

ECIO 2010

European Conference on Integrated Optics

Cambridge University, UK

Collected Manuscripts

(c) Copyright 2010 The ECIO Board. All rights reserved.

Contents

ID	Author	Title
WeA1	Meint K. Smit	Moore’s law in photonics
WeB1	B.I. Akca, N. Ismail, F. Sun, A.	Integrated AWG Spectrometer for On-chip Optical Coherence Tomography and Raman Spectroscopy
WeB2	J. Pello, J.J.G.M. van der Tol,	Design of a new ultra-small polarization converter in InGaAsP/InP membrane
WeB3	Kenji Iwamoto, Junya Odori, Jiro	An Athermal Delay Circuit Using Trenches Filled with Silicone Resin
WeB4	A. Melloni, F. Morichetti, A. Ca	Advances in Filters and Delay Lines in Silicon Photonics
WeB5	N. Ismail, B.I. Akca, F. Sun, K.	Arrayed-waveguide-grating light collector for on-chip spectroscopy
WeB6	J.D. Doménech, M. Rius, P. Muñoz	Apodized coupled resonator optical waveguides using the longitudinal offset technique
WeB7	Moshe Nazarathy	Integrated Photonic Circuits for Ultra-fast Sampling and Inherently Linear 6-bits Flash Quantization Based on Coherent Multi-Phase Interferometry
WeC2	Anatoly V Zayats	Plasmonic components for integrated nanophotonic circuits
WeC3	I. Brunets, J. Schmitz, R.J. Wal	Fabrication of a CMOS backend-compatible electrical surface plasmon polaritons source
WeC4	Takuo Tanaka	Two-photon reduction technique for isotropic metamaterials
WeD1	G.T.Reed , F.Y.Gardes	Optical modulators in silicon
WeD2	G. F. Fan, R. Orobtchouk, J. M.	8×8 λ-router in Silicon-on-insulator Technology for Optical Networks on Chip
WeD3	Minhao Pu, Weiqi Xue, Liu Liu, H	360° Tunable Microwave Phase Shifter Based on Silicon-on-Insulator Dual-Microring Resonator
WeD4	X. Chen, C. Li, S. M. G. Lo, K.	Silicon Waveguide Grating Couplers with Engineered Coupling Strength for Optimized Coupling
WeD5	F. Morichetti, A. Canciamilla, C	Backscattering in silicon photonic devices
WeD6	Peter Lützow, Helmut Heidrich, H	Vertical optical interfacing of Silicon waveguides
WeD7	W. De Cort, J. Beeckman, K. Neyt	Tuning Silicon-On-Insulator Ring Resonators in InPlane Switching Liquid Crystal Cells
WeE1	Stéphanie Cheylan	Organic devices for photonics Progress towards ITO-free devices
WeE2	Stephen Morris, Philip Hands, Su	Simultaneous Red-Green-Blue Organic Laser Devices
WeE3	J. Yang, C. Grivas, M.B.J. Dieme	Continuous-wave Lasers in Polymer waveguides
WeE4	Alexander Colsmann, Andreas Puet	Semi-transparent polymer solar cells
WeE5	J. Clark, T. Virgili, J. Cabanil	Ultrafast all-optical switching in organic photonic devices
WeE6	R. M. Parker, J. C. Gates, H. L.	An Integrated Reconfigurable Bragg Grating utilising a Photoresponsive Co-polymer
WeF1	K. Huybrechts, L. Liu, R. Kumar,	Digital photonics using InP microdisk lasers heterogeneously integrated on Silicon-on-Insulator
WeF2	P. Muñoz, R. García-Olcina, J.D.	Multi-wavelength laser based on an Arrayed Waveguide Grating and Sagnac loop reflectors monolithically integrated on InP
WeF3	J. Pozo, B. Docter, O. Raz, N. C	Fast Integrated Tunable Laser using Filtered Feedback
WeF4	John H. Marsh	Parallel integration of high power laser arrays – technology and applications
WeG1	Marcel Kroh, Lars Zimmermann,, H	Integrated Receivers on SOI for PSK Modulation Formats

WeG2	L. Xu, C. Li, X. Chen and H. K.	DQPSK Demodulation Using Integrated Silicon Ring Resonators
WeG4	N. Bamiedakis, A. H. Hashim, J.	Hybrid-Integrated Optical Transceiver on an OE PCB
WeG5	Z. Zhang, N. Mettbach, C. Zawadz	Hybrid Integration of Optical Polymer Waveguides and 25 GHz Photo Detector Arrays
WeG6	Kenichi Nakama, Yuu Tokiwa, and	Wavelength addressed intra-board optical interconnection using plug-in alignment technique by a micro hole array
WeG7	Z. Zhang, N. Mettbach, C. Zawadz	Polymer-based Passive Photonic Components with on-chip Fiber Grooves and Thin Film Filters
ThA1	Ortwin Hess and Kosmas L Tsakmak	Slow Light in Nanophotonic Materials From 'Trapped Rainbows' to Quantum Memories
ThB1	K. Zinoviev, A.B. González, O. E	Using integrated optics for advanced point-of-care diagnostic devices
ThB2	C. Dongre, H.J.W.M. Hoekstra, M.	Multi-wavelength fluorescence sensing with integrated waveguides in an optofluidic chip
ThB3	J.S. Wilkinson, G.S. Murugan, D.	Integrated Microsphere Planar Lightwave Circuits
ThC1	M.G. Tanner, C. M. Natarajan, J.	Next generation infrared superconducting single photon detectors integrated into optical cavities
ThC2	Anthony Laing, Alberto Peruzzo,	Experimental multimode interference of two single photons in integrated waveguides
ThC3	Rupert Ursin	Space-QUEST: satellites based quantum communication
ThC4	Abu Thomas, Harald Herrmann and	Novel Source of Polarization Entangled Photon Pairs Using a PPLN Waveguide with Interlaced Domains
ThD1	Aubin, A. Martinez	Quantum dot based mode locked lasers: performance and applications
ThD2	M.S. Tahvili, M.J.R. Heck, R. Nö	Dual Wavelength Passive and Hybrid Mode-Locking of a 10GHz Quantum Dot Laser Diode at 1.5μm
ThD3	Guillermo Carpintero, Kresten Yv	Comparison of the noise performance of integrated 10GHz QW and QD Mode-Locked Laser Diodes
ThD4	L. Hou, M. Haji, R. Dylewicz, J.	Monolithic 45-GHz Mode locked Surface-Etched DBR Laser Using Quantum Well Intermixing Technology
ThD5	M. Xia, R. V. Penty and I. H. Wh	Superradiant Emission from AlInGaAs/InGaAsP Quantum-Well Waveguides
ThE1	E. H. Bernhardi, H. A. G. M van	Single-Frequency, Narrow-Linewidth Distributed Feedback Waveguide Laser in Al2O3:Er3+ on Silicon
ThE2	L. Agazzi, J. D. B. Bradley, F.	Al2O3:Er3+ waveguide amplifiers at 1.5 μm
ThE3	J. D. B. Bradley, L. Agazzi, F.	Widely Wavelength-selective Al2O3:Er3+ Ring Laser
ThE4	Lewis G. Carpenter, Christopher	Investigating Planar Integrated Glass Cantilevers Utilizing Bragg Gratings and Mechanical Resonance in a Vacuum
ThE5	D. Yudistira, D. Janner, V. Prun	Integrated acoustic and acousto-optic filters using domain inversion
ThE6	S.V. Pham, L.J. Kauppinen, M. Di	Cantilever deflection read-out with a grated waveguide optical cavity
ThF2	R. Zhang, H.-G. Bach, R. Kunkel,	Micro-pin Photodiode-Antenna Chip Packaged for Sub-THz Applications
ThF3	Kai-Daniel Büchter, Harald Herrm	Hybrid Up-Conversion Detector for Mid-Infrared Radiation using Ti:PPLN Waveguides
ThF4	B. Romeira, J. M. L. Figueiredo,	Optical Injection Locking of a Resonant Tunneling Diode-Optical Waveguide Photo-Detector
ThF5	H. Ishikawa, R. Akimoto, T. Mozu	All-optical phase modulation effect in InGaAs/AlAsSb quantum well and its application to ultra-fast alloptical signal processing
ThG1	C. J. Chang-Hasnain, V. Karagods	High-Contrast Gratings: A New Platform for Integrated Optoelectronics

ThG2	H. Wang, A. Wonfor, R.V. Penty,	A Compact Lossless Integrated 16×16 QW SOA Switch
ThG3	Xaveer Leijtens	JePPIX: the platform for InP-based photonics
ThG4	C. C. Renaud, M. Fice, L. Ponnam	A photonic, hybrid integrated, THz heterodyne source
ThG5	A. Rohit, K. A. Williams, X.J.M.	Fast Reconfigurable Cyclic Router Using Semiconductor Optical Amplifier Gate Array
ThG6	Lasse J. Kauppinen, Tjeerd J. Pi	Photonic Crystal Cavity-Based Wavelength Routers
ThH1	R. Zhang, F. Bordas, J.J.G.M. va	Submicron Active-Passive Integration for InP-based Membranes on Silicon
ThH2	T. Dupont, L. Grenouillet, A. Ch	III-V on Si distributed-feedback lasers based on exchange Bragg contradirectionnal coupling
ThH3	Shigehisa ARAI	InP-based Membrane-type Semiconductor Lasers
ThH4	M.J.H. Marell, M.T. Hill &	Side-emitting metallic waveguide lasers with InGaAsP MQWs
ThH5	Jun Sakaguchi, Takeo Katayama, a	All-Optical Memory Operation for 20-Gb/s PRBS RZ and 40-Gb/s NRZ Signals Using 980-nm Polarization-Bistable VCSEL
ThI1	Toshihiko Baba	Tunable Slow Light in Photonic Nanostructures
ThI2	D.O. Dzibrou, J.J.G.M van der To	Low-Loss Two-Dimensional Pillar Photonic Crystals Filled with Dielectrics
ThI3	I. Cestier, V. Eckhouse, G. Eise	Nonlinear GaInP Photonic Crystal Waveguides
FrA1	Katsunari Okamoto	Evolution of Planar Waveguide Devices: Communication and Sensing Applications
FrB2	Junji Kotani, Peter J. van Veldh	Single-layer InAs/InP (100) quantum-dots on well laser and mid-infrared emission
FrB3	Frank H. L. Koppens1, Abram L. F	Near-field Electrical Detection of Optical Plasmons and Single Plasmon Sources
FrC1	Masataka Nakazawa	Device Requirements for Next Generation Optical Transmission Technology
FrC2	G. de Valicourt, F. Pommereau, F	Low chirp RSOA using multi-sections devices for optical access networks
FrC3	A. Albores-Mejia, K.A. Williams,	Switching Ultrahigh Line-rate Optical Data in a Monolithic Multistage Interconnection Network
FrD1	Rahman Nouroozi, Hubertus Suche,	Optical Parametric Amplification in Ti:PPLN Channel Waveguides
FrD2	M. García-Granda, D. Janner, D.	Integrated LiNbO3 ridge modulators planarized by using a Teflon buffer layer
FrD3	Roberto Llorente, Maria Morant,	Dual-Parallel Y-Coupled Lithium Niobate Electro-Optic Modulator with 15.2 dB SFDR gain
FrD4	Nasrin Moeini, Harald Herrmann,	Electro-Optic Polarization Controller With Ti:PPLN Channel Waveguides
FrD5	Li Gui, Hui Hu, Rahman Nouroozi	Locally Poled Ridge Waveguide on X-cut LiNbO3 for Nonlinear Wavelength Conversion
FrD6	D. Janner, D. Tulli, M. Garcia-G	Electrode-free high voltage cutoff waveguide sensor in domain inverted LiNbO3
FrJA1	Ana Vukovic, Phillip Sewell, Tre	Analysis of Rotationally Symmetric Resonators
FrJA2	C. Sieutat, X. Letartre, P. Vikt	3D light confinement in air : the photon cage
FrJA3	Brian Stout, Alexis Devilez, Nic	Light localization and collection systems employing micro/nano-spheres
FrJA4	A. Di Tommaso, M. De Sario, M. F	Modeling of Rare Earth Doped Microspheres
FrJA5	P.Orlandi, M.Gnan, A.Samarelli,	Modeling of Racetrack Resonator with Grating Assisted Coupling
FrJB1	Alberto Peruzzo, Jonathan Matthe	Quantum Random Walks Circuits with Photonic Waveguides
FrJB2	Ivan B. Djordjevic	Integrated Optics Implementation of Universal Quantum Gates, Bell States Preparation Circuit, Quantum Relay and Quantum LDPC Decoders
FrJB3	Xue-Wen Chen, Vahid Sandoghdar a	Monolithic directional optical antennas for funneling photons to single emitters
FrJB4	M. George, R. Ricken and W. Sohl	Tm:Ti:LiNbO3 Waveguide for Quantum Memory Applications

FrJB5	Alberto Politi, Jonathan C. F. M	A compiled version of Shor’s quantum factoring algorithm on a waveguide chip
FrJB6	Jonathan C. F. Matthews, Alberto	Entangled Multi-Photon States in Waveguide for Quantum Metrology
WeP01	A. Larrue, O. Gauthier-Lafaye, S	Photonic Crystal DFB laser array robust to optical feedback
WeP02	Soon Thor Lim, Ching Eng Png, Ma	Widely tunable optical nanocavity photonic crystal sensor
WeP03	Minhao Pu, Liu Liu, Haiyan Ou, K	All-Optical Tunable Photonic Crystal Cavity
WeP04	A.Talneau, I. Sagnes	Ultra-sharp edge filtering in nanotethered photonic wire
WeP05	O. Horn, T. Lipka, J. Amthor, J.	Surface mounted tapered vertical Coupler for photonic Nanowires
WeP06	W. Y. Chiu, Y. H. Wu, Y. J. Chan	Photonic crystal filter integrated with photodiodes
WeP07	Jorge Barrio, Jorge Lamela, Airá	Near Field Transmission of Ordered Arrays of SubWavelength Holes Fabricated in Lithium Niobate by Femtosecond Laser Writing.
WeP08	I. H. Rey, D. M. Beggs, and T. F	Tunable optical delay line in engineered slow light photonic crystal waveguides
WeP09	A. Samarelli, M. Sorel, R.M. De	Grating Assisted Coupling in Microring Resonators
WeP10	Usman Younis, Barry M. Holmes, D	Towards Monolithic Integration of Non-linear Optical Frequency Conversion
WeP11	Chaotan Sima, J. C. Gates, B. D.	Realization of a planar Bragg grating for all-optical Hilbert transformer
WeP12	Kenji Kintaka, Yuki Kita, Katsuy	Cavity-Resonator-Integrated Grating Input/Output Coupler with Au Reflection Layer
WeP13	Hassanet Sodabanlu, Jeong Seung	Intersubband Absorption Saturation in AlN-based Waveguide with GaN/AlN Multiple Quantum Wells Fabricated by Metalorganic Vapor Phase Epitaxy
WeP14	Thorbjörn C. Buck, M.S. Müller,	Compact FBG interrogator based on a customized integrated optical arrayed waveguide grating
WeP15	Min Zhang, Martin Kristensen, As	1×3 Beam Splitter Based on Self-Imaging Phenomena in Air-Slab Photonic Crystal Waveguides
WeP16	D. Vermeulen, K. Van Acoleyen, S	Efficient Tapering to the Fundamental Quasi-TM Mode in Asymmetrical Waveguides
WeP17	J.D. Doménech, M. Rius, J. Mora,	Microwave photonics beamformer based on ring resonators and arrayed waveguide gratings
WeP18	E.V.Bekker, V.Brulis, D.Gallaghe	Accurate Design of Optical Microring Resonators
WeP19	Ranjith. R, Qing Dai, Haider But	Nanophotonic Microlens Array
WeP20	K. Voigt, L. Zimmermann,, G. Win	New Design Approach to MMI-Couplers in Photonic Wire Substrates
WeP21	Zhanxiang Zhao, Gin Jose, Animes	Tellurite Glass on Polymer Planar Waveguides
WeP22	S.M. Kostritskii, Yu.N. Korkishk	Parasitic spectral selectivity of Y-branching power dividers on proton-exchanged LiNbO3 waveguides
WeP23	Y. Hao, N. Bamiedakis, R. V. Pen	Optical Filters Based on Casacaded Point-Symmetric Mach-Zehnder Interferometers
WeP24	Nobuhiko Ishizawa, Masahiro Kand	Flexible Optical Waveguide with Tapered Structure Having Large Coupling Tolerance
WeP25	B. Royall, M. Gunes, N. Balkan,	Spectral Response of GaInNAs / GaAs Multiquantum-Well Solar Cells
WeP26	Khai Q. Le, Bjorn Maes and Peter	Numerical Study of Plasmonic Nanoparticles Enhanced Light Emission in Silicon Light-Emitting Diodes
WeP27	Ergun Simsek	A More Realistic Coupled Dipole Approximation Model for Plasmonic Waveguides
WeP28	Khai Q. Le and Peter Bienstman	Enhanced Sensitivity of Absorption-Based Surface Plasmon Interference Sensors in Silicon-On-Insulator by Adsorbed Layer
WeP29	M. Février, P. Gogol, J.-M. Lour	Localized surface plasmon waveguide integrated on dielectric waveguide
WeP30	Haider Butt, Qing Dai, Peter Far	Modeling of multiwalled carbon nanotubes based metamaterials and photonic

		crystals
WeP31	M. Rodas Verde, A. Laing, A. Per	Towards fault tolerant quantum photonics circuits
WeP32	Matthaeus Halder, Jeremie Fulcon	Fibre based Photon Pair Sources for Integrated Quantum Information
WeP33	Martin Hendrych, Roberto León Mo	Generation of entangled photons in Bragg reflection waveguides
WeP34	A. Maalouf, M. Gadonna, D. Bosc,	Study of polymer micro-ring resonator based filter in system experiment at 10 Gbit/s
WeP35	Uwe Hollenbach, Hans-J. Boehm, J	POLINA – Polymer Light Waveguides for Nanophotonics
WeP36	D. Duval, C. Godet, N. Huby and	First developments of sub-micronic waveguide structures on UV210 polymer
WeP37	C. Holmes, L.G. Carpenter, H.C.	Microfluidic Multimode Interference Device
WeP38	D.J. Wales, R.M. Parker, J.C. Ga	Integrated planar Bragg grating oxygen sensor
WeP39	Rainer Hainberger, Paul Muellner	SOI photonic wire Bragg gratings for interferometric sensor arrays
WeP40	K. E. Zinoviev, C. Dominguez, L.	Silicon Nitride Bimodal Waveguides for High Sensitivity Biosensors
ThP01	J. B. Rosas–Fernández, J. Dong,,	All Optical Switching and Label Swapping Using HNLF and SOAs for 40 Gb/s Spectrally Encoded Systems
ThP02	Y. Yu, J. B. Rosas–Fernández, R.	Single-to-four all-optical wavelength and format conversion
ThP03	Akito Ihara, Hiroki Kishikawa, N	Passive Waveguide Circuit for BPSK Label Identification Consisting of Cascaded Asymmetric X-junction Couplers
ThP04	Hiroki Kishikawa, Nobuo Goto and	Switching Characteristics of All-Optical WavelengthSelective Switch Controlled by a Single Light
ThP05	Ehab S. Awad	80Gbits/s DPSK regeneration using an SOA balanced-receiver
ThP06	J. Javaloyes, P. Stolarz, L. Hou	Passive Mode-Locking in Quantum Well Lasers
ThP07	Marco Vallone, Paolo Bardella, I	Photon-Photon Resonance Enhanced Modulation Bandwidth in CCIG lasers
ThP08	W.P. Pallmann, Y. Barbarin, M. H	Design and Continuous-Wave Characterization of Electrically Pumped VECSELs Suitable for Passive Modelocking
ThP09	Mattia Rossetti, Paolo Bardella,	Simulation and Design of Quantum-Dot Lasers Operating in Dual-wavelength Passive Mode-locking Regime
ThP10	J. P. Gauthier, C. Paranthoen, C	Polarization controlled quantum dashes VCSELs
ThP11	Z. Wang, G. Yuan,, X. Cai, S. Yu	Further miniaturized retro-reflector cavity semiconductor micro-ring lasers
ThP12	Elodie Lamothe, Lars Lundeberg a	Eigenmode analysis of phase-locked VCSELarrays using spatial coherence measurements
ThP13	Jeong Hwan Song, Marc Rensing, C	High Speed Laser Diode Packaging with Over 10GHz-Bandwidth
ThP14	B.W. Tilma, M.S. Tahvili, J. Kot	Analysis of the Current Dependency of the Small Signal Gain Spectrum in InAs/InP(100) Quantum-Dot Amplifiers
ThP15	Tim J. Karle, Fabrice Raineri,,	Temporal measurements of SOI wire racetrack resonators
ThP16	B. D. Snow, H. L. Rogers, C. Hol	UV-written planar chirped Bragg gratings for use in dispersion management
ThP17	C. J. Oton, J. Herrera, P. Sanch	150 ps all-optical switching in silicon microring resonators
ThP18	R. Stabile, K.A. Williams	Low Polarisation Conversion in Whispering Gallery Mode Micro-Bends
ThP19	E. Xifré-Pérez, J.D. Doménech, R	All Silicon Waveguide Spherical Microcavity Device
ThP20	Yunhong Ding, Xinliang Zhang, De	Bandwidth tunable filter based on silicon microring-MZI structure
ThP21	A. Marconi, A. Anopchenko, L. Pa	Potential of Si-nc MOS devices as Transceivers for interchip optical links
ThP22	D. G. Sun, S. Abdul-Majid, I. Ha	High Efficiency Silicon-on-Insulator based Corner Turning Mirrors
ThP23	V. Duc Nguyen, T.G. van Leeuwen,	SiON integrated optics elliptic couplers for Fizeau-based Optical Coherence Tomography
ThP25	F. Sun, A. Driessen, and K. Wörh	Reduction of N-H Absorption Peaks by B or P Doping of PECVD SiON Layers for Integrated Optics

ThP26	H. L. Rogers, J. C. Gates, S. Am	New Technique for Loss Measurement of a Direct UV Written Silica-on-Silicon Waveguide using Integrated Bragg Grating Structures
ThP27	F. Gity, J. M. Hayes, B. Corbett	Modelling Ge/Si Avalanche Photodiodes
ThP28	Sara Mas, José Caraquitena, José	Tailored Chromatic Dispersion in Silicon-on-Insulator Slot Waveguides
ThP29	S. J. Beecher, R. R. Thomson, N.	320 fs Pulses from an Ultrafast Laser Inscribed Waveguide Laser Utilizing a Carbon Nanotube Saturable Absorber
ThP30	J. Hauden, member, OSA, N. Gross	Ultra Low Loss Split Y- Junctions: Application to QPSK- Lithium Niobate Modulators
ThP31	E. Y. B. Pun, D.L. Zhang, and P.	Optical Damage Resistant Near-stoichiometric Ti:Mg:Er:LiNbO3 Strip Waveguides
ThP32	D.L. Yang, E.Y.B. Pun, J. Zhang,	Tm3+/Yb3+ codoped aluminum germanate ion-exchanged glass waveguide amplifiers
ThP33	Christopher J. Rowlands, Dr. Lei	Rapid Prototyping of Planar Infrared Waveguides
ThP34	K. van Dalfsen, J. Yang, F. Ay,	Nd-doped aluminum oxide integrated amplifiers at 880 nm, 1060 nm, and 1330 nm
ThP35	Rafal Dylewicz, Richard De La Ru	Electron Beam Lithography of Bulk Zinc Oxide Wafers using a Polythiophene-based Charge Dissipation Layer
ThP36	Western Bolaños, Joan J. Carvaja	Er-doped KY1-x-yGdxLuy(WO4)2 surface channel waveguides
ThP37	C. L. Sones, Y. J. Ying, R. W. E	UV laser-assisted fabrication of ridge waveguides in lithium niobate crystals
ThP38	Hong-Sik Jung	Šolc-type wavelength filters based on TE↔TM mode conversion utilizing periodically poled Ti-diffused lithium-niobate channel waveguides
ThP39	Maria Cinta Pujol, Magdalena Agu	Rare Earth Doped Epitaxial Layers of KY1-x-yGdxLuy(WO4)2 as Active Waveguides
ThP40	Qin Wang, Fei Xu, Zi-yan Yu, Xia	Acousto-optic tunable optical diode based on periodically poled LiNbO3

Moore's law in photonics

Meint K. Smit, COBRA – TU Eindhoven, The Netherlands, m.k.smit@tue.nl

Abstract—**Similarities and differences between photonic and microelectronic integration technology will be discussed and a vision on the development of photonic integration in the coming decade will be given**

Keywords-photonic integration; integrated optics

I. THE DEVELOPMENT OF CHIP COMPLEXITY

Figure 1 shows the complexity development of InP-based Photonic ICs (PICs), measured as the number of components integrated on a single chip [1,2]. The PICs based on Arrayed Waveguide Grating based wavelength demultiplexers, which play a key role in WDM systems, show a clear exponential trend, similar to Moore's law in micro-electronics, which suggests that photonics is following the technology driven development of microelectronics, albeit with a time lag of more than thirty years, and at a slower pace: doubling each 30 months.

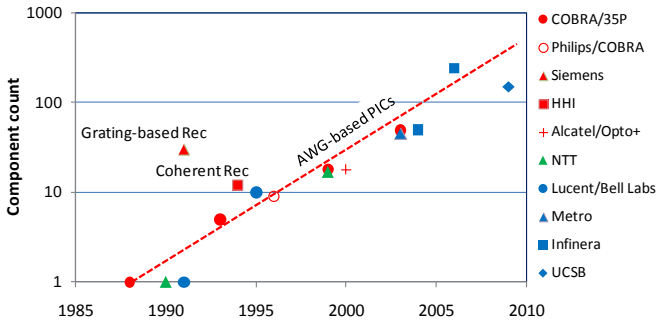


Figure 1 Development of chip complexity measured as the number of components per chip.

II. DIFFERENCES BETWEEN PHOTONICS AND MICROELECTRONICS

There is an important difference, however, between de well know Moore plot of Intel and the graph shown in Figure 1. The Intel plot lists the complexity development of commercially applied ICs, whereas most of the points in Figure 1 are about research devices. Only one of the reported devices, the chip of Infinera (■, 2004) is applied in a commercial product. It is an interesting question why so few of the advanced PICs reported in the literature have made it to the market, despite the fact that in the last two decades there has been substantial investment in the development of integration technologies in national and international projects in Europe, America and the Far East.

The problem with current project funding models is that they tie the technology development closely to an application: you get no money without a clear and challenging application. In order to meet the challenging specifications the technology has to be fully optimized for that application and, as a result, we have almost as many technologies as applications. Owing to this huge fragmentation, the market for these application-specific technologies is usually too small to justify their further development into an industrial volume manufacturing process that would really lead to low chip costs. This is quite different from the situation in micro-electronics where a huge market is served by a relatively small set of integration technologies (most of them CMOS technologies).

III. TOWARDS GENERIC PHOTONIC INTEGRATION TECHNOLOGIES

The solution to this problem seems obvious: introduce the same methodology to photonics that allowed microelectronics to change the world. This can be done by moving from application specific integration technologies to generic integration technologies. These are technologies that support integration of a small set of high performance building blocks, like passive waveguide devices (MMIs, AWGs), modulators and optical amplifiers, in different circuit configurations that support a broad range of functionalities. And by making such technologies available to a broad group of customers via foundries, similar to the foundry model in microelectronics. Reducing the huge variety of different technologies to a few generic technologies will make it attractive for Photonic CAD companies to develop dedicated design kits that will enable much faster design in the generic process. And it will allow for building a steadily growing component library that will release designers from having to develop each part of their circuit themselves. Another important advantage of a generic foundry process is that it will lead to a large reduction of the costs of product qualification. If the process is qualified than each component that is designed within the design rules should automatically qualify too.

Generic foundries are well known in micorelectronics, in Photonics they do not exist, however. Within the European FP6 Network of Excellence ePIXnet (www.epixnet.org) research platforms for foundry access to three major technologies have been established: InP-based monolithic integration technology (JePPIX), Silicon Photonics technology (ePIXfab) and a glass-based platform that covers the whole wavelength range from visible to IR (TriPleX).

The COBRA research institute of TU Eindhoven has pioneered with providing small scale foundry access to an InP-based monolithic integration process for research purposes in the framework of the JePPIX platform. Transfer of the model to industrial foundries is presently investigated in large European and Dutch research projects.

IV. LIMITS TO INTEGRATION COMPLEXITY

Once generic integration technologies are introduced in photonics we expect a development similar to what happened in micro-electronics: a dramatic reduction of the cost of R&D and chip manufacturing and a correspondingly expansion of the application market, both in volume and diversity. Applications will follow in many fields where PICs are presently too expensive, such as sensors, health care, interconnect, metrology etc.

We do not expect, however, that the complexity supported by the generic processes as described above will exceed a component count of 1000 for a number of reasons. In passive devices the complexity will be restricted due to unavoidable component losses which restrict the total number of components that can be cascaded. But in active PICs SOAs and lasers typically have a power dissipation of 100 mW or more. So their number is restricted to several tens up to a maximum of a few hundreds, because of heat sinking limitations. Secondly, although today's PICs often carry digitally modulated signals, the basic building blocks and the circuits built from them essentially operate in an analog mode, which means that on passing a number of components the signal will accumulate noise and distortion and needs to be regenerated. Regenerators can be integrated too, but they consume space and dissipate heat.

This is quite similar to the development path in microelectronic ICs, where analog circuits usually do not contain more than a few hundred transistors per circuit block. The breakthrough to VLSI did not occur in analog electronics but in digital electronics, where signal regeneration inherently occurs after each processing step, so that operations can be concatenated endlessly.

V. SILICON PHOTONICS

A larger complexity can be supported, in principle, in membrane based circuits, where component dimensions and power dissipation can be significantly smaller due to the strong light confinement in thin membranes with a high vertical index contrast, as they are presently applied in Silicon Photonics. This will allow lasers and amplifiers to operate with significantly lower injection currents and heat dissipation. Unfortunately silicon does not support integration of efficient lasers and amplifiers because of its indirect bandgap structure. Solutions are sought in heterogeneous integration of active InP-based layers on silicon waveguide layers. Efficient coupling of light from the III-V layers to the silicon layers is difficult, however. A promising novel solution is the integration of active and passive functionality in InP-based membranes with locally active regions which are created with nanoscale selective area epitaxy [3]. With this technology, which is called IMOS (InP Membrane on Silicon) a complexity increase of one order might be feasible, as depicted in figure 2.

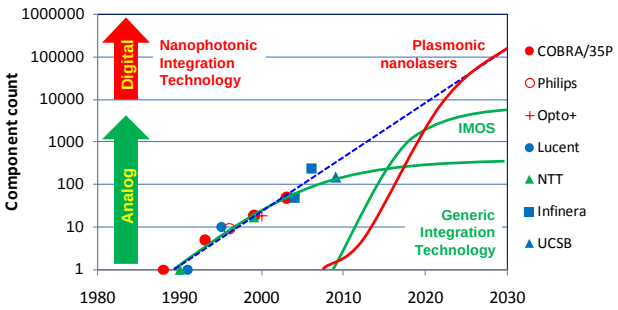


Figure 2 Vision on the future complexity development of InP-based photonic ICs

VI. TOWARDS DIGITAL PHOTONICS

For moving towards LSI or VLSI circuit complexity a change from analog to digital signal processing will be necessary. Digital Photonics is receiving increasing interest. In particular, digital photonics based on coupled micro or nanolasers is a promising candidate for integrating large numbers of digital circuits. The recent breakthrough in plasmonic lasers [4, 5], which are no larger than modern transistors and can operate with low switching energies at very high switching speeds, holds the promise that digital photonic circuits with more than 100,000 lasers operating at THz clock rate will become reality. Such circuits can avoid a lot of power-hungry electro-optic conversions in high speed internet routers and they may be used in ultrafast digital photonic signal processors.

VII. CONCLUSIONS

It is often argued that Moore's law does not apply to photonics because of the large differences between microelectronic and photonic integration technology. This is indeed true for today's R&D model in photonic integration. But as these differences are at the same time the major reason that photonic ICs have not succeeded in large scale penetration into the photonics components market, an obvious conclusion is that we have to get rid of these differences as soon as possible. By applying the methodology of microelectronics to photonics we expect a dramatic reduction of the costs of R&D and manufacturing of photonic ICs and a breakthrough to applications in telecommunications and datacommunications, as well as in sensors, medical equipment, metrology and consumer photonics.

REFERENCES

[1] R. P. Nagarajan and M.K. Smit, "Photonic integration", *IEEE LEOS Newsletter* Vol 21, Nr. 3, pp. 4-10, June 2007.

[2] M.K. Smit and C. Van Dam, "PHASAR-based WDM devices: principles, design and applications", *J. of Sel. Topics in Quantum. Electron*., Vol. 2, No. 2, pp. 236-250, June 1996.

[3] R. Zhang, "Submicron active-passive integration for InP-based membranes on silicon", Proc. ECIO'10, # ThH1.

[4] M. T. Hill et al, "Lasing in Metallic-Coated Nanocavities", Nature Photonics, Vol. 1, pp 589-594, 2007.

[5] M.T. Hill et al., Lasing in metal-insulator-metal sub-wavelength plasmonic waveguides, Optics Express, 17(13), 11107-11112, 2009.

Integrated AWG Spectrometer for On-chip Optical Coherence Tomography and Raman Spectroscopy

B.I. Akca, N. Ismail, F. Sun, A. Driessen, K. Wörhoff, M. Pollnau, and R.M. de Ridder
Integrated Optical Microsystems Group,
MESA+ Institute for Nanotechnology, University of Twente
Enschede, The Netherlands
B.I.Akca@utwente.nl

V.Duc Nguyen, J. Kalkman, and T.G. van Leeuwen
Biomedical Engineering & Physics
Academic Medical Center,
University of Amsterdam
Amsterdam, The Netherlands

Abstract—**Silicon oxynitride-based arrayed waveguide grating (AWG) spectrometers were designed for on-chip spectral-domain optical coherence tomography (OCT) systems and Raman spectroscopy of the skin. A novel geometrical layout for Raman spectroscopy was introduced to reduce loss. Measurements show that integrated optics has a good potential for miniaturizing current OCT systems.**

Keywords-arrayed waveguide grating; Raman spectroscopy; optical coherence tomography; integrated optics

I. INTRODUCTION

Spectrometers have an important role in a wide variety of fields. The most important integrated optical implementation of a spectrometer is the AWG that, with its excellent performance and compactness, has a high potential for various spectroscopic applications [1]. Two of these applications are considered here: on-chip spectral-domain OCT systems and confocal Raman spectroscopy of the skin.

The operation of an AWG [1] is briefly explained, referring to Fig. 1a. Light from an input waveguide diverges in a first free propagation region (FPR) in order to illuminate the input facets of an array of waveguides with a linearly increasing length. At a central design wavelength, the phase difference at the output facets of adjacent array waveguides is an integer multiple of 2π. Since these facets are arranged on a circle, a cylindrical wavefront is formed at the beginning of a second FPR, which generates a focal spot at the central output channel. Since the phase shift, caused by the length differences between arrayed waveguides, is linearly dependent on wavelength, the resulting wavelength-dependent phase gradient implies a tilt of the cylindrical wavefront at the beginning of the second FPR, which causes the focal spot to shift to a different output waveguide.

II. AWG SPECTROMETER FOR ON-CHIP OCT SYSTEMS

OCT is a widely used optical imaging technology which can provide non-invasive, sub-micrometer resolution diagnostic images [2]. We aimed for a miniaturized OCT system operating at 1.3 μm, a commonly used wavelength for skin imaging. In the literature there is only limited data on the implementation of OCT systems on a chip [3-4].

The free spectral range (FSR) and wavelength resolution ($\Delta\lambda$) of the AWG were determined according to the depth resolution and depth range requirements of the OCT system. For the first device, we aimed at a 19-μm depth resolution (determined by the free spectral range of the AWG) and 1-mm depth range (determined by the wavelength spacing per output waveguide). Using the standard AWG equations [1], the remaining design parameters were determined as: optical path length difference 29.176 μm; grating order 33; focal length of the slab region 5393.5 μm; number of arrayed waveguides 400; and number of output waveguides 100. We used single-mode silicon oxynitride (SiON) channel waveguides with 2 μm width and 0.6 μm height, embedded in SiO_2. The core and cladding refractive indices were 1.55 and 1.4485, respectively, at 1.3 μm. The minimum bending radius of curved waveguides was calculated to be 800 μm. In order to decrease the loss, 6-μm-wide and 200-μm-long linear tapers were applied at the interfaces between slab and arrayed waveguides. The device geometry was optimized for minimum loss and an adjacent crosstalk of -10 dB using beam propagation (BPM) simulations. The simulation result of the final design is given in Fig. 1b.

The optical transmission measurements were performed by coupling TE-polarized light from a broadband source (Fianium SC450) into the input waveguide, using a single-mode polarization-maintaining fiber. The output signal was sent to an optical spectrum analyzer (iHR 550, Horiba Jobin Yvon) through a single-mode fiber. The transmission spectra measured at the output channels were normalized with respect to the transmission of a straight channel waveguide. The transmission spectra of four central channels are given in Fig. 1c. The inset of Fig. 1c represents the complete set of 100 transmission spectra of the device. As predicted, each channel works as a bandpass wavelength filter. The resolution of the device was $\Delta\lambda$ = 0.38 nm and the FSR was 38.8 nm, which are both very close to the design values of 0.4 nm and 40 nm, respectively. The measured 3 dB bandwidth of the output channels was about 0.3 nm and the channel crosstalk was approximately –32 dB. The insertion loss was measured as –1.5 dB for the central and –6.5 dB for the outer channels, respectively. For TM polarization, we obtained a slight shift of 1.36 nm for the central wavelength, which corresponds to an effective refractive index difference of $\sim 1.54\times10^{-3}$ between the two polarizations due to the waveguide birefringence.

This work is supported by the Dutch Smartmix-Memphis and Dutch IOP Photonic Devices

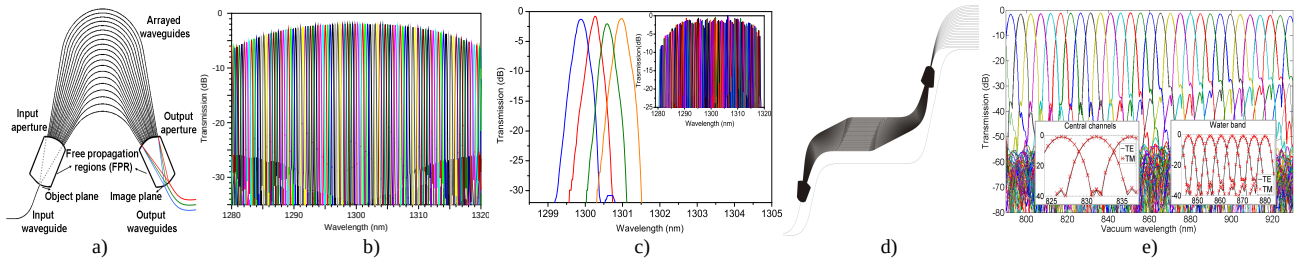


Figure 1. a) Schematic layout of an AWG. b) Beam propagation simulation result of the designed AWG. c) Optical transmission measurement results for the central output channels for TE polarization. The inset shows the complete free spectral range transmission data. d) AWG layout using identical bends (see text). e) Simulated wavelength response of the AWG for the skin application; the insets show the very low TE-TM shift.

III. AWG RAMAN SPECTROMETER

In vivo confocal Raman spectroscopy provides a possibility of accurately controlling the skin region from which the Raman signal is detected [5]. Here, we design an integrated, compact, and potentially low-cost device, specifically for the detection of water concentration in the *stratum corneum*. To this end, it is needed to measure the ratios between a broad water peak and narrow lipid and protein peaks in the Raman spectrum.

Our design is based on using SiON channel waveguides with SiO_2 cladding, having a cross-section of 1.4 µm × 0.52 µm. The core refractive index is 1.509 at 830 nm. At an excitation wavelength of 671 nm, the relevant Raman spectrum extends from 800 to 920 nm. In order to separate the lipid and protein peaks the output channel spacing is chosen as 5 nm, and to guarantee the lowest insertion loss for the lipid peak, the central wavelength of AWG is chosen at the center of the lipid band (831 nm). To cover the entire Raman signal a minimum free spectral range of 120 nm is required; the best choice of grating order is 3, resulting in 55 output channels. With our choice of channel spacing we can place only one channel in each of the L and P bands, and several channels are available for collecting the water and background signals.

The Raman signal may be up to 10^8 times weaker than the backscattered laser and fluorescence light; hence we introduce improvements in the geometrical layout of the device in order to reduce the losses. The standard anti-symmetric broadband layout [6] is modified in order to reduce the main sources of loss, which are intrinsically part of the conventional geometry. We identify these in straight-to-bend waveguide transition losses [7] and systematic phase errors due to the use of different bends for the arrayed waveguides. A method for reducing the systematic phase errors has been reported in [8], in which bends with constant bending radius (but different length) were used in all the arrayed waveguides. In our design we aimed to completely eliminate these phase errors by using identical bends in all arrayed waveguides. We use two bend types (A and B) as building blocks in all the arrayed waveguides. All arrayed waveguides are composed of two bends of type A and N-1 bends of type B, where N is the number of arrayed waveguides. In this way the phase of light propagating in each array waveguide is affected in the same way by the bends, while the optical path length difference is introduced only by straight sections. Since this approach is independent of the specific bend geometry, we could easily replace all circular bends with cosine bends in which the transition from straight to bend is gradual and can be designed to be adiabatic. In a conventional design, such a replacement would lead to an excessive calculation burden. The layout is shown in Fig. 1d and the BPM simulation results are given in Fig. 1e. We observed negligible TE-TM shifts of 0.01 nm for the central channels and 0.03 nm in the water band, see inset in Fig. 1d.

IV. CONCLUSIONS

SiON-based AWG spectrometers have been designed and fabricated for on-chip spectral-domain OCT systems and confocal Raman spectroscopy of the skin. The device for Raman spectroscopy presents improvements in the geometrical layout aimed at reducing losses and is designed to be polarization insensitive. Its optical characterization is currently under way. The device for on-chip OCT systems has been optically characterized and the measurement results are in good agreement with the simulation results. The spectrometer shows very good performance in terms of insertion loss, crosstalk, FSR, and resolution. The OCT depth resolution and the depth range were calculated as 19.2 µm and 1.1 mm, respectively, using the measurement results. In future work, we will include light delivery and collection waveguide channels as well as detector arrays connected to the AWG output channels.

V. REFERENCES

[1] M. K. Smit and C. van Dam, "PHASAR-based WDM-devices: principles, design and applications," IEEE J. Select. Topics Quantum Electron., vol. 2, pp. 236–250, 1996.

[2] D. Huang et al., "Optical coherence tomography," Science, vol. 254, pp. 1178-1181, 1991.

[3] D. Culemann, A. Knuettel, and E. Voges, "Integrated optical sensor in glass for optical coherence tomography", IEEE J. Select. Topics Quantum Electron. vol. 5, pp. 730-734, 2000.

[4] G. Yurtsever and R. Baets, "Towards integrated optical coherence tomography system on silicon on insulator", Proc. 2008 Symp. IEEE/ LEOS Benelux Chapter, Enschede, The Netherlands, pp.163-166, 2008.

[5] P. J. Caspers, G. W. Lucassen, R. Wolthuis, H. A. Bruining, and G. J. Puppels, "In vitro and in vivo Raman spectroscopy of human skin," Biospectroscopy, vol. 4, pp. S31-S39, 1998.

[6] R. Adar, C. H. Henry, C. Dragone, R. C. Kistler, and M. A. Milbrodt, "Broad-band array multiplexers made with silica waveguides on silicon," J. Lightwave Technol., vol. 11, pp. 212-219, 1993.

[7] M. K. Smit, "Progress in AWG design and technology," IEEE/ LEOS Workshop Fibers & Optical Passive Compon., pp. 26-31, 2005.

[8] F. M. Soares et al., "InP-based arrayed-waveguide grating with a channel spacing of 10 GHz," National Fiber Optic Engineers Conference (Optical Society of America, Washington DC), paper JThA239, 2008.

Design of a new ultra-small polarization converter in InGaAsP/InP membrane

J. Pello, J.J.G.M. van der Tol, G. Roelkens, H.P.M.M. Ambrosius and M.K. Smit
COBRA Research Institute, Eindhoven University of Technology (TUE)
Eindhoven, The Netherlands
j.pello@tue.nl

***Abstract*—The design of an ultra-small (4.1 µm length) polarization converter in Indium phosphide (InP) membrane is presented. The device is modelled using a vectorial 2D mode solver. Simulations show strong conversion (> 94%) and low-loss operation (< 0.5 dB) over a wavelength range of 200 nm. A description of a possible fabrication scheme for the device using standard InP technology is also given.**

Indium phosphide; integrated optics; polarization converter (PC); triangular waveguide.

I. INTRODUCTION

Recently, membrane photonics platforms such as Silicon-on-insulator (SOI) or InP-membranes-on-silicon (IMOS) have been gaining attention. The high vertical index contrast obtainable in membrane structures can lead to high density photonic integrated circuits (PICs) by reducing substantially the size of most photonic devices. Furthermore, membranes are compatible with different carrier substrates through the use of bonding technologies [1], which paves the way for intrachip communication.

Although the SOI platform benefits from the technology tools developed in the silicon industry, it lacks the ability of creating simple optical sources and amplifiers. By contrast, the IMOS platform is based on direct bandgap alloys, and we are working on butt-joint integration of active and passive components in thin InP-membrane, using sub-micron scale selective area growth. Recently, the fabrication of compact and efficient passive IMOS components was presented [2], including ultra-small couplers, ring resonators and micro-bends (see Fig. 1). In the present paper, a new device, an ultra-small polarization converter in InP membrane, is introduced, using two oppositely-oriented triangular waveguide sections.

The presented device is more than one order of magnitude smaller than the shortest polarization converters made by optical lithography [3], and was designed together with a clear fabrication plan which uses the standard technological tools available for InP processing. The polarization conversion behaviour is analyzed using the film mode matching (FMM) method [4]. This component can be applied to polarization-diversity integration schemes and in interesting devices such as light intensity modulators and polarization bit interleaving (PBI) components [5].

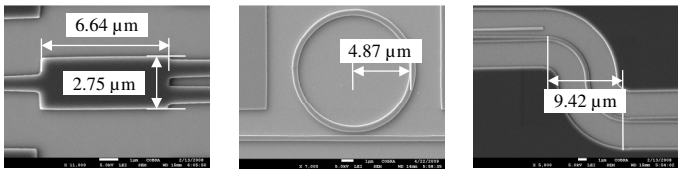


Figure 1. An ultra-small coupler, a ring resonator and an S-bend previously realized in IMOS

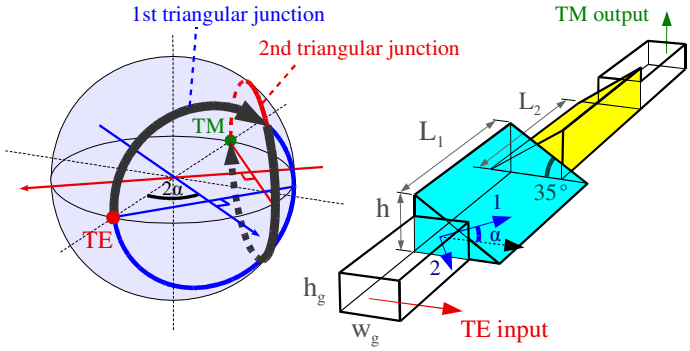


Figure 2. Schematic of the polarization converter design and Poincaré sphere diagram of the polarization conversion

II. PRINCIPLE

The idea behind the use of asymmetrical cross-section waveguides in PCs is to create a new set of two eigenmodes which are not aligned with the TE and TM polarization of the normal rectangular waveguides, and which propagate with different propagation constants β_1 and β_2. The incoming polarization state, e.g. TE in Fig. 2, is projected on these two tilted eigenmodes. As the eigenmodes propagate with different speeds, a phase-shift is created between the two that linearly increases with the propagation length L (the same birefringence principle as in bulk half-wave plates). By choosing the length L of the triangular section and coupling light back to a rectangular waveguide, different elliptical and linear polarization states can be obtained.

In this work, we consider triangular waveguides that can be obtained by dry etching of the vertical wall and wet etching of the slanted wall at an angle of 35° with respect to the (001) plane [6]. The resulting asymmetry yields a rotation α~23° (determined using the FIMMWAVE mode solver [4]) of the eigenmodes of the triangular waveguides. As a consequence, the polarization states attainable by varying the length of the first triangular waveguide are all the states represented by the first drawn circle on the Poincaré sphere in Fig. 2. We see that in order to achieve full TE to TM conversion, one triangular section is not enough. Therefore, we add another triangular section, mirrored with respect to the first one, which will enable to reach the TM polarization state by rotating along the semi-dotted circle on the sphere in Fig. 2. The two bold arrows

in the sphere show how the polarization is gradually converted from TE to TM.

The respective lengths of the two triangular sections that lead to full TE to TM conversion can be obtained by simple geometric calculations in the Poincaré sphere and expressed in terms of the half-beat length $L_\pi = \frac{\pi}{\beta_1 - \beta_2}$ and the tilt angle α as:

$$L_1 = \frac{L_\pi}{\pi} \times \left(\arcsin\left(\frac{1}{(\tan 2\alpha)^2} \right) + \frac{\pi}{2} \right) = 2L_\pi - L_2 \qquad (1)$$

The device has a total length of $2L_\pi$. As expected, the stronger the birefringence of the waveguide, the shorter the device.

III. Design Optimization and Tolerances

The structure is modelled in FIMMWAVE, taking into account the Benzocycolbutene (BCB) and air claddings of a fabricated device (see Section IV).

We first investigate the performance of the PC at a wavelength of λ = 1.55 µm. The propagation constants β_1 and β_2 of the two modes of the triangular waveguides are calculated using the mode solver FIMMWAVE for different values of the membrane height h. It is found that the highest birefringence is obtained for h = 400 nm. The corresponding half-beat length is equal to L_π = 2.06 µm, which corresponds to a total device length of only 4.12 µm. After setting h to this value, the cross-section dimensions h_g and w_g (see Fig. 2) of the input (and output) rectangular waveguides, as well as the lateral offsets between the different junctions are optimized to maximize the coupling efficiency. It is found that the coupling between rectangular and triangular waveguides is optimized for $h_g/h \sim 2/3$. This suggests the use of a very thin etch-stop layer in the membrane to enable a simple and accurate definition of these two heights. A 20 nm-thick quaternary etch-stop layer was therefore included in the simulation of the triangular waveguides.

To verify the behaviour of the complete PC and investigate its tolerance to different fabrication parameters variations, we simulate it in the propagation module of FIMMWAVE. As seen on the results graph in Fig. 3, the short length of this PC makes it very broadband. For the 1.4-1.6 µm wavelength range, the device total losses are less than 0.5 dB and the polarization conversion (defined as the TM output power divided by the total output power for a fully TE polarized input wave) is more than 94%. The use of wet-etching, which enables to set the slope of the slanted wall of the triangular junctions very accurately to 35° and to define the two heights h and h_g, makes our design intrinsically tolerant. According to our simulations, an error of 20 nm in the definition of the height h of the triangular section (respectively, an error of 100 nm in the rectangular waveguides width) increases the losses by only 0.1 dB without changing the polarization conversion.

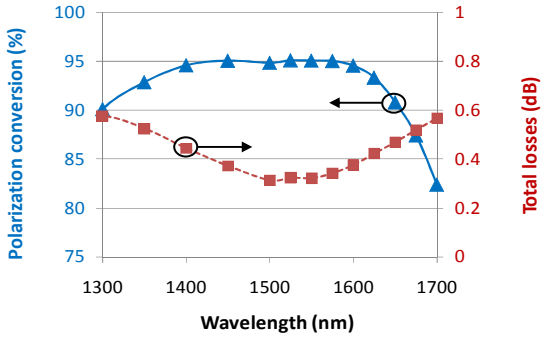


Figure 3. Spectral behavior of the proposed PC design optimized for λ = 1.55µm

IV. Fabrication Plan

Like our previous IMOS components [2], the presented polarization converter will first be fabricated on an epitaxial InP and quaternary layer structure. Then, the sample is bonded upside-down with BCB on a host wafer and the substrate and sacrificial layers are removed. In the end, only the submicron-thick patterned InP membrane is left, embedded in BCB and its bottom surface facing the air.

First the heights h and h_g are defined using the quaternary etch-stop layer mentioned in section III. The rectangular waveguides can then be fabricated by standard e-beam lithography and dry-etching as in [2]. For the triangular waveguides, we propose to adapt the process flow successfully applied in classical InP-based waveguides [3]. The vertical sidewalls are defined by dry etching in the same step as the rectangular waveguides. The area of the triangular sections is then covered with a SiN_x mask, which is dry-etched to leave only the vertical sidewalls covered. Successive wet-etchings of InP, using e.g. $1HCl:1H_3PO_4$ [6], and of the thin quaternary etch-stop layer, will stop on the (112) plane between the SiN_x covered wall and the etch-stop layer below, thus defining quasi-perfect triangular cross-section waveguides.

V. Conclusion

We present the design of a new IMOS component, used for efficient TE to TM conversion. The device shows excellent broadband capabilities, is inherently tolerant and can be fabricated using standard InP membrane technology. It is one order of magnitude smaller than the shortest PCs made to date by optical lithography. This device can be used with other devices of the IMOS platform to realize high-density and eventually fully active-passive PICs suitable for inter and intrachip communication.

References

[1] G. Roelkens, J. van Campenhout, J. Brouckaert, D van Thourhout, R. Baets, P. Rojo Romeo et al., "III-V/Si photonics by die-to-wafer bonding," Materials Today, vol. 10, no. 7-8, Jul. 2007

[2] F. Bordas, F. van Laere, G. Roelkens, E.J. Geluk, F. Karouta, P.J. van Veldhoven et al. "Compact grating coupled MMI on DVS-BCB bonded InP-membrane," 14th European Conference on Integrated Optics, ECIO08, Eindhoven, 11-13 Jun. 2008

[3] L.M.Augustin, R. Hanfoug, J.J.G.M. van der Tol, W.J.M. de Laat and M.K. Smit, "A compact integrated polarization splitter/converter in InGaAsP–InP," IEEE Photon. Technol. Lett., vol. 19, no. 17, Sep. 2007

[4] FIMMWAVE v.5.1, Photon Design, 2008

[5] P. S. Cho and J. B. Khurgin, "Return-to-zero differential binary phase-shift-keyed multichannel transmission with 25-Gbit/s polarization bit interleaving and 25-GHz spacing," Journal of optical networking, vol. 2, no. 5, May 2003

[6] S. Adachi and H. Kawaguchi "Chemical Etching Characteristics of (001) InP," J. Electrochem. Soc., vol. 128, no. 6, p. 1342, Jun. 1981

An Athermal Delay Circuit Using Trenches Filled with Silicone Resin

Kenji Iwamoto, Junya Odori, Jiro Ito and Hiroyuki Tsuda
Graduate School of Science and Technology, Keio University
Yokohama, Japan
k_iwamoto@tsud.elec.keio.ac.jp

***Abstract*—We fabricated an athermal delay circuit using trenches filled with silicone resin that has opposite temperature dependence to the silica. It was designed for the 1-bit delay circuit for 12.5 Gbit/s differential phase shift keying receiver and it exhibits wide operating temperature range.**

Keywords- Athermal waveguide; differensional phase shift keying;

I. INTRODUCTION

Silica-based planar lightwave circuits (PLCs) are reliable, low-loss, and feature low junction loss with optical fibers, so various types have been used for optical networks. However, the temperature dependence of the silica is too large for most interference circuits like 1-bit delay circuit. So the temperature of the circuit needs to be controlled. Using Athermal waveguide we can reduce fabrication cost and power dissipation [1-3]. In this paper, we have designed and fabricated the athermal 1-bit delay circuit for a differential phase shift keying (DPSK) receiver.

II. ATHERMAL WAVEGUIDE

A. Structure of the athermal waveguide

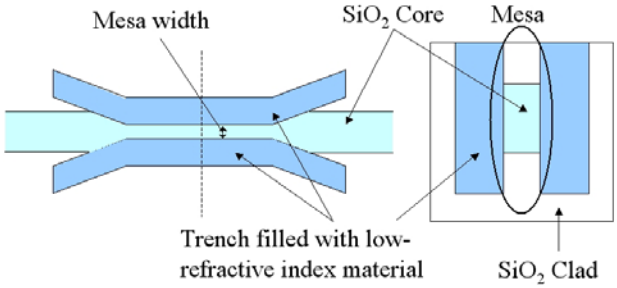


Figure 1. Structure of the athermal waveguide

The structure of the athermal waveguide is shown in Fig. 1. Trenches are fabricated along the core of the waveguide and filled with low-refractive index material [4, 5]. We used Silicone resin as a low-refractive index material. The propagation constant of the waveguide is determined by the refractive indices of the core and the low-refractive index material; their thermo-optic coefficients have opposite sign, and therefore the temperature dependence of the waveguide can be suppressed.

B. Effective index of the athrmal waveguide

The temperature dependence of the effective index of the waveguide can be described as;

$$n_{eff}(T) = A(T-25)^2 + B(T-25) + C \quad , (1)$$

where, T is temperature in degrees Celsius. A, B and C were constants calculated for mesa widths of 2.0 to 4.0 μm, as shown in Table I and II. The refractive indices of the core, the cladding layer and the resin were assumed to be 1.466, 1.444, and 1.393, and the thermo-optic coefficients of the silica and the resin were assumed to be 1.6×10^{-5} and -3.7×10^{-4}, respectively.

TABLE I. EFFECTIVE INDEX FOR TE MODE

	$A(10^{-5})$	$B(10^{-5})$	C
Normal	0.00091	1.65822	1.45632
Mesa 2.0 (μm)	0.01273	-3.76270	1.43956
Mesa 2.5 (μm)	0.00921	-1.76026	1.44493
Mesa 3.0 (μm)	0.00685	-0.62397	1.44856
Mesa 3.5 (μm)	0.00528	0.06216	1.45111
Mesa 4.0 (μm)	0.00421	0.49907	1.45296

TABLE II. EFFECTIVE INDEX FOR TM MODE

	$A(10^{-5})$	$B(10^{-5})$	C
Normal	0.00094	1.65687	1.45630
Mesa 2.0 (μm)	0.01283	-2.95334	1.44059
Mesa 2.5 (μm)	0.00907	-1.26293	1.44562
Mesa 3.0 (μm)	0.00668	-0.30314	1.44903
Mesa 3.5 (μm)	0.00513	0.27885	1.45143
Mesa 4.0 (μm)	0.00409	0.65132	1.45318

The thermo-optic coefficient of the waveguide depends on the mesa width. When the mesa width is wide, most of the light is confined in the silica core; therefore, the thermo-optic coefficient of a waveguide is positive. On the other hand, when the mesa width is narrow, some of the light is in the cladding region, and the thermo-optic coefficient is negative.

III. DESIGN OF ATHERMAL DELAY CIRCUIT

A. *Structure of 1-bit delay circuit*

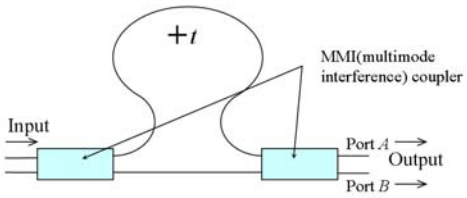


Figure 2. Schematic of 1-bit delay circuit

A schematic of the 1-bit delay circuit for the differential phase shift keying (DPSK) receiver is shown in Fig. 2. The time delay is set to the symbol period, *t*. In DPSK signaling, the symbols [0] and [1] are assigned to the phase difference between successive bits. The output light power from the output port is determined by the phase difference between the successive bits. When the phase difference between the successive bits is π, the light is output to port *A*., whereas when the phase difference is 0, the light is output to port *B*. Finally, a balanced receiver converts the output light into an electrical signal.

B. *Temperature dependence of the 1-bit delay circuit*

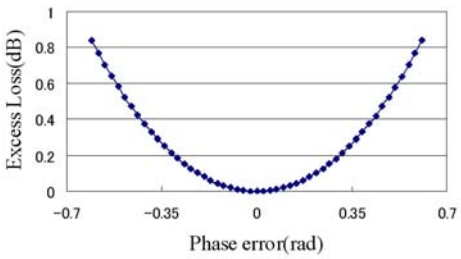


Figure 3. Excess loss caused by phase difference error.

Figure 3 shows the excess loss caused by the phase error to the second MMI. The optical length difference in the asymmetric MZI for a 12.5 Gbit/s DPSK signal is about 24 mm; therefore, the temperature change can easily lead to a phase error and the associated excess loss. The phase error range for excess loss of less than 0.5 dB is -0.45 rad to 0.45 rad.

C. *Design and Fabrication of Athermal 1-bit delay circuit*

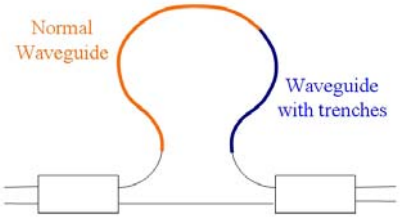


Figure 4. The athermal 1-bit delay circuit

We use normal waveguide and waveguide with trences for 1-bit delay, as shown in Figure 4. The mesa width of a waveguide with trenches is 2.0μm. We calculated the ratio of the length of both waveguides for athermal condition. Table III shows calculation results. The structure of athermal 1-bit delay circuit that we fabricated is shown in Fig. 5.

TABLE III. WAVEGUIDE LENGTH

	The Length of Normal Wavguide (mm)	The Length of Wavguide with Trench (mm)
TE mode	11294	5235
TM mode	10381	6153

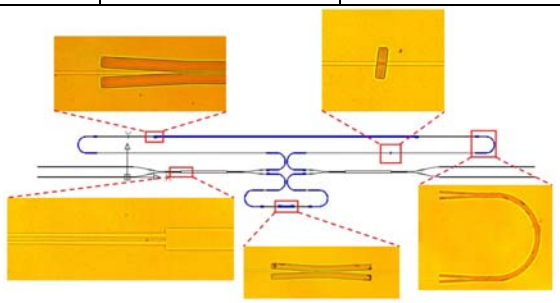


Figure 5. Structure of 1-bit delay circuit.

IV. EXPERIMENTAL RESUITS

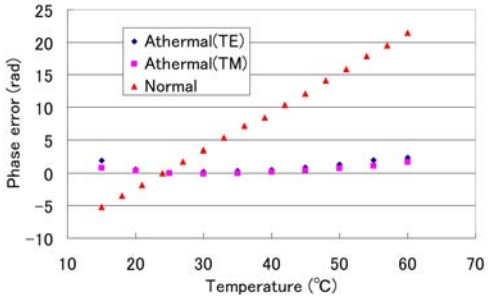


Figure 6. Temperature dependences of fabricated 1-bit delay circuits.

The experimental results of 1-bit delay circuits that we fabricated are shown in Fig. 6. By applying the athermal waveguide, the temperature range for the excess loss of less than 0.5 dB was extended from 1.5 (Normal) to 25.0 degrees (TE) and 30.0 degrees (TM).

V. CONCLUSION

We proposed a novel athermal waveguide structure. We also fabricated a 1-bit delay circuit for the 12.5 Gbit/s DPSK receiver, which had a wide operating temperature range.

REFERENCES

[1] S. Tada, H. Tanaka and Y. Kokubun, "Three-Dimensional Athermal Waveguide at 1.3μm Wavelength for Temperature Independent Lightwave Devices," OPTICAL REVIEW, vol. 3, no. 6B, pp. 478-480(1996).

[2] K. Iwamoto, J. Ito, H. Tsuda, "Design of an athermal optical waveguide using trenches filled with low-refractive index material", The 14th Microoptics Conference, P-55, Brussels, Belgium, September 2008.

[3] K. Iwamoto, J. Ito, H. Tsuda, "An athermal delay interference circuit using trenches filled with low-refractive index material", IEICE Electronics Express, vol. 6, no. 24, pp. 1769-1773(2009).

[4] J. Ito, T. Y. Fan, T. Suzuki and H. Tsuda, "Compact silica arrayed-waveguide grating with small bend radius utilizing trenches filled with low-refractive index material," IEICE Electronics Express, vol. 3, no. 23, pp. 499-503(2006).

[5] J. Ito, T. Y. Fan, T. Suzuki and H. Tsuda, "Compact Silica Arrayed-Waveguide Grating Using High-Mesa Small-Bend Waveguides," IEICE TRANSACTIONS on Electronics, Vol. E91-C, No. 1, pp. 110-112(2008).

Advances in Filters and Delay Lines in Silicon Photonics

A. Melloni, F. Morichetti, A. Canciamilla, C. Ferrari, and M. Martinelli
POLICOM – DEI, Politecnico di Milano, 20133, Milano, Italy
melloni@elet.polimi.it

G. Morea
DEE, Politecnico di Bari, 70125, Bari, Italy

M. Sorel, A. Samarelli, R. De La Rue
DEEE, University of Glasgow, Glasgow, G12 8LP, UK

***Abstract*— We report on design, characterization, exploitation and limitations of linear devices realized in Silicon Photonics. Filters and tunable delay lines are tested with picosecond pulses and PolDM DQPSK signals. Potentialities, impairments and critical aspects such as tuning, process tolerances, polarization management and waveguide sidewall roughness are thoroughly investigated and discussed.**

Keywords- silicon photonics; filters; ring resonators; slow wave; delay lines; DQPSK

I. INTRODUCTION

Silicon Photonics technology is rapidly progressing and a large number of elementary building blocks are becoming available for the implementation of devices with complex spectral characteristics. Filters, for example, are key elements in any telecom, datacom, optical interconnect and even sensor applications, with tight spectral and reconfiguration requirements. The high integration scale capability, the fast thermo-optic time response and the low power consumption place the SOI platform in a preferred position for applications where these prerequisites are mandatory.

Here we report the outcome of a long theoretical and experimental investigation on filters in SOI technology realized with Mach-Zehnder, rings, gratings and cascaded resonators. As a convincing demonstration of the capabilities of this technology, we report on an experimental investigation on the tuning delay of a 10 ps Gaussian pulse and on the management of a 100 Gbit/s signal with polarization-division-multiplexing (PolDM) differential quaternary phase shift keying (DQPSK) format. We demonstrate the compatibility of Silicon Photonics with the emerging advanced transmission systems at high bit-rate, provided that several delicate aspects (process tolerances, waveguide sidewall roughness, tuning and trimming) are taken into account.

II. TECHNOLOGY AND DEVICES

Fig. 1 (a) shows a detail of the cross-section of the fabricated waveguides (220 nm thick, 490 nm wide). The fabrication process was optimized by using an HSQ electron-beam-resist based technology in order to obtain very low propagation losses (~1 dB/cm) [1] and an accuracy of better than 0.5 nm on the waveguide dimensions. After the etching process, the residual HSQ is not removed and the waveguide is covered with 0.5-μm-thick SiO_2 layer by PECVD. The fabrication has been carried out at the James Watt Nanofabrication Centre of the University of Glasgow.

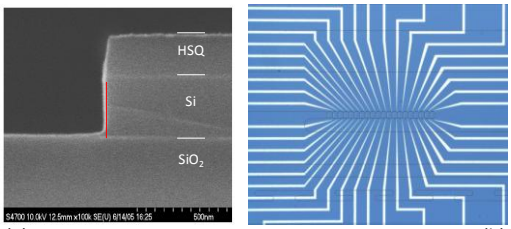


Figure 1. Photographs of (a) the waveguide cross section and (b) a 20-rings reconfigurable CROW.

A large number of circuits and devices have been realized. As an example, Fig. 1 (b) shows a coupled-resonator optical waveguide (CROW) structure, consisting of 20 identical racetrack ring resonators with a radius of 20 μm and a straight coupling section 16 μm long. All the rings have the same shape, while the coupling coefficients are optimized [2] by changing the gap size between the coupler waveguides. A heater consisting of a 50 nm-thick highly resistive metallic layer of nichrome (NiCr) patterned by lift-off to obtain a 0.9 μm wide strip is deposited on each ring, allowing a flexible and full reconfiguration of the devices and, if necessary, a fine tuning of the characteristic.

The choice of the ring dimensions is strongly related to the application and it is the result of a careful compromise between bandwidth, delay and pulse distortion, bend-induced losses, backscatter, sensitivity to technological tolerances, tuning electrical power and overall footprint and minimum number of rings to tune. Fig. 2 shows in solid lines the intensity (a) and group delay (b) spectral characteristic of a 6-rings CROW with a free spectral range FSR = 440 GHz and a -3 dB bandwidth of 100 GHz. The agreement with the theoretical response (dashed lines) demonstrates that the accuracy of the fabrication process guarantees the proper alignment of the ring resonances without the need for an active tuning of the structure. The power consumption required for the shift of an entire FSR is about 23 mW per ring and the time response is 12 μs. The thermal

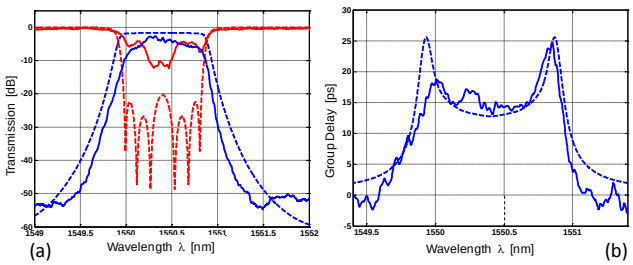


Figure 2. (a) Intensity and (b) group delay spectral characteristic of a 6-rings CROW: comparison between measures (solid) and design (dashed).

crosstalk between adjacent rings is about 1-2 % and is therefore negligible for most of the applications. Further details can be found in [3].

III. IMPAIREMENTS AND ISSUES

When dealing with high index contrast waveguides and especially with high finesse ring resonators and large circuits, several critical issues must be taken into account. Among others, the most detrimental are: uncertainties and tolerances of technological processes, distributed backscatter induced by sidewall roughness [4], structural disorder [5] and undesired polarization coupling and rotation.

Further, it must be kept in mind that an error of one nanometer on an SOI waveguide cross-section dimension typically produces a shift of one nanometer of the spectral response. Hence, trimming or tuning procedures are of prime importance to finely control the device characteristic. Thermo-optic control is a viable technique to perform fast and low power circuit tuning and reconfiguration, with the advantage that thermal crosstalk between adjacent waveguides in an SOI material platform is much lower than in glass-based devices and can be made negligible with a proper design.

IV. APPLICATIONS AT 100 GBIT/S

As a first example we investigated the tunable delay induced by a 20-rings reconfigurable CROW with a 10 ps Gaussian input pulse, the spectrum of which fits completely within the structure bandwidth. The tuning scheme is shown in Fig. 3 (a) and it is a folded CROW with each ring that can be individually tuned to change the delay [6]. The input pulse and the delayed output pulses are shown in Fig. 3 (b) when the resonance of 4, 8 and 12 rings are tuned to match the signal bandwidth. At resonance the double-transit induced-delay per ring is 7.3 ps but a suitable detuning of the last ring allows for a fine control of the delay within a fraction of a picosecond [6]. Delays up to 88 ps, corresponding to more than 1 byte, have been achieved with 12 open rings and an acceptable pulse broadening and a moderate intersymbol interference. After a delay of 8 bits the pulse FWHM is 11 ps and the extinction ratio is reduced to 7 dB, still an acceptable value for low-penalty transmission. Clearly, the relative delay on longer pulses is shorter because of the narrower spectrum of the

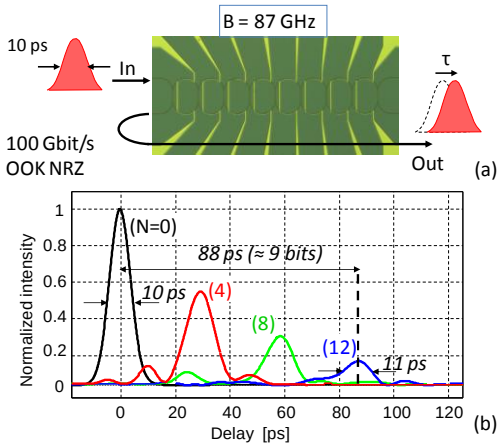


Figure 3. Sketch of the reflective tunable CROW delay line. b) Delays of a 10 ps gaussian pulse achieved by aligning the resonances of 4, 8 and 12 rings.

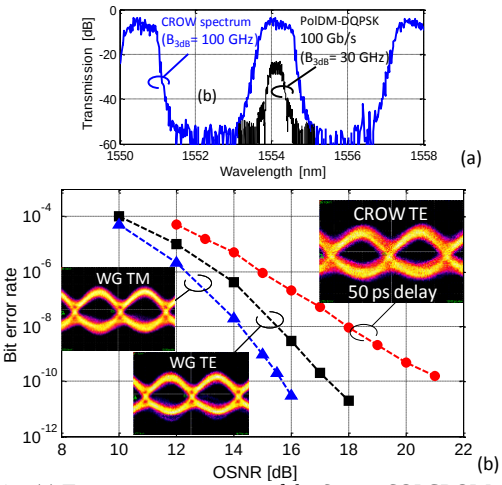


Figure 4. (a) Transmission spectrum of the 6-rings SOI CROW shown in Fig. 2 and spectrum of the 100 Gbit/s RZ-PolDM-DQPSK signal; (b) BER measurements after propagation through 1-cm-long SOI nanowire (TE and TM polarization) and through the CROW with 50 ps delay (TE only).

signal. The fractional insertion loss is 0.8 dB/bit (or 0.6 dB/ring) up to 6 delayed bits, after which the pulse intensity reduces because of the broadening induced by chromatic dispersion.

The synchronization of two 50 Gbit/s DQPSK modulated signals to form a 100Gbit/s PolDM one is the most advanced demonstration of the potential of this device. The two data streams were independently generated, combined and sent to the CROW input with the same optical power. One of the two polarizations is then aligned with the TE CROW passband and delayed with respect to the other one [7], to achieving the time-interleaving condition.

Figure 4 (a) shows the transmission spectrum at the Drop port of the CROW for a TE polarized input light. The 30-GHz-wide spectrum (evaluated at 3 dB attenuation) of the 100 Gbit/s PolDM-DQPSK signal is entirely contained within the (TE) CROW passband and the impact of chromatic dispersion and filtering is very limited. Figure 4 (b) shows that error-free propagation (BER < 10^{-9}) through the CROW is achieved with less than 3 dB OSNR penalty with respect to propagation in the straight waveguide. This penalty, which is mainly due to non optimal alignment of the rings' resonances, is expected to be largely reduced by a proper tuning of the device. At this wavelength the TM-polarized channel is not coupled to the CROW, propagates in the 1-cm-long bus line only and outcouples from the through port of the device, showing the same BER performance as the straight waveguide.

REFERENCES

[1] M. Gnan et al., Electron. Lett., vol. 44, no. 2, pp.115-116, 2008.

[2] A. Melloni and M. Martinelli, J. Lightw. Technol., vol. 20, no. 2, 2002.

[3] A. Canciamilla et al., submitted to IEEE Photonics.

[4] F. Morichetti et al., Phys. Rev. Letters , in press.

[5] C. Ferrari, F. Morichetti, and A. Melloni, J. Opt. Soc. Am. B, vol. 26, no. 4, pp. 858-866, 2009.

[6] F. Morichetti, A. Melloni, C. Ferrari and M. Martinelli, Opt. Express, vol. 16, no. 12, pp. 8395-8405, 2008.

[7] C. Ferrari et al., IEEE Photon. Technol. Lett., vol. 21, no. 20, pp. 1541-1543, 2009.

Arrayed-waveguide-grating light collector for on-chip spectroscopy

N. Ismail, B.I. Akca, F. Sun, K. Wörhoff, R.M. de Ridder, M. Pollnau, and A. Driessen
Integrated Optical Microsystems Group, MESA+ Institute for Nanotechnology, University of Twente
Enschede, The Netherlands
n.ismail@ewi.utwente.nl

Abstract—**We present a novel arrayed-waveguide-grating (AWG) device with improved external (biomedical) signal collection for use in on-chip spectroscopy. The collection efficiency of the device is compared to that of a standard AWG. We also present experimental results on the collection efficiency and size of the collection volume.**

Keywords-arrayed waveguide grating; spectroscopy; integrated optics

I. INTRODUCTION

Large efforts are currently being made to miniaturize optical devices, as for example integration of OCT systems and Raman spectrometers [1, 2]. In this work we draw the attention on on-chip spectrometers, in particular on the issues related to focusing light from the on-chip excitation laser source into the (biomedical) sample under study, and collection of the light backscattered from the sample. We propose a novel method for laser delivery and signal collection based entirely on integrated optics, and we present our first experimental results on the collection efficiency and the size of the collection volume.

II. LASER DELIVERY AND SIGNAL COLLECTION

A. Method description

The proposed method [3] makes use of two AWG devices (for the working principle of an AWG we refer to the work of M. K. Smit and C. V. Dam [4]), one for focusing the excitation beam into the sample and one for collecting the backscattered light from the focal spot. The devices are arranged in such a way that the output grating line of the focusing device, which lays on a circle, is concentric with the input grating line of the collection device. In this way the output free propagation region (FPR) of the excitation device and the input FPR of the collector device merge together forming a single free propagation region that for convenience we indicate with SFPR (sample-side FPR). The length of the SFPR region must be chosen in such a way that when brought in contact with the sample the focal spot is located inside the latter at the desired depth d (this choice depends on the refractive index of the sample). Figure 1 shows a schematic of the two devices where, for simplicity, the excitation device and the collection device have a single channel. In the most general case both devices may present more than one channel. In particular, if we are interested in performing spectroscopic measurements on the sample, the collection AWG must be designed with the appropriate number of output channels depending on the desired wavelength spacing and free spectral range (FSR) needed for the application.

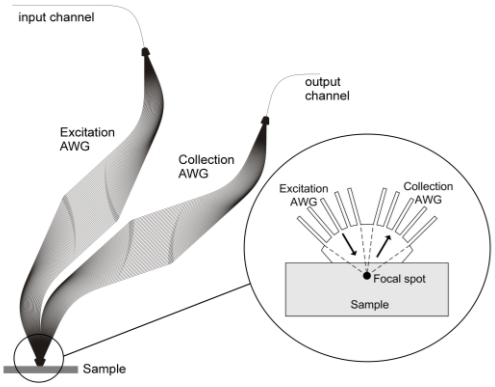


Figure 1. Schematic of the laser delivery and signal collection device with a single input and a single output channel. The inset shows the confocal arrangement of the two devices.

B. Collection efficiency

We have compared the collection efficiencies of two similar AWGs; the first is a standard AWG (the reference device) with an input FPR region of length l_{FPR} and an input channel which collects the light, whilst the other (corresponding to the collection AWG of the device proposed above) presents only part of the input FPR of length $l = l_{FPR} - d$ (its length l depends on the distance d from the source) and no input channel, i.e., light collection is made by the SFPR. For the characterization, both devices are placed at a distance d from a light source S. A schematic representation of the input sections of the two devices is shown in Fig. 2.

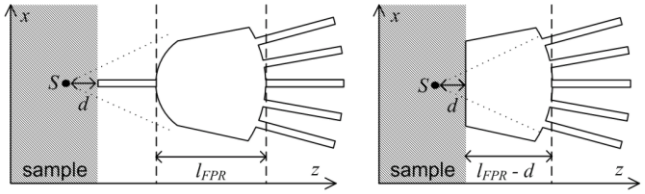


Figure 2. Input sections of a standard AWG (reference device, left-hand side) and an arrayed-waveguide-grating collector (proposed device, right-hand side) positioned at a distance d from a source S.

Financial support from the Dutch IOP Photonic Devices (Senter-Novem and STW) is acknowledged.

The collection efficiency of both devices was calculated analytically as a function of d, using the following parameters: monochromatic source emitting at wavelength λ = 1284.6 nm with a numerical aperture of NA = 0.16; sample refractive index of 1.46; device geometry and waveguide cross-sections as described in SECTION III. All chosen parameters correspond to those used in the experimental setup. The simulation results are shown in Fig. 3. In all the simulations the number of arrayed waveguides N is constant (N = 400) and the AWG spillover losses are around 0.05% for NA = 0.16. On the secondary axis of Fig. 3 we show the gain in collection efficiency achieved using our proposed device compared to the reference device as a function of d, for different values of NA. As d increases, the collection efficiency of the collector AWG increases compared to that of the standard AWG, becoming approximately 10 times larger than for the standard AWG for d = 225 μm. In order to simulate the more realistic situation in which light inside a sample is scattered in all directions, i.e., approaching a point source, we calculated the efficiency also for higher NA values of the source. We notice that for NA ≥ 0.35 there is no significant increase in the efficiency, which starts to drop for NA ≥ 0.55. This is due to an increase in the spillover losses as the emission angle of the source becomes larger. To overcome this problem the number of arrayed waveguides should be accordingly increased. We have calculated that for an ideal situation in which light is emitted over the whole solid angle, and where the number of arrayed waveguides is sufficient to capture all the light coupled into the input FPR, the power collected by the collector AWG would be around 30 times higher than that collected by the reference device already at a distance d = 100 μm.

III. EXPERIMENTAL RESULTS

Measurements were performed on two identical AWG devices fabricated in silicon oxynitride (SiON) technology [5] with a waveguide cross section of 2 μm × 0.6 μm and SiO_2 cladding. The core and cladding refractive indices were 1.55 and 1.4485, respectively, at 1.3 μm. The length of the FPR was 5393.5 μm, the number of arrayed waveguides 400, and the central wavelength 1.3 μm. Furthermore, the AWGs presented 100 output channels with a wavelength spacing of 0.38 nm. In order to perform the measurements for varying distance d, the free propagation region of the proposed AWG collector was diced for each measurement point. The dicing was performed using a 30-μm-thick diamond blade. As a source we used a tunable diode laser (New Focus 6324) at a wavelength of 1284.6 nm connected to a single-mode optical fiber with NA = 0.16. Index matching liquid with a refractive index of 1.46 was used between the source and the device. For accurate positioning of the source fiber a motion controller (Newport PM500) was used, which allows for a stable position at variable distance from the chip with nanometer precision. For each position d the output power was measured with a power sensor (HP 8153A) for both devices from the output channel centered at 1284.6 nm. The measurements, displayed in Fig. 3, are in good agreement with the simulation results. In order to determine the size of the region within the sample from which light is collected using the AWG collector, we moved the fiber

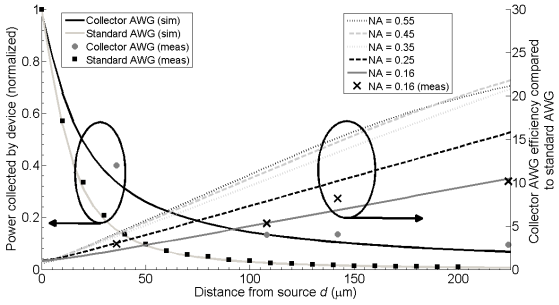


Figure 3. (primary axis) Simulation and measurement results showing the power collected by the AWG collector compared to that of the reference device as a function of the distance d from the source. The results are normalized to the collection of the reference device at d = 0. (secondary axis) Collected power ratio between the proposed AWG and the reference device as a function of d, for different values of NA.

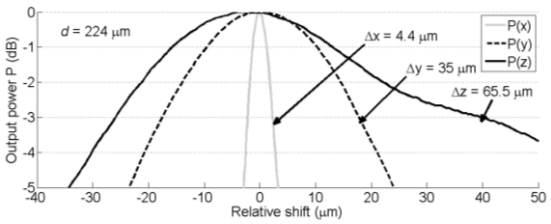


Figure 4. Measurement of the collection volume of the arrayed-waveguide-grating collector for d = 224 μm.

(originally centered on the focal point) in the three spatial directions while keeping the excitation wavelength fixed. By taking the points where the power decays by 3 dB (see Fig. 4), we calculated a volume $\Delta x \Delta y \Delta z$ of 4.4 μm × 35 μm × 65.5 μm for a distance d of 224 μm. For d = 36 μm we measured Δx = 4.4 μm, and Δy = 5 μm (we were not able to perform the measurement of Δz for this distance).

IV. CONCLUSIONS

We presented a method for focusing and collecting light from a sample, which makes use of two AWG devices in a confocal arrangement. This opens possibilities for on-chip spectroscopic measurements with no need for external optics. Our experimental and simulation results on the collection efficiency of the device showed that it can be up to 20 times higher than that achieved using an input waveguide channel connected to a standard AWG device.

V. REFERENCES

[1] E. N. Lewis, P. J. Treado, and I. W. Levin, "A Miniaturized, No-Moving-Parts Raman Spectrometer," *J. Appl. Spectrosc.* vol. 47, pp. 539-543, 1993.

[2] G. Yurtsever and R. Baets, "Towards integrated optical coherence tomography systems on silicon on insulator," in *Proc. Symp. IEEE/ LEOS Benelux Chapter*, Enschede, The Netherlands, 2008, pp. 163-166.

[3] N. Ismail, M. Pollnau, and A. Driessen, "Scattered light collector, light focusing apparatus, method for controlling the focus of a focused light source and method for measuring the light scattered or originating from a point of an object." Patent No. NL 1036920, The Netherlands, 2009.

[4] M. K. Smit and C. v. Dam, "PHASAR-Based WDM-Devices: Principles, Design and Applications," *J. Select. Topics Quantum Electron.,* vol. 2, pp. 236-250, 1996.

[5] K. Wörhoff, L. T. H. Hilderink, A. Driessen, and P. V. Lambeck, "Silicon oxynitride: a versatile material for integrated optics application," *J. Electrochem. Soc.,* vol. 149, pp. 85-91, 2002.

Apodized coupled resonator optical waveguides using the longitudinal offset technique

J.D. Doménech, M. Rius, P. Muñoz and J. Capmany
Optical and Quantum Communications Group, iTEAM-Universidad Politécnica de Valencia
C/ Camino de Vera s/n - Valencia 46470 - SPAIN
E-mail: jodogo@iteam.upv.es

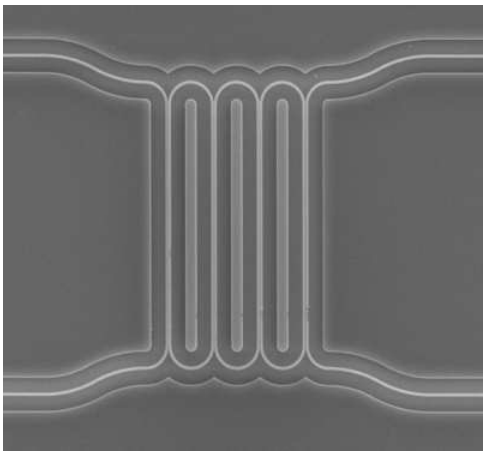
***Abstract*—In this paper, an experimental demonstration of the apodization of coupled resonator optical waveguide (CROW) devices through the longitudinal offset technique is presented for a 3 racetracks CROW device and compared against the uniform case.**

I. Introduction

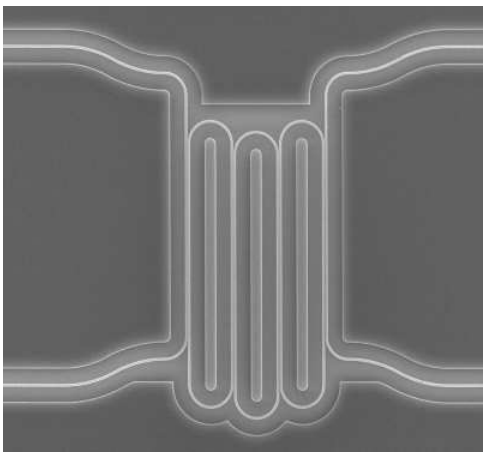
Coupled Resonator Optical Waveguide Devices (CROW) [1] are promising building blocks for the future photonic integrated devices, and their main application amongst others is for filtering purposes. The device consists on a series of directly coupled ring resonators. When the coupling constants between the pairs of resonators are equal, the spectral response of these device exhibits pass band ripples. They can be reduced by means of windowing or apodization of the inter-ring coupling coefficients as already demonstrated theoretically in [2]. Typically the apodization of the coupling coefficients has been done by increasing or decreasing the lateral coupling distance between the cavities [3], in steps that can be of the order of tens of nanometers, in order to increase/decrease the coupling coefficients. For some fabrication processes, as photolithography, these steps are below the achievable resolution. Recently we proposed the longitudinal offset technique [4], in which the change of the coupling coefficients is done by applying a longitudinal offset to the cavities and keeping constant the transversal distance between the resonators. This changes the effective length along which the resonators are coupled, and therefore the coupling constant. However, the steps required for the apodization are found to be of two orders of magnitude above those employed in the conventional technique [3], allowing a more precise control of the coupling.

II. Experimental results

The CROW devices presented in Fig. 1 are fabricate on a Silicon-On-Insulator platform. The devices are based on 3 racetracks shaped resonators with a bending radius of 5 microns and a straight coupling section of 53.3 μm. The devices were designed and fabricated with waveguides of a 500 nm x 220 nm cross-section, providing single mode operation at 1550 nm with a layerstack of 220 nm thick Silicon on top of $2\mu m$ Silicon Oxide BOX. With the aforementioned ring dimensions, the predicted Free Spectral Range is 4 nm for the wavelengths close to 1550 nm, where the group index of these waveguides is 4.25. The devices were fabricated in the ePIXfab SOI platform [5] using deep UV lithography. All the couplers were designed to have a gap of 150 nm. Two CROW devices were fabricated: the first device with a uniform distribution of the coupling coefficients shown in Fig. 1-(a), that is, the same coupling constant for all the couplers (no offset); the second one with the coupling constants following a Gaussian distribution by applying a longitudinal offset to each cavity in the CROW device depicted in Fig. 1-(b).



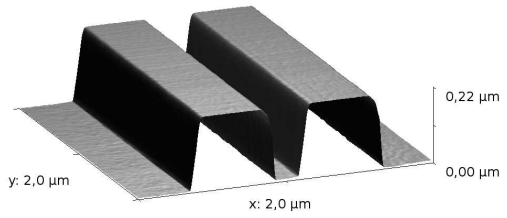
(a)



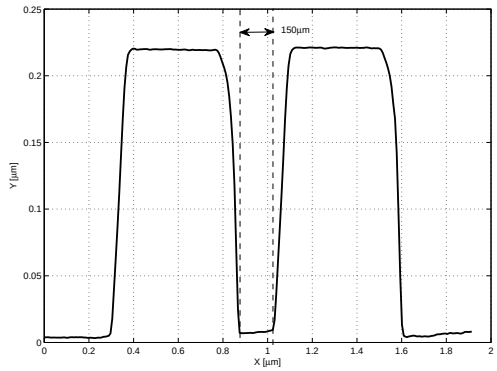
(b)

Fig. 1. SEM images of a 3 racetracks CROW uniform (a) and apodized with the longitudinal offset technique (b).

The gap amongst the coupler parallel waveguides was measured using an Atomic Force Microscope (AFM), since

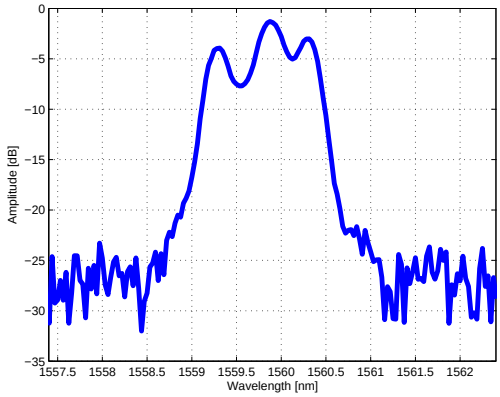


(a)

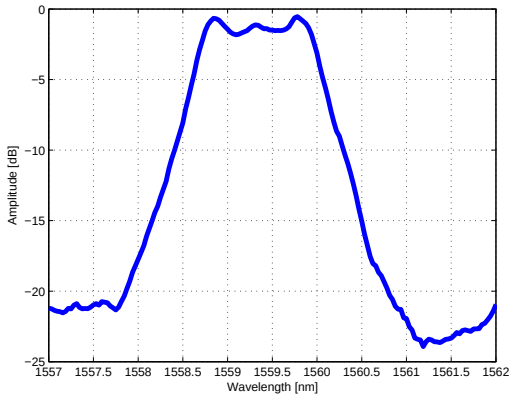


(b)

Fig. 2. AFM measurements on-chip coupler surface (a) 3D profile and (b) cross-section.



(a)



(b)

Fig. 3. Transmission spectra for 3 racetracks uniform (a) and offset apodized (b) CROWs.

it is a very relevant parameter for the control of the coupling constant. The results are shown in Fig. 2-(a) and (b), where a three dimensional reconstruction of the waveguide profile, and a cross-section with the obtained gap are shown respectively.

Light was coupled in to/out from the devices by means of grating couplers [6] optimized for TE transmission around 1550 nm, and optical fibers properly positioned and aligned. A reference transmission spectrum through a straight waveguide was acquired for normalization purpouses. The spectral response of the uniform device in Fig. 1-(a), is shown in Fig. 3-(a). The spectrum exhibits the well known pass-band ripples for this kind of devices. For the apodized device using the longitudinal offset technique, shown in Fig. 1-(a), the spectrum in provided in Fig. 3-(b). A reduction of nearly 5 dB in the pass band ripple is obtained.

III. Conclusions

In this paper, the longitudinal offset technique for the apodization of CROW devices has been experimentally demonstrated. The technique is able to perform pass-band ripple reduction in the spectral response of a CROW device. The technique allows apodization of the response using fabrication technologies with coarse resolution steps, as photolithography, at a cost of increased device footprint in the lateral dimension.

References

[1] A. Yariv, Y. Xu, R. K. Lee, and A. Scherer, "Coupled-resonator optical waveguide: a proposal and analysis," *Opt. Lett.*, vol. 24, no. 11, pp. 711–713, 1999.

[2] J. Capmany, P. Munoz, J. D. Domenech, and M. A. Muriel, "Apodized coupled resonator waveguides," *Opt. Express*, vol. 15, no. 16, pp. 10 196–10 206, Aug. 2007.

[3] F. Xia, M. Rooks, L. Sekaric, and Y. Vlasov, "Ultra-compact high order ring resonator filters using submicron silicon photonic wires for on-chip optical interconnects," *Opt. Express*, vol. 15, no. 19, pp. 11 934–11 941, 2007.

[4] J. D. Domenech, P. M. noz, and J. Capmany, "The longitudinal offset technique for apodization of coupled resonator optical waveguide devices: concept and fabrication tolerance analysis," *Opt. Express*, vol. 17, no. 23, pp. 21 050–21 059, 2009.

[5] "ePIXfab Silicon Photonics Platform," http://www.epixfab.eu/.

[6] W. Bogaerts, D. Taillaert, B. Luyssaert, P. Dumon, J. V. Campenhout, P. Bienstman, D. V. Thourhout, R. Baets, V. Wiaux, and S. Beckx, "Basic structures for photonic integrated circuits in silicon-on-insulator," *Opt. Express*, vol. 12, no. 8, pp. 1583–1591, 2004.

Integrated Photonic Circuits for Ultra-fast Sampling and Inherently Linear 6-bits Flash Quantization Based on Coherent Multi-Phase Interferometry

Moshe Nazarathy
Dept. of Electrical Engineering, Technion, Haifa (Israel)
nazarat@ee.technion.ac.il

Abstract—**We propose a novel 6 bits 40Gsamp/sec photonic-sampled-and-quantized flash ADC structure, based on parallel phase-domain interferometric comparisons, realizable over Si/InP (possibly hybrid) photonic integrated circuits with complexity commensurate with the state-of-the-art of photonic integration, achieving high linearity and resilience to a multitude of impairments.**

Integrated Photonics, Photonic Integrated Circuits, Modulators, Analog to Digital Conversion, Phase Measurement.

I. INTRODUCTION

Photonic sampling and quantization techniques for *Analog to Digital Converters* (ADC) with electronic interfaces have been intensely researched in the last three decades [1], motivated by the slow improvement trend in bandwidth-resolution performance of electronic ADC, and spurred by the unique advantages of photonics.

Recent PADC research has focused on the time-stretch architecture (e.g. [2]) providing spectacular performance, yet realized by bulky systems not amenable to miniaturization by means of *Photonic Integrated Circuits* (PIC), e.g. [3].

Unfortunately, progress in photonic quantization (e.g. [4-7]) has not been keeping up with the impressive advances in photonic sampling [8]. In this paper we propose a novel Photonic ADC (PADC) architecture, amenable to photonic integration, and quite distinct from all prior photonic sampling & quantization schemes, in that it is directly based on the Flash ADC principle, performing multiple comparisons in parallel, in the phase domain, based on interferometric principles.

The hitherto untapped photonic rationale is that interferometry is a fundamental optical technique excelling at generating comparisons between optical phases, put here to work in a PIC: the voltage under test is linearly converted into phase (referred to as the phase-under-test), then multiple parallel interferometric comparisons of the phase-under-test are performed against a sequence of angular thresholds (ADC transition levels). This realizes the flash principle, except that the signal under test and ADC thresholds are now optical phases rather than voltages.

The proposed compact flash PADC-in-a-PIC promises high performance (6 bits, ~4 effective bits at tens of GHz bandwidth), and is amenable to mass production over Si/InP PIC platforms due to its structure, further facilitated by its inherent tolerance to impairments and fabrication errors, stemming from phase- rather than intensity-domain operation.

Finally, while highly valuable in itself, the novel Flash PADC is not "the end game" but constitutes a stepping-stone, providing a building block in novel compound PADC architectures which we have conceived (pipelining and *Successive Approximation Register* (SAR) structures combining two or more flash PADCs), with resolutions potentially exceeding 10 bits effective (also with tens of GHz bandwidth, even without time-interleaving).

II. A NOVEL FLASH PADC ON-A-PIC

The proposed flash PADC block diagram is shown in Fig. 1 (for acronyms see the figure caption). A *b*-bits PADC requires an array of $N = 2^{b-1}$ PCs (e.g. N=32 for 6 bits). Each of the N interferometers (formed by the shared PP-PM, one of the ODCs, and its BPD), acts as a phase-detector. The n-th PHD amounts to an MZM with its quadrature point quasi-statically biased at $\theta^{(n)} = n\pi / N$, $n = 0,1,...N-1$ (an extra $\pi/2$ phase bias is built-in). In the k-th time interval, the phase-under-test $\phi_k = V(kT)\pi / V_\pi \in \{-\pi, \pi\}$ is interferometrically compared against each of the phases $\{\theta^{(0)}, \theta^{(1)}, ..., \theta^{(N-1)}\}$. The polarity of the n-th photocurrent sample $i_k^{(n)} \equiv i^{(n)}(kT)$ indicates whether or not $\phi_k > \theta^{(n)}$: $\mathrm{sgn}\left\{i_k^{(n)}\right\} = \mathrm{sgn}\left\{\sin\left[\phi_k - \theta^{(n)}\right]\right\}$. E.g. let $\left|\phi_k - \theta^{(n)}\right| < \pi$, then $i_k^{(n)} > 0$ iff $\phi_k > \theta^{(n)}$, i.e. the n-th PC compares the phase-under-test against the n-th ADC transition $\theta^{(n)}$. In the OEBE, the N photocurrents are TIA-amplified, sign-detected (sliced) by an array of uncoupled 1-bit ADCs, then processed by the encode-logic.

The signs assumed by the sinusoidal *transfer characteristics* (TC) (Fig. 2) describing the N interferometers, when sampled at the phase-under-test ϕ_k, suffice to uniquely determine which of the M ADC bins (quantization intervals) ϕ_k actually belongs to. Remarkably, the TC sinusoidal non-linearity is inconsequential, since the only info required in order to quantize ϕ_k (identify its ADC bin) is whether ϕ_k falls to the right or to the left of each quadrature point; as each sinusoid is odd around its quadrature point, then we just detect its sign. Hence we attain *high PADC linearity*, unrelated to the TC nonlinear shape; instead the PADC linearity is set by the C&C ability to spread the N quadrature bias phases $\{\theta^{(n)}\}$ at regular

angular intervals π / N over $\{0, \pi\}$. Our PADC integrated device (Fig. 1) has the following desirable characteristics:

(i): Amenable to compact and resilient *PIC realization*, e.g. over photonic integration platforms consisting of Silicon Photonics, SOI, InP, $LiNb0_3$ or combinations thereof, in particular hybrid Si/InP integration platforms.

(ii): Implements the equivalent of an electronic *flash* ADC in terms of its abstract system block diagram, performing multiple parallel comparisons of the signal-under-test (albeit in the phase domain).

(iii): Unlike in most photonic quantization systems, the signal-under-test here is not *intensity*, but is effectively *optical phase*, imparting extra resilience to the system. The phase comparisons required in the flash architecture are interferometrically performed, effectively amounting to parallel thresholding by means of an effective array of MZMs with regularly spaced quadrature points (the multiple MZMs are virtual, as physically just one pair of phase modulators – the front-half of a single MZM - is actually used).

(iv): Inherently linear: our PADC linearity is not limited by the sinusoidal interferometric TC, but is essentially set by the ability to adjust and stabilize multiple quasi-static phase-shifts (the quadrature settings of the effective MZMs in Fig. 2a) by means of slowly-varying *control and calibration* (C&C) procedures, adaptively actuated by either training sequences or by blind (decision-directed) equalization techniques.

(v): Resilient to a variety of PIC impairments and fabrication errors - this stems from the quantization action essentially occurring in the phase domain, rendering PIC performance impervious to most (but not all) amplitude imbalances, coupling ratios, amplitude fluctuations; the tolerances on the PIC fabrication are then relaxed compared to conventional intensity modulation based PADC schemes.

(vi): Operates in differential (balanced) push-pull mode

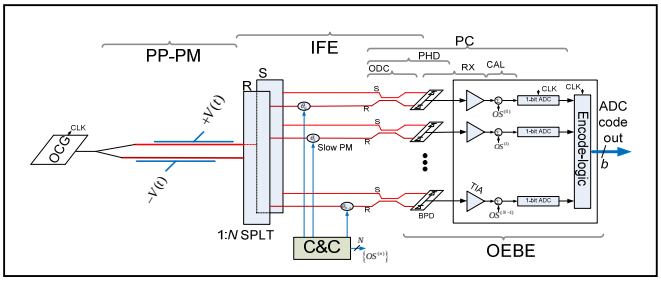


Figure 1. Integrated Flash Photonic ADC system based on coherent multi-phase interferometry. OCG=Optical Comb Generator; PP-PM=Push-Pull Phase Modulators; IFE=Interferometric Front-End; OEBE=Opto-Electronic Back-End; PC=Phase-Comparator; PHD=Phase-Detector; SPLT=(N-way) Splitter; PP-PM=Push-Pull Phase-Modulator; ODC=Optical Directional Coupler; RX=Optical Receiver; BPD=Balanced Photodiodes pair; TIA=Trans-impedance amplifier; CAL=Calibration offsets section; C&C=Control&Calibration; 1-bit ADC=Slicer (sign-detector; comparator to zero). V(t) = voltage-under-test. Notice that the two 1:N splitters (drawn for clarity on top of each other) are actually laid out side by side in integrated planar lightwave circuit implementations, wherein some waveguide interconnects from the two splitters to the ODCs cross each other.

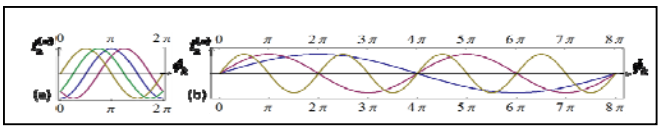


Figure 2. Transfer Characteristics (TC) : (a): TC plots of a 5-bit version of our PADC for the $N=4$ PCs. (b): TC plots for a "Tayor-like" PADC based on parallel modulators [4,5], some with excessively low V_π, or serially-cascaded modulators [6]. Notice that our PADC just requires a 2π or $\pm\pi$ phase excursion, whereas Taylor-like schemes require a $2\pi N$ phase excursion.

with antipodal phase modulations and balanced photo-detector pairs), hence gaining 3 dB in shot-noise SNR, and further reducing certain common-mode impairments (see next point).

(vii): Relaxed *optical comb generator* (OCG) requirements: tolerance to pulse-to pulse intensity fluctuations, to laser RIN.

(viii): Amenable to calibration (tuning out) of most residual impairments (those which are not automatically cancelled by the phase-based amplitude-insensitive operation in balanced mode); the calibration is achieved by having the C&C module apply quasi-static controlled offsets in the electrical domain. The other C&C function is adjustment of the slowly varying control phase-shifts to ensure the system linearity.

(ix): The phase comparators (PC) count, N, is half as large as in electronic flash ADC: $N = 2^{b-1}$ rather than $M = 2N = 2^b$, with b the number of bits). E.g., a 6-bit system requires just 32 PCs rather than 64, halving the PIC complexity.

(x): Sampling rate performance: The "speed" (bandwidth) of the system is determined by that of the electro-optic modulation (up to tens of GHz at low V_π), as well as by the speed of the terminal electronic slicing operations (the array of 1-bit electronic ADC, i.e. sign detectors).

(xi): Accuracy and bandwidth performance: High-speed electronic flash ADC systems are typically unable to exceed 6 bits, our PADC being no exception (as the comparators count rises exponentially in the number of bits b). The *effective number of bits* (ENOB) is typically 1-2 less than the number of bits. Given the beneficial PADC characteristics surveyed above, and in particular the inherent tolerance of the architecture to impairments, we expect at least 4 effective bits at tens of GHz bandwidth.

The proposed flash PADC is valuable in itself and may further serve as a building block in compound integrated pipeline PADC structures potentially exceeding 10 bits effective.

REFERENCES

[1] G. C. Valley, Photonic analog-to-digital converters, Opt. Express 15, 1955 (2007).

[2] A.M. Fard, S. Gupta, B. Jalali, Dynamic range improvement in time-stretch analog-to-digital converter, OFC'09, paper OMI2 (2009).

[3] M.J. Wale, "Photonic integration challenges for next-generation networks," in ECOC'09, paper 1.7.4

[4] H. F. Taylor, "An optical analog-to-digital converter—design and analysis," IEEE J. Quant. Electron.15, 210 (1979).

[5] B. Jalali and Y.M. Xie, "Optical folding-flash analog-to-digital converter with analog encoding," Opt. Lett. 18, 1901 (1995).

[6] M. Currie, "Optical quantization of microwaves signals via distributed phase modulation," J. Lightwave Technol. 23, 827 (2005).

[7] J. Stigwall and S. Galt, "Demonstration and analysis of a 40-Gigasample/s interferometric analog-to-digital converter," J. Lightwave Technol. 24, 1247 (2006).

[8] P. Juodawlkis et al, "Optically sampled analog-to-digital converters," IEEE Trans. Microwave Theory Tech. 49, 1840, (2001).

PLASMONIC COMPONENTS FOR INTEGRATED NANOPHOTONIC CIRCUITS

Anatoly V Zayats
Centre for Nanostructured Media
The Queen's University of Belfast
Belfast, United Kingdom
Email: a.zayats@qub.ac.uk

Abstract— **Plasmonic waveguides provide very efficient means to confine and guide photonic signals on subwavelength scales. Here we will discuss passive and active nanophotonic components based on plasmonic waveguides and crystals for optical signal manipulation, routing, modulation and amplification.**

Keywords- surface plasmon, waveguiding, nanophotonics

Surface plasmon polaritons (SPPs) have proved to be very efficient in confining and guiding photonic signal on sub-wavelength scales hardly attainable with conventional dielectric waveguides. Moreover, due to the SPP field confinement and enhancement near the metal interface, various functionalities can be efficiently implemented with SPPs through nonlinear, electro-optical or thermo-optical effects.

A surface plasmon polariton is an electromagnetic wave coherently coupled to electron oscillations and propagating in a wavelike fashion along a metal-dielectric interface [1]. Being a surface wave, a SPP is intrinsically confined near the metal surface, exponentially decaying from it at a sub-wavelength distance in dielectric and in metal. A variety of two-dimensional optical elements for surface polaritons, such as mirrors, lenses, resonators, sources, detectors, etc., have been demonstrated [2]. Moreover, it is possible to implement various SPP waveguiding structures, such as metallic stripes and wires [3–5], grooves and gaps in a metal surface [6,7], metallic wedges [8,9], chains of metallic nanoparticles [10,11] *etc.*

A SPP wave, however, experiences attenuation as it propagates due to Ohmic losses in the metal. Thus approaches to increase SPP propagation length are of outmost importance for future of plasmonic circuits [12-14]. The concept of active plasmonics for switching and modulating of SPP waves all optically or electronically has been also proposed [5,15–18].

These developments facilitate various possible applications of SPPs in telecommunication networks, integrated photonics, and lab-on-a-chip systems.

One prospective type of the waveguide is the dielectric-loaded surface plasmon polariton waveguide (DLSPPW) formed by a dielectric stripe on the top of metal surface [19–25]. The advantage of DLSPPWs compared to other SPP waveguide types is that a dielectric ridge can be easily functionalized to provide thermo-optical, electro-optical, or all-optical functionalities and can be used for the development of active plasmonic components. Moreover, DLSPPWs fabrication is compatible with current lithography process used in the fabrication of electronic circuits. Combined with intrinsic possibility to control optical signals by electronic ones and *vise versa*, this can lead to the realization of hybrid electro-optical devices.

In this paper we will discuss various realisations of plasmonic components for integrated nanophotonic circuits with particular emphasis on the active functionalities such all-optical and electro-optical modulation and amplification of SPP signals.

ACKNOWLEDGMENT

The author acknowledges A. V. Krasavin, P. Bolger, W. Dickson, G. A. Wurtz, J.-S. Bouillard and the members of the EC FP6 STREP PLASMOCOM who contributed in one or another way to the work presented here.

REFERENCES

[1] H. Raether, Surface Plasmons, Berlin: Springer-Verlag, 1988.

[2] A.V. Zayats, I. I. Smolyaninov, and A. A. Maradudin, "Nano-optics of surface plasmon polaritons," Phys. Rep., vol. 408, pp. 131-314, 2005.

[3] J. Krenn and J.-C. Weeber, ""Surface plasmon polaritons in metal tripes and wires," Philos. Trans. R. Soc. London, Ser. A, vol. 362, pp. 739-756, 2004.

[4] J. Takahara, S. Yamagishi, H. Taki, A. Morioto, and T. Kabayashi, "Guiding of a one-dimensional optical beam with nanometer diameter," Opt. Lett., vol. 22, pp. 475-477, 1997.

[5] T. Nikolajsen, K. Leosson, and S. Bozhevolnyi, "Surface plasmon polariton based modulators and switches operating at telecom wavelengths," Appl. Phys. Lett., vol. 85, pp. 5833-5835, 2004.

[6] S. Bozhevolnyi, V. Volkov, E. Devaux, J.-Y. Laluet, and T. Ebbesen, **"**Channel plasmon subwavelength waveguide components including interferometers and ring resonators**,"** Nature, vol. 440, pp. 508-511, 2006.

[7] B. Wang and G. Wang, "Planar metal heterostructures for nanoplasmonic waveguides," Appl. Phys. Lett., vol. 90, 013114, 2007.

[8] M. Yan and M. Qiu, "Guided plasmon polariton at 2D metal corners," J. Opt. Soc. Am. B, vol. 24, pp. 2333-2342, 2007.

This work has been supported by the EC FP6 STREP PLASMOCOM and EPSRC (UK).

[9] D. O'Connor, M. McCurry, B. Lafferty, and A. V. Zayats, “Plasmonic waveguide as an efficient transducer for high-density data storage,” Appl. Phys. Lett., vol. 95, 171112, 2009.

[10] S. A. Maier and H. A. Atwater, “Plasmonics: Localization and guiding of electromagnetic energy inmetal/dielectric structures,” J. Appl. Phys., vol. 98, 011101, 2005.

[11] G. A. Wurtz, W. Dickson, D. O'Connor, R. Atkinson, W. Hendren, P. Evans, R. Pollard, and A. V. Zayats, “Guided plasmonic modes in nanorod assemblies: strong electromagnetic coupling regime,” Opt. Express, vol. 16, pp. 7460-7470, 2008.

[12] J. Grandidier, G. Colas des Francs, S. Massenot, A. Bouhelier, L. Markey, J.-C. Weeber, Ch. Finot, and A. Dereux, “Gain-assisted propagation in a plasmonic waveguide at telecom wavelength,” Nanolett., vol. 9, pp. 2935-2339, 2009.

[13] A. Marini, A. V. Gorbach, D.V. Skryabin, and A. V. Zayats, “Amplification of surface plasmon polaritons in the presence of nonlinearity,” Opt. Lett., vol. 34, pp. 2864-2866, 2009.

[14] P. M. Bolger, W. Dickson, A. V. Krasavin, L. Liebscher, S. G. Hickey, D. V. Skryabin, and A. V. Zayats, "Amplified spontaneous emission of surface plasmon polaritons and limitations on the enhancement of their propagation length," Opt. Lett., in press, 2010.

[15] A. V. Krasavin, K. F. MacDonald, N. I. Zheludev, and A. V. Zayats “High-contrast modulation of light with light by control of surface plasmon polariton wave coupling”, Appl. Phys. Lett., vol. 85, pp. 3369-3371, 2004.

[16] G. A. Wurtz and A. V. Zayats, “Nonlinear surface plasmon polaritonic crystals," Laser and Photon. Rev., vol. 2, pp. 125-135, 2008.

[17] D. Pacifici, H. J. Lezec, and H. A. Atwater, Nat. Phot., vol. 1, 402-405, 2007.

[18] W. Dickson, G. A. Wurtz, P. R. Evans, R. J. Pollard, and A. V. Zayats, “Electronically-controlled surface plasmon dispersion and optical transmission through hole arrays in metal films with liquid crystal,” Nano Letters, vol. 8, pp. 281-286, 2008.

[19] A.V. Krasavin, A.V. Zayats, “Passive photonic elements based on dielectric-loaded surface plasmon polariton waveguides,” Appl. Phys. Lett., vol. 90, 211101, 2007.

[20] T. Holmgaard, Z. Chen, S. I. Bozhevolnyi, L. Markey, A. Dereux, A. V. Krasavin, A. V. Zayats, “Bend- and splitting loss of dielectric-loaded surface plasmon-polariton waveguides,” Opt. Express, vol. 16, pp. 13585-13592, 2008.

[21] A. V. Krasavin, A. V. Zayats, “Three-dimensional numerical modeling of photonic integration with dielectric-loaded SPP waveguides,” Phys. Rev. B, vol. 78, 045425, 2008.

[22] T. Holmgaard, S. I. Bozhevolnyi, L. Markey, A. Dereux, A. V. Krasavin, P. Bolger, and A. V. Zayats, “Efficient excitation of dielectric-loaded surface plasmon-polariton waveguide modes at tele-communication wavelengths,” Phys. Rev. B, vol. 78, 165431, 2008.

[23] Z. Chen, T. Holmgaard, S. I. Bozhevolnyi, L. Markey, A. Dereux, A. V. Krasavin, and A. V. Zayats, “Wavelength selection by dielectric-loaded plasmonic components,” Appl. Phys. Lett., vol. 94, 051111, 2009.

[24] Z. Chen, T. Holmgaard, S. I. Bozhevolnyi, A. V. Krasavin, A. V. Zayats, L. Markey, and A. Dereux, “Wavelength-selective directional coupling with dielectric-loaded plasmonic waveguides,” Opt. Lett., vol. 34, pp. 310-312, 2009.

[25] A. V. Krasavin and A. V. Zayats, “Silicon-based plasmonic waveguides,”, to be published.

Fabrication of a CMOS backend-compatible electrical surface plasmon polaritons source

I. Brunets, J. Schmitz
MESA+ Institute for Nanotechnology
Chair of Semiconductor Components
University of Twente
Enschede, The Netherlands
i.brunets@utwente.nl

R.J. Walters, R.V.A. van Loon and A. Polman
Center for Nanophotonics
FOM Institute for Atomic and Molecular Physics
Amsterdam, The Netherlands

***Abstract*—This paper details the low-temperature manufacturing process chosen for the first realization of a CMOS-backend-compatible surface plasmon polariton source. The optically active multilayer Al_2O_3/Si-nanodots stack is formed at low temperatures (300-325 °C) by a combination of ALD and CVD techniques. The choice of materials, precursors and dimensions is explained from materials analysis results and integration considerations.**

Keywords-component; surface plasmon polariton (SPP), 3-D integration, ALD, CVD, nanodots, silicon, electroluminescence

I. INTRODUCTION

The prospective implementation of optical data transfer within IC's requires efficient, CMOS-compatible light sources. However, integrated circuit components have nowadays reached dimensions much smaller than the dimensions of typical micro-optical components. This "size mismatch" is regarded as a practical concern for a variety of integrated optics applications. The application of surface plasmon polaritons (SPPs) generated at metal/dielectric interfaces provides light confinement and control at length scales below 100 nm, herewith overcoming this size mismatch [1], [2]. The SPP can propagate with an effective wavelength much smaller than the free-space wavelength of photons at the same frequency. In contemporary SPP research, plasmons are normally generated by external lasers. In a recent article [2] we have presented an electrical SPP source, operating at low supply voltage, and manufactured using CMOS backend compatible techniques.

In this paper we discuss the details of the manufacturing process used for these novel plasmonic devices [2]. In our devices the metal–insulator–metal (MIM) plasmon waveguide geometry is used for electrically driven SPP sources. The optically thick gold cladding layers support and guide the SPP mode and also serve as contact electrodes. When a sufficient voltage is applied across the insulator layer of alumina that contains silicon quantum dots, tunneling electrons excite the embedded quantum dots by impact ionization processes. As the insulator layer of this MIM waveguide is too thin to support photonic modes, the excited quantum dots decay radiatively predominantly by direct near-field coupling to plasmonic modes. This results in the electrically driven excitation of SPPs over a spectral range determined by the properties of the silicon quantum dots.

Usually, silicon nanodots are created in a silica host material by annealing silicon-rich silicon oxides at high temperatures (>900 °C). This approach is incompatible with back-end CMOS processing. To lower the thermal budget of fabrication the optically active layer stack with embedded silicon nanodots has been formed by sequential atomic layer deposition (ALD) of Al_2O_3 (at 300 °C) and low-pressure chemical vapour deposition (LPCVD) of silicon nanodots (at 325 °C) [3]. Encapsulation in an Al_2O_3-matrix, realized without vacuum break, provides a sufficient passivation and prevents further oxidation of the Si-ND layers during the subsequent processing steps.

II. EXPERIMENTAL

The multilayer stack was deposited on bare p-type silicon wafers with (100) orientation. First, the standard cleaning procedure was applied. Afterwards, to etch the native oxide and to avoid metal contamination, the wafers were briefly (around 1.5 minutes) dipped in a solution of 0.3% HF and 0.3% HCl.

Directly afterwards, the hydrogen-terminated silicon wafers were placed into the loadlock of a cluster system with three separate reactors [3]. Five layers of Al_2O_3 and four interstitial layers of nanodots were grown at temperatures ranging from 300 to 325 °C without a vacuum break for a total insulator layer stack thickness of 100 nm.

A. ALD of Al_2O_3

The 20-nm thick Al_2O_3 layers were deposited by atomic layer deposition at a temperature of 300 °C in reactor 3 of the cluster system. The wafer was sequentially exposed to $Al(CH_3)_3$ (Trimethylaluminum, or TMA) and H_2O, with a N_2 purge cycle in between (245 cycles in total) [4]. The deposition rate of alumina was 0.08 nm per cycle. After the deposition, the wafer was transferred to reactor 1 to perform the film thickness measurements using spectroscopic ellipsometry.

B. *LPCVD of Si-nanodots*

Without vacuum beak, the wafer was transferred to reactor 2, where silicon nanodots were deposited in LPCVD mode from trisilane (Si_3H_8) at 325 °C and 1 mbar reactor pressure. Temperature and time were optimized to achieve a high nucleation density at practical deposition times. The deposition time was varied in range between 10 and 30 minutes resulting in up to ~3 nm thick Si-nanodots with single-layer areal nanodots density reaching 2×10^{12} cm^{-2} (shown in Figure 1).

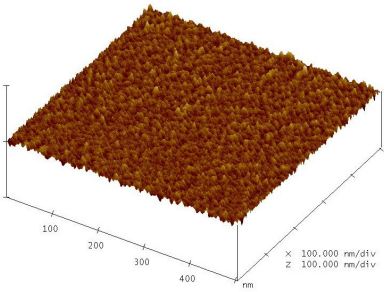


Figure 1. AFM images of oxidized Si-ND layers deposited at 325°C from Si_3H_8 at 1 mbar. To enable the observation of the nanodots, no upper protection layer was deposited. Deposition time 10 minutes.

A final structure with four layers of silicon nanodots encapsulated in Al_2O_3-matrics was formed. Figure 2 shows a transmission electron microscope (TEM) image of a cross-section of a similar structure where the thicknesses of Al_2O_3 layers were 10 nm. The energy filtered TEM analyses confirmed a discontinuous character of the silicon layers.

C. *Metalization*

After deposition of the functional layer stack, the 200-nm top gold cladding/contact layer was formed by sputtering. On the reverse side of the wafer, a 300 nm thick SiO_2 film was deposited by PECVD and patterned to serve as a hard mask for a tetramethyl ammonium hydroxide anisotropic etch solution. The wafer was back-etched to the alumina layer to create membranes of 50×100 µm. Then the top gold layer was patterned and etched after separating the dies. The bottom cladding/contact layer was then formed by sputtering 200 nm of gold to the bottom side of the die through a physical mask.

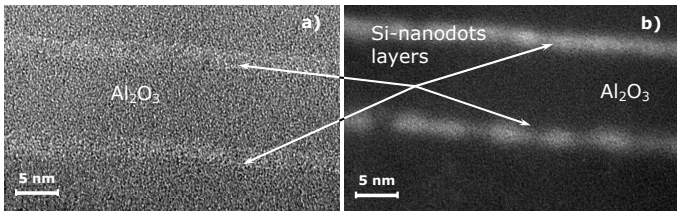


Figure 2. High Resolution (a) and Energy Filtered TEM images (b) depicting the cross-section of the multilayer stack with Si-ND embedded in an Al_2O_3-matrix.

III. Results and Discussion

The influence of process parameters on the quality of the nanodot layers was investigated. A dramatic increase of silicon nucleation and growth rate was observed, when using Si_3H_8 as a precursor in comparison to Si_2H_6 or SiH_4. Similar nucleation enhancement was previously reported for deposition temperatures between 400-500 °C [5] and higher. A decrease of the Si-ND deposition time (i.e. smaller size of Si-ND's) provided a gradual shift of the photoluminescence peak to higher photon energies (shown in Figure 3a), indicating exciton confinement in the nanocrystals. The subsequent annealing in forming gas (10% H_2:N_2) at 500 °C for 10 minutes resulted in an increase in the photoluminescence spectra maximum of up to 400% of the initial intensity, as shown in Figure 3b. The quantum efficiency for Si-ND in alumina matrix is estimated to be about 0.3%. The electroluminescence spectrum was measured at various biasing conditions, and is shown in Figure 3c.

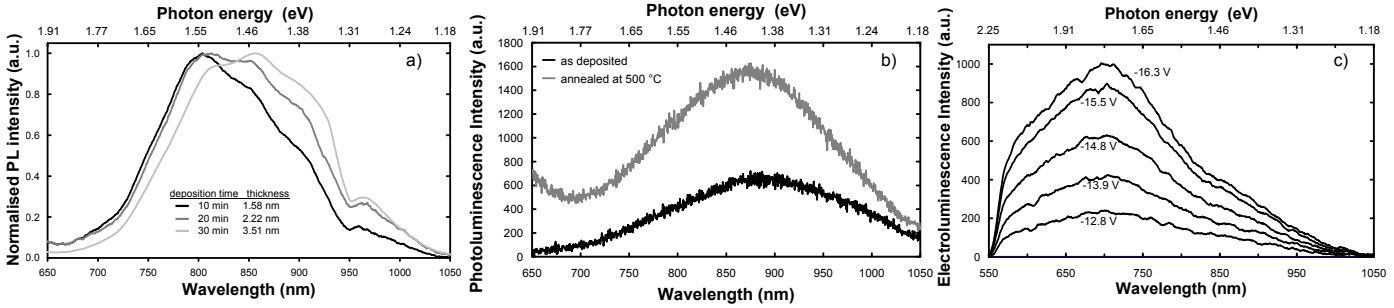


Figure 3. PL spectra measured for (a) layers with different thicknesses (excited using the 488 nm line of an Ar+ laser); (b) samples annealed in forming (10% H_2:N_2) gas atmosphere showing an enhancement of the luminescence in comparisson to as deposited sample; (c) EL spectrum at various biasing conditions,

References

[1] W. L. Barnes, A. Dereux, and T. W. Ebbesen, "Surface plasmon subwavelength optics," Nature, vol. 424, pp. 824-830, 2003.

[2] R. J. Walters, R. V. A. van Loon, I. Brunets, J. Schmitz, and A. Polman, "A silicon-based electrical source of surface plasmon polaritons," Nature Materials, vol. 9, pp. 21-25, 2010.

[3] I. Brunets, A. A. I. Aarnink, A. Boogaard, A. Y. Kovalgin, R. A. M. Wolters, J. Holleman, and J. Schmitz, "Low-temperature LPCVD of Si nanocrystals from disilane and trisilane (Silcore®) embedded in ALD-alumina for non-volatile memory devices," Surface and Coatings Technology, vol. 201, pp. 9209-9214, 2007.

[4] R. Bankras, J. Holleman, J. Schmitz, M. Sturm, A. Zinine, H. Wormeester, and B. Poelsema, "In Situ Reflective High-Energy Electron Diffraction Analysis During the Initial Stage of a Trimethylaluminum/Water ALD Process," Chemical Vapor Deposition, vol. 12, pp. 275-279, 2006.

[5] P. R. Fischer, S. Van Aerde, E. Oosterlaken, B. Bozon, P. M. Zagwijn, M. Bauer, M. Yan, and W. Verweij, "Low Temperature Silcore® Deposition of Undoped and Doped Silicon Films," ECS Transactions, vol. 3, pp. 203-215, 2006.

Two-photon reduction technique for isotropic metamaterials

Takuo Tanaka
Metamaterials Laboratory
RIKEN Advanced Science Institute
2-1 Hirosawa, Wako, Saitama, JAPAN
t-tanaka@riken.jp

***Abstract*—The electromagnetic properties and design strategy of plasmonic metamaterials in the optical spectral range are theoretically investigated. The fabrication techniques for the three-dimensional isotropic metamaterials are also proposed. Three-dimensional nano-scale silver or gold structures are demonstrated.**

Keywords-component; metamaterials; resonator; plasmonics; two-photon absorption; reduction; 3D structure

I. INTRODUCTION

Plasmonic metamaterial is a structure that consists of metal resonator array. Designing resonator array structure so that it is smaller than the wavelength of the light, metamaterials woks as a homogeneous material whose electromagnetic properties inherited from its structure. By engineering such materials, we can design and control their magnetic permeability even in the optical frequency region in which all materials in nature lose magnetic response and their relative permeability is fixed at unity. In this paper, we report on the theoretical investigations of the artificial magnetism of metamaterials in the visible light. Moreover, we also present a two-photon-induced metal-ion reduction technique in a metal-ion doped materials for fabricating 3D isotropic metamaterials.

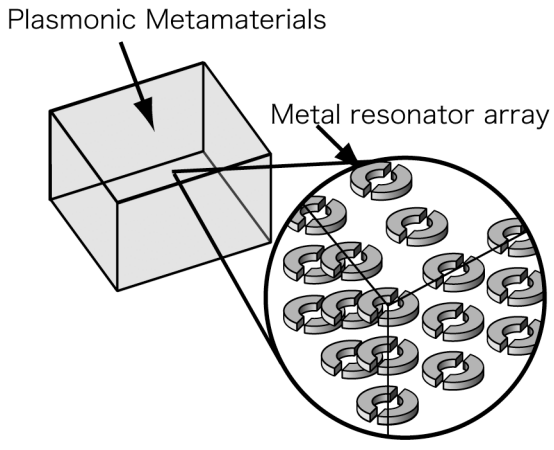


Figure 1 Plasmonic metamaterials.

II. PLASMONIC METAMATERIALS AND THEIR EFFECTIVE PERMEABILITY

We have theoretically investigated the magnetic response of plasmonic metamaterials in the optical frequency region [1-4]. Figure 2 shows the split ring-resonator (SRR) model used in our calculations. Describing the dispersion properties of the metals in the optical region, we derived the effective permeability (μ_{eff}) of the SRRs as

$$\mu_{eff} = \mu_{\mathrm{Re}} + i\mu_{\mathrm{Im}} = 1 - \frac{F\omega^2}{\omega^2 - \frac{1}{CL} + i\frac{Z(\omega)\omega}{L}}, \qquad (1)$$

where F is the filling factor, C and L are the geometrical capacitance and inductance, and $Z(\omega)$ is the ring metal impedance. Using equation (1) we calculated the frequency dispersion of μ_{eff} from 100THz to 800THz covering the entire visible light frequency region taking into account the electro-magnetic properties of the metals (silver, gold, and copper).

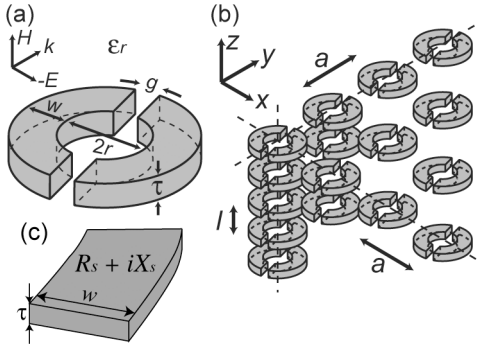


Figure 2 Models of metamaterial structure used in calculations.

As shown in Figure 3(a), the effective permeability μ_{eff} changes both positively and negatively at the resonant frequency of the SRRs array. In Figure 3(b), we plotted the calculation results of the change of μ_{eff}, which means the difference between max μ_{eff} and min μ_{eff} as shown in Fig. 3(a), for each metal SRRs array. From these results we have

clarified that a three-dimensional array of split-ring-resonators made of silver can give a strong magnetic response in the visible light frequency region. As also shown in Fig. 3(b), silver SRRs exhibit μ_{eff} changes exceeding 2.0 in the entire visible range, which means μeff can become a negative value, while the responses of gold and copper SRRs do not exceed 2.0 in the visible light region.

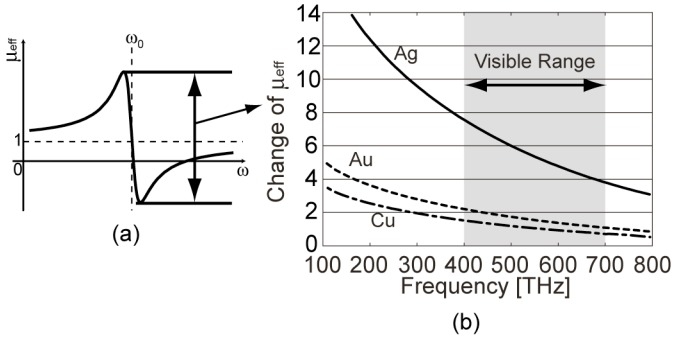


Figure 3 Frequency dependencies of the change of effective permeability (μ_{eff}) of SRRs made of silver, gold, and copper.

III. TWO-PHOTON REDUCTION METHOD

To create a plasmonic metamaterial structure, the fabrication technique requires the ability to make arbitrary three-dimensional metallic structures. To satisfy this requirement, we have proposed a new fabrication technique that uses two-photon induced reduction of metal complex ions [5-9].

Figure 4 shows a schematic of the two-photon reduction technique. A mode-locked Ti:Sapphire laser system with a center wavelength of 800 nm, a pulse width of 80 fs, and a repetition frequency of 82 MHz was used as a light source. The laser beam was focused inside the metal-ion solution using an oil-immersion objective lens. The focused laser beam was scanned in two dimensions (x-y scanning) using a pair of galvanometer mirrors, and was also scanned in the longitudinal direction (z-scanning) by translating the objective lens using a computer-controlled motor stage.

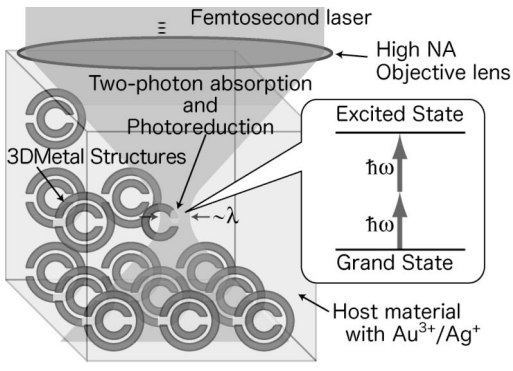


Figure 4 Schematic of two-photon-induced metal-ion reduction by focused fsec NIR laser irradiation.

Figure 5 shows the 3D metal structures fabricated using a silver ion aqueous solution with Coumarin 440 dye. Fig. 5(a) and (b) show a silver 3D gate structure and a top-heavy silver cup, respectively. Fig. 5(c) shows 3D silver pyramid structues with 200nm line width. This nano-meter scale resolution was achieved by the metal crystallization control using dopant surfactant molecules. These structures also have sufficient strength to endure cleaning with water; that is, they were not destroyed by the surface tension of the meniscus when removing the ion solution. The resistance of the 3D silver gate (Fig. 5(a)) was 4.59 kΩ as measured by connecting each foot to a silver electrode with silver wire. This result indicates that the fabricated 3D silver microstructure is also electrically conductive.

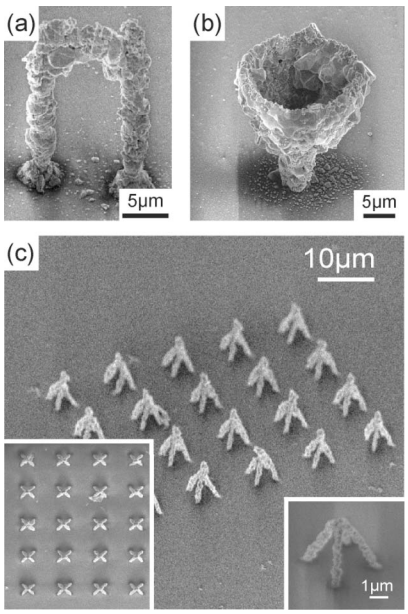


Figure 5 3D matal structures fabricated by two-photon reduction technique.

REFERENCES

[1] A. Ishikawa, T. Tanaka, and S. Kawata, Phys. Rev. Lett. **95**, 237401 (2005).

[2] A. Ishikawa, and T. Tanaka, Opt. Commun. **258**, pp. 300-305 (2006).

[3] A. Ishikawa, T. Tanaka, and S. Kawata, J. Opt. Soc. Am. B **24**, 3, pp. 510-515 (2007).

[4] T. Tanaka, A. Ishikawa, and S. Kawata, Phys. Rev. B **73**, 125423 (2006).

[5] T. Tanaka, A. Ishikawa, and S. Kawata, Appl. Phys. Lett. **88**, 81107 (2006).

[6] A. Ishikawa, T. Tanaka, and S. Kawata, Appl. Phys. Lett. **89**, 113102 (2006).

[7] N. Takeyasu, T. Tanaka, and S. Kawata, Appl. Phys. A **90**, pp. 205-209 (2008).

[8] T. Tanaka, J. Laser Micro/Nanoengineering **3**, pp. 152-156 (2008).

[9] Y. Cao, N. Takeyasu, T. Tanaka, X. Duan, and S. Kawata, Small **5**, pp. 453-458 (2009).

Optical modulators in silicon

G.T.Reed , F.Y.Gardes
Advanced Technology Institute, University of Surrey,
Guildford, Surrey, GU2 7XH, United Kingdom
G.Reed@surrey.ac.uk

Abstract—**Silicon Photonics is highly topical at present, having the potential to impact many application areas. Currently, the main focus is on various forms of optical interconnect as this is also the focus of a number of companies, some of whom have also released products into the market place. However, the implementation of silicon photonics for mass production will also benefit a range of other application areas. One of the key components that will enable silicon photonics to flourish is a high performance optical modulator. In this paper, an overview is given of the major Si photonics modulator research that has been pursued at the University of Surrey to date, as well as an overview of the state of the. We will show the trend taken toward integration of optical and electronic components with the difficulties that are inherent in such a technology**

Keywords- Silicon-On-Insulator (SOI), silicon photonics, Optical modulator, Depletion, Accumulation

I. INTRODUCTION

Recently, computer processing power has increased dramatically and nowadays common desktop computers are able to deliver a few billion floating points operation per second (FLOPs). Intel recently reported an 80 core processor capable of delivering more than 1 TFLOPs. Furthermore, storage media is moving towards solid state drives where transfer rates are steadily increasing, and requires correspondingly fast interconnects able to provide a sufficient data rate.

The computing market is leading the way with storage media and processing power for which interconnects will have to be able to deliver information in excess of 10Gb per second, up to a Tb per second in the near term. In this regard silicon photonic circuits, may be the technology of choice, primarily because of the attraction of integration of electronic and photonic functionality in a cost effective manner, and also because silicon on insulator substrates have proved successful for high volume processing of very low loss waveguides, of the order of 0.1 dB/cm. Almost every optical circuit can be replicated in silicon but in order to achieve a very high data rate, a fast and efficient optical modulation function is required, using a CMOS compatible process in Silicon on insulator.

II. RECENT DEVELOPMENT IN OPTICAL MODULATORS IN SILICON

In 2007, Liu et al.[2] experimentally demonstrated a pn carrier depletion based silicon optical modulator with a structure very similar to that proposed by Gardes et al. [3] in 2005. The structure is a horizontal pn junction inserted in a rib waveguide where the top of the rib and the slab of the waveguide are connected to a highly doped area forming a resistive contact. This device was the first to demonstrate the possibility to achieve a bandwidth of 30 GHz and a data rate of 40 Gb/s

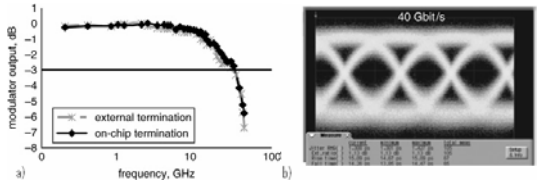


Figure 1: a) Represent the response of the modulator as a function of the RF frequency for a 1 mm active area. (b) Optical eye diagram of the modulator with a 1 mm long active area [2]

In 2008 Liu et al[4] reported a configuration of 8 MZIs based on the same modulator. The modulators were operated at 25Gb/s with an extinction ratio of 2dB. The amplified single-ended output of 3.2 V_{pp} (6.4 V_{pp} differential) was combined with 2 V_{dc} using a bias Tee to ensure reverse bias operation for the entire AC voltage swing. The DEMUX is shown Figure 2 and showed the possibility of transmitting data at an aggregate data rate of 200 Gb/s.

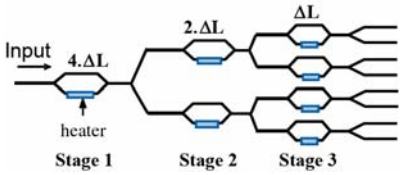


Figure 2: Schematic of the 8 channel DEMUX based on asymmetric MZIs; 4·ΔL=97.2 um for Δλ=3.2 nm around 1550 nm, where $a.\Delta L$ and $\Delta\lambda$ are the length difference between two arms of the asymmetric MZIs and optical channel spacing, respectively.

Recently, Park et al.[5] reported a carrier depletion MZI based modulator in 220 nm overlayer SOI using high p and n doping concentrations positioned vertically in a 220 nm high, 500 nm wide rib waveguide to achieve a high efficiency. They showed an eye diagram demonstrating a data rate of 12.5 Gb/s. This structure is also similar to one of the designs proposed by Gardes et al [6]. A $V_\pi L_\pi$ efficiency of 2 V.cm and a loss of approximately 4dB/mm were reported. A 3dB electro-optic bandwidth of 7.1GHz was reported and data transmission was demonstrated at 12.5 Gb/s and 4Gb/s with extinction ratios of approximately 3dB and 7dB respectively.

Modulation in a SOI based ring resonator structure has also been demonstrated with an electro-optic bandwidth in excess of 35 GHz by Gill et al [7]. The modulator here is also based

on SOI and the vertical pn junction is inserted in an overlayer of approximately 230 nm. The interesting feature of this device is the possibility to control the resonance of the ring by replacing the coupler by an MZI hence enabling a full control on the extinction ratio of the ring. Modulation is performed by switching the ring into and out of resonance.

Moving away from pn junction modulators, it is interesting to note that recently a modulator based on accumulation of carriers on both sides of an oxide region has been reported by Lightwire Inc[8, 9]. This device is based on the same principle used in [10] but reported a much higher efficiency, with a $V_\pi L_\pi$ of 2 V.mm which provides a compact device occupying (800um x 15um). The eye diagram indicates data transmission at 10 Gb/s with an extinction ratio of almost 9 dB. One of the possible drawbacks of this device and all reported devices based upon carrier accumulation, is the relative complexity of the fabrication process required to produce the MOS capacitor-like structure.

III. SURREY THE EARLY YEARS

The University of Surrey has been active in the development of innovative carrier injection devices since their inception, and more recently of depletion based modulators. Surrey experimental work on modulation was first reported by Tang et al [11] in 1994, in support of an earlier simulation paper in 1993 [12]. This showed that it was possible to obtain a net increase in the concentration of injected carriers into the waveguiding region of a phase modulator [11, 13] by changing the sidewall angle of the rib from vertical to 54.7 degrees. At the time when these devices were fabricated, the typical current densities were of the order of kA/cm^2 [14]. Therefore, with an experimental drive current of 7 mA, and current density of 175 A/cm^2, this device represented an improvement in the current density, and hence power consumption, of approximately an order of magnitude. Modulation bandwidths were in the range 5 – 20 MHz for different device variants.

In 2000, Hewitt et al. [15] used computer simulation to reconsider a simple two terminal p-i-n modulator based on a 5.5 μm SOI rib waveguide. It was predicted that even for a two terminal device, significant optimization is possible. For example, an increase in the doping concentrations of the p+ and n+ regions, from 1019 cm–3 to 1020 cm–3, results in a drive current decrease from 63 to 8 mA while the transient rise time also decreases from 110 ns to 105 ns.

At the same time, the placement of the doping windows forming the resistive contacts was also found to improve/degrade device transient characteristics. Rise time was reduced from 184 ns when the resistive contact was located 7 μm from the centre of the waveguide, to 39 ns when the distance was reduced to 3 μm [15]. Whilst the study was conducted for a specific device geometry, it was argued by the authors that the trends observed in the results, would have applicability in other device configurations.

From the work of Hewitt and others [15, 16] it is clear that three terminal devices required less drive current (2.8 mA vs 8 mA) and are faster than two terminal devices(29 ns vs 39 ns), for an equivalent injection concentration. This is because; three terminal devices offer more efficient carrier injection. The potential drawback of these devices is that additional optical attenuation may occur due to the doping contact at the rib top.

Png *et al*.[17],in 2003/4 improved upon the work of Ang *et al* [18]., by modelling devices with a three terminal geometry, but with improved performance[19-21]. In particular, a series of devices were modelled with intrinsic bandwidths ranging from 70 MHz to in excess of 1 GHz. The devices were based around a rib waveguide, approximately 1μm in height and between 0.5 μm and 0.75 μm wide. A feature of these devices was the optimized doping profile in the n^+ regions to optimize injection efficiency. In 2004 Png *et al.* [17] also reported the technique of pre-emphasis on critical device rise and fall times to increase device speed, improving the previously proposed device from 95 MHz to 5.8 GHz. Using such a scheme, a class of devices with nominal operating speeds of 1 GHz could theoretically be switched in excess of 40 GHz[22]. The pre-emphasis driving scheme is currently employed for high speed operation of silicon modulators up to 18 Gb/s [23, 24].

In order to increase the bandwidth further, a sub-micrometer modulator based on the depletion of a p-n junction was proposed in 2005 by Gardes *et al*. [3] In common with the MOS capacitor, the depletion type phase shifter is not limited by the minority carrier recombination lifetime and is based on the principle of removing carriers from the junction area when applying a reverse bias. The structure was 550 nm high 405 nm wide with a four terminal asymmetric horizontal pn structure, where the concentration of n-type doping is much higher than the concentration of p-type doping. The reason for such a structure is firstly to minimize the optical losses induced by the n-type doping and secondly to enhance the depletion overlap between the optical mode and the p-type region, in order to induce a better phase shift to length ratio. The carrier concentration variation in this kind of device is not uniform and arises on both sides of the junction over a width of around 200 nm. One way to optimize the device is by increasing the overlap between the optical mode and the p-type depleted region. The main advantage of using depletion is obviously the very fast response time, simulated to be 7 ps for this modulator. This corresponds to an intrinsic bandwidth of approximately 50 GHz. The device proposed by Gardes et al was 2.5 mm long and operated with a reverse bias swing of 5 Volts in a push-pull configuration as part of a Mach Zehnder interferometer (MZI). To further improve compactness and simplify fabrication, a modulator based on a depletion of a vertical pn junction was demonstrated by Gardes et al. [6]. The ring resonator modulator is based on a 300 nm wide, 150 nm etch depth and 200 nm high rib waveguide, which enables single mode transmission. The pn junction is asymmetrical in size and in doping concentration in order to maximize the area of hole depletion that overlaps with the optical mode. The n-type region is 75 nm wide and the p type 225 nm wide, and the net doping concentration of this particular junction varies between 6 x 10^{17}.cm^{-3} and 2 x 10^{17}.cm^{-3}, for n and p types, respectively. The junction was fabricated using ion

implantation at CEA Leti in France, and the Ion Beam Centre at the University of Surrey. The modulator exhibited a DC on/off ratio of 5 dB at -10 V, and a 3 dB bandwidth of 19 GHz.

This showed the trend in miniaturization of the devices to obtain maximum performance in terms of mode confinement, frequency of operation and power consumption, where the ultimate goal is to integrate electronic drivers and optical building blocks on the same substrate, also referred to as "front end integration".

IV. SILICON PHOTONICS IN EUROPE

Following the results obtained in the field of high speed modulation in silicon photonics two relatively large consortium based projects have been funded in Europe to demonstrate and establish the possibilities offered by silicon photonics. The first project is UK based " UK silicon photonics" [25] and the second is a European based project called "Helios" [26] . The mission of the two projects is to demonstrate building blocks that will be use to achieve large scale integration. Innovative means are to be developed to combine a photonic layer with electronic circuitry, using microelectronics fabrication processes. One of the aims of the two projects is to develop optical modulation for 10 Gb/s and 40 Gb/s while improving figures of the state of the art in terms of efficiency and modulation extinction ratio. Furthermore, extensive research is applied to the fabrication of the components to enable reliable fabrication processing in order to obtain high yields

V. SUMMARY CONCLUSION

The state of the art in silicon photonics is varying at an enormous rate, with innovations being reported very frequently. Integration is one of the most topical subject areas and within the field of integration, optical modulators is a key component as it defines most of the chip parameters such as power consumption, size and speed of operation. This paper has discussed the state of the art, with emphasis on the work at the University of Surrey. Whilst significant progress continues to be made, device performance still needs to improve to be viable for high performance optical modulation, and particularly to move towards high scale integration of silicon photonic components with electronic functionality.

Acknowledgements

This work has been funded by the Engineering and Physical Sciences Research Council (EPSRC) programme, "UK Silicon Photonics".

[1] Intel, "Intel Research Advances 'Era Of Tera'," 2007.

[2] A. Liu, L. Liao, D. Rubin, H. Nguyen, B. Ciftcioglu, Y. Chetrit, N. Izhaky, and M. Paniccia, "High-speed optical modulation based on carrier depletion in a silicon waveguide," Optics Express, vol. 15, pp. 660-668, 2007.

[3] F. Y. Gardes, G. T. Reed, N. G. Emerson, and C. E. Png, "A sub-micron depletion-type photonic modulator in silicon on insulator," Optics Express, vol. 13, 2005.

[4] L. Ling, L. Ansheng, J. Basak, H. Nguyen, M. Paniccia, Y. Chetrit, and D. Rubin, "Silicon photonic modulator and integration for high-speed applications," in Electron Devices Meeting, 2008. IEDM 2008. IEEE International, 2008, pp. 1-4.

[5] J. W. Park, J.-B. You, I. G. Kim, and G. Kim, "High-modulation efficiency silicon Mach-Zehnder optical modulator based on carrier depletion in a PN Diode," Opt. Express, vol. 17, pp. 15520-15524, 2009.

[6] F. Y. Gardes, A. Brimont, P. Sanchis, G. Rasigade, D. Marris-Morini, L. O'Faolain, F. Dong, J. M. Fedeli, P. Dumon, L. Vivien, T. F. Krauss, G. T. Reed, and J. Martí, "High-speed modulation of a compact silicon ring resonator based on a reverse-biased pn diode," Opt. Express, vol. 17, pp. 21986-21991, 2009.

[7] D. M. Gill, M. Rasras, T. Kun-Yii, C. Young-Kai, A. E. White, S. S. Patel, D. Carothers, A. Pomerene, R. Kamocsai, C. Hill, and J. Beattie, "Internal Bandwidth Equalization in a CMOS-Compatible Si-Ring Modulator," Photonics Technology Letters, IEEE, vol. 21, pp. 200-202, 2009.

[8] http://www.lightwire.com/, 2009.

[9] http://www.ofcnfoec.org/conference_program/2009/images/09-DAndrea.pdf, 2009.

[10] A. Liu, R. Jones, L. Liao, D. Samara-Rubio, D. Rubin, O. Cohen, R. Nicolaescu, and M. Paniccia, "A high-speed silicon optical modulator based on a metal-oxide-semiconductor capacitor," Nature, vol. 427, pp. 615-18, 2004/02/12 2004.

[11] C. K. Tang and G. T. Reed, "Highly efficient optical phase modulator in SOI waveguides," Electronics Letters, vol. 31, pp. 451-452, 1995.

[12] C. K. Tang, G.T. Reed, A.J. Wilson, and A.G. Rickman, "Simulation of a low loss optical modulator for fabrication in SIMOX material," in Silicon-Based Optoelectronic Materials Symposium, 12-14 April 1993, San Francisco, CA, USA, 1993, pp. 247-52.

[13] C. K. Tang, G.T. Reed, A.J. Wilson, and A.G. Rickman, "Low-loss, single-mode, optical phase modulator in SIMOX material," J. Lightwave Technol., vol. 12, pp. 1394-1400, October 1994.

[14] J. P. Lorenzo and R. A. Soref, "1.3 mm electro-optic silicon switch," Appl. Phys. Lett., vol. 51, pp. 6-8, 1987/07/05 1987.

[15] P. D. Hewitt, and G.T. Reed, "Improving the response of optical phase modulators in SOI by computer simulation," Journal of Lightwave Technology, vol. 18, pp. 443-450, March 2000.

[16] P. D. Hewitt and G. T. Reed, "Multi micron dimension optical p-i-n modulators in silicon-on-insulator," San Jose, CA, USA, 1999, pp. 237-43.

[17] C. E. Png, S. P. Chan, S. T. Lim, and G. T. Reed, "Optical phase modulators for MHz and GHz modulation in silicon-on-insulator (SOI)," Journal of Lightwave Technology, vol. 22, pp. 1573-1582, 2004.

[18] T. W. Ang, G. T. Reed, A. Vonsovici, A. G. R. Evans, P. R. Routley, and M. R. Josey, "0.15 dB/cm loss in Unibond SOI waveguides," Electronics Letters, vol. 35, pp. 977-8, 1999/06/10 1999.

[19] R. M. H. Atta, G. J. Ensell, A. G. R. Evans, C. E. Png, and G. T. Reed, "Fabrication of a highly efficient optical modulator based on silicon-on-insulator," Maspalonas, Gran Canaria, Spain, 2003, pp. 495-501.

[20] C. E. Png, G. Masanovic, and G. T. Reed, "Coupling to 1 micron silicon modulators," San Jose, CA, USA, 2002, pp. 62-9.

[21] C. E. Png, G. T. Reed, R. M. H. Atta, G. Ensell, and A. G. R. Evans, "Development of small silicon modulators in Silicon-On-Insulator (SOI)," San Jose, CA, United States, 2003, pp. 190-197.

[22] C. E. Png, "Silicon-on-insulator phase modulators," PhD thesis, University of Surrey, 2004.

[23] S. Manipatruni, X. Qianfan, B. Schmidt, J. Shakya, and M. Lipson, "High Speed Carrier Injection 18 Gb/s Silicon Micro-ring Electro-optic Modulator," in Lasers and Electro-Optics Society, 2007. LEOS 2007. The 20th Annual Meeting of the IEEE, 2007, pp. 537-538.

[24] W. M. J. Green, M. J. Rooks, L. Sekaric, and Y. A. Vlasov, "Ultra-compact, low RF power, 10 Gb/s silicon Mach-Zehnder modulator," Opt. Express, vol. 15, 2007.

[25] "http://www.uksiliconphotonics.co.uk/," 2009.

[26] "http://www.helios-project.eu/," 2009.

8x8 λ-router in Silicon-on-insulator Technology for Optical Networks on Chip

G. F. Fan, R. Orobtchouk
Institut des Nanotechnologies de Lyon (INL), CNRS UMR5270, Université de Lyon, INSA-Lyon, Bât "Blaise Pascal", 7 avenue Jean Capelle, Villeurbanne F-69621, France
e-mail: regis.orobtchouk@insa-lyon.fr

J. M. Fédéli
CEA-LETI, Minatec, CEA-Grenoble, 17 rue des Martyrs, F-38054 GRENOBLE cedex 9, France

Abstract— **In this paper, we demonstrate a compact 8x8 λ-router using multimode- interference (MMI) crossing based on the microring resonator. The 8x8 λ-router was designed and fabricated with a CMOS compatible silicon on insulator technology. The experimental results are in good agreement with the modeling. The basic add drop filters of the devices exhibit losses of -2 dB and on/off contrast of the resonance of 20 dB. The total losses for one channel are about -4 dB and the imbalance between the 8 channels is lower than 2 dB.**

Keyword Si photonics, ring resonator, add-drop filter, λ-router

I. INTRODUCTION

To satisfy the interconnect requirements of chip multiprocessors in the future, Optical network on chip (ONoC) have recently become popular as one solution for increasing bandwidth, decreasing latency and reducing power [1-3]. ONoC provides an optical link between a certain number of input ports and output ports by routing signals based on their wavelengths,and is composed of three types of blocks: (1) transmitters, (2) passive integrated photonic routing structure (λ-router) and (3) receivers [4]. The λ-router is a passive wavelength-routed optical network constituting the core of the ONoC, which is composed of add-drop filters.

II. ROUTER ARCHITECTURE

A 8x8 optical network on chip is shown in Fig.1, each square in Fig.1 represents an add-drop filter.

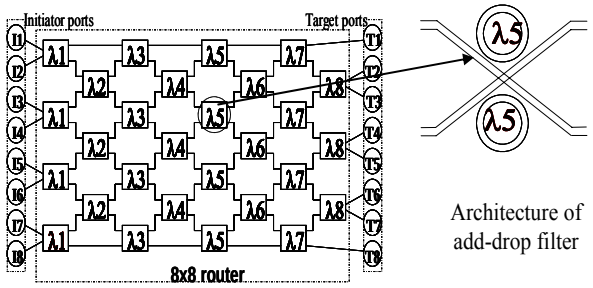


Fig.1 Schematic view of a 8x8 ONoC.

The add-drop filter is λ-router basic building block. It works in a similar way to a classical electronic switch from a functional view [4], where the non-resonant signal propagates in diagonal direction and the resonant is dropped in straight direction as shown in Fig.2.

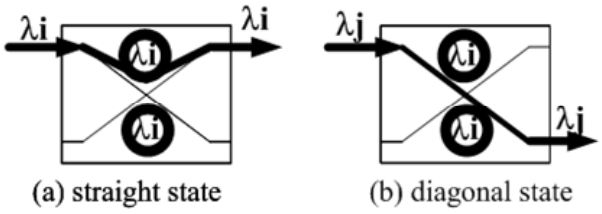


Fig.2 Functional states of add-drop filter.

The optical path of the signal in the 8x8 network depends on the signal wavelength. For example, if the initiator port I4 wants to communicate to the target port T4, then, I4 must send signal with wavelength λ8 through the λ-router.

III. ADD DROP FILTER

The microring resonator is formed by tightly bent Silicon-On-Insulator (SOI) waveguides. Compared with racetrack resonators, microring resonators have a wider free spectral range (FSR), a smaller size and a better quality factor [6-7].

The modeling of the add-drop filter is performed with full vectorial finite difference mode solvers to calculate the variation of the effective index and the losses versus the wavelength of the modes that propagate in the straight and bend waveguides. The coupled modes theory (CMT) is used to calculate the spectral response of the device. The final design of the add-drop filter is validated with a 3D FDTD calculation.

In the basic building blocks of the λ-router, 2 by 2 MMIs are used to reduce the cross talk and the crossing losses of the device. 2.5 μm radius microrings with a radius difference of 10 nm allow a free spectral range of 24 nm and a spacing between channels of 3 nm.

As the radius of the μring is very low, the width of the input and output straight waveguide of each add-drop filter is reduced to 0.38 μm in order to increase the coupling factor with the ring resonator.

This work was funded by a STREP European program "WADIMOS".

IV. FABRICATION AND CHARACTERIZATION

Based on the analysis of the previous section, we design and fabricate the 8x8 λ-router on 200nm CMOS line as shown in Fig.3. The radius difference of every close microring is 10nm.

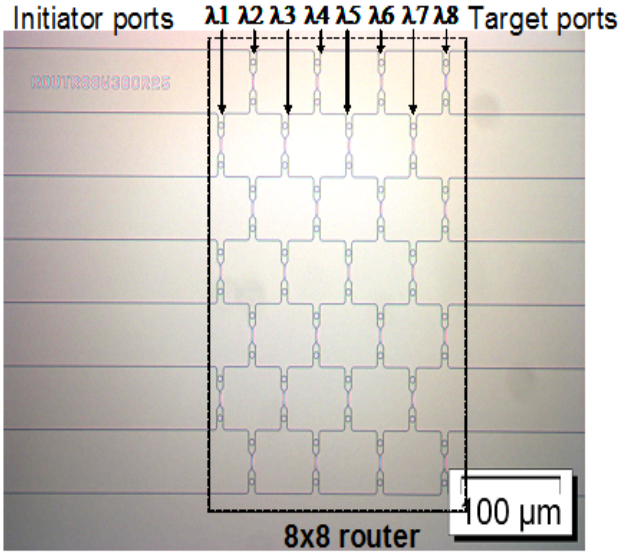


Fig.3 8x8 λ-router

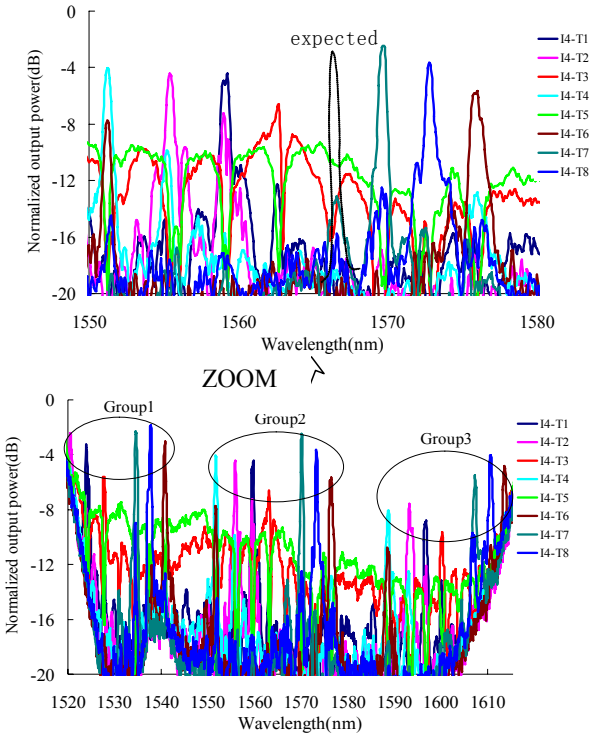


Fig.4 Measured transmission spectrum of the optical 8x8 λ-router at T1-T8 with light injected at port I4

The measured transmission spectrum of the optical 8x8 λ-router with light injected at port I4 is shown in Fig.4b. Three groups are observed presenting a good repeatability. The close up picture of the first group (Fig4a) reveals seven peaks which are equally space along the spectral range. The path I4-T5 is throughput path for the input I4: no resonance is observed. So the eighth peak misses. The red peak from I4-T3 is a little bad because the coupling from the throughput path disturbs the resonant spectra of path I4-T3,and the resonance from I4-T3 is close to the expected peak of throughput path I4-T5.

In Fig.4, the total loss of the studied channels is about -4 dB and the imbalance between the 8 channels is lower than 2 dB. The output efficiency for every path is a little weak (about 10dB to 20dB), because each path has to travel 6-8 waveguide crossings. The crosstalk between some drop channel is a little larger(about -4dB). This can be overcome by using the discrete source.

Similar measurements were performed for all input ports of the 8x8 network. There is about ⩽1nm difference for the same resonance with different input port because of the fabrication imperfection.

In conclusion, we present optical 8x8 λ-router using MMI crossing based the microring resonator. To our knowledge, this is the first experimental demonstration of such passive circuits.

ACKNOWLEDGMENT

This work was supported by a STREP European program "WADIMOS".

REFERENCES

[1] A. Kazmierczak, W. Bogaerts, E. Drouard, F. Dortu, P. Rojo-Romeo, F. Gaffiot, D. Van Thourhout, and D. Giannone, “Highly Integrated Optical 4x4 Crossbar in Silicon-on-Insulator Technology,” Journal of Lightwave Technology 27(16) , 2009, pp. 3317- 3323.

[2] N. Sherwood-Droz, H. Wang, L. Chen, B. G. Lee, A. Biberman, K. Bergman, M. Lipson, “Optical 4x4 hitless silicon router for optical Networks-on-Chip (NoC),” Optics express, 16(20), 2008, pp. 15915-15922.

[3] A. Shacham, K. Bergman, and L. P. Carloni, “Photonic networks-on-chip for future generations of chip multiprocessors,” IEEE Trans. Comput., 57(9), 2008, pp.1246–1260.

[4] M. Brière et al., “System Level Assessment of an Optical NoC in an MPSoC Platform,” Proc. Design Automation and Test in Europe (DATE), Nice, France, April , 2007, pp. 1084-1089.

[5] I. O'Connor et al., “Reduction methods for adapting optical network on chip topologies to specific routing applications,” Proc. Design of Circuits and Integrated Systems (DCIS), November 12-14, Grenoble, France, 2008.

[6] Q. Xu, D. Fattal, and R. G. Beausoleil, “Silicon microring resonators with 1.5-μm radius,” Opt. Express 16, 2008, pp. 4309-4315.

[7] R. Grover, V. Van, T. A. Ibrahim, P. P. Absil, L. C. Calhoun, F. G. Johnson, J. V. Hryniewicz, and P.-T. Ho, “Parallel-cascaded semi-conductor microring resonators for high-Order and Wide-FSR Filters,” Journal of Lightwave Technology,20(5),2002,pp.9

360° Tunable Microwave Phase Shifter Based on Silicon-on-Insulator Dual-Microring Resonator

Minhao Pu, Weiqi Xue, Liu Liu, Haiyan Ou, Kresten Yvind, and Jørn M. Hvam
DTU Fotonik, Department of Photonics Engineering
Technical University of Denmark
Lyngby, Denmark
mipu@fotonik.dtu.dk

***Abstract*—We demonstrate tunable microwave phase shifters based on electrically tunable silicon-on-insulator dual-microring resonators. A quasi-linear phase shift of 360° with ~2dB radio frequency power variation at a microwave frequency of 40GHz is obtained.**

Keywords-Integrated optics devices; microwave photonics; radio frequency photonics; silicon microring resonator.

I. INTRODUCTION

Microwave photonics has lately received increasing interests [1]. Photonic components, providing compact size, large bandwidth, immunity to electromagnetic interference and low weight, have been widely demonstrated in microwave systems. Microwave phase shifters with a full 2π phase shifting range are key components in many microwave applications, such as microwave filters. So far, several schemes for phase shifting including wavelength conversion [2], stimulated Brillouin scattering [3], slow-light effects in semiconductor devices [4] have been reported. Recently, silicon-on-insulator (SOI) microring resonators (MRRs) have also been used as phase shifters [5,6]. A 0-260° shifting range was realized in [5] with thermo-optical tuning from a high-power control light. Previously, we also demonstrated an electrically tunable phase shifter based on MRR with a phase-shifting range of 0-336° in [6]. However, it is difficult to realize a full 2π phase shift by using a single MRR. Furthermore, the radio frequency (RF) power varies dramatically during the phase shifting operation. Here, we demonstrate microwave phase shifters with tuning range larger than 2π by using two cascaded MRRs with independent electrically controllable micro heaters. A quasi-linear phase shifting rang of 0~360° with only 2dB RF power variation is obtained. These devices can be easily integrated with photonic and electronic circuits.

II. DESIGN

Fig. 1(a) shows the schematic drawing of an all-pass dual-microring resonator (DMRR). The two cascaded rings are designed to have identical geometries. Figs. 1(b) and 1(c) illustrate the transmission and the phase for the DMRR at the through port with different resonance offsets (ω_{MRR2}-ω_{MRR1}) between the two MRRs. As shown in Fig. 1(c), the optical phases experience a monotonic phase change from negative to positive detuning. If, in this case, an optical signal carrying a microwave signal with two peaks of the desired frequency

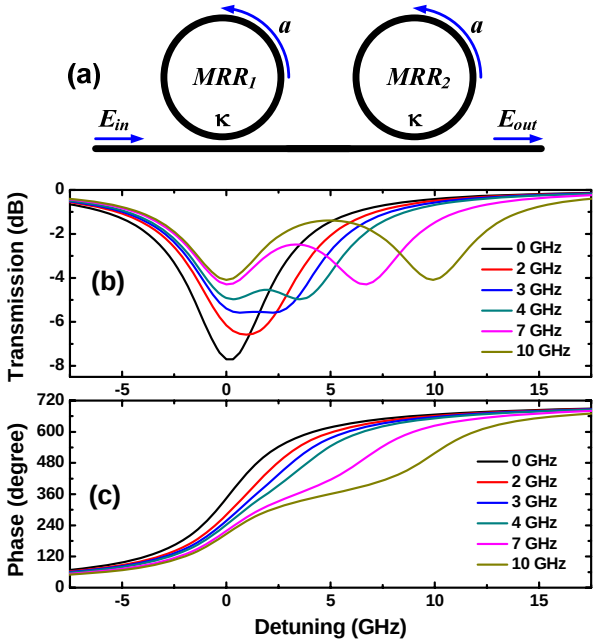


Figure 1. Schematic of a DMRR (a). Calculated transmission (b) and phase (c) as a function of optical detuning from the resonance frequency (ω_{MRR1}) at the through port for the DMRR with different resonance offsets (ω_{MRR2}-ω_{MRR1}) between the two MRRs. Here, amplitude coupling coefficient κ, power transmission coefficient a^2 and the ring diameter are assumed to be 0.2, 0.99 and 35μm, respectively.

spacing is input to the DMRR, the phase difference of the two peaks of the transmitted field can be tuned by changing the resonance frequency, and thus realizing a microwave phase shift. As shown in Figs. 1(b) and (c), the transmission spectrum and the phase curve can be altered by offsetting the resonances for the two MRRs. When the resonance offset increases from 0 to 3GHz, the notch bandwidth is increased with reduced notch depth and the notch bottom becomes flat. If the resonance offset increases further, the notch splits into two notches while the phase curve acquires a step-like shape. Therefore, the resonance offset can be tuned to a desired value (i.e., 3GHz in this case) to get a wide notch bandwidth, a decreased notch depth and a flattened notch bottom. If the RF phase shifting is operated within this bottom region, one can realize an RF phase shifting in a certain range without RF power variation, since the RF power follows the optical power.

This work was supported by the Danish Strategic Research Council and the EU FP7 via the projects NANO·COM and GOSPEL, respectively.

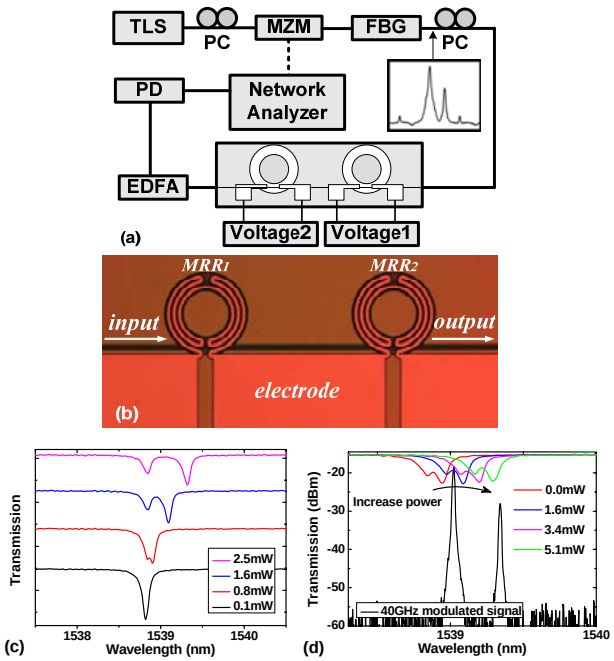


Figure 2. (a) Experimental setup for microwave phase shift measurements. (b) Optical microscope picture of the fabricated DMRR with micro heaters. (c) Measured transmission spectrum of the device with different applied power on the micro heater for MRR_1. (d) Mesured transmission spectrum of the device with extra applied power on both micro heaters (see the color curves) and the generated 40GHz microwave signal with central wavelength of 1539nm (see the black curve).

III. Experiment

The experimental setup used to measure the fabricated device is shown schematically in Fig. 2(a). Light from a tunable laser source (TLS) was modulated through a Mach-Zehnder modulator (MZM) by a microwave signal from the network analyzer. A fiber Bragg grating (FBG) notch filter was used to filter out one sideband of the modulated signal. After that, the optical signal, with the envelope modulated at the microwave frequency in the time domain (i.e., with two peaks of the desired frequency spacing in the spectral domain (see Fig.2 (d))) was generated and sent into the fabricated DMRR as shown in Fig. 2(b). All the structures were made on an SOI wafer with 250-nm thick top silicon layer and the waveguide width is 450nm. The coupling gaps between the two rings and the straight waveguide are 150nm. As shown in Fig. 2(c), the transmission spectrum can be altered by applying power on one of the micro heaters (i.e., the heater for MRR_1). In the measurement, we set 0.8mW as the reference power applied on MRR_1 to get a suitable resonance offset between the two MRRs. The polarization of the input light was adjusted to the quasi transverse electrical (TE) mode with a fiber polarization controller (PC). By equally increasing the extra electrical power applied to both micro heaters simultaneously, the resonance frequency of the DMRR can be tuned with respect to one of the peaks of the optical signal as illustrated in Fig. 2(d) and then the phase difference between the two peaks can be changed. Amplified by an erbium-doped fiber amplifier (EDFA), the output signal was detected by a high-speed photo detector (PD), and converted to the microwave signal. Then the network analyzer was used to extract the information of phase and power changes of the microwave signal.

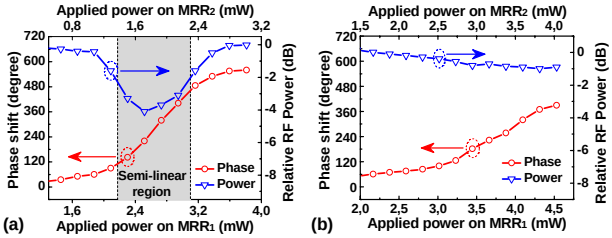


Figure 3. Measured RF phase shift and relative RF power versus the applied power on both micro heaters for the MRRs with ring-to-waveguide coupling gaps of 150nm (a) and 100nm (b).

The measured RF phase shift and RF power variation as a function of the applied electrical power on both micro heaters are also shown in Fig. 3(a). A continuously tunable RF phase shift is demonstrated, and the maximum RF phase shift of 540° is achieved with the RF power variation of ~4dB. However, if the device is operated within the gray region shown in Fig. 3(a), one can obtain not only a quasi-linear phase shift of 360°, but also an RF power variation of only 2dB. In this case, the total required operation power is ~2mW. We also tested another DMRR with a smaller ring-to-waveguide gap of 100nm which corresponds to a lower quality (Q)-factor for the resonator. As shown in Fig. 3 (b), a phase shift larger than 360° is still achieved. Although the maximum phase shift is reduced from 540° to 390°, the total RF power variation in the whole tuning range is only 1dB which is smaller than that of the high-Q device.

IV. Conclusion

We have introduced microwave phase shifters based on electrically tunable SOI DMRRs. A quasi-linear 360° phase shift has been achieved at a microwave frequency of 40GHz with 2dB RF power variation. A phase shift of 390° has also been demonstrated with only 1dB RF power variation using a DMRR with lower Q-factor. These devices are believed to be potentially useful in microwave applications.

References

[1] J. Capmany and D. Novak, "Microwave photonics combines two worlds," Nat Photon, vol. 1, Jun. 2007, pp. 319-330.

[2] M. Fisher and S. Chuang, "A microwave photonic phase-shifter based on wavelength conversion in a DFB laser," Photonics Technology Letters, IEEE, vol. 18, 2006, pp. 1714-1716.

[3] A. Loayssa and F.J. Lahoz, "Broad-band RF photonic phase shifter based on stimulated Brillouin scattering and single-sideband modulation," Photonics Technology Letters, IEEE, vol. 18, 2006, pp. 208-210.

[4] W. Xue, S. Sales, J. Capmany, and J. Mørk, "Microwave phase shifter with controllable power response based on slow- and fast-light effects in semiconductor optical amplifiers," Optics Letters, vol. 34, Apr. 2009, pp. 929-931.

[5] Q. Chang, Q. Li, Z. Zhang, M. Qiu, T. Ye, and Y. Su, "A Tunable Broadband Photonic RF Phase Shifter Based on a Silicon Microring Resonator," Photonics Technology Letters, IEEE, vol. 21, 2009, pp. 60-62.

[6] M. Pu, L. Liu, W. Xue, Y. Ding, L.H. Frandsen, H. Ou, K. Yvind, and J.M. Hvam, "Tunable Microwave Phase Shifter Based on Silicon-on-Insulator Microring Resonator," unpublished.

Silicon Waveguide Grating Couplers with Engineered Coupling Strength for Optimized Coupling

X. Chen, C. Li, S. M. G. Lo, K. Fung, and H. K. Tsang
Dept. of Electronic Engineering, the Chinese University of Hong Kong, Shatin, N. T., Hong Kong
Phone:+852 26098252 Fax:+852 26035558 E-mail: xchen@ee.cuhk.edu.hk

***Abstract*—We describe simulation and experimental results of gratings for coupling between optical fibers and nanophotonic waveguides. The coupling strength was engineered to obtained Gaussian-like output profile. 1.2dB coupling loss is achieved to single-mode fibers. Preliminary experimental result for coupling with vertical fiber with chirped grating gives a 3dB coupling loss.**

Keywords - grating coupler; silicon-on-insulator; integrated photonics; chirped grating

I. INTRODUCTION

Highly integrated photonic circuits could be realized at low cost based on silicon-on-insulator (SOI), because of small size made possible by the high refractive index contrast between the waveguide core material (silicon) and the cladding materials (air or silicon dioxide), and the availability of established semiconductor (CMOS) nanofabrication technology. End fire coupling techniques with adiabatic tapers [1] have achieved highly efficient coupling between small core area optical fibers and nanophotonic SOI waveguides. Diffractive waveguide grating couplers [2] has also been actively researched and coupling losses as low as 1.6dB were recently achieved with a high index polysilicon overlay [3]. Compared with the alternative coupling techniques, waveguide grating couplers are of immense practical interest because of their many advantages, including large alignment tolerance, simpler fabrication process since they do not require polishing of facets, and the flexibility to be placed anywhere on the chip.

The coupling efficiency of grating couplers is mainly limited by two factors. One is the bi-directional nature of grating diffraction. A large fraction of the optical power in the SOI waveguide is coupled downwards into the substrate instead of upwards to the optical fiber. Additional structures such as a polysilicon overlay [3] or a substrate mirror [4] were demonstrated to guide more light towards the fiber. Another factor that limits the coupling efficiency is the mode mismatch between the field profiles of diffracted light from waveguide grating and the fiber mode. An exponentially decaying field profile is expected when diffracted from a uniform grating, and this would theoretically limit the coupling efficiency to a maximum of 80% for coupling to the Gaussian-like mode profile of an optical fiber [5]. It was suggested that Gaussian-like output profile from SOI grating couplers may be achieved by varying the fill factor of the grating [6], but to our knowledge this has not been previously implemented.

This work was supported by a UGC special equipment grant CUHK-SEG01 and an ITF grant ITS/041/09.

In this paper, we describe the simulation and experimental measurement results of highly efficient diffractive gratings for coupling between perfectly vertical ($\theta = 0°$) or slightly titled optical fiber and nanophotonic waveguide as shown in Fig.1a, whose fill factors are engineered to achieve Gaussian-like output profile.

II. SIMULATION & EXPERMENTAL RESULTS

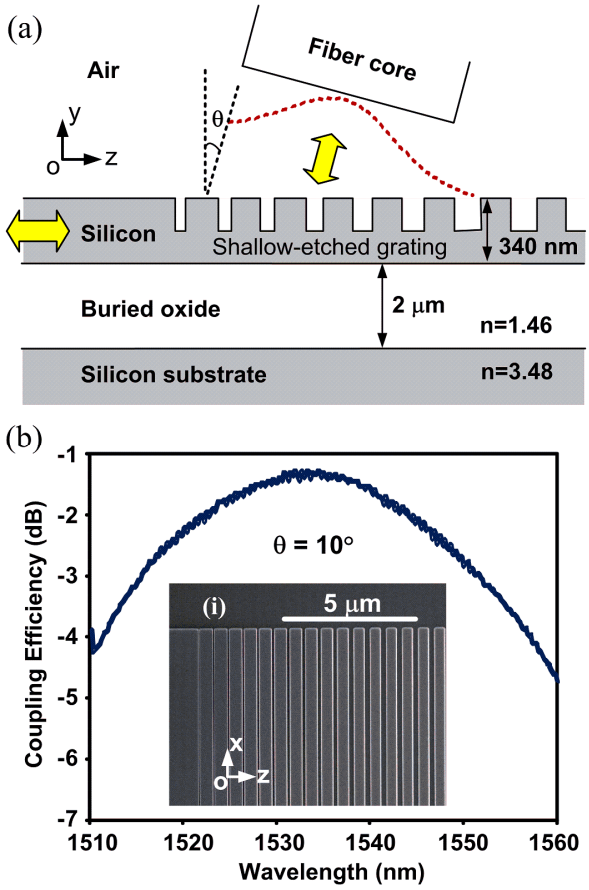


Fig.1. (a) Schematic of the fabricated grating couplers. (b) The experimentally measured coupling efficiency of the grating coupler with engineered fill factor, coupling between titled optical fiber ($\theta = 10°$) and nanophotonic waveguide. From the best measurement result, -1.2dB efficiency is achieved at 1534nm. (i) The inset shows a SEM image of the fabricated grating coupler.

The grating couplers were fabricated on a SOI wafer using electron beam lithography with 340nm thick top silicon layer and 2μm thick buried oxide. Grating was formed by 200nm shallow etch. 2D FDTD simulation was used to verify and

optimize the coupler designs. The directionality (defined as the portion of the light power coupled into fiber normalized with respect to the total coupled optical power) of the grating can be optimized up to 0.87 according to simulations with the configuration listed above. We went beyond the strict single-mode waveguide thickness constraint and used a more optimum waveguide thickness and etch depth. Although the waveguide thickness used may support a weakly guided first order mode, for most device applications, the grating coupler itself can act as an effective mode filter for both the input and output coupling and thus only the fundamental mode is present.

The fundamental mode of the nanophotonic waveguide is first expanded laterally (in x-axis) by an adiabatic taper to a 10.4μm wide waveguide which have a lateral mode size similar to the single mode fiber. The light would then be diffracted upward into the optical fiber by the grating; whose fill factor was varied according to our calculation. So that the coupling strength was engineered and a Gaussian-like output field profile was realized. When coupling to a slight titled ($\theta = 10°$) standard single mode optical fiber, the grating coupler achieved a loss of only 1.2dB from the TE mode in a 450nm (wide) by 340nm (thick) SOI waveguide. This result is the highest coupling efficiency reported to date for waveguide grating couplers.

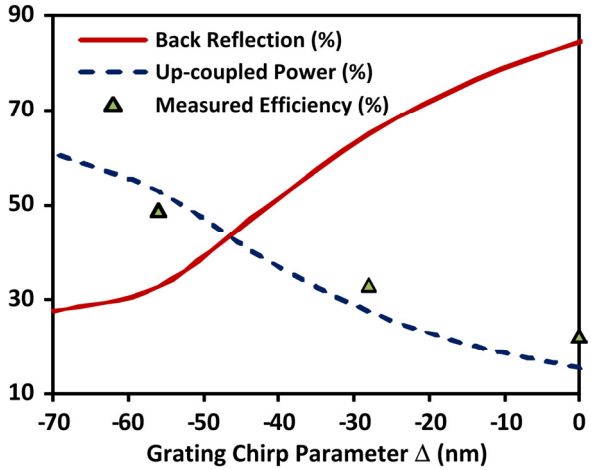


Fig.2. The simulated back reflection and up-coupled power into fiber are plotted with different grating chirped parameter. Experimentally measured coupling efficiencies are also plotted.

With slightly tilted fiber, we found that varying the fill factor of grating couplers is also able to eliminate the small back reflection caused by the comparatively large index step of the grating. But back reflection would still dominate (> 80%) when we designed the grating for coupling to perfectly vertical optical fiber. Because the vertical coupling scheme (without fiber tilting) would be more preferable for low cost photonic packaging process, preliminary work on applying linearly chirped grating to reduce the back reflection [7] was carried out with the constraint of maintaining a Gaussian-like output profile and keeping the fiber vertical to the chip surface.

Simulation result for the chirped grating coupler is plotted in Fig.2. Because we are using fill factor f (ratio of the etched groove over period) ranging from 0.08 to 0.4 to engineer the coupling strength of the grating coupler along z-axis. The average effective index of the grating region would also change with f. According to phase matching condition, the grating period Λ need to be change from 520nm to 580nm for different f in the design for vertical coupling at 1550nm wavelength. Similar to [7], we could define a grating chirp parameter Δ as the maximum deviation of the change applied to the first and last grating periods of the chirped section. The negative sign means the change of each period is decreasing. For example, if $\Delta = -40$nm, the first period would be change from 520nm to 540nm, and the last period would be changed from 580nm to 560nm. By linearly chirping the grating period (reducing Δ from 0), the back reflection can be reduced significantly. The coupling efficiency is enhanced as shown in Fig.2. Preliminary experimental results showed a 3dB coupling loss with $\Delta = -56$nm. The Fabry-Perot resonance was found to be reduced from 11dB to 2.6dB for a short waveguide with two grating couples at both ends, indicating a significant reduction of the back reflection. Further improvement of the design is under way, as we found that the coupling strength increased abruptly when reducing the coupling angle θ. Thus the output profile of the vertical grating coupler was distorted.

III. Conclusion

We experimentally demostrated waveguide grating couplers with 1.2dB and 3dB coupling loss with off-vertical and vertical optical fiber respectivley. The fill factor is varied to achieve Gassian-like output profile from the waveguide grating. Back reflection was reduced by a linear chirp of the grating period to enhance the coupling efficiency with vertical optical fiber. Further improvement is under way.

References

[1] T. Shoji, T. Tsuchizawa, T. Watanabe, K. Yamada, and H. Morita, "Low loss mode size converter from 0.3μm^2 Si wire waveguides to singlemode fibers," Electron. Lett. **38**, 1669-1670 (2002).

[2] D. Taillaert, W. Bogaerts, P. Bienstman, T. F. Krauss, P. Van Daele, I. Moerman, S. Verstuyft, K. De Mesel, and R. Baets, "An out-of-plane grating coupler for efficient butt-coupling between compact planar waveguides and single-mode fibers," IEEE J. Quantum Electron. **38**, 949-955 (2002).

[3] D. Vermeulen, S. Selvaraja, P. Verheyen, G. Lepage, W. Bogaerts, G. Roelkens, "High-efficiency Silicon-On-Insulator Fiber-to-Chip Grating Couplers Using a Silicon Overlay," IEEE 6th International Conference on Group IV Photonics, PDPF1 (2009).

[4] F. Van Laere, G. Roelkens, M. Ayre, J. Schrauwen, D. Taillaert, D. Van Thourhout, T. F. Krauss, and R. Baets, "Compact and highly efficient grating couplers between optical fiber and nanophotonic waveguides," J. Lightw. Technol. **25**, 151-156 (2007).

[5] R. Orobtchouk, A. Layadi, H. Gualous, D. Pascal, A. Koster, and S. Laval, "High-Efficiency Light Coupling in a Submicrometric Silicon-on-Insulator Waveguide," Appl. Opt. **39**, 5773-5777 (2000).

[6] D. Taillaert, P. Bienstman, and R. Baets, "Compact efficient broadband grating coupler for silicon-on-insulator waveguides," Opt. Lett. **29**, 2749-2751 (2004).

[7] X. Chen, C. Li, and H. K. Tsang, "Fabrication-tolerant waveguide chirped grating coupler for coupling to a perfectly vertical optical fiber," IEEE Photon. Technol. Lett. **20**, 1914-1916 (2008).

Backscattering in silicon photonic devices

F. Morichetti, A. Canciamilla, C. Ferrari, M. Martinelli and A. Melloni
POLICOM – Dipartimento di Elettronica e Informazione
Politecnico di Milano
20133, Milano, Italy
morichetti@elet.polimi.it

G. Morea
DEE – Dipartimento di Elettrotecnica ed Elettronica
Politecnico di Bari
70125, Bari, Italy

Abstract— **We report on the backscattering induced by sidewall roughness in silicon on insulator optical nanowires, its dependence on the waveguide geometrical and optical parameters and its impact on silicon photonic devices. In silicon ring resonators cavity-enhanced backscattering, increasing with the square of the resonator's finesse, emerges as a severe impairment.**

Keywords- optical waveguides; silicon photonics; roughness; backscattering; ring resonators

Surface roughness at the walls of optical waveguides is one of the main sources of radiation loss [1] and backward coupling with counterpropagating guided modes [2]. Both these effects become stronger when the waveguide index contrast increases and the waveguide size is reduced to sub-wavelength scale. As a result, the fabrication of low-loss silicon on insulator (SOI) nanowaveguides requires the reduction of sidewall roughness down to a few nanometers scale [3]. If propagation loss of state-of-the-art SOI waveguides are now sufficiently low (< 1 dB/cm) to fulfill the requirements of many applications, on the side of roughness induced backscattering many issues are still open. This is mainly because, to the best of our knowledge, backscattering in SOI waveguides has never been quantified experimentally, so that there is not a real awareness of its actual implications on practical applications.

In this work we report on an experimental investigation on the effects of backscattering in silicon on insulator optical nanowires, showing its dependence on the waveguide geometrical and optical parameters and evaluating its impact on silicon photonic devices. The dramatic effects of cavity enhanced backscattering on the spectral response of silicon ring resonators are shown, demonstrating that backscattering could hinder the full exploitation of SOI waveguides in many practical applications.

I. BACKSCATTERING IN SOI NANOWIRES

We measured the backscattering of conventional SOI nanowires with a rectangular silicon core of height h = 220 nm and width w, buried in a silica cladding [Fig. 1(a)]. The silicon core sidewalls have a surface roughness with a standard deviation of about 2 nm and a correlation length of about 60 nm. This roughness results in a propagation loss of 2.5 dB/cm in 490-nm-wide single mode waveguides. Details on the interferometric technique employed for the backscattering measurements can be found in [4].

Fig .1(b) shows the power spectral density (PSD) of the backscatter produced by a 1-mm-long waveguide, averaged over a spectral range of 60 nm (from 1520 to 1580 nm). Some noteworthy considerations arise from this figure. First, due to the higher sensitivity to sidewall roughness, transverse electric (TE) polarization (circles) suffers from a much higher backscattering level than transverse magnetic (TM) polarization (diamonds), the difference between the two polarizations increasing from about 10 dB in larger waveguides (w = 600 nm) to about 20 dB in narrower waveguides (w = 300 nm). Second, given a certain degree of roughness, backscattering strongly depends on the waveguide geometrical and optical parameters. Experimental data agrees with theoretical predictions (dashed lines), stating that backscattering is related to the waveguide mode effective index n_{eff} through the square of its partial derivative with respect to w, i.e. it scales as $(dn_{eff}/dw)^2$ [4]. This dependence results in the higher slope of TE backscattering versus w in Fig. 1(b). Third, even though the backscattered power represents only a small

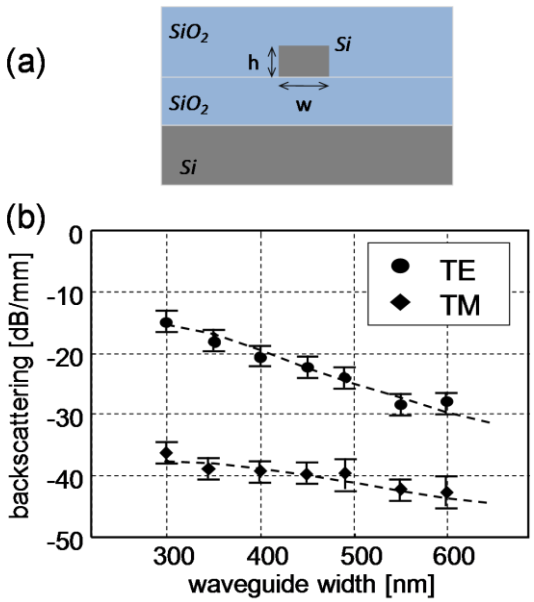


Figure 1. (a) Cross-section of a SOI nanowire; (b) measured backscattering of SOI waveguides versus *w* for TE (circles) and TM (diamonds) input polarization. Dashed lines show a numerical fit with a theoretical perturbative model.

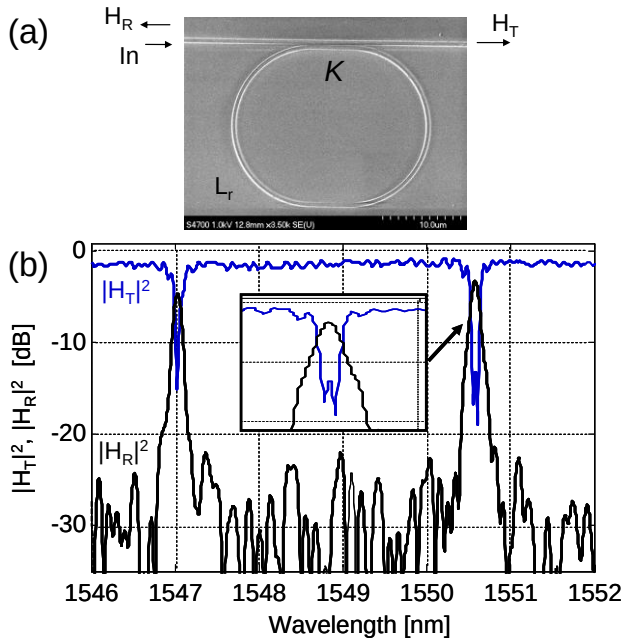


Figure 2. (a) Top view photograph of a silicon APF with a racetrack RR coupled with a bus waveguide; (b) Measured transmission ($|H_T|^2$) and backreflection ($|H_R|^2$) of the silicon APF coupled with a 3-mm-long bus waveguide for K = 0.2.

fraction of the overall radiation loss (<10 %), it can be more detrimental than propagation loss. For example, in a 490-nm-wide waveguide (α = 0.25 dB/mm), a backscattering of -24 dB/mm is responsible for only 0.015 dB/mm loss. Yet, the backscattered light is not lost, but it originates a backreflected signal that is not acceptable in many applications. Widespread examples are devices for optical communications, where return loss specifications above 40 dB are typically required. Note that this value is not fulfilled by a single mode 490-nm-wide longer than 50 μm and that the effect becomes more severe in narrower waveguides. The use of TM polarization, which is rarely employed in this kind of waveguides, could be a possible strategy to mitigate backscattering impairment.

II. BACKSCATTERING IN SILICON RING RESONATORS

The effects of backscattering in SOI nanowires are further magnified when the waveguide is employed to realize resonant structures such as ring resonators (RRs) [6,7]. In such devices, multiple round trips along the waveguide enhance backscattering according to the square of the resonator's finesse and cause strong transfer function distortions. To investigate the effect we fabricated several all-pass filters (APFs) consisting of a racetrack RRs with a radius of 20 μm and coupled to a bus waveguide by a 16-μm-long straight coupling section. In these devices, we used 490-nm-wide waveguides, with a sidewall roughness reduced below 2 nm standard deviation, resulting in a propagation loss of less than 2 dB/cm at a wavelength of 1550 nm.

Figure 2(b) shows the TE intensity transmission ($|H_T|^2$) and backreflection ($|H_R|^2$) of an APF with a power coupling coefficient K = 0.2 with the bus waveguide. As expected, at the RR's resonances (around 1547 nm and 1550.6 nm), transmission loss is enhanced. However, the roundtrip losses of the measured RR do not entirely justify the observed notches' depth. In the APF of Fig. 2(b), with a quality factor Q = 13000, the roundtrip loss of 0.2 dB would be expected to originate a notch of less than 4 dB at resonance. Our results clearly show that the missing light is actually scattered back and, for sufficiently low values of K, can even exceed the transmitted power. For instance, in the considered APF, transmission is less than -15 dB at 1550.5 nm, while reflection is as high as -5 dB. At different resonances the backscattering level (and hence the transmission notches) can change, because the RR enhances the waveguide backscattering, which varies almost randomly versus wavelength. Note also that the multiple round trips in the RR strongly correlate backscattering, so that the cavity-enhanced backscattering does not exhibit a noise-like PSD. Off-resonance the effect of the RR disappears and the backscattering of the bus waveguide emerges. The backscattering level of the straight waveguide, with a length of 3 mm, is 30 dB below transmission, resulting in -35 dB/mm average backscattering.

III. CONCLUSION

In conclusion, our results point out that in silicon optical waveguides backscattering, being three order of magnitude higher than in low index contrast waveguides, can be a severe impairment in many practical applications. For instance, it has strong implications on the behaviour of integrated RRs, where it can dramatically modify the spectral response even at moderate Q values.

ACKNOWLEDGMENT

This work was partially supported by the European Project SPLASH (6th FP). The authors are grateful to M. Sorel, R. M. De La Rue, A. Samarelli and to the technical staff of the James Watt Nanofabrication Centre at the University of Glasgow for the fabrication of the devices.

REFERENCES

[1] K. K. Lee, D. R. Lim, L. C. Kimerling, J. Shin, and F. Cerrina, "`Fabrication of ultralow-loss Si/SiO2 waveguides by roughness reduction," Opt. Lett., vol. 26, pp. 1888-1890, Dec. 2001.

[2] F. Ladouceur and L. Poladian, "Surface roughness and backscattering," Opt. Lett., vol. 21, pp. 1833-1835, Nov. 1996.

[3] M. Gnan, S. Thoms, D.S. Macintyre, R.M. De La Rue, and M. Sorel, Electron. Lett. 2, 2008.

[4] F. Morichetti, A. Canciamilla, C. Ferrari, M. Torregiani, A. Melloni, and M. Martinelli, "Roughness induced backscattering in optical silicon waveguides," Phys. Rev. Letters , in press.

[5] K. Takada and S. Mitachi, "Measurement of Depolarization Ratio and Ultimate Limit of Polarization Crosstalk in Silica-Based Waveguides by Using a POLCR", IEEE J. Light. Technol., vol. 16, pp. 639, Apr. 1998.

[6] B. E. Little, J.-P. Laine, and S. T. Chu, "Surface-roughness-induced contradirectional coupling in ring and disk resonators," Opt. Lett. , vol. 22, pp. 4-6, 1997.

[7] F. Morichetti, A. Canciamilla, M. Martinelli, A. Melloni, A. Samarelli. R. M. De La Rue, and M. Sorel, "Coherent backscattering in optical microring resonators", submitted to Appl. Phys. Lett.

Vertical optical interfacing of Silicon waveguides

Peter Lützow, Helmut Heidrich
Department of Fiber Optical Sensor Systems,
Fraunhofer Heinrich-Hertz-Institute (HHI),
10587 Berlin, Germany,
peter.luetzow@hhi.fraunhofer.de

Harald Richter, Lars Zimmermann
Technology Department,
IHP Microelectronics,
15236 Frankfurt (Oder), Germany

***Abstract*—We present a novel concept and first experimental results for vertical optical interfacing of Si-waveguides on SOI substrates. The application of bent waveguides instead of grating elements assures broad spectral bandwidth and low polarization dependence. Test elements have been fabricated by using standard CMOS processing modules.**

Keywords- Silicon photonics, optical interfacing, vertical coupling, butt-coupling

I. INTRODUCTION

The possibility for ultra dense integration of photonic circuits alongside with CMOS-electronic functionality has resulted in extensive research in the field of silicon photonics during the past two decades. One key issue is the interfacing between photonic waveguides/wires and optical fibers. Several approaches have been followed, each having its advantages but disadvantages as well. Grating couplers typically show good out-of-plane coupling efficiency but only narrow bandwidth and rather strong polarization dependence [1]. End-facet optical interfaces with integrated waveguide tapers exhibit both high coupling efficiency and large bandwidth but do not allow wafer scale testing of the photonic circuits since they have to be terminated on end-polished chip facets.

Here we describe a new and particularly promising option for silicon optical interfacing based on out-of-plane directed waveguide micro-bends which will eventually enable out-of-plane, low-polarization dependent and low insertion loss coupling. The new approach relies on the fact that the large index contrast between silicon (refractive index $n > 3.4$) and silicon dioxide ($n = 1.45$) or air ($n = 1$) allows the realization of waveguide bends with bending radii as small as 1 µm and negligible transmission loss [2]. So far such small bends have only been demonstrated to work in the wafer-plane, helping to route guided light along the surface of a chip or to realize minute optical ring resonators. This paper reports - to the best of our knowledge - the first application of waveguide micro-bends to out-of-plane (vertical) optical interfacing.

II. CONCEPT

Fig. 1 illustrates the schematic of the optical interfacing set-up. A high index a-Si waveguide terminated by an upwards directed waveguide bend with a bending radius in the range of a few micrometers is embedded into a SiO_2 buffer, assuring optical isolation from the underlying substrate as well as mechanical stability. Light, e.g. from an optical fiber, can be launched towards the upwards directed facet of the waveguide so that part of the incoupled light is guided through the bend section down to the straight embedded waveguide which itself may be part of a larger (extended) waveguide circuit. The bend section is either slab-like and connected to a single-mode part of the waveguide via a taper structure or single-mode as well.

First 2D simulations of these structures show the coupling efficiency to be comparable to that obtained with waveguides terminated at a chip end-facet and with a similar bandwidth of (in principle) hundreds of nanometers. The same holds for the polarization dependence. There is, however, the particular advantage of the vertical interfacing that no laborious preparation of end-facets of individual chips is needed. In addition, we do not see these structures necessarily as stand-alones. The polished wafer-surface on which the waveguides end may be used as a platform for additional structures serving to mode-match between optical fibers and the waveguides. As an example a silicon nitride top placed above the a-Si waveguide could implement such a function.

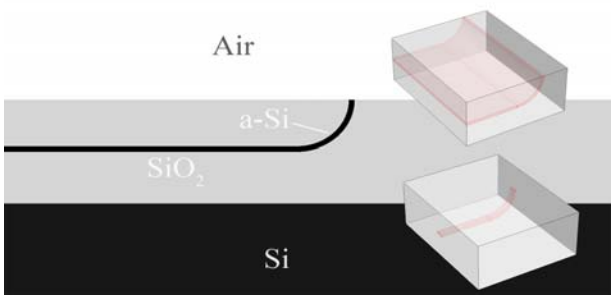


Figure 1. Schematic of the proposed design for vertical interfacing of silicon optical waveguides. The insets show a variant with a slab-like bend section (upper inset) and single-mode bend section (lower inset).

III. PROCESSING

To demonstrate the approach we fabricated test structures consisting of slab waveguides with integrated bend sections. These first test structures were fabricated on 200 mm Si wafers according to the following process flow:

First a 4.5 µm thick plasma enhanced tetraethylorthosilicate (TEOS) oxide layer is deposited on a bare Si wafer, followed by Low Pressure Chemical Vapor Deposition (LPCVD) of 200 nm silicon nitride (Si_3N_4). By i-line lithography

rectangular stripes (500 µm broad and some millimeters long) were defined and transferred into the underlying nitride by dry etching in a $CHF_3/CF_4/O_2$ plasma. For this dry etch step, a well established magnetically enhanced plasma etch equipment (MERIE) was used. The silicon nitride layer serves as a hard mask in the following wet etch step (buffered oxide etch) using hydrofluoric acid (HF). During the isotropic HF etching the silicon oxide is attacked to build a pedestal like structure underneath the Si_3N_4-remains (cf. Fig. 2a). After the silicon nitride has been removed from the wafer using hot phosphoric acid, amorphous silicon is deposited by a disilane CVD process at 575°C. Subsequently the whole wafer is covered again with 4.5 µm plasma enhanced TEOS oxide (see Fig. 2b). A two-step Chemical Mechanical Polishing (CMP) process is applied to planarize the wafer surface (Fig. 2c) and to finally remove the unwanted amorphous silicon remains that cover the upper part of the curved waveguide sections (Fig. 2d).

The process flow as described above has been implemented using CMOS compatible technology at IHP. Fig. 2d shows the cross-section of a final structure. The waveguide core layer has a thickness of approximately 250 nm and is buried underneath 1.65 µm of SiO_2. The lower oxide buffer measures about 2.54 µm. The realized structures deviate from the theoretical form presented in Fig. 1 in that the bend sections end with a smaller angle of approximately 65° with respect to the wafer-plane. This is primarily due to the wet-etching behavior of the deposited SiO_2 in the HF solution. By adjusting the process flow to include an anisotropic dry etch step directly before the wet etch or by changing the deposition procedure completely vertical alignment is expected.

IV. Experiments

In the experimental set-up for optical characterization we used specially designed pre-tilted fiber holders on 3-axis-translation stages to align tapered optical fibers (~3.5 µm spot size) to the waveguides. Preliminary transmission measurements were performed on typical slab waveguides with a length of approx. 2 mm. Fig. 3 shows wavelength scans of the laser-to-detector transmission as measured for the polarization controller being adjusted to maximum (state 1) and minimum (state 2) laser-to-detector transmission, respectively. The inset of Fig. 3 shows the normalized beam profile at the output facet of the slab waveguide, measured by moving the output fiber along the output facet. The laser-to-detector transmission shows an almost exponential increase with increasing wavelength of up to 17 dB over the accessible wavelength range from 1470 nm to 1570 nm which we tentatively attribute to multimode effects. The maximum laser-to-detector transmission as obtained at 1570 nm was about -54 dB for the polarization being in state 1 and -62 dB for the polarization being in state 2. The losses can be partly explained by the beam divergence inside the slab waveguide.

V. Conclusion and Outlook

We have demonstrated light coupling to and out of a-Si slab waveguides using upwards directed waveguide micro-bends coupled to tapered optical fibers. Further experimental investigation along with numerical simulations is currently being conducted to verify and further quantify the results as well as to identify the individual loss mechanisms. As a next step, following the fabrication of slab waveguide structures, processing of single-mode vertical micro-bends is under way. Promising applications include economic wafer-level probing, on-surface fiber pigtailing, or even optical interfacing of (individual) functionalized nano-structures on chip.

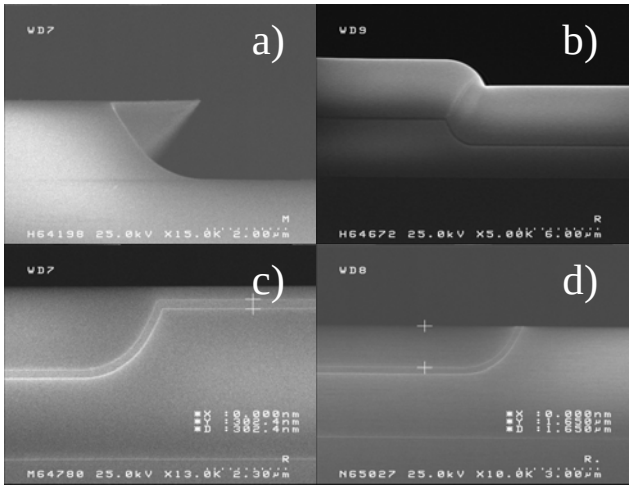


Figure 2. Si waveguide preparation process: Fig. 2a: after oxide wet etching; Fig.2b: after 2nd TEOS oxide deposition; Fig.2c: during oxide CMP; Fig.2d: after a-Si CMP

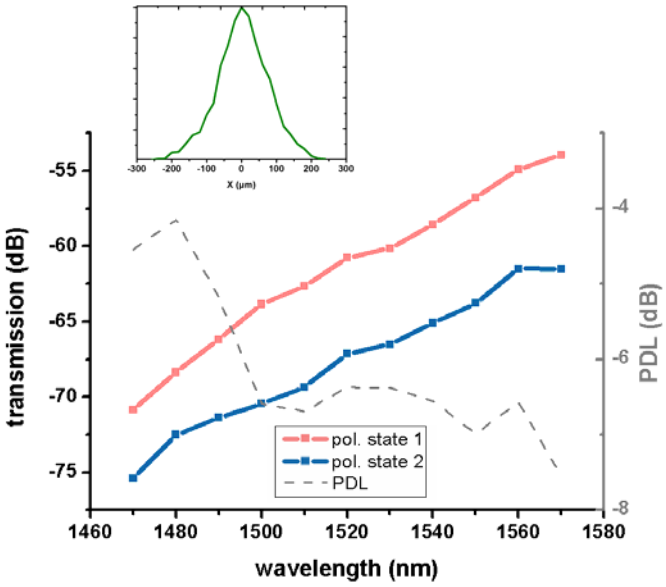


Figure 3. Laser-to-detector transmission for polarization states 1 and 2, polarization dependent loss (PDL),
Inset: Transverse beam profile at output facet.

[1] D. Van Thourhout et al, "Coupling mechanisms for a heterogeneous silicon nanowire platform," Semicond. Sci. Technol., vol. 23, pp. 064004(1-9), May 2008

[2] Y.A. Vlasov and S.J. McNab, "Losses in single-mode silicon-on-insulator strip waveguides and bends", Opt. Express, vol. 12, pp. 1622-1631, April 2004

Tuning Silicon-On-Insulator Ring Resonators in In-Plane Switching Liquid Crystal Cells

W. De Cort[1,2], J. Beeckman[2], K. Neyts[2], R. Baets[1]

[1]Department of Information Technology
Ghent University – IMEC
Ghent, Belgium
wout.decort@intec.ugent.be

[2]Department of Electronics and Information Systems
Ghent University
Ghent, Belgium

Abstract—**We show tuning of the resonance wavelength of Silicon-On-Insulator ring resonators with a liquid crystal cladding layer. In-plane switching of the liquid crystal director causes a shift towards longer wavelengths. The magnitude of the shift is 0.7 nm. We confirm our experiments with simulations using a fully anisotropic mode solver and explain the tuning mechanism.**

Keywords-Liquid crystals, silicon-on-insulator, tunable filters

I. INTRODUCTION

Ring resonators are very small and efficient optical filters. They are already used as components for (de-) multiplexers in optical networks. Reconfigurable optical networks require tunable ring resonators to control the filtering of wavelengths. The most common ways to achieve this are heating or carrier injection. In literature, tuning with a liquid crystal (LC) cladding layer has been shown [1,2]. This way, the effective index of the waveguide mode can be influenced and the resonance wavelength of the ring resonators tuned by an externally applied electric field. This is an interesting option as the optical anisotropy of LCs can be large, a birefringence Δn of 0.2 is common in nematic LCs. This allows for wide tuning ranges. It has been demonstrated that with a top-bottom electrode configuration, a shift to shorter wavelengths can be achieved [2]. In this paper we discuss Silicon-On-Insulator (SOI) ring resonators tuned by in-plane switching (IPS) of the LC cladding. In the next section we discuss the cell consisting of the chip, the LC and the electrodes, in the third section we show our experimental results and in the final section we explain our simulations and clarify the tuning mechanism.

II. CELL OVERVIEW

The SOI chip consists of a Si substrate, a 2 μm thick insulating layer of SiO_2 to prevent leakage of light to the substrate and a 220 nm thick Si layer in which the photonic structures are defined. We use ring resonators with radii between 4 and 6 μm. The waveguides are 450nm wide and 220 nm high. The structures are designed to work for TE polarized light, which allows for very small components due to the strong confinement of the mode in the waveguides. The structures are fabricated using deep UV lithography [3]. This mass production technique renders the chips very cheap. Using UV curable glue and spacers with a radius of 1.6 μm we attach a glass plate on the chip. On this glass plate we spincoated a nylon alignment layer. This forces the LC director on the glass-LC interface parallel to the input waveguides of the ring resonators. From experience we know that on the chip surface the director follows the local waveguide structures. On the glass we made Indium Tin Oxide (ITO) finger pattern electrodes of which the fingers are parallel to the waveguides (see Figure 1) and spaced 12 μm apart. When a voltage is applied, there will be an electric field between two neighbouring fingers, orthogonal to the waveguides. We fill the cell with 5CB, a common nematic LC, often used in display technology. Capillary forces draw the LC into the heated cell which is then cooled down gradually to avoid the formation of domains.

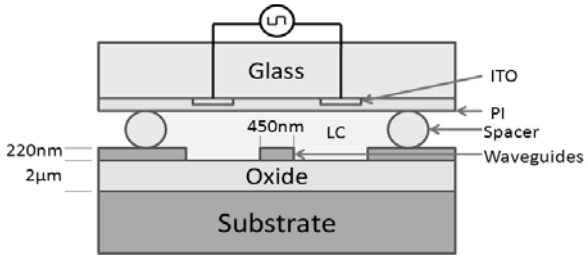


Figure 1. Schematic overview of an IPS cell

III. OPTICAL CHARACTERIZATION

The waveguides on the chip are equipped with grating couplers. These periodic structures are used to couple light (coming in vertically from an optical fiber) in and out of the chip [4]. The couplers have an efficiency of 30%. We use a tunable laser as light source and measure the output with a power meter. We apply a square wave of 1 kHz frequency between the fingers of the electrodes and measure the output spectrum of the ring resonators. For increasing voltages we clearly see a gradual increase of the resonance wavelength. For low voltage levels we see no change as the electric field is too weak to overcome the elastic forces holding the LC. For a certain voltage we can see a clear threshold where the electric fields compensate exactly for the elastic forces. After this Freedericksz transition the resonance wavelength increases until it reaches a saturation level. All the molecules are now

This project is funded by the Institute for the Promotion of Innovation through Science and Technology in Flanders (IWTVlaanderen).

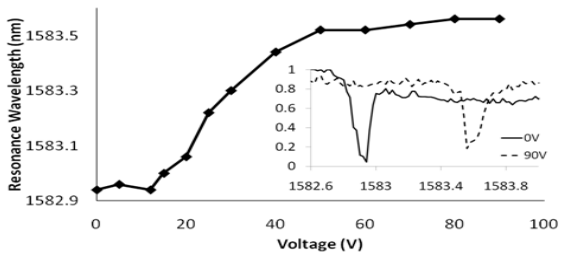


Figure 2. Experimental observation of the change in resonance wavelength for increasing voltage. Spectra for 0V and 90V are shown in inset.

fully reoriented to their maximum twist angle (i.e. perpendicular to the waveguide). We are able to tune the resonance wavelength of the ring resonators towards longer wavelengths over 0.7nm (see Figure 2), which is the largest reported shift for TE based rings.

IV. Verification of the Experiments

A. Simulations

It is not trivial to calculate the modes of a waveguide with an LC cladding in the presence of an electric field. A first problem is the calculation of the liquid crystal orientation (Figure 3). In this work a variable order calculation [5] is used based on the minimization of the Landau-deGennes free energy functional [6]. This was developed in collaboration with University College London. A second problem is the calculation of the optical waveguide modes. Commercial simulation tools often do not allow full anisotropy. We have developed in collaboration with UCL a mode solver that incorporates the full anisotropy of the dielectric tensor. The output of the liquid crystal orientation calculation is used to calculate the modes. This calculation is based on the solution of the variational form of the curl-curl equation of the electric field, implemented with higher-order edge elements [7]. These two tools allow us to calculate the effective index of the waveguide mode for different voltages. From this the resonance wavelengths can be obtained. The simulation space is 3 μm high and 5 μm wide. At the bottom there is a 1 μm thick layer of SiO_2 with a waveguide on top (220 nm high, 450 nm wide). The electrodes are in the top right and left corner and are spaced 3 μm apart. We calculate the resonance shift in ring resonators based on these waveguides for different voltages. We find a curve very similar to the experimentally found curve (Figure 4). The tuning range is smaller in the experiments. This is because the fingerpatterns only influence a part of the circular ring structure. For an optimized electrode

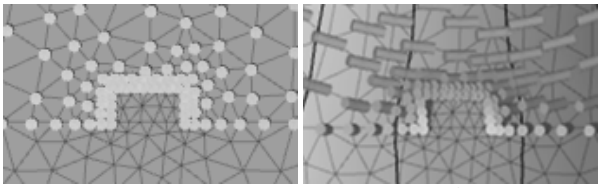


Figure 3. Simulated LC orientation without voltage (left) and with 15V applied (right). Images are close-up around the waveguide.

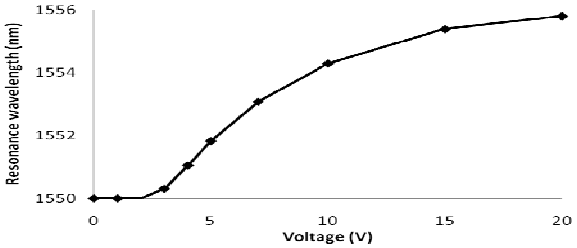


Figure 4. Simulated resonance shift

configuration, the simulations predict a range of 6 nm.

B. Tuning mechanism explained

The evanescent tails of the waveguide mode around the waveguide are for the largest part TE-polarized. Without voltage applied, the LC is oriented parallel to the waveguide and the transversal component of the electric field of the light 'sees' the short axis of the molecules and thus a low refractive index results. As the molecules turn under influence of the external field, they present their long axis. This effect causes an increase of the effective index of the mode.

V. Conclusion

We have shown tuning of SOI optical ring resonators with an LC cladding in an in-plane switching configuration. With this method we are able to tune the resonance wavelength over 0.7nm towards longer wavelengths.

Acknowledgment

W. De Cort acknowledges the Institute for the Promotion of Innovation through Science and Technology in Flanders (IWT-Vlaanderen) for a specialization grant. Jeroen Beeckman is Postdoctoral Fellow of the Research Foundation Flanders (FWO-Vlaanderen). The work has been carried out in the framework of the IAP project Photonics@be of the Belgian Science Policy.

References

[1] Maune, B., Lawson, R., Gunn, C., Scherer, A., Dalton, L., "Electrically tunable ring resonators incorporating nematic liquid crystals as cladding layers", Appl. Phys. Lett. 83, pp. 4689-4691, 2003

[2] De Cort, W., Beeckman, J., James, R., Fernandez, F.A., Baets, R., Neyts, K., "Tuning of silicon-on-insulator ring resonators with liquid crystal cladding using the longitudinal field component", Opt. Lett., vol. 34, pp. 2054-2056, 2009

[3] Dumon, P. et. al., "Low-Loss SOI Photonic Wires and Ring Resonators Fabricated With Deep UV Lithography", IEEE Photonics Technol. Lett. 16, 1328-1330 (2004).

[4] Taillaert, D., Bienstman P., and Baets, R., "Compact efficient broadband grating coupler for silicon-on-insulator waveguides", Opt. Lett., vol. 29, 2749-2751 (2004)

[5] James, R., Willman, E., Fernandez, F. A., and Day, S. E., "Finite-element modeling of liquid crystal hydrodynamics with a variable degree of order", IEEE T. Electron Dev. 53, 1575-1582 (2006)

[6] de Gennes, P. G., and Prost, J., "The Physics of Liquid Crystals", Oxford: Oxford University Press, 1995

[7] Beeckman, J., James, R., Fernandez, F. A., De Cort, W., Vanbrabant, P. J. M., and Neyts, K., "Calculation of fully anisotropic liquid crystal waveguide modes", J. Lightwave Technol., vol. 27, pp. 3812-3819, 2009

Organic devices for photonics

Progress towards ITO-free devices

Stéphanie Cheylan

ICFO - Institute of Photonic Sciences,
Mediteranean technology Park, 08860 Castelldefels (Barcelona) Spain
stephanie.cheylan@icfo.es

Abstract— **In this contribution, the most relevant and recent progress on ITO-free organic devices will be reviewed. To illustrate some of the challenges present, we have focused on a specific device, namely the organic light-emitting diode (OLEDs). The possibility to use thin metal layer as a substitute to ITO will be investigated in detail.**

Keywords: Polymer, OLED, ITO, electrode, thin metal films

I. INTRODUCTION

Since the discovery of conductivity in polymers and certain organic molecules, remarkable progress has been made in synthesizing organic materials, in understanding their properties and in developing them for use in electronic and optical devices. Currently, organic light-emitting diodes (OLEDs), photovoltaic cells (OPV) and field effect transistors (OFT) are being pushed towards commercialization. But other interesting applications are emerging such as RFID tags (radio frequency identification), memory devices, sensors, single-use diagnostic devices and more, which represent a future multi billion market. A principle advantage of organic electronics is that large, flexible substrates can be used. Polymer films (like polyester) are most widely used today, but paper, cardboard, thin glass and stainless steel are also prominent candidates.

A successful entry of organic devices into the general market requires, apart from high performance levels, a significant cost reduction of the devices. One of the limiting factor for the industrial implementation of organic devices is the use of indium tin oxide (ITO) as bottom electrode, which apart from being an expensive and scarce material also requires high temperature process for obtaining thick layers ideal for device application (Fig. 1). Therefore various alternatives with high conductivity and transparency have been studied to function as the anode.

We will give here a brief report of the various approaches investigated recently. In addition, our recent proposal and demonstration of thin metal layers as substitute to ITO for OLEDs will be discussed.

II. ORGANIC LIGHT-EMITTING DIODE

In the last decades organic light-emitting diodes (OLEDs) have been extensively investigated as the potential next generation technology for flat-panel display and lighting. The interest in this technology has been triggered due to the reports of new breakthroughs in device efficiencies, lifetimes, and achievable colors, including white [1].

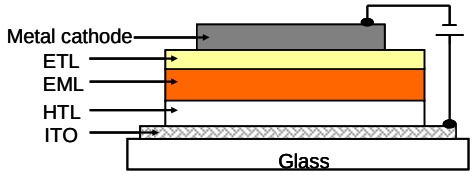


Figure 1: Schematic of the multilayer organic light-emitting device with the ITO as bottom electrode. EML is the emissive layer, ETL the electron transport layer and HTL the hole transport layer, all layers being organic.

An established method to obtain efficient OLEDs is use of multilayered device structures, consisting of many layers of organic semiconductor materials with different energy levels and functionalities, such as carrier transport, emission, and carrier blockage (Fig. 1). In such devices, indium-tin oxide (ITO), owing to its high optical transparency, good hole-injecting and commercial availability, has been used exclusively as a standard anode particularly for bottom emitting OLEDs. The surface of ITO glass is, however, chemically and physically ill-defined, which causes the detriment of its performance as the hole-injecting electrode in OLEDs. For example, its work function is known to dramatically depend on surface treatment methods and conditions. It has been reported that various species from the ITO will diffuse into the organic semiconductor layers leading to degradation in device performance.

A first approach to overcome several ITO limitations consisted in using thin metal layers (Ag, Cr) on top of ITO [2,3]. This double layer metal-ITO anode leads to an enhancement of the light output, even if its transmittance is lower than that of a single ITO layer. The metal-ITO anode is more favourable to device operation because of its optimized surface topography which leads to longer device lifetime. Adding a metal with a

high work function to the ITO surface is then considered as a method with great potential for OLED applications. However for metal-ITO anode, improvement was observed only in hole injection efficiency, but not in power efficiency. This clearly implies reduced quantum efficiency, which is undesirable. Furthermore, such metals are only semitransparent, hence diminishing potential gains in efficiencies resulting from the metal buffer layer, while still using a thick ITO layer as part of the electrode. To be able to achieve ITO-free devices, extensive efforts have been made towards finding superior transparent conductive oxides (TCO) with no or little In. TCOs are usually n-type conductors either in a pure state or doped and in principle guarantee good charge injection, high transparency, good electrical conductivities, tunable morphology and the possibility of deposition on large areas with low cost techniques. Recently interesting results have been reported either using them like anode or cathode in the device [4]. A promising material is Al doped Zinc Oxide (ZnO) or AZO, which might replace ITO due to its high transmittance and low sheet resistance [5]. Still, a relatively thick layer of around 100nm is needed in order to obtain such a low sheet resistance and further work is needed to optimize its deposition. However, the most appealing examples of the use of this class of compounds are as air-stable electrodes in hybrid LEDs (HyLEDs) [6] where very efficient devices have been reported, but unfortunately, such approach still requires the use of ITO. The closest that has been achieved so far in using ITO free contact is the recent work by J. Meiss *et al* [7]. They have shown that multilayer metal contact made of ultra thin thermally evaporated Al and Ag films can be used for the top contact of an inverted organic bulk heterojunction solar cells obtaining up to 2.2 % in efficiency.

III. Thin Metal Films to replace ITO as Electrodes

In this work, we have investigated the possibility of using a thin nickel layer instead of ITO as anodes for bottom-emitting organic light-emitting diodes [8]. Identical single-layer devices based on a blue-emitting polymer were fabricated as bottom-emitting diodes, and equipped with either an ITO or nickel hole injecting electrode. The sputtering fabrication process gives very smooth, continuous and conductive nickel films, even for a film thickness as low as 4 nm. Metal films with a thickness between 50 and 100 Å are routinely used to prepare semitransparent contacts for a variety of optoelectronic devices [9]. Similar transmittance performance as for TCOs can actually be achieved if the metal film thickness is low enough (down to a few tens of angstroms) [10]. In addition, metals intrinsically show a significantly lower resistivity with respect to TCOs, even when they are very thin.

It was demonstrated that similar efficiencies were reached for devices with either ITO or nickel films less than 10 nm [8]. The thin nickel films show higher roughness, higher square resistance and a lower transmittance of about 2.5 times compared with ITO. These characteristics lead to a less efficient hole injection in the nickel-based device, which results in lower current densities at a given voltage and a slightly higher threshold voltage than the ITO-based device. Nevertheless, similar luminance levels were obtained for ITO-based and nickel-based devices. Most importantly, no optical modes could be observed within the nickel layer because the film is too thin for a light trapping mechanism. Lifetime measurements of the devices are underway

Another important aspect of the ITO-free electrode is the possibility to be deposited on flexible substrates. Preliminary work has been done in this direction, using flexible polyethylene terephtalate (PET) substrates. So far, the nickel films deposited on PET show good quality and good properties as on glass. Devices are now being implemented.

IV. CONCLUSION

In this paper, we have reported recent advances on ITO-free electrode for organic devices, focusing mainly on OLEDs. We have shown how thin nickel films could provide a route to ITO-free devices, as a semitransparent anode material for bottom-light-emitting diodes, with several advantages including simple deposition, no need for post-deposition treatment and lower cost.

ACKNOWLEDGMENT

This work was carried out with the financial support of the Spanish Ministry of Education and Science through grant TEC2006-10665/MEC, TEC2007-60185 and the Consolider-Ingenio CSD2007-00007 and through the Ramon y Cajal program.

REFERENCES

[1] S. Reineke, F. Lindner, G. Schwartz, N. Seidler, K. Walzer, B. Lüssem, K. Leo, “White organic light-emitting diodes with fluorescent tube efficiency“ Nature vol. 459, pp. 234-238, 14 May 2009.

[2] R. Meerheim, R. Nitsche, K. Leo, “, Appl. Phys. Lett. vol. 93, pp. 043310-043313, 2008

[3] Y. Shen, D. B. Jacobs, G. G. Malliarias, G. Koley, M. G. Spencer, Adv. Mat. vol. 13, pp. 2131-2138, 2001.

[4] K. Morii, M. Ishida, T. Takashima, T. Shimoda, Q. Wang, M. K. Nazeeruddin, M. Graetzel, Appl. Phys. Lett. “” vol. 89, pp. 183510-183513, 2006.

[5] J. Meyer, P. Görrn, S. Hamwi, H.-H. Johannes, T. Riedl, W. Kowalsky, Appl. Phys. Lett. vol. 93, pp. 073308-073311, 2008.

[6] H. J. Bolink, E. Coronado, J. Orozco, M. Sessolo, Adv. Mat. vol. 20, pp. 1-8, 2008.

[7] J. Meiss, M. K. Riede, K. Leo, “Towards efficient tin-doped indium oxide (ITO)-free inverted organic solar cell using metal cathodes”, Appl. Phys. Lett. vol. 94, pp. 013303-1 – 3303-3, 2009.

[8] D. Krautz, S. Cheylan, D. S. Ghosh, V. Pruneri, “Nickel as an alternative semitransparent anode to indium tin oxide for polumer LED applications”, Nanotechnology vol. 20, pp..275204-275210, 2009.

[9] R. A. Hatton, M. R. Willis, M. A. Chesters, D. Briggs, “”, J. Mater. Chem. vol. 13, pp. 13722-13725, 2003.

[10] D. S. Ghosh, L. Martinez, S. Giurgola, P. Vergani, V. Pruneri, “Widely transparent electrodes based on ultrathin metals”, Opt. Lett. vol. 34, pp. 325-327, 2009.

Simultaneous Red-Green-Blue Organic Laser Devices

Stephen Morris, Philip Hands, Su Seok Choi, Alison Ford, Carrie Mowatt, Tim Wilkinson, and H. J. Coles*
Centre of Molecular Materials for Photonics and Electronics, Electrical Engineering Division, University of Cambridge, CB3 0FA, United Kingdom
*hjc37@cam.ac.uk

***Abstract*—This paper describes recent developments in organic laser devices based upon liquid crystalline media. The key features of a typical laser device are discussed along with a method for controlling the band gap (>100 nm) using electric fields. Finally, simultaneous red-green-blue laser arrays are demonstrated from a single device when optically pumped.**

Keywords; laser, photonic band gap, liquid crystals

I. INTRODUCTION

Liquid crystals are best known for their role in flat panel displays but recent research has shown that these materials can, in fact, be used to form low threshold organic laser devices. This technology is of significant interest for a number of applications including laser projection displays, telecommunication devices and medical diagnostic techniques. The liquid crystal laser exhibits many characteristics which make it an attractive alternative to semiconductor lasers. First and foremost, the periodic structure self-organizes without the need for any complex fabrication procedure. Secondly, any wavelength can be chosen ranging from the deep ultraviolet to the infra-red by adjusting the periodicity of the structure through chemical, mechanical, or electrical stimulus. Finally, due to the sensitivity of liquid crystals to external electric fields, the 'molecular' ordering and thus the optical properties can be altered in-situ. This can lead to a number of significant effects not least of all tuning of the emission wavelength. Laser emission from these materials is a manifestation of the large gain that exists at the edge of a photonic band-gap due to the large density of photon states. Combined with spontaneous emission from a gain medium, such as a laser dye, this can lead to laser action [1 – 5].

In recent years, we have studied these organic laser devices in detail to show low excitation thresholds, high slope efficiencies, and wavelength tuneability [2 - 8]. Our research has focused on understanding the correlations between the macroscopic properties of the liquid crystal such as birefringence, dielectric anisotropy, elasticity etc and the performance properties of the corresponding liquid crystal laser device [2 – 4]. Results have shown that high birefringence and a high order parameter are of paramount importance to the performance characteristics. Furthermore, optimization of the device thickness also has a significant effect on the emission properties [3]. The cell thickness ranges from 5 microns to 25 microns.

To demonstrate the versatility of this laser technology we have recently shown simultaneous multi-wavelength laser emission from a single liquid crystal sample by creating a two-dimensional laser array fabricated from a dye-doped chiral nematic liquid crystal [5, 6]. By forming a pitch gradient across the cell, thus varying the periodicity, and optically pumping the sample using a micro-lens array, a polychromatic laser array can be observed consisting simultaneously of Red-Green-Blue colors [6]. As an example, the two-dimensional polychromatic array could be used as a means for producing a laser-based display whereby no complex fabrication procedure is required to generate the individual 'pixels'.

II. FABRICATING A LIQUID CRYSTAL LASER

A. The liquid crystal host

There are several different liquid crystal phases that are suitable for generating band-edge laser emission. Specifically, these are phases which exhibit a macroscopic periodic structure such as a chiral nematic or chiral smectic whereby the 'local' director (the average pointing direction of the molecules) rotates about a common axis to form a helix. This helix results in a periodic refractive index which leads to a gap in the photonic bands. Examples of liquid crystal phases which exhibit a helical/periodic structure include the chiral nematic phase, the chiral smectic phase, and the blue phases. The latter exhibit a 3-d band-gap whilst the former only exhibit a band-gap that is 1-d.The majority of the research on these lasers has been carried out on the chiral nematic phase as this typically exists over wide temperature ranges, forms uniform high-quality macroscopic helices, and is miscible with commercial laser dyes.

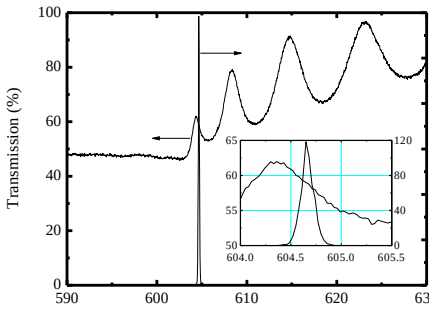


Figure 1. The transmission spectrum of the photonic band gap (left-hand axis) and the laser emission spectrum (right hand axis).

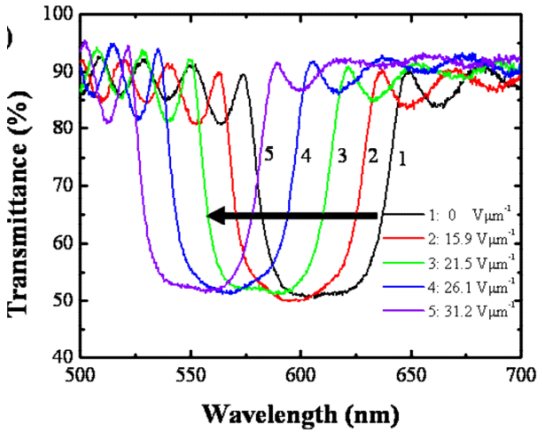


Figure 2.Wavelength tuning of the photonic band gap for an increase in the electric field strength. The frequency of the applied a.c. electric field is 1 kHz.

The position and width of the photonic band gap in terms of wavelength is governed by the first order approximation $\Delta np = \Delta\lambda$ whereby Δn is the birefringence and p is the pitch of the helix. Both of these properties can be controlled at the molecular level by adjusting the chemical structure and thus enabling the band-gap to be positioned at any desired wavelength from the ultra-violet to the infrared.

B. The gain medium

For the gain medium a laser dye is typically used although a rare-earth or transition metal may also be suitable. In order to ensure that laser emission occurs, one edge of the photonic band gap must be matched, spectrally, to the fluorescence curve of the laser dye. Moreover, so as to maximize the emission efficiency this band-edge must be matched to the gain maximum which usually occurs at, or close to, the fluorescence maximum. High quantum efficiency dyes are required for low thresholds and high slope efficiencies [7].

III. EMISSION CHARACTERISTICS

The emission from these laser devices, when optically pumped with a solid state laser such as an Nd:YAG operating with nanosecond pulse widths, have been found to be single mode with a narrow linewidth (~ 0.06 nm – limited by resolution of the apparatus, see Figure 1) although this does depend upon the uniformity and alignment of the liquid crystalline structure. If defects are present or the alignment consists of polydomains then broader linewidths and multimode emission are observed. Nevertheless, for low molar mass liquid crystalline compounds, large-area monodomains are readily achievable resulting in high quality factor structures and narrow linewidth emission. The emission profile is near-Gaussian. As for the slope efficiencies these can be as high as 70% for multi-pass device architectures.

IV. TUNING THE PHOTONIC BAND GAP

It is possible to tune the wavelength of the photonic band gap using electric fields. However, for the majority of cases this often leads to deterioration of the quality of the macroscopic periodic structure and thus a decrease in the transmission quality of the photonic band gap. Using ferroelectric electric dopants in a chiral nematic liquid crystal host we have observed broadband wasvelength tuning covering over a 100 nm without any change to the finesse of the structure (see Figure 2). This is the result of a contraction of the pitch as the electric field strength is increased.

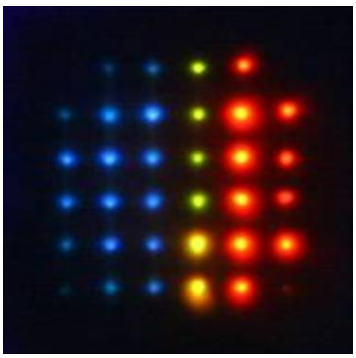


Figure 3.Simultaneous red-green-blue laser emission from a single liquid crystal device when optically pumped at 430 nm.

V. SIMULTANEOUS RED-GREEN-BLUE ARRAYS

Using a combination of dyes in a single liquid crystal cell, which exhibited a gradient in the pitch, the result was laser emission at multiple wavelengths when optically pumped at 430 nm. Figure 3 shows a 2-d array of simultaneous red-green-blue laser emission from a single liquid crystal cell.

ACKNOWLEDGMENTS

The authors gratefully acknowledge the financial support of the Engineering and Physical Sciences Research Council (UK) through the Basic Technology Research Grant “Coherent Optical Sources using Micro-molecular Structures” (COSMOS) (Grant No. EP/D04894X/1).

REFERENCES

[1] V. I. Kopp, B. Fan, H. K. M. Vithana, A. Z. Genack, “Low-threshold lasing at the edge of a photonic stop band in cholesteric liquid crystals” *Opt. Lett*. **23** (21), 1707 (1998)

[2] S. M. Morris, A. D. Ford, M. N. Pivnennko, O. Hadeler, and H. J. Coles, “Correlations between the performance properties of a liquid crystal laser and the corresponding macroscopic material properties” Phys. Rev. E., 74, 061709 (2006)

[3] S. M. Morris, A. D. Ford, C. Gillespie, M. N. Pivnenko, O. Hadeler, and H. J. Coles, “The emission characteristics of liquid crystal lasers” J. SID, 14 (6), 565-573 (2006)

[4] A. D. Ford, S. M. Morris, M. N. Pivnenko, C. Gillespies, and H. J. Coles, “Emission characteristics of a homologous series of bimesogenic liquid crystal lasers” Phys. Rev. E. 76, 051703 (2007)

[5] P. J. W. Hands, S. M. Morris, T. D. Wilkinson, and H. J. Coles, “Two-dimensional liquid crystal laser array” Opt. Lett. 33 (5), 515-517 (2008)

[6] S. M. Morris, P. J. W. Hands, S. Findeisen-Tandel, R. H. Cole, T. D. Wilkinson, “Polychromatic liquid crystal laser arrays towards display applications” Opt. Exp. 16 (23) 18827-18837 (2008)

[7] C. Mowatt, S. M. Morris, M. H. Song, T. D. Wilkinson, R. H. Friend, and H. J. Coles, Comparison of the performance of chiral nematic liquid crystal lasers with different gain media, J. Appl. Phys (in press)

[8] S. S. Choi, S. M. Morris, W. T. S. Huck, and H. J. Coles, “ Electrically tuneable liquid crystal photonic band gap” Adv. Mater.

Continuous-wave Lasers in Polymer waveguides

J. Yang, C. Grivas(*), M.B.J. Diemeer, A. Driessen, and M. Pollnau
Integrated Optical Micro Systems, MESA+ Institute for Nanotechnology,
University of Twente, Enschede, the Netherlands
* On leave from Optoelectronics Research Centre, University of Southampton,
Southampton, United Kingdom
E-mail: j.yang@ewi.utwente.nl

***Abstract*—Channel waveguides based on a polymer, 6-fluorinated-dianhydride/epoxy, which is actively doped with a rare-earth-ion-doped complex, Nd(thenoyltrifluoroacetone)$_3$ 1,10-phenanthroline, have been fabricated. Photoluminescence peaks at 880 nm, 1060 nm, and 1330 nm have been experimentally observed. By optimization of the fabrication procedure of both, host material and optical structure, continuous-wave laser operation on both, the four-level and quasi-three-level transitions near 1060 nm and 880 nm, respectively, has been demonstrated in channel waveguides.**

Keywords-photodefined polymer, organic complex, neodymium, polymer waveguide laser, continuous-wave polymer laser

I. INTRODUCTION

Polymer waveguides have emerged as a viable technology for integrated optical devices due to their low cost, capability of integration with other material systems, and ease of fabrication and modification of their chemical structure. This latter property offers enormous flexibility in the design of waveguide laser media. Research in the area of solid-state polymer lasers over the last years resulted in numerous reports on semiconducting [1] and dye-doped [2] polymer sources, which due to absorption by excitons in their excited triplet state operate in the pulsed regime. Although rare-earth-ion-doped polymers offer a suitable medium for the generation of continuous-wave (CW) laser emission, they are notably absent from the list of polymer sources realised, which is largely due to the fluorescence quenching of the dopant ions. The latter occurs by coupling of their excited state to high-energy vibrational modes of C-H and O-H bonds both in the polymer host and in the complex, where they are encapsulated in order to be dissolved in the polymer [3], thereby imposing a requirement for high pump powers, which are usually destructive for the active medium.

Here, waveguide laser operation of Nd^{3+}-complex-doped polymer channel waveguides near 1060 and 880 nm is reported, which is, to the best of our knowledge, the first demonstration of a rare-earth-ion-doped polymer waveguide laser as well as CW polymer laser.

II. WAVEGUIDE FABRICATION

The fabrication process of channel waveguides has been detailed in Ref. [4]. In brief, a neodymium complex, Nd(TTA)$_3$phen, was synthesized and incorporated into the fluorinated host 6-FDA/epoxy. The fluorine ligands and the fluorination of the host material significantly decrease the luminescence quenching originating from high-energy vibrations of C-H and O-H bonds in the polymer host.

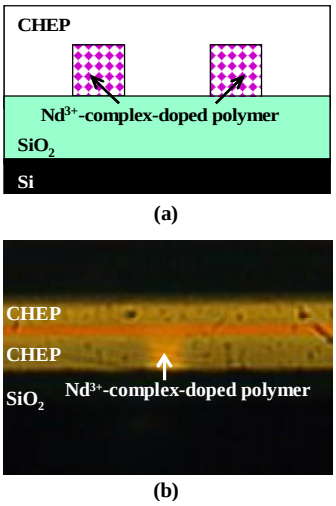


Figure 1. (a) Geometry of the buried Nd^{3+}-complex doped polymer waveguides and (b) optical microscope picture of a channel waveguide cross section

By spin-coating onto a thermally oxidized silicon wafer and subsequently photodefining a cycloaliphatic epoxy prepolymer (code name CHEP) [5], inverted channels in the low-refractive-index CHEP polymer were obtained. The core material, a Nd(TTA)$_3$phen doped 6-FDA/epoxy solution, was then backfilled via spin-coating and 5×5 μm^2 Nd-complex-doped channel waveguides were realized after thermal curing. An additional 3-μm-thick CHEP layer was spin-coated on top of the channels as the upper cladding layer. Figures 1a and b show the geometry of the Nd^{3+} doped 6-FDA/epoxy channel waveguide and an optical microscope picture of a channel waveguide cross section, respectively. The Nd^{3+} concentration for the laser experiment is 1.03×10^{20} cm^{-3}.

The photoluminescence of the Nd^{3+}-doped polymer channel waveguides was investigated by pumping the channel waveguides at 800 nm using a Ti:sapphire laser, and the resulting fluorescence collected from the output face of the waveguide was measured by a spectrometer and an InGaAs

detector (Fig. 2). Three luminescence bands near 880 nm, 1060 nm, and 1330 nm were identified, corresponding to the

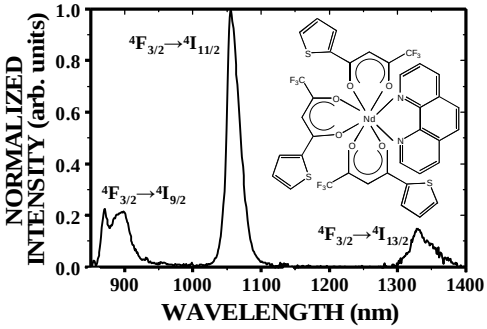


Figure 2. Luminescence spectrum of a buried Nd^{3+}-complex-doped polymer waveguide (corrected with respect to the response of the detector).

transitions between the metastable $^4F_{3/2}$ state and the lower lying $^4I_{9/2}$, $^4I_{11/2}$, and $^4I_{13/2}$ states of the Nd^{3+} ions, respectively. The luminescence lifetime of Nd^{3+} in the 6-FDA/epoxy host was measured to be 141 μs, thus demonstrating that the fluorination effectively diminishes non-radiative quenching of the luminescence.

III. Laser Experiments

Laser operation was achieved with a CW Ti:sapphire pump laser emitting at 800 nm. To form the laser cavity two high-reflective (HR) mirrors at the signal wavelength were attached at the end-faces of the 7.5-mm-long waveguides.

CW laser emission was observed near 1060.2 nm above a threshold of 50 mW of absorbed pump power, and is given in Fig. 3a. The laser power characteristics were studied using a set of four outcoupling mirrors with a transmission of 1.8%, 3%, 4%, and 5% at the laser wavelength. The laser output as a function of absorbed pump power is given in Fig. 3b (closed dots). The maximum output power of 0.98 mW and the highest slope efficiency of 2.15% were obtained with 5% outcoupling.

Laser operation was also achieved on the quasi-three-level transition near 878 nm (Fig. 3a) above an absorbed pump power threshold of 67 mW when the cavity was formed with two HR mirrors. Re-absorption losses combined with the relatively low stimulated-emission cross section at this wavelength compared to the dominant four-level transition require high pump powers, which however is in conflict with the need to maintain the pump power at a low level to avoid adverse effects on laser performance induced by thermal degradation of the material. Using 2.2% outcoupling, we obtained a slope efficiency of 0.35% and a laser threshold of 74.5 mW (open dots in Fig. 3b).

IV. Conclusion

Successful design of a polymer host material and an organic complex to encapsulate the Nd ions enabled the development of Nd-complex-doped channel waveguide lasers operating on either the four-level or the quasi-three- level

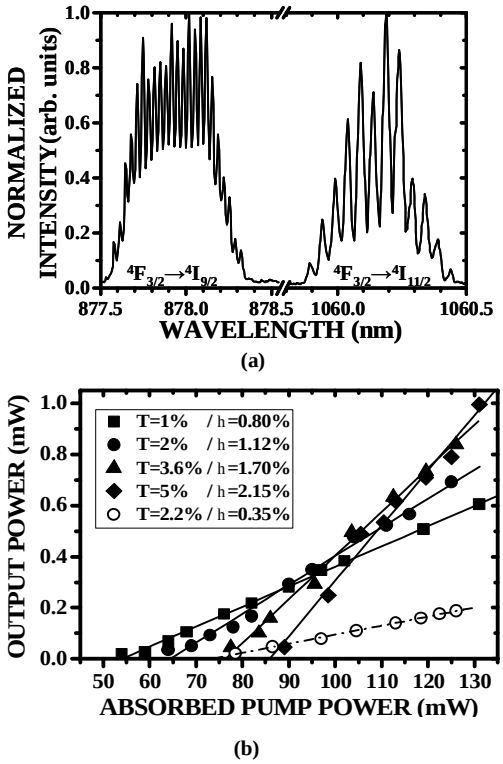


Figure 3. Laser emission of a buried Nd^{3+}-complex-doped polymer waveguide at 1060.2 nm and 878 nm: (a) typical laser spectra and (b) input-output curves.

transition near 1060.2 nm and 878 nm, respectively. The lasers exhibit remarkable lifetime stability as they can withstand at least two hours of uninterrupted operation whilst producing output powers of up to 0.98 mW. This is the first demonstration of a rare-earth-doped polymer waveguide laser as well as a CW polymer laser.

Acknowledgment

This work was supported by the Dutch Technology Foundation STW within the framework of project TOE 6986.

References

[1] I. D. W. Samuel and G. A. Turnbull, “Organic semiconductor lasers,” Chem. Rev., vol. 107, pp. 1272-1285, 2007.

[2] A. Costela, I. García-Moreno, and R. Sastre, “Polymeric solid-state dye lasers: Recent developments,” Phys. Chem. Chem. Phys., vol. 5, pp. 4745-4763, 2003.

[3] L. H. Slooff, A. van Blaaderen, A. Polman, G. A. Hebbink, S. I. Klink, F. C. J. M. Van Veggel, D. N. Reinhoudt, and J. W. Hofstraat, “Rare-earth doped polymers for planar optical amplifiers,” J. Appl. Phys., vol. 91, pp. 3955-3980, 2002.

[4] J. Yang, M. B. J. Diemeer, D. Geskus, G. Sengo, M. Pollnau, and A. Driessen, “Neodymium-complex-doped photodefined polymer channel waveguide amplifiers,” Opt. Lett., vol. 34, pp. 473-475, 2009.

[5] M. B. J. Diemeer, L. T. H. Hilderink, R. Dekker, and A. Driessen, “Low-cost and low-loss multimode waveguide of photodefinable epoxy”, IEEE Photon. Technol. Lett., vol. 18, pp. 1624-1626, 2006.

Semi-transparent polymer solar cells

Alexander Colsmann, Andreas Puetz, Felix Nickel, Manuel Reinhard, Uli Lemmer
Lichttechnisches Institut
Karlsruhe Institute of Technology (KIT)
76131 Karlsruhe, Germany
alexander.colsmann@kit.edu

Abstract—**Semi-transparent organic photovoltaic devices have great potential for integrated system applications. In this work we present highly efficient semi-transparent devices comprising a polymer:fullerene blend with absorption extending to the near infrared. We further demonstrate an approach to organic photovoltaic devices featuring a cathode from a transparent and highly conductive polymer.**

Keywords: Semi-transparent solar cell; conjugated polymer; organic optoelectronic device

I. INTRODUCTION

Due to the recent reports about organic bulk-heterojunction photovoltaic devices with power conversion efficiencies exceeding 7% [1,2] polymer solar cells made a giant leap towards economically interesting optoelectronic devices. This success of polymer solar cells can be attributed to the development of new co-polymers with an extended absorption to the infrared. Despite the ultra-thin active films in an organic photovoltaic device, these co-polymers act as efficient photon harvesting molecules due to their remarkably high absorption coefficients. Hence this material class offers the potential of a significant material cost reduction in optoelectronic devices. However, in order to dissociate generated excitons in organic photovoltaic devices, the incorporation of strong electron acceptors in the active layer is mandatory. Among these strong acceptors, the fullerene derivatives [6,6]-phenyl C_{61} butric acid methyl ester ($PC_{60}BM$) can be considered as standard material that allows for a very efficient electron transfer from the polymer, while also ensuring a good electron transport to the device cathode. By replacing the $PC_{60}BM$ with [6,6]-phenyl C_{71} butric acid methyl ester ($PC_{70}BM$) the absorption of organic solar cells can be even more enhanced in order to increase the device efficiency.

In contrast to their inorganic counterparts, organic molecules exhibit a band absorption that is limited to a certain wavelength regime, making them a predestined material class for semi-transparent optoelectronic devices. Possible applications for semi-transparent solar cells range from façade integration and window shadowing to integrated power sources for off-grid energy systems. Autonomous signage is a further field of application among many others. Due to the close relation with organic photodetectors, very similar device architectures can be implemented in low-cost lab-on-a-chip systems for integrated light detection. In particular, the combination with low-bandgap, infrared absorbing polymers that let the visible light pass are a promising approach.

In this work we present promising device architectures for highly efficient semi-transparent organic photovoltaic devices incorporating polymer/fullerene bulk-heterojunctions.

II. RESULTS AND DISCUSSIONS

A. *Semi-transparent solar cells featuring sputtered transparent cathodes.*

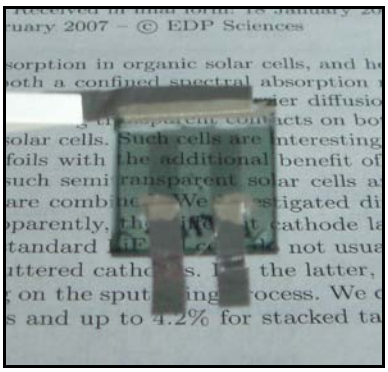


Figure 1: Photo of an organic solar cell comprising a PSBTBT:$PC_{70}BM$ absorber layer, a sputtered ZnO cathode and a LiF/Al interlayer.

The polymer poly[(4,4'-bis(2-ethylhexyl)dithieno[3,2-b:2',3'-d]silole)-2,6-diyl-alt-(2,1,3-benzothiadiazole)-4,7-diyl] (PSBTBT) makes up for highly efficient photovoltaic devices when blended with the acceptor $PC_{70}BM$ [3]. In order to build a semi-transparent device with two transparent electrodes, we fabricated polymer solar cells following established standard procedures but replaced the opaque metal cathode with a transparent, sputtered zincoxide electrode following the procedure described in [4]. An ohmic contact between the high work function zincoxide and the absorber was established by introducing a combination of ultrathin layers of lithiumcobaltoxide ($LiCoO_2$, 0.5 nm) and aluminum (3 nm) below the zincoxide cathode. In the presence of aluminum alkalihalogenides dissociate. While the halogen atom reacts with the aluminum cathode, the alkali (here: lithium) atom migrates into the upper parts of the active layer and subsequently establishes n-doping [5]. The resulting solar cell exhibits a power conversion efficiency of $\eta \approx 3\%$. A reference device comprising an opaque aluminum electrode and a $LiCoO_2$ interlayer, however, exhibits exactly the same electrical properties within the measurement accuracy. Subsequently it can be concluded, that semi-transparent devices can exhibit comparable high efficiencies as non

transparent devices. However, it is important to point out that the vacuum chamber was loaded from ambient atmosphere before cathode deposition. Thus the samples were contaminated with air. Keeping the entire process under inert atmosphere will very likely account for significantly enhanced semi-transparent cell efficiencies, as we were able to fabricate 5.5% efficient solar cells from PSBTBT:$PC_{70}BM$ comprising a calcium cathode under nitrogen atmosphere.

B. Polymeric electrodes for semi-transparent solar cells

One of the expected advantages of organic photovoltaic devices is the potential for significant fabrication cost reduction through printing processes. Subsequently, it is favorable to use printable, i.e. solution processable, functional layers instead of vacuum deposited films. The transparent anode can easily be replaced by the highly conductive polymer system poly(3,4-ethylenedioxythiophene):poly(styrenesulfonate) (PEDOT:PSS) [6-8]. Unfortunately, there is no low work function material system with similar properties that is suitable for the extraction of electrons from the device.

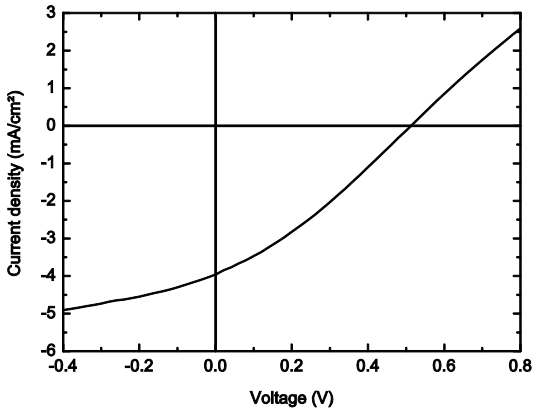


Figure 2: JV curve of a semi-transparent solar cell comprising Indium tin oxide (125nm)/PEDOT:PSS (25nm)/P3HT:PCBM (200nm)/BPhen:Li (20nm)/Gold (3nm)/PEDOT:PSS (50nm).

However, by first establishing an n-doped interlayer below the cathode, conductive polymers with high work functions become interesting materials for cathodes, too [9]. With a polymeric electrode n-doping by $LiCoO_2$ does not work since a reaction partner for $LiCoO_2$ is missing in order to create diffusing lithium atoms. Subsequently, intentional n-doping of an additional electron transport layer must be carried out. In this case we decided to co-evaporate a lithium doped bathophenanthroline (BPhen:Li) [10] followed by nominal 3 nm gold on top of a poly-(3-hexylthiophene-2,5-diyl):$PC_{60}BM$ bulk heterojunction before cathode deposition. The polymer cathode then was spincast on top of the layer stack. While the BPhen:Li interlayer accounts for an ohmic contact to the PEDOT:PSS cathode, the gold with its high density of states is needed in order to convert the electron current in BPhen:Li to a hole current within the p-type PEDOT:PSS, i.e. an efficient lossless charge recombination from electrons in BPhen:Li and holes in PEDOT:PSS. This process is well known for tandem solar cells and thus often addressed in literature [11]. Though an ohmic contact is established between BPhen:Li and PEDOT:PSS, the short circuit current density and subsequently the device efficiency ($\eta \approx 0.6\%$) are quite moderate as depicted in figure 2. Partially, this moderate efficiency can be accounted to the considerable serial resistance in the polymer cathode. Further, the recombination at the BPhen:Li/PEDOT:PSS interface needs further investigations in order to improve the lossless conversion between electrons and holes.

III. CONCLUSION

In conclusion we demonstrated highly efficient semi-transparent polymer solar cells comprising a sputtered ZnO cathode. We further gave evidence that a semi-transparent device can also be formed by utilizing polymer electrodes for electron extraction.

REFERENCES

[1] Y. Liang, Z. Xu, J. Xia, S.-T. Tsai, Y. Wu, G. Li, C. Ray, and L. Yu, "For the Bright future – Bulk Heterojunction Polymer Solar Cells with Power Conversion Efficiency of 7.4%", Adv. Mater. 22 (2010) 1

[2] H.Y. Chen, J. Hou, S. Zhang, L. Yu, Y. Wu, G. Li, Y. Liang, G. Yang, and Y. Yang, "Polymer solar cells with enhanced open-circuit voltage and efficiency", Nat. Photon. 3 (2009) 649

[3] H.Y. Chen, J. Hou, A. Hayden, H. Yang, K. Houk, and Y. Yang, "Silicon Atom Substitution Enhances Interchain Packing in a Thiophene-Based Polymer System", Adv. Mater. 21 (2009) 1

[4] J. Hanisch, E. Ahlswede, and M. Powalla, „All-sputtered contacts for organic solar cells ", Thin Solid Films 516 (2008) 7241

[5] G. Greczynski, M. Fahlman, and W. Salaneck, „Hybrid interfaces of poly(9,9-dioctylfluorene) employing thin insulating layers of CsF: A photoelectron spectroscopy study", J. Chem. Phys. 114 (2001) 8628

[6] A. Colsmann, F. Stenzel, G. Balthasar, H. Do, and U. Lemmer, "Plasma patterning of poly(3,4-ethylenedioxythiophene):poly(styrenesulfonate) anodes for efficient polymer solar cells", Thin Solid Films 517 (2009) 1750

[7] H. Do, M. Reinhard, H. Vogeler, A. Pütz, M.F.G. Klein, W. Schabel, A. Colsmann, and U. Lemmer, „Polymeric anodes from poly(3,4-ethylenedioxythiophene):poly(styrenesulfonate) for 3.5% efficient organic solar cells", Thin Solid Films 517 (2009) 5900

[8] E. Ahlswede, W. Mühleisen, M.W. Bin Moh Wahi, J. Hanisch, and M. Powalla, „Highly efficient organic solar cells with printable low-cost transparent contacts", Appl. Phys. Lett. 92 (2008) 143307

[9] F. Nickel, A. Puetz, M. Reinhard, H. Do, C. Kayser, Alexander Colsmann, and Uli Lemmer, „ Cathodes comprising highly conductive poly(3,4-ethylenedioxythiophene): poly(styrenesulfonate) for semi-transparent polymer solar cells", Org. Electron. doi:10.1016/j.orgel.2009.12.009

[10] A. Colsmann, J. Junge, T. Wellinger, C. Kayser, and U. Lemmer, „ Optimization of electron transport and cathode materials for efficient organic solar cells", SPIE-Eur. Conf. Proc., Strasbourg 6192 (2006) 6195

[11] A. Colsmann, J. Junge, C. Kayser, U. Lemmer, „Organic tandem solar cells comrising polymer and small-molecule subcells", Appl. Phys. Lett. 89 (2006) 203506

Ultrafast all-optical switching in organic photonic devices.

J. Clark
OE, Cavendish Laboratory,
J J Thomson Avenue,
Cambridge, CB3 0HE, UK
jc414@cam.ac.uk

T. Virgili, J. Cabanillas-Gonzalez,
K.C. Vishnubhatla,
S. Perissinotto and
G. Lanzani
IIT, Dipartimento di Fisica and
IFN-CNR, Politecnico di Milano,
Milano 20133, Italy

R. Xia
Blackett Labs,
Imperial College, London,
Prince Consort Road,
London SW7 2AZ, UK

L. Bazzana
LUCEAT S.p.A., Viale G. Marconi 31,
Dello (BS),
Italy

Abstract—**Using the knowledge gained by studying fundamental light-matter interactions in conjugated polymers, we have developed novel organic photonic devices which are capable of all-optical ultrafast gain switching for applications in data communication networks.**

Keywords-organic photonics; all-optical switching

I. Introduction

Currently, modulation and switching are achieved by a combination of light and electronics: optoelectronics. This limits the speed and density of communications. *All-optical* modulation, on the other hand, performs the whole process with photons providing much higher achievable speeds. All-optical ultrafast switching is currently an open field in terms of materials and mechanisms. Here we demonstrate all-optical gain switching in conjugated polymer-based photonic devices. Organics, and conjugated polymers in particular, are promising candidates for photonic applications as they have large optical cross-sections, are tuneable across a range of wavelengths and are cheap, robust and flexible.

Figure 1 demonstrates a schematic of light-matter interactions in conjugated polymers. (1) Absorption of light ($S_0 \rightarrow S_1$) forms a tightly bound electron-hole pair (exciton). From this excited state (S_1), stimulated emission (2) can occur to produce amplification (gain) or lasing. In addition, charges can be generated through exciton dissociation. The exact mechanisms behind charge generation in these materials is still hotly debated, although it has become clear that (i) it is more likely to occur from higher-lying states (shown by process (3) in Figure 1), and (ii) interactions between chains increase the charge generation yield. Increased charge photo-generation yield, although useful for solar cell applications, is often detrimental for other photonic applications such as lasers and amplifiers, as the charge absorption band overlaps spectrally with the stimulated emission, shown by (4) in Figure 1. Therefore, charge generation acts to quench the stimulated emission, gain and lasing action.

It is therefore critically important to be able to control the charge generation (3) and recombination dynamics (5) in conjugated polymers for optical amplification applications. A step towards this control is to fully understand charge photo-generation. To that end, we study the effect of interchain interactions on charge photo-generation by isolating conjugated polymers in an inert matrix and using a time-resolved technique known as *pump-push-probe* spectroscopy [4].

II. Results

We find that exciton dissociation can occur even in isolated chains, forming *on-chain* charge pairs that recombine rapidly (within 150 fs) owing to the one-dimensional nature of the conjugated polymer chain [3]. Furthermore, intra-chain charge pairs are efficiently photo-generated only through excitation to higher-lying states. Using this knowledge, we can control charge generation using a 'gating' pulse to re-excite polymer chains to higher-lying states. Charges are produced and the stimulated emission is efficiently quenched. Then, fast recombination occurs and the gain recovers.

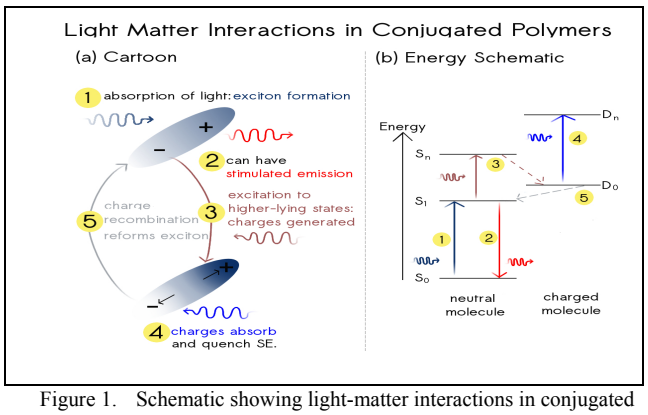


Figure 1. Schematic showing light-matter interactions in conjugated polymers. (a) Cartoon, (b) Energy Level Schematic demonstrating (1) absorption of light ($S_0 \rightarrow S_1$) and formation of exciton, (2) stimulated emission (SE), (3) re-excitation to S_n, to form charges (D_n) (4) absorption by the charges (which overlaps spectrally with SE) and (5) recombination of the charges to form an exciton (S_1) and recovery of the stimulated emission.)

This work was funded by the European Union under framework FP6, project POLYCOM, contract number 026365.)

As an example, Figure 2 shows the stimulated emission (SE) as a function of time in a plastic optical fiber (POF) doped with a fluorene oligomer. The pump arrives at t=0 ps (1) producing SE, (2). The gate arrives at ~2 ps (3) and completely quenches the SE (4). Recovery of SE (5) depends on the photo-generated charge lifetime, which depends on the sample morphology and chemical structure, but is largely independent of polymer length.

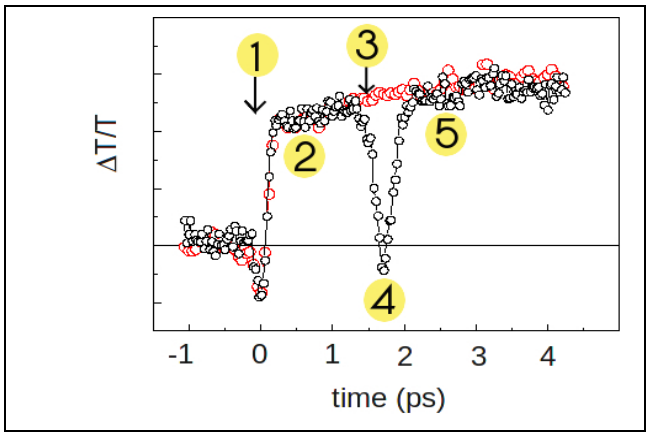


Figure 2. Pump-probe (red) and pump-push-probe (black) dynamics of polyfluorene-doped POF.

III. Applications

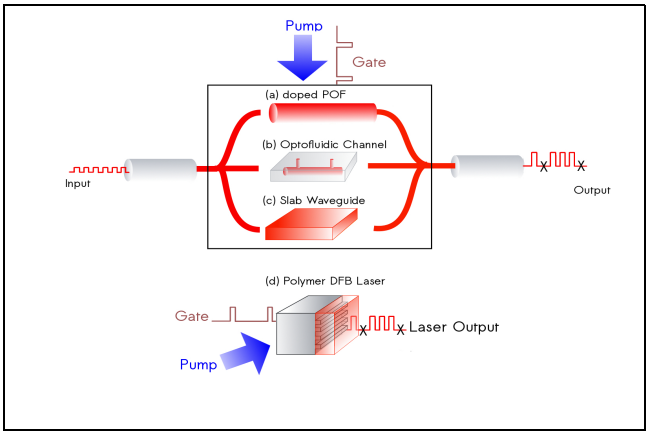


Figure 3. Schematic showing photonic devices using ultrafast switching (a) doped plastic optical fiber (POF), (b) optofluidic channel, (c) slab waveguide and (d) polymer distributed feedback (DFB) laser.

These discoveries have lead to the development of a new generation of organic lasers and amplifiers that can be optically controlled, with a gating pulse acting to switch off the gain. In particular, we have developed four different photonic devices, based on the principle of ultrafast switching (Figure 3): (a) Conjugated polymer/oligomer doped plastic optical fiber amplifiers (POF) for integration in data communication networks [1], (b) Optofluidic channel, capable of lasing, amplification and switching for integration in lab-on-a-chip type applications [4], (c) Conjugated polymer slab waveguides capable of optical amplification and switching, and (d) Conjugated polymer distributed feedback (DFB) lasers capable of being optically controlled [2, 5].

IV. Impact

The work outlined here is a breakthrough in all-optical switching for organic photonics as we demonstrate a *resonant* switching process with high on/off ratios and ultrafast response times. In the future, these findings may increase the data transmission rates in data communications, allow a move towards time-devision multiplexing (TDM) to increase bandwidth and could have implications for all-optical computing.

References

[1] J. Clark, L. Bazzana, D. D. C. Bradley, J. Cabanillas-Gonzalez, G. Lanzani, D. G. Lidzey, J. M. Morgado, N. A., T. W. C., T. Virgili, and R. Xia. Blue polymer optical fiber amplifiers based on conjugated fluorene oligomers. *J. Nanophotonics*, 2:023504, 2008.

[2] S. Perissinotto, G. Lanzani, M. Zavelani-Rossi, M. Salerno, and G. Gigli. Ultrafast optical switching in distributed feedback polymer laser. *Appl. Phys. Lett.*, 91(19):191108, 2007.

[3] T. Virgili, D. Marinotto, C. Manzoni, G. Cerullo, and G. Lanzani. Ultrafast intrachain photoexcitation of polymeric semiconductors. *Phys. Rev. Lett.*, 94(11):117402, 2005.

[4] K. C. Visnubhatla, J. Clark, G. Lanzani, R. Ramponi, R. Osellame, and T. Virgili. Ultrafast optofluidic gain switch based on conjugated polymer in femtosecond laser fabricated microchannels. *Appl. Phys. Lett.*, 94:041123, 2009.

[5] R. Xia, C. Cheung, A. Ruseckas, D. Amarasinghe, I. D. W. Samuel, and D. D. C. Bradley. Wavelength conversion from silica to polymer optical fibre communication wavelengths via ultrafast optical gain switching in a distributed feedback polymer laser. *Adv. Mater.*, 19(22):4054, 2007.

An Integrated Reconfigurable Bragg Grating utilising a Photoresponsive Co-polymer

R. M. Parker, J. C. Gates, H. L. Rogers, M. C. Grossel, P. G. R. Smith
Optoelectronics Research Centre and the School of Chemistry
University of Southampton
Southampton, UK
rmp@orc.soton.ac.uk

***Abstract*— Reconfigurable Bragg grating devices are of significant interest for telecomm applications. Such devices can be fabricated by combining a UV-written silica Bragg grating with an azobenzene-based polymer – a photoresponsive material that undergoes reversible refractive index change on exposure to ultraviolet light. The preliminary 17 GHz tuning response suggests future applicability.**

Keywords- reconfigurable Bragg grating; photoresponsive polymer; direct UV written.

I. INTRODUCTION

We shall present a proof of concept for a reconfigurable Bragg grating filter using the refractive index change on photo-induced isomerism of an azobenzene functionalised methacrylate co-polymer.

Reconfigurable optical devices are of great interest for telecomm applications; such as dispersion compensation, switching, and wavelength multiplexing. Bragg gratings are important elements in such systems and, therefore, reconfigurable optical Bragg grating structures with fine wavelength control and wide tuneability are desirable. Previous approaches to this problem are to incorporate a degree of reconfiguration into existing Bragg devices through tuning of the refractive index by temperature [1], piezoelectric [2], magnetostrictive [3], or mechanically induced strain [4]. With some exceptions, these all require a continual supply of electrical power to maintain the altered wavelength.

Azobenzene-based polymers can act as photosensitive, nonlinear optical, or photorefractive materials with ever increasing fields of application, including: programmable optical interconnects, electro-optic modulation, coherent image amplification, and holographic storage [5]. The simple azobenzene motif can undergo reversible isomerism from the *trans* to the *cis*-isomer upon exposure to ultraviolet light, as shown in Fig. 1.

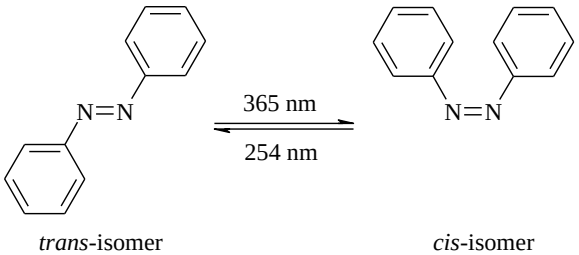


Figure 1. The reversible photoisomerism of the azobenzene motif, upon exposure to UV light.

We would like to thank the EPSRC for funding this research.

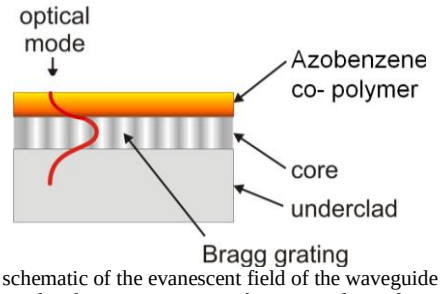


Figure 2. A schematic of the evanescent field of the waveguide penetrating into the photo-responsive azobenzene polymer layer.

Upon isomerisation between the *trans* and *cis*-isomer there is a change in the polarisability of the azobenzene molecule, resulting in a change in refractive index. Barley [6] has reported an example of a siloxane-based polymer functionalised with an azobenzene derivative. The polymer contained only 5% azobenzene but still exhibited a change in refractive index of 3.5×10^{-3}. Incorporation of such a polymer into an integrated Bragg grating device will allow for a latched reconfiguration of the Bragg wavelength without the need for continual electrical input.

II. EXPERIMENTAL

In this work, a methacrylate based co-polymer was synthesised incorporating 4.8% *p*-methoxy azobenzene units along the polymer backbone.

A silica-on-silicon sample was fabricated via flame hydrolysis deposition where the core layer was doped with germanium to provide photosensitivity. On exposure to UV light ($\lambda = 244$nm) the refractive index of the germanium doped glass was locally increased, forming the waveguide. Using an interferometer, Bragg gratings of different period may be simultaneously written into the device [7]. No overclad was deposited onto the core layer allowing the evanescent optical mode to penetrate up a micron from the waveguide surface onto which a ~100 nm film of the azobenzene functionalised co-polymer was spun (Fig. 2). The presence of the film and its ability to photoisomerise was confirmed by diffuse-reflectance UV-visible spectroscopy.

Interrogation of the Bragg grating was carried out with by a 780 nm broadband source, generated from a frequency doubled 1550 nm femtosecond laser source. A 600 nm band pass filter was used to remove any third harmonic light at 515 nm that would interfere with photoisomerism.

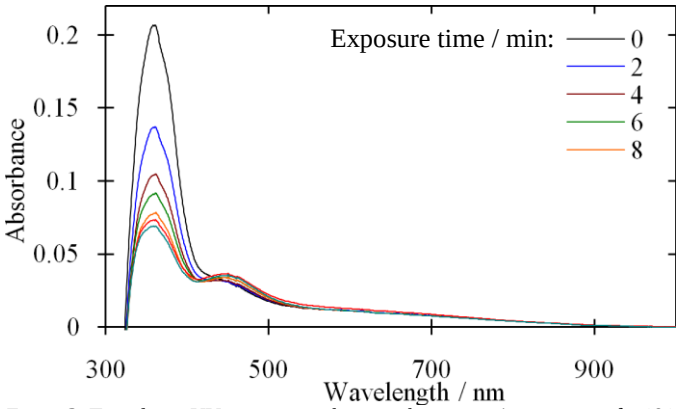


Figure 3. Time-lapse UV-vis spectra showing the *trans- cis* transition of a 191 nm thick *p*-methoxy azobenzene containing methacrylate co-polymer spun onto a silica surface, on exposure to ultraviolet light (354 nm) over 8 minutes.

III. Results

Azobenzene can undergo photoisomerisation efficiently on irradiation with UV light. The transmission UV-visible spectra for the co-polymer film (Fig. 3) shows that there is an intense absorption peak at 361 nm corresponding to the π-π* electronic transition of the *trans*-isomer and a weak peak at 451 nm which originates from the weak n–π* electronic transition of the *cis*-isomer [8]. When the film is irradiated by UV light at 365 nm, the azobenzene units inside the co-polymer undergo *trans-cis* isomerisation, with no further change detected after ~8 minutes. In contrast the reverse *cis-trans* isomerisation takes ~15 minutes. This results in the absorption at the *trans*- isomers π-π* peak decreasing while the weaker *cis*- isomer's n–π* peak increases.

Initial work focused on the interrogation of the Bragg response at 780 nm, spectrally near to the absorption feature. At this wavelength, the co-polymer induced high optical loss to the waveguide device, with almost total loss of the optical mode after travelling only 6 mm along the polymer coated waveguide. This was sufficient, however, to interrogate two Bragg gratings within the waveguide. The sample was alternately exposed to ultraviolet light at 365 and 254 nm; with thermal changes monitored by a thermocouple in thermal contact with the optical device. The Bragg response demonstrated reproducible switching between the two isomeric states, separated by 35 pm – a well resolved transition (Fig. 4). The index change shows the *trans-cis* transition is faster than the reverse, consistent with observations in the time-lapse UV-visible absorption measurements.

The *cis*-isomer is unstable at room temperature, with Barley [6] reporting ~20 h for a 50 % reconversion. For this methacrylate polymer, a slower thermal reconversion occurred linearly over 5 days, with a 17 pm reconversion taking ~60 h.

Initial work investigating if this effect is observable at 1550 nm has observed a slightly smaller shift for this same polymer film. However the high loss observed at 780 nm is not present at 1550 nm, allowing for the entire waveguide to be interrogated. The low loss allows for a thicker polymer film to be deposited onto the sensor surface that will further increase the isomeric shift to an order of a nanometre.

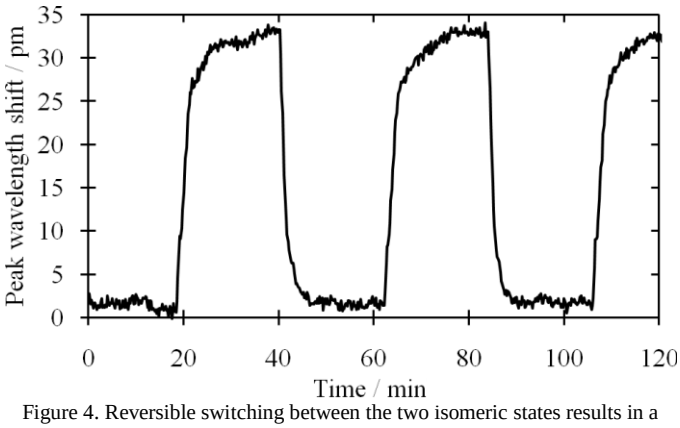


Figure 4. Reversible switching between the two isomeric states results in a detectable optical switch in the Bragg wavelength.

IV. Conclusion

A *p*-methoxy azobenzene functionalised methacrylate co-polymer has been synthesised. This has been shown to undergo reversible photoisomerism when exposed to UV light, producing a corresponding significant change in refractive index that is thermally stable. When deposited upon an optical surface a reconfigurable Bragg grating is formed that has potential for a range of applications. In this initial device the maximum observed tuning was 35 pm, corresponding to 17 GHz. This indicates that future devices could find application for wavelength trimming of lasers or for reconfigurable dispersion compensation. We will present our latest developments of this device, focusing on enhancing the magnitude of the refractive index response at 1550 nm.

Acknowledgment

This project was sponsored by the EPSRC, UK.

References

[1] H.G. Limberger, N. Hong Ky, D.M. Costantini, R.P. Salathe, C.A.P. Muller, G.R. Fox, "Efficient miniature fiber-optic tuneable filter based on intracore Bragg grating and electrically resistive coating", IEEE Photon. Technol. Lett., 10, 361–363, 1998.

[2] S.Y. Kim, S.B. Lee, S.W. Kwon, S.S. Choi, J. Jeong, "Channel-switching active add/drop multiplexer with tuneable gratings", Electron. Lett., 34, 104–105, 1998.

[3] L. Cruz, A. Diez, M.V. Andrés A. Segura, B. Ortega, L. Dong, "Fibre Bragg gratings tuned and chirped using magnetic fields", Electron. Lett., 33, 235–236, 1997.

[4] M. Le Blanc, S.Y. Huang, M.M. Ohn, R.M. Measures, "Tunable chirping of a fibre Bragg grating using a tapered cantilever beam," Electron. Lett., 30, 2163–2165, 1994.

[5] P.S. Ramanujam, S. Hvilsted, F. Ujhelyi, P. Koppa, E. Lörincz, G. Erdei, G. Szarvas, "Physics and technology of optical storage in polymer thin film," Synth. Met., 124, 145–150, 2001.

[6] S.H. Barley, A. Gilbert, G.R. Mitchell, "Photoinduced reversible refractive-index changes in tailored siloxane-based polymers",J. Mater. Chem., 1, 481-482, 1991.

[7] G.D. Emmerson, S.P. Watts, C.B.E. Gawith, V. Albanis, M. Ibsen, R.B. Williams, P.G.R. Smith, "Fabrication of directly UV-written channel waveguides with simultaneously defined integral Bragg gratings," *Elec. Lett*., 38, 1531-1532, 2002.

[8] M. Sun, W. Que, X. Hu, "Preparation and trans–cis isomerization of azobenzene-containing TiO2/ormosils hybrid films derived at a low temperature sol–gel process for photonic applications", J. Sol-Gel. Sci. Technol., 50, 415–420, 2009.

Digital photonics using InP microdisk lasers heterogeneously integrated on Silicon-on-Insulator

K. Huybrechts[1], L. Liu[1], R. Kumar[1], T. Spuessens[1], G. Roelkens[1], E.-J. Geluk[2], T. de Vries[2], M. Smit[2], P. Regreny[3], P. Rojo-Romeo[3], D. Van Thourhout[1], R. Baets[1], G. Morthier[1]

[1] Photonics Research Group, INTEC Department, Ghent University – IMEC, B-9000 Ghent, Belgium
[2] COBRA Research Institute, Technische Universiteit Eindhoven, 5600MB Eindhoven, The Netherlands
[3] Universite de Lyon, Institut des Nanotechnologies de Lyon, Ecole Centrale de Lyon, Ecully, F-69134, France

***Abstract*— We demonstrate the use of heterogeneously integrated microdisk lasers for application in low-power and high-speed all-optical flip-flops and gates. Flip-flop operation is experimentally demonstrated using pulse energies of 1.8 fJ in lasers with a diameter of 7.5 μm. Potential optimization of the performance and future photonic integrated circuits are also described.**

Keywords- microdisk laser, heterogeneous integration, digital photonics

I. INTRODUCTION

All-optical networks would benefit greatly from an increased use of all-optical signal processing, especially with the introduction of all-optical packet/burst switching [1-3]. In addition to wavelength conversion and signal regeneration, photonic devices implementing digital or logic functions are greatly desired, e.g. for header processing, routing or storing header information.

Solutions for the all-optical implementation of logic functions so far have suffered from a relatively large power consumption [4] and/or a slow operation. Sometimes they require complex photonic circuits that are difficult to integrate and comprise several power-hungry SOAs or laser diodes as well as optical filters or even isolators [5].

We have recently demonstrated the first low-power all-optical flip-flop on a silicon chip, making use of heterogeneously integrated microdisk lasers with diameter as small as 7.5 μm. The small footprint, the low power consumption and the use of the Silicon-on-Insulator (SOI) platform make this approach ideally suited for the realization of photonic integrated circuits comprising a number of gates, set-reset flip-flops and passive devices.

Below we will give more details on the fabrication technology and the operation principle, the first experimental results and the plans for the near future work.

II. FABRICATION TECHNOLOGY AND OPERATION PRINCIPLE

Figure 1 shows a schematic of the bonded microdisk lasers. The III-V/SOI heterogeneous integration is obtained through adhesive die-to-wafer bonding using DVS-BCB as a bonding agent [6]. The fabrication of the microdisks is discussed in more detail in [7]. The flip-flop operation is based on the switching between the clockwise (CW) and the counter clockwise (CCW) whispering gallery modes (WGM) in the disk laser. Unidirectional operation is only possible if the coupling between the CW and CCW modes is sufficiently small and if the gain suppression is sufficiently large. Therefore, extra care was taken to minimize the sidewall surface roughness of the disks and to obtain good power efficiency. A low sidewall surface roughness was obtained by using an optimized lithography and etch processes. A large internal power density results from the good mode confinement of the InP membrane, due to the high index contrast, and from the extra heat sinking we introduced by making the Au layer of the top contact thicker. This last measure avoided degradation at higher currents due to self-heating. The microdisk lasers are coupled to SOI wire waveguides and the light from these waveguides is coupled to fiber using grating couplers. The SOI wafers were fabricated through a MPW-approach by the Silicon Photonics platform ePIXfab [8].

The same microdisks that are used for all-optical set-reset flip-flops can in principle be used as all-optical gates for logic functions.

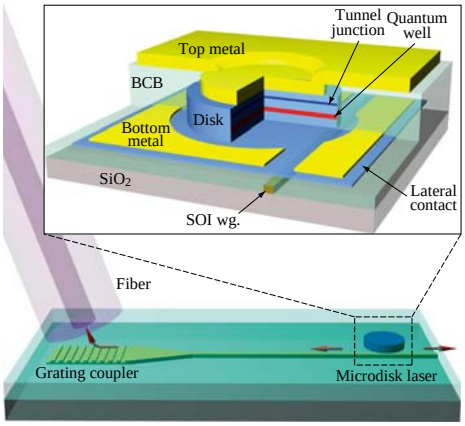


Figure 1. Structure of the whole circuit and the microdisk laser.

III. First Experimental Results

The L-I characteristic shows the typical behavior of disk lasers evolving from bidirectional towards unidirectional operation (Figure 2). The typical threshold current of the 7.5 μm microdisk lasers is below 0.5 mA. In Figure 2, the threshold current for lasing in the bidirectional regime is 0.33 mA. Bistable unidirectional behavior starts typically between 1 and 2 mA and at 1.7 mA in Figure 2. Due to the small dimensions, the lasers are single mode with a side mode suppression of over 40 dB.

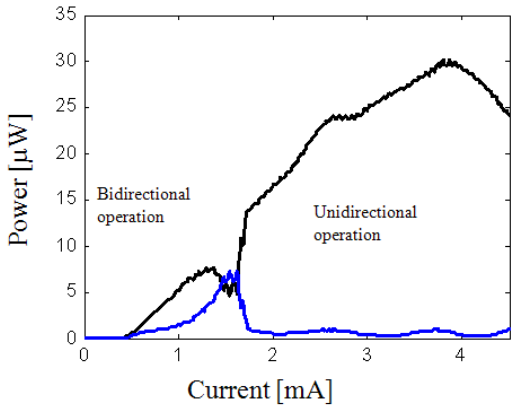


Figure 2. Typical L-I characteristic of a microdisk laser depicting the optical output power at both sides of the disk.

Switching between CW and CCW modes is achieved through injection locking. In our switching experiments we biased the laser at 3.5 mA to avoid self-switching due to noise and used 100 ps long switching pulses (generated using a 10 Gb/s pulse pattern generator). Figure 3 shows the typical time dependence of the on- and off-switching of a laser mode, measured on one side of the straight waveguide. Because the disk is only coupled to a single straight waveguide, it is not possible to separate the switch pulses and the laser signal. Therefore the switch pulses always cover the transient of the microdisk signal, making it difficult to measure the exact switching times. However, we found switch off times as low as 60 ps. Required switching energy is as low as 1.8 fJ, which is a record low value at the 1.55 μm wavelength.

The total power consumption of this all-optical set-reset flip-flop is estimated to be about 6 mW, but could be reduced down to 1.5 mW. This corresponds with 0.15 pJ per bit at 10 Gb/s and is a number that is very competitive with current and even near future opto-electronic solutions, especially if the power consuming interconnections are taken into account for the opto-electronic approach.

All-optical gates have been demonstrated at 10 GHz so far using pump-probe experiments. The disks did not have to be biased for this purpose.

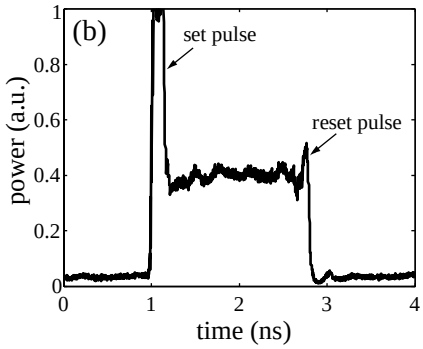


Figure 3. Waveform of the optical signal measured on one side.

IV. Conclusion and Future Work

The demonstration of set-reset all-optical flip-flops and all-optical gates based on heterogeneously integrated microdisk lasers opens the way for the exploration of more complicated devices such as D-flip-flops and shift registers. These can be made by simply interconnecting different S-R flip-flops and gates. However, for this purpose it is very important that all microdisk lasers and gates have laser or resonance wavelengths within small tolerances.

Acknowledgment

This work is supported by the European FP7 ICT-projects HISTORIC, WADIMOS, and PhotonFAB, the Belgian Fund for Scientific Research Flanders (FWO), and the IAP-project “Photonics@be”. The work of K.H. and T.S. is supported by the Institute for the Promotion of Innovation through Science and Technology (IWT) under a specialization grant.

References

[1] R. Van Caenegem, J. A. Martinez, D. Colle, M. Pickavet, P. Demeester, F. Ramos, and J. Marti, "From IP over WDM to all-optical packet switching: Economical view," Journal of Lightwave Technology, **24**, 1638-1645 (2006).

[2] Pleros, N., Apostolopoulos, D., Petrantonakis, D., Stamatiadis, C. & Avramopoulos, H. Optical Static RAM Cell. *IEEE Photon. Technol. Lett.* **21**, 73-75 (2009).

[3] H. J. S. Dorren, M. T. Hill, Y. Liu, N. Calabretta, A. Srivatsa, F. M. Huijskens, H. de Waardt, and G. D. Khoe, "Optical packet switching and buffering by using all-optical signal processing methods," Journal of Lightwave Technology, **21**, 2-12 (2003).

[4] Tucker, R. S. Role of Optics and Electronics in High-Capacity Routers. *IEEE J. Lightwave Technol.* **24,** 4655-4673 (2006).

[5] Malacarne, A., Wang, J., Zhang, I, Das Barman, A, Berrettini, G., Poti, L., Bogoni, A., 20-ps transition time all-optical SOA-based flip-flop used for photonic 10Gb/s switching operation without any bit loss, *IEEE Journ. Sel. Top. Quant. El.*, **14**, 808-815 (2008).

[6] G. Roelkens, J. Van campenhout, J. Brouckaert, D. Van Thourhout, R. Baets, P. Romeo, P. Regreny, A. Kazmierczak, C. Seassal, X. Letartre, G. Hollinger, J.M. Fedeli, L. Di Cioccio, C. Lagahe-Blanchard, “III-V/Si photonics by die to wafer bonding,” Materials Today 10(7), p.36-43 (2007)

[7] L. Liu, R. Kumar, K. Huybrechts, T. Spuessens, G. Roelkens, E-J. Geluk, T. de Vries, P. Regreny, D. Van Thourhout, R. Baets, G. Morthier, An ultra-small, low-power all-optical flip-flop memory on a silicon chip, *Nature Photonics*, 2010

[8] Silicon Photonics Platform ePIXfab: www.epixfab.eu

Multi-wavelength laser based on an Arrayed Waveguide Grating and Sagnac loop reflectors monolithically integrated on InP

P. Muñoz, R. García-Olcina, J.D. Doménech, M. Rius and J. Capmany
Optical & Quantum Comms. Group
iTEAM Research Institute
Univ. Politécnica de Valencia (Spain)
E-mail: pascual@ieee.org

L.R. Chen and C. Habib
Photonics Systems Group
Electrical & Computer Eng. Dept.
McGill University (Canada)
E-mail: lawrence.chen@mcgill.ca

X.J.M. Leijtens, T. de Vries, M.J.R. Heck, L. Augustin, R. Notzel and D. Robbins
Opto-Electronic Devices group
COBRA Research Institute
TU Eindhoven (The Netherlands)
E-mail: x.j.m.leijtens@tue.nl

***Abstract*—In this paper, a multi-wavelength laser monolithically integrated on InP is presented. A linear laser cavity is built between two integrated Sagnac loop reflectors, with an Arrayed Waveguide Grating (AWG) as frequency selective device, and Semiconductor Optical Amplifiers (SOA) as gain sections. The power is out coupled from the cavity using a side diffraction order of the AWG. Simultaneous laser operation is provided for four wavelengths/cavities in the device. The termination of the laser cavities with integrated Sagnac loop reflectors avoids using high reflection coating. Only anti-reflection coating is used in the output facet of the chip.**

I. Introduction

Multi-wavelength lasers monolithically integrated on an Indium Phosphide chip are very relevant devices for optical communications [1]. They usually consists on combinations of Arrayed Waveguide Gratings (AWGs) and Semiconductor Optical Amplifiers (SOAs), and two configurations are mainly used, linear and ring lasers [2]. The linear lasers are assisted by reflectors to provide the needed feedback to the cavity, and they are typically implemented either using High-Reflection (HR) coating at the ending side of the cavity on the chip facet [3], or by means of Distributed Bragg Reflectors (DBR) [4]. Ring lasers do not require HR coating, but the lasing preferred direction cannot always be determined [2]. In this paper we present a multi-wavelength linear laser based on AWGs and SOAs, in which the linear cavity is enclosed by Sagnac loop reflectors, therefore no HR coating is needed. Although HR coating is not a complex process at InP manufacturing, this and other material systems can benefit of this novel configuration.

II. Results

The devices were designed and fabricated on InP active/passive technology, where selective etching and regrowth are used to provide active/passive butt-coupled integration. Full technology details are given in [5], where the layer stack, process flow, waveguide types (deep, shallow) and devices are described. The AWG was designed to work at λ_0=1550 nm, with 2 input and 5 output spectral channels spaced $\Delta\lambda_c$= 1.6 nm. The design is for a cyclic response, FSR=5*1.6=8 nm, and for two diffraction orders [6] to be available at the input/output slab couplers. Hence 50:50 out coupling from the laser cavity can be performed without the need of an additional power splitter, since input waveguides have the same spectral transfer function, as labeled in Fig. 1 as 'FSR out-coup'. The loop reflectors are Sagnac interferometers with a 2x2 MMI coupler [7] that provides a $\pi/2$ phase shift [8] between the two outputs, necessary for total reflection [8]. Although just one waveguide in the Sagnac is used, the other one is terminated in a pigtail/spiral shaped waveguide, Fig. 1, to minimize unwanted reflections due to possible imperfections. The SOA sections have a length of 500 μm. The amplifiers SOA_2 and SOA's L_i, i=1..4, are used to obtain sufficient gain for lasing to occur at each cavity. Additionally, thermo-optic heaters are laid between the SOAs and the Sagnacs, to control the cavity phase. The device was soldered to a copper support and its temperature was kept at 25 C during the measurements. A multi-contact wedge was used to probe the SOA's, and a lensed fiber was aligned with the output waveguide using a nano-positioning stage. Alternate lasing of the 4 available wavelengths was obtained for a SOA_2 bias of 25 mA, and SOA's L_1 to L_4 alternated bias of 75 mA, as shown in Fig. 2-(a). In the present device, for a given SOA L_i, i=1...4, the lasing wavelength can hop between the AWG spectral periods, due to the SOA gain maximum shift with the applied current. This can be prevented if a larger size AWG design, with finer channel bandwidth, is used [2]. With SOA_2 at 25 mA, the threshold currents for alternate lasing are 30 mA, for SOA L_1 and 25 mA for SOA's L_2 to L_4. The Optical Spectrum Analyzer (OSA) peak powers, measured at the wavelengths shown in Fig. 2-(a), for SOA's L_i biased at 75 mA, are 70.795, 141.254, 112.202 and 89.125 mW/0.1 nm respectively. Simultaneous lasing of 4 wavelengths within the same AWG FSR was obtained, as shown in Fig. 2-(b), by biasing SOA_2 at 33.2 mA, and SOA's L_i 1 to 4 at 121.3 mA, 65 mA, 49 mA, and 74 mA respectively. Finally, the length

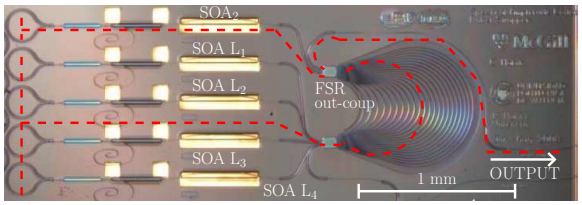


Fig. 1. Device micro graphs, output and SOA's labeled.

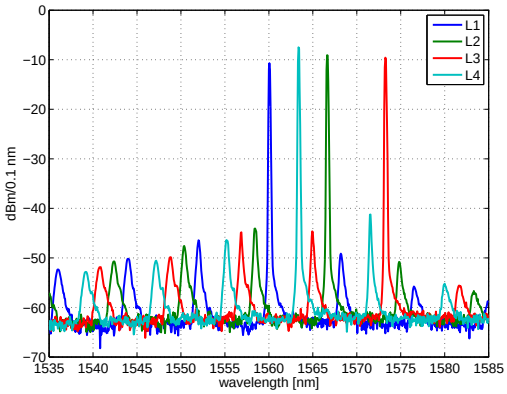
of the Fabry-Perot (FP) cavity between the two mirrors was confirmed by means of a 10 pm resolution Optical Spectrum Analyzer. Fig. 3 shows the acquired spectrum for SOA_2 and SOA L_4 biased at 25 mA and 75 mA respectively. The FP mode spacing averaged amongst five modes yields 51.4 pm, corresponding to a cavity length of 6.7 mm, for a group index of 3.5, marked in Fig. 1 between two Sagnac reflectors with a dashed red line. The length for the SOA_2 to SOA L_4 cavity is: Sagnac reflectors, ring of 85 μm, hence a perimeter of $2\pi 85$ μm each; straight sections between the Sagnac and bent waveguides to the AWG, 1.8 mm each; bent waveguides, 325 μm each; the AWG optical length is $l_0 + N/2 * \Delta l$ [6], where $l_0 = 500$ μm is the shortest path length, $N = 22$ is the number of arrayed waveguides and $\Delta l = m\lambda_0/n_c$ is the path length increment between consecutive waveguides, with $m = 194$ the AWG diffraction order and $n_c = 3.4$ the propagation effective index in the arms, therefore, AWG path length 1.5 mm; total length 2*(1.8+2π*0.085+0.325)+1.5=6.7 mm.

III. Conclusion

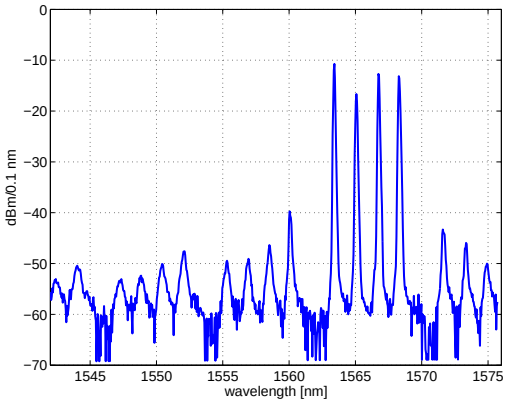
A multi-wavelength laser based on AWGs, SOAs and integrated Sagnac loop reflectors, monolithically integrated on InP, has been demonstrated. The device can be operated either as a discretely tunable or simultaneous four wavelength laser.

Acknowledgments

The authors acknowledge financial support from the European Commission FP6 project 004525 ePIXnet and the Canadian Institute for Photonic Innovations. The devices were fabricated through the InP Photonic Integration Platform JePPIX (coordinator D J Robbins), at the COBRA fab.



(a)



(b)

Fig. 2. (a) Alternate lasing and (b) simultaneous 4 laser operation

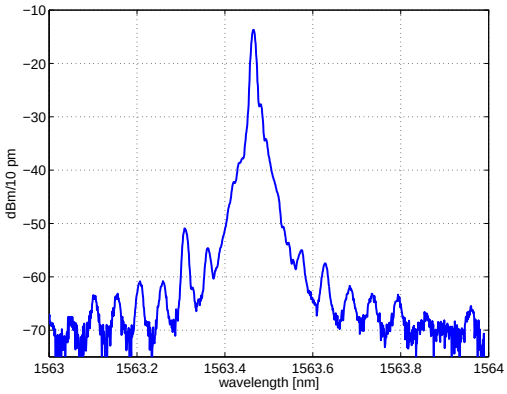


Fig. 3. 10 pm OSA resolution laser spectrum trace.

References

[1] D. Welch, F. Kish, S. Melle, R. Nagarajan, M. Kato, C. Joyner, J. Pleumeekers, R. Schneider, J. Back, A. Dentai, V. Dominic, P. Evans, M. Kauffman, D. Lambert, S. Hurtt, A. Mathur, M. Mitchell, M. Missey, S. Murthy, A. Nilsson, R. Salvatore, M. Van Leeuwen, J. Webjorn, M. Ziari, S. Grubb, D. Perkins, M. Reffle, and D. Mehuys, "Large-scale inp photonic integrated circuits: Enabling efficient scaling of optical transport networks," *IEEE J. Sel. Topics Quantum Electron.*, vol. 13, no. 1, pp. 22–31, Jan.-feb. 2007.

[2] J. den Besten, "Integration of multiwavelength lasers with fast electro-optical modulators," Ph.D. dissertation, TU Eindhoven, 2004.

[3] A. La Porta, M. Heck, X. Leijtens, L. Augustin, T. d. Vries, E. Smalbrugge, Y. Oei, R. Notzel, R. Gaudino, D. Robbins, and M. Smit, "Monolithic awg-based discretely tunable laser with nanosecond switching speed," in *Proc. LEOS Annual Meeting*, 2008, p. CThM3.

[4] L. Coldren, "Monolithic tunable diode lasers," *IEEE J. Sel. Topics Quantum Electron.*, vol. 6, no. 6, pp. 988–999, Nov/Dec 2000.

[5] E. Bente and M. Smit, "Ultrafast InP optical integrated circuits," in *Proc. of SPIE*, vol. 6124, 2006, p. 612419.

[6] P. Munoz, D. Pastor, and J. Capmany, "Modeling and design of arrayed waveguide gratings," *J. Lightw. Technol.*, vol. 20, no. 4, pp. 661–674, 2002.

[7] L. Soldano and E. Pennings, "Optical multi-mode interference devices based on self-imaging: principles and applications," *J. Lightw. Technol.*, vol. 13, no. 4, pp. 615–627, Apr 1995.

[8] B. Saleh and M. Teich, *Fundamentals of Photonics*, 2nd ed. Wiley, 2007, ch. 2.

Fast Integrated Tunable Laser using Filtered Feedback

J. Pozo[1], B. Docter[1], O. Raz[2], N. Calabretta[2], S. Beri[3,4], I.V. Ermakov[3], J. Danckaert[3,4] and M.K. Smit[1]

[1]OED group and [2]ECO group, COBRA, Technische Universiteit Eindhoven,The Netherlands
[3]Department of Applied Physics and Photonics, Vrije Universiteit Brussel, Belgium
[4]Department of Physics, Vrije Universiteit Brussel, Belgium
j.m.pozo.torres@tue.nl

Abstract— **A novel integrated tunable laser is presented which combines a simple tuning method with ns switching speed. The Photonic Integrated Circuit consists of a Fabry-Perot laser with deeply-etched DBR mirrors. The Fabry-Perot modes can be selected independently using an Arrayed Waveguide Grating and then re-injected into the laser cavity, forcing single mode operation at the wavelength of that mode. 4ns switching time as well as 15 dB SMSR is demonstrated on the prototype device.**

Keywords-tunable laser; fast switching; filtered feedback; DBR mirrors;AWG; active passive integration.

I. INTRODUCTION

Fast switching tunable lasers (TLs) are key components in the pursuit of all-optical reconfigurable telecom networks. Traditional solutions for TLs rely on complex and costly control schemes for selection of the desired wavelength and stabilization of the output signal. For instance, a continuously tunable, multi-section laser based on Distributed Bragg Reflector (DBR) mirrors has at least 4 analog control sections; a set of look-up tables is necessary to address each section with the proper control current and frequency drifts due to temperature effects need to be compensated in order to achieve the desired operation. Such lasers are available with high power (> 10 dBm), a wide tuning range (> 40 nm) and tuning speeds in the ms-range [1]. So far, attempts to simplify the control scheme have not yet led to competitive devices.

We have reported the invention, fabrication, modeling and characterization of a new Integrated Filtered-Feedback Tunable Laser (IFF-TL) [2,3,4]. The device is composed of two integrated cavities which are separated by high reflection DBR mirrors: a short lasing cavity allowing for very fast switching speed and a filtered-feedback cavity allowing for easier control. Improved chirp performance has been demonstrated in [5], where the filtered feedback cavity contained a coupled micro-ring filter. It was shown that with this approach the frequency drift can be reduced to less than 1 GHz. In this paper we report dynamic measurements on an IFF-TL laser with a discretely tunable feedback filter, consisting of an AWG with an SOA gate array, which demonstrate 4 ns switching speed.

II. DEVICE DETAILS, DESIGN AND FABRICATION

A schematic picture of the IFF-TL is shown in fig 1. A Fabry-Perot (FP) laser is formed by a Semiconductor Optical Amplifier (SOA) and two deeply etched Distributed Bragg Reflector (DBR) mirrors. The laser cavity length (L_{cav} = 822 µm) is chosen such that the mode spacing (given by $\Delta\lambda = \lambda^2 / 2N_g L_{cav}$) equals 50 GHz (0.4 nm) –the channel spacing in the standard ITU-grid used for telecom applications. N_g is the group index of the waveguide (3.65) and λ is the central wavelength (1.55 µm).

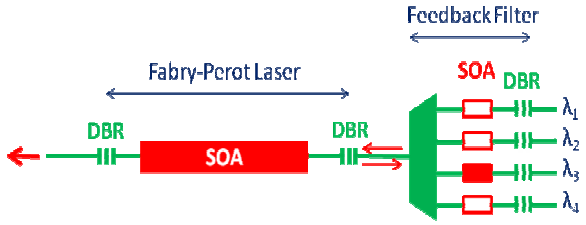


Figure 1. Schematic diagram of the Integrated Filtered-Feedback Tunable Laser.

The FP laser is coupled to an AWG filter, with a 400 GHz (3.2 nm) channel spacing, that routes the modes of the lasing cavity into several waveguide branches according to their wavelength –4 in the case of the device reported in this paper. Each branch contains a 100-µm-long SOA that works as an optical gate. The SOA length is chosen in such a way that an unbiased gate will absorb the light in the waveguide, and a forward biased one will amplify it. The light is then fed back into the lasing cavity reflected either by a cleaved chip facet, another DBR mirror or any other form of broadband mirror. The feedback light causes the laser mode with the largest feedback strength to dominate over the other modes and single-mode operation is achieved. The feedback strength and phase are controlled by the gates in the feedback branches. The output light leaves the chip through the opposite DBR mirror. The DBR mirrors, which have been deeply etched as shown in [6], can be used to obtain high reflectivity over a broad wavelength range and allow us to control the cavity length very accurately.

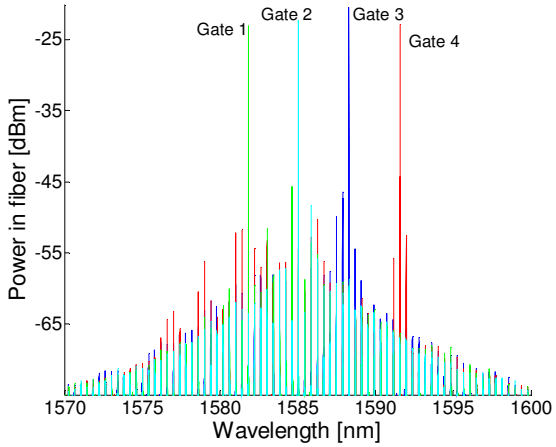


Figure 2. Optical spectra of the IFF-TL

III. CHARACTERIZATION

We measured a threshold current of 40 mA at 15 ^{0}C. For the characterization of the tunability, the device has been forward biased at 45 mA; at this operation point an output power of 20 µW has been collected using a lensed fiber. The performance of the device as a tunable laser is shown in fig. 2, where the 4 spectra, corresponding to each of the SOA gates operated in forward bias separately, are plotted. The separation between the 4 possible lasing wavelengths is equal to 3.2 nm, or 400 GHz corresponding to the channel spacing of the AWG. The sub-threshold peaks show the mode-spacing of the FP laser, which are positioned 50.5 GHz apart; only 1% mismatch with the designed 50 GHz. These sub-threshold peaks collide for all 4 lasing spectra, providing a good indication that the carrier density in the main laser cavity is the same, and the temperature does not vary much at all. This also confirms that the wavelength is tuned due to small feedback received from the gates, and the device does not operate as an extended cavity laser.

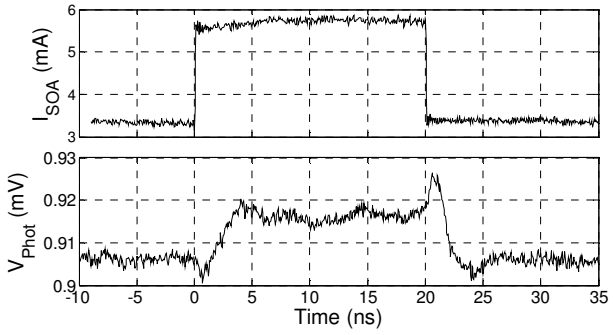


Figure 3. Characterization of the switching speed. (top) I_{SOA} is the signal applied to one of the SOA gates. (bottom) V_{PHOT} is the signal received from the laser by a photodiode at the wavelength corresponding to that gate.

In order to characterize the switching speed, a square signal like the one shown in fig. 3 (top) was applied to one of the SOA gates. The signal shows transitions of high and low values. The current values on the SOA are chosen such that the high value is sufficient to induce single mode operation, whereas at the low value the device operates in multimode regime. At the output of the laser a tunable filter was used to filter the wavelength of interest. The output of the filter is connected to a 10-GHz photodiode and electrical amplifier. The resulting RF signal is studied in a digital oscilloscope. A sample of the output signal is shown in fig. 3 (bottom), demonstrating a transition time of 4-5ns for both the rise and decay. The switching characteristics of the IFF-TL were investigated numerically using a multimode Lang-Kobayashi model with frequency selective feedback [4]. Simulations based on this model (not shown) predict a switching time of 0.8 ns. The difference between the modeled and experimental result is attributed to an impedance mismatch between the SOA and the signal generator.

IV. CONCLUSIONS

The new concept of the IFF-TL combines high switching speeds with simple wavelength control. While the latter promises a reduction in cost of the control electronics compared to continuously tunable lasers, we believe that the fast switching speed is the biggest advantage of this novel device. Together with the fact that the device can be integrated with other active and passive components, we expect that fast switching will enable new applications in packet routing techniques for all-optical telecommunication networks. This research was supported by the Dutch Technology foundation STW and the Belgian Science Policy Office under Grant No. IAP-VI10. I.V.E., S.B. and J.D. Acknowledge support from the Research Foundation-Flanders (FWO).

V. REFERENCES

[1] J. Buus and E. J.Murphy, “Tunable lasers in optical networks,” J Lightw. Technol., vol. 24, no. 1, pp. 5–11, Jan. 2006.

[2] B. Docter, J. Pozo, F. Karouta, S. Beri, I.V. Ermakov, J. Danckaert, M.K. Smit, “Novel Integrated Tunable Laser using Filtered Feedback for simple and very fast tuning,” Proc. 35th European Conference on Optical Communication (ECOC), 2009, Vienna, Austria.

[3] B. Docter, S. Beri, F. Karouta, and M. K. Smit, “Semiconductor laser device,” Int. Patent #PCT/NL/2008/000185, filed Aug. 1, 2008.

[4] B. Docter, J. Pozo, S. Beri, I.V. Ermakov, J. Danckaert, M.K. Smit, "Discretely Tunable Laser Based on Filtered Feedback for Telecommunication Applications", J. Sel. Top. on Quantum Electronics, accepted for pub., DOI 10.1109/JSTQE.2009.2038072

[5] S. Matsuo, T. Segawa, T. Kakitsuka, T. Sato, R. Takahashi, H. Suzuki, B. Docter, F. Karouta, and M. K. Smit, “Integrated filtered feedback tunable laser using double-ring-resonator-coupled filter,” in Proc. IEEE 21st Int. Semicond. Laser Conf. (ISLC 2008), Sep.14–18, pp. 155–156.3.

[6] B. Docter, F. Karouta, E. A. J. M. Bente, T. de Smet, and M. K. Smit, “Short-cavity lasers with deeply etched DBR mirrors for photonic integrated circuits,” Proceedings of IEEE/LEOS Benelux Chapter, Twente, The Netherlands, 2008.

Parallel integration of high power laser arrays – technology and applications

John H. Marsh
Department of Electronics and Electrical Engineering
University of Glasgow
Glasgow, G12 8LT, United Kingdom
j.marsh@elec.gla.ac.uk

The author is also with Intense Ltd, 4 Stanley Boulevard, Blantyre, Glasgow G72 0BN, United Kingdom

Abstract—**Massively parallel individually addressable laser arrays are reported, delivering 500 mW per element at 800-980 nm with 100 monolithic elements. By placing arrays side by side powers can be scaled further, with uncooled modules delivering 150 W cw.**

Keywords- Optoelectronics; photonic integrated circuits; semiconductor lasers; laser arrays; monolithic integration

I. INTRODUCTION (HEADING 1)

It has long been recognized that integration of photonic components into photonic integrated circuits (PICs) is necessary for complex optoelectronic systems to penetrate into mass markets. Monolithic PICs have evolved rapidly since the year 2000, with the two monolithic integration technologies of greatest importance being selective area epitaxy and quantum well intermixing (QWI) [1]. Either of these techniques may be combined with regrowth. For telecom applications, integrated transmitter and integrated receiver chips have been combined with silicon electronics in optical-electronic-optical (OEO) transceivers and these modules are now widely deployed in the telecom backbone. For non-telecom applications there has been considerable interest in monolithic, individually addressable arrays of semiconductor lasers. Highly parallel arrays of semiconductor lasers each delivering 100s of mW are already used in high-end printing [2] and materials processing. As the technical and cost challenges associated with PICs are overcome, new applications and commercial opportunities are opening.

This paper focuses on non-telecom applications, showing how integration using QWI can be used to manufacture wide parallel arrays of semiconductor lasers.

II. INDIVIDUALLY ADDRESSABLE LASER ARRAYS

The integration of parallel arrays of semiconductor lasers in a single chip appears at first to be a trivial problem, simply involving leaving the lasers cleaved from the wafer in the form of bars. However, many applications allow for zero redundancy and so significant technology development has been required to achieve an acceptable yield at array level. Exceptional reliability is needed because the entire module fails as soon as a single emitter in the array fails. Achieving high reliability at powers of several 100 mW requires careful design of the laser and a robust technique for passivating the facet. Moreover, many applications require a high uniformity of laser parameters, such as kink power and optical beam profile. Some applications require uncooled operation with the junction temperature approaching 100 °C.

The primary challenges in manufacturing semiconductor laser arrays are, therefore, to design a reliable laser that delivers a power of several 100 mW in a single transverse mode and that is robust against manufacturing tolerances. Here we use QWI to create relatively long (>100 µm) passive waveguides immediately adjacent to each facet of a ridge waveguide laser. As a result of the QWI processing, the passive waveguides have a larger bandgap than the gain section so raising the threshold power at which catastrophic optical mirror damage (COMD) of the facet mirror occurs [3]. The length of the passive waveguides enables large monolithic arrays to be cleaved from a wafer with high yield and also relaxes packaging tolerances as the passive waveguide sections can overhang the laser carrier. A novel 'V-profile' layer [4] has also been included in the structure to reduce the fast axis far-field divergence and to make the laser performance less vulnerable to processing variations across the wafer and from wafer to wafer.

III. ARRAY PERFORMANCE

Full 3 inch wafer processing using state-of-the-art photolithography and dry-etching techniques, in combination with passive waveguides and the V-profile laser design, allows very large element arrays of high-performance single-mode lasers to be fabricated with high yield. The design has been optimized to give extremely good uniformity across arrays containing up to 100 individually addressable lasers. An 86

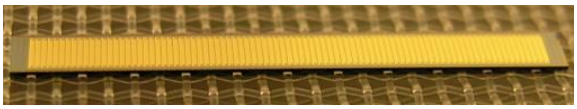


Figure 1. Processed array containing 86 lasers.

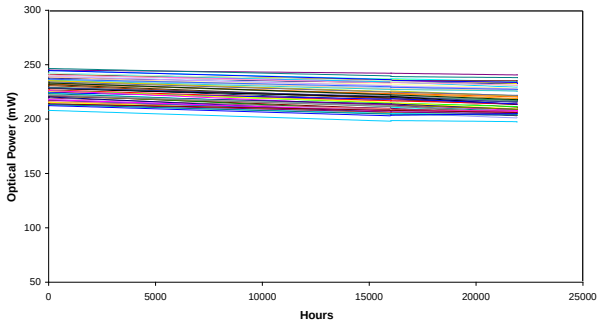


Figure 2. 22,000 hour lifetest of 64 element 200 mW, 8xx nm single mode laser module.

element array is shown in Fig. 1. The laser arrays are then die-bonded to a Cu:W composite metal carrier, using a hard solder.

IV. Reliability

Extensive reliability data have been collected for 2 µm wide ridge lasers operating at 808 and 830 nm in a single transverse mode at 200 mW per channel. Fig. 2 shows typical lifetest curves for a 64 element array operating at 200 mW per channel up to 22,000 h with a junction temperature >65 °C. More than 30,000,000 device hours of data have been collected with the lasers running continuously at 200 mW. The FIT rate (10^9 h) for individual elements is 118 and the resulting module MTTF is >17,000 h. The key to achieving this level of reliability is the use of quantum well intermixing (QWI).

V. Super Arrays

Monolithic laser arrays are limited in size, partly by processing and handling considerations and partly by the by the need to have a reasonable yield from the size of wafer used in production (currently 3 inch). In applications such as coding and marking more elements may be required, e.g. for printing bar codes in a single pass of a label. In order to build larger arrays, monolithic arrays are placed side by side using precision die bonding to maintain a constant laser pitch across the super array.

Fig 3 shows a super array built using arrays of 16 elements. Current designs use individual bars with typically 100 lasers on a pitch of 125 µm at wavelengths of 808, 830 and 980 nm. Moreover, individual lasers can deliver up to 500 mW with good uniformity in continuous wave operation with all elements 'on' (Fig. 4). Uncooled modules with 300 elements are now capable of delivering 150 W of power under precision

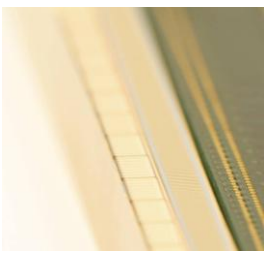


Figure 3. Part of a super array assembled using monolithic lasers containing 16 elements.

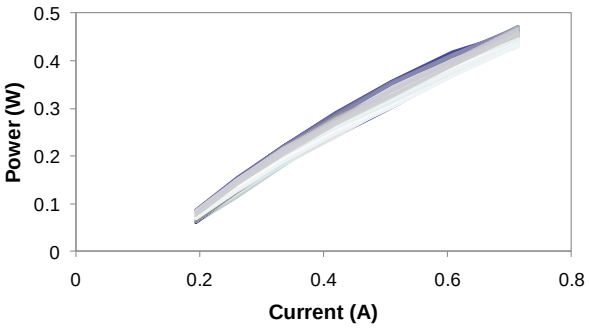


Figure 4. Light-current characteristics of 250 elements of a 980 nm super array.

control to precision locations.

Higher powers are possible in pulsed operation. 2 µm wide ridge lasers deliver >7 W for 50 ns pulses without exhibiting facet failure, the power being limited by the maximum drive current. For longer pulses (200 ns) 10 µm wide ridge lasers deliver >8 W, although roll-over is observed for the longer pulses.

VI. Conclusions

This paper has focused on technology for non-telecom applications, in particular technology for manufacturing wide arrays of semiconductor lasers. It is clear that integration of passive waveguides within laser cavities has led to significant improvements in yield and in device performance, particularly reliability. Such arrays have many applications in printing [2], where they are already deployed in computer to plate systems and digital presses. They are also being used in coding and marking applications, and have potential applications in LADAR, bio-sensing, processing of plastics and laser displays. It is now possible to deliver more that 150 W of optical power from a single compact semiconductor laser module under precision control to precise locations.

Acknowledgments

The author thanks numerous past and present colleagues at Intense Ltd who have contributed to this work, in particular G. Bacchin, S. Gorton, C. J. Hamilton, O. P. Kowalski, X. F. Liu, S. P. Najda, S. D. McDougall, G. Palmer, B. C. Qiu, B. Schmidt and M. Silver.

References

[1] J. H. Marsh, 'Quantum well intermixing', *Semiconductor Science and Technology*, vol 8, pp. 1136–1155, 1993.

[2] S. P. Najda, J. H. Marsh, 'Laser printing - Laser arrays transform printing', *Nature Photonics*, vol **1** (7), pp387-389, 2007.

[3] S. P. Najda, G. Bacchin, B. Qiu, X. Liu, O. P. Kowalski, M. Silver, S. D. McDougall, C. J. Hamilton, J. H. Marsh, 'Benefits of quantum well intermixing in high power diode lasers', *Proc SPIE*, vol 5365, pp. 1 – 13, 2004.

[4] B. C. Qiu, S. D. McDougall, X. F. Liu, G. Bacchin, J. H. Marsh, 'Design and fabrication of low beam divergence and high kink-free power lasers', *IEEE J. Quantum Electron.*, vol 41, 1124 – 1130, 2005.

Integrated Receivers on SOI for PSK Modulation Formats

Marcel Kroh[1], Lars Zimmermann[2,3], Heinz-G. Bach[4], Mads L. Nielsen[1], Jürgen Bruns[3], Günter Unterbörsch[1]

1: u2t Photonics AG, Reuchlinstr. 10/11, 10553 Berlin, Germany, kroh@u2t.de
2: IHP Microelectronics GmbH, Im Technologiepark 25, 15236 Frankfurt (Oder), Germany, lzimmermann@ihp-microelectronics.com
3: Technische Universität Berlin, Hochfrequenztechnik, HFT 4, Einsteinufer 25, 10587 Berlin, Germany, juergen.bruns@tu-berlin.de
4: Fraunhofer Heinrich-Hertz-Institute, Einsteinufer 37, 10587 Berlin, Germany, bach@hhi.fhg.de

***Abstract*— Phase coded modulation formats require the deployment of more complex receiver configurations. Waveguide integrated SOI boards are investigated to provide versatile optical functions for compact DPSK and QPSK detectors.**

Keywords- PSK, direct detection, coherent detection, SOI, hybrid integration.

I. INTRODUCTION

Novel data modulation formats such as Phase Shift Keying (PSK) modulation require receiver configurations of increased complexity, which include an optical decoder to detect and evaluate phase differences between received data bits. To handle the increasing complexity solutions by free space optics, fiber optics or planar waveguide technology are used. Integrated solutions offer the strongest potential for scalability and high volume. This requires advanced integrated devices such as delay line interferometer (DLI) and 90°-optical hybrids, which will enable the set-up for direct or coherent detection. However, advanced photonic circuits still pose challenges such as low insertion loss and low polarization dependence. In the following, a hybrid integration scheme of active InP components on silicon-on-insulator (SOI) is proposed and investigated for the examples of 40 Gbps DPSK and 40 Gbaud/s QPSK modulation format. Our approach facilitates a modular system of building high-performance receiver chips.

II. CONCEPT

A. Integration concept

Monolithic integration of all components in one material system such as InP allows to build sophisticated receivers, e.g. for coherent detection [1]. However, the increase in chip size leads to higher costs. Moreover, high performance necessitates a large number of process steps. Alternatively, we propose a hybrid integration concept using a motherboard with planar lightwave circuits (PLC) in SOI as introduced in [2]. It provides the required larger integration area for optical decoding and phase evaluation at an affordable price while high performance active components for detection and amplification are manufactured on separate InP wafers and flip-chip assembled after initial testing.

InP technology provides active components such as photodiodes (PDs) and Semiconductor Optical Amplifiers (SOAs) with low polarization dependence and high RF bandwidth. The integration of optical waveguides enables a high-speed design and operation. Practicable flip-chip integration is achieved by end-fire coupling.

PSK receivers can then be fabricated for a wide spectrum of applications using hybrid integration technology without compromise in performance. The hybrid assembly technology used here relies on AuSn flip-chip soldering.

B. SOI motherboard

The optical network is based on SOI rib waveguides (3.5 x 4 µm). SOI rib waveguides are particularly well suited for the trimming of the polarization dependence. Silicon itself does not exhibit a material birefringence, but the choice of rib geometry and cladding overlay leaves two independent parameters for birefringence tuning. This technique is used to build optical waveguide circuits with a low polarization dependency. Recently [3], state-of-the-art performance was demonstrated for the DPSK demodulators using a DLI with a low polarization dependence on SOI of 0.4 GHz polarization dependent frequency shift (PDFS) and <0.5 dB polarization dependent loss (PDL).

The same waveguide technology was used to fabricate fully passive 90°-optical hybrids [6]. The operation of the optical hybrids relies on self imaging as a result of interference between the supported modes in the multimode region. A geometry using 4µm waveguides allows to build robust devices with respect to process tolerances. Standard silicon technology allows fabrication of devices on 200mm wafers, which can accommodate an adequate number of receiver chips with increased size.

C. Active InP flip-chip components

The concept of wideband waveguide integrated PDs was deployed to enable hybrid flip-chip integration on SOI maintaining a horizontal waveguiding throughout the assembly. Previously, the PDs had achieved bandwidths of 80 GHz and beyond [4]. The diodes were grown by a one-step MOVPE process on a semi-insulating InP substrate. P-I-N-diodes employ evanescent coupling from a single mode rib waveguide.

The PDs for upside-down assembly were modified and processed with a layout regarding mechanical, electrical and optical issues for flip-chip integration. Details of the PD layout can be found in [2]. The balanced PDs for flip-chip

This work was partly funded in the frame of the project Eibone, activity 01BP559, 560, 561, by the German Federal Ministry of Research and Education.

integration show a responsivity of 0.5 A/W, a polarization dependent loss < 0.5 dB and a band-width > 75 GHz.

III. Experimental Results

A. *Investigation of integrated hybrids for DPSK receivers*

The increased complexity of receivers also requires new evaluation procedures. Previous to the assembly of subcomponents, critical parameters of the DLIs and the PDs are investigated by wavelength scan and polarization scrambling in order to identify remaining birefringence, PDL and imbalance [3]. After the flip-chip integration of PDs onto the SOI DPSK decoder boards (Fig. 1a), the direct measurement of the frequency bandwidth is hampered by the transfer function of the DLI. The bandwidth evaluation requires the compensation of the transfer function, following a method described in [5]. The S21 characteristics of the hybrid and the calculated o/e bandwidth are shown in Fig. 1b.

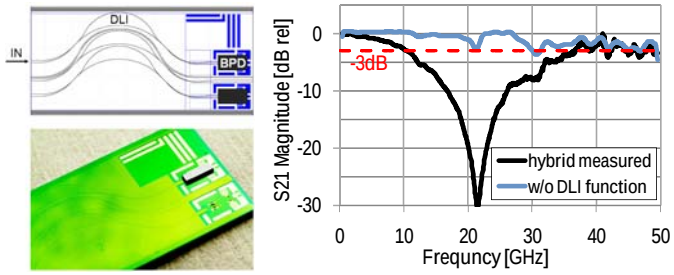


Fig 1a: DPSK receiver board. Fig. 1b: S_{21} characteristics of the assembly and calculated o/e bandwidth.

The 3 dB bandwidth of this hybrid was determined to be 30 GHz. However, the frequency bandwidth evaluation in Fig. 1b shows some ripple due to imperfections of the RF connection. Taking this into account the flattened bandwidth clearly exceeds 40 GHz.

B. *Investigation of 90° hybrids for QPSK receivers*

90° hybrids were fabricated on SOI. The hybrids are based on multimode interference (MMI) 4×4 devices, enabling fully passive operation [6].

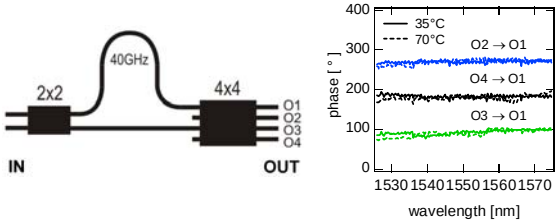


Fig. 2a: Layout of a 4x4 MMI test structure and Fig. 2b: results of phase measurements.

Fundamental performance characteristics of the hybrid are output phase relations, insertion loss, and imbalance. The evaluation of the MMI function was based on an auxiliary DLI to enable a homodyne measurement. The local oscillator signal for coherent detections was replaced by a delayed copy of the test signal itself (Fig. 2a). The phase relations between output channels were measured by wavelength scan. Fig. 2b shows the measured output phase relations across the C band. Phase deviations remained below 5°. Insertion loss and imbalance stayed below 1 dB and 0.5 dB, respectively.

IV. System Test

A DPSK receiver module comprising SOI DLI board and flip-chip integrated balanced PD was tested in a system experiment. The packaged module had a footprint of 48 x 28 mm. The RF-connection is accomplished by a coplanar line onto the PLC board between the PD chip and the RF connector. The set-up for the 40 Gbps back-to-back measurements is shown in Fig. 3a. The measured bit-error rate (BER) vs. optical signal to noise ratio (OSNR) is shown in Fig. 3b.

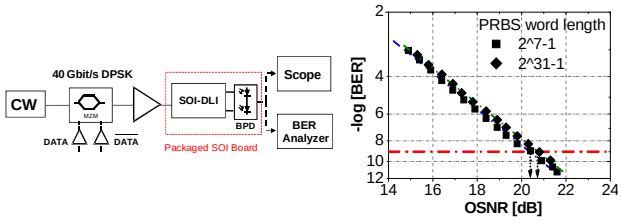


Fig. 3a: Test-bed for 40 Gbps non-return to zero (NRZ) DPSK, Fig. 3b: BER vs. OSNR for pseudo random bit sequences (PRBS) with word lengths of 2^7-1 and 2^{31}-1.

The input power was set to +19 dBm. Error free operation was achieved for an OSNR of 20.4 dB (PRBS 2^7-1) and 20.8 dB (PRBS 2^{31}-1).

V. Conclusion

Hybrid integration on SOI motherboards is a versatile technology to provide solutions for the detection of PSK modulated data signals. We have shown assembly and successful testing of a 40 Gbps DPSK receiver comprising a waveguide integrated demodulator on SOI and flip-chip integrated InP-based photodetectors.

Coherent detection with 4x4 MMIs for 90° hybrids was investigated using the same integration platform. Low phase deviations and operation over the entire C-Band enable integrated solutions of QPSK detectors. Potential receiver bandwidths of > 40 GHz permit symbol rates of up to 57 Gbaud/s and receiver designs for 200 Gbps QPSK.

Acknowledgment

The authors acknowledge the contribution of the project team Eibone [2] of HHI, TUB and u2t to the results reported here.

References

[1] C. Doerr et al., “High-Speed InP DQPSK Receiver“ in Proc. OFC 2008, PD paper 23.
[2] M. Kroh et al., “Hybrid Integrated 40 Gb/s DPSK Receiver on SOI” paper OMK3, in Proc. OFC 2009, San Diego, 2009.
[3] K. Voigt et al., “Performance of 40-Gb/s DPSK Demodulator in SOI-Technology”, IEEE PTL, 20(8), pp.614-6, 2008.
[4] A. Beling, “PIN Photodiode Modules for 80 Gbit/s and Beyond” in Proc. OFC 2006, paper OFI1.
[5] M. L. Nielsen et al., “Method for Measuring Conversion Gain Response and O/E Bandwidth of Integrated D(Q)PSK Receivers” accepted as poster JWA33 on OFC 2010, San Diego, USA, 2010.
[6] L. Zimmermann et al., “C-band optical 90°-hybrids based on silicon-on-insulator 4x4 waveguide couplers” IEEE PTL, 21 (3), pp. 143-45, 2009.

DQPSK Demodulation Using Integrated Silicon Ring Resonators

L. Xu, C. Li, X. Chen and H. K. Tsang
Dept. of Electronic Engineering, the Chinese University of Hong Kong, Shatin, N. T., Hong Kong
Phone:+852 26098254 Fax:+852 26035558 Email: hktsang@ee.cuhk.edu.hk

***Abstract*—We experimentally demonstrated an ultra-small 20Gb/s differential quadrature phase-shift keying (DQPSK) demodulator using silicon based microring resonators. The double-waveguide microring resonators enable detection of *I* and *Q* signals as well as inverted *I* and *Q* signals.**

Keywords-Differential quadruture phase-shift keying (DQPSK); silicon integration

I. INTRODUCTION

Phase-shift keying provides enhanced sensitivity and tolerance to fiber nonlinearities when compared with on-off-keying (OOK). Differential quadrature phase-shift keying (DQPSK) doubles the spectral efficiency when compared with binary formats such as OOK or differential phase-shift keying (DPSK). The most common approach for DQPSK demodulation employs a Mach–Zehnder delay interferometer (MZDI) for demodulation of each quadrature [1], followed by balanced detection. Optical frequency discriminator with direct detection is also an alternative approach [2]. DPSK demodulation based on a frequency discriminator implemented with a silicon microring resonator was recently demonstrated [3] to operate over a wider range of bit rates than the conventional MZDI approach. Zhang, et al [4] recently analyzed the performance of DQPSK demodulation using microring resonators. Compared to the MZDI approach, microring structures occupy a much smaller chip area and are thus easy to stabilize thermally and can be integrated with other devices such as waveguide photodetectors.

In this paper, we report the performance of a pair of integrated silicon microring resonators for 20 Gb/s DQPSK demodulation. The testing of the frequency discriminator employed 10Gb/s DPSK for each quadrature channel, and we showed that tuning of the resonator frequency to match the requirements of DQPSK demodulation may be achieved by localized optical heating of each resonator.

II. DEVICE DESIGN

The integrated microring resonators were fabricated at IMEC on silicon-on-insulator (SOI) wafer with a 0.22-μm thick top silicon layer and a 2-μm thick buried oxide (BOX) layer. The waveguides were nominally 500nm wide and the device layout was defined by193nm-deep-UV photolithography, and transferred onto the device layer by dry etching. The entire device was clad with a 0.75-μm-thick high density plasma (HDP) oxide. Fig.1 shows the top-view scanning electron micrograph of the fabricated microring

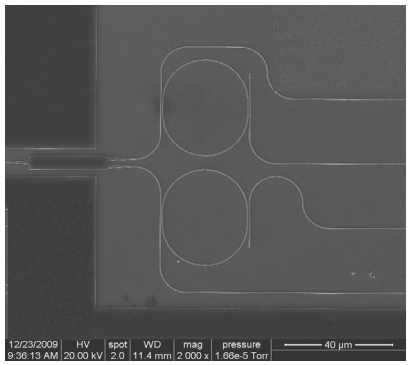


Fig.1 Top view of the device

device. The racetrack microring arc radius is 15 μm, and the straight interaction length is 8 μm. The fabricated air-gap spacing g between the ring and the waveguide is about 200nm.

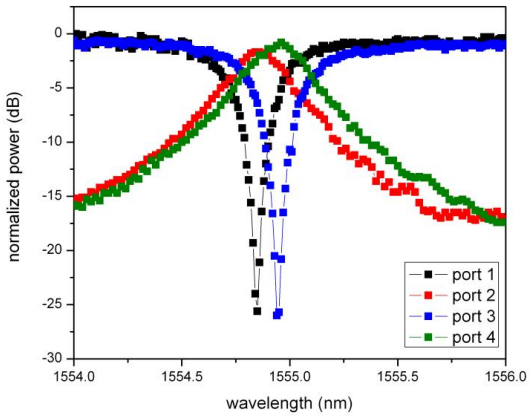


Fig.2 Measured TE-polarized through-port and drop-port spectra of the fabricated silicon microring resonators.

The spectra of TE-polarized light at the through port and drop port, measured using a narrow linewidth tunable laser with 0.01 nm spectral resolution, are shown in Fig.2. It is found that the transmitted power at the on-resonance wavelength drops by more than 25 dB with respect to that of the off-resonance wavelengths. The quality factor (Q) for both resonators were measured to be about 6500. Input and output coupling to the microresonators were via integrated fiber grating couplers [5] coupling to single mode optical fibers orientated at about ten degrees off-vertical.

This work was supported by the University Grants Committee of Hong Kong Special Administrative Region, China under special equipment grant CUHK-SEG01 and direct grant 2050460.

III. EXPERIMENT

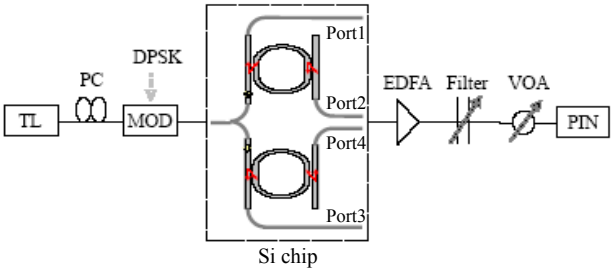


Fig. 3 Experimental set up. TL: tunable laser; MOD: modulator; VOA: variable optical attenuator; PIN: Pin diode

The experimental setup is shown in Fig.3. A CW light at the wavelength of 1554.85/1554.94nm was generated by a tunable laser (HP 8168F) with 0.001nm tuning step and was tuned exactly to the resonance of one resonator. It was then phase modulated with the data generated from a pseudo-random binary sequence (PRBS) pattern generator with a pattern length of 2^{31}-1 at 10Gb/s data rate. The generated DPSK signal was coupled into a microring resonator through input port of 1x2 MMI and then coupled out from output port 1/port 3, which extracted the AMI format from the DPSK spectrum for detection.

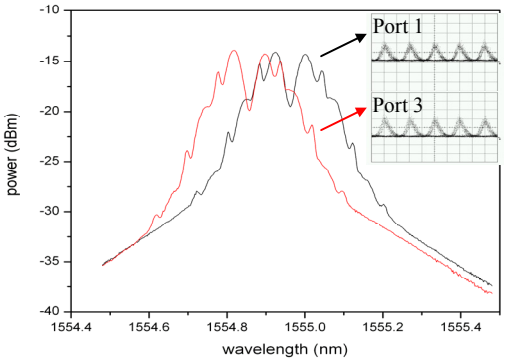


Fig. 4 The spectra after filtering and respective eye diagrams

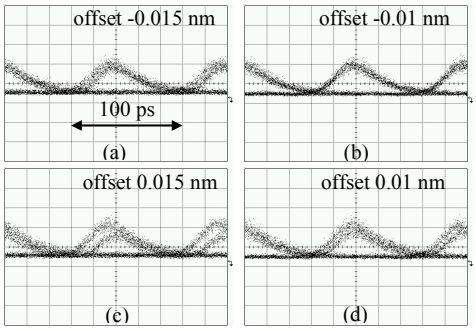


Fig. 5 Eye diagrams of demodulated signal at different offset frequencies

Fig.4 shows spectra after demodulation measured with a nominal 0.01nm 3dB-bandwidth spectral resolution optical spectrum analyzer. The inset pictures show clean and open demodulated eye diagrams at 10Gb/s. Wavelength detuning against the resonance wavelength was investigated for port 1 shown in Fig. 5. Here a negative detuning is defined as tuning the signal towards shorter wavelength while positive detuning means tuning towards longer wavelength. Fig.5(a)-(d) show demodulated eye diagrams of negative detuning of -0.015 nm to positive detuning of 0.015 nm. It is shown that the negative detuning has a better tolerance for signal demodulation.

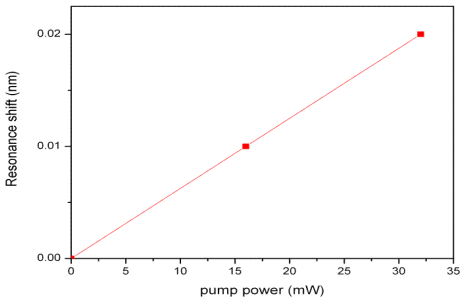


Fig. 6 Resonance shift against injected pump power

Precise tuning of the two microrings may be carried out using electrical wire heaters. However for this proof-of principle experiment, we used the local heating from the absorption of 980 nm wavelength light to tune the resonator's refractive index. The absorption of light produces free carriers (reduces the refractive index) and local heating (increases the refractive index). It is observed that the thermo-optic effect is the larger effect since the resonant wavelength shifts to longer wavelength as shown in Fig.6. It is thus possible to tune the resonance separation of the two rings match the required ¼ symbol rate for DQPSK demodulation (2.5 GHz separation for 20 Gb/s DQPSK demodulation) [4].

IV. CONCLUSION

We experimentaly demonstrated a silicon integrated microring resonator device for DQPSK demodulation. The performance was studied using DPSK for each channel for proof-of-principle. We show that the resonance seperation between I and Q channel can be tuned to match the ¼ symbol rate for DQPSK demodulation.

Acknowledgments: We thank ePIXfab (www.epixfab.eu) for device fabrication.

References

[1] Y. K. Lizé, M. Faucher, É. Jarry, P. Ouellette, É. Villeneuve, A.Wetter, and F. Séguin, "Phase-tunable low-loss, S-, C-, and L-band DPSK and DQPSK demodulator," IEEE Photon. Technol. Lett., vol. 19, no. 3, pp.1886–1888, 2007.

[2] C. C. Chien, Y. H. Wang, I Lyubomirsky, and Y. K.. Lizé, "Experimental Demonstration of Optical DQPSK Receiver Based on Frequency Discriminator Demodulator", J. Lightw. Technol. vol. 27, no. 19, pp. 4228-4232, 2009

[3] L. Xu, C Li, C. Y. Wong, and H. K. Tsang, "Optical Differential-Phase-Shift-Keying Demodulation Using a Silicon Microring Resonator", IEEE Photon. Technol. Lett., vol. 21, no. 5, 2009

[4] L. Zhang, J. Y. Yang, Y. C. Li, M. P. Song, R. G. Beausoleil, and A. E. Willner, "Monolithic modulator and demodulator of differential quadrature phase-shift keying signals based on silicon microrings", Optics Lett., vol. 33, no. 13, pp. 1428-1430, 2008

[5] D. Taillaert, F. V. Laere, M. Ayre, W. Rogaerts, D. V. Thourhout, P. Bienstman and R. Baets, "Grating couplers for coupling between optical fiber and nanophotonic waveguide", Jap. J. Appl. Phys., vol. 45, pp. 6071-6077, 2006.

Hybrid-Integrated Optical Transceiver on an OE PCB

N. Bamiedakis, A. H. Hashim, J. Beals IV, R. V. Penty, I. H. White
Electrical Engineering Division, Department of Engineering
University of Cambridge
Cambridge, UK
nb301@cam.ac.uk

***Abstract*—An optical transceiver, integrating the receiver and transmitter optoelectronic modules with a polymer Y-splitter onto a low-cost single-layered FR4 substrate, is reported. The transceiver is produced with conventional PCB manufacturing methods, employs simple electro-optic connectors and supports bidirectional 10 Gb/s data transmission along a single optical fiber.**

Keywords- optical interconnects; opto-electronic printed circuit boards; polymer waveguides;

I. INTRODUCTION

Board-level optical interconnects have constituted an area of intensive research in recent years due to the increasing demand for large interconnection bandwidth in datacommunication systems and supercomputing applications. Successful integration of photonic components with electronics on conventional printed circuit boards (PCBs) requires the use of materials with suitable mechanical, thermal and optical properties and the development of cost-effective packaging and assembly processes. Polymer multimode waveguides are a promising candidate for use in board-level optical links as they can be cost-effectively integrated onto standard PCBs and offer relaxed alignment tolerances. Various board-level optical interconnection schemes deploying such waveguide structures have been demonstrated. These differ with respect to the board design, integration method and packaging and assembly schemes employed. In most cases, however, the on-board electro-optic integration is based on the use of either advanced optical components such as mirror structures and micro-lenses to achieve efficient optical coupling [1, 2] or multi-layered substrates pre-processed in order to interface the optical transmission medium with the electrical layer of the board [3, 4]. As a result, the overall cost and complexity of the fabrication and assembly of the opto-electronic (OE) PCB increase. In this paper, a straightforward alternative scheme for integrating optical waveguides onto low-cost single-layered FR4 substrates is reported. The integration method is based on the use of simple through-board connectors which are compatible with pick-and-place assembly processes and enable end-fired optical coupling schemes. The use of such optical coupling simplifies the design and fabrication of the optical transmission layer as the need for beam-turning elements is eliminated. An optical transceiver, integrating a polymer Y-splitter with the transmitter (Tx) and receiver (Rx) electrical modules on the same board, is produced with conventional PCB manufacturing processes. This transceiver, intended as a board-level optical network unit, can currently provide bidirectional communication either along a single optical fiber at data rates up to 10 Gb/s or between similar units at 6 Gb/s.

II. ELECTRO-OPTIC PCB INTEGRATION AND ASSEMBLY

The design of the OE PCB is based on a single-layer FR4 substrate and assumes that the electronic and photonic components reside on different sides of the board. The top side of the board accommodates all electronic components and signal tracks, while the underside of the board supports the optical waveguides (Fig. 1). The interface between the optical and electrical layers of the board is achieved with simple electro-optic connectors that accommodate the active optoelectronic devices (laser and photodiode). These connectors are mounted in through-board slots appropriately produced to expose the waveguide facets and allow end-fired optical coupling in and out of the waveguides.

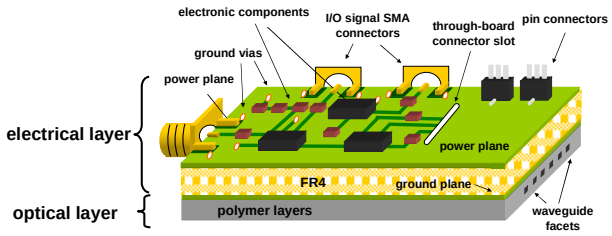


Figure 1. Schematic of OE PCB with various features noted.

The process flow for manufacturing the OE PCB comprises the following steps: (i) production of the electrical layouts on low-cost substrates, (ii) fabrication of the optical waveguides on the bottom board surface, (iii) attachment of the electronic components to the board with solder reflow process and (iv) production of the through-board connector slots using a milling machine. The substrate employed in this work consists of a 1 mm thick single-layered FR4 board with copper-plated vias and a uniform solder mask on the bottom copper surface (Fig. 2a). The electrical vias are employed to connect the ground tracks on the top of the board to the ground plane (bottom copper surface) while the uniform bottom solder mask is used to cover the vias, planarize the surface and minimize any mechanical and thermal stresses induced on the polymer layers during soldering. The polymer siloxane materials (OE-4140 and OE-4141) employed in this work are developed by Dow Corning and exhibit the essential mechanical and thermal properties to withstand the high-temperature environments associated with the soldering and lamination processes of standard PCB manufacturing [5]. The polymer materials are directly deposited over the solder mask on the underside of the

This work is funded by the Dow Corning Corporation and the UK Engineering and Physical Science Research Council.

board and can be patterned with various techniques such as printing and stamping. In this work, spin coating and photolithography are employed.

Having formed the optical and electrical layers of the OE PCB, compact L-shaped electro-optic connectors are used to accommodate the active devices, accurately position them opposite the waveguide facets and electrically connect them to the on-board circuits. The shape of the connectors is compatible with pick-and-place assembly tools and facilitates vertical and angular alignment with the waveguides owing to the two inside connector surfaces that serve as reference planes. Lateral alignment is achieved with alignment marks produced on the board surface and recognized by pick-and-place tools. The connectors are attached to the board with common adhesives, in this case Araldite. The electro-optic connectors used in this work are produced from 1.6 mm-thick FR4 substrates and carry device positioning pads as well as signal tracks and vias to efficiently route the signals from the board to the active devices (Fig. 2b).

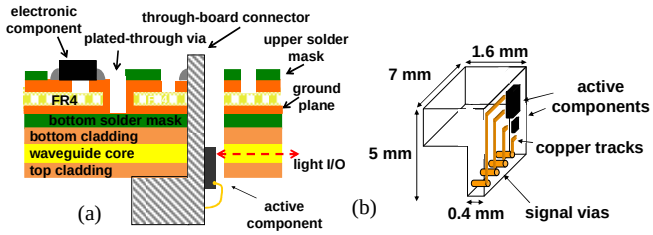


Figure 2. (a) Cross section of realised OE PCB with fitted electro-optic connector and (b) schematic of the L-connector with dimensions noted.

III. Optical Transceiver

The optical transceiver incorporates the Tx and Rx electrical modules and the polymer Y-splitter on a single-layered FR4 substrate (Fig. 3). The electrical layer comprises the laser and photodiode driving circuits, edge-mounted SMA connectors to provide the I/O data signals and voltage regulators to provide over-voltage protection to the circuits. All employed electronic components consist of low-cost commercially-available chips (Texas Instruments ONET8501V, ONET8511T) and surface-mount components. A low-cost multimode 850 nm 10 Gb/s VCSEL source and a 8 GHz GaAs photodiode with an aperture of 75 μm are used as the active components. The polymer Y-splitter has a cross section of 50×50 μm^2 and an index step of 0.2 to match standard 50/125 multimode fiber.

The data transmission performance of the optical transceiver is assessed with a digital communication analyzer and a bit-error-rate (BER) tester when the unit is interfaced with (i) external optical components (fiber-coupled high-speed receiver or VCSEL Fig. 4a) and (ii) a similar transceiver unit connected in a link configuration (Fig. 4b). When external optical components are employed, error-free ($BER<10^{-12}$) data transmission at 10 Gb/s is achieved for both the transmit and receive operation modes of the transceiver (Fig. 4c and 4d). For the link configuration, error-free data transmission at a lower rate of 6 Gb/s is obtained due to imperfections in the electrical driving circuits (Fig. 4e). The optimization of the electrical layer of the OE PCB is expected to enable 10 Gb/s operation for the link configuration. Results obtained from the optimized transceiver units will be presented in the conference.

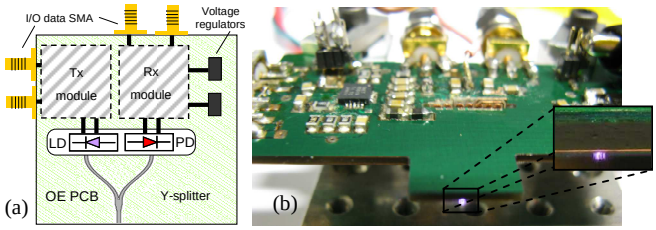


Figure 3. (a) Schematic of realised optical transceiver and (b) photograph of the actual unit with inset picture of illuminated output waveguide facet.

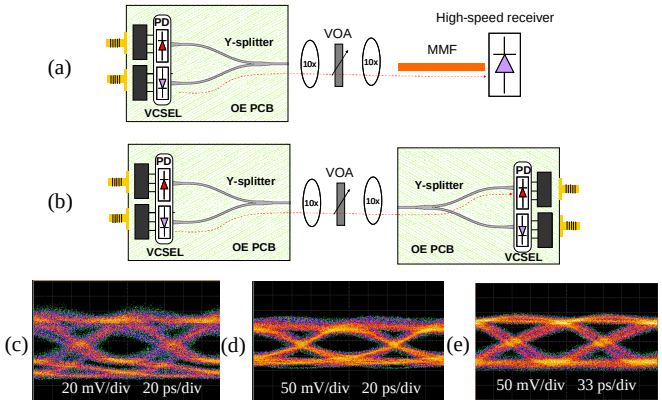


Figure 4. Link configurations when the optical transceiver is employed with: (a) an external optical component (high-speed fiber-coupled receiver) and corresponding received eye diagrams for (c) transmit and (d) receive operation mode at 10 Gb/s, and (b) in a link configuration with (e) corresponding received eye diagram at 6 Gb/s.

IV. Conclusion

A simple method of integrating photonics with electronic components onto low-cost substrates using conventional PCB manufacturing and pick-and-place assembly processes is presented. An optical transceiver incorporating a polymer Y-splitter along with the electronic circuitry on a single-layered FR4 substrate is produced. The transceiver supports bidirectional transmission along a single optical fiber at data rates up to 10 Gb/s.

References

[1] S. Nakagawa, et al., "High-density optical interconnect exploiting build-up waveguide-on-SLC board," in Proc. of the 58th Electronic Components and Technology Conference, pp. 256-260, 2008.

[2] L. Dellmann, et al., "120 Gb/s optical card-to-card interconnect link demonstrator with embedded waveguides," Proc. of the 57th Electronic Components & Technology Conference, pp. 1288-1293, 2007.

[3] C. L. Schow, et al., "A Single-Chip CMOS-Based Parallel Optical Transceiver Capable of 240-Gb/s Bidirectional Data Rates," Journal of Lightwave Technology, vol. 27, pp. 915-929, 2009.

[4] H. Zhaoran Rena, et al., "Hybrid Integration of End-to-End Optical Interconnects on Printed Circuit Boards," IEEE Transactions on Components and Packaging Technologies, vol. 30, pp. 708-715, 2007.

[5] J. V. DeGroot Jr., "Cost-effective optical waveguide components for printed circuit applications," in Passive Components and Fiber-based Devices IV, pp. 678116-12, 2007.

Hybrid Integration of Optical Polymer Waveguides and 25 GHz Photo Detector Arrays

Z. Zhang, N. Mettbach, C. Zawadzki, D. Schmidt, W. Brinker, J. Wang, N. Keil*, and N. Grote
Fraunhofer Institute for Telecommunications,
Heinrich-Hertz-Institut,
Einsteinufer 37, D-10587 Berlin, Germany
*norbert.keil@hhi.fraunhofer.de

***Abstract*— We demonstrate hybrid integration of very high-speed (25 GHz) photodetector arrays vertically coupled with polymer waveguides via a 45º mirror. The fiber-waveguide-detector insertion loss is less than 2dB, the detector responsivity is larger than 0.4mA/mW, and the crosstalk level is around -30dB.**

I. INTRODUCTION

Recent progress in optical communication networks has led to the growing need for highly functional, small footprint, low power consumption and low-cost optical modules. Integrating multiple optical functions into a single device is a key step for achieving these goals. With hybrid integration technology, discrete elements can be made each on the best suited material system and can be tested and selected prior to assembly. Hybrid integration can offer the benefits of micro-optical packaging and allow for further miniaturization, higher degree of machine-assisted assembly, less fiber connections and potentially higher performance and reliability.

Polymer planar light wave circuit (P2LC) technology is attractive because it offers the potential of fairly simple and low cost fabrication based on low-temperature processes and low-cost packaging involving passive alignment [1-2]. The optical loss of optical polymers has been reduced to less than 0.1dB/cm recently [3]. Polymer waveguides can be patterned into different geometries, allowing different optical signal processing functions such as wavelength routing, multiplexing and switching to be performed. Passive optical functions can also be implemented in the form of thin film elements featuring very small size, high optical performance and virtually temperature independence. Furthermore, optoelectronic devices such as photodetectors (PDs) and laser diodes (LDs) can be incorporated into the polymer board, perspectively in a (semi)automatic manner by means of a pick-and-place machine.

In this paper, we address the hybrid integration of single PDs and photo detector arrays (PDAs) into the P2LC platform using a vertical coupling scheme via 45° turning mirrors. Particularly, we focus on very-high speed PDs with cut-off frequencies in the 25 GHz range which play a crucial role in the current development of 100GHz transmission systems (e.g. DQPSK; 4x 25 Gb/s wavelength multiplexing). Figures for insertion loss, detector responsivity, crosstalk level and high frequency response will be presented.

II. FABRICATION TECHNOLOGY

Fig. 1 depicts the vertical coupling scheme for a bottom illuminated PD coupled to the P2LC waveguide via an integrated 45° mirror. Inserted are the side view of the 45° mirror and the top view of a mounted PD. The polymer material is commercially available and utilized in qualified devices. Buried waveguides are formed using conventional spin-on and reactive ion etching techniques. Silicon is used as substrate. The refractive index contrast (Δn) can be readily adjusted between 0.06 and 0.20 by varying the composition of the waveguide core material. Using e.g. $\Delta n = 0.06$ the cross-section of the single-mode waveguide core measures about 6x6 μm^2. The typical waveguide loss is around 0.5dB/cm at 1550nm and 0.4dB/cm at 1310nm.

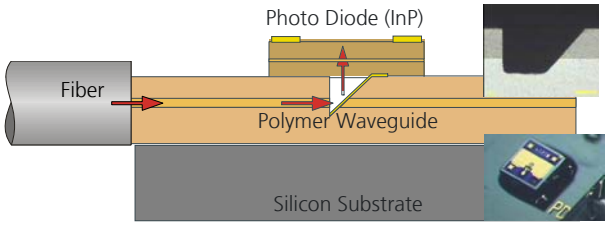


Fig. 1 Coupling of a planar photo diode to the polymer optical motherboard via an integrated 45° mirror

The 45° mirror can be created either by using an angled dicing saw or by locally etching the polymer material with the aid of grey-tone mask lithography and subsequent reactive ion etching. It should be emphasized that the sawing process leaves optically smooth waveguide and mirror facets, thanks to an inherent polishing effect. This behavior is believed to be unique to polymer materials, as contrasted to inorganic substances. After trench formation a thin reflecting Au metal layer is deposited on the mirror facet by oblique thermal evaporation ensuring the waveguide output facet to be left uncoated. The PD is placed on top of the polymer chip in a purely passive way, by a state-of-the-art bonder with positioning precision of ~1um. The PD is fixed by UV glue with adequate index matching to suppress back reflection. Shear force tests showed critical bonding values of up to 20 N/mm^2. The backside of the PD is AR coated against this glue which completely fills the mirror trench. The mirror loss measured with a multi-mode fiber is around 1 dB. The actual PD coupling loss of course also depends on the diameter of the

PD active area, its alignment position, and how it matches the actual beam spot. Using a 25 Gb/s capable PD with a typical active diameter of some 20 µm an insertion loss of only 1.8 dB was obtained at best so far, including fiber/chip coupling loss and the propagation loss of a 3 mm long polymer waveguide.

The bottom illuminated PD is designed with a full p-metal contact on its top side which facilitates uniform current flow and serves as optical reflector for the laser light to double-pass the absorbing layer. This is beneficial regarding achievable responsivity particularly with very high-frequency PDs, the absorption layer thickness of which is limited by the transit time to the order of 1 µm. On the other hand, the back illuminated PD is more sensitive to beam divergence because of the longer optical path of the beam between waveguide output and the active PD region. By thinning the PD substrate and applying a tapered waveguide output, especially when using waveguides of higher index contrast, the effective beam diameter at the active PD region can be kept as small as ~10µm ($1/e^2$). This value is fairly well below the active diameter of PDs suitable for 25 Gb/s reception, a bit rate which is in the focus now for 100 Gb/s transmission applications (4x25 Gb/s wavelength multiplexed or DQPSK schemes).

III. PHOTODETECTOR ARRAY COUPLING

Fig. 2 schematically illustrates a 4-channel fiber-waveguide-detector array (PDA) which was fabricated and characterized. The photograph at the bottom shows a completed device comprised of the surface-mounted detector array chip with four individual PDs (20 µm diam.), the P2LC waveguide board and four input fibers attached to the polymer waveguides using on-chip alignment grooves. The center spacing between the waveguides is 250 µm, which allows the use of standard fiber ribbons. The total chip measures 5 mm (length) by 1.3 mm (width).

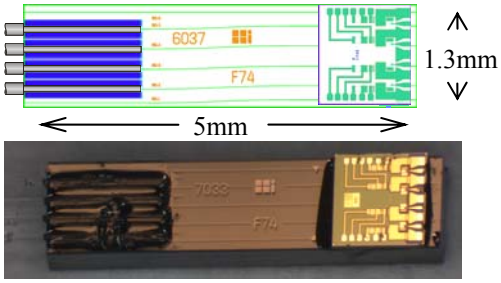


Fig. 2 4-channel fiber-waveguide-detector array.

The optimal coupling position was carefully defined in terms of waveguide position, cladding/core layer thickness and width of the mirror trench. The PDA is then mounted on top of the 45° mirror at the proper location and fixed with UV glue. Finally the fiber array is plugged in and glued for the measurements. The measured responsivity mostly varied between 0.3 mA/mW to 0.4 mA/mW, with the highest value being 0.43 mA/mW. The results have to be compared to the reference value of 0.65 mA/mW of the sole PD obtained from direct fiber illumination. The static crosstalk level was found to be on a similar level, -28 dB to -30 dB, for any of the individual PD elements within the array, suggesting stray light to be a limiting factor. The polarization dependent loss is around 0.6 dB and the optical return loss into the launching fiber (back-reflection) was determined to be lower than -35 dB.

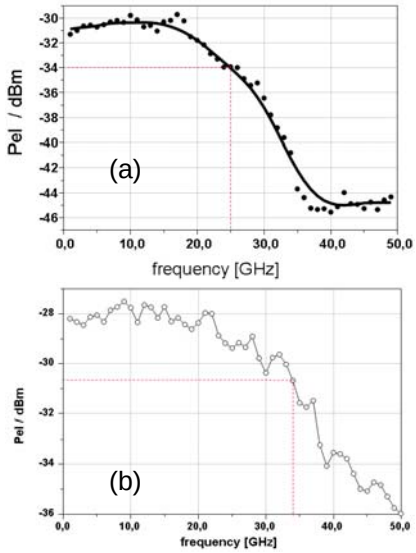


Fig. 3 PD frequency response, (a) without impedance matching and (b) with impedance matching.

Fig. 3 shows the small-signal frequency response of a mounted PD chip. The measurement was performed directly on the chip using a suitable RF probe head. Without dedicated electronics for 50 Ω impedance matching, the 3 dB bandwidth is at 25 GHz, and by applying impedance matching the bandwidth increases to 34 GHz (Fig. 3(b)), however at the expense of responsivity.

IV. CONCLUSION

To summarize, we have demonstrated hybrid integration of polymer waveguides and photodetectors using a vertical coupling scheme. The easy-to-fabricate, yet efficient 45° mirror is one of the key features of the polymer platform. Integrated 4-channel arrays with 25 Gb/s capability showed low insertion loss, good responsivity, fairly low crosstalk and back-reflection, which will allow their application to advanced receiver architectures for 100 Gb/s optical transmission systems.

V. ACKNOWLEDGEMENTS

This work was conducted in the frame of the *POLYPLANAR* project funded by the German Ministry of Education and Research (BMBF) and the *100x100 Optics* project funded by the Berlin Future Fund, co-sponsored by the European Fund for Regional Development (EFRE).

[1] S. Lehmacher and A. Neyer, "Integration of polymer optical waveguides into printed circuit boards", Electron. Lett., 36(12), pp. 1052-1153, 2000.

[2] N. Keil, H. Yao, C. Zawadzki, N. Grote, and M. Schell, "Polymer Optical Motherboard Technology", Photonics West 2008, San José (USA), Invited Paper, Proc. SPIE, Vol. 6899, pp. 689914, 2008.

[3] A. Yeniay, R. Gao, K. Takayama, R. Gao, and A. F. Garito, "Ultra-low-loss polymer waveguides", J. Lightwave Technol., 22(1), pp. 154-158, 2004.

Wavelength addressed intra-board optical interconnection using plug-in alignment technique by a micro hole array

Kenichi Nakama, Yuu Tokiwa, and Osamu Mikami
Graduate School of Science and Technology
Tokai University
1117 Kitakaname, Hiratsuka, Kanagawa, 259-1292 JAPAN
mikami@tokai.ac.jp

Abstract— We proposed a novel intra-board optical interconnection combining both a micro passive wavelength selector (MPWS) and a micro hole array (MHA) for a plug-in alignment. We found that the wavelength addressing operation of the MPWS was good solution for an intra-board interconnection by simulations and experiments.

Keywords- optical inerconnecton; wavelength addressing; plug-in alignment; optical pin; micro hole array; diffraction grating;

I. INTRODUCTION

Optical interconnections are suitable for high capacity LAN, asynchronous transfer mode (ATM) switches, and huge parallel processing computer systems because of their high data transmission rate, small crosstalk between the adjacent lines, small signal reflection, and high density mounting. For the purpose, optical surface mount technology (O-SMT) is the best solution of these applications because of their capability of both low cost and high density mounting [1].

Previously, we have proposed a board level O-SMT which was composed of micro optical pins and optoelectronic printed wiring board (OE-PWB) [2]. In this case, a reconfigurable interconnection technique is useful for intra-board optical interconnection between buried optical layers.

In this paper, we propose a novel intra-board optical interconnection combining both an optical wavelength addressing technique by a micro passive wavelength selector (MPWS), and a passive optical waveguide alignment technique by a micro hole array (MHA). And we also report experimental results of the MHA and the wavelength addressing operation of the prototype MPWS module.

II. CONCEPT OF MPWS

A module configuration of the MPWS module is shown in Fig. 1. The configuration was based on a simple free space micro optical system of a littrow monochromator mount. The optical waveguide channels were buried in the OE-PWB, and the MPWS module was plugged the optical waveguide channels in by using tapered micro holes of the MHA.

Transmitting light from an optoelectronic surface mount device (OE-SMD) propagates the optical waveguide channel, and radiates to the collimator lens. The collimated light from the collimator lens is diffracted by a diffraction grating, and is focused on the receiving optical waveguide channel which is guide to the other OE-SMD. So, we can select the receiving optical waveguide channel by the transmitting wavelength λ.

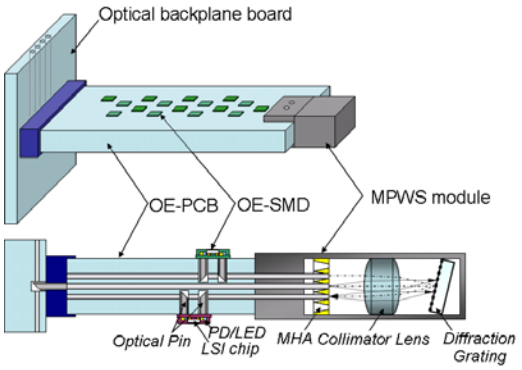


Fig. 1 Schematic figure of the OE-PWB with MPWS module

III. OPTICAL SYSTEM DESIGN

We designed and evaluated the optical system of the MPWS module by using an optical design software OSLO-EDU of Lambda Research Corporation.

We considered focusing spot positions corresponding to the wavelength dispersion from the reciprocal linear dispersion D;

$$D=d\cdot\cos\beta/m\cdot f \qquad (1)$$

where d: groove spacing, β: diffraction angle, m: diffraction order, and f: focal length of the collimator lens, respectively. When we choose the array pitch Δp of MHA and the wavelength pitch Δλ of the channel, we can decide D as Δλ/Δp, and we also select the optical elements of the MPWS.

Examples of the simulation results of the MPWS were shown in Fig. 2. In this case, we assumed that the OE-PCB had three optical waveguide channel layers. And the diffraction grating of groove spacing d=1.67μm (600 line/mm), the collimator lens of focal length f=12.5mm, the MHA of array pitch Δp=0.5mm, and wavelength pitch Δλ=65nm (460/ 525/ 590nm) were selected, respectively. And we set the littrow wavelength λl=525nm, diffraction order m=+1, and incident angle in littrow α=β=9.06 deg, respectively.

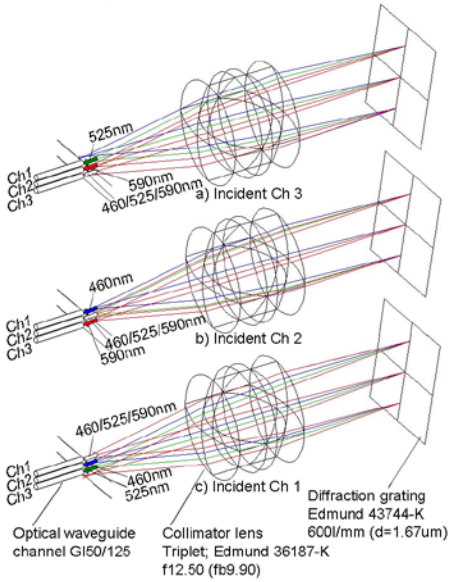


Fig. 2 Simulation results of the MPWS module

From Fig. 2, we could understand obviously, in the case of the incident channel was Ch2, Ch1 and Ch3 were addressed by 460 and 590nm, respectively. And we realized the interconnection from Ch3 to Ch1, or from Ch1 to Ch3 were addressed by the littrow wavelength of 525nm. And from the simulation, we evaluated that the spot diameter was within 60 microns and the maximum sift of the spots from the accurate positions were below 5 microns.

IV. Experimental Results

The MHA, which was the key device of plug-in alignment, was made of acrylic UV curable resin. We fabricated the MHA by the mask transfer method [3]. A microscope photograph of a fabricated 4 x 4 arrayed MHA is shown in Fig. 3.

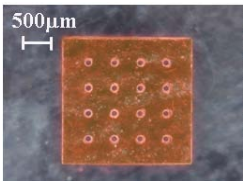


Fig. 3 Microscope photograph of a fabricated MHA

In this case, UV irradiation power and exposure time were 0.54 W/cm2 and 0.5 s, respectively. And the diameter, pitch, tapered angle, and thickness of the MHA were evaluated at 0.131 mm, 0.50 mm, 0.4 deg., and 0.95 mm, respectively.

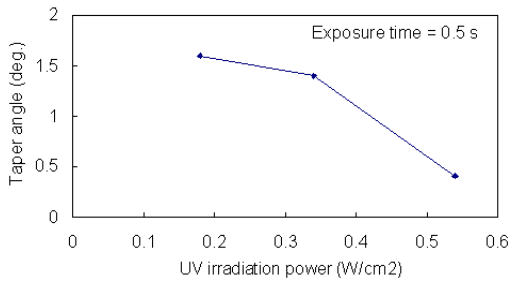


Fig. 4 Relationship of taper angle and irradiation power

The relationship of the taper angle and the irradiation power are shown in Fig.4. From the results, we found that it was applicable to control the taper angle from 0.4 deg. to 1.6 deg. by adjusting the UV irradiation power.

Fig. 5 shows a photograph of a prototype MPWS module, which was arranged on a test bench. In this case, we assumed that the OE-PCB had four optical waveguide channel layers of GI50/125 optical fibers. Other optical elements were same as Fig. 2, and the optical system size was about 8 x 8 x 30mm. The optical fibers were plugged in the MHA of the prototype MPWS module, passively.

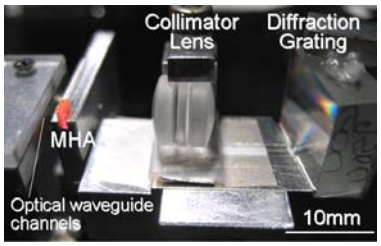


Fig 5 Photograph of the prototype MPWS module

The MPWS module was demonstrated as shown in Fig. 6. In this case, the transmitting channel was Ch1, and blue (λ 470nm), green (λ 525nm), and amber (λ 470nm) LEDs were lighted on, in order to interconnect to the receiving channels of Ch2, Ch3, and Ch4, respectively. From the results, we confirmed that the wavelength addressing operation of the MWPS module was effective for intra-board optical interconnection.

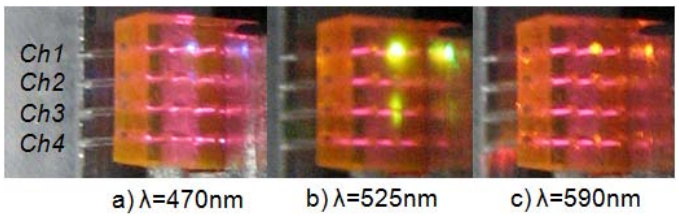


Fig. 6 Wavelength addressing operation of the MPWS module

V. Conclusions

We proposed a novel intra-board optical interconnection combining both an optical wavelength addressing technique by the MPWS, and a passive optical waveguide alignment technique by the MHA. It was found that the wavelength addressing operation of the MWPS was proved good solution for intra-board optical interconnection of the OE-PCBs.

References

[1] T. Uchida and O.Mikami, “Optical surface mount technology”, IEICE Trans. Electron. vol. E80-C, no. 1, pp. 81-87, Jan. 1997.

[2] O. Mikami, Y. Mimura, H. Hanajima, and M. Kanda, “Optical connection wirh optical pins and self-written waveguides for board-level optical wirings”, IEICE Trans. Electron., vol. E90-C, no. 5, pp.1071-1080, May 2006.

[3] Y. Obata, M. Kanda, O. Mikami, “Self-written waveguide on a VCSEL-emitting window using a photomask transfer method”, IEEE Photo. Technol. Lett., Vol.18, No.12, pp.1308–1310 , June 2006 J. Clerk Maxwell, A Treatise on Electricity and Magnetism, 3rd ed., vol. 2. Oxford: Clarendon, 1892, pp.68–73.

Polymer-based Passive Photonic Components with on-chip Fiber Grooves and Thin Film Filters

Z. Zhang, N. Mettbach, C. Zawadzki, C. Wagner, N. Keil*, and N. Grote
Fraunhofer Institute for Telecommunications,
Heinrich-Hertz-Institut,
Einsteinufer 37, D-10587 Berlin, Germany
*norbert.keil@hhi.fraunhofer.de

A. Scheibe, H. Ehlers, and D. Ristau
Laser Zentrum Hannover,
Hollerithallee 8,
D-30419 Hannover, Germany

***Abstract*— Passive photonic components based on polymer planar waveguides combined with integrated thin film filters are demonstrated. Etched on-chip grooves provide the possibility of automatic and passive fiber attachment with high coupling efficiency. 1x2 multiplexers show extremely low insertion loss (< 1 dB) and low crosstalk level (< -30 dB). Integrated polarization splitters exhibit more than 35dB TE/TM extinction ratio over a 20nm wavelength window.**

I. INTRODUCTION

Modern optical fiber based communication networks are in increasing demand for highly functional, small footprint, low power consumption, and low-cost optical modules. Photonic integration - monolithic or hybrid - is considered a key technology to achieving these requirements. The latter approach relies on planar light wave circuits (PLC) serving as integration platform. To this end various material platforms are being utilized. We have been developing polymer-based PLC technology (P2LC) which is attractive in several respects: flexible and potentially low-cost fabrication including passive alignment packaging [1]; applicability of different substrates and incorporation of heterogeneous materials because of low-temperature processes; easy micro-machineability, amongst others. We are pursuing a "toolbox" concept [2, 3] in which on-chip fiber grooves, thin film filters (TFFs), and 45° turning mirrors are involved as crucial elements. The toolbox also encompasses hybridized integration of active devices, in particular photo- and laser diodes. In this paper, we focus on passive fiber attachment and the integration of thin film filters for wavelength (de)multiplexing and polarization splitting.

II. ON-CHIP FIBER ATTACHMENT

Fiber/waveguide coupling has proven to be challenging for PLC due to the refractive index and/or the optical mode mismatch. The coupling issue becomes more serious with high-index contrast PLCs, based on e.g. silicon (SOI) and III-V semiconductors. The solutions are either expensive (with spot size converters) or bulky (with vertical grating couplers). For low-index contrast PLCs, such as silica or SiNx platforms, the coupling issue is less severe and can be solved by end-fire coupling with the aid of anti-reflection coatings. However, the end-fire coupling often suffers from poor mechanical support and the need for an extra sub-mount to hold the fiber in place.

On the polymer platform we have performed fiber/waveguide coupling by means of on-chip U grooves, as shown in Fig. 1. The U-groove width matches the fiber diameter and is etched down to the point where the fiber core and the waveguide centre are aligned. Horizontally, they are defined to the respective waveguides in a self-aligned manner thus providing virtually perfect lateral adjustment. In addition, the fiber/waveguide interface can be angled at 8° to reduce back reflection. The deep groove is etched by standard oxygen reactive ion etching utilizing a thin metal mask. The uniformity achieved across a whole 4-inch wafer is within 1µm for both width and depth.

With proper index-matching glue and waveguide tapering for mode matching, the typical loss per-facet for the U-groove based fiber/waveguide coupling is as low as 0.25 dB over a broad spectral range from 1300-1600nm. Together with a company partner an automated "pick-and-place" fiber attachment process is under development.

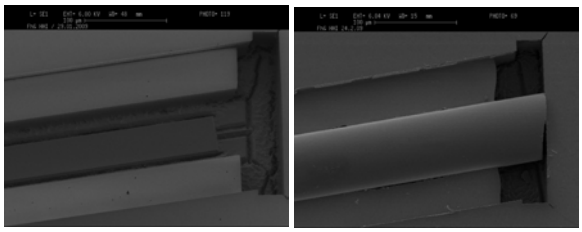


Fig. 1: SEM photos of U grooves with (right) and without (left) angled fiber inserted.

III. THIN FILM FILTERS

Optical filters are key components in any optical network using different operating wavelengths. We have studied the implementation of filter functions using thin film filter elements. These are vertically inserted into dedicated slots crossing the PLC waveguide, as schematically shown in Fig. 2. The TFF slots are etched in the same process as used for the fiber U-groove formation but may also be simply formed by applying a dicing saw, subject to wafer and chip layout. The width of the slot needs to be well adjusted to the thickness of

the filter platelet. The verticality of the mounted filter and its thickness are determining parameters for the excess loss. The thin film filters themselves are made by ion beam sputter deposition of appropriate dielectric layers onto a polymer film (same polymer material as used for the waveguide cladding) which again is spun on a sacrificial Si substrate. The total thickness of the eventual filter element measures between some 15-25 µm only, depending on the spectral requirements.

As an application example we demonstrate a 1x2 1310/1490 (or 1550) nm (de)multiplexer, as utilized in FTTH networks (Fig. 2). The total chip made on Si substrate measures 5 mm (length) by 1.3 mm (width). The input signals at wavelengths 1310 nm and 1490 nm (or 1550 nm) are launched into the input port. Using a long wavelength pass filter (LWPF), the optical signal at wavelength 1490/1550 nm will pass it to exit at output port 2 whereas the signal at 1310 nm will be reflected by the TFF to the output port 1.

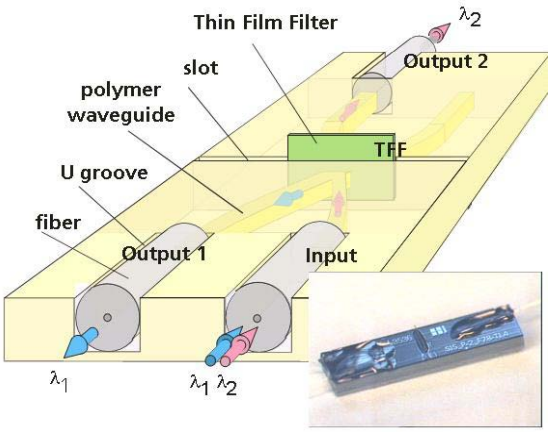


Fig. 2: The schematic of the 1X2 multiplexer

The polymer material used is commercially available and employed for qualified components. The buried waveguide core has a typical cross-sectional dimension of about 6 µm in both width and height to ensure single-mode operation. The waveguide loss is around 0.5 dB/cm at 1550nm and 0.4dB/cm at 1310nm. The full angle between the two waveguides is 16°, which efficiently suppresses back-reflection while keeping the slot loss at a minimum.

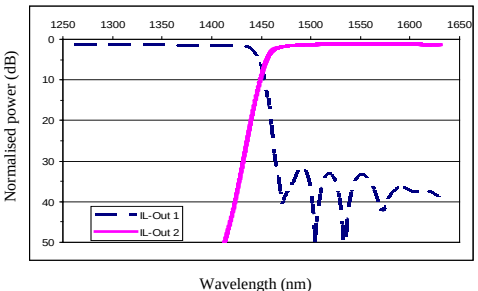


Fig. 3 Spectral characteristics of the 1X2 multiplexer, with the blue curve indicating the signal at output #1 (reflected) and the purple curve the signal at output #2 (transmitted).

The measurement result is shown in Fig. 3, displaying the filter performance of the LWPF. At 1310nm, the insertion loss at output port 1 is around 1.2 dB. The other channel at 1550nm exhibits an even smaller loss of 1.0 dB. The crosstalk level is below -30dB. Across the whole wavelength range, the back reflection into the input fiber (optical return loss) is well below -50 dB. If we subtract the loss from the fiber connectors and only consider the net insertion loss from the input fiber to the output fiber, the device itself features a loss well below 1 dB. The maximum polarization dependent loss is 0.5 dB.

IV. Polarization Beam Splitter

Polarization splitting is another key function, especially with polarization diversity type PLCs. There have been many integrated polarization splitters reported, using gratings, waveguide birefringence, photonic bandgap effect, and others. We propose, however, a fairly easy solution by again using a thin film element (PSTFF). The schematic architecture of the device is similar to Fig. 2. Depending on the characteristics of the PSTFF, one polarization will be reflected to output 1 and the other will pass through to output 2. The incident angle from the waveguide to the PSTFF, i.e. the half-angle between the two waveguides, can be varied to optimize the splitting ratio for a desired bandwidth.

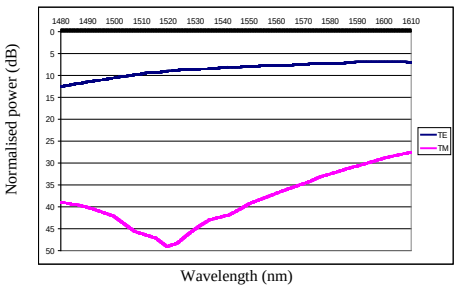


Fig. 4 Spectral characteristics of the polarization beam splitter at output 2 (transmitted). The blue curve indicates the TE polarization and the purple curve shows the TM polarization.

As an early result, Fig. 4 shows the spectra for TE and TM signals at the output port 2. At 1520nm, the splitting ratio is around 40dB with a 3dB bandwidth of ~20nm. Further studies are in progress to optimize the device in terms of smaller insertion loss, larger splitting radio and bandwidth.

V. Acknowledgement

This work was conducted in the frame of the national projects MiniWDM and POLYPLANAR funded by the German Federal Government, and of the project “100x100 Optics” funded by the Berlin Future Fund, co-sponsored by the European Fund for Regional Development (EFRE).

[1] N. Keil, H. H. Yao, C. Zawadzki, C. Dreyer, and J. Bauer, M. Bauer, OFC 2001, Post-Deadline paper PD7, 2001.

[2] N. Keil, H. Yao, C. Zawadzki, N. Grote, and M. Schell, Photonics West 2008, San José (USA), Invited Paper, Proc. SPIE, Vol. 6899, pp. 689914, 2008.

[3] N. Keil, Z. Zhang, C. Zawadzki, C. Wagner, A. Scheibe, H. Ehlers, D. Ristau, J. Wang, W. Brinker, and N. Grote, Electronics Letters, Vol. 45, Issue 23, pp. 1167–1168, 2009.

Slow Light in Nanophotonic Materials

From 'Trapped Rainbows' to Quantum Memories

Ortwin Hess and Kosmas L Tsakmakidis
Advanced Technology Institute and Department of Physics
University of Surrey
Guildford, Surrey, GU2 7XH, UK
o.hess@surrey.ac.uk

Abstract—**We analyze and compare the salient features of slow-light propagation in a variety of nanophotonic structures, including metamaterial, plasmonic and photonic crystal waveguides. We discuss the possibility of stopping light in nanoplasmonic metamaterials, and coherently storing quantum information in semiconductor quantum dot ensembles.**

Keywords—slow light; metamaterals; plasmonics; photonic crystals; quantum dots; waveguides

I. INTRODUCTION

Metamaterials (MMs) [1], [2] and 'slow light' (SL) [3], [4] have, in the last decade, evolved to two of the largest and most exciting realms of contemporary science, enabling a wealth of useful applications, such as *sub*-diffraction-limited lenses, 'invisibility' cloaks, and ultra-compact photonic devices.

Recently, it has been theoretically demonstrated [5] that these two highly technologically important areas of research, which were until now following separate tracks, could in fact be combined, with the potential of leading to novel metamaterial-enabled slow-light structures that can improve (in terms of the degree to which light can be decelerated, as well as in terms of performance, functionality and efficiency) on existing slow-light designs and structures.

In what follows, we begin by concisely reviewing the basic premises of slow/stopped light in metamaterial and plasmonic waveguides featuring negative electromagnetic constitutive parameters (permittivity/permeability/refractive-index). We explain how and why these structures can enable complete stopping of light even in the presence of disorder *and*, simultaneously, dissipative losses. Section III provides a brief overview of various, so called, 'trapped rainbow' light-slowing/stopping schemes that have recently been reported, along with their merits and limitations. Further, on the basis of full-wave numerical simulations, it will be reported (during the course of the presentation) that the incorporation of thin layers made of an active medium adjacently to the core layer of a negative-refractive-index waveguide can *completely* remove dissipative losses. In section IV we explain that it is, in principle, possible to realize controlled storage and release of photonic space-time quantum coherences in quantum dot nanomedia subjected to coherent tunable light signals. Finally, section V summarizes the paper, presenting the main conclusions of the present review.

II. SLOW AND STOPPED LIGHT IN METAMATERIALS

Some of the most successful slow-light designs at present, based on photonic crystals (PhCs) [6] or coupled-resonator optical waveguides (CROWs) [7], can so far efficiently slow down light by a factor of 40 – otherwise, large group-velocity dispersion *and* attenuation-dispersion occur, i.e. the guided light pulses broaden and the attainable bandwidth is severely restricted. Furthermore, it has by now been realised that such *positive*-index slow-light structures are, unfortunately, extremely sensitive to the presence of (even weak) fabrication disorder [8] – to the point that a disorder of only 5-10 nm (at a wavelength of 1550 nm) leads to group velocities that can *never*, even in the presence of dispersion, be smaller than approximately $c/300$ (refs. [3], [9]).

In an effort to overcome the above intrinsic limitations of *positive*-index slow-light schemes, a fundamentally new approach has been recently proposed [5]. This method relies on the use of negative-refractive-index, NRI, (or negative-refraction) waveguides, wherein the power-flow direction inside the NRI regions is opposite to the one in the positive-index regions, resulting in a pronounced deceleration of the guided electromagnetic energy (see Figure 1). The scheme is resilient to fabrication disorder/imperfections because it does not rely on the use of stringent conditions (such as a 'perfect' photonic-crystal lattice or attainment of ultralow temperatures, etc) for decelerating and stopping light, but rather on the deployment of *negative* bulk/effective electromagnetic parameters (such as, e.g., negative refractive index or, simply, negative permittivity) that can be realised by even *amorphous* and *highly disordered* metamaterials [10], [11] – a situation which is similar to, e.g., crystalline or amorphous silicon, where the presence or not of a periodic atomic lattice does not preclude the attainment of a bulk/effective (positive) refractive index.

Moreover, these metamaterial heterostructures can be designed in such a way that they exhibit *zero* group-velocity-dispersion *and* attenuation-dispersion, even in the 'stopped-light' regime [12]. In doing so, we are able to allow for extremely large bandwidths over which the slowing or stopping of the incoming optical signals can be achieved, as well as for ultrashort device lengths. This ability of metamaterial-based heterostructures to dramatically decelerated or even *completely stop* [5] light under realistic

experimental conditions, has recently led to a series of experimental works [13], [14] that have provided spectroscopic evidence for the observation of 'trapped rainbow' light-stopping in metamaterial waveguides – to our knowledge, the first experimental works to provide a telltale spectroscopic fingerprint of 'true' light-stopping in solid-state structures.

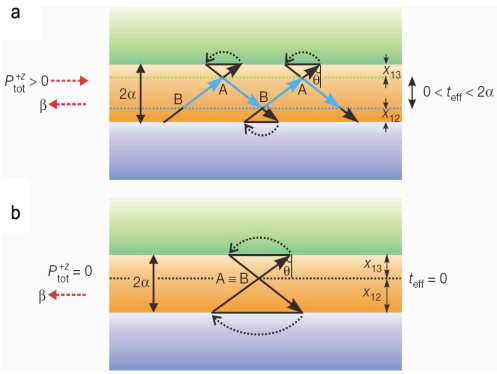


Fig.1. Slow and stopped light in negative-refractive-index hetero-structures. (a) Slow zigzag ray propagation along a NRI heterostructure. (b) Here, the ray returns exactly to its original point; the ray, thus, becomes permanently trapped (zero group velocity, $v_g = 0$) and an 'optical clepsydra' is formed.

III. Further Schemes For Slowing And Stopping Light

As was explained above, the 'trapped rainbow' method for stopping light relies critically on the presence of negative Goos-Hänchen phase shifts (see Fig. 1), as well as on the occurrence of mode-degeneracy points in the modal dispersion diagrams [5], [15], both of which require media with negative optical parameters, e.g., negative permittivity – but *not* necessarily negative refractive index. For instance, a plasmonic waveguide having a core of a material with negative (real part of) permittivity in the optical regime supports surface plasmon polaritons (SPPs) whose cycle-averaged power flow inside the negative-ε core is negative (owing to the negativity of ε). This can result in zero total cycle-averaged power flow, P_{tot} [15], at a particular (mode-degeneracy) point along the waveguide and, accordingly, in zero group (or energy) velocity at that point. As a result, in addition to the initially proposed negative-index based method towards broadband 'trapped rainbow'-stopping of light [5], scientists have now theorized a number of alternative metamaterial structures and geometries that can achieve similar feat. Some of these are, now, summarized below.

A first approach relies on the use of extremely anisotropic metamaterial wire waveguides made up of alternating metallic and dielectric discs [16]. In these structures the effective permittivity of the metamaterial wire is negative in the transverse direction but positive in the longitudinal direction, leading to zero-group-velocity (mode-degeneracy) points for the supported oscillatory modes, similar to those appearing in a negative-index waveguide. The light-stopping is achieved by an adiabatic *increase* of the wire radius to the zero-v_g point. A further interesting scheme uses, so called, 'spoof' SPPs in engineered metallic gratings in the THz regime (where the metallic losses are very small) to bring them to a complete halt at different points along the grating, depending on the frequency of the guided SPP wave [17], [18]. The authors of that work have, thus, showed that different 'colours' of light can adiabatically be stopped at different waveguide thicknesses, forming (THz) 'trapped rainbows'. In a different approach, He *et al*. [19] demonstrated that using a waveguide with a photonic crystal in its *negative*-refraction regime can, also, lead to temporarily halting individual light frequencies at distinct points along the waveguide. An advantage of this scheme is that, being all-dielectric, is almost insensitive to material dissipative losses. 'Trapped rainbow' stopping of light inside a hollow, air waveguide with anisotropic metamaterial cladding has been demonstrated numerically by Jiang *et al*. [20], while slow light propagation with very low group velocity dispersion in a negative-index waveguide with plasmonic claddings was reported by Dong *et al*. [21]. An NRI thin-cladding waveguide structure for temporarily stopping light has been proposed by Kim [22], while a detailed feasibility study for light-stopping in plasmonic waveguides has recently been reported by Park *et al*. [23]. More recently, Bai *et al*. [24] have demonstrated by using numerical simulations how optical information can controllably be stored in and released from a NRI waveguide. It should be herein noted that an advantage of the NRI (double-negative) slow-light structures as compared to their single-negative (e.g., plasmonic) counterparts is that they can facilitate slow light propagation for *both* polarizations (TM and TE) – an attribute that is important for certain slow-light applications, such as in modulators and switches [25].

Finally, it is worth pointing out that negative Goos-Hänchen shifts can exist not only for electromagnetic waves, but also for acoustic waves [26], as well as for matter (e.g., electron or atom) waves [27], [28]. This opens up the remarkable possibility of 'trapped rainbow'-stopping of *matter* waves by means of *light* (e.g., laser 'slabs'), i.e. the reverse of 'trapped rainbow'-stopping of light in meta-material waveguides.

IV. Quantum Dot Nanomaterials For Quantum Memories

Light is a promising candidate for carrying information in classical, but also *quantum* communication systems. In the realization of quantum information technologies, a key requirement is the ability to transmit a photonic qubit *and* to maintain and store quantum coherences. Various experiments have, therefore, focused on an exploration of the coupling of light and matter with the aim to preserve and store quantum coherence. In principle, the realization of such a 'quantum memory' system requires precise knowledge of the coherence properties of the particular material employed, as well as the system itself. So far, concepts and realizations of quantum memory elements have typically been based on atom and ion ensembles, and various investigations have concentrated on atomic vapours or ensembles of atoms, where the transfer of a

quantum state between matter and light has, indeed, been achieved [29].

Recently, we have theoretically demonstrated controlled storage and transfer of photonic space-time quantum coherences realized by a quantum dot nano-medium that was subjected to a coherent tunable light signal [30]. This system has a large potential for the realization of a solid-state based controllable quantum memory: Quantum dots can be positioned in a controlled way, addressed electrically and/or optically, embedded into active devices or integrated into larger structures, e.g. arrays or micro cavities to improve the efficiency. Further, they are attractive for quantum experiments, e.g. as single photon sources [31]. Our analysis of spatial coherence patterns that directly profit from the full information represented in the distributions of field-field and field-dipole correlations, demonstrated a strong dependence of *storage* and transfer of quantum coherence on, both, optical and *electrical* excitation conditions. Furthermore, the quantum correlations revealed the influence of intradot hot-carrier relaxation and shed light on the importance of disorder in the dynamic response and coupling of light and matter.

V. Conclusion

In summary, we have shown that plasmonic metamaterial waveguides featuring negative electromagnetic parameters can enable complete stopping of light under realistic experimental conditions [5], [13], [14], [17], [18], [23], [24]. This attribute is underpinned by the resilience of the deceleration mechanism in these structures to fabrication imperfections (e.g., disorder) and dissipative losses. By nature, these schemes invoke solid-state materials and, as such, are not subject to low-temperature or atomic coherence limitations. The NRI-based scheme, in particular, inherently allows for high in-coupling efficiencies, polarization-independent operation, and broadband function, since the deceleration of light does not rely on refractive index resonances. This versatile method for trapping photons opens the way to a multitude of hybrid, optoelectronic devices to be used in 'quantum information' processing, communication networks and signal processors, and conceivably heralds a new realm of combined metamaterials and slow light research.

References

[1] V. M. Shalaev and A. K. Sarychev, Electrodynamics of Metamaterials, New Jersey: World Scientific Publishing, 2007.

[2] N. Engheta and R. W. Ziolkowski, Eds. Electromagnetic Metamaterials: Physics and Engineering Explorations, New York: Wiley-IEEE Press, 2006.

[3] J. B. Khurgin and R. S. Tucker, Eds. Slow Light: Science and Applications, New York: Taylor and Francis, 2009.

[4] P. W. Milonni, Fast Light, Slow Light and Left-Handed Light, New Yorl: Taylor and Francis, 2005.

[5] K. L. Tsakmakidis, A. D. Boardman, and O. Hess, "'Trapped rainbow' storage of light in metamaterials," Nature, vol. 450, pp. 397–401, Nov. 2007.

[6] B. Corcoran, *et al*., "Green light emission in silicon through slow-light enhanced third-harmonic generation in photonic crystal waveguides," Nature Photonics, vol. 3, pp. 206–210, Mar. 2009.

[7] F. Xia, *et al*., "Ultracompact optical buffers on a silicon chip," Nature Photonics, vol. 1, pp. 65– 71, Jan. 2007.

[8] A. Petrov, *et al*., "Backscattering and disorder limits in slow light photonic crystal waveguides," Opt. Express, vol. 17, pp. 8676–8684, May 2009.

[9] D. P. Fussell, *et al*., Influence of fabrication disorder on the optical properties of coupled-cavity photonic crystal waveguides," Phys. Rev. B, vol. 78, pp. 144201-1–144201-11, Oct. 2008.

[10] C. Helgert, *et al*., "Effective properties of amorphous metamaterials," Phys. Rev. B, vol. 79, pp. 233107-1–233107-4, June 2009.

[11] N. Papasimakis, *et al*., "Coherent and incoherent metamaterials and order-disorder transitions," Phys. Rev. B, vol. 80, 041102-1–041102-4, July 2009.

[12] A. Karalis, *et al*., "Plasmonic dielectric systems for high-order dispersionless slow or stopped subwavelength light," Phys. Rev. Lett., vol. 103, pp. 043906-1–043906-4, July 2009.

[13] X. P. Zhao, *et al*., "Trapped rainbow effect in visible light left-handed heterostructures," Appl. Phys. Lett., vol. 95, 071111-1–071111-3, Aug. 2009.

[14] V. N. Smolyaninova, *et al*., "Experimental observation of the trapped rainbow," arXiv:0911.4464v1 [physics.optics], Nov. 2009.

[15] K. L. Tsakmakidis, *et al*., "Single-mode operation in the slow light regime using oscillatory waves in generalised left-handed heterostructures," Appl. Phys. Lett., vol. 89, pp. 201103-1–201103-3, Nov. 2006.

[16] Y. J. Huang, *et al*., "Nanowire waveguide made from extremely anisotropic metamaterials," Phys. Rev. A, vol. 77, pp. 063836-1–063836-11, June 2008.

[17] Q. Gan, *et al*., "Ultrawide-bandwidth slow-light system based on THz plasmonic graded metallic grating structures," Phys. Rev. Lett., vol. 100, pp. 256803-1–256803-4, June 2008.

[18] L. Chen, *et al*., "Trapping of surface-plasmon polaritons in a graded Bragg structure: Frequency-dependent spatially separated localization of the visible spectrum modes," Phys. Rev. B, vol. 80, pp. 161106-1–161106-4, Oct. 2009.

[19] J. He, *et al*., "Slow light in a dielectric waveguide with negative-refractive-index photonic crystal cladding," Opt. Express, vol. 16, pp. 11077-1–11077-6, July 2008.

[20] T. Jiang, *et al*., "Stopping light by an air waveguide with anisotropic metamaterial cladding," Opt. Express, vol. 17, pp. 170-177, Dec. 2008.

[21] J. W. Dong and H. Z. Wang, "Slow electromagnetic propagation with low group velocity dispersion in all-metamaterial based waveguide," Appl. Phys. Lett., vol. 91, pp. 111909-1–111909-3, Sep. 2007.

[22] K.Y. Kim, "Tunneling-induced temporary light trapping in negative-index-clad slab waveguide," Jpn. J. Appl. Phys., vol. 47, pp. 4843-4845, June 2008.

[23] J. Park, *et al*., "Trapping light in plasmonic waveguides," Opt. Express, vol. 18, 598-623, Jan. 2010.

[24] Q. Bai, *et al*., "Controllable optical black hole in left-handed materials," Opt. Express, vol. 18, pp. 2106-2115, Jan. 2010.

[25] F. Y. Gardes, *et al*., "Micrometer size depletion-type photonic modulator in silicon on insulator," Opt. Express, vol. 15, pp. 5879-5884, Apr. 2007.

[26] L. Zeng, *et al*., "Trapped phonon in acoustic metamaterial," Mod. Phys. Lett. B, vol. 23, pp. 2853-2859, 2009.

[27] C. W. J. Beenakker, *et al*., "Quantum Goos-Hänchen effect in graphene," Phys. Rev. Lett., vol. 102, pp. 146804-1–146804-4, Apr. 2009.

[28] J. Huang, *et al*., "Goos-Hänchen-like shifts in atom optics," Phys. Rev. A, vol. 77, pp. 063608-1–063608-7, June 2008.

[29] D. N. Matsukevitch and A. Kuzmich, "Quantum state transfer between matter and light, Science, vol. 306, pp. 663-666, Oct. 2004.

[30] E. gehrig and O. Hess, "Controlled storage and transfer of photonic space-time quantum-coherence in active quantum dot nanomaterials," Opt. Express, vol. 16, pp. 3744-3752, Mar. 2008.

[31] C. Santori, et al., "Indistiguishable photons from a signle-photon device," Nature, vol. 419, pp. 594-597, Oct. 2002.

This work was supported by the UK Engineering and Physical Sciences Research Council (EPSRC) and the Royal Academy of Engineering.

Using integrated optics for advanced point-of-care diagnostic devices

K. Zinoviev[1], A.B. González, O. E. Hidalgo, J. Elizalde[2], L. Fernández[2] and L. M. Lechuga
Nanobiosensors and Bioanalytical Application Group,
Research Center on Nanoscience and Nanotechnology, CIN2 (CSIC-ICN)
[1]Instituto de Microelectrónica de Barcelona (IMB) CNM-CSIC
Campus UAB, 08193, Cerdanyola del Valles, Barcelona Spain
[2] IKERLAN S Coop, MEMS Department, E-20500 Mondragón, Guipúzcoa, Spain

laura.lechuga@cin2.es

Abstract—**Integrated optics is an extreme useful technology for the production of high sensitive and compact devices for biosensing purposes. Devices can be further integrated in complete lab-on-a-chip platforms for point-of-care diagnostics.**

Keywords-optical biosensor; interferometer; point-of-care; microfluidics, grating couplers.

I. INTRODUCTION

Most clinical tests are based on time-consuming, expensive, and sophisticated techniques performed by specialized technicians in laboratory environments. These techniques typically require labeling of the samples or reagents with fluorescent or radioactive markers. There is an unmet need of having reliable diagnostic tools that ensure a sensitive, rapid, affordable and simple analysis, particularly in the clinical practice. Such reliable diagnostic tools could afford the decentralization of clinical diagnostics to point-of-care (POC) settings, allowing tests in primary care facilities and outpatient clinics, in hospital units, workplaces and homes, among others.

Advances in micro- and nanobiosensor technology is offering the implementation of diagnostic tools with increased sensitivity, specificity, and reliability for *in vivo* and *in vitro* applications. Such a device could contain enough hard wired intelligence and robustness to be used by the patient and deliver a multitude of data to the practitioner or the central database of a hospital. It is clear that the application of a portable, easy-to-use and highly sensitive biosensor lab-on-a-chip platform for real-time clinical diagnosis could offer significant advantages over current methods [1].

Taking into account this demand, we are seeking to develop highly-competitive label-free biosensing systems which could be integrated in a portable platform. Different photonic biosensor technologies are pursued in parallel: integrated interferometer devices (Mach-Zender and bimodal waveguides), plasmonic nanostructures and waveguided microcantilevers. Our main aim is to develop a highly sensitive platform for POC analysis based on label-free biosensing detection and integrated in a microsystem instrument fabricated with low-cost technologies of polymer and silicon, and meeting the requirements of disposability and portability.

II. BIOSENSOR LAB-ON-CHIP DEVELOPMENT

The biosensor microsystem is being assembled by integrating the following parts: (i) micro/nano sensors fabricated with standard silicon technology, (ii) a polymer microfluidic cartridge monolithically integrated with the sensor and with the corresponding tube connections, (iii) novel grating coupler devices for the in and out coupling of the light in all the photonic channels for multisensing (iv) robust immobilisation and regeneration protocols for the biological receptor (iv) CMOS photodetectors, electronic & software control (v) final integration and packaging. In the following, we will show our last developments in the sensor, microfludics and grating couplers steps and the integration between them.

A. Interferometric nanobiosensor

The key element of the microsystem is an array of photonic microsensors based on Mach–Zehnder interferometer devices of high sensitivity. The interferometer devices were fabricated on silicon technology and constructed from rib waveguides of nanometer dimensions (and wavelength in the visible range). Detection of the biomolecular interactions is done through the interaction with the evanescent wave of the light circulating in the sensor area. For the array of sensors, each sensing arm can be functionalised with a different biological receptor specific to the substance to be detected. In this way, we can obtain a device for the real-time detection of substances at the pico/femtomolar level without using fluorescent labels. The high sensitivity of the analysis is guaranteed by the design of the photonic structures in which the evanescent wave

interaction is maximized. Experimental evaluation of the devices indicate a detection limit of $\Delta n_{min} = 1 \cdot 10^{-7}$ [2].

B. Integrated microfluidic network

One key issue is the way to bring the sample in contact with the sensing area. The volume of the sample and the flow rate are critical parameters, especially for clinical testing, where it is extremely important to reduce the sample volume as much as possible. The size of the channels in the fluidic network, their design, fabrication, connection and alignment to the sensor area are critical steps. We have performed the integration of the MZI biosensor with a microfluidic polymeric network at the wafer level [3]. The microfabrication technique is based on an adhesive bonding process and releasing steps of two photolithographic patterned SU-8 polymeric resist layers on separate wafers: the bottom substrate (the wafer containing the MZI devices) and a temporary top substrate (Kapton™ on borosilicate glass wafer). Once the two-dimensional SU-8 layers were generated, the patterned wafers were aligned and bonded together to form a three-dimensional (3D) microchannel structure between them. After the bonding, the top glass wafer and the Kapton™ film were detached from the SU-8 stack and bottom substrate.

The generated microfluidic channels have a height close to 50 µm and 100 µm width. The microchannel is homogeneous with the same height along the 15 mm length of the MZI sensor area. The successful results are showed in Figure 1 with a top overview of the microfluidic with one microfluidic channel over a sensor window with a perfectly coupled mode propagating and exposed to the channel environment.

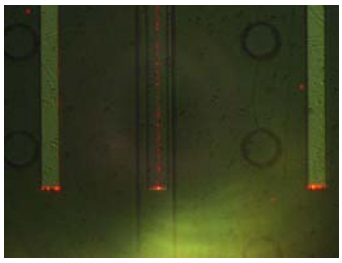


Figure 1. Light propagating in a waveguide sensor window integrated with a 56 µm microfluidic channel.

The platform can operate at pressure drops up to 1000 kPa under steady-state flow rates ranging from 1 to 1000 µl/min in laminar flow regime.

C. Mountable diffraction grating coupler

Light coupling in/out of the waveguides can be realized by using diffraction gratings (DG) with sub-micron period. But usually the compatibility and complexity of the technologies for batch fabrication of the DG couplers and the waveguides on the same wafer is a challenge. In order to solve the known problems, we have proposed a novel approach where grating couplers were fabricated separately and then were attached to the waveguides. We used hard dielectric thin film couplers supported by a polydimethylsiloxane (PDMS) film. We developed a technique to mount thin film dielectric grating couplers onto planar waveguides. The couplers were batch fabricated, fixed on the elastomer film, characterized and then installed on the chip containing the waveguides (see Figure 2). The property of the elastomer film to adapt or to stick to even nonplanar surfaces is employed to press the couplers against the waveguides. Similar to the prism couplers concept, the gratings can be reliably pressed against the waveguides by the elastomer and can be safely released from it. Our method has assured a good and reproducible contact of the waveguides with the thin film grating couplers, both fabricated separately. We have called this approach “mountable gratings”.

No air gaps were observed at the interface between the gratings and the waveguides, confirming that the DGC was in contact with the waveguide surface, except on defects The out-of-plane light coupling into the rib waveguide using the proposed hybrid DGC-PDMS system was obtained focusing a He-Ne laser (632.8 nm) on the grating using a plano–convex lens. Preliminary results indicate a coupling efficiency of 5% (TE polarization). This value could be further improved.

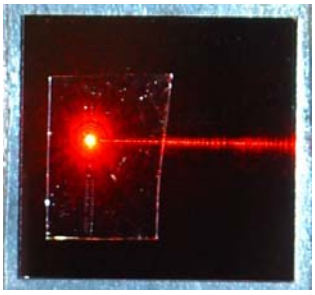


Figure 2. Out of plain coupling of light into a waveguide. Mountable DG couplers were attached to a chip with silicon nitride waveguides.

ACKNOWLEDGMENT

Authors acknowledge the financial support from Fundación M. Botín and the SENA project (TSI-020301-2008-11) from the Spanish Ministry of Industry.

REFERENCES

[1] B. Kuswandia, Nurimana, J. Huskensb, W. Verboomb. ”Optical sensing systems for microfluidic devices: A review”. Anal. Chim. Acta, vol 601 pp 141–155 (2007)

[2] K. Zinoviev, L.G. Carrascosa, J. Sánchez del Río, B. Sepúlveda, C. Domínguez and L.M. Lechuga, “Silicon Photonic Biosensors for Lab-on-a-Chip Applications”, Advances in Optical Technologies, doi:10.1155/2008/383927 (2008)

[3] F.J. Blanco, M. Agirregabiria, J. Berganzo, K. Mayora, J. Elizalde, A. Calle, C. Dominguez and L.M. Lechuga, “Microfluidic-optical integrated CMOS compatible devices for label-free biochemical sensing”, J. of Micromechanics and Microengineering, vol. 16,pp. 1006–(2006).

Multi-wavelength fluorescence sensing with integrated waveguides in an optofluidic chip

C. Dongre, H.J.W.M. Hoekstra, M. Pollnau
Integrated Optical Microsystems (MESA+),
University of Twente, Enschede, The Netherlands

R. Martinez Vazquez, R. Osellame, G. Cerullo
Dipartimento di Fisica, IFN-CNR,
Politecnico di Milano, Milan, Italy

J. van Weerd, R. van Weeghel
Zebra Bioscience BV, Enschede, The Netherlands

G.A.J. Besselink, H.H. van den Vlekkert
LioniX BV, Enschede, The Netherlands

***Abstract*—Femtosecond-laser-written integrated waveguides enable multi-wavelength fluorescence sensing of flowing biomolecules in an optofluidic chip. Fluorescence from differently labeled biomolecules with distinct absorption wavelengths, encoded by uniquely modulating each excitation beam, is detected by a color-blind photodetector, and the origin of each signal is unraveled by Fourier analysis.**

Keywords-optofluidics; biophotonics; fluorescence sensing

I. INTRODUCTION

Optical sensing, specifically fluorescence sensing, is the preferred detection technique in a number of biochemical analyses due to the high sensitivity that is achievable. Most systems consist of a single excitation wavelength in order to induce fluorescence in the labeled analytes. While a few approaches report multi-wavelength fluorescence sensing [1] for bioanalysis, these tend to apply complicated bulk optical schemes to separate signals at different fluorescence wavelengths, which is critical to any multi-wavelength approach.

We present an elegant approach to achieve multi-wavelength sensing in an optofluidic chip with integrated optical waveguides, by means of *a priori* encoding of the fluorescence originating in different biomolecules by intensity-modulating the excitation light sources, followed by Fourier decoding of the detected biophotonic signals, thereby tracing back the origins of the biomolecules. We implement capillary electrophoresis (CE) as a powerful method to separate differently sized biomolecules in a tiny microfluidic (MF) lab-on-a-chip (LOC) device, where high-speed operation and low reagent volumes pave the way to solving real-life challenges in medicine. We post-processed integrated optical waveguides (WGs) into such commercially mass-produced MF LOCs on a fast (few minutes / chip), flexible, chip-by-chip basis by femtosecond-laser micromachining [2]. This approach allows the exploitation of the existing mature MF fabrication infrastructure, while achieving integrated-WG laser-induced fluorescence (LIF) monitoring during on-chip migration and separation of biomolecules [3].

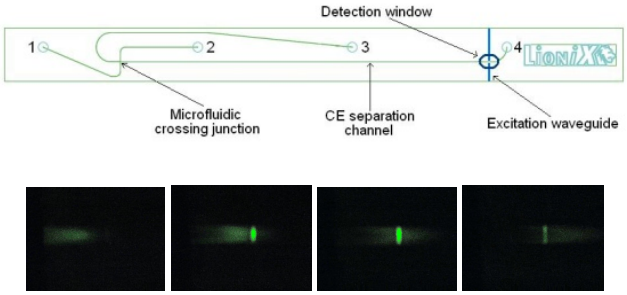


Fig. 1. (a) Schematic of the optofluidic chip showing MF reservoirs, injection (reservoir 1 → reservoir 2) and CE separation (reservoir 3 → reservoir 4) channels, integrated optical WG and detection window; (b) movie recorded with a CCD camera showing transient fluorescence from several molecule plugs formed by CE separation of the DNA ladder as these plugs pass by the point of integrated-WG laser excitation at 488 nm.

II. OPTOFLUIDIC INTEGRATION

The integrated optical WG intersecting the MF channel perpendicularly in plane was written at a speed of 20 µm/s into a fused-silica LOC device (Fig. 1a) by translating it perpendicular to a focused Ti:sapphire laser beam consisting of 150-fs, 4-µJ pulses emitted at a repetition rate of 1 kHz and a wavelength of 800 nm. The WGs were tuned by astigmatic beam shaping to have an elliptical cross section with a width of ~12 µm and a height of 50 µm (identical to the MF channel height, to maximize the excitation volume). They have a graded refractive index profile, and a maximum refractive index increase of 1×10^{-3}. Propagation losses were measured to be in the range of 0.5–0.9 dB/cm at a wavelength of 543 nm. Initial tests in this setup indicated that fluorescently labeled DNA molecules could be flown and detected (Fig. 1b) as bright fluorescent segments appearing at the WG-MF-channel interface, with a sizing accuracy of 99% (comparable to the state of the art in DNA sequencing). The current spatial resolution of this setup is limited by the MF plug width (>248 µm), while the integrated-WG width (12 µm) would allow for a 20-fold better resolution, demonstrating that integrated optics can handle the resolution demands of future MF-chip generations.

III. MULTI-WAVELENGTH FLUORESCENCE SENSING

Two sets of fluorescence-labeled biomolecules, each set consisting of two differently sized molecules, m_1 and m_2, which migrate with different speeds served as analytes. One set was red-labeled, the other blue-labeled. Two laser beams at the absorption wavelengths of the labels, intensity-modulated at frequencies f_1 and f_2, respectively, were launched into the excitation/detection area via a single integrated optical WG. For fluorescence detection, a cooled PMT was aligned to collect the fluorescence signal from the excitation/detection area. The modulation of each laser induced an accordingly time-varying fluorescence signal emitted by those dye molecules absorbing this specific laser wavelength, and the resulting time-modulated fluorescence signal at both wavelengths was simultaneously recorded by the ultrasensitive, albeit color-blind PMT, as shown in the upper part of Fig. 2. Fourier analysis was implemented for post-processing the recorded total fluorescence signal, resulting in the frequency spectrum of Fig. 3, which consists of signals at the different modulation frequencies. Only a narrow band of frequencies around each modulation frequency (f_1 = 17 Hz, f_2 = 31 Hz) was selectively passed by a flat-top transfer function and extracted back into the time domain by an inverse Fourier transform, leading to the blue and red colored graphs in the lower part of Fig. 2. This scheme enables an unambiguous extraction of the signals corresponding to specific excitation wavelengths and the regeneration of corresponding individual time-domain signals.

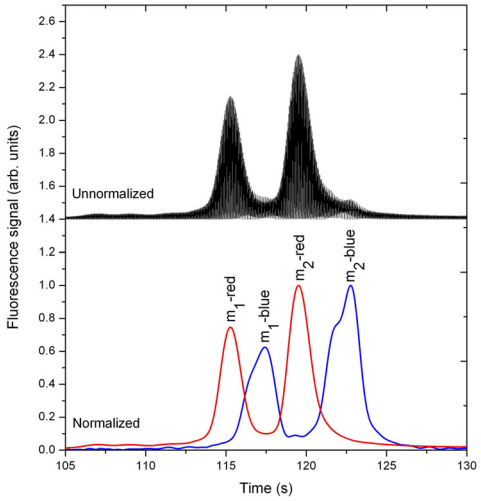


Fig. 2. Fluorescence intensity vs. time as measured by a color-blind PMT during the migration of two sets of blue- and red-labeled biomolecules through the integrated optical excitation/detection area under modulated excitation: cumulative signal from all four molecules (upper part) and corresponding individual signals resolved by Fourier decoding (lower part).

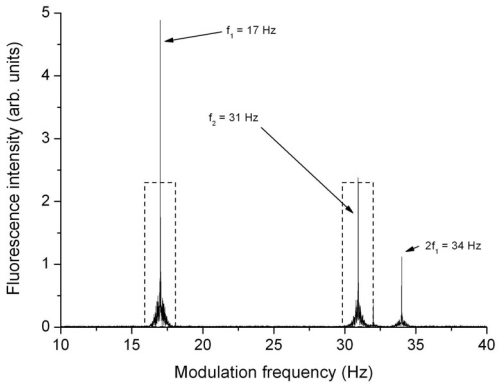


Fig. 3. Fourier transform of the cumulative signal showing signals at the individual modulation frequencies of the excitation laser beams.

Extracting specific, narrow frequency bands in the Fourier domain back into the time domain also resulted in an enhanced signal-to-noise ratio, leading to a limit of detection of 130 femto-molar (corresponding to merely 5 molecules in the excitation volume), which is a record-low value as far as on-chip-integrated fluorescence monitoring is concerned.

IV. CONCLUSIONS

The proposed integrated optical detection scheme enables exciting possibilities whenever wavelength multiplexing or ultrasensitivity can add value to an existing biophotonic system. We are currently building upon the example described in this paper making simultaneous investigation of several diagnostically relevant regions of a gene become feasible in a single optofluidic experiment, based on exclusive wavelength labeling of the different genetic origins and encoding of their fluorescence by different modulation frequencies, thereby leading to multiplex genetic diagnostics in an integrated optofluidic chip. Efforts are also in progress to further enhance the sensitivity, allowing us to eventually reach the Holy Grail of single molecule detection in an on-chip-integrated dynamic migration experiment.

ACKNOWLEDGMENT

We acknowledge financial support by the FP6 EU project "Hibiscus".

REFERENCES

[1] R. Iten, "Apparatus for emitting and detecting light in a nucleic acid amplification reaction," European Patent 1962084, 2007.

[2] R. Martinez Vazquez, et al, "Integration of femtosecond laser written optical waveguides in a lab-on-chip," Lab Chip, vol. 9, pp. 91–96, January 2009.

[3] C. Dongre, et al, "Fluorescence monitoring of microchip capillary electrophoresis separation with monolithically integrated waveguides," Opt. Lett., vol. 33, pp. 2503-2505, November 2008.

Integrated Microsphere Planar Lightwave Circuits

J.S. Wilkinson, G.S. Murugan, D.W. Hewak,
M.N. Zervas, Y. Panitchob & G.R. Elliott
Optoelectronics Research Centre,
University of Southampton
Southampton, Hampshire, UK
jsw@orc.soton.ac.uk

P.N. Bartlett, E.J Tull & K.R. Ryan
School of Chemistry
University of Southampton
Southampton, Hampshire, UK
pnb@soton.ac.uk

Abstract—**Multicomponent glass microspheres self-assembled on optical waveguides combine tailored optical properties with strong light/material interaction potentially leading to compact low-power photonic devices. Progress and prospects for microsphere/waveguide integration will be described.**

Keywords:Integrated optics; optical resonators; self-assembly

I. INTRODUCTION

Resonant cavities are key components in photonic circuits, providing feedback, wavelength selectivity and energy storage to allow dispersion control and enhanced nonlinearity, resonant filtering, waveguiding with low bend radius and ultra-low threshold lasing. Silica microspheres and microcylinders with diameters ranging from a few microns to a hundred microns or more have been shown to exhibit high quality factors of order 10^9 when an appropriate whispering-gallery mode (WGM) is excited [1], and lend themselves to evanescent coupling to optical waveguides to provide integrated resonant functions in an optical circuit. Planar lightwave circuits (PLCs) can potentially offer low-cost mass-manufacturable solutions to complex optical circuit requirements, but conventional optical waveguide technology suffers from two problems which limit dense integration for multiple circuit functions. The first is that exploitation of many optical phenomena requires long optical path lengths to achieve, for example, sufficient delay in dispersion compensation, or sufficient growth of power in a nonlinear interaction. Coupling of waveguides to arrays of microresonators potentially allows energy storage, long delays and high-efficiency nonlinear interactions. The second problem is that, so far, no one material has emerged as ideal for photonic circuits, and microsphere integration with conventional waveguides allows flexible configuration of multiple materials systems. The most elegant demonstrations of microsphere resonators to date have employed light delivery by tapered optical fibres where the modes evanescently couple to WGMs of the spheres. Ultra-high Q microtoroid resonators based on silicon processing [2] exhibit excellent performance but are difficult to integrate directly in waveguide circuits, while photolithographically-defined ring resonators [3] and disk resonators [4] are limited in their materials flexibility. Planar lightwave circuits offer a platform for stable placement of microspheres or microsphere arrays, for example by self-assembly, along with evanescent coupling to single or multiple waveguides, to realise highly functional circuits in a more robust configuration than fibre devices, and with greater flexibility than monolithically integrated microresonators.

This work was funded by the UK EPSRC under grant GR/S96500/01

II. GLASS MICROSPHERES

High-quality unsupported microspheres were formed from exemplar multicomponent glasses with specific optical functionality. We have chosen Nd and Er-doped BK7 borosilicate glasses for their good laser and amplifier properties [5] and gallium lanthanum sulphide chalcogenide glasses for their high third-order nonlinearity for switching [6], and in both materials have obtained microspheres with (waveguide-coupled) loaded Q-factors >60,000, suitable for low-threshold lasing and high-bandwidth communications devices. Tellurite glass [7] microspheres have also been realised to exploit their excellent Raman gain properties. Microspheres of radius 15μm to 100μm were fabricated from crushed and sieved custom glass which was doped, purified and melted in our laboratories, by annealing in a specialised drop-furnace [8]. It was confirmed that the Nd-doped borosilicate and chalcogenide glass spheres lased when pumped with a focused free-space beam.

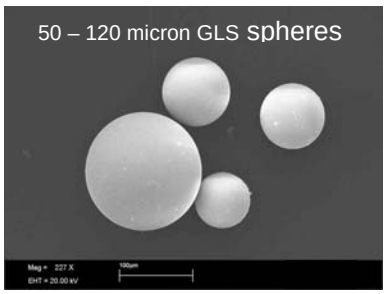


Figure 1. Gallium Lanthanum Sulphide glass microspheres

III. MICROSPHERE ASSEMBLY

Most conventional self-assembly techniques are unsuitable for assembly of microspheres greater than about 5 microns in diameter, due to the reduced influence of convective forces [9]. A novel technique of selective chemical modification of structured substrates has been used to realise surfaces tailored to the assembly of glass microspheres from aqueous solution, allowing realisation of individual spheres in etched wells sparsely distributed over a substrate, as required for integrated microsphere planar lightwave circuits, and as shown in Figure 2, for 60μm diameter spheres in etched pits in borosilicate glass substrates [10]. The assembly process parameters have been studied in detail in terms of their influence on accuracy of positioning and defect density, to allow well-controlled construction of waveguide integrated devices.

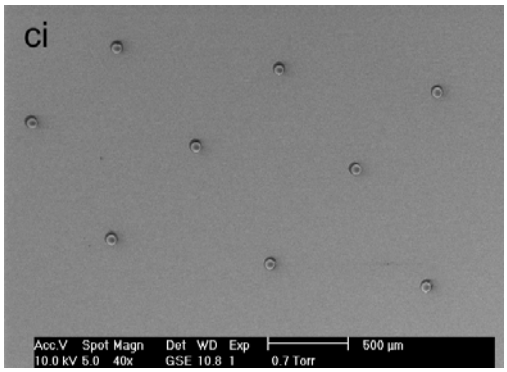


Figure 2. Glass microspheres assembled in pit array [10]

IV. Microsphere-Coupled Waveguides

Microspheres coupled to optical waveguides with variable separation have been characterised using both ion-exchanged glass waveguides [11] and tantalum pentoxide rib waveguides, the latter allowing a wide range of effective indices for phase-matching to WGMs in high-index spheres. Whispering-gallery mode spectra were obtained using a tunable line-narrowed source at wavelengths between 1440nm and 1640nm, and modes were assigned by fitting to sphere, waveguide and coupled-mode models. Typical data for a well-coupled microsphere (in this case Er-doped borosilicate glass) are shown in Figure 3, and mode-assignment allowed experimental confirmation of coupling coefficients, microsphere round-trip losses and WGM effective path lengths, enabling fine-tuning of device designs where the control of coupling coefficient through waveguide-microsphere separation is crucial. Controllable positioning of microspheres has also allowed the study of WGM mode-splitting in non-ideal microspheres, enabling determination of ellipticity and orientation.

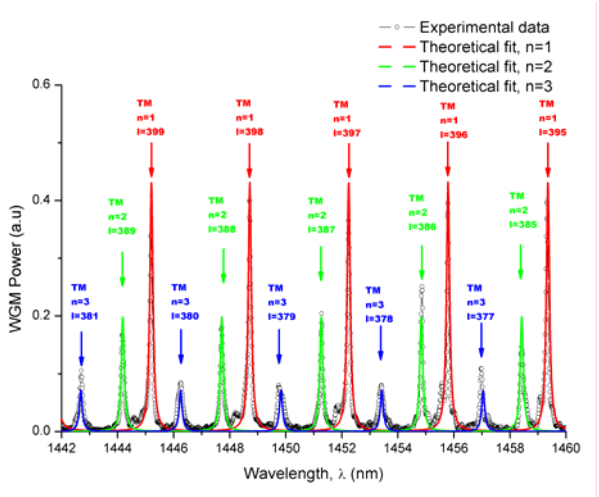


Figure 3. Typical WGM spectrum and mode-assignment.

Glass microspheres have been assembled between two otherwise uncoupled monomode Ta_2O_5 rib waveguides, as shown in Figure 4, with the aim of providing strongly wavelength-dependent coupling and to demonstrate nonlinear functionality. Arrays of microspheres may be readily formed on waveguide substrates and used to select WGM resonances and shape the transmission spectrum of sphere-coupled waveguides. Initial results from coupling two spheres to form a so-called "photonic molecule" [12] show the mode-splitting and enhanced wavelength selectivity expected from coupling two resonators.

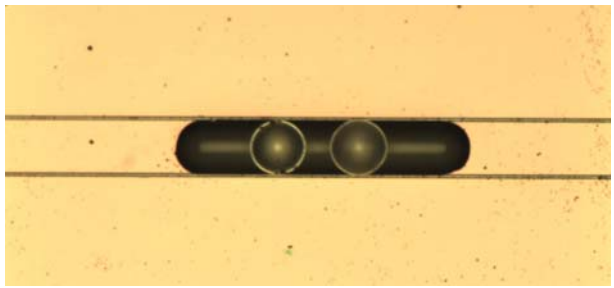


Figure 4. 60 micron microspheres assembled between waveguides

V. Conclusions

High-quality microspheres suitable for all-optical switching and lasing have been realised from advanced glasses and assembled on photolithographically structured substrates. Coupling to waveguides shows promise for the realisation of compact, highly functional photonic devices.

Acknowledgement

The authors thank Prof Y. Ohishi of Toyota Technological Institute, Nagoya, Japan, for providing the tellurite glasses.

References

[1] M.L.Gorodetsky A.A. Savchenkov and V.S. Ilchenko, "Ultimate Q of optical microsphere resonators", Opt. Lett., **21**, pp. 453-455 (1996).

[2] D.K. Armani, T.J. Kippenberg, S.M. Spillane and K.J. Vahala, "Ultra-high-Q toroid microcavity on a chip", Nature, **421**, pp. 925-929 (2003).

[3] Q. Xu, D. Fattal and R.G. Beausoleil, "Silicon microring resonators with 1.5-µm radius", Optics Express, **16**, pp. 4309-4315 (2008).

[4] K. Djordjiev, S.J. Choi, S.J. Choi and P.D. Dapkus "Microdisk tunable resonant filters and switches", IEEE Photon. Technol. Lett., **14**, pp. 828-830, (2002).

[5] T. Feuchter, E.K. Mwarania, J. Wang, L. Reekie and J.S. Wilkinson, "Erbium-doped ion-echanged waveguide lasers in BK-7 glass", IEEE Photon. Technol. Lett., **4**, pp. 542-544, (1992).

[6] J. Requejo-Isidro, A.K. Mairaj, V. Pruneri, D.W. Hewak, M.C. Netti and J.J. Baumberg, "Self-refractive nonlinearities in chalcogenide based glasses", J. Non-Crystalline Solids, **317**, pp. 241-246 (2003).

[7] G.S. Murugan, T. Suzuki and Y. Ohishi, "Raman characteristics and nonlinear optical properties of tellurite and phosphotellurite glasses containing heavy metal oxides with ultrabroad Raman bands", J. Appl. Phys., **100**, 023107 (2006).

[8] G.R. Elliott, D.W. Hewak, G.S. Murugan and J.S. Wilkinson "Chalcogenide glass miorospheres; their production, characterization and potential", Optics Express, 15, pp17542-17553 (2007).

[9] E.J. Tull, P.N. Bartlett and K.R. Ryan, "Controlled assembly of micrometer-sized spheres: Theory and application", Langmuir, **23**, pp. 7859-7873 (2007).

[10] E.J. Tull, P.N. Bartlett, G.S. Murugan and J.S. Wilkinson "Manipulating spheres that sink:assembly of micrometer sized glass spheres for optical coupling", Langmuir, **25**, pp. 1872-1880 (2009).

[11] Y. Panitchob et al., "Whispering gellery mode spectra of channel waveguide coupled microspheres", Opt. Express, **16**, pp. 11066 (2008).

[12] G.S. Murugan, J.S. Wilkinson and M.N. Zervas, "Waveguide coupling to size-mismatched bispheres", MOC 07, Japan (2007).

Next generation infrared superconducting single photon detectors integrated into optical cavities

M.G. Tanner, C. M. Natarajan, J. A. O'Connor, R.J. Warburton, R. H. Hadfield
Heriot Watt University
Edinburgh, EH14 4AS, UK
M.Tanner@hw.ac.uk

B. Baek, S. Nam
National Institute of Standards and Technology
325 Broadway, Boulder, CO 80305, USA

S. Dorenbos, E. Bermúdez Ureña, T. Zijlstra, T. Klapwijk, V. Zwiller
Kavli Institute for Nanoscience, Delft University of Technology
Lorentzweg 1, 2628 CJ Delft, The Netherlands

***Abstract*— Single-photon detectors are a key enabling technology for optical quantum information processing. A major challenge is integrating new detector technologies with photonic systems. This paper demonstrates enhanced efficiency in practical fibre coupled infrared superconducting single photon detectors through the integration of an optical cavity.**

Single-photon detectors are a key enabling technology for optical quantum information processing (QIP). A new type of single-photon detector based on a superconducting nanowire holds particular promise, offering infrared single-photon sensitivity with low dark counts and excellent timing resolution, at an operating temperature of 4 K. These detectors have been integrated into practical closed-cycle refrigerator systems[1] and have been successfully employed in a succession of QIP experiments, including characterization of single and entangled photon sources and quantum key distribution over 200 Km of optical fibre[2].

Current work on Superconducting Nanowire Single Photon Detectors (SNSPDs) is focused towards improving Detector Efficiency (DE) at telecommunications wavelengths, whilst exploiting low dark count rates and picosecond timing resolution[3,4]. Devices fabricated in a new material, NbTiN, offer improved signal to noise characteristics[5]. In this work we present high efficiency measurements of practically fibre coupled NbTiN SNSPDs at telecoms wavelengths. Efficiency is significantly enhanced as the SNSPDs have been fabricated on silicon substrates with a 225nm thermally grown SiO_2 layer directly underneath the active device layer. The reflection at the SiO_2 – Si interface increases absorption in the NbTiN layer yielding practical efficiencies in excess of 20% at 1310 nm and 7% 1510 nm, at dark count rates ~1 kHz. The efficiency drop off at lower bias current is slight, yielding 10% efficiency with only 20Hz dark counts at 1310nm.

Absorption in the superconducting layer has a significant effect on device efficiency. Simple plane wave Fresnel equation simulations of the NbTiN device with inclusion of the underlying reflector layers enables estimation of the absorption as a function of incident photon wavelength. Inclusion of a probability of hotspot formation dependent on the photon energy and additional cavity oscillations from the fibre to device separation yields a simulation closely matching measured DE vs wavelength data as shown in the figure below. These insights will enable us to optimise devices for high efficiency at 1550 nm wavelength. This methodology will also be used to examine the relationship between absorption and device efficiency as a function of wavelength. There is much interest in enhancing coupling through use of cavities[6]. Further simulations suggest more complex optical reflectors will significantly increase efficiency, whilst allowing convenient front side fibre coupling to devices. Thus devices of this type promise to provide a practical solution to the demand for high efficiency single photon detection at telecom wavelengths.

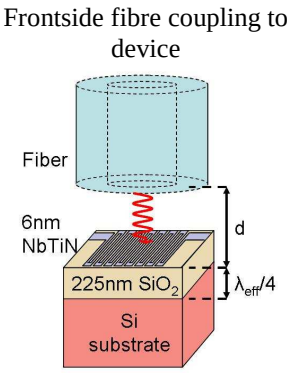


Figure 1. Full chip and fiber arrangement, not to scale.

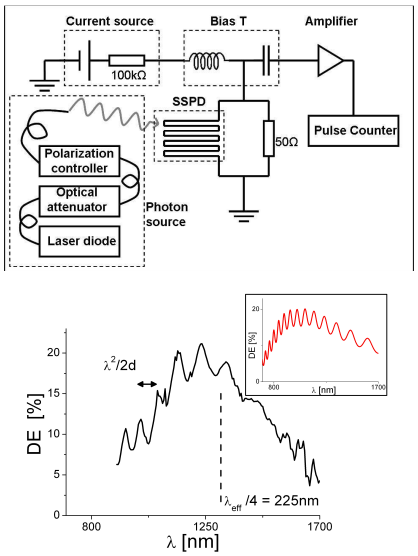


Figure 2. Top - Experimental setup. Bottom – Experimental dependence of DE with varying wavelength at 1.7 kHz dark count rate. Inset red line is simulated device efficiency plotted with the same scale as the experimental data. Black dashed line marks the designed adsorption maximum from the device layer cavity structure.

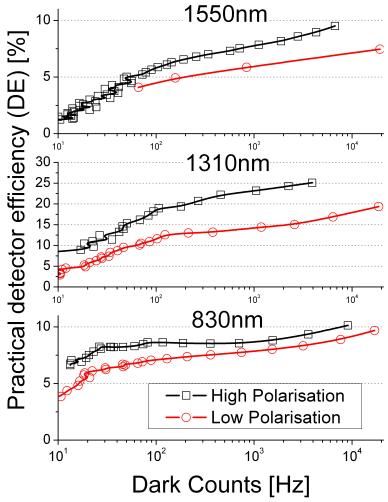


Figure 3. NbTiN device efficiency versus dark count rates at 3 wavelengths. Polarization optimised for high (low) efficiency shown in black (red). Note, vertical scale varies, while horizontal axis matches between the figures.

ACKNOWLEDGMENT

This work is supported by the UK Engineering and Physical Science Research Council. RHH is supported by the Royal Society of London (UK) via a University Research Fellowship. We thank Ryan Warburton and Gerald Buller for assistance with the timing jitter measurements.

REFERENCES

1 R. H. Hadfield, M. J. Stevens, S. S. Gruber, A. J. Miller, R. E. Schwall, R. P. Mirin, and S. W. Nam, Optics Express 13 (26), 10846 (2005).

2 H. Takesue, S. W. Nam, Q. Zhang, R. H. Hadfield, T. Honjo, K. Tamaki, and Y. Yamamoto, Nat. Photonics 1 (6), 343 (2007).

3 G. N. Gol'tsman, O. Okunev, G. Chulkova, A. Lipatov, A. Semenov, K. Smirnov, B. Voronov, A. Dzardanov, C. Williams, and R. Sobolewski, Appl. Phys. Lett. 79 (6), 705 (2001).

4 S. Miki, M. Fujiwara, M. Sasaki, B. Baek, A. J. Miller, R. H. Hadfield, S. W. Nam, and Z. Wang, Appl. Phys. Lett. 92 (6) (2008).

5 S. N. Dorenbos, E. M. Reiger, U. Perinetti, V. Zwiller, T. Zijlstra, and T. M. Klapwijk, Appl. Phys. Lett. 93 (13) (2008).

6 K. M. Rosfjord, J. K. W. Yang, E. A. Dauler, A. J. Kerman, V. Anant, B. M. Voronov, G. N. Gol'tsman, and K. K. Berggren, Optics Express 14 (2), 527 (2006).

Experimental multimode interference of two single photons in integrated waveguides

Anthony Laing, Alberto Peruzzo, Alberto Politi & Jeremy L. O'Brien
Centre for Quantum Photonics, H. H. Wills Physics Laboratory & Department of Electrical and Electronic Engineering,
University of Bristol,
Bristol, UK,
Jeremy.Obrien@Bristol.ac.uk

Abstract—Multiport beam splitters are interesting and useful to the field of quantum information. (QI) They have applications including the production of highly entangled photonic states that form the basis of many of the powerful protocols in QI. We report details on multiport interferometers on integrated devices that rely on multimode interference.

Keywords-component; quantum entanglement; multiport beamsplitter

I. INTRODUCTION

Integrated quantum photonic devices promise the miniaturization and scaling of the quantum logic circuits that will be required in future quantum technologies [1-4]. The basic building blocks in these circuits are beam splitters. Beam splitters are fundamental devices in quantum optics enabling classical interference of a single photon with itself and quantum interference (or the Hong Ou Mandel dip) [5] between different photons. This multi-photon interference allows the generation of non-classical states of light that have applications in quantum communication, quantum computation, quantum metrology, and quantum lithography.

We give details of the experimental investigation of beam splitter devices based on the interference of different Gaussian light modes: multimode interferometers in silica-on-silicon waveguide. MMI devices are based on the self-imaging principle, by which an input field profile is reproduced in single or multiple images at periodic intervals along the propagation direction of a multimode guide [6]. This is designed to support a large number of lateral modes. These devices allow the design of N by M splitters and with a greater tolerance to wavelength variations and relaxed fabrication requirements compared to the other main beam splitting technology, directional couplers.

We give data on the two-photon quantum interference in a 2x2 MMI. We also discuss results from quantum interference in a 4x4 MMI (see Figure 1), which exhibits both Hong-Ou-Mandel dips and anti-dips. This is the first realization of quantum interference via multimode interferometry.

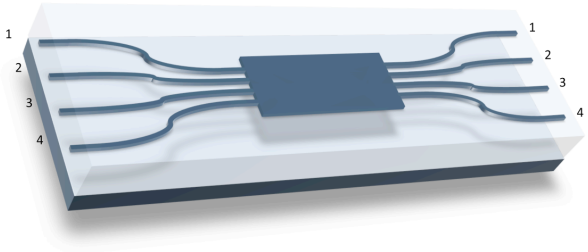


Figure 1. A 4x4 multimode interferometer, silica on silicon waveguide.

II. METHOD

Testing the MMI devices to their full potential required the construction of a spontaneous parametric down conversion (SPDC) source: the process by which a nonlinear crystal splits a very small proportion of photons from a strong pump beam into pairs of daughter photons (See Fig 2). A 402 nm continuous wave laser was focused to a waist of around 40 μm in a 2 mm thick Type-I BiBO crystal. The crystal was cut to output degenerate photon pairs (804 nm) at 3 degrees either side of the pump beam. The daughter photons were filtered to a bandwidth of 2nm and focused into polarisation maintaining fibres. The source was then fine tuned to ensure indistinguishable properties of polarisation and centre wavelength of the daughter photons.

This photon pair source was previously tested for quantum interference in a directional coupler waveguide and was found to produce a Hong Ou Mandel Dip of near unit visibility [7]. This provided a useful benchmark for the testing of the MMI devices.

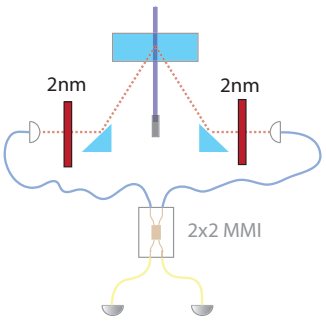


Figure 2. An SPDC two photon soure with 2x2 MMI waveguide

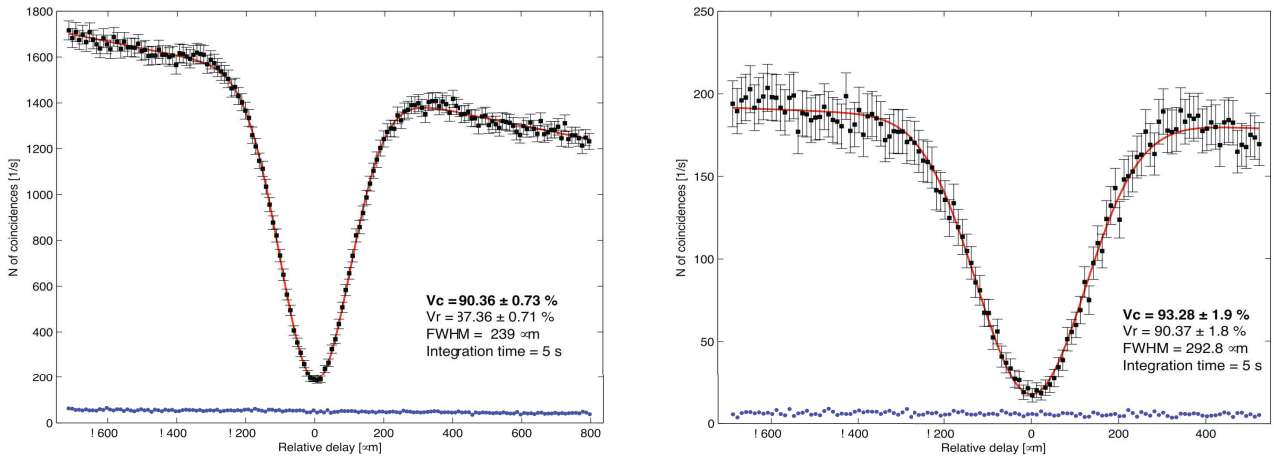


Figure 3. Quantum interference in a 2x2 MMI quantified by Hong Ou Mandel Dips. The two dips are from the same experimental set up, with the only difference being that the one on the right received post-filtering with a 0.5nm bandwidth interference filter inserted between the chip and the detector.

III. Results

We find that that the quantum interference visibility at 89.74 ± 1.3% is significantly lower than that of a directional coupler with the source described above. A major reason for the reduced visibility is the coherence length of the photons, which is set by the 2nm interference filters. Since the different modes see different effective refractive indices within the interferometer, a jitter is introduced which allows distinguishibility between the photons. To overcome this problem we introduced a narrower 0.5nm filter in one of the channels between the device and the detector, i.e. not affecting the source. This quantum erasure technique increases the visibility significantly to 95.12 ± 2.5%. This difference can be appreciated in Fig 3, although here the dips are shown with a Sinc function that gives slightly different visibilities than the more usual Gaussian fitting, which produces the data quoted here.

IV. On-Going Work

Finally, we observed the novel interference effects from a 4x4 interferometer. Here, one observes the very interesting multiport interference effects of dips and anti-dips. One can use the sign of the dips (dip or anti dip) and their visibilities to determine an internal free parameter that occurs for multiport interferometers of dimension greater than four [8]

References

[1] A.Politi, M.J. Cryan, J.G. Rarity, S. Yu, and J.L. O'Brien, Science 320, 646 (2008)

[2] A. Politi, J.C.F Matthews, M.G. Thompson, J.L. O'Brien, IEEE Journal of Selected Topics in Quantum Electronics, 15, 6, 1673-1684 (2009)

[3] J.C.F Matthews, A.Politi, A Stefanov and J.L. O'Brien, Nature Photonics, 3, 346 (2009)

[4] A. Politi, J.C.F Matthews and J.L. O'Brfien, Science, 325, 1221 (2009)

[5] C. K. Hong, Z. Y. Ou, and L. Mandel, Phys. Rev. Lett. 59, 2044 (1987)

[6] L. Soldano and E. Pennings, "Optical multi-mode interference devices based on self-imaging: principles and applications" Lightwave Technology, Journal of, vol. 13, no. 4, pp. 615-627, Apr 1995.

[7] A. Laing, A. Peruzzo, A. Politi, M. R. Verde, M. Halder, T. C. Ralph, M. G. Thompson, and J. L. OBrien, (To appear) (2009).

[8] G. J. Pryde and A. G. White, Physical Review A (Atomic, Molecular, and Optical Physics) 68, 052315 (2003).

Space-QUEST: satellites based quantum communication

Rupert Ursin
AInstitute for Quantum Optics and Quantuminformation, Austrian Academy of Sciences, Austria
Vienna, Austria
Rupert.Ursin@oeaw.ac.at

***Abstract*— The European Space Agency (ESA) has supported a range of studies in the field of quantum physics and quantum information science in space and a mission proposal Space-QUEST (Quantum Entanglement for Space Experiments) was submitted. We propose to perform space-to-ground quantum communication tests from the International Space Station (ISS). We present the proposed experiments in space as well as the design of a space based quantum communication payload.**

Keywords-component; quantum optics, quantum key distribution,

I. INTRODUCTION

Quantum entanglement is, according to Erwin Schrödinger in 1935 [1], the essence of quantum physics and inspires fundamental questions about the principles of nature. By testing the entanglement of particles we are able to ask fundamental questions about realism and locality in nature [2, 3]. Local realism imposes certain constraints in statistical correlations of measurements on multi-particle systems. Quantum mechanics, however, predicts that entangled systems have much stronger than classical correlations that are independent of the distance between the particles and are not explicable with classical physics. It is an open issue whether quantum laws, originally established to describe nature at the microscopic level of atoms, are also valid in the macroscopic domain such as long distances. Various proposals predict that quantum entanglement is limited to certain mass and length scales [4, 5] or altered under specific gravitational circumstances [6].

II. PROPOSED EXERPIMENTS SO FAR

Testing the quantum correlations over distances achievable with systems placed in the Earth orbit or even beyond 7] would allow to verify both the validity of quantum physics and the preservation of entanglement over distances impossible to achieve on ground.

Using the large relative velocity of two orbiting satellites, one can perform experiments on entanglement where—due to special relativity—both observers can claim that they have performed the measurement on their system prior to the measurement of the other observer. In such an experiment it is not possible anymore to think of any local realistic mechanisms that potentially influence one measurement outcome according to the other one. Moreover, quantum mechanics is also the basis for emerging technologies of quantum information science, presently one of the most active research fields in physics. Today's most prominent application is quantum key distribution (QKD) [8], i.e. the generation of a provably unconditionally secure key at distance, which is not possible with classical cryptography. The use of satellites allows for demonstrations of quantum communication on a global scale, a task impossible on ground with current optical fiber and photon-detector technology. Currently, quantum communication on ground is limited to the order of 100 of kilometers [9, 10]. Bringing quantum communication into space is the only way to overcome this limit with state-of-the-art technology.

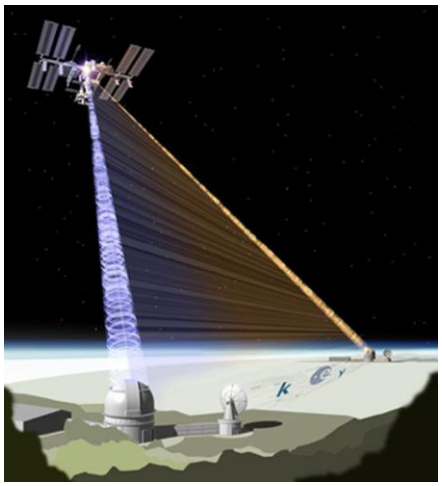


Figure 1 Distribution of pairs of entangled photons using the International Space Station (ISS). Entangled photon pairs are simultaneously distributed to two separated locations on Earth, thus enabling both fundamental quantum physics experiments and novel applications such as quantum key distribution. (Image courtesy ESA/GSRP).

Another area of applications is in metrology, where quantum clock synchronization and quantum positioning [11] are studied. Furthermore, sources of quantum states in space may have applications in the new field of quantum astronomy [12].

We propose to ESA to perform these experiments in space by placing a quantum transceiver on the external pallet of the European Columbus module at the ISS.

In our talk we will present the scientific background and the technological development to be tackled with within this project. We will present theoretical as well as experimental studies [13-16] performed so far as well as ongoing studies performed by several partners from academia as well as from industry.

III. PROOF-OF-PRINCIPLE EXPERIMENTS

We report a proof-of-principle experiment where we were able to generate a quantum cryptographic key over a record-breaking distance 144 km over a free-space link between the Canary Islands La Palma and Tenerife [14,15]. One photon from the entangled pair was measured locally. The second photon was sent via a transmitter telescope over the 144 km long free-space link to the Optical Ground Station (OGS) of the European Space Agency (ESA) on Tenerife. The OGS, originally built to act as a transmitter and receiver for classical laser communication to and from satellites, a 1 m Richey-Chrétien/Coudé telescope was used to collect the single photons. The atmospheric turbulence caused significant beam wander in the focal plane. A suitable optical system was implemented to prevent the beam from wandering off the single photon detectors with a quantum efficiency of about 40%. We measured a loss of -30 dB on the entire quantum link.

Each event in one of the detectors was locally labelled with a 64-bit computer generated tag, containing the detector channel and a time tag with a timing resolution of 156 ps synchronized with a 10 MHz oscillator directly disciplined by the Global Positioning System (GPS) with a relative drift of about 10-11 over 100 s. The identification of the coincident events where implemented by cross-correlating both sets of time tags using software which determined the offset (~487 µs) and unavoidable drift of the two timescales online. Future experiments with entangled photons will benefit from the increased precision of clock synchronization.

Entangled photons shared between the two parties were used to establish 178 bits unconditional secure key [**Fehler! Verweisquelle konnte nicht gefunden werden.**] in total. Any attempt by an eavesdropper to intercept and copy the key is obvious to the receiving party, who notices errors in the transmission. This experiment demonstrated for the first time the use of an entangled photon source delivering the pair production rate required to realize an optical downlink from low-Earth satellites, such as the International Space Station (ISS) [13], to optical ground stations on Earth. This would allow a separation of the two entangled photons by more than 1400 km, clearly exceeding the possible distances for today¹s fiber technology [9].

IV. CONCLUSIONS

We emphasize that the space environment will allow quantum physics experiments with photonic entanglement and single photon quantum states to be performed on a large, even global, scale. The Space-QUEST proposal aims to place a quantum communication transceiver containing the entangled photon source, a weak pulsed (decoy) laser source and single photon counting modules in space and will accomplish the first-ever demonstration in space of fundamental tests on quantum physics and quantum-based telecom applications. The unique features of space offer extremely long propagation paths to explore the limits of the validity of quantum physic's principles. In particular, this system will allow for a test of quantum entanglement over a distance exceeding 1000 km, which is impossible on ground.

[1] E. Schrödinger. Die gegenw¨artige Situation in der Quantenmechanik. Naturwissenschaften, 23:807–812; 823–828; 844–849, 1935.

[2] J. S. Bell. On the Einstein Podolsky Rosen paradox. Physics, 1:195–200, 1964.

[3] A. J. Leggett. Nonlocal hidden-variable theories and quantum mechanics: An incompatibility theorem. Found. Phys., 33:1469–1493, 2003.

[4] G. C. Ghirardi, A. Rimini, and T. T. Weber. Unified dynamics for microscopic and macroscopic systems. Phys. Rev. D, 34:470, 1986.

[5] R. Penrose. On gravity's role in quantum state reduction. Gen. Rel. Grav., 28:581, 1996.

[6] T. C. Ralph, G. J. Milburn, and T. Downes. Gravitationally induced decoherence of optical entanglement. arXiv:quantph/0610093v1.

[7] R. Kaltenbaek, M. Aspelmeyer, M. Pfennigbauer, T. Jennewein, C. Brukner, W. R. Leeb, and A. Zeilinger. Proof-of-concept experiments for quantum physics in space. Proc. of SPIE, 5161:252–268, 2003.

[8] N. Gisin, G. Ribordy, W. Tittel, and H. Zbinden. Quantum cryptography. Rev. Mod. Phys., 74(1):145–195, Mar 2002.

[9] E. Waks, A. Zeevi, and Y. Yamamoto. Security of quantum key distribution with entangled photons against individual attacks. Phys. Rev. A, 65:52310, 2002.

[10] H. Takesue, E. Diamanti, T. Honjo, C. Langrock, M. M. Fejer, K. Inoue, and Y. Yamamoto. Diff erential phase shift quantum key distribution experiment over 105 km fibre. New Journal of Physics, 7:232, 2005.

[11] A. Valencia, G. Scarcelli, and Y Shih. Distant clock synchronization using entangled photon pairs. Appl. Phys. Lett., 85:2655 (2004).

[12] G. Naletto, C. Barbieri, T. Occhipinti, F. Tamburini, S. Billotta, S. Cocuzza, and D. Dravins. Very fast photon counting photometers for astronomical applications: from quanteye to aqueye. In Photon counting applications, Quantum Optics, and Quantum Cryptography. SPIE Proc. 6583, pp. 65830B-1/14, (2007).

[13] M. Pfennigbauer, M. Aspelmeyer, W. Leeb, G. Baister, T. Dreischer, T. Jennewein, G. Neckamm, J. Perdigues, H. Weinfurter, and A. Zeilinger. Satellite-based quantum communication terminal employing state-of-the-art technology. J. Opt. Netw., 4(9):549–560, 2005.

[14] T. Schmitt-Manderbach, H. Weier, M. F¨urst, R. Ursin, F. Tiefenbacher, T. Scheidl, J. Perdigues, Z. Sodnik, C. Kurtsiefer, J. G. Rarity, A. Zeilinger, and H. Weinfurter. Experimental demonstration of free-space decoy-state quantum key distribution over 144 km. Phys. Rev. Lett., 98:010504, 2007.

[15] R. Ursin, F. Tiefenbacher, T. Schmitt-Manderbach, H. Weier, T. Scheidl, M. Lindenthal, B. Blauensteiner, T. Jennewein, J. Perdigues, P. Trojek, B. Oemer, M. Fuerst, M. Meyenburg, J. Rarity, Z. Sodnik, C. Barbieri, H. Weinfurter, and A. Zeilinger. Entanglement-based quantrum communication over 144 km. Nature Physics, 3:481 – 486, 2007.

[16] P. Villoresi, T. Jennewein, F. Tamburini, M. Aspelmeyer, C. Bonato, R. Ursin, C. Pernechele, V. Luceri, G. Bianco, A. Zeilinger, and C. Barbieri. Experimental verification of the feasibility of a quantum channel between space and earth. New J. Phys., 10:033038, 2008.

Novel Source of Polarization Entangled Photon Pairs Using a PPLN Waveguide with Interlaced Domains

Abu Thomas, Harald Herrmann and Wolfgang Sohler
Angewandte Physik, Department Physik
Universität Paderborn
Paderborn, Germany
abu@mail.upb.de

Abstract: **A novel source of polarization entangled photon pairs has been developed based on spontaneous parametric down conversion (SPDC) in a periodically poled Ti:$LiNbO_3$ waveguide. The domain structure consists of interlaced domains with two periodicities designed for type II quasi-phase-matching. Design issues as well as experimental results on second harmonic and SPDC characterization and entanglement measurements are reported.**

Keywords-SPDC; PPLN; entanglement; interlaced

I. INTRODUCTION

Entangled photon pair sources are essential devices for quantum key distribution. Different approaches have been demonstrated to generate entangled photon pairs. The most promising devices rely on spontaneous parametric down conversion (SPDC) especially in integrated optical structures. High efficiency and brightness can be achieved using nonlinear optical waveguides in periodically poled $LiNbO_3$ (PPLN). To generate in such waveguides polarization-entangled photon pairs, either both photons must have the same wavelength (operation at degeneracy) [1] or a hybrid – and thus less robust and compact - Sagnac scheme [2] has to be used.

In this contribution we present a novel scheme to generate non-degenerated polarization-entangled photon pairs in a PPLN waveguide with a specifically designed poling structure consisting of interlaced domains.

II. DESIGN AND FABRICATION

A. Principle of Operation

Via nonlinear optical SPDC a pump photon can decay into a signal and an idler photon. In LN waveguides this process can be exploited taking advantage of the strong d_{33} nonlinear coefficient (type I) or via the d_{31} nonlinearity (type II). In the latter case the generated photons are orthogonally polarized. An efficient pair generation requires quasi-phase-matching, achievable by choosing the proper poling period. For type II phase-matching the signal- and idler wavelengths are shown in Fig. 1 as function of the pump wavelength for two different poling periods Λ_1 and Λ_2. Using a sample with one fixed poling period, polarization entangled photon pairs can be generated, if the device is operated at degeneracy and the pairs are subsequently spatially separated via a beam splitter [1]. However, half of the created photon pairs get lost if they are routed to a common output port of the splitter. To overcome this drawback, we apply a new scheme – which has recently been proposed in [3] - to create polarization-entangled pairs at non-degeneracy.

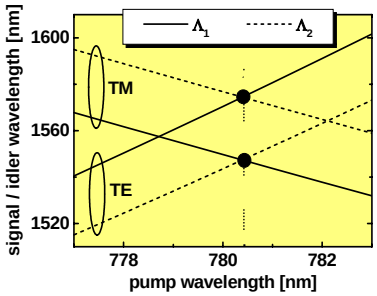


Figure 1: Phase-matching characteristics of type II SPDC for two different poling periodicities. The operating points of the novel entangled source are indicated by the black dots.

If the Ti:PPLN waveguide is poled with two periodicities Λ_1 and Λ_2, two different photon pairs, one corresponding to Λ_1 and the other to Λ_2 can be created. Non-degenerated orthogonally polarized entangled pairs can be generated if the device is operated at a pump wavelength where the TE emission of Λ_1 coincides with the TM emission of Λ_2 and vice versa (see Fig. 1).

B. Waveguide Design and Fabrication

To investigate this new scheme PPLN waveguides with different poling patterns have been designed. Segments with N domains of Λ_1 and N domains of Λ_2 are interlaced as shown in Fig. 2. The spacing δ_i between the segments was adjusted to maintain the proper phase relation between adjacent segments of the same period. Interlacing the two periods instead of a sequential arrangement should enhance the photon indistinguishability. To prove this, different structures with N=10, 100, 500 and 3000 have been designed and fabricated.

57 mm long single mode waveguides were fabricated by in-diffusion of photolithographically defined 7μm wide, 80 nm

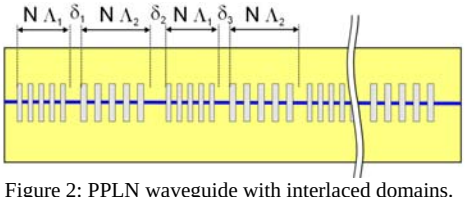


Figure 2: PPLN waveguide with interlaced domains.

thick Titanium stripes for 9 hours at 1060°C. Afterwards the waveguide is periodically poled. The poling periods (Λ_1=9.30 μm and Λ_2=9.37 μm) were chosen to obtain SPDC in the 1550 nm range with the wavelengths of the operating point separated by around 25 nm.

III. CHARACTERISATION

A. *Second Harmonic Generation (SHG) and SPDC*

At first, the sample was characterized by SHG. At 45° linear polarized light from a tunable extended cavity laser (ECL) was coupled into the waveguide to excite TE and TM modes simultaneously. The generated SH power was measured as function of the ECL wavelength as shown in figure 3. A structure with only two segments (N=3000) provides two distinct SH peaks (left diagram). The second diagram corresponds to the waveguide with multiple segments (N=500). Due to the segmentation satellite peaks appear in addition to the main peak. Similar satellite peaks can be expected for SPDC. The satellites can be pushed away from the wavelength range of interest by decreasing the number of domains per segment. With 10 domains per segment, the satellite peaks are outside the measurement window as shown in the right diagram.

The measured SH efficiency was about 5 % / W. The full width at half maximum (FWHM) of each peak is about 0.2 nm.

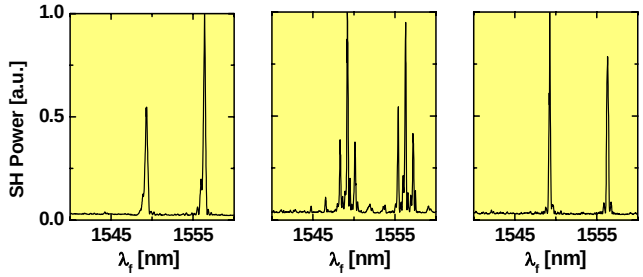


Figure 3. Measured SH phase-matching spectra with N=3000, 500 and 10 domains per segment, respectively.

SPDC spectra of a waveguide with 10 domains per segment were investigated. The pump radiation from an ECL (λ_p~775 nm) was coupled into the waveguide. The spectrum of the down-converted radiation was measured by an InGaAs PIN diode behind a monochromator. The residual pump radiation was blocked by a combination of absorption and dielectric filters. Measured SPDC spectra are shown in figure 4 for a pump wavelength slightly offset (left) and exactly at the operating point. The amplitude of the TM peaks is smaller compared to the TE peaks because of the higher losses in the waveguide and in the measurement setup. The measured SPDC

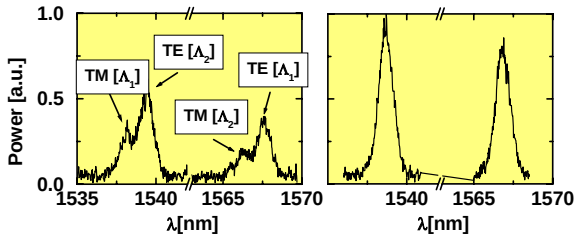


Figure 4: Measured SPDC spectra: Pump wavelength slightly offset from the correct point of operation (left) and at the correct value (right).

efficiency was ~ 4×10^{-9} % and the FWHM was 0.4 nm.

B. *Characterisation of Entanglement*

The experimental setup to study entanglement is shown in figure 5. The photons are butt-coupled into an optical fiber and spatially separated using a circulator and a fiber bragg grating (0.5 nm spectral width). The reflected photons enter the single photon detector (SPD) after passing through a half wave plate (HWP) and a polarization beam splitter (PBS). The transmitted photons are routed via a band pass filter (1 nm width) and a

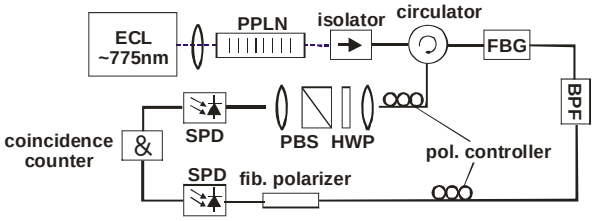


Figure 5: Experimental set-up to analyse polarization entanglement.

fiber PBS to a second SPD. Coincidence counts were measured for different orientations of the HWP as shown in Fig. 6. As predicted for entangled states the coincidence count rate oscillates with a period of 90° as we rotate the HWP. A quantitative analysis of the quality of entanglement is currently under progress.

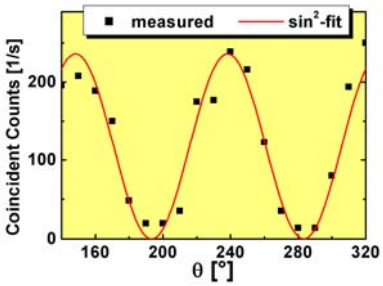


Figure 6: Coincident counts for different orientations of the HWP.

IV. CONCLUSIONS

We have demonstrated a novel type of polarization entangled photon pair source using interlaced domains in a Ti:PPLN waveguide. This novel scheme strongly simplifies the development of efficient, compact and robust sources of entangled photon pairs for applications especially in quantum key distribution.

REFERENCES

[1] T. Suhara, H. Okabe,M. Fujimura, "Generation of polarization entangled photons by Type-II Quasi-Phase-Matched Waveguide Non-linear-Optic Device.," *IEEE Photon. Tech.Lett.*, vol. 19, pp. 1093-1096 (2007)

[2] Y. Jiang, A. Tomita, "The generation of polarization-entangled photon pairs using periodically poled lithium niobate waveguides in a fibre loop," *Journal of Physics B*, vol. 40, pp. 437-443 (2007)

[3] K. Thyagarajan, J. Lugani, S. Ghosh, K. Sinha, A. Martin, D. B. Ostrowsky, O. Alibart and S. Tanzilli, "Generation of polarization entangled photons using type-II doubly periodically poled lithium niobate waveguides," *Phys. Rev. A* , vol. 80, 052321 (2009)

Quantum dot based mode locked lasers: performance and applications

A. Ramdane, K. Merghem, A. Akrout, R. Rosales, S. Azouigui, J.-P. Tourrenc, G. Aubin, A. Martinez
CNRS Laboratory for Photonics and Nanostructures
Route de Nozay, Marcoussis 91460, France
Abderrahim.ramdane@lpn.cnrs.fr

F. Lelarge, A. Shen, F. Van Dijk, G.-H. Duan
Alcatel-Thales III-V Laboratory, a joint Laboratory of Alcatel Lucent Bell Laboratories and Thales Research and Technology, Route de Nozay, Marcoussis 91460, France

***Abstract*-Recent progress in semiconductor quantum dot based mode locked lasers is discussed. Sub-picosecond pulse generation and extremely low phase noise have been demonstrated for both InAs/GaAs and InAs/InP material systems. Applications include e.g. OTDM sources and frequency comb generation for WDM systems, all-optical clock recovery at high bit rate or microwave photonics .**

Keywords- self-assembled quantum dots; semiconductor mode locked lasers; pulse generation; phase noise; fiber optic telecommunications; microwave photonics

I. INTRODUCTION

Self-assembled semiconductor quantum dot (QD)-based lasers are attracting considerable interest owing to their predicted remarkable properties that result from the three-dimensional carrier confinement. Extremely low threshold currents [1] as well as high temperature stability have readily been demonstrated in the InAs/GaAs material system together with temperature independent transmission experiments at 10 Gbit/s [2].

Monolithic mode locked laser (MLLs) diodes are very attractive short pulse sources for a number of applications including Optical Time Division Multiplexing (OTDM), all-optical clock recovery, microwave photonics,…[3]. III-V QD-based active layers have recently been used in the fabrication of MLLs. Inhomogeneous broadening of the gain spectrum due to QD size distribution is indeed an asset for MLLs as this should result in pulsewidth reduction. Ultra-fast carrier dynamics is also a major advantage in the short pulse generation. Finally the low optical confinement factor leads to very small phase noise and this results in low timing jitter as compared to the quantum well based MLLs.

II. SHORT PULSE GENERATION AT HIGH REPETITION RATE

Early demonstration of a monolithic passively mode locked laser using QD based active layer was reported at ~1.3 µm using InAs/GaAs QDs [4]. 17ps wide pulses were generated at a repetition rate of 7.4 GHz, both values being limited by the available optical modal gain in a two-QD layer stack. Advances in Molecular Beam Epitaxy (MBE) material growth allowed to stack several QD layers thus enabling mode-locking with much improved performance in terms of pulse width, repetition rate, noise properties,...

A recent review summarizes the main achievements in this field [5]. Sub-picosecond pulse durations were readily demonstrated by several groups using InAs/GaAs QDs, without resorting to pulse compression schemes [6-8]. This was made possible owing to the wide inhomogeneously broadened optical gain spectrum as well as extremely fast absorption recovery under reverse bias in the saturable absorber section of the devices. Increased peak powers were also reported as mode locking occured in a large range of injection currents above threshold.

Many applications require high repetition rates which are given by the inverse of the round trip cavity time. High modal gain active layers are hence necessary to achieve the highest repetition rates corresponding to the shortest laser cavities. Enhancement of the optical gain using 15 QD layers allowed a record repetition rate of 80 GHz to be achieved associated with a 1.9 ps pulsewidth obtained from a 0.5 mm long passive mode locked laser based on InAs/GaAs [8].

MBE growth of InAs quantum dots on InP (100) substrates generally leads to the formation of quantum " dash " nanostructures (elongated dots). These nanostructures however exhibit very interesting properties pertaining to short pulse generation using mode-locked lasers. They in particular provide a higher optical gain compared to that of QDs grown on GaAs susbstrates [9]. Sub-picosecond pulse generation was reported at a very high repetition rate of 134 GHz [10]. Of particular interest, these results were achieved using a single section self-pulsating Fabry–Perot laser, i.e. without resorting to an absorber section. In this latter configuration, enhanced four-wave mixing (FWM) is invoked as the driving mechanism of the passive mode locking which induces a strong correlation between the longitudinal modes. Similar results were reported for InAs QDs grown by Chemical Beam Epitaxy (CBE) on InP [11]. Other investigations used Metal Organic Vapour Phase Epitaxy (MOVPE) for the growth of InAs QDs on InP [12].

Further growth optimization of quantum dash (QDash) nanostructures allowed laser emission for very short cavities down to ~120 µm, which resulted in the generation of sub-picosecond pulses with a record high repetition rate of 346 GHz [13].

III. NOISE PROPERTIES OF QD MLLs AND APPLICATIONS

QD-based mode locked lasers have shown very interesting noise properties related to the expected low n_{sp} noise factor and to the small coupling of the amplified spontaneous emission (ASE) to the optical mode owing to the relatively small optical confinement in these material systems.

They have demonstrated very narrow radio-frequency (RF) linewidths, ~two orders of magnitude less than those of quantum well MLLs [10, 14]. A record low RF linewidth of 500 Hz has recently been reported for a 10 GHz passively mode locked InAs/GaAs device [15]. Phase-noise measurements on the same device yielded an integrated timing jitter of 147 fs (4 MHz to 80 MHZ) for passive and 197 fs (20 kHz to 80 MHz) for hybrid mode-locking.

The effect of optical feedback on the noise properties of a InAs/InPQDash based laser has been investigated in [16], with the demonstration again of a 500 Hz RF linewidth, which indicates low phase noise and hence low 'high frequency' timing jitter.

These monolithic mode locked lasers are hence promising sources for many applications that require high repetition rates, low timing jitter, narrow RF linewidths such as high bit rate optical communications, millimeter wave signal generation, or optical sampling [17].

All-optical clock recovery, based on the optical injection locking of a QDash based MLL, has been performed at 40 Gbit/s, compliant with ITU-T recommendation [18]. The one-section self-pulsating QDash laser realizes high-frequency jitter suppression owing to its inherently narrow free-running RF spectral linewidth. This result paves the way to all-optical clock recovery up to 160 Gbit/s.

The wide optical spectrum (~10 nm) of mode locked QDash lasers has recently been exploited in WDM comb generation consisting of 100 GHz –spaced channels [19]. Separate error-free transmission of eight channels was successfully performed at 10 Gbit/s.

The very narrow RF linewidth makes QD MLLs very attractive for high frequency signal generation for radio transmission or radar applications. They have been successfully implemented for the generation of 60 GHz carriers for wireless transmission of high speed data streams [20]. It has also allowed significant phase noise reduction in millimeter-wave coupled opto-electronic oscillators [21].

[1] G. T. Liu, A. Stintz, H. Li, K. J. Malloy, and L. F. Lester, "Extremely low room-temperature threshold current density diode lasers using InAs dots in $In_{0.15}Ga_{0.85}As$ quantum well", Electron. Lett . vol. 11, 1999, pp. 1527-1529

[2] M. Ishida et al., " Low-driving current temperature stable 10 Gbit/s operation of p-doped 1.3 µm quantum dot lasers between 20 and 90 °C", Electron. Lett. Vol. 43, pp. 219-221 (2007)

[3] K. A. Williams, M. G. Thompson, and I. H. White, "Long wavelength monolithic mode locked diode lasers", New J. Phys. vol. 6, 2004, pp. 179

[4] X. Huang , A. Stintz , H. Li , L.F. Lester , J. Cheng , and K.J. Malloy , "Passive mode-locking in 1.3 µm two-section InAs quantum dot lasers", Appl. Phys. Lett. vol. 78 (19) , pp. 2825 – 2827 (2001)

[5] E. U. Rafailov, M. A. Cataluna, and W. Sibbett, "Mode-locked quantum-dot lasers", Nature Photonics vol. 1, pp. 395-401 (2007)

[6] E.U. Rafailov , M.A. Cataluna , W. Sibbett , N.D. Il'inskaya , Yu.M. Zadiranov , A.E. Zhukov , V.M. Ustinov , D.A. Livshits , A.R. Kovsh , and N.N. Ledentsov , "High-power picosecond and femtosecond pulse generation from a two-section mode-locked quantum-dot laser" , Appl. Phys. Lett. vol. 87 , 081107 (2005)

[7] M.G. Thompson , A. Rae , R.L. Sellin , C. Marinelli , R.V. Penty , I.H. White , A.R. Kovsh , S.S. Mikhrin , D.A. Livshits , and I.L. Krestnikov , "Subpicosecond high-power mode locking using fl ared waveguide monolithic quantum-dot lasers" , A ppl. Phys. Lett. vol.88 , 133119 (2006)

[8] M. Laemmlin , G. Fiol , C. Meuer , M. Kuntz , F. Hopfer , A.R. Kovsh , N.N. Ledentsov , and D. Bimberg , "Distortion-free optical amplification of 20–80 GHz mode-locked laser pulses at 1.3 µm using quantum dots", IEE Electron. Lett. vol.42 (12) , pp. 697 – 699 (2006)

[9] G. Moreau et al., "Effect of layer stacking and *p* -type doping on the performance of InAs/InP quantum-dash-in-a-well lasers emitting at 1.55 µ m", Appl. Phys. Lett. vol. 89 , 241123 (2006)

[10] C. Gosset , K. Merghem , A. Martinez , G. Moreau , G. Patriarche , G. Aubin , and A. Ramdane , "Subpicosecond pulse generation at 134 GHz using quantum dash-based Fabry–Perot laser emitting at 1.56 µm", Appl. Phys. Lett. vol.88, 241105 (2006)

[11] J. Liu, Z. G. Lu, S. Raymond, P. J. Poole, P. J. Barrios, and D. Poitras, "Dual-wavelength 92.5 GHz self-mode locked InP-based quantum dot laser", Opt. Lett. vol. 33 (15), pp. 1712-1704 (2008)

[12] M. J. R. Heck etal., "Observation of Q-switching and mode locking in two-section InAs/InP (100) quantum dot lasers around 1.55 µm", Opt. Exp. Vol. 15 (25), pp. 16292-16301 (2007)

[13] K. Merghem et al., "Pulse generation at 346 GHZ using a passively mode locked quantum-dash-based laser at 1.55 µm", Appl. Phys. Lett. vol. 94, 021107 (2009)

[14] F. Kefelian, S. O.'Donoghue, M. T. Todaro, J. G. McInerney, and G. Huyet, "RF linewidth in monilithic passively mode-locked semiconductor laser", IEEE Photonics Technology Letters vol. 20 (16), pp. 1405-1407 (2008)

[15] G. Carpintero, M. G. Thompson, R. V. Penty, and I. H. White, "Low noise performance of passively mode-locked 10 GHz quantum dot laser diode", IEEE Photonics Technology Letters vol. 21 , pp. 389-391 (2009)

[16] K. Merghem et al., "Low noise performance of passively mode locked quantum-dash- based lasers under external optical feedback", Appl. Phys. Lett. vol. 95, 131111 (2009)

[17] G. H. Duan et al., "High performance InP-based quantum dash semiconductor mode-locked lasers for optical communications", Bell Labs Technical Journal vol. 14 (3), pp. 63-84 (2009)

[18] J. Renaudier et al., "Standard-compliant jitter transfer function of all-optical clock recovery at 40 GHz based on a quantum-dot self-pulsating semiconductor laser" , IEEE Photon. Tech. Lett. vol. 18 (11) , pp. 1249 – 1250 (2006)

[19] A. Akrout et al., "Separate error-free transmission of eight channels at 10 Gbit/s using comb generation in a quantum dash-based mode locked laser", IEEE Photonics Technology Letters vol. 21 (23) , pp. 1746-1748 (2009)

[20] M. Huchard et al., "Millimeter wave photonic up-conversion based on a 55 GHz quantum dash mode locked laser", Proc. 34th Eur. Conf. On Optical Commun. (ECOC'08), Brussels, Belgium, (2008)

[21] F. Van Dijk, A. Enard, X. Buet, F. Lelarge, and G.-H. Duan, "Phase noise reduction of a quantum dash mode locked laser in a millimeter-wave coupled opto-electronic oscillator", J. Lightwave Technol. Vol. 26 (15), PP. 2789-2794 (2008)

Dual Wavelength Passive and Hybrid Mode-Locking of a 10GHz Quantum Dot Laser Diode at 1.5μm

M.S. Tahvili, M.J.R. Heck*, R. Nötzel, M.K. Smit, E.A.J.M. Bente
COBRA Research Institute, Eindhoven University of Technology
Eindhoven, the Netherlands
s.tahvili@tue.nl

Abstract— **We report on stable dual-wavelength operation in passive and hybrid mode-locking of a 10GHz two-section InAs/InP(100) quantum dot laser diode operating at 1.5μm. The range of stable passive mode-locking, the locking range of hybrid mode-locking and detailed measurements of the phase modulation in the output pulses will be presented.**

Keywords- mode-locked laser diode; quantum dot; hybrid mode-locking; dual-wavelength;

I. INTRODUCTION

Quantum dot (QD) material has been shown to be a promising gain medium for mode-locked laser diodes (MLLDs). The inhomogeneous broadening leads to a broad gain spectrum, which can in principle bring about ultra-short pulse generation. The QDs show reduced amplified spontaneous emission levels compared to bulk or quantum well material which can lead to a lower phase noise. Recently, we have been investigating mode-locking (ML) behavior in lasers incorporating InAs/InP(100) QD gain material, operating around 1.55μm [1]-[2]. The QD laser structure is grown on n-type (100) InP substrates by metal–organic vapor phase epitaxy [3]. The laser structure has five layers of InAs QDs stacked and located at the centre of a 500nm thick InGaAsP optical waveguiding core. Fabry–Perot type (FP) laser devices with two electrically isolated sections have been realized. The structures are cleaved to create the mirrors of the FP cavity. A high reflection (HR) coating is applied to the relatively short absorber-side facet of the lasers to decrease the cavity losses and reduce the pump current density. We intend to develop a short pulse laser light source based on the quantum dot gain material operating at 1.55um wavelength region. Combining the operation of such a laser source with an integrated pulse shaper will enable us to employ the miniature pulsed laser systems into a variety of applications including metrology and biomedical imaging.

In this paper, experimental results including verification of dual-wavelength operation, locking range of hybrid ML and evaluation of chirp profile of generated pulses, obtained from a 4mm (10GHz) MLLD with 120μm absorber section are presented. The output light from the device is collected by a lensed fiber and all measurements are performed at 12°C.

II. PASSIVE MODE-LOCKING

The two-section devices are operated by forward biasing the longer section, creating a semiconductor optical amplifier (SOA) and by reversely biasing the shorter section, creating a saturable absorber (SA). An operating range can be defined where stable ML is achieved in terms of the values of injected current of the SOA-section and bias voltage of the SA, I_{SOA} and V_{SA} respectively. To determine the stable ML operating range of the MLLD, I_{SOA} is sweep-scanned and the RF spectra traces are recorded. The measurement is repeated for a range of values of V_{SA}. The height of RF peak at the fundamental frequency over the noise floor, is mapped as a function of operating parameters and a plot is presented in Fig.1.

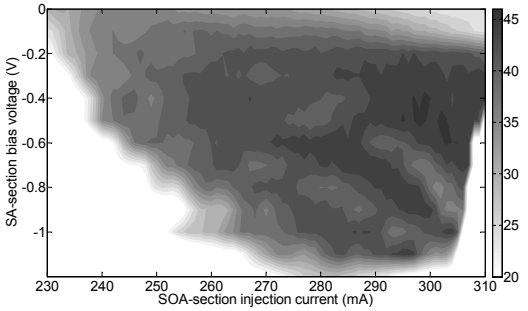


Fig.1. Height of the peak (grey scaled in dB) at the fundamental frequency over noise floor, recorded by the electrical spectrum analyzer. The electrical bandwidth used to obtain the spectra is 50kHz.

A. Dual wavelength operation

The optical spectrum shows that over the whole range of stable ML two separated groups of modes exist together. E.g. at I_{SOA}=270mA and V_{SA}=−0.5V the two groups are separated by 13nm. The longer wavelength group of modes has a FWHM of 5nm and shows relatively higher optical power as compared to the other lobe which has a FWHM of 3nm.

The output in the two groups of modes was studied in more detail. A tunable 1.2nm bandpass filter (BF) is tuned over the whole optical spectrum to filter the MLLD output signal. The filtered signal is then amplified using a booster SOA. If only the SOA is used at the output of the laser, the short wavelength group is effectively filtered out due to the gain properties of the booster amplifier. Fig.2 shows the RF spectra of the optical signals with the filter tuned at the centre of the two mode groups (light and dark grey) and an RF spectrum from the total long wavelength mode group (LWMG) (black). It appears that both mode groups generate pulses. The total output from the LWMG shows little or no amplitude noise at low frequencies, while the 1.2nm filtered output, which contains only a fraction of the output of a group, does show increased amplitude noise. This observation is similar to [1]. The changes in relative height of peaks at harmonic frequencies in the RF spectrum

This work is supported by the IOP Photonic Devices program managed by the Technology Foundation STW and SenterNovem.

*M.J.R. Heck is currently with the Department of Electrical and Computer Engineering, University of California Santa Barbara, Santa Barbara, USA.

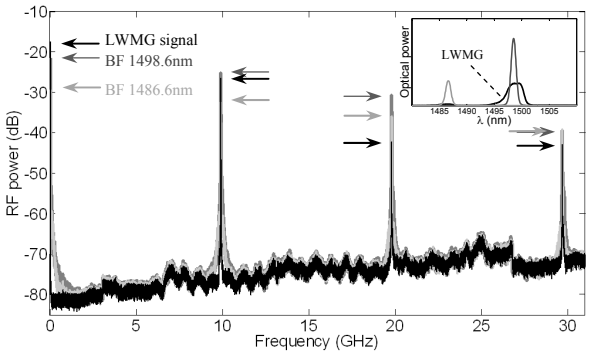


Fig.2. RF spectra obtained at I_{SOA}=260mA, V_{SA}=−0.5V, recorded with resolution bandwidth of 3MHz. The arrows on the plot point to the top of RF peaks. The inset shows optical spectra of the signals.

reveal not only that there is a difference in total optical power of the signals, but also a difference in the shape and modulation depth of the pulses in the two mode groups.

The pulsed operation of the QD laser at both wavelength mode groups is confirmed by autocorrelator traces which show FWHM of 16.2ps and 8.8ps for the 1.2nm filtered signal from long and short wavelength mode groups respectively. The total LWMG signal shows a FWHM of 45ps indicating a large chirp in the pulse, similar to earlier observations [1].

III. HYBRID MODE-LOCKING

In hybrid ML of a two-section MLLD, a stable electrical modulating signal at a frequency close to the free spectral range of the laser cavity is applied on the absorber section. The RF signal can be applied to slightly tune the repetition rate of the pulsed laser, but more importantly it reduces the timing jitter. Furthermore, hybrid ML enables broader range of measurement and characterization possibilities, e.g. with high-speed electrical sampling oscilloscopes, due to the availability of a clean electrical trigger.

A. Locking range

To define a locking range in terms of frequency and power of the modulating signal and evaluate the stability of optical pulses, the value of timing jitter is used. Such a value has been determined by integration of the single sideband phase noise signal over 20kHz-80MHz offset around the fundamental RF peak.

A good operating point for the free running QD MLLD is at I_{SOA}=280mA and V_{SA}=−0.5V with f_{rep}=9.904GHz where the laser shows a timing jitter of 14.5ps. Fig.3 shows the timing jitter results obtained with hybrid ML over a range of RF power levels and frequencies where the jitter remains below 5.5ps. At P_{RF}=15dBm, a maximum locking range of ~22MHz is achieved. The minimum jitter in this range is about 1ps.

B. Chirp evaluation

The RF signal can be used to trigger a 50GHz sampling oscilloscope with optical input and record traces of optical pulses. As an example, a recorded trace of the LWMG signal is shown in the inset of Fig.4. The figure shows that the output pulse expands over 40ps (FWHM) in one period. The autocorrelator shows a FWHM of 43ps for the optical pulse.

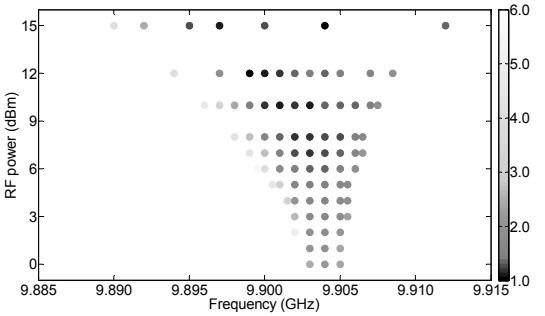


Fig.3. Time jitter (grey scaled in ps) for hybridly mode-locked QD MLLD over a range of applied RF power levels and frequencies.

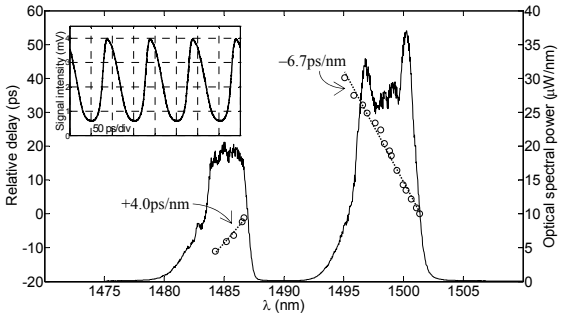


Fig.4. Relative time delay of pulses with different spectral components superimposed on a plot of the optical spectrum. The inset shows an oscilloscope trace for the LNW signal at I_{SOA}=290mA, V_{SA}=−0.5V, and P_{RF}=3dB.

A similar approach as reported in [2] is employed to evaluate the value of chirp. In this method, the BF is tuned over the spectrum, and oscilloscope traces are recorded and then analyzed to determine the relative time delay of the different spectral components. The result is shown in Fig.4 for the QD MLLD operating at P_{RF}=3dB. The overall output pulse from all different spectral components is around 50ps which is half the period of the repetition rate. The value of the linear chirp is determined to be –6.7ps/nm and +4.0ps/nm over the long- and short-wavelength lobes of optical spectrum respectively.

IV. CONCLUSIONS

We have demonstrated the dual-wavelength operation of a 10GHz QD MLLD. The laser can operate in a mode where two groups of wavelength modes are locked. The spectral components at different wavelengths are synchronized in pulsed operation. While the phenomenon which drives ML in 1.55μm QD material seems to be effective, the mechanism causing the chirp and giving rise to elongated optical pulses appears to be robust. These observations are consistent with our earlier work on 5GHz lasers.

REFERENCES

[1] M. J. R. Heck, et.al., “Passively mode-locked 4.6 GHz and 10.5 GHz quantum dot laser diodes around 1.55 μm with large operating regime,” IEEE J. Sel. Top. Quant. Electron., vol. 15, pp. 634–643, 2009.

[2] M.J.R. Heck, et.al., "Analysis of hybrid mode-locking of two-section quantum dot lasers operating at 1.5 μm," Opt. Exp., vol. 17, pp. 18063-18075, 2009.

[3] R. Nötzel, et.al., “Self assembled InAs/InP quantum dots for telecom applications in the 1.55 um wavelength range: wavelength tuning, stacking, polarization control, and lasing,” Jap. J. of Appl. Physics, 45(8B), pp. 6544-6549, 2006.

Comparison of the noise performance of integrated 10GHz QW and QD Mode-Locked Laser Diodes

Guillermo Carpintero
Tecnología Electrónica
Universidad Carlos III de Madrid
Leganés, Madrid, Spain
guiller@ing.uc3m.es

Kresten Yvind
Department of Photonics Engineering
DTU Fotonik
Lyngby, Denmark

Mark G. Thompson
Department of Electrical and Electronic Engineering
University of Bristol, Bristol, United Kingdom
(previously: Engineering Department, University of Cambridge, Cambridge, United Kingdom)

R.V. Penty, I.H. White
Engineering Department
University of Cambridge
Cambridge, United Kingdom

***Abstract*—This paper reports the experimental characterization of the noise performance of monolithically integrated quantum dot and quantum well 10GHz passively mode locked laser diodes.**

Keywords-passive mode locking, quantum dot, quantum well, phase noise.

I. INTRODUCTION

Semiconductor mode-locked lasers are key components for optical data transmission and for optical signal processing as a result of their compactness, robustness, performance stability, power consumption and low cost [1]. These integrated devices commonly comprise two sections, a saturable absorber (which represents its main difference with continuous wave lasers) and a gain section. The shape of the generated pulses depends heavily on the pulse interactions in these sections, which produce opposite effects on the pulse, namely shortening in the saturable absorber and broadening in the gain section [2]. The interactions in turn depend on the material structure of the active layer, which is commonly either a quantum-well (QW) or quantum dot (QD) structure. Both are low-dimensional structures but the intrinsic differences between QWs and QDs (such as the density of states) gives rise to very different dynamics which can account for the improvement of the QD performance as well as improving key device parameters such as the threshold current density or mode overlap factor [3]. In addition, a recent review has pointed that the passive mode locking (PML) regime of QD devices has a far superior performance over QW in terms of noise [3, 4]. The RF frequency noise for PML lasers is dominated by the spontaneous emission noise, having a Lorentzian shaped single side band (SSB) PSD, given by [5]:

$$S_{\phi RF}(f) = \Delta\nu_{RF} / \pi f^2 \qquad (1)$$

which is completely defined by the full width at half maximum (FWHM) of the first harmonic ($\Delta\nu_{RF}$). In this paper we report an experimental comparison of the passive mode locking regime in a 10GHz QD laser versus a QW device.

II. QW & QD DEVICES

Both devices have an all-active two-section structure with 4mm total length for a 10GHz repetition rate. Both devices were processed using state-of-the-art gain material structures, having similar threshold current densities, 250 A/cm^2 for the QD and 262 A/cm^2 for the QW lasers, both measured at 20ºC with the absorber in the open circuit condition..

The QD device has a 580µm long absorber section and a 3420µm long gain section, which have an ~1300nm bandgap wavelength. The active region contains a five fold stack of InGaAs QD in well layers [6]. Horizontal confinement of the optical field is achieved by the formation of 6µm wide ridge waveguide structure. The device is packaged in a case that includes a microwave 50Ω microstrip line port to the saturable absorber section and a thermoelectric cooler/thermistor that allows temperature stabilization. Laser facets are as cleaved, and light is coupled via a fiber lens to a single mode fiber pigtail with an angled connector.

The QW device has an 85µm long absorber section and a 3915µm gain section. The active region contains one well InGaAsP/AlGaInAs QW laser emitting at ~1512nm [3]. Horizontal confinement of the optical field is achieved by the formation of a 2µm width ridge waveguide structure. The facet at the absorber end is HR coated, and light is coupled on the gain facet (which is as cleaved) via single mode AR coated lensed fiber.

Both devices have been characterized on the same set-up. The gain current is injected from a 3724B ILX diode controller and the reverse bias to the saturable absorber from a HP E3631A voltage source. Both devices are mounted on a thermoelectric cooler/thermistor stage that allows temperature stabilization, and an optical isolator is used following the output coupling fiber.

The optical spectrum is measured on a HP 86140 analyzer and the electrical RF spectrum on a 22-GHz Lightwave analyzer HP 70000 system.

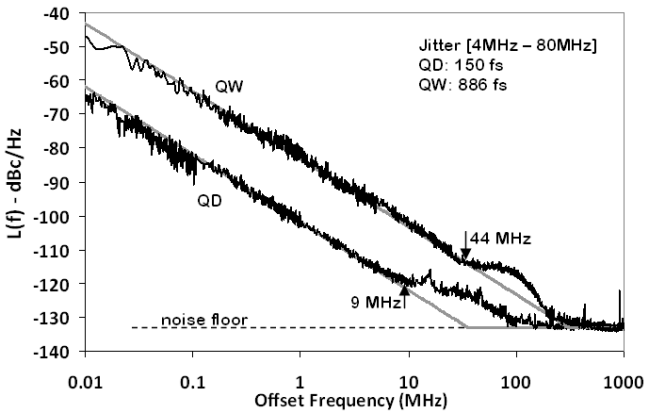


Figure 1. SSB phase noise power spectral density of the mode-locked lasers

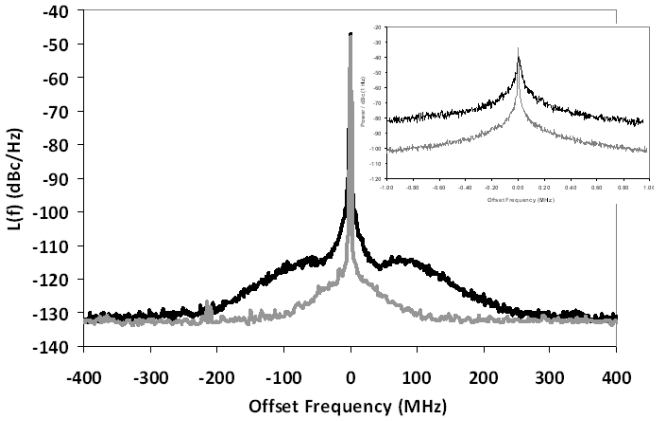


Figure 2. RF electrical spectrum showing the phase noise relative to the 10GHz carrier for the QW (black) and the QD (gray). The inset has a span of 1 MHz, and a RBW of 10 KHz

III. RESULTS

Figure 1 shows the SSB phase noise spectra for both devices, operating at the conditions which provide the best jitter figure. In agreement with the theory, the lowest noise performance on both corresponds to the highest gain current at which the device remains mode locked [3]. The bias settings are I_{gain} = 70 mA and V_{abs} = -7 V for the QW device, and I_{gain} = 130 mA and V_{abs} = -6 V for the QD laser. The grey straight lines correspond to the Lorentzian lineshape in Eq. 1, fitted down to the noise floor at -133 dBc, with the resulting $\Delta\nu_{RFfitQD}$ = 200 Hz for the QD and $\Delta\nu_{RFfitQW}$ = 15 kHz for the QW lasers. The figure shows that the two SSB phase noise traces follow the ideal -20 dB/dec roll-off up to a given frequency, f_D, namely 9 MHz for the QD and 44 MHz for the QW lasers (see Figure 1), departing at higher frequencies. The most significant difference is that after a plateau, the QD rolls off at -20 dB/dec while the QW decreases with a -40 dB/dec slope. This difference is in agreement with theoretical results which attribute it to amplitude fluctuations [7]. The integrated timing jitter ([4 MHz – 80 MHz]) of the SSB phase noise is shown on the graph, with $\sigma_{T\,QD}$ = 150 fs for the QD and $\sigma_{T\,QW}$ = 886 fs for the QW. When the jitter is calculated by integration of the Lorentzian fit, we obtain σ_{TfitQD} = 91 fs for the QD and σ_{TfitQW} = 760 fs for the QW. The result suggests that the lower jitter in the QD laser is mainly due to the narrower linewidth of this device, which can be attributed to a reduction of the spontaneous emission rate coupled to the lasing mode, due to the interaction with a small fraction of the injected carriers [3].

To confirm this point, the 10GHz RF beat signal for the QD and the QW devices are shown on Figure 2, both exhibiting a carrier-to-noise ratio greater than 42 dB. The beat signal shows a narrow frequency peak with Lorentzian lineshape (see the inset) sitting on a broad noise pedestal. When the frequency peak is fitted to a Lorentzian, the -3 dB linewidth is $\Delta\nu_{RFQD}$ = 500 Hz for the QD [6] and $\Delta\nu_{RFQW}$ = 16 kHz for the QW lasers. The results show a strong agreement between theory ($\Delta\nu_{RFfitQW}$, σ_{TfitQW}) and observed data ($\Delta\nu_{RF\,QW}$, $\sigma_{T\,QW}$) for the QW device, where the difference between σ_{TfitQW} and $\sigma_{T\,QW}$ can be attributed to the difference between the two curves above f_D in Figure 1. Similarly, for the QD, the lower f_D increases the impact of the non-Lorentzian components of the SSB phase noise on the rms timing jitter from the RF linewidth, which explains the observed difference between $\sigma_{T\,QD}$ and σ_{TfitQD}.

IV. CONCLUSSIONS

In conclusion, our results on the passive mode locked SSB phase noise confirm that the extremely good timing jitter performance of the QDs laser is due to the narrower linewidth on the QD device, as these are intrinsically linked. However, the dynamics of the device, which cause a slow roll-off of the pedestals, impact on the resulting jitter from the QD.

ACKNOWLEDGMENT

This work was supported by the U.K. Engineering and Physical Sciences Research Council, The Danish Independent Research Council FTP and the European Commission through the ePIXnet Network of Excellence (www.epixnet.org). One of the authors (G.C.) thanks Spanish Ministerio de Educación, supporting this work through mobility grant ref. PR2009-0056.

REFERENCES

[1] Kaiser, R. and Hüttl, B. "Monolithic 40-GHz Mode-Locked MQW DBR lasers for high-speed optical communication systems" IEEE J. of Sel. Topics in Quantum Electronics 13(1), 125 – 135 (2007)

[2] Williams, K.A.; Thompson, M.G.; White, I.H. "Long-wavelength monolithic mode-locked diode lasers" New J. Phys. **6** 179 (2004).

[3] Yvind, K.; Larsson, D.; Mørk, J.; Hvam, J.M.; Thompson, M.; Penty, R.; White, I.H. "Low-noise monolithic mode-locked semiconductor lasers through low-dimensional structures" Proc. of the SPIE, Vol. 6909, pp. 69090A-69090A-9 (2008).

[4] Thompson, M.G.; Rae, A.R.; Mo Xia; Penty, R.V.; White, I.H. "InGaAs Quantum-Dot Mode-Locked Laser Diodes" IEEE J. Sel. Topics in Quantum Electronics 15(3), pp. 661 – 672 (2009).

[5] Kéfélian, F.; O'Donoghue, S.; Todaro, M.T.; McInerney, J.G.; Huyet, G. "RF Linewidth in Monolithic Passively Mode-Locked Semiconductor Laser" IEEE Phot. Tech. Lett. 20(16), pp. 1405 – 1407 (2008)

[6] Carpintero, G.; Thompson, M.G.; Penty, R.V.; White, I.H. "Low Noise Performance of Passively Mode-Locked 10-GHz Quantum-Dot Laser Diode" IEEE Phot. Tech. Lett. 21(6), pp. 389-391 (2009)

[7] Mulet, J.; Moerk, J.; Kroh, M. "Identification of amplitude and timing jitter in external-cavity mode-locked semiconductor lasers" in CLEO/IQEC San Francisco, CA, May 16-21 (2004)

Monolithic 45-GHz Mode locked Surface-Etched DBR Laser Using Quantum Well Intermixing Technology

L. Hou, M. Haji, R. Dylewicz, J. M. Arnold, A. C. Bryce
Department of Electronics and Electrical Engineering, University of Glasgow, G12 8LT Glasgow, U.K.
lhou@elec.gla.ac.uk

***Abstract*—45-GHz passively mode locked AlGaInAs/InP 1.55 μm lasers integrated with surface-etched distributed Bragg mirrors have been fabricated. Quantum well intermixing was used to provide low absorption loss gratings with accurate wavelength control. The lasers produce 3.6-ps Gaussian-pulses with TBP of 0.57.**

Keywords—mode locked laser; monolithic integrated circuits; surface-etched Bragg gratings; quantum well intermixing.

I. INTRODUCTION

Semiconductor mode locked lasers are attractive as compact pulse sources in high-speed optical communication systems, microwave photonics, and high speed optical sampling. Distributed Bragg reflectors (DBRs) are indispensable for controlling the spectral bandwidth, the centre wavelength, and repetition rate tuning of the pulses. So far, conventional 40-GHz mode locked DBR lasers require at least one growth interruption, resulting in a low yield and higher cost per unit [1, 2]. Surface-etched DBRs require only a single epitaxial grown step, and can be simultaneously fabricated with the ridge waveguide. Therefore, the fabrication process is much simpler than the methods used in traditional DBR structures. In particular, Al-containing active layers can be used below the grating without the risk of oxidization. Larsson et al. [3] have demonstrated 10-GHz all-active monolithic mode locked lasers with surface-etched Bragg gratings, but the DBR coupling efficiency κ was very low ($\kappa \sim 7$/cm). Quantum well intermixing (QWI) permits post-growth modification of the QW band edge, offering a simple, flexible and low cost alternative technique to selective etching and re-growth. The refractive index discontinuity at the interface between adjacent sections is negligible, which eliminates parasitic reflections that can degrade performance [4]. Recent advances in the AlGaInAs/InP material system make it a more promising candidate due to better intrinsic characteristics in comparison with the conventional InGaAsP/InP material system [5]. In this paper, we present for the first time a monolithic 45-GHz passively mode locked AlGaInAs/InP 1.55 μm multi-quantum-well (MQW) laser integrated with surface-etched Bragg gratings with moderate coupling efficiency ($\kappa \sim 40$/cm), low absorption loss, and accurate wavelength control using a relatively simple fabrication approach. QWI technology was used to blue-shift the bandgap of DBR and phase section relative to the active sections, e.g. gain and saturable absorber (SA) section, to reduce the direct bandgap absorption.

II. DEVICE STRUCTURE AND FABRICATION

The epitaxial structure is described in [5]. The top $Al_{0.423}Ga_{0.047}In_{0.53}As$ (60-nm-thick) waveguide layer behaves as a reactive ion etching (RIE) etch-stop layer to define the height of the ridge waveguide, while reducing the RIE lag effect in the grating. The monolithic integrated mode locked DBR laser is shown in Fig. 1. The device has a total length of 1080 μm and consists of a 700-μm-long gain section, saturable

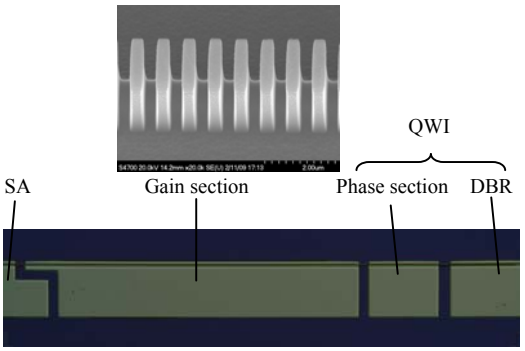


Figure 1. Optical microscope picture of monolithic AlGaInAs/InP mode locked DBR laser and SEM picture of 734-nm-period gratings.

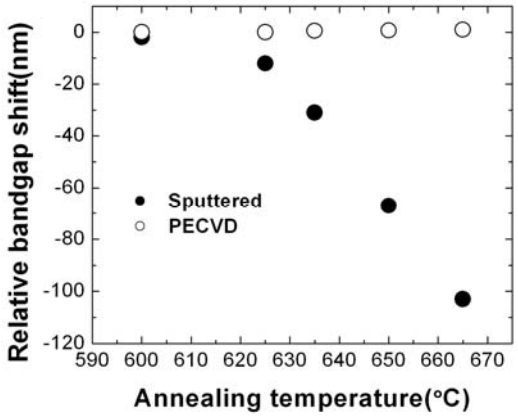


Figure 2. Relative bandgap shift vs. annealing temperature for samples covered with sputtered and PECVD SiO_2 after 60 seconds of rapid thermal annealing (RTA) process.

The work was financially supported by EPSRC UK (project EP/E065112/1–*High Power, High Frequency Mode-locked Semiconductor Lasers*)

absorber (20 μm), phase section (150 μm) and a DBR section (150 μm). Electrical isolation between the electrodes was obtained by wet etching 20 μm slots in the contact layer. A 200 nm of sputtered SiO_2 film was selectively deposited on the passive waveguide areas (DBR and phase sections) then the whole wafer was covered with a protective 200-nm-thick PECVD SiO_2 film. The sample was subsequently annealed at 660 °C for 60 seconds leading to a targeted bandgap shift of 100 nm for the passive section, while the gain and SA section did not exhibit any significant shift at the same rapid thermal annealing (RTA) temperature (see Fig. 2). The 2.5-μm-wide ridge and 3rd order gratings (367-nm-wide grating slots with 50% duty cycle) were defined by electron beam lithography and a CH_4:H_2:O_2 RIE dry etching process, terminated at the etch-stop layer (1.92 μm total ridge etch depth). Following the normal passivation, p-contact window opening, p-contact deposition, thinning and n-contact deposition, the sample was cleaved into individual laser bars with both SA facets and the DBR facets left uncoated. The devices were mounted epilayer-up on a copper heat sink and tested under CW conditions at a temperature of 20 °C.

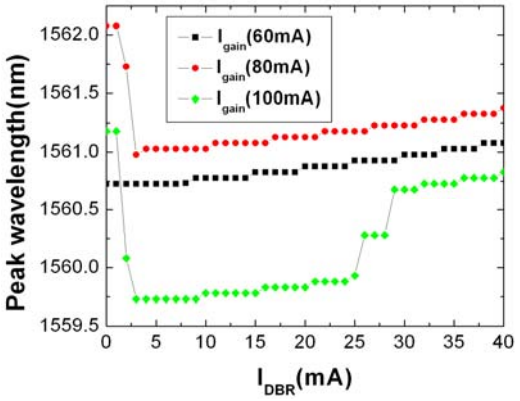


Figure 3. Emission peak wavelength vs. DBR currents for I_{gain} = 60, 80, and 100 mA, while the phase section is floating and V_{SA} = -2.0 V.

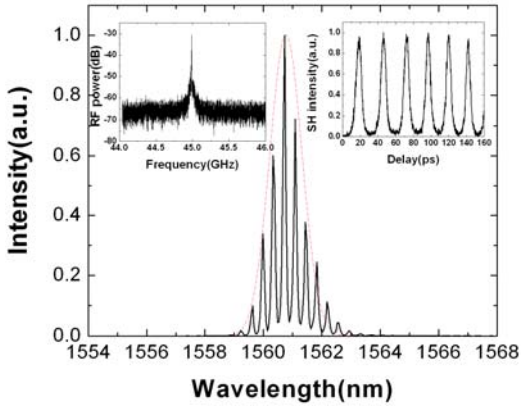


Figure 4. Optical spectrum, corresponding RF spectrum (left inset) and autocorrelation trace (right inset) for I_{gain} = 60 mA, I_{DBR} = 2 mA, phase section floating, and V_{SA} = -2.0 V.

III. DEVICE PERFORMANCE

Pure mode locking characteristics were observed when forward biasing gain section I_{gain} varied from 44 mA to 136 mA and SA reverse bias voltage $|V_{SA}| \geq 2.0$ V.

Fig. 3 summarizes the dependence of the peak wavelength on the DBR tuning current, where the total injection current to the gain sections and the absorber reverse bias were fixed at 60, 80, 100 mA and -2.0 V, respectively. The results clearly show that when I_{gain} is set to 80 or 100 mA, the peak wavelength is reduced as I_{DBR} increases from 0 mA to 3 mA due to the plasma effect. At higher DBR currents, the wavelength increases again due to heating effect. At discrete current levels a jump in wavelength occurs, which is equivalent to the length of one longitudinal mode (~ 0.35 nm). For I_{gain} = 60 mA, the plasma effect is less pronounced as the tuning was dominated by the heating effect.

The shortest pulse width was observed at I_{gain} = 60 mA, I_{DBR} = 2 mA, where the autocorrelation width of an isolated pulse was 5.1 ps, which deconvolves to 3.6 ps pulse duration if a Gaussian pulse shape is assumed. The period of the emitted pulse train measured is 22.2 ps, which is in accordance with the RF spectrum frequency of 45.0 GHz (see Fig. 4). The optical spectrum is centered at 1560.8 nm with a 3 dB bandwidth of 1.29 nm. The time-bandwidth product of the pulse is equal to 0.57, which is very close to the transform limit (≈ 0.441) of a pulse with Gaussian profile.

IV. CONCLUSION

In conclusion, we have fabricated and characterized a 45-GHz passively mode-locked AlGaInAs/InP 1.55 μm laser with highly selective and low-loss DBR mirrors by using QWI technology. The mode locking results show that our device offers a real alternative to and a cheaper solution than conventional DBR mode locked lasers.

Reference

[1] S. Arahira, Y. Matsui, T. Kunii, S. Oshiba, and Y. Ogawa, "Transform-limited optical short-pulse generation at high repetition rate over 40 GHz from a monolithic passive mode-locked DBR laser diode," IEEE Photon. Technol. Lett., vol. 5, pp. 1362-1365, 1993.

[2] R. Kaiser and B. Huttl, "Monolithic 40-GHz mode-locked MQW DBR lasers for high-speed optical communication systems," IEEE J. Sel. Top Quantum Electron., vol. 13, pp. 125-135, 2007.

[3] D. Larsson, K. Yvind, and J. M. Hvam, "Long all-active monolithic mode-locked lasers with surface-etched Bragg gratings," IEEE Photon. Technol. Lett., vol. 19, pp. 1723-1725, 2007.

[4] F. Robert, A. C. Bryce, J. H. Marsh, A. J. SpringThorpe, J. K. White, "Passive mode locking of InAlGaAs 1.3-μm strained quantum wells extended cavity laser fabricated by quantum-well intermixing," IEEE Photon. Technol. Lett., vol. 23, pp. 374-376, 2004.

[5] L. Hou, P. Stolarz, J. Javaloyes, R. Green, C. Ironside, M. Sorel, and A. C. Bryce, "Subpicosecond pulse generation at quasi-40-GHz using a passively mode locked AlGaInAs/InP 1.55 μm strained quantum well laser," IEEE Photon. Technol. Lett., vol. 21, pp. 1731-1733, 2009.

Superradiant Emission from AlInGaAs/InGaAsP Quantum-Well Waveguides

M. Xia, R. V. Penty and I. H. White
Centre for Photonic Systems
Department of Engineering, University of Cambridge
Cambridge CB3 0FA, UK
E-mail: mx207@cam.ac.uk

P. P. Vasil'ev
PN Lebedev Physical Institute
53 Leninsky Prospect
Moscow 119991, Russia
E-mail: peter@lebedev.ru

Abstract—**Superradiant emission from a quantum-well semiconductor structure has been experimentally demonstrated at room temperature for the first time, resulting in a 5MHz train of 390fs pulses with 7.2W peak power at 1580nm wavelength.**

Keywords: Superradiance; femtosecond phenomena

I. INTRODUCTION

Owing to its ability to generate ultrashort high power optical pulses, superradiance (SR) has been investigated both theoretically and experimentally [1-3] since the concept was first proposed in 1954 [4]. SR emission has been of particular interest because of its unique properties of femtosecond pulse generation, spatial coherency and large field amplitude. It has shown great potential for many applications such as medical systems, imaging systems, sensing devices and bio-photonics [5]. The main difficulty in obtaining SR emission from semiconductor structures is to attain the extremely high concentrations of the electron-hole (e-h) pairs necessary to achieve an excitonic condensate at ordinary temperatures. This is required to achieve cooperative radiation of the inverted quantum oscillator. Until recently, SR has only been experimentally reported in bulk semiconductor (GaAs/AlGaAs heterostructures) at room temperature at wavelengths around 880 nm [1].

However, in this work, we have for the first time experimentally demonstrated SR emission from a quantum-well device at room temperature. SR is confirmed by analyzing the evolution of the optical spectra, and superradiant trends and regimes are studied as a function of driving condition. A 5 MHz optical pulse train has been obtained in the 1.55 μm wavelength window, with pulse durations as short as 390 fs and pulse peak powers of 7.2 W.

II. DEVICE DESCRIPTION

The active region of the device under investigation, Fig. 1(a), incorporates a 5 AlGaInAs QW active structure which is grown on an InP substrate using MBE. Standard photolithography and ICP dry etch processes are used to fabricate the 3 μm wide ridge waveguide structures. The device is operated at a room temperature of 20 ^{o}C and has an emission wavelength of ~1.55 μm. The back facet is HR coated and the front facet is AR coated. Light is coupled out of the system via the front facet using a lensed fiber. The total length of the device is 1.03 mm, Fig. 1(b), comprising two 415 μm long gain sections and one 200 μm long absorber section. Two gain sections are connected to an electrical pulse generator that has a tunable amplitude from 0 to 2 A, a tunable pulse repetition rate up to 5 MHz and minimum pulse width of 9 ns, whilst a dc reverse bias voltage from 0 to 8 V is applied to the absorber section.

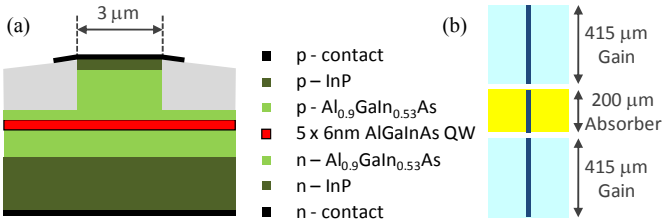


Figure 1. (a) Schematic diagram of the QW waveguide and epitaxial structure; (b) structure of the multi-section design.

III. EXPERIMENTAL RESULTS

In classic SR theory, the properties of SR emission are determined by two fundamental effects: mutual phasing of emitters and the collective spontaneous emission of the correlated emitters. It is shown in [1] that there are three critical criteria to achieve SR emission in semiconductor structures at room temperature: (i) high current pumping, (ii) larger internal carrier density and (iii) high gain, namely the realization of the condition $\alpha L >> 1$, where α is the small-signal gain and L is the length of the structure. These criteria can be experimentally implemented by applying a strong current pulse to the one section of the device. With the other section in a strongly absorptive state, high optical gain can build up and suppress the phase relaxation processes at the early stage of evolution. In turn, this can induce the generation of SR pulses. A pulsed drive current of 0-400 mA is therefore used in the investigated QW structure to increase the inversion of the system and overcome the destructive role the phase relaxation in the early stage of the SR pulse generation. A dc reverse bias from 0 to 8 V is applied to the absorber in order to prevent lasing and achieve higher levels of e-h densities in the structure.

The investigated device has a lasing threshold of 75mA with both gain sections pumped and 0 V absorber applied. However, SR, as a result of simultaneous recombination of a

large number of the correlated emitters, can only be observed for currents over 275 mA due to the requirement of high pumping and large carrier density for e-h condensates [6]. As a result strong absorption is required to prevent conventional lasing in the device.

Fig. 2 shows the evolution of SR pulse generation. The drive pulse amplitude is fixed at 400 mA while the reverse bias voltage is varying from 0 to 8 V to control the optical gain profile. Initially, stimulated emission can be observed at lower bias voltage (i.e. low e-h density) in the form of gain-switching and Q-switching. There is a transition between the Q-switching and SR regimes and the optical spectrum drifts dramatically (>20 nm) toward longer wavelength during the transition. This red shift corresponds to the band gap shrinkage as the e-h density increases with the increase in reverse bias. SR emission from an e-h condensate can be observed when mutual phasing of the individual e-h pairs occurs and a coherent cooperative state forms right at the band gap. In contrast to the gain and Q-switching spectra, which exhibit longitudinal modes, the SR spectrum is continuous without any mode structure and hence SR is considered as collective spontaneous emission of the correlated e-h pairs (rather than lasing). The shape of the continuous spectra of the cooperative recombination is asymmetric with the long wavelength edge being steeper than the short wavelength.

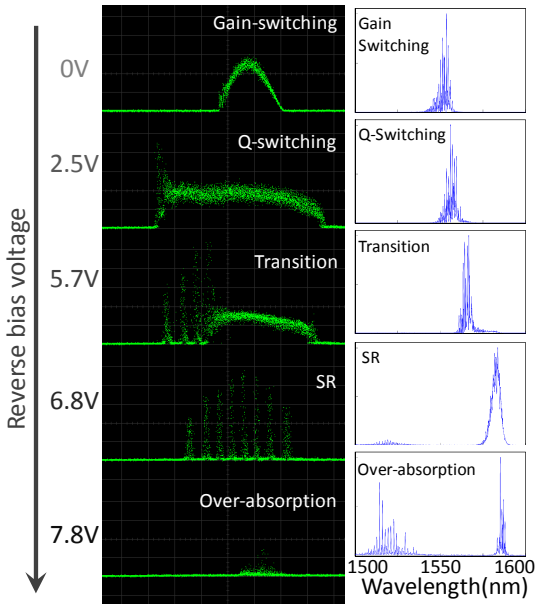


Figure 2. SR pulse evolution: drive pulse amplitude fixed at 400 mA while reverse bias voltage changing from 0 to – 8 V. Pulse development observed from oscilloscope (upper, 1 ns/div.) and optical spectrum analyzer (lower, res. BW = 0.07 nm).

Fig. 3 (a) shows the regimes of SR emission. The device can work in different operating regimes under different driving conditions. A train of single SR pulses with femtosecond pulse duration can be observed for drive currents from 275 to 325 mA while bursts of multiple SR pulses (see Fig. 2) are detected at higher drive currents. Multiple SR pulses can also be observed for electrical drive pulse widths greater than 9 ns for lower drive currents. The individual pulse width however always lies in the hundreds of femtosecond range. The average output power as a function of driving conditions can be seen in Fig. 3(b). The average power decreases rapidly during the transition (along with the associated red shift of the optical spectrum), which leads to a relatively low SR average power.

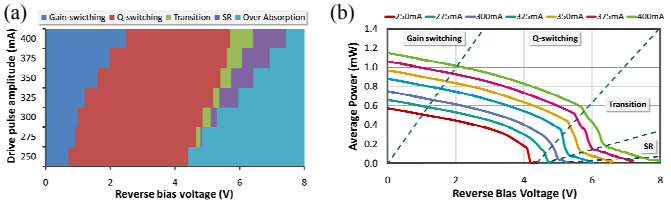


Figure 3. (a) SR regimes and (b) measured average output power as a function of driving conditions.

For optimized SR operation, the gain section is driven at 325 mA, whilst a 5.95 V bias voltage is applied to the absorber section. As shown in Fig. 4(a), a SR pulse is obtained with an optical pulse duration of 390 fs at a pulse repetition rate of 5 MHz. The estimated pulse peak power is 7.2 W with a pulse energy of 3.3 pJ. Fig. 4(b) shows the optical spectrum under such operation. The central emission wavelength is 1583.6 nm, with a spectral width of 3.67 nm. It should be noted that the small peak observed from the shorter wavelength (~1515 nm) corresponds to the spontaneous emission with much higher photon energies in the QW structure.

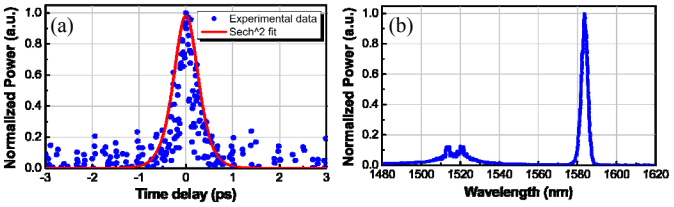


Figure 4. (a) Autocorrelation trace for SR emission under 325 mA driving current and -5.95 V reverse bias voltage; (b) corresponding optical spectrum.

IV. Conclusion

We have experimentally demonstrated superradiant emission from an AlGaInAs quantum-well semiconductor structure at room temperature for the first time. SR trends and regimes have been measured as a function of driving conditions. A 5 MHz SR pulse train has been obtained at an emission wavelength of 1.58 μm, with a pulse width as short as 390 fs and 7.2 W pulse peak power.

References

[1] P. P. Vasil'ev, "Femtosecond superradiant emission in inorganic semiconductors," Rep. Prog. Phys. 72, 076501 (2009)

[2] M. O. Scully and A. A. Svidzinsky, "The super of superradiance," Science, 325, 1510-1511 (2009).

[3] L. I. Men'shikov, "Superradiance and related phenomena," Phys. Usp. 42, 107 (1999).

[4] R. H. Dicke, "Coherence in spontaneous radiation processes," Phys. Rev. 93, 99 (1954).

[5] C. M. Eigenwillig, B. R. Biedermann, G. Palte, and R. Huber, "K-space linear Fourier domain mode locked laser and applications for optical coherence tomography," Optics Express, 16, 8916-8937 (2008)

[6] P. P. Vasil'ev, "Conditions and possible mechanism of condensation of e-h pairs in bulk GaAs at room temperature," Phys. Stat. Sol. (b) 241, 1251-1260 (2004)

Single-Frequency, Narrow-Linewidth Distributed Feedback Waveguide Laser in $Al_2O_3:Er^{3+}$ on Silicon

E. H. Bernhardi, H. A. G. M van Wolferen, L. Agazzi, M. R. H. Khan,
C. G. H. Roeloffzen, K. Wörhoff, M. Pollnau and R. M de Ridder
MESA$^+$ Institute for Nanotechnology, University of Twente,
Enschede, The Netherlands
E-mail: e.h.bernhardi@utwente.nl

***Abstract*—A distributed feedback channel waveguide laser in erbium-doped aluminum oxide on a silicon substrate is reported. The optically pumped laser has a threshold pump power of 15 mW and emits 3 mW in single-frequency operation at 1545.2 nm wavelength with a slope efficiency of 6.2% and linewidth of 15 kHz.**

Keywords—Distributed feedback (DFB) laser; waveguide laser; erbium-doped laser; Bragg gratings; aluminum oxide

I. INTRODUCTION

Dense wavelength division multiplexing (DWDM) in telecommunication networks has been one of the main driving forces behind the development of single-frequency lasers operating in the telecommunication C-band (1530-1565 nm). Monolithic erbium-doped dielectric distributed feedback (DFB) waveguide lasers are of particular interest for this application due to their stable, single-mode, single-polarization, extremely narrow-linewidth and low-noise emission [1,2].

Erbium-doped aluminum oxide ($Al_2O_3:Er^{3+}$) has been identified as a very promising gain medium to realize such integrated single-frequency waveguide lasers due to its favorable optical properties and compatibility with existing silicon waveguide technology. $Al_2O_3:Er^{3+}$ waveguides with low propagation losses and an internal optical gain over an 80 nm wavelength range, by far exceeding the range of the telecommunication C-band, with a peak gain of 2.0 dB/cm have recently been realized [3]. The first $Al_2O_3:Er^{3+}$ integrated waveguide laser was consequently demonstrated soon thereafter [4].

In this work we present the first monolithic single-frequency distributed feedback channel waveguide laser in $Al_2O_3:Er^{3+}$. Its output power is in the milliwatt range, with a low pump threshold and high slope efficiency being achieved due to tight light confinement and small propagation losses in our channel waveguides, while also providing the additional feature of single-frequency, narrow-linewidth operation. The laser power and spectral characteristics make it an excellent competitor against well-established optical waveguide technologies such as erbium-doped phosphate glass and lithium niobate channel waveguide lasers [1,2,5].

Funding was provided by the MEMPHIS project which is part of the Smart Mix Programme of the Netherlands Ministry of Economic Affairs and the Netherlands Ministry of Education, Culture and Science.

II. FABRICATION

The channel waveguides were fabricated in $Al_2O_3:Er^{3+}$ layers which were deposited onto standard thermally oxidized silicon wafers [6]. The erbium doping concentration has been set to ~3×10^{20} cm^{-3}. The ridge waveguides were 1 cm long, 3 μm wide and were etched 0.1 μm deep via a reactive ion etching process [7]. The waveguide geometry was designed to support only single transverse-mode operation at the pump and laser wavelengths. A 650-nm-thick plasma-enhanced chemical vapor deposition (PECVD) SiO_2 cladding layer was deposited on top of the ridge waveguides.

Optical feedback in the cavity was provided by a 1-cm-long surface relief Bragg grating. The grating pattern was defined in a 120-nm-thick negative resist layer on top of the SiO_2 by means of laser interference lithography (LIL). Finally, the grating pattern was etched into the SiO_2 layer using a $CHF_3:O_2$ reactive ion plasma, after which the residual resist was removed by an O_2 plasma. The resultant Bragg grating had an etch depth of ~150 nm with a period of 488 nm and a duty cycle of ~50%. In order to ensure single longitudinal mode operation, a distributed quarter-wave phase shift was introduced to the cavity by means of a 2-mm-long adiabatic sinusoidal tapering of the waveguide width in the center region of the cavity [8].

III. CHARACTERIZATION

The laser was optically pumped by a 1480 nm laser diode where a maximum pump power of 67 mW was launched into the waveguide via a 1480/1550 nm wavelength division multiplexing (WDM) fiber. The laser emission was collected from the pumped side of the cavity with the WDM fiber and sent to a power meter. The power characteristic of the laser is shown in Fig. 1. The DFB laser threshold occurs at a launched pump power of 15 mW. The maximum laser emission from the pumped side of the cavity is more than 3 mW, which results in a slope efficiency of 6.2% versus launched pump power. The unabsorbed pump power that was collected at the unpumped side of the cavity indicated that only approximately 20% of the launched pump power is absorbed in the cavity so that a pump power threshold of below 3 mW and slope efficiency of more than 30% are

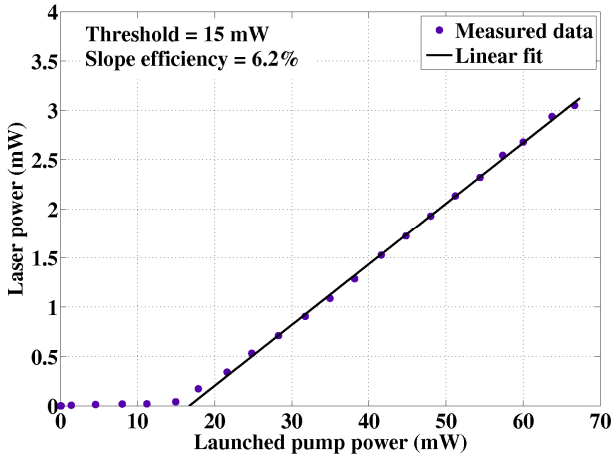


Figure 1. Laser output power laser as a function of launched pump power

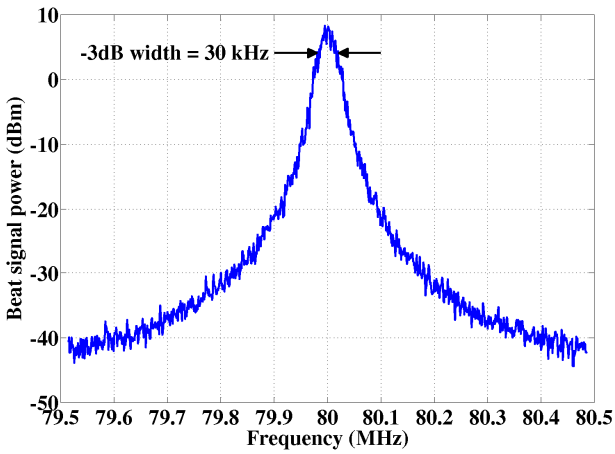


Figure 2. The heterodyne RF beat signal with a –3dB linewidth of 30 kHz

derived versus absorbed pump power. The low threshold is a consequence of the strong light confinement due to the comparatively high refractive index of Al_2O_3 of ~1.65 which allows the fabrication of compact integrated optical structures and small waveguide cross-sections.

The laser emission from the unpumped side of the cavity was collected with a WDM fiber and sent to an optical spectrum analyzer (OSA) with a resolution of 0.1 nm. The laser operated at a wavelength of 1545.2 nm (TE polarized) and the single emission peak is more than 40 dB above the amplified spontaneous emission noise floor. Since characterization of the Bragg gratings showed that the Bragg reflection of the TM mode occurs at ~1533 nm, we conclude that the laser was operating TE-polarized at all times. Although single-mode behavior could be confirmed with the OSA measurement, the linewidth of the laser emission was limited by the resolution of the OSA.

Consequently a delayed self-heterodyne interferometer with a much higher resolution of ~10 kHz was implemented to measure the laser linewidth [9]. The setup was constructed with two 50/50 couplers, a 9.5 km fiber, an 80 MHz acousto-optic modulator, photo-detector and an RF spectrum analyzer. The measured –3 dB linewidth of the beated RF signal was 30 kHz, which implies a laser linewidth of 15 kHz for a Lorentzian lineshape (Fig. 2). We believe that the actual laser linewidth is in fact significantly narrower and that the current measured value for the linewidth is a result of excessive noise in the heterodyning measurement setup. We are currently in the process of extending the heterodyne interferometer to a recirculating delayed self-heterodyne interferometer which will reduce the linewidth resolution of the setup to the sub-kilohertz regime. Additionally we are also addressing the issue of excessive noise in the measurement setup.

IV. Conclusion

A monolithic distributed-feedback waveguide laser in $Al_2O_3:Er^{3+}$ was presented. The low-threshold laser demonstrated narrow-linewidth, single-longitudinal-mode, and single-polarization emission. A maximum output power of more than 3 mW was achieved with a linewidth of <15 kHz. To the best of our knowledge, this is the first rare-earth-ion-doped DFB laser that is fabricated on a silicon substrate. This result holds many promising opportunities for the integration of such single-frequency lasers with existing dielectric waveguide technology on silicon substrates.

References

[1] A. Blaize, L. Bastard, C. Cassagnetes, G. Vitrant, and J. E. Broquin, “Ion-exchanged glass DFB Lasers for DWDM,” Proc. SPIE, vol. 4640, pp. 218-225, Jan. 2002.

[2] L. Bastard, S. Blaize, and J.E. Broquin, “Glass integrated optics ultranarrow linewidth distributed feedback laser matrix for dense wavelength division multiplexing applications,” Opt. Eng., vol. 42, pp. 2800-2804, Oct. 2003.

[3] J. D. B Bradley, L. Agazzi, D. Geskus, F. Ay, K. Wörhoff, and M. Pollnau, “Gain bandwidth of 80 nm and 2 dB/cm peak gain in $Al_2O_3:Er^{3+}$ optical amplifiers on silicon,” J. Opt. Soc. Am. B, vol. 27, pp. 187-196, Feb. 2010.

[4] J. D. B. Bradley, R. Stoffer, L. Agazzi, F. Ay, K. Wörhoff, and M. Pollnau, “Integrated $Al_2O_3:Er^{3+}$ ring lasers on silicon with wide wavelength selectivity,” Opt. Lett., vol. 35, pp. 73-75, Jan. 2010.

[5] B. K. Das, H. Suche, and W. Sohler, “ Single-frequency Ti:Er:$LiNbO_3$ distributed Bragg reflector waveguide laser with thermally fixed photorefractive cavity,” Appl. Phys. B, vol. 73, pp. 439-442, Oct. 2001.

[6] K. Wörhoff, J. D. B. Bradley, F. Ay, D. Geskus, T. P. Blauwendraat, and M. Pollnau, “Reliable low-cost fabrication of low-loss $Al_2O_3:Er^{3+}$ waveguides with 5.4-dB optical gain,” IEEE J. Quantum Electron. vol. 45, pp. 454-461, May 2009.

[7] J. D. B. Bradley, F. Ay, K. Wörhoff, and M. Pollnau, “Fabrication of low-loss channel waveguides in Al_2O_3 and Y_2O_3 layers by inductively coupled plasma reactive ion etching,” Appl. Phys. B, vol. 89, pp. 311-318, Oct. 2007.

[8] L. Bastard, J. E. Broquin, “Realization of a distributed phase shifted glass DFB laser,” Proc. SPIE, vol. 5728, pp. 136-145, Jan. 2005.

[9] T. Okoshi, K. Kikuchi, and A. Nakayama, “Novel method for high resolution measurement of laser output spectrum,” Electron. Lett. vol. 16, pp. 630-631, Jul. 2007.

$Al_2O_3:Er^{3+}$ waveguide amplifiers at 1.5 μm

L. Agazzi, J. D. B. Bradley, F. Ay, K. Wörhoff, and M. Pollnau
Integrated Optical MicroSystems Group, MESA+ Institute for Nanotechnology,
University of Twente, Enschede, The Netherlands
l.agazzi@ewi.utwente.nl

***Abstract*— We report optical amplification in $Al_2O_3:Er^{3+}$ with a gain bandwidth of 80 nm and peak gain of 2.0 dB/cm at 1533 nm, data transmission at 170 Gbit/s without added bit-error penalty and monolithic integration of these active $Al_2O_3:Er^{3+}$ waveguides with passive silicon-on-insulator waveguides.**

Optical amplifiers; Integrated optics materials; High-speed amplification; Monolithic integration with SOI waveguides

I. INTRODUCTION

Silicon-on-insulator (SOI) is emerging as a platform for realizing compact integrated photonic circuits at wavelengths in the telecom range. However, SOI devices – though highly integrated – show relatively high losses [1]. Amplifiers are thus an indispensable feature of integrated optical systems, with the task of regenerating signals that have been attenuated during their propagation within an optical circuit. We have selected Er-doped amorphous aluminum oxide ($Al_2O_3:Er^{3+}$) as the amplifier material due to its high Er solubility and higher refractive index contrast compared to other typical glass hosts, which allows more compact devices. Our straightforward fabrication process allows deposition on a variety of substrates such as silicon [2], resulting in low background losses (typically 0.1-0.2 dB/cm). Here we report on internal net gain over a wavelength range of 80 nm, with a peak value of 2 dB/cm at 1533 nm [3]. The great potential of this material is demonstrated by high-speed amplification at 170 Gbit/s without noise penalty or patterning effects and wafer-scale monolithic integration of active Er-doped Al_2O_3 waveguides with passive SOI waveguides.

II. GAIN IN $Al_2O_3:Er^{3+}$ WAVEGUIDE AMPLIFIERS

$Al_2O_3:Er^{3+}$ layers with a thickness of approximately 1.0 μm were deposited on thermally oxidized silicon substrates by reactive co-sputtering [2] and 4.0-μm-wide ridge waveguides were defined by reactive ion etching to a depth of 50 nm [4]. The Er concentration varied from 0.27 to 3.66×10^{20} cm^{-3}. Gain measurements were carried out by launching simultaneously 977-nm pump light from a Ti:Sapphire pump source and 1533-nm signal light from a tunable laser into the channel waveguides using a lens-coupling setup. The output signal light was separated from the residual pump light by a silicon filter and acquired by a detector and lock-in amplifier. For optimum Er concentrations in the range of 1 to 2×10^{20} cm^{-3}, internal net gain of up to 2.0 dB/cm was obtained. Furthermore, net gain was obtained over a wavelength range of 80 nm with a peak gain of 9.3 dB at 1533 nm (Fig. 1), for an amplifier length of 5.4 cm and Er concentration of 1.17×10^{20} cm^{-3}. These high gain values demonstrate that $Al_2O_3:Er^{3+}$ is a competitive technology for active integrated optics.

III. 170 Gbit/s HIGH-SPEED AMPLIFIER

In collaboration with colleagues from the University of Rennes, France, we performed signal transmission experiments at 170 Gbit/s in an integrated $Al_2O_3:Er^{3+}$ waveguide amplifier to investigate its potential application in high-speed photonic integrated circuits [5]. Figure 2 shows typical eye diagrams measured (a) without the EDWA and (b) with the EDWA included in the experimental transmission setup. In the case with the EDWA included 0.1 mW of signal and 65 mW of pump power were launched into the device, and a single input signal polarization was selected. The eye pattern is open and the pulse FWHM is 2 ps in both cases. Bit error rate (BER) assessments were also performed with and without the device in the transmission setup. Identical bit error rate vs. received optical power curves were obtained with and without the EDWA in the system, verifying that negligible noise is added by the amplifier.

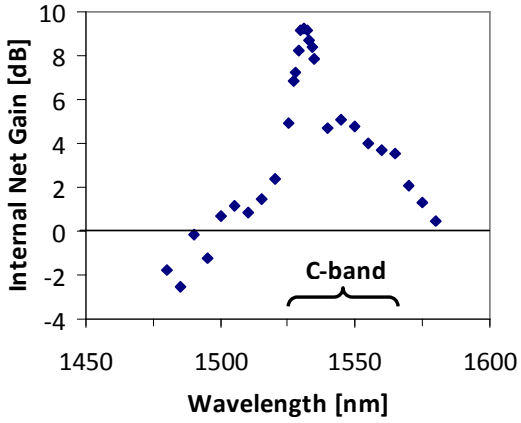


Figure 1. Internal net gain in an Al_2O_3 channel waveguide amplifier with an Er^{3+} concentration of 1.17×10^{20} cm^{-3} as a function of wavelength

Funding was provided by the Smartmix Memphis programme of the Dutch Ministry of Economic Affairs.

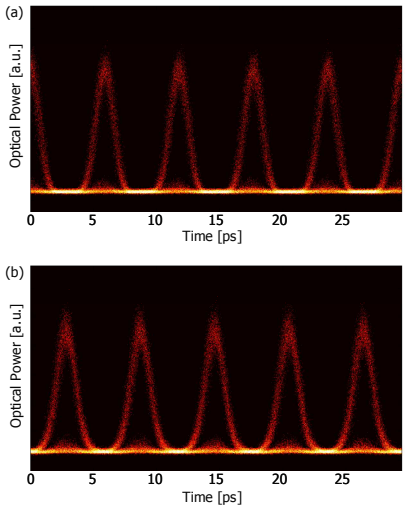


Figure 2. Transmission eye diagrams at 170 Gbit/s (a) without EDWA and (b) with EDWA and a launched signal power of 0.5 mW and counter-propagating pump power of 65 mW

IV. MONOLITHIC INTEGRATION OF $Al_2O_3:Er^{3+}$ WITH SOI WAVEGUIDES

In collaboration with colleagues from Ghent University, Belgium, the $Al_2O_3:Er^{3+}$ waveguide amplifiers were integrated with SOI passive waveguides [6]. SOI rib waveguides with a cross section of 450 nm × 220 nm were defined by deep UV lithography. A 1-µm-thick $Al_2O_3:Er^{3+}$ layer was grown directly on top by reactive co-sputtering [2] and 2.0-µm-wide ridge waveguides were defined by reactive ion etching to a depth of 270 nm [4]. The Er concentration was approximately 2×10^{20} cm^{-3}. In order to achieve highly efficient coupling the Si waveguides were tapered down to 100 nm over a length of 400 µm (inset, Fig. 3) to adiabatically transform the silicon waveguide mode to that of the $Al_2O_3:Er^{3+}$ waveguide. Losses in the Si-$Al_2O_3:Er^{3+}$ couplers were measured by comparing the transmission of 1533-nm light in $Al_2O_3:Er^{3+}$ waveguides both with and without Si-taper couplers, resulting in a value of 2.5 dB per coupler. Simulations indicate that this loss can be reduced to 0.5 dB. Signal enhancement measurements were performed in an $Al_2O_3:Er^{3+}$-Si-$Al_2O_3:Er^{3+}$ structure, with a method similar to that described in Sect. I, but with a pump wavelength of 1480 nm. The two $Al_2O_3:Er^{3+}$ sections had a total length of 9.5 mm, while the Si waveguide was 4 mm long, including the tapers. Figure 3 shows the signal enhancement as a function of pump power coupled into the waveguide at 1533 nm, indicating saturation at around 50 mW of input power.

To our knowledge, this is the first time that monolithic integration of rare-earth-ion-doped waveguides with SOI waveguides is achieved and signal enhancement is measured. These fundamental results will allow us to make use of potential Er-doped gain devices and their performance in passive Si photonic circuits. By improving the coupling losses and exploiting Yb^{3+} co-doping [7], significantly less than 1 cm of amplifier length will potentially provide net amplification at high speed across the entire telecom C-band, making such an amplifier highly interesting for silicon photonics.

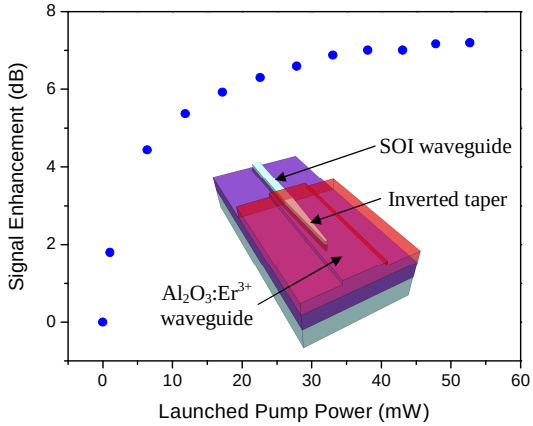


Figure 3. Signal enhancement (dB) vs. launched pump power in an $Al_2O_3:Er^{3+}$-Si-$Al_2O_3:Er^{3+}$ structure

V. CONCLUSIONS

Internal net gain over a wavelength range of 80 nm with a peak gain of 2.0 dB/cm at 1533 nm was obtained in $Al_2O_3:Er^{3+}$ amplifiers. A high-bit-rate amplifier was demonstrated, and active $Al_2O_3:Er^{3+}$ waveguides were monolithically integrated with passive SOI waveguides.

ACKNOWLEDGMENTS

The authors thank M. Dijkstra from the MESA+ Institute for Nanotechnology for assisting with fabrication of the samples, M. Costa e Silva, M. Gay, L. Bramerie, and J.C. Simon from the FOTON Laboratory, University of Rennes for assistance with the high-speed transmission measurements as well as G. Roelkens and R. Baets from the Photonics Research Group, Ghent University for preparing the SOI chip.

REFERENCES

[1] M. Lipson, “Guiding, modulating, and emitting light on silicon – challenges and opportunities,” J. Lightwave Technol., vol. 23, pp. 4222-4238, December 2005.

[2] K. Wörhoff, J. D. B. Bradley, F. Ay, D. Geskus, T. P. Blauwendraat, and M. Pollnau, “Reliable low-cost fabrication of low-loss $Al_2O_3:Er^{3+}$ waveguides with 5.4-dB optical gain,” IEEE J. Quantum Electron., vol. 45, pp. 454-461, May 2009.

[3] J. D. B. Bradley, L. Agazzi, D. Geskus, F. Ay, K. Wörhoff, and M. Pollnau, “Gain bandwidth of 80 nm and 2 dB/cm peak gain in $Al_2O_3:Er^{3+}$ optical amplifiers on silicon,” J. Opt. Soc. Am. B, vol. 27, pp. 187-196, February 2010.

[4] J. D. B. Bradley, F. Ay, K. Wörhoff, and M. Pollnau, “Fabrication of low-loss channel waveguides in Al_2O_3 and Y_2O_3 layers by inductively coupled plasma reactive ion etching”, Appl. Phys. B, vol. 89, pp. 311-318, October 2007.

[5] J. D. B. Bradley, M. Costa e Silva, M. Gay, L. Bramerie, A. Driessen, K. Wörhoff, J. Simon, and M. Pollnau, "170 Gbit/s transmission in an erbium-doped waveguide amplifier on silicon," Opt. Express, vol. 17, pp. 22201-22208, November 2009.

[6] L. Agazzi, J. D. B. Bradley, F. Ay, G. Roelkens, R. Baets, K. Wörhoff, and M. Pollnau, “Monolithic integration of erbium-doped amplifiers with silicon waveguides”, submitted.

[7] F. D. Patel, S. DiCarolis, P. Lum, and J. N. Miller, “A compact high-performance optical waveguide amplifier,” IEEE Photon. Technol. Lett., vol. 16, pp. 2607-2609, December 2004.

Widely Wavelength-selective $Al_2O_3:Er^{3+}$ Ring Laser

J. D. B. Bradley, L. Agazzi, F. Ay, K. Wörhoff, and M. Pollnau
Integrated Optical Microsystems Group,
MESA+ Institute for Nanotechnology, University of Twente
Enschede, The Netherlands
m.pollnau@ewi.utwente.nl

R. Stoffer
PhoeniX BV
P.O. Box 545, 7500 AM Enschede
The Netherlands

***Abstract*—Integrated $Al_2O_3:Er^{3+}$ channel waveguide ring lasers were realized on thermally oxidized silicon substrates. High pump power coupling into- and low output power coupling from-the ring is achieved in a straightforward design. Wavelength selection in the range 1532 to 1557 nm was demonstrated by varying the length of the output coupler from the ring.**

Keywords—waveguide laser; ring laser; erbium-doped laser; aluminum oxide

I. INTRODUCTION

Er-doped waveguide lasers are of interest for their emission at wavelengths around 1.55 µm in the third telecommunication window. A ring resonator laser offers a simple and straightforward solution with a low number and complexity of processing steps. Previously rare-earth-ion-doped ring lasers have been demonstrated in SiO_2 [1,2] and $LiNbO_3$ hosts [3]. $Al_2O_3:Er^{3+}$ offers several advantages compared with these materials. Compared to silica, it has a larger emission bandwidth, increasing the potential for tunability and generation of ultrashort pulses. In addition, its larger refractive index of ~ 1.65 (as compared to 1.45 in silica) allows for more compact devices and potentially reduces the threshold pump power due to a more tightly confined optical mode. As opposed to lithium niobate, it can be deposited on a number of substrates, including thermally oxidized silicon. This flexibility of deposition allows for monolithic integration of $Al_2O_3:Er^{3+}$ with other common integrated optical materials. Recently optical gain over a large bandwidth of 80 nm has been demonstrated in $Al_2O_3:Er^{3+}$ channel waveguides [4], opening the possibility for a tunable ring laser in this material.

We report on an integrated ring laser in $Al_2O_3:Er^{3+}$. By varying the degree of output coupling several laser wavelengths in the range 1532-1557 nm were demonstrated, exploiting the broad emission spectrum of this material.

II. FABRICATION AND DESIGN

A 500-nm-thick $Al_2O_3:Er^{3+}$ layer was deposited on an 8-µm-thick thermally oxidized 10-cm-wide standard Si wafer by reactive co-sputtering from high-purity metallic targets [5]. The resulting Er concentration was approximately 1×10^{20} cm^{-3}. Subsequently, 1.5-µm-wide channel waveguides were defined in the $Al_2O_3:Er^{3+}$ layer using standard lithography and reactive ion etching [6]. A 5-µm-thick SiO_2 top-cladding layer was deposited by plasma-enhanced chemical vapour deposition and end facets were prepared by dicing. The resulting channel waveguides were single-mode around 1550 nm for both TE and TM polarization and multimode at the 980-nm pump wavelength.

A schematic of the $Al_2O_3:Er^{3+}$ ring laser is shown in Fig. 1. The ring cavity was designed such that a high Q-factor of the ring resonator is obtained when the ring coupler (Coupler 1 in Fig. 1) permits strong coupling. Such a directional coupler exhibits stronger coupling for longer wavelengths, i.e. for the laser wavelength in a Stokes-shifted emitting laser, while coupling at the shorter pump wavelength can be minimized in order to launch a significant part of the pump power into the ring. The coupler lengths were varied from 350 to 600 µm in increments of 50 µm. The resonator length was varied from 2.0 to 5.5 cm.

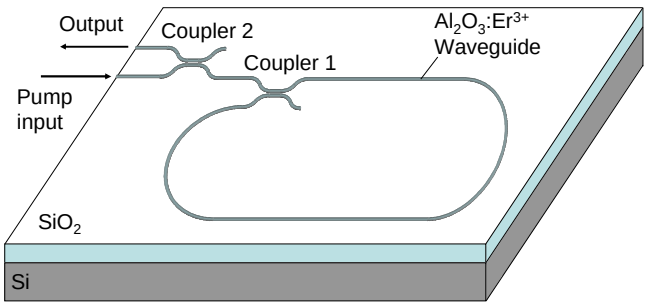


Figure 1. Schematic of $Al_2O_3:Er^{3+}$ ring laser.

A fiber array unit (FAU) was aligned simultaneously to the input and output ports of the chip. Pump light from a 980-nm diode laser was coupled to the chip through one fiber of the FAU. The output signal was collected in a second fiber of the FAU and the optical power and spectral behavior was measured.

III. LASER PERFORMANCE

The laser output power is shown as a function of launched pump power for devices with coupler lengths ranging from 400 to 550 µm in Fig. 2. The coupler length and main lasing wavelength are indicated. The highest slope efficiency of 0.11% was observed in a 5.5-cm-long resonator, with a TE-polarized output power of up to 9.5 µW measured at 19 mW launched pump power. The threshold pump power varied from 6.4 to 15.5 mW. This threshold power is significantly lower than those reported in previous Er-doped ring lasers [1,3].

This work is supported by the Dutch Smartmix-Memphis project.

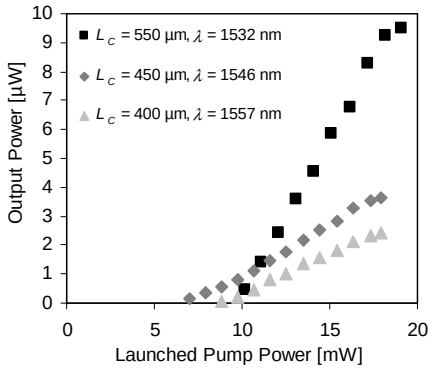


Figure 2. On-chip integrated laser output power vs. pump power launched into the chip for varying output coupler length. The coupler length and main lasing wavelength are indicated.

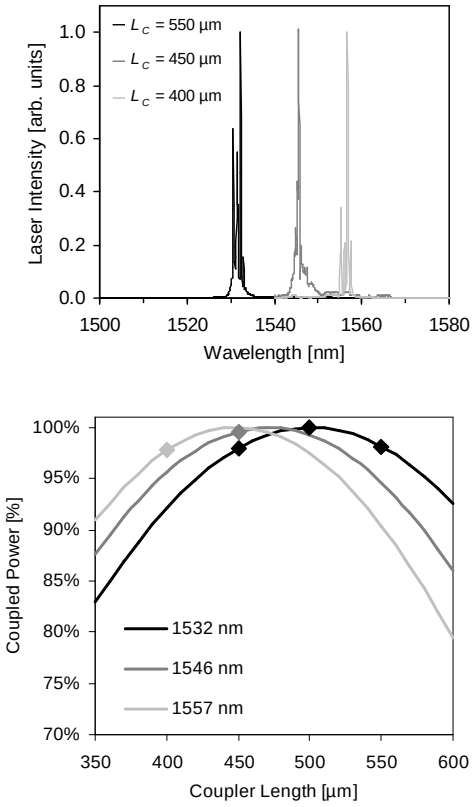


Figure 3. (a) Laser output spectra for coupler lengths L_C of 550, 450, and 400 µm.; (b) simulated coupled power in Coupler 1 vs. coupler length for the observed laser wavelengths and TE polarization. The coupler lengths for which lasing was observed are indicated by the diamonds on the curves.

Laser output spectra for three devices with different wavelengths are shown in Fig. 3a. Because of the long resonator length, which results in a free spectral range of between 0.3 and 0.8 pm, the spectra include many longitudinal modes. The laser selects the wavelength and polarization with lowest threshold power, which is directly affected by the resonator roundtrip losses and the percentage of coupled power at Coupler 1. A greater amount of coupled power results in a lower total roundtrip loss and a lower lasing threshold. Accordingly, in Fig. 3b the predicted percentage of coupled power is shown versus Coupler 1 length for the three observed main laser wavelengths and TE polarized light. At a coupler length of 400 µm a significantly higher percentage of coupled power is predicted at 1557 nm where lasing was observed. When the coupler length is increased to 550 µm, greater coupling is predicted at 1532 nm, and the laser output shifts to this wavelength.

Besides the outcoupling degree, the emission cross section also determines the roundtrip gain. The most common lasing wavelength was close to 1532 nm, at the peak emission cross section of the $^4I_{13/2} \rightarrow {}^4I_{15/2}$ Er^{3+} transition [4]. The high gain per unit length at this wavelength makes it more likely that round-trip net gain is achieved in the cavity, and lasing is possible even for a lower degree of coupling at Coupler 1. This effect is apparent for a coupling length of 450 µm (Fig. 3b). Besides the primary laser output around 1546 nm where the predicted coupling efficiency was 99.6%, a second set of laser lines around 1532 nm, where the coupling efficiency was 97.9%, is emitted.

The wavelength variation of the laser output is supported by the broadband gain observed [4]. By adjusting the coupling length of Coupler 1 in a single device, it would be possible to change the lasing wavelength. This concept could be applied to achieve a tunable on-chip ring laser.

IV. CONCLUSIONS

We have demonstrated an $Al_2O_3:Er^{3+}$ laser based on a ring-resonator design which allows strong coupling of pump light into the ring while simultaneously allowing only a small percentage of output coupling at the signal wavelength. Due to the broad gain spectrum in $Al_2O_3:Er^{3+}$, the output wavelength varied between 1532 to 1557 nm, over a large section of the telecom C-band, in devices with different output coupler lengths. Design enhancements will lead to wavelength tunability.

V. REFERENCES

[1] K. Hattori, T. Kitagawa, M. Oguma, Y. Hibino, Y. Ohmori, and M. Horiguchi, "Er-doped silica-based planar ring resonator," Electron. Commun. Jpn., vol. 77, pp. 62-72, November 1994.

[2] H.-K. Hsiao and K. A. Winick, "Planar glass waveguide ring resonators with gain," Opt. Express, vol. 15, pp. 17783-17797, December 2007.

[3] W. Sohler, B. K. Das, D. Dey, S. Reza, H. Suche, and R. Ricken, "Erbium-doped lithium niobate waveguide lasers," IEICE Trans. Electron., vol. E88-C, pp. 990-997, May 2005.

[4] J. D. B. Bradley, L. Agazzi, D. Geskus, F. Ay, K. Wörhoff, and M. Pollnau, "Gain bandwidth of 80 nm and 2 dB/cm peak gain in $Al_2O_3:Er^{3+}$ optical amplifiers on silicon," J. Opt. Soc. Am. B, vol. 27, pp. 187-196, February 2010.

[5] K. Wörhoff, J. D. B. Bradley, F. Ay, D. Geskus, T. P. Blauwendraat, and M. Pollnau, "Reliable low-cost fabrication of low-loss $Al_2O_3:Er^{3+}$ waveguides with 5.4-dB optical gain," IEEE J. Quantum Electron., vol. 45, pp. 454-461, May 2009.

[6] J. D. B. Bradley, F. Ay, K. Wörhoff, and M. Pollnau, "Fabrication of low-loss channel waveguides in Al_2O_3 and Y_2O_3 layers by inductively coupled plasma reactive ion etching," Appl. Phys. B, vol. 89, pp. 311-318, October 2007.

Investigating Planar Integrated Glass Cantilevers Utilizing Bragg Gratings and Mechanical Resonance in a Vacuum

Lewis G. Carpenter, Christopher Holmes, Helen L. Rogers, James C. Gates and Peter G.R. Smith
Optoelectronic Research Centre
University of Southampton
Southampton, UK
lc906@orc.soton.ac.uk

Abstract—**Glass-micro-cantilever Bragg grating devices incorporate both micro-machining and direct UV writing. This novel combination of fabrication techniques reduce construction times on photolithography and allow rapid prototyping. It utilizes the cantilevers mechanical resonance to allow it to be used to detect the change in the air's damping coefficient with pressure.**

Keywords-component; Cantilevers; Planar Integrated Optics; Bragg Gratings;

I. INTRODUCTION

We demonstrate a glass cantilever based on a unique micromachining and etching approach, combined with UV writing. Here we explore the changes in the resonant mechanical flexure modes with pressure. Cantilevers are ubiquitous ultra sensitive force sensors used in applications such as Atomic Force Microscopy (AFM), mass sensing, and acoustic transducers. Conventionally cantilevers are fabricated by photolithography; however in this paper we demonstrate a new approach based on micromachining silica-on-silicon substrates. Furthermore this approach is compatible with Direct UV writing of optical waveguide channels and Bragg gratings [1]. The Bragg gratings provide a method of interrogating the deformation of the cantilever.

II. GLASS CANTILEVER FABRICATION

A. Fabrication

The planar substrates consist of three layers of matched refractive index silica on silicon substrate. The middle core silica layer is doped with germanium promoting photosensitivity and allowing the ability to UV write waveguides. Definition of the cantilever is achieved by micromachining, grooves into the silica layer with a precision dicing saw. This allows the length and width of the cantilever to be predefined. After micromachining waveguides and Bragg reflectors are direct UV written into the photosensitive layer. Finally the silicon substrate is etched with heated KOH to liberate the silica cantilever from the substrate.

B. Micromachining Advantages

There are several advantages of micromachining over standard etching with masks, these include:

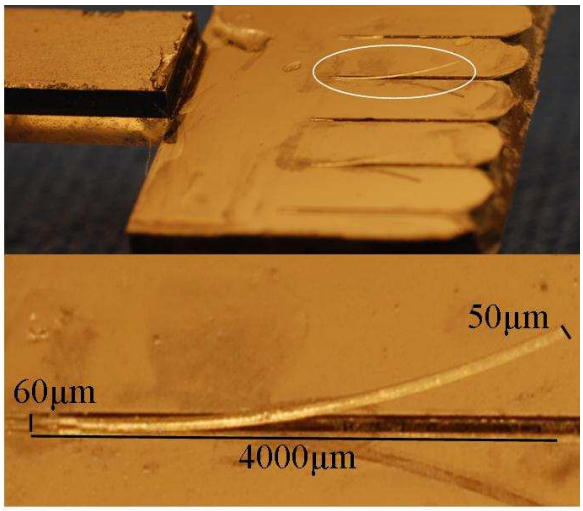


Figure 1. The top image shows the 20mm by 10mm substrate with the pigtail, the cantilever is circled. The bottom image shows a close up of the cantilever with approximate measurements.

- Well defined vertical side walls, rather than sloping ones caused by etching along crystal boundaries
- Overall roughness (R_a) of ~10nm.
- Freedom from mask expense and time investment, thus allowing rapid prototyping

The combination of micromachining, UV writing and the planar geometry allows for smaller devices with many cantilevers and more than one Bragg grating on each cantilever. Simple fiber coupling allows these devices to be multiplexed and distributed over a large area.

III. GLASS CANTILEVER OPERATION

A. Cantilever Selection

The experiment was undertaken using a 20mm by 10mm substrate, with 9 cantilevers, each having 9 Bragg gratings along its length with central wavelengths each 5nm apart from 1525nm to 1560nm.

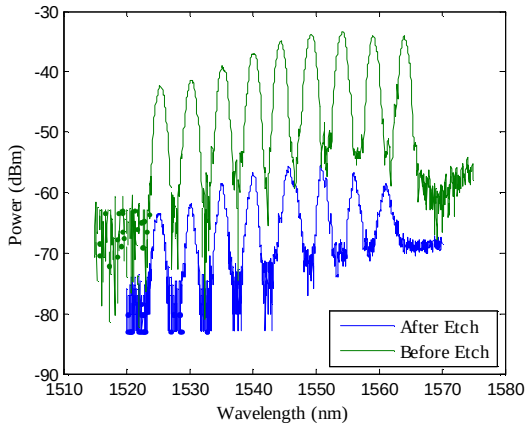


Figure 2. Shows the reflected spectra from the Bragg gratings of cantilever, the final grating at 1565nm was damaged during etching.

B. *Finding the Mechanical Resonace*

The reflection spectra were collected from a cantilever using a broadband source and an optical spectrum analyzer, as shown in figure 2. The 6th grating was chosen to be interrogated because it had the biggest central Bragg wavelength shift from pre and post etching thus it was assumed to be the most sensitive to further stress induced shifts. A tunable laser was used to match the point of highest gradient of reflection of grating 6, which was on the grating's shoulder at 1550.9nm. A piezoelectric transducer was then attached to the substrate and an acoustic signal was sent through the transducer and swept in frequency from 0 to 100 kHz. The reflected optical signal was measured with a photodiode and phase sensitive technique. The largest mechanical resonance was found to be at 25.7 kHz.

IV. Investigating the Cantilever's Mechanical Resonance with Pressure

A. *Mechanical Resonance at vacuum*

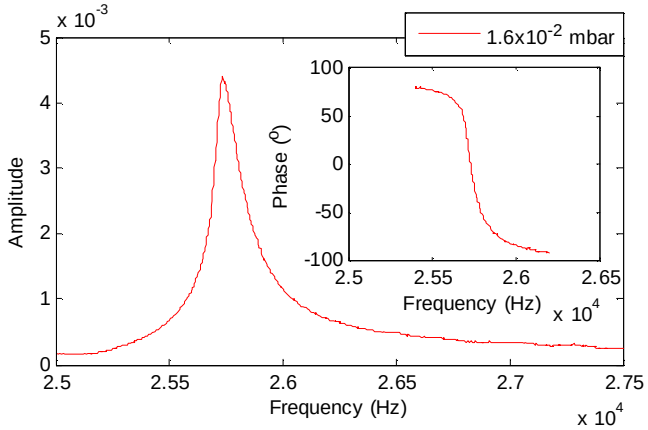


Figure 3. Frequency response showing mechanical resonce of the cantilever. The phase response is shown in the inset and exhibates the expected π phse.

By placing the sample in a vacuum chamber the resonance response of the sample was investigated as a function of pressure. Figure 3 shows the resonance at $1.6\text{x}10^{-2}$ mbar. Resonance curves were taken over a pressure range of $1.6\text{x}10^{-2}$ mbar to atmosphere.

B. *Analytical Data Fit*

A damped driven oscillator model [2] was used to fit the resonance data according to Equation 1:

$$A(\omega) = \frac{\frac{F_o}{m}}{[(\omega_o^2 - \omega^2)^2 + 4\gamma^2\omega^2]^{\frac{1}{2}}}. \quad (1)$$

Where A is the amplitude, F_o is the maximum applied force, m is the mass, ω is the angular frequency, ω_o is the resonant angular frequency and γ is the damping coefficient.

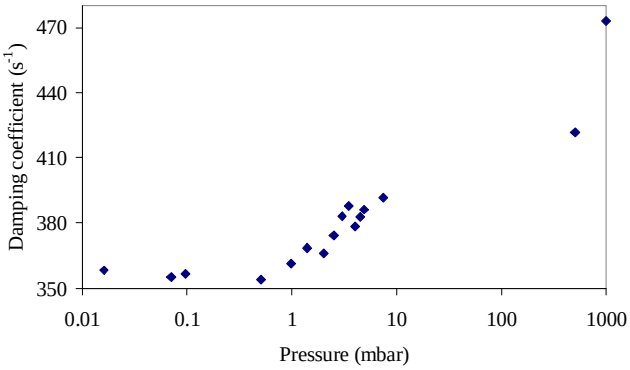


Figure 4. Fitted damping coefficient as a function of pressure.

The damping coefficient is shown in figure 4 and agrees with the trends reported by Kumazaki [3], for a resonant optical fiber. Figure 4 also exhibits the characteristic transition from molecular flow to viscous flow at 1 mbar as the pressure is increased.

Conclusion

Here we have demonstrated an integrated glass cantilever using Bragg gratings to interrogate the resonant mechanical characteristics. We have also shown that placing the glass cantilever in a vacuum changes the characteristics of the resonance curve for its fundamental mechanical flexure mode. Similar results have been shown by Kumazaki. We shall show our latest application of these fabrication techniques.

References

[1] James C. Gates, Christopher Holmes, Benjamin D. Snow, Corin B.E. Gawith and Peter G.R. Smith, "UV written evanescent devices fabricated in micro-structured substrates for optofluidics", Optical sensing and sensors OCIS codes: (280.4788), (130.3120) Integrated optics devices.

[2] G. R. Fowles and G. L. Cassiday, Analytical Mechanics. Fort Worth: Harcourt Brace College, 1986.

[3] H. Kumazki, S. Inaba and K. Hane, "Pressure dependence of resonce characteristics of the microcantilever fabricated form optical fibre," in Vacuum, vol. 47, numbers 6-8, Elsevier Science, 1996, pp. 475–477.

Integrated acoustic and acousto-optic filters using domain inversion

D. Yudistira, D. Janner
ICFO-Institut de Ciencies Fotoniques
Castelldefels (Barcelona), Spain
didit.yudistira@icfo.es

V. Pruneri
ICFO-Institut de Ciencies Fotoniques
Castelldefels (Barcelona), Spain
ICREA -Institució Catalana de Recerca i Estudis Avançats
Barcelona, Spain

Abstract—**Domain inversion superlattices combined with co-planar electrodes allow novel waveguide acoustic and acousto-opic filtering. In this paper we show that efficient devices can be achieved through an appropriate fabrication of domain inverted and electrode geometries.**

Domain inversion; acoustic superlattices; acousto-optics fitlers.

I. INTRODUCTION

In the last decades, the introduction of interdigitated transducers (IDTs) [1] to generate surface acoustic wave (SAW) in ferroelectric crystals, lead to the spreading of acoustic-based devices in many fields. Among the applications are: RF filter for wireless communications, non-destructive testing (NDT), and bio-medical sensing. Recently, the use of periodically poled lithium niobate (PPLN) in combination with coplanar RF electrodes was used for SAW and bulk waves in novel configurations, named acoustic superlattices (ASLs) [2]. One of the main advantages of ASL based transducers is that the elastic wavelength is related to the period Λ of the PPLN compared to IDTs' period that needs to be Λ/2. Moreover, the coplanar electrode configuration is much simpler and easier to impedance-match.

The combination of acoustic and optical signals brings many interesting applications, particularly in the field of polarization converters. Acousto-optic (AO) polarization converters are key elements in many photonic applications, such as wavelength division multiplexing (WDM), spectral filtering of supercontinuum sources. State-of-the-art integrated AO filters typically combine IDTs and optical medium (waveguide) in a single piezoelectric crystal. The potential drawback of using IDTs for this device, however, lies in the fact that the optical waveguide is usually covered by the metallic layer of the IDTs, thus increasing the optical loss. Employing ASL for acoustic wave generation can potentially overcome the loss issue [3].

In this work we will present recent results and improved geometries for acoustic wave generation based on ASL using co-planar linear electrodes and on their application in AO filters. Along the way we demonstrate the generation of acoustic longitudinal bulk wave (L-BAW) with high efficiency using a tapered electrode on ASL.

II. SUPERLATTICE COUSTIC FILTERS

Co-planar electrode geometry is employed allowing the electric field to be confined in the crystal region between the electrodes and close to the substrate surface[4]. This allows for direct excitation of both SAW and bulk acoustic waves, reported for the first time in ref. 2.

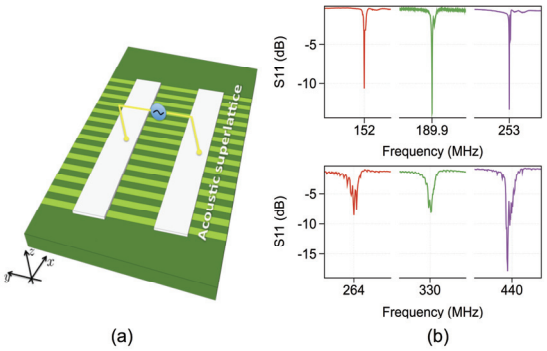


Figure 1. (a) Proposed coplanar electrode ASL transducer. (b) S_{11} for SAW (*upper*) and L-BAW (*lower*) generation in different ASL's period Λ.

The scheme of the fabricated device is outlined in Fig. 1(a). The ASLs were prepared on a 500 μm thick ZX-cut LiNbO3 substrate with various lattice periods Λ=15, 20, and 25 μm with total length 10 mm. The domain inversion was realized through electric field poling and 200 nm-thick coplanar aluminum (Al) electrodes oriented along the x-axis were deposited on the ASL. The electrode width was chosen to be 100 μm with a metallization ratio (MR) of 0.5. The RF characterization shown in Fig. 1(b) was performed with PNA-X Agilent network analyzer. In the upper part of Fig. 1(b) the measured dips in the S11 correspond to the resonance frequencies f_{SAW}= 253, 189.7, and 152 MHz. At those frequencies the SAW velocities are 3795, 3794, and 3800 m/s, respectively. The comparison with the theoretical velocity of SAW on ZX-cut $LiNbO_3$ is 3798 m/s, confirming SAW generation. As reported in Fig. 1(b)-bottom, L-BAW that travels with $v_{L\text{-}BAW}$=6600 m/s was also observed with resonance frequencies measured at around 440, 330, and 264

MHz. There is thus a good agreement between calculated and measured frequencies for both SAW and L-BAW. Furthermore, the transduction efficiency of the SAW represented by the effective electromechanical coupling coefficient is about 0.3 %, which is close to 0.53 % obtained from the calculation for ZX-cut $LiNbO_3$.

III. SUPERLATTICE ACOUSTO-OPTIC FILTERS

The above ASL transducer configuration was used for AO filters. As the ASL transducer is able to generate both SAW and L-SAW, two types of AO device were considered depending on the type of the acoustic wave being employed, namely surface AO and bulk AO filters. In both cases, the AO filtering relies on the transverse electric (TE) to transverse magnetic (TM), or vice versa (TM to TE), polarization conversion of optical wave. The conversion efficiency between TE-TM is defined by $\eta(\Delta=0)=P_M(x=L_i)/P_E(x=0)=\sin^2(\kappa L_i)$, where κ denotes the coupling coefficient and L_i is the interaction length.

For surface AO filter, a mono-modal Ti-$LiNbO_3$ optical waveguide was fabricated. The waveguide was positioned parallel to and at the center between the electrodes. The edges of ASL were polished at $\theta=8^o$ to minimize back reflection from the acoustic wave.

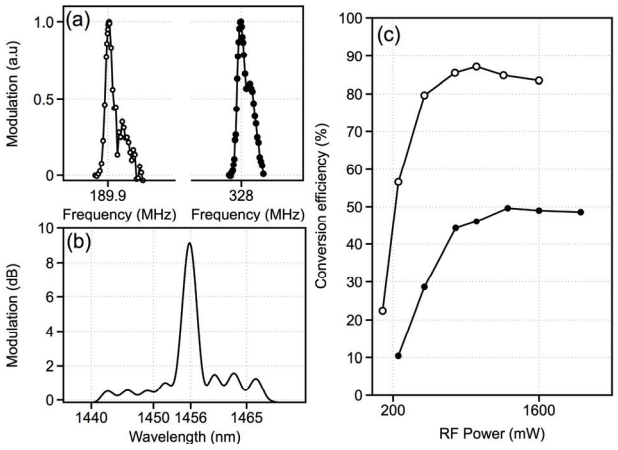


Figure 2. (a) AO modulation of (*left*) bulk and surface (*right*) AO filter as a function of RF frequency for RF power of 500 mW. (b) AO modulation vs optical wavelength from surface AO filter. (c) Power conversion efficiency versus RF power from (opened circle) surface AO and (filled circle) bulk AO, respectively.

A Supercontinuum laser source was used to generate a broad spectrum in the wavelength region of interest. To couple the light into and out of the device, a pair of fiber collimator and of single mode fiber block was used for the bulk AO and surface AO samples, respectively. For acoustic wave generation, an amplified RF signal generator was employed and finally an Optical Spectrum Analyzer (OSA) was used to monitor the optical output.

Measurements were carried out using various RF input power P_{rf} ranging from 200 mW to 1600 mW. For each P_{RF}, RF frequency (f_{RF}) was swept around resonance frequency of the ASL transducer with Λ =20 μm, f_{SAW} (f_{BAW}), f_{SAW}=189.7 MHz and f_{BAW}=330 MHz (Fig. 2(a)). After that, the optical output was measured around the phase matching wavelengths, λ_S=1456 nm (surface AO) and λ_B=1472 nm (bulk AO), respectively. The result of surface AO filter is shown in Fig. 2(b); the -3-dB optical bandwidth was measured around $\Delta\lambda_S$=2.51 nm. The polarization conversion efficiency (η), i.e. the ratio between converted and transmitted power in the absence of RF signal, as a function of RF power for surface and bulk AO is shown in Fig. 2(c).

IV. TAPERED ELECTRODES ON ASL

With straight co-planar electrodes, the surface AO device shows good performance while the bulk AO device does not perform as good as the surface one (Fig. 2(c)). For this reason a special design based on a coplanar curved electrode approach is proposed to increase the efficiency of the bulk AO device. Using a tapered geometry for the RF electrodes, an improved impedance matching at the frequencies of bulk waveguides can be obtained [5].

The MR was fixed at 0.5 along x-axis and the ASL transducer with period Λ of 15 μm was used. Fig. 3 shows a broader S11 spectrum as a result of tapered electrode. A strong dip (-60 dB) at frequency around 440 MHz was obtained showing a quite large transduction from microwave to acoustic wave (L-BAW) compared to the ASL using uniform (straight) electrode shown previously. These results are expected to improve the bulk AO. AO measurements are being performed and will be presented at the conference.

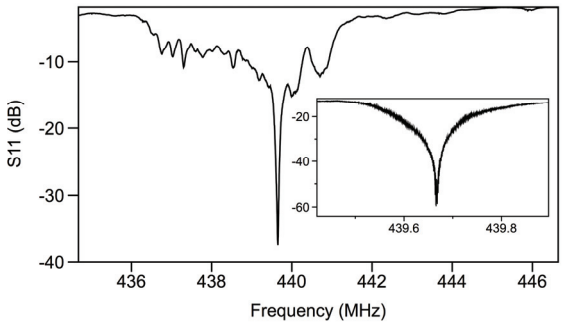


Figure 3. S11 as a function of RF frequency for L-BAW from ASL transducer with curved electrode. Inset is an expanded view around the dip.

REFERENCES

[1] R. M. White and F. W. Voltmer, "Direct piezoelectric coupling to surface elastic waves", App. Phys. Lett., vol.7, pp. 314-316, 1965.

[2] D. Yudistira, S. Benchabane, D. Janner and V. Pruneri, "Surface acoustic wave generation in zx-cut linbo3 superlattices using coplanar electrodes", App. Phys. Lett., vol.95, no.5, pp. 052901, 2009.

[3] D. Yudistira, D. Janner, S. Benchabane and V. Pruneri, "Integrated acousto-optic polarization converter in a ZX-cut LiNbO3 waveguide superlattice", Opt. Lett., vol.34, no.20, pp. 3205-3207, 2009.

[4] Y.-q. Lu, Y.-y. Zhu, Y.-f. Chen, S.-n. Zhu, N.-b. Ming and Y.-J. Feng, "Optical properties of an ionic-type phononic crystal", Science, vol.284, no.5421, pp. 1822-1824, 1999.

[5] N. Goto and Y. Miyazaki, " "Design of tapered SAW waveguide for wavelength-selective optical switches using weighted acoustooptic interaction", Electrical Engineering in Japan, vol.154, no.1, pp. 36-46 2006.

Cantilever deflection read-out with a grated waveguide optical cavity

S.V. Pham, L.J. Kauppinen, M. Dijkstra, H.A.G.M. van Wolferen, R.M. de Ridder and H.J.W.M. Hoekstra
MESA$^+$ Institute for Nanotechnology, University of Twente
P.O. Box 217, 7500 AE Enschede, The Netherlands
Tel.+31 53 489 2816, Fax. +31 53 489 3343
s.v.pham@ewi.utwente.nl

***Abstract* - We propose a novel and highly sensitive mechano-optical device for gas-sensing through nano-displacements, based on micro-cantilevers, supplied with a selective gas absorbing layer (Pd), suspended above a Si_3N_4 grated waveguide (GWG). We present the simulation and preliminary experimental results, which indicate the sensing of nanodisplacements, an important intermediate step for the gas-sensing purpose.**

Keywords - grated waveguide; microcantilever; gas-sensing; mechano-optical sensor

I. INTRODUCTION

Waveguide gratings are often referred to as one-dimensional (1D) photonic crystals, which have a periodic variation of the dielectric constant along the propagation direction. An important property of a grated waveguide (GWG) is the occurrence of fringes in the transmission spectrum near the stop-band edges. It is well known that these oscillations are due to Fabry-Perot resonances of Bloch modes propagating in the cavity defined by the grated section [1]. Based on this property of GWGs, a demonstration of the potential of such structures for sensing of index changes was reported using a cavity with a high quality factor (high Q) [2]. In addition, the potential of micro-cantilevers to convert concentration changes efficiently into displacements was also demonstrated [3-6]. For these reasons, we were motivated to integrate a GWG and a microcantilever into one chip as a novel compact mechano-optical sensor for hydrogen gas. Such a sensor enables the detection of the concentration of hydrogen gas through the change of nanodisplacements of the microcantilever, which is monitored optically by shifts of resonance peaks of the transmission spectrum [7]. In this paper we present the simulation results and preliminary optical characterization results of the fabricated chips, which confirm the possibility of such a GWG-cantilever integration as a platform for gas-sensing.

II. WORKING PRINCIPLE AND SIMULATION

A picture of the envisioned device is given in Fig.1. The device consists of two main components which are integrated: a grated waveguide as an optical read-out, and a micro-cantilever suspended above the GWG. The device is functionalized by depositing a sensitive layer on top of the cantilever; for hydrogen (H_2) sensing, palladium (Pd) can be used. Absorption of H_2 into Pd will cause the cantilever to bend [3-6]. This bending of the cantilever can then be optically detected by exploiting the properties of the GWG. The presence of a dielectric object, in this case a cantilever, in the evanescent-field region of the GWG may lead to the occurrence of propagating modes for wavelengths inside the stop band of the grating, and so to resonances (defect modes) inside the stop band [2,7]. As the cantilever approaches the grating, the first near band edge resonance peak is pulled inside the stop band and its spectral width decreases. This effect can be used for the detection of cantilever displacements and so the detection of gas concentration.

Figure 2 shows the 2D cross-sectional model of the device. A 2D bidirectional eigenmode propagation (BEP) method [6] was applied to this model to analyze the nanodisplacement sensing, through the effect of the suspended microcantilever on the output transmission spectrum. As a result, the spectral shift due to the change of the gap between the GWG and the cantilever was observed. A critical gap width, at which the microcantilever starts influencing the evanescent-field region of the GWG, is calculated to be ~ 400 nm (as shown in Fig.3). On the other hand, if a thin cantilever is coated with a metal layer, the evanescent field of the GWG may reach the metal layer through the thin-film and cause an optical loss. Partial metal coating can be used to avoid such a loss. Simulations using a channel mode solver were carried out to estimate the optical absorption. The result shows that the safety distance between the metal tip and the oxide tip, where the cantilever is not covered in the region that overlaps the modal field, is estimated to be 15 μm.

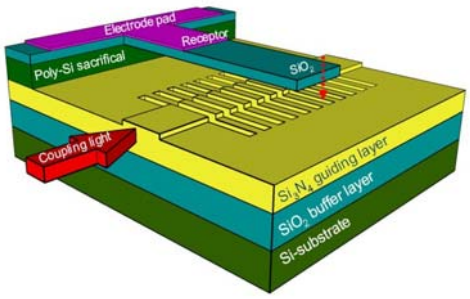


Fig.1 . The grated waveguide-cantilever device

This research is financially supported by MEMSland, a project of the Point One program funded by the Ministry of Economic Affairs and the STW Technology Foundation through project TOE. 6596

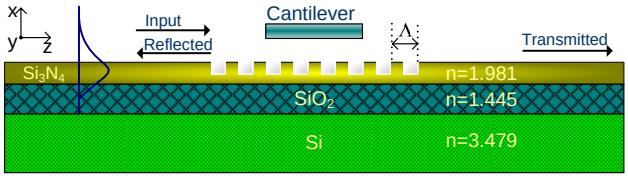


Fig.2. 2D cross-sectional model of the device

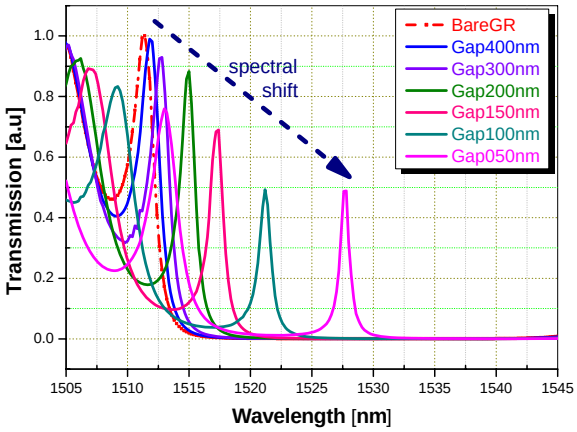


Fig.3. Simulated transmission spectra of a 125-period grating, with a 800 nm thick cantilever suspended above it. A spectral shift due to the change of the gap between the GWG and the cantilever was observed

III. Fabrication and Characterization

A fabrication process was designed and optimized in order to obtain good devices with a uniform grating and a low initial bending of the cantilever. A grating was defined in a shallow ridge silicon nitride (Si_3N_4) waveguide (WG), using laser interference lithography (LIL). The cantilever was released using sacrificial layer etching techniques. The cantilever core material was chosen to be silicon dioxide (SiO_2). Further details of the fabrication process will be described and published elsewhere. For preliminary optical characterization, a series of cantilevers with various lengths of the metal-pads was fabricated. The purpose of changing lengths of metal-pads is to cause a difference in the surface stress, and so in initial bending of the cantilevers. This resulted in different gaps between the GWG and the cantilever (as illustrated in Figs. 4a and 4b). A small metal area (Fig.4a) produces a very flat cantilever and the gap is the same as the thickness of the sacrificial layer of ~250 nm, while a large metal area (Fig.4b) causes an initial bending of ~130 nm, corresponding to a gap of ~380 nm. The difference in gaps leads to different spectral shifts of the transmission spectra as shown in Fig.4c. The first resonant peak next to the band edge of the bare grating (without a suspended cantilever) is at a wavelength of 1488.8 nm. This peak is shifted to wavelengths of 1489.2 nm and 1490.2 nm for gaps of ~380 nm and ~250 nm, respectively. These experimental results are in agreement with simulation results and give good confidence in the gas sensing capability of the device.

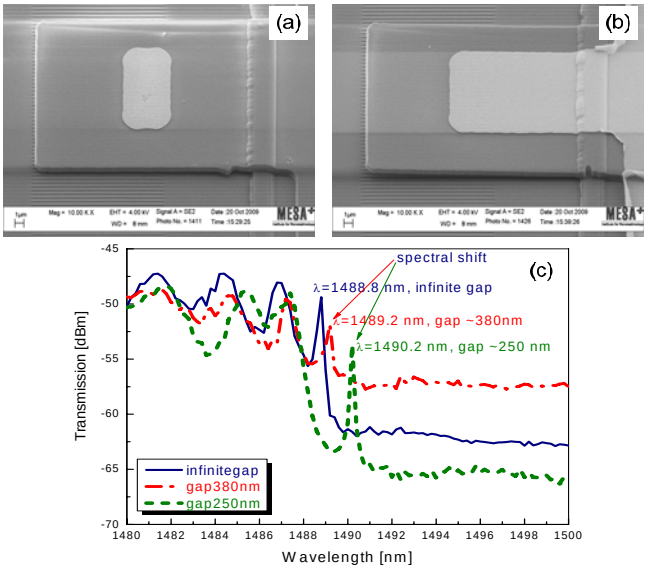


Fig.4. Fabricated chips (a) & (b) and their measured transmission spectra (c) of a 250-period grating, with a 800 nm thick cantilever suspended above it. Gaps between the GWG and the cantilever in (a) and (b) are different, owing to different metal pad lengths leading to differences in stress and so initial bending

IV. Conclusions

We have presented simulations and preliminary experimental results of a novel and compact mechano-optical sensor for nanodisplacements aimed for gas-sensing. The experimental results prove the potential of the considered integrated GWG-cantilever set-up as a platform for gas sensors.

References

[1] G.J. Veldhuis, J.H. Berends, R.G. Heideman, and P.V. Lambeck, “An integrated optical Bragg-reflector used as a chemo-optical sensor,” Pure and Applied Optics, vol. 7, pp. L23-L26, 1998.

[2] W.C.L. Hopman, H.J.W.M. Hoekstra, R. Dekker, L. Zhuang, R.M. de Ridder, “Far-field scattering microscopy applied to analysis of slow light, power enhancement, and delay times in uniform Bragg waveguide gratings,” Opt. Express, vol. 15, pp. 1851-1870, 2007.

[3] Y.-I. Chou, H.-C. Chiang, and C.-C. Wang, “Study on Pd functional-ization of microcantilever for hydrogen detection promotion,” Sensors and Actuators B: Chemical, vol. 129 pp. 72-78, 2008.

[4] M. Álvarez, and J. Tamayo, “Optical sequential readout of micro-cantilever arrays for biological detection,” Sensors and Actuators B: Chemical, vol. 106, pp. 687-690, 2005.

[5] J. Fritz, “Cantilever biosensors,” The Analyst, vol. 133, pp. 855-863, 2008.

[6] Z. Hu, T. Thundat, and R.J. Warmack, “Investigation of adsorption and absorption-induced stresses using microcantilever sensors,” J. Appl. Phys., vol. 90, pp. 427–431, 2001.

[7] L.J. Kauppinen, H.J.W.M. Hoekstra, M. Dijkstra, R.M. de Ridder, and G.J.M. Krijnen, “Grated waveguide optical cavity as a compact sensor for sub-nanometre cantilever deflections,” Proc. 14th European Conference on Integrated Optics (ECIO2008), pp. 111-114, 2008.

Micro-pin Photodiode-Antenna Chip Packaged for Sub-THz Applications

R. Zhang, H.-G. Bach, R. Kunkel, G.G. Mekonnen, D. Schmidt and Ö. Karpuzi
Fraunhofer Institute for Telecommunications, Heinrich-Hertz-Institute
Berlin, Germany
Ruiyong.Zhang@hhi.fraunhofer.de

***Abstract*—A Sub-THz transmitter module based on a micro-pin-antenna chip and a silicon lens for focusing RF radiation is presented. The radiated power of the module is up to -13.5 dBm and exhibits a power radiation of 1 µW at 200 GHz and higher.**

Keywords-waveguide integrated micro-pin photodiode; monolithic antenna; sub-THz; heterodyne signal generation and detection

I. INTRODUCTION

The THz-technology has been impressively developed in the last years due to great interest in applications of fiber-based radio and THz-spectroscopy. One of the great challenges in the THz technology is the realization of emitters and receivers. The advantage of using photodiodes (PD) for the generation of CW THz signals is the high output power. An UTC-PD with 148 µW and 25 µW output power at 457 and 914 GHz, respectively, has being reported in [1].

In one of our recent papers [2], we described the fabrication and the characteristics of the monolithically integrated pin photodiode and a planar antenna chip. In [3] a short report on a packaged sub-THz transmitter module was published. The main work of this paper is to present the detailed results of the module characteristics and its applications also to higher frequencies.

II. MICRO-PIN PHOTODIODE AND MODULE PACKAGING

To build widely tunable THz transmitters, not only the photodiode but also the antenna should have broadband characteristics. Therefore we designed a 5x7 µm^2 photodiode with more than 150 GHz bandwidth as shown in Fig. 1 and a frequency independent antenna, which comprises a logarithmic periodic circularly-toothed structure which is indicated in Fig. 1 (inset-lower). The micro-pin photodetector chip with optimized evanescent coupling scheme comprises a pin-mesa PD, an antenna and a spot size converter for effective fiber-chip coupling. All devices are integrated on a semi-insulating waveguide layer stack being composed of three quaternary optical guiding layers embedded within InP and an upper thicker waveguide layer (Fig.1, inset-top). A contact and matching layer with protrusion length L controls the optical intensity distribution in the device, it provides the refractive index match between the waveguide and the absorber and serves as n-contact layer with low resistance [4]. The intrinsic InGaAs absorption layer with 200 nm thickness provides a short transit time within the PD. The pin-mesa with a size of 5x7 µm^2 has a capacitance of about 21 fF and drives the antenna with approximately 70 Ω feedpoint impedance. The whole transmitter was fabricated on InP:Fe substrate employing metal organic vapor phase epitaxy (MOVPE) for the layer stack of the micro-pin PD.

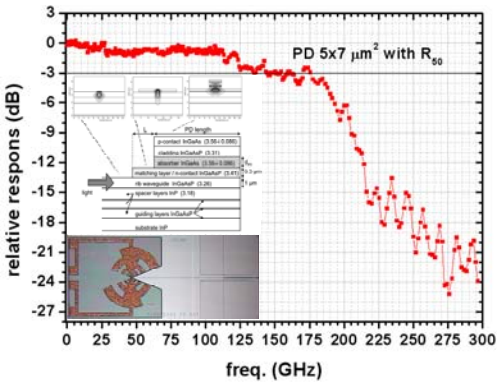


Figure 1. Frequency response of a micro-pin photodiode, inset-top: layer stack of the chip, fabricated micro-pin antenna chip (inset-lower).

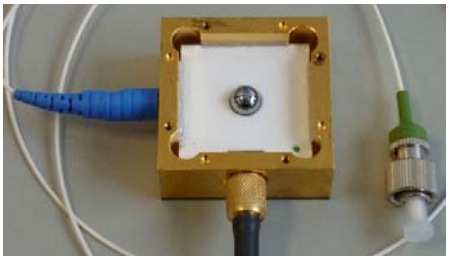


Figure 2. Packaged micro-pin antenna transmitter module with a Si-lens and a pig-tailed fiber.

The pin-antenna chip was packaged into a transmitter module with a fiber pigtail and a Si-lens located on the backside of the chip (Fig. 2). At (sub)mm-wavelengths Si-lenses are normally applied to eliminate the loss of the integrated circuit antennas due to substrate modes. The advantage of mounting the chip on such a Si-lens is that 97.8% [2] of the radiated power from the antenna is being directed to the lens side.

III. MEASUREMENTS

After module packaging, we have measured the transmitter with a heterodyne source and a power meter with a feed horn antenna as a receiver. The optical signal is monitored by an OSA. The measurement setup is shown in Fig. 3.

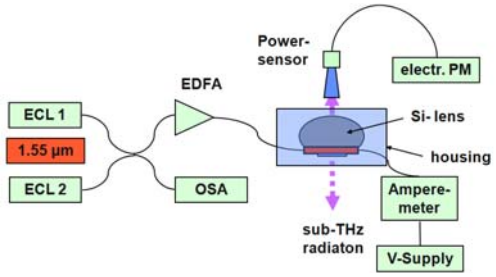


Figure 3. Heterodyne based measurement setup.

For the power measurement the horn antenna is mounted directly above the Si-lens, so that the emitted electrical power could be optimally received. The relation between the output electrical power and the input optical power is measured at 2 V reverse bias and 100 GHz beating frequency. The transmitter module exhibits a responsivity of 0.22 A/W and has a linear characteristic up to 15 dBm optical input power, as is shown in Fig. 4, which additionally indicates that the output power from the Si-lens is nearly 10 dB higher than that from the antenna side.

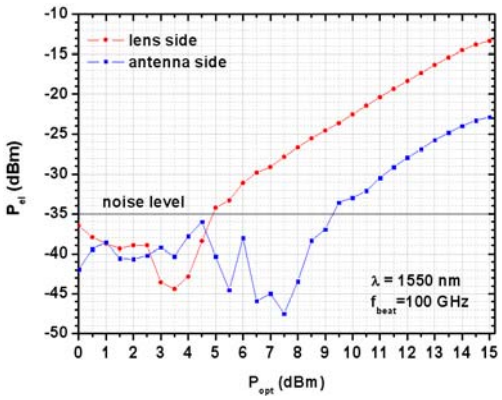


Figure 4. Output power vs. optical input power.

The heterodyne measurement was carried out in the frequency range of 50 to 300 GHz and at about 13.6 dBm optical power (corresponds to 5 mA photocurrent) for both sides. The results are illustrated in Fig. 5. The power meter is adjusted very carefully before the measurements. For the antenna side, the measurement was done only up to 200 GHz because of low power. The transmitter provides a maximal power of -13.5 dBm at about 65 GHz and 1 µW at 225 GHz. The resonance frequencies of the antenna lay approximately at 75 GHz, 110, 155 and 220 GHz. These are with some deviations well recognized in the smoothed curve of the lens side, whereas the original curve fluctuates strongly because of polarization mismatch between the radiated field and the receiver antenna. The tilting angle of the polarization plane is detected as ±35°. A good signal to noise ratio up to 1.6 THz of a coherent CW THz system with the same micro-pin PD in combination with a bow-tie antenna as the emitter and a photoconductor as the receiver has been reported in [5].

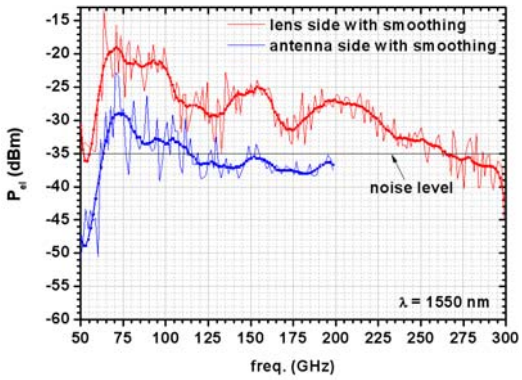


Figure 5. Frequency response of micro-pin antenna chip.

IV. CONCLUSION

A micro-pin antenna chip comprising a waveguide integrated pin PD and a logarithmic periodic circularly-toothed antenna was packaged into a fiber-fed transmitter module. The maximal radiated power of the device was -13.5 dBm and 1 µW output power at 225 GHz was obtained. The device could be optimized by applying DDR or UTC layer stacks for high power capability. Alternative antenna structures such as bow-tie antenna could be used to minimize the polarization tilting. Dipole antennas are suitable for resonant applications. An antenna array could be combined with some micro-pin PDs to control the THz far field pattern through changing the optical delay time or phases of the optical control signals.

ACKNOWLEDGMENT

The authors acknowledge gratefully the contributions from their colleagues T. Rosin and D. Pech at FhI Heinrich-Hertz-Institute, Berlin, Germany. Furthermore they acknowledge the cooperation with the TU-Darmstadt (C. Sydlo, P. Meisner).

REFERENCES

[1] C. C. Renaud et al., "A high responsivity, broadband waveguide uni-travelling carrier photodiode," Proc. SPIE, Vol. 6194, 2006, pp. 61940C.1-61940C.8.

[2] Reinhard Kunkel et al., "Monolithic Integration of a Waveguide-Integrated p-i-n-Photodiode and a Planar Antenna for THz Applications," OTST, March 18-21, 2007, Orlando, Florida.

[3] H.-G. Bach et al., "Integration Potential of Waveguide-integrated Photodiodes: Self-powered Photodetectors and sub-THz pin-Antennas," Optical Fiber Communication Conference (OFC), February 2008, San Diego, California.

[4] A. Beling et al., "High-Speed Miniaturized Photodiodes and Parallel-fed Traveling Wave Photodetector based on InP," IEEE J. of Selected Topics in Quantum Electronics, special issue on High-Speed Photonic Integration, Vol. 13, No. 1, 2007, pp. 15-21.

[5] B. Sartorius et al., "Continuous wave terahertz systems exploiting 1.5 µm Telecom technologies," Optics Express, Vol. 17, Issue 17, 2009, pp. 15001-15007.

Hybrid Up-Conversion Detector for Mid-Infrared Radiation using Ti:PPLN Waveguides

Kai-Daniel Büchter, Harald Herrmann, Viktor Quiring, Raimund Ricken, and Wolfgang Sohler
Angewandte Physik, Department Physik
Universität Paderborn, Paderborn, Germany
sol_db@physik.upb.de

***Abstract*—We developed a fiber-coupled "hybrid detector" for mid-infrared radiation. Ti-indiffused waveguides in periodically poled $LiNbO_3$ are exploited to perform sum-frequency generation, followed by near-infrared detection. Superior sensitivity in comparison with a commercial HgCdTe mid-infrared detector has been achieved at 3.4 µm wavelength, yielding an improvement in detectivity by a factor of 3.5.**

Keywords-nonlinear optics; infrared detectors; PPLN; integrated optics.

I. INTRODUCTION

Mid-infrared (MIR) wavelengths in-between 3 and 4 µm are of considerable interest, especially because fundamental rovibrational transitions of carbon-hydrogen bonds are to be found in this wavelength range. Since there is still a lack of practical lasers for the MIR, nonlinear difference frequency conversion is a popular approach to generate these wavelengths [1]. Suitable detector materials for MIR wavelengths have long been available, e.g. HgCdTe, InSb, GaSb and PbSe. However, the detectivities of MIR detectors are typically two orders of magnitude lower than those of near-infrared (NIR) detectors. Thus, wavelength conversion of MIR radiation to the NIR with power conversion efficiencies above one percent would increase detection sensitivity, if added noise is kept under control. This scheme can also be combined with single photon detectors [2]. The sensitivity improvement relates mainly to the conversion efficiency, filtering of residual (pump-) radiation, and the ratio of detectivities of the respective MIR and NIR detectors used. In addition, such a scheme enables the use of conventional telecom fibers to guide radiation from the location of measurement to the actual photodetector.

In this contribution, we describe our development of such a hybrid detector using optical waveguides, and present results achieved. Compared to a commercial HgCdTe detector, our hybrid detector yields a detectivity improvement by a factor of 3.5. We see the potential to enhance current performance of the hybrid detector by one order of magnitude.

II. DESCRIPTION OF THE HYBRID DETECTOR

In fig. 1, a scheme of the hybrid detector is shown. We use Ti-indiffused waveguides, monomode at λ = 3.4 µm, in periodically poled $LiNbO_3$ (Ti:PPLN) to get an efficient nonlinear interaction. A poling periodicity of 26.65 µm is chosen for quasi-phase-matched (QPM) sum-frequency generation (SFG).

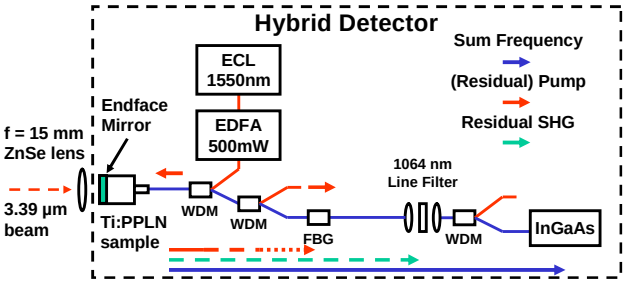


Figure 1. Schematic of Hybrid Detector. ECL: External Cavity Laser, EDFA: Erbium Doped Fiber Amplifier, FBG: Fiber Bragg Grating, SHG: Second Harmonic Generation, WDM: Wavelength Division Multiplexer, InGaAs: InGaAs detector. Lock-In and polarization control not shown.

The waveguide sample with an overall length of 92 mm, including a tapered section of 4 mm, is clamped in an 85 mm long oven. To detect radiation from a HeNe laser (P = 60 µW, λ = 3.39 µm) using a pump of λ = 1549.5 nm, a sample temperature of 165.1°C is necessary to generate phase-matched sum-frequency (SF) of λ = 1063.4 nm (fig. 2). A dielectric end face mirror is employed to reflect the pump at the free-space interface and to enable co-directional SF generation (see [3] for details). Pump source is a tunable ECL together with an EDFA (see fig. 1 for abbreviations). An InGaAs detector (Femto GmbH OEC-200) with an integrated amplifier and conversion gain up to 10^{11} V/W detects the SF signal. To remove unwanted (residual pump) radiation, a filtering scheme consisting of three fiber WDM filters (with 20 dB separation of 1064 nm from 1550 nm and ca. 1dB loss at 1064 nm each) as well as a tunable fiber Bragg grating, centered at 1549.5 nm (ca. 1dB loss at 1064 nm), is employed. Overall, a pump suppression of -77.5 dB is achieved. In addition, a dielectric line filter (centered at 1064 nm, transmission is 40% including free-space coupling losses) is used to remove spurious non-phase-matched second harmonic of the pump at 775 nm. A scan of the signal wavelength reveals the phase-matching characteristics of the device (fig. 2). Some asymmetries due to waveguide inhomogeneities are apparent.

III. HYBRID DETECTOR PERFORMANCE

A figure of merit to describe photodetectors is the specific detectivity

$$D^* = (A\,\Delta f)^{1/2} / NEP, \qquad (1)$$

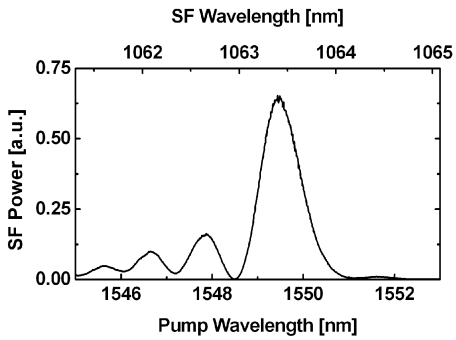


Figure 2. SFG tuning curve. Fundamental wavelength is 3.39 µm.

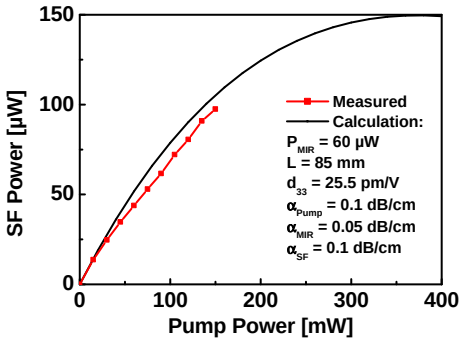


Figure 3. Sum-frequency power as function of pump power (waveguide internal conversion). Calculation parameters are given in the inset.

A is the active detector area, Δf the detection bandwidth, and NEP the Noise Equivalent Power. NEP can be expressed as

$$NEP = S_n \Delta f^{1/2} / R, \quad (2)$$

with S_n being the noise spectral density and R the detector responsivity at the specific wavelength. In our experiments, we use a lock-in amplifier (Signal Recovery DSP7265) to measure S_n. NEP can then be determined using the detector's specifications. Note that in such measurements S_n includes intrinsic detector noise as well as additional electrical noise due to electric circuitry. To describe the upconversion detector, we introduce an additional, overall (total) conversion efficiency

$$\eta_{tot} = \tau_{opt} \eta_{nl}, \quad (3)$$

where τ_{opt} is the transmission through all optical components (including e.g. coupling efficiencies and fiber optic insertion losses) and η_{nl} the nonlinear conversion efficiency (note that we are considering power, not quantum efficiency). Now we define for the hybrid detector

$$NEP_{hd} = 1/\eta_{tot} \times NEP = 1/\eta_{tot} \times S_n \Delta f^{1/2} / R, \quad (4)$$

where NEP is the noise equivalent power of the detector at SF wavelength, with pump switched on, and NEP_{hd} is the noise equivalent power in terms of incident MIR radiation.

For signal detection using the lock-in amplifier, a mechanical chopper wheel is used to modulate the MIR beam with 1 kHz modulation frequency. With 60 µW MIR power and 500 mW pump power, we determined the overall conversion efficiency to be η_{tot} = 5.5 %. We estimate τ_{opt} = 3 %, determined by coupling and propagation losses as well as insertion losses of fiber optic components. Pump transmission (from EDFA output to reflected power at endface mirror) is estimated to be 30 %. With these approximations, η_{nl} yields 174 %, even though the utilized pump power is ~ 150 mW only (cp. fig. 3).

The noise spectral density was determined as S_n = 14.4 µV/$Hz^{1/2}$ with pump enabled. Using (2) and (4), and taking Δf = 1 Hz, as well as R(SF) = 0.7×10^9 V/W, leads to NEP_{hd}(MIR) = 0.36 pW at 500 mW pump power. To compare this result to a conventional MIR detector, we characterized the noise properties of a thermoelectrically cooled HgCdTe detector (OEC GmbH) with integrated current amplification. The characterization reveals S_n = 14 µV/$Hz^{1/2}$, corresponding in this case to NEP = 14 pW at 1 Hz measurement bandwidth. Hence, directly comparing both hybrid and conventional detector gives an improvement in NEP by a factor of 39. In order to make a truly fair comparison however, the different detector areas need still be considered, leading us to an "overall" specific detectivity D*. The detector area of the InGaAs detector is roughly 7.85×10^{-5} cm^2, whereas the detector area of the HgCdTe detector is about 0.01 cm^2. Taking (1), this gives D* (HgCdTe) = 7.1×10^9 cm·$Hz^{1/2}$/W and D* (Hybrid) = 2.5×10^{10} cm·$Hz^{1/2}$/W. According to these normalized values, an improvement by a factor of 3.5 is achieved with the hybrid detector.

To estimate the improvement in conversion efficiency η_{nl} by raising pump power, conversion was modeled using a numeric solver of coupled mode equations (fig. 3). To compare experimental results to theory, the waveguide internal power levels were deduced from measured data. We conclude that an increase in conversion efficiency by a factor of 1.5 is possible by doubling pump power.

IV. Conclusion and Outlook

We have demonstrated a hybrid-MIR-detector, using nonlinear frequency conversion from 3.4 µm to 1064 nm, with a cw pump and a fW-range InGaAs detector. We could show a factor of 3.5 improvement in "overall" detectivity, compared to a thermoelectrically cooled HgCdTe detector. We see the potential to reduce fiber optic losses of the hybrid detector setup by a factor of 6, by replacing several fiber optic components with a more simple and robust wavelength filtering scheme. Also, pump power and thus nonlinear conversion efficiency may be increased (we are limited to about 500 mW by fiber optic WDM-couplers in use). Doubling of pump power, together with the enhancements in the experimental setup, may well lead to an improvement of the overall conversion efficiency by one order of magnitude.

References

[1] O. Tadanaga et al., "Efficient 3-µm difference frequency generation using direct-bonded quasi-phase-matched $LiNbO_3$ ridge waveguides," Appl. Phys. Lett., Vol. 88, Art. 061101, February 2006.

[2] G. Temporão, S. Tanzilli, H. Zbinden, and N. Gisin, "Mid-infrared single-photon counting," Opt. Lett., Vol. 31, No. 8, pp. 1094-1096, April 2006.

[3] K.-D. F. Büchter, H. Herrmann, C. Langrock, M. M. Fejer, and W. Sohler, "All-optical Ti:PPLN wavelength conversion modules for free-space optical transmission links in the mid-infrared," Opt. Lett., Vol. 34, No. 4, pp. 470-472, February 2009.

Optical Injection Locking of a Resonant Tunneling Diode-Optical Waveguide Photo-Detector

B. Romeira, J. M. L. Figueiredo
Centro de Electrónica, Optoelectrónica e Telecomunicações
Universidade do Algarve, Faro, Portugal
bmromeira@ualg.pt; jlongras@ualg.pt

C. N. Ironside, A. E. Kelly, T. J. Slight
Department of Electronics and Electrical Engineering
University of Glasgow, Glasgow, United Kingdom
ironside@elec.gla.ac.uk

***Abstract*—We report photo-detection and optical injection locking of a resonant tunneling diode - optical waveguide (RTD-OW) voltage controlled oscillator (VCO). When incorporated in a resonant tank the RTD-OW photo-detector is capable of locking to optical radio-frequency sub-carriers, with considerable reduction of VCO phase noise and locking ranges above 15 MHz.**

Keywords-Optical injection locking; optoelectronic devices; optical waveguides; photo-detectors; resonant tunneling diodes

I. INTRODUCTION

Photonic radio-frequency (RF) receivers extract RF signals from optical carriers with a wide range of applications in RF-over-fiber communication systems. Efficient and low noise receivers are being currently object of intense developments towards low cost photonic-microwave communication systems. An interesting approach is the capability of the optical RF sub-carrier to control the receiver circuitry [1]. Also of interest is the capability of transferring phase shift keyed (PSK) digitally encoded signals from the optical to the wireless domain [2]. Among the photo-detection devices, waveguide photo-detectors promise both the high-speed and high internal quantum efficiency.

In this paper we present a photo-detection device based on a resonant tunneling diode (RTD) embedded in an optical waveguide (OW), the RTD-OW. The RTD-OW can work both as electro-absorption modulator and as photo-detector at optical communication wavelengths [2] [3]. Here we show RTD-OW operation as a voltage controlled oscillator (VCO) capable of locking to optical injected RF carriers.

RTDs have attracted much interest due to their nonlinear N-shape current–voltage (*I-V*) characteristic, exhibiting negative differential conductance (NDC). The NDC provides wide bandwidth electronic gain that can give rise to high frequency self-sustained oscillations (up to 831 GHz [4]). RTD-based photo-detectors have been proposed for low noise optical injection and optical-to-RF conversion taking advantage of the nonlinear NDC [2] [5]. In what follows we describe the recent developments on monolithic RTD-OW photo-detectors operating as microwave-photonic receivers capable of low noise optical injection locking with exceptional frequency-locking range.

Fundação para a Ciência e Tecnologia, Portugal, Grant SFRH/BD/43433/2008.

II. DEVICE STRUCTURE AND EXPERIMENTAL SETUP

The RTD-OW consists of an AlAs/InGaAs/AlAs double barrier quantum well (DBQW) resonant tunneling diode integrated with a InAlAs/InGaAlAs/InP optical waveguide (more details can be found in [3]). The InGaAlAs waveguide core was made 1 μm thick with a ridge waveguide 3 μm wide providing light confinement along the double barrier quantum well plane.

Figure 1 shows the schematic diagram of the typical RTD-OW band structure when DC biased in the valley region (see inset the *I-V* characteristic). A light pulse with photon energy close to the waveguide core band gap energy produces photo-charges which under the presence of an electric field give rise to a photocurrent. The current flow depends on bias voltage and the incident optical power.

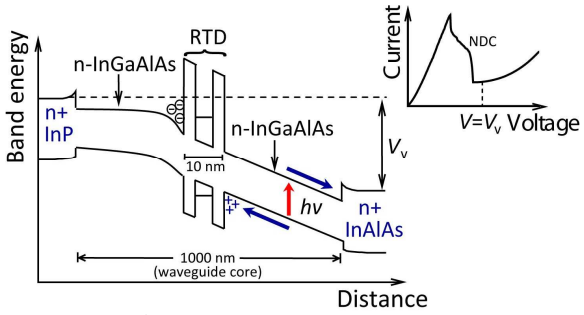


Figure 1. Diagram of the RTD-OW band structure when DC biased in the valley region. Inset is shown the schematic *I-V* characteristic.

Figure 2 shows the experimental arrangement used to characterize RTD-OW photo-detection and optical injection locking operations. Continuous light-wave from a tunable single mode laser was modulated up to 10 dB extinction ratio

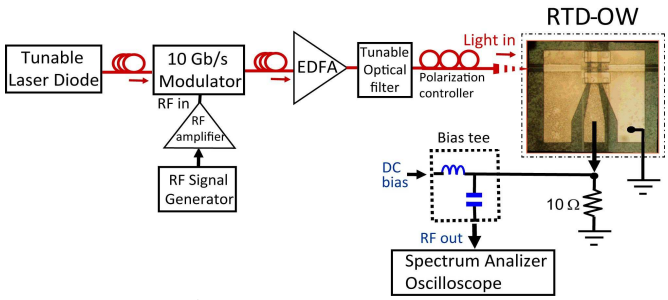


Figure 2. Diagram of the experimental arrangement used to characterize RTD-OW photo-detection and optical injection locking operations.

(ER), using an electro-optical 10 Gb/s external modulator driven by a RF signal generator. The modulated light signal was amplified by an Erbium Doped Fiber Amplifier (EDFA), passing through a tunable optical filter and then coupled to the RTD waveguide using a standard lensed fiber.

The RTD-OW circuitry includes a 10 ohm resistor shunting the RTD-OW coplanar waveguide (CPW) transmission line, which decouples the DC bias circuit from the resonant tank formed by the CPW inductance and bonding wires and the RTD-OW intrinsic capacitance [2]. This arrangement provides the appropriate resonant conditions for operation as a self-sustained microwave VCO with fundamental frequency ranging from 0.98 GHz to 1.25 GHz.

III. Results and Discussion

The RTD-OW photo-detector works as follows. Light at wavelengths around 1550 nm coupled to the DC biased RTD-OW is progressive absorbed as it propagates along the waveguide. The light absorption generates charge carriers resulting in a photocurrent that adds to the current flowing through the device. Such current increase can be interpreted as a device series resistance reduction, which leads to an overall shift to lower voltage of the *I-V* characteristic. Figure 3(a) shows RTD-OW illuminated and dark *I-V* characteristics.

Figure 3(b) presents device responses for biasing at peak and valley regions as a function of incident optical power. The light was modulated at 1.2 GHz with 10 dB ER. If the coupling loss is estimated at 8 dB, then the responsivity in the valley is 1.5 A/W. As shown in Fig. 3, the peak-to-valley transition gives rise to 14 dB increase on the photo-detection response in the range of optical powers used. The improvement on the response in this region occurs because the holes photo-generated in the depletion region accumulate around the collector barrier (see Fig. 1), causing a local enhancement field which leads to higher current, Fig. 3(a).

When DC biased in the NDC region, the RTD-OW self-sustained oscillations lock to the photo-detected signal, i.e., the oscillator synchronizes to the optical sub-carrier. Figure 4(a) shows electrical spectra of free-running and synchronized oscillations, of a RTD-OW DC biased in the NDC region, near the valley, where it produces free-running oscillation at around 1.2 GHz. The 4 mW injected power was modulated at 1.2 GHz with 10 dB extinction ratio. The results show single side band (SSB) phase noise of -104 dBc/Hz at 20 kHz (the reference source was < -110 dBc/Hz), a ~36 dB phase noise reduction compared to free running oscillation (-68 dBc/Hz). The free-running oscillator's phase noise was < -70 dBc/Hz at 100 kHz offset and compares with previous reported RTD-based photo-detectors [5]. Figure 4(b) presents the corresponding frequency-locking capture range as a function of power level, for extinction ratios of 5 dB and 10 dB. Optical powers around 10 mW with 10 dB extinction ratio leads to locking capture ranges up to 15.9 MHz, almost four times the maximum reported in [5] for comparable incident optical power levels. This is a promising performance considering the fiber to waveguide light low coupling efficiency, mainly due to the thin absorption layer.

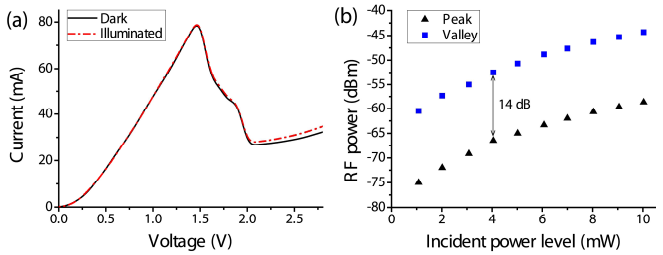


Figure 3. (a) RTD-OW illuminated and dark *I-V* curves for an incident optical signal λ=1550 nm and 4 mW power modulated at 1.2 GHz. (b) Photo-detection in the peak and valley regions as a function of power level.

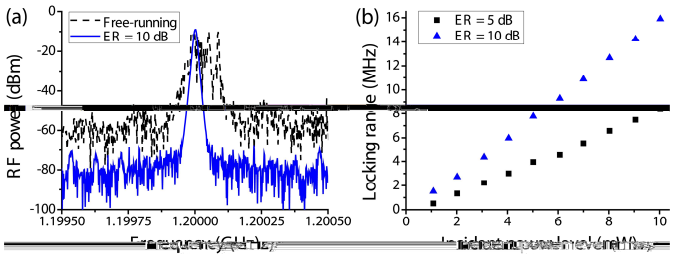


Figure 4. (a) Free-running RTD-OW VCO oscillation at around 1.2 GHz and optical injection locking for a 4 mW optical signal at λ=1550 nm, modulated at 1.2 GHz. (b) Frequency locking range as a function of power level.

The frequency-locking range and spectral measurements reported here indicate clear advantages of using the RTD optical waveguide configuration design when compared to standard RTD photo-detection schemes to obtain higher optical-to-RF conversion efficiency, since the limitations imposed by the low optical coupling between the lensed fiber and the RTD optical waveguide can be substantially improved.

IV. Conclusion

In conclusion, we have employed a resonant tunneling diode-optical waveguide to perform photo-detection and optical injection locking to gigahertz RF sub-carriers at input power levels as low as 1 mW. The locking range went up to 15.9 MHz for incident power of 10 mW. The device can be the basis of a low cost optoelectronic receiver for error free timing extraction. This application is currently under investigation towards the implementation of new digital communication schemes. Because of the small physical dimensions and low noise optical injection locking, RTD-OW-based optical-to-RF interfaces have interesting applications as optoelectronic receivers for radio-over-fiber communications.

References

[1] A. J. Seeds, "Microwave Photonics," IEEE Trans. Microwave Theory Tech., vol. 50, pp. 877-887, March 2002.

[2] B. Romeira et al., "Nonlinear Dynamics of Resonant Tunneling Optoelectronic Circuits for Wireless/Optical Interfaces," IEEE J. Quantum Electron., vol. 45, pp. 1436-1445, November 2009.

[3] J. M. L. Figueiredo, C. N. Ironside, C. R. Stanley, "Electric field switching in a resonant tunneling diode electroabsorption modulator," IEEE J. Quantum Electron., vol 37, pp. 1547-1552, December 2001.

[4] Safumi Suzuki et al., "Fundamental Oscillation of up to 831 GHz in GaInAs/AlAs Resonant Tunneling Diode," Appl. Phys. Express, vol. 2, 054501, April 2009.

[5] T. M. Ramond, L. Hollberg, P.W. Juodawlkis, S.D. Calawa, "Low-noise optical injection locking of a resonant tunneling diode to a stable optical frequency comb," Appl. Phys. Lett., vol. 90, p. 171124, April 2007.

All-optical phase modulation effect in InGaAs/AlAsSb quantum well and its application to ultra-fast all-optical signal processing

H. Ishikawa, R. Akimoto, T. Mozume, G. Cong, S. Gozu, K. Akita, M. Nagase, T. Ogasawara, H. Kuwatsuka
Network Photonics Research Center
National Institute of Advanced Industrial Science and Technology (AIST)
Tsukuba, Japan
hiroshi-ishikawa@aist.go.jp

***Abstract*—Ultrafast all-optical cross phase modulation (XPM) effect in InGaAs/AlAsSb quantum well is reviewed and its application to ultrafast all-signal processing is presented. Error free demultiplexing operation from 160-Gb/s to 40-Gb/s with low gating power is demonstrated.**

Keywords; ultrafast signal processing; quantum well; cross phase modulation; 160-Gb/s

I. INTRODUCTION

The InGaAs/AlAsSb quantum well exhibits ultrafast optical cross phase modulation (XPM) effect. The TM pump pulse corresponding to the intersubband transition (ISBT) energy causes the phase modulation in the TE polarized signal light which is inherently transparent to the quantum well [1]. So far mechanism of this new all-optical phase modulation effect has been made clear ant the guiding principle to realize large XPM has been given [2]. Owing to the response speed of this XPM effect of an order of 1ps, and the inherently lossless XPM for the TE light, this can be used to realize ultrafast all-optical signal processing devices with low insertion loss. We developed Mach-Zehnder type all-optical gate module using a mesa type InGaAs/AlAsSb ISBT device [3]. Achieved are error free demutiplexing (DEMUX) operation from 160-Gb/s to 40-Gb/s with low gating pulse energy of 1.5pJ/pulse, and wavelength conversion for 160-Gb/s signal [4]. Here, we review the achievement so far with this new device.

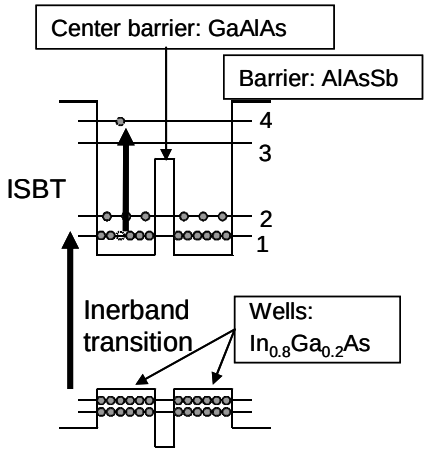


Fig.1 Band structure of coupled quantum well

This work was partially supported by New Energy and Industrial Technology Development Organization (NEDO)

II. XPM EFFECT AND QUANTUM WELL

Figure 1 shows typical quantum well structure. We employed a coupled double quantum well structure (CDQW). This structure gives 1.55 μm transition wavelength for the 1 to 4 transition in the conduction band. While the band to band transition wavelength is shorter than 1.55 μm. Then the 1.55μm wavelength range light is not absorbed by the interband transition. TM pump pulse of 1.55μm range causes the phase modulation to the lossless 1.55μm TE light. We investigated the TE light (signal) wavelength dependence of this XPM efficiency. It was shown that shorter the signal wavelength the larger the XPM efficiency. This indicates that this XPM takes place due to the band to band dispersion. Analysis of XPM efficiency using **kp** calculation for the

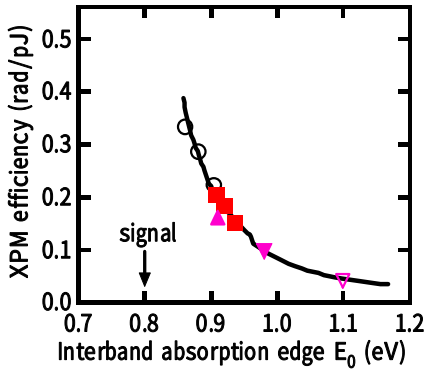


Fig.2 Calculated and measured XPM efficiency as a function of interband transition energy. Plots in the figure are experimental results for various samples [2].

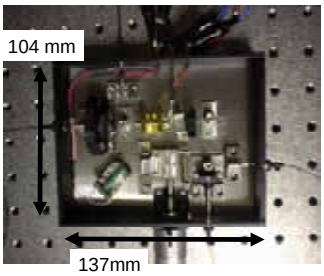


Fig.3 A photograph of Mach-Zehnder module with ISBT device

valence band showed good agreement with experimental results as shown in Fig.2 [2]. Then the guideline for the design of CDQW to achieve large XPM efficiency is to design the quantum well so that the band to band transition energy is close the intersubband transition energy, but within the limit that real band to band transition does not takes place.

Stacked CDQW was grown by molecular beam epitaxy. Initially we fabricated the CDQW with $In_{08}Ga0_{.2}As$ well layer using AlAs center barrier. However, we changed the center barrier to AlGaAs. This barrier enables us to tune the coupling between two quantum wells by adjusting the Al composition. Then we can tune the ground state energy of conduction subband to adjust the band to band transition energy. The other advantage of AlGaAs center barrier is that it compensates the strain of quantum well enabling us to grow high crystal quality stack of CDQWs for the waveguide structure. The mesa type waveguide structure with width of 1μm was fabricated. Tapered structure was attached on both facets for the fiber coupling. Using this mesa type device, the largest XPM efficiency of 0.5rad/pJ was obtained for the Al composition of 0.5 in the center barrier [5].

III. SIGNAL PROCESSING CHARACTERISTICS

Using bulk optics, Mach-Zehnder type gate device as shown in Fig.3 was developed [3]. Owing the low insertion loss of ISBT device for TE mode, total insertion loss of the module was 5-6dB which is mostly due to fiber coupling loss. We performed all-optical demultiplexing (DEMUX) operation form 160-Gb/s to 40-Gb/s. The XPM efficiency of the ISBT device used here was 0.5 rad/pJ. Figure 4 shows the eye pattern,

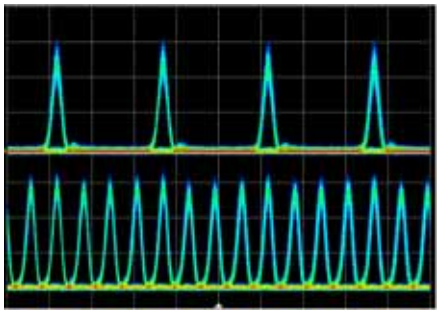


Fig. 4 Input 160-Gb/s signal to Mach-Zehnder ISBT module (lower picture) and DEMUXED 40-Gb/s signal (upper picture).

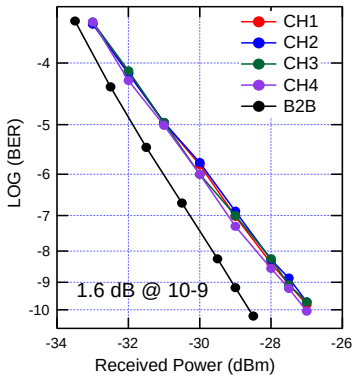


Fig. 5 Bit-error-rates for DEMUX operation form 160Gb/s to 40Gb/s.

and Fig. 5 shows the bit error rate. The gate pulse energy here was 1.5pJ to the fiber. We can confirm clear eye opening and the error free DEMUX operation. We also performed wavelength conversion. Modulated TM polarized RZ signal acts as gating pulse to code the TE CW light. Then the wavelength of the gate signal is converted to other wavelength. We obtained good eye opening even for 160-Gb/s signal [4].

IV. CONCUSIONS

Using the all-optical XPM effect of the ISBT device, all-optical signal processing for 160-Gb/s was attained. This new XPM effect is highly promising for ultrafast signal processing because of its fast response and lossless characteristics.

REFERENCES

[1] H. Tsuchida, T. Simoyama, H. Ishikawa, T. Mozume, and M, Nagase, “Cross-phase-modulation-based wavelength conversion using intersubband transition in InGaAs/AlAs/AlAsSb coupled quantum wells,” Optics Lett., vol. 32, pp.751-753, April 2007.

[2] G. W. Cong, R. Akimoto, K. Akita, S. Gozu, T. Mozume, T. Hasama and H. Ishikawa, “Experimental and theoretical study of cross-phase modulation in InGaAs/AlAsSb coupled double quantum wells with a AlGaAs coupling barrier,” Phys. Rev. B, vol. 80, 035306, 2009.

[3] R. Akimoto, T. Simoyama, H. Tsuchida, S. Namiki, C.G. Lim, M. Nagase, T. Mozume, T. Hasama, and H. Ishikawa, “All-optical demultiplexing of 160-10Gb/s signals with Mach-Zehnder interferometric switch utilizing intersubband transition in InGaAs/AlAs/AlAsSb quantum well,” Appl. Phys. Lett., vol.91, 221115, 2007.

[4] R. Akimoto, S. Gozu, T. Mozume, K. Akita, G. W. Cong, T. Hasama, H. Ishikawa, “All-optical wavelength conversion at 160Gb/s by intersubband transition swithces utilizing efficient XPM in InGaAs/AlAsSb coupled double quantum well,” European Confernce on Optical Communication, paper 1.2.2, Viena, Austria, Sep. 2009..

[5] S. Gozu, T. Mozume, R. Akimoto, K. Akita, C. G. Cong, and H. Ishikawa, “Cross phase modulation efficinecy enhanement in $In_{0.8}Ga_{0.2}As/Al_{0.5}Ga_{0.5}As/AlAs_{0.56}Sb_{0.44}$ coupled double auantum wells by tailoring interband transition wavelength,” Applied Physics Express, vol.2, 042201, 2009.

High-Contrast Gratings:

A New Platform for Integrated Optoelectronics

C. J. Chang-Hasnain, V. Karagodsky, F. Sedgwick, B. Pesala, C. Chase
Electrical Engineering and Computer Sciences
University of California
Berkeley, CA, 94720, USA
cch@eecs.berkeley.edu

Abstract—**A new concept of dielectric subwavelength grating has emerged. This grating leverages a high contrast in refractive indices for the grating medium and its surrounding (and hence the name). We will discuss how HCG can manipulate light to achieve various extraordinary properties and its potential as a new platform for integrated optics.**

Keywords-component; subwaveelngth gratings, VCSELs, integrated optics (key words)

I. INTRODUCTION

Recently, we reported extraordinary properties from a simple, one-dimensional, single-layer, subwavelength grating fully surrounded by media that has a large contrast of refractive index (Fig. 1) [1-4]. Leveraging this large index contrast with subwavelength dimensions, light can be manipulated in ways that were totally unexpected. The different designs that will be reviewed in this talk include (a) broadband, high-reflectivity mirror for light incident in surface-normal direction and at a glancing angle [1-4], (b) ultra high-Q resonator with surface-normal output [5], (c) as a cladding for an ultralow loss hollow-core waveguide [6-8], and (d) ultra-compact optical coupler and splitter [9,10]. The prospect for HCG as a new platform for integrated optics will be discussed.

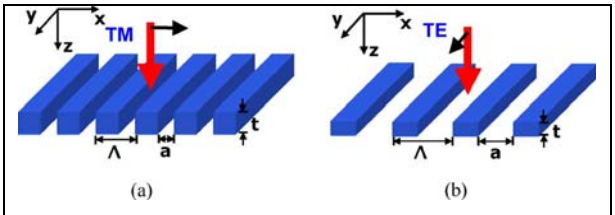


Figure 1. Schematic of high contrast grating (HCG). High index gratings (blue) are fully surrounded by low index material. They can be designed to reflect primarily TE or TM waves.

II. 2. BASIC PRINCIPLE

The origin of high reflectivity can be understood by noting that when a light beam is incident on an HCG, the light is reflected and transmitted into multiple diffraction orders. However, when the period of the grating is less than the wavelength ($\Lambda<\lambda$), all higher order modes are evanescent in air (low index medium). When the grating parameters are optimally designed, destructive interference is obtained between the directly transmitted waves, which leads to an extremely high reflectivity. Due to the high index contrast between the gratings and their surroundings, there are only two modes of significant energy [11]. Hence, the matching of boundary conditions to result in constructive interference can be satisfied over a broad wavelength range, leading to an enormously broadband high reflectivity $\Delta\lambda/\lambda\sim65\%$. With a simple change of parameters to yield destructive interference also at the input plane, on the other hand, an extremely narrow band resonance can be attained $\Delta\lambda/\lambda\sim10^{-6}$. Though both are a direct result of interference, the design tolerance is remarkably large due to the large index contrast [3,4].

III. BROADBAND MIRRORS

Broadband mirrors with very high reflectivity are the fundamental building block for numerous device applications, including lasers, modulators, detectors, sensors and imaging, ranging from 0.7μm to 12μm wavelength regimes. Semiconductor-based distributed Bragg reflectors (DBRs) have been used to achieve high reflectivity required for devices such as vertical cavity surface emitting lasers (VCSEL), detectors and filters. Because of the very short gain length in VCSELs, a very high reflectivity (>99%) is required in the DBRs. Hence, the DBRs are typically very thick, consisting of 20-40 pairs of alternating index materials. This has been the most critical bottleneck for the realization of VCSELs in wide wavelength regimes.

The fact that HCG was suitable to be used in the near-field regime was not proven until its incorporation in a VCSEL as the top mirror [3]. Figure 2 shows the schematic of a typical HCG-VCSEL. The device consists of a conventional semiconductor-based bottom *n*-DBR mirror, a λ-cavity layer with the active region, and an HCG-based top mirror. The structure of the HCG consists of periodic stripes of $Al_{0.6}Ga_{0.4}As$ that are freely suspended with air as the low-index cladding layers on the top and bottom. Typical single mode with 40 dB side mode suppression ratio is routinely obtained for both designs. Lithographically defined polarization was demonstrated with a mode discrimination as large as 25-36 dB. Extraordinarily large fabrication tolerance is demonstrated with ±20% variation of the HCG critical dimension. Emission wavelength of HCG-VCSEL varied only 0.2% with 40 % change in lithography linewidth.

The HCG is naturally suitable for forming a tunable VCSEL structure. With its ultra-thin layer, 20-40 times thinner than a typical DBR, the other two dimensions of

the micro-electro-mechanical (MEM) structure can be reduced by similar numbers, resulting a 1,000-8,000 times mass reduction and >160 times increase in tuning speed. We demonstrated a tunable VCSEL with a tuning range of 18 nm and tuning speed ~20 ns, the fastest MEM tunable device reported to date.

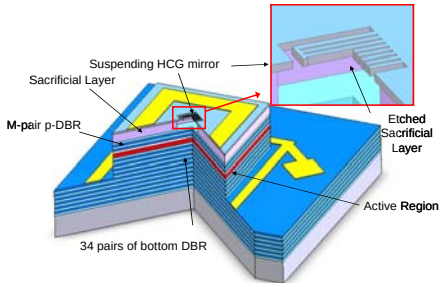


Figure 2. Schematic of HCG-VCSEL

IV. High Quality Factor (Q) Resonators

High Q resonators have attracted much attention recently. Grating structures including distributed Bragg reflectors (DBRs) and distributed feedback (DFB) structures have been widely studied as optical resonators, in which the incident beam, resonance optical mode and optical output are all collinear. While this configuration facilitates device integration in a cascaded fashion, they are often difficult to couple with free space or fiber optics. Recently, we present a novel high-Q resonator using the high contrast subwavelength grating concept (Fig. 3). The in-plane high-contrast grating forms a high-Q resonator which couples light in the surface-normal direction. Unlike our previous HCG work, the HCG design presented in this paper offers a narrow band high-Q resonator instead of a broadband mirror. A Q-factor of ~500,000 is obtained from numerical simulation. Experimentally, a Q-factor of 14,000 is measured from fabricated devices. The design shown in this paper can be potentially used to make a simple surface-emitting laser.

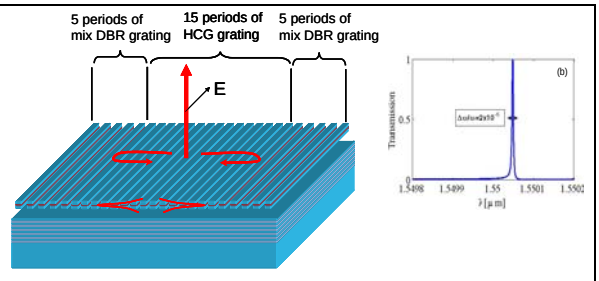


Figure 3. HCG Resonator and calculated spectrum

V. Hollow-core Waveguide

The ability to generate long optical delays with low intrinsic loss is useful for a wide range of applications including optical signal processors, RF filtering, optical buffers, and optical sensing. Lithographically defined, chip-scale waveguides are compact, light-weight, and can be integrated with other optoelectronic devices. The lowest reported loss achieved to-date in chip-based waveguides is ~1 dB/m. Hollow-core waveguides are highly promising for achieving ultra-low loss, nonlinearity and dispersion because of the elimination of the core material. There have been advances in hollow-core waveguides using a metallic shell, DBR, or photonic crystals, etc. The basic principle is to guide the optical beam propagating through air by multiple reflections at the cladding mirrors. The lowest loss for a chip-based hollow-core waveguide is still high because the reflectivity of the cladding DBR not being high enough. Ultrahigh reflectivity is essential to achieve ultra-low loss. We propose using HCGs as the high reflectivity cladding to reflect light at a small glancing angle (Fig. 4). The most peculiar property, perhaps of all, is that HCG with periodicity parallel to the direction of propagation can confine light in the waveguide. Instead of causing backward wave reflection normally expected of traditional periodic structures, the HCG forms a high reflectivity glancing incidence mirror for the guided wave. We show a HCG hollow-core slab waveguide design with an exceedingly low propagation loss (<0.01 dB/m) using numerical simulation [6,7]. Preliminary experimental results indicate that HCG may be used to control polarization dependent dispersion [8].

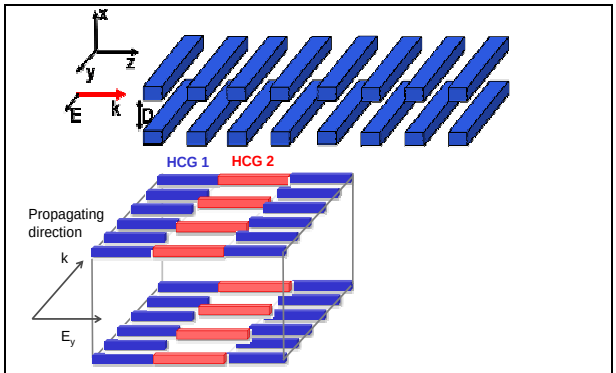


Figure 4. 1D (top) and 2D HCG hollow-core waveguide

VI. Ultra-compact Optical Coupler and Splitter

As light is tightly confined by HCG-HW, it can be shown that two adjacent, parallel hollow-core waveguides sharing one common layer of HCG can be totally isolated. This means the two waveguides are separated by a dimension less than 1 λ, in sharp contrast to conventional waveguides needing a separation up to ~10λ. Leveraging this phenomenon, we can construct an ultra-compact 3dB splitter and 2×2 coupler.

An extremely compact 2×2 coupler with a length of 26um (16 λ), and a footprint (length×width) of 85um^2 (35 λ^2) and a 3dB splitter with a length of 3.6um (2.4 λ), and a footprint of 12 um^2 (5 λ^2) are realized with finite-difference time-domain (FDTD) simulation. Low insertion loss is obtained through the coupler (~0.35dB) and the splitter (~0.28 dB). The design presented [9] can be easily extended to form a variety of on-chip photonic components (N×M couplers, arbitrary ratio splitters) that

are useful for optical signal processing and routing applications.

For a 2×2 coupler, the coupling length can be expressed as: $L_{MMI} = 4n_r W_{MMI}^2 / \lambda_o$, where n_r is the refractive index of the core and W_{MMI} is the effective width of the MMI region [12]. Similarly for a 3dB-splitter, $L_{MMI} = n_r W_{MMI}^2 / 2\lambda_o$. For conventional waveguide design, the input/output waveguides have to be separated by at least $w \sim 2w$, w being the width of each waveguide, to avoid unwanted coupling. Hence, the width of the MMI region becomes $3w \sim 4w$. For the case of hollow-core waveguide, the refractive index of the core is 1 and more importantly stronger confinement of light in the core region means that the waveguides can be literally adjacent to each other. In this case, the width of the MMI region is reduced to $2w$. These two factors contribute to a large reduction in the area of the splitter and the coupler by a factor of 10 (see Table 1). Figure 5 shows the results of a splitter for a 1.5um waveguide. As we can see from the figure, light is indeed strongly confined to the core and there is negligible coupling between the output waveguides. The coupling length in this case is 3.6um (2.4 λ) giving rise to an extremely small device footprint of 12um^2 (5 λ^2).

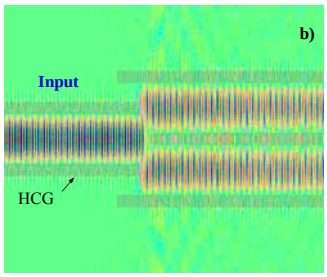


Figure 5. Finite-difference time domain simulation showing the splitting of light in a HCG-HW based MMI splitter.

Quantity	Conventional waveguide	HCG hollow-core waveguide
n_{core}	1.5 - 3	1
W_{MMI}	$3w - 4w$	$2w + t_{HCG}$
$L_{Splitter}$	~ 12*(w^2/λ_o)	~ 2*(w^2/λ_o)
$L_{Coupler}$	~ 100*(w^2/λ_o)	~ 16*(w^2/λ_o)
$A_{Splitter}$ ($W_{MMI} * L_{splitter}$)	~ 40*(w^3/λ_o)	~ 4*(w^3/λ_o)
$A_{Coupler}$ ($W_{MMI} * L_{Coupler}$)	~ 300*(w^3/λ_o)	~ 30*(w^3/λ_o)

Table 1. Comparison between conventional waveguide MMI splitter/coupler with a HCG hollow-core waveguide MMI splitter/coupler of same waveguide width w. Low refractive index of the core and stronger confinement of light in the core region leads to a factor of 10 reduction in the footprint of HCG based splitter and coupler.

VII. Conclusion

The HCG can potentially be a new platform to revolutionize chip-scale integrated optics. We envision many other novel devices including power combiner, WDM multiplexer, demultiplexer, optical modulators, fixed and tunable filters, and resonators to be built on the same platform. The HCG-HW can be highly useful for sensing applications as well as a vehicle for nonlinear optics experiments, having the unique property of confining a high optical intensity in the middle of a core that can be filled with anything desirable.

Acknowledgment

This work was supported by DARPA UPR Award HR0011-04-1-0040, NSF CIAN ERC #EEC-0812072, and a DoD National Security Science and Engineering Faculty Fellowship via Naval Post Graduate School N00244-09-1-0013.

References

[1] C.J. Chang-Hasnain, C.F.R. Mateus, and M.C.Y. Huang, US Patent 7304781

[2] C.F.R. Mateus, et. al. IEEE Photon. Technol. Lett., vol. 16, pp. 518-520, 2004

[3] Chang-Hasnain, C.J et. al. J. Selected Topics in Quantum Electronics, Vol. 15, Issue 3, 2009 Page(s):869 – 878

[4] Zhou, Y, et. al., J. Selected Topics in Quantum Electron., Digital Object Identifier 10.1109/JSTQE.2009.2021145

[5] Y. Zhou, et. al. Opt. Express 16, 17282–17287 (2008).

[6] Ye Zhou, et. al. Opt. Express 17, 1508-1517 (2009).

[7] M. Kumar, et. al. Photonics Journal, IEEE, Volume 1, Issue 2, Aug. 2009 Page(s):135 - 143

[8] Bala Pesala, et. al. CLEO, Baltimore, MD, June 1-5 2009.

[9] Bala Pesala, Vadim Karagodsky and Connie Chang-Hasnain, "Ultra-compact Optical Coupler and Splitter using High-Contrast Grating Hollow-Core Waveguide", submitted to CLEO 2010

[10] Christopher Chase and Connie J. Chang-Hasnain, "Transparent High Contrast Gratings for Tunable Optical Phase and Birefringence Engineering", submitted to CLEO 2010

[11] Vadim Karagodsky and Connie Chang-Hasnain, unpublished

[12] L. B. Soldano et. al., "Optical multi-mode interference devices based on self-imaging: principles and applications" JLT, 615-627 (1995).

A Compact Lossless Integrated 16×16 QW SOA Switch

H. Wang, A. Wonfor, R.V. Penty, I.H. White
Centre for Photonic Systems, Electrical Engineering Division, Engineering Department, University of Cambridge, 9 JJ Thomson Avenue, CB3 0FA
Cambridge, UK
Hw288@cam.ac.uk

K.A Williams
Technische Universiteit Eindhoven, P.O. Box 513, 5600 MB
Eindhoven, The Netherlands
k.a.williams@tue.nl

Abstract — **A monolithically integrated 16×16 Quantum Well Semiconductor Optical Amplifier switch is demonstrated. The switch has a 2dB facet-to-facet gain, a mean power penalty of 3dB and worst path power penalty < 5.5dB operating at 10Gb/s.**

Keywords-SOA;Optical switch

I. INTRODUCTION

The use of photonics for switching applications has become increasingly necessary owing to the demand for optical networks able to rapidly re-route signals between moderate numbers of input and output ports in new applications such as datacenters [1]. However, current optical switches using MEMs technology and the like have limited reconfiguration speed [2]. Semiconductor optical amplifier switches have the ability to switch on nanosecond timescales and have therefore undergone much development, with 8×8 port switches being reported [3]. However, these are realised with multiple integrated 1x8 switching elements which are separately packaged and require fibre interconnections and timing synchronization. To meet the energy and cost points for high capacity switching, integrated devices with port counts of at least 16×16 are needed for practical system applications [4]. It has been shown that 16x16 port counts can be achieved using cascaded 4x4 devices with fibre interconnections [5]. In this paper, therefore we report the first monolithically integrated 16×16 port SOA based optical switch, incorporating ~1100 individual components. The switch is re-arrangably non-blocking and has a chip area of only 6.3mm×6.5mm.

II. DEVICE DESIGN

The switch is based on a 3-stage hybrid Clos-Tree structure, which has three columns of four 4×4 port switch building blocks being connected by two fixed shuffle networks. Each of the 4x4 switching elements contains its own input and output shuffle networks and 16 SOA gates, as shown in Figure 1. In this all active switch, the waveguides in each shuffle network are forward biased to result in only a small loss between successive SOA gates. The SOA gates provide routing functionality and sufficient gain to allow lossless operation of the entire switch.

An integrated SOA switch should be compact with minimized internal loss, allowing the SOA gates to operate in a low gain regime, in order to minimize distortion and the build up of amplified spontaneous emission (ASE) noise. Therefore, the total length of the waveguides, the split and combine loss, and the number of cascaded SOA gates should be kept to a minimum. The use of beam splitters and beam turning components introduce excess losses, and hence the number of these components must also be minimized.

Table 1 shows that the 3-stage hybrid Clos structure used in this work requires the lowest number of gating SOAs and a modest number of SOA cascading stages for a re-arrangably non-blocking integrated 16x16 switch [6]. The tree architecture uses many SOAs which, whilst not cascaded, must overcome large split/combine losses. A Benes network based on 2x2 switches has a low loss per stage, but must cascade many SOAs and thus suffers from a low input power dynamic range.

TABLE I. COMPARISON OF SWITCH ARCHITECTURES FOR 16X16 PORT COUNT

Switch architecture	No. of SOA gates	No. of cascading stages	Max No. of SOA gates in each stage	Splitting loss per stage
Tree	256	1	256	24dB
Benes	224	7	32	6dB
3-Stage hybrid Clos-Tree	192	3	64	12dB

III. DEVICE IMPLEMENTATION

The switch used for this demonstration is fabricated from all active material with a 6 QW AlGaInAs active region, grown on an InP substrate, and operates with a gain peak around 1550nm. The chip layout is shown in Figure 1(a) and (b).

The shuffle network is constructed from 2μm wide shallow etched ridge waveguides, with an etch depth of 1.84μm. This relatively narrow waveguide width enables short taper lengths, where necessary for compatibility with etched turning mirrors and splitters, described later. This therefore reduces the overall path length and allows a compact switch to be developed. The SOA gates are 4μm wide shallow etched waveguide and 1mm in length (Fig. 1(c)). Adiabatic tapers are used to interface between the 2 and 4 μm waveguide widths. Thus a compact switch with dimensions of 6.3mm×6.5mm can achieve high extinction ratio and low system crosstalk.

In order to make the chip as compact as possible, 45 degree total internal reflection (TIR) mirrors (Fig 1(d)) are used to turn

the light to a perpendicular waveguide, rather than curved waveguides. These mirrors are 3.16μm deep etched and connected to 2.4μm wide waveguides on each side. The waveguides are then tapered back to 2μm. Two types of beam splitters are used in the shuffle networks, side splitters (Fig. 1(e)) and T-type splitters. They have similar structure to the beam splitters used in [7] and [8] respectively. Waveguides are linearly or parabolic tapered to the splitters. TIR mirrors are also used inside the splitters to the route half of the light to the perpendicular side waveguide. A full angle of 1 degree is used for all the linear tapers on the switch.

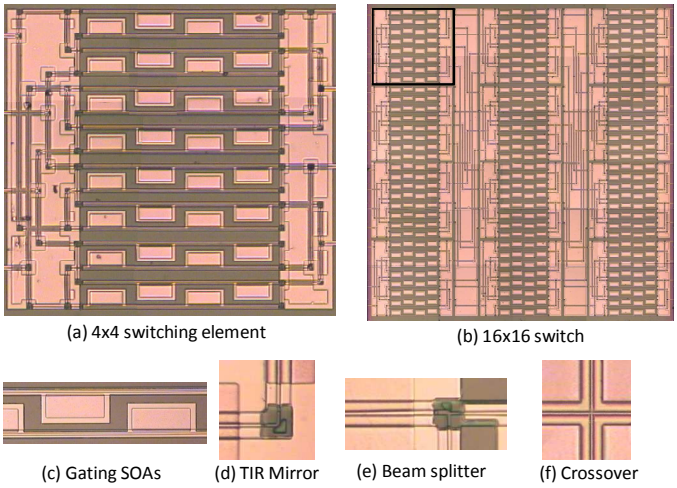


Figure 1 (a) shows a 4x4 switching element. 12 such elements are used in the 16x16 switch (b) . Key building blocks for the switch are (c) gating SOAs, (d) TIR mirrors, (e) and beam splitters and (f) waveguide crossings.

The current switch is re-growth free i.e. without active-passive interfaces. It is believed that the inclusion of, for example, passive shuffle networks would reduce ASE, nonlinear distortion and power consumption. As can be seen from figure 1, each path has three gating SOAs and goes through eight shuffle sections. Each specific input to output path on the 4×4 switch elements has a fixed length, ranging from 1.9mm to 3.35mm. Each of the two main shuffle networks has 16 paths, whose lengths are between 0.625mm and 4.225mm. As the switch is re-arrangably non-blocking, there are 4 different possible paths for each specific input to specific output, i.e. through the first to fourth 4×4 switch element in the second column. Therefore, the possible path lengths vary from 6.95mm to 16.8mm, while the shortest possible path for specific input to output pairs are range between 6.95mm and 12.7mm. Most of the paths have 13 mirrors, 12 beam splitters/combiners and a minimum possible length of less than 10mm. The switch contains 192 gating SOAs, 288 beam splitters/combiners, 424 deep etched turning mirrors and 210 waveguide crossings, a total of 1114 functional components integrated onto the same chip.

IV. EXPERIMENT DETAILS AND RESULTS

The switch is mounted on a thermo-electric cooler and operated at 15°C, with lensed fibres used to couple light on and off the chip. The switch is operated with selected gating SOAs biased between 0 (OFF) and 100mA (ON). This ensures good crosstalk performance. The shuffle networks inside the 4×4 switch elements are driven at 450mA, while the two large intermediate shuffle networks are each biased at 1000mA. This drive current is equivalent to 750mA per path. For this drive current, the switch has a facet-to-facet gain of >0dB at 1557.5nm for all tested paths with fibre coupling losses measured to be 4dB per facet. The TIR mirror loss has been measured to be 4dB. Optimisation of the design is expected to improve this. The 1dB on-chip output saturation power is -11.5dBm with a 3dB spectral bandwidth of >9nm.

Routing measurements are performed using a 10Gb/s 2^{31}-1 PRBS signal from a Mach-Zehnder modulator and an optically pre-amplified and filtered receiver. The switch output has an in-band optical signal-to-noise ratio (OSNR) of > 14.5 dB. The BERs for several selected paths are shown in figure 2. The switch operates with a power penalty of 5.5dB at a BER of 10^{-9} for the longest path (16.7mm). However, each input to output port pair has 4 possible paths and controlled re-arrangement of the switch can normally avoid this long path and keep the majority of path lengths to around 10mm or less. The shortest path and two paths which have average lengths are tested and show a minimum power penalty around 2.5dB.

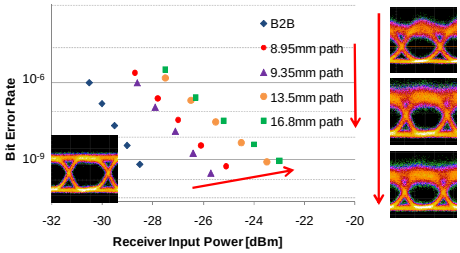


Figure 2 shows bit error rates and eye diagrams for selected paths, with red arrows showing the inceases in path length.

V. CONCLUSIONS

A monolithically integrated 16×16 SOA switch is demonstrated. The switch is compact and lossless. Routing of a 10Gb/s signal and error-free operation for different path lengths, including the shortest and longest, is achieved. The switch has a minimum power penalty around 2.5 dB, showing its potential for high speed switching applications such as packet switching.

REFERENCES

[1] M. Glick, "Optical Switching for Next Generation Data Centers", in PS2009, p ThII1-1

[2] D.T. Neilson et al., "256 256 Port Optical Cross-Connect Subsystem", J. of Lightwave Technol., vol. 22, no. 6, pp. 1499-1509, JUNE 2004.

[3] Y. Kai et al., "A compact and lossless 8×8 SOA gate switch subsystem for WDM optical packet interconnections", in ECOC 2008, p. We.2.D.4.

[4] L. Dittmann et al., "The European IST Project DAVID: A Viable Approach Toward Optical Packet Switching", J. of Selected Areas in Comm., vol. 21, no. 7, pp. 1026-1040, September 2003.

[5] H. Wang et al., "Lossless Multistage SOA Switch Fabric using High Capacity Monolithic 4x4 SOA Circuits", in OFC2009, OWQ2.

[6] I. H. White et. al. "Scalable optical switches for computing applications", Journal of Optical Networking, vol 8, no 2, pp 215-224, 2009.

[7] E.T. Aw et al., "Dynamic Range Studied of a Monolithic 2x2 Quantum Dot Switch" in CLEO2007, CTuII2

[8] H. Wang et al., "High Capacity Demonstration of a Compact Regrowth-Free Integrated 4×4 Quantum Well Semiconductor Optical Amplifier Based Switch", in ECOC2008, p. Th.1.C.6

JePPIX: the platform for InP-based photonics

Xaveer Leijtens
COBRA Research Institute, Eindhoven University of Technology, the Netherlands
Email: X.J.M.Leijtens@TUe.nl

***Abstract*—JePPIX is the European platform that offers access to Indium Phosphide based technology for proof of concept, prototyping and large volume manufacturing. This is enabled by using a generic integration technology.**

I. Introduction

The joint European platform for InP-based components and circuits, JePPIX, is a technology platform for the development and promotion of Photonic Integrated Circuits (PICs) in Indium Phosphide. JePPIX aims at a generic integration technology in which a variety of photonic integrated circuits can be designed and fabricated using the same process. This concept is well known in electronics; in photonics it is new and can lead to huge cost reductions by realizing photonic ICs for a broad variety of applications using a small set of basic building blocks that are integrated in a generic foundry process.

JePPIX is one of the three photonic integration platforms that were started from ePIXnet, the EU FP6 Network of Excellence, besides ePIXfab (silicon photonics) and TriPleX (dielectric waveguides).

II. Generic integration technology

One of the main challenges for photonic integration is to develop a technology that supports a small set of building blocks with good performance, with which a broad class of functionalities can be realized. At COBRA we use a technology that offers active-passive butt-joint integration: three-step epitaxy by MOVPE, self-aligned CH_4-H_2 RIE process for etching, planarization and metallization. This process integrates the following building blocks:

1) Passive waveguide devices (PHMs), including the most widely used components such as waveguide bends, multi-mode interference couplers, arrayed waveguide grating demultiplexers (AWGs), and tapers. Shallow and deep-etched PWDs are available, figure 1 and 2, for low and high contrast, respectively.

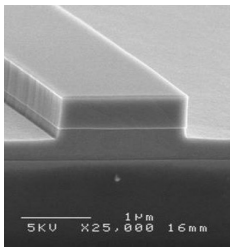


Figure 1. Shallow etched waveguide.

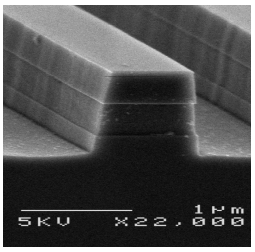


Figure 2. Deep etched waveguide.

2) Phase modulators (PHMs) to control the phase of the optical signals. When used in an interferometric configuration, such as a Mach-Zehnder interferometer, phase modulators provide a means for signal intensity modulation or space switching as well.
3) Semiconductor optical amplifiers (SOAs), figure 3. The importance of the SOA for photonics is similar to that of the transistor for electronics: it provides amplification but it also supports a broad class of non-linear signal operations, like wavelength conversion, 2R and 3R signal regeneration, optical time-domain demultiplexing, clock extraction and other digital signal operations. When operating the SOAs in reverse bias, they can be used as high-speed photo-detectors.

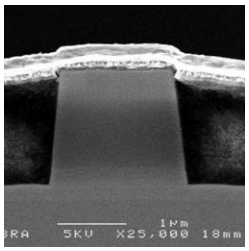


Figure 3. Shallow etched SOA or photo-detector.

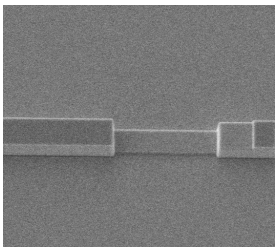


Figure 4. Isolation section, where top layer is locally removed (angled top-view).

4) Isolation sections, figure 4. These are regions where the highly conductive p^+-layer is locally removed to provide electrical isolation between different SOAs and/or phase modulators.

At the moment JePPIX is offering small-scale access to the COBRA generic integration process of TU Eindhoven.

III. Access to Multi-Project Wafer Runs

Having a technology that makes use of standard building blocks will greatly reduce the costs of photonic ICs, because the development cost of that technology will be shared by all users of that technology. For smaller-scale projects, those costs can be even further reduced, by making use of multi-project wafer runs. In this approach, different users share cells on the same wafer, and thereby they share the cost of that run, typically proportional to the total chip area that they use.

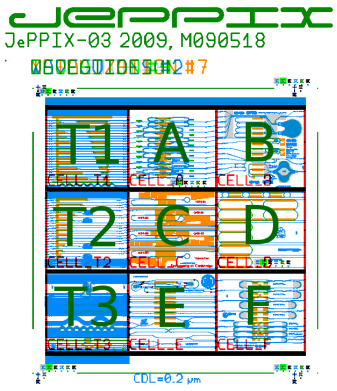


Figure 5. View of the cell layout of a JePPIX MPW-run at COBRA, consisting of test cells (T1–T3) and multi-project user cells (A–F).

COBRA offers access to multi-project runs to external users, who are first trained in the design of photonic ICs in a two-week course at the COBRA institute in Eindhoven. The runs then consist of processing active-passive 2-inch epi-wafers, split into 9 cells (typically 4×4 mm^2), see figure 5; three of which are reserved for test structures (T1–T3, to qualify the processing) and 6 cells host the designed PICs of the users (A–F). Each user can make an independent design, even without the need to know anything about the neighboring cell. This is achieved by using pre-defined positions and dimensions of the input and output waveguides, see figure 6. These waveguides may be placed on a 25 µm pitch, either straight or angled, where the 7° angle greatly reduces the reflections from the cleaved chip-facet.

A number of novel devices made from these basic building block in a JePPIX multi-project wafer run at COBRA have been demonstrated, including a mode-locked ringlaser [1], which uses a combination of the SOA, isolation and PWD building blocks; a pulse-compressor [2], using combinations of PHM and PWD building blocks; a fast tunable laser [3], integrating SOAs with PWD building blocks. Figure 7 shows a photograph of that tunable laser. Clearly visible are the gold contact pads for the current injection of the SOAs (three bottom contacts), eight contact pads on the top, which connect to short SOA-sections that act as optical gates which select the wavelength, and an AWG acting as wavelength filter is visible on the right side of the picture.

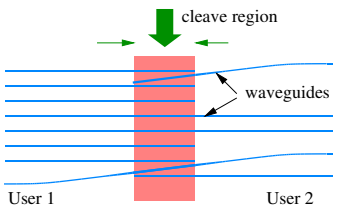


Figure 6. Standardized waveguide locations at cell boundary.

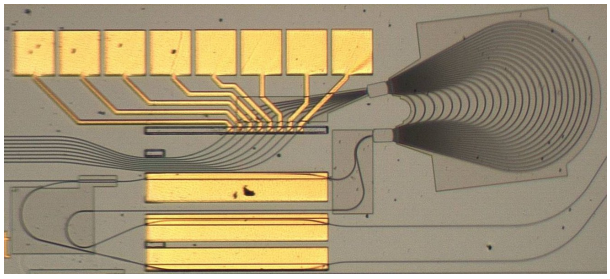


Figure 7. Discretely tunable laser with ns switching time.

IV. Outlook

COBRA offers small scale access to its process for gaining experience with the generic foundry process. In the EuroPIC project, http://europic.org, transfer of this model to industrial fabs is presently being investigated. Two EuroPIC partners, Oclaro Technology in the UK and the Fraunhofer Heinrich Hertz Institute in Germany, whose processes are conceptually similar to the process of COBRA, are presently preparing their processes for experimental generic foundry runs. When the EuroPIC project is succesful, COBRA will move its activity to development of improved or novel features for later integration in the industrial foundry processes.

References

[1] Y. Barbarin, E. Bente, M. Heck, J. den Besten, G. Guidi, Y. Oei, J. Binsma, and M. Smit, "Realization and modeling of a 27-GHz integrated passively mode-locked ring laser," *IEEE Photon. Technol. Lett.*, vol. 17, pp. 2277–2279, Nov. 2005.

[2] M. Heck, P. Muñoz, B. Tilma, E. Bente, Y. Barbarin, Y. Oei, R. Nötzel, and M. Smit, "Design, fabrication and characterization of an InP-based tunable integrated optical pulse shaper," *IEEE J. Quantum Electron.*, vol. 44, pp. 370–377, Apr. 2008.

[3] M. Heck, A. L. Porta, X. Leijtens, L. Augustin, T. de Vries, E. Smalbrugge, Y. Oei, R. Nötzel, R. Gaudino, D. Robbins, and M. Smit, "Monolithic AWG-based discretely tunable laser diode with nanosecond switching speed," *IEEE Photon. Technol. Lett.*, vol. 21, pp. 905–907, July 2009.

A photonic, hybrid integrated, THz heterodyne source

C. C. Renaud, M. Fice, L. Ponnampalam, D. C. Rogers*, D. G. Moodie*, G. D. Maxwell*, I. F. Lealman*, P. J. Cannard*, R. Harmon*, L. Pavlovic†, L. Naglic†, M. Vidmar† and A. J. Seeds
Department of Electronic and Electrical Engineering
University College London
London UK
*CIP Technologies, Ipswich UK
†Univerza v Ljubljani, Ljubjana, Slovenia

Abstract—**We present the first results on the integration of a photonic heterodyne source using a hybrid integrated optical phase lock loop to minimise loop propagation delay. The loop achieved phase noise of less than -80dBc/Hz at 10KHz offset and generated high spectral purity signals at frequencies up to 300GHz with an output power of -20dBm.**

Hybrid Integration; Heterodyne; Optical Phase Lock Loop; Photonic integration

I. INTRODUCTION

Photonic techniques are being used increasingly for frequency generation to access the millimetre-wave band (30 – 300 GHz) and beyond (terahertz waves). Potential applications in the mm-wave band include high-speed fixed wireless access and home area networks, with wireless links at 10 Gb/s data rates already having been demonstrated at 60 GHz [1] and 120 GHz [2] over spans of tens to hundreds of metres. At higher terahertz (THz) frequencies, there is interest in medical imaging, spectroscopy, and security screening [3].

This paper shows the potential of photonic hybrid integrated systems for high spectral purity frequency generation at frequencies above 30 GHz [4]. The high purity photonic heterodyne source was based on an hybrid integrated optical phase lock loop (OPLL) [5] with an overall delay of 1.4 ns, where the two slave tuneable lasers offered the potential for the generation of up to 1.8 THz. The integrated OPLL allowed for the generation of signals with a phase noise of – 80 dBc/Hz at 10 kHz offset.

II. THE HYBRID OPLL BOARD

The board was based on hybrid technology where active InP based components are integrated with passive silica waveguides on silicon substrates [6]. The advantage of such a technology is that while the overall optical delay of the loop is reduced, the individual active components (lasers and photodetectors) and the electronic filters are easily integrated with the board. The optical part of the board, shown in Fig. 1, comprise the mother board with the optical passive waveguides, coupler and the electrical connections for integration with the active optical components and electronic filters. The board also include a daughter board with a twin distributed Bragg reflector (DBR) laser chip. These twin DBR lasers are buried heterostructure lasers fabricated 30μm apart on a single InP/InGaAsP chip, each laser having 4 sections: front and rear grating, gain section and phase section. The waveguide of each laser was of different width to achieve a wavelength offset between them. The outputs were combined by a coupler, which was further integrated onto an angle tapered semiconductor optical amplifier (SOA) to boost the output power with minimum facet reflections to 10 dBm maximum per laser. Importantly, for the OPLL, the two laser output linewidths were about 1 MHz, thus permitting an overall loop delay of up to 1.5 ns [1]. The board also included two daughter boards for the 10 GHz 3dB bandwidth photodetectors. The integration meant that the optical part of the delay was only 40 ps.

This board was connected to a multilayer printed circuit board containing the electronic loop filter. The filter was based on two parallel paths. The first path was a short delay gain loop offering a total 1.4 ns delay that was essential to the operation of the phase lock loop. The second loop was a lower bandwidth integrating loop that was used to track the slow thermal drift of the slave laser frequency and allow for tuning of the frequency difference between the slave and the master. That frequency difference was limited to a 2 GHz to 7 GHz range, where the lower limit was due to the 90-degree power splitter used for reference signal distribution and the upper limit was due to the photodiode amplification stage.

III. LOCKING PERFORMANCE

The tuning performance of the integrated OPLL was studied by measurement of the heterodyne signal between the master and locked slave laser using a spectrum analyzer. The quality of the lock was measured in terms of phase noise with

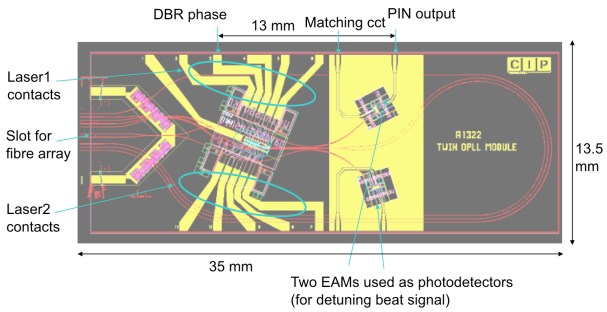


Fig. 1: Hybrid OPLL board with a dual DBR laser and two EAM detetectors

This work was sponsored by the European Commission through the Framework 6 integrated project IPHOBAC.

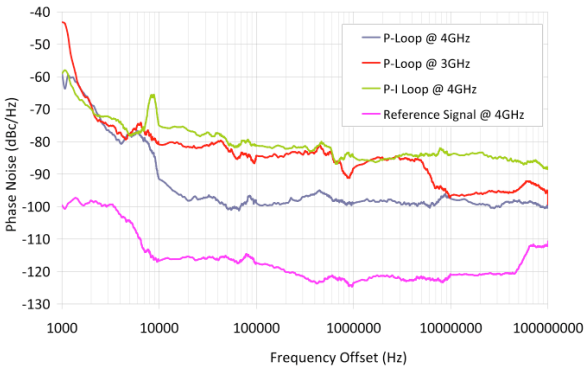


Fig. 2: Phase noise up to 10 MHz offset for the locked laser signal.

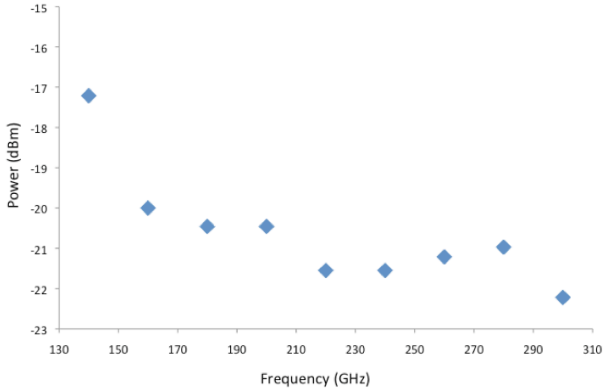


Fig. 3: Emitted power from a fast photodetector integrated with antenna connected to the hybrid OPLL

and without the slow tracking integrating loop. The measured phase noise results are shown in Fig. 2, together with the frequency reference source phase noise. The heterodyne linewidth (3 dB) was less than 1 kHz (instrument resolution bandwidth limited). At 10 kHz offset the phase noise was -80 dBc/Hz. As the gain of the proportional loop (P-loop) was frequency dependent, differences could be seen at different frequency offsets.

With the integral tracking loop on and an optimized photocurrent on the photodetector, the slave laser could be tuned over the full 2 GHz to 7 GHz offset range while remaining locked to the master laser.

IV. Frequency Generation

To generate Frequencies above the maximum 9 GHz frequency offset an optical frequency comb generator was used as the master optical source [4]. Two comb lines were then used respectively to provide the optical reference signal to the OPLL and to lock a Distributed Bragg Reflector (DBR) laser by injection locking. The OPLL was first tuned close to the frequency of one of the comb lines before turning on the phase lock loop.

First this heterodyne system was tested at 100 GHz with a fast Uni-Travelling Carrier (UTC) photodetector [4] connected through a coplanar probe and an harmonic mixer to a spectrum analyzer. Figure 3 shows the resulting heterodyne spectrum at 1 kHz resolution bandwidth, with the expected high spectral purity (heterodyne linewidth < 1 kHz, resolution bandwidth limited). The system was then connected to partially depleted absorber photodetector integrated with a bow tie antenna on top of a silicon hemispherical lens with an injected optical power of 100 mW, while the lock quality was monitored. The power was then measured using a large area THz Thomas Keating power meter for frequencies between 130 GHz and 300 GHz, obtained by locking to different comb lines. Fig. 4 shows that the THz power was varied from -17 dBm to -22 dBm, thus demonstrating the potential of the integrated source for the generation of high spectral purity signals at frequencies up to 300 GHz.

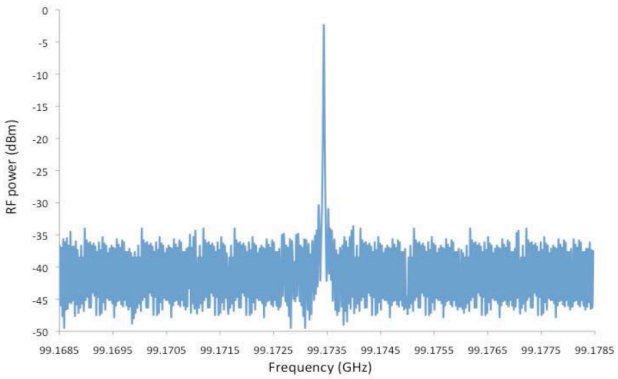


Fig. 4: Spectrum of the heterodyne signal at 99 GHz with 1 kHz resolution.

V. Conclusion

We have presented the first demonstration of an hybrid integrated photonic heterodyne OPLL frequency source. The required short loop delay that was achieved through integration enabling high spectral purity frequency generation from 2 GHz to 300 GHz with less than -80 dBc/Hz phase noise at 10 kHz offset. The optical output power of the photonic source was about 10 dBm per laser and with external amplification up to -3 dBm was generated at 110 GHz with an and -22 dBm at 300 GHz using UTC photodiodes.

References

[1] A. J. Seeds and K. J. Williams, *J. Lightw. Technol.*, vol. 24, no. 12, pp. 4628-4641, 2006.

[2] A. Stöhr *et al*., *J. Optical Networking.*, vol. 8, no. 5, pp. 471-487, 2009..

[3] A. Hirata *et al., IEEE Trans. Microwave Theory and Techniques*, vol. 54, no. 5, pp. 1937-1944, 2006.

[4] C. C. Renaud, L. Ponnampalam, F. Pozzi, E. Rouvalis, D. Moodie, M. Robertson, A. J. Seeds, (invited) International Topical Meeting on Microwave Photonics (MWP 2008), pp. 55-58, Gold Coast Australia, 2008.

[5] A. J. Seeds, F. Pozzi, C. C. Renaud, M. J. Fice, L. Ponnampalam, D. C. Rogers, I. F. Lealman, R. Gwilliam, (invited) 14th European Conference on Integrated Optics and Technical Exhibition, pp. 123-132, 2008

[6] G. Maxwell et al, "Very low coupling loss, hybrid-integrated all-optical regenerator with passive assembly" ECOC, Post Deadline Paper, 2002.

Fast Reconfigurable Cyclic Router Using Semiconductor Optical Amplifier Gate Array

A. Rohit, K. A. Williams, X.J.M. Leijtens, T. de Vries, Y.S. Oei, M.J.R. Heck, L.M. Augustin, R. Notzel, D.J. Robbins and M.K. Smit

COBRA, Technische Universiteit Eindhoven, PO Box 513, 5600MB Eindhoven, The Netherlands. Email: a.rohit@tue.nl

Abstract— **A fast reconfigurable monolithic wavelength router with highly compact semiconductor optical amplifier gate arrays is proposed and demonstrated. Time and wavelength multiplexed data is dynamically routed with a power penalty of 3.0dB for guard times as low as 2ns.**

Keywords: Optical communication, Wavelength division multiplexing, Tunable filters, Semiconductor optical amplifier

I. INTRODUCTION

Nanosecond time-scale, wavelength-tuneable, optical filters offer an important enabler for a wavelength agile networking in metropolitan area telecommunications [1], interconnection systems [2] and access networks [3]. However, cost and energy consumption place stringent demands on the required hardware. Photonic integration can reduce the assembly complexity and remove unnecessary losses from fiber to chip interfaces. Arrayed waveguide grating (AWG) cyclic routers in particular offer a manufacturable and highly scalable route to reconfigurable networking. However, most work has required their combined use with wavelength tuneable transmitters or wavelength convertors. Recently, fast re-configurability in AWG based tunable filters has been made possible through electro-optic phase tuning [4]. Wideband unicast operation has been demonstrated but complex analog control is required.

In this work, we propose a novel digitally controlled, monolithic nanosecond re-configurable wavelength router consisting of multiband cyclic AWG integrated with a highly compact SOA gate array. Power penalty for the routed data is studied for both static and dynamically reconfigured operation. Nanosecond re-configurability for very short guard bands is analyzed by means of full bit error assessment to quantify fast reconfigured circuit performance.

II. DESIGN AND FABRICATION

The reconfigurable wavelength router consists of a highly compact 4x4 cyclic AWG with densely integrated array of four SOA gates. The device has been fabricated using an active-passive re-grown epitaxy [5]. The microscope image in figure 1 shows the functional part of the circuit. The input on the top-right is split using cascaded 1x2 multimode interference couplers to the four compact SOA gates. Each SOA gate is 140µm in length and is angled at 12 degrees relative to the active island length. These SOA gates are accommodated within one single active island of 30µm x 750µm, as shown in inset of figure 1.

This work is supported by the Dutch Technology Foundation STW. The chip has been fabricated on the Photonic Integration Platform JePPIX on a multi-project wafer.

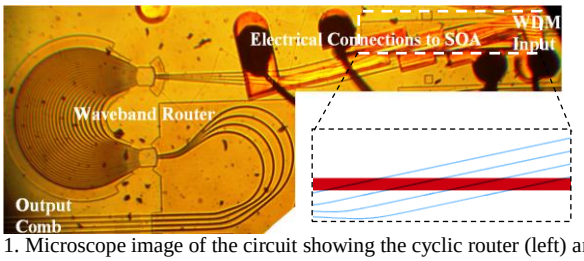


Figure 1. Microscope image of the circuit showing the cyclic router (left) and the gate array (upper right). (Inset) Mask layer representation of the four SOA gates across the active region

Wide shallow etched waveguide widths of 3µm are used for the SOAs and the 2µm widths are used for passive shallow etch waveguides. Waveguide tapers and shallow to deep waveguide transitions are implemented each side of the active island. Deep etched low radius curved waveguides allow for further circuit size reduction. The total circuit area is less than 5mm^2, including the waveguide fan-out for the fiber interface. Input and output waveguides are angled at 7 degrees to the cleaved facets for reduced reflections. Lensed fibers are used for fiber-chip coupling.

The circuit transfer function is evaluated by biasing one of the SOA gate at 50mA and measuring the amplified spontaneous emission at the input and each of the four outputs. The four output side spectra are overlaid in figure 2 for SOA gate 1 enabled. The free spectral range is five times the channel separation, leaving one band unconnected for each free spectral range. A uniform spectral performance with 2dB variation is observed across the measured 100nm bandwidth. The unfiltered spontaneous emission from the input side is also shown with a variation of under 4dB over the 100nm measurement range. Selective electrical biasing within the SOA array enables a reprogramming of the transfer function allocating wavelength comb to each of the output ports.

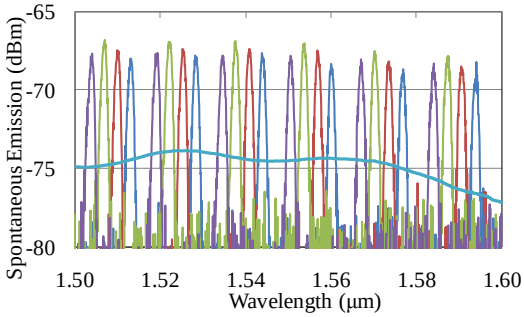


Figure 2. Cyclic router transfer function for SOA 1 enabled. Overlaid spontaneous emission spectra to the input and the four outputs.

III. Dynamic Switching Characteristics

The experimental arrangement to study the dynamic optical routing is shown in figure 3(a). Firstly, the assessment of switching performance of the SOA gate is performed. Two multiplexed wavelength channels at 7dBm (in fiber) each are input to the device. The two wavelength channels are individually routed to the same outport by sequentially changing the bias states for SOA gates 1 and 2.

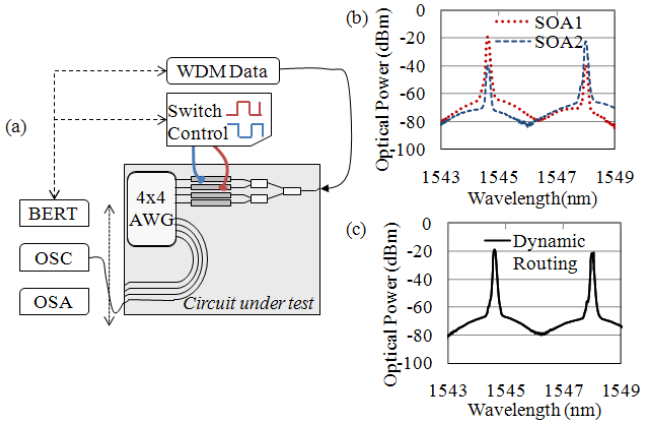


Figure 3. (a) Dynamic routing experiment, (b) For SOA1 and SOA2 on, (c) SOA1 and SOA2 alternating. (0.1nm resolution bandwidth)

Extinction ratio is measured for dc bias conditions for individual SOAs at 40mA.The output is measured on the optical spectrum analyzer. As shown in figure 3(b), extinction ratios of greater than 15dB are achieved for both switch states. Figure 3(c) shows the output spectrum when the SOAs are biased using 0 to 2V complementary square wave signal for the fast reconfigurable routing experiments.

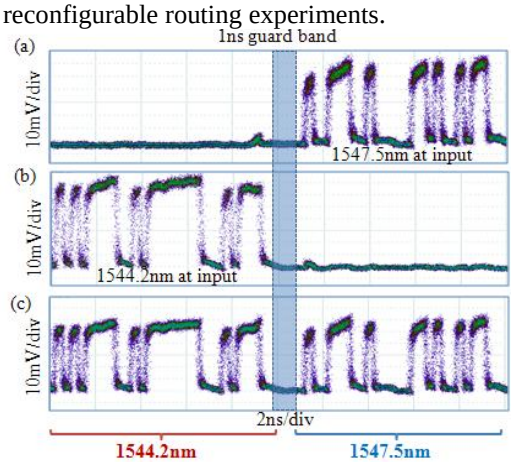


Figure 4. Fast reconfigurable routing monitoring the circuit output (a) Only channel 1547.5nm at input (b) Only channel 1544.2nm at input (c) Channels 1544.2nm and 1547.5nm at input.

The impact of nanosecond switch transitions on data integrity is studied with data at 3Gbit/second on two different wavelength channels. Two tuneable lasers are multiplexed and modulated with the same pseudorandom sequence of 2^{15} -1 bit length data. These are input to the wavelength router. The switch state is reconfigured at the rate of 5.7 kHz with 1ns electronic transition times. The oscilloscope traces in figure 4 shows the optical data during switch reconfiguration. Output port 1 is monitored for the periodically gated router for the two wavelengths individually input (a) and (b) and then simultaneously (c). The time traces show that the data sequence is transmitted only for the on-state of the corresponding SOA gate. For the off-state, the transmission is suppressed. When both the wavelength channels are present, a continuous data sequence is received as shown in figure 4(c). The oscilloscope trace shows a stable transition between wavelength channels as the circuit is reconfigured with no evidence of ringing or overshoot. The figure also shows a guard time of less than 2ns between the wavelength packets thus enabling very high link utilization.

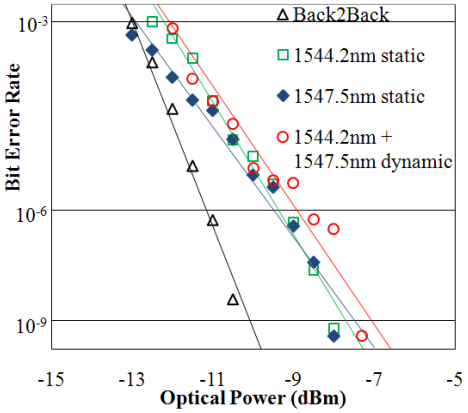


Figure 5. Power penalty assessment for all received bits, switching between 1544.2nm and 1547.5nm.

Bit error rate measurements for the received static and dynamically routed optically time multiplexed data are performed and shown in figure 5. No clock recovery is performed for the synchronized data streams in this study. No circuit dependent transient degradation is observed. Power penalty of 3.0dB is observed which is only marginally higher than the values measured for static operation.

IV. Conclusion

A gated cyclic wavelength router with nanosecond timescale re-configurability is demonstrated for the first time. The highly compact SOA gate array provides digital control and the use of cyclic router enables an intrinsically scalable architecture. A power penalty of 3.0dB is observed for both static and for dynamic wavelength routing.

References

[1] L. Dittmann et al, "The European IST project DAVID: A viable approach toward optical packet switching", IEEE Journal on Selected Areas in Communications, 21, 7, 1026-1040, 2003.

[2] R.P. Luijten and R. Grzybowski, "The OSMOSIS optical packet switch for supercomputers", Proceedings of the Optical Fiber Communication Conference, Paper OTuF3. 2009.

[3] M.C. Parker et al., "Wavelength-tolerant optical access architectures featuring N-dimensional addressing and cascaded arrayed waveguide gratings", Journal of Lightwave Technology, 16, 12, 2296-2302, 1998.

[4] T. Tanemura et al, "InP/InGaAsP integrated 1x5 optical switch using arrayed phase shifters", IEEE PTL, 20, 12, 1063-1065, 2008.

[5] M.J.R. Heck et al, "Monolithic AWG-based discretely tunable laser diode with nanosecond switching speed", IEEE PTL, 21,13, 905-907,2009.

Photonic Crystal Cavity-Based Wavelength Routers

Lasse J. Kauppinen, Tjeerd J. Pinkert, Hugo J.W.M. Hoekstra, and René M. de Ridder
Integrated Optical MicroSystems Group, MESA+ Research Institute for Nanotechnology
University of Twente
Enschede, The Netherlands
l.j.kauppinen@ewi.utwente.nl

***Abstract*— We have characterized the optical properties of wavelength routers in a 2D photonic crystal with a triangular lattice of air holes. The router designs are aimed for realization of monolithically integrated mechano-optical switches.**

Keywords- photonic crystal; cavity; filter; switch;router; silicon

I. INTRODUCTION

We have studied the optical properties of two different photonic crystal (PhC) cavity-based wavelength routers. The first one is based on a Y splitter with an asymmetric cavity at the junction; the second one, known as a channel drop filter, consists of two parallel waveguides, coupled through a cavity. The optical designs are aimed at monolithic integration with a nanomechanical actuator, in order to actuate the switching function. For such an integration the small size of PhC structures is beneficial due to compactness and fast actuator operation [1].

The Y splitter device is designed for operation at a specific wavelength; the input signal can be switched between two output ports by selectively filling either of two holes, thus effectively mirroring the structure, see Fig 1. The channel drop filter is designed to drop a certain wavelength band from the "bus" channel to the "drop" channel, see Fig. 3. By changing the effective index of the structure with a mechanical element, the drop wavelength can be tuned [2].

The optical structures have been fabricated by the silicon photonics platform of IMEC, Leuven [3]. In the process the devices are patterned into a 220-nm thick silicon device layer of a SOI wafer with a 2 μm buried silicon dioxide layer.

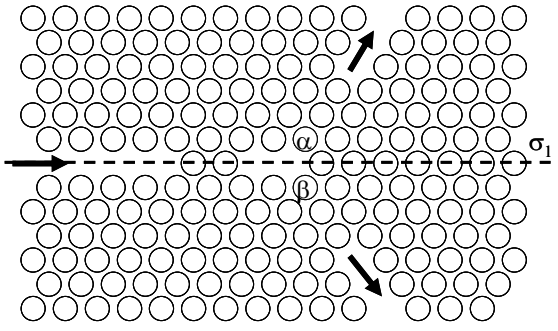


Figure 1. Principle of a PhC cavity-based Y splitter. The labels α and β indicate the positions of the switching holes. The asymmetric cavity at the junction (α or β filled) couples input light to only one of the output ports at a specific wavelength. By selectively filling either hole, the structure is effectively mirrored about the dashed line, thus interchanging the output ports.

This work is supported by NanoNed, a national nanotechnology program coordinated by the Dutch ministry of Economic Affairs.

II. Y SPLITTER DEVICE

The functionality of the Y splitter design is based on symmetry of the cavity. By filling either hole α or β, the device symmetry is changed, and at a resonance wavelength light is coupled to either one of the output ports.

Based on our modeling results we have chosen a PhC lattice period of 420 nm and a hole diameter of 255 nm, in order to obtain an operating wavelength of 1550 nm. The actual hole diameter depends on the lithographic exposure dose. A SEM image of the fabricated device (hole β filled) is shown in Fig 2a.

Fig. 2b shows the measured transmission spectrum (hole β filled) and the result of a corresponding 2D FDTD simulation [4]. Light was coupled into the PhC device using a vertical fiber coupling method [5]. The measured transmission spectra have been normalized with respect to a straight Si photonic wire waveguide, similar to the access waveguides. For the simulation we assumed a hole diameter of 250 nm and an effective index of 2.82. The simulated curve has been fitted to the experimental data by shifting it in horizontal direction by –23 nm (accounting for inaccuracy introduced by using the effective index method in 2D calculations) and in vertical direction by -7 dB (average excess loss). The typical loss of a 25 periods long PhC W1 waveguide was measured to be 5 dB; near the mode cut-off it is 10-15 dB. The near mode cut-off loss is attributed to the slow light [6].

From Fig. 2b it can be seen that at resonance wavelength 1560 nm most of the light is coupled through the cavity to the *out1* waveguide branch, operating similar to a Fabry-Perot resonator. The on/off ratio at 1560 nm between ports *out1* and *out2* is about 12 dB.

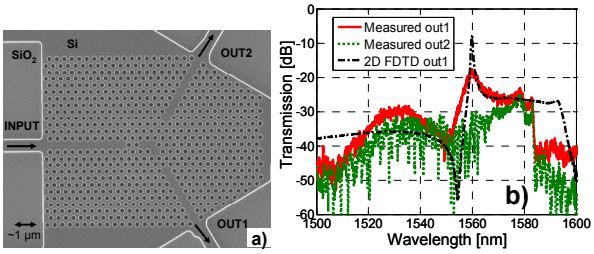


Figure 2. a) SEM image (top view) of the PhC Y splitter. b) Measured and simulated transmission spectra for the asymmetric cavity design; transmission from the *input* to the *out1* waveguide branch, using the normalization procedure mentioned in the main text.

III. CHANNEL DROP FILTER DEVICE

A SEM image of the cavity-based PhC channel drop filter is shown in Fig. 3. In the ideal case the light at a specific wavelength propagating along the bus channel is transmitted to the drop port (*out2*) while the light at the other wavelengths continues travelling through the bus channel to output port *out1*. The cavity should be designed such that the power at the drop wavelength is fully coupled to the drop port. This kind of performance requires (quasi)degenerate resonance modes with different field symmetries [7] at the operation wavelength. These resonant modes should have opposite symmetry with respect to the mirror plane centered on the cavity and perpendicular to the waveguides. The odd resonant mode excites forward and backward travelling guided modes in the PhC waveguides with π phase shift, whereas the even resonant mode excites them in phase, thus causing destructive interference for the backward travelling waves [7].

For the PhC structure we have selected a period of 440 nm and a hole diameter of 240 nm, as according to our simulations these parameters give device operation that is in the desired wavelength range of 1530-1565 nm. The PhC structure under study, shown in Fig. 3, consists of two symmetrically arranged W1-type waveguides, separated by 7 rows of holes, with a cavity in between. The diameter of the boundary holes adjacent to the W1 waveguides are made larger than the rest of the slab holes, in order to obtain single mode operation [8] and to adjust the dispersion curves for the cavity cross-section such that the desired wavelength drop performance is achieved.

Two versions of the device were fabricated; one with a boundary hole diameter (BHD) of 320 nm and the other with a BHD of 330 nm. Figs. 4a and 4b show the measured transmission spectra of the channel drop devices, normalized with respect to the transmission of a straight W1 waveguide of equal dimensions. Due to measurement noise, the transmission seems to be slightly above 0 dB in some regions.

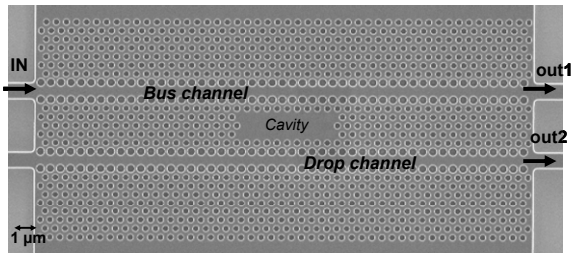


Figure 3. SEM image (top view) of a PhC channel drop filter. Ideally the cavity drops one wavelength from the bus to the drop channel, while other wavelengths continue in the bus channel.

As seen from the measured transmission spectra, both channel drop filters have a drop wavelength of 1561 nm. For a design with BHD of 330 nm the on/off ratio between ports *out1* and *out2* is higher; 16 dB compared to 10 dB. The full width at half maximum of the drop band is approximately 2.5 nm for both designs. Fig. 4a also shows the transmission spectrum of a reference device without a cavity but otherwise similar. From this reference curve (OUT2 Ref.), it can be seen that the device suffers from considerable cross talk at wavelengths longer than 1570 nm. Therefore the device should not be operated at wavelengths larger than the drop wavelength. The device with 320 nm BHD appears to have less crosstalk outside the drop band.

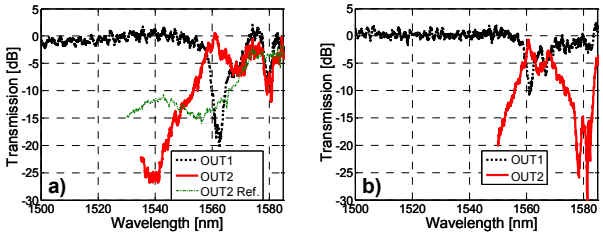


Figure 4. Measured transmission spectra of channel drop filters from the *in* to the *out1* and *out2* ports. a) device with 330 nm boundary hole diameter (BHD). Also shown a reference curve (see text). b) device with 320 nm BHD.

IV. CONCLUSIONS

Photonic crystal cavity-based devices for integrated mechano-optically actuated wavelength router devices have been designed and fabricated. The optical properties of the devices were characterized. For the Y splitter device a 12 dB on/off ratio between the output ports at the operation wavelength was measured. For the two slightly different channel drop filter devices cross talk values of 16 dB and 10 dB respectively have been measured at the drop wavelength. The optical loss of the deep UV fabricated PhC waveguides (25 periods long) are from 5 dB to 15 dB, depending on the wavelength.

ACKNOWLEDGMENT

We thank Anton Hollink and Meindert Dijkstra for their technical help.

REFERENCES

[1] S.M. Chakkalakkal Abdulla et al., "Optimisation study of micro cantilevers for switching of photonic band gap crystals," in Proc. Photonics in Switching 2009, Italy, PT 5, 2009.

[2] G.N. Nielson, et al., "Integrated wavelength-selective optical MEMS switching using ring resonator filters," IEEE Photon. Technol. Lett, vol. 17, pp. 1190-1192, 2005.

[3] Silicon Photonics Platform, http://www.epixfab.eu/

[4] A. Farjadpour, et al., "Improving accuracy by subpixel smoothing in FDTD," Opt. Lett., vol. 31, pp. 2972–2974, 2006.

[5] D. Taillaert, et al., "Grating couplers for coupling between optical fibers and nanophotonic waveguides," Jpn. J. Appl. Phys., vol. 45, pp. 6071-6077, 2006.

[6] L.O'Faolain, et al., "Dependence of extrinsic loss on group velocity in photonic crystal waveguides," Opt. Express, vol. 15, pp. 13129-13138, 2007.

[7] S. Fan, et al., "Theoretical analysis of channel drop tunneling processes," Phys. Rev. B, vol. 59, pp. 15882-15892, 1999.

[8] A. Adibi, R.K. Lee, Y. Xu, A. Yariv, and A. Scherer, "Design of photonic crystal optical waveguides with singlemode propagation in the photonic bandgap," Electron. Lett., vol. 36, pp. 1376-1378, 2000.

Submicron Active-Passive Integration for InP-based Membranes on Silicon

R. Zhang, F. Bordas, J.J.G.M. van der Tol, H. Ambrosius, G. Roelkens, M.A.Dundar and M.K. Smit
COBRA Research Institute
Technische Universiteit Eindhoven
Eindhoven, The Netherlands
r.zhang@tue.nl

P. Thijs
PHILIPS
High tech Campus,
Eindhoven, The Netherlands

Abstract—**The high vertical index contrast and the small thickness of thin InP-based membrane structures bonded with BCB on Silicon allow the realization of very small devices. To make photonic integrated circuits with both passive and active components in these membranes, active-passive integration on a small scale is essential. In this paper we will present our results on sub-micrometer active areas for membrane applications.**

Keywords-InP-based membrane; active-passive integration; interface morphology; photoluminescence;

I. INTRODUCTION

The complexity of photonic integrated circuits (PICs) has been raised significantly these last few years, following Moore's law in Photonics[1]. But to satisfy the need for even further complexity, devices have to be made smaller and less power consuming. InP-based membrane bonded on Si[2](See Fig.1) is a qualified candidate to fulfill this demand. The advantages of this PIC platform are multiple. First of all, we have the main advantage of a membrane structure: high vertical refractive index contrast and low power consumption because of the ultra small size. Secondly, both passive and active functions can be realized in the platform of InP-based materials[3]. Finally, the platform is compatible with Si-on-Insulator (SOI) and CMOS platforms. This makes it possible to use the mature and advanced CMOS Fab technology.

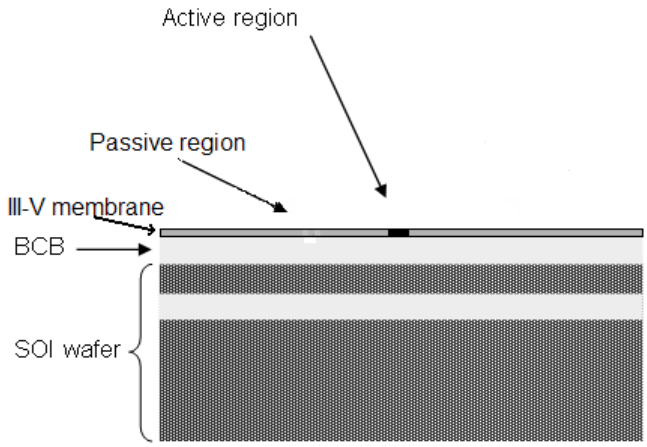


Figure 1. Schematic of InP membrane on SOI platform

Ultra small passive components in the InP membrane, such as waveguides, ring cavities and MMIs, have already been fabricated and these basic components of PICs shows good performance[4] . Since PICs consist of both passive and active components, a successful active-passive integration with sub-micrometer active regions in membranes is an essential step towards complete PICs. In this paper we will present our results on active-passive integration with sub-micrometer active areas. The interface between active and passive areas shows a good quality in terms of morphology. Moreover, we find that in the sub-micrometer size active area, the degradation of the active material(InGaAsP quantum wells) due to processing is limited.

II. IDEA AND DESIGN

A successful active-passive integration test should satisfy two critical conditions. On one hand, a smooth and flat interface should be realized between the active and passive materials. A coarse interface causes both reflection and scattering loss when light is coupled between active region and the passive regions. Meanwhile a good surface flatness is necessary for processing and bonding of membranes. On the other hand, since the smallest active regions are only around submicron size, it is possible that the active quantum well materials are damaged by the processes, which means that they cannot emit light anymore.

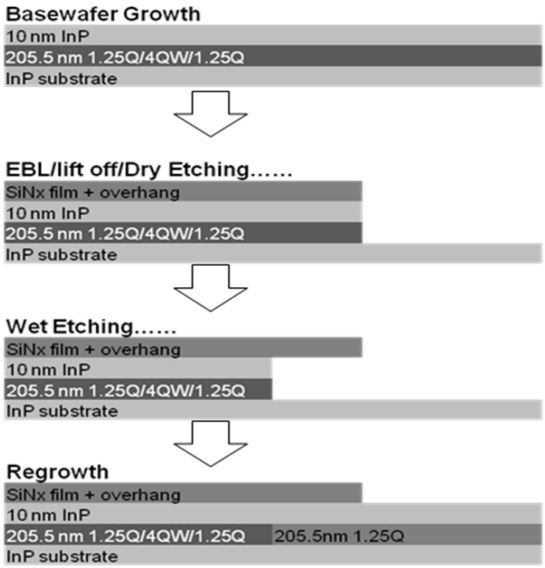


Figure 2. Fabrication process flow

To check the quality of active-passive integrations, active regions of multiple shapes (such as hexagons and octagons) and different orientations are designed. Moreover the sizes of the active regions varies from 250 nm to 2.5 µm in side length.

III. FABRICATION

As it is shown in Fig.2, the starting point is a 200nm quaternary layer (InGaAsP) on InP substrate and this is a typical thickness for membranes. quantum wells which are designed to emit light at 1.55 µm are embedded in InGaAsP layer,. The thin quaternary layer is etched away, except for the places where an active medium is required. Then a regrowth of passive material leads to a passive quaternary layer with local active medium. The wet etching time is optimised so that a flat surface can be realized around the interface between active and passive regions.

IV. CHARACTERIZATION

The characterization focuses on two aspects. On the one hand, the quality of the interface between active and passive materials is checked using Focused Ion Beam etching and SEM inspection. On the other hand, the photoluminescence of small active regions is measured to determine the quality of the remaining quantum well materials.

A. Interface morphology

Fig.3 shows a top view SEM picture of an achieved structure(hexagon bar) with a submicron size. The SiNx mask used for the regrowth is left on the sample, in order to make the active areas visible. The line indicates the position where the cross section picture of Fig.4 is made, by the use of Focused Ion Beam(FIB) etching and SEM. The good quality of the interface and the flatness of the surface can be seen in Fig.4

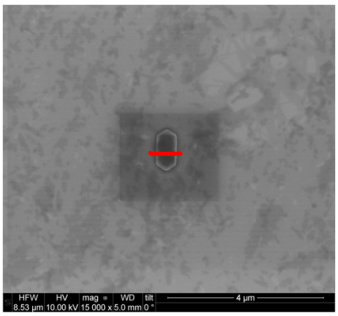


Figure 3. SEM picture

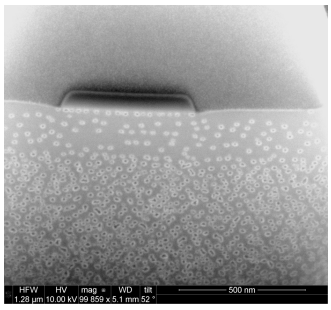


Figure 4. Cross section made by FIB

B. Photoluminescence measurement

Fig.5 shows the photoluminescence of a realized structure under CW pumping by a red laser diode at 660 nm. This spectrum corresponds to the quantum wells emission with a peak centred at 1500nm and this means quantum wells are usable.

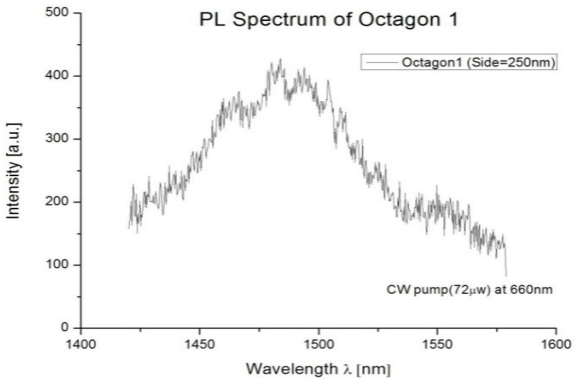


Figure 5. PL spectrum of the submicron achieved region

We observed a blue shift when the size of the active region decreases. We believe that this is due to the quantum intermixing effect[5] caused by defects from dry etching and high temperature during the regrowth process.

V. CONCLUSION

In this paper, we explored the feasibility of active-passive integration within the submicron scale on a quaternary material system (InGaAsP). This is the essential step towards membrane PICs including ultra small active and passive components. The interface between active and passive areas shows a good quality in terms of morphology. Moreover, by using photoluminescence measurement, we find that in the sub-micrometer size active area, the degradation of the active material(InGaAsP QWs) due to processing is limited.

A successful active-passive integration within submicron range will enable us to make very small lasers in InP-based membranes with very small threshhold current and power consumption. Naturally, this is of great interest for applications like single photon sources and digital photonics, such as all optical flip-flops based on coupled lasers

ACKNOWLEDGMENT

The authors thank EU Project HISTORIC for financial support. Particularly, we would like to thank B. Barcones Campo for her help in Focus Ion Beam etching.

REFERENCES

[1] R. P. Nagarajan and M.K. Smit, “Photonic integration”, IEEE LEOS Newsletter. vol 21, Nr. 3, pp. 4-10, June, 2007.

[2] G. Roelkens, et al”III-V/Si Photonics by die to wafer bondig”,Materials Today. vol 10, Nr 7-8, pp.36-43,July-August,2007.

[3] J.J.G.M. van der Tol,Y.S Oei,U. Khalique,R. Notzel and M.K. Smit, ”InP-based photonic circuit: comparison of integration techniques ” , unpublished.

[4] F. Bordas, et al “Compact passive devices in InP membrane on silicon”, in Proceedings of the Conference ECOC, 2009

[5] J. Micallef, A. Brincat and W. C. Shiu, **“**Cation inter-diffusion in GaInP/GaAs single quantum wells”, Proceeding of Material. Resource Society. Symposium. Vol. 484, 1998.

III-V on Si distributed-feedback lasers based on exchange Bragg contradirectionnal coupling

T. Dupont, L. Grenouillet, A. Chelnokov
CEA-LETI, MINATEC, 17 rue des Martyrs,
38054 Grenoble, France.
tiphaine.dupont@cea.fr

P. Viktorovitch
Institut des Nanotechnologies de Lyon,
INL, UMR 5270, 36 avenue Guy de Collongue,
Ecully, France.

***Abstract*— We propose a novel III-V on silicon distributed-feedback laser design that takes advantage of exchange Bragg coupling between a III-V stack and a silicon-on-insulator corrugated waveguide. Numerical simulations indicate that the structure design is compatible with bonding thicknesses up to 200 nm, which relaxes the constraints to the integration technology.**

Silicon photonics; heterogeneous integration; semiconductor laser; distributed feedback laser; mode coupling

Over the past few years, the heterogeneous integration of III-V material on Silicon-On-Insulator (SOI) wafers has appeared as a promising solution for the integration of active optical devices on CMOS substrates. Molecular bonding (using a SiO_2 layer) and adhesive bonding (using a polymer layer) have recently enabled the demonstration of several types of III-V on SOI lasers, from microdisk resonators [1] to distributed-feedback (DFB) lasers [2]. In particular, DFB lasers are attractive for wavelength division multiplexing applications due to their monomodicity. This type of laser traditionally uses an index grating along the gain material that acts as a distributed reflector. In the case of III-V on SOI lasers, the grating is preferably placed in the silicon part since the fabrication process would benefit from the maturity and the scalability of the SOI platform. Hybrid evanescent DFB lasers demonstrated by the Intel/UCSB research team have shown noteworthy results [2]. In their design, the fundamental mode of the structure is guided by the SOI waveguide and benefits from gain only on its evanescent tail which overlaps the III-V waveguide. This type of design relies necessarily on a trade-off between modal gain and coupling efficiency into the SOI waveguide. This trade-off requires the use of a very thin bonding layer between the III-V stack and the SOI (5nm in [2]) since the modal overlap on the neighbouring waveguide decreases exponentially with increasing distance between the waveguides. Such an approach can be very demanding from a technological point of view, and intrinsically leads to a device performance that is very sensitive to the bonding thickness accuracy. So as to relax the constraints on the bonding thickness and break the trade-off between modal gain and coupling efficiency, we propose to take advantage of contradirectional coupling between the III-V and the SOI eigenmodes (so called exchange Bragg coupling [3]). The originality of our design is that the grating is not only used to provide distributed feedback but also to couple the III-V and the SOI eigenmodes.

Let us consider the laser structure sketched in Fig. 1. A 580 nm-thick III-V laser stack is bonded on a SOI square-wave corrugated waveguide using a 100 nm thick SiO_2 bonding layer. The silicon thickness is set to 260 nm and the grating depth to 40 nm. The numerical simulations shown hereafter are performed in two dimensions so the structure width is considered as infinite. The laser gain wavelength is centred at 1500nm. The effective indices of the fundamental eigenmodes of the III-V and SOI waveguides are 3.16 and 2.98 respectively. Note that the SOI thickness and grating depth are both optimised so as to minimize codirectional coupling between the various modes of the structure.

The Fig. 2 represents the dispersion diagram of the whole system calculated with the plane wave expansion algorithm. Resonant contradirectional coupling between the various guided modes occurs at anticrossings points. Resonant coupling is associated with the opening of a frequency gap which amplitude increases with the coupling strength. Three distinct coupling points of interest are found at the normalized frequencies u_1=0.158 (a/λ), u_2=0.162 (a/λ) and u_3=0.168 (a/λ). Those coupling frequencies correspond respectively to III-V/III-V direct Bragg coupling, III-V/SOI exchange Bragg coupling and SOI/SOI direct Bragg coupling. Direct Bragg coupling corresponds to a simple mode reflection without any power transfer from a waveguide to the other. This type of coupling is used to create feedback in traditional DFB lasers.

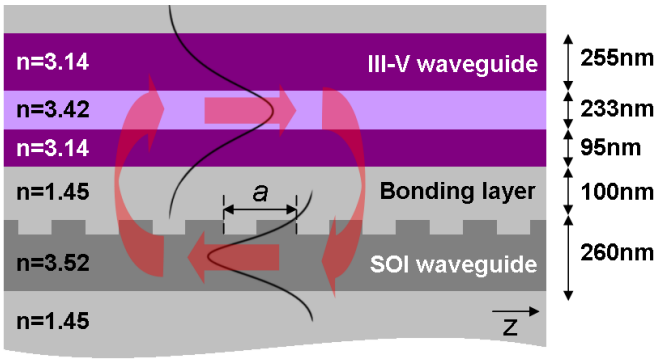


Figure 1. Schematic of a III-V laser stack bonded on a SOI corrugated waveguide. The field circulation at the exchange Bragg frequency is illustrated.

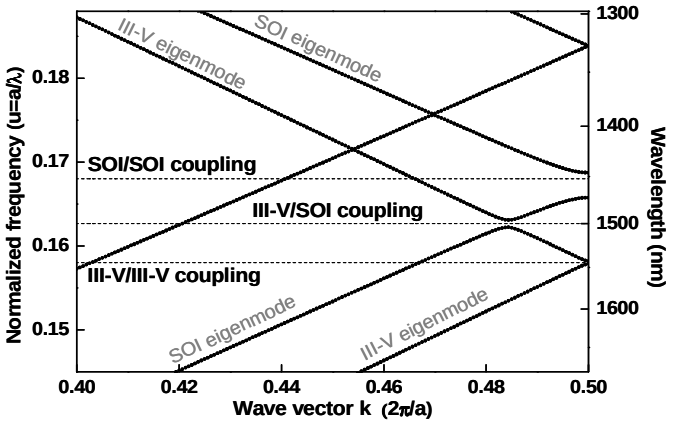


Figure 2. Dispersion diagram of the III-V on SOI structure. Wavelengths on the right axis are calculated for a grating period of 244 nm.

On the other hand, exchange Bragg coupling corresponds to a power transfer from the mode that travels in one direction in the first waveguide to the mode that travels in the opposite direction in the other waveguide [3]. Note that the exchange Bragg coupling point is not placed at the band edge of the dispersion diagram, in contrast to direct Bragg coupling. If the period of the grating is set so that the frequency u_2 is in the gain spectrum of the III-V stack, one should be able to force the optical field to circulate between the III-V and the SOI waveguide and obtain distributed feedback. This circulation of the field would allow the mode to benefit from gain on its highest amplitude part while still allowing for an efficient power extraction to the SOI waveguide. From the dispersion diagram, we calculate that a period of 244 nm would be appropriated for an emission wavelength at 1500 nm, which is achievable by deep-UV lithography.

The spectral width Δu of the gap at the exchange Bragg coupling frequency is related to the coupling constant κ by the following expression [4]:

$$\Delta u = \frac{a}{2\pi} \frac{4\kappa}{n_{gIII-V} + n_{gSOI}} \qquad (1)$$

The group indices of the III-V and SOI modes n_{gIII-V} and n_{gSOI} can be calculated from the slopes of the dispersion curves. From the dispersion diagram of Fig. 2, we extract $\Delta u=8.68.10^{-4}$ and $n_{gIII-V}=3.44$ and $n_{gSOI}=3.63$ which gives $\kappa=39.5$ mm^{-1}. The same numerical simulation performed with a bonding layer thickness of 200 nm lead to $\kappa=13.2$ mm^{-1}, stressing the tolerance of the device regarding waveguide spacing.

The spectral response of the device calculated by 2D-FDTD is shown in the Fig. 3. The structure is two hundred periods long and a quarter-wave shift defect has been added in the middle of the grating so as to break the grating symmetry and force the monomode behaviour of the DFB laser. A pulsed source is placed at the middle of the III-V waveguide and a Gaussian excitation field is launched from the right to the left of the structure. A time monitor that collects the field flowing from the left to the right is placed in the SOI waveguide. Another monitor placed one period away behind the source collects the feedback field flowing from the right to the left of the III-V waveguide. Monitor responses are normalized by the source excitation spectrum. Resonant peaks appear at the three coupling frequencies identified on the dispersion diagram of Fig. 3. The power in the III-V waveguide is more than ten times higher at the III-V/SOI coupling frequency than at the SOI/SOI coupling frequency. The latter is therefore not likely to lase due to the poor modal overlap with the gain material. On the other hand, at the exchange Bragg III-V/SOI coupling frequency, the field distribution is equally shared between the III-V and the SOI waveguides allowing for both a high amount of gain and an efficient power extraction to the SOI waveguide.

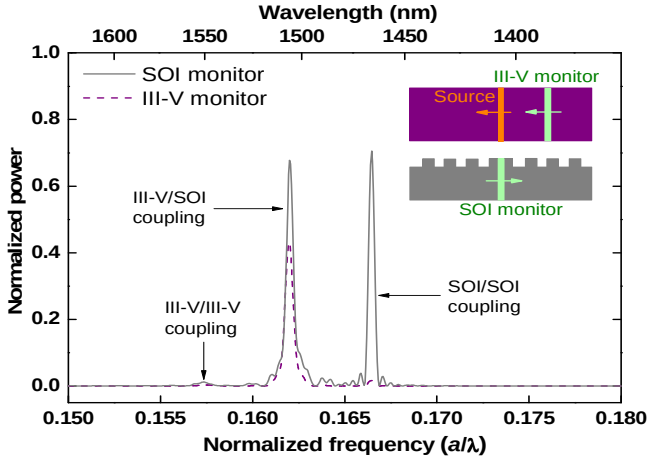


Figure 3. Spectral response of the device calculated by 2D-FDTD. The grating period is 244 nm. A quarter-wavelength shift is added in the middle of the grating. Inset : simulation layout.

In summary, we propose a new type of III-V on Si DFB laser. The distributed feedback action, which is based on an exchange Bragg III-V/SOI coupling scheme, provides an optimum trade-off between modal gain and coupling efficiency to the SOI waveguide. This optimum operation is obtained owing to the generation of a laser mode which is "ideally hybrid", since it provides an equal share of the optical field between the III-V gain material layer and the SOI waveguide. This coupling scheme is compatible with bonding thicknesses as high as 200 nm and therefore relaxes the constraints to the integration technology. FDTD simulations show that mono-mode laser emission should be obtained by using a quarter-wavelength shift in the centre of the grating just as in traditional DFB lasers.

REFERENCES

[1] J. Van Campenhout, P. Rojo-Romeo, P. Regreny, C. Seassal, D. Van Thourhout, S. Verstuyft, et al., “Electrically pumped InP based microdisk lasers integrated with a nanophotonic silicon on insulator,” Optics Express, vol. 15, pp. 6744–6749, May 2007.

[2] A. W. Fang, E. Lively, Y. -H. Kuo, D. Liang and J. E. Bowers, "A distributed feedback silicon evanescent laser," Optics Express, vol. 16, pp. 4413–4419, March 2008.

[3] P. Yeh, H. F. Taylor, "Contradirectional frequency-selective couplers for guided-wave optics," Applied Optics, vol. 19, pp. 2848–2855, August 1980.

[4] S. Olivier, H. Benisty, C. Weisbuch, C. J. M. Smith, T. F. Krauss, R. Houdré, "Coupled-mode theory and propagation losses in photonic crystal waveguides," Optics Express, vol. 11, 1490–1496, June 2003.

InP-based Membrane-type Semiconductor Lasers

Shigehisa ARAI
Quantum Nanoelectronics Research Center
Tokyo Institute of Technology
Tokyo, Japan
arai@pe.titech.ac.jp

Abstract—**With an aim of ultra-low power operation, membrane-type distributed-feedback (DFB) lasers consisting of wirelike active regions are realized with an InP-based high index-contrast waveguide by using benzocyclobutene (BCB) as well as direct boding on a silicon-on-insulator (SOI) substrate. Lateral current injection (LCI) type lasers on a semi-insulating (SI) InP substrate are also presented.**

Keywords-semiconductor laser; distributed feedback laser; BCB bonding; wafer bonding; silicon on insulator

I. INTRODUCTION

To solve the bottle neck problem of Si-LSIs, i.e. speed and power consumption limit, due to transmission time delay caused by long total global transmission line distance, an introduction of optical interconnects / on-chip optical wirings became a very important and challenging issue in next generation electronics [1],[2]. At the same time another research trend to realize not only LSIs but also photonic integrated circuits (PICs) on the same platform with matured CMOS technologies became very active [3], and very low-loss Si waveguides [4],[5] and a very high-Q cavity [6] were achieved on an SOI substrate. Ultrahigh speed detectors and modulators based on Si or Ge/Si on SOI substrates have been demonstrated [7]-[10]. Si Raman lasers on an SOI substrate as well as Ge on Si laser [11]-[13], and hybrid materials system lasers based on AlGaInAs/InP directly bonded on an SOI substrate were also realized [14]-[16].

Looking at the requirements for the light source of optical interconnects [1],[2], the capability of low-power consumption is considered to be essential, hence vertical cavity surface emitting lasers (VCSELs) [17], micro disk lasers [18], and 2-D photonic crystal (PC) lasers [19], which can operate with very low threshold current, have been intensively investigated. A very low threshold current operation of micro disk lasers integrated with Si wire waveguide on an SOI substrate was also demonstrated [20],[21]. On the other hand we have been investigating single-mode lasers, i.e. DFB and distributed-reflector (DR) lasers with strongly index-coupled gratings, which can be operated with very low threshold current, and demonstrated sub-mA threshold currents [22]-[24].

For further reduction of the threshold current, we proposed a membrane buried-heterostructure (BH) DFB laser to enhance an optical confinement factor of the active layer by adopting a high index-contrast waveguide and obtained a room-temperature continuous-wave (RT-CW) operation under optical pumping [25]. In this paper, research activities on InP-based membrane lasers and lateral current injection lasers formed on a SI-InP are presented.

This research was supported by a Grant-in-Aid for Scientific Research (#19002009) from the Ministry of Education, Culture, Sports, Science and Technology (MEXT).

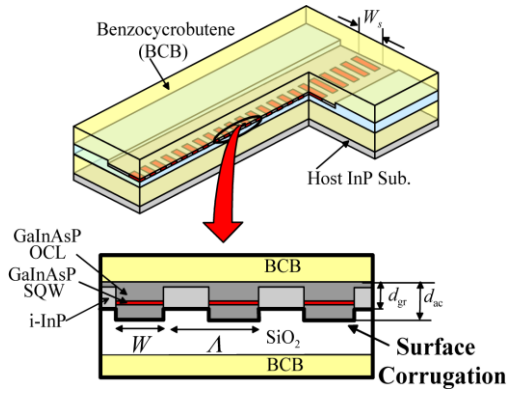


Fig. 1 Schematic of membrane BH-DFB laser with surface corrugations [27].

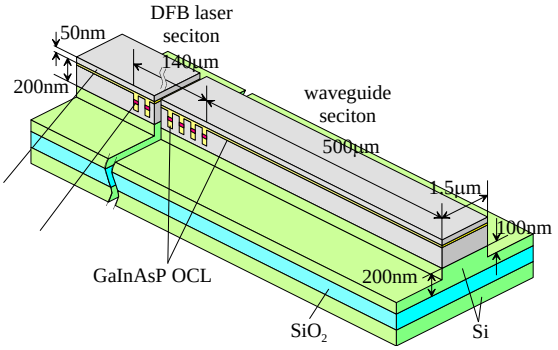


Fig. 2 Schematic of membrane BH-DFB laser directly bonded on SOI with rib-waveguide [30].

II. MEMBRANE BH-DFB LASERS

A. Low Threshold Operation Capability

Due to a strong index-contrast as well as a very thin (only 150 nm) waveguide, an optical confinement factor of the active layer is enhanced by a factor of 3. Furthermore by adopting a DFB structure with wirelike active regions, a threshold current of less than 50 μA for the stripe width of 1 μm was predicted [26], and a low threshold operation was confirmed under an optical pumping (threshold pump power P_{th} = 0.34 mW for W_s = 2 μm and L = 80 μm) with RT-CW condition (Fig. 1)[27]. By thinning the semiconductor core so as to cancel the temperature coefficient of the core by that of the BCB, temperature coefficient of the lasing wavelength was reduced to 1/5 of that of conventional lasers emitting at 1.5-1.6 μm [28].

B. Direct Bonding on SOI Substrate

Aiming at an integration with low-loss Si waveguides, a direct bonding of a membrane BH-DFB laser wafer on an SOI substrate was carried out. P_{th} of 2.8 mW for W_s = 2 μm and L =

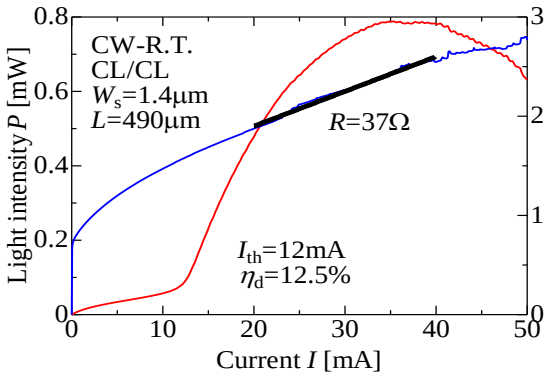


Fig. 3 Light output and voltage-current characteristics of LCI-BH laser grown on SI-InP substrate [33].

120 μm was obtained at RT-CW condition [29]. Similar BH-DFB lasers directly bonded on an SOI with a rib-waveguide structure was fabricated (Fig. 2) [30]. As a step toward current injection of this type of lasers, BH-DFB lasers with 2 μm-thick InP cladding layer was realized and a threshold current density of 400 A/cm^2 was obtained [31].

III. Lateral Current Injection (LCI) Lasers

Since a current injection operation is essential for optical interconnects, we fabricated LCI type lasers with 400-nm-thick GaInAsP core layer grown on a SI-InP substrate [32]. Recently a moderately low threshold operation was achieved (Fig. 3)[33], hence an extremely low threshold current operation can be expected with the membrane BH-DFB laser in near future.

Acknowledgment

The author would like to acknowledge Prof. N. Nishiyama Tokyo Inst. Tech.), Prof. T. Maruyama (Kanazawa Univ.), Mr. T. Okumura, Mr. S.-H. Lee, and other students for fruitful discussions and hard working for experiments.

References

[1] D. A. B. Miller, "Rationale and challenges for optical interconnects to electronic chips," *Proc. IEEE*, Vol.88, No. 6, pp. 728-749, June 2000.

[2] J. Rattner, "The mega-center," Intel Developer Forum, Mar. 2006.

[3] R. Soref,. "The past, present, and future of Silicon photonics," *IEEE J. Sel. Top. Quantum Electron.*, Vol. 12, No. 6, pp. 1678-1687, Nov./Dec. 2006.

[4] L. C. Kimerling et al., "Electronic-photonic integrated circuits on the CMOS platform," *Proc. SPIE* 612502 (2006).

[5] Y. A. Vlasov and S. J. McNab, "Losses in single-mode Silicon-on-insulator strip waveguides and bends," *Opt. Express.*, Vol. 12, No. 8, pp. 1622-1631, Apr. 2004.

[6] T. Asano et al., "Analysis of the experimental Q factors (~ 1 million) of photonic crystal nanocavities," *Opt. Express.*, Vol. 14, No. 5, pp. 1996-2002 Mar. 2006.

[7] M. Rouviere et al., "Ultrahigh speed germanium-on- silicon-on-insulator photodetectors for 1.31 and 1.55μm operation," *Appl. Phys. Lett*. Vol. 87, 231109-1. Nov. 2005.

[8] T. Yin et al., "31Ghz Ge –n-i-p waveguide photodetectors on Silicon-on-Insulator substrate," *Optics Express*, Vol. 15, No. 21, pp. 13965-13971, Oct. 2007.

[9] L. Liao et al., "40Gbit/s silicon optical modulator for high-speed applications," *Electron. Lett.* vo. 43, No. 22, DOI 20072253, Oct. 2007.

[10] S. Manipartruni et al., "50 Gbit/s wavelength division multiplexing using silicon microring modulators," *Int'l Conf. on Group IV Photonics* 2009, San Francisco, U. S. A., FC3, pp. 244-246, Sept. 2009.

[11] H. Rong et al., "A continuous-wave Raman silicon raman laser," *Nature*, Vol. 433, No.7027, pp. 725-728, Feb. 2005.

[12] H. Rong et al., "Low-threshold continuous-wave Raman silicon laser," *Nature Photonics*, Vol. 1, No. 4, pp. 232-237, Apr. 2007.

[13] J. Liu et al., "Optical gain from the direct gap transition of Ge-on-Si at room temperatue," *Int'l Conf. on Group IV Photonics* 2009, San Francisco, U. S. A., FD2, pp. 262-264, Sept. 2009.

[14] A. W. Fang et al., "Electrically pumped hybrid AlGaInAs- silicon evanescent laser," *Optics Express*, Vol. 14, No. 20, pp.9203-9210, Oct 2006.

[15] A. W. Fang et al., "Integrated AlGaInAs-Silicon evanescent race track laser and photodetector," *Optics Express*, Vol. 15, No. 5, pp.2315-2322, Mar 2007.

[16] A. W. Fang et al., "A distributed feedback silicon evanescent laser," *Optics Express*, Vol. 16, No. 7, pp.4413-4419, Mar 2008.

[17] K Iga, "Surface emitting laser - Its birth and generation of new optoelectronics fiel," *IEEE J. Select. Topics Quantum Electron.*,, Vol. 6, No. 6, pp. 1201-1215, Nov/Dec, 2000.

[18] M Fujita et al., "Continuous wave lasing in GalnAsP microdisk injection laser with threshold current of 40μA," *Electron. Lett*., Vol 36, No.9, pp. 790-791, Apr. 2000.

[19] H.-G. Park et al., "Electrically driven single-cell photonic crystal laser," Science, Vol 305, No.9, pp. 1444-1447, Sept. 2004.

[20] J. Van Campenhout et al., "Electrically pumped InP-based microdisk lasers integrated with a nanophotonic Silicon- on-insulator waveguide circuit," *Optics Express*, Vol. 15, No.11, pp. 6744-6749, May 2007.

[21] T. Spuesens et al., "Improved design of an InP-based microdisk laser heterogeneously integrated with SOI," *Int'l Conf. on Group IV Photonics* 2009, San Francisco, U. S. A., FA3, pp. 202-204, Sept. 2009.

[22] N. Nunoya et al., "High-performance 1.55μm wavelength GaInAsP- InP distributed-feedback lasers with wirelike active regions," *IEEE J. Sel. Top. Quantum Electron.*,Vol. 7, No. 2, pp. 249-258, June 2001.

[23] K. Ohira et al., "Low-threshold and high-efficiency operation of distributed reflector lasers with width-modulated wirelike active regions," *IEEE J. Select. Topics Quantum Electron*., Vol. 11, No. 5, pp. 1162-1168 , Sept./Oct. 2005.

[24] T. Shindo et al., "Low-threshold and high-efficiency operation of distributed reflector laser with wirelike active regions," *IEEE Photon. Technol. Lett*., Vol. 21, No. 19, pp. 1414-1416 , Oct. 2009.

[25] T. Okamoto et al.,, "Low threshold singlemode operation of membrane BH-DFB lasers," *Electron. Lett.*, Vol. 38, No. 23, pp. 1444-1445 ,Nov. 2002.

[26] T. Okamoto et al.,, "Optically pumped membrane BH-DFB lasers for low-threshold and single-mode operation," *IEEE J. Select. Topics in Quantum Electron*., Vol. 9, No. 5, pp. 1361-1366 , Sept./Oct. 2003.

[27] S. Sakamoto et al., "Strongly index-coupled membrane BH-DFB lasers with surface corrugation grating," *IEEE J. Select. Topics Quantum Electron.*, Vol. 13, No. 5, pp. 1135-1141, Sept./Oct. 2007.

[28] S. Sakamoto et al., "Reduced temperature dependence of lasing wavelength in membrane buried hetero-structure DFB lasers with polymer cladding layers," *IEEE Photon. Technol*. Lett., Vol. 19, No. 5, pp. 291-293, Mar. 2007.

[29] T. Maruyama et al., "GaInAsP/InP Membrane BH-DFB lasers directly bonded on SOI substrate," *Optics Express*, Vol. 14, No. 18, pp. 8184-8188, Sept. 2006.

[30] T. Okumura et al., "Single-mode operation of GaInAsP/InP- membrane distributed feedback lasers bonded on Silicon-on-insulator substrate with rib-waveguide structure," *Jpn. J. Appl. Phys.*, Vol. 46, No. 48, pp. 1206-1208, Dec. 2007.

[31] T. Okumura et al., "Injection-type GaInAsP-InP-Si distributed-feedback laser directly bonded on silicon-on-insulator substrate," *IEEE Photon. Technol. Lett*., Vol. 21, No. 5, pp. 283-285, Mar. 2009.

[32] T. Okumura et al., "Lateral current injection GaInAsP/InP laser on semi-insulating substrate for membrane-based photonic circuits," *Optics Express*, Vol. 17, No. 15, pp. 12564-12570, July 2009.

[33] T. Okumura et al., "Room-Temperature CW operation of lateral current injection lasers with thin film lateral cladding layers," *The 21st Int. Conf. on Indium Phosphide and Related Materials* (IPRM2009), Newport Beach, U. S. A., WP12, pp. 298-301, May 2009.

Side-emitting metallic waveguide lasers with InGaAsP MQWs

M.J.H. Marell, M.T. Hill & M.K. Smit
Opto-Electronic Device Group
Eindhoven University of Technology
Eindhoven, The Netherlands
m.j.h.marell@tue.nl

***Abstract*— Metal-coated cavities can be used to fabricate lasers with nanometer-scale dimensions. So far, these lasers were fully enclosed by metal and emitted their light, scattered from within the cavity, through the substrate on which they are fabricated. In this paper we present the first side-emitting metal-insulator-metal waveguide laser.**

Keywords:

I. INTRODUCTION

The arrival of the first electrically pumped metal-coated nano-laser has opened a whole new range of possibilities for integrated optics. It has been shown that despite high internal losses, lasing is possible in metallic or plasmonic cavities with dimensions well below the diffraction limit of light [1,2,3,4]. Cavities with moderate Q-values can reproducibly be fabricated and lasing can be achieved at very low currents (µA range). Due to the small size and high pump density, it is possible that future metallic nano-lasers will have switching speeds in the THz range.

Integration of these lasers with other optical components is difficult, since they are fully enclosed by a metal layer of several hundreds of nanometers thick. Side-emission of metal-coated lasers is desirable. In this paper we demonstrate the first side-emitting metallic waveguide laser.

II. FABRICATION

The side-emitting, metal-coated lasers are fabricated on an n-doped InP substrate on which a InP/InGaAsP/InP heterojunction is grown; in the 510 nm thick InGaAsP layer, 8 InGaAs quantum wells of 4.1 nm thickness are incorporated. The structures are defined by electron beam lithography in a 140 nm thick PMMA resist layer at 30 kV. The pattern is inverted by covering the sample with 30 nm of Cr and performing lift-off in acetone. The chrome pattern is then transferred to a 440 nm SiO_2 hard mask layer by etching the SiO_2 for 30 minutes with a pure CHF_3 process in our RIE reactor. The sample is etched in a CH_4/H_2 ICP-RIE process to transfer the patterns to the semiconductor layer stack. After dry etching the structures, surface damage, caused by the dry etching, is removed by repeatedly oxidizing the sidewall surface and etching away the oxidized material. A 20 nm thin SiN_x layer is then deposited to protect the sidewalls and to electrically insulate the silver cladding from the semiconductor stack. After the whole structure is covered in silver and the electrical contacts have been fabricated, the structures are cleaved and the facets polished with an Ar^+ cross-section polisher, resulting in Fabry-Perot cavities of 65 µm long and with a core width of 200 nm.

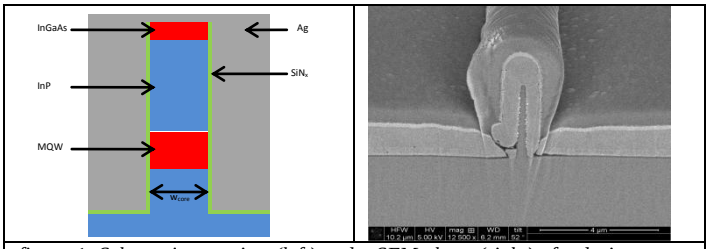


figure 1: Schematic overview (left) and a SEM photo (right) of a device cross-section. The waveguide width is 220 nm.

III. SIMULATION RESULTS

Simulations show that, in a metallic waveguide with perfect rectangular shape, two modes are sustained. From these simulations an estimate of the propagation loss can be made. We find that the propagation loss is in the order of 0.14 dB/µm for the TE polarization and 0.09 dB/µm for TM polarized light. In reality, the propagation loss is expected to be even higher.

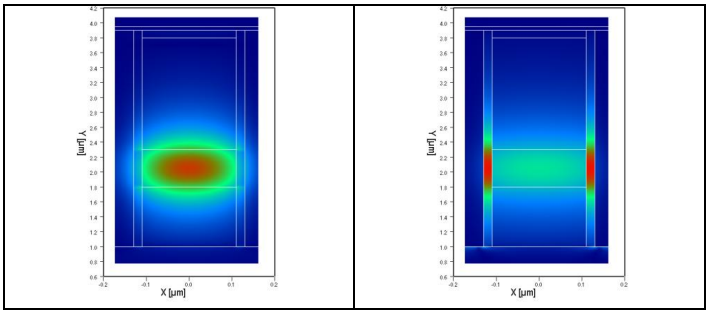


figure 2: Mode profile of the modes sustained by the metallic waveguide

IV. MEASUREMENTS

A schematic overview of the measurement setup is shown in figure 3. Groups of 8 devices are placed inside a cryostat and cooled down to a temperature of 80K. Current was sent through the devices, while monitoring the voltage across the

device and the spectral output of the device. Light emitted by the devices is collected by a microscope objective with a 17 mm working distance and 0.42 N.A. and coupled into a single mode fiber.

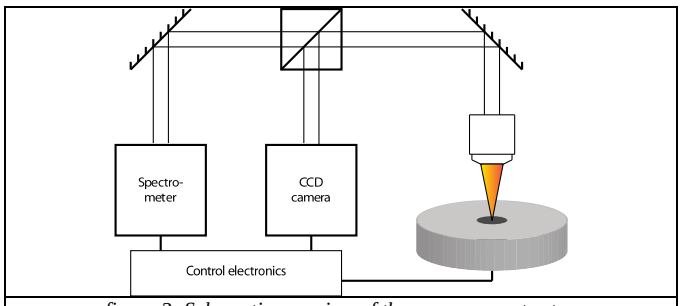


figure 3: Schematic overview of the measurement setup

From figure 4 & 5 it can be seen laser operation is achieved starting at a threshold current of approximately 75 µA. The light collected from the devices is TE polarized, due to the width of the waveguide and better overlap of the electric field with the quantum wells. The measured L-I curve shows super-linear behavior due indicative for typical Fabry-Perot lasers.

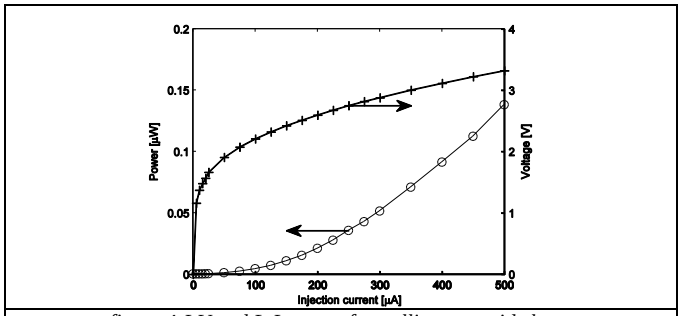


figure 4:I-V and L-I curve of metallic waveguide laser

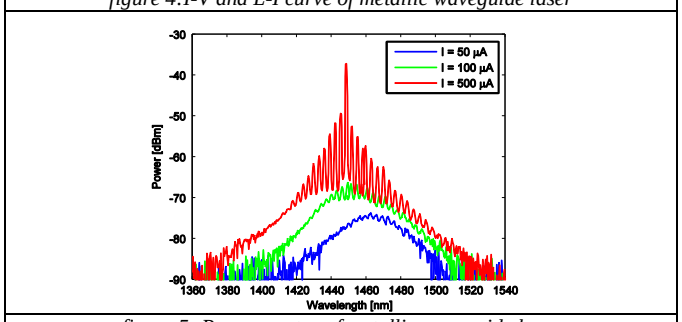


figure 5: Powerspectra of metallic waveguide laser

The wavelength of the main laser peak is located close to 1450 nm. The considerable blue shift is due to the high current density inside the device, the high gain required for lasing and the low operating temperature. The output power level at the wavelength peak 0.14 µW (in-fiber).

At I_{pump} = 500 µA, the power level in the main laser peak is 30 dB above the background ASE level. Figure 7 shows high resolution scans of the highest spectral peak for three values of the injection current. The FWHM decreases from 0.719 nm at I_{pump} = 150 µA to 0.102 nm at I_{pump} = 500 µA.

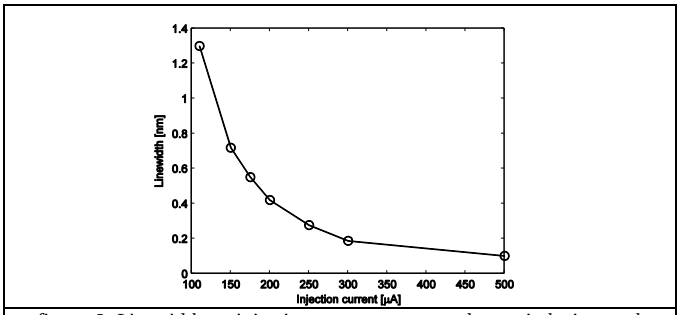


figure 6: Linewidth vs. injection current, measured at main lasing peak

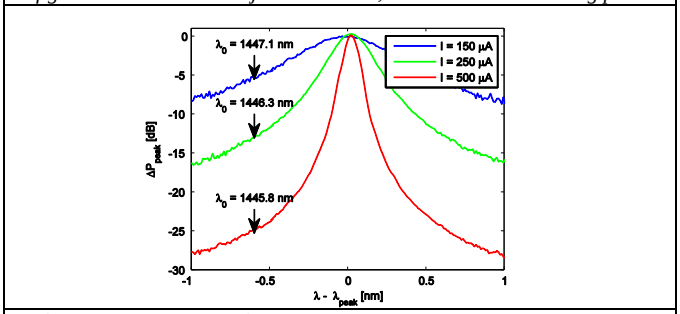


figure 7: Comparison of main laserpeaks at various injection currents

The wavelength of the peaks is 1447.1 nm, 1446.3 nm and 1445.8 nm respectively. The smallest linewidth measured for these devices is 68 pm, but is possibly smaller due to the limited resolution of the spectrum analyzer. The Fabry-Perot cavity modes are spaced 3 nm apart, which corresponds to a FSR = 444 GHz.

V. Conclusions and Outlook

We have shown that side-emission of a nanometer-sized, metallic waveguide laser is possible. Lasers based on metallic waveguides can operate at very low injection currents, similar to their fully enclosed counterparts (albeit currently at cryogenic temperatures only).

Work on truly plasmonic side-emitting lasers, with waveguide widths down to 80 nm, is in progress. Better performance is expected due to a more optimal shape of the waveguide's cross-section and a bulk active layer. Results on these lasers are expected soon.

VI. References

[1] M. A. Noginov et al., "Demonstration of a spaser-based nanolaser," Nature vol. 460, 1110-1112 (2009).

[2] R. F. Oulton et al.,"Plasmon lasers at deep subwavelength scale" Nature, vol. 461, 629-632 (2009)

[3] M. T. Hill et al., "Lasing in metal-insulator-metal sub-wavelength plasmonic waveguides", Opt. Express 17, 11107-11112, 2009

[4] M. T. Hill et al., "Lasing in metallic-coated nano-cavities", Nature Photonics, vol. 1, 589-594, 2007

All-Optical Memory Operation for 20-Gb/s PRBS RZ and 40-Gb/s NRZ Signals Using 980-nm Polarization-Bistable VCSEL

Jun Sakaguchi, Takeo Katayama, and Hitoshi Kawaguchi
Graduate School of Materials Science
Nara Institute of Science and Technology
Ikoma, Japan
tkatayam@ms.naist.jp

Abstract—**Ultrafast all-optical memory operation was experimentally demonstrated using a 980-nm polarization-bistable vertical-cavity surface-emitting laser. 1-bit data signals were arbitrarily sampled and memorized from a 2^6-1 pseudorandom bit sequence return-to-zero signal at 20 Gb/s and a 6-bit non-return-to-zero signal at 40 Gb/s by AND gate and memory functionalities.**

Keywords-VCSEL; polarization bistable switching; optical buffer memory

I. INTRODUCTION

All-optical buffer memories are desirable as key elements of all-optical packet-switched networks. We previously proposed an optical buffer memory with shift register function consisting of a two-dimensional array of polarization-bistable vertical-cavity surface-emitting lasers (PB-VCSELs) [1]. We have demonstrated that such buffer memory consisting of four VCSELs can store and regenerate 4 bits in a 1550-nm range [2]. The fastest 1-bit buffering achieved so far has been for 10-Gb/s return-to-zero (RZ) signals in a 980-nm range [3].

In this presentation, we report 1-bit memory operation of 20-Gb/s RZ signals and 40-Gb/s non-return-to-zero (NRZ) signals using a 980-nm PB-VCSEL. We have succeeded in memorizing an arbitrary bit of the pseudorandom bit sequence (PRBS) data signal as long as 2^6-1 bits at 20-Gb/s. In 40-Gb/s operation, we have achieved memorizing each bit of 6-bit NRZ signals. These are the fastest operation of optical bistable flip-flop memories to the best of our knowledge.

II. PRINCIPLE

A PB-VCSEL has a square mesa structure and has two lasing modes with polarization directions orthogonal to each other (0 and 90°). Since one of the two modes suppresses the other through cross gain saturation, the VCSEL stably oscillates with one of these polarizations. By injection of a control light with sufficient power and at the polarization direction orthogonal to that of the lasing mode, we can switch the lasing polarization of the VCSEL as shown in Fig. 1.

The 1-bit memory function is achieved as follows (Fig. 2). The 90 or 0° polarization state of the PB-VCSEL is used to store the "0" or "1" of the target bit in the data signal, respectively. A data signal with 0° is injected into the VCSEL. The injection power of the data signal is set to less than the polarization switching threshold of the VCSEL. We also inject a set pulse with 0°. If the set pulse is injected together with a "1" data pulse and the combined power of the data pulse and the set pulse exceeds the polarization switching threshold, the polarization state of the VCSEL switches from 90 to 0°. Therefore, the polarization state of the VCSEL reflects the "0/1" of the target bit in the data signal. The stored target bit can be read out at any timing using an optical gate device.

III. OPERATING CONDITIONS OF MEMORY

As we increase the data rate, the temporal width of each data pulse and set pulse needs to be shortened. We then need higher injection power for these pulses to obtain polarization switching. When the bit length of the data signal becomes long,

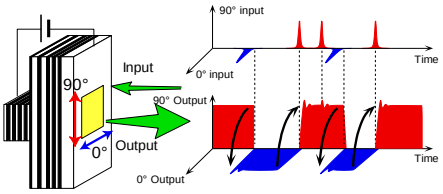


Figure 1. Polarization bistable operation by injection of optical pulses in a VCSEL.

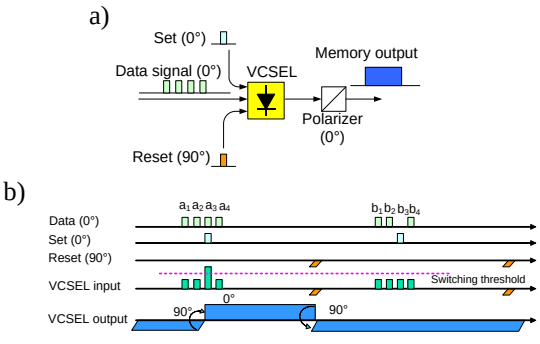


Figure 2. 1-bit buffering using a PB-VCSEL. a) Implementation and b) Timing chart.

This research was supported in part by the Strategic Information and Communications R&D Promotion Programme (SCOPE) and by the Ministry of Education, Culture, Sports, Science, and Technology of Japan, Grant-in-Aid for Scientific Research (B) (21360034).

change in the number of carriers in the active region of the VCSEL, caused by each data pulse, accumulates and causes undesired polarization switching even without set-pulse injection. One solution for this problem is to detune the carrier frequency of the data signal f_{data} from the oscillation frequency of the VCSEL f_0 [3]. Since larger frequency detuning Δf (= f_{data} - f_0) requires higher signal power P_{data} for polarization switching to occur, it is important to grasp the conditions for memory operation without errors in the Δf - P_{data} relation.

We performed a numerical simulation of the polarization switching using a two-mode rate equation model in order to obtain the operation conditions. We calculated two criteria for the signal power P_{data} as functions of Δf. The first was the threshold for the polarization switching to occur with injection of a data pulse and a set pulse. This curve provides the lower limit of P_{data}. Here, the data pulse power and the set pulse power were assumed to be equal. The wavelength tolerance of the input optical pulse was wider on the longer wavelength side. The second criterion was the switching threshold for long-bit data pulses (2^6-1 bits, PRBS) without a set pulse. This curve provides the upper limit of P_{data}. In our simulation for a 20-Gb/s data signal, resonant structures appeared in the upper limit curve at around -20 and -15 GHz due to the sidebands of the input data signals and the relaxation oscillation. Since the upper limit power becomes larger than the lower limit power for Δf < -22 GHz, memory operation without errors can be expected at this condition for 20-Gb/s PRBS RZ signals.

IV. All-Optical High Bit-Rate Memory Operation

We performed 1-bit memory operation for a 20-Gb/s PRBS RZ data signal using an InGaAs/GaAs VCSEL with a square mesa of 6×6 μm^2 in a 980-nm range [4]. The bias current was set to about 9.28 mA. The output power of the VCSEL was about 430 μW. Optical data signals and optical set and reset pulses were generated by tunable external cavity laser diodes and $LiNbO_3$ modulators. The input signal to the VCSEL was monitored using a sampling oscilloscope, while the VCSEL output waveform through a polarizer was monitored using a photodiode and a digital storage oscilloscope.

An example of the memory operation for a 2^6-1-bit PRBS data signal is shown in Fig. 3. For three successive groups of data signals, three set pulses were positioned to sample "1", "0", and "1" data (Fig. 3 b). When the "1" data pulse and the set pulse were injected simultaneously, the polarization state of the VCSEL switched from 90 to 0° (Fig. 3 c). The frequency detuning Δf of the data signal against the lasing wavelength of the 0° polarization mode was set to be about -23 GHz. The peak power of the data signal and set pulses were 250 and 190 μW, respectively. This data signal power was lower than the VCSEL output power. Thus, this all-optical memory operation has an optical gain even for such a high data rate. Without changing the power and the wavelength, i.e., by only changing the timing of the set pulses, we have successfully demonstrated sampling of 2^6-1-bit PRBS data. These results show the ability of the current PB-VCSEL memory to handle RZ data signals of 20 Gb/s.

We also examined memory operation for 40-Gb/s NRZ signals. In the NRZ data signal, because the set pulse interfered with the pulse tails of the adjacent bits of a target bit, the difference in the optical power of the "0" or "1" sampled bit became indistinct. Despite this problem, we have achieved the memorization of each bit of NRZ signals with a 6-bit length as shown in Fig. 4.

V. Conclusion

We have demonstrated all-optical 1-bit memory operation for 20-Gb/s PRBS RZ signals and 40-Gb/s NRZ signals using a PB-VCSEL in a 980-nm range for the first time. A 1-bit data signal was arbitrarily sampled and memorized from the 2^6-1-bit, 20-Gb/s data signals and 6-bit, 40-Gb/s data signals by changing only the time position of the set pulses.

References

[1] H. Kawaguchi, T. Mori, Y. Sato and Y. Yamayoshi, "Optical buffer memory using polarization bistable vertical-cavity surface-emitting lasers," Jpn. J. Appl. Phys., Express Lett., vol. 45, pp. L894-L897, September 2006

[2] T. Katayama, T. Ooi and H. Kawaguchi, "Experimental Demonstration of Multi-Bit Optical Buffer Memory Using 1.55-μm Polarization Bistable Vertical-Cavity Surface-Emitting Lasers," IEEE J. Quantum Electron., vol. 45, pp. 1495-1504, Novmber 2009.

[3] T. Mori and H. Kawaguchi, "10-Gb/s optical buffer memory using a polarization bistable VCSEL," IEICE Trans. Electron., vol. E92-C, pp. 957-963, July 2009.

[4] Y. Sato, T. Mori, Y. Yamayoshi and H. Kawaguchi, "Polarization bistable characteristics of mesa structure 980nm vertical-cavity surface-emitting lasers," Jpn. J. Appl. Phys., vol. 45, pp. L438-L440, April 2006.

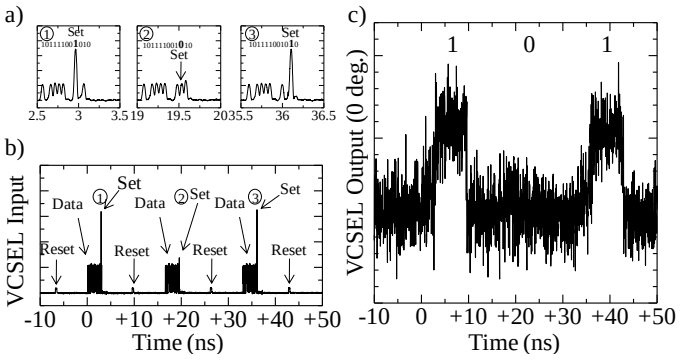


Figure 3. Memory operation for 20-Gb/s, 2^6-1 bit PRBS RZ signals.
a) Magnified VCSEL input, b) VCSEL input, and c) VCSEL output.

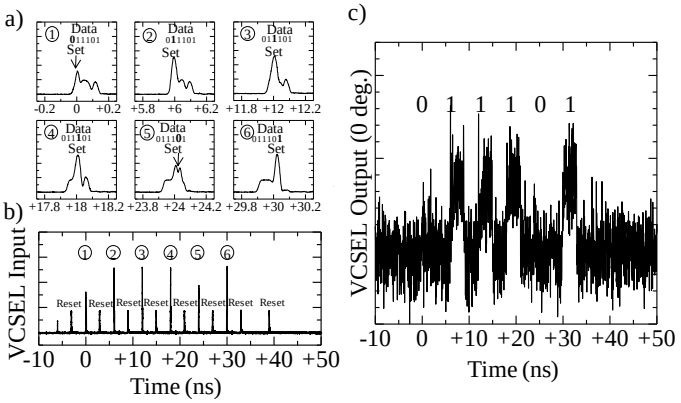


Figure 4. Memory operation for 40-Gb/s, 6-bit NRZ signals.
a) Magnified VCSEL input, b) VCSEL input, and c) VCSEL output.

Tunable Slow Light in Photonic Nanostructures

Toshihiko Baba
Department of Electrical and Computer Engineering
Yokohama National University
79-5 Tokiwadai, Hodogayaku, Yokohama 240-8501, Japan
baba@ynu.ac.jp

Abstract — **On-chip slow light in photonic nanostructures allows 100 ps order delay and tunability with sub-THz bandwidth. This paper reports the state-of-the-art performance of SOI slow light devices fabricated by e-beam or Si CMOS technology, related topics such as nonlinear enhancement and dynamic tuning, and its application to fast optical correlator.**

Keywords-slow light; photonic nanostructure; photonic crystal; silicon photonics; optical correlator

Slow light having a group velocity much smaller than that in vacuum has been studied in these ten years toward advanced time-domain optical signal processing (optical buffers and memories, re-timing and MUX/DMUX of optical signals, fast correlators and pump-probe systems, etc.) and enhancement of light-matter interaction (nonlinearity, phase shift, etc.). Photonic nanostructures such as photonic crystals are powerful tools that allow on-chip slow light devices [1].

We have reported slow light devices based on photonic crystal waveguides (PCWs) fabricated on SOI substrate by using *e*-beam lithography and ICP etching. The photonic crystal coupled waveguide of 250 – 700 μm length has achieved a 100 ps class delay and its tunability based on thermo-optic effects, maintaining a sub-THz bandwidth. Clear time-domain shift of picosecond optical pulses were successfully observed in the device [2]. In a lattice-shifted PCW, >40-fold enhancement of self-phase modulation and two-photon absorption was evaluated with the slow light effect [3].

The next issues are longer delay and wider tunability, stronger enhancement of nonlinearity with lower losses, more functionalities, and development of applications. For the first issue, we expect the silicon CMOS technology to provide a new class of large-scale integration. In comparison with e-beam technology, the CMOS technology allows easy integration of wire waveguides and optical coupler with fibers, as shown in Fig. 1, and ensures higher uniformity. The insertion loss can be dramatically reduced and so we can discuss practical device applications. The device length is easily elongated to millimeter order and sub-nanosecond delay and tunability will be available. For the second issue, a more efficient material beyond Si is desired. We have developed a Ag-As_2Se_3 chalcogenide glass PCW and observed more than 10-fold enhancement in third order nonlinearity than in Si [4]. The four-wave mixing was observed for < 0.5 W input peak power in a 400-μm-long PCW. It is promising to high efficiency tuning and switching based on optical Kerr effect with negligible two-photon absorption and related free carrier absorption. For the third issue, dynamic tuning of the device and optical pulse are of great interest [5]. The instantaneous change of device index changes wavelength components of optical pulses and allows the complete stopping of light and shuffling of the order of pulses. It will be experimentally demonstrated by using fast nonlinear effects as a tuning mechanism. As an application, we are considering a fast optical correlator. In conventional correlators, mechanically tunable delay line restricts data acquisition speed. Using the thermo-optic tunable delay in the PCW slow light device, 100-fold faster tunable delay is available. We achieved the correlation measurement up to 4 kHz repetition frequency [7]. It is effective for 2D and 3D data mapping of OCT and THz TDS.

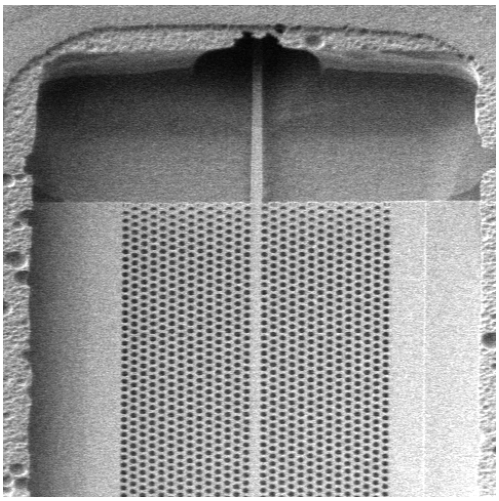


Fig. 1 Si PCW integrated with photonic wire by using CMOS technology

[1] T. Baba, "Slow light in photonic crystals", Nature Photon., vol. 2, no. 8, pp. 465-473, 2008.

[2] J. Adachi, N. Ishikura, H. Sasaki and T. Baba, "Wide range tuning of slow light pulse in SOI photonic crystal coupled waveguide via folded chirping", IEEE J. Sel. Top. Quantum Electron., vol. 16, 2010 (in press).

[3] Y. Hamachi, S. Kubo and T. Baba, "Slow light with low dispersion and nonlinear enhancement in a lattice-shifted photonic crystal waveguide," Opt. Lett., vol. 34, no. 7, pp. 1072-1074, 2009.

[4] K. Suzuki, Y. Hamachi and T. Baba, "Fabrication and characterization of chalcogenide glass photonic crystal waveguides", Opt. Express, vol. 17, no. 25, pp. 22393-22400, 2009.

[5] M. F. Yanik, S. Fan, "Stopping light all-optically," Phys. Rev. Lett., vol. 92, no. 8, pp. 083901, 2004.

[6] N. Ishikura, J. Adachi and T. Baba, "Fast optical correlator via thermal delay tuning in photonic crystal coupled waveguide", SPIE Photonics West, San Francisco, no. 7612-24, 2010.

This work was supported by JST-CREST project.

Low-Loss Two-Dimensional Pillar Photonic Crystals Filled with Dielectrics

D.O. Dzibrou, J.J.G.M van der Tol and M.K. Smit
COBRA Research Institute
Eindhoven University of Technology
Eindhoven 5600 MB, The Netherlands
d.o.dzibrou@tue.nl

Abstract—**Optimization of two-dimensional pillar photonic crystals is presented. In the interpillar spaces, three-layer stacks of dielectrics were introduced. The simulation predicts the lowest coupling loss for such structures reported so far and lower etching depths for the pillar fabrication than in previous studies.**

Keywords-pillar photonic crystal; low loss; ; filling with dielectrics; high refractive index contrast.

I. INTRODUCTION

The concept of photonic integrated circuits (PIC's) is drawing a body of attention from academic as well as industrial prospects. A unique offer given by PIC's resides in monolithic integration of discrete optical components onto a single chip. Such a circumstance enables drastic reduction in size and power consumption of PIC-based devices. Several issues, however, have to be solved for achieving decent performance of PIC's. Control of polarization represents one of those since polarization dependence of PIC components produces an additional source of loss. Two-dimensional (2D) pillar photonic crystals (PhC's) showed substantial potential for dealing with the issue [1]. Further reduction in loss requires vertical confinement in the interpillar space. A vertical waveguide layer stack (VWLS) made of a material layer with high refractive index enclosed by two low-index layers was proved workable for the case of polymers theoretically and experimentally [2]. Low contrast between refractive indices of the polymers yielded appropriate loss for the pillars higher than 3 μm.

The present paper is aimed at demonstrating that introduction of a VWLS composed of materials with higher contrast in refractive index n allows: i) obtaining the lowest coupling loss among pillar PhC's reported so far and ii) lowering the pillar heights to 2-2.5 μm which leads to dramatic mitigation of the fabrication process.

II. DESCRIPTION OF SIMULATION

Transverse magnetic (TM) photonic band gap width $\Delta\omega$ and coupling loss were simulated for 2D pillar PhC's. An illustration of the top view of the crystals is given in Fig. 1a. The PhC designs differed in radius r while their lattice constants a's were kept the same (see Fig. 1b). The pillars

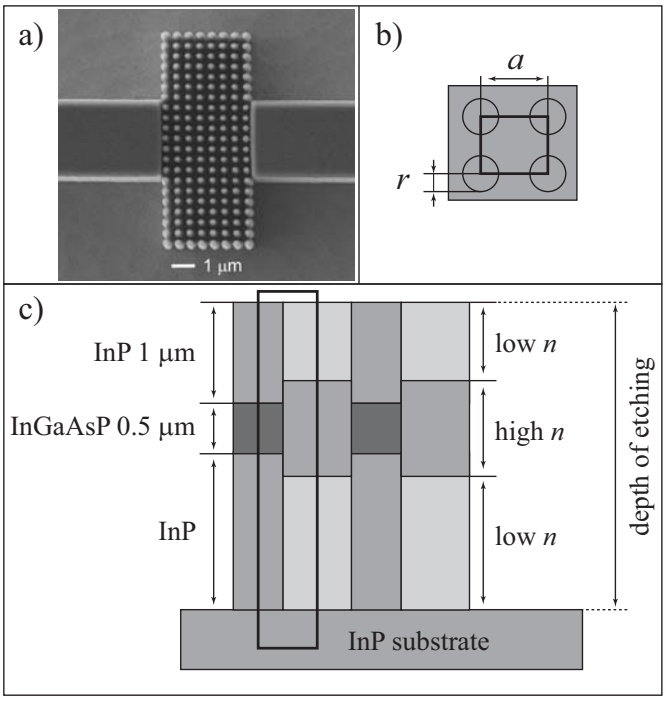


Figure 1. a) Top view of 2D pillar photonic crystal; b) Unit cell (by black square) of 2D photonic crystal used for band gap calculation; c) Cross section of photonic crystal: pillar composition (in darker colours): 1-μm-high InP part, 0.5-μm-high InGaAsP part and InP one of varying height depending on depth of etching, followed by InP substrate; composition of vertical waveguide layer stack: low n/ high n/ low n layers all with varying thicknesses. Black rectangle in bold denotes calculation window for simulation of coupling loss. n stands for refractive index, r, pillar radius, a, lattice constant of photonic crystal. The structure is periodic in the horizontal

were made to ensure compatibility with the generic integration technology. In the interpillar space, a VWLS was introduced (see Fig. 1c). Being designed for an operational wavelength of 1.55 μm, the PhC's yielded: i) propagation control of the TM-polarized mode and ii) minimal coupling loss of light on its advance through a PhC interface.

All the simulations employed the CrystalWave software of Photon Design. The band solver of CrystalWave was used to calculate $\Delta\omega$ as a function of effective refractive index n_{eff} and normalized pillar radius r/a. A 2D unit cell depicted by the

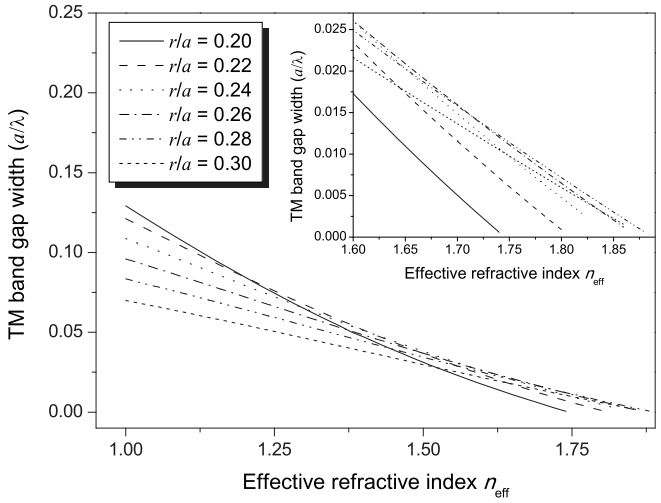


Figure 2. TM band gap width as a function of effective refractive index of the mode in vertical waveguide layer stack and normalized pillar radius r/a for 2D pillar photonic crystals. r denotes pillar radius, a, photonic crystal lattice constant, λ, wavelength.

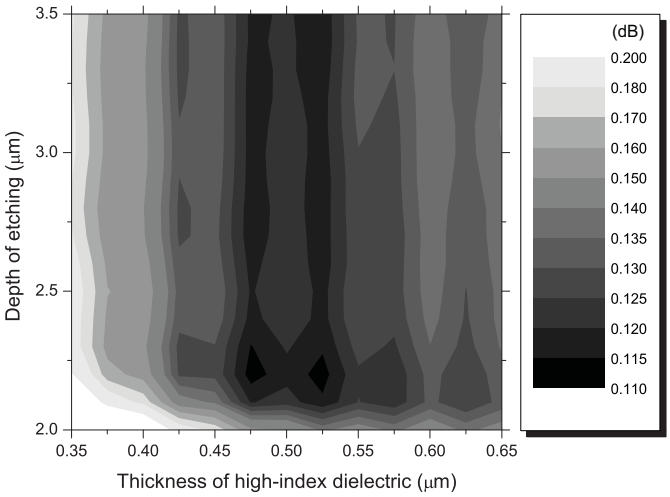


Figure 3. Coupling loss on advance through an interface of 2D pillar photonic crystal as a function of thickness of high refractive index material and depth of etching. Plot is limited by thickness of high refractive index material = 0.65 μm since larger values cause closure of photonic band gap.

black square in Fig. 1b was defined for that purpose. The pillar area was given $n_{eff} = 3.26$ while the n_{eff} of the interpillar region was varied. Normalized pillar radius varied between 0.20 and 0.30 with a step of 0.02.

The finite difference time domain engine computed loss as a function of etching depth and thickness of high n material in the VWLS. That necessitated definition of the calculation window (see Fig. 1c, black rectangle). Coupling loss of light on transition from the pillar into the VWLS is computed using the overlap integral of the mode profiles in the pillar and the VWLS. For the pillars, the InP area is given $n = 3.17$ and for InGaAsP $n = 3.36$. The low refractive index material in the VWLS has $n = 1.45$ corresponding to SiO_2 whereas its high-index counterpart was given $n = 2.10$ associated with Ta_2O_5.

III. Results

A. TM Photonic Band Gap Width

TM photonic band gap widths as functions of n_{eff} for different r/a values were simulated for the PhC's to ensure rejection of the TM modes over all the C-band (1.53-1.57 μm). The modelling results are presented in Fig. 2. All of the curves follow the same trend: Δω becomes narrower with increasing n_{eff} leading to complete closure of photonic band gap. Larger r/a values yield a wider range of acceptable n_{eff} values. Rejection of all frequencies in the C-band (1.53-1.57 μm) requires the TM photonic band gap to be larger than 0.01 a/λ, with λ representing the wavelength, for all r/a values. The inset of Fig. 2 shows that such a condition is met at $n_{eff} < 1.75$ for the designs with $r/a > 0.24$.

B. Coupling Loss

An optimal etching depth and thickness of the high n material in the VWLS was found by the simulation of coupling loss. The results are given in Fig. 3. It is seen that an acceptable level of loss is already achieved at thicknesses of the high n layer from 0.45 μm to 0.6 μm. The preceding study [2] used a polymer stack with lower n contrast in comparison with ours. It reported a loss value of 0.2 dB per interface between the pillar and the VWLS for etching depths larger than 3 μm. In the current study, a value of 0.12 dB per pillar-VWLS interface was calculated for etching depths of 2-2.5 μm. This is the lowest value of coupling loss reported so far for pillar PhC's. Moreover, etching depths of 2-2.5 μm alleviate the pillar fabrication substantially.

IV. Conclusion

Two-dimensional pillar photonic crystals with a vertical waveguide layer stack of dielectrics in the interpillar space were investigated. Examination of the TM band gap width as a function of effective refractive index for different values of the normalized radii showed that safe rejection of frequencies from the C-band occurs for PhC designs with a normalized radius > 0.24. The study of loss vs depth of etching and thickness of high refractive index layer in the stack emanated coupling loss = 0.12 dB per pillar-VWLS interface for etching depths of 2-2.5 μm. This loss value was found to be the lowest reported so far for pillar photonic crystals. The said values of etching depths and coupling loss indicate substantial mitigation of the pillar fabrication process and the possibility of constructing a very low-loss pillar photonic crystal, compatible with standard photonic integrated circuits, using dielectrics such as SiO_2 and Ta_2O_5.

Acknowledgement

The authors gratefully acknowledge the financial support from the NRC Photonics.

V. References

[1] A. A. M. Kok, E. J. Geluk, F. K. Karouta, J. J. G. M. van der Tol, R. Baets, M. K. Smith, "Short polarization filter in pillar-based photonic crystals", IEEE Photonic Technol. L., vol. 20, pp. 1369-1371, August 2008.

[2] A. A. M. Kok, J. J. G. M. van der Tol, R. Baets, M. K. Smith, "Reduction of propagation loss in pillar-based photonic crystal waveguides", J. Lightwave Technol., vol. 27, pp. 3904-3911, April 2009.

Nonlinear GaInP Photonic Crystal Waveguides

I. Cestier, V. Eckhouse, G. Eisenstein
Electrical Engineering Dept.
Technion
Haifa, Israel

S. Combrié, P. Colman, A. De Rossi
Thales Research and Development
Thales
Palaiseau, France

Abstract — **We report highly nonlinear GaInP photonic crystal waveguides. An extremely large hybrid nonlinearity was demonstrated in a static experiment as well as in a wavelength conversion scheme at 10 Gbit/s. Highly efficient four wave mixing was also demonstrated for either CW or pulsed pump signals.**

Photonic crystyals; Nonlinear optics; Nonlinear wave mixing

I. INTRODUCTION

The small cross section [1] and large group index [2] are responsible for the attractive nonlinear properties of Photonic crystal (PhC) waveguides. Indeed, many nonlinear experiments exploiting mainly the instantaneous Kerr effect have been reported [3-8] in Si, GaAs, AlGaAs, GaInP and chalcogenide glass based PhC structures. Materials with wide band gaps, such as AlGaAs and GaInP are favorable since nonlinear losses [4] are avoided at 1.55 μm so that the effective nonlinearities are enhanced.

In this paper we describe two nonlinear GaInP PhC waveguides. The two waveguides comprise a thin, 170 nm, GaInP free standing membrane into which a triangular lattice of holes was etched. The lattice constant is a = 480 nm, the air holes have a radius of r = 0.19a. The waveguides were 1.3 mm long.

The first device is a low finesse nonlinear Fabry Perot resonator constructed by the ~40% reflectivity of the cleaved end facets. In this device we make use of a hybrid nonlinear phenomenon which combines a thermal effect with the Kerr nonlinearity. The structure enables to extract the phenomenological nonlinear coefficient γ by a direct observation of the phase shift experienced by the Fabry-Perot fringes as a response to an optical pump. A very efficient static response as well as wavelength conversion at 10 Gbit/s was demonstrated. The second device is similar except that it contains mode converters [9] which raise the coupling efficiency and eliminate the end facet reflectivities. This device was used to demonstrate highly efficient four wave mixing (FWM) for CW and for pulsed pump signals with powers in the mW range.

II. NONLINEAR RESONATOR

The nonlinear resonator was characterized using a static pump probe scheme with which the phase shift experienced by the Fabry Perot fringes was observed. In the static experiment, the pump was a low power CW signal and the probe was a broad band, low power ASE signal from an EDFA. The linear transmission (obtained with the pump off) is shown in Fig. 1 (a) as a blue line. The other traces in Fig. 1 (a) show the measured Fabry Perot fringes for different input pump powers. The pump induces a clear red shift in the phase of the Fabry Perot fringes, which increases with power. The largest observed shift is $\varphi = \pi/3$ for a pump power of 800 μW. We quantify the nonlinearity by the common phenomenological nonlinear parameter γ according to the experimentally observed phase shifts. γ is formulated for the cross phase modulation configuration and takes on the large value of $\gamma = 3.5 \times 10^5$ $m^{-1}W^{-1}$ for the mode at λ=1537 nm (group velocity V_g ~c/7). The effect of the group velocity in the PhC waveguide is demonstrated by measuring the phase shift values for various pump wavelengths. Fig. 1 (b) shows the wavelength dependence of γ, together with a quadratic fit of the slowdown factor S (dashed curve). Near the band-edge, the nonlinear parameter of the slow guided mode (V_g ~c/15) is enhanced and reaches the high value of $\gamma = 2.2 \times 10^6$ $m^{-1}W^{-1}$. These γ values are much larger than those obtained in experiments that rely solely on the Kerr effect [3-5]. This suggests that the observed nonlinearity is due to a hybrid phenomenon of Kerr and some thermal effects.

To evaluate the dynamic properties we performed a wavelength conversion experiment. The pump was externally modulated at 10 Gbit/s and had an average power of 2 mW. The probe was a CW signal of ~1 mW. The probe was filtered

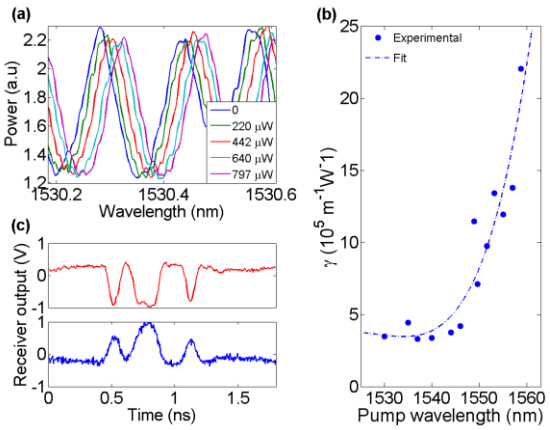


Figure 1. (a) Fabry Perot fringes as a function of wavelength for various input pump powers. (b) γ values as a function of pump wavelength (dots). (c) Pump (red trace) and probe (blue trace) dynamics for a 10 Gbit/s pattern.

at the output following amplification, detected and measured on a fast sampling oscilloscope. Wavelength conversion results are illustrated in Fig. 1 (c). A portion of the data pattern is shown in the case of the probe wavelength with no pump chosen to coincide with a peak of a Fabry Perot fringe. Consequently the converted signal (blue trace) exhibits the complimentary data of the pump (red trace). The probe signal follows the pump pattern very well, proving that even though the thermal effect dominates, the hybrid nonlinearity is sufficiently fast to enable switching at rates of 10 GHz.

III. NON DEGENERATE FOUR WAVE MIXING

For the FWM measurements, the probe was a tunable CW signal while the pump was either a CW or a pulsed signal. In the latter case the pulses were 100 ps wide and had a duty cycle of 1:16. Fig. 2 (a) shows the output spectrum when the pump was pulsed. Pump and probe, detuned here by 1.3 nm, had input power levels of 25 mW (peak) and 1.8 mW, respectively. Two clear first order idler signals are seen. The real levels of the pump and FWM products were 16 times (12 dB) larger than that exhibited due to the averaged detection of the OSA (this is denoted by black arrows in Fig. 2 (a)). The conversion efficiency, defined as the ratio between the output power of the idler on the pump side to the probe input power takes the large value of η = -36 dB. Fig. 2 (b) shows the conversion efficiency dependence on the pump-probe detuning at constant pump and probe levels for a pump wavelength of λ_p = 1550 nm. The experimental data were quantified by a simple model [10]. For co-polarized pump and probe the conversion efficiency is

$$\eta = \gamma P_p(L)(\sinh(gL))^2 e^{-\alpha L}/g \qquad (1)$$

with $P_p(L)$, L, γ , α and g being the average pump power, waveguide length, third order nonlinear coefficient, loss coefficient, and parametric gain respectively. The parametric gain is defined as

$$g = [(\gamma P_p(L))^2 - (\Delta k_L + \Delta k_{NL})/2]^{1/2}. \qquad (2)$$

The phase mismatch has two contributions: a linear part due to dispersion $\Delta k_L \approx 2\beta_2\Omega^2$ and a nonlinear part $\Delta k_{NL} = \gamma P_p(L)$. β_2 is the linear dispersion and Ω the pump-probe frequency detuning.

The fit shown as a solid line is Fig. 2 (b) matched the measurements very well. The parameters used were a linear dispersion β_2 = -1.47 ps^2/mm (extracted from the linear transmission function of the waveguide), a measured loss coefficient α = 1000 m^{-1}, and a nonlinear coefficient γ = 2900 m^{-1}W^{-1}.

IV. CONCLUSIONS

To conclude, we have demonstrated two nonlinear PhC waveguides based on GaInP membranes. One device exhibits an extremely large hybrid nonlinearity which is sufficiently fast to allow for switching at 10 Gbit/s. The second device was used to demonstrate highly efficient FWM for both a CW and a pulsed pump.

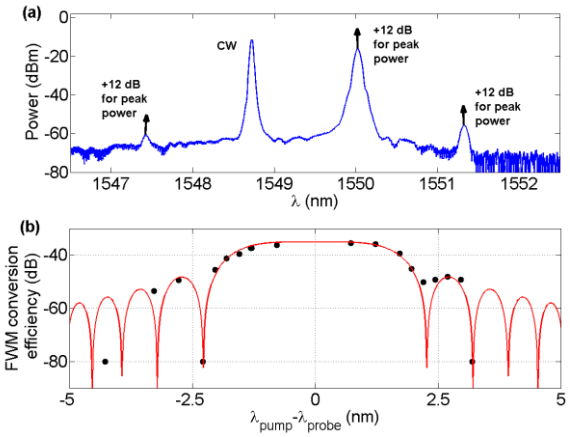


Figure 2. (a) FMW optical spectrum for a CW probe and a modulated pump. (b) FWM efficiency dependence on pump probe detuning for the pump wavelenght of λ_p = 1550 nm (dots). The solid line represents a simulation.

ACKNOWLEDGMENT

This research was partially supported by the project GOSPEL within the seventh framework of the European commission. Dr. Vardit Eckhouse acknowledges the Aly Kaufman fellowship.

REFERENCES

[1] Y. Akane, T. Asano, B. Song, and S. Noda, "High-Q photonic nanocavity in a two-dimensional photonic crystal", Nature 425, 944-947 (2003).

[2] M. Soljacic, S. G. Johnson, S. Fan, M. Ibanescu, E. Ippen, and J. D. Joannopoulos, "Photonic-crystal slow-light enhancement of nonlinear phase sensitivity", J. Opt. Soc. Am. B 19, 2052-2059 (2002).

[3] S. Combrie, Q. Vy Tran, C. Husko, P. Colman, and A. De Rossi, "High quality GaInP nonlinear photonic crystals with minimized nonlinear absorption", Appl. Phys. Lett. 95, 221108 (2009).

[4] K. Inoue, H. Oda, N. Ikeda, and K. Asakawa, "Enhanced third-order nonlinear effects in slow-light photonic-crystal slab waveguides of line-defect", Opt. Express 17, 7206-7216 (2009).

[5] K. Suzuki, Y. Hamachi, and T. Baba, "Fabrication and characterization of chalcogenide glass photonic crystal waveguides", Optics Express, 17, 22393-22400 (2009).

[6] C. Becker, M. Wegener, S. Wong, and G. von Freymann, "Phase-matched nondegenerate four-wave mixing in one-dimensional photonic crystals", Appl. Phys. Let., 89, 131122, (2006).

[7] A. M. Malvezzi, G. Vecchi, M. Patrini, G. Guizzetti, L. C. Andreani, F. Romanato, L. Businaro, E. Di Fabrizio, A. Passaseo, and M. De Vittorio, "Resonant second-harmonic generation in a GaAs photonic crystal waveguide, " Phys. Rev. B 68, 161306-1–161306-4 (2003).

[8] H. Oda, K. Inoue, A. Yamanaka, N. Ikeda, Y. Sugimoto and K. Asakawa, "Light amplification by stimulated Raman scattering in AlGaAs-based photonic-crystal line-defect waveguides", Appl. Phys. Let., 93, 051114 (2008).

[9] Q. Vy Tran, S. Combrié, P. Colman, and A. De Rossi, "Photonic crystal membrane waveguides with low insertion losses", Appl. Phys. Let. 95, 061105 (2009).

[10] M. Ebnali-Heidari, C. Monat, C. Grillet, and M. K. Moravvej-Farshi, "A proposal for enhancing four-wave mixing in slow light engineered photonic crystal waveguides and its application to optical regeneration", Opt. Express 17, 18340 (2009).

Evolution of Planar Waveguide Devices: Communication and Sensing Applications

Katsunari Okamoto
AiDi Corporation, Tsukuba, Ibaraki, 305-0032 Japan
katsu.okamoto@aidicorp.com

Abstract. *The talk will review progress and future prospects of two kinds of planar waveguide devices; they are (a) silicon photonics multi/demultiplexers for communications and (b) a novel spectrometer based on Fourier transform spectroscopy for sensing applications.*

Silicon photonics is widely regarded as a promising technology to meet the requirements of rapid bandwidth growth and energy-efficient on-chip communication while reducing cost per bit. Si photonics devices will have to deal with several tens of different wavelengths of light in the next-generation multi-core chips. There are mainly four kinds of devices capable of multi/demultiplexing tens of WDM signals; they are ring resonators, lattice-form filters, arrayed waveguide gratings (AWG) and planar concave gratings (PCG). The former two are cascaded devices relying on temporal multi-beam interference effect and the latter two utilize spatial multi-beam interference effect. Performance limitations in these filter devices due to the conventional SOI manufacturing processes will be described and a possible way of overcoming the problem will be discussed.

In the latter part of the talk, an integrated-optic spectrometer based on Fourier-transform spectroscopy will be described. A novel planar waveguide spectrometer consists of interleaved Mach-Zehnder interferometer (MZI) array. Practical importance of Fourier-transform spectrometer is the ability to correct for interferometer defects (phase errors) in data processing stage. Successful measurement results of the signal spectrum with 20-GHz resolution by the spectrometer implemented in silica-based planar waveguide will be presented. Miniature spectrometers will be important for daily health care and environmental sensing applications since they are compact in size (wearable) and potentially very low-cost (disposable).

Single-layer InAs/InP (100) quantum-dots on well laser and mid-infrared emission

Junji Kotani, Peter J. van Veldhoven, Tjibbe de Vries, Barry Smalbrugge,
Erwin.A.J.M. Bente, Meint K. Smit, and Richard Nötzel
COBRA Research Institute on Communication Technology,
Eindhoven University of Technology,
Eindhoven, The Netherlands

***Abstract*— We report a single layer InAs/InP (100) quantum dot (QD) laser operating in continuous wave mode at room temperature on the QD ground state transition grown by metal organic vapor phase epitaxy. The necessary high QD density is achieved by growing the QDs on a thin InAs quantum well (QW). This QDs on QW laser exhibits a high slope efficiency and a lasing wavelength of 1.74 µm. An extremely long-wavelength emission centered at 2.46 µm at 6 K is also observed from such QDs on QW structure.**

Keywords- III-V semiconductors; semiconductor quantum dots; semiconductor lasers; mid-infrared emission

I. INTRODUCTION

InAs/InP (100) quantum dot (QD) lasers operating in continuous wave (CW) mode at room temperature (RT) on the QD ground state (GS) transition require multiple stacked QD layers for sufficient gain [1-2]. A single layer InAs QD laser was reported on InP (311)B where the QD density is higher than on InP (100) [3]. Here we report a single layer InAs/InP (100) QD laser operating in CW mode at RT on the QD GS transition and an extremely long-wavelength emission centered at 2.46 µm at 6 K.

II. DEVICE FABRICATION

The QD lasers were grown by low-pressure metalorganic vapor-phase epitaxy (MOVPE) on n-type InP (100) substrates using trimethyl-indium (TMI), trimethyl-gallium (TMG), tertiarybutyl-arsine (TBA), and tertiarybutyl-phosphine (TBP) as gas sources. The InAs QDs on QW structures and conventional InAs QDs for reference were placed in the center of a 500 nm thick lattice-matched InGaAsP waveguide core with a RT band gap at λ_Q= 1.25 µm (Q1.25). For the InAs QDs on QW structure, a 1.6 nm-thick InAs QW was formed under metal stable conditions [4]. 1 ML InAs was deposited for QD formation which is already sufficient due to a large amount of surface segregated In on the InAs QW. The conventional InAs QDs (single and multiple stacked layers separated by 40 nm Q1.25) were formed by 3 ML InAs on a 1.5 ML GaAs interlayer. The GaAs interlayer allows the formation of pure InAs QDs on Q layers [5]. The InAs growth rate and growth temperature were 0.70 ML/s and 515 ^{o}C, and the TBA flow rate was 30 sccm which shifts also the lasing wavelength of the conventional QD lasers to around 1.75 µm. Bottom and top claddings of the laser structures were 500 nm n-InP and 1.5 µm p-InP completed by a compositionally graded 75 nm p-InGaAsP contact layer.

III. RESULTS

A. *Single-layer InAs/InP(100) QD laser*

Fig. 1 (a) and (b) show schematic drawing of the InAs QDs on QW structure and the InAs QDs grown with GaAs interlayer. Fig. 1 (c) and (d) are the atomic force microscopy (AFM) images of the QDs corresponding to the structures in Fig. 1 (a) and (b). The QD density is increased 5 ~ 6 times in the presence of the InAs QW from 6 x 10^9 cm^{-2} for the QDs grown on Q1.25 to 3.4 x 10^{10} cm^{-2}. This increase of the QD density on the InAs QW is attributed to the large amount of strain and surface segregated In [6].

Fig. 2 (a) - (c) show the electroluminescence and lasing spectra of the single layer InAs QDs on QW laser and the five-fold and three-fold stacked InAs QD lasers taken in CW mode at RT. Fig. 2 (d) shows the electroluminescence of the single layer InAs QD laser. QD GS lasing is obtained for the single layer InAs QDs on QW laser with lasing wavelength of 1.74 µm and for the five-fold stacked InAs QD laser. Excited state (ES) lasing of the single layer InAs QDs on QW laser sets in with increasing injection current, confirming GS lasing at

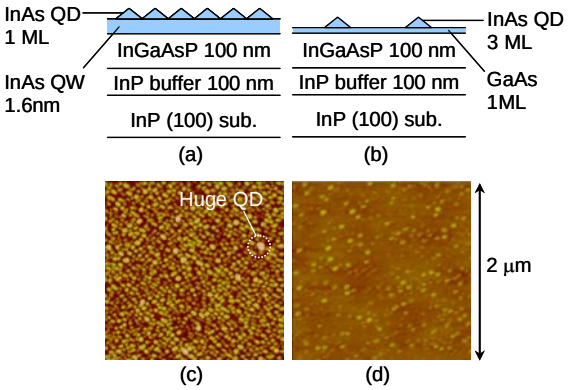


Fig. 1 Sample structure of the InAs QDs grown on (a) InAs QW and (b) GaAs interlayer on Q1.25. [(c) and (d)] AFM images of the corresponding QDs. The height contrast is 40 nm.

This work is supported by the IOP Photonic Devices program managed by the Technology Foundation STW and SenterNovem

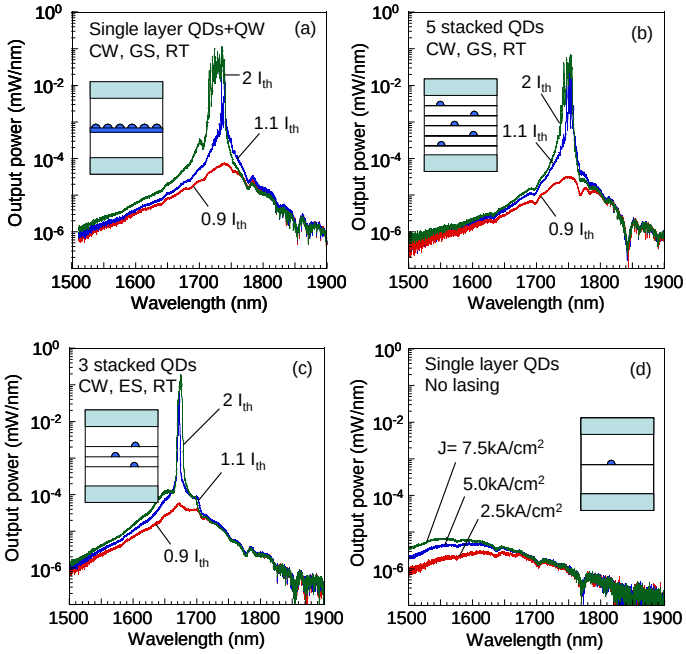


Fig. 2. Electroluminescence and lasing spectra of the four different laser structures. (a) single-layer InAs QDs on QW laser, (b) and (c) five-fold and three-fold stacked InAs QD laser, and (d) single-layer InAs QD laser.

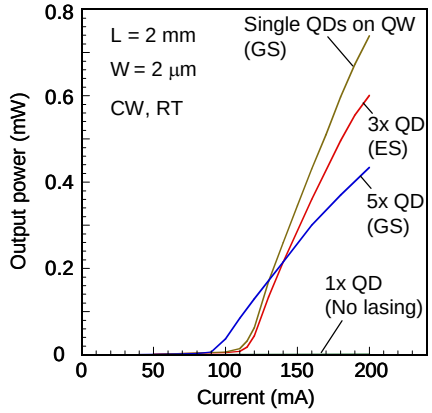


Fig. 3. Light output versus injection current curves of the four InAs QD lasers.

threshold, shown in Fig. 2 (a) at twice the threshold current (I_{th}). For the three-fold stacked InAs QD laser only lasing from ES is observed. For the single layer of InAs QDs lasing is not achieved.

Fig. 3 shows the single facet (as-cleaved) light output versus injection current curves of the four QD lasers. I_{th} of the single layer InAs QDs on QW laser and the five-fold stacked InAs QD laser are comparable. For the three-fold stacked InAs QD laser I_{th} density per QD layer is increased significantly to 0.97 kA/cm^2 from 0.46 kA/cm^2 for the five-fold stacked InAs QD laser due to the three-fold degeneracy of the ES. The slope efficiency of the single layer InAs QDs on QW laser is larger than that of the five-fold stacked InAs QD laser. This is attained by the high density QDs on QW, the related larger confinement factor for the single layer QDs on QW due to their location in the center of the waveguide (see insets in Fig. 2), and a better carrier injection into this single layer.

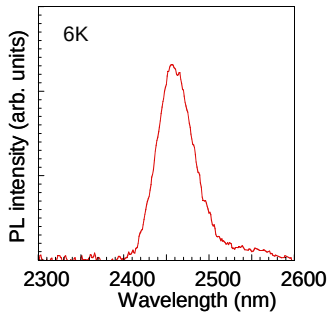


Fig. 4. PL spectrum at 6 K of the InAs QDs on QW structure in the wavelength range of 2.3 – 2.6 µm.

B. Mid-infrared emission from InAs QDs on QW structure

Fig. 4 shows the PL spectrum taken at 6 K in the wavelength range 2.3 – 2.6 µm of the InAs QDs on QW structure, revealing an extremely long-wavelength emission centered at 2.46 µm. This emission is found only for the QDs on QW samples. We believe this emission originates from the huge InAs QDs seen in the AFM image in Fig. 1 (c). They are nearly 20 nm high and over 100 nm wide and only found on the InAs QW, probably triggered by the large amount of surface segregated In after QW growth.

IV. Conclusion

We have successfully achieved lasing in CW mode at RT on the QD GS transition of a single layer InAs QDs on QW structure grown by MOVPE on InP (100) substrates. This is enabled by the 5 ~ 6 times increased QD density on the InAs QW compared to that of conventional QDs. The single layer QDs on QW laser exhibits a higher slope efficiency compared to that of multiple stacked InAs QD lasers. The lasing wavelength is 1.74 µm. Moreover, an extremely long-wavelength PL centered at 2.46 µm is observed at 6 K from the QDs on QW structure.

References

[1] S. Anantathanasarn et al., "Lasing of wavelength-tunable (1.55 µm region) InAs/ InGaAsP/ InP (100) quantum dots grown by metal organic vapor-phase epitaxy," Appl. Phys. Lett., 2006, 89, pp. 073115-1 - 073115-3

[2] S. G. Li et al., "Room temperature continuous-wave operation of InAs/ InP (100) quantum dot lasers grown by gas-source molecular-beam epitaxy", Appl. Phys. Lett., 2008, 93, pp. 111109-1 - 111109-3

[3] E. Homeyer et al., "First demonstration of a 1.52 µm RT InAs/InP (311)B laser with an active zone based on a single QD layer," Semicond. Sci. Technol., 2007, 22, pp. 827 – 830

[4] E. Tournié and K. H. Ploog, "Surface stoichiometry, epitaxial morphology and strain relaxation during molecular beam epitaxy of highly strained InAs/$Ga_{0.47}In_{0.53}As$ heterostructures," J. Cryst. Growth, 1994, 135, pp. 97 – 112

[5] J. M. Ulloa, S. Anantathanasarn, P. J. van Veldhoven, P. M. Koenraad, and R. Nötzel, "Influence of an ultrathin GaAs interlayer on the structural properties of InAs/ InGaAsP/ InP (001) quantum dots investigated by cross-sectional scanning tunneling microscopy," Appl. Phys. Lett., 2008, 92, pp. 083103-1 - 083103-3

[6] J. Kotani, P. J. van Veldhoven, and R. Nötzel, "Mid-infrared emission from InAs quantum dots, wells, and dots on well nanostructures grown on InP (100) by metal organic vapor phase epitaxy," J. Appl. Phys., 2009, 106, pp. 093112-1 - 093112-5

Near-field Electrical Detection of Optical Plasmons and Single Plasmon Sources

Frank H. L. Koppens[1,4], Abram L. Falk[1], Chun L. Yu[2], Kibum Kang[3], Nathalie de Leon Snapp[2], Alexey V. Akimov[1], Moon-Ho Jo[3], Mikhail D. Lukin[1], and Hongkun Park[1,2]

[1]Department of Physics and [2]Department of Chemistry and Chemical Biology, Harvard University, 12 Oxford Street, Cambridge, MA 02138, USA. [3]Department of Materials Science and Engineering, Pohang University of Science and Technology, San 31, Hyoja-Dong, Nam-Gu, Pohang, Gyungbuk, 790-784, Korea

[4]ICFO-Institut de Ciencies Fotoniques, Mediterranean Technology Park, 08860 Castelldefels (Barcelona), Spain

frank.koppens@icfo.es

We demonstrate an efficient nanoscale electrical detector for propagating surface plasmons, an essential component for integrated plasmonic nanocircuits. Our technique is based on the near-field coupling between guided plasmons and a nanowire field-effect transistor. We demonstrate that this near-field circuit can efficiently detect the plasmon emission from a single quantum dot that is directly coupled to the plasmonic waveguide.

Photonic circuits can be much faster than their electronic counterparts, but they are difficult to miniaturize below the optical wavelength scale. Nanoscale photonic circuits based on surface plasmon polaritons (SPs) are a promising solution to this problem because they can localize light below the diffraction limit. However, there is a general tradeoff between the localization of an SP and the efficiency with which it can be detected with conventional far-field optics. Here we describe a new all-electrical SP detection technique based on the near-field coupling between guided plasmons and a nanowire field-effect transistor (Fig. 1a,b) [1]. The Ag NW guides SPs to the Ag/Ge junction, where they are converted to electron-hole (e-h) pairs [2-4] and detected as current through the Ge NW. The Ag NWs are highly crystalline and defect-free, allowing SPs to propagate over distances of several microns without scattering into free-space photons.

Electrical plasmon detection is demonstrated by scanning a focused laser beam across an Ag/Ge crossbar device and recording the current (I) through the Ge NW as a function of the diffraction-limited laser spot position. These data, recorded at zero bias voltage (V_b), show that current flows through the Ge NW only when the laser beam is focused on four distinct spots on the device (Fig. 1b). First, current is detected when the laser is focused near the Ag/Ge junction, due to the direct photoresponse of the Ge NW [5]. The photocurrent induced on the left (I_{left}) and right (I_{right}) sides of the junction have opposite signs (discussed below). Moreover, current through the Ge NW (I_{plas}) is recorded when the laser is focused at either end of the Ag NW. This I_{plas} signal is the key signature for electrical SP detection. Propagating SPs can be launched in the Ag NW only when the excitation laser is incident on the Ag NW ends. Away from the ends, free space photon-to-SP conversion is strongly suppressed by the wave vector mismatch between the two modes. If light scattered off the Ag NW were responsible for the current flowing through the Ge NW, a photocurrent signal would also be detected when the laser is focused on the middle of the Ag NW, in clear contrast to the data shown in Fig. 1b.

An important figure of merit for our detector is the overall plasmon-to-charge conversion efficiency (η), defined as the ratio of detected charges to the number of SPs reaching the Ag/Ge junction. The values of η in our devices typically ranged from 0.01 – 0.1 This efficiency can be tuned by applying a gate voltage (V_{gate}) to an additional electrical contact defined at one end of the Ag NW (data not shown).

These results can be understood by considering electrical plasmon detection as a multistep process. First, the AC electric field of the SP generates e-h pairs in the Ge NW via near-field coupling. Second, the DC electric field within the Ge NW separates these e-h pairs into free charges before recombination takes place. The separated *e-h* pairs are then detected as current. The shape of the built-in DC electric potential, a potential well (Fig 1a, inset), can be inferred from the sign of the Ge photocurrent at either side of the Ag/Ge junction. The depth of this well is tuned by V_{gate}. Asymmetric electrical contacts to the Ge can cause the potential well in the Ge to be off center with respect to the Ag NW. This asymmetry explains the difference in magnitude of I_{right} and I_{left}, and determines the sign of the plasmon-induced current. The DC electric field in the Ge NW is nonzero even at $V_b = V_{gate} = 0$, due to charge transfer across the Ag/Ge junction and/or the occupation of surface charge traps.

We demonstrate the utility of our near-field SP detector by electrically detecting emission from a CdSe quantum dot acting as a single plasmon source (Fig. 1c). The tight field confinement around Ag NWs causes a large fraction of the spontaneous emission from nearby emitters (i.e. 30-100 nm away) to be captured as SP modes [6,7]. These SPs are then converted into an electrical signal at a Ge NW detector. Individual quantum dots (QDs) are coupled to an Ag NW by covering an Ag/Ge device with a 30 nm film of poly(methyl methacrylate) containing a dilute concentration of chemically

synthesized CdSe QDs. Optical fluorescence measurements (Fig. 1f) show that some QDs are close to the Ag NW. When the laser excites one of these QDs, a current signal in the Ge NW detector is observed (pink circle in Fig. 1c) in addition to optical fluorescence from the QD. The dependence of this signal on the excitation wavelength is a clear proof that the current signal results from QD emission (Fig. 1d). Significantly, photon correlation measurements of the far-field fluorescence (Fig. 1e) demonstrate a clear anti-bunching signature, indicating that this spot corresponds to an individual QD.

Nanoscale near-field SP detection opens up several directions for further research. An electrical SP detector could be mounted on a scanning tip, providing a new SP imaging technique. In conjunction with an electrically driven plasmon source [8], a near-field SP detector could be integrated into a "dark" optoelectronic-plasmonic nanocircuit in which all coupling is in the near field. The plasmon detection sensitivity could be improved by using a nanoscale avalanche photodiode or a superconducting film [9] as the SP detector, enabling efficient electrical detection of individual plasmons. Electrical plasmon detectors could lead to new applications for optical sensing without collection optics, including the measurement of plasmon states whose coupling to the far field is suppressed by symmetry. Finally, the strong near-field coupling between single-plasmon emitters and plasmonic nanocircuits could lead to completely new capabilities that are not available with conventional photonics, such as nonlinear switches, single-photon transistors, and quantum non-demolition detectors.

[1] Near field electrical detection of optical plasmons and single plasmon sources, A. L. Falk, F. H. L. Koppens, C. Yu, K. Kang, N. P. de Leon Snapp, A. V. Akimov, M-H. Jo, M. D. Lukin, H. Park

[2] De Vlaminck, I., Van Dorpe, P., Lagae, L. & Borghs, G. Local electrical detection of single nanoparticle plasmon resonance. Nano Lett. 7, 703-706 (2007).

[3] Mapel, J.K., Singh, M., Baldo, M.A. & Celebi, K. Plasmonic excitation of organic double heterostructure solar cells. Appl. Phys. Lett. 90, 121102 (2007).

[4] Ditlbacher, H. et al. Organic diodes as monolithically integrated surface plasmon polariton detectors. Appl. Phys. Lett. 89, 161101 (2006).

[5] Ahn, Y. & Park, J. Efficient visible light detection using individual Germanium nanowire field effect transistors. Appl. Phys. Lett. 91, 162102 (2007).

[6] Akimov, A.V. et al. Generation of single optical plasmons in metallic nanowires coupled to quantum dots. Nature 450, 402-406 (2007).

[7] Chang, D.E., Sorenson, A.S., Hemmer, P.R. & Lukin, M.D. Strong coupling of single emitters to surface plasmons. Phys Rev. B 76, 035420 (2007).

[8] Koller, D.M. et al. Surface plasmon coupled electroluminescent emission. Appl. Phys. Lett. 92, 103304 (2008).

[9] Heeres, R.W., Dorenbos S.N., Koene, B., Solomon, G.S., Kouwenhoven L.P., Zwiller, V., On-Chip Single Plasmon Detection, Nano Letters, volume 10, Issue 2, Page 661-664, (2010).

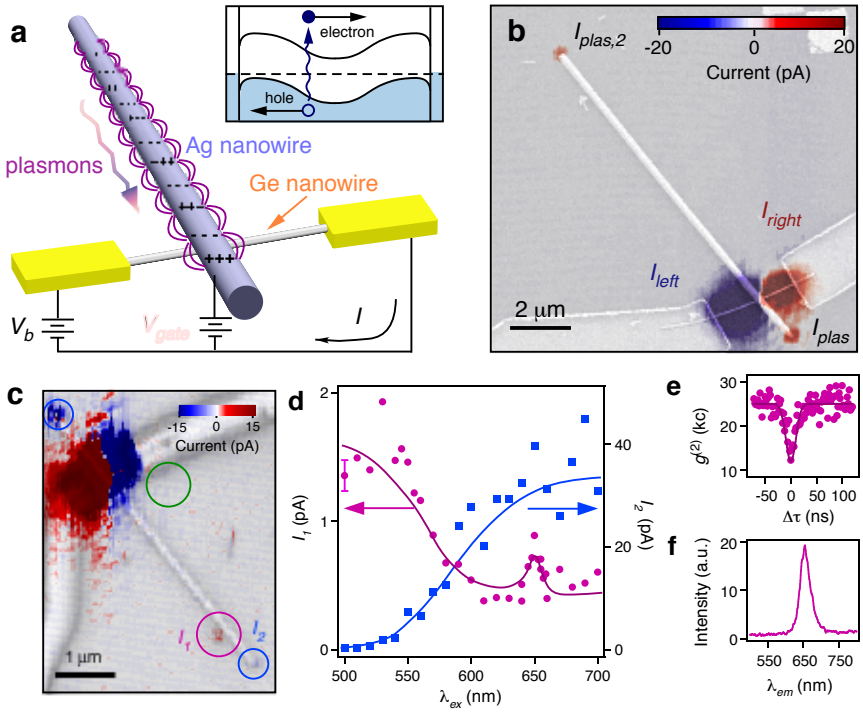


Figure 1. **a.** Schematic of electrical plasmon detector operation. Inset: electron-hole pair generation and separation in the Ge NW detector. **b.** Scanning electron micrograph of Device 1, overlaid with the current through the Ge NW as a function of excitation laser position. Excitation laser power P = 2.0 μW, wavelength λ_{ex} = 532 nm, V_b = 0, V_{gate}=0. **c**. Electrical detection of emission from a single CdSe colloidal QD. I as a function of laser position, overlaying a reflection image of Device 4. P = 1.5 μW, λ_{ex} = 530 nm. V_b = 0, V_{gate} = 0. The violet circle indicates the detector signal corresponding to QD emission into the Ag NW plasmon modes. The blue circles correspond to detection of surface plasmons launched directly by the laser, at the ends of the NW. The green circle corresponds to the position of a QD that is not near the Ag NW, and hence does not generate a current in the detector. **d.** I_1 (QD emission, violet circles) and I_2 (direct laser-to-plasmon signal, blue squares) as a function of λ_{ex}. **e.** Second-order self-correlation function $g^{(2)}(\tau)$ of the QD fluorescence,.The coincidence rate at τ = 0 approaches the 0.5 mark, confirming that a single QD is present. **f.** QD emission spectrum.

Device Requirements for Next Generation Optical Transmission Technology

Masataka Nakazawa
Research Institute of Electrical Communication, Tohoku University, Sendai, Japan
nakazawa@riec.tohoku.ac.jp

***Abstract*— We describe fundamental optical devices for ultrahigh-speed and ultra-multilevel coherent optical transmission in the next generation. Key components such as ultrashort and coherent optical sources, advanced optical modulators, ultrafast switches and coherent receivers are overviewed, and their application to 640 Gbit/s/channel OTDM and 256 QAM transmissions are presented.**

Keywords- Ultrahigh-speed OTDM transmission; coherent QAM transmission; mode-locked laser; all-optical switch; frequency-stabilized laser; IQ modulator; OPLL; coherent receiver

I. INTRODUCTION

Two trends have recently emerged in optical communication technology. One is ultrahigh-speed transmission using ultrashort pulses, which is the driving force behind attempts to realise an advanced high-speed optical network. The other trend is ultrahigh spectral density coherent transmission employing multi-level modulation formats, whose aim is to expand the capacity of WDM transmission systems within a finite transmission bandwidth. These advanced optical transmission technologies are enabled by the progress in light sources, optical modulators, and receivers. In this talk, we present recent progress and future prospects for ultrahigh-speed and coherent optical devices toward Terabit/s OTDM and 256 QAM transmissions.

II. ULTRAHIGH-SPEED OTDM DEVICES

First we describe key devices used in OTDM systems by referring to a 640 Gbit/s/channel-525 km transmission experiment that we demonstrated recently [1]. The experimental set-up is shown in Fig. 1. As an optical pulse source, we used a 40 GHz mode-locked fibre laser (MLFL) that generates a 2.0 ps pulse train. MLFL is an attractive pulse source because of low timing jitter around 100 fs, but because of harmonic mode locking, it suffers from a frequency fluctuation as a result of mode hopping. We developed a mode-hop-free MLFL by installing an etalon in the cavity [2], which greatly improved the stability in the optical phase. To generate an ultrashort pulse for 640 Gbit/s, we employed external pulse compression based on spectral broadening using self-phase modulation in a highly-nonlinear fibre with normal dispersion. After chirp compensation and optical bandpass filtering, a pedestal-free (< – 30 dB), 600 fs pulse train was obtained. It should be noted that the phase coherence is well maintained with this pulse compression scheme as noise-induced modulational instabilities do not occur in a normal dispersion fibre. This property is very important for generating a phase-

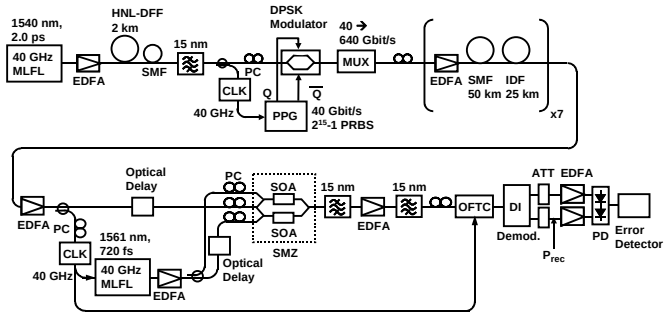


Figure 1. Experimental set-up for a 640 Gbit/s-525 km DPSK transmission.

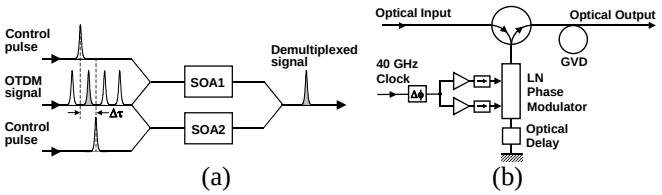


Figure 2. Basic configuration of ultrafast SMZ switch (a) and OFTC (b).

modulated data signal with a subpicosecond pulse. The compressed pulse was then DPSK modulated at 40 Gbit/s and multiplexed to 640 Gbit/s in a single polarisation

After 525 km transmission, the 640 Gbit/s OTDM signal was demultiplexed to 40 GHz with an all-optical semiconductor symmetric Mach-Zehnder (SMZ) switch [3]. The basic configuration of the SMZ switch is shown in Fig. 2(a). By canceling the slow relaxation components of the phase shifts introduced in each SOA with a time delay $\Delta\tau$, an ultranarrow switching gate can be realised. For such an ultrahigh-speed demultiplexing, fibre-based all-optical switches such as a nonlinear optical loop mirror (NOLM) [4] and Kerr switching with parametric amplification [5] have also been demonstrated. Fibre-based switches offer the potential for ultrafast operation owing to a femtosecond response time of the Kerr nonlinearity. The demultiplexed pulse was then launched into an optical Fourier transform circuit (OFTC), in which the spectral profile is converted into a waveform in the time domain and waveform distortions are eliminated [6]. The OFT for a 640 Gbit/s signal was realised by applying a strong chirp to a subpicosecond pulse with a phase modulator operated in a round-trip configuration as shown in Fig. 2(b). Based on this set-up, a bit-error rate (BER) performance sufficiently below a standard FEC threshold (2×10^{-3}) for error-free operation was successfully achieved for all OTDM channels.

III. Devices for Ultra-multilevel QAM Coherent Transmission

In order to overview fundamental devices for ultra-multilevel coherent transmission, here we describe key components that we adopted in a 256 QAM transmission experiment [7]. The transmission set-up is shown in Fig. 3. As a coherent light source, we employed a C_2H_2 frequency-stabilised fibre laser [8], whose linewidth is 4 kHz and the frequency stability is 1.3×10^{-11}. Recently, a C_2H_2 frequency-stabilised external-cavity laser diode has also been demonstrated with an RIN of –135 dB/Hz and a linewidth of 4 kHz [9]. The coherent light is QAM modulated with an IQ modulator, whose configuration and operation principle are shown in Fig. 4(a). It is composed of three Mach-Zehnder (MZ) inteferometers, in which in-phase (I) and quadrature-phase (Q) data are modulated with MZ_A and MZ_B, respectively, and combined with MZ_C with a 90-deg phase shift between I and Q [10]. In a $LiNbO_3$ (LN)-based IQ modulator, surface acoustic waves generated by the piezoelectric effect in the LN crystal should be suppressed to avoid degradation in the low-frequency response, which is very important for increasing the multiplicity level in QAM transmission. Recently a semiconductor IQ modulator has also been demonstrated using InP as shown in Fig. 4(b) [11], which is beneficial for compact integration. A more complicated IQ modulator can be fabricated using PLC-LN hybrid integration as shown in Fig. 4(c) [12]. After the modulation, the QAM signal is coupled with a pilot tone signal whose frequency is 10 GHz down-shifted against the data signal.

After the transmission, the QAM signal is homodyne-detected with a local oscillator (LO) to convert the QAM data into a baseband signal. Here we employed an optical phase-locked loop (OPLL) technique to lock the optical phase between LO and QAM signal using the transmitted pilot tone, in which a high-speed free-running fibre laser is used as an LO [13]. A configuration of a coherent receiver used for homodyne detection is shown in Fig. 5. The LO output is divided with a 90-deg phase shift each other and coupled with the QAM signal in a 90-deg optical hybrid circuit so that the cosine (I) and sine (Q) components are obtained after balanced detection. The phase noise of the detected signal was as low as 0.3 deg., which is sufficiently small for demodulating a 256 QAM signal. Finally they are A/D converted and demodulated into a binary sequence in the DSP. Because of the software demodulation, this transmission system operates in an off-line condition.

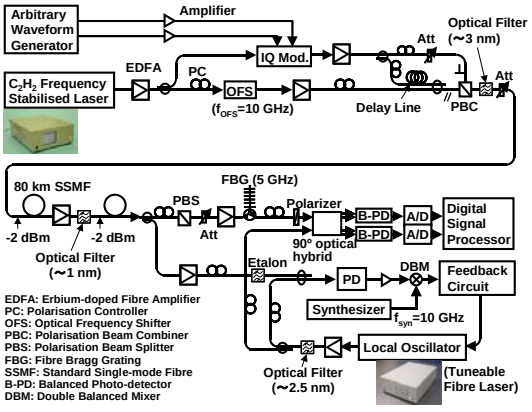


Figure 3. Experimental set-up for 4 Gsymbol/s, 256 QAM transmission.

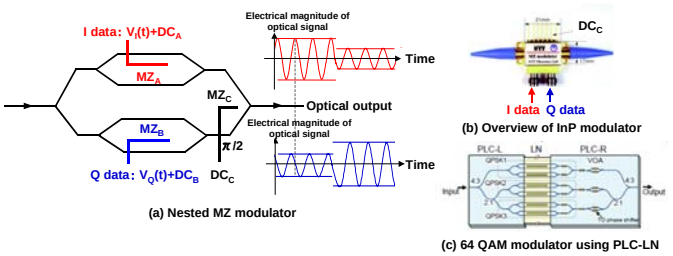


Figure 4. Nested Mach-Zehnder modulators used as an IQ modulator.

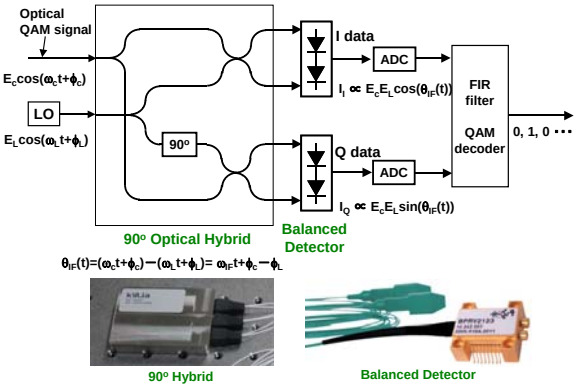


Figure 5. Coherent detection of QAM signal using a 90-deg hybrid and balanced detectors.

In this set-up, we successfully transmitted a polarisation-multiplexed, 4 Gsymbol/s 256 QAM (64 Gbit/s) signal over 160 km within an optical bandwidth of 5.4 GHz, indicating the possibility of spectral efficiency as high as 11 bit/s/Hz. Such an ultrahigh spectral efficiency is substantially beneficial not only for expanding the WDM transmission capacity but also for reducing power consumption.

References

[1] T. Hirano, P. Guan, T. Hirooka, and M. Nakazawa, OFC2010, OTh7.

[2] M. Yoshida, K. Kasai, and M. Nakazawa, IEEE J. Quantum Electron., vol. 43, no. 8, pp. 704-708, 2007.

[3] K. Tajima, Jpn. J. Appl. Phys., vol. 32, no. 12A, pp. L1746-L1749, 1993.

[4] T. Yamamoto, E. Yoshida, and M. Nakazawa, Electron. Lett., vol. 34, no. 10, pp. 1013-1014, 1998.

[5] S. Watanabe, R. Okabe, F. Futami, R. Hainberger, C. Schmidt-Langhorst, C. Schubert, and H. G. Weber, ECOC 2004, Th4.1.6.

[6] M. Nakazawa, T. Hirooka, F. Futami, and S. Watanabe, IEEE Photon. Technol. Lett., vol. 16, no. 4, pp. 1059-1061, 2004.

[7] M. Nakazawa, S. Okamoto, T. Omiya, K. Kasai, and M. Yoshida, to be published in IEEE Photon. Technol. Lett.

[8] K. Kasai, A. Suzuki, M. Yoshida, and M. Nakazawa, IEICE Electron. Express, vol. 3, no. 22, 487-492, 2006.

[9] K. Kasai and M. Nakazawa, Opt. Lett., vol. 34, no. 14, pp. 2225-2227, 2009.

[10] S. Shimotsu, S. Oikawa, T. Saitou, N. Mitsugi, K. Kubodera, T. Kawanishi, and M. Izutsu, IEEE Photon. Technol. Lett., vol. 13, no. 4, pp. 364-366, 2001.

[11] N. Kikuchi, H. Sanjoh, Y. Shibata, T. Sato, K. Tsuzuki, E. Yamada, T. Ishibashi, and H. Yasaka, ECOC 2007, 10.3.1.

[12] H. Yamazaki, T. Yamada, T. Goh, Y. Sakamaki, and A. Kaneko, ECOC 2009, 2.2.1

[13] K. Kasai, J. Hongo, M. Yoshida, and M. Nakazawa, IEICE Electron. Express, vol. 4, no. 3, pp. 77-81, 2007.

Low chirp RSOA using multi-sections devices for optical access networks

G. de Valicourt, F. Pommereau, F. Poingt, M. Lamponi, G.H. Duan, and R. Brenot
Alcatel-Thalès III-V labs, a joint Laboratory of "Alcatel Lucent Bell Labs" and "Thales Research & Technology"
Campus Polytechnique, 1, Avenue A. Fresnel, 91767 Palaiseau cedex, France,
guilhem.devalicourt@3-5lab.fr

P. Chanclou[2] and M. A. Violas[3]
(2) Orange Labs,
2 Avenue Pierre Marzin, 22307 Lannion, France
philippe.chanclou@orange-ftgroup.com
(3) Instituto de Telecomunicações, Universidade de Aveiro,
Campus Universitário, Aveiro 3810-193, Portugal
manuelv@ua.pt

Abstract—**Optimized bi-electrode reflective semiconductor optical amplifier is used as remote modulator. It is demonstrated both theoretically and experimentally that multi-sections devices reduce the chirp, enabling only 4.5 dB penalty for transmission on standard fibre at 2.5 Gbit/s over 50 km.**

Keywords-Access control; Modulation; Optical fiber communication; Semiconductor optical amplifiers

I. INTRODUCTION

Today, high speed connectivity is required to fill users demand. Wavelength division multiplexed (WDM) passive optical networks (PONs) is one of the possible scenario for the next generation of access network. Colorless remote modulator such as injection-locked Fabry-Perot lasers [1], reflective electro-absorption modulator (EAM) [2] and Reflective EAM-semiconductor optical amplifier (SOA) [3] are considered as potential candidates. However, in order to develop large scale commercially available services, low cost solutions have to be investigated. Its large optical bandwidth, high gain and large electro-optic bandwidth make RSOA an ideal candidate fullfilling most requirements [4]. Recently, the first commercial service with R-SOA based hybrid PON has been announced for 1024 subscribers at 1.25 Gbps over 20 km[5]. However the performance of SOAs is still to be improved for higher bit-rate and longer transmission distance. In particular, the chirp due to direct modulation of the RSOA becomes a limiting factor for transmission distance approaching 50 km and bit rate up to 10 Gbit/s. In this paper, we demonstrate, for the first time, both theoretically and experimentally the chirp reduction by using adequate RSOA electrodes configuration. The penalty introduced over a 50 km transmission at 2.5 Gbps is reduced to 4.5 dB, corresponding to 1.5 dB of improvement compared to the single electrode RSOA configuration.

II. MULTI-ELECTRODES MODEL AND CARRIER DENSITY SIMULATION

In SOA devices, the modulation of refractive index, upon carrier density modulation, introduces a phase change of the incoming continuous wave signal, commonly called chirp. Because the carrier density along a RSOA is not homogenous, the location where is applied the current modulation strongly affect the device behaviour. A time domain model for RSOAs was developed based on the carrier rate and wave propagation equations. In this model, the non linear gain saturation effect and the amplified spontaneous emission on carrier density have been included. The analytical approach follows the same analytical formalism of Connelly static model [6]. The active zone thickness and width are 0.5 µm and 0.6 µm respectively. A constant DC current of 30 mA with ± 20 mA modulation is used with bi-electrode devices as in the experimental set up. A DC current of 35 mA is applied on the input electrode when modulating the mirror electrode (SOA2) and a DC current of 100mA is used in the other case (modulation of the input section: SOA1). Both current values correspond to optimized conditions in order to obtain low penalties. In classic SOA, strong carrier depletion at the input section is observed, due to the high amplified spontaneous emission (ASE) power in the RSOA at ON state, and this effect is reduced at OFF state. Due to spatial hole burning (SHB), both electrodes are not independent in the different configuration and the modulation of one electrode strongly affects the carrier density level of the

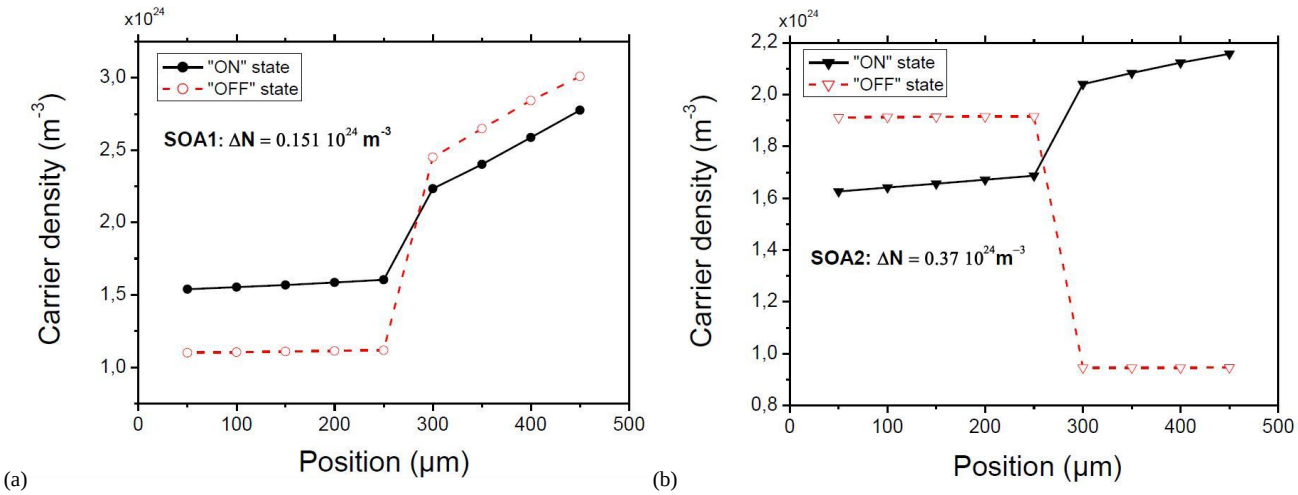


Figure 1. Simulated carrier density along bi-electrode RSOA with input (a) and mirror (b) electrode modulation for ”ON” and ”OFF” state

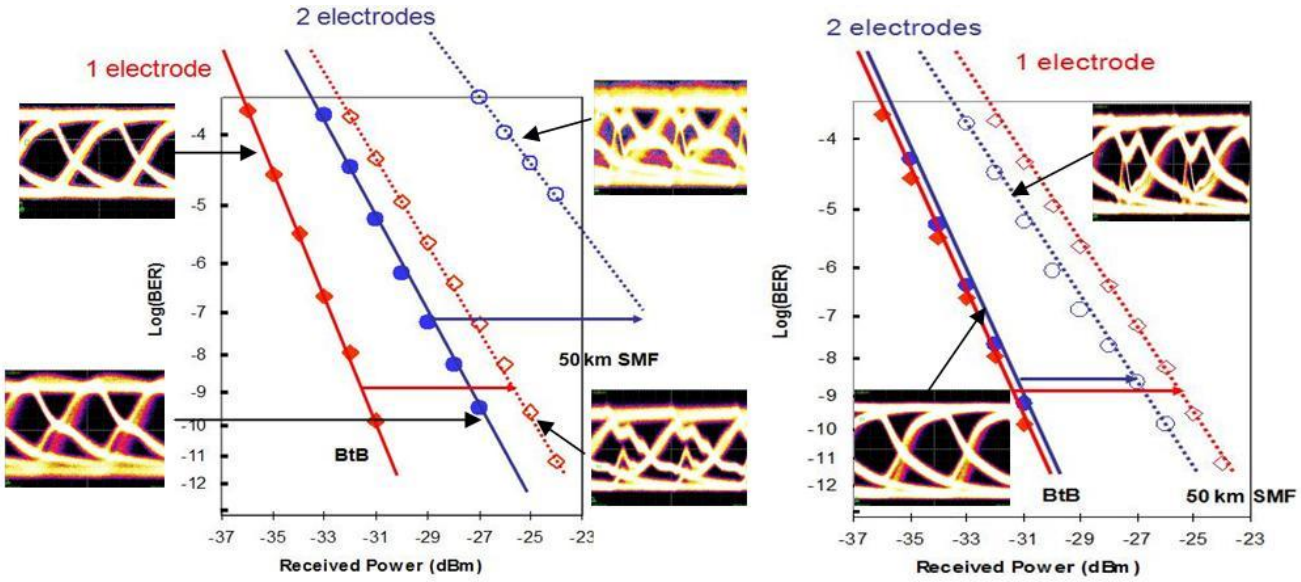


Figure 2. BER curves as a function of the received power in Back-to-Back and after 50 Km transmission for one and two electrodes configurations. In bi-electrode configuration, the modulation I_{HF} is applied to the mirror section and DC current I_{DC} to the input section (left) or inversely (right)

second one. As a result, large carrier density variation is observed in the input section when modulating the mirror section (SOA2, Fig. 1 (b)), which explains the limitation of this configuration. On the contrary, modulating the input section mainly affects this section (SOA1, Fig. 1 (a)), since in the mirror region carrier density is less impacted by photon density distribution variations.

III. Device Characteristics and Experimental Results

The RSOA structure consists of thick tensile-strained InGaAsP active zone with high optical confinement value (around Γ~80%) and polarization independent gain. We minimize internal reflections using 7° tilted facet and AR coating. Coupling losses lower than 2dB and gain values up to 25 dB have been measured. The gain peak and gain bandwidth values were respectively 1510 nm and 50 nm. Proton implantation was used in order to isolate electrically the two electrodes. A standard reflective scheme is used including a transmission link over 50 km of fiber. An external cavity laser or a standard DFB is used to launch a CW signal into the system at $\lambda = 1540$ nm through an optical circulator (OC). The CW signal is coupled into the RSOA whose current is modulated to generate the upstream signal. The RSOA is biased with a 2^{31}-1 pseudo-random bit sequence (PRBS) at 2.5 Gbps, and the output of RSOA is coupled back into the OC. The modulated signal propagates through a 50 km long Single Mode Fiber (SMF). A variable optical attenuator is placed before the receiver in order to analyze the performances of the transmission. Bit-error-rate (BER) measurements were performed using an error analyzer. A back-to-back and transmission through 50 km SMF at 2.5 Gbps has been achieved using RSOA with one and two electrodes. Fig. 2 displays BER measurements and unfiltered eye diagrams performed at 1540 nm and 2.5 Gbps as a function of the received power for one electrode and bi-electrode RSOA. The penalty due to the transmission with a single electrode device is equal to 6 dB. With the bi-electrode device, penalties of 8 or 4.5 dB are obtained respectively for configurations SOA1 and SOA2. These transmission results clearly show the correlation between the penalty and the chirp: higher is the SOA chirp, larger is the transmission penalty. The minimum transmission penalty is achieved using an adequate bi-electrode configuration. However, the configuration SOA1 corresponds to a moderate average current in the input section, and leads to a degradation of the noise factor. This drawback can be overcome with a tri-electrode configuration.

IV. Conclusions

We demonstrate that penalties due to the transmission over 50 km SMF at 2.5 Gbps are reduced from 6dB to 4.5dB using an optimized multi-electrodes device. However the use of a non adequate bi-electrode configuration increases transmission penalties up to 8 dB. We believe this effect will be even more pronounced when 10 Gbps RSOA will be used. Further works are underway to study more complex, optimized multi-electrodes schemes (Tri-electrode and more).

Acknowledgment

This work was supported by ICT-FUTON and ANR-AROME projects.

References

[1] Wai Hung, Chun-Kit Chan, Lian-Kuan Chen, and Frank Tong, "An Optical Network Unit for WDM Access Networks With Downstream DPSK and Upstream Remodulated OOK Data Using Injection-Locked FP Laser," IEEE Photonics technology letters, Vol. 15, No. 10, 2003

[2] E. K. MacHale, G. Talli, P. D. Townsend, A. Borghesani, I. Lealman , D. G. Moodie, and D. W. Smith, "Extended-Reach PON Employing 10Gb/s Integrated Reflective EAM-SOA, "in Proc. ECOC'08, Th.2.F.1, Bruxelles, 2008

[3] A. Garreau, J. Decobert, C. Kazmierski, M.-C Cuisin, J.-G Provost, H. Sillard, F. Blache, D. Carpentier, J. Landreau, P. Chanclou, "10Gbit/s Amplified Reflective Electroabsorption Modulator for Colourless Access Networks," Indium Phosphide and Related Materials Conference Proceedings, pp.168-170, 2006

[4] G. de Valicourt, D. Maké, J. Landreau, M. Lamponi, G.H. Duan, P. Chanclou and R. Brenot, "New RSOA Devices for Extended Reach and High Capacity Hybrid TDM/WDM -PON Networks", in proc. ECOC'09, P9.5.2, Vienna, 2009

[5] Han-Hyub Lee, Seung-Hyun Cho, Jie-Hyun Lee, Eui-Suk Jung, Jea-Hoon Yu, Byoung-Whi Kim, Sang-Soo Lee, Sang-Hyeun Lee, Jai-Sang Koh, Back-Heung Sung, Suk-Jin Kang, Jin-Hee Kim, and Ki-Tae Jeong, "First commercial Service of a Colorless Gigabit WDM/TDM Hybrid PON System", in Proc. OFC'09, PDPD9, San Diego, 2009

[6] M. J. Connelly, ―Semiconductor Optical Amplifiers‖, Boston, MA Springer-Verlag, 2002

Switching Ultrahigh Line-rate Optical Data in a Monolithic Multistage Interconnection Network

A. Albores-Mejia, K.A. Williams, X.J.M. Leijtens, T. de Vries, Y.S. Oei, M.J.R. Heck, D.J. Robbins and M.K. Smit
Electrical Engineering, University of Technology Eindhoven
COBRA Research Institute
Eindhoven, The Netherlands
a.a.m.albores.mejia@tue.nl

Abstract—**A monolithic multistage interconnection network with minimum two and maximum four stages of cascaded crossbar switches is designed, fabricated and demonstrated. Record ultrahigh data line-rates of 160Gb/s are dynamically switched between paths exploiting the high 43.4dB extinction ratio and optical signal to noise ratio of 41.7dB/0.1nm.**

Keywords- Monolithic Integration; Optoelectonic Switching

I. INTRODUCTION

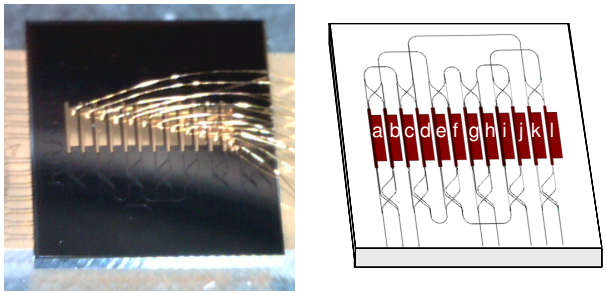
The increasing demand for high-capacity data transfer with increasing number of network connections is driving research into large capacity photonic switching systems. Nanosecond-switched, broadband semiconductor optical amplifier (SOA) based circuits have received particular attention owing to the promise of low control complexity and monolithic integration. Higher serial line-rates per wavelength offer a route to reduced inventory, simplified network management and payload-agnostic routing. Important energy savings are also anticipated as line rates increase in ultrabroadband photonic circuits. However there is little understanding of the limits to serial data rates in such monolithic multistage interconnection networks.

In this work we study, for the first time, the switching behaviour of an intrinsically scalable optoelectronic monolithic multistage interconnection network. Nanosecond timescale reconfigurable operation is demonstrated for the first time at 160Gb/s.

II. PHOTONIC INTEGRATED CIRCUIT

A. Circuit

The four input, four output multistage optoelectronic switching circuit is implemented on an active-passive regrown InGaAsP/InP epitaxial multiproject wafer [1]. The InGaAsP/InP multiquantum-well active layer is designed for 1550nm operation. Twelve active islands with area 30 µm × 1000 µm are defined on a 250 µm pitch within a larger passive waveguiding area. Fig. 1a shows a photograph of the circuit attached to a gold plated AlN subcarrier. Wire bonds connect each of the electrodes. Fig. 1b explicitly shows the implemented waveguide and electrode arrangements. Pairs of SOA gates are placed within each of the twelve active islands for enhanced integrated density. Each active island is invidually addressed using the twelve rectangular electrodes visible in the centre of the circuit. The total circuit area is implemented within chip dimensions of only 4.3mm × 2.8mm.



a) b)

Fig. 1. a) Microscope photograph of the monolithic multistage interconnection network. b) Schematic waveguide layout.

B. Architecture

The multistage interconnection network allows an increase in the number of network connections while using identical 2x2 crossbar switch cells. In this work, an N-stage planar network [2] is implemented with our previously demonstrated two-electrode crossbar switch concept [3], which is now configured for active passive integration. The four input and four output waveguides are placed at the front facet and connect to the row of crossbar cells across the centre of the circuit. Each crossbar switch has four SOA gates which are configured to occupy only two active islands. The two electrodes define either cross or bar state. Six such crossbar switches are interconnected by means of deeply etched 100 µm radius curved waveguides integrated within the low-loss, passive-waveguide shuffle network. Waveguide crossings are implemented with shallow waveguides to reduce path dependent crosstalk. Splitters and combiners are implemented with multimode interference couplers. Eleven of the sixteen paths are successfully implemented despite a wiring error.

III. EXPERIMENTS

Operating fibre to fibre loss is measured to be –13.7dB and –14.0dB for the two stage paths studied here. Losses are dominated by the 6.0dB fibre to chip coupling loss leading to estimated on chip losses of only 1.7dB and 2.0dB. Net chip gain is feasible, but facets are not anti-reflection coated, and therefore modest operating currents are selected to avoid spectral ripple and subsequent signal impairments.

The chip has been fabricated on the Photonic Integration Platform JePPIX. A. Albores-Mejia acknowledges the support of CONACyT-Mexico.

Switching is initially characterised in terms of a static extinction ratio. Optical transmission is compared for two bias currents at one SOA gate electrode: low state 0mA and high state 120mA. A polarisation-aligned, continuous-wave signal is input with 3dBm (in-fibre) power at 1550nm. Fig. 2 shows the measured extinction ratio of 41.2dB. Optical signal to noise ratio is measured to be 39.5dB/0.06nm. These good values are indicative of high gain and low loss within the circuit.

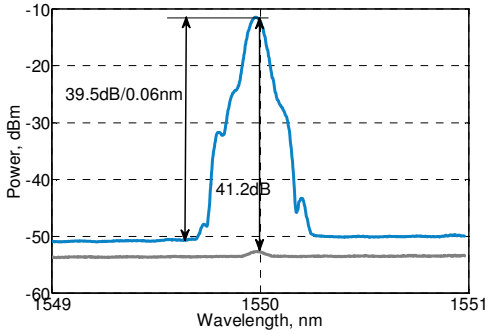


Fig. 2. Switching extinction ration and OSNR for a polarization optimized CW input signal.

High serial line rate transmission is studied by inputting 160Gb/s signals into two different ports and assessing via the same output. The experimental arrangement is shown in figure 3. The switch is controlled with a combination of current sources and fast transition pulse generators clocked at 2.6MHz.

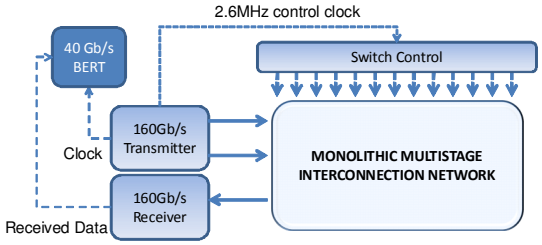


Fig. 3. Experimental setup for 160Gb/s data routing.

The 160Gb/s serial data is an aggregate of sixteen optically time division multiplexed 10Gb/s tributary channels. An aggregate optical power of +7dBm in-fibre is injected into the circuit. Fig. 4a shows the static performance of the circuit when 160Gb/s signals are routed through a two-stage path. The performance is assessed with bit error rate measurements showing a power penalty of 0.8dB. Fig. 4b shows that the data integrity is maintained on all the multiplexed channels while maintaining error free operation at -19.5dBm. Error free operation has also been achieved when routing through the maximum four stages with a different multiplexing scheme [4].

Dynamic routing is studied by addressing the crossbar electrodes with fast pulse generators. The optical state transition time is measured to be 1.2ns. Electrode *j* is biased at the low state and electrodes *g* and *h* are reconfigured during the measurements. Fig. 5 shows one tributary of the dynamically routed 160Gb/s signal. The upper time-traces highlight the switching response when only one path is selected at a time. A complete suppression of the signal is achieved with the electrodes in the off state. The bottom time-trace shows the time aggregated channels from the two paths.

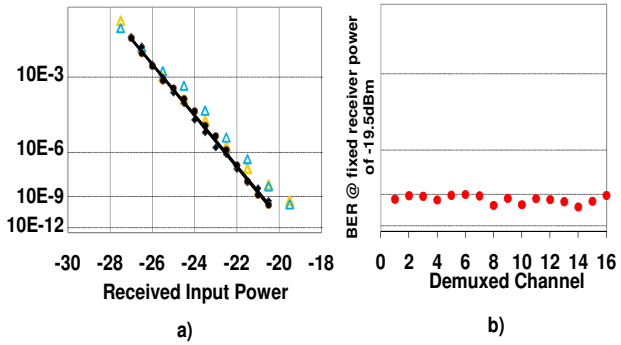


Fig. 4. a) Bit Error Rate performance showing for clarity two out of sixteen demultiplexed channels. b). Error performance at receiver power -19.5dBm for all sixteen demultiplexed tributrary channels.

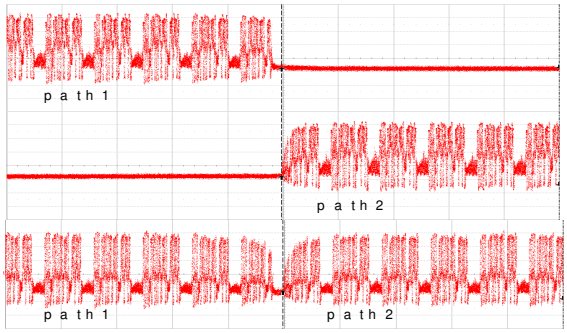


Fig. 5. Dynamic routing of a OTDM 160Gb/s input signal. (73ns timebase)

IV. Conclusion

The first monolithic multistage interconnection network using active passive integration is presented. A high extinction ratio, good optical signal to noise ratio, low loss and fast nanosecond rise time are all exhibited within the same circuit. The presented architecture is intrinsically scalable to higher network connections. The record 160Gb/s line-rate highlights a highly promising route to high-capacity and large scale photonic circuit integration.

References

[1] M.J.R. Heck, A. La Porta, X.J.M. Leijtens, L.M. Augustin, T. de Vries, E. Smalbrugge, Y.S. Oei, R. Nötzel, R. Gaudino, D.J. Robbins, M.K. Smit, "Monolithic AWG-based discretely tunable laser diode with nanosecond switching speed". IEEE Photonics Technology Letters, 2009, 21, 13, 905-907.

[2] Spanke, R A., Benes, V. E., "N-stage planar optical permutation network", Appl. Opt. 1987, 26, 7, 1226-1229.

[3] A. Albores-Mejia, K.A. Williams, T. de Vries, E. Smalbrugge, Y.S. Oei, R. Nötzel, M.K. Smit, "Integrated 2x2 quantum dot optical crossbar switch in 1.55 µm wavelength range", IET Electronics Letters, 2009, 45, 6, 313-314.

[4] A. Albores-Mejia, K.A. Williams, F. Gomez-Agis, S. Zhang, H.J.S. Dorren, X.J.M. Leijtens, T. de Vries, Y.S. Oei, M.J.R. Heck, R. Notzel, D.J. Robbins and M.K. Smit, "160Gb/s Serial Line Rates in a Monolithic Optoelectronic Multistage Interconnection Network", 17th IEEE Symposium on High Performance Interconnects, 2009.

Optical Parametric Amplification in Ti:PPLN Channel Waveguides

Rahman Nouroozi*, Hubertus Suche, Werner Grundkötter, Raimund Ricken, Viktor Quiring and Wolfgang Sohler
Angewandte Physik, Department Physik, Universität Paderborn,
D 33098 Paderborn, Germany
*Rahman.nouroozi@upb.de

Abstract—**Optical parametric amplification via cascaded SHG/DFG in Ti:PPLN channel waveguides has been investigated using a Q-switched DPSS-laser of low pulse duty cycle as fundamental source to avoid photorefraction. More than 26 dB of parametric gain was achieved in a 95 mm long waveguide with 15 W of fundamental peak power.**

Keywords- nonlinear optics; optical parametric amplifier; PPLN, waveguide

I. INTRODUCTION

Optical parametric amplification (OPA) is a very promising way to get large bandwidth, low (quantum-limited) noise, coherent and phase sensitive amplification. Therefore, corresponding devices are completely transparent, attractive in particular for telecom applications. Among the different OPA approaches [1,2], cascaded second harmonic generation and difference frequency generation with simultaneous signal amplification (cSHG/DFG(OPA)) in periodically poled $LiNbO_3$ (PPLN) waveguides [3] is of particular interest: (i) the largest nonlinear coefficient can be exploited enabling the development of integrated amplifiers much shorter than fiber-optical devices, (ii) stimulated Brillouin scattering (SBS), self- and cross phase modulation (SPM, XPM) do not deteriorate the OSNR and, therefore, need not to be overcome by sophisticated pump modulation schemes [2], (iii) the cascaded process allows using telecom devices for pumping, and (iv) the actual pump wave is generated internally by SHG.

Pulsed OPA in PPLN was first demonstrated in 1998 in the bulk [4] and later in proton-exchanged waveguides with two successive sections of different domain periodicities for SHG and OPA using a mode-locked Er-doped fiber laser as fundamental source [1].

In this contribution we report pulsed OPA by cSHG/DFG (OPA) in a low-loss Ti-indiffused PPLN waveguide of constant poling periodicity using a Q-switched diode pumped solid state (DPSS) laser fundamental source. A gain of up to 26 dB was demonstrated at 15 W fundamental peak power.

II. PRINCIPLE OF OPERATION

In cSHG/DFG(OPA) the actual pump wave for the DFG/OPA process is generated internally by SHG of the fundamental wave. The signal is amplified and a wavelength converted (idler) wave is generated at the difference frequency $\omega_i = \omega_p - \omega_s$ (Fig. 1). Due to quasi phase-matched SHG a selective excitation of a single spatial pump mode is guaranteed.

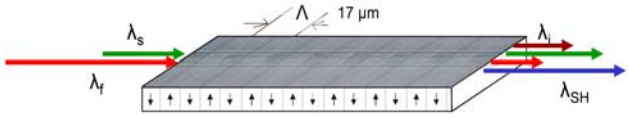


Fig.1: Scheme of OPA of a signal (λ_s) wave by cSHG/DFG(OPA) in a Ti:PPLN channel guide. The fundamental wave (λ_f) generates its second harmonic (λ_{SH}) as pump wave for the DFG/OPA-process. The idler (λ_i) is the wavelength-converted signal (λ_s) wave.

The evolution of fundamental-, SH-, signal- and idler power levels in the waveguide has been calculated for cw-operation. An effective interaction length of 45 mm, homogeneous quasi-phase matching, and ~3 W coupled fundamental power have been assumed for the example presented in Fig. 2. The fundamental wave is continuously depleted mainly due to SHG but also due to DFG and OPA (here ~ 16 dB).

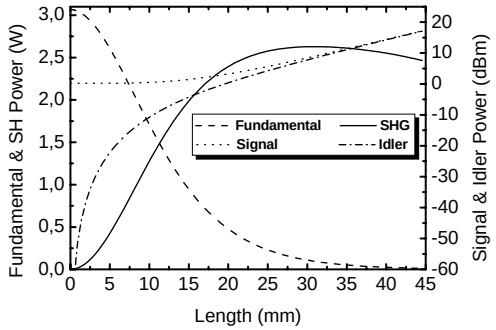


Fig. 2: Calculated evolution of cw-fundamental-, SH-, signal-, and idler power levels along the waveguide for 3 W of coupled fundamental power.

III. FABRICATION AND EXPERIMENTAL SETUP

7 µm wide strip waveguides of low propagation losses (< 0.1 dB/cm @ 1550 nm) were fabricated by indiffusion (9h/1060°C) of photolithographically delineated 100 nm thick Ti-stripes into Z-cut $LiNbO_3$. Afterwards, the waveguides were periodically poled with a period Λ=16.3 µm using the field assisted poling method [5]. To avoid Fabry-Perot cavity effects, which might lead to the onset of parametric oscillation, the waveguide end-faces were angle-polished and AR-coated.

This work was funded by the Deutsche Forschungs-gemeinschaft (DFG) within the framework of the project "Contention Resolution in Optical Burst Switching (OBS) using Wavelength Conversion".

To avoid photo-refraction at high power operation, 2.5 ns long pulses of a low duty cycle (8.2×10^{-6}) passively Q-switched laser at 1535 nm wavelength were used as the fundamental radiation. The cw signal was combined with the pulsed fundamental wave using a dichroic mirror and launched together into the temperature stabilized waveguide. To achieve quasi-phase-matching the waveguide was heated to 165°C. At the output a tunable bandpass filter selected the signal. It was monitored by an InGaAs-PIN-photodiode of 15 GHz bandwidth and a digital oscilloscope of 1.5 GHz bandwidth.

IV. RESULTS AND DISCUSSION

In Fig. 3, transmitted fundamental-, generated SH- and amplified signal are displayed for low (0.8 W, left) and high (6 W, right) of coupled fundamental peak power as example.

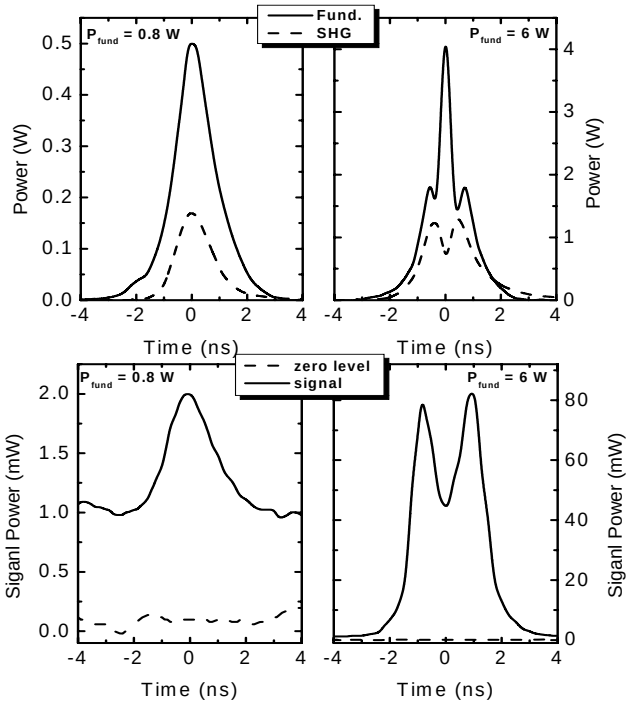


Fig. 3: Upper diagrams: measured output fundamental (solid), SHG (dashed) pulses; lower diagrams: measured output signal pulses without (dashed) and with (solid) parametric gain; coupled fundamental power levels: 0.8 W (left) and 6 W (right).

At low fundamental power the fundamental pulse is continuously depleted leading to an single peaked SH pulse (left). At high fundamental power the depletion of the fundamental pulse becomes nonmonotonic resulting in a distorted double peaked SH-pulse (right). We attribute this effect to the shrinking of the quasi-phase matching (QPM) acceptance bandwidth [6]. Even small deviations from exact QPM (e.g due to temperature fluctuations and/or waveguide inhomogeneities) lead to a power level dependent non-monotonic evolution of the fundamental wave along the guide. As a consequence the shape of the SH-pulse can significantly deviate from the square of the pulse shape of the input fundamental wave.

The pulse shape of the amplified signal follows the SH-pulse envelope (Fig. 3, lower diagrams). By comparing the peak power level during amplification with the cw-signal power level without amplification a parametric gain of about 3 dB for 0.8 W and 20 dB for 6W coupled fundamental power has been achieved.

In Fig. 5 the measured and calculated (for cw and 45 mm effective interaction length) parametric gain is plotted versus the coupled fundamental power. With about 15 W more than 26 dB of parametric gain has been achieved. In the range of undistorted SHG (up to about 4 W of coupled fundamental power) a good agreement between measured and calculated parametric gain has been achived.

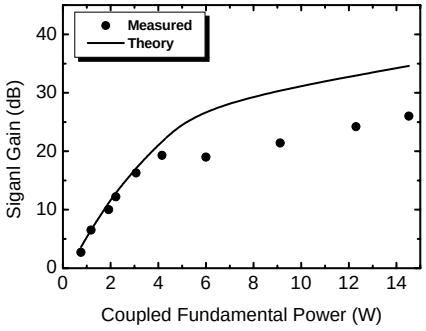


Fig. 5: Measured and calculated signal gain versus coupled fundamental peak power in a Ti:PPLN channel waveguide of 45 mm long effective interaction length and 16.3 µm micro-domain period, operated at 165°C.

V. CONCLUSIONS

Pulsed optical parametric amplification by cSHG/DFG (OPA) in a 95 mm long (45 mm long effective interaction length) Ti:PPLN channel waveguide is reported. To avoid photorefraction in high power operation a Q-switched DPSS-laser emitting short pulses of low duty cycle has been used. With 15 W of fundamental peak power ~ 26 dB of signal gain has been measured. This result is in reasonably good agreement with numerical simulations.

REFERENCES

[1] A. Galvanauskas, K. K. Wong, K. El Hadi, M. Hofer, M. E. Fermann, D. Harter, M. H. Chou, M. M. Fejer, "Amplification in 1.2-1.7 µm communication window using OPA in PPLN waveguides", Elec. Lett. 35, p. 731-733 (Apri1 1999).

[2] Thomas Torounidis, Peter A. Andrekson, and Bengt-Erik Olsson, "Fiber-Optical Parametric Amplifier With 70-dB Gain", IEEE Photonics Technology Letters, Vol. 18, No. 10, May 15, 2006.

[3] W. Sohler, W. Grundkötter, J.H. Lee, Y.L. Lee, Y.H. Min, V. Quiring, H. Suche, R. Schiek, T. Pertsch, F. Lederer, R. Iwanow, G.I. Stegeman: "All-optical signal processing in periodically poled LiNbO3 waveguide structures", Proc. ECOC2004, Vol. 2, paper Tu3.4.1 (invited) pp 192-195, Stockholm, September.

[4] A. Galvanauskas, A. Hariharan, and D. Harter, "High-Energy Femtosecond Pulse Amplifi-cation in a Quasi-Phase-Matched Parametric Amplifier", Opt. Lett. 23, p. 210-212 (February 1998).

[5] G. Schreiber, H. Suche, Y.L. Lee, W. Grundkötter, V. Quiring, R. Ricken, and W. Sohler:"Efficient cascaded difference frequency conversion in periodically poled Ti:LiNbO3 waveguides using pulsed and cw pumping", Applied Physics B, Special Issue on Integrated Optics, vol. 73, 501-504 (2001).

[6] K. R. Parameswaran, J. R. Kurz, R. V. Roussev, M. M. Fejer, "Observation of 99% pump depletion in single-pass second-harmonic generation in a periodically poled lithium niobate waveguide", Optics Letters, 27, p. 43-45 (January 2002).

Integrated $LiNbO_3$ ridge modulators planarized by using a Teflon buffer layer

M. García-Granda, D. Janner, D. Tulli
ICFO – Institut de Ciencies Fotoniques
Mediterranean Technology Park
08860, Castelldefels (Barcelona), Spain
miguel.garcia-granda@icfo.es

Valerio Pruneri
ICFO – Institut de Ciencies Fotoniques
Mediterranean Technology Park
08860, Castelldefels (Barcelona), Spain
ICREA – Institució Catalana de Recerca i Estudia Avançats
Barcelona, Spain

***Abstract*—Novel electro-optical ridge-guide modulators in $LiNbO_3$ are proposed. Spun Teflon AF polymer is used as buffer and planarization layer, improving modulator performance and fabrication process. Simulation results show low driving voltage (< 8 V•cm) for nearly velocity and impedance matched devices. Electro-optical characterization will be presented at the conference.**

Modulators, lithium niobate, ridge waveguides, Teflon.

I. INTRODUCTION

External modulators based on lithium niobate ($LiNbO_3$) are nowadays key components for high-bit-rate optical communication systems. Current commercial devices offer a modulation bandwidth (Δf) exceeding 40 GHz combined with a low driving voltage (V_π) in the range of 4 to 5 V, with a voltage-length product ($V_\pi L$) of the order of 12 to 15 V•cm.

Many technological approaches have been made in order to improve modulator performance. For example, thin sheet designs, [1], ferroelectric domain inversion [2], or even photonic crystal structures [3]. However, one of the most promising structures is the ridge waveguide modulator. These devices are able to shrink the size of optical modes so that the overlap of applied electric field and optical fields is maximized. Ridge structures also provide a lower effective index of the modulating microwave with thinner buffer layers, which means that the bandwidth of the devices is larger, while having low driving voltage.

High-bandwidth devices with $V_\pi L$ in the range of 8 to 9 V·cm have been demonstrated [4] based on $LiNbO_3$ ridge waveguides coated with SiO_2 buffer layer. However, a drawback of these structures is the need to deal with the different levels of the ridge structure, which make the fabrication process more sensitive and complicated. This can also result in additional electrical losses.

In this work we propose a novel combination of ridge waveguides in $LiNbO_3$ with Teflon AF as buffer and planarization layer. For the first time, we show that Teflon can be deposited via straightforward spin-coating on ridge waveguides, leading to a top planarized surface. The resulting surface morphology allows the further fabrication of electrode structures.

II. DEVICE DESIGN

Our proposed device is based on recently developed ridge waveguide modulators, in which a high-confinement, complete-ridge interferometer is made by means of a wet etching process [5]. Teflon AF, used as buffer layer material provides a good confinement of light, as its refractive index at 1.55 μm wavelength is 1.3 whereas that of SiO_2 is 1.44. Its lower dielectric constant (ε=1.9) in comparison with SiO_2 (3.9) also makes it a better choice in order to achieve velocity matching. Moreover, it has been measured that the dielectric losses of Teflon AF at high frequency are lower than those of SiO_2, which is a great advantage for high bandwidth devices [6]. The proposed cross section is sketched in figure 1.

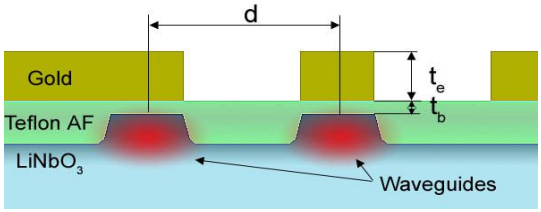


Figure 1. Cross section of proposed modulator.

In order to evaluate the performance of these modulators, their main parameters ($V_\pi L$, effective microwave index n_{eff}^{MW}, and characteristic impedance Z) were calculated.

Selected results are shown in figure 2. In figure 2(a) we can see how the $V_\pi L$ evolves as function of the ridge height (h) with the buffer layer thickness on top of the ridges (t_b) and the separation between waveguide centers (d) as parameters. As expected, the lower t_b is, the lower the driving voltage becomes. We also indentify the range of h beyond 3 μm as the one that provides a lower value of $V_\pi L$. Values even below 8 V·cm are found for t_b = 0.2 μm. In figure 2 (b), characteristic impedance and microwave effective index are shown for devices with t_b=0.2μm, with the distance between waveguides and the electrode thickness (t_e) as parameters. We can see that velocity matching condition (n_{eff}^{MW}=2.14) can be obtained with this buffer thickness for different configurations. For example, with d=24μm and t_e=8μm, a nearly velocity and impedance

matched design can be made with a ridge height between 4 and 7 μm. This devices yields a $V_\pi L$ of 8 V·cm.

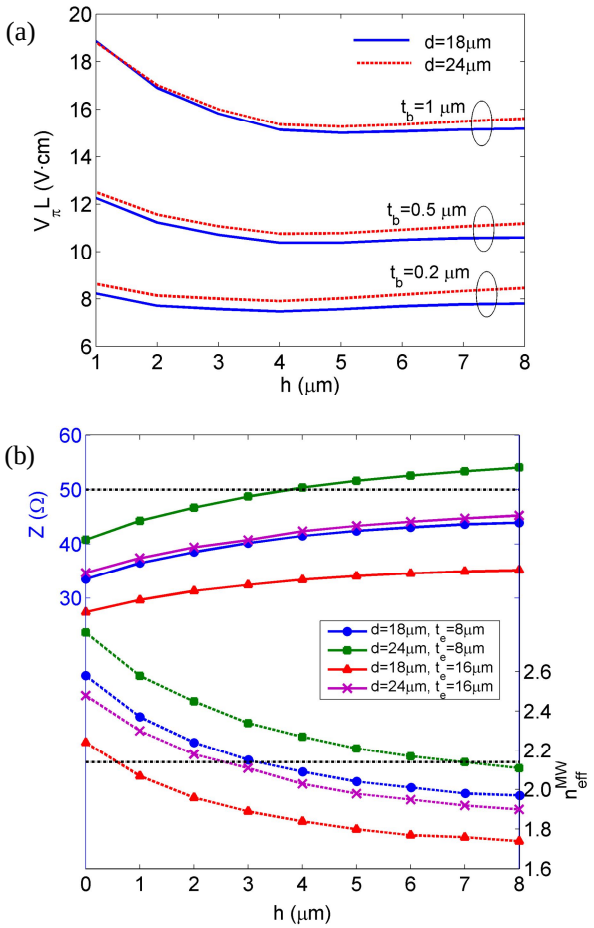


Figure 2. Calculated driving voltage-length product (a) and characteristic impedance and effective index of modulating microwave (b). In (b) all the results are for t_b=0.2 μm. The impedance matching (Z=50Ω) and velocity matching n_{eff}^{MW}=2.14 conditions are shown by horizontal dashed lines.

III. FABRICATION

The fabrication of the ridge interferometers is carried out by a wet etching technique based on an HF, HNO_3 and ethanol mixture, which provides smooth ridge walls. The guiding in the vertical direction is obtained by the proton exchange technique. After the ridges are fabricated, diluted Teflon AF is spun on the samples at 2500 rpm and then baked at 180ºC. Figure 3 shows a SEM image of an etched ridge coated by a Teflon AF layer with a thickness of 4 μm above the ridge top. In order to reduce the thickness and planarize the surface of the deposited layer, different processes are being developed, such as fine mechanical polishing as well as oxygen plasma etching. A thinned layer can be shown in the lower picture of figure 3.

In order to fabricate the electrodes on top of the planarized Teflon AF layer, a fluorocarbon surface treatment to improve adhesion is used (Tetra-etch). In this way, a reactive film is created on the Teflon surface making possible to deposit thin metal layers as well as photoresist. Finally, the electrodes are fabricated on top of the buffer via electroplating. In figure 4, an example of an electrode and impedance-matching transition is shown on top of a planar Teflon AF layer.

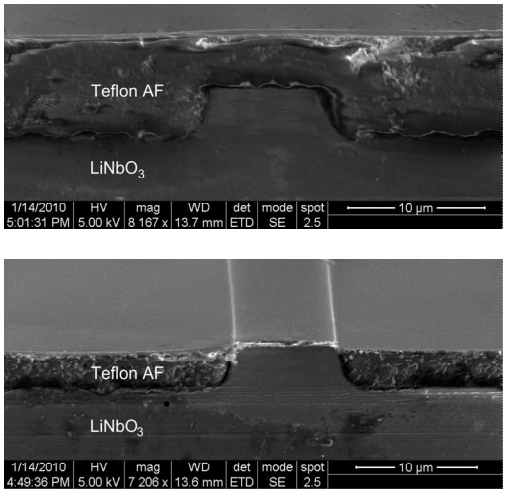


Figure 3. $LiNbO_3$ ridges covered by Teflon AF layers with a thickness above the ridge top of 4μm (upper) and 0.6μm (lower).

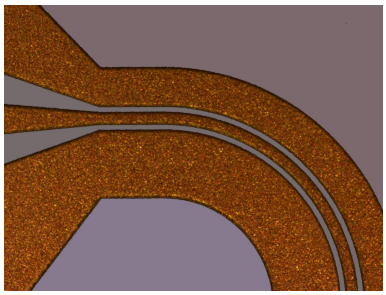


Figure 4. Electroplated electrode and tapered transition grown on top of a planar Teflon AF later.

Currently, the electro-optical characterization of the devices is being carried out and the results will be presented at the conference.

REFERENCES

[1] G. Poberaj, M. Koechlin, F. Sulser, A. Guarino, J. Hajfler, P.Günter, "Ion-sliced lithium niobate thin films for active photonic devices," Opt. Mater., vol. 31, no. 7, pp. 1054–1058, 2009

[2] F. Lucchi, D. Janner, M. Belmonte, S. Balsamo, M. Villa, S. Giurgola, P. Vergani, V. Pruneri, "Very low voltage single drive domain inverted $LiNbO_3$ integrated electro-optic modulator," Opt. Exp., vol. 15, no. 17, pp. 10739–10743, 2007.

[3] M. Roussey, M. P. Bernal, N. Courjal, D. V. Labeke, F. I. Baida, "Electro-optic effect exaltation on lithium niobate photonic crystals due to slow photons," Appl. Phys. Lett., vol. 89, pp. 241110-1–241110-3, 2006

[4] W. K. Burns, M. M. Howerton, R. P. Moeller, R. Krähenbühl, R. W. McElhanon, and A. S. Greenblatt, "Low drive voltage, broad-band LiNbO modulators with and without etched ridges," J. Lightw. Technol., vol. 17, no. 12, pp. 2551–2555, 1999.

[5] M. García-Granda, H. Hu, J. Rodríguez-García, W. Sohler, "Design and Fabrication of Novel Ridge Guide Modulators in Lithium Niobate,", J. Lightw. Technol., vol. 27, no.24, pp. 5690-5697, 2009.

[6] P.R. Resnick, W. H. Buck, Fluoropolymers 2-Properties,. Springer US, 2006, pp.25–33.

Dual-Parallel Y-Coupled Lithium Niobate Electro-Optic Modulator with 15.2 dB SFDR gain

Roberto Llorente, Maria Morant
Valencia Nanophotonics Technology Center
Universidad Politécnica de Valencia
Valencia, Spain
{rllorent, mmorant}@ntc.upv.es

Jerome Hauden, Henri Porte, Nicolas Grossard
Photline Technologies
Besancon, France
{jerome.hauden, henri.porte,
nicolas.grossard}@photline.com

***Abstract*—The concept of dual-parallel linearization of Y-coupled $LiNbO_3$ electro-optic modulation is presented in this paper. Characterization of a fabricated device exhibits 15.2 dB SFDR enhancement over a conventional Mach-Zehnder interferometer, finding application in photonic-ADC technology.**

Keywords- electro-optic devices, parallel linearization

I. INTRODUCTION

Analog applications as radio-over-fiber (RoF) optical transmission of wireless signals [1] or optical signal processing techniques like photonic-ADC sensing of ultra-low power radio [2] require electro-optic modulators (EOM) with excellent dynamic range. This is of special importance when the final application involves the photonic processing of several radio signals in coexistence, i.e. different wireless signals with different dynamic ranges are jointly processed. The most restrictive case, considering the wireless state of the art, is sensing and/or RoF transmission of ultra-wide band (UWB) radio [2], which exhibits powers spectral densities (PSD) lower than -41.3 dBm/MHz in the frequency band from 3.1 to 10.6 GHz, in presence of WiMAX. This paper proposes a linearized EOM based in a dual-parallel $LiNbO_3$ Y-junction to address the dynamic range limitation.

II. DUAL-PARALLEL Y-COUPLED WITH E-WALL LINEARIZATION CONCEPT

The linearized EOM concept herein proposed is a dual architecture comprising two parallel active $LiNbO_3$ Y-branch directional couplers with phase reversal travelling wave electrodes and ferroelectric domain inversion. This architecture derives from [3] and is enhanced integrating two couplers staked with $\pi/2$ electrical phase shift and e-wall isolation [4]. Fig. 1 depicts the device structure. The incoming light is optically split in two arms (E_1 and E_2) which are fed to two parallel Y-junctions. Each of the Y-branch directional couplers is comprised by an integrated Z-cut Lithium-Niobate crystal substrate. Adequate operation requires isolation by a metallic e-wall between the junctions.

Both upper and lower Y-junctions shown in Fig. 1 are formed by two parallel waveguide in $\Delta\beta$ reversal configuration [5]. The gap between the waveguides is calculated allowing optical coupling via evanescent field. One waveguide in each Y-junction has a positive ferroelectric orientation while the other has a negative one, i.e. each arm include a central RF electrode (L_1) which applies electric field into the waveguide generating a positive phase variation in one arm and negative in the other. This is actually a push-pull configuration as in the second section (L_2) the ferroelectric domain inversion is applied to the opposite waveguide, resulting in an inverted situation when the light propagates though the waveguides.

Successful linearization of the electro-optic response of the overall architecture depends on two factors: First, the L_1 and L_2 parameters, which stand for the length of the first and second section electrodes respectively. And second, the V_U and V_L voltages applied to the upper and lower Y-junctions respectively. Both voltages must be precisely set to produce a phase shift of $\pi/2$ in order to achieve adequate linearization.

After simulation studies, the target parameters selected for fabrication are: L_1=27.88 mm, L_2=12.12 mm, Lc=12.12 mm, and gap of 15.35 µm (total length 40 mm). The Y-junctions fabricated were named UCELLS5 and UCELLS21. The main characteristics measured after fabrication are shown in Table I.

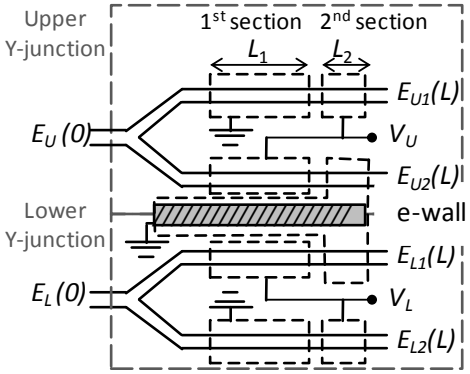


Figure 1. Proposed dual-parallel Y-coupled device structure with e-wall

TABLE I. FABRICATED Y-JUNCTION SPECIFICATIONS

	UCELLS5	*UCELLS21*
Optical losses @ 1542 nm [a]	4.1 dB	4.2 dB
Exctinction Ratio on DC @ 1542 nm	35 dB	24 dB
Vπ on DC port @ 1550 nm	5.5 V	7 V

a. Including splicing and optical connectors

This work was supported in part by the European 7th Framework Program project UCELLS FP7-ICT-216785. Maria Morant's work is supported by Spain FPU MEC grant AP2007-01413. The Network of Excellence BONE FP7 ICT-216863 is also acknowledged.

III. Experimental Characterization

Fig. 2 shows the experimental set-up to evaluate the performance of the proposed dual-parallel Y-junction structure. The characterization of the proposed dual-parallel Y-junction structure is compared with single and dual-parallel architectures with conventional Mach-Zehnder modulators measuring the spurious free dynamic range (SFDR) as:

$$SFDR = P_{1\text{st harmonic}} / \max(P_{\text{distortions}}, P_{\text{noise}}) \quad (1)$$

The setup includes the dual-parallel Y-junction architecture fed by a 3.1 GHz (10 dBm) RF tone. This frequency is the first frequency of the UWB band. Applied V_U corresponds directly to the RF tone, and V_L includes a $\pi/2$ phase shift. The RF tone is modulated on a continuous wave (CW) light (1550 nm, 11 dBm) splitted in two branches (7 dBm, E_U and E_L) polarization controlled. Both Y-junctions are biased at quadrature (0.9 V UCELLS5, 2.88 V UCELLS21). The resulting optical signals are combined and photodetected (PIN, 0.7 A/W). Electrical amplification (21 dB gain, 5.8 dB noise figure) is used at the RF ports and after photodetection. Fig. 3 shows the electrical spectrum measured with the dual-parallel linearized architecture proposed. The SFDR is labeled in the figures. Fig. 4 shows the laboratory setups for single and parallel architectures with conventional Mach-Zehnder modulators (Photline MX-LN-10-PD).

It can be observed that in the case of conventional optical links, the 3rd harmonic leads to the highest degradation, as can be observed in the case a single Mach-Zehnder modulator (Fig. 5(a), SFDR of 19 dB). In the case of the parallel architectures, the higher distortion component falling inside the UWB band is the 2nd order harmonic (SFDR of 34.2 dB for the proposed dual-parallel Y-junction, SFDR 24 dB for a parallel Mach-Zehnder). The proposed dual-parallel Y-coupled structure gives 15.2 dB gain in SFDR compared with a single Mach-Zehnder, and 10.2 dB improvement compared with the parallel Mach-Zehnder arrangement.

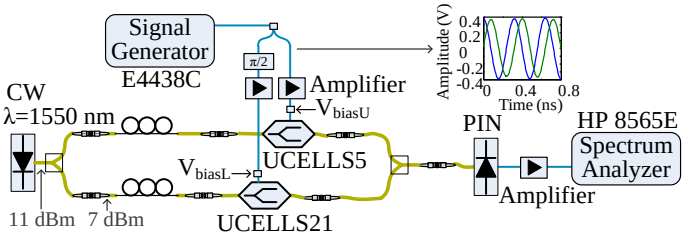


Figure 2. Experimental setup for dual-parallel Y-coupled linearized characterization

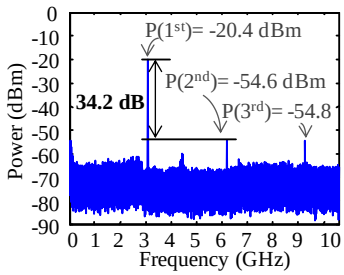


Figure 3. Measured electrical spectrum for dual-parallel Y-coupled linearized proposed architecture

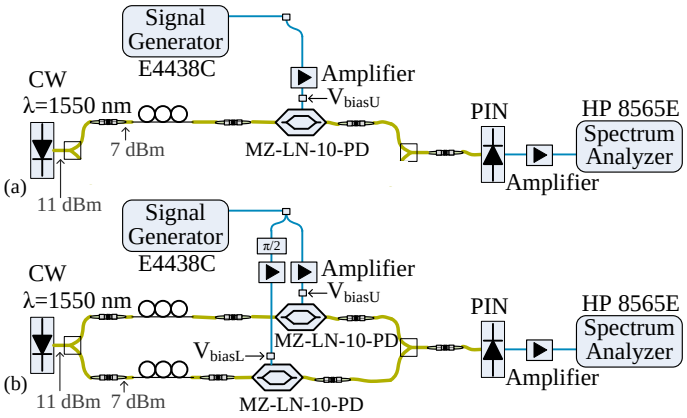


Figure 4. Experimental setup (a) single and (b) dual-parallel architecture with conventional Mach-Zehnder modulators

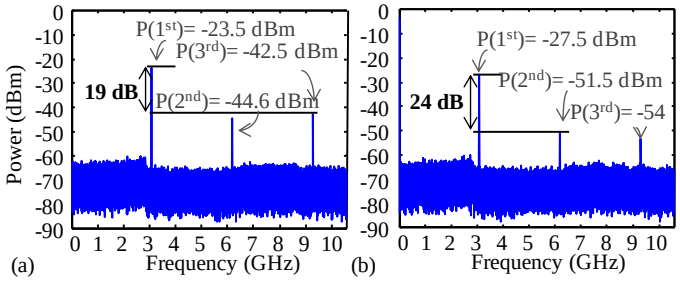


Figure 5. Measured electrical spectrum for (a) single and (b) dual-parallel architecture with conventional Mach-Zehnder modulators

IV. Conclusion

The concept dual-parallel $LiNbO_3$ Y-Coupled linearized electro-optic modulation has been proposed. Two linearized Y-junctions have been fabricated, being the performance especially sensible to the fabrication process. Fabricated devices have been characterized exhibiting 15.2 dB SFDR gain over a conventional $LiNbO_3$ Mach-Zehnder modulator and 10.2 dB SFDR gain over a parallel Mach-Zehnder architecture. This linearization concept finds application in highly-linear applications like radio-over-fiber transmission of wireless signals in coexistence and photonic-ADC sensing.

References

[1] R. Llorente, T. Alves, M. Morant, M. Beltran, J. Perez, A. Cartaxo, J. Marti, "Optical distribution of OFDM and impulse-radio UWB in FTTH networks", OFC 2008, JWA100, San Diego, CA, Feb. 2008.

[2] R. Llorente, M. Morant, J. Puche, J. Romme and T. Alves, "Sensing ultra-low-power radio signals by photonic analog-to-digital conversion", ECOC2009, Vienna, Austria, 20-24 Sept. 2009.

[3] R. F. Tavlykaev, R.V Ramaswamy, "Highly linear Y-fed directional coupler modulator with low intermodulation distorsion". Journal of Lightwave Techn., Vol. 17, No. 2, Feb 1999, pp.282-291.

[4] K. Higum, S. Oikawa, Y. Hashimoto, H. Nagata and M. Izutsu, "X-cut lithium niobate optical single sideband modulator", Electronics Letters, Vol. 37, No. 8, April 2001, pp. 515-516.

[5] H. Kogelnik and R. V. Schmidt, "Switched directional couplers with alternating," IEEE J. Quantum Electron., vol. 12, pp. 396–401, 1976.

Electro-Optic Polarization Controller With Ti:PPLN Channel Waveguides

Nasrin Moeini, Harald Herrmann, Raimund Ricken, Viktor Quiring and Wolfgang Sohler
Angewandte Physik, Department Physik
Universität Paderborn
Paderborn, Germany
nmoeini@mail.uni-paderborn.de

Abstract—**An electro-optic polarization controller consisting of a PPLN based polarization converter followed by a phase-shifter is reported. The integrated device is fabricated in Z-cut $LiNbO_3$ with X-propagation. Design and characterization of the single components are discussed and polarization transformation is demonstrated.**

Keywords: integrated optics, polarization conversion, PPLN

I. INTRODUCTION

Controlling the state of polarization (SOP) is a key task in various applications. Especially in communications systems polarization control is essential for polarization multiplexing or to mitigate polarization mode dispersion (PMD). In recent years several different schemes for polarization control have been investigated. Among them integrated optical approaches offer the potential to enable fast electro-optic polarization control with low drive voltages.

In $LiNbO_3$ polarization controllers have been realized using X-cut material with Z-[1] or with Y-propagation [2]. These devices consist of a structure composed of electro-optic mode converter and phase-shifter. Endless, reset-free polarization control has been demonstrated. Although a good performance has been obtained, the devices have also some drawbacks. The Y-propagating structure requires interleaved transducer electrodes on top of the waveguide which might induce additional propagation losses. Devices with Z-propagation can hardly be integrated with other devices as most functions cannot be obtained in this orientation. Therefore, we have realized a polarization controller in Z-cut $LiNbO_3$ capable to be integrated with other electro-optic or nonlinear optical components. Benefiting from a periodically poled substrate, the electrode configuration is much simpler than that of previously demonstrated devices in X-cut $LiNbO_3$.

In this contribution we report the first realization of a polarization controller composed of a polarization converter in periodically poled $LiNbO_3$ (PPLN) - which has recently been demonstrated in [3] - and a phase-shifter.

II. PRINCIPLE OF OPERATION

The integrated optical polarization controller as shown in Fig. 1 consists of an electrooptic polarization converter followed by a phase-shifter in Z-cut, X-propagating $LiNbO_3$. The converter itself consists of a Ti-diffused waveguide in a periodically poled region [3]. An electrical field is generated in the waveguide via a control voltage applied to lumped type electrodes deposited on top of the sample on both sides of the waveguide. A polarization conversion, i.e. TE→TM or vice versa, can be induced via the r_{51} coefficient of the electro-optic tensor by the Y-component of the electric field. The poling period Λ must be chosen to provide phase-matching for the desired wavelength λ according to $\Lambda=\lambda/(n_{TM}-n_{TE})$, where n_{TM} and n_{TE} are the effective indices of the TM and TE mode, respectively. The conversion efficiency as function of the applied voltage varies according a $\sin^2$-characteristics. In terms of polarization transformation the conversion can be interpreted as a rotation around the S_2 axis on the Poincare-sphere [4].

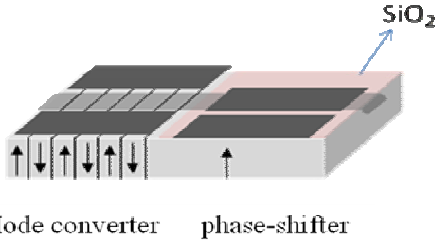


Fig. 1. Schematic drawing of the polarization controller.

In the phase shifter a voltage can be applied to vary the birefringence in the waveguide, and, hence, the relative phase between the TE- and TM-waves at the output of the guide. This corresponds to a rotation of the SOP around the S_1 axis on the Poincare sphere.

The cascading of the converter and phase-shifter enables the transformation from almost any input SOP to any desired output SOP via two control voltages. Only for certain input SOPs (for instance circular polarization) the polarization transformation is limited. To overcome this drawback and to provide full flexibility in the polarization transformation another phase-shifter in front of the converter can be implemented.

III. DEVICE FABRICATION

Optical waveguides were fabricated in Z-cut $LiNbO_3$ by an indiffusion of 7 µm wide and 96 nm thick titanium stripes. Diffusion was carried out for 8.5 h at 1060 °C. This fabrication process leads to single mode waveguides in both polarizations in the 1550 nm range. Waveguide losses are typically about 0.1 dB/cm.

Subsequently, a 15 mm long region out of the 35 mm long sample was periodically poled with a poling period of 22 µm. The unpoled phase-shifter region was covered with a 400 nm thick SiO_2 layer. Electrodes for the converter and the phase-shifter were fabricated by depositing 15 mm long titanium films with a gap of 15 µm directly on the $LiNbO_3$ surface and on the SiO_2 film, respectively.

Finally, the polished end-faces of the waveguides were AR coated and the sample was mounted on a copper holder which can be temperature stabilized to about 0.1 °C.

IV. Experimental Results and Discussion

At first polarization converter and phase-shifter were studied separately. A tunable external cavity laser (ECL) was used to investigate the spectral characteristics of the polarization converter. TE-polarized light was launched into the waveguide and the TE- and TM-polarized powers at the output were recorded. In Fig. 2 such spectral characteristics are shown. A converter voltage of U_c=10 V lead to a complete conversion at the phase-match wavelength λ=1587.2 nm with a spectral width of 2 nm. The measured curve coincides well with the theoretically predicted one, which is also given in the diagram. At the phase-matchwavelength the converted power was measured as function of the applied voltage (Fig. 2, bottom). The predicted $\sin^2$-behaviour could be observed. A small offset on the horizontal axis, i.e. a conversion at U_c=0 V, was observed. This offset can be attributed to local electric fields already present in the crystal without any applied voltage.

The phase-shifter was characterized using a linear input polarization at 45°. The voltage required to obtain a relative phase-shift of π was determined from the observed beating at the output to be $U_{p,\pi}$=15 V.

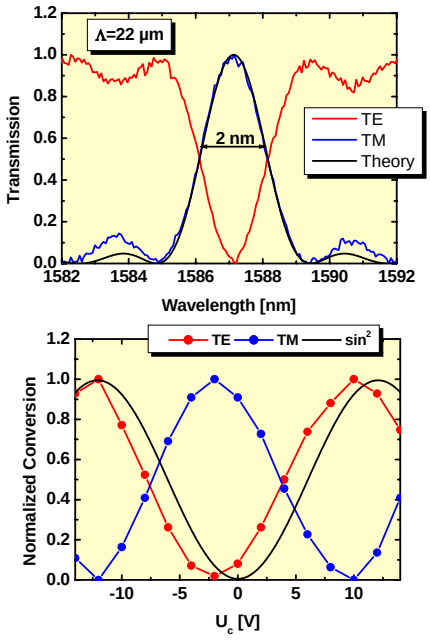


Fig. 2: Top: Measured and calculated spectral characteristics of the electro-optic polarization converter. Bottom: Conversion efficiency at phase-matching as function of the applied voltage.

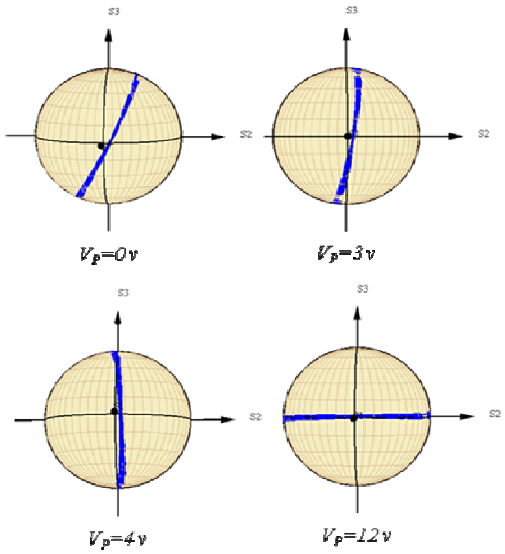


Fig. 3: Measured polarization transformation of the device

To demonstrate the applicability of the combined converter and phase-shifter as polarization controller a TE polarized wave was coupled into the waveguide. A static voltage was applied to the phase-shifter and a ramp voltage (- 15 V … 15V) to the converter electrodes. The output SOP was monitored using a commercial polarimeter.

In Fig. 3 traces on the Poincare sphere are shown for several phase-shifter voltages. Closed circles on the Poincare-sphere were observed. Their orientation depends on the phase-shifter voltage. By a proper choice of the converter voltage U_c and the phase-shifter voltage U_p any desired SOP can be obtained at the output.

V. Conclusions

We have demonstrated a new electro-optic waveguide device, which can be used as a polarization controller consisting of a TE↔TM mode converter followed by a phase shifter. Such devices will find applications where fast electro-optic polarization control is required as for instance polarization multiplexing and PMD compensation in communication systems or polarization state preparation in quantum communications.

References

[1] F. Heismann, M.S. Whalen, "Broadband reset-free automatic polarization controller", *Electron. Lett.*, vol. 27, pp. 377-379 (1991)

[2] F. Heismann, M.D. Divino, L.L. Buhl, "Integrated-optic polarization controller with unlimited transformation range", *Appl. Phys. Lett.* , vol. 57, pp. 855-857 (1990)

[3] C. Y. Huang, C. H. Lin, and Y. H. Shen, "Electro-optic Ti:PPLN waveguide as efficient optical wavelength filter and polarization mode converter," *Opt. Express* , vol. 15, No. 5, March 2007, pp. 2548-2554.

[4] F. Heismann, R. C.Alferness, "Wavelength-Tunable electrooptic Polarization conversion in Birefringent Waveguides," *IEEE J. Quantum Electronics,* vol. QE-24, NO. 1,1988, pp. 83-93

Locally Poled Ridge Waveguide on X-cut $LiNbO_3$ for Nonlinear Wavelength Conversion

Li Gui, Hui Hu, Rahman Nouroozi and Wolfgang Sohler
Angewandte Physik, Department Physik
Universität Paderborn
Paderborn, Germany
lgui@mail.upb.de

Abstract—**Fabrication of a periodically poled Ti in-diffused ridge waveguide on X-cut $LiNbO_3$ using local poling and doping techniques is reported. Stable second harmonic generation of 50 mW at λ=775 nm was achieved at room temperature. Wavelength conversion in the C-band of optical communication was also demonstrated using cascaded nonlinear interaction.**

Keywords-ridge waveguide; periodic poling; second harmonic generation; wavelength conversion

I. INTRODUCTION

To enhance the efficiency of nonlinear interactions in optical waveguides, smaller cross section and higher index contrast are required leading to a strong enhancement of the guided mode intensity. Therefore, $LiNbO_3$ (LN) ridge waveguides are of increasing interest. Nishida et al. reported highly efficient wavelength conversion using a Z-cut direct-bonded PPLN ridge waveguide [1, 2]. Iwai et al. reported high power blue generation from an X-cut adhered MgO:LN ridge waveguide by frequency doubling [3]; Sugita et al. also demonstrated efficient second harmonic generation (SHG) in a Y-cut direct-bonded MgO:LN ridge waveguide [4]. The fabrication of the PPLN ridge waveguide in all existing work is based on adhering or direct-bonding a periodically poled bulk substrate to another substrate followed by lapping, polishing and either sawing or dry etching in order to shape the ridge. We have recently reported novel local poling and doping techniques to fabricate a periodically poled Ti in-diffused ridge waveguide on X-cut LN [5]. In this work, we improved the fabrication techniques and thus enhanced the efficiency of second harmonic generation (SHG) by a factor of two. Moreover, for the first time we demonstrated wavelength conversion using a cascaded scheme of SHG and difference frequency generation (DFG).

II. WAVEGUIDE FABRICATION AND LOCAL POLING

A. *Fabrication of Ridge Waveguide*

The ridge was fabricated using ICP etching in a mixture of C_4F_8 and He. The etching process was repeated several times until the ridge height was 3.5 µm. A Ti layer of 80 nm was then deposited only on the top of the ridge as the doping source. Ti in-diffusion was done at 1060 °C for 8.5 hours. A fabricated ridge waveguide is shown in Fig. 1(a). The propagation loss of such a ridge waveguide at λ=1550 nm is around 1 dB/cm for TE and 0.8 dB/cm for TM polarization.

B. *Local Periodic Poling*

Local periodic poling was performed as depicted in Fig. 1(b). Comb-like electrodes were deposited on the sides of the ridge using a lift-off technique. Since the ridge is typically 7 - 9 µm wide, a low voltage of a few hundred volts was sufficient to overcome the coercive field of ~ 21 KV/mm. Generally, a voltage pulse of 400 Volts and 30 ms duration was used. By cutting through the ridge (Fig. 1(c)) and using selective chemical etching in $HF:HNO_3$ solution, the inverted domains are revealed as shown in Fig. 1(d). However, the quality of the poling, especially the domain shape and the duty cycle, could be further improved.

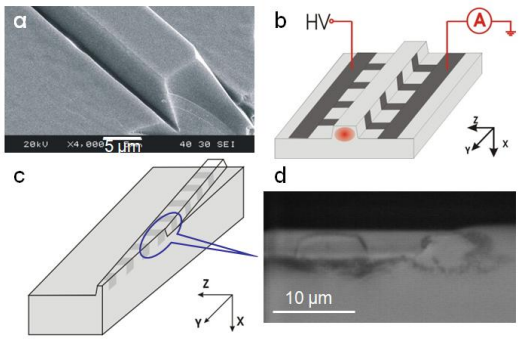


Figure 1. (a) SEM micrograph of a Ti in-diffused ridge waveguide; (b) Scheme of local periodic poling; (c) Sketch of cutting a ridge; (d) selectively chemical etched periodic domains in the ridge waveguide.

III. WAVELENGTH CONVERSION

Nonlinear interactions were investigated using a 13 mm long locally poled ridge guide on X-cut LN at room temperature. The height and width of the ridge guide are 3.5 µm and 7 µm respectively. The domain period is 16.6 µm throughout the waveguide. The end faces of the waveguide have been carefully polished and an anti-reflection coating at λ=1550 nm was deposited.

A. *Second Harmonic Generation*

The fundamental wave was provided by a tunable extended cavity semiconductor laser (ECL) with the wavelength λ_f tuned in steps of 1pm around 1548 nm. The light was coupled into the waveguide by fiber butt coupling. Fig. 2 presents the SHG tuning characteristic as generated SH power versus λ_f. The

measured bandwidth of 0.8 nm agrees with the calculated result. This indicates the excellent homogeneity of the periodically poled ridge guide along the interaction length.

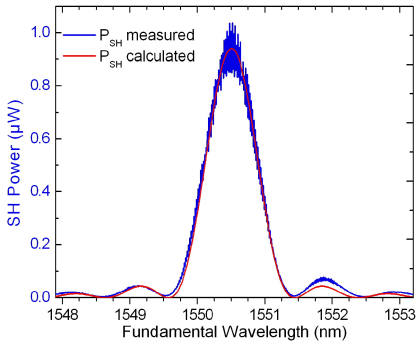


Figure 2. Generated SH power as function of the fundamental wavelength.

SHG was also investigated as function of the fundamental power as shown in Fig. 3. A parabolic dependence between the SH power and the fundamental power was observed, well described by a power normalized efficiency of 28 % W^{-1} (or 16.5 % W^{-1} cm^{-2}). It is calculated as the ratio of out-coupled SH power and the square of in-coupled fundamental power. The normalized efficiency was improved by a factor of two compared to [5] mainly due to the reduced cross sectional area of the ridge guide. It is important to note that the ridge guide shows a higher resistance to the photorefractive damage at room temperature compared to a conventional Ti:PPLN channel waveguide. A stable SH power up to 50 mW was measured at the fundamental power of 700 mW as a function of time as shown in the inset of Fig. 3. A similar phenomenon was reported in [1] but on a Z-cut direct-bonded LN ridge guide.

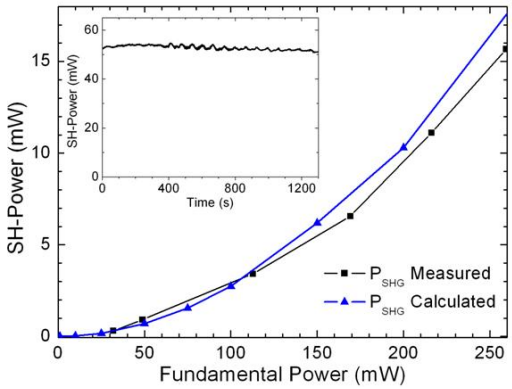


Figure 3. Generated SH power as function of coupled fundamental power. Inset: Measured SH power as function of time.

B. Cascaded SHG/DFG

Wavelength conversion based on a cascaded scheme as shown in Inset 1 of Fig. 4, was demonstrated using the ridge guide. The fundamental wave from the ECL at λ_f =1548.5 nm and the signal wave at λ=1555.5 nm from a DFB laser diode were both coupled into the ridge guide. The generated SH wave at λ=774.25 nm served as the pump of the successive DFG. In this first experiment, we observed a conversion efficiency from the signal to the idler of -29 dB when the coupled fundamental power was around 200 mW. The idler power is relatively stable as shown in Inset 2 of Fig. 4.

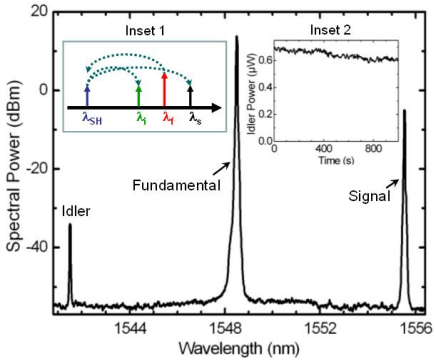


Figure 4. Wavelength conversion by cascaded SHG/DFG at a coupled pump power of ~200 mW (Resolution: 0.1 nm). Inset 1: Scheme of the wavelength conversion. Inset 2: Measured idler power as function of time.

IV. CONCLUSION

We demonstrated SHG and cascaded SHG/DFG using a locally poled Ti in-diffused ridge waveguide on X-cut LN. Such a ridge guide shows a high resistance to the photorefractive damage at room temperature. There is a large potential to improve the conversion efficiency by using a longer waveguide with smaller cross section and further optimizing the domain shape and the duty cycle.

ACKNOWLEDGMENT

This work was funded by the Deutsche Forschungsgemeinschaft (DFG) within the framework of the project “Materials World Network: Nanoscale Structure and Shaping of ferroelectric Domains”.

REFERENCES

[1] Y. Nishida, H. Miyazawa, M. Asobe, O. Tadanaga and H. Suzuki, “Direct-bonded QPM-LN ridge waveguide with high damage resistance at room temperature,” Electronics Letters, vol. 39, pp. 609–611, April 2003.

[2] Y. Nishida, H. Miyazawa, M. Asobe, O. Tadanaga and H. Suzuki, “0-dB wavelength conversion using direct-bonded QPM-Zn:$LiNbO_3$ ridge waveguide,” IEEE Photonics Technology Letters, vol. 17, pp. 1049-1051, May 2005.

[3] M. Iwai, T. Yoshino, S. Yamaguchi, M. Imaeda, N. Pavel, I. Shoji and T. Taira, “High-power blue generation from a periodically poled MgO:$LiNbO_3$ ridge-type waveguide by frequency doubling of a diode end-pumped Nd:$Y_3Al_5O_{12}$,” Applied Physics Letters, vol. 83, pp. 3659-3661, November 2003.

[4] T. Sugita, K. Mizuuchi, K. Yamamoto, K. Fukuda, T. Kai, I. Nakayama and K. Takahashi, “Highly efficient second-harmonic generation in direct-bonded MgO:$LiNbO_3$ pure crystal waveguide,” Electronics Letters, vol. 40, pp.1359-1360, October 2004.

[5] L. Gui, H. Hu, M. Garcia-Granda and W. Sohler, “Local periodic poling of ridges and ridge waveguides on X- and Y-Cut $LiNbO_3$ and its application for second harmonic generation,” Optics Express, vol.17, pp.3923-3928, February 2009.

Electrode-free high voltage cutoff waveguide sensor in domain inverted $LiNbO_3$

D. Janner, D. Tulli, M. Garcia-Granda
ICFO-Institut de Ciencies Fotoniques,
Mediterranean Technology Park
08860 Castelldefels (Barcelona), Spain
davide.janner@icfo.es

R. Ricken
Applied Physics Department,
University of Paderborn
33098 Paderborn, Germany

V. Pruneri
ICFO-Institut de Ciencies Fotoniques,
Mediterranean Technology Park
08860 Castelldefels (Barcelona), Spain
ICREA - Barcelona, Spain

***Abstract*—We present the design and fabrication of a novel electric field optical sensor in $LiNbO_3$. The design is based on a waveguide near cutoff, centered on a few microns wide domain inverted region. Electric fields as high as 20 MV/m can be measured thanks to the electrode-free surface geometry.**

Electric field sensor, Electrode-less sensing, lithium niobate

I. INTRODUCTION

In the last few years, the need for intense electromagnetic field sensing technology has widely increased playing a critical role in various scientific and technical areas, especially in the power industry and in the electromagnetic compatibility (EMC) measurements. Conventional electric field meters normally use conductive parts, which can interfere with the field to be measured, and are very sensitive to electromagnetic noise. Moreover, frequency bandwidth limitation and 50-Ω characteristic impedance in the case of RF waveguide sensors limits the scope of applicability of such technology. Electro-optic (EO) devices present several advantages compared to their electronic counterparts such as noise immunity, the feasibility of electrode-free operation, and consequently the possibility of operating even in harsh or dangerous environments.

So far, several configurations of EO sensors have been proposed, mostly based on waveguide interferometers [1] or bulk polarization/phase rotation in a piezoelectric crystal [2]. This second approach is based on polarization or phase measurements which require interrogation systems that are rather expensive to implement and may present long-term stability issues. On the contrary, waveguide based sensors directly translate the electric field value into an optical power variation, thus simplifying the interrogation system and potentially lowering the costs. In this context, Mach-Zehnder interferometers are employed for their sensitivity. However, they require additional metal electrodes and controlled biasing to work properly. To overcome some limitations, schemes without any conductive parts based on ferroelectric poling of the two interferometer arms have been proposed [3]. Alternative designs are based on Bragg grating in $LiNbO_3$ [4] or cutoff modulators with dummy electrode structure [5]. Field intensities measurable with the aforementioned approaches are typically below the fields present in some installations, like electric plants or railways electric network where very bulky sensors need to be employed [6].

In this work, we propose an electrode-free lithium niobate electric field sensor that can measure fields up to 20 MV/m. The novel design leverage on a combination of an optical waveguide near or below cutoff and domain inversion.

II. DEVICE DESIGN

The scheme of the proposed device is sketched in fig. 1. A proton exchange (PE) y-propagating waveguide in z-cut $LiNbO_3$ is designed to be near cutoff at the working wavelength (λ=1550 nm) and centered in a domain inverted region. The waveguide has a width of 6 μm and a depth of 4 μm, where the vertical profile was assumed to be half-gaussian with an index step of 0.01. On application of an external electric field parallel to the z axis of the device, the refractive index in the central inverted domain will decrease while the in the external domains will increase. Thus, the index difference change $\Delta n_{\pm}$ between positive and negative domains is given by:

$$\Delta n_{\pm} = 2 \cdot \frac{n_e^3}{2} r_{33} E \,, \qquad (1)$$

where E is the intensity of the externally applied electric field, n_e=2.14 and r_{33}=30.8 pm/V are respectively the refractive indices and the electro-optic coefficient along the z-axis. Limiting the external field below the coercive field of $LiNbO_3$ along z-axis (E_c= 21.4 MV/m), from eq. (1) we estimate that we are able to induce index changes of $\Delta n_{\pm}$ =6.5·10^{-3} for electric fields of 20 MV/m.

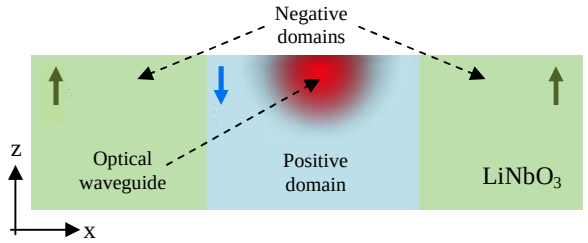


Figure 1. Scheme of cutoff electric field sensor. Optical waveguide is centered in the domain inverted region.

In order to find the optimal configuration, we studied with a BPM simulation software the behavior of the sensor under variation of the width of the central poled region (W_p=6, 10, 15, 20 μm). In fig. 2 we report the optical power in the waveguide mode after a fixed propagation length L=10 mm against the external electric field applied. From these results we

see that the best sensitivity is obtained for a poling region width W_p=10 µm.

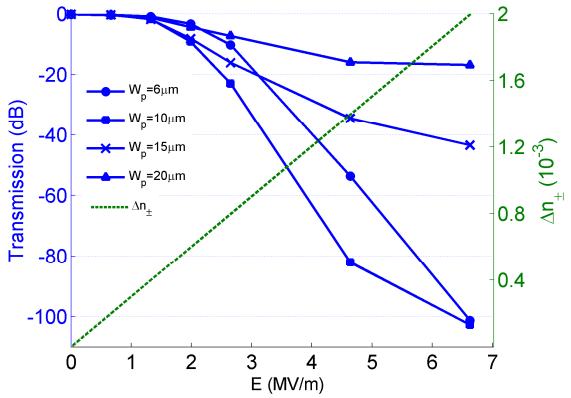


Figure 2. Transmitted power vs. external electric field after 10 mm propagation for different poling region widths.

In fig. 3 we plot the evolution of the optical power in the waveguide along the propagation. Those simulations suggest that sensors may be optimized for a specific electric filed range by reducing the overall length to target for very intense field while increasing it for weaker fields. To further improve the sensitivity and allow the sensor to work in reflection a multi-layer dielectric mirror could be deposited on one face.

AC operation of the device can be achieved by using a waveguide below cutoff for which the positive or negative electric field would increase or decrease respectively the transmitted power. In this case the poling length and pattern could be optimized to improve the linearity and dynamic range of the response.

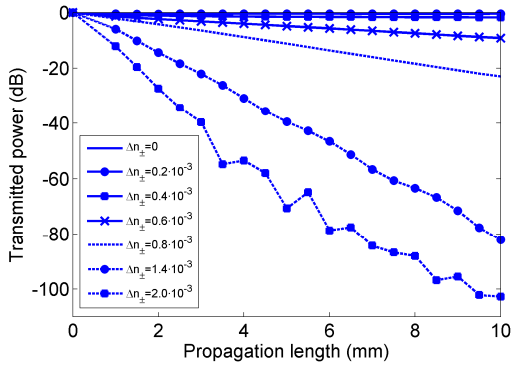


Figure 3. Evolution of the optical field along propagation direction for different values of index change induced by external electric field.

III. FABRICATION

The device was fabricated starting from the domain inversion by electric field poling. To this aim a 3.3 µm-thick layer of resist AZ4533 was spun on the z- face and was used as an insulator layer after patterning and baking at 140ºC for 1 hour. The inverted domains were then revealed via differential etching in hydrofluoric acid for alignment purposes. The final difference between z+ and z- domains was around 90 nm. Fig. 4 shows the poled domains and illustrates the position of the waveguides in their center. According to our simulations, the etching step is not affecting the optical mode even in the presence of the external electric field. Waveguide mask was aligned with the center of the inverted regions and a 200-nm-thick aluminum mask layer was deposited by lift-off technique. Waveguides were fabricated by 30 minutes PE in molten benzoic acid with a subsequent annealing step of 11 hours at 360ºC. The aluminum mask was then removed and the sample was diced and the faces were end polished.

Preliminary measurements confirm the simulation results and the possibility to measure electric fields as high as 20 MV/m. More details on the characterization and results will be presented at the Conference.

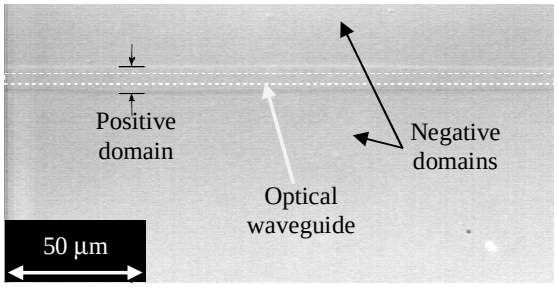


Figure 4. Domain inverted regions revealed by HF differential etching and position of the optical waveguides.

REFERENCES

[1] T.H. Lee, et al.,''Electromagnetic field sensor using mach-zehnder waveguide modulator'' Microwave and optical technology letters, vol. 48, no .9, September 2006.

[2] G. Gaborit, L. Duvilaret, "Electro-optic sensors: towards vectorial electric field characterization", ECIO '05, Grenoble, 2005

[3] D.H. Naghski, et al. ''An Integrated Photonic Mach-Zehnder Interferometer with No Electrodes for Sensing Electric Field", J. Lightwave Technol., vol. 12, no. 6, June 1994.

[4] D. Runde, et al., " Integrated optical electric field sensor based on a Bragg grating in lithium niobate", App. Phys. B, vol. 86, 91-95, 2007.

[5] S.S. Lee, M.C. Oh, S.Y. Shin, and K.H. Keh,"Integrated Optical High-Voltage Sensor Using a Z-Cut $LiNbO_3$ Cutoff Modulator", Photonics Technology Letters, vol.5, no.9, September 1993.

[6] P. P. Chavez, et al. "230 kV Optical Voltage Transducer Using a Distributed Optical Electric Field Sensor System ",Transmission and Distribution Conference and Exposition, 2001 IEEE/PES,Atlanta (2001)

Plan Nacional TEC2007-60185 and Juan de la Cierva programs

Analysis of Rotationally Symmetric Resonators

Ana Vukovic[1], Phillip Sewell[1], Trevor M. Benson[1]

[1] *George Green Institute for Electromagnetics Research, Nottingham University, UK*
ana.vukovic@nottingham.ac.uk

Introduction

Dielectric resonators are important components in modern photonic circuits as they exhibit high Q-factor, high sensitivity and directional emission and can be used in many communication and sensor applications. Three-dimensional analysis of these structures has been undertaken mainly with numerical methods such as Finite Difference Time Domain (FDTD) whilst analytical methods have been applied to simplified two-dimensional models [1]. In this paper we report a combination of Body of Revolution Method (BOR) [2] with the method of analytical Regularization (MAR) [3] for modeling of rotationally symmetric bodies. In the BOR method the azimuthal symmetry of the structure is integrated within the free space Greens's function to give a Modal Green's Function (MGF). This enables reduction of the 3D body to the equivalent 2D one without any loss of accuracy. The MGF function is highly oscillatory and an equivalent series representation of the MGF integral has been reported in [4]. The BOR equations are reduced to the integral equations of the Fredholm type by extracting the frequency dependent part corresponding to a suitable canonical shape [3], in this case perfect sphere.

Results

The BOR-MAR method is initially applied to the analysis of the resonant frequencies of metal spheroidal resonators. In particular modes with high azimuthal order are analysed. The spheroidal resonator with the major axis a=1μm and the minor axis b=0.9μm is considered. Fig.1 compares the resonant frequencies of the spheroidal resonator with those of the perfect sphere for the azimuthal order m=5. It can be seen that the resonance shift of the spheroid modes is not trivial and the additional resonances present can be attributed to TE-TM coupling.

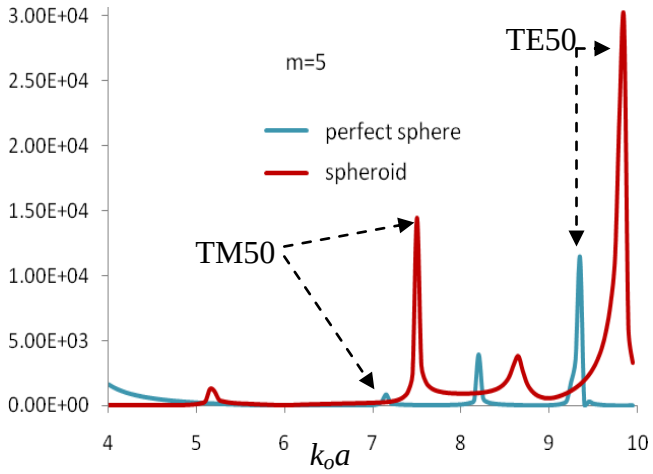


Fig.1.Comparison of resonant frequencies of the perfect sphere and spheroid for m=5

References

[1] Boriskina S., Sewell, P., Benson T.M., J. Opt. Soc. Am A, vol.21, no.3, pp.393-402, (2004).
[2] Glisson W., Willton D.R.,, IEEE Trans. Antennas Propagat., vol.28, pp.593-603., (1980).
[3] Nosich A., *IEEE Antennas and Propagation Magazine*, vol. 41, pp.34-49, (1999).
[4] Abdelmageed K., Progress in Electromagnetics Research, PIERS 27, pp.337-357, (2000).

3D light confinement in air : the photon cage

C. Sieutat[1], X. Letartre[1], P. Viktorovitch[1], J.L. Leclercq[1], A. Danescu[1], G. Grenet[1], H. Magoariec[2]

[1] *Université de Lyon, Institut des Nanotechnologies de Lyon (INL), UMR CNRS 5270*

Ecole Centrale de Lyon, 36 avenue Guy de Collongue, F 69134 Ecully Cedex, France

xavier.letartre@ec-lyon.fr

[2] *Université de Lyon, Laboratoire de Tribologie et Dynamique des Systèmes (LTDS), UMR CNRS 5513*

Ecole Centrale de Lyon, 36 avenue Guy de Collongue, F 69134 Ecully Cedex, France

It is emphasing that Micro-Nano-Photonics can be defined as the control of photons within the tiniest possible space during the longest possible time. Optical microresonators are considered as the basic conceptual and technological bricks for that purpose. They are meant to provide strong spectral and spatial confinement of photons, which is essential for the efficient operation of a wide range of active micro-nano-photonic devices, including low threshold micro-lasers, non-linear optical devices and biochemical sensors. The general approach to achieve strong confinement of photons consists in high index contrast structuring of space at the wavelength scale. The progress in micro-nano-photonic integration technology has resulted in a large variety of photonic devices, fabricated along planar technological schemes, but mainly restricted to 2D operation. This way, multiple demonstrations have been made based on microdisk-, micropillar- and photonic crystals microcavities.

Significant progress for quasi 3D control of photons has been achieved in our group along a 2.5D nanophotonics approach which can be considered as an extension of planar 2D photonic crystal-based technology exploiting the vertical direction[1-4].

In this paper we propose a new concept for the 3D control of light in real 3D optical microresonators that can be assimilated to 'cages', where photons are trapped efficiently. The main attractive feature of this photon cages lies in their ability to result in a considerable enhancement of the electromagnetic field in the central part of the cage, that is in the air region, opening the way to new sensing or trapping of nanoparticles in fluidic (gas or liquid) ambiances.

We will present the basic concepts we exploit to confine photons in air using cylindrical or spherical structures based on a periodic lattice of pillars (or stripes). These structures act as 2D/3D mirrors to trap photons in a small volume of low index material (e.g. air). Numerical results, based on FDTD simulations, will illustrate this new idea. Finally, an original technological approach, based on mechanical relaxation of strained microstructures, will be proposed for the fabrication of such 'photon cages'.

References

[1] X. Letartre et al, *Journal of Lightwave Technology*, 21, 1691 (2003).

[2] B. Ben Bakir et al, *Appl. Phys. Lett.* 88, 081113 (2006) and *Virtual Journal on Nanoscale Science & Technology* (2006), 13 n°10.

[3] S. Boutami et al, *Appl. Phys. Lett.* 91, 071105 (2007)

[4] L. Ferrier et al, *Optics Express* 16, 3136-3145 (2008)

Light localization and collection systems employing micro/nano-spheres

Brian Stout*, Alexis Devilez, Nicolas Bonod
Institut Fresnel, Aix – Marseille université, Domaine universitaire de St Jérôme, 13397 Marseille, France
brian.stouts@fresnel.fr

Abstract

We demonstrate the utility of quasi-analytic calculations to accurately design light localization, collection, and emission systems using dielectric microspheres or metallic nano-spheres.

Dielectric microspheres can focus light in their near field with low divergence, A phenomenon called photonic nano-jets [1]. We have demonstrated the utility of analyzing the properties of these beams in reciprocal space. Notably, one can demonstrate that the illumination of the microsphere by a focused beam already containing large k-vectors enables the suppression the large z-axis extension of the emerging beam [2,3]. These subwavelength properties recommend photonic jets as a useful tool for high resolution nano-particles detection, fluorescence microscopy improvements and nano-patterning. Despite some their highly desirable properties of low loss and high directivity, systems involving dielectric systems are mico-meter scaled and largely limited by diffraction.
Truly sub-wavelength manipulation of light apparently require systems involving localized plasmon resonances.[4-6]. Recent investigations have been undertaken to move the localized EM field in the metallic structure by modulating the frequency, the polarization and more interestingly the phase of the excitation beam [7-11]. These studies nicely demonstrate that basic manipulation of the excitation beam can produce various field distributions in the near field of the metal structure. In this presentation, we demonstrate through simulations how antennas made of spherical nano-particles enable the control of light localization at nanometer scale. We demonstrate that by simply tuning the angle of illumination of an excitation plane wave, one can control the localization of the EM enhancement with a spatial resolution on the order of $\lambda/10$ [12].
An unfortunate drawback of nano-particles, particularly for nano-antenna applications is the high loss intrinsic to plasmonic systems. We address the issue of loss in a variety of antenna configurations and address issues concerning optimizing the directivity of emitted radiation and increasing intrinsic properties of the emitter such as its quantum efficiency [13].

References

1. A. Heifetz, S.-C. Kong, A. V. Sahakian, A. Taflove, V. Backman, "photonic Nanojets," J. Comput. Theor. Nanosci. **6**, 1979-1992 (2009).
2. A. Devilez, N. Bonod, J. Wenger, D. Gérard, B. Stout, H. Rigneault, E. Popov, "Three-dimensional subwavelength confinement of light using dielectric microspheres," Opt. Express **17**, 2089 – 2094 (2009).
3. A. Devilez, B. Stout, N. Bonod, E. Popov, "Spectral analysis of three-dimensional photonic jets," Opt. Express **16**, 14200 – 14212 (2008).
4. K. Li, M. I. Stockman, D. J. Bergman, "Self-similar chain of metal nanospheres as an efficient nanolens," Phys. Rev. B **91**, 227402 (2003).
5. W. Rechberger, A. Hohenau, A. Leitner, J. R. Krenn, B. Lamprecht, F. R. Aussenegg, "Optical properties of two interacting gold nanoparticles," Opt. Comm . **220,** 137 - 141 (2003).
6. H. Tamaru, H. Kuwata, H. T. Miyazaki, K. Miyano, "Resonant light scattering from individual Ag nanoparticles and particle pairs", Appl. Phys. Lett. **80**, 1826 (2002).
7. M. I. Stockman, S. V. Faleev, D. J. Bergman, "Coherent control of femtosecond energy localization in nanosystems," Phys. Rev. Lett. **88**, 067402 (2002).
8. M. Aeschlimann, M. Bauer, D. Bayer, T. Brixner, F. J. Garcia de Abajo, W. Pfeiffer, M. Rohmer, C. Spindler, F. Steeb, "Adaptative subwavelength control of nano-optical fields," Nature **446**, 301 (2007).
9. A. F. Koenderink, J. V. Hernandez, F. Rochibeaux, L. D. Noordam, A. Polman, "Programmable Nanolithography with plasmon nanoparticle arrays," Nanoletters **7**, 745 – 749 (2007).
10. J. Le Perchec, P. Quémerais, A. Barbara, T. Lopez-Rios, "Controlling strong electromagnetic fields at subwavelength scales," Phys. Rev. Lett. **97**, 036405 (2006).
11. G. Volpe, S. Cherukulappurath, R. J. Parramon, G. Molina-Terriza, R. Quidant, "Controlling the optical near field of nanoantennas with spatial phase-shaped beams," Nanoletters **9**, 3608 (2009).
12. A. Devilez, N. Bonod, B. Stout, "Far field control of light localization in nanoantennas," (submitted).
13. J-. J. Greffet, "Nanoantennas for light emission," Science 308, 1561 (2005).

Modeling of Rare Earth Doped Microspheres

A. Di Tommaso[1*], M. De Sario[2], M. Ferrari[3], L. Mescia[2], T. Palmisano[1], G.C. Righini[4], F. Prudenzano[1],

[1] *DIASS, Politecnico di Bari, 74100 Taranto, Italy*

* *ditommaso@deemail.poliba.it*

[2] *DEE, Politecnico di Bari, 70125 Bari, Italy;* [3] *CNR-IFN, CSMFO Lab., 38100 Trento, Italy*

[4] *CNR-IFAC, MDF Lab., 50019 Sesto Fiorentino, Italy*

Two computer codes for the design of active microspheres coupled with tapered fibers have been developed. The former code models the amplification of the Whispering-Gallery Modes (WGMs) propagating into rare earth doped microspheres. The latter code solves the rate equations and the power propagation equations in frequency domain (FD).

Introduction

High Q quality factor dielectric microspheres are very attractive for many applications: nonlinear optics, evanescent-wave sensing, amplification. In particular, active microspheres allow to design novel devices, e.g. in active biosensing area. In this work, two different versatile models are ad hoc developed/optimized for the design of rare earth doped dielectric microspheres. The design of an Er^{3+} doped silica microsphere, surrounded by air and coupled to a tapered silica fibre permits to show the code effectiveness. The tapered fibre can couple the light at both pump and signal wavelengths into low order WGMs closely confined to the sphere surface and equator. In the former home made computer code, the cavity resonances and the amplification due to rare earth have been modelled by means of an advanced FDTD (Finite Difference Time Domain) algorithm. The latter home made computer code takes into account the FD (Frequency Domain) analytical WGM solution, the coupling between microsphere and the tapered fiber, the rate equations, pertaining to ion population of the Er^{3+} energy levels and the power propagation equations, in the frequency domain. The simulated results are compared and their agreement validates each other both the codes.

Results

The investigated amplifying system consists of an erbium doped silica microsphere having radius R_s=15 μm. A tapered fibre having waist radius R_f=0.45 μm excites and extracts both the pump and the signal and it is far 300 nm from the microsphere. In this way the phase matching between the microsphere WGM at the signal wavelength and the fibre fundamental mode occurs. The fibre fundamental modes are considered for both signal and pump. The pump wavelength is 980 nm, the signal wavelength envelopes a sinusoidal carrier at 1.53 um. The pump power is 0.8 mW, because this value allows the complete ion population inversion. By means FDTD approach the transient response of the amplifying system to the CW input signal is simulated. In order to simplify the amplifying system model, a two-dimensional (2-D) approach can be used to study the WGMs along the sphere equator. The electromagnetic field profile of the microsphere WGMs are analytically calculated for both pump and signal. In regime-state, the 2D FDTD method is less rigorous than 3D FD. Thus, the WGM electromagnetic field profiles and the propagation constants show a slight displacement. Nonetheless, by means of 2D FDTD approach it is possible to investigate other different structures.

Acknowledgements: The work has been developed within the COST ACTION MP0702: Towards Functional Sub-Wavelength Photonic Structures.

References L. Mescia, F. Prudenzano, M. De Sario, T. Palmisano, M. Ferrari, G.C. Righini, "Design of Rare Earth Doped Microspheres", accepted on Optics & Laser, Technology.

Modeling of Racetrack Resonator with Grating Assisted Coupling

P.Orlandi[1], M.Gnan[1], A.Samarelli[2], G.Bellanca[3], A.Melloni[4], R.M.De La Rue[2], M.Sorel[2], P.Bassi[1]
[1] *DEIS, University of Bologna, Viale Risorgimento 2, I 40136, Bologna, Italy*
piero.orlandi@unibo.it
[2] *Electronics and Electrical Engineering Department, Glasgow University, Glasgow, UK*
[3] *Dipartimento di Ingegneria, University of Ferrara, Via Saragat 1, I 44100 Ferrara, Italy*
[4] *Dipartimento di Elettronica e Informatica, Politecnico di Milano, via Ponzio 34/5, I 20133, Milano, Italy*

We study the properties of Grating Assisted Couplers (GACs) included in a racetrack resonator geometry. A more detailed theoretical model of the coupling than is usually performed is shown to be necessary to describe correctly the behaviour of devices fabricated in SOI.

Introduction

The GAC is an optical component successfully applied in integrated optics ($LiNbO_3$) [1] and fibre optics [2]. Recently, it has been used in SOI to demonstrate channel dropping with dispersion control, with devices as long as 100 μm [3]. In order to reduce the device length and retain high selectivity, we have arranged it into a racetrack resonant cavity, thus obtaining a novel device. Such a device can be functional for add-drop behavior of a limited set of channels in DWDM systems.

Results

Using the simplified Coupled Mode Theory and the transfer matrix approach implemented by ASPIC modeling software [4], the inclusion of the GAC into the racetrack geometry limits the frequency range over which the resonance occurs (Fig.1). Characterization of devices fabricated in SOI having grating regions made by sinusoidal sidewall modulation shows an overall similarity to the simulated behavior, but also discrepancies that the model cannot encompass, such as coupling of the isolated port and split resonance peaks. In this paper, we shall show that correct device modeling requires accurate description of the modal coupling within the GACs. The hypotheses of weak coupling and weak perturbation of the high confinement modal regime will be progressively released and discussed in relation to the accurate modeling of the racetrack resonance.

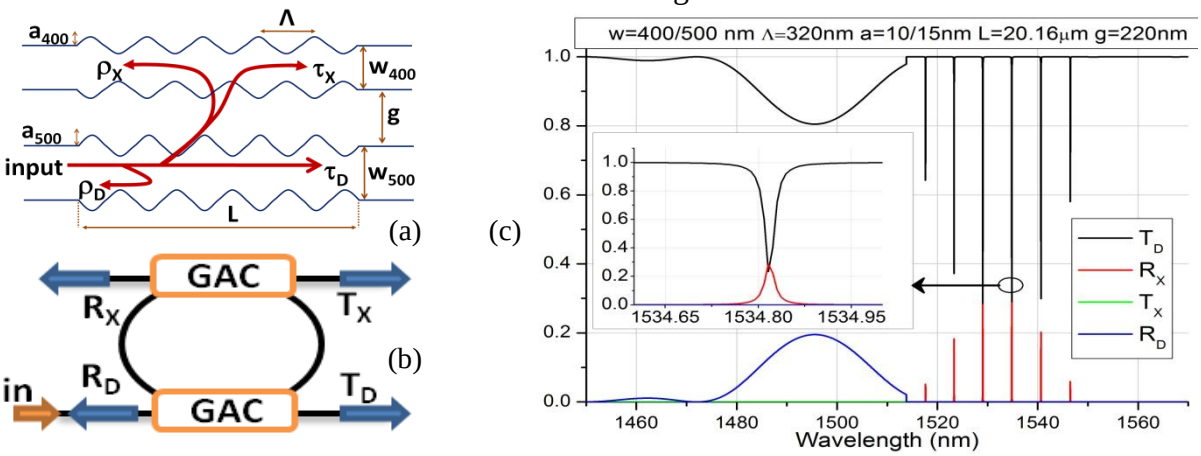


Fig.1 (a) GAC schematic. (b) Schematic of GAC in racetrack geometry and (c) its simulated behavior.

References

[1] P. Yeh and H.F. Taylor, *Appl. Optics*, **19**, 2848-2855, (1980).

[2] S. Orlov et al. *Opt. Lett.*, **22**, 688-690, (1997).

[3] D. Tan et al., *Appl. Phys. Lett.*, **95**, 141109, (2009).

[4] ASPIC, *www.aspicdesign.com*, Filarete, Italy.

Quantum Random Walks Circuits with Photonic Waveguides

Alberto Peruzzo, Jonathan Matthews, Alberto Politi, Mirko Lobino, Xiao-Qi Zhou, Mark G. Thompson, and Jeremy O'Brien
Department of Electrical and Electronic Engineering
University of Bristol, Bristol, United Kingdom

Nobuyuki Matsuda
Research Institute of Electrical Communication
Tohoku University, Sendai, Japan

Nur Ismail, Kerstin Wörhoff
Institute for Nanotechnology
University of Twente, Enschede, The Netherlands

Yaron Bromberg, Yoav Lahini, Yaron Silberberg
Department of Physics of Complex Systems, The Weizmann Institute of Science, Rehovot, Israel

Abstract—**Arrays of 21 evanescently coupled waveguides are fabricated to implement quantum random walks and a generalized form of two-photon non-classical interference, which was observed via two photon correlation.**

Keywords-component; quantum optics; waveguides; quantum computing; quantum random walks.

I. INTRODUCTION

Quantum random walks, the quantum analogue of statistical random walks, have great potential for designing a new generation of quantum algorithms and can be regarded as a primitive for universal quantum computation. Derived from Richard Feynman's original proposal in the 1960s, physical observation of random walks based upon quantum mechanical behaviour has been an important pursuit in modern quantum physics. Demonstrations of discrete time quantum walks have so far included Nuclear Magnetic Resonance [1], the phase space of trapped ions [2], the position space of trapped ions [3], and the path of a single photon in a network of (bulk) linear optics [4].

Continuous time quantum walks (CTQW) have been demonstrated using NMR [5] and in a so called ``optical version of Galton's board'' in the optical frequency space of an optical resonator [6] and in the tunnelling of light in coupled arrays of integrated waveguide structures [7].

The effective de-coherence free properties of photons make them an attractive test-bed for realizing quantum walks (as well as many other quantum mechanical behaviour). Quantum circuits are typically a series of nested interferometers (including [4]), which due to the nature of interferometry realized with bulk optics, is severely limited in size and complexity.

One of the most promising architectures for realizing CTQW is based on inherently stable integrated waveguide structures, already demonstrated in realizing optical circuits for quantum application [8-12].

For any circuit that would realize a quantum walk based on linear optics using an n-mode unitary, one could construct the circuit as a decomposition of 2-mode unitaries [13]. Decomposing circuits in this manner is, however, costly with respect to repeated bending circuitry into and out of interferometers. Instead, observation of larger CTQW (currently of the order 20-30 vertices) can be achieved using the direct tunnelling of light between coupled, ordered waveguide on a single array [7] (Fig. 1). By using this same architecture, the effects of Anderson localization on propagating quantum information [14] has been experimentally simulated using coherent light [15].

The statistics from measuring CTQW can be also predicted with a classical treatment. This provides motivation for the theoretical study into the distinctly non-classical effects of interfering more than one identical photon in an array of coupled waveguides [16]. This generalization of Hong-Ou-Mandel interference leads to various patterns of correlated statistics dependent upon the input state. While part of the model can be verified with classical correlation statistics (as they do in [16]), no experiment to date has been reported using quantum states of single photons to reproduce the full quantum correlation behaviour.

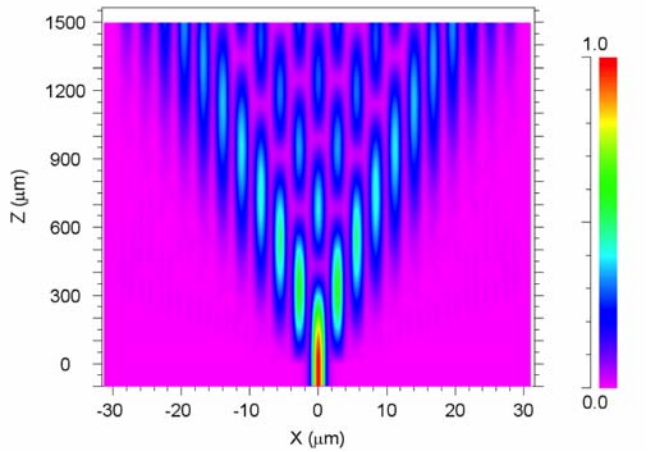


Figure 1. A BPM simulation of the light propagation along the waveguides array when the light is injected into the central waveguide.

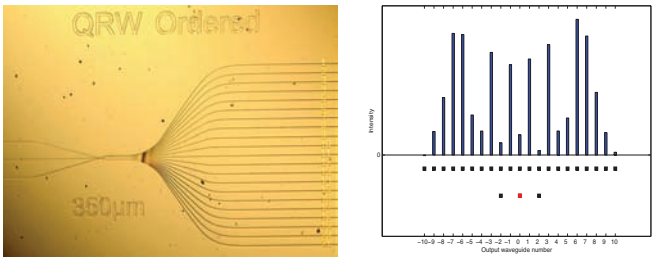


Figure 2 Left: An optical micrograph of a 21 waveguide quantum random walk device. Three input waveguides, initially separated by 250 micron, fan in to the 350 micron long coupling region, and 21 waveguides fan out to a 125 micron spacing. Right: Single photon quantum random walk data.

II. METHODS

For the device fabrication silicon oxynitride (SiON) layers are grown on thermally oxidized (8µm) Si <100> wafers (Fig. 2). The deposition is carried out in an Oxford parallel plate PECVD reactor utilizing SiH_4 and N_2O precursors. After annealing the channel waveguides are obtained by standard lithography and reactive ion etching in CHF_3 / O_2 chemistry. The channel structures are covered by a PECVD silicon oxide (SiO_2) cladding layer.

We coupled single photon pairs into the waveguides arrays and detected with silicon avalanche single photon detectors. To generate the single photon pairs a type I spontaneous parametric downconversion process was used. This is a $\chi^{(2)}$ nonlinear process where a bismuth borate BiB2O6 crystal is pumped by a 402 nm wavelength, 60 mW laser. The single photons are collected with polarization mantaining fibre arrays and injected into the waveguides. At the output a single mode fibre array was used to connect each waveguide to each detector.

The characterization of the QRW arrays has been done by measuring the single photon distribution (Fig. 2 left).

III. RESULTS AND CONCLUDING REMARKS

Fig. 2 left reports the output intensity when a single photon is injected into the central input waveguide.

When two photons are coupled into the waveguides, two photon correlation can be measured and the results are shown in Fig. 3. Remarkably the general behaviour of the quantum walks is demonstrated for the first time and it is in accordance with the predictions (Fig. 4). These results represent a first step highlighting the quality of these structures and their potential for quantum computing applications.

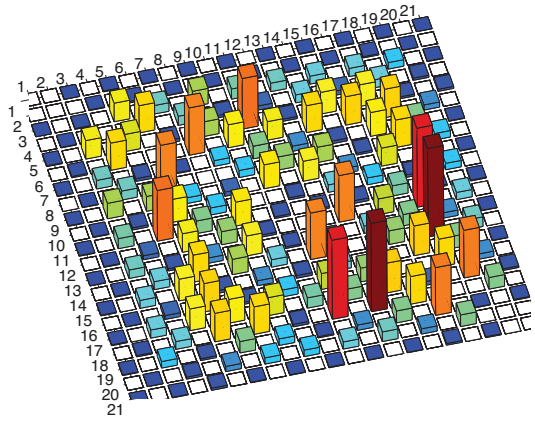


Figure 3. Measured 2-photons quantum correlation matrix when the photons are coupled to two adjacent waveguides.

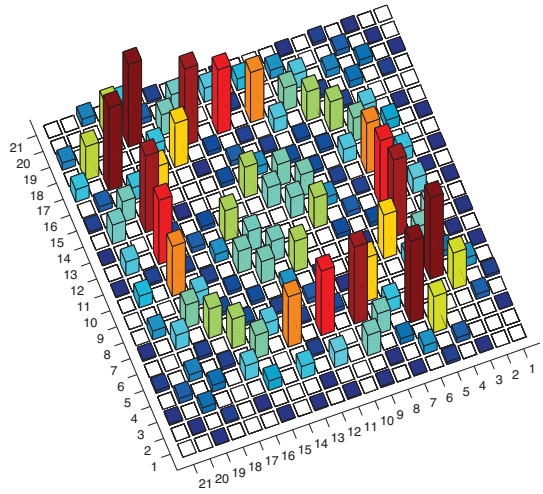


Figure 4. Simulation of the 2-photons quantum correlations when the photons are couple to adjacent waveguides.

REFERENCES

[1] C. A. Ryan, M. Laforest, J. C. Boileau, R. Laflamme, PRA 72, 062317 (2005).

[2] H. Schmitz et al. arxiv.org/abs/0904.4214 (2009).

[3] M. Karski et. al. Science 325,174 (2009).

[4] B. Do et al., J. Opt. Soc. Am. B 22, 499 (2005).

[5] J. Du et. al. PRA 67, 042316 (2003).

[6] D. Bouwmeester, I. Marzoli, G. P. Karman, W. Schleich, J. P. Woerdman, PRA 61, 013410 (1999).

[7] H. B. Perets et al., PRL 100, 170506 (2008).

[8] A. Politi, et. al. Science 320, 646 (2008).

[9] J. C. F. Matthews, A. Politi, A. Stefanov, J. L. O'Brien Nature Photonics 3 346 (2009)

[10] A. Politi, J. C. F. Matthews, J. L. O'Brien Science 325, 1221 (2009).

[11] G. D. Marshall, A. Politi, J. C. F. Matthews, P. Dekker, M. Ams, M. J. Withford, J. L. O'Brien, Optics Express, 17, 15, 12546 (2009).

[12] A. Politi, J. C. F. Matthews, M. G. Thompson, J. L. O'Brien, IEEE Journal of Selected Topics in Quantum Electronics, 15, 6, 1673-1684 (2009).

[13] M. Reck, A. Zeilinger, H. J. Bernstein, P. Bertani PRL 73, 58 (1994).

[14] J. P. Keating, N. Linden, J. C. F. Matthews, A. Winter PRA, 76, 1, 012315 (2007).

[15] Y. Lahini, A. Avidan, F. Pozzi, M. Sorel, R. Morandotti, D. N. Christodoulides , Y. Silberberg, PRL 100, 013906 (2008).

[16] Y. Bromberg, Y. Lahini, R. Morandotti, Y. Silberberg, PRL, 102, 253904 (2009).

Integrated Optics Implementation of Universal Quantum Gates, Bell States Preparation Circuit, Quantum Relay and Quantum LDPC Decoders

Ivan B. Djordjevic
University of Arizona, Department of Electrical and Computer Engineering
1230 E. Speedway Blvd., Tucson, AZ 85721, USA
ivan@ece.arizona.edu

Abstract— **We show that arbitrary family of universal quantum gates can be implemented in integrated optics based on single optical hybrid/Mach-Zehnder interferometer/directional coupler and highly nonlinear optical fibers (HNLFs). We also show how to implement the Bell states preparation circuit and quantum relay, needed in quantum teleportation systems, using the same technology. Finally, we study the implementation of sparse-graph quantum decoders in integrated optics.**

Keywords- quantum teleportation; quantum information processing; integrated optics devices; quantum error-correction codes (QECCs); sparse-graph quantum codes

I. INTRODUCTION

Quantum information processing (QIP) is an active research area with numerous applications, including quantum teleportation and quantum computing [1]. In order to perform an arbitrary quantum computation operation a minimum number of gates, known as universal quantum gates [1],[2]-[4], is needed. In this paper, we show that arbitrary single-qubit gate can be implemented based on single optical hybrid (OH)/Mach-Zehnder interferometer (MZI)/directional coupler (DC). We also show how to implement the deterministic CNOT gate based on OH/MZI/DC and highly nonlinear optical fiber (HNLF), which completes the implementation of arbitrary set of universal quantum gates in all-fiber technology. Two basic quantum circuits needed in quantum teleportation are Bell states preparation circuit and quantum relay. We also show how to implement them in integrated optics. The QIP, unfortunately, relies on delicate superposition states, which are sensitive to interactions with environment, resulting in decoherence. Moreover, the quantum gates are imperfect and the use of quantum error correction coding (QECC) is essential to enable the fault-tolerant computing and to deal with quantum errors [1]. In our recent paper [5] we proposed several structured quantum LDPC codes based on the balanced incomplete block designs (BIBDs), which offer a number of advantages thanks to the sparness of their quantum check-matrix. We show that encoder/decoder for arbitrary quantum LDPC code can be implemented in integrated optics as well.

II. INTEGRATED OPTICS IMPLEMENTATION OF UNIVERSAL QUANTUM GATES AND PAULI GATES

In what follows, the logical "0" is represented by a horizontal (H) photon $|H\rangle=[1\ 0]^T$ and the logical "1" is represented by a vertical (V) photon $|V\rangle=[0\ 1]^T$. An arbitrary single-qubit gate can be implemented in integrated optics based on OH, MZI or DC as shown in Figs. 1 (a)-(c), respectively. By expressing the power splitting ratio of OH as $k=\cos^2(\gamma/2)$ where angle γ is used to parameterize the power splitting ratio, the output qubit $[\psi_{H,o}, \psi_{V,o}]^T$ is related to the input qubit $[\psi_H, \psi_V]^T$ by

$$\begin{bmatrix}\psi_{H,o}\\ \psi_{V,o}\end{bmatrix}=U\begin{bmatrix}\psi_H\\ \psi_V\end{bmatrix},\ U=\begin{bmatrix}\cos\left(\frac{\gamma}{2}\right)e^{j(\alpha-\beta/2-\delta/2)} & -\sin\left(\frac{\gamma}{2}\right)e^{j(\alpha-\beta/2+\delta/2)}\\ \sin\left(\frac{\gamma}{2}\right)e^{j(\alpha+\beta/2-\delta/2)} & \cos\left(\frac{\gamma}{2}\right)e^{j(\alpha+\beta/2+\delta/2)}\end{bmatrix}. \quad (1)$$

The matrix U in eq. (1) represents the matrix representation of an arbitrary single-qubit quantum gate according to the Z-Y decomposition theorem (see equation (4.12) in [1]). The same equation holds for MZI-based and DC-based single-qubit quantum gate (see Figs. 1(b,c)). By setting $\gamma=\delta=0$ rad, $\alpha=\pi/4$ and $\beta=\pi/2$ rad U-gate described by (1) operates as the phase gate; by setting $\gamma=\delta=0$ rad, $\alpha=\pi/8$ and $\beta=\pi/4$ rad the U-gate operates as $\pi/8$ gate; while by setting $\gamma=\pi/2$, $\alpha=\pi/2$, $\beta=0$ rad and $\delta=\pi$, the U-gate operates as Hadamard gate.

To complete the implementation of the following set of universal quantum gates {Hadamard, phase, $\pi/8$, CNOT}, the implementation of CNOT-gate is needed. The authors in [2] proposed the use of directional couplers to implement the CNOT-gate. However, in that proposal, the control output qubit is affected by input target qubit, which violates the definition of CNOT-gate operation (control qubit must be unaffected by target qubit) [1]. The CNOT gate from [2] operates correctly only with probability of 1/9, and is essentially a probabilistic gate. In Fig. 2 we show the deterministic implementation of CNOT-gate based on optical hybrid shown in Fig. 1 and HNLF. By using the quantum-mechanical description provided in [1], it can be shown that output control $|C_o\rangle=[c_{H,o}\ c_{V,o}]^T$ and target qubits $|T_o\rangle=[t_{H,o}\ t_{V,o}]^T$ are related to corresponding input qubits by:

$$\begin{bmatrix}c_{H,o}\\ c_{V,o}\\ t_{H,o}\\ t_{V,o}\end{bmatrix}=\underbrace{\frac{1}{\sqrt{2}}\begin{bmatrix}1&1&0&0\\1&-1&0&0\\0&0&1&1\\0&0&1&-1\end{bmatrix}}_{I\otimes H}\underbrace{\begin{bmatrix}1&0&0&0\\0&1&0&0\\0&0&1&0\\0&0&0&-1\end{bmatrix}}_{K}\underbrace{\frac{1}{\sqrt{2}}\begin{bmatrix}1&1&0&0\\1&-1&0&0\\0&0&1&1\\0&0&1&-1\end{bmatrix}}_{I\otimes H}\begin{bmatrix}c_H\\ c_V\\ t_H\\ t_V\end{bmatrix} \quad (2)$$

$$=U_{CNOT}\begin{bmatrix}c_H\\ c_V\\ t_H\\ t_V\end{bmatrix},\ U_{CNOT}=\begin{bmatrix}1&0&0&0\\0&1&0&0\\0&0&0&1\\0&0&1&0\end{bmatrix}$$

This paper was supported in part by the NSF under Grant IHCS-0725405.

The Kerr nonlinearity device in Fig. 2 performs the controlled-Z operation. In the absence of control c_V-photon the target qubit is unaffected because $H^2=I$ (identity operator). In the presence of control c_V-photon, thanks to the cross-phase modulation in HNLF, the target vertical photon experience the phase shift χL, where χ is the third order nonlinearity susceptibility coefficient and L is the HNLF length. By selecting appropriately the fiber length we obtain $\chi L=\pi$ and the overall action on target qubit is $HZH=X$, which corresponds to the CNOT gate action.

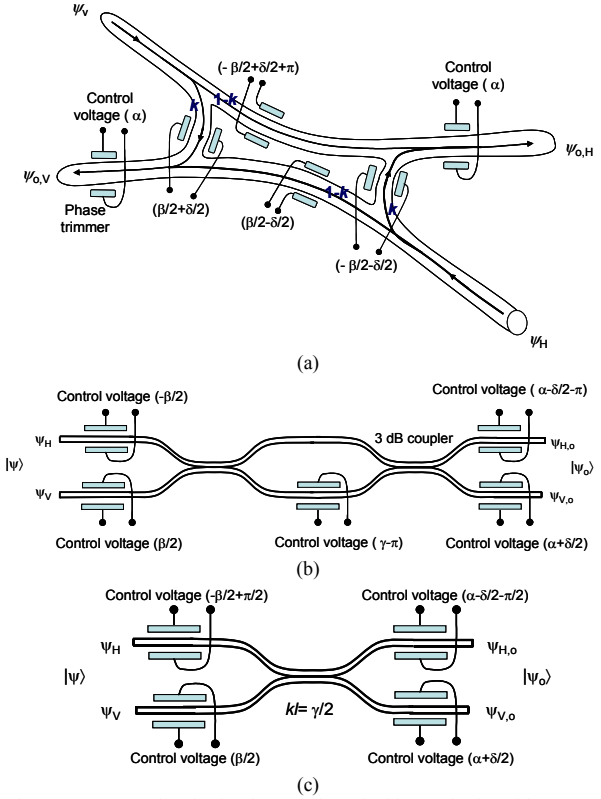


Figure 1. Integrated optics implementation of arbitrary single-qubit quantum gate based on single: (a) optical hybrid, (b) Mach-Zehnder interferometer and (c) directional coupler (k-the coupling coefficient, l-the coupling region length).

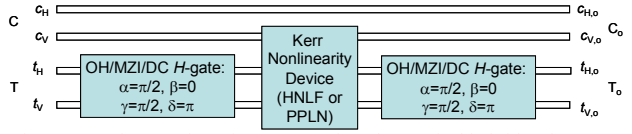


Figure 2. Implementation of CNOT gate based on optical hybrid and HNLF. OH/MZI/DC H-gate: OH/MZI/DC based Hadamard gate, PPLN: periodically poled LiNbO3.

With small modifications in (1) and by using similar approach to that described in Fig. 2, we can easily obtain the Barenco gate; while Deutsch gate can be obtained by employing three control qubits, instead of one used in Fig. 2.

By using the U-gate shown in Fig. 1 and by appropriately setting the phase shifts α, β, γ, and δ we can obtain the corresponding Pauli gates. The Y-gate is obtained by setting $\gamma=\pi$, $\beta=\delta=0$ rad and $\alpha=\pi/2$; the Z-gate is obtained by setting $\gamma=\delta=0$ rad, $\alpha=\pi/2$ and $\beta=\pi$; while the X-gate is obtained by setting $\gamma=\pi$, $\delta=0$ rad, $\alpha=\pi/2$ and $\beta=-\pi$.

III. Integrated Optics Implementation of Bell States Preparation Circuit and Quantum Relay

We further describe the implementation of Bell states preparation circuit based on OH/MZI/DC, which is shown in Fig. 3(a). The upper OH/MZI/DC circuit operates as Hadamard gate, while the rest of the circuit operates as CNOT gate. In Fig. 3(b) we describe how to implement the quantum relay based on Bell states preparation circuit (shown in Fig. 3(a)), Hadamard, controlled-X and controlled-Z gates described above. We employ the principle of differed measurement and perform corresponding measurements only in last intermediate node, which is a key difference with various quantum relay architectures described in [6]. The measurements circuits in Fig. 3(b) represent avalanche photodetectotors (APDs), which are used to detect the presence of c_V-photons in corresponding control qubits. The detection of c_V-photons triggers the application of required control voltages on phase trimmers to perform controlled-X and controlled-Z operation.

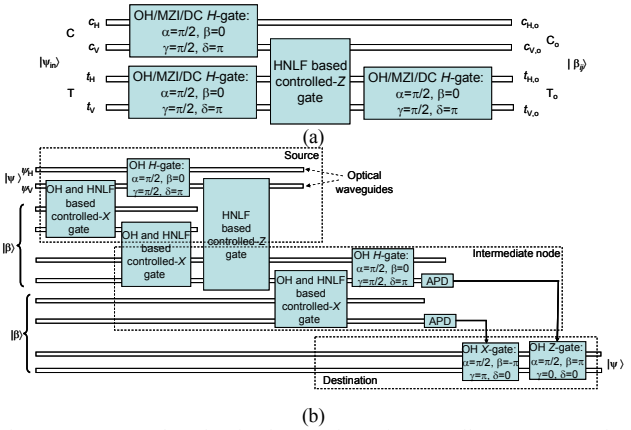


Figure 3. Integrated optics implementation of: (a) Bell states preparation circuit, and (b) quantum relay.

IV. Integrated Optics Implementation of Quantum LDPC Encoders/Decoders

The QECC encoders/decoders are essentially based on Pauli gates, whose implementation in integrated optics is already described in previous section. We have recently shown [5] that encoders and decoders for quantum LDPC codes can be implemented based on Hadamard and CNOT gates only. Therefore, arbitrary quantum LDPC encoder and decoder can be implemented in integrated optics based on OH/MZI/DC.

References

[1] M. A. Neilsen, and I. L. Chuang, *Quantum Computation and Quantum Information*. Cambridge University Press, 2000.

[2] T. C. Ralph *et al.*, "Linear optical controlled-NOT gate in the coincidence basis," *Phys. Rev. A*, vol. 65, paper 062324, 2002.

[3] A. Barenco, "A universal two-bit quantum computation," *Proc. R. Soc. London. A*, vol. 449, pp. 679-683, 1995.

[4] D. Deutsch, "Quantum computational networks," *Proc. R. Soc. London. A*, vol. 425, pp. 73-90, 1989.

[5] I. Djordjevic, "Photonic quantum dual-containing LDPC encoders and decoders," *IEEE Photon. Technol. Lett.*, vol. 21, pp. 842-844, 2009.

[6] S.-T. Cheng *et al.*, "Quantum communication for wireless wide-area networks," *IEEE J. Sel. Areas Comm.*, vol. 23, pp. 1424-1432, 2005.

Monolithic directional optical antennas for funneling photons to single emitters

Xue-Wen Chen, Vahid Sandoghdar and Mario Agio
Laboratory of Physical Chemistry, ETH Zurich, 8093 Zurich, Switzerland
mario.agio@phys.chem.ethz.ch

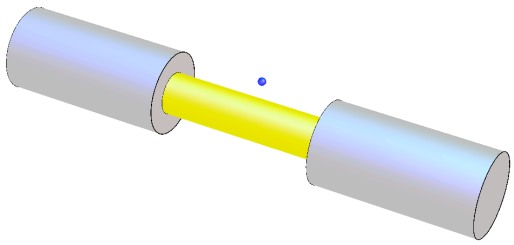
An emerging strategy for achieving efficient coupling of single emitters with photons relies on optical antennas. Here, we propose a class of metal nanostructures that feature directionality, strong field enhancement, and low losses for applications in quantum photonics and quantum nano-optics.

Introduction

Coupling single photons with single quantum emitters has become central to nanophotonics, for the implementation of integrated quantum networks and computing, but also for improving classical ways of processing information such as optical switching [1]. Progress in nano optics has shown that optical antennas [2] and plasmonic waveguides [3] can lead to large coupling efficiencies with broadband operation and better miniaturization in comparison to micro-resonators. However, optical antennas suffer from dipolar radiation patterns, which require high numerical-aperture optics for achieving strong couplings, and directional antenna arrays imply accurate handling of each individual element at the nanoscale [4]. On the other hand, practical exploitations of plasmonic waveguides need a rapid and effective conversion of surface plasmon-polaritons (SPPs) into photons, especially in the near infrared spectral range. Here, we propose a class of optical antennas that combines the high directionality of plasmonic waveguides with the performances and simplicity of dipole antennas.

Results

The figure below illustrates the concept of integrated monolithic directional antennas, where a finite metal nanostructure acts as an efficient light-matter interface between a nearby quantum emitter and photons, as well as a mode converter for coupling to a lossless waveguide. As an illustrative example, we consider metal nanowires butt-coupled to a dielectric fiber. Under appropriated conditions, we show that more than 95% of the incident guided photons are converted into SPPs and vice versa. The mechanism that boosts the coupling efficiency relies on the formation of a weak resonance at the nanowire-fiber interface, which entails a relationship between the operating wavelength and the nanowire and fiber radii. When we replace the nanowire with a truncated metal cone, SPPs nanofocus towards the cone tip to yield intensity enhancements of more than three orders of magnitude and, when propagating backward, collection efficiencies above 70% in the near infrared spectral range [5,6].



References

[1] J. L. O'Brien, A. Furusawa, J. Vučković, *Nat. Photonics*, **3**, 687-695, (2009)

[2] S. Kühn, U. Håkanson, L. Rogobete, V. Sandoghdar, *Phys. Rev. Lett.*, **97**, 017402, (2006)

[3] D. E. Chang, A. S. Sørensen, P. R. Hemmer, M. D. Lukin, *Phys. Rev. Lett.*, **97**, 053002, (2006)

[4] J. Li, A. Salandrino, N. Engheta, *Phys. Rev. B*, **76**, 245403, (2007)

[5] X.-W. Chen, V. Sandoghdar, M. Agio, *Nano Lett.*, **9**, 3765-3761, (2009)

[6] X.-W. Chen, V. Sandoghdar, M. Agio, *submitted*, (2010)

Tm:Ti:$LiNbO_3$ Waveguide for Quantum Memory Applications

M. George, R. Ricken and W. Sohler
Angewandte Physik, Department Physik
Universität Paderborn, Paderborn, Germany
mathew.george@uni-paderborn.de

E. Saglamyurek, N. Sinclair, C. La Mela and W. Tittel
Institute for Quantum Information Science,
and Department of Physics and Astronomy
University of Calgary, Calgary, Canada

Abstract—**We report fabrication and characterization of a Tm:Ti:$LiNbO_3$ optical waveguide, single mode around 800 nm wavelength, in view of photon-echo quantum memory applications. In particular, room- and low-temperature properties were investigated via loss and absorption measurements, spectral hole burning, photon echo, and Stark spectroscopy.**

Keywords: rare-earth-ion doped crystal; optical waveguide; lithium niobate; photon-echo; quantum memory.

I. INTRODUCTION

Quantum memories are key elements for quantum repeaters, which promise overcoming the distance barrier of quantum communication [1]. A currently extensively studied approach relies on photon echoes [2,3]. Tm:Ti:$LiNbO_3$ optical waveguides combine interesting features arising from the specific rare-earth dopant, the host material, as well as the waveguide. Specifically, thulium features a transition at 795 nm (Fig. 1), a wavelength where air is transparent, entangled photons are conveniently generated in non-linear crystals or optical fibres, and high-efficiency and easy-to-operate single photon detectors are commercially available. Furthermore, when implemented into Lithium Niobate, its electronic states acquire permanent electric dipole moments, allowing for modification of the transition frequencies through the application of an electric field [4]. Finally, the use of a waveguide where travelling wave electrodes can be spaced closely and light intensities can be large, promise simple integration with fibre optics and quantum networks, sub-ns Stark frequency control, and large Rabi frequencies, which benefits the optical pumping procedure required for spectral tailoring of the inhomogeneously broadened absorption line [2,3].

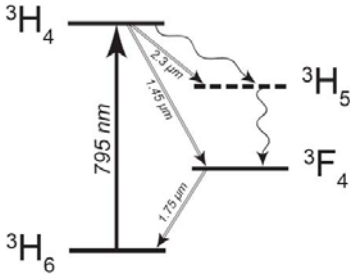


Figure 1. Simplified energy level diagram of Tm:LiNbO3 showing the electronic levels relevant to this work.

II. WAVEGUIDE FABRICATION AND CHARACTERIZATION

A. *Tm diffusion doping of $LiNbO_3$*

Commercially available 0.5 mm thick Z-cut wafers of undoped optical grade congruent lithium niobate were Tm-doped near the +Z-surface before waveguide fabrication. A vacuum deposited Tm layer of 19.6 nm thickness was in-diffused at 1130 ^{0}C during 150 hrs in an argon-atmosphere followed by a post treatment in oxygen (1 h). The diffusion profile was determined by secondary neutral mass spectroscopy (Fig. 2). The maximum Tm concentration of about 1.35 x 10^{20} cm^{-3} corresponds to a concentration 0.74 mole %.

B. *Ti indiffused waveguides in Tm:$LiNbO_3$*

On the Tm-doped surface 3.0 µm wide, 40 nm thick Ti-stripes were deposited and subsequently in-diffused at 1060 ^{0}C for 5 hrs to form 30 mm long optical strip waveguides. In the wavelength range around 775 nm, these waveguides are single mode for TE and TM-polarization (see also Fig. 2).

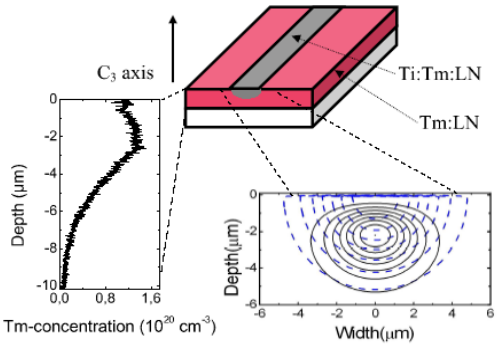


Figure 2. Scheme of the waveguide geometry with the measured Tm concentration profile on the left and the calculated intensity distribution of the fundamental TM-mode superimposed on the profile of the extraordinary index of refraction induced by the Ti-doping. The latter data are for 795 nm wavelength. Iso-intensity lines are plotted for both, the index and the mode profile, corresponding to 100%, 87.5%, 75% etc. of the maximum index increase ($\Delta nmax$ = 4.0 x 10^{-3}) and mode intensity, respectively.

C. *Characterization*

The total waveguide propagation losses, consisting of absorption and scattering loss, were measured around 800 nm wavelength at room temperature by the Fabry-Perot method [5]. In addition, the waveguide propagation loss was determined at 729 nm wavelength where negligible absorption by the Tm-

ions is expected. In this way the scattering loss was determined alone; it is 0.2 dB/cm for both polarizations.

Moreover, polarization dependent transmission spectra of a 30 mm long waveguide were measured, yielding the inhomogeneously broadened spectrum depicted in Fig. 3.

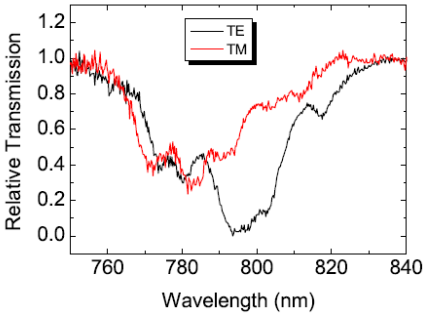


Figure 3. Relative transmission through the Tm:Ti:$LiNbO_3$ waveguide for TM- and TE-polarization, respectively, as a function of wavelength.

III. Thulium Spectroscopy

To characterize Tm:Ti:$LiNbO_3$ waveguides for photon-echo based quantum memories, we studied a large variety of low-temperature (3K) properties (for more information see [6,7]).

First, we repeated the measurement of the inhomogeneously broadened $^3H_6 \leftrightarrow {}^3H_4$ absorption line at 3.5 K, which confirmed the strong polarization dependence that we already found at room temperature. Furthermore, the measurement reflected the temperature dependent distribution of atomic population in the ground state Stark levels, and enhanced absorption for transitions starting in the ground state Stark level.

Next, we investigated relaxation avenues and population dynamics of the $^3H_4$ and $^3F_4$ atomic. This impacts on the possibility to tailor the inhomogeneously broadened absorption line by frequency selectively transferring absorbers to long-lived states. Figure 4 depicts the results of time-resolved spectral hole burning, yielding radiative lifetimes of 82 µs and 2.4 ms for the $^3H_4$ and $^3F_4$ levels, respectively, and a branching ratio from the $^3H_4$ into the $^3F_4$ level of ~ 44%.

We repeated these studies under application of magnetic fields between 100 and 1250 Gauss, oriented parallel to the crystal C_3-axis. This led to the appearance of two atomic ground state sub-levels with lifetimes exceeding 1 second.

An important property that determines the storage time of quantum states in optical atomic is the width of the sharpest spectral feature that can be generated. It depends on the homogeneous linewidth of the $^3H_6 \leftrightarrow {}^3H_4$ transition (which itself is limited by the inverse radiative lifetime) as well as on spectral diffusion, which leads to time dependent broadening. Using two- and three-pulse photon echoes, we found an effective homogeneous linewidth of 1.082 MHz, and hence a minimum spectral feature of around 2 MHz.

Finally, in order to control dephasing and rephrasing of atomic coherence through electric fields [2], we measured the DC Stark effect, again using spectral hole burning techniques. We observed a linear frequency shift (reflecting the symmetry properties of Tm in $LiNbO_3$) of 24.6 ± 0.7 kHz·cm/V.

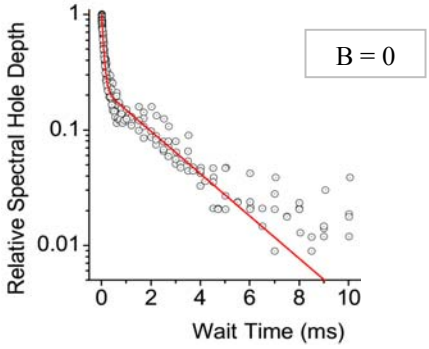


Figure 4. Spectral hole decay under zero magnetic field. Plotted circles denote the normalized spectral hole depth as a function of the waiting time between burning and reading pulses. Two exponential decays are easily identified, yielding radiative lifetimes of 82µs and 2.4 ms for the $^3H_4$ and $^3F_4$ levels, respectively. The branching ratio into the $^3F_4$ level is approximately 44%.

IV. Conclusions

Our findings demonstrate the suitability of Tm:Ti:$LiNbO_3$ waveguides cooled to 3 K for implementations of photon-echo quantum memory protocols. Level structure, lifetimes, and branching ratios allow tailoring of the natural, inhomogeneously broadened absorption profile. The minimum width of spectral holes of ~2 MHz, as determined by spectral diffusion, will limit storage of quantum information in optical coherence to roughly a hundred nanoseconds. While longer times may be achievable at lower temperature, this is still sufficient for mapping coherence onto long-lived ground state coherence, as Rabi frequencies exceeding hundred MHz can be obtained, due to the high power densities achievable inside waveguiding structures. Finally, the existence of a linear Stark shift, together with the possibility to space electrodes closely, allows shifting of resonance frequencies by more than 100 MHz within sub-nanosecond times, thus enabling novel phase control techniques. The first demonstration of a quantum memory protocol, using this waveguide, will be reported elsewhere [8].

References

[1] H. J. Briegel, W. Dür, J. I. Cirac and P. Zoller, "Quantum repeaters: The role of imperfect local operations in quantum communications," Phys. Rev. Lett. 81, 5932 (1998).

[2] W. Tittel *et al.*, " Photon-echo quantum memory in solid state systems" Laser and Photonics Rev. DOI 10.1002/lpor.200810056.

[3] H. de Riedmatten *et al.*, "A solid-state light-matter interface at the single-photon level, " Nature 456, 773 (2008).

[4] R. Macfarlane, "Optical Stark spectroscopy of solids", J. Lumin. 125, 156 (2007).

[5] R. Regener and W. Sohler, "Loss in low-finesse Ti:$LiNbO_3$ waveguide resonators". App. Phys. B, vol 36 p 143 (1985).

[6] N. Sinclair *et al.*, "Spectroscopic investigations of a Ti:Tm:$LiNbO_3$ waveguide for photon echo quantum memory", J. Lumin., in press.

[7] C.W. Thiel *et al.*, "Optical Decoherence and Persistent Spectral Hole Burning in Tm^{3+}:$LiNbO_3$", J. Lumin., in press.

[8] E. Saglamyurek et al., "Integrated quantum memory for quantum communication", to be presented at OFC 2010.

A compiled version of Shor's quantum factoring algorithm on a waveguide chip

Alberto Politi, Jonathan C. F. Matthews & Jeremy L. O'Brien
Centre for Quantum Photonics, H. H. Wills Physics Laboratory & Department of Electrical and Electronic Engineering,
University of Bristol,
Bristol, UK,
Jeremy.Obrien@Bristol.ac.uk

Abstract—**Realization of a compiled version of Shor's quantum factoring algorithm is realized on a waveguide chip. Utilizing quantum and classical interference, multiple quantum gates are integrated within silica-on-silicon waveguide to realize a proof-of-principle of quantum computation within a single optical chip. This demonstration illustrates the importance of integrated optics for future quantum technology.**

Keywords-component; quantum information; algorithm; single photons; integrated waveguides

I. INTRODUCTION

Realizing computation based on quantum physics is one of the main goals for modern science and engineering. Fifteen years ago, Peter Shor proposed an algorithm [1] that would harness the unique quantum mechanical properties of superposition and entanglement to efficiently factorize a product of two large prime numbers [2]. To date, no known algorithm exists using conventional classical computation to solve this problem in time less than exponentially large in the input, making factorization intractable and forms the basis for most modern cryptographic security.

Progress towards proof-of-principle demonstration of Shor's factoring algorithm have included liquid state nuclear magnetic resonance [2] and bulk optical implementations using simplified quantum logic gates [3,4]. While the latter demonstrate the necessary use of entanglement required for improvement over classical computation, they cannot be scaled to the required large number of quantum gates and quantum bits (qubits). Instability and physical size remain as amongst the largest of limitations in complexity implementing practical quantum technology.

Recent demonstrations of using both lithographic and directly written monolithic waveguide circuits for quantum optical experiments [5,6,7,8,9] allows the use of integrated optics as an important platform for future quantum optical schemes. We report the subsequent application of waveguide quantum gates to realize a circuit implementing a compiled version of Shor's quantum algorithm to factorize 15 [10].

This work was supported by Engineering and Physical Sciences Research Council, Quanutm Information Processing Interdisciplinary Research Collaboration, Intelligence Advanced Research Projects Activity, and the Leverhulme Trust. J.L.O'B acknowledges a Royal Society Wolfson Merit Award.

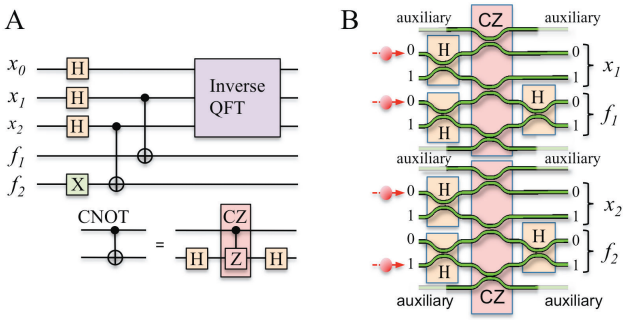


Figure 1: Realizing a compiled version of Shor's algorithm on a waveguide chip. (A) The quantum circuit compiled to factorize 15. (B) Schematic of the waveguide circuit including photonic inputs.

II. METHOD

The full process of Shor's algorithm can be partitioned into conventional classical processing and a quantum sub-routine known as order finding [1,3,4]. Figure 1A shows the quantum circuit for the compiled order finding routine designed specifically to factorize 15 with designed success rate of 1/2. The circuit comprises of a number of single qubit rotations (Hadamard (H), NOT (X)) and two two-qubit entangling gates (controlled π-phase shift (C-Z)) acting on qubits in two registers known as the argument (x_i) and function (f_i). An inverse quantum fourier transform (QFT) acting on the argument register is achieved for certain compiled circuits using classical post-processing [4]. The integrated waveguide version of this circuit consists of directional couplers to realize the quantum optical gates [5] and is shown schematically in figure. The 3.5μm core waveguides, designed to guide the fundamental mode for λ=790nm, are defined by doped silica on a silicon substrate and are fabricated using standard lithographic techniques [5].

Photonic quantum bits are encoded using the path of four 790nm photons simultaneously prepared via spontaneous parametric down-conversion. A 157fs Ti:sapphire laser tuned

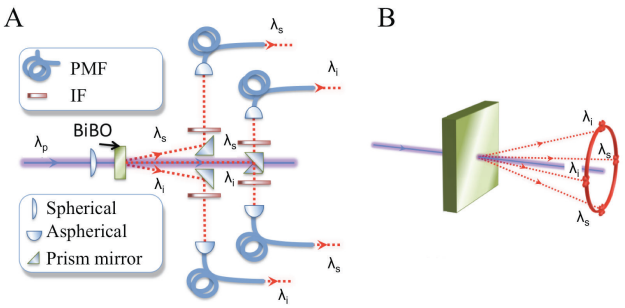


Figure 2: The down conversion based photon source. (A) Schematic of the down conversion source pumped by 390nm light to produce two pairs of 790nm photons, filtered by high transmission interference filters (IF) and collected in four spacial modes (B) into polarization maintaining fibre (PMF).

to 790nm is up-converted using a 2mm thick nonlinear bismuth borate BiB_2O_6 (BiBO) crystal (cut for second harmonic generation) to produce a beam of λ_p=385nm. This is then focused down onto a second BiBO crystal cut for spontaneous parametric down-conversion, producing pairs of signal and idler photons $\lambda_s=\lambda_i$=790nm, which are first filtered through high transmission interference filters (λ_0=790nm), before being collected in polarization maintaining fibres as shown in figure 2.

The photons are injected into the waveguide chip using butt-coupled arrays of polarization maintaining fibre matched to the dimensions of the waveguide circuit, and detected after the waveguide circuit using single photon counting avalanche photodiodes to yield the outcome of the quantum algorithm.

III. Results & Concluding Remarks

Detecting photons in the argument registers yields the outcome of the order finding routine. The two expected failure and two success events are predicted to occur with equal probability (1/4). Our experimental results (given in figure 3) agree with this with a similarity 99±1%. Together with final steps of classical processing, the factors of 15 are correctly determined [10].

While complete scalability of using photons to realize quantum computation is still an open area of research, needing efficient single photon sources and efficient single photon detectors, the ongoing progress in these fields together the use of ultra-stable and miniaturized integrated optical circuits, will

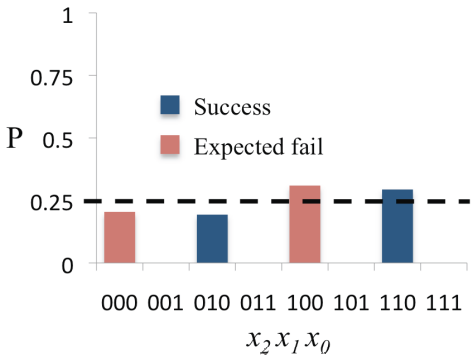


Figure 3: argument register outputs are normalized to a statistical distribution. With classical post-processing, these results reveal the factors of 15 to be 3 and 5 with success rate ½ [4,10]. The dashed line shows the ideal level of the four possible outcomes of the value, while the blue and red bars display expected success and failure outcomes of the circuit.

allow the development of sophisticated quantum circuits and the implementation of large-scale quantum algorithms.

Acknowledgment

We thank R. Jozsa, A. Laing, A. Montanaro, S. Takeuchi, M. G. Thompson and X.-Q. Zhou for helpful discussions.

References

[1] P. W. Shor, in *Proceedings of the 35th Annual Symposium on the Foundations of Computer Science* (IEEE `Computer Science Press, Los Alamitos, CA, 1994), pp. 124-134.

[2] L. M. K. Vandersypen *et. al.*, *Nature* **414**, 883 (2001).

[3] C.-Y. Lu, D. E. Browne, T. Yang, J. W. Pan, *Phys. Rev. Lett.* **99**, 250504 (2007).

[4] B. P. Lanyon *et. al.*, *Phys. Rev. Lett.* **99**, 250505 (2007).

[5] A. Politi, M. J. Cryan, J. G. Rarity, S. Yu, and J. L. O'Brien, *Science* **320**, 646 (2008).

[6] A. Politi, J. C. F. Matthews, M. G. Thompson, J. L. O'Brien, *IEEE Journal of Selected Topics in Quantum Electronics*, **15**, 6, 1673-1684 (2009).

[7] G. D. Marshall, et al., *Optics Express*, **17**, 12546 (2009).

[8] J. C. F. Matthews, A. Politi, A. Stefanov and J. L. O'Brien, *Nature Photonics,* **3**, 346 (2009).

[9] B. J. Smith, D. Kundys, N. Thomas-Peter, P. G. R. Smith, I. A. Walmsley *Opt. Exp.* **17**, 13516 (2009).

[10] A. Politi, J. C. F. Matthews and J. L. O'Brien, *Science*, **325**, 1221 (2009).

Entangled Multi-Photon States in Waveguide for Quantum Metrology

Jonathan C. F. Matthews, Alberto Politi,
Damien Bonneau & Jeremy L. O'Brien
Centre for Quantum Photonics, H. H. Wills Physics Laboratory & Department of Electrical and Electronic Engineering,
University of Bristol, Bristol, UK
Jeremy.Obrien@Bristol.ac.uk

André Stefanov
Now at: Federal Office of Metrology METAS,
Bern-Waberm, Switzerland

Abstract—**Entangled photonic states known as "NOON" states are manipulated within monolithic waveguide circuitry. The resulting quantum interference has sufficient visibility to measure phase beyond the shot noise limit using integrated waveguide. We also demonstrate a scheme for heralding two- and four-photon entangled states which can be generalized to arbitrarily large NOON states.**

Keywords-component; quantum metrology; integrated waveguides; single photons

I. INTRODUCTION

Harnessing quantum superposition and quantum entanglement of single photon is already providing enhanced security with quantum cryptography [1] and is one of the leading platforms for other technologies derived from quantum information science, including quantum computation [2], quantum lithography [3] and quantum metrology [4].

In each of these technologies, quantum mechanics offers additional improvement over what can be achieved by applying classical physics alone. Quantum metrology uses large superposition states of photons, entangled in number and one other type of (typically path or polarization), known as "NOON" states. Related to so-called "Schrödinger cat states", NOON states of photon number N are mathematically defined by

$$|N::0\rangle = \frac{1}{\sqrt{2}}\left(|N\rangle_a |0\rangle_b + |0\rangle_a |N\rangle_b\right) \qquad (1)$$

where $|n\rangle_j$ represents the Fock state of n photons populating a mode labeled j. These states have an increased sensitivity to relative phase relative to un-entangled light, allowing a precision in phase measurement towards the Heisenberg limit (HL) $\Delta\phi \sim 1/N$, beyond the classical shot noise limit (SHL) of $\Delta\phi \sim 1/\sqrt{N}$ [4].

Previous experiments to demonstrate the increased resolution in phase sensitivity gained by NOON states have been demonstrated using bulk optics by encoding the quantum states in polarization and path (for example [5] and [6] respectively). We present here the manipulation of NOON states in integrated waveguide circuits and experimentally implement a theoretical proposal to herald the creation of NOON states of up to four photons using only linear optics and projective measurements [8].

This work was supported by IARPA, EPSRC, QIP IRC and the Leverhulme Trust

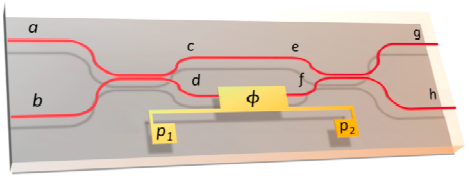


Figure 1: An integrated waveguide Mach-Zehnder interferometer used to manipulate entangled states of light using a resistive heater (labeled ϕ).

II. MANIPULATING NOON STATES

A. Method

The waveguide circuit for manipulating path entanglement is a Mach Zehnder interferometer with lithographically patterned thermal resister to control the internal phase as shown in figure 1. The 3.5μm core waveguides are lithographically patterned from doped Silica fabricated on a Silicon substrate using standard methods and are designed for single mode operation in the 780nm region. On applying a voltage across the thermal resister, the relative optical phase of quantum states guided through the interferometer is varied in a stable, controlled manner.

Multi photon states of two- and four-photons are produced by pumping spontaneous parametric down conversion (SPDC). A Ti:sapphire pulsed laser (157fs) laser is tuned to 780nm and upconverted to 390nm via second harmonic generation in a 2mm thick nonlinear Bismuth Borate BiB_2O_6 (BiBO) crystal. This is then focused onto a second BiBO crystal cut for non-collinear down-conversion to produce pairs of signal and idler photons with wavelength 780nm. The pairs are filtered spectrally using high transmission interference filters and spatially into two modes by focusing onto polarization maintaining fibres (PMF). The photons are injected into the chip using butt-coupled arrays of PMF pitched to match those of the waveguide. Coincidental events are then detected using

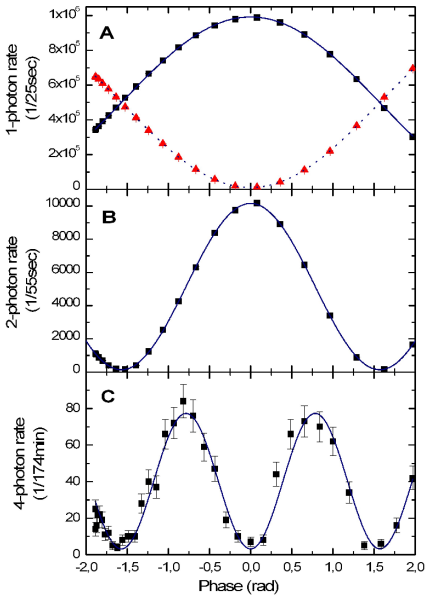


Figure 2: Quantum interference inside a waveguide interferometer. (A) The single photon interference patterns from inputting single photons in waveguide *a* (see figure 1); black squares are plotted from detecting photons on output *h*, red triangles correspond to detections at output *g*. (B) Two photon interference pattern of a two-photon NOON state. (C) Four photon interference pattern on post-selecting a four-photon NOON state inside the interferometer. All plots use sinusoids as a best fit.

commercially available silicon avalanche photo diode single photon counting modules (SPCM).

B. Results

Figure 1A displays the single photon interference fringe obtained on inputting single photons into mode *a* and detecting them independently at modes *g* and *h* with respect to variation of phase inside the interferometer. While this interference pattern is equivalent to the pattern observed from inputting classical light, the contrast of 0.982±0.003 indicates an average fidelity of 0.99984±0.00004 for manipulating single bits of quantum information (qubits) encoded across two spatial modes—the natural encoding for integrated waveguide circuitry[cite integrated quantum circuits].

On inputting two coherent identical photons on inputs *a* and *b* deterministically yields a two photon NOON state; varying the phase of the device by causes the two photon NOON state to be shifted in phase by 2. On post selecting two photon coincidences across the outputs of *g* and *h* allows an interference pattern of twice the resolution of the single photon case to be observed. The fringe given in figure 2B has a contrast of 0.972±0.004, sufficient to beat the standard quantum limit (assuming high efficiency photon sources and perfect detectors).

Producing four photon NOON states is not so straightforward as the two photon case and cannot be achieved by using non-classical interference of Fock states alone. To observe a four-fold interference fringe, we use a method to post select the presence of a four photon NOON state inside the interferometer, hence allowing the observation of a four-photon interference fringe with four times the resolution of the single photon case [6]. The plot given in figure 2C has a contrast of 0.92±0.04, which despite the detection scheme required to post select the four photon NOON state, is sufficient to beat the standard quantum limit (again, assuming high efficiency detectors and photon sources).

III. HERALDING NOON STATES

The generation of large photon number NOON states is unlikely to be achieved by using non-classical interference alone. It has been theoretically proposed [8] that using linear optics and projective measurements, large photon number NOON states can be constructed from Fock states. Demonstrate this experimentally in waveguide circuit designed to herald the presence of two- and four-photon NOON states with, in principle, perfect fidelity. This requires two extra ancillary photons for each case. Using projective measurements in this manner can also be generalized to yield arbitrarily large NOON states [9].

IV. CONCLUDING REMARKS

The inherent stability and near perfect mode-overlap of lithographic waveguide architecture is ideal for the application to quantum metrology. They have already been demonstrated to yield high levels of non-classical interference for components for quantum computation [10,11,12], and the results presented here highlight their potential for quantum metrology realized in an integrated optics platform.

ACKNOWLEDGMENT

We thank A. Laing, T. Nagata, S. Takeuchi, X. Q. Zhou, J. P. Hadden, A. Lynch and J. G. Rarity for helpful discussion.

REFERENCES

[1] N. Gisin, G. Ribordy, W. Tittel, H. Zibenden, *Rev. Mod. Phys.* **74**, 145-195 (2002).

[2] M. A. Nielsen, I. L. Chuang, *Quantum Computation and Quantum Information* (Cambridge Univ. Press, 2000).

[3] A. N. Boto *et. al. Phys. Rev. Lett.* **85**, 2733-2736 (2000).

[4] V. Gioveannetti, S. Lloyd, L. Maccone, *Science* **306**, 1330-1336 (2004).

[5] M. W. Mitchell, J. S. Lundeen, A. M. Steinberg *Nature* **429**, 161-164 (2004).

[6] T. Nagata, R. Okamoto, J. L. O'Brien, K. Sasaki, S. Takeuichi, *Science* **316**, 726-729 (2007).

[7] J. C. F. Matthews, A. Politi, A. Stefanov, J. L. O'Brien, *Nature Photon.* **3** 346 (2009).

[8] H. Lee, P. Kok, N. J. Cerf, J. P. Dowling *Phys. Rev. A* **65** 030101 (2002).

[9] P. Kok, H. Lee, J. P. Dowling, *Phys. Rev. A* **65** 052104 (2002).

[10] A. Politi, M. J. Cryan, J. G. Rarity S. Yu, J. L. O'Brien *Science*, **320**, 646-649 (2008).

[11] A. Politi, J. C. F. Matthews and J. L. O'Brien, *Science*, **325**, 1221 (2009).

[12] A. Politi, J. C. F. Matthews, M. G. Thompson, J. L. O'Brien, *IEEE Journal of Selected Topics in Quantum Electronics*, **15**, 6, 1673-1684 (2009).

Photonic Crystal DFB laser array robust to optical feedback

A. Larrue, O. Gauthier-Lafaye, S. Bonnefont, A. Monmayrant, F. Lozes-Dupuy
CNRS ; LAAS ; 7 avenue du colonel Roche, F-31077 Toulouse, France
Université de Toulouse ; UPS, INSA, INP, ISAE ; LAAS ; F-31077 Toulouse, France
antoine.monmayrant@laas.fr

Abstract—**We demonstrate experimentally a new design for arrays of photonic crystal DFB lasers with precise wavelength spacing and high robustness to optical feedback.**

Distributed-feedback (DFB) lasers, optical feedback, photonic crystals (PhCs), semiconductor lasers

I. INTRODUCTION

Recently, it has been shown that photonic crystal defect waveguides can be used to fabricate second-order single-mode DFB lasers [1, 2]. Using affine deformation, these lasers can be arranged in array with a fine control over the frequency spacing between lasers [3]. The main limitation of this approach is optical feedback that introduces unpredictable frequency shifts and mode-hoping. Here, we present a novel approach dubbed "double deformation" that combines affine deformation of the photonic crystal and precise control of the width of the defect waveguide to achieve precise control of the laser frequency together with high robustness to optical feedback. The latter is obtained by a careful optimization of the Q factor of the cavity.

II. DFB ARRAY USING AFFINE DEFORMATION

Here we consider lasers based on W3 ΓK defect waveguides (obtained by omitting 3 rows of holes along the ΓK direction in an hexagonal lattice, see figure 1. (b)). These lasers are fabricated on a InGaAs/GaAs membrane (of effective index 3.27 at 990 nm), using a lattice constant a=304nm and a filling factor of 25%, as described in [3]. We compare two different approaches to build an array of such lasers with a precise control of the emission frequency. In the first approach, each laser is deformed using affine deformation (see figure 1. (a)): the lattice period along a direction perpendicular to the waveguide is scaled: b'=αb together with the defect width w'=αw, where α is called the deformation. Using this approach, we designed arrays of fifteen 300µm-long lasers (see figure 2. (a)). A particular attention was devoted to cavity ends. First, the ends of the photonic crystal waveguide were slanted along the ΓM direction (see figure 2. (b) and (c)) in order to avoid optical feedback at that point. Second, two different types of output mirrors (corresponding to the end of the membrane itself) were designed: tilted ones (see figure 2. (b)) which provide the lowest possible level of feedback and normal ones (see figure 2. (c)) which introduce a moderate level of feedback. Across the array, deformation α increases from 0.86 to 1.00 (ie an increase of Δα=0.01 from one laser to the next). (This deformation range was chosen as is provided us with the best performances). To test the impact of optical feedback on laser performances, 4 arrays where fabricated: 2 with tilted output mirrors at both ends of the membrane, hereafter called "TT" geometry, and two with a tilted output mirror at one end and a normal output mirror at the other end, hereafter called "TN" geometry.

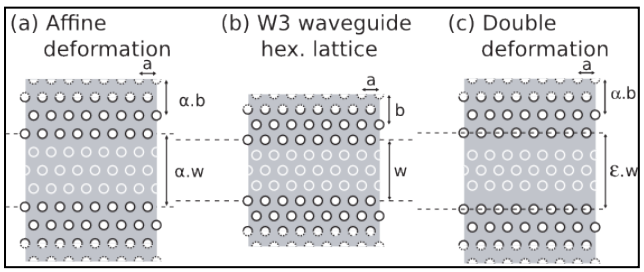


Figure 1. Geometry description: (b) undeformed W3 waveguide; (a) affine deformation; (c) double deformation

Lasers were tested under pulsed optical pumping (532nm – 10 ns – 1 KHz) and showed narrow DFB emission around 990 nm with an average pumping threshold around 500 µW.

On figure 3. , we report the difference of DFB emission wavelength between the center laser and each laser of the array as a function of the deformation used to design each laser. Arrays of the "TN" geometry (moderate feedback) are reported in (a) and arrays of the "TT" geometry (low feedback) in (b). In both (a) and (b), an overall increase of the emission wavelength across the array can be seen. However, with moderate level of optical feedback (a), several lasers are no longer single mode in particular in the range α=[0.93,0.97]. Moreover, unpredictable mode-hopping occurs and the two identical arrays TN1 and TN2 show different emission wavelengths for similar lasers. For low level of optical feedback (b), things get smoother: most the lasers remain single-mode and the wavelength dispersion around the overall trend is smaller. However, the two identical arrays still don't exhibit the same emission frequency for each laser as some lasers seem to have hoped to a different mode. Even in this favorable condition of low feedback, the behavior of the array departs from what was expected (in particular all single-mode laser array with precisely tuned emission wavelength) and in an unpredictable manner that depends on minute changes of the feedback conditions at the laser output. Wavelength difference Δλ from two identical lasers in different arrays can be as high as 2 nm.

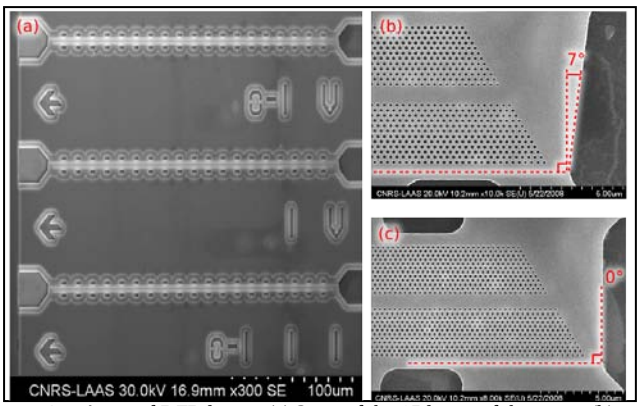


Figure 2. Array of DFB lasers: (a) 3 out of the 15 lasers of the array; (b) close-up on a tilted output mirror; (b) close-up on a normal output mirror.

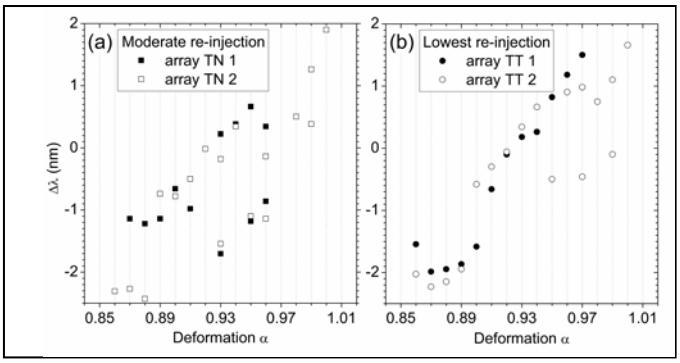


Figure 3. DFB laser arrays using affine deformation: evolution of the emission wavelength difference Δλ: (a) with one normal end introducing moderate level of feedback and (b) with two tilted ends ensuring lowest possible feedback.

III. DFB ARRAY USING DOUBLE DEFORMATION

In order to overcome the limitation of the affine deformation approach, we designed a novel approach that we called "double deformation". The main issue with affine deformation is that deformation α impacts on both the emission wavelength and the Q-factor of the waveguide. Indeed, using FDTD-3D simulations we have shown that Q goes down from $3.5x10^4$ to 10^4 across the deformation range we used[4]. The other DFB degenerated mode experiences a Q factor that stays around 10^4. The problem is twofold: the Q factor is not high enough and the discrimination between the two degenerated modes gets too small for increasing deformations. Thus we need a way to optimize both the emission wavelength and the Q-factor discrimination, which requires at least two design parameters.

In double deformation approach (see figure 1. right), affine deformation is applied to the crystal: b'=αb, but for the defect width that is scaled independently w'=εw. We rely on closed-loop optimization: first α is used to aim at a target emission wavelength, then ε is used to optimize the Q factor of the most favorable mode and last we loop over until a stationary solution is achieved.

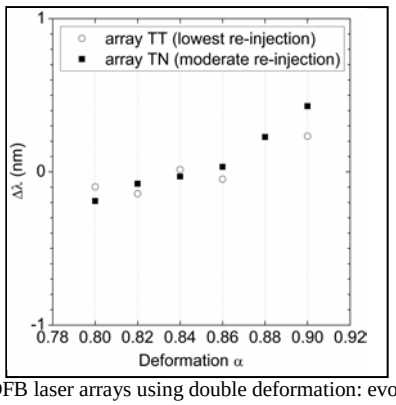


Figure 4. DFB laser arrays using double deformation: evolution of the relative emission wavelength with one normal end introducing moderate level of feedback (black squares) and with two tilted ends ensuring lowest possible feedback (white circles).

With this approach Q factors around $7x10^5$ were achieved for the most favorable mode, while the other degenerated one exhibits Q factor of around $2x10^4$. In fact, a broad optimum was found for ε=1.04 and α=0.7 to α=0.9. To demonstrate experimentally the benefits of this approach two arrays of 6 lasers each were designed and fabricated with a fixed ε=1.04 and α increasing from 0.8 to 0.9 across the array. One array uses the TN geometry for the output mirrors (moderate feedback) and one the TT geometry (low feedback). On figure 4. , we report the difference of DFB emission wavelength between the center laser and each laser of the array as a function of the deformation used to design each laser. For both geometries, ie for low feedback (white circles) and moderate feedback (black squares), the emission wavelength increases smoothly across the array. There are no major differences between the two (as opposed to affine deformation as can be seen comparing figure 3. (a) and (b)). Moreover, wavelength differences between two similar lasers stays below 0.2 nm, a tenfold improvement over affine deformation. Last, emission frequency evolution with deformation is 6 times slower than with affine deformation. This paves the way towards better frequency control and denser arrays.

IV. CONCLUSION

Here we have demonstrated that "double deformation" is an efficient way to fabricate arrays of single mode DFB photonic crystal lasers with a precise control of the emission frequency and a high robustness to optical feedback.

REFERENCES

[1] X. Checoury, et al, "Distributed feedback regime of photonic crystal waveguide lasers at 1.5 µm," Appl. Phys. Lett., vol. 85, pp. 5502-5504, 2004.

[2] O. Gauthier-Lafaye, S. Bonnefont, F. Lozes-Dupuy, D. Mulin, "Square lattice W1 waveguide photonic crystals lasers for telecommunications," Microtechnologies Conference for the New Millennium 2005, Séville (Espagne), 9-11 mai 2005.

[3] A. Larrue, et al , "Precise frequency spacing in photonic crystal DFB laser arrays," IEEE Photon.Tech. Lett., vol. 20, pp. 2120-2122, 2008.

[4] O. Gauthier-Lafaye, A. Larrue, A. Monmayrant, S. Bonnefont, F. Lozes-Dupuy, "Ultra-High Q photonic crystal waveguides for DFB laser operation," CLEO Europe, Munich (Allemagne), 14-19 juin 2009.

Widely tunable optical nanocavity photonic crystal sensor

Soon Thor Lim, Ching Eng Png
Advanced Photonics and Plasmonics
IHPC, A*Star
Singapore
limst@ihpc.a-star.edu.sg

Maoqing Xin, Aaron Danner
Dept. of Electrical and Computer Engineering
National University of Singapore
Singapore
adanner@nus.edu.sg

Abstract— **A large peak shift of 12 nm is reported from a silicon-on-insulator waveguide with photonic crystal filter. With high Q and 10dB modulation depth, fast and accurate sensing may be possible.**

Keywords-photonic bandgap, sensing, modulators

I. INTRODUCTION

Optical sensing often relies on the detection of a small change in refractive index, usually caused by a fluid or gas passing through an optical resonator, or a small change in absorption. Photonic crystals-based sensors are often plagued by the inability to fabricate photonic crystals with resonance peaks that are reproducible run-to-run. In this presentation, we show that adding a small amount of electrical tunability (with low power consumption) can both allow active correction for fabrication errors—a sort of way to calibrate away fabrication errors—and allow sensing at multiple wavelengths or even to scan through a series of wavelengths. With as much as a 12 nm tuning range for a single resonator, multiple resonators could be arrayed to achieve broadband tunability.

II. DEVICE CONFIGURATION

Fig. 1 shows an optical nanocavity sensing device that can be scalable to include array of sensors that are formed by photonic bandgap structures. Although a passive device is shown, active devices could just as easily be incorporated into the device as will be described. Two possible structures are discussed; first a one dimensional (1-D) periodic air hole similar to [1-2], where the local defect inside the photonic crystal leads to highly confined optical states, such structure are optimized for large peak shift with low power consumption. Second, a cross waveguide resonator, where two identical one dimensional (1D) subwavelength Fabry –Perot (FP) waveguide resonators [3] are configured perpendicular to each other to form a microcavity at the central intersection, therefore optimized for device speed through a more efficient carrier injection scheme as compared to a single FP waveguide resonator approach.

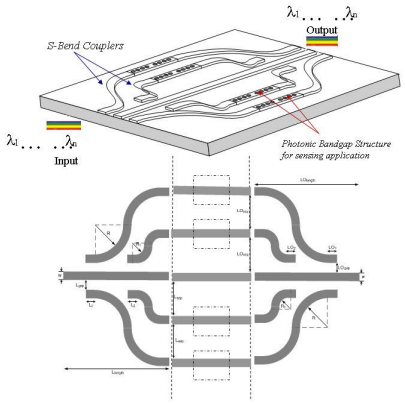


Fig. 1 Schematic diagram of a passive nanocavity sensor suitable for multiple sensing applications

III. 1-D PHOTONIC BANDGAP FOR OPTIMIZED PEAK SHIFT

An optical nanocavity is configured by using a rib waveguide of 470 nm width and an optimized etch depth of 180 nm with an ultra-thin silicon slab layer of 23 nm as shown in Fig. 2 with five etching air-holes on both sides of the structure creating a central defects. Such configuration reduces the doping volume and more significantly, reduces the total number of injected free carriers, whilst maintaining sufficient modal overlap thus allows the reduction in power consumption without sacrificing the modulation depth. The device is a two terminal *p-i-n* structure where both *n* and *p* regions were modeled using ATLAS device simulation package from SILVACO, as highly doped regions with constant doping concentrations of 10^{20} cm^{-3}.

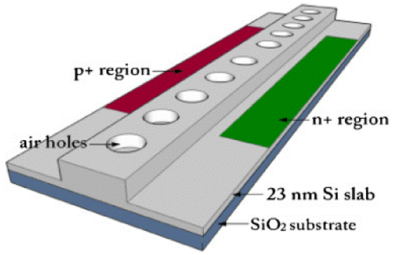


Fig. 2 3D schematic of 1D photonic bandgap nanocavity with p+ and n+ doping region

The device is biased at various voltage points as shown in Fig. 3. It can be noted that the rise and fall times are approximately 6.2 ns and 3.8 ns which is suitable for fiber to the home (FTTH) and sensing applications. The level of carrier concentration is converted to its equivalent optical properties, e.g. refractive index change and absorption coefficient for optical characterization. Fig. 4 shows the relationship of power density between resonance peak-shift and modulation depth, where the power density, P_{DC} is defined as:

$$P_{DC} = V_{bias} I \quad (1)$$

where V_{bias} is the bias voltage and i is the current density. Therefore, from figs. 3 and 4, a 10dB modulation depth at a power of 186 µW/µm with a large peak shift of 12nm is expected. This peak shift is an order of magnitude larger than what was reported in [4].

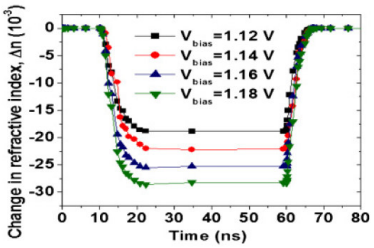


Fig 3 Transient characteristic of the photonic bandgap at different bias voltages.

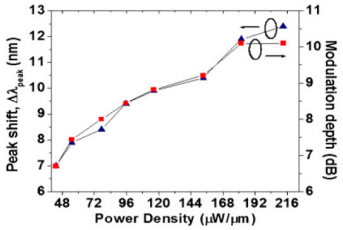


Fig. 4 Relationship between resonance peak shift, modulation depth and power density

IV. CROSS WAVEGUIDE RESONATOR FOR OPTIMIZED DEVICE SPEED

Alternative configuration for optimized device speed can be achieved by creating an optical nanocavity at the intersection of two identical 1D photonic bandgap structures know as a cross waveguide resonator. A localized transverse-electric (TE) mode is allowed due to the central defects of the 1D photonic bandgap and the two opposite branches are partially doped with p+ and n+ regions so that a transverse p-i-n diode is embedded into the cross waveguide as shown in fig. 5. It can be observed from fig. 6 that the bias voltage and the drive current decrease with increasing carrier concentration, hence allowing the same modulation depth with a lower power consumption. However, optical absorption increases with increased dopant concentration. At a concentration level of 4 x 10^{19} cm^{-3}, the optical loss is at 1.68 dB. The transient refractive index change of the nanocavity is shown in fig. 7. The voltage is varied from 1.22V to 1.8V. A modulation speed of 2.9 GHz is expected when the bias voltage is at 1.65V, DC power consumption of 17.3 mW, with a 3dB frequency around 4 GHz.

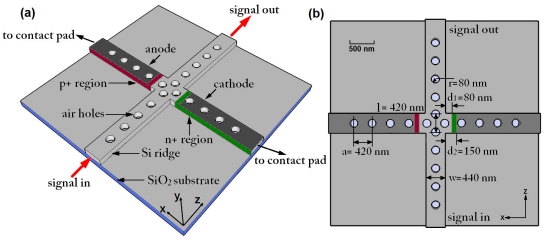


Fig. 5 (a) 3D schematic of the cross waveguide resonator based modulator; (b) top view of the device with notations of the optimum device dimensions.

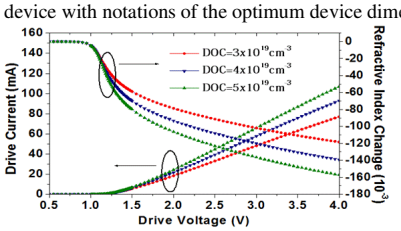


Fig. 6 I-V characteristics of the p-i-n diode shows a lower bias voltage is needed to achieve the same RI change for higher doping concentrations

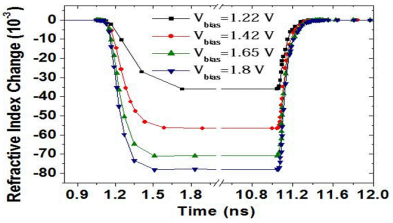


Fig. 7 DC and transient characteristics of the device performance: the relationship between modulation depth, peak shift and power consumption

V. CONCLUSIONS

Our results suggest that very small photonic crystal structures can be placed in an arrayed on-chip environment for broadband active sensing.

ACKNOWLEDGMENTS

A research grant from Singapore's Ministry of Education is acknowledged.

REFERENCES

[1] J. S. Foresi, P. R. Villeneuve, J. Ferrera, E. R. Thoen, G. Steinmeyer, S. Fan, J. D. Joannopoulos, L. C. Kimerling, H. I. Smith, and E. P. Ippen, "Phonotic-bandgap mocrocavities in optical waveguides," *Nature*, vol. 390, pp. 143-145, 1997.

[2] C. E. Png, S. T. Lim, E. P. Li, and Graham. T. Reed, "Tunable and sensitive biophotonic waveguides based on photonic-bandgap microcavities," *IEEE Trans. on NanoTechnol,*. vol. 5, no. 5, pp 478-484, 2006.

[3] N. Moll, R. Harbers, R. F. Mahrt, and G.-L. Bona, "Integrated all-optical switch in a cross-waveguide geometry," Appl. Phys. Lett., vol. 88, 171104, 2006.

[4] B. Schmidt, Q. Xu, J. Shakya, S. Manipatruni, and M. Lipson, "Compact electro-optic modulator on silicon-on-insulator substrates using cavities with ultra small modal volumes", *Optics Express*, vol. 15, no. 6, pp. 3140-3148, 2007.

All-Optical Tunable Photonic Crystal Cavity

Minhao Pu, Liu Liu, Haiyan Ou, Kresten Yvind, and Jørn M. Hvam
DTU Fotonik, Photonics Engineering Department
Technical University of Denmark
Lyngby, Denmark
mipu@fotonik.dtu.dk

Abstract—**We demonstrate an ultra-small photonic crystal cavity with two resonant modes. An all-optical tuning operation based on the free-carrier plasma effect is, for the first time, realized utilizing a continuous wave light source. The thermo-optical effect is minimized by isopropanol infiltration of the photonic crystal structure.**

Keywords-All-optical devices; integrated optical devices; microcavity devices; photonic crystal.

I. INTRODUCTION

Photonic crystal (PhC) cavities, which offer high quality factors (Q) and small modal volumes (V), have been used in many applications including ultra-small filters, low-threshold lasers, photonic chips, nonlinear optics and optical information processing [1]. Recently, an all-optical switch based on a PhC cavity with two resonant modes has been demonstrated [2],[3]. Typically, a four-hole defect (L4) cavity is necessary to support two resonant modes. Here we demonstrate a PhC cavity with only three missing holes (L3) supporting two resonant modes. The smaller cavity mode volume makes it more suitable for this application due to the enhanced light confinement. In this paper, we experimentally demonstrate all-optical tuning of the proposed photonic crystal cavity based on the plasma effect from free carriers generated by two-photon absorption (TPA).

II. DESIGN

Fig. 1(a) shows a schematic of the proposed structure consisting of a triangular-lattice of air holes with a line-defect (W1) waveguide and an L3 cavity. The dispersion diagram for the structure is shown in Fig. 1(c). Here we investigate the waveguide band in two spatial regions (waveguide region and cavity region). The solid lines are the bands for the W1 waveguide region and the upper blue one shows the waveguide mode within the band-gap. Since the L3 cavity is of the size of the light wavelength, only one resonant mode is supported within the pass band of the W1 waveguide. This mode can be seen as a dip in the transmission spectrum (the upper dotted line in Fig. 1(c)). On the other hand, the cavity region can also be considered as two coupled W1 waveguides. The band of such a coupled waveguide structure is plotted as the two blue dashed lines illustrated in the dispersion diagram (see Fig. 1(c)). One can see that the waveguide modes are different from those of a single W1 waveguide. In this case, photons with a specific frequency can only exist in the cavity region due to the mode-gap (MG) effect [1]. Thus, the frequencies that photons can take in this cavity region become quantized due to the short

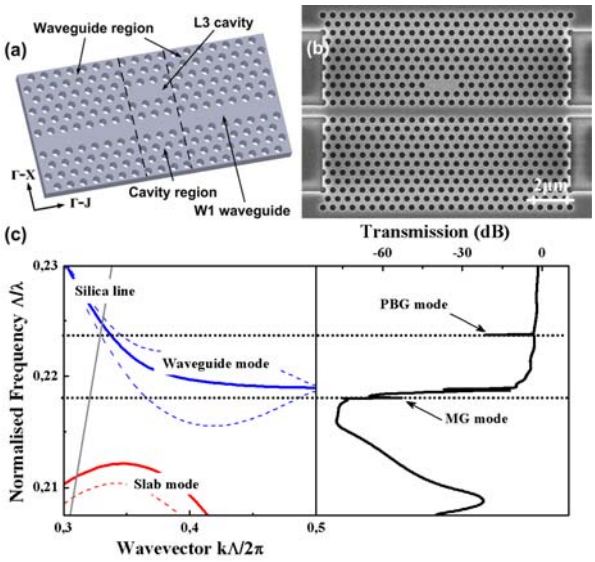


Figure 1. (a) Schematic of the L3 based PhC cavity. (b) SEM picture of the fabricated structure. (c) (Left) Dispersion diagram for the PhC structure in waveguide region (solid lines) and the cavity region (dashed lines). (Right) Simulated transmission for the proposed structure.

length of the cavity region in the Γ-J direction. Therefore, another resonant mode is formed below the cut-off frequency of the W1 PhC waveguide as the lower dotted line shown in Fig. 1(c).

III. EXPERIMENT

The photonic crystal structure is fabricated in silicon-on-insulator (SOI) material with a top silicon thickness of 340nm and a 1-μm buried silicon dioxide (see Fig. 1(b)). The lattice constant of the structure is 380nm and the diameter of the holes is 220nm. The length of the whole PhC structure is 10μm. Fig. 2(a) shows the measured transmission spectrum of the fabricated structure for the TE mode. As we expected, there is one notch above the cutoff frequency due to the PBG effect of the L3 cavity, which is denoted as PBG mode in Fig. 2(a). One can also find that there is one peak below the cutoff frequency. This is the resonant mode (MG mode) due to the MG effect. The loaded Q factors for the two modes are 11,000 and 8,800, respectively. The Q factors are comparable to the cavity used for all-optical switching in [2], but V is smaller in our L3 cavity, which makes it possible to further reduce the operation power in the all-optical switch and memory applications since the operation energy scales as V/Q^2 in the device.

This work was supported by the Danish Strategic Research Council via the NANO·COM project.

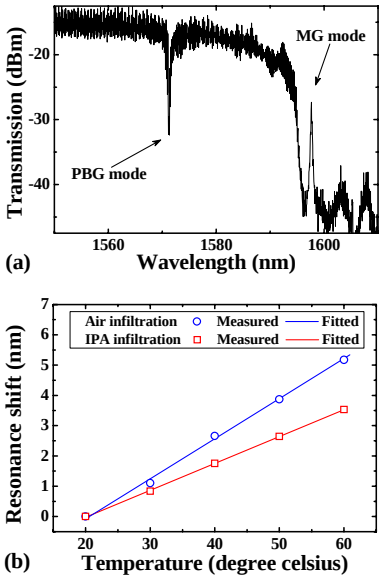


Figure 2. (a) Measured transmission spectrum of the fabricated structure (b) Measured resonance shift with different temperature for different infiltrations.

In the above measurement, the optical power was kept low during the wavelength sweeping of a tunable laser to avoid any nonlinear effect in the cavity. When the light intensity in the cavity increases, the enhanced light-matter interaction will result in TPA. The free carriers generated by TPA induce a decrease of the refractive index. However, TPA also introduces heat, and the thermo-optical (TO) effect increases the refractive index of silicon. Normally, the TO effect dominates over the plasma effect. Thus, to observe the carrier effect, an ultra-short pulsed light source is needed to avoid the slow thermal effect (in the order of a microsecond) [4]. The carrier effect can induce optical bistability in the cavities which has been demonstrated for many applications including optical switching, memory and fundamental logic functions, such as a flip-flop. However, the TO effect prevents the carrier-induced bistability from operating at steady state. Typically, the holding time for the steady state is less than 10ns [4]. This hampers the applications mentioned above. Since the TO coefficient of Si material is positive, infiltration for the air holes of the PhC cavity with a liquid of a negative TO coefficient can be used to reduce the temperature dependence of the PhC cavity [5]. In our experiment, the PhC holes were infiltrated with isopropanol (IPA). Fig. 2(b) shows the resonance (PBG mode) shift with temperature before and after the IPA infiltration. It is seen that the temperature dependency of the resonance has been decreased after the infiltration, which would make the carrier effect dominate as shown below in the measurement results.

To achieve all-optical tuning, we choose the PBG mode for the control wavelength and MG mode for the signal wavelength. As the light intensity at the PBG mode increases in the cavity, the TPA-induced free-carrier effect will change the refractive index of cavity which also affects the resonance wavelength of the MG mode. In our experiment, one laser with fixed wavelength at 1570.8nm was used as the control light. The intensity of the light was controlled by a combination of an

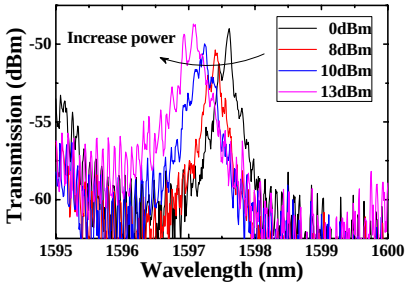


Figure 3. Measured resonance blue-shift of the MG mode with different input power for the PBG mode.

optical amplifier and an attenuator. Another tunable laser with a low power was used to sweep wavelength around the MG mode. Fig. 3 shows the measured resonance shift for the MG mode. A clear blue-shift of 1nm is observed by applying 13dBm input power, which is an evidence of the dominant carrier effect induced by TPA in the proposed device since the TO effect results in a resonance red-shift. To our knowledge, this is the first experimental demonstration of all-optical tuning by carrier effect for a silicon PhC cavity using a continuous wave (CW) laser source. This will make it more practical to utilize the carrier-based bistability in some applications. Though the required power to realize the carrier-based all-optical tuning for the device using CW laser is relatively high, the problem can be resolved by using ultra-high Q factor L3 cavity [6].

IV. CONCLUSION

We have demonstrated a PhC L3 cavity supporting two resonant modes with ultra-small V. It is also demonstrated that the temperature dependence of the device could be reduced by infiltrating the air hole with isopropanol. By minimizing the thermo-optical effect, we experimentally demonstrated all-optical tuning operation for the PhC cavity by the plasma effect of free carriers induced by TPA. This is the first experimental demonstration, to our knowledge, of carrier-based all-optical tuning using a CW laser source. We believe that the device is of potential use for many applications including all-optical switching, memory and fundamental logic functions.

REFERENCES

[1] B. Song, S. Noda, T. Asano, and Y. Akahane, "Ultra-high-Q photonic double-heterostructure nanocavity," Nat Mater, vol. 4, Mar. 2005, pp. 207-210.

[2] T. Tanabe, M. Notomi, S. Mitsugi, A. Shinya, and E. Kuramochi, "Fast bistable all-optical switch and memory on a silicon photonic crystal on-chip," Optics Letters, vol. 30, Oct. 2005, pp. 2575-2577.

[3] M. Notomi, A. Shinya, S. Mitsugi, G. Kira, E. Kuramochi, and T. Tanabe, "Optical bistable switching action of Si high-Q photonic-crystal nanocavities," Optics Express, vol. 13, Apr. 2005, pp. 2678-2687.

[4] Q. Xu and M. Lipson, "Carrier-induced optical bistability in silicon ring resonators," Optics Letters, vol. 31, Feb. 2006, pp. 341-343.

[5] C. Karnutsch, C.L.C. Smith, A. Graham, S. Tomljenovic-Hanic, R. McPhedran, B.J. Eggleton, L. O'Faolain, T.F. Krauss, S. Xiao, and N.A. Mortensen, "Temperature stabilization of optofluidic photonic crystal cavities," Applied Physics Letters, vol. 94, Jun. 2009, pp. 231114-3.

[6] Y. Akahane, T. Asano, B. Song, and S. Noda, "Fine-tuned high-Q photonic-crystal nanocavity," Optics Express, vol. 13, Feb. 2005, pp. 1202-121.

Ultra-sharp edge filtering in nanotethered photonic wire

A.Talneau, I. Sagnes
CNRS-Laboratoire de Photonique et de Nanostructures, F- 91460 Marcoussis
Corresponding author : anne.talneau@lpn.cnrs.fr

Abstract : An InP-based photonic wire including periodically spaced nanotethers can demonstrate a complex resonant behaviour leading to an ultra-sharp filter edge. This coupled resonant mechanism is investigated mainly experimentally but also with first theoretical views.

Keywords: Optical waveguide filters, coupled resonators, photonic wires, suspended membrane

I- Introduction

Optical filtering is a key function in all-optical networks. Simultaneously to a large –at least 20dB– rejection, the highest sharpness is desired for a very selective spectral response. Additionally, such a reflector can be used in optical modulation or switches. Ring resonators based filters have been extensively investigated, and in such an environment, filters can be custom-designed implementing a large number of coupled ring resonators [1,2]. A very sharp edge filter has also been proposed in a photonic crystal –PhC- environment, including phase-shift elements aside the PhC waveguide [3].

We propose here and demonstrate, both theoretically and experimentally, that a photonic wire including regularly spaced nanotethers can behave as a reflector exhibiting a very sharp band-edge.

II- Simulation

A photonic waveguide including a periodic perturbation exhibits a transmission stop-band – forbidden frequency range – due to the in-phase feedback contribution coming from all the grating elements, the well-known Distributed Bragg Reflector (DBR) effect.

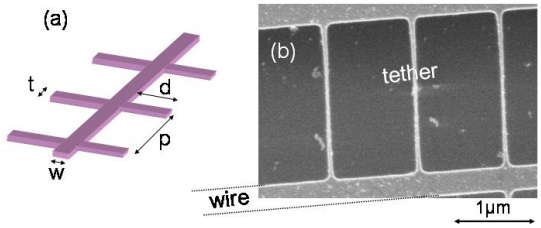


Fig.1: (a) schematic of the tethered wire
(b) SEM picture of a suspended wire (period p=1 µm, tether length d=2µm, wire width w=0.3 µm)

The stop-band width is determined by the feedback strength, and the stop-band edge sharpness is determined by the overall grating shape. On this basis, addition of dissipative elements damps the filter shape while, on the contrary, reactive elements sharpen it.

In our case, the photonic wire is suspended in air through regularly spaced nanotethers (fig.1-a). These nanotethers operate as a Bragg reflector. Furthermore, for a specific wavelength, each tether operates as a weak reactive element that can be viewed as a resonator or a stub : the tethers are transverse waveguides with a sizable reflection at their ends (Fig.1b). The photonic wire is coupled to the series of all these stubs.

We have simulated the spectral response generalizing the archetypal model proposed by S. Fan for the increased sharpness of a side-coupled waveguide-cavity system arising when including a partially reflecting element in the waveguide [4].
In our case, the reflecting element is the cross section between the tether and the wire, and the resonant cavity is the tether itself.

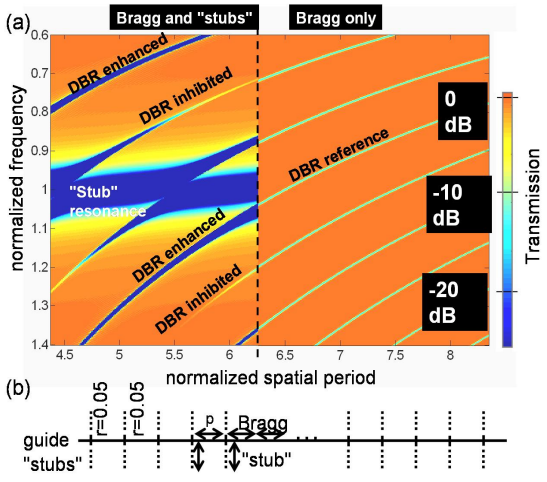


Fig.2 : (a) Calculated transmission (colour scale) versus frequency and tether period p. Each reflector features r=0.05. See text. (b) Sketch of the multiple cavity+stub arrangement.

We have extended the calculation including 36 cavities and as many coupled elements (Fig.2b). We have plotted on Fig.2 the calculated transmission (colour scale) versus the frequency and spatial period which is the distance between tethers. The usual frequency gaps due to the Bragg effect alone are plotted on Fig.2-a right. The abscissa is equivalent to period *p*.

We see on Fig.2-a left the transmission when both the DBR effect due to the periodic reflectors and the resonance in each stub take place: a large frequency gap is visible additionally to the narrow gaps due to the low reflectivity of the crossing sections set to r=0.05. Additionally, as for the single cavity case [4], the depth of the DBR dip is much enhanced even far from the stub resonance, and its edge is also sharper (detail not shown). For this simulation, every other Bragg resonance is "enhanced", and the other one is "inhibited", likely for symmetry reasons.

III- Experiments

Suspended tethered wires have been fabricated on a 260 nm thin suspended InP membrane. An established process based on ICP etching of the nanopatterns followed by a selective etching of the sacrificial layer and a super critical drying is used [5], see Fig.1-b. Investigated parameters are the following: wire width *w*= 0.3, 0.4 and 0.6 µm, tethers spacing *p*=1 or 2 µm, tethers length *d*= 1 to 2 µm, tethers width *t*= 40 to 100 nm. Closely spaced tethers have been chosen for a single transmission dip in the measured 1410-1620 nm wavelength domain. Measurement of 680-µm-long photonic wires are performed on an end-fire fibre set-up including a polarisation-maintaining tuneable source in TM-like polarisation (E vertical), and plotted in Fig.3 for two selected cases. Transmission in case (a), when p = 1µm is smaller than the one in case (b) where p = 2µm, because the number of tethers is twice larger, thus leading also to higher propagation losses.

The spectral dip shape is qualitatively in agreement with the trends of S.Fan work [4] (Fig.2), but more firm connections have to be established as the stub resonance is not evidenced in the limited experimental spectral range. Reducing the wire width gives rise to a dip with a larger spectral width and a sharper edge, because the overlap of the swollen field profile with the tether is larger. Inversely, going to wider wires w>0.4 µm was found to lead to the disappearance of the coupled resonant effect.

Additional structures are currently investigated.

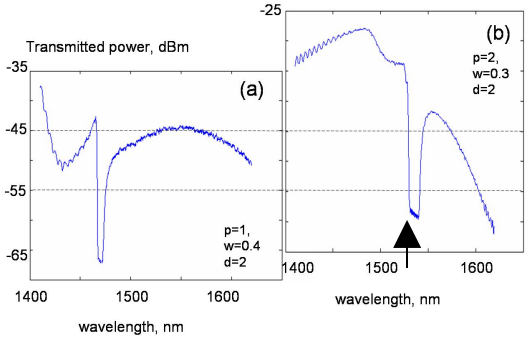


Fig.3 : Measured transmission for tethered wires ;
(a) in the case of p=1µm, w=0.4µm, d=2µm and t=70nm
(b) in the case of p=2µm, w=0.3µm, d=2µm and t=70nm. The falling edge (arrow) drops by 14 dB in a 1 nm span at 1529 nm.

Conclusion

We have experimentally evidenced that a photonic wire including regularly spaced nanotethers on both sides exhibit sharp edges in its transmission spectrum that we attribute to a complex coupled–resonator behaviour, reminiscent of both "all-pass" and "coupled-optical-resonator waveguide" behaviours. We propose that the resonance takes place in each tether much like in a stub, and all resonators are coupled through the waveguide wire. We will report more in detail on the parametric range, notably the wire widths and the tethers cross sections, for which this effect is best observed.

References

[1] D.G. Rabus, M. Hamacher, U. Troppenz, and H. Heidrich, "Optical filters based on ring resonators with integrated semiconductor optical amplifiers in GaInAsP-InP" IEEE Journal of Selected Topics in Quantum Electronics, Vol. 8, pp.1405-1411; Nov/Dec 2002 .

[2] B. E. Little, S. T. Chu, P. P. Absil, J. V. Hryniewicz, F. G. Johnson, F. Seiferth, D. Gill, V. Van, O. King, and M. Trakalo, "Very High-Order Microring Resonator Filters for WDM Applications", vol.16, pp.2263-2265 (october 2004)

[3] Chao Chen, Xuechun Li, Hanhui Li, Kun Xu, Jian Wu, and Jintong Lin , "Bandpass filters based on phase-shifted photonic crystal waveguide gratings", Opt. Express, vol.15, pp.11278-11284 (2007).

[4] S. Fan, "Sharp asymmetric line shapes in side-coupled waveguide-cavity systems", Appl. Phys. Lett., vol. 80, pp. 908-910 (2002).

[5] A. Talneau, K.-H. Lee, S. Guilet, I. Sagnes "Efficient coupling to W1 photonic crystal waveguide on InP membrane through suspended access guides" Appl. Phys. Lett. vol. 92, pp. 061105 (2008).

Surface mounted tapered vertical Coupler for photonic Nanowires

O. Horn, T. Lipka, J. Amthor, J. Mueller
Hamburg University of Technology, Department of Microsystems Technology
Eissendorfer Strasse 42, 21073 Hamburg, Germany
Email: o.horn@tuhh.de

***Abstract*—A vertical nanowire coupler enables incoupling of Vertical-Cavity Surface-Emitting Lasers (VCSEL) into silicon photonic nanowires and connects electronic and photonic devices on the same substrate.**

I. Introduction

Single mode, high refractive index contrast silicon photonic wires offer small bending radii high integration density on a chip. High data rates on CMOS-CPU can be achieved due to the absence of electric interference. Typical dimensions for single mode waveguides with an oxide cladding are 220nm times 600nm, the losses are in the range of 2 dB/cm, but only a few millimetres are required for on chip systems.

An efficient coupler for the interface between the electric signal and the photonic wire is the key feature for the photonic integration on CMOS-CPUs. Grating couplers e.g. show coupling losses of less than 3 dB, but they need a certain angle of incidence (often 10°) to insert the light without any reflections [1]. Since the wavelength range of gratings is limited as well, they have to be designed carefully to fit the bandwidth windows of other wavelength selective components. Filters showing production tolerances may run out of the coupler's bandwidth window. Coupling into cleaved wave guides ("endfire") overcomes those limitations, but a cleaved sidewall of the chip is required. The distance from the fiber to the system may be long, leading to increased costs (due to a higher demand of area) and higher signal losses. The number of "endfire"-couplers per chip depends on the edge length, which grows linearly, while the area grows quadratically.

In general, the output mode of an optical fiber or a semiconductor laser does not match the nanowire mode. In inverse tapers [2] the mode is enlarged, when the waveguide dimensions becomes smaller than the wavelength inside the material. These inverse tapers are short (a few 10 μm) in comparison to conventional adiabatic tapers, but an additional polymer wave guide is needed to guide the light exactly to the inverse tapers[3]. The critical aligment is done in the photolithography.

In this paper a 45°-mirror turns perpendicular irradiated light, which can be placed everywhere on the chip surface, into a polymer wave guide. An inverse taper couples the light from the polymer waveguide into a silicon nanowire.

II. Design and Fabrication

DUV (248 nm wavelength) contact lithography is used to fabricate the photonic wires. The wave guides are additionally smoothed and shrunk by thermal oxidation. This shrinkage enables the fabrication of very small tip widths (<50 nm) for the inverse tapers, having larger sizes (> 300 nm) on the mask. The fabrication steps are shown in fig. 1. A more detailed description is given in [4]. The topside of the waveguide is protected by a LPCVD-TEOS (Tetraethyl orthosilicate) silica to reduce unwanted height loss during oxidation. After DUV-lithography an anisotropic ICP-oxide and ICP-silicon etch is used for structuring. After photoresist removal, a low loss silicondioxide cladding is built up by thermal oxidation. The oxidation temperature is 1100 ° C in a dry process using 3 l/min pure O_2.

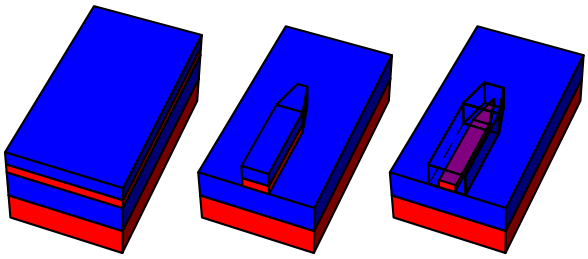


Fig. 1. Wave guide and inverse taper fabrication steps: TEOS deposition, lithography and TEOS/Silicon etch, thermal oxidation

The further fabrication steps are shown in fig. 2. The lithography for the mirror fabrication is done by a collimated laser beam with a wavelength of 405 nm and a power of 50 mW, which can irradiate the substrate under

angles from 10° to 90°. For this design, an angle of 45° is chosen. A 200 nm thick aluminium layer was sputtered as a mirror, using a low power process to avoid thermal damage to the photoresist. I-line contact lithography and wet chemical etch were used to remove the aluminium from the substrate except the mirror and the contact plane for the VCSEL. The photoresist on top of the aluminium is removed by an oxygen-plasma, while the photoresist beneath is protected by the aluminium. The polymer for the connection wave guide is spun on with a thickness of 2 μm. A negative photoresist (SU-8-2) is used, because it has low absorption at 1550 nm [5] and can be structured by I-line contact lithography. The system is completed and a VCSEL or a fiber can be applied.

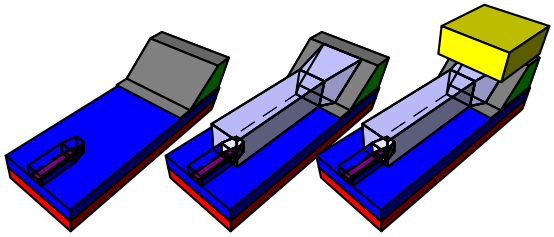


Fig. 2. Mirror and polymer wave guide fabrication steps: 45°-lithography and aluminium (sputtered and structured), SU-8 lithography, VCSEL application

III. Simulation

Fig.3 shows a cross section SEM-picture of the 45° mirror with a polymer spun on. Using this cross section a FEM-simulation is done, which is shown in fig.3. The simulation results in fig. 4 show only a few percent change in coupling efficiency over a 100 nm wavelength band, which is more than a grating coupler can achieve. The VCSEL or fiber has to be positioned in a 1.5 μm range in propagation direction.

IV. Conclusion

In this paper a short, broadband and polarization independent vertical coupler is described. A misalignment up to 1.5 μm does not change the coupling efficiency. The coupling efficiency can even be improved with an optimization of the mirror angle and thicknesses. The measurements are currently under investigation and will be presented at the conference.

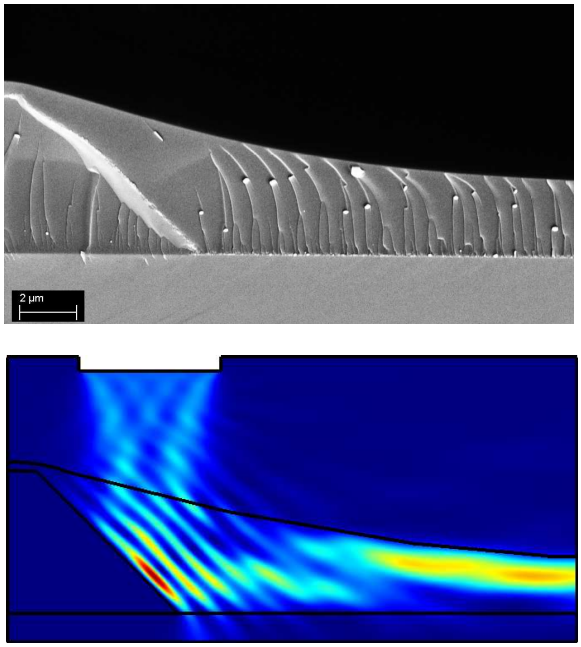


Fig. 3. a) SEM-Picture of a cross section through the mirror, b) a FEM-simulation (time-average powerflow is shown)

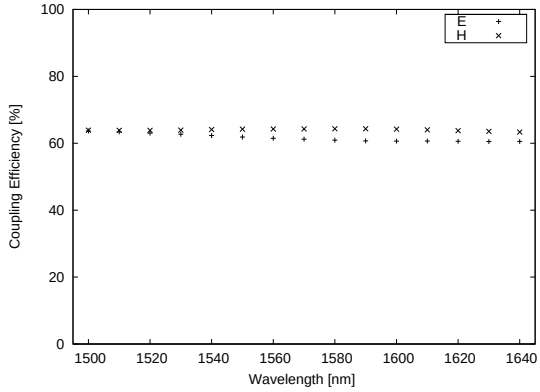


Fig. 4. Simulation results: Wavelength dependancy of coupling efficiency

References

[1] D. Taillaert, W. Bogaerts, P. Bienstman, T. Krauss, I. Moerman, P. Van Daele, and R. Baets, "An out-of-plane grating coupler for efficient butt-coupling between compact planar waveguides and single-mode fibers," *IEEE Journal of Quantum Electronics*, vol. 38, no. 38, pp. 949–955, July 2002.

[2] V. R. Almeida, R. R. Panepucci, and M. Lipson, "Nanotaper for compact mode conversion," *Optics Letters*, vol. 28, no. 15, pp. 1302–1304, August 2003.

[3] T. Shoji, T. Tsuchizawa, T. Watanabe, K. Yamada, and H. Morita, "Low loss mode size converter from 0.3 μm square si wire waveguides to singlemode fibres," *Electronics Letters*, vol. 38, no. 25, pp. 1669–1670, 2002.

[4] O. Horn, J. Amthor, T. Lipka, and J. Müller, "Tunable silicon photonic wires fabricated by contact lithography and thermal oxidation," in *Microtechnologys for the new Millenium*, A. Serpenguzel, Ed., vol. 7366, no. 1. SPIE, 2009, p. 73660C. [Online]. Available: http://dx.doi.org/10.1117/12.821694

[5] M. Nordstrom, D. A. Zauner, A. Boisen, and J. Hubner, "Single-mode waveguides with su-8 polymer core and cladding for moems applications," *Lightwave Technology, Journal of*, vol. 25, no. 5, pp. 1284–1289, May 2007.

Photonic crystal filter integrated with photodiodes

W. Y. Chiu, Y. H. Wu, Y. J. Chan
Department of Electrical Engineering
National Central University
Jhongli 320, Taiwan

Chia-Hung Hou, Hung-Ta Chien, Chii-Chang Chen*
Department of Optics and Photonics
National Central University
Jhongli 320, Taiwan
trich@dop.ncu.edu.tw

Abstract—**We demonstrate the monolithic integration of photonic crystal waveguides, a photonic crystal demultiplexer, a conventional waveguide and photodiodes in InGaAsP-based material. The photonic crystal demultiplexer consists of hexagonally arranged air holes. The inputted light at the wavelengths of 1530nm and 1550nm can be separated by the demultiplexing system.**

Keywords-component; Photonic crystals; filter; photodiodes; waveguides

I. INTRODUCTION

The photonic bandgap (PBG) effect of PC provides the highly confined mode needed to be control the propagation of the light. Due to their nanometer feature size, the device packing density can be increased. PC-based devices are potentially integrated into a monothilic material with electronic devices which are in nanometer scale. Several PC devices have been developed such as directional couplers[1], ring resonators[2], hollow waveguides[3], laser[4], lenses[5], etc. To integrate these devices, the fabrication process including the conventional pthotolithography and the e-beam lithography should be utilized for the patterns of micrometer and nanometer scales, respectively. In this study, we realize the integrated nano-optics system consisting of a PC demultiplexer which separates the incoming light of the wavelengths at 1530nm and 1550nm, a PC taper coupler, PC waveguide as well as two photodiodes for the detection of the light.

II. DEVICE DESIGN AND FABRICATION

InGaAsP-based materials are chosen for the fabrication of the device to obtain high absorption efficiency at the operating wavelengths. The refractive index of the guiding material is designed to be higher than that of the cladding layer to obtain the vertical confinement in the input/output conventional slab waveguides. For the photodiodes, the partially p-doped photo-absorption layer is adopted to accelerate the diffusion of the electron form absorption layer to the depletion layer [6]. The PC demultiplexer is formed by periodically arranged air-holes in hexagonal lattice. The radius is chosen to be 0.33a. The normalized frequency of the complete photonic bandgap is between 0.2 and 0.3. The normalized frequency of 0.24 is chosen for the wavelength at 1.55μm. The corresponding lattice constant and radius of the air-holes are 0.375μm and 0.125μm, respectively. The corresponding photonic bandgap in wavelength is between 1.25μm and 1.875μm. This result confirms that the operating wavelengths at 1.53μm and 1.55μm are in the photonic bandgap. The sample is grown by metal-organic-chemical-vapor-deposition (MOCVD) on a semi-insulating InP substrate. The conventional waveguide and the photodiodes are fabricated by the conventional photolithography processes. The pattern of the PC region is defined onto the photoresist by electron-beam lithography. The inductively coupled plasma (ICP) etcher was used to transfer the PC patterns into the InGaAsP layers to form the PC waveguides and demultiplexer. PC taper couplers are used between the conventional waveguides and the PC waveguides to reduce the coupling loss. Figure 1 shows the scanning electron microscope images of the systems including the conventional waveguide, PC taper coupler, PC waveguides, PC demultiplexer and photodiodes

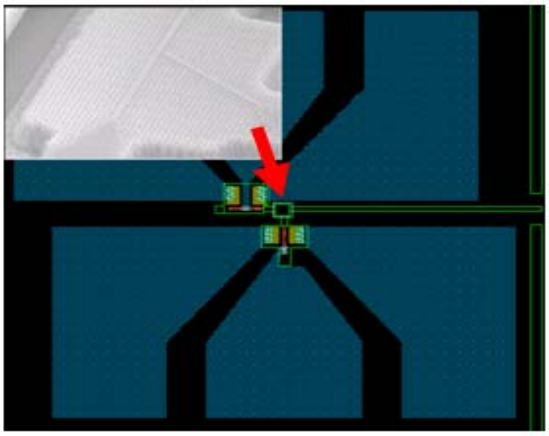


Figure 1. Layout of integrated nano-optics system. The inset is the PC demultiplexer.

III. MEASUREMENT RESULTS

A tunable semiconductor laser with its power of 0dBm is used as the light source. The input light is polarized in the TE mode. The wavelength of the input light is scanned from 1.52μm to 1.57μm. Figure 2 shows the measured photocurrent ratios between two photodiodes. From the measured result, we can observe that the PC demultiplexer can successfully separate the different wavelengths. The photocurrent ratio is 3.2 (5dB) and 3.8 (5.8dB) for the photodiodes of 1530nm and 1550nm, respectively.

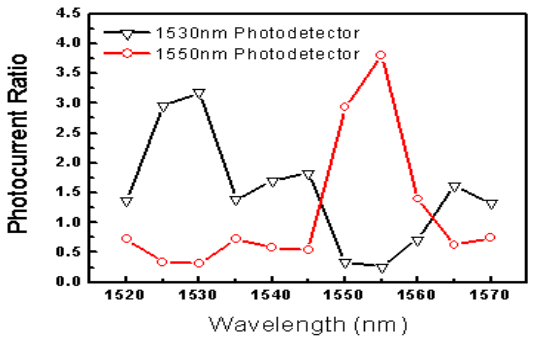


Figure 2. Response spectra measured from photodetectors.

The bandwidth of the photodiode is measured with a heterodyne beating system which the optical signal is generated by mixing two tunable lasers with different wavelength into a 3-dB coupler and through the lensed fiber with a diameter of 2.5μm. The result shows that the electric-bandwidth performance is achieved about 25GHz.

IV. CONCLUSIONS

In this work, we demonstrate an integrated nano-optics system consisting of conventional waveguide, PC taper coupler, PC waveguide, PC demultiplexer and partially p-doped photodetector. The results show that the system can separate the wavelengths at 1.53 and 1.55μm simultaneously for the wavelength division multiplexer application with a bandwidth of 25GHz. By introducing a PC laser source in the system, a complete optical communication system can be achieved in a chip for the application of optical computing.

[1] Chii-Chang Chen, Chih-Yu Chen, Wen-Kai Wang, Fan-Hsiu Huang, Cheng-Kuo Lin, Wei-Yu Chiu, Yi-Jen Chan, "Photonic crystal directional couplers formed by InAlGaAs nano-rods," Opt. Express, vol. 13, pp. 38-43, January 2005.

[2] Wei-Yu Chiu, Tai-Wei Huang, Yen-Hsiang Wu, Yi-Jen Chan, Chia-Hung Hou, Hung-Ta Chien, Chii-Chang Chen, “A photonic crystal ring resonator formed by SOI nano-rods,” Optics Express, vol. 15, pp. 15500-15506, November 2007.

[3] Hua-Kung Chiu, Fu-Li Hsiao, Chia-Hua Chan, Chii-Chang Chen, “Compact and low-loss bent hollow waveguides with distributed Bragg reflector,” Optics Express, vol. 16, pp.15069-15073, September 2008.

[4] Li-Ming Chang, Chia-Hung Hou, Yu-Chen Ting, Chii-Chang Chen, Che-Lung Hsu, Jenq-Yang Chang, Chien-Chieh Lee, Guan-Ting Chen, Jen-Inn Chyi, "Laser emission from GaN photonic crystals," Appl. Phys. Lett., vol. 89, pp. 071116-071119, August 2006.

[5] Hung-Ta Chien, Chii-Chang Chen, “Focusing of electromagnetic waves by periodic arrays of air holes with gradually varying radii,” Opt. Express, vol. 14, 10759-10764, October 2006.

[6] W.-Y. Chiu, J.-W. Shi, W.-K. Wang, Y.-S. Wu, Y.-J. Chan, Y.-L. Huang, and R. Xuan “Leaky-Wave photodiodes with a partially p-doped absorption layer and a Distributed-Bragg-Reflector (DBR) for high-power and high-bBandwidth responsivity product performance” IEEE Photon. Technol. Lett., vol. 18, pp.1267-1269, June 2006.

Near Field Transmission of Ordered Arrays of Sub-Wavelength Holes Fabricated in Lithium Niobate by Femtosecond Laser Writing.

Jorge Barrio, Jorge Lamela, Airán Ródenas, Daniel Jaque, Ginés Lifante, Francisco Jaque
Departamento Física de Materiales, F. Ciencias, Universidad Autónoma de Madrid, 28049 Madrid, Spain
e.mail: daniel.jaque@uam.es
Guangyong Zhou, and Min Gu
Centre for Micro-Photonics and Centre for Ultrahigh-bandwidth Devices for Optical Systems, Faculty of Engineering and Industrial Sciences, P. O. Box 218, Hawthorn, Victoria 3122, Australia.
mgu@swin.edu.au

***Abstract*— In this work direct femtosecond laser ablation of ordered arrays of sub-λ/4 (80-200 nm) holes in $LiNbO_3$ crystals is presented. The near field transmission properties of the fabricated arrays of sub-micrometric holes have been investigated by means of Near Field Scanning Microscopy. We have found a rich variety of phenomena all of them in agreement with beam propagation simulations. We have found that the near field intensity distribution created by the fabricated arrays could lead, under certain conditions, to intensity enhancements in excess of 50%, behaving as efficient near field lenses.**

Keywords: femtosecond ablation, SNOM, sub-wavelength

I. INTRODUCTION

The possibility of creating controlled periodic nanostructures at the surface of ferroelectric nonlinear lithium niobate (LN) crystals is nowadays attracting much attention because of its numerous applications including the fabrication of two-dimensional (2D) photonic crystals [1], micro-diffraction elements [2], 2D photonic crystals [3], and novel focusing structures when combined with metallic coatings [4]. Among the different techniques capable of controlled surface structuring in LN crystals at the sub-micrometric scale (such as focused ion beam milling, ion beam enhanced etching, or mask assisted plasma etching), femtosecond laser ablation (FLA) is of special relevance because its simplicity, reduced processing times and absence of sample preparation requirements [5]. Nevertheless, for most of the above mentioned applications (especially those involving visible light control) reduced hole sizes are required. The possibility of using high-NA (NA > 1) optics has been already demonstrated in several materials (including glasses and self-assembled monolayers) [6,7], but its potential application in LN crystals for beating the 200 nm limit is still unexplored. In addition to the above mentioned practical applications, the creation of sub-200 nm surface structures in a high refractive-index nonlinear medium such as LN (n ~ 2.2 - 2.4) is also interesting from a fundamental point of view since they could open the avenue novel fundamental effects, such as extraordinarily high transmission or polarization-sensitivity effects [8].

In this work we report on the femtosecond laser fabrication of orders arrays of sub-λ/4 holes in a LN crystal by multi-pulse ablation, with a full control over the hole diameter in the 80-200 nm range. We demonstrate that the presence of the fabricated nano-holes strongly modulates the near-field optical transmission of the LN surface. We show that the near-field transmitted intensity almost vanishes at hole´s central position, whereas a significant near-field enhancement is produced at its surroundings. The increment observed in the near field intensity in the surroundings of the nano-holes has been found to be weak for single nano-holes but of relevance in the case of ordered arrays of nanoholes. By comparing the measured and FDTD simulated NSOM images we found nanometric surface relief in combination with cooperative multiple-scattering as the key factors for the optical contrast mechanisms.

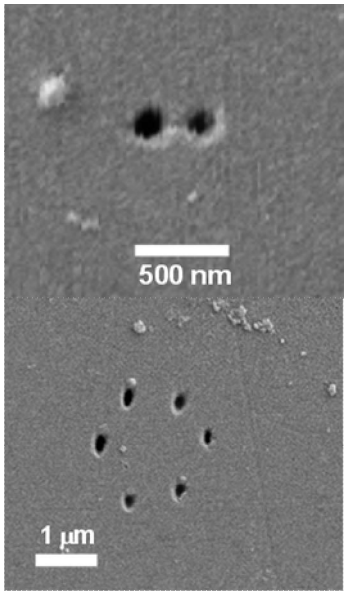


Fig 1.- Ordered arrays of nano-holes fabricated in LN by fs laser ablation.

II. EXPERIMENTAL

The LN samples used in this work were 0.5x1x10 mm^3 prisms in both x-cut and z-cut orientation. Femtosecond laser ablation was done by using a Spitfire (Spectra Physics) regenerative amplifier generating ~150 fs laser, linearly polarized pulses at 800 nm wavelength, with a 1 kHz repetition rate. The laser beam was focused onto the LN surface by using an oil immersion Olympus PlanAPO 60X TIRFM microscope objective with a numerical aperture (NA) of 1.45. The size of the ablated nano-holes was controlled by a careful adjust of the irradiation energy. The NSOM image was obtained with a Nanonics near-field microscope (MultiView 200 TM) working in non-contact tapping mode using a visible 532 nm continuous wave laser for back illumination of the sample and a ~100 nm aperture fibre for near-field collection. The fibre was kept at a constant separation of ≈20 nm above the LN surface.

III. RESULTS AND DISCUSSION

Figure 1 shows an example of two simple arrays (consisting of two and six nanoholes) fabricated at the surface of the LN sample. The particular experimental conditions used for this structure lead to nano-holes with an average size well below 200 nm. As it can be seen fs laser writing well allows for surface relief with a spatial control in the nanometric scale with a complete absence of extended damage regions.

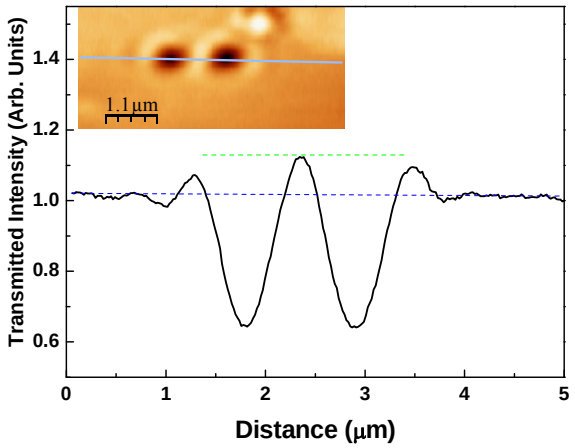


Fig 2.- Inset shows the SNOM transmission image obtained from a pair of nano-holes separated 1 μm. Black line corresponds to the intensity profile as obtained along the scan direction indicated in the inset. Blue and red dashed lines indicate the background and enhanced intensity, respectively.

Once the structures were fabricated then the near field transmission was characterized by SNOM measurements. Some results are summarized in Figure 2. In this Figure we show as an inset the near field transmission image obtained for a pair of nano-holes separated 1 μm. In this Figure it is clear that the near field intensity is strongly reduced at the centre of both holes. This is compensated by a near field increment in the hole's surroundings, in accordance to previous experimental and theoretical works [9]. The most relevant result can be appreciated in the intensity profile shown by the black line. In this profile it is clear that the near field intensity is enhanced in the region between holes (see the different intensity levels indicated by the blue and red lines). This effect can be understood in terms of the constructive overlap between the scattering filed distributions created by each hole, denoting a cooperative scattering phenomenon. The validity of this assumption was checked by numerical simulations, that have shown an excellent agreement from both the qualitative and quantitative point of view.

We have found that when the number of scattering centers is increased (as in the array shown at the bottom of Fig.1) the Near Field enhancement induced between these sub-wavelength scattering centers is increases even further, reaching a total amplification at the middle of the structure exceeding 40% in respect to the background intensity.

IV. CONCLUSIONS

We have fabricated ordered arrays of sub-wavelength scattering centers in Lithium Niobate crystals by femtosecond laser ablation. The Near Field Optical images of the obtained structures denote the presence of cooperative scattering. We state at this point that the fabricated structures emerge as very promising structures for their use as potential lenses in the Near Field.

ACKNOWLEDGMENT (HEADING 5)

This work has been supported by the Spanish Ministerio de Educación y Ciencia (MAT2004-0334 and MAT2007-64686), by the Universidad Autónoma de Madrid and Comunidad Autónoma de Madrid (projects MICROSERES-CM and CCG07-UAM/MAT-1861), and by the Australian Research Council (ARC) Centre of Excellence for Ultrahigh-bandwidth Devices for Optical Systems (CUDOS, No. CE0348259), and ARC Discovery grant (No. DP0665868).

REFERENCES

[1] S. Diziain, J. Amet, F.I. Baida, and P.M. Bernal. Appl. Phys. Lett. **93**, 261103 (2008).

[2] G.A. Torchia, C. Méndez, I. Arias, L. Roso, A. Ródenas, D. Jaque. Appl. Phys. B. **83**, 559 (2006).

[3] K. Kokkonen, M. Kaivola, S. Benchabane, A. Khelif, and V. Laude. Appl. Phys. Lett. **91**, 083517 (2007).

[4] M. Merano, G. Boyer, A. Trisorio, G. Chériaux, and G. Mourou. Opt. Lett. **32**, 2239 (2007).

[5] F. Korte, J. Serbin, J. Koch, A. Egbert, C. Fallnich, A. Ostendorf and B. N. Chichkov. Appl. Phys. A. **77**, 229 (2003).

[6] Y.V. White, X. Li, Z. Sikorski, L.M. Davis and W. Hofmeister. Opt. Express **16**, 14411 (2008).

[7] N. Hartmann, S. Franzka, J. Koch, A. Ostendorf and B. N. Chichkov. Appl. Phys. Lett. **92**, 223111 (2008).

[8] A. Battula, S. Chen, Y. Lu, R. J. Knize and K. Reinhardt. Opt. Lett. **32**, 2692 (2007).

[9] A. Ródenas et al, Appl. Phys. Lett. **95**, 181103 (2009)

Tunable optical delay line in engineered slow light photonic crystal waveguides

I. H. Rey, D. M. Beggs, and T. F. Krauss
School of Physics and Astronomy
University of St Andrews
St Andrews, Fife, KY16 9SS, UK
ir21@st-andrews.ac.uk

T. Kampfrath and L. Kuipers
FOM Institute AMOLF
Science Park 113
1098 XG Amsterdam, The Netherlands

Abstract—**We propose a new design for compact tunable optical delay lines, based on adiabatic wavelength conversion and group velocity dispersion, in engineered silicon slow light photonic crystal waveguides. For a 3nm adiabatic wavelength shift, we obtain a simulated change in group index from n_g=25 to n_g=124.**

Keywords-tunable optical delay line; adiabatic tuning; photonic crystal waveguide; slow light; dispersion

I. Introduction

Tunable optical delay lines will provide an important functionality in future all-optical signal processing systems, to be employed in applications such as optical memories, optical packet switches and time division multiplexing. Different schemes have been proposed for generating tunable delays in miniaturised systems, mainly involving tuning chains of coupled cavities [1] or trapping and releasing optical pulses in a few resonators by dynamically varying their quality factors Q [2]. The former approach, however, requires the ability to precisely align and uniformly tune the resonant frequencies of many cavities; in the latter, the maximum achievable delay is limited by the photon lifetime. An alternative approach to realising tunable delay is based on wavelength conversion and dispersion: if an input signal is shifted in wavelength and coupled into a dispersive medium, it will propagate at a different speed with respect to an unshifted pulse, experiencing a different delay. Several demonstrations of tunable delay based on this technique have been reported using optical fibres as a dispersive medium, resulting in the highest optical delays to be observed [3]. Nevertheless, these solutions are extremely bulky and not suitable for integration with optoelectronic devices.

In this paper we investigate the possibility of realising a tunable optical delay line based on wavelength conversion and dispersion in compact silicon slow light photonic crystal (PhC) waveguides. Low-power adiabatic tuning is proposed as a means of achieving wavelength conversion.

II. Adiabatic Wavelength Conversion

Wavelength conversion in silicon is usually achieved through nonlinear optical effects such as four-wave mixing, which requires high pump powers and has very low efficiency (-20-30dB). Wavelength conversion may also be obtained through adiabatic tuning of an optical resonator, which is instead a linear effect: if the resonant frequency of a cavity is tuned whilst storing light, the wavelength of the light in the cavity follows the change in resonant wavelength [4]. This phenomenon is the optical equivalent of tuning a guitar string, and is relatively new in photonics, since it requires tuning of the system within the photon lifetime, which was not possible before the fabrication of high-Q cavities. Experimental observation of adiabatic wavelength conversion in a PhC cavity was reported in [5].

The same effect can also be obtained through use of slow light, since we may tune the properties of a waveguide while photons are present if light propagates slow enough, which is equivalent to a long photon lifetime in a cavity. This was recently demonstrated in the slow light regime of a short silicon W1 PhC waveguide, whose band diagram was blue-shifted by 0.39THz by illuminating the material with a pump pulse [6], with an estimated absorbed pump pulse energy of ~6pJ. Fig. 1 shows the output spectrum of the probe pulse as a function of the pump-probe delay τ. For τ<4ps the probe arrives before the pump, and therefore propagates in the unshifted band diagram. For τ>1ps the probe arrives after the pump and is reflected, since its frequency falls in the band gap of the blue-shifted band diagram. Around τ=-1ps pump and probe have maximum overlap, and the probe spectrum is adiabatically blue-shifted by 0.39THz, with an efficiency better than 80%.

III. Design

As adiabatic tuning is a linear effect, the relative frequency shift is proportional to the relative refractive index change, of the order of 10^{-3}-10^{-4}. Nevertheless, such a small frequency

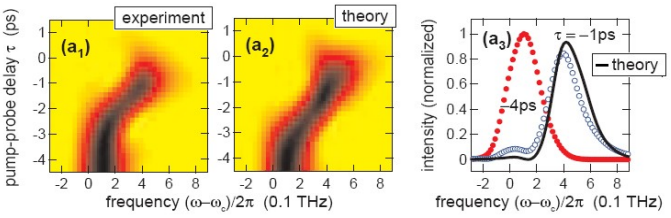


Figure 1. Adiabatic wavelength conversion in the slow light regime of a W1 PhC waveguide. (a1) Experimentally determined and (a2) calculated intensity spectra of the W1 waveguide response to a 1.3ps long input probe pulse at centre frequency $\omega_c/2\pi$=202THz, for different pump-probe delays τ. (a3) Measured and calculated output spectra at τ=-4ps and 1ps.

shift is sufficient for delay tuning if the dispersion of the subsequent medium is strong enough. This is in fact the case for the transition region from fast to slow light regime of dispersion-engineered slow light PhC waveguides obtained by shifting the position of the first two rows of holes adjacent to the line defect [7]. Such a waveguide will be therefore used as a dispersive section for a tunable delay line. The slow light modes of the very same waveguide, instead of the standard W1 used in [6], will be employed for adiabatic wavelength conversion.

The proposed photonic structure for achieving tunable delay through wavelength conversion and dispersion is an engineered slow light waveguide which acts both as a dispersive medium and, in its initial section, as frequency conversion component (Fig. 2). A signal pulse enters the structure in the slow light regime (Fig. 3a). Here, low group velocity and compression in space are both fundamental to accomplishing adiabatic blue-shift of light due to refractive index tuning. The blue-shifted pulse propagates through the waveguide and enters the untuned region (Fig. 3b), where its new frequency is associated with a faster mode.

IV. Results

A concrete example is given by the TE band diagram of Fig. 3 (red line), obtained through a 3D MPB (MIT Photonic Band) simulation of an engineered slow light waveguide realised in a 220nm thick silicon membrane (refractive index of 3.5), with lattice constant a=448nm, radius r=0.29a and displacements of the first and second rows of holes s_1=-0.11a and s_2=0.08a respectively, where shifts towards the waveguide centre are defined to be positive. The input wavelength of 1685.5nm corresponds to a group index n_g of ~124. According to [6], we may assume to be able to adiabatically blue-shift the signal wavelength up to ~3nm, where n_g is decreased to ~25. Given these quantities, the maximum achievable delay range Δt depends on the waveguide length L as $\Delta t = L\Delta n_g/c$. On the other hand, L is related to the minimum pulse duration T_0 allowed by group velocity dispersion, through the dispersion length expression $L=T_0^2/|\beta_{2,max}|$, where $\beta_2=d^2k/d\omega^2$. If we aim at a delay-bandwidth product $\Delta t/T_0$ of 8 pulsewidths (i.e. one byte), the pulse duration T_0 may be taken as short as 7.8ps, corresponding to a dispersion length L of 189μm.

For the same band structure we can instead choose to maximise $\Delta t/T_0$ by increasing L. The maximum allowed length will depend on propagation loss α. Assuming that α increases linearly with n_g in the transition region between fast and slow light regime [8], we may estimate the maximum propagation loss α_{max} to be comparable with the maximum n_g. By setting the maximum overall loss to a reasonable value of 10dB, we find that a ~808μm long waveguide delays a 16ps pulse (allowed by dispersion) by 334ps for n_g~124 (untuned) and by 67ps for

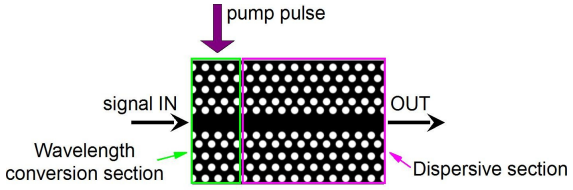


Figure 2. Schematic of the proposed tunable delay line based on wavelength conversion and dispersion in an engineered slow light PhC waveguide.

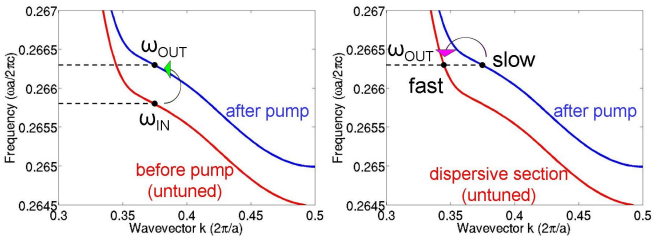


Figure 3. (a) Adiabatic wavelength conversion in an engineered PhC waveguide: an input pulse is blue-shifted, following the frequency shift of the fundamental TE mode. (b) Coupling of the blue-shifted pulse to the untuned dispersive section, where it propagates with a higher group velocity.

n_g~25 (tuned). This corresponds to a delay range of 267ps (~16 pulsewidths).

The length of the initial section for wavelength conversion is equal to the physical size of the input pulse which, propagating in a slow mode, is compressed in space. This is the only part of the waveguide needing tuning through carrier injection. The size of a pulse of time duration T_0 propagating at a group index n_g may be evaluated as $l=cT_0/n_g$. If n_g~124, we have l~19μm for T_0=7.8ps.

V. Conclusion

We have proposed a new design for realising a miniaturised tunable optical delay line, based on adiabatic wavelength conversion and group velocity dispersion in a silicon engineered slow light PhC waveguide.

Acknowledgements

This work has been partially funded by the UK Engineering and Physical Sciences Research Council (EPSRC) programme, "UK Silicon Photonics", as well as the EU-FET project "Splash".

References

[1] S. Fan, M. F. Yanik, Z. Wang, S. Sandhu, and M. L. Povinelli, "Advances in theory of photonic crystals," J. Lightwave Technol., vol. 24, pp. 4493–4501, 2006.

[2] J. Upham, Y. Tanaka, T. Asano, and S. Noda, "Dynamic increase and decrease of photonic crystal nanocavity Q factors for optical pulse control," Opt. Express, vol. 16, pp. 21721–21730, 2008.

[3] E. Myslivets, N. Alic, S. Moro, B. P. P. Kuo, R. M. Jopson, C. J. McKinstrie, M. Karlsson, and S. Radic, "1.56-μs continuously tunable parametric delay line for a 40-Gb/s signal," Opt. Express, vol. 17, pp. 11958–11964, 2009.

[4] M. Notomi and S. Mitsugi, "Wavelength conversion via dynamic refractive index tuning of a cavity," Phys. Rev. A, vol. 73, p. 051803, 2006.

[5] T. Tanabe, M. Notomi, H. Taniyama, and E. Kuramochi, "Dynamic release of trapped light from an ultrahigh-Q nanocavity via adiabatic frequency tuning," Phys. Rev. Lett., vol. 102, p. 043907, 2009.

[6] T. Kampfrath, D. M. Beggs, T. P. White, A. Melloni, T. F. Krauss, and L. Kuipers, "Ultrafast adiabatic manipulation of slow light in a photonic crystal," unpublished.

[7] J. Li, T. P. White, L. O'Faolain, A. Gomez-Iglesias, and T. F. Krauss, "Systematic design of flat band slow light in photonic crystal waveguides," Opt. Express, vol. 16, pp. 6227–6232, 2008.

[8] L. O'Faolain, S. Schulz, D. M. Beggs, T. P. White, A. Di Falco, A. Samarelli, M. Sorel, R. M. De La Rue, F. Morichetti, A. Canciamilla, A. Melloni, and T. F. Krauss, "Low loss dispersion engineered photonic crystal waveguides for optical delay lines," unpublished.

Grating Assisted Coupling in Microring Resonators

A. Samarelli, M. Sorel, R.M. De La Rue
Electronic and Electrical Department,
Glasow University,
Glasgow, United Kingdom
antonios@elec.gla.ac.uk

A. Melloni
Dipartimento di Elettronica e Informazione,
Politecnico di Milano
Milano, Italy

P. Orlandi, M. Gnan, P.Bassi
Dipartimento di Elettronica, Informatica e Sistemistica,
Università di Bologna
Bologna, Italy

Abstract—**Grating Assisted Couplers (GACs) in Silicon-on-Insulator waveguides are studied experimentally as building blocks for optical integrated devices. By including them in a microring resonator configuration, we enhance the GAC wavelength selectivity and limit the resonance range of the microring. This device has the potential for small footprint, highly selective, wavelength filters and sensors.**

Keywords-grating assisted coupler; microring resonator; silicon-on-insulator;

I. INTRODUCTION

Silicon-on-insulator (SOI) technology is a promising platform for constructing functional micro-scale optical devices for high-density photonic integration. Among the various unit elements that can be developed as building blocks for SOI photonic circuits, the Grating Assisted Coupler (GAC) can perform optical routing among different waveguides while being highly wavelength selective. GACs have been realized in $LiNbO_3$ [1], optical fibers [2], and, recently, also in SOI [3]. If they are designed to operate on nanometer sized bandwidths (e.g. for applications such as WDM add-drop filters or sensors) the grating is weak, resulting in many hundreds of micrometre long devices [3]. In this paper, after demonstrating the coupling properties of weak sidewall GACs in SOI, we show numerically and experimentally that a GAC in a microring resonator configuration takes advantage of the optical feedback to reduce both its coupling bandwidth and device footprint.

II. GRATING ASSISTED COUPLER

A GAC consists of two waveguides placed side by side where a common grating mediates the coupling between the modes of the waveguides (Fig. 1). When two counter-propagating modes belonging to the same waveguide are coupled, their Bragg condition is $\beta_i = \pi/\Lambda$, where *i* specifies the waveguide, Λ is the grating period, and β_i is the propagation constant. When two modes of different waveguides are involved, the Bragg condition is $\beta_i + \beta_j = 2\pi/\Lambda$, which is halfway between the two previous coupling regimes. If the grating is sufficiently weak, the Coupled Mode Theory (CMT) approach can be used. Furthermore, the three coupling regimes can be modeled separately if they are sufficiently spaced in wavelength [4]. In order to use GACs as building blocks for optical devices, we have studied the properties of a set of GACs fabricated in SOI, made out of waveguides having weak sidewall modulation.

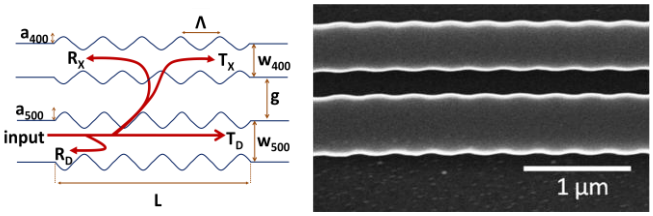


Figure 1 Schematic and micrograph of fabricated GAC.

A 220-nm silicon core layer on a 1-μm buried oxide sample of SOI wafer from SOITEC was patterned using electron beam lithography and HSQ resist – and subsequently dry-etched [5]. Inverse tapers coupled to polymer SU8 waveguides were used to terminate all the silicon waveguides so as to minimize back reflection at the waveguide ends and improve the coupling efficiency. The fabricated devices were finally embedded in 900 nm of oxide formed as a bi-layer of HSQ and deposited SiO_2.

The waveguides of the GACs were 500 nm and 400 nm wide, providing different propagation constants in single modal regimes with low propagation losses [5]. Each sidewall has a sinusoidal modulation with an amplitude parameter *a*. The wider waveguide has a larger modulation so that $a_{500} > a_{400}$. The average gap between the two waveguides is *g* and the length of the coupling region is *L*.

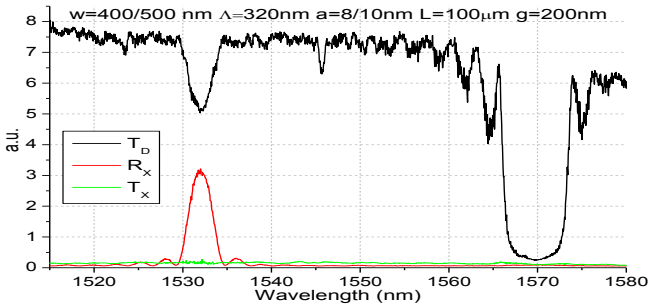


Figure 2 – Experimental transmission of GAC (dimensions specified in figure heading)

Fig. 2 shows experimental direct transmission (T_D), cross transmission (T_X), and cross reflection (R_X) curves of a GAC with Λ = 320 nm, a_{400} = 8 nm, a_{500} = 10 nm, L = 100 μm g = 200 nm. The right-most stop-band shape in T_D (centered at λ~1570 nm) is the direct stop-band of the feeder 500 nm wide waveguide. The left-most stop-band (at $\lambda_0 \sim 1532$ nm) is the exchange coupling stop-band, where direct transmission drops in favor of cross-reflected power (R_X). The "missing" other direct stop-band (at λ_0~1494 nm, according to CMT) would be

visible if the input power were inserted into the 400 nm wide waveguide. The cross-transmission is always isolated from the feeder waveguide. The weak modulation of the transmittance is presumably due to residual co-directional coupling.

The experimental cross-coupling coefficients of various geometrical configurations obtained varying the sidewall modulation amplitude (*a*), gap (*g*) are shown in Table 1.

a_{400} / a_{500} → g ↓	4nm / 6nm	8nm / 10 nm	10nm / 15 nm
200 nm	0.00397±0.00005	0.0062 ± 0.0002	0.0074 ± 0.0002
220 nm	0.003± 0.00008	0.0049 ± 0.0005	0.0072 ± 0.0004
240 nm	0.0025±0.0002	0.0043 ± 0.0006	0.0048 ± 0.0003

Table 1 Experimental exchange coupling coefficients (units are μm^{-1})

The very small value of the exchange coupling coefficients is closely related to the nanometre sized bandwidth of the exchange stop-band shown in Fig. 2. Because of the weak coupling factors, large exchange reflections can only be obtained by hundreds of micrometres of propagation, which would result in too large a device footprint. In the next section, we propose a configuration where the length of the device can be kept short by using the optical feedback of a microring resonator configuration.

III. GAC IN MICRORING CONFIGURATION

The schematic of the microring resonator with two GAC elements is shown in Fig. 3. ASPIC software [6] with transfer matrix and CMT methods was used to simulate the device behavior. Fig. 4 shows results with Λ = 320 nm, a_{400} = 10 nm, a_{500} = 15 nm, L = 20.16 µm, g = 220 nm, and coupling coefficients as detailed in Table 1. The input and output waveguides are 400 nm wide, while the ring waveguide is 500 nm wide with a 20 µm radius.

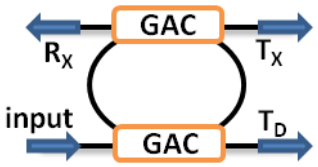


Figure 3 Sketch of the microring resonator with GAC elements.

Besides the direct stop-band of the feeder waveguide, the main feature of the simulated behavior is the set of ring resonance dips limited to the exchange coupling bandwidth of the GACs. From the point of view of the GACs, the optical resonance of the ring enhances its effective length, thus making it more wavelength selective. We believe that this device can be tailored so as to allow only the set of wavelengths that are needed, for example, in WDM filters or sensing devices. The simulated device was then fabricated and its measured characteristics are shown in Fig. 5. On the whole, the curves reproduce the simulated ones very closely. The main difference is found in the fact that the cross-transmission (T_X) is as large as the cross-reflection (R_X). This can be explained by spurious reflections within the resonator, possibly at the interface between the grating and the feedback wires – or by roughness-induced backscatter.

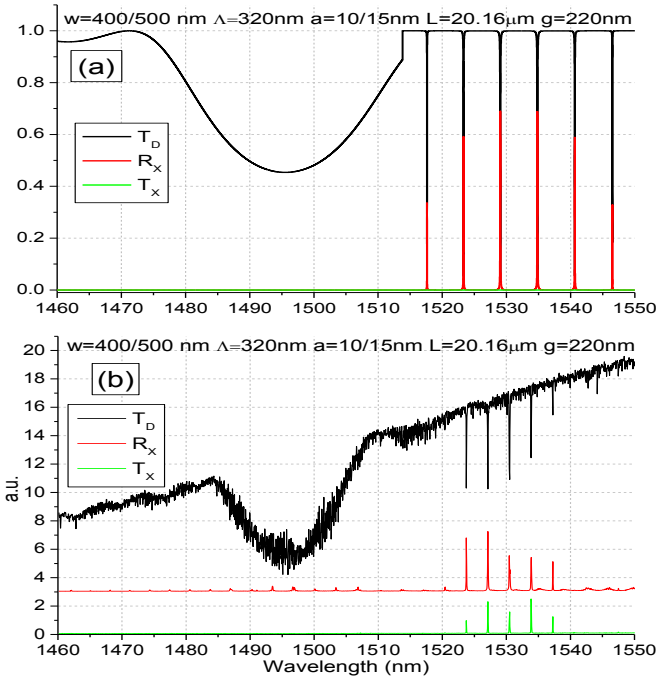


Figure 4 (a) Simulated and (b) experimental behavior of GAC in microring configuration. Note that R_x has been offset by 3 for readability.

IV. CONCLUSION AND FUTURE WORK

The experimental behavior of sidewall GACs fabricated in SOI with various geometries was demonstrated. By arranging two GACs in a microring resonator configuration we have demonstrated numerically and experimentally, enhancement of the selectivity of the GAC or, conversely, the limitation of the resonance of the microring resonator. This device has the potential to be tailored to become a highly wavelength selective add-drop filter or sensor – while maintaining a compact footprint.

ACKNOWLEDGMENT

We thank the JWNC staff at GU for support in fabrication of the devices and Gaetano Bellanca for helpful discussions. We acknowledge SPLASH and PROMINER projects for funding.

REFERENCES

[1] P. Yeh and H.F. Taylor, "Contradirectional frequency-selective couplers for guided-wave optics," Appl. Optics, vol. 19, pp. 2848-2855, 1980.

[2] S. Orlov, A. Yariv, and S. Van Essen, "Coupled-mode analysis of fiber-optic add drop filters for dense wavelength-division multiplexing," Opt. Lett., vol. 22, pp. 688-690, 1997.

[3] D.H. Tan, K. Ikeda, and Y. Fainman, "Coupled chirped vertical gratings for on-chip group velocity dispersion engineering," Appl. Phys. Lett., vol. 95, p. 141109, 2009.

[4] R. Syms, "Optical directional coupler with a grating overlay," Appl. Optics, vol. 24, pp. 717-726, 1985.

[5] M. Gnan, S. Thoms, D. Macintyre, R. De La Rue, and M. Sorel, "Fabrication of low-loss photonic wires in silicon-on-insulator using hydrogen silsesquioxane electron-beam resist," Electron. Lett., vol. 44, pp. 44-45, 2008.

[6] ASPIC Design. Filarete, Italy, 2009 – website www.aspicdesign.com

Towards Monolithic Integration of Non-linear Optical Frequency Conversion

Usman Younis, Barry M. Holmes, David C. Hutchings
Dept. of Electronics & Electrical Engineering
University of Glasgow
Glasgow, United Kingdom, G12 8QQ
younis@elec.gla.ac.uk

John S. Roberts
EPSRC National Centre for III-V Technologies
University of Sheffield
Sheffield, United Kingdom, S1 3JD

***Abstract*—The monolithic integration of an all optical frequency converter is developed. The wavelength routing is demonstrated with a di-chroic MMI coupler, which has a minimum cross talk of -12 dB. The stimulated emission at 801 nm has been achieved in a half ring superlattice laser.**

Keywords-Nonlinear optics; di-chroic MMI coupler; semiconductor superlattice laser

I. INTRODUCTION

Compound semiconductors are an attractive choice for non-linear optical frequency conversion applications. They benefit from mature fabrication technologies – and, with the inclusion of an on-chip pump source, it is possible to achieve a fully integrated all optical frequency converter. GaAs/AlGaAs superlattices can be used to obtain a substantive modulation in the non-linear optical properties through post-growth quantum-well intermixing (QWI) techniques. We have engineered the $\chi^{(2)}$ modulation in our domain-disordered quasi-phase matching (DD-QPM) GaAs/AlGaAs superlattices using ion-implantation induced QWI, and have demonstrated the second order non-linear processes of continuous wave (CW) second harmonic generation (SHG) [1] in type-I polarization configuration, pulsed type-II SHG [2], and, more recently, we have achieved difference frequency generation (DFG) [3]. In this paper, we demonstrate the components required in a monolithically integrated optical frequency converter, which include: (1) a di-chroic multimode interference (MMI) coupler for wavelength routing, and (2) superlattice laser, which in a ring configuration, would serve as an on-chip pump.

II. DI-CHROIC MMI COUPLER

The simultaneous conversion of different wavelengths requires the routing components in our designed integrated optical frequency converter for 1.5 µm telecommunication band, shown in Fig. 1. The material structure, which has been previously presented in [2], has a band gap near 775 nm. The pump wavelength (band gap excitation) couples into the DD-QPM waveguide, and then couples back into the ring laser cavity. However, due to the di-chroic nature of couplers, signal and idler wavelengths (near the half band gap excitation) do not enter the ring.

The designed MMI coupler cavity is 220 µm long and 6.5 µm wide – the design has been optimized with beam-propagation-based simulations using a commercial package[1]. The access waveguides to the coupler are 3 µm wide. Considering these parameters, MMI couplers with a range of cavity lengths were fabricated. The fabrication process involved electron beam (E-beam) patterning and subsequent definition with $SiCl_4$ reactive ion etching (RIE). RIE was assisted with an *in-situ* laser reflectometry to achieve an etch depth of 1.35 µm.

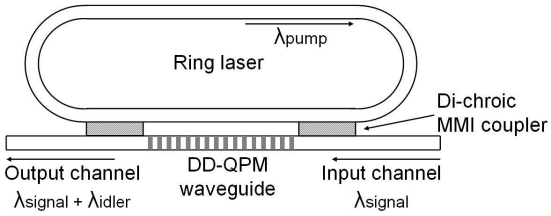


Figure 1. The designed integrated optical frequency converter

The couplers were characterized with a CW Ti:sapphire laser and a CW C-band laser, for the measurements near the band gap and the half band gap wavelengths, respectively. The coupled light was detected using both Silicon and Germanium photo-detectors. The cross talk, which in this case is the ratio between the unwanted signal and the wanted signal, is given in Fig. 2 (a) for the measurements near the band gap, and in Fig. 2 (b) for the measurements near the half band gap. The peak coupling in both cases occurred for ~220 µm MMI cavity length, which is consistent with the initial design. The minimum cross talk of -12 dB is satisfactory under the given design constraints – and the high performance is achievable in the integrated chip with reduced out coupling of the ring laser mode.

III. SUPERLATTICE LASER

The laser action has been achieved using a thinner superlattice core material structure, to demonstrate an on-chip pump source. The *p-i-n* laser diode has a 600 nm thick intrinsic core, which includes a 100 nm 14:14 monolayer

[1] BeamPROP from Research Software (Rsoft) Inc.

GaAs/$Al_{0.85}Ga_{0.15}As$ superlattice active medium, with 250 nm $Al_{0.45}Ga_{0.55}As$ buffers on either side. The claddings are similar to the previous material structure, but are doped with C and Si to make them p-type and n-type, respectively. The wafer was grown using metalorganic vapor phase epitaxy (MOVPE), and has an intense measured electroluminescence (EL) of 772 nm.

Low pressure MOVPE growth was undertaken using a robot loading 6x2 Aixtron showerhead reactor. A high quality superlattice was deposited using the precursors trimethylgallium, trimethylaluminium and arsine in combination with an *in-situ* oxygen gettering. The precise control of the superlattice period was achieved using an array of purged four-way vent/run valves and the growth process was monitored using a Laytec EpiTT reflectivity/pyrometer system.

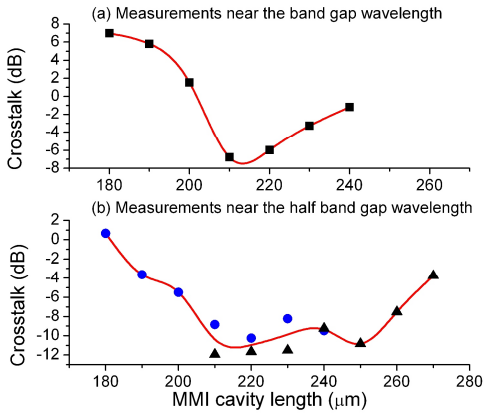


Figure 2. (a) Measured cross coupling near the band gap wavelength, (b) measured bar coupling near the half band gap wavelength. The solid lines are a smoothed fit to the data

The 3 μm wide ridge waveguide lasers were fabricated in half rings, with the ring radii of 450 μm and 475 μm. The laser patterns were designed such that the cleaved samples have 2200 μm long half ring cavities. The fabrication process included an initial rapid thermal annealing at 775 °C for 60 sec – which is mandatory as a post QWI treatment in fabrication of the final device. The waveguides were patterned in E-beam and defined by $SiCl_4$ RIE, again with an *in-situ* laser reflectometry to achieve 1.35 μm etch depth. The Ti-Pt-Au P-contacts and Au-Ge-Au-Ni-Au N-contacts were deposited by E-beam metal evaporation. The lasers were finally cleaved and mounted on the brass pads for testing.

The lasers were tested CW at the room temperature. The optical power was measured with a power meter. The lasing wavelength was obtained by coupling the light into a lens fiber and measuring it on an optical spectrum analyzer. The L-I curves for the half rings are given in Fig. 3. The higher lasing threshold of 450 μm half ring is caused by its higher bending losses, as compared to that of 475 μm half ring.

The inset in Fig. 3 shows the lasing wavelength of 801 nm, which was measured for a 500 μm long annealed Fabry-Perot (FP) ridge. A red shift of 29 nm is observed between the EL and the laser excitation, which can be attributed to a relatively high threshold current density of 3.5 kA/cm^2 for the device [4]. The loss factor for the annealed material is 3.21 cm^{-1} – calculated by plotting external quantum efficiency against FP cavity length. This shows an excellent structural quality and is confirmed by the X-ray measurements. Therefore, the growth defects – as a potential source of higher threshold – can be confidently ruled out; however, laser action was undetected for the devices fabricated using un-annealed material – and the turn-on voltage was reduced from ~4 V to ~2 V after annealing. Further investigations of the lasing characteristics are ongoing.

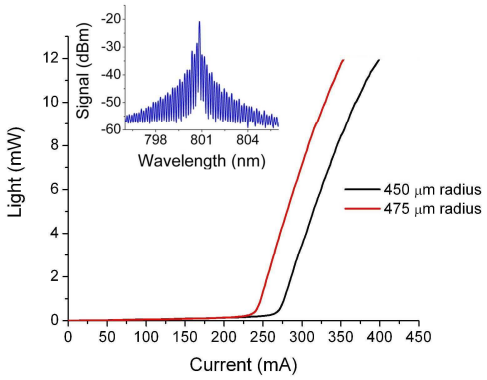


Figure 3. The L-I curves of the half rings - stimulated emission at 801 nm (the power meter saturated above 12 mW)

IV. CONCLUSIONS

Our recent demonstrations of various second order non-linear processes in a same material system [1-3], have reported higher conversion efficiencies; which is highly encouraging towards integrated all optical conversion devices. In this paper we have demonstrated the components that are required for the monolithic integration of our designed optical frequency converter. The wavelength routing has been demonstrated with a di-chroic MMI coupler, and the half ring superlattice laser has been demonstrated towards an on-chip pump source.

REFERENCES

[1] S. J. Wagner, B. M. Holmes, U. Younis, A. S. Helmy, J. S. Aitchison, and D. C. Hutchings, "Continuous wave second-harmonic generation using domain-disordered quasi-phase matching waveguides," Applied Physics Letters, vol. 94, pp. 151107-3, 2009.

[2] B. M. Holmes, U. Younis, D. C. Hutchings, S. J. Wagner, A. S. Helmy, and J. S. Aitchison, "Type-II quasi-phase-matched second-harmonic generation in domain-disordered semiconductor waveguides," in Conference on Lasers and Electro-Optics, and Conference on Quantum electronics and Laser Science Conference (CLEO/QELS 2009), Baltimore, USA, 31 May – 5 June 2009.

[3] S. J. Wagner, I. Sigal, A. S. Helmy, J. S. Aitchison, U. Younis, B. M. Holmes, *et al.*, "Difference Frequency Generation in Domain-Disordered Quasi-Phase Matching Semiconductor Waveguides," unpublished.

[4] R. D. Dupuis, P. D. Dapkus, J. Nick Holonyak, E. A. Rezek, and R. Chin, "Room-temperature laser operation of quantum-well $Ga_{(1-x)}Al_xAs$-GaAs laser diodes grown by metalorganic chemical vapor deposition," Applied Physics Letters, vol. 32, pp. 295-297, 1978.

Realization of a planar Bragg grating for all-optical Hilbert transformer

Chaotan Sima, J. C. Gates, B. D. Snow, H. L. Rogers, M .N. Zervas, P. G. R. Smith
Optoelectronics Research Centre
University of Southampton
Southampton, United Kingdom
cs4g09@orc.soton.ac.uk

***Abstract*—An all-optical Hilbert transformer is proposed and demonstrated experimentally. We preliminarily show that an all-optical Hilbert transformer can be implemented using an apodized planar Bragg grating with a single π phase-shift. The proposed planar Bragg grating is fabricated by Direct UV writing technology in silica-on-silicon.**

Keywords-Planar Bragg grating; photonic Hilbert transformer; optical signal processing; Direct UV writing

I. INTRODUCTION

Hilbert transformers are important devices widely used in communication, information processing and signal analysis in the electronic domain [1]. An all-optical Hilbert transformer or photonic Hilbert transformer (PHT) could be expected for a similar range of applications, which would enable the direct processing of optical signals at high speeds as well as operation bandwidths far beyond current electronic technologies.

Based on discrete free space photonic components, PHTs have been realized, e.g., multi-tap fiber-optics transversal filters and sampled fiber Bragg gratings [2–5]. Recently, derived from the first-order Born approximation (weak-coupling FBG), a single phase-shifted Fiber Bragg grating (FBG) with a proper apodization profile for PHT has also been presented [6]. However, most of the references mentioned above are mainly about theoretical simulation or with multiple components; to date no simple PHT device has been experimentally reported. Here we present initial efforts to fabricate an integrated PHT, which provides a route to realize compact optical modules for applications such as single sideband (SSB) modulation.

In this letter, we practically demonstrate that an all-optical Hilbert transformer can be implemented using an appropriate apodized planar Bragg grating with a π-phase shift in the grating length. The planar Bragg grating is fabricated by direct UV grating writing technology [7].

II. OPERATION PRINCIPLE

The Hilbert transform H[g(t)] of a signal g(t) is defined as [1]:

$$H[g(t)] = \hat{g}(t) = g(t) * \frac{1}{\pi t} = \frac{1}{\pi} P\int_{-\infty}^{\infty} \frac{g(\tau)}{t-\tau} d\tau \qquad (1)$$

P stands for the Cauchy principal value of the singular integral. Its Fourier transform is given as [1]:

$$\hat{H}[g(\omega)] = -j\,\mathrm{sgn}(\omega)\hat{g}(\omega) \qquad (2)$$

Where sgn(ω) is the sign function (which is +1 for ω>0 and -1otherwise), and ω is the baseband frequency. Thus, the frequency response of the HT filter has a π-phase shift at ω=0, whereas the amplitude remains constant.

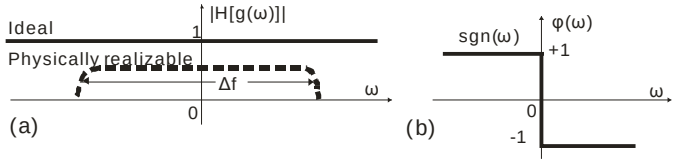


Figure 1. The magnitude responses (a) and phase response (b) of an ideal Hilbert transformer (solid lines) and physically realizable PHT (dashed lines) [8].

The π-phase shift which is the primary function of a Hilbert transformer is simply induced by placing a π-phase shift in the refractive index modulation of the Bragg grating. However in practice such a filter would have a limited frequency bandwidth and temporal impulse response. The ideal practical Bragg device could incorporate an apodization profile with the necessary π-phase shift, similar to the simple weak-coupling uniform FBG in [6]. To obtain the temporal impulse response given by (1) along a finite-time interval, the grating apodization profile is given by [6]:

$$\Delta n(z) \propto \frac{\sin^2(\pi n_{av}\Delta f\,(z-z_0)/c)}{(z-z_0)} \qquad (3)$$

For $0 \le z \le L$, where n_{av} is the average refractive index of the planar Bragg grating, c is the light speed in vacuum, L is the total grating length, z_0 is the zero-crossing point in the apodization function, and Δf is the operative bandwidth. z_0 is set to the centre of the grating length for simplicity. The grating period is $\Lambda=\lambda_B/2n_{eff}$.

As anticipated, the resulting grating apodization profile requires a single π-phase shift along the grating length. Besides, the zero-to-zero width of the side lobes Δz in the apodization profile is directly related to the full operation spectral bandwidth Δf of the PHT, where $\Delta z = c/(n_{av}\Delta f)$.

This project is sponsored by EPSRC

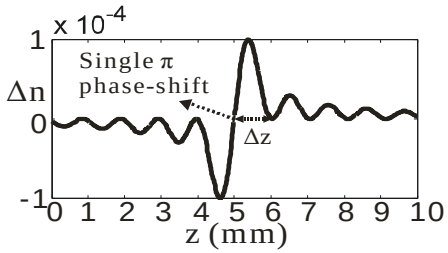


Figure 2. The apodization profile of the refractive index change Δn of the planar Bragg grating, with a single π-phase shift.

III. FABRICATION AND PRELIMILARY RESULTS

The proposed planar Bragg grating was fabricated using direct UV grating writing (DGW) technology. This method involves focusing two crossed laser beams (λ=244nm) into a photosensitive core of a planar sample. Precise translation of the sample and modulation of the interference pattern create grating structures and simultaneously define the channel waveguide [7]. This spot size is approximately 6μm in diameter, providing the unique ability over traditional FBG to manipulate the grating's structure at the micron level. This ability allows precise engineering of the amplitude and phase response of the gratings for PHT.

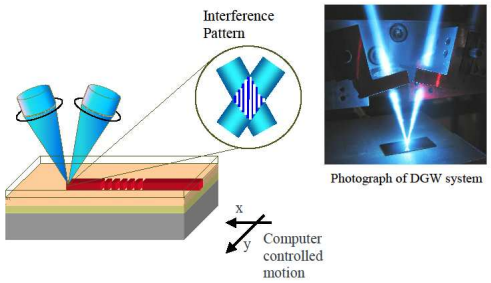


Figure 3. Illustration of the fabrication process with direct UV grating writing in silica-on-silicon.

The preliminary step is to fabricate a planar Bragg grating with exact π-phase shift. The effective refractive index of the mode within the Bragg grating was n_{eff} =1.4472, the total grating length was L = 2mm, the grating period was Λ=540.5nm and the zero-crossing point (π-phase shift point) was z_0=1mm. For this first step the grating was given a Gaussian apodization. The grating group delay in reflection was directly measured using the modulation phase-shift technique in [9].The reflection power and relative group delay are shown in Fig. 4.

IV. CONCLUSIONS

We have presented preliminarily data demonstrating the ability to fabricate exact π-phase shifted Bragg gratings with a simple apodization profile, for application as a PHT. We will present our latest work on more complex apodized gratings required to obtain the ideal realizable frequency and temporal bandwidth responses for all-optical Hilbert transformers.

In the future, the integrated nature of planar geometry will allow these devices to be combined with other functions, such as liquid crystals and thermal tuning elements to generate reconfigurable devices.

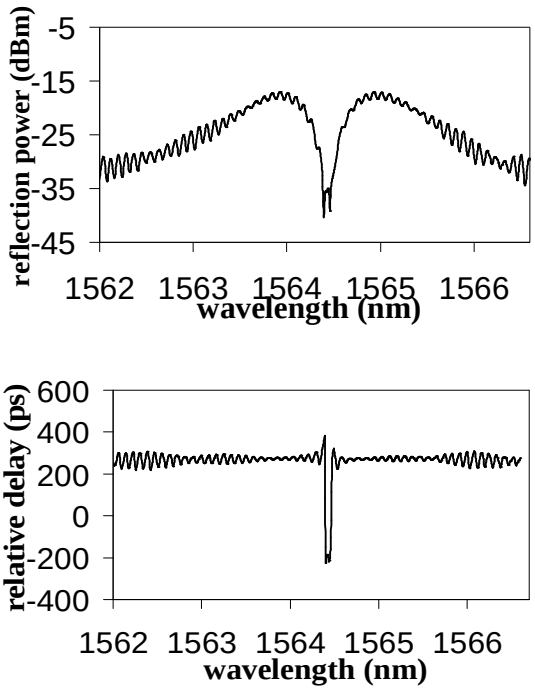


Figure 4. The measured reflection spectrum (a) and relative group delay (b) of the single π phase-shifted planar Bragg grating

REFERENCES

[1] S. L. Hahn, The Transforms and Applications Handbook, 2nd ed., A. D. Poularikas, ed. CRC Press, 2000, pp. 551.

[2] K. Takano, N. Hanzawa, S. Tanji, and K. Nakagawa, "Experimental Demonstration of Optically Phase-Shifted SSB Modulation with Fiber-Based Optical Hilbert Transformers", Optical Fiber Communication Conference, OSA Technical Digest Series (CD), [Optical Society of America, 2007], paper JThA48.

[3] H. Emami, N. Sarkhosh, L. A. Bui, and A. Mitchell, "Wideband RF photonic in-phase and quadrature-phase generation". Opt. Lett., vol. 33, pp. 98–100, January 2008.

[4] H. Emami, N. Sarkhosh, L. A. Bui, and A. Mitchell, "Amplitude independent RF instantaneous frequency measurement system using photonic Hilbert transform". Opt. Express, vol. 16, pp. 13707–13712, August 2008.

[5] M. Hanawa, K. Nakamura, K. Takano, and K.Nakagawa, Proceedings of the European Conference on Optical Communication (ECOC) (VDE-Verlag), paper 01.5.6., September 2007.

[6] M. H. Asghari and J. Azaña, "All-optical Hilbert transformer based on a single phase-shifted fiber Bragg grating: Design and analysis," Opt. Lett., vol. 34, pp. 334–336, February 2009.

[7] G. D. Emmerson, S. P. Watts, C. B. E. Gawith, V. Albanis, M. Ibsen, R. B. Williams, and P. G. R. Smith. "Fabrication of directly UV-written channel waveguides with simultaneously defined integral Bragg gratings". Electronics Letters, vol. 38, pp. 1531–1532, November 2002.

[8] Ming Li and Jianping Yao. "All-fiber temporal photonic fractional Hilbert transformer based on a directly designed fiber Bragg grating". Opt. Lett. , vol. 35, pp. 223–225, January 2010.

[9] Rongqing Hui and Maurice O' Sullivan. Fiber Optic Measurement Techniques. Elsevier Inc, pp. 346–350, 2009.

Cavity-Resonator-Integrated Grating Input/Output Coupler with Au Reflection Layer

Kenji Kintaka
Photonics Research Institute
AIST
Tsukuba, Japan
kintaka.kenji@aist.go.jp

Yuki Kita, Katsuya Shimizu, Hitoshi Matsuoka, and Shogo Ura
Department of Electronics
Kyoto Institute of Technology
Kyoto, Japan
ura@kit.ac.jp

Junji Nishii
Research Institute for Electronic Science
Hokkaido University
Sapporo, Japan
nishii@es.hokudai.ac.jp

***Abstract*—A cavity-resonator-integrated grating input/output coupler (CRIGIC), which consisted of a grating coupler and two distributed Bragg reflectors, was designed and fabricated in a thin-film SiO_2-based waveguide with an Au reflection layer for the first time. Output coupling efficiency of 58% was obtained by 20-μm-aperture CRIGIC.**

Keywords-integrated optics; grating couplers; distributed Bragg reflectors; cavity resonators; waveguides; optical interconnects

I. INTRODUCTION

Grating couplers (GCs) have attracted much attention as one of key components in inter-/intra-chip optical interconnects for future ultra-high-speed signal processing units. We have proposed and investigated an intra-board chip-to-chip optical interconnect device using focusing grating couplers (FGCs) integrated in a thin-film waveguide for two-dimensional parallel signal transmission [1-3]. The channel width of the device was a few hundreds micrometer, which was determined by the aperture size of FGCs. In order to increase the wiring density, the radiation decay factor of GC has to be increased so that the coupling length as well as the aperture size can be reduced. The radiation decay factor depends on and is limited by the modulation depth of refractive index and the groove depth of the grating structure. Short GCs have been recently reported in semiconductor waveguides with large refractive index difference [4–6]. Such large index difference, however, is not obtained in dielectric waveguides, resulting in small radiation decay factors. In order to achieve high-efficiency vertical coupling with smaller aperture size in dielectric waveguides, we have proposed and investigated a new-type GC, namely a cavity-resonator integrated grating input/output coupler (CRIGIC) [8, 9]. CRIGIC consists of one GC and two distributed Bragg reflectors (DBRs). In previous works, we have theoretically investigated [7] and have fabricated [8] the CRIGIC in a thin-film SiO_2-based waveguide on a Si substrate. In this work, we design and fabricated CRIGIC integrated in a thin-film SiO_2-based waveguide with an Au reflection layer on a substrate for the first time. The Au reflection film was introduced to suppress a substrate radiation and to enhance an output air radiation from GC. Output coupling of a guided wave to a free-space wave was demonstrated experimentally.

II. DEVICE CONFIGURATION AND DESIGN

The cross-sectional structure of the waveguide device for TE mode is illustrated in Fig. 1. The waveguide consists of a Ge-SiO_2 core layer (refractive index of 1.54), a SiO_2 buffer layer (refractive index of 1.464), and an Au reflection layer with a Cr adhesion layer on a glass substrate. An electron-beam (EB) resist layer (refractive index of 1.55) is coated on the core for CRIGIC. In CRIGIC, a GC is integrated between a front and a rear DBRs with phase-shifting spaces (PSs).

The incident guided wave is partially reflected by the front DBR, partially coupled out to a radiation wave by GC, and reflected by the rear DBR with reflection efficiency of almost unity. The reflected guided wave from the rear DBR is partially coupled out to another radiation wave by GC, partially reflected by the front DBR, and transmitted the front DBR to eliminate the reflection by CRIGIC. The rear PS between GC and the rear DBR is determined so that the radiation wave from backward guided wave is phase-matched with that from forward guided wave. The coupling efficiency of the front

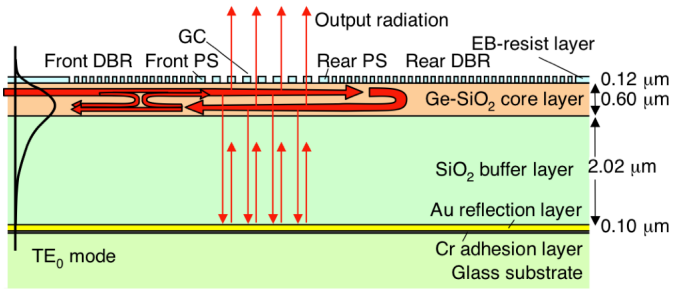


Figure 1. Cross-sectional structure of the designed CRIGIC.

DBR and the front PS between the front DBR and GC are determined so that the reflected wave by the front DBR is canceled by the transmitted backward wave through the front DBR. The thickness of the buffer layer is chosen so that the indirect air radiation wave reflected from the reflection layer is phase-matched with the direct air radiation wave. Therefore, CRIGIC generates only output air radiation.

The device characteristics were predicted by using a coupled mode analysis. The effective index of TE_0 mode was 1.4896, and the grating period of GC and DBRs were 565.7 nm and 282.8 nm, respectively, for operating wavelength of 842.6 nm. The radiation decay factor of GC and the coupling coefficient of DBR were calculated to be 4.46 mm^{-1} and 17.9 mm^{-1}, respectively. The lengths of the front and rear PSs and the front and rear DBRs were calculated to be 212.1 nm, 212.1 nm, 46.9 μm, and 141.4 μm, respectively, for the GC length of 20 μm. Fig. 2 shows the theoretically calculated wavelength dependence of output, transmission, and reflection efficiencies. The maximum output efficiency was calculated to be 96%, which was 6 times as high as that of a conventional GC with the same aperture size. Full width at half maximum (FWHM) of wavelength selectivity was 1.2 nm.

III. Fabrication and Experimental Results

A Cr adhesion layer and an Au reflection layer were sequentially deposited by thermal evaporation on a SiO_2 substrate. A SiO_2 buffer layer and a Ge-SiO_2 core layer were sequentially deposited by plasma-enhanced chemical vapor deposition (PECVD). After an EB resist layer was spin-coated, CRIGIC pattern was formed by EB direct writing and developing. GCs of 1.3 μm and 0.6 μm periods with 0.5 mm aperture were also fabricated for exciting TE_0 mode and for reference, respectively.

Cr atoms diffused through the Au layer, and were oxidized on the Au layer to form Cr_2O_3 during the following PECVD [3]. The Cr_2O_3 was needed for the adhesion between the Au and buffer layers, but also increased the optical path length between the CRIGIC and Au layers. The output efficiency seriously depends on the optical path length due to interference between the direct radiation and the indirect radiation reflected from the reflection layer. Therefore, the optical path length of the fabricated waveguide was measured from a reflection spectrum, and the thickness of the buffer layer was estimated to be 2.24 μm. The maximum output efficiency of the fabricated device

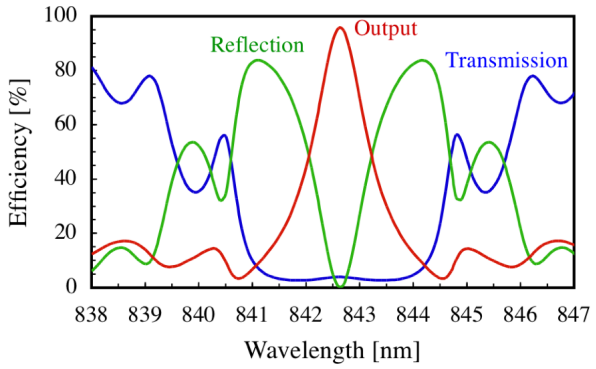


Figure 2. Theoretically calculated wavelength dependence of output, transmission, and reflection efficiencies of CRIGIC.

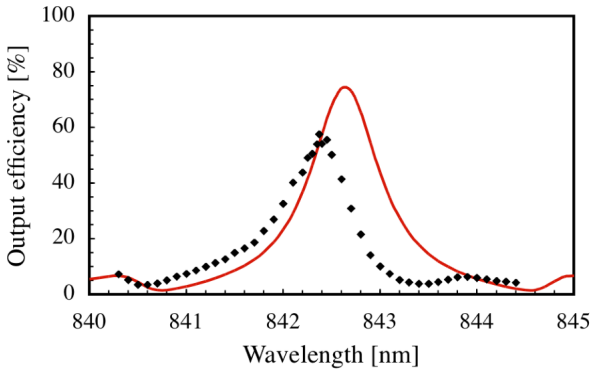


Figure 3. Measured and theoretical wavelength dependence of output efficiency.

was predicted to be 74%.

A tunable laser diode was used as a light source, and TE_0 mode was excited by the GC. Effective index of TE_0 mode was measured to be 1.486 from the incident angle. The radiation decay factor of the reference GC was measured to be 0.8 mm^{-1} from near-field intensity profile of the diffracted wave. Fig. 3 shows measured wavelength dependence of the output efficiency. A theoretical dependence calculated by using the measured effective thickness of the buffer layer is also shown by the red curve in Fig. 3. The maximum efficiency of 58% was obtained at 842.4 nm with FWHM of 0.8 nm.

IV. Conclusions

We have designed and fabricated a CRIGIC with an Au reflection layer on a substrate for high-efficiency coupling with small aperture. The maximum output efficiency of 58% was obtained for 20-μm-aperture CRIGIC, which was 78% of the predicted value. Improvement of device characteristics is now under study by precise control of the effective thickness of the buffer layer. Application of the CRIGIC to optical interconnect devices is also being investigated.

References

[1] S. Ura, "Selective guided mode coupling via bridging mode by integrated gratings for intraboard optical interconnects," Proc. SPIE, vol. 4652, pp. 86–96, 2002.

[2] K. Kintaka, J. Nishii, K. Shinoda, and S. Ura, "WDM signal transmission in a thin-film waveguide for optical interconnection," IEEE Photon. Technol. Lett., vol. 18, pp. 2299-2301, 2006.

[3] K. Kintaka, J. Nishii, S. Murata, and S. Ura, "8-channel WDM optical interconnect divice using add-drop multiplexers integrated in a thin-film waveguide," Tech. Dig. IPNRA, ITuA2, Boston, July 13–16, 2008.

[4] D. Taillaert et al., "Grating couplers for coupling between optical fibers and nanophotonic waveguides," Jpn. J. Appl. Phys., vol. 45, pp. 6071–6077, 2006.

[5] F. Van Laere et al., "Compact and highly efficient grating couplers between optical fiber and nanophotonic waveguide," J. Lightwave Technol., vol. 25, pp. 151–156, 2007.

[6] C. Gunn, "CMOS photonics for high-speed interconnects," IEEE Micro., vol. 26, pp. 58–66, March–April 2006.

[7] S. Ura, S. Murata, Y. Awatsuji, and K. Kintaka, "Design of resonance grating coupler," Opt. Express, vol. 16, pp. 12207–12213, 2008.

[8] Y. Kita, K. Kintaka, K. Shimizu, Y. Awatsuji, and S. Ura, "Aperture miniturization of grating coupler by integration of cavity-resonator," Tech. Dig. Microoptics Conf., pp.350–351, Tokyo, Oct. 25–28, 2009.

Intersubband Absorption Saturation in AlN-based Waveguide with GaN/AlN Multiple Quantum Wells Fabricated by Metalorganic Vapor Phase Epitaxy

Hassanet Sodabanlu, Jeong Seung Yang, Masakazu Sugiyama, and Yukihiro Shimogaki
School of Engineering
The University of Tokyo
Tokyo, Japan
e-mail address: sodabanlu@hotaka.t.u-tokyo.ac.jp

Takuo Tanemura, Yoshiaki Nakano
Research Center for Advanced Science and Technology
The University of Tokyo
Tokyo, Japan

***Abstract*—The intersubband absorption saturation in a ridge AlN-based waveguide with MOVPE fabricated GaN/AlN MQWs was examined. A 1.56-µm short-pulse laser with a temporal width of 0.4-ps FWHM and a repetition rate of 63 MHz was employed to elucidate a 5-dB saturation using a pulse energy of 115 pJ.**

Keywords—MOVPE, intersubbnd transition, GaN/AlN MQWs, absorption saturation

I. INTRODUCTION

The demands placed on optical communication bandwidth have propelled the research into high speed optical components including all-optical switches. Among the potential technologies, intersubband transition (ISBT) in GaN multiple quantum wells (MQWs) has the potential to answer this requirement. This is owing to the unique properties of nitride semiconductors especially ultrafast intersubband relaxation time promoting GaN-based all-optical switch which is capable for Tb/s data operating. So far, the optical switching utilizing the absorption saturation effect in GaN MQWs has been demonstrated only in molecular beam epitaxy (MBE) grown samples [1], [2]. Although metalorganic vapor phase epitaxy (MOVPE) can provide high-quality buffers favorable for low loss and good performance optical devices, the strong intersubband transition at communication wavelength, 1.55-µm, was only recently realized with MOVPE-grown GaN/AlN MQWs [3]. In this work, we demonstrate the intersubband absorption saturation in a ridge AlN-based waveguide with MOVPE-grown GaN/AlN MQWs.

II. SAMPLE PREPARATION

A. Growth of Nitride Layers by MOVPE

The crystal growth of nitride semiconductors was done by AIXTRON 200/4 RF-S low-pressure MOVPE. Trimethyl-gallium, trimethyl-aluminium, ammonia and silane were used as gas precursors. The reactor pressure was maintained at 100 mbar during the growth. The sample was prepared on 0.4-µm-thick high-quality AlN buffer on a c-plain sapphire substrate. A 0.1- µm-thick AlGaN interlayer was grown on the top of the AlN buffer at 1150 °C followed by 10-period GaN/AlN MQWs (1.2 nm/3.0 nm) at 800 °C using pulse injection method [3]. To prevent the GaN/AlN MQWs from effects of sputtered Si_3N_4, the sample was capped with a 0.1-µm-thick AlN layer grown at 850 °C.

B. Waveguide Fabrication

In this work, sputtered Si_3N_4 was utilized as a cladding layer for AlN-based waveguide because of its properties: (i) transparent at 1.5-µm range, (ii) can be deposited at low temperature by sputtering method, and (iii) reflective index matching that of nitride semiconductor. A 0.5-µm-thick Si_3N_4 was deposited at 250 °C using Si target under Ar and N_2 ambient. After that, the 2-µm-wide ridge waveguide structure was fabricated by etching Si_3N_4 layer using ICP-RIE dry etching. The back-side of the sample was polished and a 400-µm-long waveguide was cleaved using a diamond pen.

III. MEASUREMENT RESULTS

Prior to measurement, the functionality of fabricated waveguide was verified by observing a near-field image of propagating light from the output facet. The circular of light spot was observed confirming the successful fabrication. The polarization dependent loss (PDL) and the intersubband absorption saturation were evaluated.

A. Polarization Dependent Loss

The propagation spectra of TE- and TM-polarized light were investigated by direct coupling the signal from a supercontinuum light source covering 1.10 µm to 1.75 µm wavelength range to the ridge waveguide. At output facet, the propagating light was focused by a 100x lens and coupled to a large-diameter multimode fiber via a pinhole and a collimating lens. The polarization of light was controlled by placing a polarization filter between the 100x lens and the pinhole. The output light was then analyzed by optical spectrum analyzer. The PDL was defined by the ratio of transmittances of TE- and TM-polarized light and plotted as function of wavelength in Fig. 1. Note that, the noise around 1.75-µm wavelength was

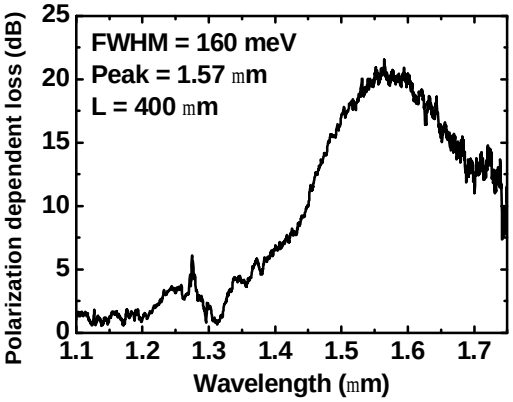


Figure 1. Polarization dependent loss defined by ratio of transmittances of TE- and TM-polarized light

originated from the limitation of the supercontinuum light source. From a 400-μm-long ridge waveguide, we could observe 20-dB PDL including absorption via intersubband transition. The inhomogeneous linewidth of PDL curve was 160 meV with an absorption peak at 1.57 μm. At short wavelength range, the PDL could also be observed. This TM-polarization loss was ascribed to edge dislocations in nitride semiconductors as supported by [4].

B. Intersubband Absorption Saturation

The intersubband absorption saturation in fabricated waveguide was evaluated by self-saturation measurement. A 1.56-μm-wavelength laser with a pulse full-width at half-maximum (FWHM) of 0.4 ps and a repetition rate of 63 MHz was directly coupled to the waveguide. The power of optical pulse was adjusted by an optical attenuator. The energy of input pulse could be determined by the average power of input pulse and repetition rate. The polarization of input light was controlled via fiber-type polarization controller. The output light from the waveguide was coupled to a multimode fiber using a 100x lanes, a pinhole and a collimating lens. The average power of output light was measured by a power meter. Therefore, the transmittances of both TE- and TM-polarized light could be determined by subtracting the output power with the input power (in dBm) and plotted as functions of input energy as presented in Fig. 2.

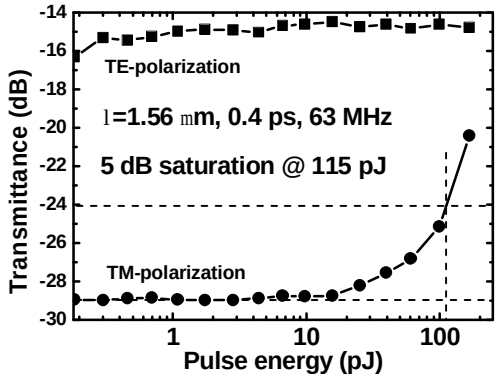


Figure 2. Transmittances of TE- and TM-polarized light as functions of input pulse energy.

For TE-polarization, the non-saturated loss was around 15 dB for a 400-μm-long ridge waveguide. Simulating by the beam propagation method, about 36% of input power can be guided in this ridge structure or 4.4-dB coupling loss equivalent (ideal case). The coupling loss at output facet to the multimode fiber was 9 dB estimated by fiber-to-fiber measurement. Hence, the loss 1.6 dB at most was the propagation loss and scattering loss at waveguide facets highlighting the capability of MOVPE-grown high-quality nitride layers for the fabrication of low loss devices. Considering TM-polarization, the optical nonlinearity via intersubband absorption was observed and 5-dB saturation level could be achieved by using an input energy of 115 pJ. However, this result cannot be directly compared with the records from MBE-grown GaN/AlN MQWs samples reported to have a 10-dB saturation using 38-pJ input energy [1] and a 5-dB saturation using 25-pJ input energy [2]. This is due to input pulse width of 0.4 ps in this work was relatively longer than that of 160 fs in [1] and that of 130 fs in [2]. The saturation energy in this work is expected to decrease with decreasing input pulse width as predicted from the simulation in [5].

IV. CONCLUSIONS

We have demonstrated the intersubband absorption saturation in ridge AlN-based waveguide with GaN/AlN MQWs fabricated by MOVPE. Pumped by 0.4-ps-FWHM pulse laser at 1.56-μm wavelength, 5-dB absorption saturation was achieved with 115-pJ of input pulse energy. This achievement has revealed the potential of MOVPE-grown GaN/AlN MQWs for intersubband optical devices capable of operating at communication wavelength.

REFERENCES

[1] Y. Li, A. Bhattacharyya, C. Thomidis, T. D. Moustakas, and R. Paiella, "Ultrafast all-optical switching with low saturation energy via intersubband transitions in GaN/AlN quantum-well waveguides," Opt. Express, vol. 15, pp. 17922-17927, December 2007.

[2] N. Iizuka et al., "Integration of GaN/AlN all-optical switch with SiN/AlN waveguide utilizing spot-size conversion," Opt. Express, vol. 17, pp. 17922-17927, December 2007.

[3] H. Sodabanlu, J. S. Yang, Y. Shimogaki, M. Sugiyama, and Y. Nakano, "Strain effects on the intersubband transitions in GaN/AlN multiple quantum wells grown by low-temperature metal organic vapor phase epitaxy with AlGaN interlayer" Appl. Phys. Lett., vol. 95, pp. 161908, October 2009.

[4] N. Iizuka, K. Kaneko, and N. Suzuki, "Polarization dependent loss in III-nitride optical waveguides for telecommunication devices," J. Appl. Phys., vol. 99, pp. 093107, May 2006.

[5] N. Suzuki, N. Iizuka, and K. Kaneko, "FDTD simulation of femtosecond optical gating in nonlinear optical waveguide utilizing intersubband transition in AlGaN/GaN quantum wells," IEICE Trans. Electron., vol. E83-C, pp. 981-988, June 2000.

Compact FBG interrogator based on a customized integrated optical arrayed waveguide grating

Thorbjörn C. Buck
Institute for measurement systems and sensor technology
Technische Universität München
Munich, Germany
t.buck@tum.de

M. S. Müller and A. W. Koch

Abstract—**Fiber Bragg gratings (FBG) are attracting more and more attention for use in aeronautical systems. We present an integrated optical robust interrogator for fiber Bragg gratings based on a customized arrayed waveguide grating. The interrogator is capable of simultaneously monitoring four FBGs with strong anti-aliasing capabilities and a cutoff frequency of 20 kHz.**

Keywords-FBG, Arrayed wavgeuide grating, structural monitoring, Fiber Bragg Gratin, interrogator

I. INTRODUCTION

Fiber Bragg grating sensors have great potential for sensing applications, especially where conventional electrical sensors are not reliable, as it is the case, for example, under the influence of high electromagnetic fields. Several interrogation methods for FBGs are well known, as there are for example spectrometers, scanning lasers, etc.[1]. However, these approaches suffer from issues like cost, size and the ability to implement anti-aliasing filtering, which is crucial for sensing applications with dynamic signals. Within the scope of an ESA (European Space Agency)-funded project we developed an interrogator based on a customized manufactured integrated optical arrayed waveguide grating (AWG). The interrogation of FBGs with an AWG-based interrogator was first demonstrated by Sano et al, whereas a commercial of the shelf AWG was used. Our interrogator design allows high speed interrogation of up to four FBGs. The interrogator is being tested at INTA (Instituto Nacional de Técnica Aeroespacial).

II. SPECIFICATION

A. Interrogator specification

The measurement task poses a number of restrictions with respect to the useable wavelength range per sensor and to the minimum acceptable wavelength resolution and accuracy. A minimum of four sensors has to be interrogated at the same time. Each sensor has an wavelength operation range of approx. 5 nm, which corresponds to a temperature range of ±100°C at a dynamic axial mechanical load of approx. 1500 µstrain [2].

The dimensions of the interrogator unit need to be in accordance with the very tight size restrictions of the Ariane launcher electronic interface system. The main task of the interrogator is to monitor structural loads during lift off of the launcher, so the system has to be constructed considering the potentially occurring high vibrational and thermal loads on the interrogator during operation. The minimum permissible measurement frequency is 20 kHz.

III. MEASUREMENT PRINCIPLE

For the intended measurement task, an interrogator based on an arrayed waveguide grating as an optical filter was developed, as AWGs offer the potential for integrating a large number of optical filter edges at minimum device size. Together with the possibility of integrating passive optical devices as PIN photodetectors on the AWG die and thus due to the ability to precisely control the temperature of all electro-optical and optical parts of importance for the measurement, this interrogation device allows good performance for this measurement task.

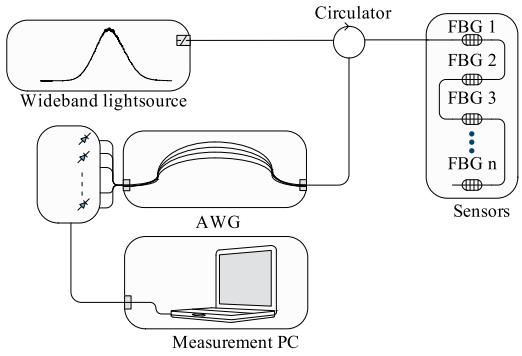


Figure 1 Schematic of the designed AWG-based FBG-interrogator

In AWG based FBG interrogators, a number of serially multiplexed FBGs are illuminated by a large bandwidth light source. Depending on the load acting of an FBG, a spectrally well defined part of the illuminating spectrum is reflected by each FBG. The reflected light portion is guided to the input waveguide of an AWG. A schematic of the measurement setup is shown in Figure 1. Depending on the reflection wavelength of the FBG, this fact gives rise to light intensities in two adjacent output channels of the AWG, which are measured by photodiodes.

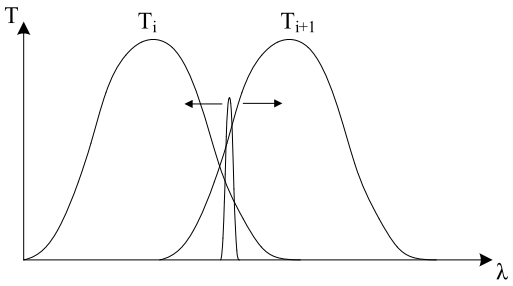


Figure 2 AWG-based measurement principle. narrow peak indicates FBG reflection. Broad Peaks indicate two adjacent output channel transmission characteristics

The measurement principle is indicated in Figure 2. The narrow spectral peak indicates the spectral FBG reflection. The two broad spectral curves indicate schematically the spectral transmission of two adjacent AWG output channels. The FBG center wavelength is determined by the logarithmic ratio of the measured intensities in the adjacent channels [3]

$$\rho = \frac{\log(I_i - I_b)}{\log(I_{i+1} - I_b)},$$

where I_i and I_{i+1} denote the light intensities in the adjacent channels caused by the FBG and I_b denotes the photocurrent contribution of the background reflected light in the fiber.

The spectral measurement uncertainty of the interrogator is dependent on a number parameters [6], as there is for example the light source intensity, the FBG peak reflectivity, the AWG channel spacing and channel width.

For the described measurement task, a measurement uncertainty of 10 pm at a maximum frequency of 20 kHz is acceptable. Considering this restriction in combination with the desired spectral measurement range per sensor, simulations according to [6] were performed. An AWG with a channel spacing of 3.33 nm and a spectral channel FWHM of 2.33 nm, considering a Gaussian channel transmission profile, is applied in the simulations.

Inevitable noise contributions present in the detected signals in the adjacent channels give rise to measurement uncertainties. Figure 3 shows the estimate useable measurement bandwidth for a system with a standard draw tower grating, dependent on the first stage amplifier electronics bandwidth and on the AWG channel width. The useable measurement range decreases for with increasing electronic bandwidth. On the one hand high electronics bandwidth is needed for precise measurement of high frequency loads on the sensor, on the other hand signal amplitudes larger than the adjacent channel spacing desire high electronic bandwidths for the necessary amplification of higher signal frequency harmonics, as it is discussed below.

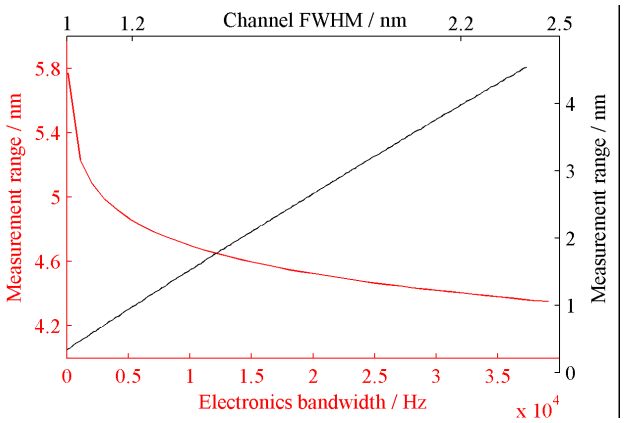


Figure 3 Measurement range at a measurement accuracy below 10 pm, dependent on (black) AWG channel FWHM and on (red) amplification electronics bandwidth

Larger spectral channel widths give rise to higher signal levels at the detectors, reducing the noise contribution for signal evaluation. Thus, considering quasi-static signals, the useable measurement range per channel pair can be increased by designing the AWG for larger output channel widths at a fixed channel spacing.

Large signal amplitudes, i.e. large dynamic wavelength shifts of the FBGs, lead to the generation of higher signal harmonics at the opto-electronic detector due to the nonlinear shape of the channel transmission functions at the channel center wavelengths. Thus, a first amplification stage needs to have a cutoff frequency much higher than the expected signal frequencies, in order to provide distortion free signal sampling. This seems to be partially in conflict with the above mentioned increasing measurement uncertainty with increasing electronics bandwidth. However, this can be encountered by proper signal oversampling, averaging and application of appropriate deskewing filters.

IV. System Realization

A. Arrayed waveguide grating

A planar photodiode array has been integrated in the output channels of the manufactured AWG after device characterization and the device has been integrated in a customized butterfly package. The packaging is prepared for a hermetic sealing which is needed during the intended operation on the ARIANE launcher during lift off, as influences from condensing moisture on the optical performance of the AWG have to be eliminated.

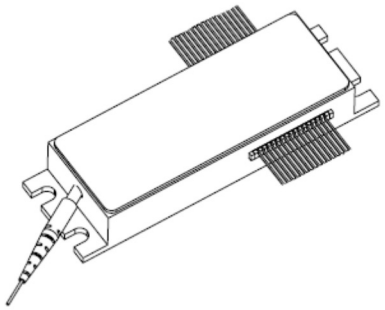


Figure 4 AWG packaging with implementable hermetic sealing for space applications

B. Device performance

From the measured AWG channel transmission curves, the performance of the interrogator can be estimated. Figure 5 exemplarily shows the evaluation function for the two adjacent output channels of the customized AWG. The evaluation function shows a good linear behavior over a wavelength range of approximately 4.6 nm. This is in very good accordance with the expected useable measurement range of approximately 4.5 nm, considering the measurement system electronical and optical configuration.

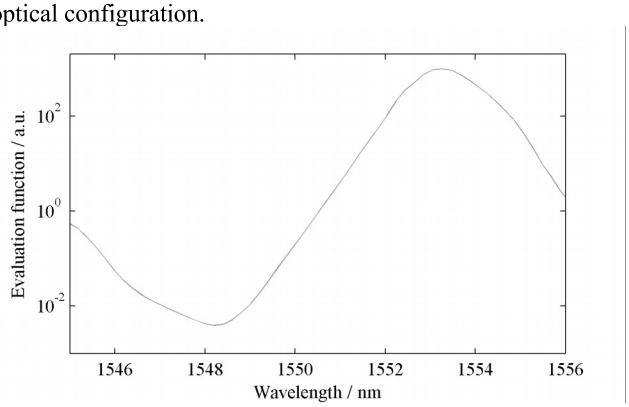


Figure 5 Exemplary interrogation function for a FBG sensor

C. Conclusion and Outlook

We have developed an AWG-based compact FBG interrogator for use under harsh environmental conditions. The interrogator is designed for a measurement uncertainty below 10 pm at a maximum signal frequency of 20 kHz. The optical core component is packaged packaging adapted for use in space.

The device will be extensively tested at the test facilities at INTA.

For further improvement of AWG-based FBG interrogators, further investigation with respect to on shaping the spectral transmission curves of the AWG output channels needs to be carried out

ACKNOWLEDGMENT

The authors acknowledge funding of the project by ESA and KayserThrede GmbH. Furthermore, the authors would like to acknowledge the contributions of OptriCon and Fraunhofer Heinrich Hertz Institute to the project.

REFERENCES

[1] Zhao Y., Liao Yanbiao, “Discrimination methods and demodulation techniques for fiber Bragg grating sensors,” Optics and Lasers in Engineering, 41, pp. 1-18, 2004

[2] A. Othonos, “Fiber Bragg Gratings”, Review of Scientific Instruments, 68:4309-4341 ,1997

[3] “Fast Optical Wavelength Interrogator Employing Arrayed Waveguide Grating for Distributed Fiber Bragg Grating Sensors”, Journal of Lightwave Technology, Y. Sano, T. Yoshino, Vol. 21, pp.132-139,2003

[4] C.M. Lopatin, S. Mahmood, E. Mendoza, B. Moslehi, R. Black, K. Chau, L. Oblea , “Progress in miniaturization of a multichannel optical fiber Bragg grating sensor interrogator,” Proc. SPIE, Vol. 6619. 66193X (2007), doi:10.1117/12.738785

[5] T. Zeh, Optical Fiber Bragg Sensors, Dissertation, TU München, 2004, in: Reports on Measurement and Sensor Systems, Shaker Verlag

[6] T. Buck, M.S. Mueller, M. P. Plattner, A. W. Koch, “Performance analysis of interrogators for Fiber Bragg Grating sensors based on arrayed waveguide gratings”, Proceedings of SPIE, Vol 7389 (2009), doi: 10.1117/12.827526

1x3 Beam Splitter Based on Self-Imaging Phenomena in Air-Slab Photonic Crystal Waveguides

Min Zhang, Martin Kristensen, Asger Christian Krüger
INANO, IFA and ASE
Aarhus University
Ny Munkegade 120, DK-8000 Aarhus C, Denmark
minz@inano.dk, mk@phys.au.dk

Radu Malureanu
Plasmonics and Metamaterials group, Department of Photonics Engineering
Technical University of Denmark
Ørsteds Plads, DK - 2800 Kgs. Lyngby, Denmark

Abstract— **A 1x3 beam splitter using multi-mode interference based on self-imaging is demonstrated theoretically and experimentally in PhCWs. The total transmission of the 1x3 splitter is almost equal to the corresponding length of W1 PhCW. The input power is distributed equally between the output ports within 1dB from 1541nm to 1552nm.**

Keywords- Splitter; Self-imaging; multi-mode interference; Photonic Crystal; Waveguides; e-beam lithography

I. INTRODUCTION

Beam splitters are central building blocks in large-scale photonic integrated circuits (PICs). There are different ways to equally split the introduced signal into output ports based on photonic crystal waveguides (PhCWs). Some of the most successful structures in PICs are based on slab photonic crystals (PhCs) [1]. In such waveguides, the optical field is confined, horizontally, by a photonic band-gap (PBG) provided by the PhC and, vertically, by total internal reflection due to the refractive index differences between different layers. Various PhCW components can be made by slab PhC, such as bend structures, 1x2 optical beam splitters, including Y- or T-junctions and directional couplers. Most work focuses on single-mode operation in the performance of PhCW. However, multi-mode interference (MMI) in line-defect PhCWs also exhibit extraordinary features [2]. In recent years, there has been a growing trend in the application of MMI effects in integrated optics. The technology for both PhCW and MMI fabrication is well developed.

The wavelength de-multiplexer based on self-imaging phenomena in line-defect PhCWs has been theoretically investigated [3]. TE and TM polarization splitters based on the simulation using self-imaging phenomena in PhCW were studied by Hong *et al.* [4]. Liu *et al.* first investigated theoretically 1x2 splitter based on self-imaging phenomena in line-defect PhCWs [5]. The 2D simulation of Yu *et al.* indicated that the self-imaging phenomena also exist in every other-line defect PhCWs for 1xN (N≥2) splitter [6,7]. The beating length in this every-other-line defect PhCWs is shorter than the conventional coupling length in line-defect PhCWs. Rod slabs were adapted in Liu *et al.*'s research, but high transmittance can only be obtained for very high rods in the slab. High transmittance can be obtained in thin air-slab PhCW, and integration with other building blocks is easily carried out. Standard SOI wafers and e-beam lithography provide our fabrication platform. Here we report the theoretical and experiment result of a 1x3 beam splitter based on self-imaging phenomena in the 340nm top silicon layer of a SOI wafer.

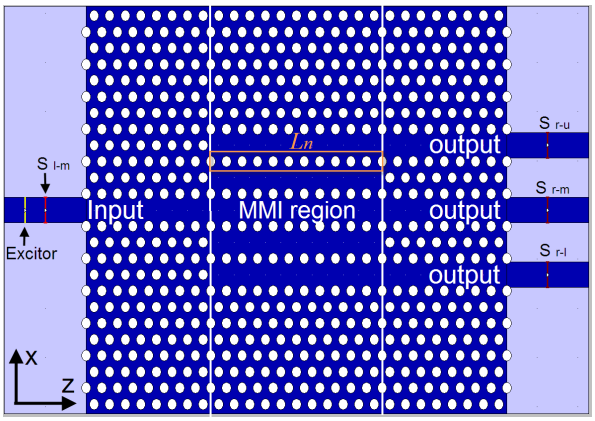


Figure 1. Schematic layout of 1x3 beam splitter consisting of input, MMI and output PhCWs, and excitor and sensors arranged in the ridge waveguides.

II. SELF-IMAGING PRINCIPLE

Bryngdahl *et al.* suggested the possibility of achieving self-imaging in slab waveguides [8], and Urich *et al.* explained the principle in detail [9]. Self-imaging is a property of multi-mode waveguides by which an input field profile is reproduced in single or multiple images at periodic intervals along the propagation direction [2].

The proposed 1x3 beam splitter based on planar PhCW is shown in Fig. 1. It consists of three sections of PhCW, a single-mode input, MMI region with length L_n (L_n needs to be optimized. n is the number of holes and must be an integer) and three single-mode outputs. The lengths of input and output ports were fixed in the theoretical design. The interaction between adjacent output ports can be ignored, due to the separation by three rows of air holes.

III. MODEL AND THEORETICAL SIMULATION

The PhC structure has a pitch of Λ=380 nm in a triangular configuration of air holes with 222nm diameter. This arrangement in silicon (refractive index n=3.476) gives rise to a high transmittance and a band-gap below the silica line for TE-polarized light. The traditional W1 waveguide is obtained by removing a single row of air-holes in the Γ-K direction of the

lattice. The in-plane normalized dispersion diagrams for single- and multi-mode PhCWs are shown in Fig. 2. Super-cells are depicted as insets, calculated by 3D plane wave expansion (PWE). It is seen that the frequency range of PhC in both super-cells are similar. One even mode is supported in single-mode PhC, and three even modes are supported in multi-mode PhC. This means that a 1x3 beam splitter is conceivable in this slab design near the frequency of 0.241(Λ/λ).

The configuration of Fig. 1 is directly used in 3D FDTD modeling. Different L_n's were simulated (with grid Λ/24). The calculations show that the component with L_n=11Λ splits the input equally and exhibits the highest transmittance. This means that the first 3-fold images are obtained around 11Λ due to MMI. The net normalized transmittance is obtained by the net transmittance through the sensors in the right ridge waveguides divided by that through the input sensor. The net transmittance for W1 PhCW and the optimized splitter are shown in Fig. 3. From the 3D simulation, the best wavelength is 1567.4 nm and the total normalized transmittance is close to that for a W1 PhCW. The H_y field distribution at 1567.4 nm is depicted in the inset.

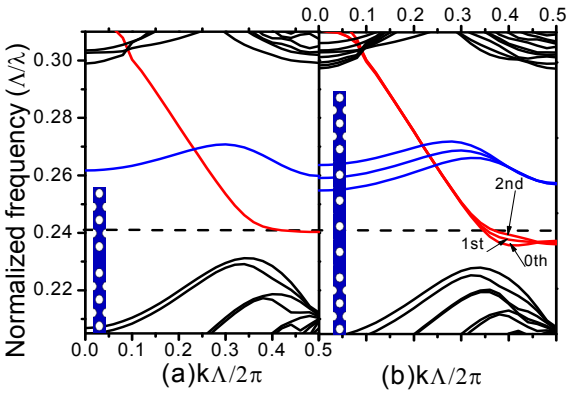


Figure 2. Dispersion diagram for TE polarization of the PhCWs calculated using 3D PWE method. The supercells are shown in the insets. Black lines are PhC modes. Red (blue) line are even (odd) gap-guided modes.

IV. Fabrication and Characterization

The optimized splitter was fabricated using e-beam lithography and standard anisotropic reactive-ion etching to define the PhCW structure into the 340 nm top silicon layer. A SEM photograph of the optimized splitter is shown as inset in Fig. 4. The air holes have a diameter of 220 +/- 5nm.

The optical properties were characterized by observing the normalized transmittance spectra for TE from 1480 to 1580 nm. The experimental results are shown in Fig. 4. The experimental result is consistent with that of the numerical modeling. The small difference is attributed to the finite gridding, ignoring a few nm native oxide in the modeling and fabrication errors. The total output of the 1x3 splitter is close to the analogue length of W1 PhCW. The power is divided equally into three parts between 1541 and 1552 nm, with the biggest difference among the output ports less than 1dB.

In summary, the numerical and experimental results show that the input beam is split equally into three outputs within a ~ 10nm range near 1550nm. The 1x3 splitter is important for many applications including telecommunications.

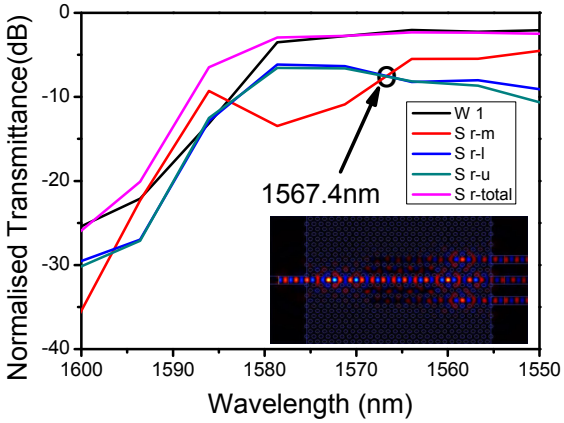


Figure 3. Normalised TE-polarized transmittance (dB) for the splitter with L_n=11Λ, simulated by 3D FDTD. The inset is a snapshot of H_y at 1567.4 nm.

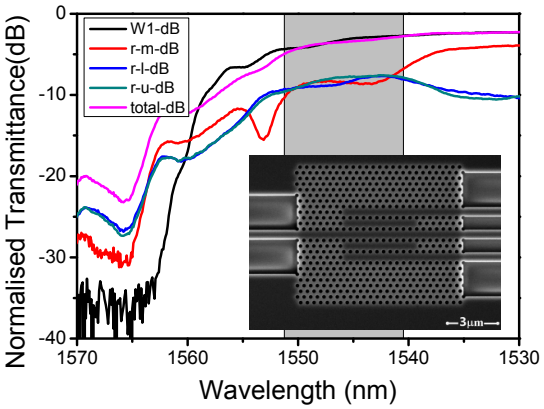


Figure 4. Measured normalised TE-polarized transmittance (dB) for the 1x3 splitter in Fig. 4, the inset is an SEM photograph of the component.

References

[1] J. D. Joannopoulos, S. G. Johnson, J.N. Winn and R. D. Meade, Photonic Crystals: Molding the Flow of Light, 2nd ed., Princeton, NJ: Princeton University Press, 2008.

[2] L. B. Soldano and E. C. M. Pennings, "Optical multimode interference devices based on self-imaging - principles and applications", J. Lightwave Technol., vol. 13, pp 615-627, 1995.

[3] H. J. Kim, I. Park, B. H. O, S. G. Park, E. H. Lee and S. G. Lee. "Self-imaging phenomena in multi-mode photonic crystal line-defect waveguides: application to wavelength de-multiplexing", Opt. Express, vol. 12, pp 5625-5633, 2004.

[4] H. B. Chen, Y. Xu, J. L. He and Z. Hong, "A polarization splitter based on self-imaging phenomena in an anisotropic photonic crystal with an absolute photonic band gap", Opt. Comm, vol. 282, pp 3626–3629, 2009.

[5] T. Liu, A. R. Zakharian, M. Fallahi, J. V. Moloney and M. Mansuripur,, "Multimode interference-based photonic crystal waveguide power splitter" J. Lightwave Technol., vol. 22, pp 2842-2846, 2004.

[6] T. B. Yu, M. H. Wang, X. Q. Jiang, Q. H. Liao and J. Y. Yang, "Ultracompact and wideband power splitter based on triple photonic crystal waveguides directional coupler" J. Opt. A: Pure Appl. Opt. vol. 9, pp 37-42, 2007.

[7] T. B. Yu, H. F. Zhou, Z. Gong, J. Y. Yang, X. Q. Jiang, and M. H. Wang, "Ultracompact multiway beam splitters using multiple coupled photonic crystal waveguides", J. Phys. D: Appl. Phys. vol. 41, pp. 095101, 2008.

[8] O. Bryngdahl, "Image formation using self-imaging techniques," J. Opt. Soc. Amer., vol. 63, no. 4, pp. 416-419, 1973.

[9] R. Ulrich, "Image formation by phase coincidences in optical waveguides," Opt. Comm., vol. 13, no. 3, pp. 259-264, 1975.

Efficient Tapering to the Fundamental Quasi-TM Mode in Asymmetrical Waveguides

D. Vermeulen, K. Van Acoleyen, S. Ghosh, S. Selvaraja, W.A.D. De Cort, N.A. Yebo, E. Hallynck, K. De Vos, P.P.P. Debackere, P. Dumon,W. Bogaerts, G. Roelkens, D. Van Thourhout and R. Baets
Photonics Research Group, Department of Information Technology (INTEC)
Ghent University - IMEC
Sint-Pietersnieuwstraat 41, 9000 Ghent, Belgium
Diedrik.Vermeulen@intec.ugent.be

Abstract—**The tapering problem of the fundamental quasi-TM mode in thin asymmetrical waveguides is investigated. Mode conversions are found to be at the origin of the failing adiabatic tapers. We propose and investigate three non-adiabatic taper solutions, a focusing grating coupler, a lensed taper and a discontinuous taper, which circumvent these mode conversions.**

Keywords-taper; quasi-TM; polarization; integrated photonics; asymmetrical waveguide; Silicon Photonics;

I. INTRODUCTION

Optical waveguides are the fundamental building blocks of integrated photonic devices. Besides waveguide loss, substrate loss, optical confinement and footprint one has to deal with polarization issues when designing a waveguide. In high index contrast platforms such as Silicon-On-Insulator (SOI), thin (subwavelength) waveguides are used resulting in quasi-polarized modes which differ substantially in effective refractive index (birefringence), optical confinement and waveguide loss. Besides the traditional optical communication application for integrated circuits where polarization diversity is required, interest in using the quasi-TM polarization is rising. One advantage is that because of a weaker optical confinement and because of a large evanescent field at the top of the waveguide, the quasi-TM mode is more suited for field interactions with deposited and bonded materials or for biosensing [1]. Another example is where the quasi-TM polarization is used to excite plasmons in a gold clad layer [2]. All these applications can result in highly asymmetrical waveguide structures. The problem is that asymmetrical waveguide circuits, unlike symmetrical ones, don't transmit any quasi-TM polarized light if adiabatic tapering from a multi-mode waveguide to a single-mode waveguide is present.

II. ADIABATIC MODE CONVERSIONS

All calculations have been performed for an SOI strip waveguide with a thickness of 220nm. When the top cladding of the waveguide is equal to the bottom cladding, we speak of a symmetrical waveguide. This vertical symmetry introduces a plane along which the mode is purely polarized, resulting in quasi-TE and quasi-TM modes. For waveguides where top and bottom cladding are different or in the case of a rib waveguide,

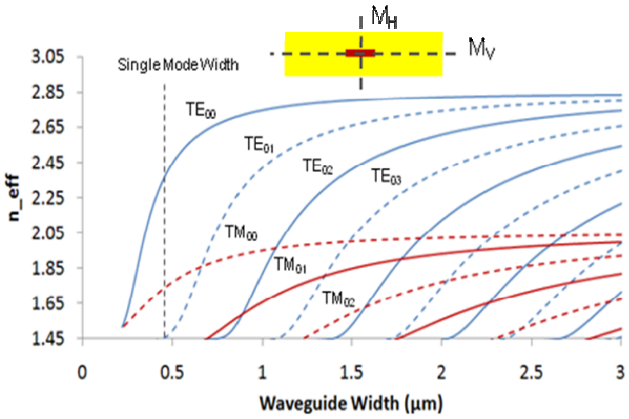


Figure 1. Adiabatic Mode Profile of a symmetric waveguide.

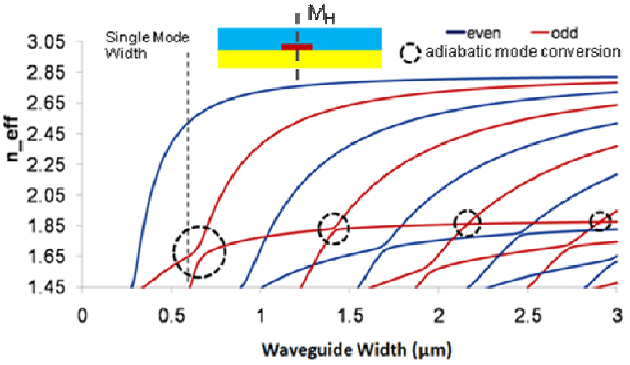


Figure 2. Adiabatic Mode Profile of an asymmetric waveguide.

the symmetry is broken and one cannot make a distinction between different quasi-polarized modes. As a convenience we shall use quasi-polarized mode naming in these asymmetrical waveguides referring to the quasi-polarized counterpart of the mode in the symmetrical case. Fig. 1 and 2 show the effective refractive index as a function of the waveguide width for all guided modes of respectively a symmetrical waveguide and asymmetrical waveguide. In a symmetrical waveguide two symmetry planes are present by which the modes can be

classified. Using the vertical symmetry (M_V), modes are split into quasi-TE and quasi-TM modes. The horizontal symmetry (M_H) subdivides these polarizations into even and odd modes. In an asymmetrical waveguide the symmetry plane for quasi-polarization classification disappears such that quasi-TE and quasi-TM modes can couple to each other in adiabatic tapers. The circles in Fig. 2 show the mode conversions from the fundamental quasi-TM mode to higher order quasi-TE modes. The latter are not guided in a single-mode waveguide what explains the breakdown of adiabatic tapering.

III. NON-ADIABATIC TAPERS

We will investigate different solutions which circumvent the mode conversion problem for tapering to the fundamental quasi-TM mode in an asymmetrical strip waveguide.

A. Focusing Fiber-To-Chip Grating Coupler

With a focusing grating coupler, see Fig. 3(a), one can couple and at the same time focus the light into a photonic wire [3]. This approach is experimentally verified and an efficiency of 13% is demonstrated for coupling from an optical fiber to the fundamental quasi-TM mode of a 220nm thick SOI single-mode photonic 500nm wire. The etch depth of the grating is 70nm and the top cladding is air, making the waveguide highly asymmetrical. The 1dB and 3dB bandwidth were respectively 45nm and 80nm.

B. Lensed Focusing Taper

Another way of avoiding the mode conversion problem due to adiabatic tapering is to use a focusing effect as is done in focusing grating couplers. This focusing effect can also be obtained by using in-plane lenses. These lenses can for example be fabricated in silicon using doping or by etching. The lenses considered here are made by etching 70nm of the 220nm high silicon area as shown in Fig. 3(b). Since the effective index of the etched area is smaller, a focusing lens has a concave shape. One can now design bi-concave and plano-concave lenses. From lensing theory it is known that the latter result in fewer aberrations when using them for focusing purposes. 2D effective index FDTD simulations were performed for focusing from a 10µm waveguide to a 450nm waveguide using bi-concave lenses. For a radius of curvature ranging from 5µm to 10µm, the focal length ranges from 9µm up to 23µm and the efficiency increases from 85% up to 90% respectively. The use of plano-concave lenses roughly doubles the focal distance but no significant improvement in efficiency was seen. The increase in efficiency for larger focal distances can be explained due to matching of the focused light to the diffraction of a 450nm waveguide. 3D-FDTD simulations were performed as well but these show a decrease in efficiency to about 30%. This is mainly due to the etch step which will scatter the light since the TM mode has the largest field intensity at the top and the bottom of the waveguide.

C. Discontinuous Taper

By avoiding the waveguide widths in a taper for which mode conversions take place, one can design a discontinuous taper as shown in Fig. 3(c). By optimizing the waveguide widths of the discontinuous sections of the taper with a 3D vectorial mode solver, 90% efficiency has been obtained for tapering from a 10µm waveguide to a 450nm waveguide of the fundamental quasi-TM mode.

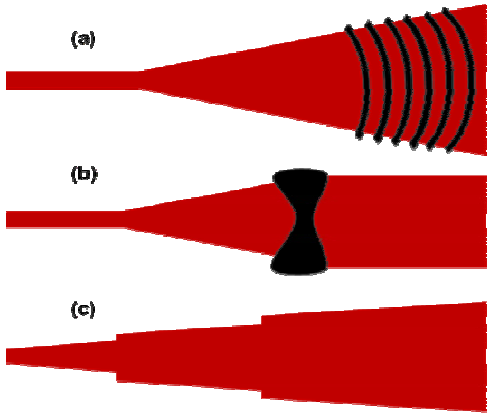


Figure 3. Non-Adiabatic tapers: (a) Focusing Grating Coupler (b) Lensed Focusing Taper (c) Discontinuous Taper

IV. CONCLUSION

We have found that asymmetrical adiabatic tapers exhibit a lot of mode conversions and are unsuitable for tapering of the fundamental quasi-TM mode. 13% coupling efficiency has been measured for a focusing grating coupler that couples and focus the light into a single-mode waveguide. 2D and 3D-FDTD simulations predict respectively 90% and 30% taper efficiency for a lensed focusing taper. According to 3D vectorial mode solving, an optimized discontinuous taper can have 90% taper efficiency. In symmetrical waveguides, process variations can break the symmetry resulting in mode conversions. In general one should avoid the waveguide widths near a mode conversion. For the same reason it is desirable to not make an adiabatic taper unnecessary long for symmetrical waveguides.

ACKNOWLEDGMENT

D. Vermeulen, W.A.D. De Cort and K. De Vos thank the Institute for the Promotion of Innovation by Science and Technology in Flanders (IWT) for a grant. K. Van Acoleyen, W. Bogaerts and G. Roelkens acknowledge the Research Foundation-Flanders (FWO-Vlaanderen) for a research grant.

REFERENCES

[1] A. Densmore, D. X. Xu, P. Waldron, S. Janz, P. Cheben, J. Lapointe, A. Delge, B. Lamontagne, J. H. Schmid, and E. Post, "A silicon-on-insulator photonic wire based evanescent field sensor," IEEE Photonics Technology Letters, 18:23 (2006), 2520-2522.

[2] P. Debackere, R. Baets, and P. Bienstman, "Bulk sensing experiments using a surface-plasmon interferometer," Optics letters, 34:18 (2009), 2858-2860.

[3] F. Van Laere, T. Claes, J. Schrauwen, S. Scheerlinck, W. Bogaerts, D. Taillaert, L. O'Faolain, D. Van Thourhout, and R. Baets, "Compact focusing grating couplers for silicon-on-insulator integrated circuits," IEEE Photonics Technology Letters, 19:23 (2007), 1919-1921.

Microwave photonics beamformer based on ring resonators and arrayed waveguide gratings

J.D. Doménech, M. Rius, J. Mora, P. Muñoz and J. Capmany
Optical Communications Group. ITEAM Research Institute
Universidad Politécnica de Valencia, Camí de Vera s/n, 46020 Valencia (Spain)
E-mail: jodogo@iteam.upv.es

***Abstract*—In this paper a novel microwave photonics beamformer device concept, for single side band (SSB) modulated signals, is presented. The device is based on tunable lasers, arrayed waveguide gratings and an all-pass ring resonator. The reconfiguration accuracy and time depend on the laser switching characteristics.**

I. Introduction

Microwave photonics is becoming a strong field where the processing of high frequency microwave signals is done completely in the optical domain [1], avoiding the common limitations of the electric domain. Amongst the applications, beamforming is of great interest. On the other hand, integrated optics ring resonators (RR) are key devices due to their small foot print and filtering response. Several approaches exist in the literature for optically controlled tunable beamformers, amongst them some using all-pass RR. In the work by Adams et al. [2] tunability is done by means of the thermo-optic effect with heaters. Chang et al. [3] use the thermal nonlinear effect of Silicon. However, despite the change in refractive index with the temperature can be large (for instance in Silicon [4] $\partial n/\partial T = 1.86 \cdot 10^{-4} K^{-1}$), the response times are not better than 1 μs [5]. The approach presented in this paper is limited by the switching speed of the tunable lasers, which are well below the nanosecond scale [6].

II. Microwave phase shifter

Consider a single-side band (SSB) optical signal, with optical carrier frequency f_c and radio frequency (RF) f_{RF}. The signal is filtered using an all-pass ring-resonator, hence a relative phase shift is induced between the optical carrier and the RF sub-carrier frequencies [7]. The RR response is periodic, hence the phase shift depends on both the position of the optical carrier within the spectral period (Free Spectral Range, FSR) and the relative difference between the optical carrier and RF sub-carrier frequencies. The characterization of a RR limited to two FSR span is shown in Fig. 1. For a given optical carrier and accompanying RF sub-carrier, by tuning the former, the relative phase shift changes, due to the shape of the phase response of the all-pass RR. A power penalty takes place, due to the non-flat power transfer function in practical devices as in Fig. 1. The penalty depends on the RR coupling constant and round trip losses.

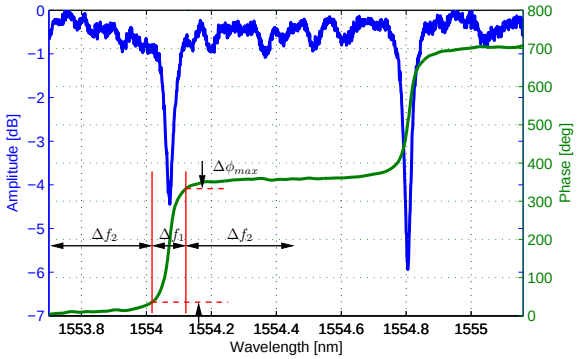


Fig. 1: Power transmission and phase characterization of an all-pass single RR in two FSRs.

III. Tunable beamformer concept

The beamformer device is depicted in Fig. 2 and consists of N tunable lasers multiplexed by an Nx1 AWG. The lasers are externally modulated by a dual-drive Mach Zender Modulator (MZM), filtered with an all-pass RR and then demultiplexed by an 1xN AWG. The phase shift for each antenna can be selected by tuning the corresponding laser in the range allowed by the passband of the AWG, and within the RR FSR. The spectral response of the all-pass RR is periodic with period $FSR = \frac{c}{n_g L_c}$, where c is the speed of light in vacuum, n_g is the group refractive index of the waveguides and L_c the RR cavity length. For the phase shifter design it is useful to partition the RR FSR as shown in Fig. 1. The maximum phase shift ($\Delta\phi_{max}$ in the figure) is given by both a) the spectral separation of the optical and RF signals and b) the phase response slope. From the figure, to be able to change $\Delta\phi$ in the range [0,$\Delta\phi_{max}$] by tuning the laser, $\Delta f_1 \leq f_{RF} \leq \Delta f_2$. The pair $\Delta\phi_{max}$ and Δf_1 depends on the slope of the phase transfer function around resonance. This slope depends on the power coupling constant K between the ring and the access waveguide. The lower the K value, the higher the slope, and the wider the flat regions in the phase transfer, out of resonance [8]. A steep slope turns into a small fraction of the FSR (Δf_1) needed to attain the targeted maximum phase shift ($\Delta\phi_{max}$). The maximum achievable phase shift for a single ring device will be always lower than 360 degrees with this configuration, but this can be solved by using multistage

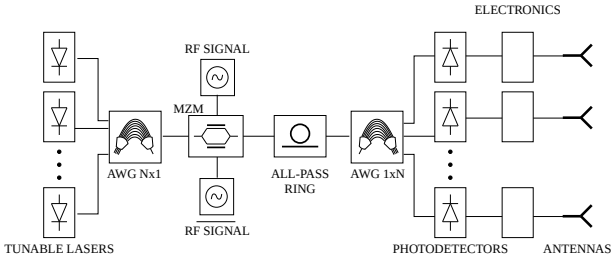


Fig. 2: Schematic of the integrated beamformer.

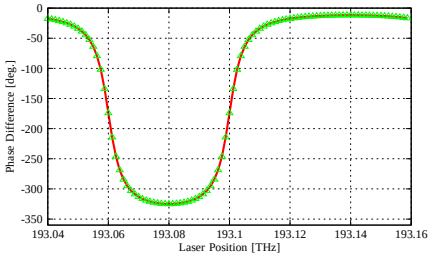


Fig. 3: Induced phase shift for a 40 GHz RF signal in one channel vs laser position in the ring FSR. The triangle symbols indicate the tunable laser discrete steps.

resonators.

The AWG frequency channel spacing must be designed to be equal to an integer multiple of the RR FSR. A critical part of the design is the spectral alignment of the AWG multiplexer and demultiplexer. Either individual thermal tuning or an advanced design with a single 2Nx2 AWG in loopback configuration [9] can solve the problem.

A 4 element beamformer design based in a single ring all-pass section designed in Silicon-On-Insulator is presented. The device simulations are based in a fabricated and characterized RR with waveguide cross-section of 220x500 nm. This waveguide has a group index of 4.25 for TE mode near 1.55 μm wavelength and propagation losses of about 3 dB/cm. The cavity length is set to 711.68μm leading to a FSR close to 99 GHz at the mentioned wavelength. The pair $\Delta\phi_{max}$ and f_{RF} are set to be to 270 degrees and 40 GHz respectively. Fig. 3 shows the induced phase shift between the optical and RF signals while the laser is swept inside an AWG channel. A typical laser step of 10 pm (1.25 GHz) is assumed, though many commercially available tunable have smaller steps. The smaller the laser step, the higher the accuracy of the device beamforming, in terms of both the pointed direction and the available (discrete) set of directions. In Fig. 3 96 positions corresponding to 1.25 GHz steps within a 120 GHz range are shown. Note the aforementioned laser step trade-off, for instance from laser step 16 to 17 there is a phase increment of more than than 30 degrees. The AWGs passbands are designed [10] to have a bandwidth equal to the RR FSR. The full device has been modelled with commercial software [11].

Fig. 4 shows the ideal radiation diagram of the 4 isotropic elements linear array for several progressive phases and the diagram obtained with the simulated device. The main lobe

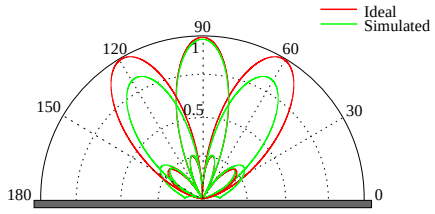


Fig. 4: Radiation diagram vs. Θ [deg.] for a uniform linear 4 element array, for different α values and $d = \lambda/2$

angular mean deviation from theoretical calculations is 0.923 degrees but can easily improved by reducing the tunable laser step. Moreover, the diagram shows a reduced radiation efficiency in the main lobe due to the non-flat RR power transfer function. This could be compensated if the device is implemented in InP technology, with a Semiconductor Optical Amplifier (SOA) placed before each photodetector.

IV. Conclusions

A novel optical beamformer architecture has been presented where the reconfiguration accuracy and time depend on the tunable laser characteristics. The former is easily around 1 pm, therefore providing a nearly continuously tunable device, while the later is in the nanosecond time scale. The device can provide phase shifts up to 360 degrees with a multistage RR design. To optically control the amplitude of the radiant elements, and hence the sidelobe level and null position in the radiation directions, the device can be completely designed in InP with semiconductor optical amplifiers.

References

[1] J. Capmany and D. Novak, "Microwave photonics combines two worlds," *Nature Photonics*, vol. 1, pp. 319–330, 2007.

[2] D. Adams and C. Madsen, "A novel broadband photonic RF phase shifter," *IEEE Journal of Lightwave Technology*, vol. 26, no. 15, pp. 2712–2717, 2008.

[3] Q. Chang, Q. Li, Z. Zhang, M. Qiu, T. Ye, and Y. Su, "A tunable broadband photonic RF phase shifter based on a silicon microring resonator," *IEEE Photonics Technology Letters*, vol. 21, no. 1, pp. 60–62, 2009.

[4] G. Cocorullo and I. Rendina, "Thermo-optical modulation at 1.5 μm in silicon etalon," *Electronics Letters*, vol. 28, no. 1, pp. 83–85, 1992.

[5] V. Almeida and M. Lipson, "Optical bistability on a silicon chip," *Opt. Letters*, vol. 29, no. 20, pp. 2387–2389, 2004.

[6] G. Alibert, F. Delorme, P. Boulet, J. Landreau, and H. Nakajima, "Subnanosecond tunable laser using a single electroabsorption tuning super structure grating," *IEEE Photonics Technology Letters*, vol. 9, no. 7, pp. 895–897, 1997.

[7] C. K. Madsen and G. Lenz, "Optical all-pass filters for phase response design with applications for dispersion compensation," *IEEE Photonics Technology Letters*, vol. 10, pp. 994–996, July 1998.

[8] J. E. Heebner, R. W. Boyd, and Q.-H. Park, "Scissor solitons and other novel propagation effects in microresonator-modified waveguides," *J. Opt. Soc. Am. B*, vol. 19, no. 4, pp. 722–731, 2002.

[9] P. Munoz, J. D. Domenech, M. Manzanedo, J. Den Besten, E. Verdumen, and J. Capmany, "Design of arrayed waveguide sagnac interferometers for OTDM-WDM optical networks," *5th Reunión Española de Optoelectrónica*, 2007.

[10] P. Munoz, D. Pastor, and J. Capmany, "Modeling and design of arrayed waveguide gratings," *IEEE Journal of Lightwave Technology*, vol. 20, no. 4, pp. 661–674, 2002.

[11] VPItransmissionMaker/VPIcomponentMaker Version 8.0, VPIsystems Inc., www.vpiphotonics.com.

Accurate Design of Optical Microring Resonators

E.V.Bekker, V.Brulis, D.Gallagher
Photon Design Ltd
34 Leopold Street, Oxford, OX4 1TW, UK
e-mails: ebekker@photond.com, vbrulis@photond.com

***Abstract*— In this article we present and test a model for large microring resonators based on implementation of the bi-directional Eigenmode Expansion Method for rigorous modelling of vectorial field propagation in the coupling region and using accurate solutions for the bend mode propagating in the ring.**

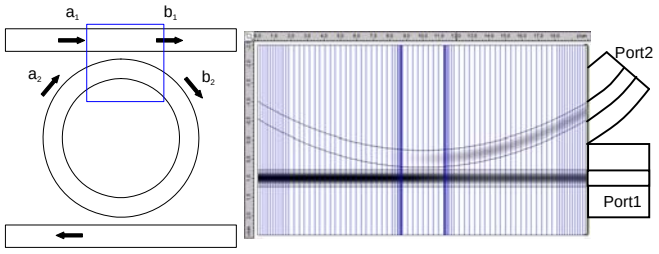
Keywords – microring resonator; Eigenmode Expansion Method; EME; bend modes;

INTRODUCTION

The Finite-Difference Time-Domain (FDTD) method is the most commonly used methodology for modelling of smaller MicroRing Resonators (MRR). It can account for many material properties, such as refractive index anisotropy, various types of dispersion characteristics and nonlinearity. Although FDTD is efficient in modelling MRRs of small dimensions, long computation times and large memory requirements arise when dealing with microring resonators of larger radii.

I. DESCRIPTION OF THE METHODOLOGY

The microring resonator is divided into two computational domains (see Fig. 1a): the coupling region, which is simulated using EigenMode Expansion (EME) [1,2], and the propagation in the ring, which is modelled by calculating the bend mode. Both calculations are performed with the software package FIMMWAVE/FIMMPROP [3].



(a) (b)

Figure 1. (a) Schematic view of the microring resonator (blue square limits the coupling region); a1, a2, b1 and b2 represent optical fields propagating in the corresponding microring resonator regions. (b) Intensity profile for the coupler; the vertical lines show the discretisation along the z-axis.

A. Modelling of Coupling Region a via EME method

The EME method is used to model the field propagation in the coupling region between the bus waveguide and the ring. EME provides a fully-vectorial and bi-directional modelling of the coupling region relying on rigorous resolution of Maxwell's Equations [1]. It can therefore model high refractive index contrasts and wide angles and can be applied to the simulation of Silicon-On-Insulator (SOI) devices. The EME technique discretises the coupler into z-direction invariant waveguide sections (see Fig. 1b). The optical field in each section is expressed in terms of a superposition of the forward- and backward-propagating guided modes and discretised radiation modes. The solutions are obtained in the form of scattering matrices, giving the transmission and reflection coefficients between the modes of the ring waveguide and the modes of the bus waveguide. Coupling to the bend modes of the ring waveguide is calculated via the construction of *port waveguides* with a new tilted and curved frame of reference (Fig. 1b – Port2) in which the bend modes are calculated with an advanced Finite-Difference bend mode (FDM) solver [3] (used also for the rest of the ring). Overlap integrals between fields in the domain of the coupler and the bend modes of the port waveguides are then computed, taking the rotation of the reference frames into account.

B. The Microring Resonator Model

For single mode waveguides, the relationship between the amplitudes (see Fig. 1a) in the coupling region can be written as a linear system:

$$\begin{bmatrix} b_1 \\ b_2 \end{bmatrix} = \begin{bmatrix} t & i\kappa \\ i\kappa^* & t^* \end{bmatrix} \begin{bmatrix} a_1 \\ a_2 \end{bmatrix}, \quad (1)$$

where t and κ are the transmission and coupling coefficients. The feedback after one loop of the ring can be expressed as: $a_2 = b_2 e^{i\phi}\alpha$ with $\phi = 4\pi^2 R \cdot neff(\lambda_0)/\lambda_0$, where *neff* and α are computed by the bend mode solver, R is the radius of the ring, and λ_0 the free-space wavelength. Solving the linear system allows us to calculate the transmission for the microring:

$$T = \frac{|t|^2 + |\alpha|^2 - 2\alpha t \cos\phi}{1 + |\alpha t|^2 - 2\alpha t \cos\phi}. \quad (2)$$

II. NUMERICAL MODELLING RESULTS

C. Modelling of SOI Microring Resonators

The methodology was applied to simulate an SOI MRR based on the design presented in [4]. The ring waveguide has a radius of 40μm and is coupled to two diametrically opposed straight bus waveguides. The silicon waveguide has a cross-section width of 450nm and height 250nm and is placed on top of a thick silica layer. The width of the gap between the ring and the bus waveguides was varied between 30 and 140nm. The modes in the coupler and the bend modes in the port waveguide were calculated using the fully vectorial FDM mode solver [3].

Convergence of the results was observed for a mode solver grid size of 22nm. Mode calculations showed that the bus and bend waveguides were single mode. The bend modes were calculated with both PMLs and transparent boundary conditions and were found to be virtually lossless. The evolution of the transmission spectrum at resonance and the coupling coefficients for different gap widths are shown in Figure 2 below. The coupler was simulated in 3D in 25 minutes by FIMMPROP running on an Intel® Core™2 CPU at 2.4GHz.

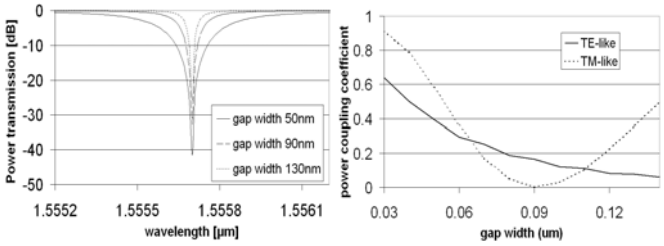


Figure 2. (left) Transmission spectrum around resonance for the TE-like polarisation, plotted in dB for a gap width of 50nm, 90nm and 130nm. (right) Evolution of the coupling coefficient between the bus and the ring plotted against gap width.

D. Modelling of Fluorine-Implanted Lithium-Niobate MRR

In this example we consider the microring resonator of 80 μm radius similar to that shown in Fig.1a. The MRR was fabricated from fluorine-implanted $LiNbO_3$ and presented in [5]. The bent and bus guides are slanted-wall rib waveguides, with refractive indices in the guiding region of 2.2 in horizontal and 2.14 in vertical direction, correspondingly (z-cut $LiNbO_3$ crystal). The refractive indices in the material on top of the rib is 1.5, and in the amorphised substrate 2.03, the width of the guiding region is 3.2 μm, and height 1.2 μm.

In the coupler and in the bent waveguide regions we solve anisotropic Maxwell Equation in order to take into account the crystal anisotropy. The bend mode effective indices and corresponding losses are calculated by fully-vectorial finite-difference method and shown at the Figure 3. For a wide range of bend mode curvature the effective index of the zero-order TE mode is significantly larger than that of the zero-order TM and first-order TE modes, resulting in the weaker confinement of the latter modes and, consequently, bigger bent losses.

Weaker confinement of the zero-order TM mode is caused by the crystal anisotropy ($n_{yy}<n_{xx}$). For the anisotropic bent waveguide of 80 μm radius the loss for the fundamental TE mode is 0.000228 1/cm, what is about 1000 times less than that for the zero-order TM mode, while for the isotropic case the modal loss for the zero-order TM mode is even smaller and of the same order as for the zero-order TE mode. mode.

Moreover, the anisotropy affects the polarisation mixing in the coupling region changing the coupling coefficient from TE bus mode to TM bend mode from 0.41% to a negligible 0.0149%, as the TM mode is further suppressed by 1000 times higher losses in the ring. The combination of these two effects explains the fact that TM mode is not observed in the experiment reported in [5].

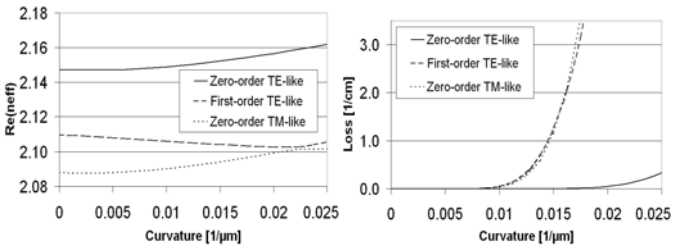


Figure 3. (left) The refractive indices and (right) the modal losses for zero-order TE (solid line), first-order TE mode (dashed line) and zero-order TM mode (dotted line) as a function of bend curvature (1/R).

The solid line at the Fig.4 presents the results for normalised transmission of the MRR reported in [5]. The gap between the bus and bend waveguides is equal to 0.2μm. The depth of the resonance matches that reported in the experiment.

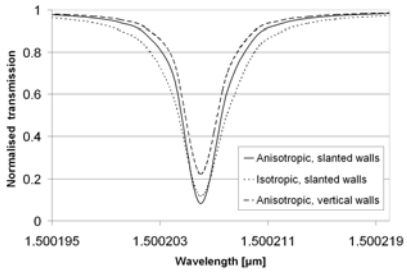


Figure 4. Numerical results for normalised transmission of the original fluorine-implanted LiNbO3 microring resonator (solid line), of the same resonator with vertical wall waveguides (dashed line) and of the same waveguide with isotropic refractive index (dotted line).

The dashed and dotted lines present the results of calculations for isotropic material approximation and for the case of vertical wall approximation. As one can see the depth and width of the calculated resonances are affected by the approximations.

III. MODEL POTENTIAL

The EME-based MRR model described in I.B can be readily improved to include bend mode phase deviation in the coupler, higher-order modes and to take account of reflections off waveguide wall fabrication imperfections. For multimode, eqn. (2) can be readily replaced with a matrix solution. In comparison, though FDTD can model reflections and phase effects it is limited in ring size, while use of BPM plus a matrix solution of the ring cannot deal with reflections or high index contrast accurately.

REFERENCES

[1] D.F.G. Gallagher, T.P. Felici, Proc. SPIE, vol 4987, p. 69 (2003).

[2] Sztefka, G. et al, IEEE Phot. Tech. Lett., vol. 5: 554 (1993).

[3] FIMMWAVE/FIMMPROP by Photon Design Ltd., http://www.photond.com

[4] F. Liu et al, Optics Express vol. 16, p. 15880 (2008).

[5] A. Majkic et al, IEEE Phot. Tech. Lett., vol. 21, p. 639 (2009).

Nanophotonic Microlens Array

Ranjith. R, Qing Dai, Haider Butt, Kanghee James Won and Timothy D Wilkinson
Department of Engineering, Centre of Molecular Materials for Photonics and Electronics,
University of Cambridge, 9 J.J. Thomson Avenue, Cambridge CB3 0FA, UK
Email: tdw13@cam.ac.uk

Abstract—We demonstrate a nanophotonic device fabricated with multiwall carbon nanotubes as electrode sites on a silicon or quartz substrate, covered with nematic liquid crystal. The device acts as a switchable microlens array. Electro optic characterization of the device is presented while discussing potential applications.

Keywords-nanophotonic; carbonnanotube; liquid crystal; microlens array

I. INTRODUCTION

Carbon based nanoparticles are a promising technology because of their excellent electrical properties and strong interaction with the aromatic mesogenic groups of liquid crystals. Jeong et al. [1] showed the formation of unusual double-four-lobe nematic textures in a carbon nanotube-doped liquid crystal under the application of an external voltage. From the hybrid combination of carbon nanotubes and liquid crystals, it has been found that there is a strong interaction between carbon nanotubes and liquid crystals despite the size difference between liquid-crystal molecules (1–2 nm) and carbon nanotubes (a few nanometers to micrometers). This interaction can be interpreted as an optical interaction through the optical anisotropy of the liquid crystal. Hence carbon nanotubes attached to a surface of a substrate in a liquid-crystal cell can be used to form electrodes and defect centers in the medium, and the liquid crystal can be manipulated by applying an external electric field. Based on this technique, an electrically reconfigurable nanophotonic device has been fabricated with light modulation capability [2]. The carbon nanotube electrode arrays were grown on silicon and quartz substrates by plasma enhanced chemical vapor deposition after employing e-beam lithography to nickel catalyst layer into an array. This allowed the growth of a single multiwall carbon nanotube of around 50 nm diameter at each point in the array [2]. Then the nanotubes on the silicon substrate were sputtered with 100 nm thick aluminum and on quartz substrate with 100 nm thick boron oxide for an electric contact between the nanotube array. The nanotube array was then assembled with a top electrode containing indium tin oxide on 0.5-mm-thick borosilicate glass into a cell filled with nematic liquid crystal (BL048) using a 20 um cell gap set by spacer balls in UV glue. The top electrode alone was given a planar alignment by rubbing a thin film of polyimide and hence the resultant alignment of the device was hybrid. The device fabricated on the silicon substrate operated in reflective mode and on quartz functioned in transmissive mode. In this paper we discuss electro optic characterization of the device while explaining potential applications.

II. ELECTRO OPTICS CHARACTERIZATION

Three-dimensional phase recovery from the nanophotonics device is essential for studying the phase modulation capabilities of the device. The phase was retrieved from the device using interference techniques [3]. A Fourier-transform-based fringe analysis [4] was used to retrieve the phase from the device, as it requires only one interferogram and gives higher accuracy by eliminating the background intensity distribution, speckle noise, and optical noise from higher spatial frequencies. The nanophotonic device was characterized using a modified Fourier transform technique. By using the above technique, the microscopic phase profile of each lenslet was recovered using an interference setup constructed with an optical microscope. The microscopic phase profile of each lenslet is of interest as it decides the real modulation capability and applications of the device. The experimental setup consisted of a He–Ne laser along with a beam expander as the illuminating source. An optical microscope was used to detect the beam in reflective mode and for capturing the image. An eye piece having a magnification of ×20 was used in the microscope. The device was mounted on a fine three-axis tilting stage and attached to the microscope. The rubbing direction of the device was kept at 45° to the polarizer. The interference fringes were formed owing to the interference between the ordinary and extraordinary beams being combined by an analyzer that was crossed with polarizer [5]. A rotating diffuser (transparent plastic sheet) was used to average out speckle noise. The fringes were captured by a CCD camera and frame grabber. The interferogram of four lenslets and retrieved unwrapped phase profile of one lenslet at 0Vrms, 1.1 Vrms and 6Vrms of a transparent device with six nanotube group with each nanotube separated by 1μm and a period of 10μm are shown in Fig. 1. It was found that in the absence of an external voltage circular fringes were observed, which showed an alignment deformation of the liquid-crystal molecules near the carbon nanotubes, even though the macroscopic alignment was planar. The change in phase modulation (the phase difference between the center and circumference of lenslet) was bigger at lower voltages than at higher voltages, as shown in Fig. 2. The phase modulation of the hybrid grating lenslet is 3.7 π at 0 Vrms and increased to 4.2 π at 1.1 Vrms because maximum refractive index gradient was created between centre and edge of each hybrid grating lenslet by aligning liquid crystal molecules in response to Gaussian electric field spawned by

nanotubes[2]. The phase modulation decreased after 1.1 Vrms as shown in figure 3. The focal length of each hybrid grating lenslet was calculated using the equation $f=\rho^2/ 2OPD$ [5,6] as shown in Fig.3, where OPD is the peak-to valley optical path difference from the centre to the edge of the hybrid grating lenslet and ρ is the radius of the test area 5 µm. The focal length variation was due to the change in phase profile with respect to applied voltage. The focal length was varied from 10 µm (0Vrms) to 36 µm (2.2 Vrms) and hence the micro lens array became more concave in nature with increased applied voltages. The lensing nature of the microlens arrays disappeared after 3 Vrms because the liquid crystal molecules aligned randomly at higher electric fields. The CNT-liquid-crystal nanophotonic device can be used as an electrically reconfigurable optical diffuser. Optical diffusers change the angular divergence of incident light as well as act as a random phase modulator. At the same time the current device acts as a grating because of the periodically arranged CNTs at 10 µm separation and microlenses due to the liquid crystal. Thus the device can be used for homogenous illumination that is reconfigurable with an external voltage. The device has over 1000×1000 lenslets within the 10 ×10 mm area.

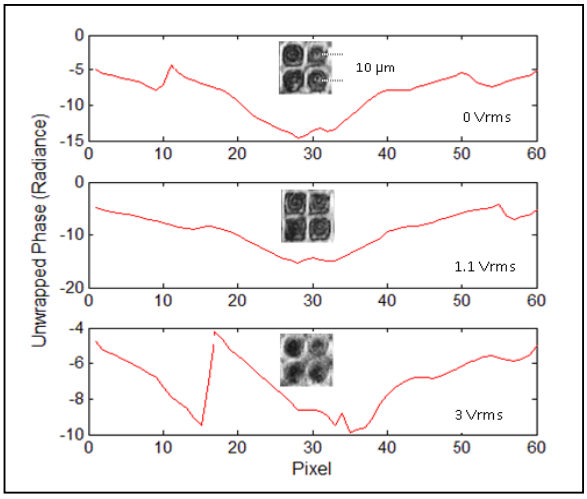


Figure:1 Interferograms of four lenslets along with unwrapped phase profile across one lenslet at 0Vrms, 1.1 Vrms and 3 Vrms. The phase profile is smooth and parabolic like at 1.1 Vrms.

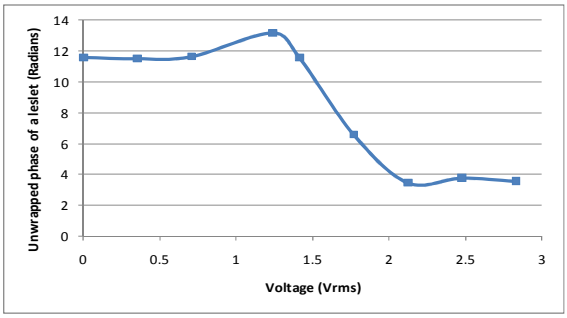


Figure:2 The variation of unwrapped phase of one lenslet with respect to applied voltage

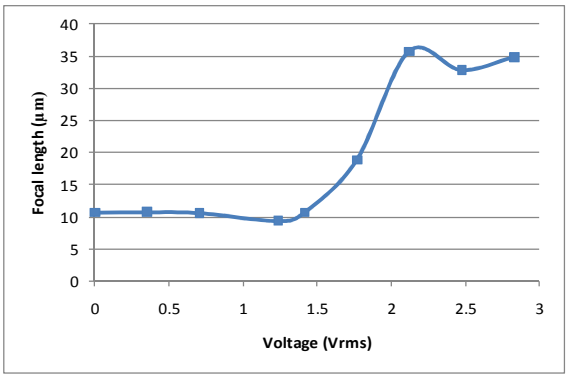


Figure:3 Focal length variation of one lenslet with respect to applied voltage.

III. CONCLUSION

We present a nanophotonic device functioning as a voltage reconfigurable micro lens arrays. The device was fabricated using conducting multiwall carbon nanotubes and liquid crystals. An interference set up attached to a microscope was used to recover the interference fringes. The phase profile was retrieved using Fourier transform techniques and the phase profile of the device was more or less parabolic at 1.1 Vrms, but distorted the parabolic profile at higher voltages. The focal length of the device varied from 10 µm to 36 µm. The device performance was elaborated while explaining the potential applications.

ACKNOWLEDGMENT

The authors thank Stephen Morris, Damian Gardiner, Christoph Bay and Jon Freeman for fruitful discussions. Ranjith. R specially thanks UK-India Education and Research Initiative (UKIERI, British Council) and Cambridge Commonwealth Trust (CCT) for giving funding to pursue PhD.

REFERENCES

[1] Seok Jin Jeong, Palanivelu Sureshkumar, Kwang-Un Jeong, Anoop K. Srivastava, Seung Hee Lee, Seok Ho Jeong, Young Hee Lee, Ruibo Lu, and Shin-Tson Wu, "Unusual double four-lobe textures generated by the motion of carbon nanotubes in a nematic liquid crystal," Opt. Express , vol. 15, pp. 11698-11705 , 2007.

[2] T. D. Wilkinson , X. Wang, K. B. K. Teo and W. I. Milne, "Sparse Multiwall Carbon Nanotube Electrode Arrays for Liquid-Crystal Photonic Devices, " Adv. Mater. (Weinheim, Ger.) , vol. 20, pp. 363 - 366, 3 Jan 2008.

[3] Mitsuo Takeda, Hideki Ina, and Seiji Kobayashi, "Fourier-transform method of fringe-pattern analysis for computer-based topography and interferometry," J. Opt. Soc. Am. , vol. 72, pp. 156-160, 1982.

[4] Claude Roddier and François Roddier, "Interferogram analysis using Fourier transform techniques," Appl. Opt., vol. 26, pp. 1668-1673 ,1987.

[5] Hongwen Ren and Shin-Tson Wu, "Variable-focus liquid lens," Opt. Express, vol. 15, pp. 5931-5936, 2007.

[6] Ranjith Rajasekharan-Unnithan, Haider Butt, and Timothy D. Wilkinson, "Optical phase modulation using a hybrid carbon nanotube-liquid-crystal nanophotonic device," Opt. Lett., vol. 34, pp. 1237-1239 ,2009

New Design Approach to MMI-Couplers in Photonic Wire Substrates

K. Voigt[1], L. Zimmermann[1,2], G. Winzer[1], K. Petermann[1]
[1]TU Berlin, Institut für Hochfrequenztechnik – Photonics, Einsteinufer 25, 10587 Berlin, Germany
[2]IHP, Im Technologiepark 25, 15236 Frankfurt/Oder, Germany
e-mail: Karsten.Voigt@tu-berlin.de

***Abstract*—In this paper we present a new design approach for multimode-interference devices exemplified by 2×2 couplers based on photonic wire substrates with excellent performance. We discuss the influence of guided modes in multimode section. Excess loss and imbalance values can be adjusted to better than 0.1 dB.**

***Keywords*—2×2, multimode-interference (MMI) coupler, silicon-on-insulator (SOI), rib waveguide, Si-wire, photonic wire**

I. INTRODUCTION

In the recent past, photonic wires have shown their high potential for innovations in the field of integrated optics. Based on the high-index contrast between core and cladding material, the pushed miniaturization of devices enables very high integration densities. Amongst others, this leads to a reduction of required footprint of interferometric devices due to the small waveguide-dimensions and minimal bend radii.

Advanced silicon technology now offers the possibility of considerable length-reduction of multimode-section of MMI couplers compared to low-index contrast devices. The question remains whether the high performance of low index-contrast MMIs (e.g. in 4µm SOI rib waveguide technology [1]) can be transferred to nanowire technology. We ought to keep in mind that high index-contrast MMI devices have to deal with phase deviations proportional to the order of modes differing considerably from low-index materials [2, 3].

So far, 1×2 MMI-couplers were most promising candidates for splitting and combining devices on photonic wire substrates. They offer high design flexibility due the symmetric layout of this type of MMI-coupler. Simulations show excess losses of better than 0.1 dB [4]. 2×2 MMI couplers would be more versatile devices due to input/output symmetry. However, 2×2 devices are also considerably more prone to performance degradation. We would therefore like to present our design approach using the example of 2×2 couplers. In this paper we argue that maximum length reduction of the MMI section will not lead to optimum performance. To this end, we shall provide simulation results as well as experimental evidence.

II. MMI-COUPLER SIMULATION

Optimum performance of MMI-coupler devices will show low excess loss and imbalance. Therefore, simulations are used to obtain these performance characteristics while varying geometrical dimensions. Rough estimation of geometry can be done by extrapolation of the waveguides on chip defined by single-mode (SM) condition. Considering the 2×2 MMI-coupler with two input and output waveguides, we need obviously multiple widths of SM-waveguide. This sets a lower limit to the MMI-coupler width, minimizing the final dimensions. We also need to take into account the quadratic scaling between width and length of the multimode section. Additional optimization is required for positioning of the access waveguides, as well as width and shape. Here we will focus on the effect of changing the width of the multimode-section.

Generally, as predicted for symmetric slab waveguides, we can at the same waveguide width expect a higher number of modes for high-index guiding systems compared to low-index systems. This is in accordance with the value of normalized thickness of the guide $V = k_0 \cdot W_{MMI} \cdot (n_F^2 - n_{Cl}^2)^{1/2}$, which is higher for high-index case. Here k_0 is the free space wave number, W_{MMI} the effective width of multimode section, n_F and n_{Cl} the effective refractive indices of the guiding and the cladding layer, respectively. Therefore, by changing the width of multimode section (W_{MMI}), we also change the number of guided modes (see Fig. 1a) that should have influence on the imaging quality at output-side of the MMI-coupler.

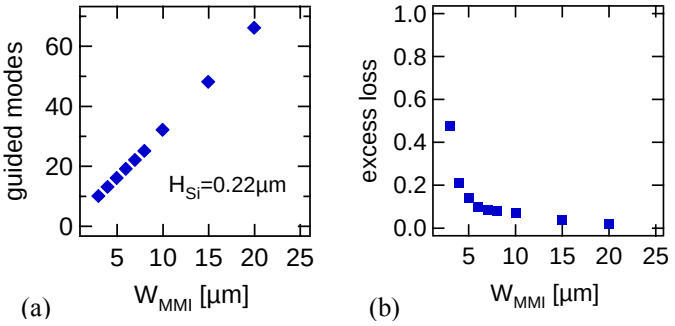


Fig.1a Relation between guided modes and width of multimode-section in silicon-on-insulator material with Si-thickness H of 0.22µm. Fig. 1b shows the excess loss of 2×2 MMI-coupler realized in the same substrate for TE-mode.

This work was supported in the frame of European project HELIOS under the grant of 224312.

Here we implement a paired interference device. We change the width of 2×2 MMI-coupler (H = 220 nm) and estimate the overall excess loss of the device. The width of in- and outgoing sections scales in both cases with the width of the multimode-section with factor of ~ 0.3. Figure 1b shows the calculated excess loss at the two 3 dB-points for 2×2 MMI-coupler depending on W_{MMI} at wavelength of 1550 nm. We can observe the convergence of the excess loss adapted to a given width of the MMI-coupler. From $W_{MMI} > 4\mu m$ we keep the excess loss below 0.2 dB. Moreover, from mode number of about 50 (W_{MMI} ~ 15 µm), we can reduce the loss to about 0.05 dB. Here, the imbalance is better than 0.01 dB. Another important design parameter is the optical bandwidth of the MMI-coupler. In Fig. 2 is plotted the excess loss around the C-band for three different widths of multimode-section, i.e. 4 µm, 6 µm and 10 µm. As shown before, the excess loss at 1550 nm increases for reduced W_{MMI}. The same trend is observed towards the boarders of C-band and beyond.

III. Experiment

For a first fabrication of selected MMI-coupler with $W_{mmi} < 5$ µm we prepared an SOI wafer with a BOX-layer of 2 µm thickness and a silicon layer of 0.22 µm. To determine the basic performance characteristics of the 2×2 MMI-coupler we put them into a MZI-interferometer consisting of a delay line with 25 ps. For the delay line we used additional bends with stretched radius of 20 µm as shown in Fig. 3a. The corresponding free spectral range (FSR) can be calculated with $\lambda / (n_g \Delta L)$. Here λ is the free space wavelength, n_g the group index and ΔL the length difference between the two interferometer arms (~ 2 mm, corresponding to delay time). We used 248nm Deep-UV-lithography and decoupled plasma source etching (Applied Materials) for structuring. The samples were furthermore separated per dicing and polished at the facets. Finally anti-reflection coating was applied. The footprint of the device is about 200 × 1000 µm^2 with potential for further reduction by use of smaller bending radii. A typical measured filter curve of a 2×2 MZI around 1550 nm is shown in Fig. 3b. We achieve, as expected for precise phase correlations at the outputs of the MMI-coupler, π - shifted transfer curves between bar and cross port.

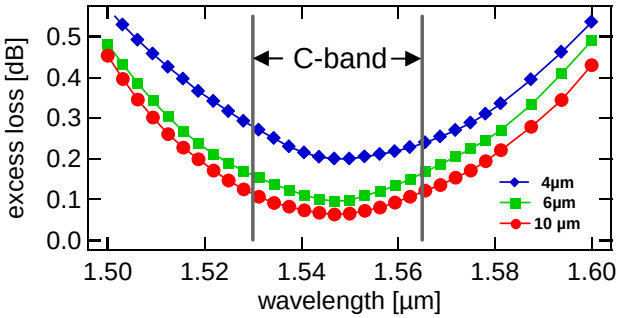
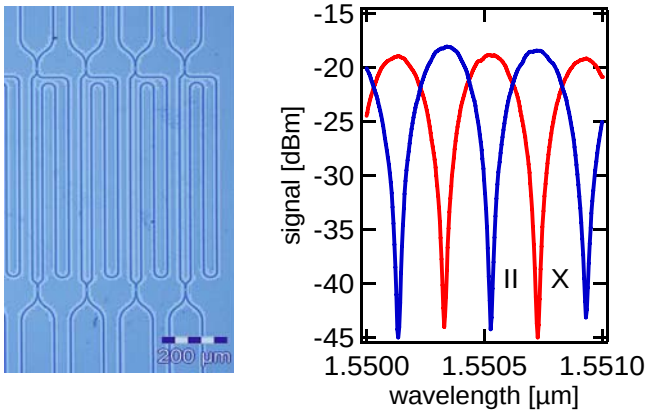


Fig.2 Excess Loss of 2×2 MMI-coupler over wavelength around 1550nm and as function of W_{MMI}.



(a) (b)

Fig.3 Realized 2×2 Mach-Zehnder Interferometers with delay line of 25 ps (3 a) and measured transfer curve at 1550nm for TE-mode (3 b). Extinction ratios for bar and cross port exceed 20 dB.

The extinction ratio over C-band never goes below 20 dB. Because of degrading effects, induced by noticeable different loss in the interferometer arms, the ratio is certainly higher for devices with bigger FSR. The excess loss of MMI-coupler was estimated by employing a 1×1 delayless MZI realized in the same wafer run. We measured excess loss of < 0.5 dB per MMI-coupler, which is in accordance with the simulations above.

IV. Conclusions

We presented a promising approach for the design of MMI-couplers in thin silicon. The approach based on consideration of the number of guided modes conditions in the multimode section. For SOI-wafer with thickness of 0.22 µm, excess loss can be minimized depending on the number of guided modes to be less than 0.1 dB and better. We have also shown high bandwidth operation with slightly increasing losses to the borders of C-band. The experimental data show the applicability of this design method for practical use. Finally, we also see potential for applicability of the presented approach in other substrate types.

References

[1] K. Voigt, L. Zimmermann, G. Winzer, M. Schnarrenberger, T. Mitze, J. Bruns, K. Petermann, "Performance of 40-Gb/s DPSK Demodulator in SOI-Technology", IEEE Photonics Technology Letters, vol. 20, no. 8, April 2008, pp. 614-616.

[2] L. Zimmermann, K. Voigt, G. Winzer, K. Petermann, „ Towards Silicon on Insulator DQPSK Demodulators", paper OThB3, OFC 2010.

[3] J. Z. Huang, R. Scarmozzino, R.M. Osgood, "A New Design Approach to Large Input/Output-Number Multimode Interference Couplers and Its Application to Low-Crosstalk WDM Routers", IEEE Photonics Technology Letters, vol.10, no.9, September 1998, pp. 1292-1294.

[4] P. Dumon et al., "Basic photonic wire components in silicon-on-insulator", in IEEE Proc. Group IV Photonics 2005, 21-23 September 2005, pp. 189–191.

Tellurite Glass on Polymer Planar Waveguides

Zhanxiang Zhao[1], Gin Jose[1], Animesh Jha[1],
Paul Steenson[2]
[1]Institute for Material Research, School of Process, Environmental and Materials Engineering.
[2]Institute of Microwave and Photonics, School of Electronic and Electrical Engineering.
University of Leeds, Leeds, LS2 9JT, UK
g.jose@leeds.ac.uk

Nikos Bamiedakis, Jianji Dong, Ian H White, Richard V Penty
Center for Photonic Systems, Electrical Engineering Division, Department of Engineering,
University of Cambridge, 9 JJ Thomson Avenue, Cambridge, CB3 0FA UK
rvp11@cam.ac.uk

***Abstract*-Tellurite glass thin films were deposited by excimer laser ablation onto silica and polymer covered silica. The transmittance, fluorescence and refractive index of the films have been studied. The films on both substrates were fabricated using identical process parameters and the results show promise and indicate that further optimization is required for producing high quality glass films on polymer suitable for integrated optical device fabrication. Furthermore, the films deposited on silica were etched using CHF_3 based reactive ion etching, and an etch rate of 68nm/min in preparation for integrated device patterning.**

Key words: tellurite glass; thin film; polymer; PLD; planar waveguide; reactive ion etching

I. INTRODUCTION

The ever increasing demand for bandwidth in many data communication and imaging systems is the motivation for forming optical interconnects in backplane systems [1]. A terabit capacity passive polymer optical backplane architecture has recently, been demonstrated [2], which shows that polymer waveguides offer a cost effective way to build optical interconnects due to straightforward patterning techniques and the capability to integrate these with printed circuit boards. Several polymer materials possess adjustable physical properties and low propagation losses, making them desirable for applications in light transmission devices [3]. Specifically, siloxane polymers are regarded as one of the most promising materials for optical waveguiding due to their high transparency and low Rayleigh scattering in addition to the excellent thermal and mechanical properties [4]. Adding active functionality to a polymer integrated device has been demonstrated by doping the polymer with fluorescent dye molecules [5]. In this paper, we propose the alternative approach of using a rare earth doped glass film as the "active" or gain element in a glass-polymer integrated structure. We used an erbium doped tellurite glass having high dopant solubility and broad emission bandwidth for potential amplification in the C and L bands of optical communication networks. The pulsed laser deposition (PLD) of the glass was first optimized for silica glass substrates and its suitability for patterning and integration is studied using reactive ion etching (RIE) experiments. The glass was then deposited using PLD on a polymer film pre-deposited by spin coating on a silica substrate. The fabrication procedure, light propagation characteristics, and photoluminescence properties of the fabricated thin films are also reported.

II. EXPERIMENTS

The molar composition of the glass target used for pulsed laser deposition was $72TeO_2.17WO_3.11La_2O_3$ and was doped with 1wt% Er_2O_3 (TWL). The glass was prepared by conventional melting and quenching processes. Commercial high quality silica substrates were used for a series of experiments to optimize the deposition condition for the TWL glass. The Dow Corning PDMS polymer films on silica substrate have an approximate thickness of 25 µm and a refractive index of 1.507 at 633 nm. The pulsed laser deposition was carried out in a Dual-PLD system (PVD Products, USA) under controlled atmosphere. The chamber was first pumped down to below 10^{-5} mTorr, and the substrate was rotated at the speed of 20 rpm and at a distance of 50 mm from the target, during the deposition. The substrate temperature was maintained at 100^oC during the deposition process and the output from an ArF laser (193nm, 10Hz) was incident on the target at the angle of 60°, whilst the target was rotated at 40 rpm. The ablation was carried out with laser fluence of 1.3 mJ/cm^2 and under a partial pressure of oxygen of 135 mTorr. The deposition time for the film on silica was 3 hrs while that for the film on polymer was 6 hrs. The films on silica were used for reactive ion etching (RIE) to assess their suitability for patterning. The RIE was carried out at a pressure of 36 mTorr and RF power of 200 W for 10 min, with a CHF_3 gas flow rate of 2 sccm. The refractive index and propagation loss of the films were measured using a Metricon Model 2010 prism coupler using He-Ne laser (633nm), and an ultraviolet-visible-NIR spectrometer (Lambda 19, Perkin Elmer), was used to measure the transmittance of the thin films. The fluorescence spectrum of the thin film was measured using a Spectrofluorimeter (Model FS 920, Edinburgh Instruments, UK), and the thickness and image of the etched channels were obtained using Alfa-IQ surface profiler and optical microscope respectively.

III. RESULTS AND DISCUSSION

A. Glass films on silica and patterning

A series of thin films of the TWL glass was deposited on silica glass substrates of refractive index 1.46 (at 633nm) to optimize the PLD process parameters prior to selecting the parameters listed in the experimental section. The surface morphology of films was studied using high resolution SEM and the image shown in Fig. 1 corresponds to the film fabricated under those conditions. The refractive index of the glass film is 1.8, which is lower than that of the target glass

refractive index of 2.10. This may be due to the defects at nanoscale in the films shown in the inset of the figure and is currently under investigation. The loss of the film on silica is about 0.2 dB/cm at 633 nm and the thickness was 1.07 µm. An optical micrograph of a portion of two etched channels is shown in Fig. 2a. The height of the channel is 0.68µm after 10 minutes etching as shown in Fig. 2b.

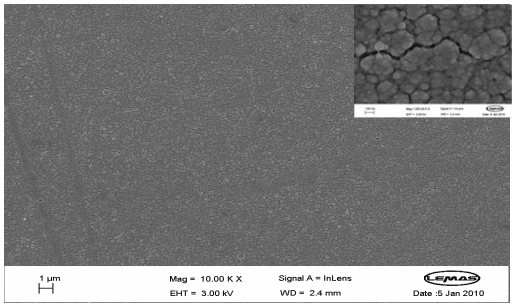


Figure 1. SEM image of the TWL film on silica. Inset showing image at higher magnification.

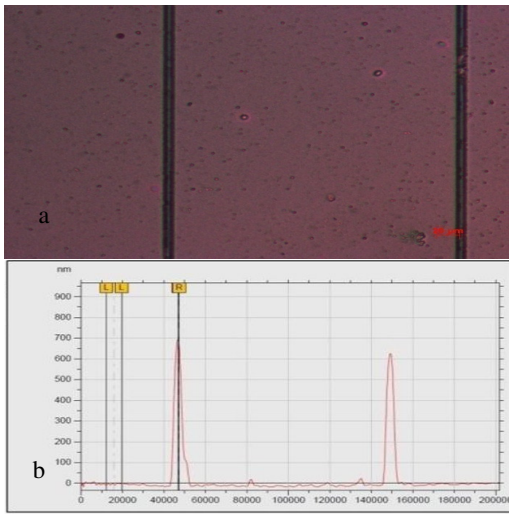


Figure 2. a. Microscopy image, b. height measurement of etched channels.

B. Glass films on polymer

The thin films on polymer substrates were deposited under the same conditions as used for those deposited directly on silica substrates. In Fig. 3 the transmittance spectra of the glass thin films on silica and on polymer are compared. The transmittances of both films are higher than 90% in the wavelength range from 900nm to 2500nm. However, the apparent reduction in the transmittance for the film on polymer is evident. This implies that further optimization of the PLD process is necessary to obtain improved optical quality glass thin films on polymer. The thickness of the glass film on polymer is 1.87 µm. The photoluminescence spectrum of the film is reported in Fig. 4 and the FWHM of this spectrum is 88 nm. Propagation loss in the film and waveguide patterning and transmission experiments using glass on polymer waveguides, are currently under progress and the results of these experiments will be reported at the conference.

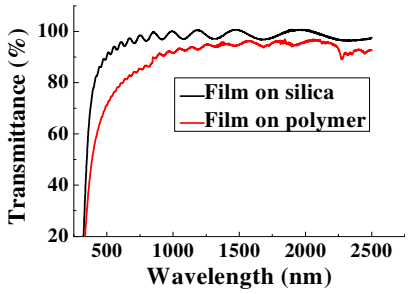


Figure 3. Transmittance of the glass film on silica and polymer substrates.

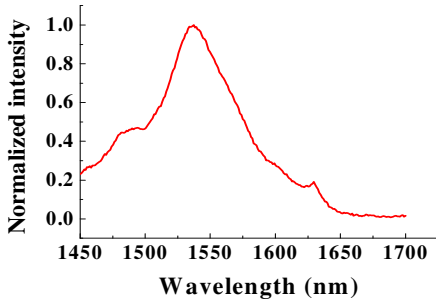


Figure 4. Normalized PL spectrum of the thin film on polymer.

IV. Conclusion

Tellurite glass thin films were fabricated on silica and polymer substrates using pulsed laser deposition technique. The glass films were patterned using RIE technique in CHF_3 gas and a good etching rate of 68 nm/min was obtained. The propagation loss of the film on silica is as low as 0.21 dB/cm. Optical properties of pulsed laser deposited films on polymers need further improvement. The FWHM of the PL of the Er^{3+}-ion doped tellurite glass film on polymer is 88 nm. These preliminary results show excellent prospect for integration of glass based active devices on polymer platform using pulsed laser deposition and RIE.

Acknowledgment

Authors acknowledge the RCUK Basic Technology Research grant (Ref: **EP/D048672/1**).

References

[1] S. Uhlig and M. Robertsson, "Limitations to and solutions for optical loss in optical backplanes," J. Lightwave Technol., vol. 24, pp. 1710-1724, 2006.

[2] J. Beals, et al, "A terabit capacity passive polymer optical backplane based on a novel meshed waveguide architecture," Appl. Phys. A-Mater. Sci. & Proces., vol. 95, pp. 983-988, 2009.

[3] M. Zhou, "Low-loss polymeric materials for passive waveguide components in fiber optical telecommunication," Opt. Eng., vol. 41, pp. 1631-1643, 2002.

[4] N. Bamiedakis, et al, "Cost-effective multimode polymer waveguides for high-speed on-board optical interconnects," IEEE J. Quantum Electron., vol. 45, pp. 415-424, 2009.

[5] M. A. Reilly, C. Marinelli, C. N. Morgan, R. V. Penty, I. H. White, M. Ramon, M. Ariu, R. Xia, and D. D. C. Bradley, "Rib waveguide dye-doped polymer amplifier with up to 26 dB optical gain at 625 nm," Appl. Phys. Lett., vol. 85, pp. 5137-5139, 2004.

Parasitic spectral selectivity of Y-branching power dividers on proton-exchanged $LiNbO_3$ waveguides

S.M. Kostritskii, Yu.N. Korkishko, V.A. Fedorov,
E.I. Maslennikov, A.A. Dikevich
Optolink Ltd, Zelenograd, Proezd 4806, bd.5, 124498,
Moscow, Russia;
skostritskii@optolink.ru

Abstract **- Insertion losses, splitting ratio and its spectral dependence were measured for Y-splitters based on channel proton-exchanged $LiNbO_3$ waveguides. The parasitic spectral selectivity was suppressed by optimization of branching topology.**

Keywords - Lithium niobate, waveguides, Y-branching

I. INTRODUCTION

Optical channel waveguides in lithium niobate are very useful elements for building a variety of integrated optical components. For example, the key component of fiber optical gyroscope (FOG) is the multi-function integrated optic chip (MIOC), which is an important part of the Sagnac interferometer. Proton exchange (PE) is now an established technique for fabricating integrated optical devices in $LiNbO_3$ and offers possibility of obtaining low-loss MIOC [1]. As the MIOC consists inherently a Y-branching splitter, the wavelength sensitivity of Y-splitter can present the dramatic problem if uncertainty of the light source centre wavelength is sufficient to induce marked variations in the mode coupling between two channel waveguides in branching region of Y-splitter. Moreover, suppression of parasitic spectral selectivity is rather difficult task for real devices because of inherent asymmetry of Y-branching region, appearing due to technological uncertainty of photolithography and etching processes [2]. Thus, a careful design of the Y-branching is mandatory to obtain high performance MIOCs, that demands an optimisation of Y- branching topology.

II. EXPERIMENTAL

A series of power dividers utilizing the different geometries of Y-branching splitters and straight channel guides were delineated in X-cut $LiNbO_3$ substrates, using standard photolithographic technique. The channel width W of waveguides forming an Y-splitter was varied in the range from 5.6 to 6.2 μm, where formation of a low-loss single mode channel waveguide, operating within a wavelength region from 1500 to 1580 nm, is expected [1,2]. To fabricate these waveguide structures with the aid of the APE technique, the substrates were proton exchanged at 175 °C for 50÷70 min in pure benzoic acid and annealed at 360 °C for 6÷7.5 hours. It allows us to fabricate the low-loss Y-splitter, utilizing a Y-branching (section II in Fig.1) formed by three single-mode channel waveguides (sections I and III, Fig.1).

The different geometries of Y-branching were used to fabricate three different types of Y-splitter for further comparative study, aiming to find geometry. The most reliable geometries for MIOC design are found to be described by the following equations:

$$y(x) = y_s + \frac{y_e - y_s}{x_e - x_s}(x - x_s) \qquad (1)$$

$$y(x) = y_s + A\left\{1 - \cos\left[\frac{2\pi}{p}(x - x_s)\right]\right\} \qquad (2)$$

for so-called linear and cosine branching, respectively. The parameters x_s and y_s have values within the ranges of 7÷16 mm and 0.16÷0.2 mm, respectively. The width of tapered subsection of the section II near branching point is 2W.

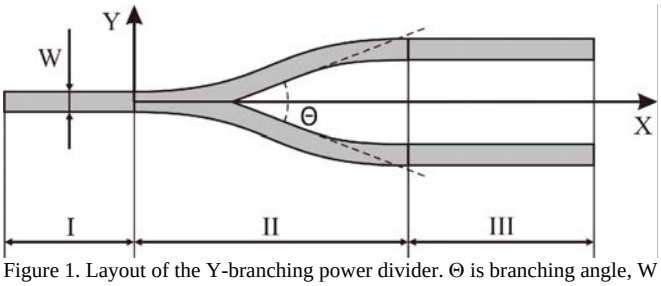


Figure 1. Layout of the Y-branching power divider. Θ is branching angle, W is channel waveguide width.

The main parameters of MIOCs were measured by coupling depolarized light into the waveguides with the aid of an isotropic single mode fiber. A fiber Lyot depolarizer utilizing PM fiber was used to decrease sharply DOP of a superluminescent diode (SLD) radiation (central wavelength is ~1540 nm) and, hence, minimize a polarization-dependent error in measurement results. To determine insertion losses and splitting ratio, we use a fiber-to-fiber coupling set-up. The IR-radiation from the output ports of Y-splitter was directed into a photodiode, operating in its linear region. Spectral dependence of output power at each output ports was measured with the aid of an optical spectral analyzer YOKOGAWA AQ6370.

III. EXPERIMENTAL RESULTS AND DISCUSSION

The power transfer coefficient (PTC) is established to be critical parameter of the Y-branching, as this parameter is most sensitive to the variations in Y- branching topology and fabrication conditions. PTC is evaluated experimentally as ratio between smaller output power and sum of both output powers, i.e. PTC is directly related to a splitting ratio that is main parameter characterizing performance of the power divider. A perfect Y-branching power divider should have PTC = 0.5, and deviation of actual PTC from this value is caused by parasitic asymmetry of Y-branching section due to technological imperfections and modes interaction, as this branching section may be regarded as analog of the directional coupler with weighted coupling [3], i.e. a normalized deviation parameter (0.5 – PTC) is proportional to $\Delta\beta/\Theta \cdot \gamma_3$,

where $\Delta\beta$ is accidental asymmetry of Y- branching caused by technological imperfections, Θ is branching angle, γ_3 is transverse component of phase constant, giving the strength of local normal mode coupling. According to the theory of Y-branching splitter [3], the shaped branching (2) has a resulting length advantage over the linear branching (1). To reach an appropriate value of PTC near 0.5, the branching angle should be large enough to decrease sufficiently the mode coupling. However the insertion losses represent the important limiting factor for further improvement of Y-branching splitter via Θ increase.

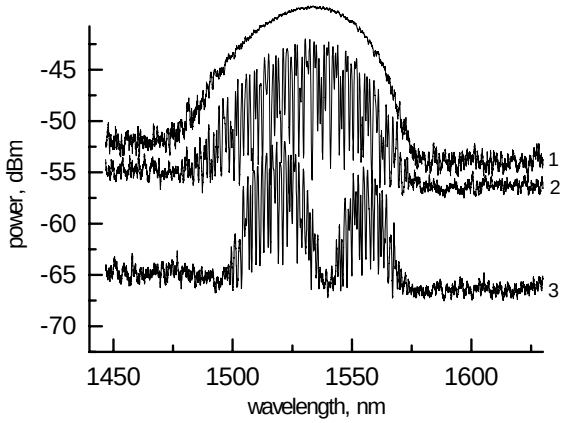


Figure 2. Spectral dependence of the power of IR radiation: (1) at SLD output fiber, (2) at output pigtail of straight channel waveguide (channel width W = 6.0 μm), (3) at output port of Y-branching power divider with cosine geometry (see Eq.(2)) and branching angle Θ is 1.4°. The power at second output port has spectral dependence oscillations of opposite sign. Thus, PTC varies from 0 to 0.5 within spectral band of SLD. To escape spectra overlapping, curve 3 is shifted for -10 dBm relative to curves 1 and 3.

In fact, the following statement may be derived from experiments with the Y-branching power dividers based on annealed PE $LiNbO_3$ waveguides: a larger value of Θ is higher insertion losses for the power dividers of any studied geometry (1,2). At the same, the cosine branching (2) provides a smallest insertion loss among the geometries studied at any fixed value of Θ. Thus, optimisation of Y-branching power divider should find the compromise between smaller PTC and higher losses via choice of geometry and fabrication conditions providing appropriate values of both parameters. Simulation with beam propagation method shows that the cosine branching (2) with average branching angle Θ = 1.4° is the optimal geometry, as it allows to obtain the branching loss (α_b) about 0.3 dB at PTC ≤ 0.485. Our experimental study confirms this theoretical finding. However, very strong parasitic spectral selectivity is observed for output of MIOC, that utilizes this Y-branching geometry, Fig.2(3). It has been attributed to the inherent asymmetry of Y-branching region, appearing due to technological uncertainty of the photolithography and etching processes.

To suppress this parasitic effect, the extra taper was introduced into section II of theY-branching power dividers in order to decrease the influence of technological uncertainty on mode coupling within initial stage of channel branching (Fig.3). This modification of Y-branching geometry gives the only partial suppression of the spectral selectivity (see Fig.4(1)), when appropriate levels of PTC and losses is obtained with growth of length and width of this extra taper.

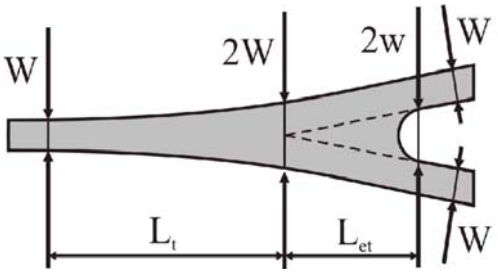


Figure 3.Topology of branching region: L_t – taper length, L_{et} and 2w – length and width of extra taper. Dashed lines show Y-branching without extra taper.

Note, that even such a small wavelength-selective variation of PTC may present a dramatic problem for some particular applications, e.g. high-precision FOG [4]. To minimize the spectral selectivity, the branching angle Θ should be increased, but a branching loss (α_b) must grow [2,3]. Thus, $\Theta = 1.9^\circ$ is evaluated as the optimal value for the cosine-branching with extra taper of L_{et} = 100 μm, 2w = 1.18 μm and W= 6 μm, when α_b = 0.6 dB, Fig. 4(2).

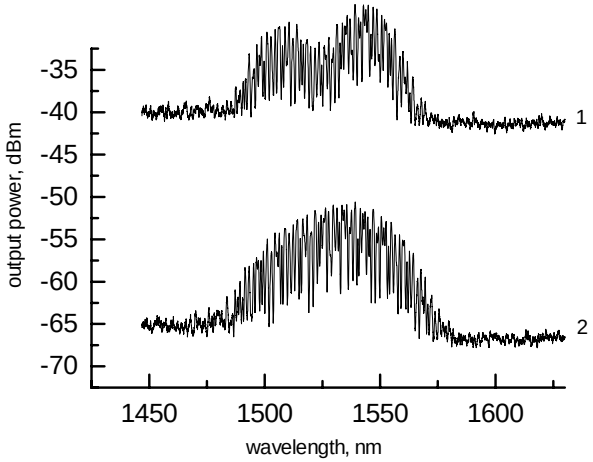


Figure 4. Spectral dependence of the power of IR radiation at output port of Y-branching power divider with cosine topology and the extra taper introduced in branching region (see Fig.3): (1) Θ =1.4° and the extra taper has L_{et} = 130 μm and 2w = 1.26 μm, (2) Θ = 1.9°, L_{et} = 100 μm and 2w = 1.18 μm. To escape overlapping, curve 2 is shifted for -24 dBm relative to curve 1.

Further increase of Θ, L_{et} and 2w is out of practical interest, as it will induce sharp growth of α_b. Note, that the cosine-branching Y-splitter with the same Θ but a much smaller extra taper, including the case of extra taper absence, demonstrates marked parasitic spectral selectivity.

REFERENCES

[1] M.M. Howerton, W.K. Burns, P.R. Skeath, and A.S. Greenblatt, "Dependence of refractive index on hydrogen concentration in proton exchanged $LiNbO_3$." IEEE J. Quant. Electron., vol. 27, pp. 593-600, 1991.
[2] S.M. Kostritskii, "Photorefractive effect in $LiNbO_3$-based integrated optical circuits at wavelengths of third telecom window", Applied Physics B, vol. 95, pp. 421-428, May 2009.
[3] W.K. Burns, and A.F. Milton, Waveguide transitions and junctions, In: Guided-wave optoelectronics, T. Tamir (ed.), Springer-Verlag, 1988.
[4] H. Lefevre, "The Fiber-Optic Gyroscope", Artech House, 1993.

Optical Filters Based on Casacaded Point-Symmetric Mach-Zehnder Interferometers

Y. Hao*, N. Bamiedakis, R. V. Penty and I. H. White
Electrical Division, Department of Engineering, University of Cambridge, CB3 0FA, Cambridge, UK.
*Email: yh277@cam.ac.uk

Abstract — **A design method for cascaded point symmetrical MZI based WDM filters is reported. An MZI-WDM filter design is simulated and optimized to achieve < –1.5dB insertion loss and –20 dB crosstalk. Characterization results for the proposed MZI WDM ONU filter are discussed.**

Keywords: Mach-Zehnder Interferometer, WDM filter, point-symmetrical configuration.

I. INTRODUCTION

Wavelength-Division-Multiplexing (WDM) filters are essential components in Optical Network Units (ONU) for Fibre-To-The-Home (FTTH) networks. There is a variety of optical structures that can be used to realize WDM filters, such as wavelength add/drop filters, multimode interferometers, directional couplers and Y-branch splitters [1-3]. However for the FTTH application, the WDM filter is used to separate the upstream (1260nm-1360nm band) and downstream (1480nm-1500nm band) signals as described by the ITU-T standards [4]. The Broadband PON and Ethernet PON standards require filter channel insertion loss < 1.5 dB, unidirectional crosstalk < –10 dB and bidirectional crosstalk < –40 dB. Therefore an optical filter based on point-to-point symmetrically connected MZIs is particularly attractive due to the super-broad optical bandwidth and low crosstalk for both up- and down- stream directions. In this paper, the principle of point symmetrical connected MZIs is illustrated and an optimized novel WDM filter design based on cascaded MZIs is proposed.

II. PRINCIPLE OF POINT-SYMMETRICAL CONNECTED MZIS

Figure 1 shows the configuration of a WDM filter composed of two point symmetrically connected MZIs. The transmittances of first MZI sub-circuit, the connecting waveguide sections and the second (identical) MZI sub-circuit are T_A, T_B, and T_C respectively. The overall transmittance of the full point-to-point symmetrically connected MZIs WDM filter is T expressed in Equation 1.

$$T=T_A\times T_B\times T_C \qquad \text{Equation 1}$$

where,

$$T_A=\begin{pmatrix} x & -y^* \\ y & x^* \end{pmatrix}, T_B=\begin{pmatrix} e^{-j\frac{\Delta\varphi_M}{2}} & 0 \\ 0 & e^{j\frac{\Delta\varphi_M}{2}} \end{pmatrix}, T_C=\begin{pmatrix} x^* & -y^* \\ y & x \end{pmatrix},$$

and x and y are the wavelength dependent complex transfer functions at the through and cross ports of the MZI sub-circuit respectively.

The coupling ratio of the complete filter photonic circuit, μ, is

$$\mu=4\eta(1-\eta)\cos^2\left(\frac{\Delta\Psi_M}{2}\right) \qquad \text{Equation 2}$$

where $\Delta\Psi_M=2\pi n\Delta L_M/\lambda$, λ is wavelength, η is the coupling ratio of the basic MZI and $\eta=|y|^2$ [5], which is expressed as

$$\eta=4\alpha(1-\alpha)\cos^2\left(\frac{\Delta\Psi}{2}\right) \qquad \text{Equation 3}$$

where $\Delta\Psi=2\pi n\Delta L/\lambda$, α is the coupling ratio of the directional coupler used in the MZI sub-circuit, ΔΨ is the phase shift resulting from the length difference of two arm waveguides (ΔL) in the MZI sub-circuit.

If the length difference of the waveguide arms connecting the two MZI sub-circuits is zero, i.e. ΔL_M=0 μm (i.e. $\Delta\Psi_M$=0), the transmittance matrix T of the full circuit reduces to:

$$T=\begin{pmatrix} |x|^2-|y|^2 & -2x^*y^* \\ 2xy & |x|^2-|y|^2 \end{pmatrix} \qquad \text{Equation 4}$$

It is clear that the phase components of x and y do not appear in the full circuit transmittance T. This gives the advantage of simplicity when designing point symmetrical MZI WDM filters.

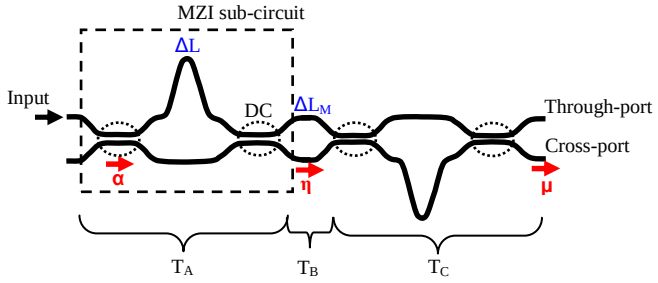


Figure 1. Configuration of WDM filter based on point-symmetrical connected MZIs.

III. DESIGN OF AN POINT-SYMMETRICAL MZI WDM FILTER

We have used this approach to design a WDM filter to demultiplex the 1310 nm wavelength band to the through-port and the 1490 nm band to the cross-port of a filter design similar to that in Figure 1. The waveguides are designed with refractive index difference Δn = 0.003 at 1490 nm wavelength, equivalent to the index step of a commercially available

polymer system, and a core size of 9 μm × 9 μm. The design process was as follows:

1. In order to obtain μ=0 at λ_{th}=1310 nm (i.e. at the through-port), η could be set to either 0 or 1 according to Equation 2. Here we use η=0 as an example. To set η=0 in Equation 3, ΔL is set so that ΔΨ/2=π, 3π, 5π, 7π...

2. To obtain μ=1 at λ_{cr}=1490 nm (i.e. at the cross-port), η is required to be as close to 0.5 as possible. We find the DC coupling ratio α at λ_{cr}=1490 nm, by using the ΔL obtained from condition 1.

3. By trial and error, we find that when ΔΨ/2=7π at λ_{th}=1310 nm, the physical length difference ΔL is 3.06 μm, which results in the coupling ratio of the MZI sub-circuit being η=0 regardless of the DC coupling ratio α at λ_{th}=1310 nm. Consequently μ=0 at λ_{th}=1310 nm at the through-port is obtained. Meanwhile, at λ_{cr}=1490 nm, for the length difference ΔL=3.06um in the basic MZI circuit and η=0.5, the DC coupling ratio is approximately 0.8. This results in μ=1 at λ_{cr}=1490 nm at the cross-port.

4. By using the FIMMWAVE software package to obtain the parameters of the simulated directional couplers and MZIs, the optimized deign of the point symmetrically connected MZI WDM filter is shown in Table 1.

DC gap	DC coupling length	Length difference ΔL	Length difference ΔL_M
7 μm	5000 μm	3.06 μm	0 μm

Table 1. Summary of the optimized point symmetrical MZI WDM filter design.

IV. Simulation Results for the Optimised Point-Symmetric MZI WDM Filter

The simulation work is carried out by utilizing a 3D mode solver, based on the film mode matching method within the FIMMWAVE software package, to find all modes in the waveguide and then FIMMPROP is employed to simulate the 3D optical propagation in the MZI device based on the beam propagation method.

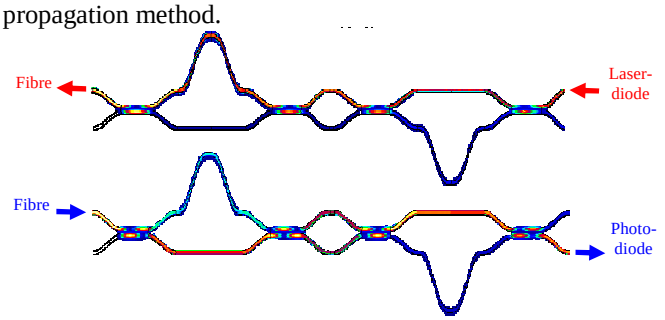


Figure 2. Optical light field intensity plots at λ_{th}=1310 nm (upper) and λ_{cr}=1490 nm (lower) of the proposed MZI WDM filter.

It can be seen from the light intensity plots in Figure 2 that the optimized WDM filter based on point symmetric MZIs proposed in Table 1 passes the upstream 1.31 μm wavelength at the through-port and the 1.49 μm downstream signal at the cross-port.

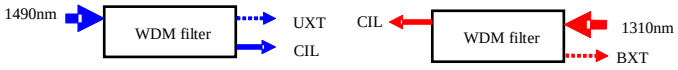


Figure 3. Illustration of unidirectional crosstalk (UXT) and bidirectional crosstalk (BXT) in optical filter.

The channel insertion loss (CIL), unidirectional crosstalk (UXT) and bidirectional crosstalk (BXT) are defined in figure 3. The wavelength dependent transmission of the optimized point symmetrical MZI WDM filter is shown in Figure 4. The shadowed areas show the 1260 – 1360 nm and the 1480 – 1500 nm wavelength windows defined in the ITU standard. The channel insertion loss within both wavelength ranges is less than –1.5 dB, and the unidirectional crosstalk is as low as –20 dB. The bidirectional crosstalk is lower than –40 dB.

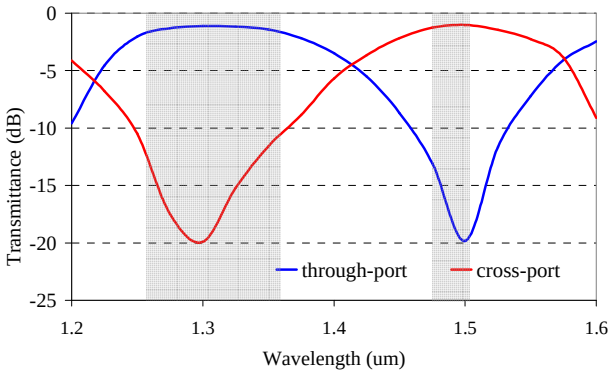


Figure 4. Optical spectrum of the proposed MZI WDM filter with point symmetrical configuration. The shadowed areas show the ITU specified 1310nm upstream window and 1490nm down stream window.

V. Conclusion

The method of cascaded MZIs WDM filter with point symmetrical configuration is demonstrated. Furthermore, the proposed WDM filter design shows less than –1.5 dB insertion loss and –20 dB crosstalk across the broad up-/down-stream wavelength windows. The performance meets the requirements of the ITU-T standards for ONUs.

Acknowledgment

The authors would like to acknowledge the support of Dow Corning Corporation, for the STOIC research project, and of the Engineering and Physical Sciences Research Council (EPSRC).

References

[1] Yaffe, C. H. Henry, M. R. Serbin, and L. G. Cohen, “Resonant couplers acting as add-drop filters made with silica-on-silicon waveguide technology, ” J. Lightwave Technol., vol. 12, pp.1010-1014, June 1994.

[2] M. H. Ibrahim, N. M. Kassim, A. B. Mohammad, “A novel 1×2 multimode interference optical wavelength filter based on photodefinable benzocyclobutene (BCB 4024-40) polymer,’’ Microwave and Optical Technology Letters, Vol. 49, No. 5, 2006.

[3] Ilic, I. Scarmozzino, R. Osgood, R.M., Jr. ‘‘Modeling multimode-input star couples in polymers,’’ J. Lightwave Technol., vol. 12, June 1994

[4] ITU-T G983.1 standards (2005) and ITU-T G984.1

[5] Y. Hida, K. Jinguji, N. Takato, ‘‘Wavelength demulti/multiplexers with non-sinusoidal filtering characteristics composed of point-symmetrically connected Mach-Zehnder interferometers,’’ Electronics and Communications in Japan, Vol. 81, No.4, 1998.

Flexible Optical Waveguide with Tapered Structure Having Large Coupling Tolerance

Nobuhiko Ishizawa, Masahiro Kanda, Osamu Mikami
Tokai University
Hiratsuka, Kanagawa, 259-1292, Japan
mikami@tokai.ac.jp

Tsuyoshi Shioda
Mitsui Chemicals, Inc.
Sodegaura, Chiba, 299-0265, Japan

Abstract—A flexible polymeric waveguide with a tapered structure in core thickness in the vicinity of the input port was proposed. The core thickness for the uniform core region was designed to be 50μm. The tapered waveguide with a core thickness of 150μm at the input port revealed three times higher coupling tolerance performance than that for an uniform core thickness of 50μm, as designed.

Keywords- optical interconnection; polymeric waveguide; coupling tolerance

I. INTRODUCTION

Optical interconnection technology has attracted much attention to solve some problems for electronic conventional interconnection, such as signal degradation, high power consumption, electromagnetic interference (EMI), heavy weight and large footprints. The optical interconnection has several advantages such as lower power consumption and high density package [1]. However, in this approach, precise positional alignment between optical devices and the optical circuit is required, which may significantly increase the cost and time required for packaging and mounting optical devices. These days, the hinge part of mobile phones and laptops needs flexible optical waveguides. If the waveguide thickness is reduced for improvement of flexibility, the waveguide core thickness should be also reduced. As a result, it is difficult to align easily and cost effectively between an optical component and an optical circuit such as waveguide. In order to overcome these difficulties, we have proposed a flexible polymeric waveguide having a tapered region in the core thickness at the input port. On the other hand, the core thickness for the uniform core region that was large portion of waveguide was designed to be 50μm. The tapered waveguide with the core thickness of 150μm at the input port revealed three times higher coupling tolerance performance than that for a uniform core thickness of 50μm, as we expected.

II. PROPOSED OPTICAL WAVEGUIDE

A. Structure of the Optical Waveguide

Fig. 1 shows the schematic structure of the proposed flexible polymeric waveguide. There are two regions. One is a taper region and another is an uniform one. At the uniform region, the core thickness and the length were designed to be 50μm and 80mm, respectively. At the taper region, the maximum core thickness at the edge was designed to be 90, 110, 130 and 150μm. The core thickness decreased continuously from the maximum to 50μm as shown in Fig. 1, and the length of the taper region was 45mm. The three-layered structure, such as upper cladding / core / under cladding, with a taper core was formed by our coating technique using a designated blade. The core pattern formed by two grooves was fabricated by a conventional dicing process as shown in Fig. 1 (b). The refractive indices of the core and the cladding polyimide at the wavelength of 850nm were 1.56 and 1.51, respectively. Fig. 2 shows a photograph of the cross-section of the input port of the waveguide.

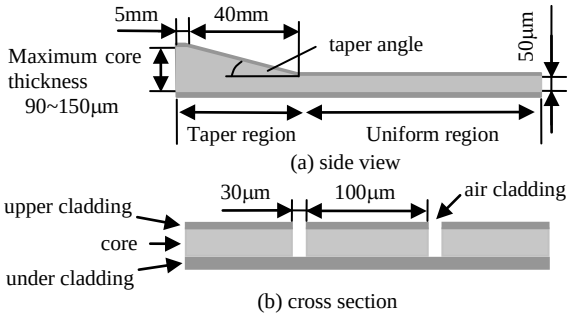


Figure 1. Schematic structure of proposed flexible waveguide.

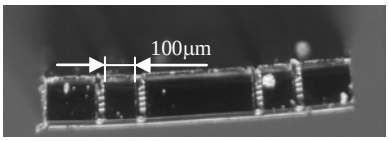


Figure 2. Photograph of cross section of the waveguide.

B. Core ThicknessProfile at the Tapaer Region

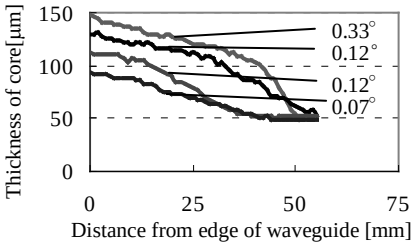


Figure 3. Core thickness profile for tapered waveguide fabricated.

Fig. 3 shows the core thickness profile by observing with an optical microscope. The core thickness decreased gradually from the maximum to 50 μm. We obtained the maximum slope

of the profile as a taper angle for all samples. Table 1. shows the taper angles of design and experimental. When we designed the maximum core thickness of 150μm, we found that the taper angle for experimental was 2.4 times larger than that for design. This was due to slight flow of a poly (amic acid) solution, which was precursor of polyimide, at a core coating process.

TABLE 1. TAPER ANGLE

Core of thickness	Taper angle	
	Design	*Experimental*
90μm	0.06°	0.07°
110μm	0.09°	0.12°
130μm	0.11°	0.12°
150μm	0.14°	0.33°

III. TOLERANCE AND OPTICAL INSERTING LOSS

A. Positional Tolerance Measurement

We evaluated the positional tolerance for optical coupling between a graded index multimode fiber (GI-MMF) with a core diameter of 50μm and the input port of the waveguide. Fig. 4 shows the optical insertion loss measurement system. The near field pattern of launching light was inserted in this figure. The fiber end was butt-coupled to the input port of waveguide. The output power from the output port of waveguide was measured by a large area photo-detector and then we calculated optical insertion loss. The change in optical insertion loss by changing the taper angle corresponds to that in the optical coupling loss by assuming fixed optical propagation loss of waveguide. We evaluated the positional tolerance for the optical insertion loss higher than the minimum optical insertion loss by 1dB. We called the positional tolerance "1dB tolerance".

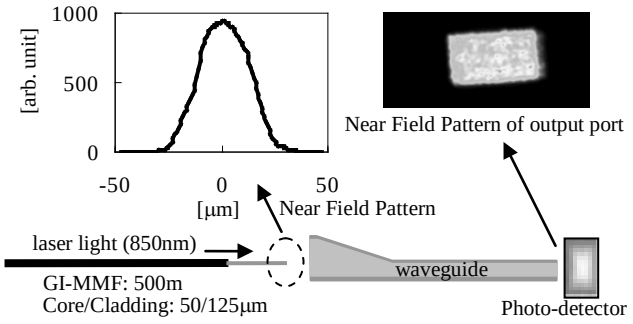


Figure 4. Optical insertion loss measurement system.

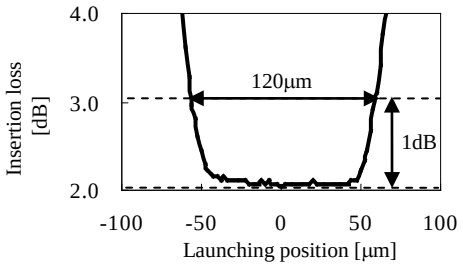


Figure 5. Example of 1dB tolerance.

Fig. 5 shows optical insertion loss change by launching position change of the fiber core center for the maximum core thickness of 130μm. We obtained the 1dB tolerance of 120μm, as shown in Fig. 5.Fig. 6 shows the maximum core thickness dependence of the 1dB tolerance. The broken line shows the relationship that the maximum core thickness is equal to the 1dB tolerance. We observed that the 1dB tolerance for all samples including the waveguide without the taper region and a core thickness of 50μm was almost similar to the maximum thickness of waveguide, as designed.

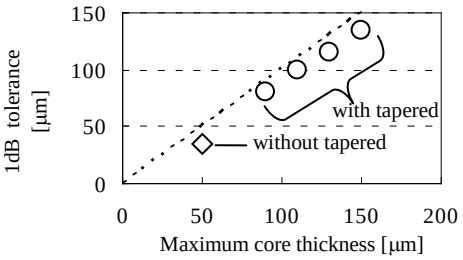


Figure 6. Maximum core thickness dependence of 1dB tolerance.

B. Optical Inserting Loss Change

Fig. 7 shows the taper angle dependence of the optical insertion loss. We had found that the optical insertion loss and its three times standard deviation (3σ) for 1,000 samples in the waveguide with the formed core thickness were obtained to be 2.5dB and 0.4dB, respectively, for the optical insertion loss measurement system. We observed no change in optical insertion loss with increasing the taper angle as designed. In general, optical insertion loss depends on launching condition for optical insertion loss measurement. The launching condition dependence on optical insertion loss and 1dB tolerance for the waveguide with tapered structure is ongoing.

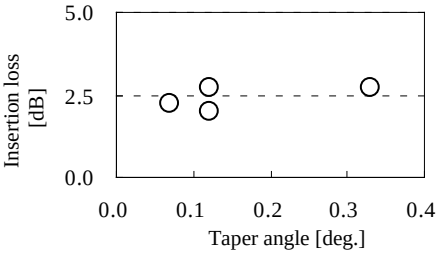


Figure 7. Taper angle dependence of optical inserting loss.

IV. CONCLUSIONS

We demonstrated a flexible polymeric waveguide with a tapered structure in core thickness in the vicinity of the input port. The core thickness for the uniform core region was designed to be 50μm. The tapered waveguide with the core thickness of 150μm at the input port revealed three times higher coupling tolerance performance than that for a uniform core thickness of 50μm, as designed. The waveguide having small portion for thick core and large portion for thin core has an advantage for easy assembly with optical components and a potential for high flexible durability.

REFERENCES

[1] M.A. Meis, "Opto-electronic backplane technology for cost effective bandwidth management," Proc.ECTC2003, 2003, pp.1073-1076

Spectral Response of GaInNAs / GaAs Multiquantum-Well Solar Cells

B. Royall*, M. Gunes, N. Balkan,
Department of Computing and Electronic Systems,
University of Essex,
Wivenhoe Park, CO4 3SQ, United Kingdom.
*broyal@essex.ac.uk

M. Saarinen
Optoelectronics Research Centre,
Tampere University of Technology,
Korkeakoulunkatu 10,
FI-33720, Tampere, Finland.

***Abstract*—The current-voltage and spectral response of a GaAs / $Ga_{0.96}In_{0.04}N_{0.015}As_{0.985}$ pin diode is measured. Its determined that the inclusion of GaInNAs increases the spectral response of the cell beyond that of GaAs but due to the low number of quantum wells employed the response at longer wavelengths is very low.**

Keywords: Multiquantum well solar cell, GaInNAs

The efficiency of a single junction conventional solar cell is limited due to low and high wavelength cut-offs[1], for example material with band gaps of 1.42 eV yielding the highest possible efficiencies of approximately 33% for AM1.5G radiation. So far efficiencies of 25.9% have been realised for GaAs and 24.7 for single crystal Si cells, while efficiencies of 18% and 19.5% have been achieved for CdTe and CIGS thin film cells respectively[2].

A number of methods to increase efficiency further exist. One is to stack solar cells of different band-gaps connecting them in series both optically and electrically creating a tandem cell [3]. This method has so far provided the highest efficiencies with a $Ga_{0.44}In_{0.56}P/Ga_{0.92}In_{0.08}As/Ge$ cell giving an efficiency of 40.7% [4]. One significant challenge when designing tandem cells is the current of each junction must match if optimum efficiencies are to be achieved.

Another approach is to include multiple quantum wells within the intrinsic region of a p-i-n cell. The combination of the wide band gap barrier and low band gap quantum well allow the absorption of photons in a wider spectral range [5]. Such cells may prove very useful if incorporated into tandem designs as they will allow the absorption edge and hence the short circuit current of each junction to be carefully chosen. In this paper we present our results covering a GaAs pin diode which incorporates multiple quantum wells using a selection of compositions of the quaternary alloy $Ga_{1-x}In_xN_yAs_{1-y}$ (dilute nitrides).

There has been much interest in $Ga_{1-x}In_xN_yAs_{1-y}$ for solar cells due to the ability to choose both its lattice constant and band gap independently. By increasing the Indium concentration the band gap is reduced and the lattice constant is increased, while increasing the Nitrogen concentration reduces both the band gap and the lattice constant [6] However, it has not been possible to create an efficient GaInNAs solar cell as the addition of nitrogen causes imperfections and dislocations. Therefore, the carrier mobilities and lifetimes are reduced [7] leading to very low diffusion lengths [8]. This results in reduced efficiencies particularly in the bulk material where the high strain causes high dislocation densities.

In our design we chose a dilute nitride composition $Ga_{0.96}In_{0.04}N_{0.015}As_{0.985}$ which gives a band gap of 1.1eV and is lattice matched to GaAs. Our design is a p on n pin solar cell with 10 GaInNAs/GaAs quantum wells with widths varying between 38Å and 110Å included in the intrinsic region. Using the infinite barrier approach together with strain we calculated the effective gap of the widest quantum well to be 1.16 eV and that of the narrowest well is 1.25eV.

Two identical devices were grown by Molecular Beam Epitaxy at Tampere University of Technology. Beryllium and silicon were used as p and n type dopants respectively. One of the devices was annealed at 720° for 5 minutes. No antireflective coating was applied to the sample. Nickel / Germanium / Gold contacts were made to the substrate and Zinc / Gold ring contacts with a diameter of 1.4 mm were formed on the top of the structure by photolithography and then etched to give an active area of $4.52mm^2$.

Photoluminescence measurements were performed on the annealed device for temperatures between 8 and 300K and are shown in figure 1. The peak at room temperature corresponds to a value of 1.17eV, close to the calculated value.

The AM1.5G IV characteristics of the devices were measured for the AM1.5G spectrum at 25C and plotted in Fig. 2. The annealed structure has a higher short circuit current but lower open circuit voltage. This can be attributed to the red shift in bandgap which occurs during annealing. The open circuit voltage of 0.44V is low but probably due to the decrease in photocurrent and increase of dark current which occur due to surface recombination. The annealed structure also shows a better fill factor of 49% and an efficiency of 0.8%.

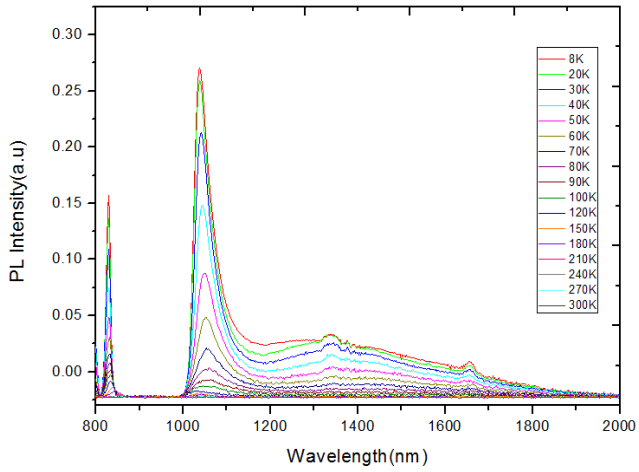


Figure 1: The photoluminescence results for the annealed structure.

The spectral response of the device was measured by illuminating the device for the wavelength range 500 to 1150 nm using a Bentham's M300 monochromator and the IL1 white light source and measuring the current of the device produced. The results are normalised with respect to the spectral dependence of the incident light and detector. These are plotted for the annealed sample in Fig. 3. It is clear the GaInNAs quantum wells extend the cells spectral response beyond that of a GaAs cell (1.42eV) to 1.17eV. The lower achieved at low photon energies can be attributed to the low number of quantum wells. With a total thickness of 64.2 nm and assuming an absorption coefficient of $1um^{-1}$ they are likely to absorb approximately 6% of photons with energies lower than 1.42eV. This coupled with the low diffusion length explains the relatively lower powers compared to GaAs wavelengths. The photoresponse begins to decrease at 1.6eV due to the lack of a window layer and by 2.4eV almost all photons are being lost to surface recombination.

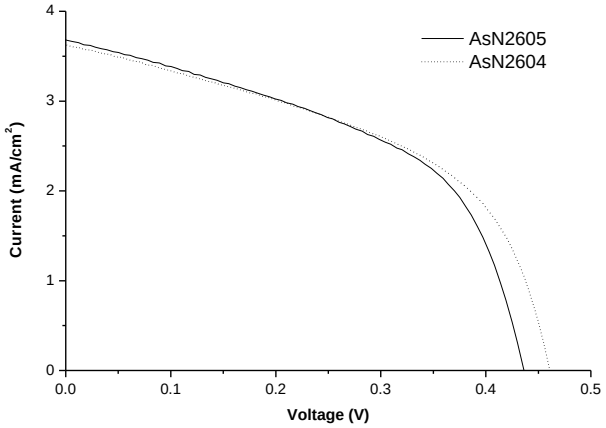


Figure 2: A graph showing the AM1.5G I-V charecteristics for the annealed (solid) and unannealed (dotted) structures

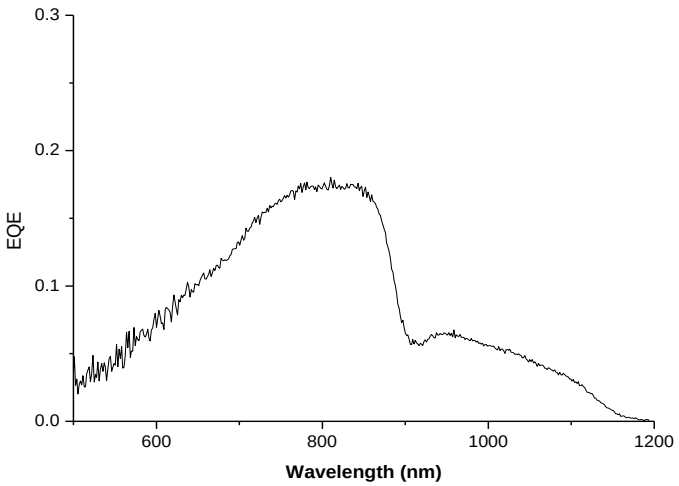


Figure 3: The spectral response for the annealed structure.

In conclusion we have demonstrated that the spectral response of a GaAs cell can be extended by the inclusion of dilute nitride quantum wells into the intrinsic region of a p-i-n GaAs cell. While the increase in photocurrent at longer wavelengths was small in this structure it maybe be possible to increase the efficiency by both increasing the number of quantum wells and designing cells with high indium and lower nitrogen in dilute nitrides to improve the optical and electrical quality. The work for this is underway and will be reported shortly.

ACKNOWLEDGMENTS

We are grateful to Professor Hari Reehal, Jeremy Ball and Badar Ahmed at London South Bank University Thin Film Materials and Devices research group for the use of their solar simulator facilities.

REFERENCES

[1] J. Nelson, "The physics of solar cells", Imperial College Press, 2003.

[2] M. A. Green, K. Emery, D. L. King, Y.Hishikawa, W. Warta, "Solar cells efficiency tables", Progress in Photovoltaics: Research and Applications 15, pp35 – 40 , 2006.

[3] D. J Friend man, J. F Geisz, S. R Kurtz, J. M Oloson, "1eV solar cells with a GaInNAs active layer", Journal of Crystal Growth 195, pp 409 – 415 , 1998.

[4] R. R. King, D.C. Law, K.M Edmondson, C. M. Fetzet, G. S. Kinsey, H. Yoon, "40% efficiency metamorphic GaInP/GaInAs/Ge multijunction solar cells", Applied Physics Letters 90, 183516 , 2007.

[5] D. B Bushnell, T. N. D Tibbits, K.W. J Barnham, "Effect of well number on the performance of quantum-well solar cells", Journal of Applied Physics 97, 124908 2005.

[6] N. Balkan, "The physics and technology of dilute nitrides", Journal of Physics: Condensed Matter, Volume 16, 3387-3412 , 2004.

[7] D. J Friedman, J. F Geisz, W.K Metzger and S. W Johnston, "Trap-dominated minority-carrier recombination in GaInNAs pn junctions", Applied Physics Letters 83, pp 698-700 , 2003.

[8] Y. Shimizu, N. Miyashuta, Y. Mura, A. Uedono, Y. Okada, "Optimization and growth of GaInNAs dilute nitrides for multi-junction solar cell applications", Conference Record of the 2006 IEEE 4th World Conference on Photovoltaic Energy Conversion volume 1, pp 811 – 814, 2006.

Numerical Study of Plasmonic Nanoparticles Enhanced Light Emission in Silicon Light-Emitting Diodes

Khai Q. Le, Bjorn Maes and Peter Bienstman
Department of Information Technology
Ghent University-IMEC, 41 Sint-Pietersnieuwstraat, Ghent 9000, Belgium
khai.le@intec.ugent.be

***Abstract*—We theoretically investigate the influence of metallic nanoparticles on light emission in silicon light-emitting diodes (LEDs) by an improved effective mode volume model proposed in this paper. We show that an enhancement of the radiative efficiency of silicon LEDs can be achieved by localized surface plasmons on silver (Ag) nanoparticles. The calculated result of optimal Ag nanoparticle size to enhance light emission of silicon LEDs at 900 nm wavelength is in very good agreement with those obtained from the experimental results.**

Keywords-component; enhanced light emission; metallic nano-particles; silicon LEDs

I. INTRODUCTION

Silicon-on-insulator (SOI) light-emitting diodes (LEDs) are very promising light sources for optical communication technologies. However, the development of these components is hampered by their low efficiencies. Efforts to improve the limitations of the efficiency have amongst others made use of plasmonic nanostructures [1]. Large efficiency enhancement of luminescence was achieved by placing metal nanoparticles close to light emitters. This has attracted intense research interests devoted to demonstrating such an enhancement in various media [2-3]. Since the surface plasmon resonance frequency is determined by various parameters such as shape, size and distribution of nanoparticles, an accurate theoretical model is very important in the design of nanoparticle enhanced light emitters.

There exist various methods developed to investigate the efficiency enhancement of electroluminescence. Among these, the recently introduced method based on the effective mode volume theory is known as a systematic and rigorous model to predict emission enhancement of quantum well LEDs in the vicinity of metal nanoparticles [4]. However, the method failed to explain the experimental results of an enhanced light emission of SOI-LEDs due to silver (Ag) nanoparticles. While the experiment demonstrated that a significant enhancement in electroluminescence from SOI-LEDs at 900 nm via excitation of surface plasmons in silver nanoparticles was obtained at the average particle size of a radius of 50-70 nm, those obtained by the theory of [4] (referred to as the conventional approach thereafter in this work) for the particle radius is only around 20-30 nm. This is attributed to the use of the Drude approximation in determining the enhanced Purcell factor. To overcome this problem, the Lorentz-Drude model for metal dispersion, which is well-known as a more accurate model [5], combined with a calculation without approximations of the enhanced Purcell factor due to nanoparticles are proposed in this paper. The calculated results by the improved approach are shown to be in very good agreement with the experiment.

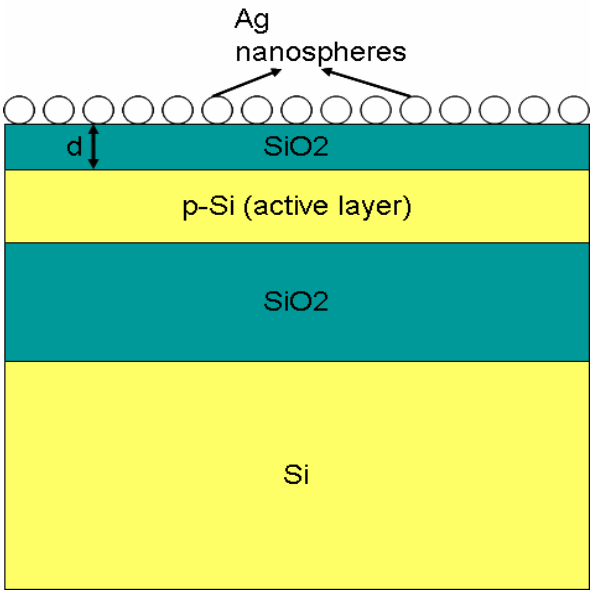


Fig. 1. Geometry of silicon-on-insulator LEDs with Ag nanospheres embedded on top

.

II. AN IMPROVED MODEL OF PLASMONIC NANOPARTICLES ENHANCED LIGHT EMITTERS

The theoretical model employed to evaluate the radiation enhancement of SOI-LEDs is usually described as a two-step process. The first step describes an energy transfer from matter to a surface plasmon-polariton (SPP) mode at the metal-dielectric interface. Owing to the high mode density in the SPP, the Purcell factor $\boldsymbol{F_p}$ [6] is significantly enhanced. The second step is a conversion of the energy from the confined SPP modes to actual propagation modes with a certain coupling rate, and this process competes with

nonradiative loss due to absorption in metal nanoparticles. Typically, tightly-confined large wavevector SPPs are more difficult to couple to the outside world. Hence, the overall radiative efficiency from the excited matter to free-propagating waves has a complicated dependence on the SPP characteristics. It was shown that for a given original radiative efficiency η_{rad} there exists an exact value of SPP enhancement [4].

The geometry of isolated metal nanospheres being placed on top of a SOI-LED is shown in Fig. 1. The effective volume of the SP mode supported by the metal sphere is given as follows [4]:

$$V_{eff} = \frac{4}{3}\pi a^3\left(1+\frac{1}{2\varepsilon_D}\right) \tag{1}$$

with a being the radius of the nanoparticle and ε_D being the dielectric constant of the surrounding media.

For the dipole positioned at the distance d from the particle surface and oriented in z direction normal to the surface, the effective density of the SP modes is

$$\rho_{SP} = \frac{L(\omega)}{V_{eff}}\left(\frac{a}{a+d}\right)^6, \tag{2}$$

where the normalized line shape of the dipole oscillation is

$$L(\omega) = \frac{\mathrm{Im}[(\varepsilon_M(\omega)+2\omega_D)^{-1}]}{\int \mathrm{Im}[(\varepsilon_M(\omega)+2\omega_D)^{-1}]d\omega}, \tag{3}$$

with ε_M being the metal dispersion. In [4], Eq. (3) was calculated by a Drude approximation. This is the main reason the method failed to explain the enhancement of the light emission from SOI-LEDs due to large nanoparticles. However, this can be remedied by considering the more accurate Lorentz-Drude model [5] combined with no approximation of the line shape of the dipole oscillation, as performed in this work.

For Ag nanoparticles embedded in a silica (SiO2) medium, the enhanced fields that occur near metal particles as a result of SP resonance give rise to an enhanced absorption. According to a generalized form of Kirchoff's law which is valid for luminescent emission, enhanced absorption corresponds to an enhanced emission [1]. Figure 2 shows the scattering and absorption cross-sections for 100 nm diameter of Ag sphere embedded in air and SiO2 calculated by Mie theory [7]. Cross sections are normalized to the geometry particle cross section. For each embedded medium, a dipole resonance is observed. At resonance frequency ω_0, the Purcell factor $F_p(\omega_0)$ can be estimated as a ratio of the effective density of the SP modes to that of the radiation components as follows:

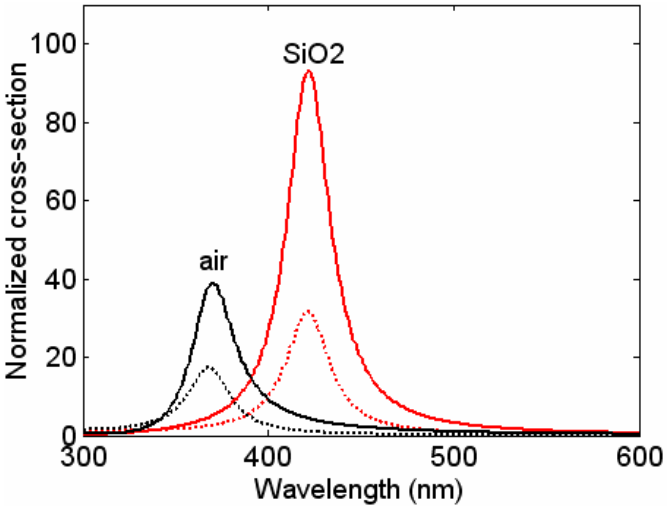


Fig. 2. Scattering (solid lines) and absorption (dotted lines) cross-sections for a 100 nm diameter Ag sphere embedded in air (black) and SiO2 (red) normalized by the projected area of the sphere.

$$F_p(\omega_0) = \frac{\rho_{SP}}{\rho_{rad}} = \frac{L(\omega_0)}{V_{eff}}\left(\frac{a}{a+d}\right)^6\left[\frac{1}{3\pi^2}\left(\frac{2\pi}{\lambda_D}\right)^3\frac{1}{\omega_0}\right]^{-1}, \tag{4}$$

with $\lambda_D = \lambda/n$ being the emission wavelength in the dielectric.

Now, given an original radiative efficiency, the expression for the enhancement factor due to a single metal nanoparticle is described as [4]:

$$F_{\mathrm{sin}\,gle} = \frac{\eta_{SP}}{\eta_{rad}} = \frac{1+F_p\eta_{pr}}{1+F_p\eta_{rad}}, \tag{5}$$

where η_{pr} is the radiative coupling efficiency of the SP mode.

For the example of InGaN quantum well LEDs, with isolated silver nanoparticles placed in close proximity to the active region, it was shown that the output enhancement due to isolated silver nanoparticles is significant while only modest enhancement can be achieved with an ordered array of nanoparticles. Furthermore, a random assembly of isolated particles may hold an advantage over the ordered arrays for light emitter devices of finite area.

III. Enhanced Light Emission by Isolated Nanoparticles

We now apply the developed model to evaluate the enhancement of the electroluminescence efficiency of silicon LEDs in which the active layer is placed in the vicinity of isolated Ag nanoparticles. The distance d from the active layer to a Ag particle is 35 nm as in the LED devices used in the experiments described in [8]. The calculated enhancement factor of the electroluminescence efficiency for a range of the original radiative efficiency of the emitter with respect to the sphere radius is shown in Fig. 3. We can see that the enhancement factor exhibits a strong dependence upon the nanosphere dimensions with the peak occurring when the radius is small enough to yield smaller effective mode volume

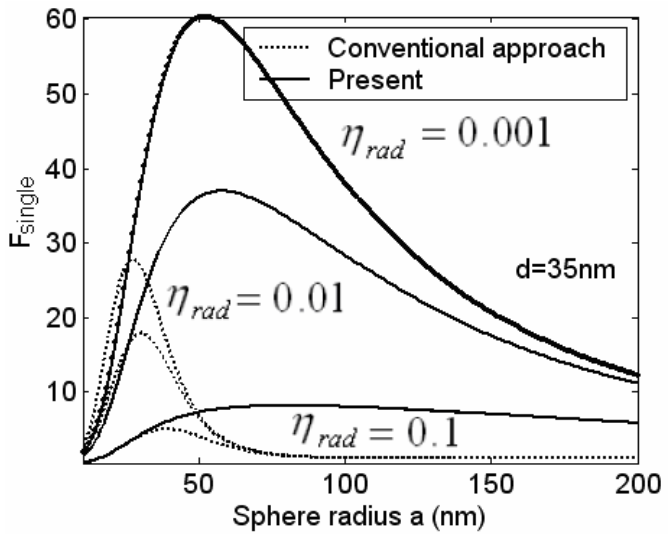


Fig. 3. Enhancement due to a single Ag sphere on SOI-LEDs with a distance of 35 nm from active layer to metal layer as a function of sphere radius for various original radiative efficiencies calculated by the conventional approach (dotted lines) and the present approach (solid lines).

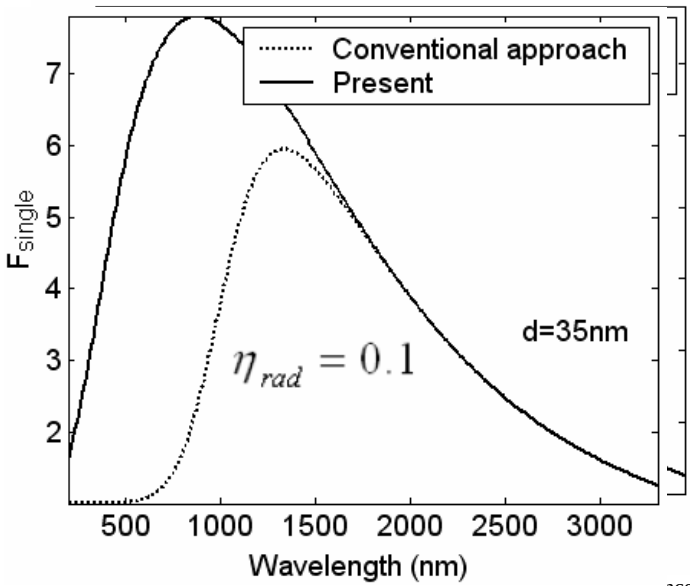


Fig. 4. Enhancement due to a single Ag sphere on SOI-LEDs with a distance of 35 nm from active layer to metal layer as a function of emission wavelengths calculated by the conventional approach (dotted line) and the present approach (solid line).

for an enhanced Purcell factor, yet is still sufficiently large to assure strong radiative coupling of the SP mode. Furthermore, the figure suggests that the higher the original radiative efficiency, the more important the concern for the efficient energy transfer from the SP mode into free-space radiation modes. This situation favors larger nanoparticles that can emit the SP energy photons into the free space prior to get lost in the metal. At the emission wavelength of 900 nm the enhancement of electroluminescence efficiency calculated by the present method can be found in the range of the particle radius to be around 50-60 nm which is very good agreement with the experimental results reported in [8], whereas those obtained from the conventional approach is only 20-30 nm.

In addition, Figure 4 shows the calculated enhancement factor of the electroluminescence efficiency as a function of emission wavelengths. It is seen that for a given original radiative efficiency of 0.1, the maximum enhancement factor is observed at the emission wavelength of around 890 nm. It is in good agreement with those obtained by the experimental result of the emission wavelength at around 900 nm while those obtained by the conventional method is around 1330 nm.

For a single nanosphere, although it may enhance light emission of only a very small emitter, an enhancement of light emission can be observed at certain optimal sizes. Therefore, with found optimal particle sizes one can consider disordered arrays of these isolated nanospheres to achieve practical enhancement of such devices as SOI-LEDs.

IV. Conclusions

The systematic and rigorous model based on the effective volume mode theory has been improved to evaluate the enhancement of the electroluminescence efficiency of SOI-LEDs due to isolated Ag nanoparticles. The improved model has well explained the plasmonic enhanced light emission of SOI-LEDs as reported in the experiment. Hence, it is very useful for the design of metal nanoparticles enhanced light emitters.

Acknowledgment

Parts of this work were performed within the context of the Belgian IAP project Photonics@Be.

References

[1] K. R. Catchpole and S. Pillai, “Surface plasmons for enhanced silicon emitting diodes and solar cells,” J. Lumin. 121, 315-318 (2006).

[2] K. Okamoto, I. Niki, A. Shvartser, Y. Narukawa, T. Mukai, and A. Scherer, “Surface-plasmon-enhanced light emitters based on InGaN quantum wells,” Nature 3, 601–605 (2004).

[3] S. Kuhn, U. Hakason, L. Rogobete, and V. Sandoghdar, “Enhancement of single-molecule fluorescence using a gold nanoparticle as an optical nanoantenna,” Phys. Rev. Lett. 97, 017402 (2006).

[4] G. Sun, J. B. Khurgin, and R. A. Soref, “Plasmonic light-emission enhancement with isolated metal nanoparticles and their coupled arrays,” J. Opt. Soc. Am. B 25, 1748-1755 (2008).

[5] A. D. Rakic, A. B. Djurisic, J. M. Elazar, and M. L. Majewski, “Optical properties of metallic films for vertical-cavity optoelectronic devices,” App. Opt. 37, 5271-5283 (1998).

[6] M. Purcell, “Spontaneous emission probabilities at radio frequency,” Phys. Rev. 69, 681 (1946).

[7] C. F. Bohren and D. R. Huffman, Absorption and scattering of light by small particles (Wiley-Interscience, New York, 1993).

[8] S. Pillai, K. R. Catchpole, T. Trupke, G. Zhang, J. Zhao, and M. A. Green, “Enhanced emission from Si-based light-emitting diodes using surface plasmons,” Appl. Phys. Lett. 88, 161102 (2006).

A More Realistic Coupled Dipole Approximation Model for Plasmonic Waveguides

Ergun Simsek
Department of Electrical & Electronics Engineering
Bahcesehir University, Istanbul, TURKEY
ergun.simsek@bahcesehir.edu.tr

Abstract— **Well-known coupled dipole approximation method is extended to multilayered media to obtain a more realistic model for plasmonic waveguides. The key component of the developed method is the layered medium Green's functions. Theoretically calculated resonance frequencies show a very good agreement with the experimental results found in the literature.**

Keywords-plasmonic waveguides; dispersion; propagation length; layered medium.

I. INTRODUCTION

Surface plasmon resonance modes of periodically placed metal nanoparticle chains and arrays, which are the main element of plasmonic waveguides, have been studied extensively in last two decades. Experimentalists have used transmission and/or reflection spectroscopy in order to obtain dispersion relations of the surface plasmons, whereas theoreticians have developed novel models both in time and frequency domains. Since most of the frequency domain models, developed based on the coupled dipole approximation (CDA), assume a homogeneous background, they are not sufficient and robust to design an optical waveguide for real world applications.

We can summarize the four strategies -applied so far- to validate experimentally obtained dispersion curves/resonance frequencies with a theoretical/numerical model as follows:

(i) *Full Wave Solvers:* One can solve Maxwell Equations in 3D space and apply appropriate boundary conditions to simulate the wave propagation through MNP chain. Such solution is an exact solution (100 percent robust) but might require very long computation time [5-7, 9].

(ii) *CDA with Image Theory:* Koenderink *et al* already applied this solution to calculate the resonance frequencies of MNP chains fabricated on a glass slide [6]. The drawback is the formulation is only valid for the two-layer case (e.g. air-glass).

(iii) *CDA with Effective Refractive Index Approximation (ERIA):* In [7], researchers approximate the whole inhomogeneous background with a single homogeneous medium whose refractive index depends on each layer's thickness and refractive indices. Even though this simple method can estimate resonance modes quite accurately, it still cannot explain the effect of an interface on dispersion modes.

(iv) *Semi-Analytical CDA:* In [9], researchers use a full wave solver to calculate the polarizability of a single MNP first, and then use this result for coupled dipole approximation. This is another very reliable method but requires a full wave solver.

In this work, we extend the CDA to multilayered media by implementing layered medium Green's functions (LMGFs). LMGFs are used not only to calculate the electric field created by the oscillating point dipoles, which are MNPs, but also to modify the polarizability of MNP embedded in multilayered media, appropriately. The formulation is not limited to any fixed number of layers, unlike [10], and does not require an external full wave solver. This fully analytical method includes the effects of retardation, radiative damping and dynamic depolarization due to the finite size of NPs. Theoretically calculated resonance frequencies show a very good agreement with the experimental results found in the literature. Theoretical results suggest that surface plasmon propagation lengths of 1μm are possible using silver or gold nanoparticles embedded in a multilayered medium.

II. LAYERED MEDIUM COUPLED DIPOLE APPROXIMATION

Assume there is a finite chain of equally spaced metal NPs along the **x**-axis in a multilayered medium; *M* is the number of NPs and *d* is the inter-particle spacing. Again assume NPs can be represented as oscillating dipoles ($\mathbf{p}_j$, j=1, 2, ..., *M*) and ω is the oscillating frequency in the absence of an applied field. The induced dipole moment on particle-*n* because of field generated by dipole-*m* can be calculated as

$$\mathbf{p}_n = \overline{\overline{\mathbf{G}}}(r_n, r_m)\begin{bmatrix} \alpha_x(\omega) & 0 & 0 \\ 0 & \alpha_y(\omega) & 0 \\ 0 & 0 & \alpha_z(\omega) \end{bmatrix}\mathbf{p}_m \qquad (1)$$

where $\alpha_\eta(\omega)$ is frequency dependent polarizability of NP along the $\boldsymbol{\eta}$-direction, $\boldsymbol{\eta}$ is **x**, **y**, or **z**; $\mathbf{G}(\mathbf{r}_n, \mathbf{r}_m)$ is the dyadic layered medium Green's function matrix that gives the relationship between each component of the electric field vector at $\mathbf{r}_n$ and the oscillating electric dipole located $\mathbf{r}_m$. For the complete formulation of LMGFs, the reader is referred to [11].

Surface plasmon resonance occurs when the dipole moment of a single NP becomes equal to the induced dipole moment on that NP due to all the other dipoles. Using (1) and the fact that any vector in 3D space can be written as a combination of 3 orthogonal unit vectors, we can build three independent dispersion modes: one longitudinal and two transverse as

This research was supported by a Marie Curie International Reintegration Grant within the 7th European Community Framework Programme. Contract No. PIRG05-GA-2009-247876.

$$1-\alpha_\eta(\omega)\sum_{n=1}^{M-1}G_{\eta\eta}(r_0,r_n)=0, \qquad (2)$$

where $\mathbf{r}_n = nd\mathbf{x}$, assuming $\mathbf{r}_0$ is located at the origin, $\boldsymbol{\eta}$ is $\mathbf{x}$ for the longitudinal, $\mathbf{y}$ for the first transverse, or $\mathbf{z}$ for the second transverse mode. For a chain of M metal NPs, (2) becomes a set of M coupled equations in the M unknown moments of NPs. One can put these equations in a matrix form as explained in [3] and calculate resonance frequencies for which the matrix coupling the dipoles is singular. For the complete procedure, reader is referred to [3]. Replacing free space Green's functions with layered medium Green's functions is not enough to extend CDA to layered media; the polarizability of NPs should be handled appropriately as well: reflection terms of the layered medium Green's function should be subtracted from α.

III. Numerical Results

In [5,7,9], *Crozier et al.* present a systematic study on the dispersion relations of a metal nanoparticle chain fabricated on top of an indium tin oxide coated (ITO) glass slide. For the experiment, they use cylindrical gold nanoparticles with heights of 55 nm, diameters of ~90 nm, and center-to-center distances of 140 nm along the length of the chain. The thickness of ITO-coating is 20 nm. In [5], they also apply CDA technique to calculate SPR modes: first they assume point dipoles exist in the air, second they assume point dipoles exist in the glass. They observe that experimentally obtained dispersion results lay in between those two cases.

We analyze the same structure theoretically using layered medium CDA (abbreviated as LM-CDA). For the optical constants of gold, the experimental values are used rather than the Drude model to avoid the concerns about the selection of the appropriate values for plasmon and relaxation frequencies. We model cylinders as ellipsoids and calculate their polarizability using (2). The refractive indices of glass, ITO and air are assumed to be 1.51, 1.45 and 1, respectively and the procedure described in the previous section is followed on the complex ω domain using 20 NPs. Fig. 1 compares experimentally (dots and crosses) [5] and theoretically (lines) obtained dispersion relations. Compared to the classical CDA solutions [5], LM-CDA provides more accurate results. Both transverse modes interact strongly with the light line. Maximum propagation length for the first transverse mode is about 1μm, which is slightly higher than the case where NPs are situated in air. This means that we can increase the surface plasmon propagation length, supported by the plasmonic waveguide, based on the constructive backscattering phenomenon.

We repeat the same numerical study for the silver NPs and conclude that silver NP chain support longer propagation lengths. More detailed analysis of these results will be discussed at the conference.

IV. Conclusions

We implement layered medium dyadic Green's functions to obtain the dispersion relations for nanoparticle structures embedded in multilayered media. The polarizability of metal nanoparticles is approximated analytically by taking multilayered medium into account. We numerically show the existence of two different transverse modes. Both of these transverse modes strongly couple with the light line. Propagation lengths of 1μm are possible.

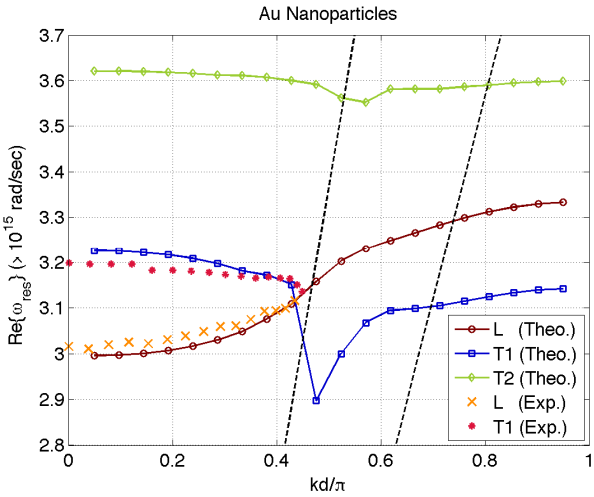


Figure 1 Experimentally (dots and crosses) and theoretically (lines) obtained dispersion curves. Dashed black lines depict light lines in air and glass.

References

[1] M. Quinten, A. Leitner, J.R. Krenn and F.R. Aussenegg, "Electromagnetic energy transport via linear chains of silver nanoparticles," Opt. Lett. 23, 1331-1333, 1998.

[2] S.Y. Park and D. Stroud, "Surface-plasmon dispersion relations in chains of metallic nanoparticles: an exact quasistatic calculation," Phys. Rev. B 69, pp. 125418-1-7, 2004.

[3] W.H Weber and G.W. Ford, "Propagation of optical excitations by dipolar interactions in metal nanoparticle chains," Phys. Rev. B 70, 125429, 2004.

[4] A.F. Koenderink and A. Polman, "Complex response and polariton-like dispersion splitting in periodic metal nanoparticle chains," Phys. Rev. B 74, 033402-1-4, 2006.

[5] K. Crozier, E. Togan, E. Simsek, T. Yang, "Experimental measurement of the dispersion relations of the surface plasmon modes of metal nanoparticle chains," Opt. Express 15, 17482-17493, 2007.

[6] F. Koenderink, R. de Waele, J. C. Prangsma and A. Polman, "Experimental evidence for large dynamic effects on the plasmon dispersion of sub-wavelength metal nanoparticle waveguides," Phys. Rev. B 76, 201403:1-4 Rapid Communication, 2007.

[7] T. Yang, K. B. Crozier, "Dispersion and extinction of surface plasmons in an array of gold nanoparticle chains: influence of the air/glass interface," Optics Express 16, 8570, 2008.

[8] E. Simsek, "On the Surface Plasmon Resonance Modes of Nanoparticle Chains and Arrays," Plasmonics, vol. 4, no. 3, pp. 223-230, Sept. 2009.

[9] T. Yang and K. B. Crozier, Surface plasmon coupling in periodic metallic nanoparticle structures: a semi-analytical model, Opt. Express, vol. 16, pp.13070--13079, 2008.

[10] E. Bae, H. Zhang, and E. D. Hirleman, "Application of the discrete dipole approximation for dipoles embedded in film," J. Opt. Soc. Am. A 25, 1728–1736 (2008).

[11] E. Simsek, Q. H. Liu, and B. Wei, "Singularity subtraction for evaluation of Green's functions for multilayer media," IEEE Trans. on Microwave Theo. and Tech., vol. 54, no. 1, pp. 216-225, Jan. 2006.

Enhanced Sensitivity of Absorption-Based Surface Plasmon Interference Sensors in Silicon-On-Insulator by Adsorbed Layer

Khai Q. Le and Peter Bienstman
Department of Information Technology
Ghent University-IMEC, 41 Sint-Pietersnieuwstraat, Ghent 9000, Belgium
khai.le@intec.ugent.be

***Abstract*—We present an numerical investigation of a planar waveguide surface plasmon resonance (SPR) sensor in silicon-on-insulator (SOI) for detecting a change in the imaginary part of the refractive index. By adding a thin adsorbed layer between the metal-analyte boundary it is found that an enhanced sensitivity of the sensor is obtained, suggesting the possibility of realizing a highly integrated and highly sensitive absorption-based SPR sensor in SOI.**

Keywords-component: SPR biosensors; silicon-on-insulator

I. INTRODUCTION

Surface plasmon resonance sensors have attracted tremendous interest in the past decade for optical detection of small biological or chemical entities in liquids [1]. Furthermore, the SPR sensors can detect changes in not only the real but also the imaginary parts of the refractive index resulting in the so-called absorption-based SPR sensor [2-3]. In general, the conventional absorption-based SPR sensors have been restricted to the cases with the conventional Kretschmann configuration. Unfortunately, the conventional configuration is not suitable for the integration into optical circuits, because of the bulk structure composed of a prism coated with a thin metal [4]. To integrate the traditional absorption-based sensor into optical circuits, input/output parts were replaced with optical waveguides. There has been a growing interest in the development of robust, portable and highly sensitive SPR sensing devices capable of out-of-laboratory measurements. Recent progress in sensitive fiber and waveguide SPR provide options for miniaturization and integration of SPR sensor systems. However, the integration of fiber-SPR to other biosensor components raises some design issues. Among those include the high precision requirement for the insertion of the fiber in to a planar substrate containing fluidic circuit and chambers and the requirement of additional optical components to achieve efficient coupling of light in and out of the fiber [5]. The proposed alternative approach to fiber-based SPR has been the planar optical waveguide structure.

Recently we proposed a highly integrated and sensitive SPR interferometer sensor based on silicon-on-insulator technology. The basic element of the sensor was a surface plasmon interferometer consisting of a thin layer of gold embedded in a silicon membrane. It was demonstrated that the device could achieve a sensitivity of 463.5 nm/ RIU (refractive index unit) and a resolution of $1x10^{-6}$ RIU with regards to wavelength interrogation [6]. That sensor, however, treats only the real part of the refractive index and no literature has examined so far the potential applicability of the planar waveguide sensor in SOI for the use as an absorption-based SPR sensor in SOI.

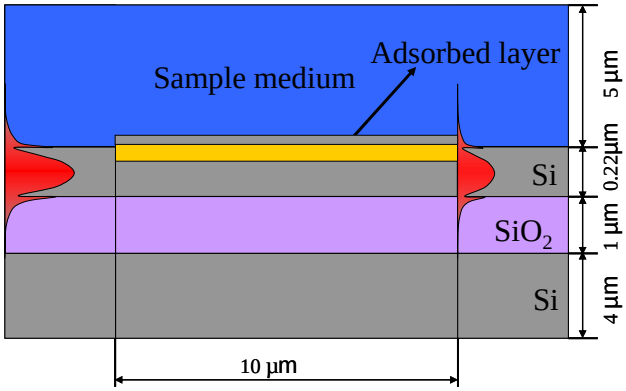


Fig. 1. Cross section of the planar waveguide SPR sensor with a 20 nm-thick adsorbed layer.

In this paper, we apply the SPR interferometer sensor in SOI to detect a change in the imaginary part of the refractive index. The resulting sensitivity of the sensor calculated by an in house-developed eigenmode expansion solver [7] is relatively low. This can be improved, however, by adding a nanoscaled adsorbed layer. Numerical results show a sensitivity enhanced by a factor 5 in comparison to the SPR interferometer without the adsorbed layer. This leads to the possibility of realizing a compact and highly sensitive absorption-based SPR sensing device in SOI.

II. SIMULATION RESULTS AND DISCUSSIONS

The cross section of the SPR interferometer sensor is shown in Fig. 1. The interferometer consists of a gold layer (refractive index calculated by the well-known Lorentz-Drude model [8]) embedded into the silicon membrane (n=3.47) on top of a supporting silica layer (n=1.45), all dimensions and

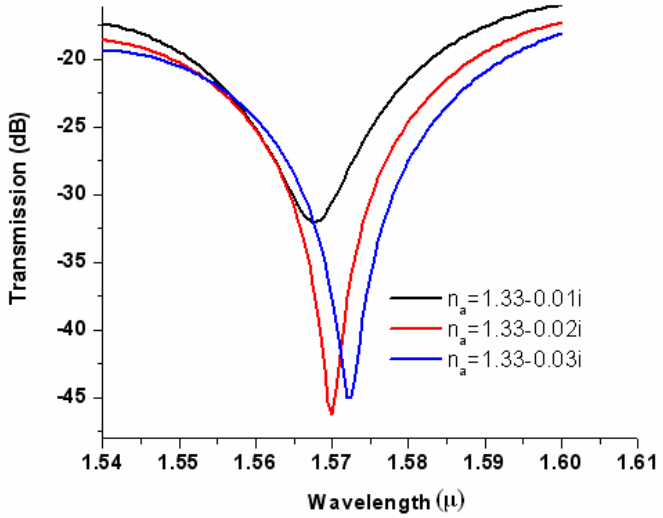


Fig. 2. Shift in resonance wavelength with respect to refractive index of analyte for the sensor without adsorbed layer.

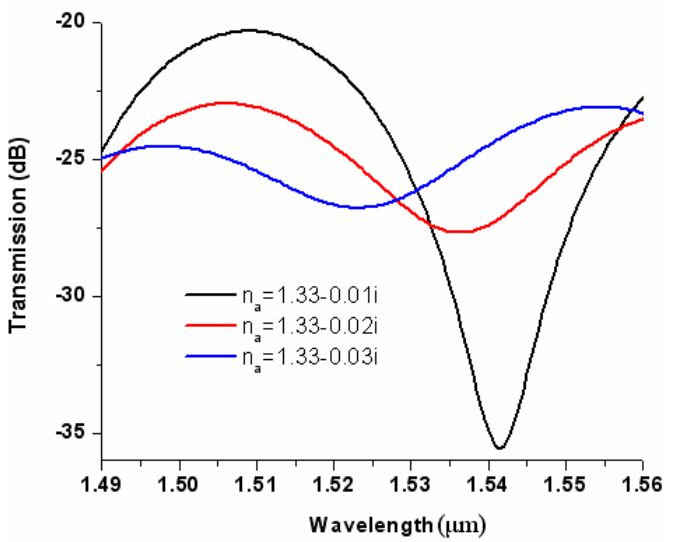


Fig. 3. Shift in resonance wavelength with respect to refractive index of analyte for the sensor with 20 nm-thick adsorbed layer.

length scales are depicted in the figure. TM polarized light is coupled into the waveguide and the transmission characteristics of the entire system are observed for variation of the imaginary part of the refractive index of analyte. We here define the refractive index of the analyte by n_a-k_ai.

The absorption-based SPR sensor can observe changes in both real and imaginary parts of the refractive index. To investigate the basic performance of the sensor, however, we deliberately vary only the value of the imaginary part k_a, whereas the real part is fixed to be n_a=1.33 [9,10]. By varying the imaginary part of the analyte k_a from 0.01 to 0.03 the transmission spectrum of the entire sensor with a 60 nm-thick gold layer is shown in Fig. 2. For each analyte the resonance wavelength has been observed. However, the small shift in resonance wavelength demonstrated the low sensitivity of the sensor. To improve the sensitivity, we propose to add a nanoscaled adsorbed layer with high refractive index between the metal-analyte boundary. In fact, using the adsorbed layer as a means to enhance the sensitivity of biosensors is not new, and SPR sensors using this approach have been realized in Kretschmann-type SPR sensors [11]. Figure 3 shows the transmission spectrum of the sensor with respect to the refractive index of the analyte. From the figure it is clearly seen that there is a large shift in resonance wavelength leading to the high sensitivity of the sensor. Furthermore, to demonstrate an enhancement of the sensitivity of the sensor by adding adsorbed layer we investigate the sensitivity of the sensor with various thickness of the gold layer. Numerical results show that by adding a 20 nm-thick silicon layer with refractive index of 3.47 the enhanced sensitivity is observed and depicted in Fig. 4. Indeed, with 50 nm-thick gold layer the sensitivity of the sensor without adsorbed layer is 225 nm/RIU whereas those of the sensor with the 20 nm-thick adsorbed layer is 1125 nm/RIU.

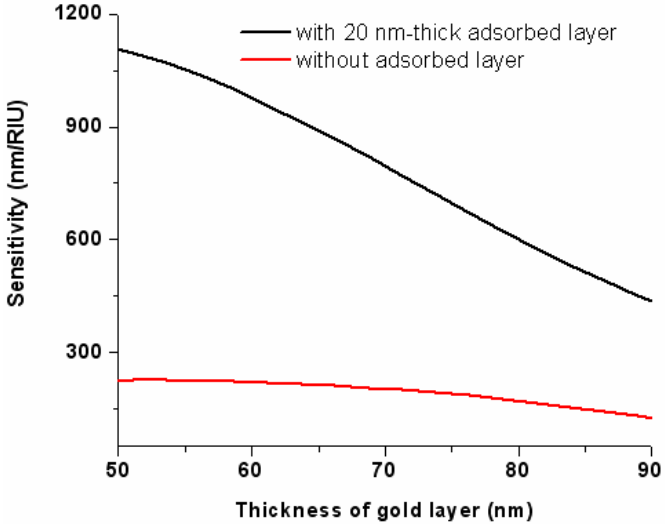


Fig. 4. Enhanced sensitivity of the sensor by a 20 nm-thick adsorbed layer for various thickness of gold layer.

III. Conclusions

The absorption-based SPR interferometer sensor in SOI has numerically been investigated. By adding an adsorbed layer an enhanced sensitivity of the sensor was obtained. It is worth mentioning that the SPR response of the sensor is quite sensitive to the changes in the imaginary part of the refractive index of the analyte leading to the possibility of realizing the highly integrated and highly sensitive absorption-based SPR interferometer sensor in SOI.

Acknowledgment

Parts of this work were performed within the context of Belgian IAP project Photonics@Be.

References

[1] J. Homola, S. Yee, and G. Gauglitz, “Surface plasmon resonance sensors: review,” Sens. Actuators B Chem., vol. 54, pp. 3–15, 1999.

[2] H. Kano and S. Kawata, “Surface-plasmon rensor for absorption-sensitivity enhancement, ” Appl. Opt., vol. 33, pp. 5166-5170, 1994.

[3] K. Kurihara, K. Nakamura, E. Hirayama, and K. Suzuki, “ An absorption-based surface plasmon resonance sensor applied to Sodium

ion sensing based on an ion-selective optode membrane," Anal. Chem., vol. 74, pp. 6323-6333, 2002.

[4] K. Kurihara and K. Suzuki, "Theoretical understanding of an absorption-based surface plasmon resonance sensor based on Kretschmann's theory," Anal. Chem., vol. 74, pp. 696-701, 2002.

[5] X. D. Hoa, A. G. Kirk, and M. Tabrizian, "Towards integrated and sensitive surface plasmon resonance biosensors: a review of recent progress," Biosens. Bioelectron., vol. 23, pp. 151-160, 2007.

[6] P. Debackere, S. Scheerlinck, P. Bienstman, and R. Baets, "Surface plasmon interferometter in silicon-on-insulator: novel concept for an intergrated biosensor" Opt. Express, vol. 14, pp. 7063-7072, 2006.

[7] CAMFR, http://camfr.sourceforge.net.

[8] A. D. Rakic, A. B. Djurisic, J. M. Elazar, and M. L. Majewski, "Optical properties of metallic films for vertical-cavity optoelectronic devices," App. Opt., vol. 37, pp. 5271-5283, 1998.

[9] T. Iwata and S. Maeda, "Simulation of an absorption-based surface plasmon resonance sensor by means of ellipsomettry," App. Opt., vol. 46, pp. 1575-1582, 2007.

[10] J. Shibayama, "A Kretschmann-type absorption-based surface plasmon resonance waveguide sensor.," Microwave Opt. Technol. Lett., vol. 50, pp. 2497-2499, 2008.

[11] A. Lahav, M. Auslender, and I. Abdulhalim, "Sensitivity enhancement of guided-wave surface-plasmon resonance sensors," Opt. Lett., vol. 33, pp. 2539-2542, 2008.

Localized surface plasmon waveguide integrated on dielectric waveguide

M. Février, P. Gogol, J.-M. Lourtioz, P. Beauvillain, B. Dagens
Institut d'Electronique Fondamentale CNRS UMR 8622, Université Paris-sud XI
Centre d'Orsay, Bâtiment 220, 91405 Orsay cedex, France

Abstract—**We first study theoretically the behavior of metallic nanoparticles chains in vacuum excited by a plane wave, with a coupled-dipole approximation method and with a 3D FDTD software. Then we consider the integration of nanoparticule chains on a dielectric waveguide, and their excitation by evanescent coupling, in the telecom range.**

Keywords- guided optics; plasmons; nanoparticule; simulation

I. INTRODUCTION

Scale reduction of optical components can be realized by manipulating light at the subwavelength scale. Especially metallic nanoparticle (MNP) chains supporting localized surface plasmons (LSP) can propagate light at the subwavelength scale [1] and realize specific function like very compact coupler [2]. However insertion of such waveguide in integrated circuit or devices requires optical coupling optimisation between dielectric waveguide and plasmonic waveguide. This paper is organized as follows. In the section II we theoretically study the behaviour of a finite MNP chain in vacuum excited with a plane wave, and the influence of NP spacing. Simulations are performed with a coupled-dipole approximation (CDA) analytical method and with a commercial FDTD 3D method (Finite Difference Time Domain Lumerical Solutions). Then the section III is dedicated to the evaluation of transmission in these MNP chains excited by evanescent coupling from a dielectric waveguide. Integration of such LSP waveguide on dielectric waveguide is discussed.

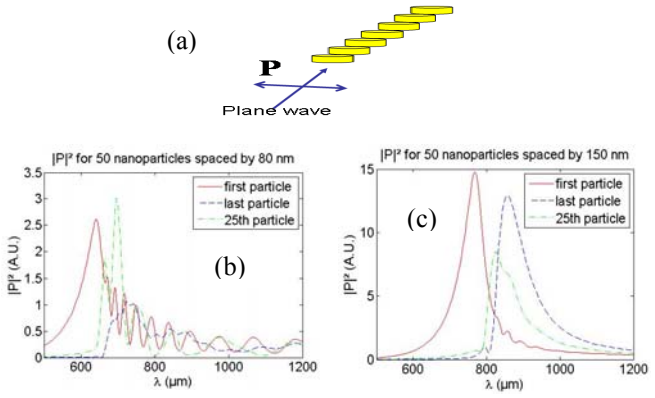


Figure 1. (a) Excitation by a plane wave along the NP chain for 50 gold nanorods spaced by a distance center to center d. The ohmic dissipated power is plotted for the first (solid red curve), the 25th (green dashed point) and the last (bleu dashed) rod as a function of the wavelength. The rods are spaced by 80 nm (b) or 150 nm (c).

II. MNP WAVEGUIDE IN VACUUM

The coupled-dipole approximation method considers each nanoparticle (NP) as a point. The response of this point to an external electric field is dipolar. In this approximation a single dipole has a polarization $\mathbf{p}e^{-i\omega t}$ oscillating with frequency ω which results from the multiplication of the local electric field by the NP polarisability. For a finite linear chain of N point dipoles the induced dipole moment on the nth NP results from the external applied field $\mathbf{E}^{(ext)}e^{-i\omega t}$ and the electric fields generated by each NP:

$$\mathbf{p}_n = \alpha(\omega)\left\{\mathbf{E}_n^{(ext)} + \frac{1}{4\pi\varepsilon_0}\sum_{m\neq n}^{N}\left[\left(1-\frac{i\omega|n-m|d}{c}\right)\frac{3(\hat{\mathbf{r}}\cdot\mathbf{p}_m)-\mathbf{p}_m}{|n-m|^3 d^3} + \frac{\omega^2}{c^2}\frac{\mathbf{p}_m-(\hat{\mathbf{r}}\cdot\mathbf{p}_m)}{|n-m|d^3}e^{i\omega|n-m|d/c}\right]\right\}, \quad (1)$$

with $\alpha(\omega)$ is the polarisability and $\hat{\mathbf{r}}$ is the unit vector pointing from the dipole to the field point. The electric field and the polarisability fully take into account retardation effects [3, 4, 5]. The NP chain supports a transverse mode of propagation (**P** perpendicular to the chain) and a longitudinal mode (**P** parallel to the chain). Our structure is composed by 50 gold nanorods spaced by a distance d (center to center distance Fig. 1(a)). Dimensions of the rods are 240 nm × 60 nm × 25 nm, and they are positioned parallel to their longer dimension. We consider only a transverse excitation (the electric field is parallel to the longer rods dimension). We use the "Drude" model for the dielectric function of gold where the plasma frequency is $\omega_p = 1.29\cdot10^{16}$ rad/s and the electron scattering rate is $\gamma = 1.14\cdot10^{14}$ s^{-1} [6].

Considering a continuous transverse excitation by a plane wave at an extremity of the chain (defined as the "first" NP), we plot the ohmic dissipated powers spectra in the range 500-1200 nm for different value of d and for different positions in the chain (the first, the 25th and the last NP) (Fig. 1). The dissipated power is proportional to $|\mathbf{P}_n|^2$. It is concentrated differently on the first, the 25th and the last particle depending on the wavelength. Its repartition is also strongly dependent on the spacing d.

The same structures are simulated with FDTD 3D commercial software (Fig. 2). Chain resonance 150 nm shift is attributed to different refractive index models used in both

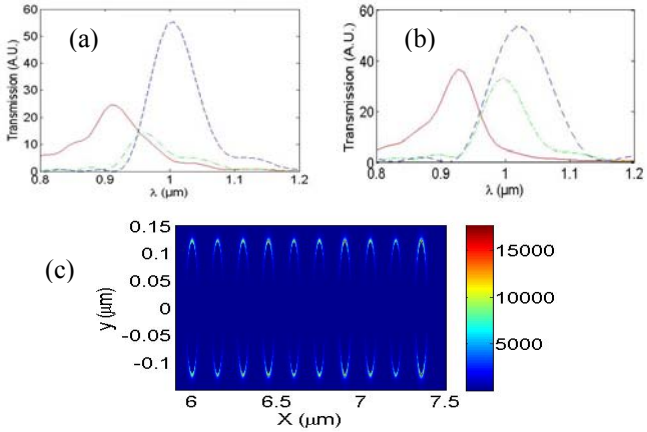


Figure 2. Excitation by a plane wave along the NP chain for 50 gold nanorods the Transmission power is plotted for the first (solid red curve), the 25th (green dashed point) and the last (bleu dashed) rod in function of the wavelength. (a) The rods are spaced by 80 nm (a) or 150 nm (b). (c) Intensity mapping for the last ten nanorods with a150 nm spacing at λ=1.04μm.

softwares, respectively "Palik" model in FDTD [6] and "Drude" model in CDA. Fig. 2(c) shows the intensity mapping along the 150 nm spacing chain. The nanorod LSP response to the excitation appears as a dipole that validates the approximation in CAD. But for a spacing of 80 nm (Figs. 1(b) and 2(a)) the results for both models are different. One hypothesis is that the point dipole approximation is no more valid: taking into account of the nanorod shape through only the polarisability is no more sufficient. More generally, the comparison between the models shows that the CDA is a good approximation for a chain with nanorods spacing higher than 120 nm. In the case of a 150 nm spacing (Figs. 1(c) and 2(b)) both models give the same global behavior, despite a higher difference between the power of the first and the last NP with FDTD.

In the figs. 2(a) and 2(b) the first and the last NP are preferentially excited by respectively short and long wavelength waves. This phenomenon is explained by the phase of the excitation plane wave respect to the LSP response of each particle, the phase matching being function of wavelength and propagation distance. We can see for intermediate wavelengths about 950 nm that all the NP of the chain are excited.

III. COUPLING OF LSP AND DIELECTRIC WAVEGUIDES

Such LSP waveguides could be integrated in photonic circuits in order to generate specific functions. Integration of LSP waveguide requires optical coupling with circuits waveguides. Taking into account the geometry of such structure, we use 3D FDTD for simulation of nanorods chain deposited on a monomode Si_3N_4 waveguide (Figs. 3). Nanoparticles are the same as in the section II. Due to the interaction with the dielectric medium, the resonance of LSP shifts up to λ = 1410 nm. We inject a 1410 nm transverse electric (TE) guided mode at the entrance of the Si_3N_4 waveguide, and we calculate the evolution of the light

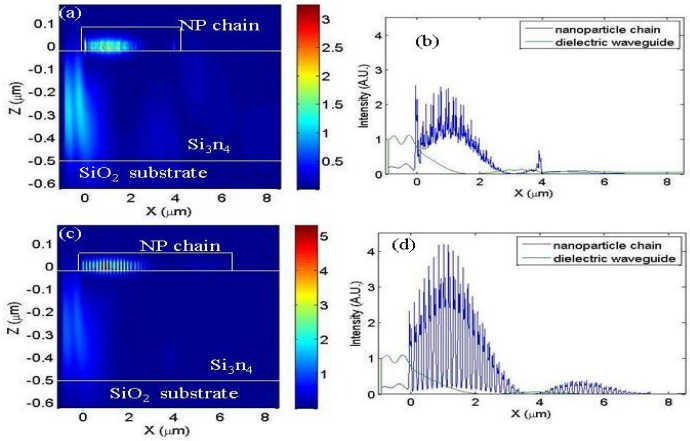


Figure 3. Intensity mapping of a coupling of a LSP waveguide a dielectric waveguide for λ = 1410 nm and for 80 nm (a) and 150 nm (c) NP spacing. Intensity as a function of the propagation direction, inside the dielectric waveguide (green curve) and the nanoparticles chain (blue curve) for 80 nm (b) and 150 nm (d)spacing at λ = 1410 nm.

along the structure. At this wavelength, the 150 nm spacing chain seems more uniformly excited than the 80 nm spacing one (Fig.3). Moreover the injected power is almost totally transferred in the NP chain before to re-couple in the dielectric waveguide. Decrease of the power in the NP chains after 1 μm propagation is attributed to both the ohmic losses in the metal and the re-coupling in the dielectric waveguide. Interestingly, the two waveguides (dielectric and LSP) behave as almost balanced coupled waveguides with a characteristic distance of around 3μm similar for the two considered NP spacing. Such behavior could be used to define a complex effective index for the LSP waveguide, thanks the coupled mode theory.

In this paper, we compare the CDA and FDTD methods to study metallic nanoparticle periodic chains in vacuum. We also show by FDTD the possibility to excite LSP waveguide by evanescent coupling from a dielectric waveguide in the telecom range.

This work was supported by the French ANR project PLACIDO and by Region Ile de France.

REFERENCES

[1] J. R. Krenn, A. Dereux, J. C. Weeber, E. Bourillot, Y. Lacroute, J. P. Goudonnet, G. Schider, W. Gotschy, A. Leitner, F. R. Aussenegg, and C. Girard, "Squeezing the optical near-field zone by plasmon coupling of mettalic nanoparticles," Phys. Rev. Lett., 82, pp. 2590-2593, 1999.

[2] M. L. Brongersma, J. W. Hartman, and H. A. Atwater, "Electromagnetic energy transfer and switching in nanoparticle chain arrays below the diffraction limit," Phys. Rev. B, 62, pp. R16356-R16359, 2000

[3] J. D Jackson, Classical Electrodynamics, 3rd ed. Wiley, New York, 1967

[4] C. F. Bohren and D. R. Huffman, Absorption and Scattering of Light by Small Particles. Wiley: New York, 1983.

[5] A. Femmius Koenderink, and A. Polman, "Complex response and polariton-like dispersion splitting in periodic metal nanoparticle chains," Phys. Rev. B, 74, 033402(1)-033402(4), 2006.

[6] E. D. Palik, Handbook of Optical Constants of Solids. Academic, Orlando,FL, 1985.

Modeling of multiwalled carbon nanotubes based metamaterials and photonic crystals

Haider Butt, Qing Dai, Peter Farah, Ranjith. R, Kanghee James Won, *Timothy D. Wilkinson and Gehan Amaratunga
Department of Engineering, University of Cambridge, Cambridge, United Kingdom
*Email: tdw13@cam.ac.uk

***Abstract*—Highly dense periodic arrays of multiwalled carbon nanotubes can be utilized as sub-wavelength structures for metamaterials and photonic crystals. We have established a metamaterial structure which acts as a plasmonic high pass filter using a 400nm spacing nanotube array and also utilized its band-gaps to construct photonic crystals based waveguides and switches.**

Keywords-component; periodic arrays of multiwalled carbon nanotubes; metamaterials; photonic crystals; optical waveguides and swictches

I. INTRODUCTION

Multiwalled carbon nanotubes (MWCNTs) since their discovery by Iijima have been the focus of extensive research. Two-dimensional periodic arrays of vertically aligned MWCNTs can be grown at precisely determined locations by plasma-enhanced chemical vapor deposition (PECVD). They present great potential for applications requiring periodic metallic structures and dielectric function, such as nano-antennas, metamaterials and photonic crystals. In this manuscript we present the utilization of 2D periodic arrays of MWCNTs as sub-wavelength structures for constructing very interesting plasmonic and photonics devices, i.e. metamaterials and photonic crystals. These devices utilize the optical properties of individual CNTs to display interesting plasmonic filtering effects and perform effective wave guiding/switching in the optical regime.

II. MWCNT BASED METAMATERIALS

Metamaterials can be formed artificially by sub-wavelength components to display properties beyond those available in naturally occurring materials. It has been reported by Pendry et al. [1] that the periodic arrays of thin metal wire structures, excited by an electric field parallel to the wires, act as metamaterials and display plasmonic response in the frequency domains depending on the array geometry. They demonstrate plasma frequencies which are much lower than in the metal structures and can be utilized for filtering in microwave and terahertz frequency domains. Here we demonstrate that two-dimensional high density arrays of metallic MWCNTs (metallic nano-wire structures) can be used to realize such plasmonic filters which operate in the optical regime.

Highly dense array of MWCNTs, excited by an electric field parallel to the wires, will perform similar to a low-density plasma of very heavy charged particles, with a plasma frequency ω_p, given by

$$\omega_p^2 = (2\pi c_0^2)/(a^2 \ln(a/r)) \quad (1)$$

where c_0 is the velocity of light in vacuum, a is the lattice constant of the 2D MWCNT array and r is the radius of the nanotubes. The lowering of the plasma frequency is due to the increase in the effective electronic mass on the nanotubes due to the induced current and corresponding magnetic field around them. According to (1), the effective plasma frequency strongly depends on the nanotube radius and lattice constant. Their values can be discretely chosen to engineer the MWCNT arrays of the desired plasma frequency.

The resultant frequency dependent permittivity of the metamaterial can be calculated using the Drude model for metals, which shows that the effective permittivity $\varepsilon(\omega)$ is negative for frequencies less than ω_p, therefore no wave propagation will take place inside the metamaterial. Electromagnetic waves propagation only occurs above ω_p, due to which the structure acts as a nanotube based nanophotonic high-pass filter.

Theoretical study, using (1), showed that a square lattice MWCNT array, with a = 400 nm and r = 50 nm, displays a plasma frequency $f_p = \omega_p/2\pi$ of 207.5 THz (λ_p of 1.44 μm). To confirm the filtering effect a Finite Element Method modeling of the same MWCNT array was performed using the "*RF Waves*" application mode of COMSOL Multiphysics® to study the propagation of optical/terahertz waves through it. The dielectric properties of individual MWCNTs were obtained from reference [2].

The modeled geometry and simulated results for the Transverse Electric (TE) mode propagation (incident electric field parallel to the nanotubes) are presented in Fig. 1. The results show that the MWCNT array allowed transmission to the waves having wavelengths of about 1 μm and less. The wavelengths above 1.25 μm were completely reflected showing that the high density MWCNT array displayed a plasmonic filtering effect for a plasmonic wavelength λ_p of about 1.25 μm, which is in close proximity to the plasmon wavelength λ_p of 1.44 μm calculated using (1). The mismatch can be explained by the difference in the dielectric properties used.

The fabrication of the MWCNT based high pass filter was also performed and a scanning electron microscope (SEM) image is shown in Fig. 1 (a). The growth of such high *a/r* aspect ratio array was a difficult task. The characterization

Haider Butt specially thanks Professor Gehan Amaratunga, Cambridge Commonwealth Trust (CCT) and Hughes Hall College for granting the funding to pursue this research.

results for the MCWNCT array based plasmonic filter showed a good match with the calculated results and will be published elsewhere.

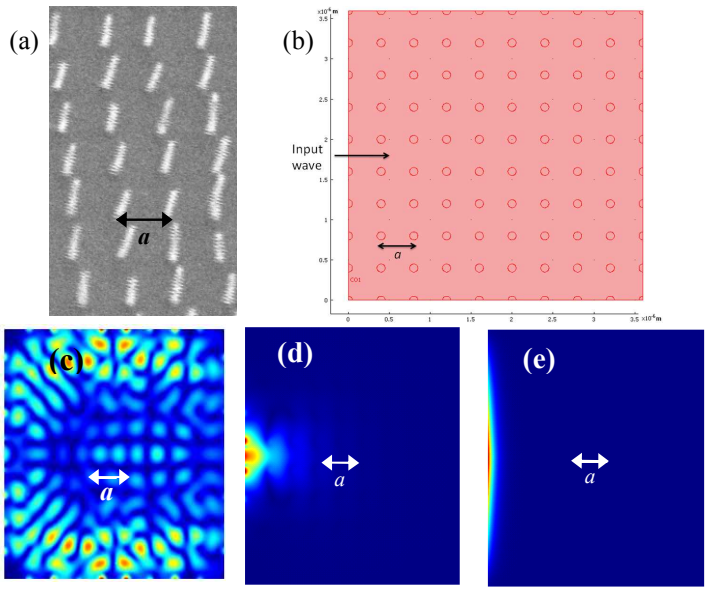


Figure 1. (a) SEM image of a 2D MWCNT array with tube radius of 50 nm and lattice constant *a* of 400 nm, grown on silicon substrate using PECVD after employing e-beam lithography to pattern a 5 nm thick nickel catalyst dots. (b) TE modeling of the same with incident wave from the left. Wavelengths of (c) 0.5 um and (d) 1 um propagate into the array. After a cut-off wavelength of (e) 1.25 um all the waves are reflected by the metamaterial.

III. PHOTONIC CRYSTALS BASED WAVEGUIDES & SWITCHES

Periodic arrays of MWCNTs have shown to act as photonic crystals [3]. The dielectric periodicity in the arrays gives rise to the Bragg-scattering of the propagating electromagnetic waves and also to the opening of energy band gaps. No real wave vector exists for any mode at the frequencies belonging to the band gap, however, by placing defects in the array these modes can be guided without significant loss. To demonstrate this photonic wave guiding effect we modeled and fabricated a 2D MWCNT array (with tube radius 50 nm and lattice constant 400 nm) having 800 nm wide line defects. Fig. 2 displays the simulated result for the propagation of a wave having 800 nm wavelength through the line defect. The fabricated MWCNT based waveguide structure is also shown in Fig. 2 (c).

Similarly, wavelength switching can also be achieved by introducing multiple line defects with varying dimensions in the MWNT based photonic crystals. Only the frequency modes having their wavelengths comparable to the line defect dimensions are able to propagate through them. Modeled results demonstrated the switching of wavelengths as shown in Fig. 3.

IV. CONCLUSION

Our results demonstrate that the periodic arrays of MWCNTs promise great potential towards the nano-scale photonic devices which can be utilized for optical filtering, wave guiding, switching and wavelength multiplexing.

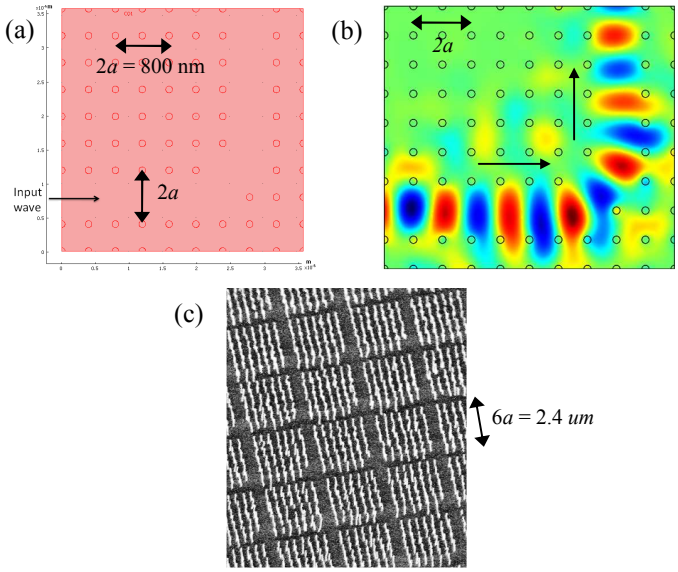


Figure 2. (a) Modeled MWCNT based photonic waveguide, with a line defect of 2*a* = 800 nm and tube radius = 50 nm. (b) Simulated (TE mode) propagation of a 800 nm wavelength wave through the line defect. (c) SEM image of the fabricated MWCNT based waveguide; the line defects in the array are visible.

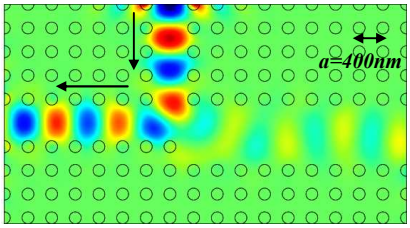
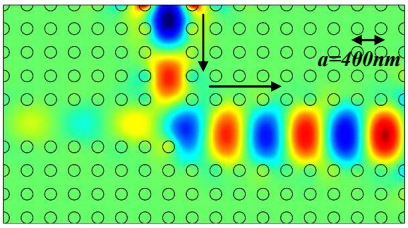
(a) An incident wave (from the top), of wavelength 810 nm, propagates through the left line defect, having a width of 2*a* =800nm.	
(b) Incident wave (from the top), of wavelength 1160 nm, propagates through the right line defect (width 3*a*=1200 nm).	

Figure 3. MWCNT based 2D photonic crystal wavelength switch. Incident waves (from the top) of lower wavelengths are deflected to the left and higher wavelengths are deflected to the right. The figure shows the simulated TE mode propagation of (a) λ= 810 nm and (b) λ=1160 nm. The lattice constant of MWCNT array is 400nm.

REFERENCES

[1] J. B. Pendry, A. J. Holden, D. J. Robbins, and W. J. Stewart, "Low frequency plasmons in thin-wire structures," Journal of Physics: Condensed Matter, vol. 10, pp. 4785-4809, 1998.

[2] F. Bommelia, L. Degiorgia, P. Wachtera, W. S. Bacsab, W. A. d. Heerb, and L. Forroc, "Evidence of anisotropic metallic behaviour in the optical properties of carbon nanotubes," Solid State Communications, vol. 99, pp. Pages 513-517 1996.

[3] K. Kempa, B. Kimball, J. Rybczynski, Z. P. Huang, P. F. Wu, and D. Steeves, "Photonic Crystals Based on Periodic Arrays of Aligned Carbon Nanotubes," Nano Letters, vol. 3, pp. 13-18, 2002.

Towards fault tolerant quantum photonics circuits

M. Rodas Verde, A. Laing, A. Peruzzo, A. Politi, M. Halder, M. G. Thompson and J. L. O'Brien
CQP, H. H. Wills Physics Laboratory & Department of Electrical and Electronic Engineering
University of Bristol, Bristol, UK

T. C. Ralph
Department of Physics
University of Queensland
St Lucia, Queensland, Australia

Abstract— **We report our latest progress in integrated quantum photonics within Silica-on-Silicon waveguide chips: a unit visibility Hong Ou Mandel Dip and CNOT truth table, with single photons from a two photon Spontaneous Parametric Down Conversion (SPDC) Source. The increase in performance, compared to previous results, is due to polarisation and spectral fine tuning of the SPDC source, and the stability inherent in silica waveguide devices.**

I. Introduction

Quantum information science promises profound new technologies in communication [1], information processing [2,3], and ultra-precise measurement [4]. However, these quantum technologies must be robust to imperfections in their components and to the effects of environmental noise. Encoding quantum information in photons is promising for fast transmission and low noise [5, 6]. Integrated photonics holds great promise for miniaturizing and scaling quantum logic circuits [7], and high fidelity single qubit operations have been demonstrated [8]. We report integrated photonic devices that exhibit near-unit fidelity quantum interference and two-photon entangling logic operation. This high fidelity operation relied on a spectrally tuned photon source producing near-identical photons. These results show that photonic quantum circuits can perform at the high fidelities required for quantum technologies.

II. Experimental Setup

A. Introduction and Setup

In the last two years we have developed silica-on-silcon waveguides quantum circuits that can process individual photons and reduce the limitations in scalability and stability of previous large-scale (bulk) systems [9]. Quantum phase stability and generation of entanglement within a chip, together with high-fidelity two-photon entangling gates have been demonstrated [7].

The CNOT gate shown in Fig. 1A shows a schematic of an integrated controlled-NOT (CNOT) gate. The silica –on-silicon waveguides guide photons via total internal reflection in much the same way as single mode optical fibres. Waveguides are brought into proximity (several μm) to realize directional couplers whose reflectivity η is controlled via the length of the coupling region. The major factors determining the performance of such devices are photon loss (typically approx.

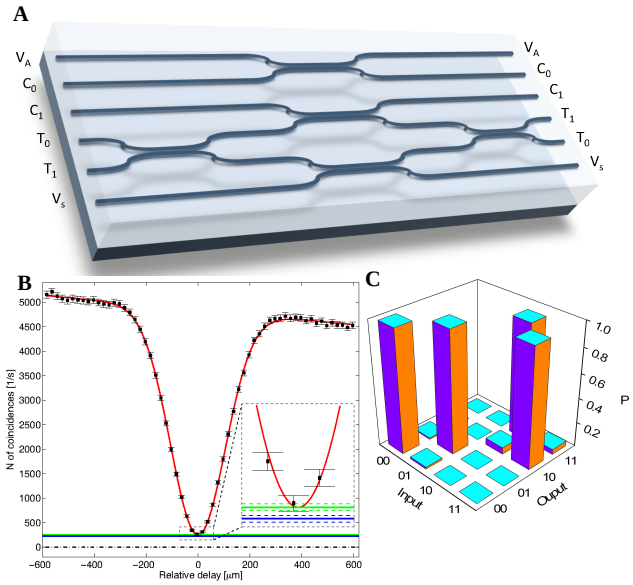


Figure 1. High-fidelity of photonic quantum circuits. (A) Achematic of a waveguide CNOT gate. (B) High visibility quantum interference in a waveguide directional coupler. (C) Experimentally measured 'truth table' for a CNOT gate circuit.

0.1dB/cm); the quality of single photon interference [10] at directional couplers; and the quality of multiphoton interference in interferometers formed by two or more directional couplers.

B. Results

We measured the rate of detecting a single photon in each output of an $\eta = 0.5267 \pm 0.0004$ directional coupler as a function of the arrival time of the photons. The measured rate of detecting photons from different pairs is plotted in Fig. 1B (blue line).The single photon interference visibility taking this rate into account is $V_{meas} = 0.995 \pm 0.004$ which corresponds to a relative visibility of $V_{rel} \equiv V_{meas}/V_{ideal} = 1.001 \pm 0.004\%$. The green line shows the expected level of the minimum for an $\eta = 0.5267$ coupler. These data correspond to perfect single photon interference, within error bars.

A CNOT gate (Fig. 1A) is ideal for testing the performance limits of quantum waveguides circuits, as it contains all of the elements of a general circuit. This CNOT gate works with probability 1/9 – the presence of only one photon in the control and one photon in the target signals success of the gate. We

measured the '1/3' coupler in the control part of the circuit (top one of Fig. 1A) to be $\eta = 0.3078 \pm 0.0009$ and assume all 1/3 couplers have this value (due we are not able to measure the other two for being embedded in the circuit). The two '1/2' couplers were measured to be $\eta = 0.442 \pm 0.001$ and $\eta = 0.452 \pm 0.001$. This is a reasonable given previous data on lithographic devices [7]. Fig. 1C shows the measured operation of our device, taking into account the rate of detecting photons form different pairs, as described above. It has a fidelity of F= 0.969± 0.002 and a similarity of $S = 0.993 \pm 0.002$ with that expected for the circuit with the measured reflectivities.

III. Experimental Details of the Photon Source

Fig. 2 shows a schematic of the photon pair source. A 402 nm CW laser was focused to a waist of 40 μm in a 2 mm thick biaxial Type-I BiBO (BiB3O6) crystal. The crystal was cut to generate photon pairs at the degenerate wavelength of 804 nm at an opening half angle of 3 degrees. Due the small spatial spectral spread, we assume that the waist of these 'daughter' photons is the same as the waist of the pump beam in the crystal. The daughter photons with the calculated waist at the crystal were then collected into PMF fibres using a single 11 mm aspheric lens, after passing through interference filters with a 2 nm FWHM, centred at 804 nm.

The two main factors in obtaining indistinguishable photon pairs from this source were ensuring that they share the same spectral mode and the same polarisation, both of which should be pure. To ensure that the photons shared the same spectral mode, the spatial collection point and the tilt of the interference filters were matched so that the profile of the transmitted photons had Gaussian shapes that were centred at the same (degenerate) wavelength. To maximise the polarisation purity of the photons collected into PMF fibres, either the slow or fast axis of the fibre must be perfectly parallel (or orthogonal) to the plane formed by the direction of the pump beam and the optic axis of the crystal, since PMFs decohere the polarisation of any photon that projects onto both axes. A polarisation purity test on the photons that exit the PMF confirmed this alignment.

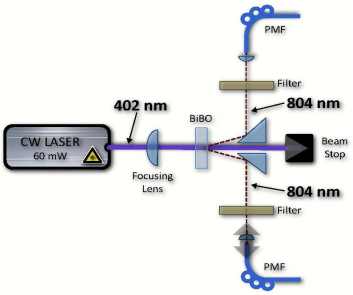


Figure 2. A schematic of the spectrally tuned two photon source. A CW laser was focused to a 40 μm waist at a Type-I BiBO crystal to produce degenerate photon pairs via spontaneous parametric down conversion. The daughter photons were collected into polarisation maintaining fibers (PMFs) after passing through interference filters with a 2 nm FWHM. The source was fine tuned with a spectrometer to ensure fully degenerate photons. The photon pairs were injected into the waveguides from Fig. 1A.

IV. Conclusion and Outlook

We shown the first implementation of optical quantum circuits operating within the limits required for fault tolerant operation needed towards the realization of a quantum computer.

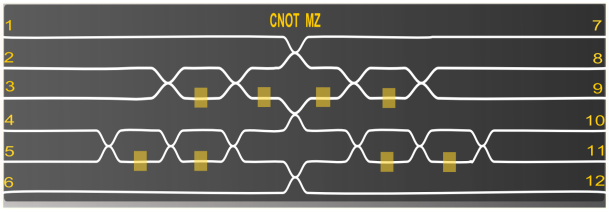


Figure 3. Sketch of an integrated photonic circuit made up of a central CNOT gate and eight phase shifters in integrated interferometers used in order to have a complete characteristion of different quantum dinamical systems.

In order to get a full characterisation of an unknown two qubit process, a new silica-on-silicon waveguide quantum circuit is being tested (Fig. 3) This circuit is made up of a CNOT gate and eight independently controlled phase shifters in integrated interferometers to control two-photon qubit states (Four to control input states and four to act on the output states). We will report on progress and details on this experiment.

References

[1] N. Gisin, G. Ribordy, W. Tittel and H. Zbinden, Rev. Mod. Phys., vol. 74, pp. 145, 2002.

[2] M. A. Nielsen and I. L. Chuang, Quantum Computation and Quantum Information, Cambridge University Press, 2000.

[3] D. Deutsch, Proc. R. Soc. Lond. A, vol. 400, pp. 97, 1985.

[4] V. Giovannetti, S. Lloydand L. Maccone, Science, vol 306, pp. 1330, 2004.

[5] E. Knill, R. Laflamme and G. J. Milburn, Nature, vol. 409, pp. 46, 2001.

[6] J. L. O'Brien, Science, vol. 318, pp. 1567, 2007, and references therein.

[7] A. Politi, M. J. Cryan, J. R. Rarity, S. Yu and J. L. O'Brien, Science, vol. 320, pp. 646, 2008.

[8] J. C. F. Matthews, A. Politi, A. Stefanov and J. L. O'Brien, Nature Photonics, vol. 3, pp. 346, 2009.

[9] J. L. O'Brien, Science, vol. 318, pp. 1567, 2007

[10] C. K. Hong, Z. Y. Ou and L. Mandel, Phys. Rev. Lett., vol. 59, pp. 2044, 1987

Fibre based Photon Pair Sources for Integrated Quantum Information

Matthaeus Halder, Jeremie Fulconis, Alex Clark, Bryn Bell, John Rarity
Centre for Quantum Photonics
University of Bristol
Bristol, UK
John.rarity@bristol.ac.uk

Chunle Xiong, William J. Wadsworth
Centre for Photonics and Photonic Materials
Department of Physics
University of Bath
Bath, UK

Mark Tame, Myungshik Kim
School of Mathematics and Physics
The Queen's University
Belfast, UK

***Abstract*—We report on the creation of entangled photon pairs in nanostructured photonic crystal fibres in an intrinsically pure state. Quantum interference between independent photons is shown and the creation of cluster state creation is demonstrated. We will present a photon pair source for integrated photonic devices.**

Keywords: Entangled photon pairs; Quantum information; Photonic crystal fibres.

I. INTRODUCTION

Single photons are at the heart of integrated optical quantum technologies such as quantum cryptography, quantum computing and quantum metrology. To achieve high visibility two-photon interferences, the photons need to be in a pure state which usually is achieved by narrow band filtering. This reduces the overall efficiency of detection (μ) and hence limits current experiments to a photon number in the order of 4-6. To achieve significant count rates for higher order multi-photon experiments (e.g. integrated cascaded CNOT or Cluster states) an improvement in μ to over 20% is essential. Here we report on the creation of photon pairs via four-wave-mixing (FWM) in birefringent Photonic Crystal Fibres (PCF) [1]. It has recently been suggested that for thoroughly engineering the phase matching condition of a birefringent PCF (Fig. 1), photon pairs can by created in an intrinsically pure state and narrow band [2,3]. This can be achieved for cross-polarized phase matching, where two pump photons in the slow axis (ss)

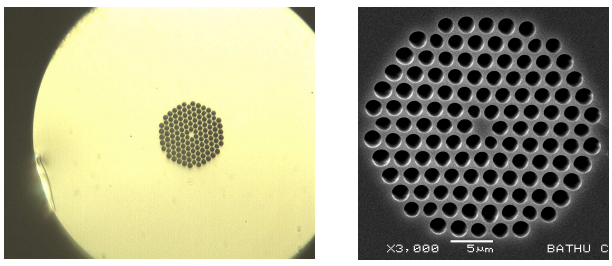


Figure 1. Profile of a nanostructured Photonic Crystal Fibre.

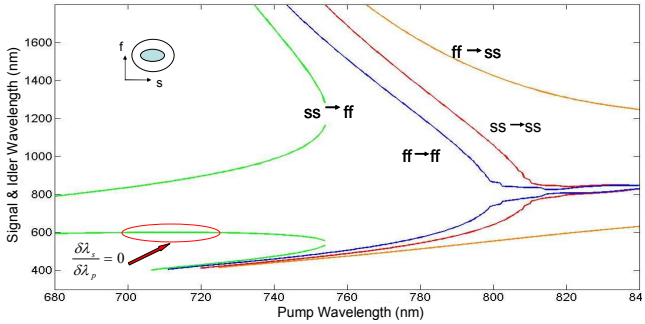


Figure 2. Phasematching curve for a birefringent fibre, with pairs annihilated and created in the fast (ff) and slow (ss) axis, respectively.

are converted into a pair of photons, polarized in the orthogonal fast (ff) axis (Fig. 2, ss-ff). The aim is to produce such intrinsically pure and narrow-band photons and hence to achieve high non-classical interference visibility without any requirement for spectral filtering. A direct consequence is an increase in the collection efficiencies μ. The absence of any filters makes FWM hence a very promising approach for photon pair generation in integrated photonic technologies.

II. THE EXPERIMENT

A. Experimental Setup

Pairs of signal (s) and idler (i) photons are created in an uncorrelated spectral state with factorable joint amplitude *f*:

$$f(\omega_s,\omega_i) = f_s(\omega_s) \otimes f_i(\omega_i) \quad (1)$$

with f_s and f_s the spectral distribution of signal and idler photon, respectively. In this case detecting one photon of the pair can be used to herald the other one in a pure quantum state. In order to experimentally test the purity of our single photons, we perform a Hong-Ou-Mandel experiment [4] using

two heralded signal photons generated in two separate PCF sources. A pulsed laser (TiSa, 705 nm, 80 MHz, 1ps) pumps two 40 cm long separate pieces of PCFs. Photon pairs are created via FWM with an intrinsic bandwidth of $\Delta\lambda_s$=0.13nm and $\Delta\lambda_i$=2nm, respectively and split up by dichroic mirrors. Band pass filters of 40 nm and 10 nm bandwidth ($\gg\Delta\lambda_{s,i}$) block the residual pump light in each two arms. Raman background is significantly reduced by spatial and polarization filtering. The idler photons are launched into single mode fibres and the signal photons into a single-mode 50:50 coupler. All four outputs are connected to Silicon avalanche photodiodes linked to a four-fold coincidence electronics [5]. When the two signal photons arrive simultaneously on the beam splitter and polarization is controlled, a 78% reduction in the 4-fold coincidence count rate can be observed with μ_s ~0.21 and μ_i ~0.18.

B. Source of entangled photon pairs

In a further setup, we are using one piece of PCF in a Sagnac loop configuration (Fig. 3), in order to create pairs of entangled photons. Pump pulses with diagonal polarization are sent onto a PBS, propagating along the PCF in both directions and giving raise to photon pairs. By tilting the optical axis of the fibre on one end by 90° (as depicted), the pairs always take the same output, but with orthogonal polarizations. They are in a coherent superposition of horizontal and vertical polarization $\frac{1}{\sqrt{2}}\left(|H_s H_i\rangle + e^{i\varphi}|V_s V_i\rangle\right)$ and hence entangled. Fig. 4 shows real and imaginary part of a full quantum state tomography with a fidelity of 86%.

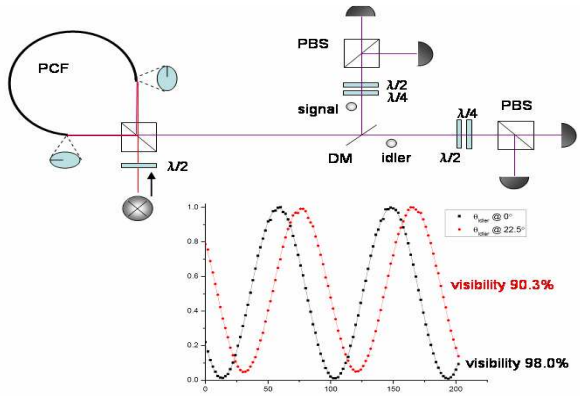


Figure 3. Setup of the entangled photon pair source.

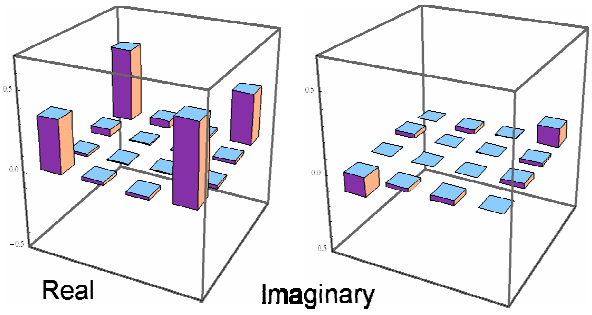


Figure 4. Quantum tomography of the entangled state.

III. Conclusion and Application

These sources of heralded and entangled photons now allow us to build integrated multi-photon setups as for example a cluster state or a teleportation gate. We will report on progress and details on these experiments at the conference and give an outlook on an integrated photon pair source for quantum information.

Acknowledgment

The work was supported by the UK EPSRC (QIP IRC and EP/F002424/1), the EU Integrated Project Qubit Applications (IP QAP) and ACDET. W.J.W. is a Royal Society University Research Fellow, J.G.R. is supported by a Wolfson Merit award and M.H. is supported by an AXA fellowship.

References

[1] J. Fulconis, O. Alibart, W. J. Wadsworth and J. G. Rarity, "Quantum interference with photon pairs using two micro-structured fibres" *New J. Phys.* **9** 276 doi:10.1088/1367-2630/9/8/276 (2007)

[2] K. Garay-Palmett et al., "Photon pair-state preparation with tailored spectral properties by spontaneous four-wave mixing in photonic-crystal fiber" *Opt. Exp.*,**15**, Issue 22, pp. 14870 (2007)

[3] O. Cohen, J. S. Lundeen, B. J. Smith, G. Puentes, P. J. Mosley, and I. A. Walmsley, "Tailored photon-pair generation in optical fibers" *Phys. Rev. Lett*. **102**, 123603 (2009)

[4] Hong, C.K., Ou, Z.Y. and Mandel, L. "Measurement of subpicosecond time intervals between two photons by interference" Phys. Rev. Lett. **59**, 2044 (1987)

[5] M. Halder, J. G. Rarity et al. "Nonclassical 2-photon interference with separate intrinsically narrowband fibre sources" *Opt. Exp.,* **17,** Issue 6, pp.4670 (2009)

Generation of entangled photons in Bragg reflection waveguides

Martin Hendrych, Roberto León Montiel, Radek Machulka, and Juan P. Torres
ICFO – Institute of Photonic Sciences
Castelldefels (Barcelona), Spain
martin.hendrych@icfo.es

Payam Abolghasem and Amr S. Helmy
The Edward S. Rogers Sr. Department of Electrical and Computer Engineering
University of Toronto
Toronto, Canada

Abstract—**It will be shown that Bragg reflection waveguides can be used to generate entangled photons through the process of spontaneous parametric down-conversion. The design of the structure allows control of the dispersive properties of the modes that in turn control the properties of the generated photons.**

Keywords-Bragg reflection waveguides, entangled photons, spontaneous parametric down-conversion

An increasing number of quantum optics applications, ranging from quantum information processing and quantum communications to quantum metrology and quantum imaging, show enhanced capabilities when biphotons with quantum frequency correlations (entanglement) are used. A successful technological implementation of these new applications depends on the existence of efficient and robust sources that would offer a high flux of paired photons while they would allow tailoring the biphoton's quantum state for a particular application. The use of integrated structures to construct sources of entangled photons is straightforward as they greatly simplify the alignment and reduce the power requirements and costs.

It will be shown that $Al_xGa_{1-x}As$ Bragg reflection waveguides (BRW) can be employed to generate entangled photons through the nonlinear process of spontaneous parametric down-conversion (SPDC). Also, their design enables control of the bandwidth of the generated photons and, by extension, of their temporal correlations. Tailoring temporal correlations or spectral bandwidth is essential for practical purposes. Certain applications demand short correlation times such as clock synchronization and analogous quantum positioning and timing measurements. Other applications demand long temporal correlations or narrow spectral bandwidth, such as atom-photon interfaces or long-haul quantum communications.

$Al_xGa_{1-x}As$ waveguides are attractive because the current fabrication technology is mature, they have a large nonlinear coefficient, broad transparency window, large damage threshold, low linear propagation loss, and are convenient for integration [1]. They can also be monolithically integrated with a laser diode pump [2] which would eliminate the coupling difficulties. The main drawback of $Al_xGa_{1-x}As$ is its lack of natural birefringence. Birefringence is a very easy means to fulfill the phase-matching condition of the frequency-conversion process. Engineering techniques based on quasi-phase matching and artificial birefringence are widely used to achieve phase matching in III-V semiconductors.

The scheme employed here is based on Bragg reflection waveguides where exact phase matching between the frequencies involved in the nonlinear process can be achieved [3]. The properties of the generated entangled photons are given by the dispersive properties of the waveguide, including material dispersion, waveguide dispersion or a combination of both. Material dispersion is often controlled by temperature or electro-optic tuning which are in general weak in $Al_xGa_{1-x}As$. On the other hand, waveguide dispersion can significantly be controlled by a proper choice of the ridge width of the waveguide, which can easily be implemented with the help of standard lithographic techniques. The strong dependence of waveguide dispersion on the ridge width can serve to tailor the properties of the entangled photons generated using the SPDC.

In the SPDC process, a pump photon from time to time splits into two daughter photons whose energies sum up to that of the pump photon. The BRW's take advantage of the possibility of letting the pump mode propagate through Bragg reflection from periodic claddings while down-converted modes propagate by means of total internal reflection . In this way, it is possible to independently control the dispersive properties of the individual fields according to the needs of the application.

A representative ridge BRW along with typical intensity profiles of the pump and down-converted photons is schematically illustrated in Fig. 1. The periodic claddings

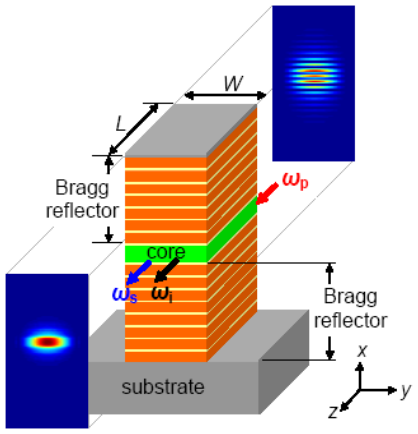


Figure 1. Schematic of a typical BRW with intensity profiles of the pump ω_p and of the downconverted photons ω_s and ω_i.

consist of 12 periods of $Al_{0.40}Ga_{0.60}As/Al_{0.90}Ga_{0.10}As$ with associated thicknesses of 89 nm/200 nm. The core is $Al_{0.65}Ga_{0.35}As$ with a thickness of 246 nm.

We assume the pump beam to be a continuous-wave source with frequency ω_p. The frequencies of the down-converted signal and idler photons are denoted as ω_s and ω_i, respectively. The two-photon state at the center of the nonlinear medium writes

$$|\Psi\rangle = \int d\omega_s d\omega_i \Phi(\omega_s,\omega_i) a_s^\dagger(\omega_s) a_i^\dagger(\omega_i) |0\rangle_s |0\rangle_i, \text{ where} \quad (1)$$

$$\Phi(\omega_s,\omega_i) = E_p(\omega_s+\omega_i)\,\mathrm{sinc}(\Delta_k L/2), \quad (2)$$

$E_p(\omega_s+\omega_i)$ is the frequency amplitude distribution of the pump beam, L is the sample length and $\Delta_k = k_p - k_s - k_i$ is the phase-mismatch function with k_j being the longitudinal component of the pump, signal and idler wavevectors, respectively.

Expanding the *k*-vectors in a Taylor series about the central wavelength, we can see the phase mismatch, and so the joint spectrum of the down-converted photons, is a function of the group velocities, group velocity dispersion and higher dispersive terms of the interacting fields. These parameters can expediently be controlled by the ridge width, $Al_xGa_{1-x}As$ composition, etch depth or the thicknesses of the Bragg layers. Only by changing the ridge width of the waveguide, it is possible to tailor the spectra of entangled photons over more than 2 orders of magnitude – from extremely broad spectra of hundreds of nanometers around the central wavelength of 1550 nm to very narrow spectra of less than 1 nm [4].

Figure 2 shows the dependencies of the phase-matching wavelength and the group velocity dispersion on the ridge width with the generated spectrum for one specific ridge width for type-I phase matching. The large bandwidth of 61 THz can be translated into a very narrow correlation time of some 15 fs.

Changing the ridge width and using type-II phase matching, a very narrow spectrum of the order of 1 nm can be obtained. On the other hand, the type-I structure used to generate the broad spectrum mentioned above can also be used to produce a narrow spectrum. It was designed to satisfy type-II phase matching as well and by only rotating the pump polarization we can reduce the spectrum from 450 nm to 5 nm.

Currently, an experiment is under way to generate down-converted photons. A single-frequency laser at 775 nm illuminates a spatial light modulator (SLM) that encodes a computer-generated hologram (CGH) to form an

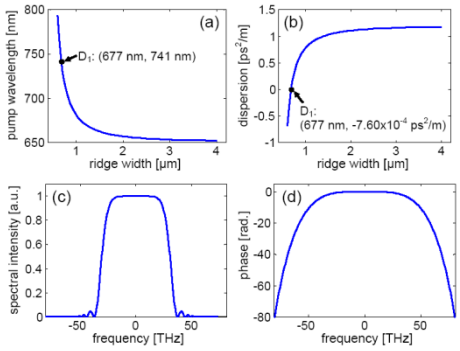


Figure 2. (a) Pump wavelength versus ridge width. (b) Signal group velocity dispersion versus ridge width. (c) Normalized joint spectral intensity $|\Phi|^2$ with a FWHM bandwidth of ~ 61 THz (~ 456 nm). (d) Phase of the spectral amplitude.

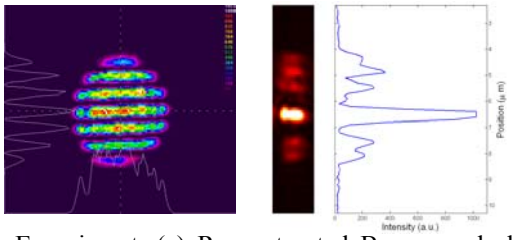


Figure 3. Experiment. (a) Reconstructed Bragg mode before the input coupling stage using an SLM. (b) Profile of the pump mode at the output facet of the waveguide along with the transverse intensity profile.

image with the form of the Bragg mode of the size of ~ 1 mm. An optical system reduces the size of this image 1000 times and couples it into the waveguide. The position and angle of the waveguide with respect to the optical setup are adjusted by piezoelectric elements. The generated photons are collected by an objective, separated by a beamsplitter and fed into a pair of InGaAs/InP avalanche photodiodes to detect coincidental counts. A picture of the Bragg mode formed in the air before the coupling stage is shown in Fig. 3(a). Figure 3(b) shows a picture of the output facet of the waveguide taken by a CCD camera with the coupled Bragg mode mixed with the fundamental Gaussian mode.

Recent success in developing an integrated edge-emitting Bragg reflection waveguide laser [2] is expected to remove the need for the preparation of the Bragg mode using the SLM, as the output mode of the Bragg laser becomes directly the input pump mode of the down-converting waveguide.

In summary, it has been shown that Bragg reflection waveguides can be used as compact, low cost and efficient source of entangled photons. By a suitable design of the structure it is possible to tailor the properties of the generated photons according to the needs of the application. Integration of the waveguide together with a Bragg reflection laser will provide a robust source of entangled photons. Currently, an experiment is under way to confirm the theoretical results.

[1] X. Caillet, V. Berger, G. Leo, and S. Ducci, "A semiconductor source of counterpropagating twin photons: a versatile device allowing the control of the two-photon state", J. Mod. Opt. **56**, 232 (2009).

[2] B. Bijlani and A. S. Helmy, "Bragg reflection waveguide diode lasers", Opt. Lett. **34**, 3734 (2009).

[3] A. S. Helmy, "Phase matching using Bragg reflection waveguides for monolithic nonlinear optics applications", Opt. Express **14**, 1243 (2006).

[4] P. Abolghasem, M. Hendrych, X. Shi, J. P. Torres, and A. S. Helmy, "Bandwidth control of paired photons generated in monolithic Bragg reflection waveguides", Opt. Lett. **34**, 2000 (2009).

Study of polymer micro-ring resonator based filter in system experiment at 10 Gbit/s

A. Maalouf[1], M. Gadonna[1], D. Bosc[2], S. Lobo[3], L. Bramerie[3]
Université européenne de Bretagne
FOTON-CCLO[1,2], et FOTON-PERSYST[3], CNRS UMR 6082
[1] Institut Télécom; Télécom Bretagne ; Brest
[2,3] ENSSAT, BP 80518, 22305 Lannion Cedex
azar.maalouf@telecom-bretagne.eu

***Abstract*—In this paper, the design and the fabrication process of a micro-ring resonator using polymer waveguides is reported. After static tests results, report on transmission test at 10 Gbit/s is given.**

Keywords: micro-ring resonator, polymer waveguides, optical filter

I. INTRODUCTION

Polymer materials, with their large available optical indexes, are potentially a basis to develop optical functions at low cost and high integration level for applications in the telecom access network. For these applications a low cost, a small footprint and flexibility are known as important issues. Other advantages of polymer materials are a good transparency at the telecom wavelengths and the ability to tune their properties by thermo-optic or electro-optic effects.

The next generation access network will use WDM technology. A tunable optical filter at the home's premises is able to provisioning the flexibility and could be an interesting alternative to AWG. The requirement for the device studied in this paper is a tunable filter on eight ITU channels at 100 GHz based on a polymer micro-ring resonator suitable for this application. Micro-ring resonators have been extensively studied for numerous applications including the filtering [1, 2]. In section II the design and the fabrication process are reported. In section III the static measurements and the dynamic response at 10 Gbit/s are presented.

II. FILTER DESIGN AND FABRICATION

A. Polymer micro-ring design

The filter structure we consider is a ring resonator coupled to two straight bus waveguides. The ring and the straight guides have the same section size. The first step is to calculate the section of the waveguide that must be a trade off between the loss in the ring, the single mode conditions and the ring/ bus waveguide coupling. Considering an index contrast of 0.15 between the core and the cladding, a square waveguide of 1.5 x 1.5 μm^2 is determined. The free scale range (FSR) of the resonator is related to the effective index and the ring round-trip length. The Full Width at Half Maximum (FWHM) is determined by the round-trip loss and the power coupling with the straight guides. The index contrast leads to a minimum radius for the ring of 100 µm to have an acceptable bend loss in the ring. In another side the bandwidth must be low enough to limit the inter-channel crosstalk. We set the objective to have a FSR of 2.04 nm and a FWHM from 0.08 nm to 0.4 nm, which lead to a ring radius of 120 µm and gaps from 0.5 to 1 µm.

B. Implementation

The core structure was performed using the polymer PVCi poly(Vinyl Cinnamate) [3] (n = 1.555 at λ = 1550 nm). This polymer was irradiated by UV for stabilization. Lower and higher claddings were made with PMATRIFE (Poly(2,2,2 MethAcrylate of TRIFluoro-Ethyle)) (n= 1.409 at λ = 1550 nm). Polymer layers were performed by spin coating. The techniques used in the process were photolithography at 365 nm and Reactive Ion Etching (RIE).

In order to improve the resolution, two masking layers were used (Fig 1). The photolithography step allows achieve photo-resist patterns. These patterns are useful for masking SiO_2 during SF_6 plasma etching. Then SiO_2 patterns serve as mask to etch polymer during O_2 plasma etching. 40 nm thickness of silica is enough to etch up to 1.5 µm of PVCi layer. In fact, effective improvement is due to the very thin photo-resist layer of 0.13 µm. This thickness can be obtained by spin-coating a commercial photo-resist under particular conditions (diluted solution) optimized in our laboratory [4].

Fig. 2 is a SEM photo of PVCi micro-ring resonator. It shows the high resolution in the definition of the gap size between the straight waveguide and the ring. The gap of fig 2 is about 0.8 µm. Finally, a layer of PMATRIFE was spin coated and then micro-ring resonators were optically characterized.

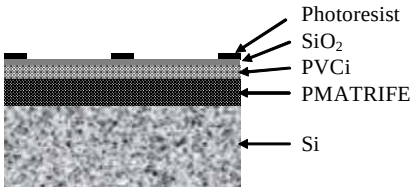


Figure 1. Representation of different layers before photolithography step

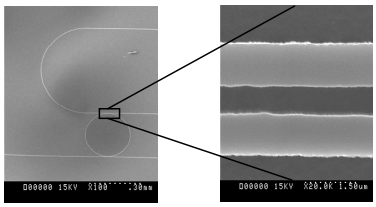


Figure 2. SEM photos of PVCi etched structure

III. RESULTS AND DISCUSSION

A. *Filter measurements*

The transmission spectra are measured by means of a tunable laser source and a power meter. The input coupling fiber has a micro-lens at the end, and the output fiber is a standard SMF. The measurements have been done on the through port and the drop port in the wavelength range 1528 – 1538 nm with a step of 2.5 pm. Fig 3 shows the drop output power for TE and TM mode for the micro-resonator with a ring diameter of 120 µm and a gap of 0.8 µm To resolve more precisely the resonant peak and the bandwidth the filter has also been measured with a step of 1 pm (Fig 4).

The mean FSR is 2.01 nm, the shift of resonant wavelength for TE and TM is around 0.7 nm. The extinction ratio is about 20 dB and the FWHM is 0.12 nm (15 GHz). The finesse (FSR/FWHM) of the filter reaches 17 and the quality factor about 12,000. These results are in good agreement with the theory.

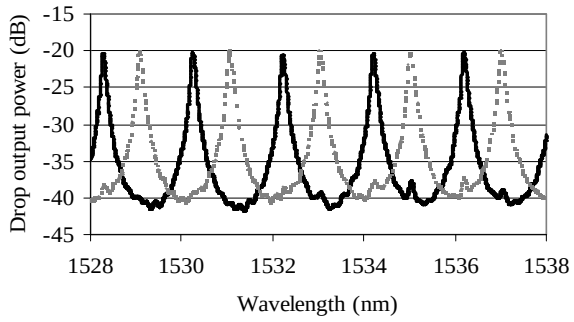


Figure 3. Drop output power with 2.5 nm step wavelength (TE / TM)

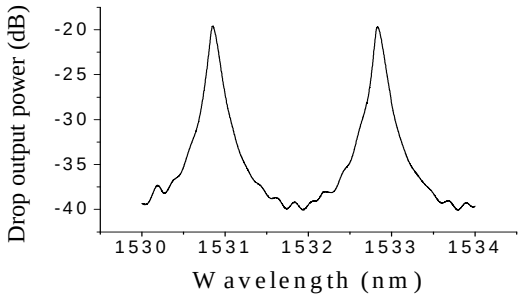


Figure 4. Drop output power with 1 nm step wavelength

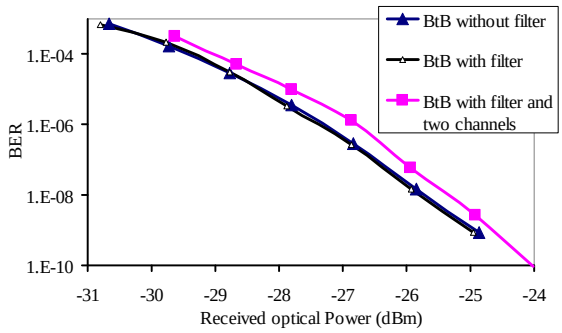


Figure 5. Experimental results at 10 Gbit/s

B. *Experimental results at 10 Gbit/s*

The precedent structure has been tested in system experiment. The transmitter (Tx) produces an NRZ optical signal modulated at 10 Gbit/s with a 2^{31}-1 bits PRBS at 1550.5 nm. To align the resonant wavelength of the filter with the transmitter wavelength, the temperature of the device is controlled by a thermo-electric cooler. The dependence of the resonant wavelength of the resonator with the used polymers has been measured at 0.11 nm/K. At the reception, the signal is directly detected by an avalanche photodiode (APD) having 10 GHz bandwidth.

Fig 5 shows there is no penalty for the Bit Error rate (BER) measured in back to back configuration (BtB) with and without the filter. Next, a second wavelength emitter corresponding to the adjacent channel of the 100 GHz ITU grid (1549.7 nm) is inserted in the line test to characterize crosstalk channel. With this neighbor channel a penalty of 0.5 dB has been measured.

IV. CONCLUSIONS

We have described the design and the fabrication process of a polymer micro-ring filter. In this paper, the emphasis is on the experimental results in system at 10 Gbit/s which show that the filter bandwidth is enough for this rate.

ACKNOWLEDGMENT

Authors acknowledge support from ANR and Pôle Images@réseaux in the project SELECTACESS and the Regional project, PONANT including FEDER funds.

REFERENCES

[1] S. Yamagata, Y. Yanagase, Y. Kokubun, “Wide range tunable microring resonator filter by thermo-optic effect in polymer waveguide”, Japanese Journal of Applied Physics, vol 43, N° 8B, 2004, pp 5766-5770

[2] A. Maalouf, D. Bosc, P.Grosso, M.Gadonna, M. Thual, F. Henrio, S. Haesaaert, “Wide tunable thermo-optical filters with polymer micro-ring resonators”, proceedings of SPIE “Silicon Photonics and Photonic Integrated Circuits”, vol. 6996, 69991S, may 2008.

[3] I. Assaïd, D. Bosc, I. Hardy, “Improvements of the Poly(vinyl cinnamate) photo-response in order to induce high refractive index variation”, Journal of Physical Chemistry B, vol.108, 2004, pp. 2801-2806.

[4] A. Maalouf, M Gadonna, D Bosc, “An improvement in standard photolithography resolution based on Kirchhoff diffraction studies”, Journal of Physics D, vol. 42, n° 1, 2009, 015106.

POLINA

Polymer Light Waveguides for Nanophotonics

Manufacturing Process and Refractive Index Profile Analysis

Uwe Hollenbach[1], Hans-J. Boehm[1], Jürgen Mohr[1], Heinrich Sieber[1], Jürg Leuthold[2], Nicole Lindenmann[2]
Karlsruhe Institute of Technology (KIT)
[1]Institute of Microstructure Technology (IMT)
[2]Institute of Photonics and Quantumelectronics (IPQ)
Karlruhe, Germany
uwe.hollenbach@kit.edu

Ute Ostrzinski, Karl Pfeiffer
Micro Resist Technology (MRT)
Berlin, Germany
k.pfeiffer@microresist.de

***Abstract*— We report a novel manufacturing method to imprint buried SM waveguides by UV lithography in polymer. The method is suitable for different multilayer structuring for all optical or opto – fluid layers. The optical layer bases on a doped polymer and is specified by high temperature stability, chemical resistance and low fluid absorption properties.**

Single mode waveguides, Integrated Optics, Nanophotonics, Polytronics

I. INTRODUCTION

Imprinting waveguides in PMMA using a DUV photolithographic mask process [1] results in asymmetrical single modes (SM) and some defects in the far field are on a high order of mismatch compared to standard SM fibers. Therefore, higher insertion loss and also modal birefringence caused by strain and stress can be found [2]. In addition, standard multimode (MM) waveguides can not be realized in PMMA by the lithography technique due to a penetration limit for the DUV light.

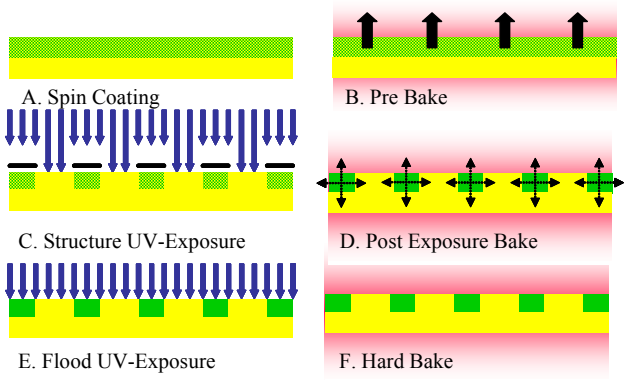


Figure 1. Schematical drawing of the main manufacturing steps.

Other different optical polymers for MM application structured as 3D rib or groove waveguides must be over covered or filled with a second polymer to build buried waveguides and can not really be used for SM waveguide production because the structure molding and/or embossing quality is limited for the small core geometry and the side wall roughness. Consequently we have been discussing to solve these problems by taking a novel chemical approach for a two component polymer based on SU 8 (Epon® oligomer). Different approaches are tested to decide on the two materials with different refractive index and the possibility for its easy adjustment by the process parameters.

II. MANUFACTURING PROCESS

The manufacturing process can be described on six main steps: A. Spin Coating, B. Pre Bake (PB), C. Structure UV-Exposure, D. Poste Exposure Bake (PEB), E. Flood UV-Exposure, F. Hard Bake (HB).

A. The epoxy based doped material (NAM) is applied to a 4 inch silicon wafer by a conventinal spin coating process. We build first a passive layer - the under cladding- which is understood as the substrate under the wave guide (WG) cores. It has a thickness of app. 20 µm. The second process step builds on the optical NAM- layer and the spin coating parameters in speed and time are optimized to get the necessary and adjusted core thickness. After finishing the following process steps, for a first order application as a mono layer WG a passivation layer – the over cladding – covers the WG cores and protects them from most influences of the environment. Especially we like to use the same NAM mixed polymer for all cover layers to realize a whole homogeneous cladding to get buried WG cores. The process technique can be seen as a unique feature for this type of WG fabrication.

B. The PB process step is variable in temperature over time. This is one parameter for refractive index tuning which is easy to handle within a range below 100 °C. The tuning works as an out diffusion process for the dopant monomer over the whole layer thickness evaporating through the surface into the air and resulting in a concentration C_x. This

Sponsored by the Government of Germany BMWi-AIF (ZIM)
KF 2308201MF9

tuning process defines the index step betwenn the cladding around the later fabricated WG cores and should be app. Δn ~ 0.0035…0.0050 for SM applications.

C. The first UV- exposure causes a photo chemical reaction in NAM because it contains also a standard PAG (photo acid generator) mobilizing H^+- ions if UV light is absorbed in the NAM layer. The H^+- ions crack the end groups of the polymer rings of the SU 8 oligomer and start the polymer network linking.

D. The dopant monomer, still available in a concentration of C_x is build in into the polymer network while the cross-linking process is running. The more the monomer groups are covalently linked the lower the value of the refractive index of the UV irradiated part forming the cladding layer. Furthermore the concentration of moveable monomers decreases over time in this part. This generates a concentration gradient from the none-exposed part, forming later the core volume, to the direction of the cladding. As long as the process temperature in the PEB is held on a high level the dopant can diffuse out. Some diffuses out into the direction of the substrate and some leaves the core volume into the direction of air via the surface.

E. In the first UV- exposure the volume forming the core structures has not been illuminated. Therefore, in general, no H^+ ions from the PAG have been activated in the core volume and this part is not cross-linked yet. The flood exposure assures an activation of the H^+ ions and starts the network linking also in the core volume.

F. Finally to stabilize the network linking process for the first optical WG layer a last bake is necessary. The temperature is much higher than that of the PB and the PEB, aiming for very high temperature stability. The softening point is shifted to T_g ~ 230 °C which is nearly the same as for a pure SU 8 polymer.

III. Refractive Index Profile Characterisation

Full information about the refractive index distribution around the WG cores is very important before using BPM simulations [4] and designing more functional structures (e.g. coupling devices). Therefore we measured all refractive index profiles depending on the structure mask widths by the RNF (refractive near field) method. The measurement system we used was developed by RINCK Electronik, Jena (step size 0.1 µm, spot size ~0.5 µm @ 671 nm, index res. 0.0001, scan area up to 400 µm x 400 µm).

The WG cores were varied by using different nominal mask structure widths of 2.0 µm ≤ w ≤ 9.4 µm. Fig. 2a) shows exemplary a measured index distribution of one SM core WG in NAM designed for visible light application around 600 nm. The used nominal mask width is about w = 3.8 µm. Fig. 2b) gives three data read outs along the horizontal line scan across different cores with a nominal mask width of w = 3 / 6 / 9 µm. The horizontal scan across the core section has a gradual function and decreases from the core center in the direction of the substrate. Its function looks fully symmetrical. The vertical scan across the layer thickness has nearly a step function as assumed in a spin coated layer.

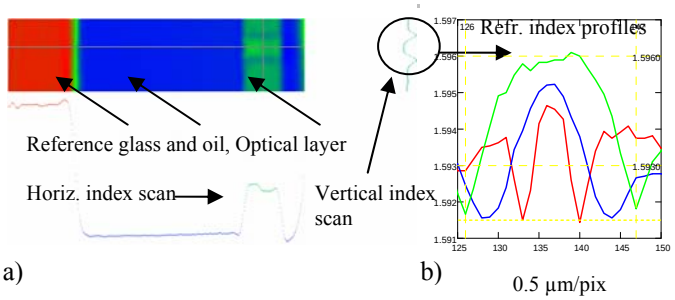


Figure 2. a) Measured refractive index scanning area on a SM WG core end face by the RNF method. b) Horizotal refr. index distribution cross over the center of SM WG cores of different mask widthes w = 3 / 6 / 9 µm

IV. Summary

We demonstrate a single material process for fabrication of embedded SM waveguides in a cladding layer with defined thickness. The used novel photo sensitive polymer mix bases on the negative resist SU 8. The mixture (C_{1-x} + C_x) of the host – guest system named NAM is variable in the concentration ratio and can be adjusted via a temperature process. Because the refractive index of the guest monomer is significantly lower than the host index of SU 8 the index of NAM can be tuned always below the refractive index of the pure SU 8. Generally a diffusion process is used for the description of an index step adjustment by UV exposure and temperature treatment. The manufacturing process technique can be used for both SM and MM waveguides. The core profiling referenced on different standard fibers for the visible and the near infrared range of wavelengths depends on the requested application in the fields of data communications. The lithographic imprinting into the used NAM polymer shows significant better mode guiding behaviors which have nearly exact Gauss symmetry. Furthermore, mode distribution analysis comes up with excellent mode field diameters (MFD) [3]. The numerical aperture (NA) referenced on standard SM fibers was measured by FFP analysis and matches well. An extensive RNF analysis shows nearly a step index profile in the vertical direction of the layer thickness and a fully symmetrical gradually growing core index from out side the substrate in the direction of the core center.

References

[1] U. Hollenbach, H.-J. Boehm, J. Mohr, D. Ross, D. Samiec, "UV Light Induced Single Mode Waveguides in Polymer for Visible Range Application", Pric. Of European Conf. on Integrated Optics (ECIO), Paper THD3, Copenhagen, Denmark, April 25-27, 2007.

[2] G. Golojuch, U. Hollenbach, T. Mappes, J. Mohr, A. Urbanczyk, W. Urbanczyk, "Investigation of birefringence in PMMA channel waveguides inscribed with DUV radiation". Measurement Science and Technology, Vol. 19, pp. 025304/1-6, 2008.

[3] H. Sieber, H.-J. Boehm, J. Mohr, U. Hollenbach, J. Leuthold, N. Lindenmann, „Polymer Light Waveguides for Nanophotonics; Near Field Intensity Distribution Analysis", to be published.

[4] U. Hollenbach, H.-J. Boehm, J. Mohr, H. Sieber, J. Leuthold, N. Lindenmann, „Polymer Light Waveguides for Nanophotonics; Comparison Between Theoretical and Experimental Results", to be published.

First developments of sub-micronic waveguide structures on UV210 polymer

D. Duval, C. Godet, N. Huby and B. Bêche
Institute of Physics
UMR CNRS 6251
Rennes, France
daphne.duval@univ-rennes1.fr

H. Lhermite
Institute of Electronics and Telecommunications
UMR CNRS 6164
Rennes, France

***Abstract*— First developments of sub-micronic waveguide structures on UV210 polymer are presented. The UV210 refractive index increases with exposure to DUV light ($\Delta n=2.10^{-2}$). Propagation losses are performed by a cut-back method in single-mode UV210 waveguides: values as low as 3.4 and 6.2 dB/cm are obtained for, respectively, TE_{00} and TM_{00} polarizations.**

Integrated optics; polymer rib waveguides; UV210 photo-resist; DUV lithography

I. INTRODUCTION

Over the last decades the use of polymers in integrated optics has been widely developed for the fabrication of low-cost devices such as sensors or optical telecommunication systems [1, 2]. However, as most photo-resists require classical lithographic processes within a 365 nm exposure wavelength, the resolution can be hardly better than 1 µm. Higher resolution can be obtained by using deep ultraviolet (DUV) lithography [3] on photo-resists such as the UV210 polymer. Moreover, exposure to DUV light can cause a variation of the refractive index of some polymers [4]. The interest of the UV210 resist has already been demonstrated in micro- / nano-electronic applications [5] but any use for photonic applications has been reported yet. The goal of this paper is to demonstrate the interest of the UV210 photo-resist for applications in integrated optics. At first, the study of the influence of DUV irradiation dose on the refractive index of the UV210 film is leaded by spectroscopic ellipsometry. Then, the photonic structure fabrication is described. Finally, optical losses at λ = 980 nm are measured for both TE_{00} and TM_{00} polarizations.

II. PHOTO-INDUCED INDEX VARIATION IN UV210 FILMS

In order to study the variation of the UV210 refractive index as a function of the DUV irradiation dose, ellipsometric measurements (*Jobin Yvon-Horiba*) were carried out on as deposited UV210 film and on UV210 films exposed to DUV energy doses ranging from E = 20 mJ/cm^2 to E = 30 J/cm^2. The ellipsometric parameter $\rho = \tan(\psi).\exp(j\Delta)$ is inferred from the conventional ellipsometric angles ψ and Δ. The refractive index n of the UV210 film, spin-coated on silicon wafer, is obtained from a 3-layer model (Si-UV210-air) using an absorbing Cauchy dispersion law. As a result, n at λ = 980 nm is plotted as a function of the DUV irradiation doses on Fig. 1. Such as deposited UV210 film (E = 0 J/cm^2) has a refractive index of 1.565 at 980 nm. This value increases with the irradiation dose: for an exposure of 15 J/cm^2, we measure an enhancement of 2.10^{-2} in the refractive index value. For higher irradiation doses, the refractive index appears to remain constant. Thus, the following study will be limited to irradiation doses ranging from 20 mJ/cm^2 to 15 J/cm^2.

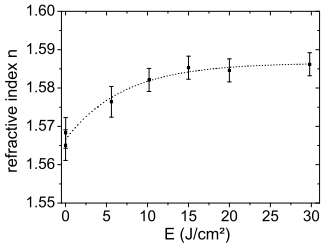


Figure 1. Refractive index values at λ = 980 nm as a function of DUV irradiation doses.

III. FABRICATION PROCESSES

The UV210 being a positive photo-resist, the UV-exposed part of the resist is dissolved during the development step. Thus, two different optical microstructures have been realized: structures of family 1 consist of as deposited UV210 waveguides while for family 2, UV210 waveguides have been exposed to DUV light after the development step in order to study the influence of DUV-induced modifications on the polymer optical properties. Both families consist of UV210 rib waveguides on a (1 0 0) silicon substrate. A SiO_2 layer is first obtained by thermal oxidation of the silicon wafer yielding a 1.2 µm-thick layer (n_{SiO2}=1.45 at 980 nm). Then, the UV210 film (*Rohm and Haas*) is deposited by spin-coating leading to 1 µm-thick film, followed by a softbake step to remove the solvent. By way of DUV-lithography (20 mJ/cm^2 at λ_{DUV} = 248 nm), the waveguide pattern defined on a quartz/chromium mask is transferred onto the UV210 guiding layer and followed by a post-exposure bake to cross-link the polymer. Then a development process with a basic developer is necessary to obtain the rib waveguides. The optical structures of family 2 are re-exposed to the DUV light source: four samples have been made with post-development irradiation doses of 0.02, 5, 10 and 15 J/cm^2. Finally, an annealing is carried out for both family structures to stabilize the UV210 material. As a result, scanning electron micrographs (SEM) of 400 nm- and 4 µm-width rib waveguides of family 1 before the annealing step are presented on Fig. 2. These pictures highlight the utilization of an appropriate set of development

This work was supported by Rennes Métropole, Région Bretagne, CNRS and ANR-08-JCJC-0136-01 programs.

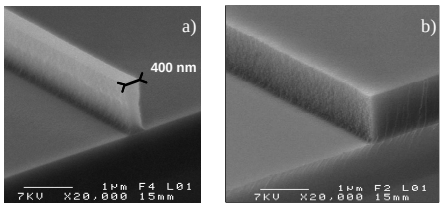


Figure 2. SEM view of rib waveguides of family 1 before the annealing step: a) 400 nm- and b) 4 µm- widths.

parameters: waveguides present low surface roughness and vertical sidewalls, which is important for the achievement of efficient light confinement.

IV. INTEGRATED OPTICAL CHARACTERIZATION AND DISCUSSIONS

A specific optical coupling set up has been developed to characterize optical losses in such UV210 waveguides by using the cut-back method. A laser source operating at λ=980 nm with an enhanced control in temperature is used for the optical injection. The output signal, after propagation through the sample, is monitored with a camera (*Pulmix*) and an optical powermeter (*Ophir* – PD300). First, the detected output optical field characterizes a single-mode propagation with a suitable optical confinement in the core region. The cut-back method is based on the relative measurement of output optical power for different lengths of waveguides that can be expressed as

$$10\log\left(P_{L_1}^{TE-TM} \Big/ P_{L_2}^{TE-TM}\right) = -\alpha^{TE-TM}\Delta L \qquad (1)$$

with, $\Delta L = (L_1 - L_2)$ the distance between two respective output cleaved faces, P_{L_1,L_2}^{TE-TM} the optical power measured after propagation at lengths L_1 and L_2 for the TE_{00} and TM_{00} optical modes and α^{TE-TM} the optical propagation losses in dB/cm for each polarization. With this method, optical losses have been evaluated on five rib waveguides (4µm-width and 1µm-height): one of family 1 and four of family 2 (irradiation doses: 0.02, 5, 10 and 15 J/cm^2). As an example, for one sample of family 2 with an irradiation dose of 0.02 J/cm^2, the exit power P has been assessed for four stabilized laser operating currents I and five waveguide lengths (L_1 to L_5), always into a fixed waveguide structure and with the same input cleaved face in order to cancel the variation of injection coupling losses. Considering (1), the quantity $10\log\left(P_{L_5}^{TE-TM} \Big/ P_{L_i}^{TE-TM}\right)$ has been plotted as a function of $(L_i - L_5)$ for TE_{00} mode (Fig. 3a) with L_5 the shortest length and L_i the five studied lengths (i=1 to 5). Then, by fitting the experimental points, we obtain four straight lines, one for each laser operating current. Since such lines almost overlaid, we conclude that propagation losses, obtained from the slopes, are independent of the laser current. Thus, for a 0.02 J/cm^2 irradiated UV210 waveguide, optical losses have been evaluated as 4.0 ± 0.2 dB/cm for TE_{00} polarization and, with the same method, as 7.0 ± 0.2 dB/cm for TM_{00} polarization. The methodology described previously has been applied to all

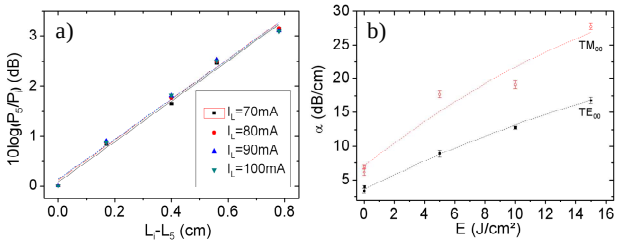


Figure 3. a) $10\log\left(P_{L_5}^{TE} \Big/ P_{L_i}^{TE}\right)$ vs. $(L_i - L_5)$ measured on a specific 0.02 J/cm^2 irradiated rib waveguide for TE_{00} mode. b) Propagation losses vs. irradiation dose for both polarizations.

the other samples. For both TE_{00} and TM_{00} modes, Fig. 3b shows the relationship between average propagation losses and irradiation doses. This highlights the increase of propagation losses with the irradiation dose: α^{TE} ranges from 3.4 ± 0.4 dB/cm for an as deposited waveguide to 16.8 ± 0.5 dB/cm for a 15 J/cm^2 irradiated waveguide. In the same way, α^{TM} ranges from 6.2 ± 0.5 dB/cm to 27.7 ± 0.5 dB/cm. This enhancement can be due to the new chemical species produced during DUV-induced transformations, leading to higher absorption at 980 nm.

V. CONCLUSION

The realization of sub-micronic rib waveguides has been validated by DUV lithography thanks to the UV210 photo-resist. First, this work presents ellipsometric measurements highlighting the refractive index variation as a function of DUV exposure doses on an UV210 film. A large index contrast up to 2.10^{-2} can be achieved between areas either irradiated or unexposed. So as to measure optical losses with the cut-back method, we have realized relevant single-mode TE_{00} and TM_{00} rib waveguides based on UV210 polymer with proper confinement of the optical modes. As a result, unexposed UV210 rib waveguides feature propagation losses α^{TE} = 3.4 ± 0.4 dB/cm and α^{TM} = 6.2 ± 0.5 dB/cm regarding both polarizations. Such properties prove that this photo-resist comes up as a promising material for the realization of sub-wavelength structures in integrated optics. Further works are under investigation to understand and reduce such an increase of optical losses in post-development irradiated waveguides in order to enhance the UV210 optical properties.

REFERENCES

[1] J. S. Kim, J.W. Kang and J. J. Kim, "Simple and low cost fabrication of thermally stable polymeric multimode waveguides using a UV-curable epoxy," Jpn. J. Appl. Phys., vol. 42, pp. 1277–1279, 2003.

[2] B. Bêche, N. Pelletier, E. Gaviot and J. Zyss, "Single-mode TE_{00}-TM_{00} optical waveguides on SU-8 polymer," Opt. Commun., vol. 230, pp. 91–94, 2004.

[3] P. B. Sahoo, R. Vyas, M. Wadhwa and S. Verma, "Progress in deep-UV photoresists," Bull. Mater. Sci., vol. 25, pp. 553–556, 2002.

[4] W. J. Tomlinson, I. P. Kaminow, E. A. Chandross, R.L.Fork and W. T.Silfvast, "Photoinduced refractive index increase in poly(methylmethacrylate) and its applications," Appl. Phys. Lett., vol. 16, pp. 486–489, 1970.

[5] S. Jagar et al., "A FinFET and Tri-gate MOSFET's channel structure patterning and its influence on the device performance," Thin Solid Films, vol. 462, pp. 1–5, 2004.

Microfluidic Multimode Interference Device

C. Holmes, L.G. Carpenter, H.C. Hunt, J.C. Gates, P.G.R. Smith
Optoelectronics Research Centre
University of Southampton
Southampton
chh@orc.soton.ac.uk

***Abstract*—A multimode interference device has been fabricated using a novel ultra-precision micromachining technique. The micromachining technique defines the interfaces of the device by cutting microfluidic channels into a silica-on-silicon substrate. Changing the refractive index of fluid within these microfluidic channels is shown to alter the optical characteristics of the device.**

Keywords- MMI; microfluidics; micromaching; silica-on-silicon

I. INTRODUCTION

Multimode interference (MMI) devices have many applications in photonic integrated circuits such as optical power splitting, switching and demultiplexing [1]. They typically exhibit a simple structure, with low loss, a compact size, polarization insensitivity, low cross talk and a good fabrication tolerance.

The use of etched trenches to define MMI interfaces has previously been suggested as a design improvement for platforms with associated low index contrast, such as silica-on-silicon [2]. Trenches can act to improve optical confinement, thus enhancing image quality and device performance. Trenches can also have the advantages of reduced heat dissipation, thermal cross talk [3], bend loss [4] and stress birefringence [5]. In this work the concept of using trenches is extended to form microfluidic channels.

Microfluidics allows the manipulation of small volumes, with precise dynamic control [6]. Interfaced with integrated optics the possibilities of device design can enhance microanalysis, including optical trapping and separation, monolithic integration of lasers and optical detection, all of which has been recently reviewed [7].

The presented work highlights a novel way of fabricating MMI components using a computer controlled ultra-precision micromachining process, illustrated in Figure 1. The sawing process is similar to that used in the microelectronics industry and is capable of fabricating ridges, trenches and V-grooves. Trenches of 10 µm can be defined with typical side wall roughness Ra value of 9 nm. The technique gives the freedom from expense and time investment associated with photolithography and etching, whilst allowing rapid prototyping, design flexibility and the potential of three-dimension structure fabrication.

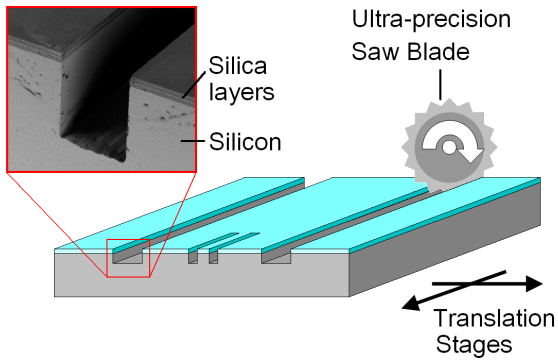


Figure 1. A conceptual illustration depicting multimode inteference device fabrication through ultra-precision micromachining

If the side walls of the MMI device are defined by microfluidic channels the device's optical characteristics can be changed by simply replacing the fluid in the microfluidic channel with another. Changing the refractive index of a fluid will alter the Goos-Hänchen shift associated with the device and thus alter its effective width [8]. This phenomenon is illustrated in Figure 2 (a) and (b), which show simulations of the novel MMI construction in silica-on-silicon, with an index of 1.3 and 1.44 in the microfluidic channels respectively. Over identical lengths the image shifts from a 1x3 fold image to a 1x4 fold image.

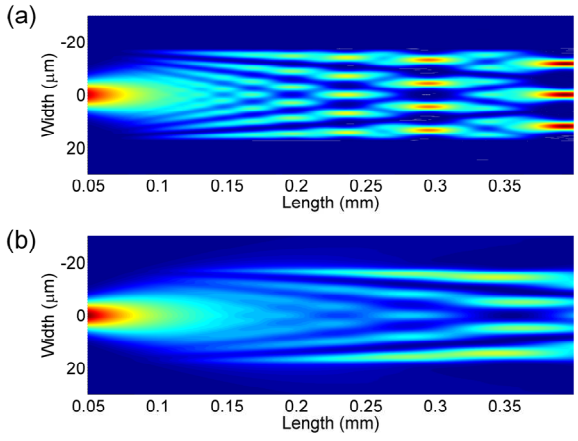


Figure 2. A beam propagation simulation of a multimode inteference device with microfluidic sidewalls, depicting a fluid of refractive index (a) 1.3 and (b) 1.44 in the microfluidic channels

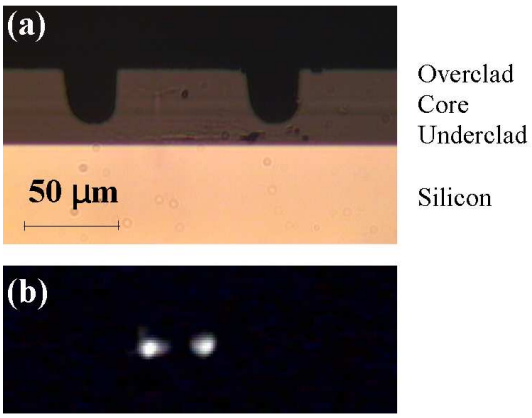


Figure 3. An endface of the fabricated device as viewed by (a) a light-microscope and (b) an IR-CCD camera with 1550 nm launch

II. FABRICATION

The reported device has been micromachined from a silica-on-silicon composite, fabricated using flame hydrolysis deposition. The composite consists of three silica layers, an underclad, a core layer and an overclad, as shown in Figure 3. To ensure lateral single mode operation the 5 µm thick central core layer was doped with germanium such to achieve a higher index than the surrounding cladding layers. For this first proof-of-principle device two trenches were micromachined into the silica using a 30 µm width saw blade, pictured in Figure 3 (a). Light was launched into the device via a single mode direct UV written channel [9]. The resulting MMI device had a width of 72 µm a length of 2.46 mm and had an antisymmetric launch offset of 7 µm. To assist characterization of the fabricated device the end face was polished.

III. RESULTS

Launching 1550 nm TE light into the fabricated MMI device resulted in an antisymmetric image as the input launch was antisymmetric. The image observed from an IR-CCD camera is shown in Figure 3 (b). The resulting mode profile was characterized by scanning an optical fiber mounted upon a translation stage along the output facet of the device and monitoring the coupled power. The input power was set to 6.3 mW and the positional error of the translation stage was approximated to be 0.5 µm. Figure 4 compares the empirical data collected with respect to simulated data for such a device. The simulation is computed using a fast Fourier transform beam propagation method. The end face power is convoluted with a Gaussian profile comparable to that of the fiber optic used to collect the empirical data.

The empirical data shows significant correspondence to the simulated data. For both an air clad and an index of 1.44 in the micromachined trenches.

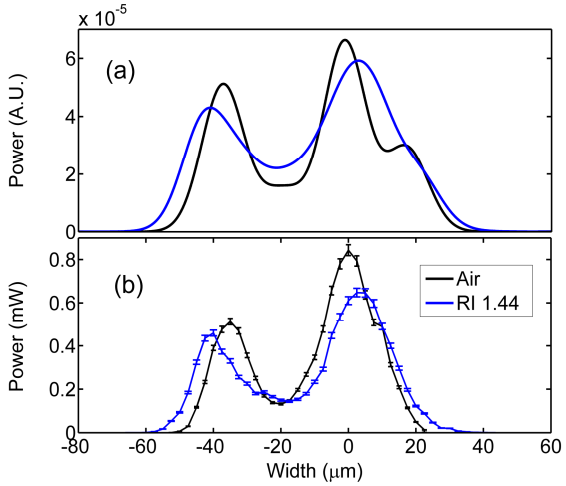


Figure 4. Characterisation of the output face of the fabricated MMI device interpreted through (a) simulation and (b) empirical measurements

IV. CONCLUSIONS

A novel ultra-precision micromachining technique for fabricating multimode interference devices has been reported. Through exploiting the fabricated trenches as microfluidic channels the optical characteristics of the device can be manipulated.

The work shall report upon micromachined MMI devices and the considerations required for optimizing optical surface quality, including insertion loss measurements and minimum achievable feature size. MMI architectures which utilize microfluidic properties shall also be explored, including optical trapping and separation, monolithic integration of lasers and optical detection.

REFERENCES

[1] P.A. Besse et al, “Optical Bandwidth and Fabrication Tolerances of Multimode Interference Couplers”, J. Lightwave Tech., vol. 12, issue 6, June 1994, pp. 1004-1009.

[2] C.J Kaalund, Z. Jin, “Novel multimode inteference devices for low index contrast materials systems featuring deeply etched air trenches”, Optics Communications, vol. 250, issue 4-6, February 2005, pp. 292-296

[3] J. Hong, J. Kim, S. Lee, “Low-power thermo-optic silica-on-silicon MZI switch using multimode interference couplers”, Proc. SPIE vol. 4654, March 2002, pp. 157-163

[4] J. Cardenas, L. Li, S. Kim, G.P. Nordin, “Compact low loss single air interface bends in polymer waveguides“ Optical Express, vol. 12, issue. 22, October 2004 pp. 5314-5324

[5] C. Nadler, M. Lanker, E. Wildermuth, W. Hunziker, H. Melkchior, “Polarization insensitive wavelength multiplexers using stress release grooves “, Proc. ECOC’98, September 1998, pp. 129-130

[6] G.M. Whitesides, “The origins and future of microfluidics”, Nature, vol. 442, July 2007, pp.368-373

[7] H.C. Hunt J.S. Wilkinson, “Optofluidic integration for microanalysis”, Microfluid Nanofluid, vol. 4, September 2007, pp. 53-79

[8] K. Okamoto, Fundamentals of Optical Waveguides, 2nd ed., Elsevier, 2006

[9] M Svalgaard, M Kristensen, “Directly UV written silica-on-silicon planar waveguides with low loss”, Elec. Let., vol. 33, issue 10, May 1997, pp. 861-862

Integrated planar Bragg grating oxygen sensor

D.J. Wales, R.M. Parker, J.C. Gates, M.C. Grossel, P.G.R. Smith
Optoelectronics Research Centre & School of Chemistry
University of Southampton
Southampton, U.K.
dw405@soton.ac.uk

Abstract— **We demonstrate an integrated planar Bragg grating sensor for the detection of oxygen by modification of the surface with a silica sol–gel containing immobilized methylene blue.**

Keywords: oxygen sensing; Bragg gratings; evanescent field; methylene blue; silica sol–gel.

I. INTRODUCTION

The detection of oxygen is required in a diverse set of scientific fields. We shall present a planar integrated Bragg grating sensor with a chemically modified overclad for the detection of oxygen in gaseous or liquid environments.

A. Oxygen sensing

Quantitative and qualitative oxygen sensing is required for the understanding of many chemical processes across a diverse set of fields including medicine, environmental science and chemical synthesis. For example, in zymology, quantitative oxygen sensing is required to determine and understand the enzyme kinetics of particular fermentation processes [1].

Typically oxygen sensing, in the liquid phase, can be achieved through the use of modified Clark electrodes [2]. However, there are many limitations associated with the Clark electrode including long – term sensitivity, as the active electrolyte within the probe is consumed over time, and potential electrical interference issues [2]. Furthermore, interrogation is unsuitable in flammable environments.

Optical fiber and integrated optics chemical sensors overcome these limitations of electrical signal based sensing methods because optical fibers are relatively inert to environmental noise and no spark risk.

B. Bragg grating chemical sensors

It has been previously shown that an optical waveguide containing a Bragg grating is an effective method of detecting minute changes in refractive index [3]. Removal of the part of the waveguide's clad allows the evanescent field of the optical mode to interact with an analyte.

The device works by detecting the associated effective index change when the analyte medium is altered. The change in effective index across the Bragg grating causes a shift in the Bragg wavelength of the grating. The relationship between effective index, n_{eff}, and Bragg wavelength, λ_B is shown in Equation (1),

$$\lambda_B = 2\, n_{eff} \Lambda \qquad (1)$$

where Λ is the period of the Bragg grating. For a silica waveguide with a Bragg grating in the telecoms region, Λ is ~ 530 nm.

II. FABRICATION OF PLANAR BRAGG GRATING SENSORS

The waveguides are fabricated in flame hydrolysis deposited layers of silica. Doping of the core layer allows a channel waveguide to be defined using a process known as Direct Grating Writing is a UV laser technique that allows simultaneous definition of channel waveguide and Bragg grating. This system differs from conventional direct writing by using an interferometer to generate a ~6 micron spot with a periodic interference pattern. Precise temporal modulation of the UV beam results in the generation of a periodic refractive index with the waveguide. Reference [4] provides a thorough review on the fabrication and development of planar Bragg grating sensors.

An aqueous solution of hydrofluoric acid is used to etch a "window" into the overclad (see Figure 1) and thus exposing the Bragg grating to the surrounding environment [3]. In addition, a ~ 50 nm thick layer of tantalum pentoxide is sputtered on to the exposed Bragg grating. The thin layer of higher refractive index tantalum pentoxide (relative to silica) "pulls" the evanescent wave of the mode into the analyte medium and thus increases the sensitivity of the device [3].

The Planar Bragg grating devices are "pigtailed" to polarizing maintaining fiber and typically interrogated using a broad band optical source and an optical spectrum analyzer.

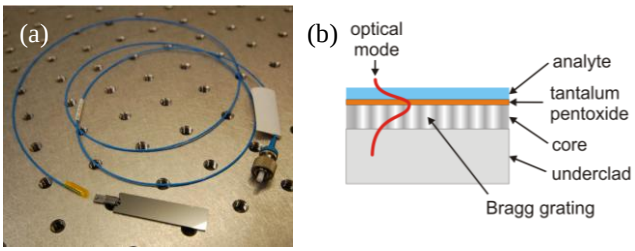


Figure 1. (a) Photograph of a pigtailed etched Bragg grating device (b) Schematic of a chemical sensing integrated planar Bragg grating waveguide

III. INTEGRATED BRAGG GRATING OXYGEN SENSOR

Cao *et al.* has previously demonstrated an optical fiber based oxygen sensor incorporating methylene blue (MB) in a silica sol – gel [5]. It was shown that the absorption spectra of an evanescent field changed relative to the concentration of oxygen passed over the fiber. Therefore it was proposed that a

We would like to thank the EPSRC for funding this research

planar integrated Bragg grating could be used to interrogate MB in a similar way. Replacement of the overclad layer above the Bragg grating with a silica sol–gel, containing immobilized MB, could be used as oxygen sensor in gaseous and liquid phases. This device differs from Cao's system as it detects the change in refractive index of MB.

A. Methylene blue

MB is an organic dye that forms intense blue colored solutions. Amongst other uses, MB is the main reagent of the notable "blue bottle" experiment in chemistry; the oscillating reaction between methylene blue and its reduced form, *leuco*-methylene blue (LMB) [6]. The oxidation of LMB to MB, due to ambient oxygen present, exhibits an explicit color change from colorless to blue, as shown in Figure 2.

B. Silica sol- gels

The photochemistry of MB in a silica sol-gel matrix has been investigated [7]. Silica sol-gels are inorganic materials that consist of a porous silica matrix [8]. Thin glass films of silica sol-gel can be formed through conversion of the initial colloidal suspension of silica, known as a sol, into thin layers of a viscous silica gel by spin or dip-coating. Additional heat treatment promotes further densification into solid materials [8]. Examples of these silica sol-gel thin glass films have been used in optical applications.

IV. PRELIMINARY RESULTS

It was believed that the significant color change upon oxidation of an aqueous solution of LMB to MB would have an associated change in refractive index, detectable by a Bragg grating sensor. The sensor consisted of four Bragg gratings, three etched sensor gratings and one buried reference grating.

A blue colored aqueous solution of MB (of concentration $3x10^{-4}$ mol/L) was reduced to colorless LMB in a nitrogen environment. An exposed planar Bragg grating device was immersed in this stirred solution and before exposing to a restricted flow of air. Gradual color change from colorless to blue was observed, suggesting that LMB was oxidized to MB, confirmed by UV-visible spectroscopy. The average Bragg wavelength shift monitored on oxidation is shown in Figure 3.

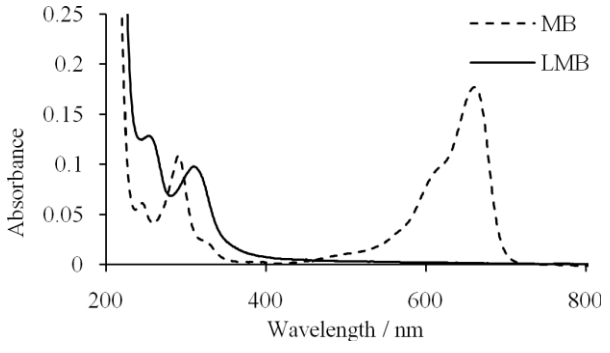


Figure 2. UV-visble spectra comparing methylene blue and leuco-methylene blue showing the loss of the absorption peak at ~660 nm.

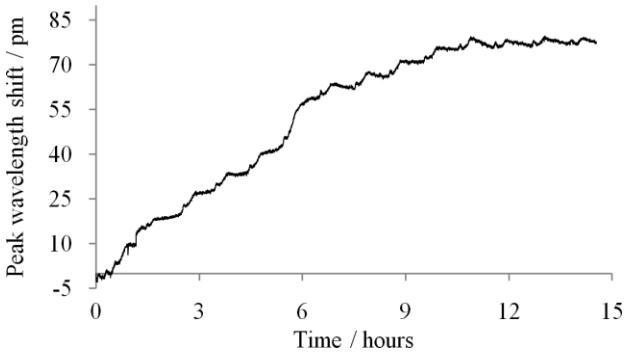


Figure 3. A shift of ~80 pm in Bragg wavelength during the oxidation of aqueous *leuco*-methylene blue to methylene blue was observed when exposed to a restricted flow of air. This demonstrates the high sensitivity to changes in oxygen concentration of the simple Bragg device. The data is corrected for temperature variation.

A Bragg wavelength shift of ~80 pm, corresponding to an effective index change of ~ 7 x 10^{-5}, was observed during the oxidation of LMB to MB. The restricted air flow allowed for gradual oxidation over ~12 hours, highlighting the sensitivity to subtle changes in oxygen concentration. Temperature compensation was achieved using a localized buried Bragg grating within the device and a scaling factor of 0.7 was applied to account for the different thermo-optic coefficients for silica and aqueous solvent.

V. CONCLUSIONS:

Here we show preliminary results that a planar Bragg grating can detect changes in the refractive index of methylene blue in solution on exposure to oxygen. We will further develop Bragg grating sensors by immobilizing methylene blue into a sol-gel overlayer that will enhance sensitivity and allow for gas phase sensing. We shall present our latest work towards the production of a robust and reversible oxygen sensor.

REFERENCES

[1] V. Bellon – Maurel, O. Orliac, Christen, P., "Sensors and measurements in solid state fermentation: a review," Process Biochemistry, vol. 38, pp. 881 – 896, 2003

[2] G. Rao, S.B. Bambot, S.C.W. Kwong, H. Szmacinski, J. Sipior, R. Holavanahali, G. Carter, "Application of Fluorescence Sensing to Bioreactors," in Topics in Fluorescence Spectroscopy: Probe design and chemical sensing, vol. 4, J.R. Lakowicz, Ed. New York: Plenum Press, 1994, pp. 417 – 444

[3] R.M. Parker, J.C. Gates, M.C. Grossel, P.G.R. Smith, "In vacuo measurement of the sensitivity limit of planar Bragg grating sensors for monolayer detection," App. Phys. Lett.., vol. 95, p. 173306, 2009

[4] I.J.G. Sparrow, P.G.R. Smith, G.D. Emmerson, S.P. Watts, C. Riziotis, "Planar Bragg grating sensors – fabrication and applications: a review," Journal of Sensors, vol. 2009, pp 1 – 12, 2009

[5] W., Cao, Y. Duan, "Optical fiber evanescent wave sensor for oxygen deficiency detection," Sensor Actuat B-Chem., vol. 119, pp. 363-369, 2006

[6] J.A. Campbell, "Kinetics – Early and often," J. Chem. Educ., vol. 40, pp. 578–583, 1963

[7] U. Gupta, D. Mohan, S.K. Ghoshal, V. Nasa, "Dual fluorescence of methylene blue encapsulated in silica matrix," J. Photoch Photobio A, vol. 209, pp. 7-11

[8] J.D. Wright and N.A.J.M. Sommerdijk, Sol-gel Materials Chemistry and Applications. London, U.K., Taylor and Francis, 2001.

SOI photonic wire Bragg gratings for interferometric sensor arrays

Rainer Hainberger, Paul Muellner, Roman Bruck
AIT Austrian Institute of Technology GmbH, Health and Environment, Nano Systems, Vienna, Austria
rainer.hainberger@ait.ac.at

Abstract— **A novel wavelength multiplexing concept for an integrated sensor array based on SOI photonic Mach-Zehnder interferometers is presented. The characteristics of the entire device are discussed and the design of the key element – a photonic wire Bragg grating with SU8 cladding for quasi-TM polarisation – is optimised on the basis of 3D FDTD simulations.**

Integrated optics, Bragg grating, silicon photonics

I. INTRODUCTION

Evanescent wave sensors for the detection of biomolecules employing integrated Mach-Zehnder interferometers (MZI) or micro rings resonators (RR) [1] based on SOI technology have attracted much interest due to their potential for a high level of integration. In order to keep the coupling of light into and out of the sensor chip as simple as possible an efficient multiplexing scheme is required. A single grating coupler input port with subsequent passive power splitting is certainly one option for addressing either multi channels of MZI or RR sensing elements. Passive power splitting inherently decreases the optical power level supplied to each channel and, moreover, prevents the use of a common output port. In the case of MZI array it would, however, offer the possibility to operate at a fixed wavelength [2]. Active optical routing by means of electro- or thermo-optical path switches would in principle be another option [3]. Considering the large area that the switching array would consume and the increased complexity in fabrication and operation this approach does not appear to be the best choice for single-use sensor chips. The third option is wavelength multiplexing employing a wavelength tunable laser source. Efficient SOI based grating couplers can be realized with <1dB coupling loss over a operation wavelength range of 35 nm [4]. In the case RR are used as sensing elements this approach allows allocating several RR provided that their resonance wavelengths are not overlapping. Since the RRs change their resonance wavelength in the course of the sensing event additional spectral distance between the individual channels has been allocated. Instead of employing the RR as sensing elements, we propose to use them as drop ports to route the optical power to MZIs that provide the sensing function. Arrayed waveguide gratings (AWG) could also be used for distributing the different wavelengths to individual channels but they have a much larger foot print than RRs. Regardless whether RRs or AWGs are used as wavelength routing component, the multiplexing of the different wavelength channels after passing through the sensing elements would require the identical spectral characteristic of the components. In particular, in case of RRs, this represents a highly challenging task because even very small deviations in the fabrication process result in a wavelength shift of the resonance characteristic.

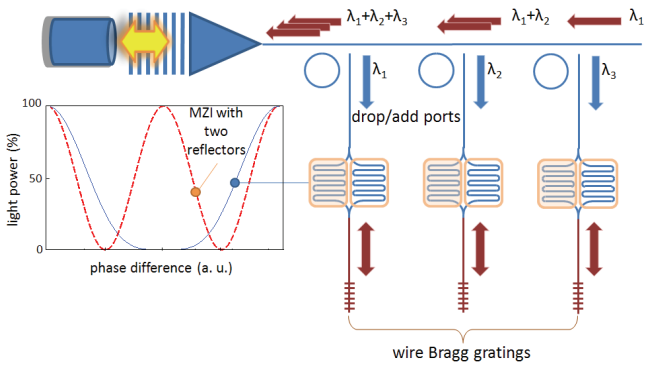


Figure 1. Wavelength multiplexing concept with one ring resonator per channel employing wire Bragg grating reflectors. The inset shows the characeteristics of an MZI with one wire Bragg grating reflector (line) and of an MZI with reflectors in both interferometer arms (dashed).

II. CONCEPT

We propose the use of photonic wire Bragg gratings that reflect the light back to the same RR that dropped the light from the input waveguide in order to eliminate the risk of a wavelength mismatch between drop and add port. This also offers the advantage that light can be coupled into and out of the chip via the same grating, which reduces the alignment effort. A fiber optic circulator is employed to separate input and output light path.

There are two possible implementations of this scheme: a) each MZI arm is terminated by a reflector, and b) the reflector is placed after recombining the light of the two MZI arms as shown in Fig. 1. In the first case, a doubling of the phase response is achieved but an almost identical reflectivity of the two Bragg gratings is required to ensure a high modulation depth of the interference pattern. The output-to-input power ratio of the light after passing forth and back through the MZI can be written as

$$P_{out}/P_{in} = (1+\cos(2\Delta\phi))/2, \quad (1)$$

where $2\Delta\phi$ represents the accumulated double pass phase difference between the sensing and the reference arm.

In the second case, the output-to-input power ratio can be expressed as

$$P_{out}/P_{in}=(1+\cos(\Delta\phi))^2/4. \quad (2)$$

The quadratic cosine term increases the gradient of the power characteristics as shown in the inset of Fig. 1.

III. Simulation Results

The key component in this concept is a photonic wire Bragg grating that reflects the light back to the input port. In a photonic wire Bragg grating the width of a wire waveguide varies periodically. The high degree of freedom with respect to the geometry of the structure provides a good control of the optical characteristics such as reflectance and wavelength dependence. In-depth studies by Gnan et al. [5,6] demonstrated that photonic wire Bragg gratings can fulfil the requirement of a band gap over a wavelength range of several tens of nanometers.

3D FDTD studies so far focused on the quasi-TE polarisation [5], which is less sensitive than the quasi-TM mode of a SOI photonic wire. Moreover, in these studies the maximum wire width in the Bragg region w_2 is kept at the width of the wire w (see Fig. 2).

In our studies, 3D FDTD simulations were carried out for varying geometry parameters (w_1, w_2, Λ) using MEEP [7]. For that purpose, the reflected and transmitted fields of photonic wire Bragg gratings were calculated for structures as depicted in Fig. 2 by placing monitors in front and behind the grating structure. The thickness of the silicon photonic wire was set to 220 nm. Figure 2 shows the transversal electric field component for a CW excitation at a wavelength of 1.57 µm of an optimised structure with an outer Bragg grating width of w_2=650 nm. The low field amplitude at the output on the right side indicates the existence of a band gap.

The wavelength response was analysed with the implemented DFT algorithm for a Gaussian pulse as source. For the structure shown in Fig. 2 more than 80% of the light is reflected over a wavelength range of ~50 nm (see Fig. 3). About 10% of the power is transmitted, whereas the remaining 10% can be attributed to radiation losses.

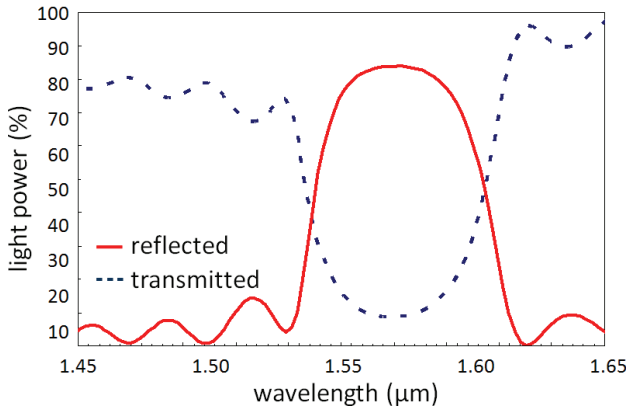


Figure 3. Reflected and transmitted optical power of the simulated photonic wire Bragg grating reflector for quasi-TM polarisation.

IV. Summary

A novel concept for the realization of a wavelength multiplexed MZI sensor array based on SOI technology was presented. The key element - a photonic wire Bragg grating reflector with SU8 cladding for quasi-TM polarisation - was designed employing 3D FDTD simulations.

Acknowledgment

This work was supported by the Austrian NANO Initiative under the grant PLATON Si-N (project no. 819655).

References

[1] X. Fan et al.," Sensitive optical biosensors for unlabeled targets: A review", Analytica Chimica Acta, vol. 620, 2008, pp. 8-26.

[2] A. Densmore et al., "Silicon photonic wire biosensor array for multiplexed real-time and label-free molecular detection", Optics Letters, vol. 34, 2009, pp. 3598-3600.

[3] A. Densmore et al., "Compact and Low Power Thermo-Optic Switch Using Folded Silicon Waveguides", Optics Express, vol. 17, 2009, pp. 10457-10465.

[4] D. Taillaert et al., "Compact efficient broadband grating coupler for silicon-on-insulator waveguides", Optics Letters, vol. 29, 2009, pp. 2749-2751.

[5] M. Gnan et al., "Modelling of photonic wire Bragg gratings", Optics and Quantum Electronics, vol. 38, 2006, pp. 133–148.

[6] M. Gnan et al., "Closure of the stop-band in photonic wire Bragg gratings", Optics Express, vol. 17, 2009, pp. 8830-8842.

[7] A. F. Oskooi et al. "MEEP: A flexible free-software package for electromagnetic simulations by the FDTD method," Computer Physics Communications, vol. 181, 2010, pp. 687-702.

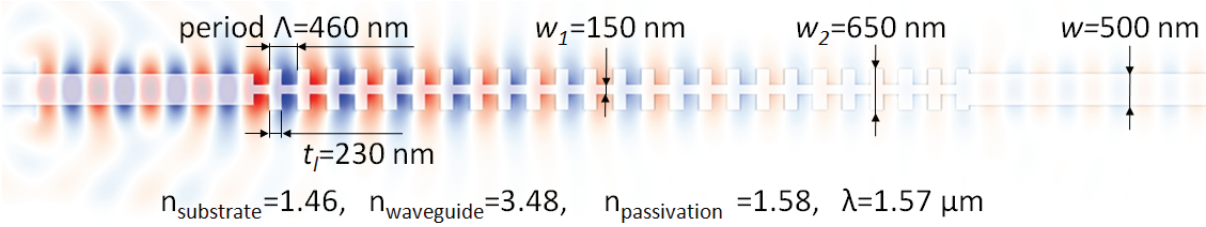


Figure 2. 3D FDTD simulation result of a 220 nm thick photonic wire Bragg grating with quasi-TM polarized CW excitation at λ=1.57µm. The transversal electric field component is shown.

Silicon Nitride Bimodal Waveguides for High Sensitivity Biosensors

K. E. Zinoviev, C. Dominguez
Micro and Nanosystems Department,
Instituto de Microelectronica de Barcelona, CNM (CSIC)
Campus UAB, 08193, Cerdanyola del Valles, Barcelona
Spain
kirill.zinoviev@imb-cnm.csic.es

L. M. Lechuga
Nanobiosensors and Bioanalytical Applications Group
CIN2 (CSIC-ICN)
Campus UAB, 08193, Cerdanyola del Valles, Barcelona
Spain
laura.lechuga@cin2.es

Abstract—**The fundamental properties of a bimodal waveguide interferometer were studied to evaluate its suitability for high sensitive biosensing applications.**

Keywords- Bimodal waveguide, biosensors,, integrated optics, multimode waveguides, optical waveguides

I. INTRODUCTION

Among the interferometric devices widely used for sensing applications the most common are the ones based on Mach Zehnder and Young interferometers. These devices have two separated in space single mode waveguide branches, one of which is provided with a sensing window. The speed of the light propagation along the sensing arm of the waveguide depends on the optical properties of the analyte deposited over this waveguide window. The relatively simple design, high integration level, well developed read out techniques, and high sensitivity (2×10^{-8} refractive index unit (RIU) [1]) made these devices very attractive for label-free biosensing applications. Y-shape junction or more complicated structures are employed to deliver the light in the two branches with 3 dB split ratio in order to achieve 100% modulation at the output. Fundamentally, the sensitivity is limited by the length of the sensing window, but in practice is limited by other factors, such as the noise in the detection system, the accuracy of sensor fabrication, by the stability of the light coupling. In order to make the device insensitive to temperature fluctuations, the waveguide branches are placed very close to each other, ~50 μm, thus, the temperature fluctuations affect both waveguides simultaneously. A substrate made of a material with high thermal conductivity, silicon for example, is preferred; so that no significant temperature gradients are expected to appear over the chip.

The devices dealing with modal interference employ single waveguide supporting the interfering modes [2, 3]. The modes propagating with different velocities create at the exit an interference pattern where the intensity distribution depends on the physical parameters of the structure, and, in particular, on the refractive index of the cladding layer. The sketch of the device is presented in Fig.1. The simplicity of the design of bimodal waveguide (BW) devices is attractive for fabrication of biosensors on their basis; there is no need for the design and fabrication of Y-shape splitters, which are the most complex component of MZI device responsible for the modulation depth of the output signal and, subsequently, for the sensitivity.

For implementation of the BW device a light source with a narrow spectral line, stable in time, and with a coherency length of several millimeters is required. This allows creating a high contrast interference at the output of the BW. Temperature sensitivity of BW device is an intrinsic property resulting from the fact that propagation constants of the modes are differently affected by temperature changes. To take advantage of this, the temperature might be used for initial adjustment of the interference pattern.

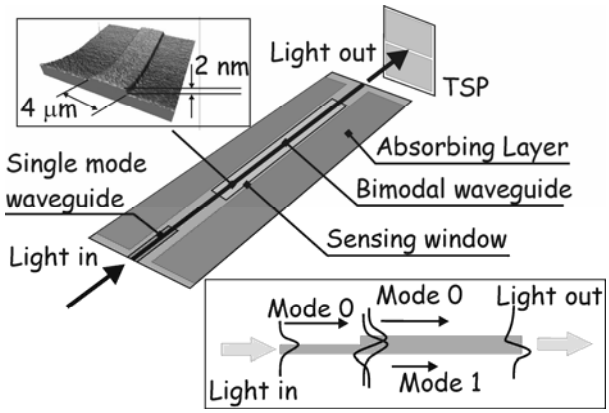


Figure 1. Sketch of the device. Top inset: an AFM image of the ridge designed for single mode operation of the waveguide in lateral direction. Inset below: the principle of mode splitting is sketched.

The interference pattern is independent on the light intensity and the output signal is not sensitive to fluctuations in coupling efficiency. The quality of the end facet, either polished or cleaved, should be good enough to register the interference of the modes. Both modes, once excited, are suffering of scattering on surface imperfections. The first order mode is normally scattered more than the zero order mode, because the concentration of the electromagnetic field of this mode is stronger at the interface waveguide-cladding. The waveguide should be maintained defects-free as much as possible in order to reduce scattering. Relatively strong defects

might result in regeneration of the modes with additional phase shifts.

In this work we discuss the above mentioned issues which are important for the implementation of a BW device as a high sensitive biosensor.

II. EXPERIMENT

The sensor is fabricated over a silicon substrate. A silicon nitride layer with thickness of 340 nm was deposited using LPCVD technique on a thermally grown silicon dioxide buffer layer. A ridge type channel waveguide with ridge height of 2 nm was formed by BHF etching through a photoresist mask patterned by conventional photolithography. We used a step junction in order to excite two modes inside the BW. The fundamental mode propagating down a single mode waveguide in the beginning is split in fundamental and first order modes on the junction. According to our calculations in order to obtain more than 70% modulation, single mode part must be less than 160 nm thick. It is difficult to achieve 100% modulation using this method. In the experiment the single mode part of the waveguide was 150 nm thick.

Light exiting the waveguide is projected on two sectional photodetector (TSP). The signals U_{up}, U_{down} generated by correspondingly the upper and the lower sections of the photodetector are recalculated into a parameter S_r, according with the expression:

$$S_r = \frac{U_{up} - U_{down}}{U_{up} + U_{down}} \qquad (1)$$

The chip was mounted on a thermoelectric element with temperature stabilization of 0.001 degrees. Light from He-Ne (633 nm) laser was coupled into the chip using direct focusing of light by an objective lens to a polished waveguide facet. The temperature of the chip support was constantly monitored together with the parameter S_r.

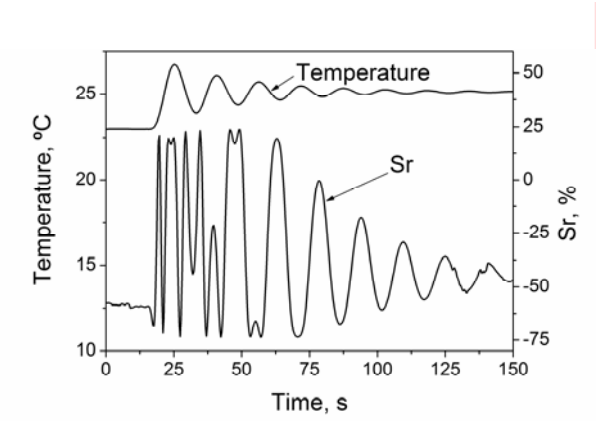


Figure 2. Response of the sensor to the temperature changes

Temperature fluctuations resulted in a chip displacement which can affect the coupling efficiency, but this did not affect the modulation depth and the sensitivity of the device. The time diagram of temperature and the readout signal are shown in Fig. 2. The parameter S_r changed by 14.3 % per 0.1 degree of temperature change.

Experiments on sensitivity to the changes in the refractive index of the cladding layer were performed by injecting a varying water:glycerin solution over the sensing window. For this purpose the chip was mounted in a PMMA fluidic cell connected to a peristaltic pump. Prior to the measurements, the signal was stabilized by injection of deionised water. Afterwards, two solutions with refractive indexes different from one of water by 1.4×10^{-4} and 5.2×10^{-4} were injected into the channel, respectively.

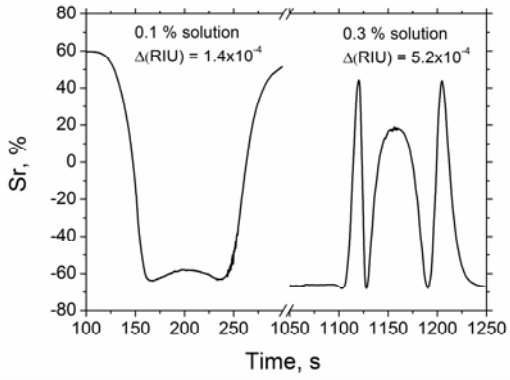


Figure 3. Response of the sensor to injection of glycerin solutions with concentrations of 0.1 % and 0.3 % (both by volume)

Fluctuations of S_r with amplitude of more than 60% can be observed in Fig.3. A phase change of more than π radian per 0.00014 cladding RIU change was observed. At the most sensitive position, where the curve slope is at the maximum, detection of a refractive index change of 10^{-6} is possible if the accuracy in detection of the parameter S_r is better than 1%.

In order to prove the expected sensitivity of the biosensor, experiments are in progress for the immunodetection of two pituitary peptide hormones with relevant biological interest and diagnostic value. We are evaluating the human growth hormone (hGH) and the follicle stimulating hormone (hFSH), which have been previously evaluated with our commercial SPR biosensor (Sensia SL., Spain).

ACKNOWLEDGMENT

Authors acknowledge the financial support from Fundación M. Botín and the SENA project (TSI-020301-2008-11) from the Spanish Ministry of Industry.

REFERENCES

[1] A. Ymeti, J. S. Kanger, R. Wijn, P. V. Lambeck, J. Greve, "Development of a multichannel integrated interferometer sensor," Sensors and Actuators B, vol. 83, pp. 1-7, 2002

[2] M. Lohmeyer, L. Wilkens, O. Zhuromskyy, H. Dötsch, and P. Herte "Integrated magnetooptic cross strip isolator," Optics Communications, vol. 189, no. 4-6, pp. 251-259, 2001.

[3] A. Irace and G. Breglio, "All-silicon optical temperature sensor based on Multi-Mode Interference," Optics Express, vol. 11, no. 22, pp. 2807-2812, 2003.

All Optical Switching and Label Swapping Using HNLF and SOAs for 40 Gb/s Spectrally Encoded Systems

J. B. Rosas–Fernández[1], J. Dong[1,2], Y.Yu[1,2], G.Huang[1], X.Zhang[2], D. Huang[2], R.V.Penty[1] and I.H. White[1]
[1]Centre for Photonic Systems, Electrical Engineering Division, University of Cambridge, 9 JJ Thomson Avenue, Cambridge CB3 0FA, UK, jbr28@cam.ac.uk
[2] Wuhan National Laboratory for Optoelectronics, Huazhong University of Science and Technology, Wuhan, 430074, P.R. China

Abstract—**HNLF and nonlinear SOA components are used to perform all-optical self-switching and label swapping of spectrally label encoded 40 Gb/s signals. A Q-factor of >6 is obtained after self-switching and label swapping for 21 channels.**

Keywords- Semiconductor Optical Amplifier, Highly Nonlinear fiber, Coding, Networks

I. INTRODUCTION

Label swapping is an important function of future networks based on optical label switching [1]. Here, one or more labels are renewed or added in an intermediate node of a multi-hop switched network. The labels are used as headers to determine the forwarding path or for the management of other networking functions such as quality of service (QoS). Previously, spectral amplitude code (SAC) labels have been proposed for label switching since they have benefits such as fast label recognition and the potential for a large label set of codes [2]. A SAC label consists of wavelength tones with a code weight (wavelengths with high amplitudes or "1" and code length (total number of wavelengths). All optical label swapping has been demonstrated for SAC labels with weight 4 using a semiconductor ring laser for label swapping [2]. However, this system needs a bank of optical decoders to recognize the SAC labels and multi-wavelength conversion for label swapping since the SAC labels have weight > 2.To alleviate the use of a bank of correlators, multiple SAC labels can be recognized by a single correlator using four wave mixing (FWM) sideband (SB) allocation and selective optical filtering [3]. Label switching of signals with separate payload was demonstrated in [3]. Recently, a control-less fast self switching system that self-switches the signal to a FWM sideband according to its specific SAC have been demonstrated [4].

The approach here does not need switch fabrics or other complex items, such as complex de/encoders, short pulses, envelope detection, etc. In this paper, we demonstrate for the first time all-optical self switching with label swapping for the two-weight code self switching system using FWM and cross gain modulation (XGM) respectively. Since the codes are built with only two wavelengths, this alleviates the cost, power consumption and complexity of the label swapping section since multi-wavelength conversions for swapping one code to another are not necessary. Here, new bins are formed by converting the wavelength of the switched signal to a new bin via XGM whilst the second bin is a local cw signal to form the new label. A schematic of the self switched network with label swapping is shown in fig. 1.

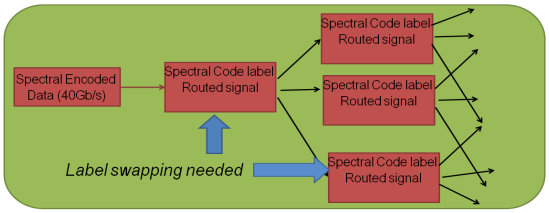


Fig.1. Multi-hop spectral coded label self switched network

II. OPERATIONAL PRINCIPLE AND EXPERIMENTAL SETUP

Fig. 2 shows the optical packet format. Each SAC label is modulated by the data payload. Thus, the label is implicit in the payload bits (each bit has two wavelengths) allowing the payload to be self-switched by FWM according to table 1 (which is developed using an algorithm similar to the one used for FWM long distance transmission [3]). The code family used has a length of 7, a weight of 2 and a total set of 21 codes. The bins are separated by a multiple of a frequency slot (Δf), in this case 100 GHz, which is also the minimum bin separation. The frequencies that overlap with others cannot be used for self-switching and these are highlighted in grey in table 1. It is important to notice that in [3], a nonlinear SOA was used and a shorter table was demonstrated since its FWM efficiency response less than the HLNF. The HNLF allows to have enough FWM reponse for about 15nm bandwidth. Figure 3 shows the experimental setup. Two tunable lasers, TL1 and TL2, generate the spectral code labels and they are modulated by the data, thus producing the spectrally encoded bits. As an example we use code 20 in table 1.

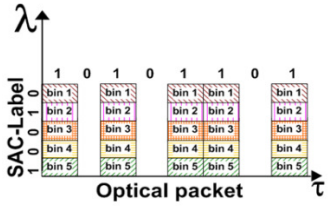


Fig.2. Optical packet format

TABLE 1. WAVELENGTH BIN ALLOCATION FOR SAC-LABEL FAMILIES

in nm	0	2	6	9	13	17	20	Δf=100GHz	
Code	1544.1	1545.7	1548.9	1551.3	1554.5	1557.8	1560.2	FWM 1	FWM 2
1	1	1	0	0	0	0	0	1547.32	1542.5
2	1	0	1	0	0	0	0	1539.37	1553.7
3	1	0	0	1	0	0	0	1537	1558.9
4	1	0	0	0	1	0	0	1533.86	1565.1
5	1	0	0	0	0	1	0	1530.72	1571.7
6	1	0	0	0	0	0	1	1528.38	1576.6
7	0	1	1	0	0	0	0	1542.54	1552.1
8	0	1	0	1	0	0	0	1540.16	1557
9	0	1	0	0	1	0	0	1537	1563.5
10	0	1	0	0	0	1	0	1533.86	1570
11	0	1	0	0	0	0	1	1531.51	1575
12	0	0	1	1	0	0	0	1546.52	1553.7
13	0	0	1	0	1	0	0	1543.33	1560.2
14	0	0	1	0	0	1	0	1540.16	1566.7
15	0	0	1	0	0	0	1	1537.79	1571.7
16	0	0	0	1	1	0	0	1548.11	1557.8
17	0	0	0	1	0	1	0	1544.92	1564.3
18	0	0	0	1	0	0	1	1542.54	1569.2
19	0	0	0	0	1	1	0	1551.32	1561
20	0	0	0	0	1	0	1	1548.91	1565.9
21	0	0	0	0	0	1	1	1555.34	1562.6

After 25 km of SMF transmission and the corresponding DCF, at the intermediate node we implement all optical self switching and label swapping.

Firstly, the 40Gb/s spectrally encoded signal is propagated through a highly nonlinear fibre (HNLF) where it is wavelength switched to only one FWM SB (output port) following table 1 - in this case to a wavelength of 1548.91 nm (port 20). The HNLF has a zero dispersion wavelength at 1552nm, a length of 135 m and a nonlinear coefficient of 20 $(W.km)^{-1}$. Suppose we desire to transmit to the next node identified by Code 19, we need to implement a label swapping section. This is achieved using two local lasers in the intermediate nodes (TL3 and TL4), and a SOA which has 15 dB gain and saturation power of 12 dBm. XGM in the SOA is used to convert the signal from 1548.91nm (incoming signal from Port 20) to 1554.54nm using TL3 (this signal becomes one bin of new Label 19). The cw signal from TL3 is transmitted in the counter propagation direction in the SOA so filtering of this signal is avoided after the XGM process.

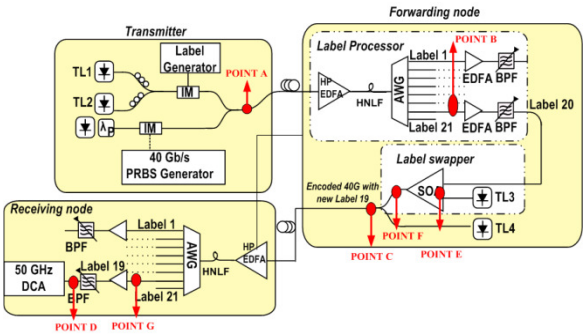


Fig.3. Experimental setup

After the self-switched data signal has been converted, it is combined with TL4, which provides the second bin of the new SAC label. To build label 19, it is tuned to 1557.8 nm. At the receiver node, the Code label 19 is self routed to Port 19 and its Q factor is measured using a 50 GHz digital communications analyser (DCA).

III. RESULTS AND DISCUSSION

Figures 4(a) to 4(d) show the eye diagrams of the 40 Gb/s signal at different stages in the system (the stages are labelled in Fig. 3). Fig 4(a) shows the transmitted eye of the original label code 20 which has with Q-factor of 10.1 (point A in the setup). Fig. 4(b) shows the eye diagram of the Code 20 after FWM self switching, with Q=7.33 (point B). Fig. 4(c) and 4(d) show the wavelength routed signals converted from 1548.91 nm to 1554.54 nm, with Q factors of 6.5 and 6.02, respectively (points C and D). Fig. 4(e) to Fig 4(h) show the spectrum of the signal at the corresponding stages. Fig. 4(e) shows the Code 20 spectrum after FWM at the intermediate node (point B), where we can see the input bins and the two SBs. The SB at 1548.91nm is filtered and input to the swapping processor. Fig. 4(f) shows the incoming Code 20 data together with the CW signal used in the XGM wavelength conversion process (point E). It should be noted that the data is inverted from the original. The signal after wavelength conversion and filtering is shown in Fig 4(g) (point F). Finally, the spectrum of the 40 Gb/s signal encoded with the new Code 19 is shown in Fig 4(h) (point G).

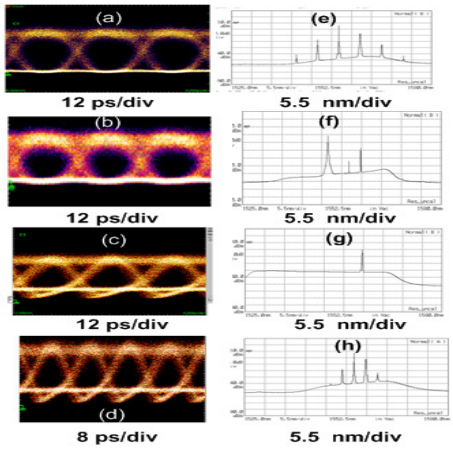


Fig. 4. (a) Original eye diagram of the 40 Gb/s Code 20 spectrally encoded data; (b) 40 Gb/s encoded signal after self routing by FWM; (c) 40 Gb/s encoded signal after wavelength conversion by XGM; (d) 40 Gb/s encoded signal with Code 19 after self routed by FWM; (e) Spectrum of Code 20 after FWM in the forwarding node; (f) spectrum of filtered 40 Gb/s signal and the CW used in the XGM process; (g) converted 40Gb/s data (h) 40Gb/s coded signals after FWM at the receiver.

IV. CONCLUSIONS

We have demonstrated for the first time a self switching system based on two weight codes and FWM in a HNLF with long bandwidth response. Furthermore, it is demonstrated all optical label swapping of spectrally label encoded 40 Gb/s signals is optimized using XGM in a nonlinear SOA for a 21-port self routing system. In contrast to previous SAC label swapping demonstrations, multi-wavelength conversion is not needed. A Q-factor of >6 is obtained after self-switching by FWM and label swapping. It is possible to route 21 different 40 Gb/s signals in a multi-hop self switched label system with a total throughput of 0.84 Tb/s.

REFERENCES

[1] U. Black, MPLS and Label Switching Networks, 2nd Edition, Prentice Hall, 2002.

[2] J.B. Rosas-Fernandez, et. al, Photonics North 2006, Proceedings of SPIE Volume: 6343, 634310.

[3] J.B. Rosas-Fernandez, JSTQE, May-June (2008), Volume: 14, Issue: 3 pp: 868-878

[4] J.B. Rosas-Fernandez, OFC, Feb (2008), paper OTuL6

Single-to-four all-optical wavelength and format conversion

Y. Yu, J. B. Rosas–Fernández, R. V. Penty and I. H. White
Centre for Photonic Systems, Electrical Engineering Division, Engineering Department, University of Cambridge,
9 JJ Thomson Avenue, Cambridge, CB3 0FA, UK
E-mail: yy297@cam.ac.uk

Abstract—**Single-to-four all-optical format conversions and wavelength conversions are demonstrated based on a single semiconductor optical amplifier (SOA). Using the four-wave-mixing effect, one input non-return-zero (NRZ) signal can be converted to four corresponding return-to-zero (RZ) signals, by pumping with two recovered clock signals. Bit error ratio measurements indicate a ~1.5 dB power penalty for the conversion at 10 Gb/s.**

Keywords - Wavelength conversion; format conversion; semiconductor optical amplifier; four wave mixing; non-return to zero; return to zero.

I. INTRODUCTION

All-optical wavelength and format conversion are key functions in providing flexible management and interfacing for wavelength division multiplexed (WDM) and optical time division multiplexed (OTDM) networks. In the past, the semiconductor optical amplifier (SOA) has been demonstrated as a good candidate for high speed all-optical signal processing including wavelength and format conversion, by utilizing nonlinear effects such as cross gain modulation (XGM), cross phase modulation (XPM) and four wave mixing (FWM). Comparing to XGM and XPM, FWM has some inherent advantages that include large spectral and dynamic range, and relative modulation format and bit-rate transparency. As a result, many papers have proposed and demonstrated FWM based all-optical wavelength conversion as well as format conversion, both for on-off keying (OOK) and phase shift keying (PSK) signals [1, 2]. Non-return-to-zero (NRZ) and return-to-zero (RZ) are the most conventional OOK formats and are widely used in current WDM and OTDM networks, due to their different time and spectral characteristics. However, most of the published papers were based on single-to-single [3] or single-to-dual [4] NRZ-to-RZ operations, which can not provide multicasting capability in addition to wavelength and format conversion.

In this paper, we propose and demonstrate single-to-four wavelength and format conversion using a single SOA. The input NRZ signal is input into the SOA as well as two synchronized clock signals, which are recovered from the input NRZ signal and used as two pump lights. Using both non-degenerate and degenerate FWM effects in the SOA, four resulting RZ signals can be achieved simultaneously at the output, showing that the ability of multicasting. Bit error ratio (BER) measurements show ~1.5 dB power penalty for the proposed conversion at 10 Gb/s. By using an SOA with higher nonlinearity, conversions at higher bit-rates can be achieved.

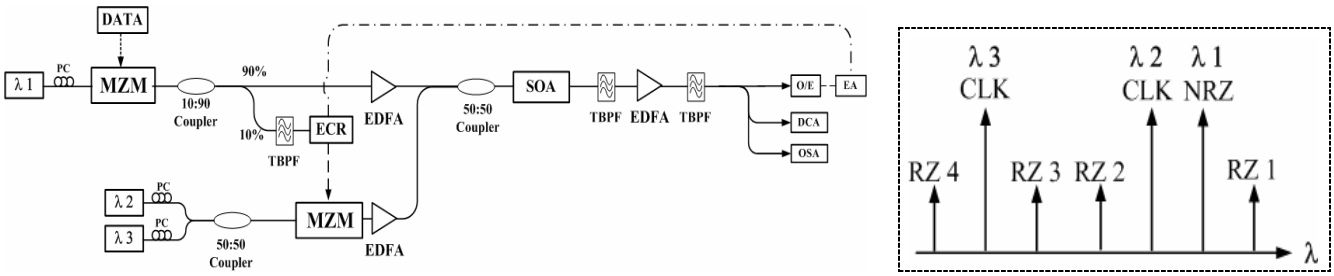
II. EXPERIMENTAL SETUP AND OPERATION PRINCIPLE

The experimental setup is shown in Fig. 1(a). The input NRZ signal is generated by modulating cw light at 1549.5 nm with a Mach-zehnder modulator (MZM). The resulting 10 Gb/s NRZ signal with 2^{31}-1 PRBS length is divided into two parts by a 10:90 coupler, the 10% tap being preprocessed via an optical filter [5] and then used to extract a synchronized RF clock signal; the 90% part being sent to the SOA to achieve wavelength and format conversion. Clock recovery (CR) is performed by a high Q electrical filter (Q≈750), this allowing a low jitter (660 fs) RF clock signal to be achieved. The recovered clock is then used to modulate two other cw channels at 1548.3 and 1543.5 nm using a second MZM, resulting in two synchronized optical clock signals. The three signals are amplified to a sufficient power by EDFAs to achieve the desired FWM effect in the SOA. The input power is 9 dBm for the NRZ signal and 12 dBm for the two clock signals. The SOA used in the experiment is a Kamelian OPA biased at 180 mA. After the SOA, a narrow band optical filter with 0.3nm 3 dB bandwidth and another EDFA are used to extract one of the converted RZ signals, which is analyzed using a digital communication analyzer (DCA), an optical spectrum analyzer (OSA) and an error analyzer (EA).

The format conversion and wavelength conversion are achieved by both non-degenerate and non-degenerate FWM in the SOA, as indicated in Fig. 1(b). Assuming the wavelength for the input NRZ and the two optical clock signals are λ_1, λ_1 and λ_3, the four converted RZ signals will be at $2\lambda_1-\lambda_2$, $2\lambda_2-\lambda_1$, $\lambda_1+\lambda_3-\lambda_2$ and $\lambda_2+\lambda_3-\lambda_1$.It should be noted that although there will also be other new wavelengths generated from the FWM process (for instance $\lambda_1+\lambda_2-\lambda_3$), the conversion efficiency is too low to obtain an RZ signal with a useful optical signal to noise ratio.

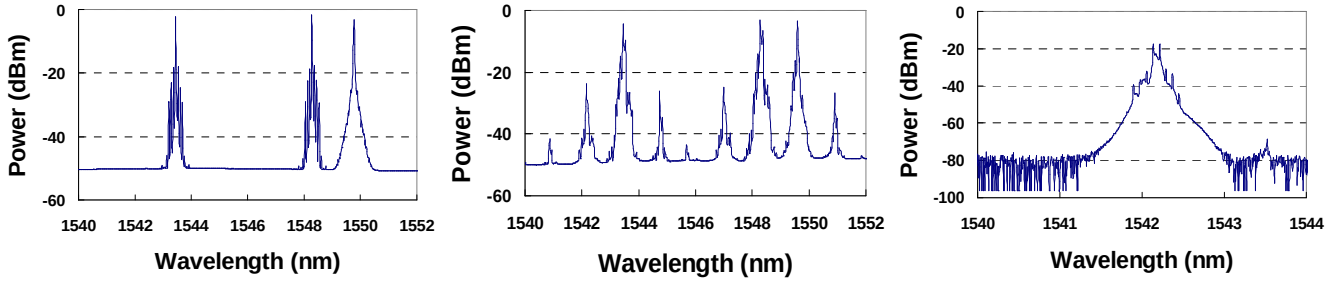
III. EXPERIMENTAL RESULTS AND DISCUSSION

Figure 2(a) shows the input spectra before the SOA. The output spectra after the SOA are presented in Fig. 2(b), showing that four main new wavelength are generated due to the FWM effect. Owing to the use of the clock signals, the wavelength conversions occur along with an NRZ to RZ format conversion. One of the converted RZ spectra is shown in Fig. 2(c).



(a) (b)

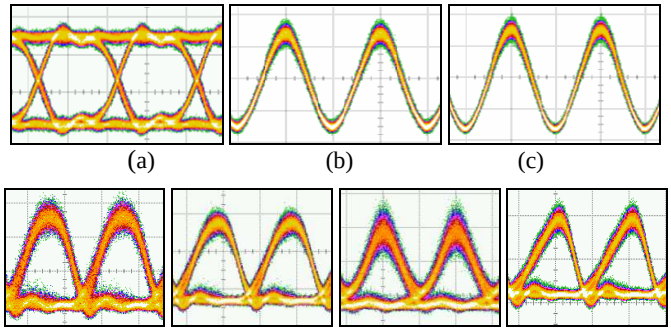
Fig. 1 (a) Experimental setup (b) operation principle



(a) (b) (c)

Fig. 2 Measured optical spectra (a) before SOA (b) after SOA (c) one converted RZ signal

The eye diagrams during the conversion process are shown in Fig. 3. Fig. 3(a) is the input NRZ signal; Fig. 3(b) and (c) are the recovered optical clock signals; Fig. 3(d) to (g) are the four converted RZ signals, corresponding to the RZ1 to RZ4 in Fig. 2(b). From these results we can see that all the converted RZ signals have good open eyes.



(a) (b) (c)

(d) (e) (f) (g)

Fig. 3 Measured eye diagrams before and after the conversions (Time scale: 50 ps/div)

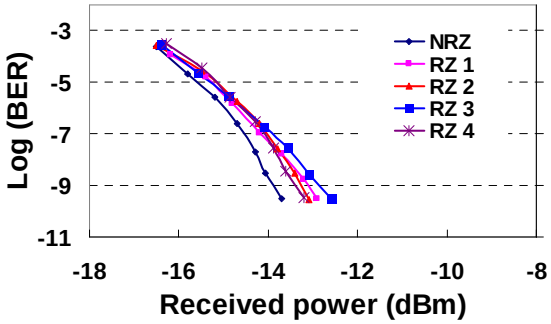


Fig. 4 BER results for the proposed conversion

In order to evaluate the conversion performance, we measured the BER for the input NRZ and output RZ signals, as shown in Fig. 4. Results show that the power penalties for the single-to-four wavelength and format conversion are about 1.5 dB.

IV. Conclusion

In conclusion, we have proposed and demonstrated a one-to-four wavelength and format conversion based on a single SOA. Thanks to the use of non-degenerate and degenerate FWM, four corresponding RZ signals can be realised simultaneously at the output by dual pumping the SOA with two recovered clock signals. BER measurements show ~1.5 dB power penalty for the demonstrated conversion at a data rate of 10 Gb/s.

References

[1] T. Simoyama, H. Kuwatsuka et al., "High-efficiency wavelength conversion using FWM in an SOA integrated DFB laser," *IEEE Photonics Technology Letters*, 12 (1), 31-33 (2000).

[2] H. Wen, H. Jiang, X. Zheng, H. Zhang, and Y. Guo, " Synchronous Clock Pumping to Improve Performance of All-Optical Wavelength Conversion for RZ-DPSK Based on Four-Wave Mixing in SOA," in *OFC/NFOEC* 2007, paper JThA35.

[3] A. Reale, P. Lugli and S. Betti, "Format conversion of optical data using four-wave mixing in semiconductor optical amplifiers," *IEEE J. Sel. Top. Quantum Electron.*, **7**(4), 703-709 (2001).

[4] J. Dong, X. Zhang, F. Wang, Y. Yu, and D. Huang, "Single-to-dual channel NRZ-to-RZ format conversion by four-wave mixing in single semiconductor optical amplifier," *Electron. Lett.*, 44, 763 (2008).

[5] Y. Yu, X. Zhang, E. Zhou and D. Huang, "All-Optical Clock Recovery From NRZ Signals at Different Bit Rates via Preprocessing by an Optical Filter," *IEEE Photonics Technology Letters*, 19 (24), 2039-2041 (2007).

Passive Waveguide Circuit for BPSK Label Identification Consisting of Cascaded Asymmetric X-junction Couplers

Akito Ihara, Hiroki Kishikawa, Nobuo Goto and Shin-ichiro Yanagiya
Department of Optical Science and Technology
The University of Tokushima
2-1 Minamijosanjima-cho, Tokushima 770-8506, Japan
Email: {a.ihara, h.kishikawa, goto, giya}@opt.tokushima-u.ac.jp

Abstract— **In photonic label networks, recognition of optical labels is one of the key functions. We propose a passive waveguide device to identify of BPSK labels with high scalability. The device was numerically confirmed by FD-BPM.**

Keywords- label identification; passive circuit; asymmetric X-junction coupler

I. INTRODUCTION

Optical processing is expected to be applied in routing nodes for improving the processing speed and reducing power consumption.[1,2] In label routing networks, a function to recognize optical labels is one of the key function. Various optical circuits have been proposed to realize optical label identification. Various systems distinguishing optical labels expressed by optical codes have been studied.[3,4] We have investigated passive optical circuits for recognition of optical coded labels in binary phase-shift-keying (BPSK) and quadric PSK (QPSK). [5,6] These devices have a drawback in scalability because the output signals do not have enough contrast between the destination output port and the other output ports. In this report, we propose to improve the contrast of outputs with a scalable structure for a restricted code set. The basic module device is numerically confirmed by finite-difference beam-propagation-method (FD-BPM).

II. BASIC MODULE FOR INTEGRATED CIRCUIT

Fig.1 shows the basic module for identifying optical four-bit BPSK coded label. The module consists of four asymmetric X-junction couplers. One of the asymmetric X-junction coupler is shown in Fig.2. The output depends on the incident phases. The electric fields of the output optical waves are related with the input fields by

$$\begin{pmatrix} A_{out} \\ B_{out} \end{pmatrix} = \frac{1}{\sqrt{2}} \begin{pmatrix} 1 & 1 \\ -1 & 1 \end{pmatrix} \begin{pmatrix} A_{in} \\ B_{in} \end{pmatrix}, \quad (1)$$

where phase terms due to the propagation along the waveguides are eliminated for simplicity. The basic module in Fig.1 consists of spatially aligned four couplers. The input to output relation of the fields is derived as

$$\begin{pmatrix} D_{out1} \\ D_{out2} \\ D_{out3} \\ D_{out4} \end{pmatrix} = \frac{1}{2} \begin{pmatrix} 1 & 1 & 1 & -1 \\ -1 & -1 & 1 & -1 \\ -1 & 1 & -1 & -1 \\ -1 & 1 & 1 & 1 \end{pmatrix} \begin{pmatrix} A_{in1} \\ A_{in2} \\ A_{in3} \\ A_{in4} \end{pmatrix}. \quad (2)$$

It is noted that the center crossed waveguides is ideally just the crossing without interaction. The waveguide pattern has to be carefully designed to suppress the path-length difference between the connecting waveguides, that is, between B_1-C_1 and B_3-C_2 and between B_2-C_3 and B_4-C_4.

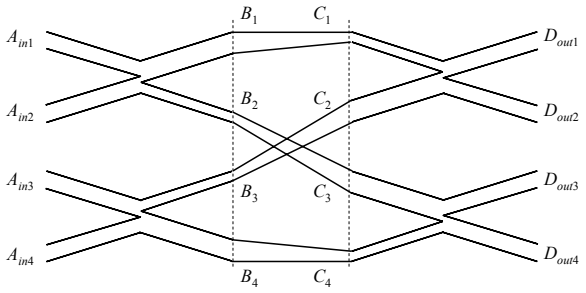


Fig.1 Basic module for four-bit coded labels.

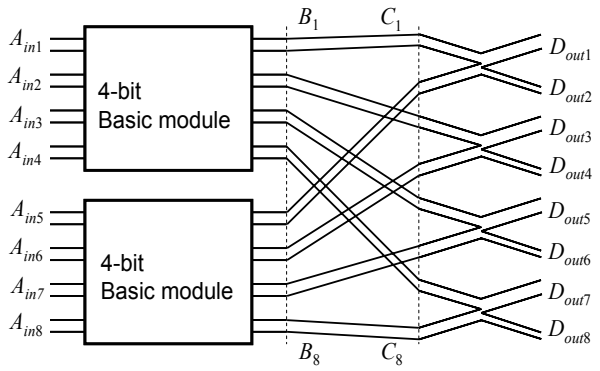


Fig.2 A scaled-up circuit for eight-bit coded labels.

We consider BPSK coded labels as given by

$$\left(\boldsymbol{A}_1^{(1)}\boldsymbol{A}_2^{(1)}\boldsymbol{A}_3^{(1)}\boldsymbol{A}_4^{(1)}\right) = \left(\boldsymbol{A}_1\boldsymbol{A}_2\boldsymbol{A}_3\boldsymbol{A}_4\right) = \begin{pmatrix} 1 & -1 & 1 & 1 \\ -1 & 1 & 1 & 1 \\ 1 & 1 & 1 & -1 \\ 1 & 1 & -1 & 1 \end{pmatrix}, \quad (3)$$

When these labels are incident in parallel at four input ports, we obtain the output fields given by

$$\left(\boldsymbol{D}_1^{(1)}\boldsymbol{D}_2^{(1)}\boldsymbol{D}_3^{(1)}\boldsymbol{D}_4^{(1)}\right) = 2 \begin{pmatrix} 0 & 0 & 1 & 0 \\ 0 & 0 & 0 & -1 \\ -1 & 0 & 0 & 0 \\ 0 & 1 & 0 & 0 \end{pmatrix}. \quad (4)$$

This means that the incident coded labels have their own output at only one destination output port for each label.

Next, we consider scalability to eight coded labels. The identifying circuit is shown in Fig.2, where the basic module is the circuit shown in Fig.1. The output fields can be related to the input fields by

$$\begin{pmatrix} D_{out1} \\ D_{out2} \\ D_{out3} \\ D_{out4} \\ D_{out5} \\ D_{out6} \\ D_{out7} \\ D_{out8} \end{pmatrix} = \frac{1}{2\sqrt{2}} \begin{pmatrix} 1 & 1 & 1 & -1 & 1 & 1 & 1 & -1 \\ -1 & -1 & -1 & 1 & 1 & 1 & 1 & -1 \\ -1 & -1 & 1 & -1 & -1 & -1 & 1 & -1 \\ 1 & 1 & -1 & 1 & -1 & -1 & 1 & -1 \\ -1 & 1 & -1 & -1 & -1 & 1 & -1 & -1 \\ 1 & -1 & 1 & 1 & -1 & 1 & -1 & -1 \\ -1 & 1 & 1 & 1 & -1 & 1 & 1 & 1 \\ 1 & -1 & -1 & -1 & -1 & 1 & 1 & 1 \end{pmatrix} \begin{pmatrix} A_{in1} \\ A_{in2} \\ A_{in3} \\ A_{in4} \\ A_{in5} \\ A_{in6} \\ A_{in7} \\ A_{in8} \end{pmatrix} \quad (5)$$

We consider the coded labels as given by

$$\begin{aligned} &\left(\boldsymbol{A}_1^{(2)}\boldsymbol{A}_2^{(2)}\boldsymbol{A}_3^{(2)}\boldsymbol{A}_4^{(2)}\boldsymbol{A}_5^{(2)}\boldsymbol{A}_6^{(2)}\boldsymbol{A}_7^{(2)}\boldsymbol{A}_8^{(2)}\right) \\ &= \begin{pmatrix} \boldsymbol{A}_1 & \boldsymbol{A}_1 & \boldsymbol{A}_2 & \boldsymbol{A}_2 & \boldsymbol{A}_3 & \boldsymbol{A}_3 & \boldsymbol{A}_4 & \boldsymbol{A}_4 \\ \boldsymbol{A}_1 & \overline{\boldsymbol{A}}_1 & \boldsymbol{A}_2 & \overline{\boldsymbol{A}}_2 & \boldsymbol{A}_3 & \overline{\boldsymbol{A}}_3 & \boldsymbol{A}_4 & \overline{\boldsymbol{A}}_4 \end{pmatrix}, \end{aligned} \quad (6)$$

where $\overline{\boldsymbol{A}}_i$ is the complement of $\boldsymbol{A}_i$. The output for these coded labels are given by

$$\begin{aligned} &\left(\boldsymbol{D}_1^{(2)}\boldsymbol{D}_2^{(2)}\boldsymbol{D}_3^{(2)}\boldsymbol{D}_4^{(2)}\boldsymbol{D}_5^{(2)}\boldsymbol{D}_6^{(2)}\boldsymbol{D}_7^{(2)}\boldsymbol{D}_8^{(2)}\right) \\ &= 2\sqrt{2} \begin{pmatrix} 0 & 0 & 0 & 0 & 1 & 0 & 0 & 0 \\ 0 & 0 & 0 & 0 & 0 & -1 & 0 & 0 \\ 0 & 0 & 0 & 0 & 0 & 0 & -1 & 0 \\ 0 & 0 & 0 & 0 & 0 & 0 & 0 & 1 \\ -1 & 0 & 0 & 0 & 0 & 0 & 0 & 0 \\ 0 & 1 & 0 & 0 & 0 & 0 & 0 & 0 \\ 0 & 0 & 1 & 0 & 0 & 0 & 0 & 0 \\ 0 & 0 & 0 & -1 & 0 & 0 & 0 & 0 \end{pmatrix}. \end{aligned} \quad (8)$$

It is found from eq.(8) that only one different output port has the value for each code. Therefore these eight labels can be identified with this circuit.

III. BPM SIMULATION

As mentioned in the previous section, the path-length difference should be suppressed in the device designing. A two-dimensional model of the basic module for BPM simulation is shown in Fig.3. The fundamental waveguide made of Ge-doped silica waveguide has width of W=3.0μm. The core and the cladding regions have refractive indices of 1.45 and 1.461, respectively. The wider and the narrower waveguide of the asymmetric X-junction couplers have widths W_w=3.4 μm and W_n=2.6 μm, respectively.

Two curved arc waveguides at the top and the lowest waveguides around the center part are introduced to adjust the path length. The output intensities from the four output ports for input label $\boldsymbol{A}_1$ vary as a function of the offset of the arc waveguides as shown in Fig.4. When the arc offset is 26.5μm, path lengths are equally adjusted.

The fields along the circuits for four input labels are shown in Fig.5, where the intensity of the electric fields is plotted. Four input labels are found to have one output at each destination output port as shown in Fig.6. The contrast ratio of the output from the destination port to the outputs from the other ports is larger than 25dB.

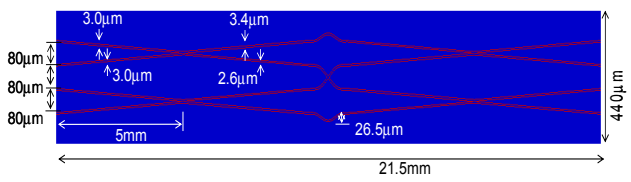


Fig.3 Two-dimensional BPM model.

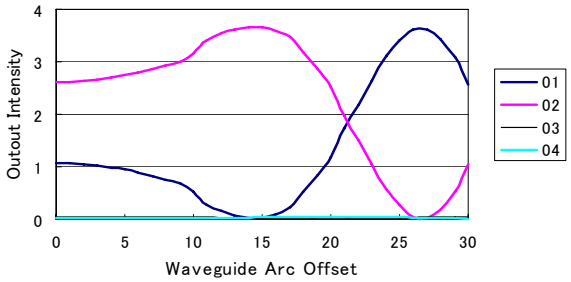


Fig.4 Output intensities for input $\boldsymbol{A}_1$ as a function of offset of arc waveguides.

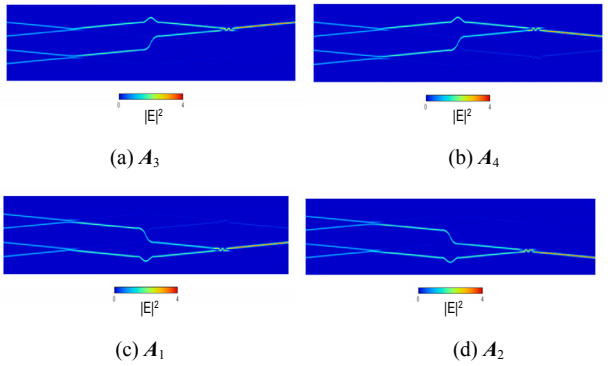


Fig.5 BPM simulation results for input labels.

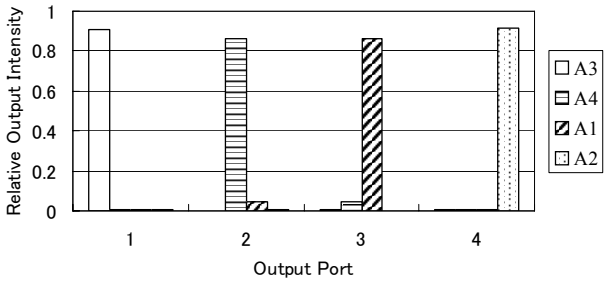


Fig.6 Relative output intensities for four input labels.

IV. CONCLUSIONS

We proposed integrated-optic passive circuits for identifying BPSK coded labels. The processing characteristics were verified by FD-BPM simulation. More refined analysis and experimental verification will be investigated.

ACKNOWLEDGEMENT

This work was supported in part by the grant from Japan Science and Technology Agency and CASIO Science Promotion Foundation.

REFERENCES

[1] D.J. Blumenthal *et al*., J. Lightwave Technol., vol.18, no.12, pp.2058-2075, (2000).
[2] K. Kitayama, N. Wada and H. Sotobayashi, J. Lightwave Technol., vol.18, no.12, pp.1834-1844 (2000).
[3] O. Moriwaki, T. Kitoh, T. Sakamoto and A. Okada, IEEE Photon. Thechnol. Lett., vol.17, no.2, pp.489-491 (2005).
[4] G. Cincotti. J. Lightwave Technol., vol.22, no.2, pp.337-342 (2004).
[5]H. Hiura, J. Narita and N. Goto, IEICE Trans. Electron., vol.E90-C, no.12, pp.2270-2277 (2007).
[6] Y. Makimoto, H. Hiura, N. Goto amd S. Yanagiya, Journal of Lightwave Technology, Vol.27, No.1, pp.60-67 (2009).

Switching Characteristics of All-Optical Wavelength-Selective Switch Controlled by a Single Light

Hiroki Kishikawa, Nobuo Goto and Shin-ichiro Yanagiya
Department of Optical Science and Technology
The University of Tokushima
2-1 Minamijosanjima-cho, Tokushima 770-8506, Japan
Email: {h.kishikawa, goto, giya}@opt.tokushima-u.ac.jp

Abstract—**We reports operating condition of a modified architecture of all-optical wavelength-selective switch controlled by a single light. Switching characteristics in a proposed circuit are analyzed with regard to their phase dependence.**

Keywords- optical switch; asymmetric X-junction coupler; Raman amplifier; wavelength-selective; Integrated optics; Optical waveguide; Wide wavelength range

I. INTRODUCTION

Wavelength-selective processing in switching, routing systems will become key technologies in order to efficiently handle signals of multiple wavelengths in network nodes. Integrated-optic switches are essential devices in such processing systems, in particular, high-speed wavelength-selective switches are required for processing wavelength-division multiplexed (WDM) packets. The authors have proposed all-optical wavelength-selective switches controlled by light intensity in cascaded optical couplers [1-5]. They consist of waveguide-type Raman amplifiers and attenuators as light intensity control elements, and 3-dB directional couplers or asymmetric X-junction couplers as optical couplers. Our latest study [5] has investigated the operation principle and characteristics of the switch employing asymmetric X-junction couplers, that have shown broadening its operating wavelength range. In this paper, we make clear another architecture of the switch, condition for switching, and additional characteristics affecting the operation of the switch, namely, dependence of signal phase variation.

II. PRINCIPLE OF SWITCHING

The architecture of the broadband wavelength-selective switch reported in [5] and the architecture reported here are shown in Fig.1 and Fig.2, respectively. They consist of cascade connection of two interferometers, which formed with three asymmetric X-junction couplers. In addition, there are two waveguide-type Raman amplifiers and an optical attenuator in Fig.1, and a Raman amplifier and two attenuators in Fig.2. Multiple WDM signals can be simultaneously and wavelength-selectively switched with the single switch because the Raman amplifiers made of crystalline waveguides can wavelength-selectively amplify optical signals with narrow gain bandwidth.

In order to explain the switching condition of these switches, we focus on an X-junction coupler and signal with a certain wavelength. Optical electric fields of input and output waves in this coupler can be written as [6-8]

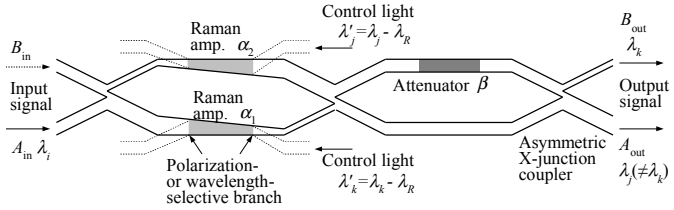


Figure 1 Schematic diagram of the previously reported switch.

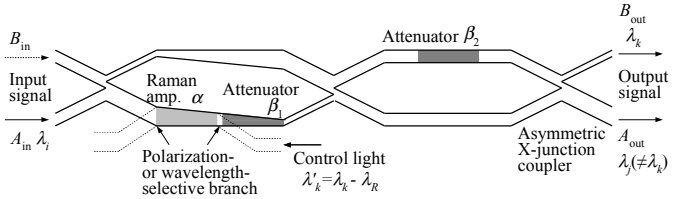


Figure 2 Schematic diagram of the modified switch.

$$\begin{pmatrix} A_{\text{out}} \\ B_{\text{out}} \end{pmatrix} = \frac{1}{\sqrt{2}} \begin{pmatrix} 1 & 1 \\ -1 & 1 \end{pmatrix} \begin{pmatrix} A_{\text{in}} \\ B_{\text{in}} \end{pmatrix} \tag{1}$$

where phase terms due to the propagation along the waveguides are eliminated for simplicity. The output fields through the switch shown in Fig.1 are related to the input fields as reported in [5]. As a similar manner, the output fields of the architecture in Fig.2 are calculated as

$$\begin{pmatrix} A_{\text{out}} \\ B_{\text{out}} \end{pmatrix} = \begin{pmatrix} \dfrac{-E_{\text{in}}}{(1+\sqrt{2})} \\ 0 \end{pmatrix} \quad \text{when} \quad \alpha = 1,\ \beta_i = \frac{1}{1+\sqrt{2}} \tag{2}$$

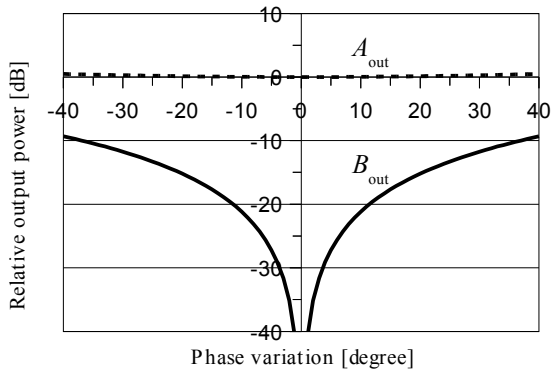
$$\begin{pmatrix} A_{\text{out}} \\ B_{\text{out}} \end{pmatrix} = \begin{pmatrix} 0 \\ -E_{\text{in}} \end{pmatrix} \quad \text{when} \quad \alpha = (1+\sqrt{2})^2,\ \beta_i = \frac{1}{1+\sqrt{2}} \tag{3}$$

where α is amplification coefficient, β_i (i=1,2) is attenuation coefficient. From these equations, it is found that incident wave is switched into each port when proper amplification and attenuation are maintained.

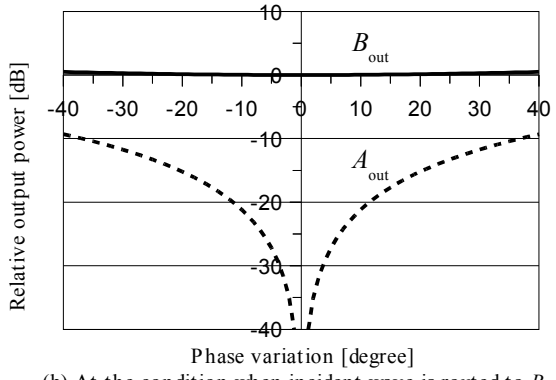
III. SWHITCHING CHARACTERISTICS

The wavelength range of switching is expected to be as wide as 400 nm as reported in [5]. Here we mention about the dependence on phase. When input waves are separated into their amplitude and phase factors, $A_{\text{in}} = |A_{\text{in}}| \exp(j\phi_{\text{Ain}})$ and $B_{\text{in}} = |B_{\text{in}}| \exp(j\phi_{\text{Bin}})$ where j is imaginary unit, (1) is calculated to

$$A_{\text{out}} = |A_{\text{out}}| \exp(j\phi_{\text{Aout}}) \tag{4}$$

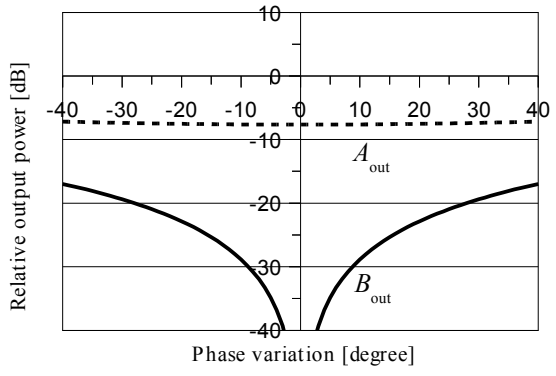


(a) At the condition when incident wave is routed to A_{out}

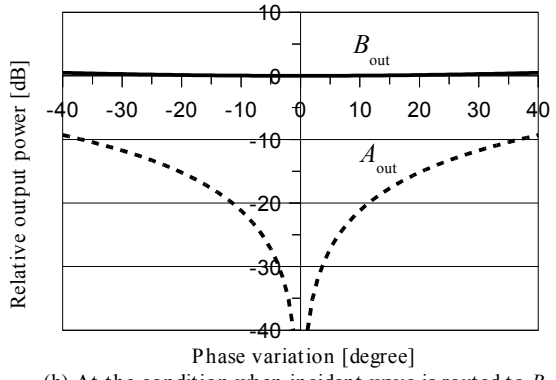


(b) At the condition when incident wave is routed to B_{out}

Figure 3 Phase dependence of the switch shown in Fig.1.



(a) At the condition when incident wave is routed to A_{out}



(b) At the condition when incident wave is routed to B_{out}

Figure 4 Phase dependence of the switch shown in Fig.2.

$$B_{out} = |B_{out}| \exp(j\phi_{Bout}) \tag{5}$$

where

$$|A_{out}| = \frac{1}{\sqrt{2}} \{ |A_{in}|^2 + |B_{in}|^2 + 2|A_{in}||B_{in}| \cos(\phi_{Ain} - \phi_{Bin}) \}^{1/2} \tag{6}$$

$$|B_{out}| = \frac{1}{\sqrt{2}} \{ |A_{in}|^2 + |B_{in}|^2 - 2|A_{in}||B_{in}| \cos(\phi_{Ain} - \phi_{Bin}) \}^{1/2} \tag{7}$$

$$\phi_{Aout} = \arctan \frac{A_{in} \sin\phi_{Ain} + B_{in} \sin\phi_{Bin}}{A_{in} \cos\phi_{Ain} + B_{in} \cos\phi_{Bin}} \tag{8}$$

$$\phi_{Bout} = \arctan \frac{-A_{in} \sin\phi_{Ain} + B_{in} \sin\phi_{Bin}}{-A_{in} \cos\phi_{Ain} + B_{in} \cos\phi_{Bin}} \quad . \tag{9}$$

Fig.3 shows phase dependence of the switch shown in Fig.1. Phase change will occur between the upper and lower arms in front of the second coupler because the signal amplified in either amplifier may cause a nonlinear refractive index change. The phase change taking place in front of the third coupler can be neglected on installing phase shifting components such as optical delay lines or thermooptic devices. This is because the distribution of amplitudes of the signal in the waveguides between the second and the third couplers is the same whether the light wave is routed to one port or the other. Therefore, in this calculation, a virtual variation of phase is generated in front of the second coupler using (6)-(9).

Fig.4 shows phase dependence of the switch shown in Fig.2. There is slightly difference between Fig.4 and Fig.3, i.e. relative output power in Fig.4(a) is smaller than that of Fig.3(a) as expressed in (2).

It is found from Fig.3 and Fig.4, the extinction ratio over 20 dB is achieved within approximately ±12 degrees of phase variation. Moreover, this phase range is similar to our previously reported architecture employing 3-dB directional couplers [4].

IV. Conclusion

This paper reports operating condition and switching characteristics of a modified architecture for all-optical wavelength-selective switch. In future, we will investigate numerical simulation using a precise model and experimental verification with integrated-optic waveguides.

References

[1] H. Kishikawa and N. Goto, J. Lightw. Technol., vol. 23, no. 4, pp. 1631–1636, Apr. 2005.

[2] H. Kishikawa and N. Goto, IEICE Trans. Electron., vol. E89-C, no. 7, pp. 1108–1111, Jul. 2006.

[3] H. Kishikawa and N. Goto, IEICE Trans. Electron., vol. E90-C, no. 2, pp. 492–498, Feb. 2007.

[4] H. Kishikawa and N. Goto, Opt. Eng., vol. 46, no. 4, pp. 044602-1–044602-10, Apr. 2007.

[5] H. Kishikawa, K. Kimiya, S. Yanagiya and N. Goto, J. Lightw. Technol., vol. 28, no. 1, pp. 172-180, Jan. 2010.

[6] H. Hiura, J. Narita, and N. Goto, IEICE Trans. Commun., vol. E90-C, no. 12, pp. 2270–2277, Dec. 2007.

[7] M. Izutsu, A. Enokihara, and T. Sueta, Opt. Lett., vol. 7, no. 11, pp. 549–551, Nov. 1982.

[8] W. K. Burns and A. F. Milton, IEEE J. Quantum Electron., vol. QE-16, no. 4, pp. 446–454, Apr. 1980.

80Gbits/s DPSK regeneration using an SOA balanced-receiver

Ehab S. Awad
Department of Engineering Applications of Lasers
NILES, Cairo University
Cairo, Egypt.
esawad@ieee.org

Abstract— **A technique for 2R-regeneration of received RZ and NRZ 80Gbit/s DPSK data is demonstrated using numerical simulations. Balanced gain-compression and amplification inside an SOA are used to reshape and reamplify demodulated DPSK. The technique is tested by wide range of random phase and amplitude noise. It shows >4dB receiver-sensitivity improvement.**

Keywords-optical communications; optical regeneration.

I. INTRODUCTION

Encoding digital data as differential phase shifting between adjacent bits in differential phase-shift keying (DPSK) format has recently found many applications in optical communications. The DPSK gives a better receiver-sensitivity than OOK (≅3dB) in case of balanced detection. That allows extended transmission distance and/ or less optical transmitted power [1]. However, the DPSK amplitude and differential-phase could suffer degradations due to transmission nonlinearities [1, 2]. These degradations reduce the transmission distance and increase the received power-penalty. Different techniques have been reported on DPSK regeneration along transmission distance to compensate for such degradations [3-7].

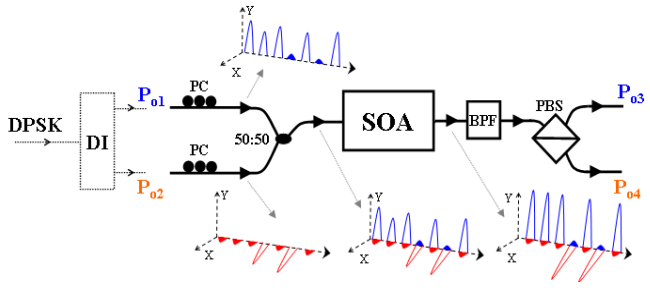


Figure 1. SOA balanced-receiver. Insets shows RZ-DPSK case.

An alternative approach is to improve the DPSK receiver sensitivity by regeneration at receivers. That could reduce transmitted power and thus channel nonlinearities. In this work, a novel technique to regenerate received RZ and NRZ DPSK and improve receiver-sensitivity is demonstrated at 80Gbit/s using numerical simulations. The technique is based on balanced gain-compression and balanced amplification inside a polarization-insensitive SOA, which re-shapes and re-amplifies demodulated DPSK (OOK) data. This balanced configuration is achieved by simultaneous co-propagation of orthogonally-polarized and complementary demodulated OOK streams inside SOA. Thus, the two OOK streams are re-amplified without adding much amplitude-noise (i.e. re-shaped) and the data quality-factor (Q) is improved. The input DPSK phase-noise is inherently suppressed as it is initially converted to amplitude-noise by the one-bit-delay interferometer (DI). The achieved single-ended receiver-sensitivity improvement is better than that of conventional balanced-detection (≅3dB [1]).

II. PRINCIPALS OF OPERATION

Fig.1 shows a schematic setup for the SOA balanced-receiver together with qualitative plots of propagating signals in case of RZ-DPSK input. The input DPSK is initially demodulated by common one-bit DI. The two demodulated complementary OOK data outputs 'P_{o1}' and 'P_{o2}' co-propagate simultaneously inside SOA. The SOA is simulated using nonlinear pulse-propagation model and optical amplifier rate equations [8]. The modeled SOA has 29dB gain, 10dBm output saturation power, 100ps recovery time, and 6dB noise-figure. The SOA is assumed to be polarization-insensitive (i.e. polarization-sensitivity <0.3dB). The two polarization controllers (PC) are utilized to ensure that 'P_{o1}' and 'P_{o2}' are orthogonal linearly-polarized with each launched along one SOA polarization-axes (X, Y). The SOA two inputs experience same gain and get re-amplified. The SOA gain saturation depends on the total power of both marks and spaces in each bit-period. However, the gain saturation mainly depends on marks amplitude as it has much power than spaces. The power-dependent gain saturation (i.e. gain-compression) suppresses amplitude-noise on marks in each bit-period. The marks amplitude-noise is a combination of input DPSK amplitude-noise in addition to phase-to-amplitude converted phase-noise. The re-amplification and reshaping improves data quality-factor at SOA output. It is important to note that the compressed-gain sees alternating orthogonal-polarized marks during signals co-propagation, which effectively seems as 'all-marks' data pattern because of SOA polarization-insensitivity. Thus the SOA does not introduce pattern-dependence to the output data. A band-pass filter (BPF) is utilized at the SOA output to reduce its ASE noise. Finally, a polarization beam splitter (PBS) is utilized to separate the SOA orthogonally-polarized OOK outputs 'P_{o3}' and 'P_{o4}'.

III. SYSTEM PERFORMANCE

The SOA balanced-receiver operation and performance is evaluated using degraded input 80Gbit/s RZ and NRZ DPSK

data. The DPSK is running at exactly 83.33Gbit/s (12ps bit-period) and it carries 2^{10}-1 PRBS data at 1550nm. The short PRBS is chosen to reduce the required simulation time. The Gaussian pulse-width in case of RZ-DPSK is 4ps. A one-bit-delay Mach-Zehnder interferometer (MZI) is chosen as a DI in these simulations. The DPSK average input power is set to 5dBm, and the BPF bandwidth is 1.32nm. The DPSK is degraded with simultaneous random differential phase-noise and amplitude-noise. The differential phase-noise is Gaussian with zero mean and standard deviation '$\sigma_{\Delta\phi}$'. The random amplitude-noise is also Gaussian with zero mean and it affects the input DPSK optical signal-to-noise ratio ($OSNR_D$). The degraded DPSK data quality is estimated from the demodulated OOK eye-histograms which carry both input amplitude-noise and phase-to-amplitude converted noise. The quality-factor of the demodulated data is evaluated from the OOK eye-histograms by examining each data bit [9].

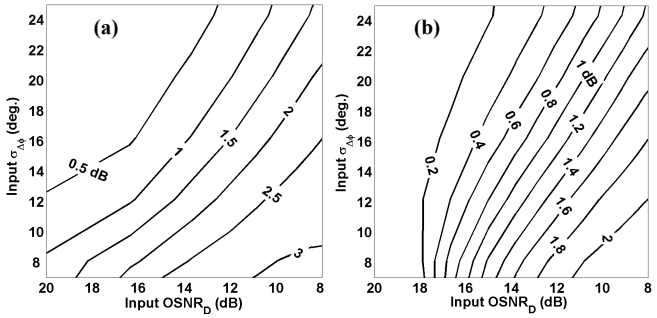


Figure 2. 2-D contour plots of ΔQ for: (a) RZ-DPSK, (b) NRZ-DPSK.

Fig. 2 shows the quality-factor improvement (ΔQ) in case of input RZ-DPSK (a) and NRZ-DPSK (b) for wide range of input noise. The input differential phase-noise '$\sigma_{\Delta\phi}$' ranges from 7° to 25°, whereas input $OSNR_D$ ranges from 20dB to 8dB. The Q always improves at SOA balanced-receiver output even for small input noise. That is because the marks standard-deviation is reduced by balanced gain-compression whereas data is re-amplified without pattern-dependence. Thus the quality-factor always improves (i.e. ΔQ is positive) for the entire tested noise range. Also, the Q improvement indicates that the relatively long SOA recovery-time (100ps), compared to the data bit-period (12ps), is uncritical for proper operation at 80Git/s. This is because co-propagation of complement orthogonally-polarized streams allows marks to exist in each bit-period and thus no pattern dependence is introduced. As shown in Fig. 2, the Q improvement increases as the $OSNR_D$ reduces, because more input amplitude-noise is suppressed by gain-compression inside SOA. However, the Q improvement reduces as the phase-noise ($\sigma_{\Delta\phi}$) increases, as the OOK extinction-ratio at DI output becomes smaller. Therefore, the receiver capability to reduce input amplitude-noise is better than that for converted phase-to-amplitude noise.

The received data probability-of-error (i.e. Bit-error-ratio) is evaluated at 80Gbit/s for RZ and NRZ DPSK in case of single-ended and balanced detection before SOA and at the system output, Fig. 3. The $OSNR_D$ of received DPSK is degraded using an attenuator followed by an EDFA before the SOA balanced-receiver. The BER is estimated by carefully analyzing the received marks and spaces probability-density functions [2]. For the case of RZ-DPSK, the estimated improvement of receiver-sensitivity at 10^{-9} BER (onset of error-free), compared to the single-ended input, is ≅4.6dB in case of single-ended output and ≅7dB in case of balanced-detected outputs. For the case of NRZ-DPSK, the estimated improvement is ≅4.2dB in case of single-ended output, and ≅5.6dB in case of balanced-detected outputs. Although the technique does not correct bit-errors (i.e. mark or space flipping), it re-amplifies received OOK data without adding much amplitude-noise, which improves overall optical signal-to-noise ratio and thus receiver-sensitivity.

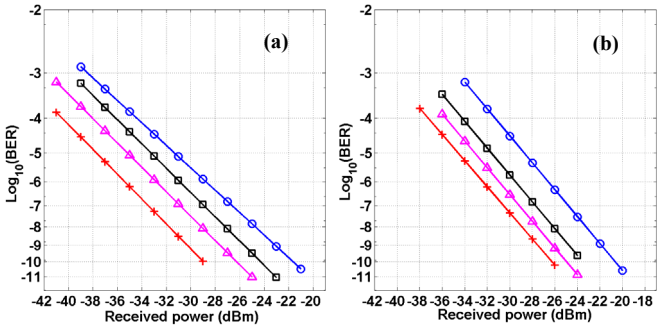


Figure 3. 80Gbit/s BER of demodulated (a) RZ-DPSK, and (b) NRZ-DPSK in case of: single-ended input (circles), balanced-detected inputs (squares), single-ended output (triangles), and balanced-detected outputs (plus).

IV. Conclusions

A single polarization-insensitive SOA is utilized to improve receiver-sensitivity for 80Gbit/s RZ (NRZ) DPSK data using balanced gain-compression and amplification. The single-ended receiver-sensitivity improvement is better than common balanced-detection technique. The SOA long recovery-time proves to be uncritical for proper operation. The receiver could be easily implemented by any kind of DI and commercially available components. It also could be monolithically integrated to reduce the system overall footprint and cost.

References

[1] A. H. Gnauck, et al, "Optical Phase-Shift-Keyed Transmission," J. of Lightwave Tech. 23, 115-130, Jan. 2005.

[2] H. Kim, et al, "Experimental Investigation of the Performance Limitation of DPSK Systems Due to Nonlinear Phase Noise," Photon. Technol. Lett. 15, 320-322, Feb. 2003.

[3] M. Matsumoto, et al, "Performance improvement of DPSK transmission by PS amplitude limiter," Opt. Exp. 15, 8094-8103, Jun. 2007.

[4] V. S. Grigoryan, et al, "SOA-Based Regenerative Amplification of Phase-Noise-Degraded DPSK Signals: Dynamic Analysis and Demonstration," J. Lightwave Technol. 24, 135-142, Jan. 2006

[5] K. Cvecek, at al, "2R-Regeneration of an 80Gbit/s RZ-DQPSK signal by a Nonlinear Amplifying Loop Mirror," Photon. Technol. Lett. 19, 1475-1477, Oct. 2007.

[6] K. Croussore, et al, "Demonstration of phase-regeneration of DPSK signals based on phase-sensitive amplification," Opt. Exp. 13, 3945-3950, May 2005.

[7] E. S. Awad, "A Technique for Rephasing+2R regeneration of 40 Gbit/s NRZ-DPSK data," Photon. Tech. Lett. 20, 848-850, May 2008

[8] A. E. Siegman, Lasers, (University science books, 1986).

[9] N. S. Bergano, et al, "Margin Measurements in Optical Amplifier Systems," Photon. Tech. Lett. 5, 204-206, Mar. 1993.

Passive Mode-Locking in Quantum Well Lasers

J. Javaloyes, P. Stolarz, L. Hou, M. Sorel and A.C. Bryce
Department of Electronics and Electrical Engineering,
University of Glasgow, Glasgow, G12 8LT, United Kingdom

S. Balle
Institut Mediterrani d'Estudis Avançats (IMEDEA),
CSIC-UIB, C/ M. Marques, 21, 07190 Esporles, Spain.

***Abstract*—We study the Mode-Locking dynamics of 40-GHz semiconductor Fabry-Pérot lasers with intracavity saturable absorber by using a Travelling-Wave-Model and a time-domain response of the semiconductor material. We analyze the influence of several key parameters and compare our predictions with the performance of AlGaInAs 1.55-μm Strained Quantum Well laser.**

***Index Terms*—Mode Locked lasers, Semiconductor Lasers.**

I. Introduction

Mode-locking (ML) of lasers is a subject of intense research both theoretically and experimentally. The theoretical challenge arises from the complex nonlinear dynamics involving the self-organization of many laser modes while the experimental motivation comes from the large number of applications of short pulse sources in medicine, metrology and telecommunications [1]. ML has led to the shortest and most intense optical pulses ever generated. Semiconductor mode-locked lasers have the added attraction of being compact, low cost and adaptable to many cavity geometries [2].

Haus' master equation [1] is a widely used approach to study passive mode-locking in the time domain. Analytical predictions on the pulse properties can be assessed under the assumption of weak saturation. However, even if pulse iterative models have provided some useful insight into the mode-locking problem, these approaches when applied to a particular design provide only a qualitative predictions, due to the many simplifying hypothesis involved. On the other hand, approaches based on finite difference time domain description [3] of the electromagnetic field and the semiconductor Bloch equations description of the active medium [4], require enormous computational power which impede parametric studies.

To circumvent these limitations and shed some light onto the mode-locking scenario, we describe the dynamics of the device by resolving the propagation of the electromagnetic waves under the Slowly-Varying-Approximation. The light-matter interaction is described by means of a frequency-domain analytical approximation to the optical susceptibility [5] that we recently transformed into a time-domain description [6]: Our approach provides important spectral features usually disregarded as for instance the abrupt spectral variations of the absorption in the saturable absorber. However, the effectiveness of our approach still allows for parametric studies: a typical 125 ns simulation run [7] is achieved in 15 minuts on a standard PC. As such our model allows for the construction of bifurcation diagrams.

J.J. and S.B. acknowledge financial support from EPSRC (EP/E065112/1) and project BLANCO (TEC2006-13887-C05-03), respectively.

II. Model

We shall consider a Fabry-Pérot cavity divided in two sections. The first one, from $z = 0$ to $z = 1 - l$ is electrically pumped and corresponds to the amplifier section; the second one, from $z = 1 - l$ to $z = 1$, corresponds to a saturable absorber (SA) section of relative length l. We consider that there is no reflectivity at the amplifier-SA interface, and that the cavity is defined by simple cleaved facets, i.e. $r \simeq 30\%$.

Within each section, the slowly-varying amplitudes of the forward and backward waves [8], $E_\pm$, evolve according to

$$\begin{aligned}(\partial_t \pm \partial_z) E_\pm(z,t) &= i\Gamma P_\pm(z,t) - \alpha_i E_\pm(z,t) \ , \quad (1)\\ \partial_t N_0(z,t) &= J - R(N_0)\\ &- i\left(P_+ E_+^\star + P_- E_-^\star - c.c.\right) \ , \quad (2)\\ \partial_t N_{\pm 2}(z,t) &= -\left(R'(N_0) + 4\mathcal{D}q_0^2\right) N_{\pm 2}\\ &- i\left(P_\pm E_\mp^\star - E_\pm P_\mp^\star\right) \ , \quad (3)\end{aligned}$$

where α_i are the internal losses of the system, Γ is the optical confinement factor, and for numerical purposes we have scaled time and space to the cavity transit time and to the optical length of the cavity, respectively. J is the current density injected per unit time (normalized to the electron charge) into the section and $q_0 = (2\pi n_g)/\lambda$ is the optical carrier wavevector. The recombination is assumed to be of the form $R(N) = AN + BN^2 + CN^3$ where A, B and C are the non radiative, bi-molecular and Auger recombination coefficients, respectively. In addition, $N_0(z,t)$ is the quasi-homogeneous component of the spatially dependent, time evolving carrier density, $N_{+2}(z,t) = N_{-2}^\star(z,t)$ is the complex amplitude of the carrier density grating at half the wavelength which is generated by the presence of the two counter-propagating waves and $\mathcal{D}$ is the ambipolar diffusion coefficient. We assume that the SA is reverse biased and presents a sweep out rate of the carriers A_{SA} much larger than in the gain section A_G.

The closure of our model is achieved by providing the link between the polarization and field amplitudes according to [6]

$$\begin{aligned}P_\pm(z,t) &= \int_0^\infty \tilde{\chi}\left[s, N_0(z,u)\right] E_\pm(z,u) ds \quad (4)\\ &+ \int_0^\infty N_{\pm 2}(z,u) \frac{\partial \tilde{\chi}}{\partial N}\left[s, N_0(z,u)\right] E_\mp(z,u) ds \ ,\\ \tilde{\chi}(s,N) &= \chi_0 e^{-(\gamma_\perp + i\Omega)s} \frac{2e^{-i\frac{N}{N_t}\gamma_\perp s} - e^{-ib\gamma_\perp s} - 1}{s} \ , \quad (5)\end{aligned}$$

where $u = t - s$, $\tilde{\chi}(s,N)$ is the Fourier transform of the frequency-dependent susceptibility of the active material found in [5], $\gamma_\perp$ is the intraband dephasing rate and b the top band.

III. Results

In order to assess the operating range and the ML quality and stability, we calculated several bifurcation diagrams as a function of some key parameters [7], e.g. bias current, length and recovery time of the SA and bandgap offset between the gain and the SA section. We used the typical method of numerical continuation: the final solution found for one value of the control parameter is used as an initial condition for the next, slightly different, value of the control parameter.

The typical sequence of bifurcations found upon increasing of the bias current is: steady emission, weak multimode dynamics, stable ML, a bubble of Self-Pulsation (SP) if the SA modulation is sufficiently strong and finally a partial degradation of the pulse train for high drive current (ten times threshold). A similar scenario is also found in Fig. 1 by varying the length of the SA section for a fixed value of the recovery time $A_{SA}^{-1} = 10$ ps.

1) For l ranging from 0% up to 1.25% of the cavity length only a weakly multimode dynamics can be seen.
2) For l from 1.5% to 2%, a transition to stable shallow Harmonic ML is found, see Fig.1a) obtained with 1.5%.
3) For l ranging from 2% to 3% unstable ML appears, with substantial modulation of the pulse amplitudes which is accompanied by a considerable jitter as can be seen in the pulse train in Fig.1 b), obtained with $l = 3\%$.
4) For l ranging from 3% to 5% stable ML exists with very low noise triggered jitter, see Fig.1 c) with $l = 3.75\%$.
5) For l greater than 5.25% the device enters a SP regime, see Fig.1 d) obtained with $l = 6.5\%$.

This phenomenology is in good agreement with the bifurcation map of passively Mode-Locked AlGaInAs 1.55-m strained quantum well laser [9]. The lasers were fabricated with varying saturable absorber lengths at one side of the chip and a 2.5μm wide and 1170μm long straight ridge waveguide define the laser cavity after cleaving. The modal separation is 37.58 GHz. ML is achieved by reverse biasing the SA section thereby increasing the sweep out rate of the photogenerated carriers. Preliminary studies indicate that a reverse Voltage of -3 Volts corresponds to a sweep out time of 10 ps.

Fig. 2 shows the current-Reverse Voltage map of a device with $l = 3\%$. A broad range of stable ML is obtained for reverse Voltages between -2.5 and -3.5 Volts and bias current ranging from two to four times threshold. For this value of the SA length, a small region of SP can be seen. The typical pulsewidth is 1.2 ps with a time bandwith product of 0.6.

IV. Conclusion

The ML dynamics of a semiconductor Fabry-Pérot laser has been explored using a TWM complemented by a new description of the active medium polarization presented in [6]. The effectiveness of our approach allowed us to systematically explore the influence of several important control parameters, and to compare with experimental data. This good qualitative agreement indicates that our modelling approach can be used, upon proper fitting of the material parameters, for optimization of the design of semiconductor ML lasers.

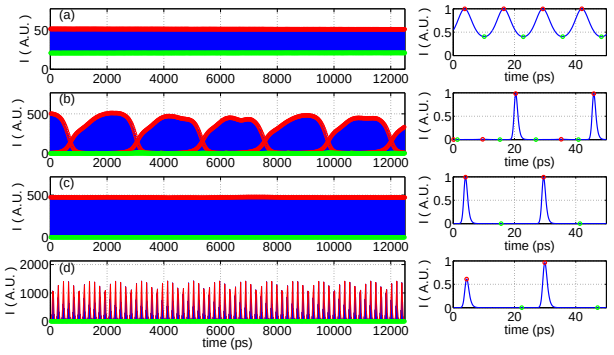


Fig. 1. Long time behavior of the time traces of the field intensity (left) and details of the pulse shape (right). The panels a), b), c) and d) correspond to $l = 1.5\%$, $l = 3\%$, $l = 3.75\%$ and $l = 6.5\%$,respectively

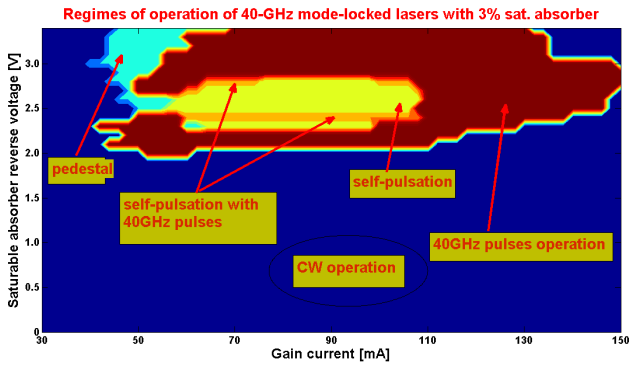


Fig. 2. Experimental operating regime map as a function of the bias current applied to the gain section (horizontal axis) and the reverse voltage applied to the SA section (vertical axis). Blue, light blue, yellow and red indicate no ML, incomplete ML, ML with SP and stable ML, respectively.

References

[1] H. A. Haus, "Mode-locking of lasers," *IEEE J. Selected Topics Quantum Electron.*, vol. 6, pp. 1173–1185, 2000.

[2] E. A. Avrutin, J. H. Marsh, and E. L. Portnoi, "Monolithic and multi-GigaHertz mode-locked semiconductor lasers: Constructions, experiments, models and applications," *IEE Proc.-Optoelectron.*, vol. 147, pp. 251–278, 2000.

[3] K. Yee, "Numerical solution of initial boundary value problems involving maxwell's equations in isotropic media," *Antennas and Propagation, IEEE Transactions on*, vol. 14, no. 3, pp. 302–307, May 1966.

[4] J. Hader, J. Moloney, and S. Koch, "Microscopic theory of gain, absorption, and refractive index in semiconductor laser materials-influence of conduction-band nonparabolicity and coulomb-induced intersubband coupling," *Quantum Electronics, IEEE Journal of*, vol. 35, no. 12, pp. 1878–1886, 1999.

[5] S. Balle, "Simple analytical approximations for the gain and refractive index spectra in quantum well lasers," *Phys. Rev. A*, vol. 57, pp. 1304–1312, 1998.

[6] J. Javaloyes and S. Balle, "Time domain response of the semiconductor media," *Phys. Rev. A*, submitted.

[7] ——, "Mode-locking in semiconductor fabry-pérot lasers," *Quantum Electronics, IEEE Journal of*, submitted 2010.

[8] L. Narducci and N. B. Abraham, *Laser Physics and Laser Instabilities*. Singapore: World Scientific, 1988.

[9] L. Hou, P. Stolarz, J. Javaloyes, R. Green, C. Ironside, M. Sorel, and A. Bryce, "Subpicosecond pulse generation at quasi-40-ghz using a passively mode-locked algainasinp 1.55- $muhboxm$ strained quantum-well laser," *Photonics Technology Letters, IEEE*, vol. 21, no. 23, pp. 1731–1733, Dec.1, 2009.

Photon-Photon Resonance Enhanced Modulation Bandwidth in CCIG lasers

Marco Vallone, Paolo Bardella, Ivo Montrosset
Dipartimento di Elettronica
Politecnico di Torino
Torino, Italy
marco.vallone@polito.it

Abstract— **The combined use of static and dynamic (FDTD) models allowed to determine the operation conditions of photon-photon resonance to increase lasers -3dB modulation bandwidth. The procedure, applied successfully to different laser structures exploiting this effect, is here applied to three-sections Coupled Cavity Injection Grating (CCIG) laser.**

Multisection lasers, modulation bandwidth, transfer matrix, FDTD.

I. INTRODUCTION

The continuous demand for high data rates in data communication systems increases the need of high speed, low cost light sources. Conventional lasers are internally limited by material properties, mainly the carrier transport time, determining a relatively low relaxation frequency. The possibility to use higher longitudinal modes, exploiting a photon-photon resonance (PPR) to obtain Extended Modulation Bandwidth (EMB) operation has been already studied both theoretically and experimentally, for DFB, DBR and in multi-section lasers such as Coupled Cavity Injection Gratings [1-5].

In this work we present a systematic procedure to find EMB condition that we applied to all the previous cases and we report here the application to a CCIG laser composed by two cavities (active and passive) separated by a grating section. The occurrence of this condition has been explored by varying the refractive index of the passive sections and evaluating the mode spacing between the lasing mode and the adjacent ones with a static model program. In this way, the conditions to obtain PPR are found exploiting the compound cavity interference effects. Successively the occurrence of these conditions for the three-sections laser has been verified using a Finite Difference Time Domain (FDTD) dynamic model [6].

II. THE MODEL

We studied the behavior of a three-section 1550 nm emitting multi-quantum wells AlGaInAs laser, made by a 100 µm active section, a 400 µm grating region with 20 cm^{-1} coupling coefficient, and a 100 µm passive cavity. The last two sections allow selecting the stationary mode positions and fine-tuning the frequency-distance of PPR from the main resonance. Both cavity terminal facets are cleaved.

A. Static Model

The static model is based on the well-known coupled modes equation relating the slow varying components of the co-propagating and contra-propagating fields in each section. Exploiting the transfer-matrix formalism, we end with a resonance condition on roundtrip gain (G=1) that allows for finding threshold lasing wavelength λ_m, the corresponding modal gain g_m and the threshold current. In this analysis refractive index changes due to dispersion and induced by gain variation are represented as in [5]. Resonance wavelengths for the other cavity modes at the laser threshold current are obtained searching for the wavelengths λ_n satisfying the roundtrip phase condition for integer n $\phi = 2n\pi$ with $n \neq m$ and $|G_n| < 1$.

B. FDTD Dynamic Model

The investigation of the dynamic properties of the device is performed using a FDTD model where all the effects introduced in the static model are considered. This model was initially used to validate the results obtained by the static model by computing the optical spectra at threshold, thus verifying the position of the modes. The dynamic model was then employed to calculate the electrical small signal modulation response of the device and the eye diagrams at different injected currents and bit frequencies.

III. MODELS RESULTS

Two conditions are required to obtain the EMB behavior: the lasing mode should be detuned respect to the reflectivity peak (detuned loading) and its distance respect to the cavity mode at the longer wavelength side should be below the Free Spectral Range (FSR). An example of solution exploiting this feature is reported in Fig. 1. The inset of the Fig. 1b reveals that the lasing mode belongs to a 3-folded solution, namely the lasing one (on the left), a central, unstable solution, and a stable competing one (on the right). This feature is due to the compound cavity [1] that allows for modes separation Δf_0 closer than the FSR.

Varying the effective index in grating (n_{grat}) and passive (n_{phase}) sections, a map for Δf_0 (n_{grat}, n_{phase}) has been built-up and it is shown in Fig. 2; the mode frequency separation below 40 GHz localizes operation conditions with possible EMB.

The research leading to these results has received funding from the European Community's Seventh Framework Programme (FP7/2007-2013) under grant agreement n°224366 (De light project).

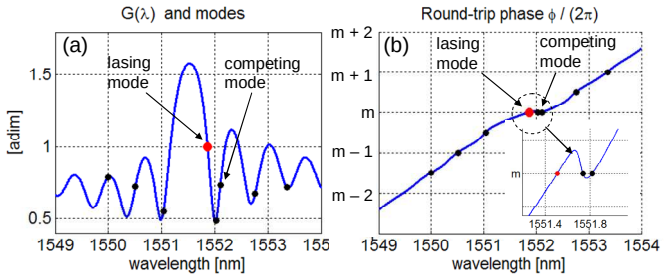


Figure.1: Example of round trip gain $|G|$ (a) and phase $\phi(G)$ (b), versus wavelength. Dots represent lasing (red) and competing (black) modes.

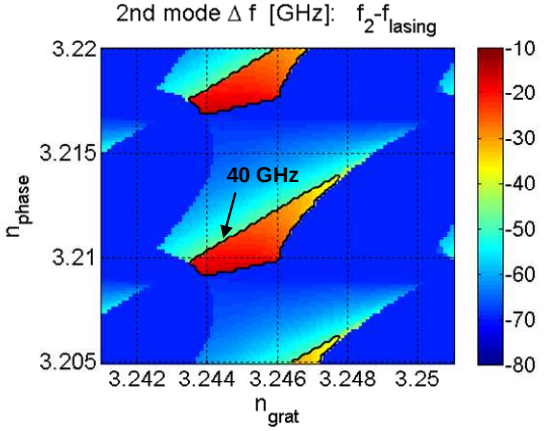


Figure 2: Frequency separation Δf_0 map in the space of effective indexes of grating and passive sections. An arrow indicates the 40 GHz contour.

Having fixed n_{phase} at 3.21 and varying n_{grat}, static and dynamic models yield the results shown in Fig. 3, where the modes position in the (n_{grat}, λ) plane is shown. EMB can take place only when a mode (blue track: static model, crosses: FDTD) is very near ($\delta\lambda$ < 0.2-0.3 nm) and on the longer wavelength side to the lasing mode (red track and circles respectively).

In order to verify the effect of PPR on CCIG modulation bandwidth, many FDTD simulations have been performed for different values of n_{grat} to calculate the small signal modulation (IM) response. This modulation map, reported in Fig. 4, shows that, for values of n_{grat} near 3.2425, in addition to the resonance peak around 8GHz, a strong peak appears at 58 GHz. This second peak is originated by PPR and its position is exactly the frequency separation between the lasing mode and its closest one. By increasing n_{grat}, the frequency distance between the modes reduces (see Fig. 3), and the gap between the relaxation oscillation peak and the PPR is also progressively reduced (A), until a 33 GHz -3dB modulation bandwidth condition is obtained (B). For an additional increase of n_{grat} (C), the two modes merge leading to the formation of a strong peak in the IM.

We finally report in Fig. 5 the eye diagrams obtained by a large signal modulation at 33GHz and 40GHz of the CCIG at the maximum EMB small signal modulation condition. The results are comparable to what presented in [3] for a DFB with feedback controlled by an integrated external cavity.

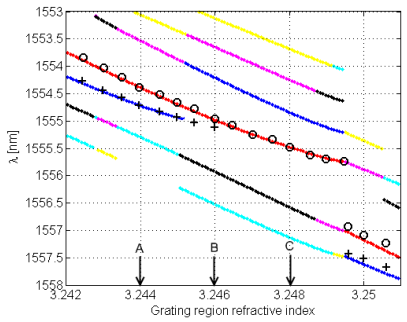


Figure 3: Modes map (static model: solid line; FTDT: circles and crosses). EMB may occurs for n_{grat} in [3.244, 3.246] range between lasing (o) and side (x) modes.

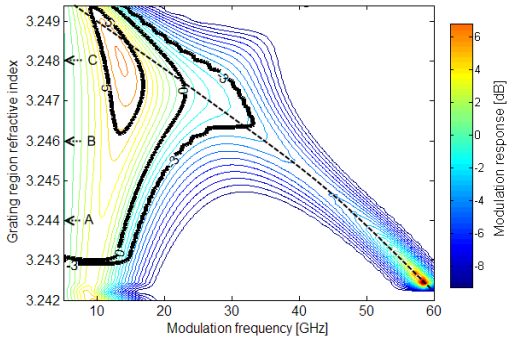


Figure 4: Map of the small signal modulation responses, calculated at 70 mA (2 I_{th}) as a function of n_{grat}. Black lines +3, 0 ,-3dB contours.

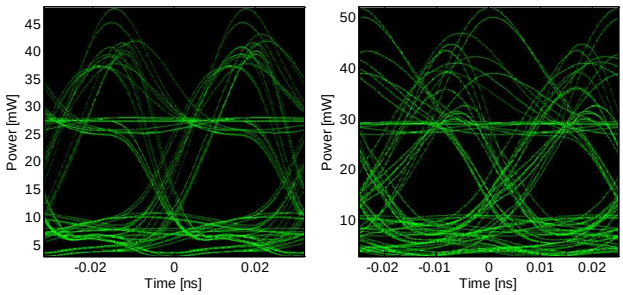


Figure 5: CCIG eye diagrams obtained by a directly current modulation between 45mA and 100mA at 33GHz (left) and 40GHz (right).

IV. Conclusions

Two complementary models have been proposed to search for EMB operation. First, a static analysis of the laser cavity modes allows finding proper PPR conditions, then with FDTW the condition for EMB is verified by computing both the small and large signal modulation responses. As an example, we reported the results obtained for a CCIG laser. A correct positioning of the cavity modes through a fine-tuning of the device parameters allowed obtaining a -3dB EMB of around 33GHz.

References

[1] G. Mortier et al., *IEEE J. Quantum Electron.*, vol. 36, n. 12, Dec. 2000.

[2] U. Feiste, *IEEE J. Quantum Electron.*, vol. 34, n. 12, Dec. 1998.

[3] M. Radziunas et al., *IEEE J. Sel. Top. Quantum Electron.*, vol. 13, 2007

[4] U. Troppenz et al., EOS Annual Meeting 2008

[5] W. Kaiser et al., *IEEE Photon. Technol. lett.*, vol. 16, n. 9, Sept. 2004.

[6] P. Bardella et al., *IEEE J. Sel. Top. Quantum Electron.*, vol. 11, 2005

Design and Continuous-Wave Characterization of Electrically Pumped VECSELs Suitable for Passive Modelocking

W.P. Pallmann[1], Y. Barbarin[1], M. Hoffmann[1], P. Kreuter[2], B. Witzigmann[2,3], M. Golling[1], T. Südmeyer[1] and U. Keller[1]

[1]Department of Physics, Institute for Quantum Electronics, ETH Zurich, Switzerland
[2]Department of Information Technology and Electrical Engineering, Integrated Systems Laboratory, ETH Zurich, Switzerland
[3]Dep. of Electrical Engineering and Computer Science, Computational Electronics and Photonics Group, University of Kassel, Germany
Author e-mail address: pallmann@phys.ethz.ch

***Abstract*—An ultrafast electrically pumped VECSEL design suitable for passive modelocking requires an acceptable trade-off in cw output power. Validating our design guidelines, 120 mW of cw output power are generated. Homogenous current injection is achieved even for large devices, as predicted by our simulations.**

Keywords-Semiconductor lasers, vertical emitting lasers, passive modelocking

I. INTRODUCTION

Optically pumped vertical external cavity surface emitting lasers (OP-VECSELs) are ideally suited for passive modelocking [1], achieving sub-100-fs pulses [2] and high average power (2.1 W in 4.7 ps pulses [3]). Furthermore, these ultrafast VECSELs generate diffraction-limited, circular output beams making them highly attractive for numerous applications such as biomedical imaging or optical clocking of multi-core processors. However, optical pumping substantially increases packaging requirements. In 2003, Novalux Corporation reported a continuous-wave (cw) output power of 900 mW from their proprietary electrically pumped VECSEL (EP-VECSEL), referred to as the NECSEL [4]. Despite this impressive cw performance, modelocked NECSELs have only generated <40 mW average output power in 15 ps pulses so far [5]. Unfortunately the detailed design parameters of the NECSEL have not been published.

Passive modelocking of EP-VECSELs requires a design optimization with an acceptable trade-off in cw output power with less field enhancement in the gain structure. This is necessary for stable modelocking which requires reduced dispersion and fundamental transverse mode operation even in larger devices. Recently, we have performed a detailed numerical analysis of EP-VECSELs and developed optimized designs compatible with passive modelocking [6]. Here we present the first experimental verification of our design in cw operation. Scaling of the average power can be achieved by different aperture diameters. We have generated a cw average output power of 120 mW with a bottom disc contact diameter (Fig. 1) of 180 µm. We realized a series of 60 EP-VECSELs of different sizes, enabling us to study the current profile as function of various design parameters. For all devices, the measured spatially resolved electroluminescence matches our numerical simulations. Even for devices with large mode diameter, a homogenous inversion profile can be realized. In a next step we will investigate the modelocking performance of our devices.

II. EP-VECSEL DESIGN AND FABRICATION

The design of our EP-VECSELs has been previously simulated and the trade-off between electrical and optical properties has been discussed in [6]. Fig. 1 shows a schematic diagram of our electrically pumped semiconductor gain structure. The EP-VECSEL is a linear cavity using this structure and an external curved output coupler as the two end mirrors. A good confinement of the injected current into the center of the device is ensured by an optimized p-doped distributed Bragg reflector (DBR), a small bottom disc contact, and a thick current spreading layer (CSL) with a top ring electrode. The low mobility of the holes in the p-DBR confines the carriers to the space above the bottom disc contact and the high mobility of the electrons in the thick current spreading layer allows their recombination in the center of the device [6]. Our simulations show a homogeneous transverse inversion profile even for larger device diameters, which enables TEM_{00} mode control.

A low reflective n-DBR between the active region and the current spreading layer and an anti-reflection (AR) section on top of the structure are introduced to enhance the gain of the structure and to reduce the cavity losses by decreasing the field strength in the doped top layers. The AR section and the moderate thickness of the current spreading layer reduce the dispersion, favoring stable modelocking.

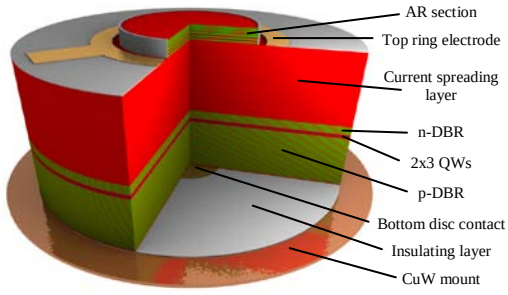


Figure 1. Sketch of our EP-VECSEL gain structure.

The structure was grown by molecular beam epitaxy (MBE) in reverse order for substrate removal. The growth of a p-doped DBR with low optical losses and low electrical resistance is challenging. To reduce the resistance of the 30 pairs p-DBR, a 16 nm "staircase grading" with five $Al_{(1-x)}Ga_xAs$ layers of different composition was inserted between each AlAs/GaAs interface. Additionally, the doping levels were increased in layers where the electrical field is low, which adds no significant additional optical losses. The doping levels in the p-DBR going from bottom to top are $[5, 4, 3, 2]\cdot10^{18}$ cm^{-3} for the pairs [1-15, 16-20, 21-25, 26-30], respectively. The active region consists of two groups of three InGaAs Quantum Wells (QWs) spaced by 10 nm and placed in two antinodes of the electrical field. In this first realization, the n-DBR has 11 AlAs/GaAs pairs without any grading, the doping concentration is $2\cdot10^{18}$ cm^{-3}. The GaAs current spreading layer is 6 µm thick and n-doped at a concentration of $2\cdot10^{18}$ cm^{-3}. The top GaAs contact layer (between the AR section and the CSL) is 150 nm thick with a doping concentration of $6\cdot10^{18}$ cm^{-3}. The top AlAs/GaAs AR section is undoped. The EP-VECSEL's total resistance and the heat generated in the structure have been simulated for high injection currents. The epitaxial layers have been fine tuned to obtain a lasing wavelength around 965 nm at an internal temperature of about 100-120°C. Accordingly, the QWs emission wavelength has been detuned by 25 nm. The different EP-VECSELs have been processed on a single chip in the FIRST cleanroom facility at ETH Zurich. For efficient heat removal, the chip is bonded to a CuW mount, which has the same coefficient of thermal expansion as GaAs.

III. Experimental Results

The lasing performance of the 60 EP-VECSELs has been measured in a simple straight cavity and near room temperature (T=3°C) using an output coupler with a radius of curvature of 25 mm and a transmission of 10%. The output powers obtained for the different EP-VECSEL sizes are plotted in Fig. 2. The linear increase of power as function of the bottom contact diameter demonstrates power scalability up to 120 mW. The light-current-voltage (L-I-V) curves of an EP-VECSEL with more than 100 mW power using a 5% output coupler are plotted in Fig. 3, a thermal roll-over is not visible. The differential quantum efficiency at 525 mA is about 25% and the wall-plug efficiency about 5% due to the higher resistivity of the bottom p-DBR required for better laser mode control. The efficiencies will be improved by using an optimized p-doped DBR.

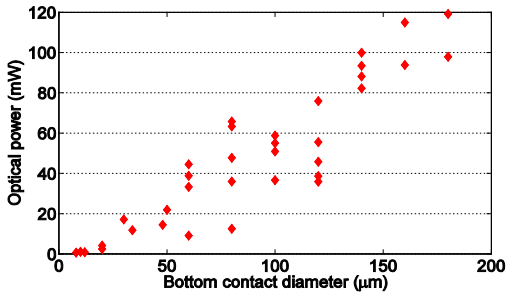


Figure 2. Output power of EP-VECSELs in a straight cavity with a 10% output coupler as function of the bottom disc contact diameter.

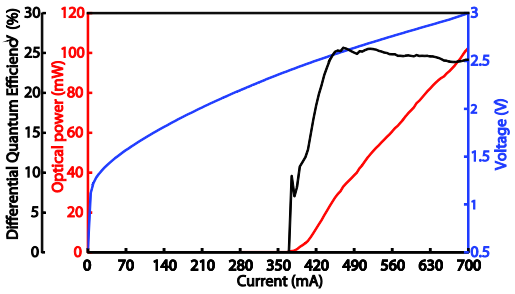


Figure 3. L-I-V curves from an EP-VECSEL with a disc contact Ø of 140 µm, top contact Ø of 300 µm and using a 5% output coupler.

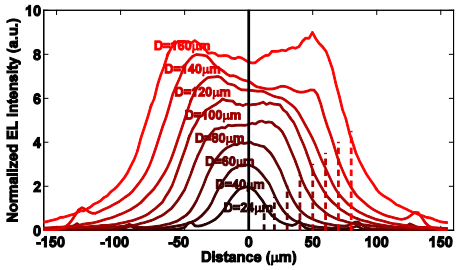


Figure 4. Electroluminescence profiles of EP-VECSELs with different back contact diameters recorded at high current injection.

A lower current threshold value could be expected but the QWs detuning of 25 nm increases the lasing threshold. The differential resistance of the laser presented in Fig. 3 is ~2.1 Ω at lasing threshold. Fig. 4 shows electroluminescence profiles of EP-VECSELs with different back contact disc diameters. Devices with p-DBR apertures larger than 100 µm diameter are not favorable for TEM_{00} beams.

IV. Conclusion And Outlook

We present a detailed experimental study on electrically-pumped VECSELs. The measured electroluminescence profiles are in very good agreement with our simulations [6]. The lasing results demonstrate scalability of the output power up to 120 mW. In a next step, we will perform modelocking experiments and further optimize the presented design.

References

[1] U. Keller, and A. C. Tropper, "Passively modelocked surface-emitting semiconductor lasers," Phys. Rep. **429**, 67-120 (2006).

[2] K. G. Wilcox, Z. Mihoubi, S. Elsmere, A. Quarterman, I. Farrer, D. A. Ritchie, and A. Tropper, "70-fs Transform-Limited Pulses Emitted by InGaAs/GaAs Quantum Well Laser," in *Advanced Solid-State Photonics (ASSP)* (Denver, USA, 2009), p. ME4.

[3] A. Aschwanden, D. Lorenser, H. J. Unold, R. Paschotta, E. Gini, and U. Keller, "2.1-W picosecond passively mode-locked external-cavity semiconductor laser," Opt. Lett. **30**, 272-274 (2005).

[4] J. G. McInerney et al., "High-power surface emitting semiconductor laser with extended vertical compound cavity," Electron. Lett. **39**, 523-525 (2003).

[5] M. E. Kurdi, S. Bouchoule, A. Bousseksou, I. Sagnes, A. Plais, M. Strassner, C. Symonds, A. Garnache, and J. Jacquet, "Room-temperature continuous-wave laser operation of electrically-pumped 1.55 µm VECSEL," Electr. Lett. **40**, 671-672 (2004).

[6] P. Kreuter, B. Witzigmann, D. J. H. C. Maas, Y. Barbarin, T. Südmeyer, and U. Keller, "On the Design of Electrically-Pumped Vertical-External-Cavity Surface-Emitting Lasers," Appl. Phys. B **91**, 257-264 (2008).

Simulation and Design of Quantum-Dot Lasers Operating in Dual-wavelength Passive Mode-locking Regime

Mattia Rossetti, Paolo Bardella, Ivo Montrosset,
Dipartimento di Elettronica
Politecnico di Torino
Torino, Italy
mattia.rossetti@polito.it

Stefan Breuer, Wolfgang Elsäßer
Institute of Applied Physics
Technische Universität Darmstadt
Darmstadt, Germany

***Abstract*— Simultaneous pulse generation from ground state and excited state transitions in a two-section quantum-dot laser is studied via a finite-difference travelling-wave model; design rules to obtain stable dual-wavelength mode-locking regime over a wide range of bias current and voltage are proposed.**

Quantum-dot laser; passive mode-locking; two-state lasing; finite-difference travelling-wave model;

I. INTRODUCTION

Passively mode-locked (ML) two-section lasers based on self-assembled InAs quantum-dots (QD) have shown an impressive potential for the generation of picosecond and sub-picosecond pulses thanks to their ultrafast absorption recovery, high differential absorption, low frequency chirp and large gain spectral bandwidth. The possibility to generate picosecond pulses involving either ground state (GS) or excited state (ES) interband transitions has been demonstrated and the switching between these two regimes has been obtained by simply changing the voltage applied to the saturable absorber (SA) section or the injected current supplied to the gain section [1]. Moreover self-pulsating regimes involving simultaneous GS and ES lasing have been studied both experimentally and theoretically [2][3].

Recently, operating regimes characterized by the coexistence of stable GS and ES mode-locked pulses have been demonstrated in QD lasers emitting around 1.3 μm [4][5]. In [4], such a dual wavelength mode-locking (DW ML) regime is achieved over a small range of currents in the gain section. At low currents, GS mode-locking occurs. Increasing the current up to about three times the GS threshold, ES emission takes place and DW ML is achieved. Increasing further the current however, ES lasing dominates and GS lasing tends to disappear.

Breuer et al. [5] recently observed the DW ML regime in a differently designed laser characterized by a significant wavelength chirp between the QD layers: contrary to [4], at low currents, ML pulses from the ES transition are observed, already for a SA bias of 0 V (short circuit). Increasing the gain current up to about 1.25 times the ES threshold, the GS lasing is achieved and the DW ML regime can be found over a wide range of applied currents. Clear indication of the simultaneity of GS and ES ML pulses in the DW ML regime is confirmed by four-wave-mixing (FWM) in the baseband of the radio-frequency spectrum.

In this paper we present a numerical study of the DW ML regime in a two-section QD laser using a finite-difference time-domain (FDTD) model [6][7]. Starting from the results shown in [5], we propose simple design rules for the simultaneous generation of ML pulses from both GS and ES transitions in a two-section QD laser.

II. FINITE-DIFFERENCE TIME-DOMAIN MODEL

We implemented a finite-difference time-domain travelling-wave model for the simulation of passive mode-locking in QD lasers. As described in [6][7], the propagation equations, describing the field evolution along the laser cavity at both GS and ES characteristic transition wavelengths, are solved in time domain via a finite-difference approach. The optical response of the QD active layers is introduced in the propagation equations through proper polarization terms. This terms provide the coupling between the field equations and a set of rate equations describing the population dynamics within the QD states, carrier capture and escape processes in and out the quantum well (QW) states and the carrier dynamics in the three-dimensional states of the separate-confinement heterostructure (SCH). The dependence of the population dynamics to the applied voltage in the QD system belonging to the SA section is then properly taken into account through voltage dependent thermionic escape rates and tunneling rates, affecting the SA absorption recovery.

Additional effects such as the inhomogeneous gain broadening induced by the QD size fluctuations, the related gain and refractive index dispersion and self phase modulation (SPM) have been introduced in the numerical model via a proper description of the polarization terms in the field equations, implemented using a set of infinite impulse response (IIR) numerical filters. Since their numerical implementation significantly increases the computational cost of the simulations due to the requirements on the integration time step, such effects were at first neglected in order to perform a systematic study of the role played by QD material and device parameters on the ML regime. Performing final simulations

The research leading to these results has received funding from the European Community's Seventh Framework Programme (FP7/2007-2013) under grant agreement n° 224338 (FAST-DOT project).

taking such effects into account, we found that the main features of the studied ML regimes were preserved, revealing that, in the simulated structures, they only give rise to higher order corrections on the steady-state ML regime.

III. Simulation Results and Discussion

In order to obtain a stable DW ML regime over a wide range of bias conditions in a two-section QD laser, we propose, following the results presented in [5], to consider a QD laser structure in which the maximum net modal gain achievable at the GS wavelength is slightly smaller, at ES threshold, than the overall losses in the laser cavity i.e. the sum of the mirror losses, intrinsic waveguide losses and saturable losses in the SA section. In order to satisfy this condition, one must therefore carefully design both the laser cavity (cavity length, facet reflectivities, intrinsic waveguide losses) as well as the properties of the QD active medium.

As an example, we consider a QD laser with a 3.3 mm total length, a 300 μm SA section, 3 μm ridge width, cleaved facets and intrinsic waveguide losses of 3.5 cm^{-1} as the one described in [5]. We found that a suitable value for the maximum saturated GS net modal gain allowing to satisfy the condition described above is about 8 cm^{-1}. In [5], such a low gain value was experimentally obtained thanks to the wavelength chirp between the different QD layers composing the active structure. Alternative paths however can be successfully followed in order to achieve such a low QD gain without chirping the QD layers, e.g. reducing the number of identical QD layers in the active region or reducing the QD density. Following these last approaches, in the present paper, the proper QD gain is obtained by considering 6 identical QD layers with a low QD surface density of $1.5 \cdot 10^{10}$ cm^{-2}. With this choice of the QD material properties, also the ES peak gain saturates to a low value of about 13 cm^{-1} due to Pauli-blocking effect.

In Fig. 1a, the simulated state-resolved PI characteristics for a 0V biased SA, obtained using the FDTD model is shown: due to the imposed condition on the QD GS gain, ES threshold occurs first at 105 mA. In the range of currents from 105 mA to 135 mA, a stable ES ML regime is obtained. The ES pulse width tends to decrease slightly when the current is increased (Fig. 1b). The low QD saturated ES gain, significantly contributes to achieve a stable ES ML regime. As a matter of fact, in this regime, the ES differential gain in the gain section is significantly reduced compared to standard QD lasers, guaranteeing a gain saturation energy in the gain section much larger than the absorption saturation energy in the SA which is an essential condition to achieve a stable ML regime.

The ES average output power increases with current up to 4 mW. The absorption of the ES power in the SA induces a photon-pumping process in the QD GSs. This process reduces the SA losses at the GS wavelength, so that at 137 mA GS threshold occurs. We found that at the GS threshold, due to the photon pumping process, a 10% reduction of the average GS absorption in the SA with respect to the unsaturated value is obtained proving that this is the main effect leading to GS lasing. Once the GS lasing is obtained, the DW ML regime occurs over a wide range of applied currents.

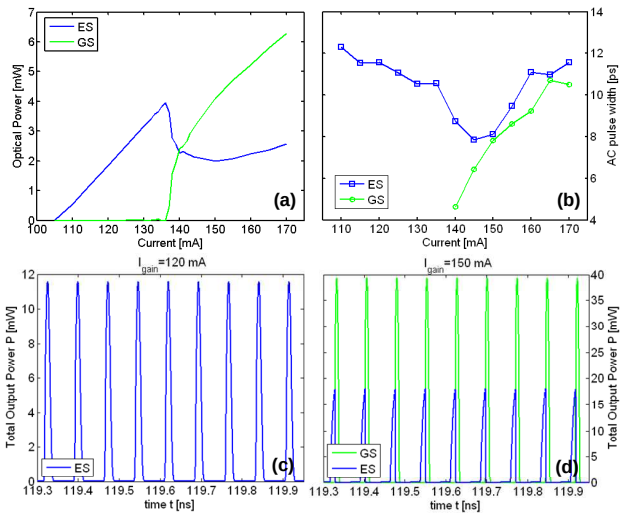


Figure 1. (a) GS and ES average output power versus injected current in the gain section at 0 V SA bias; (b) ML autocorrelation pulse width for GS and ES pulses versus the injected current in the gain section; (c) time trace of ES pulses at 120 mA; (d) time trace of GS and ES ML pulses at 150 mA.

For values of bias current just above the GS threshold, the ES average power is reduced and tends to decrease increasing current. For currents larger than 150 mA however the ES average output power grows up again with current ensuring a large regime where the GS and ES ML pulses coexist. The GS pulse width increases almost linearly with the applied current whereas the ES pulse width approximately follows the behaviour of the ES average power. In Fig. 3d, time traces of GS and ES ML pulses, referring to the DW ML regime at 150 mA, are shown: GS pulses tend to immediately follow the ES ones; this is a consequence of the coupling between the absorption dynamics at GS and ES wavelength respectively, induced by the complex carrier dynamics in the QD SA.

The simulated DW ML regime shows a very good similarity with the experimental results reported in [5], proving that the new proposed design rules represent a alternative method for the realization of QD ML lasers operating in the DW ML regime.

IV. Conclusions

Starting from the experimental results presented in [5], we simulated a DW ML regime in a two-section QD laser with low gain; a possible route for the new design of passively ML QD laser operating in a DW ML regime was shown.

References

[1] M. A. Cataluna et al., Appl. Phys. Lett., 89, 081124 , 2006.

[2] A. Markus et al., J. Appl. Phys., 100, 113104, 2006

[3] E. A. Viktorov et al., Appl. Phys. Lett., 90, 121113, 2007

[4] M. A. Cataluna et al., Digests CLEO Europe - EQEC 2009 European Conference, 14-19 June 2009.

[5] S. Breuer et al., Optics Lett., submitted.

[6] M. Rossetti et al., Digests 1st EOS Topical Meeting on Lasers, Capri, Italy 2009.

[7] M. Rossetti et al., Digests CLEO Europe - EQEC 2009 European Conference, 14-19 June 2009.

Polarization controlled quantum dashes VCSELs

J. P. Gauthier, C. Paranthoen*, C. Levallois, J. M Lamy, H. Folliot, O. Dehaese, A Le Corre
Laboratoire FOTON-INSA, UMR CNRS 6082
Rennes, FRANCE
Cyril.paranthoen@insa-rennes.fr

O. Castany, L. Dupont
Laboratoire FOTON-ENSTB, UMR 6082
Brest, FRANCE

***Abstract*— Polarization controlled quantum dashes (QDHs) VCSEL grown on InP are investigated. Using optimized growth conditions, QDHs are obtained, presenting a polarized photoluminescence at 1.55 µm at room temperature, following the [1-10] direction according to QDH length. VCSEL polarized output laser emission is demonstrated at room temperature. Output VCSEL polarization is oriented following the [1-10] direction, the extinction ratio is as high as 30 dB. Confrontation between QDH and QW VCSEL show improved performances for QDH VCSEL, in terms of polarization stability (static and dynamic) and polarization extinction ratio.**

Keywords- polarization, VCSEL, quantum dashes

I. INTRODUCTION

Vertical cavity surface emission lasers (VCSEL) operating at 1.55 µm present important interests for the telecommunication network. They present the opportunity to benefit from lasers characterized with a circular beam, a spectral purity, and a low cost of fabrication. Nevertheless, one of the most known drawbacks of such laser sources is related to the instability of the optical polarization, leading to an increase of the data bit error rate [1]. By introducing an internal loss anisotropy, nearly stabilized VCSEL have been demonstrated, using surface grating [2], birefringent mirror [3], elliptical cavity [4], and more recently high effective sub-wavelength grating [5]. Nevertheless, this approach requires complex processes. A technological process-free approach, based on the use of an anisotropic gain medium related to substrate orientation has shown polarization but unstable output VCSEL emission [6]. Recently, using InAs quantum dashes (QDHs), we have demonstrated their great interest in polarization controlled and stable output VCSEL emission [7]. In this paper, we present 1.55 µm emitting quantum dashes (QDHs) VCSELs. Polarization resolved measurements show the VCSEL output polarization control. Static and dynamic measurement will be shown.

II. QDHS GROWTH AND OPTCAL CHARACTERISTICS

Samples have been grown on (001) nominally oriented InP substrate, using gas-source molecular beam epitaxy. The nanostructures have been obtained after the deposition at 480°C, of 2.1 InAs MLs on lattice matched $Ga_{0.2}In_{0.8}As_{0.435}P_{0.565}$ quaternary alloy. For capped samples, the double cap procedure has been used in order to control the wavelength emission [8]. A 0.3 sccm low arsenic overpressure has been used, in order to favor adatom migration, and get the QDHs formed. Inset of Figure1 is a 1*1 µm² AFM measurement. QDH appears to be formed along the [1-10] crystallographic orientation. The linear density, height, width and typical length has been estimated to be respectively 30 QDH/µm, 2.5 nm, 25 nm and 200-300 nm.

In VCSEL structures, an important aspect is the maximization of the modal gain, which consists in increasing the modal gain as optimizing the overlapping between this the gain medium and the internal electric field. A peculiar attention has been focused on that point, and simulation have shown that by decreasing the '*conventionnal*' 40 nm spacer layer between each QDH layer down to 15 nm, a nearly twofold increase in the optical confinement factor is expected. Thus, we have optimized the growth of of six QDH layers stacking, separated by a 15 nm spacer layer. AFM do not show any degradation, while optical efficiency at room temperature is still quite important.

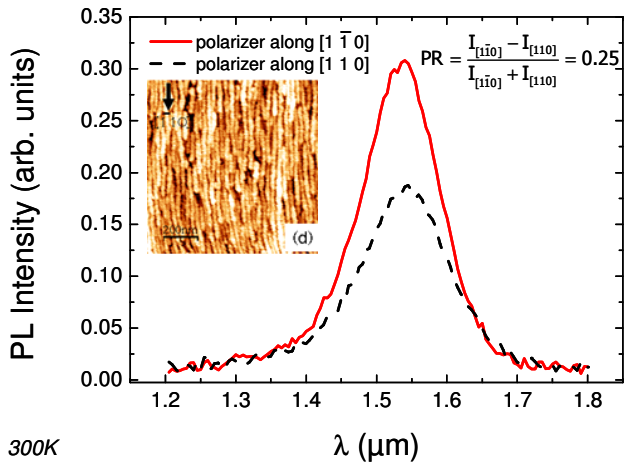


Figure 1 : RT PL of a six QDHs layers sample, separated with a GaInAsP spacer layer of 15nm, as function of the polarizer orientation (collinear with [110] or [1-10] direction). Inset is a 1*1 µm² AFM image of th sixth QDH layers

Figure 1 presents the room temperature photoluminescence (RT PL) spectrum of a six layers QDHs (15 nm spacer layer thickness) sample. The wavelength emission is well centered

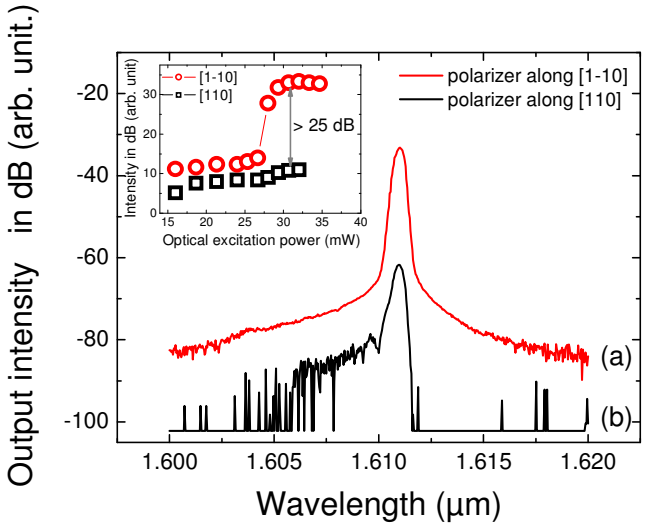


Figure 2 : RT CW laser emission spectra of a 3*6 QDHs VCSEL as function of the polarizer orientation ((a) along [1-10], (b) along [110]), at an excitation power of 30 mW. Inset represents the VCSEL light output integrated intensity versus the optical excitation power, depending on the direction axis of the polarizer, along [110] (squares) and along [1-10] (circles)

at 1.55 µm, the inhomogeneous broadening linewidth related to the size dispersion is 130 nm.

The photoluminescence spectrum appears to be strongly polarized along the [1-10] direction, in relation with the important morphology anisotropy of the QDHs structures. A polarization rate (PR) of 0.25 can be extracted from the measurement. This PR appears to be quite important compared to the value of 0.11 we have measured on a seven lattice matched InGaAs/InP quantum wells (QWs).

III. VCSEL PROCESSING

VCSEL devices containing QDHs have been realized. The active region consists in three groups of 6 QDH layers (or InGaAs QWs lattice matched on InP), each group being located at a stationary electric field maximum intensity position of the microcavity. The microcavity has been designed with two dielectric Bragg mirrors, in order to benefit from a better reflectivity and thermal conductivity in comparison with epitaxial Bragg mirrors available on InP substrate [8]. The dielectric materials used are amorphous silicon and amorphous silicon nitride deposited with a magnetron sputtering system. The lower Bragg mirror of 6 periods is deposited directly on the sample. An Au-In eutectic bonding is employed to transfer the sample on a silicon substrate. The InP substrate is removed by mechanical polishing and chemical etching. The process ends up with the deposition of an upper Bragg mirror of 6 periods.

IV. VCSEL CHARACTERIZATIONS

QDHs VCSEL are optically excited, using a 1.064 µm emitting continuous wave (CW) YAG laser, on a 10 µm diameter spot.

From L(I) curve (see figure 2 inset), laser emission is clearly demonstrated for incident excitation power above 27 mW. Sidemode suppression ratio (not shown) is over 50 dB. For incident power larger than 32mW, the output intensity saturates and even starts to decrease, mainly because of thermal effects.

Polarization resolved measurements have been carried out, to test the QDH VCSEL polarization and stability. A 30 dB extinction ratio optical polarizer has been settled between the VCSEL and the spectrum analyser. Figure 2 represents the output laser spectra of the QDHs VCSEL, depending on the polarizer orientation. Above laser threshold, the QDH VCSEL emission is strongly polarized along the [1-10] direction. The OPSR, defined as the ratio of the laser intensity polarized along [1-10] and the intensity polarized along [110], reaches a maximum value of 30 dB (mainly limited by the polarizer).

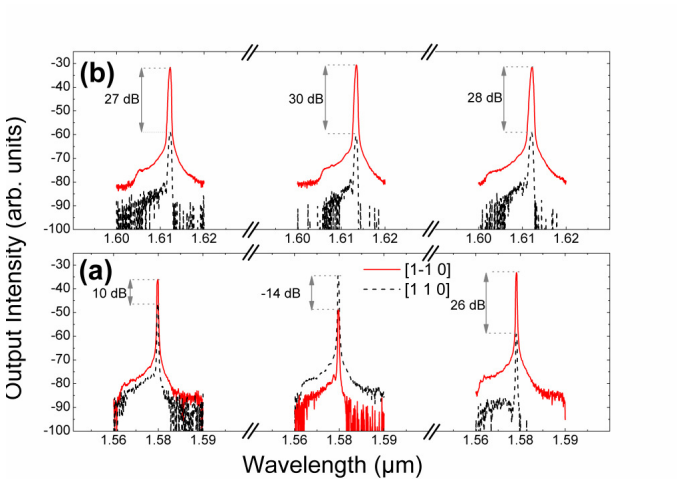


Figure 3 : Typical polarization resolved room temperature spectra from 3*3 QW VCSELs (a) and 3*6 QDH VCSELs (b), measured above threshold (in CW) at different location on samples (average spacing between VCSELs of 4 mm) Continuous line corresponds to the polarizer orientation along [1-10] direction, dashed lines along the [110]. Close to each spectra, the OPSR is indicated.

In order to confront QW VCSEL versus QDH VCSEL, we have made similar polarization resolved experiments, on both QDH and an conventional 1.55 emitting QW VCSELs. Figure 3 presents the output spectra of both VCSELs, depending on the location on a 1 cm² sample. For QDH VCSEL, the output polarization spectrum remains always oriented following the [1-10] direction, and the OPSR is rather constant at 28-30 dB. Regarding the QWs VCSEL performances, the optical polarization orientation changes from a VCSEL location to an another, and the OPSR presents important variations from 25 down to -14 dB. This QW VCSEL polarization instability has been already observed on most VCSELs in CW and modulated devices. Experiments have been investigated, in order test the dynamic stability of

VCSEL output polarization. The set-up consists in modulating the incident optical excitation, using a 1 MHz electro-acoustical modulator. Preliminary results (not shown) have shown that as expected, the QW VCSEL output polarization switches at starting, from a dominant polarization to an another at the end of the pulse. In case of QDH, stable and constant polarization is observed along the whole optical pulse.

CONCLUSION

We have successfully grown QDH nanostructures and realized a QDH VCSEL emitting at the telecommunication wavelength. QDHs exhibit a strong polarized luminescence along the [1-10], corresponding to a polarization rate of 26%. A VCSEL device based on QDHs has been realised. CW lasing is demonstrated at RT. This VCSEL exhibits a stable polarized laser emission on the whole sample without any switching, an OPSR as high as 30 dB is measured. Those QDH VCSELs have been confronted to QW VCSELs. Measurements show that QDH VCSEL output polarization is stable, oriented following the [1-10] direction, in CW and modulated mode; in opposition with QW VCSEL, for which polarization has been observed to switch.

ACKNOWLEDGMENT

This project is supported by the National Agency of Research (ANR), through the project "λ-Access".

REFERENCES

[1] M. B. Tayahi, S. Lanka, J. Wang, J. Catsten, L. Hofmann, and S. Sukanta, Proc. SPIE, **6132** (2006) 61320B.

[2] J. M. Ostermann, P. Debernardi, A. Kroner, and R. Michalzik, Photon. Technol. Lett., **19** (2007) 1301.

[3] A. Valle, L. Pesquera, and K. A. Shore, *J. Lightwave Technol.*, **14** (1996) 2062.

[4] K. D. Choquette and R. E. Leibenguth, IEEE Photon. Technol. Lett., **6** (1994) 40.

[5] M. Ortsiefer, M. Görblich, Y. Xu, E. Rönneberg, J. Rosskopf, R. Shau M. C.Amann, IEEE Photon. Technol. Lett **22**, (2010), 15

[6] Y.L. Okuno, J. Geske, K.G. Gan, Y.J. Chiu, S.P. DenBaars and J.E. Bowers, Appl. Phys. Lett,. **82** (2003) 2377.

[7] J. M. Lamy, C. Paranthoen, C. Levallois, A. Nakkar, H. Folliot, J. P. Gauthier, O. Dehaese, A. Le Corre and S. Loualiche, Appl. Phys. Lett. **95**, 011117(2009)

[8] C. Levallois, A. Le Corre, S. Loualiche, O. Dehaese, H. Folliot, C. Paranthoen, F. Thoumyre, and C. Labbe, J. Appl. Phys, **98** (2005) 43107

Further miniaturized retro-reflector cavity semiconductor micro-ring lasers

Z. Wang [1,2], G. Yuan[1,2], X. Cai[1], S. Yu[1]
1. Department of Electrical and Electronic Engineering, University of Bristol, Bristol, BS8 1TR, UK,
2. School of Optoelectronic Information, UESTC, Chengdu, 610054, China
s.yu@Bristol.ac.uk

G. Verschaflt, J. Danckaert,
Department of Applied Physics and Photonics, Vrije Universiteit Brussel, Brussel, B-1050, Belgium

***Abstract*— Novel retro-reflector cavity semiconductor ring lasers have been designed to achieve micro-sized devices. Fabricated devices lase CW at room temperature and demonstrate clear bistability down to 16μm radius. The retro-reflector is further miniaturized for smaller devices of < 10μm radius and proofed in CW lasing ring lasers.**

Keywords - semiconductor ring laser; integration; mirror; retro-reflector.

I. INTRODUCTION

Recently, semiconductor ring lasers (SRL) have attracted much interest because they offer switching, regeneration, digital and memory potentials suitable for all optical signal processing [1-4]. The intuitive circular and racetrack devices exhibit strong directional bistability [5-7]. To decrease the device size, these cavities may encounter several problems including backscattering, current leakage, and low output coupling ratio due to the strong optical confinement by the deep-etched ridge waveguides in a circular cavity. These problems can be avoided by combining shallow-etched ridge waveguides with carefully designed mirrors to form rectangular ring cavities. Here the design and fabrication of the mirrors are key to achieving not only low optical loss, but also to achieve low optical back-scattering, as back-scattering is detrimental to the directional bistability of the SRL on which all digital functions are based.

We have used a novel parabolic mirror retro-reflector (RR) mirror design instead of the conventional waveguide total internal reflection (TIR) mirror for this purpose. Two parallel straight shallow ridge waveguides (RWGs) are connected by two RR mirrors to form a closed cavity. The size of SRL can be significantly reduced while maintaining the benefits of low current leakage in the RWGs and minimizing the optical loss caused by conventional TIR mirrors. The key to this proposed SRL structure is the optimisation and fabrication of the RR mirrors.

II. RETRO-REFLECTOR MIRROR DEISGN

In our initial design, the two RWGs are placed in parallel 20 μm from each other (Fig. 1(a)). These waveguides terminate by widening abruptly, leaving the optical beam unconfined horizontally as they enter the body of the RR.

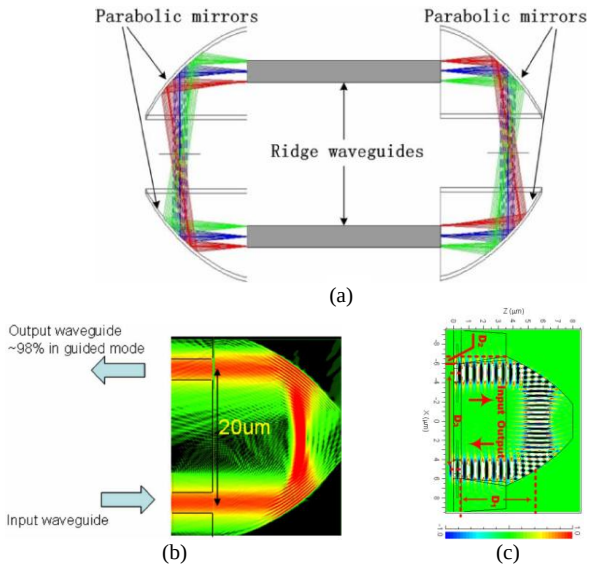


Fig. 1. (a) Design of parabolic mirror RR ring cavity, (b) FDTD simulation of the 20 μm RR, and (c) FDTD simulation of the 10μm RR.

Using parabolas with the waveguide ends on their focal plane as a starting structure, the mirror shape and positions in the RR are optimized by a ray tracing method to maximize the power transmitted via the RR between two parallel waveguides. This is necessary because pure parabolic mirrors only work for far-field while in our case the distance from end of waveguide to mirror is only 10 μm, which is comparable to the 2 μm width of the waveguide therefore cannot use the far-field assumption. Optimisation is achieved by the introduction of higher order aspheric terms into the mirror shape. The resulting mirror shape is verified with finite-difference time-domain (FDTD) simulation, which shows a 98% tansmission between the input and output waveguide modes (Fig. 1(b)).

The 20 μm distance between the waveguides limits the SRL device to a minimum of L=80 μm circumference even if the RWG length is reduced to zero. In practice the smallest devices that can be fabricated is about L=100 μm (equivalent to a R_{eq}=16 μm radius circular cavity) as some length of RWG

The work is supported by EU FP6 under project IOLOS.

is needed to form the output coupler. To further miniaturise the device, the distance between the two RWGs is reduced to 10μm. This would enable a minimum device size of 40 μm circumference (R_{eq}=6.4 μm). The mirror shape was modified and optimized again. The method of including higher order aspheric terms into to the pure parabolic curve used in the previous ray-tracing design has proven to be robust to for the even closer distance of 5 μm between the waveguide end and the mirror. This design again is verified by the finite difference time domain (FDTD) method (Fig.1 (c)). There is a futher trade-off in this even more compact design. The mirror width needs to be shortened because the access s-bend waveguides cannot be curved out too rapidly to prevent significant bending loss from occurring here, Therefore, the extension value D_2 has to be carefully chosen. When D_2 equals to 0.75μm, the transfer power ratio η defined as the output power over input power is ~96.5%, which is slightly smaller than 98% in the previous design.

III. Device Overall Design and Fabrication

All devices are fabricated on the same 5 strained InGaAlAs quantum well wafer emitting at 1550nm. The fabrication involves two different etch depth – shallow etch for the RWG and a 3.5μm deep high quality vertical etching step for the mirrors. Both etching steps are carried out using an Oxford Instrument ICP180 system. The structures achieved after the deep etching are shown in Fig.2(a) and (c).

For the 20 μm RR design (fig.2(a)), the overall device sizes implemented include circumference from 360 to 100 μm, or equivalent to circular radius of R_{eq}=50 to 16 μm. A typical L-I curve is shown in Fig.2(b) for a R_{eq}=25 mm device with 2 directional couplers and 4 output ports. Directional bistability is clearly defined above 80 mA. To achieve the smallest (R_{eq}=16 mm) devices, the directional couplers are terminated as shown in Fig.2(c), where only half the coupler length is used. The bistability in the L-I curve of fig.2(d) is not as clear-cut due to higher back-scattering in this design.

For the 10μm RR design, the main purpose at present is to achieve lasing in order to proof the design. Therefore devices of a relatively large circumference of R_{eq} of 38μm and 70μm are fabricated. The finished device is shown in Fig.2(e) and the L-I curves are shown in (f). The higher thresholds indicate that while lasing is achieved, the loss is higher than the larger RR structure, believed to be due to the extremely tight fabrication tolerance required for this design is barely achievable with the UV photolithography that we used.

I. Conclusion

Novel retro-reflector (RR) based semiconductor ring lasers have been designed to enable very small devices with potentially low threshold, good bistability, and ease of output coupling. Fabricated devcies successfully operated CW at room temperature. For RR width of 20μm, low threshold operation and clear-cut bistability has been achieved, and the smaller 10μm wide RR is also confirmed to be a viable design for even smaller devices to be fabricated. Future devices using e-beam lithography are being fabricated which should provide much better precision and therefore device performance for devices sizes of R_{eq}<10μm.

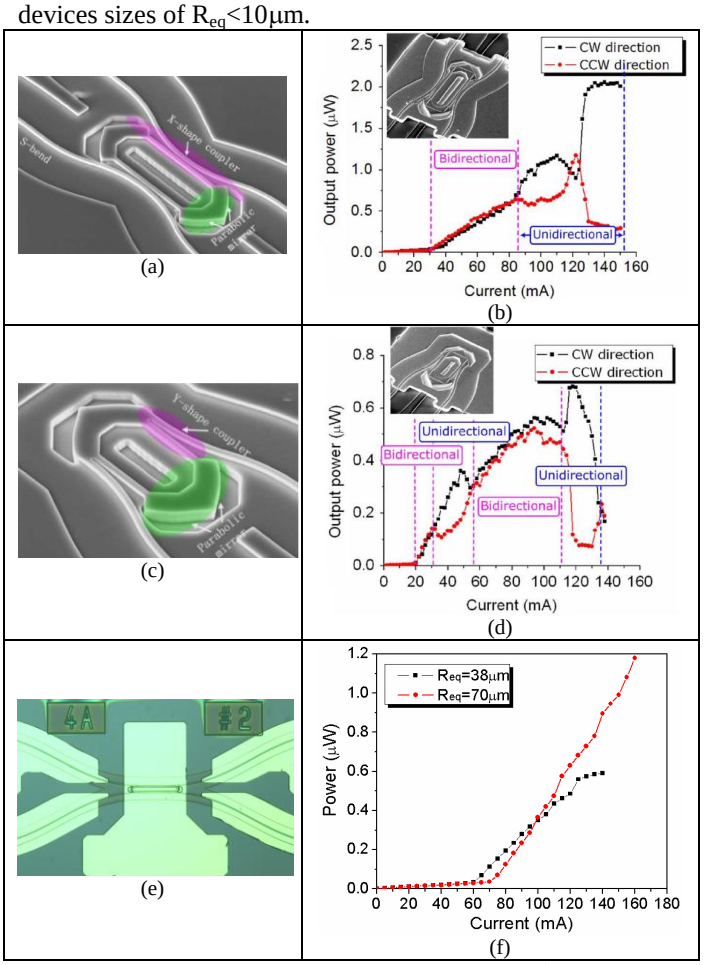


Fig. 2. (a) SRL with 20 mm RR and 4 ouputs, (b) L-I curve of device in (a) (c) SRL with 20 mm RR and 2 ouputs, (d) L-I curve of device in (c), (e)

[1] M. T. Hill et al., "A fast low-power optical memory based on coupled micro-ring lasers," Nature 432, 206–209 (2004)

[2] C.W. Tee, K.A. Williams, R.V. Penty, I.H. White. "Fabrication-tolerant active-passive integration scheme for vertically coupled microring resonator," IEEE Journal of Selected Topics in Quantum Electronics **12**, 108-116 (2006).

[3] A. W. Fang, R. Jones, H. Park1, et al. "Integrated AlGaInAs-silicon evanescent racetrack laser and photodetector," Optics express **15** 2315-22 (2007). http://www.opticsinfobase.org/abstract.cfm?URI=oe-15-5-2315

[4] M. Sorel, G. Giuliani, A. Scire', S. Donati, and P.J.R. Laybourn. "Operating Regimes of GaAs/AlGaAs Semiconductor Ring Lasers: Experiment and Model," IEEE J. Quantum Electron **39**, 1187-1195 (2003).

[5] G. Mezosi, M. J. Strain, S. Furst, Z. Wang, S. Yu, and M. Sorel. "Unidirectional bistability in AlGaInAs micro-ring and micro-disk semiconductor lasers," IEEE Photonics Technology Letters **21**, 88-90 (2009).

[6] S. Yu, Z. Wang G. Yuan, B. Li, M. I. Memon, G. Giuliani, S. Furst, and M. Sorel, "Optically triggered monostable and bistable flip-flop operation of a monolithic semiconductor ring laser," Photonics in Switching conference 2008, pp.115-116, Aug. 2007.

[7] B. Li, M. I. Memon, G. Mezosi, G. Yuan, Z. Wang, M. Sorel, and S. Yu, "All-Optical Response of Semiconductor Ring Laser to Dual-OpticalInjections",IEEE IEEE Photon. Technol .Lett., vol. 20, no. 10, pp. 770-772, May. 2008.

Eigenmode analysis of phase-locked VCSEL-arrays using spatial coherence measurements

Elodie Lamothe, Lars Lundeberg and Eli Kapon
Laboratory of Physics of Nanostructures (LPN),
Institute of Quantum Photonics and Electronics (IPEQ)
Swiss Federal Institute of Technology (EPFL)
1015 Lausanne, Switzerland
elodie.lamothe@epfl.ch

***Abstract*—We study the cavity mode structure of a 2x2 phase-locked VCSEL-array using the modal coherence theory developed by Wolf and Agarwal, coupled mode theory, and spatial coherence measurements. The eigenmode content is derived as a function of the injected current, revealing the impact of spatial hole burning and spontaneous emission coupling.**

Keywords-Vertical cavity surface emitting laser (VCSEL); eigenmode analysis; coherence; phase-locking.

I. INTRODUCTION

Arrays of phase-locked, vertical cavity surface emitting lasers (VCSELs) constitute wide aperture, coherent light sources whose design can profit from concepts related to photonic crystals [1]. In particular, phased-locked arrays of VCSELs are very attractive means for obtaining higher power beams with a high degree of spatial coherence. From a more fundamental point of view, these devices provide an interesting system for investigating partially coherent light sources.

The spatial coherence of VCSEL-arrays is traditionnally evaluated using measurements of their far field pattern, completed by model calculation of supermodes [2]. However, far field patterns give only an indication about the global coherence of the array. This coherence analysis can be refined by measuring and resolving the contribution of each mode to the emission spectrum. A more complete evaluation demonstrated recently consists in measuring the spatial degree of coherence of each VCSEL pair by performing Young's interference experiments [3]. Remarkably, the mode structure can be analyzed using the mutual coherence function, based on the modal coherence theory discussed by Wolf and Agarwal [4]. This approach is of great interest since it allows to extract the parameters of the lasing supermodes, including their corresponding relative power distribution. Here, we apply this analysis method to a 2x2 VCSEL-array and compare it with a simulation model based on coupled mode theory.

II. THEORY

We consider two different approaches to identify the spatial distribution of the modes in a VCSEL-array. The first method is an eigenmode analysis relying on modal coherence theory [4], whereas the second method employs Couple Mode Theory (CMT) which allows to calculate the spatial mode distribution [5].

A. Eigenmode Analysis

The modal coherence theory is based on the fact that the optical field $V(\mathbf{r},t)$ can be represented as an expansion of the eigenmodes ψ_n:

$$V(\mathbf{r},t) = \sum_n \alpha_n(\upsilon)\psi_n(\mathbf{r},\upsilon)e^{i2\pi\upsilon t}. \qquad (1)$$

Wolf and Agarwal demonstrated in the spectral domain that the mode functions are eigenmodes of the homogeneous Fredholm integral [4]. However, under quasi-monochromatic conditions, an analogous expression can be formulated in the space domain:

$$\int \Gamma(\mathbf{r_1},\mathbf{r_2})\psi_n(\mathbf{r_1},\upsilon)d^3r_1 = \lambda_n(\upsilon)\psi_n(\mathbf{r_2},\upsilon). \qquad (2)$$

where the variables $\mathbf{r_1}$ and $\mathbf{r_2}$ correspond to the vector positions and υ to a fixed frequency. $\Gamma(\mathbf{r_1},\mathbf{r_2})$ is the mutual coherence function of two point sources located at the positions $\mathbf{r_1}$ and $\mathbf{r_2}$, assuming zero time delay. ψ_n is the mode function of the eigenmode n and λ_n is the corresponding eigenvalue.

Considering each VCSEL of the array as a point source, the problem reduces to a linear secular equation system. In the case of a 2x2 VCSEL-array, we obtain

$$\begin{pmatrix} \Gamma_{11} & \Gamma_{12}^* & \Gamma_{13}^* & \Gamma_{14}^* \\ \Gamma_{12} & \Gamma_{22} & \Gamma_{23}^* & \Gamma_{24}^* \\ \Gamma_{13} & \Gamma_{23} & \Gamma_{33} & \Gamma_{34}^* \\ \Gamma_{14} & \Gamma_{24} & \Gamma_{34} & \Gamma_{44} \end{pmatrix} \begin{pmatrix} \psi_n^{(1)}(\upsilon) \\ \psi_n^{(2)}(\upsilon) \\ \psi_n^{(3)}(\upsilon) \\ \psi_n^{(4)}(\upsilon) \end{pmatrix} = \lambda \begin{pmatrix} \psi_n^{(1)}(\upsilon) \\ \psi_n^{(2)}(\upsilon) \\ \psi_n^{(3)}(\upsilon) \\ \psi_n^{(4)}(\upsilon) \end{pmatrix}. \qquad (3)$$

Clearly, measurements of the coherence function $\Gamma_{ij} = \Gamma(\mathbf{r_i},\mathbf{r_j})$ of all VCSEL pairs i and j (with i,j=1,2,3,4) can yield the eigenmode content $\psi_n^{(k)}$ where n can vary between one and four depending on how many eigenmodes are present in the structure. The exponent (k) indicates the eigenmode value at VCSEL location k (k=1,2,3,4). The intensities of the eigenmodes are given by their corresponding eigenvalue λ.

B. Coupled Mode Theory

CMT assumes weak coupling between the VCSELs, and of allows determining the supermodes of the VCSEL-array [5]. The mode amplitudes of a uniform 2x2 VCSEL-array in the near field derived by CMT are shown in Fig. 1(a). The in-phase mode ψ_1 corresponds to the highest loss mode. The medium loss modes are ψ_2 and ψ_3. Both have the same symmetry properties and are degenerate in terms of frequency and losses. The out-of-phase mode ψ_4, with alternating amplitude sign at adjacent VCSEL sites, is the lowest loss mode. Figure 1(b) depicts the corresponding far field patterns.

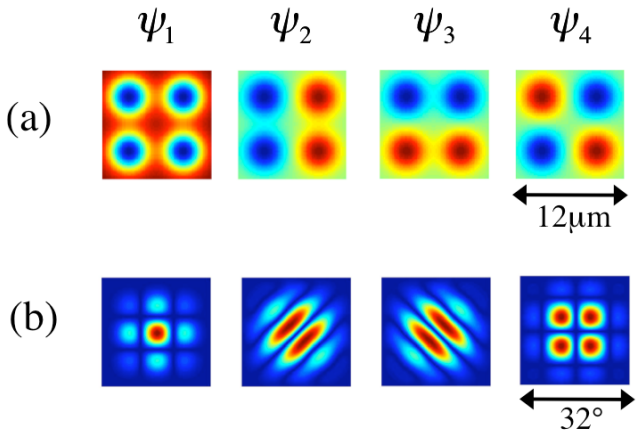


Figure 1. Calculated mode using CMT for an ideal, uniform 2x2 VCSEL-array: (a) near field amplitudes, (b) corresponding far field intensities.

III. RESULTS

Close to threshold, typical phase-locked arrays of VCSELs oscillate at the highest order supermode due to its lowest cavity losses [2]. Lower order supermodes are excited at higher excitation levels due to spatial hole burning. By using the method based on coherence theory, we were able to extract the relative intensities of all lasing supermodes. The experiments were performed with an electrically pumped VCSEL-array fabricated using Bragg-mirror patterning [1,2], emitting at 955nm wavelength. It employs strained InGaAs/AlGaAs quantum wells as the gain medium and GaAs/AlGaAs distributed Bragg reflectors (DBRs). Each square-shaped VCSEL element has a size of $4x4\mu m^2$ and the array pitch is 6.25μm. The threshold current was I_{th}=40mA.

The mutual coherence function of each pair of VCSELs within the array was measured by interefering the two corresponding near field spots using the spatial light modulator system described in [3]. Based on these measurements, equation (3) was then solved, yielding the eigenvalues and the eigenfunctions representing the array supermodes.

The eigenvalues λ, representing the relative supermode powers, are depicted by the histograms in Fig. 4 for three diode currents above threshold . The derived supermode amplitude patterns of the modes ψ_i with i = 1,2,3,4 are shown in the insets, and the total measured far field patterns are shown on the right panel. We note that the extracted near field patterns show distinct localization of the optical field, with complementary intensities of the supermodes at different array sites. This demonstrates the effect of spatial hole burning, which depletes the gain at the higher intensity peaks of each mode. The intensity of the highest order supermode is the highest at all currents, but increases with increasing pump level. This improved single mode operation results from the absence of perfect clamping of the modal gain above threshold, due to the significant coupling of spontaneous emission into the cavity mode.

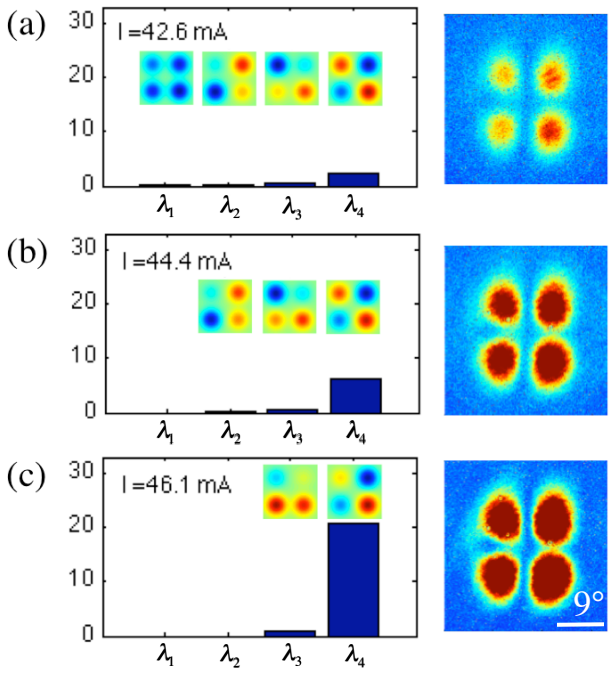


Figure 2. Histograms of normalized eigenmode intensities (λ_i ; i=1,2,3,4) including the representation of each eigenmode amplitude distribution for three different injection currents above threshold. The corresponding measured far field patterns are displayed on the right panel.

IV. CONCLUSION

We presented a modal coherence theory, which allows extracting the spatial mode distributions and the relative intensities of the lasing modes in a multimode laser cavity based on spatial coherence measurements. The method was applied to a phase-locked array of VCSELs. This approach makes possible the quantitative analysis of the mode content in such VCSELs and the assessment of new cavity designs for improved single mode operation.

REFERENCES

[1] H. Pier, E. Kapon, and M. Moser, "Strain effect and phase transitions in photonic resonator crystals" Nature, vol. 407, pp. 880-883, 2000.

[2] M. Orenstein, E. Kapon, J. P. Harbison, L. T. Florez, and N. G. Stoffel, "Large two-dimensional arrays of phase locked vertical cavity surface emitting lasers", Appl. Phys. Lett., vol. 60, pp. 1535-1537, March 1992.

[3] G. P. Lousberg, L. D. A. Lundeberg, D. L. Boiko, and E. Kapon, "Space-domain lock-in amplifier based on liquid-crystal spatial light modulator", Opt. Lett., vol. 31, no. 7, April 2006

[4] E. Wolf, and G. S. Agarwal, "Coherence theory of laser resonator modes", J. Opt. Sec. Am A, vol. 1, no. 5, May 1984, and references therein.

[5] A. Hardy, and E. Kapon, " Coupled-mode formulations for parallel-laser resontators with application to vertical-cavity semiconductor-laser arrays" IEEE J. of Quant. Elect., vol. 32, no. 6, June 1996.

High Speed Laser Diode Packaging with Over 10GHz-Bandwidth

Jeong Hwan Song, Marc Rensing, Chris LL. M. Daunt, Wei Han, Stefanie Weber, Peter O'Brien, and Frank H. Peters
Integrated Photonics Group, Tyndall National Institute, University College Cork, Cork, Ireland
jeonghwan.song@tyndall.ie

***Abstract*— A high frequency laser diode module package with over 10GHz-bandwidth is presented. The package consists of a V-connector, heat sink, and L-shaped microstrip line (MSL) on a substrate and included an integrated impedance matching resistor. For evaluation, a 1.3μm Fabry-Parot laser was included as a load on the package and the frequency response was characterized. As a result, a large modulation bandwidth of up to 15GHz was obtained. Importantly, using an L-shaped MSL with integrated impedance matching resistor design, the assembling tolerance for various optical coupling systems has been improved and the assembly process and module design have been significantly simplified.**

Keywords-impedance matching; optoelectronics packaging.

I. INTRODUCTION

For increasingly large data rates, a laser diode module for over 10Gbps may be a key component for high bit rate optical communication systems. For the bit rate of 10Gbps, the modulation bandwidth of packaged laser module must exceed 10GHz [1]. This bandwidth can be a major requirement and is determined by the electrical return loss of the input signal. This return loss may occur from the mismatched impedance of each package element such as wire bonds and microstrip line (MSL) and parasitic effects of each element as well as the characteristics of a laser diode. There are several requirements for the high performance package [2]. Electrical requirements, such as a large bandwidth, can be achieved using impedance matching techniques. Impedance matching for the achievement of large modulation bandwidth can be attained using a 50Ω transmission line and interconnecting a resistor to the laser. Optical requirements are also required such as high coupling efficiency and low optical feedback. These requirements can be achieved by various optical coupling techniques. In addition, large assembly tolerances for adopting various optical coupling systems and a simplified module for cost reduction are required. Large assembly tolerance and simplified module design can aid the ease of production for high volume manufacturing, high reliability and low cost. In this paper, we demonstrated a high frequency laser diode package with large assembly tolerances using an integrated thin-film resistor with an L-shaped MSL.

II. PACKAGE STRUCTURE AND EXPERIMENTAL RESULT

The package structure of the optical subassembly (OSA) consists of a heat sink made of Kovar as a ground plane, MSL on dielectric substrate with integrated thin film resistor, and a 1.3μm Fabry-Parot (FP) laser diode which is interconnected to the MSL via a wire bond as shown in Fig. 1. The required return loss must be less than −10dB. The return loss is mainly due to the parasitic effects of each element in the package. In particular, the inductance due to wire bonding is responsible for creating a large return loss. Generally, the length of the wire bond must be as short as possible to reduce the inductance. There are several methods to facilitate a reduction in the inductance such as using flip chip bonding which eliminates bond wires, multiple wire bonding, and ribbon wire bonding. Flip-chip is suitable for lasers with electrical transmission lines on the same plane, such as coplanar waveguide transmission lines on a laser. Flip chip bonding also has problems such as difficulty of forming solder bumps, removal of residual flux, and a reduction in the number of heat dissipation paths. For multiple wire bonding, the lasers bond pad may be small by design in order to minimize the parasitic capacitance. Among these techniques, we choose a ribbon bonding technique to reduce the inductance of a die attached laser.

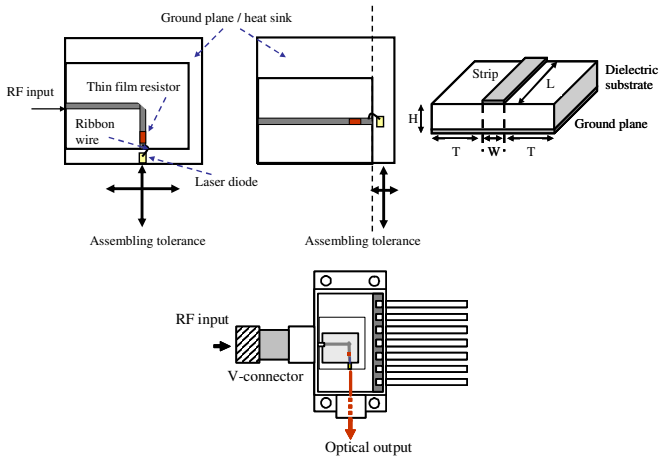


Figure 1. Microstrip line (MSL) geometry and schemetic of the package

Fig. 1 shows the comparison between using an L-shaped MSL and a conventional straight MSL. A thin-film resister integrated L-shaped MSL has been used in this experiment. The miter [3] of L-shaped design is 50%. The integrated thin-film resistor is based on a NiCr alloy and is laser trimmed to provide the required resistance value. The process used can provide a resistance of ±0.2Ω.

The working distance of an optical coupling system such as a micro lens [4] or lensed fiber [5], [6] is limited to few hundred microns or much less, respectively. As can be seen in Fig. 1, there is a large distance between the laser output facet and the edge of the ground plane due to the configuration of a

This work was supported by the Science Foundation Ireland under Grant No. 07/SRC/I1173.

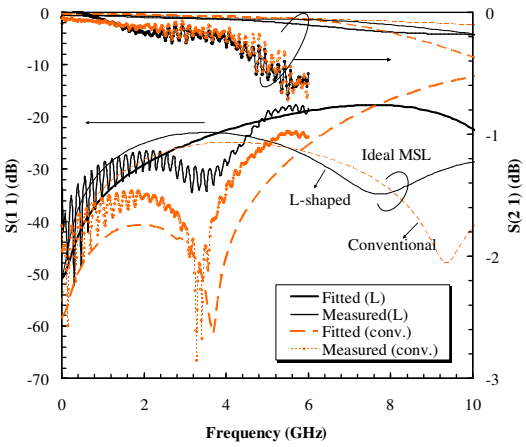


Figure 2. Convetional and L-shaped MSL measurements

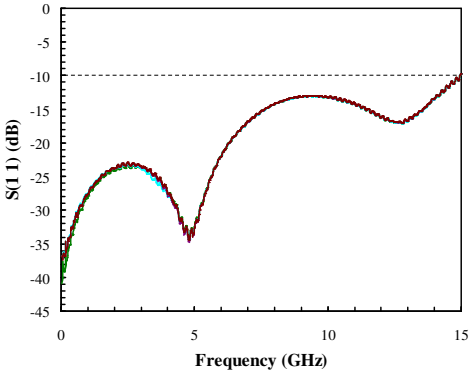


Figure 3. Reflection of frequency signal in the package with respect to various dc bias levels(40 to 70mA)

conventional MSL. This limits the alignment tolerance available when trying to achieve efficient optical coupling.

For an improved frequency response of the MSL, the conditions of T/W>2 and W/H>1 should be satisfied [7]. In the case of conventional MSL in Fig. 1, if the laser is to be aligned to the edge of the heat sink, the length of ribbon bond must be increased. However, the L-shaped MSL can overcome these limitations and can satisfy both conditions of the conventional MSL and the need for a short ribbon bond.

The fabricated MSL has the optimum width of 270μm for 50Ω impedance on the 254μm-thick Aluminum Nitride (AlN) substrate whose dielectric constant (ε) is 8.8. When W/H>1, the optimum width can be determined by equations in [8]. To investigate the frequency response of both the L-shaped and conventional MSLs, S-parameters have been measured using a vector network analyzer (VNA). Fig. 2 shows the measurement results of both MSLs. The estimated capacitances from the measurement are in the range of 0.05-0.15pF. These values of capacitance may be suitable for the package performance. The capacitance of the assembled package is an important parameter to consider because a high capacitance of the contact area would result in a large return loss when launching a high frequency signal and therefore a reduced modulation bandwidth. The results show that L-shaped and conventional MSLs have similar frequency response performance even when approaching near zero capacitance as ideal cases as shown in Fig. 2. However, the L-shaped MSL has significantly improved flexibility for adopting various optical coupling systems as mentioned previously. A 45±0.2Ω thin-film resistor has been integrated in the L-shaped MSL for impedance matching and to simplify the assembly process. The resistor integrated on the MSL is interconnected by a single ribbon bond to a laser using a K&S 4234 wedge bonder. The dimension of the gold ribbon bond was approximately 320μm×75μm×12μm which can help minimize the inductance. The measured resistance of the 1.3μm FP laser here is 4.5Ω. An entire package was assembled using a commercially available 7-pin butterfly package which included a heat sink, L-shaped MSL with impedance matching resistor and a sample laser interconnected by a ribbon bond and a V-connector. A high frequency input signal passes via a V-bead in the V-connector to the integrated impedance matched resistor on the MSL. The measurement setup for the package consists of a VNA, power meter, current source, and bias-tee. Fig. 3 shows the measurement results of our package with various injection currents. The results show that the reflection of the input signal was as low as −10dB for all signals up to 15GHz. This bandwidth is sufficient for a 10Gbps signal transmission.

III. CONCLUSION

We demonstrated a large bandwidth butterfly package for high speed laser diode modules. The package has relaxed assembly tolerances for coupling of the optical output. The package shows a large frequency bandwidth of up to 15GHz and higher flexibility for various optical coupling systems using impedance matching resistor integrated L-shape MSL. This packaging configuration is an attractive solution for high speed laser diode modules.

REFERENCES

[1] S. S. Park, M. K. Song, S. G. Kang, N. Hwang, H. T. Lee, H. R. Choo, and K. E. Pyun, “High frequency modeling for 10Gbps DFB laser diode module packaging,” Proc. Electronics Components and Technology Conference, pp.884-887, 1996.

[2] J. Schlafer, and R. B. Lauer, “Microwave packaging of optoelectronic components,” IEEE Trans. Microwave Theory Tech. vol. 38, no.5, pp.518-522, 1990.

[3] R. J. P. Douville, and D. S. James, “Experimental study of symmetric microstrip bends and their compensation,” IEEE Trans. Microwave Theory Tech. vol. MTT-26, no.3, pp.175-182, 1978.

[4] H.-G. Yun, K.-S. Choi, Y.-H. Kwon, J.-S. Choe, and J.-T. Moon, “Fabrication and characteristics of 40-Gb/s traveling-wave electroabsorbption modulator-integrated DFB laser modules,” IEEE Trans. Adv. Packag. vol.31, no.2, pp.351-356, 2008.

[5] J. H. Song, H. N. J. Fernando, B. Roycroft, B. Corbett, and F. H. Peters, “Practical design of lensed fibers for semiconductor laser packaging using laser welding technique,” J. Lightw. Technol. vol.27, no.11, pp.1533-1539, 2009.

[6] J. H. Song, P. O’Brien and F. H. Peters, “Optimal laser welding assembly sequences for butterfly laser module packages,” Opt. Express, vol.17, no.19, pp.16406-16414, 2009.

[7] C. Smith and R.-S.Chang, “Microstrip transmission line with finite-width dielectric and ground plane,” IEEE Trans. Microwave Theory Tech. vol. MTT-33, no.9, pp.835-839, 1985.

[8] H. Nakano, S. Sasaki, M. Maeda, and K. Aiki, “Dual-in-line laser diode module for fiber-optic transmission up to 4 Gbit/s,” J. Lightw. Technol. vol.LT-5, no.10, pp.1403-1411, 1987.

Analysis of the Current Dependency of the Small Signal Gain Spectrum in InAs/InP(100) Quantum-Dot Amplifiers

B.W. Tilma, M.S. Tahvili, J. Kotani, R. Nötzel, M.K. Smit and E.A.J.M. Bente
COBRA, Eindhoven University of Technology
Eindhoven, The Netherlands
b.w.tilma@tue.nl

Abstract—**InAs/InP(100) quantum-dot amplifiers have been fabricated with a 1700nm peak wavelength. The measured small-signal gain spectra have been analyzed with a quantum-dot rate-equation model. The average energies of the ground state E_{GS}=0.716eV and the excited state E_{ES}=0.760 transitions have been determined. The origin of the spectral behavior has been analyzed.**

Keywords-Semiconductor optical amplifier; quantum dot; gain measurements; rate equation; integrated optoelectronics

I. INTRODUCTION

The use of quantum-dot (QD) optical amplifiers in optical devices can have a number of benefits over the use of bulk or quantum well amplifiers. These advantages are due to the three dimensional carrier confinement in the QDs. One of the advantages is the control of the average dot size during the growth process [1] which is a direct control of the central wavelength in the operating range of the amplifier. This enables the design of active integrated optical devices for non-telecom purposes on InP substrate outside the 1550nm wavelength region. In order to be able to apply this gain material optimally in devices, we need to understand the behavior of the gain of these QD integrated optical amplifiers. In this paper we compare the measured small signal gain spectra with simulated small signal gain spectra for different injection current densities to determine the average energy levels of the ground state (GS) and the excited state (ES) and to understand the spectral behavior.

II. DEVICES AND MEASUREMENTS

The gain measurements are performed on 7mm two-section InAs/InP(100) QD devices as described in [2]. The QD wavelength is however in these devices tuned into the 1700nm region during the grow process. The photoluminescence spectrum (PL) is given in Fig. 1a. The long section of the device is used as an amplifier with a defined injection current densities and the short section is used as an absorber with a -3V reverse bias applied. The gain is determined with a measurement technique based on the analysis of the ASE spectra from different lengths of amplifiers [3]. The single pass ASE is measured from 22 parallel amplifiers on a single chip with lengths between 4.94mm and 6.48mm. The absorber is used to absorb light generated and amplified in the other direction and so prevent optical feedback. The maximum amount of feedback signal was determined to be -18dB in the most unfavorable amplifier current density and absorber length combination. The small signal gain is determined at 5 different injection current densities (continuous wave) between 1550nm and 1800nm wavelength. The resulting gain spectra are given in Fig. 1b (solid). Note that this measurement technique is not suitable for measurements below transparency due to the low signal level of the attenuated ASE far from output of the amplifier. Gain spectra at higher injection current densities could not be measured due to a to high feedback signal through the absorbers.

There are two aspects in these gain spectra which should be noted. First, we cannot make a clear distinction between gain from the GS and gain from the ES. Gain spectra as well as PL spectra from InAs QD on GaAs substrate show two clear peaks which can be assigned to the GS and ES transitions[4]. In our PL spectra (Fig. 1a) and gain spectra from InAs QD on InP substrate (Fig 1b) a single broad peak is observed, which complicates the determination of the average GS and ES energy. The second notable aspect is the continuous increase in the gain spectrum towards the shorter wavelength region with increasing injection current densities. In practice it means that when this material is used in a laser without wavelength selective devices, e.g. a simple Fabry-Perot laser, the lasing wavelength is strongly dependent on the length of the device. The longer the laser, the lower the gain per unit length needs to be, the longer the operating wavelength will be.

III. MODEL

To analyze the QD gain measurements we have set up a simulation of the QD amplifier gain with a QD rate equation model. The model we have used is based on the model presented in [4] which has been simplified for our purpose to reduce the calculation time. The model consist of 64 carrier rate equations, one for the separate confinement heterostructure (SCH) and one for the wetting layer (WL). The excited state (ES) and ground state (GS) populations are each modelled using 31 equations to describe the inhomogeneous broadening due to the dot size distribution. The rate equations are solved in

This work is supported by the IOP Photonic Devices program managed by the Technology Foundation STW and SenterNovem

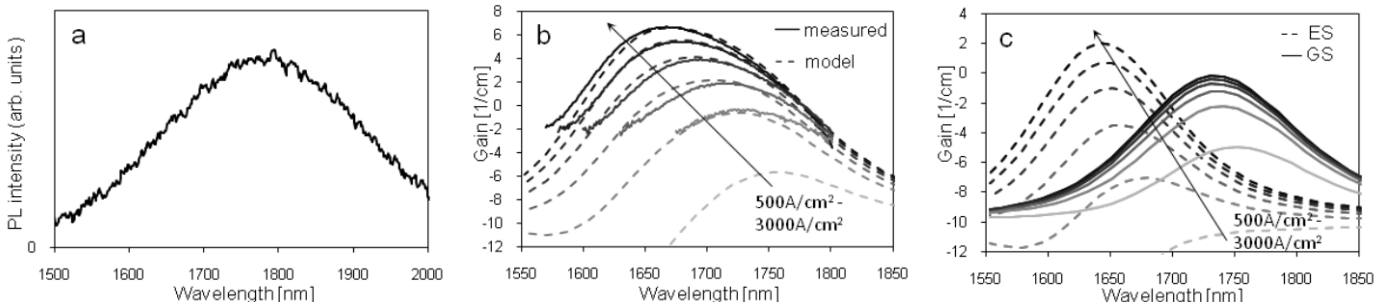


Figure 1. (a) Photoluminescence spectrum of QD amplifier structure. (b) Small signal gain spectra for a QD amplifier with current densities between 500A/cm2 (light gray) and 3000A/cm2 (black). Measured gain spectra (solid), and simulated (dashed). (c) Simulated gain spectra from GS (solid) and ES (dashed) seperately for current densities between 500A/cm2 (light gray) and 3000A/cm2 (black).

the time domain until a steady state is reached. The small signal gain is calculated from the filling probabilities in the ES and GS. The carrier losses in the dots due to stimulated emission were neglected because we only look at the low power ASE spectra far below the lasing threshold. Therefore we did not include a series of equations for the photons, which reduces the number of equations to be solved by one third.

IV. Analysis and Results

We did analyze the gain measurements by comparing the measured gain spectra with the calculated gain spectra. There are two effects which together cause the large broadening in the gain spectrum towards the shorter wavelength region with increasing injection current density. The first effect is the upcoming ES with increasing injection current densities. At low injection current densities all carriers relax to the GS and contribute to gain at the GS wavelength. At higher injection current densities part of the carriers will relax more to the ES due to the high occupation of carriers in the GS. The carriers in the ES contribute to gain at the ES wavelength. This upcoming ES gain can clearly be recognized in gain spectra from InAs QD on GaAs substrate [4] where a second peak can be detected around the ES wavelength. In our InAs QD on InP substrate we also did measure this upcoming ES gain, however, in this material system the GS and ES peak do overlap which makes there is no clear distinction between the two peaks. The large broadening in the measured gain spectrum can be assigned to this upcoming gain from the ES. It is however not the only effect which changes the gain spectrum with increasing injection current density. If it was the only effect we would have measured a jump in peak wavelength from the GS to the ES wavelength instead off a continuous shift in peak wavelength.

The second effect is the dot size dependent escape rate from the QD to the WL. After the relaxation from a carrier into a dot, it still can escape from the dot due to thermal energy in the material. The escape rate is directly dependent on the difference between the energy level in the dot and the energy level of the WL [4]. This means that due to the inhomogeneous dot size distribution the escape rate from the smaller dots is higher than the escape rate from the larger dots. The capture rate of the dots is however not dot size dependent and therefore the filling probability in the larger dots is higher than that of the smaller dots. If we look at the gain from e.g. only the ES we see that at low injection current densities the gain is higher in the relative longer wavelength region due to the relative higher filling probability in the larger dots Fig. 1c. When the injection current increases also smaller dots get occupied which extends the gain spectrum towards the shorter wavelength region. This dot size dependent escape rate causes the continuous shift in peak wavelength in the gain spectrum from GS wavelength to ES wavelength.

With the QD amplifier rate equation model we did determine the average energy level of the ES, E_{GS}=0.716eV (1730nm), and the ES, E_{ES}=0.760eV (1630nm) in our QD amplifier as well as the energy level of the WL, E_{WL}=0.843eV (1470nm) by fitting the simulated gain spectra to the measured gain spectra Fig. 1c (dashed). From the simulations we discovered that the energy difference between the GS and ES determines the amount of shift towards the shorter wavelength region with increasing injection current density. The energy difference between the ES and the WL determines the influence of the dot size dependent escape rate. Variations of the value of the basic time constants in the model do not have an influence on the shape change of the gain spectrum, only on the transparency current densities of the GS and ES gain.

V. Conclusion

The average energy level of the ES and GS as well as the energy level of the WL in our QD amplifiers could be determined by comparing the measured gain spectra with the simulated gain spectra. The simulations show that two effects together give rise to the increase in gain towards the shorter wavelength region with increasing injection current density; the upcoming ES gain with increasing injection current density and the dot size dependent escape rate from the dots to the WL.

References

[1] R. Nötzel et al., “Self Assembled InAs/InP Quantum Dots for Telecom Applications in the 1.55 μm Wavelength Range: Wavelength Tuning, Stacking, Polarization Control, and Lasing,” Jpn. J. Appl. Phys., vol. 45, pp. 6544-6549, 2006

[2] M.J.R. Heck et al., “Observation of Q-switching and mode-locking in two-section InAs/InP(100) quantum dot lasers around 1.55um,” Optics Express, vol. 15, pp. 16292-16301, December 2007.

[3] J.D. Thomson, H.D. Summers, P. Hulyer and P. Blood, “Determination of single-pass optical gain and internal loss using a multisection device,” Appl. Phys. Lett., vol. 75, pp. 2527-2529, Oktober 1999.

[4] M. Gioannini and I. Montrosset, “Numerical Analysis of the Frequency Chirp in Quantum-Dot Semiconductor Lasers,” IEEE J. Quantum Electron., vol. 43, pp. 941-949, October 2007.

Temporal measurements of SOI wire racetrack resonators

Tim J. Karle[1], Fabrice Raineri[1,3], Frederic Bordas[1], Itamar Sivan[1], Shamyr Ali[1], and Rama Raj[1]
[1]Laboratoire de Photonique et de Nanostructures, (CNRS-UPR20), 91460 Marcoussis, France
[3]Universite Paris VII, Denis Diderot
Timothy.Karle@lpn.cnrs.fr

Yacine Halioua[1,2], Gunther Roelkens[2]
[2]Photonics Research Group, IMEC/Ghent University, St-Pietersnieuwstraat 41, 9000 Ghent, Belgium

Abstract—**The temporal response of Silicon-on-Insulator racetrack resonators is measured using parametric up conversion for input pulses of duration 150fs. This allows us to study the dynamics of the coupling between the bus waveguide and the racetrack. The cavities exhibit a round trip time 660fs and a Quality Factor of 9500.**

Keywords- Racetrack Resonators, SOI, Temporal Measurements

I. Introduction

Coupling between optical waveguides and racetrack resonators has been widely studied for the promise they hold for device applications in light emission and modulation. For this, one of the important aspects which needs to be understood and controlled is their dynamic response.

We first focus on the continuous wave characteristics of the system, measuring the transmission of the waveguides, which gives the resonant frequencies of the racetrack and their quality factors. We then use the extremely temporally precise and background free method of optical parametric amplification to resolve the passage of the femtosecond pulses through the waveguide coupled racetrack resonators.

II. Samples

The silicon racetracks consist of wire waveguides with a width of 526nm and the bus waveguide have a width of 536nm, sitting atop a silica cladding. The radius of curvature of the curved sections are 4µm and within the set of samples the straight waveguide section is varied between 1 and 8µm. The coupling gap between racetrack and bus waveguide is d=180nm. The silicon waveguides are tapered up to a width of 2µm. The sample is thinned and cleaved in order to allow lens end-fire investigation in free space. In this way we avoid fibre nonlinearities which would be incurred by the short pulses. Continuous wave spectral studies show each racetrack displaying several resonances dips within the 150nm bandwidth of our tunable laser. The free spectral range of the resonances decreases as the size of the racetrack is increased as expected.

III. Measurements

The temporal measurements were performed by launching 150 femtosecond pulses, produced using a 1kHz Optical Parametric Amplifier pumped at 810nm generating tunable pulses at around 1540nm, into the silicon waveguide. The input pulses are strongly intensity filtered to avoid non-linearities in the Si such as Two-Photon Absorption and Free Carrier Absorption. The pulse propagates in the guide and is evanescently coupled to the racetrack. The coupling section of the racetrack resonator is longer than that of a circular ring resonator, allowing a larger coupling gap between the resonator and guide, for an equivalent coupling factor. Once the light is coupled into the ring it is apparent that for pulses of 150fs duration the spatial extent of the pulse is shorter than the length of the racetrack.

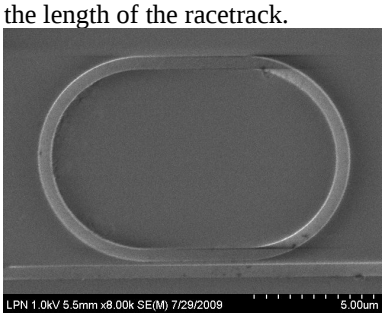


Figure 1. SEM image of racetrack resonators

The light coupled into the racetrack circulates for many round trips given the low losses in the high quality Si guides and low bending loss. At each passage though the coupler section, a percentage is recoupled to the bus waveguide. This gives rise to a sequence of output pulses with diminishing intensities. This sequence is coupled out from the Si waveguide to free space. The power levels of these pulse along with their short duration make direct detection and autocorrelation very challenging. We can however gate the pulses by making use of the original 810nm pump pulses.

The intense 810nm pump pulses are firstly converted to 405nm by second harmonic generation in a nonlinear crystal of BBO and then these blue pulses are combined with the output pulse sequence from the racetrack in a second BBO crystal. The interaction parametrically amplifies the pulses at

the idler wavelength of 1540nm (which is the wavelength of operation of our system) as well as generating an amplified signal pulse at 540nm. In order to obtain a background free signal we detect the latter using a photomultiplier, boxcar averaging and a lock-in amplifier. By optically delaying the blue gating pulse it is possible to "map" the temporal response of the pulses coming out of the waveguide-racetrack coupled system.

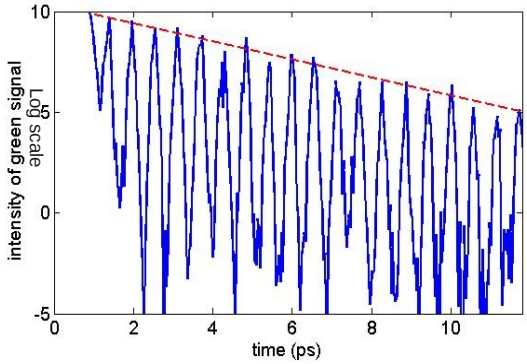


Figure 2. The intensity of the signal measured at 540nm (log scale) vs the delay time of the pump. The temporal ring-down of the racetrack shown as a sequence of diminishing peaks.

Figure 2 displays the train of pulses exiting the resonator. The racetrack gives rise to a train of pulses exiting the waveguide spaced by the round trip time of 660fs. We can deduce loaded cavity Q from the exponential decay of the peaks as 9500.

IV. Conclusion

In conclusion temporal measurements have been performed on very low intensity pulses transmitted through Si wire waveguides, having interacted with a micron scale All Pass Filter. Extending the technique to look at non-linear and active devices is now in progress.

Acknowledgment

The SOI racetrack samples were fabricated by CEA-LETI as part of the ePIXfab platform. The authors acknowledge FP7 ICT project HISTORIC for funding.

UV-written planar chirped Bragg gratings for use in dispersion management

B. D. Snow, H. L. Rogers, C. Holmes, J. C. Gates, C. Sima, M. Kaczmarek, P. G. R. Smith
Optoelectronics Research Centre and School of Physics and Astronomy
University of Southampton
Southampton, England
bds@orc.soton.ac.uk

***Abstract*—We demonstrate for the first time experimental results of chirped and chirp-apodized Bragg gratings written into planar substrates. The gratings are written using Direct Grating Writing, allowing both buried channels and gratings to be defined simultaneously. The experimental results are then compared to theory and agree well with predicted spectra.**

Keywords- Bragg gratings; planar waveguides; chirped gratings; dispersion compensation

I. INTRODUCTION

Optical filters incorporating Bragg gratings have become a powerful tool in applications such as high-speed optical telecommunications [1]. Planar Bragg grating structures have been demonstrated [2] and have the potential to address several telecoms channels simultaneously. These integrated planar optical devices have been extended to include chirped and chirped-apodized Bragg gratings.

Chirped gratings have particular interest in dispersion compensating and residual dispersion compensating devices [3]. The group delay arising from linearly chirped Bragg gratings is a linear function of wavelength. Therefore such devices can be used to recompress broadened pulses. Also, non-linearly chirped gratings can be used to correct residual dispersion due to improper dispersion slope matching from dispersion compensating fiber.

Planar chirped Bragg gratings utilize a writing technique known as Direct Grating Writing (DGW) [4]. This avoids the use of phase masks and allows buried channel waveguides and grating structures to be written simultaneously. DGW also avoids the problem of additive-only refractive index change.

In this paper we provide experimental results of planar chirped and chirped-apodized Bragg grating structures written via our DGW method. Reflection spectra for various chirp parameters are given along with their group delay curves.

II. THEORY

Linearly chirped Bragg gratings have a period of refractive index modulation that varies along the length of the grating. The consequence of this is the reflection bandwidth increases, but the peak power reflected diminishes. However, the group delay becomes a linear function of wavelength, and this can be exploited in dispersion management systems.

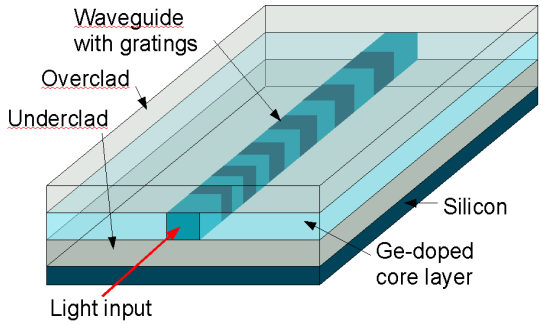


Figure 1. A DGW buried channel waveguide with integral chirped Bragg grating

Planar geometry substrates have the benefit of being able to write multiple devices on the same substrate. Therefore they provide the ability to simultaneously process multiple optical sources. Planar devices are also robust and have easily accessible gratings to allow for modification of the grating properties, such as tuning the grating period.

Fig. 1 shows a typical chirped grating written into the Ge-doped core of a 3-layer silica-on-silicon substrate. The interference pattern created by crossing two 244nm beams is periodically printed in the core, forming a grating. The grating is written by simultaneously modulating the 5µm diameter beams with an AOM whilst translating the sample under the beams using a computer-controlled air-bearing stage system.

III. RESULTS AND DISCUSSION

Shown in Fig. 2 are the reflection spectra of chirped (red) and chirp-apodized (blue) planar gratings written via DGW. The modeled data is shown in black. The chirped grating is 5mm long with a chirp rate of 5nm/cm and the apodized chirped grating uses a Gaussian apodization profile. Experimental data shows good agreement with the modeled data.

The chirped grating has a bandwidth of 2.3nm whereas the apodized grating has a bandwidth of only 0.8nm. However, this apodized grating avoids the group delay ripple as shown in the red curve, providing a more linear group delay response with a slope of -10ps/nm as shown in Fig. 3.

Further devices were fabricated to test the range of chirp available using the DGW method in the planar geometry. Fig. 4 demonstrates the range of chirp fabricated thus far using our

This project is sponsored by EPSRC

method. Fig. 5 displays the group delay spectra for these gratings. All gratings are 9mm in length. The chirp ranges from 2.8nm/cm (left, blue) up to 14.4nm/cm (right, red), however this is not the physical limit. The peak reflected power has only dropped by 3dB despite the large increase in chirp.

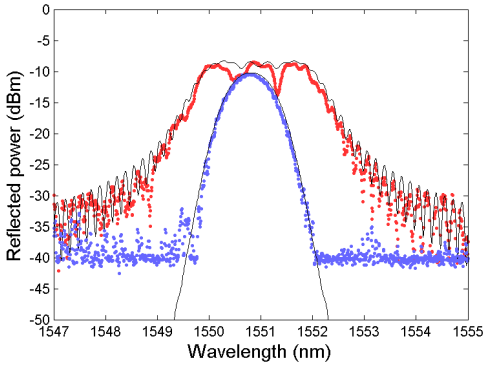


Figure 2. Reflection spectra of chirped (red) and chirp-apodized (blue) gratings with theoretical fit (black)

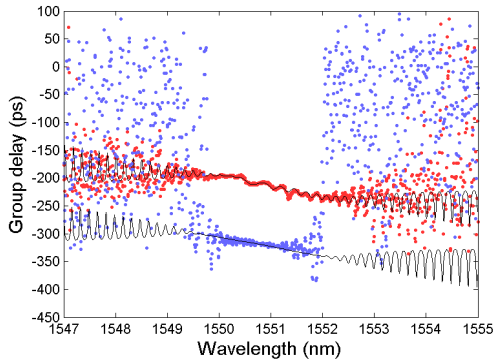


Figure 3. Group delay of chirped (red) and chirp-apodized (blue) gratings with theoretical fit (black)

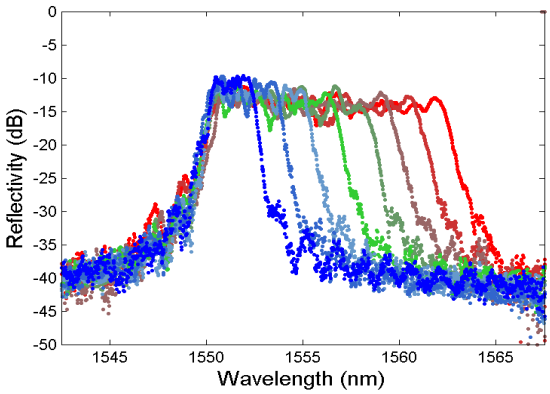


Figure 4. Reflection spectra of linearly chirped Bragg gratings with chirp rates of 2.8 - 14.4 nm/cm

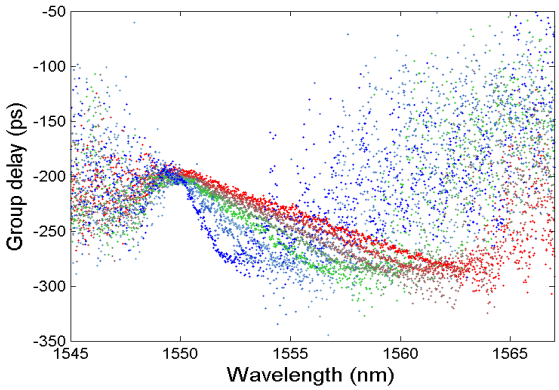


Figure 5. Group delay of linearly chirped Bragg gratings with chirp rates of 2.8 - 14.4 nm/cm

These results demonstrate that the simplified writing process can produce zero d.c. refractive index gratings. They also demonstrate that the uniformity of our planar Flame Hydrolysis Deposited (FHD) substrates and the stability of our DGW system are sufficiently high to allow fabrication of high quality gratings.

IV. Conclusions

We have demonstrated chirped and chirp-apodized planar Bragg grating devices using our Direct Grating Writing method. This produces highly configurable gratings with various chirp parameters and apodization profiles while simultaneously writing buried channel waveguides mode-matched to standard single-mode fiber. These planar devices provide a robust geometry allowing external modification of grating parameters. Chirp parameters can be controlled by thermal tuning, stress tuning, and if using an exposed channel waveguide, liquid crystal and optofluid tuning. This provides a means for producing adaptive, residual dispersion compensating devices from our planar chirped gratings.

We will present results on the use of integrated heated electrode elements to provide localized chirp correction.

References

[1] C. R. Giles, “Lightwave Applications of Fiber Bragg Gratings,” J. Lightwave Technol., vol. 15, pp. 1391-1404, August 1997.

[2] F. R. M. Adikan, J. C. Gates, A. Dyadyusha, H. E. Major, C. B. E. Gawith, I. J. G. Sparrow, G. D. Emmerson, M. Kaczmarek and P. G. R. Smith, “Demonstration of 100 GHz electrically tunable liquid-crystal Bragg gratings for application in dynamic optical networks,” Opt. Lett., vol. 32, pp. 1542-1544, June 2007.

[3] T. Duthel, S.L. Jansen, M. Otto, P.M. Krummrich and C.G. Schäffer, “Tunable all-fibre delay line filter for residual dispersion compensation in 40 Gbit/s systems,” Electron. Lett., vol. 40, pp. 1291-1293, September 2004.

[4] G. D. Emmerson, C. B. E. Gawith, R. B. Williams and P. G. R. Smith, “Simultaneous direct UV-writing of channel waveguide and bragg grating structures, ” Proceedings of SPIE, vol. 5339, pp. 156-167, January 2004.

150 ps all-optical switching in silicon microring resonators

C. J. Oton, J. Herrera, P. Sanchis, A. Martínez and J. Martí
Valencia Nanophotonics Technology Center
Universidad Politecnica de Valencia
Valencia, Spain
E-mail: coton@ntc.upv.es

We report a silicon-based optical switch controlled by a pump beam which copropagates with the signal beam. The modulator has an extinction ratio of 10dB, and a 1/*e* temporal response of 150 ps, with pump peak powers of 390 mW. The device is based on free-carrier dispersion effect produced by carriers generated through two-photon absorption.

Keywords: nonlinear silicon photonics; all-optical modulation; optical switch;

I. INTRODUCTION

Integrated silicon-based optical devices have recently emerged as a feasible technology to route, switch and modulate signals in optical networks, which are expected to dramatically reduce device costs and provide new functionalities [1]. Electrically-controlled high speed modulators have been demonstrated in the last years, most of them based on carrier injection and depletion [2]. All-optical modulators have been demonstrated too [3,4], although speeds above 1Gbps are difficult to achieve due to the carrier recombination time, which usually is in the nanosecond range. One strategy to attain high speeds consists of depleting the carriers electrically [5]. Other works have recently reported high speed optical switching without the need of electrical carrier depletion, by using polysilicon [6] or oxygen-implanted silicon [7] as guiding material. These materials are richer in recombination centers that shorten the carrier recombination time. However these works only report measurements in structures pumped from above at 800nm, which is unsuitable for an actual device. In this work, we report a high speed device where the pump copropagates with the signal and does not require electrical carrier depletion.

II. FABRICATION AND EXPERIMENT

The samples were fabricated from SOI wafers with 3 µm buried oxide and 250 nm silicon layer. The waveguides were patterned with e-beam lithography and etched with an inductively coupled plasma (ICP) etcher. The structures were covered with 2µm of silica after SEM characterization. The channels are 500 nm wide and 250 nm high, and are coupled to 20µm-radius rings through a 300 nm gap.

Light was coupled into the waveguides by butt-coupling with lensed fibers, and was extracted with an objective. The TM transmission spectrum was measured by tuning the laser, and the result is shown in Fig. 1, where one resonance is shown. The response was fitted to the theoretical equation [8] by using the propagation loss and coupling coefficient as parameters. A good agreement was found for propagation loss of 30dB/cm and coupling coefficient of 16%. Full width at half depth (FWHD) of the peak was 174 pm, which corresponds to a Q-factor of 8839.

The setup for the nonlinear characterization is shown in Fig. 2. A tunable laser was modulated with a $LiNbO_3$ modulator and amplified through Er-doped fiber amplifiers (EDFAs). The pulse train was generated with a 40Gb/s bit pattern generator, where pulses had 25 ps duration and 1.6 ns period. The peak power coupled into the waveguide was estimated to be 390mW. A continuous-wave (*cw*) probe signal was mixed with the pump with a 3dB coupler and sent to the waveguide through the same fiber with an estimated coupled power of 0.5 mW. Wavelengths of pump and probe signals were respectively 1564 and 1554 nm, chosen to match with two resonances of the microring resonator. The output signal was filtered to remove the pump component and amplified before sending the signal to a 50 GHz photodiode and collecting the data with a 40GHz sampling scope.

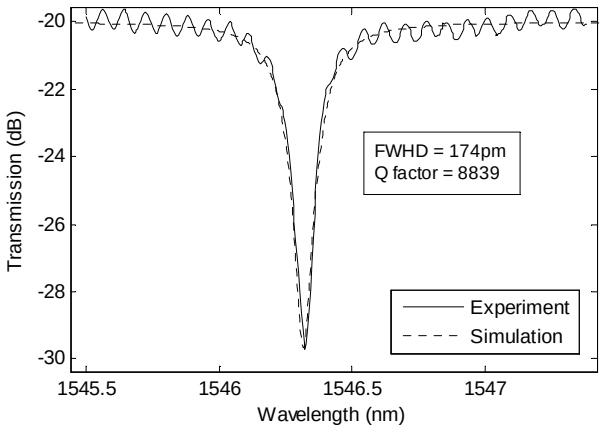


Figure 1. Transmission spectrum of the ring resonator sample (TM polarization). Solid line is the experimental data and dashed line is the result of the simulation when setting propagation loss to 30dB/cm and coupling coefficient to 16%.

This work has been sponsored by the Spanish Science and Innovation Ministry through contracts SINADEC (TEC2008-06333) and DEMOTEC (TEC2008-06360).

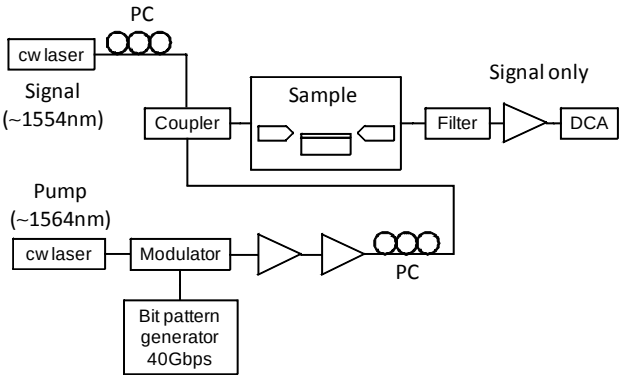


Figure 2. Setup for nonlinear characterization. Triangles represent EDFAs with ASE filters, PC stands for polarization controller, and DCA for digital communications analyzer.

III. RESULTS AND DISCUSSION

Figure 3 shows the modulation in the probe signal produced by the pump when both pump and probe are resonant with the microring. Extinction ratio is 10.2 dB and the 1/*e* recovery time is 150ps. The reason for the modulation is carrier generation through two-photon absorption (TPA), which produces a decrease of refractive index that blueshifts the resonance, taking the *cw* probe from a resonant to a non-resonant regime.

Figure 4 shows the modulation of the *cw* probe signal when probe and pump are both out of resonance. The variation of signal, which is only 5%, is due to a combination of free carrier absorption (FCA) and dispersion (FCD), as the Fabry-Pérot fringes convert phase variations into weak intensity variations. An approximate value of the carrier recombination time was extracted from the 1/*e* recovery time, which is 225 ps. This recombination rate is quite faster than values previously reported [3,4], and defects is the most likely cause. Whether these defects are surface recombination centers or produced by the electron bombardment during SEM is currently under investigation.

IV. CONCLUSIONS

We experimentally demonstrate an integrated all-optical switch based on free carrier dispersion effect with a switch time of 150 ps. The device uses a microring resonator to enhance the nonlinear effect and to commute the signal, producing ~10dB of extinction ratio.

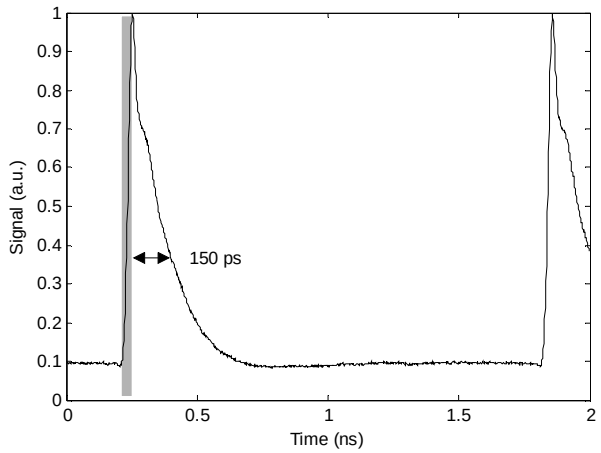


Figure 3. Variation of the probe signal when both pump and probe are resonant with two different modes of the microring. The grey box marks the pump duration.

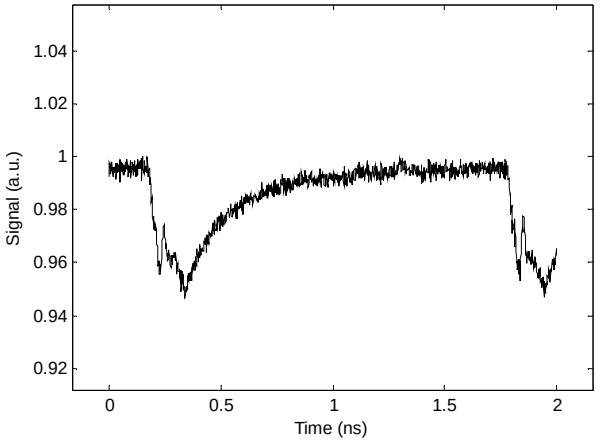


Figure 4. Variation of the probe signal when both pump and probe are out of resonance. Note that the amount of variation is only 5%.

REFERENCES

[1] R. Soref, "The past, present, and future of silicon photonics" IEEE J. Sel. Top. Quantum Electron. **12** (6), pp. 1678-1687 (2006).

[2] D. Marris-Morini, L. Vivien, G. Rasigade, J.-M. Fedeli, E. Cassan, X. Le Roux, et al, "Recent Progress in High-Speed Silicon-Based Optical Modulators," Proceedings of the IEEE **97** (7), pp.1199-1215 (2009).

[3] V. R. Almeida, C. A. Barrios, R. R. Panepucci et al., "All-optical control of light on a silicon chip" Nature **431**, pp. 1081-1084 (2004).

[4] Q. F. Xu and M. Lipson, "All-optical logic based on silicon micro-ring resonators" Opt. Express **15** (3), pp. 924-929 (2007)..

[5] S. R. Preble, Q. F. Xu, B. S. Schmidt, and M. Lipson, "Ultrafast all-optical modulation on a silicon chip" Opt. Lett. **30** (21), pp. 2891-2893 (2005).

[6] K. Preston, P. Dong, B. Schmidt, and M. Lipson, "High-speed all-optical modulation using polycrystalline silicon microring resonators" Appl. Phys. Lett. **92** (15), p. 151104 (2008).

[7] M. Waldow, T. Plötzing, M. Gottheil, M. Först, J. Bolten, T. Wahlbrink, and H. Kurz, "25ps all-optical switching in oxygen implanted silicon-on-insulator microring resonator" Opt. Express **16** (11), pp. 7693-7702 (2008).

[8] J. Heebner, R. Grover, T. A. Ibrahim, "Optical microresonators" *Springer Series in Optical Sciences* Vol. 138, Springer-Verlag, London 2008.

Low Polarisation Conversion in Whispering Gallery Mode Micro-Bends

R. Stabile, K.A. Williams
Eindhoven University of Technology
Inter-University Institute COBRA on Communication Technology
Eindhoven, The Netherlands, Postbus 513, 5600 MB

Abstract—**A new fabrication tolerant micro-bend design is proposed exploiting the unique properties of whispering gallery modes. Low polarisation conversion (<25dB/90°) is predicted for low bend radii (~20 μm). The design removes fabrication critical design parameters to provide a low variability solution for high density integrated photonics.**

Keywords-micro-bend; whispering gallery modes; polarisation conversion

INTRODUCTION

Increasing photonic integration densities require ever-smaller bends between waveguides with uncompromised waveguide modal properties. However higher order mode excitation and polarisation conversion are critically dependent on absolute waveguide dimensions for micro- and nano-photonic devices. Current lithographic processes lead to feature size deviation of order hundreds of nanometers. Total internal reflecting mirrors are heavily sensitive to such critical dimension variation through the mirror facet placement and tilt[1]. Photonic band-gap devices require high resolution fabrication[2]. Hard mask erosion during etching of waveguides can induce sidewall tilt, leading to a hybridization of guided modes and undesirable polarisation rotation. This is a particular problem for curved waveguides, where polarisation conversion is predicted to increase rapidly for reducing bend radii, even for modest radius (~50 μm) curves[3]. To this end, design focus for curved waveguide has so far been placed on enhancing polarisation rotation[4]. There is therefore little quantitative understanding of the mode of operation of optimised ultra-compact micro-bends.

In this work, a new class of deep-etched micro-bend designs is proposed, which exploits whispering gallery mode operation in disc-like micro-bends. By moving the inner sidewall beyond the caustic radius, the guided bend-modes are defined by only the outer sidewalls. The inner sidewall no longer plays a role in waveguiding and scattering loss, and so bend waveguide width is no longer sensitive to fabrication variation[5]. Critical waveguide offsetting required for optimum mode-coupling is defined in the mask and thus is similarly unaffected by feature size variations. In this work, we identify fabrication tolerant optima for radius and sidewall tilt for low polarisation conversion in such micro-bends.

The Dutch technology foundation STW is acknowledged for their support

MICRO-BEND DESIGN

The simulated structures are shown schematically in Fig. 1. Straight, deep-etched, single-mode input and output waveguides are connected via a deep-etched micro-bend.

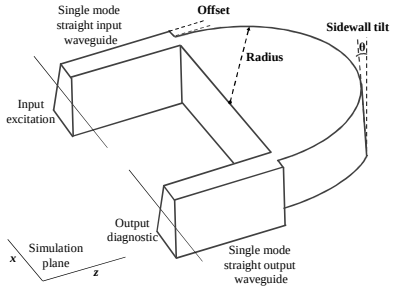


Figure 1. Schematic of the simulated waveguide core.

Assessment is performed by placing numerical 'probes' in the straight waveguides. 2D and 3D finite difference time domain (FDTD) simulations are performed with the Omnisim commercial solver[6] for 90° and 180° micro-bends. The scanned variables, shown schematically in Fig. 1, are as follows:

- Straight waveguide to micro-disc mode offset: optimizing the mode-matching at the junctions[7];
- Outer bending radius: exploring sensitivity of loss to physical size;
- Sidewall tilt angle: exploring polarisation conversion and its tolerances to fabrication parameters.

A vertical effective refractive index of 3.28 is calculated for the InGaAsP/InP waveguide using an effective index mode solver. The input and output deep etched rib waveguide widths are fixed at 1.5 μm to support a single transverse mode. Optimal offsetting between straight waveguide and micro-disc is determined iteratively for each bend radius. Vertical confinement is defined by InP cladding layers while horizontal confinement is defined by air. A screen capture from the 2D simulation tool is shown in Fig. 2. The input fundamental mode produces an excitation that propagates from the straight waveguide, around a 20 μm radius 180° disc, into a second straight waveguide. A pulse of duration 1.4 ps propagates

completely through the circuit within the calculation period. The plot shows the amplitude of the *x*-component of the electric field. After the offset, less than 3% of the input mode power is scattered at the straight-to-bend junctions. The remaining power is coupled into disc whispering gallery modes. Only a negligible amount (<1%) of input power is radiated out from the waveguide. The power coupled to the fundamental mode of the output waveguide is calculated once the light has propagated around the complete circuit. The cross-section of the device is shown as an inset in Fig. 2.

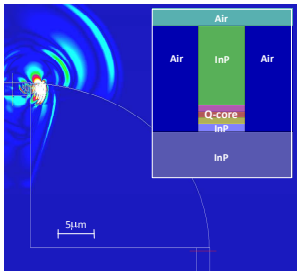


Figure 2. 2D model screen capture showing key loss mechanisms. Inset: cross section of the designed layer stacks.

Loss Mechanisms

Radiation and coupling losses are calculated for micro-bends with radii from 3 µm to 40 µm (Fig. 3). Total losses remain low (~0.3 dB) for radii in the range from 15 to 30 µm when waveguide offset is optimised, showing a relaxed fabrication tolerance. At radii exceeding 30 µm there is evidence of higher order disc mode excitation which leads to reduced coupling into an output fundamental mode. This can however be reduced by defining an inner radius close to the caustic radius limit. At radial values below 15 µm, losses increase with decreasing radius as a result of imperfect coupling into the micro-bend, despite the optimised mode offsetting.

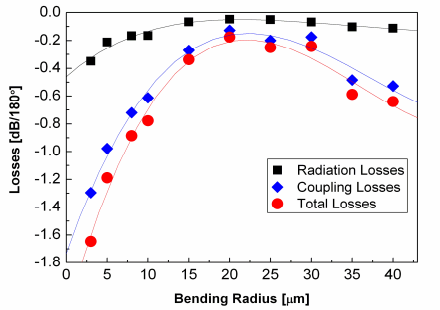


Figure 3. Total losses in 180° micro bends for varied micro-bend radius. Waveguide offsets are optimised for each radius.

Sidewall Tilt and Polarisation Conversion

Polarisation conversion results from waveguide asymmetry, which can be incurred through an off-vertical sidewall tilt in real fabricated circuits. TE-to-TM coupling is calculated for the optimum 20 µm radius micro-bends. The sidewall angle is scanned from the vertical condition at 0° to 10°, which is readily achieved with reactive ion etching. Simulations are performed for both 90° and 180° micro-bends, showing a cumulative build up in the coupling from TE-to-TM field at the output (Fig. 4). It is less straightforward to simulate intermediate angles, but there is no physical constraint.

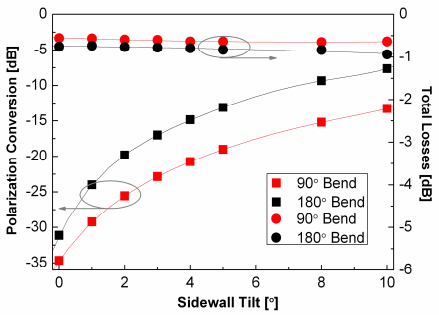


Figure 4. Polarisation conversion and loss as a function of the sidewall angle for 20 µm radius micro-bends.

A low polarisation conversion (<25dB/90°) is feasible for sidewall tilts of less than 3°. This is expected to be feasible with carefully optimised etching and masking. The increased deviation of sidewall tilt from the vertical also shows a moderate increase in the total losses (Fig. 4). The small mismatch in the losses reported in Fig. 2 (2D FDTD simulation) and Fig. 4 (3D-FDTD simulations) reflects the different description of vertical confinement.

Conclusions

A new class of micro-bend design exploiting whispering gallery modes is proposed. Relaxed fabrication tolerances and low losses, critical for high density photonic interconnection, are predicted. 20 µm radius micro-bends offer minimized total losses of ~0.5 dB/90°. Polarisation conversion is reduced to below 25 dB/90° for sidewall tilts of less than 3°, and is thus achievable with suitably optimised plasma etching.

References

[1] S. DeGui, L. Xiaoqi, W. Dongxia, H. Yuan, L. Fangliang, and J.H. Trevor, “Modeling and numerical analysis for silicon-on-insulator rib waveguide corners”, Journal of Lightwave Technology, vol. 27, pp. 4610-4618, 2009.

[2] A. Mekis, S. Fan, J.D. Joannopoulos, “Bound states in photonic crystal waveguides and waveguide bends”, Physical Rev. B, vol. 58, pp. 4809-4817, 1998.

[3] S.S.A. Obayya, B.M.A. Rahman, K.T.V. Grattan, and H.A. El-Mikati, “Analysis of polarization rotation in cascaded optical waveguide bends”, IEE Proc.-Optoelectron., vol. 142, pp. 75-80, 2002.

[4] S.S.A. Obayya, B.M.A. Rahman, K.T.V. Grattan, and H.A. El-Mikati, “Improved design of a polarization converter based on semiconductor optical waveguide bends”, Appl. Opt., vol. 40, pp. 5395-5401, 2001.

[5] R.Stabile, K.A. Williams, “Loss mechanisms in dielectric optical micro-bends”, IEEE Photonics Benelux Chapter, pp. 193-196, 2009.

[6] OMNISIM Software, Photon Design.

[7] E.G. Neumann, “Curved dielectric optical waveguides with reduced transition losses”, IEE Proc. H, 129, 278-280, 1982.

All Silicon Waveguide Spherical Microcavity Device

E. Xifré-Pérez,[1] J.D. Doménech,[2] R. Fenollosa,[1] M. Rius,[2] P. Muñoz,[2] J. Capmany,[2] F. Messeguer[1]
[1]Centro de Tecnologías Físicas, Unidad Asociada CSIC-UPV, Universidad Politécnica de Valencia, Camino de Vera s/n, 46022, Valencia, Spain, and Instituto de Ciencia de Materiales de Madrid (CSIC), Sor Juana Inés de la Cruz 3, 28049, Cantoblanco, Madrid, Spain.
[2]iTEAM Research Institute, Universidad Politécnica de Valencia, Camino de Vera s/n, Valencia, Spain
exifre@fis.upv.es

Abstract— **The characterization of silicon microspheres coupled to Si waveguides at telecom wavelengths, on a Silicon-On-Insulator technology based chip, is presented. The transmittance signal through the waveguides is strongly attenuated (up to 25 dB) at some frequencies. This effect is attributed to the coupling of light to the microphores at wavelengths corresponding to their Mie resonances.**

Keywords- silicon microspheres; microcavities; Silicon-On-Insulator technology; modal analysis; optical coupler; optical filter

I. INTRODUCTION

Optical microcavities are very relevant structures for optical processing of light, because they can trap and confine electromagnetic energy during long times in very reduced volumes, enhancing this way light-matter interaction [1]. Among the different technological platforms on which microcavities can be produced, silicon is of uttermost importance because it can combine electronics and photonics at the same time in a single device [2]. Recently, some of us reported on the synthesis of silicon microspheres, also called silicon colloids [3]. They are highly spherical particles with diameter from 0.5 to 5 μm and with a very smooth surface. This allows them working as photonic microcavities, with well defined Mie modes. The spectral characterization of these modes was also realized by means of Fourier Transform Infrared spectroscopy (FTIR) [3].

Here, we report on the coupling of silicon microspheres to Silicon-On-Insulator (SOI) waveguides at telecom wavelengths (C-band). For this purpose, devices consisting of SOI waveguides with microspheres deposited onto them are developed and their transmitted signal is measured. These measurements are compared with theoretical calculations of Mie modes of the microspheres. Previous reports about similar devices include 2D photonic crystal (PC) nanocavities coupled to PC waveguides [4], ring shaped cavities coupled to SOI waveguides [5], and half millimeter diameter silicon spheres coupled to optical fiber half couplers [6].

II. EXPERIMENTAL PROCEDURES

The silicon waveguides for this study have a cross section of 500x220 nm^2. They were produced on a standard SOITEC wafer by deep UV lithography in a ePIXfab platform. Their length is about 3 mm and they finish at their both ends by a grating coupler so that light can be easily in/out coupled to/from the waveguides [7]. Both, waveguides and couplers were designed for transmitting only TE polarized light around 1550 nm. Light from an ASE source was coupled to the waveguide and the transmitted signal was measured by an spectrum analyzer.

Silicon microspheres are obtained by chemical vapor deposition means, using di-silane as a precursor gas [3]. This method allows synthesizing amorphous and poly-crystalline silicon microspheres. For this work, poly-crystalline microspheres were chosen. Because the as-grown samples consist of a substrate with many isolated and clustered spheres and because some of them have defects, we observed the microspheres by optical microscopy and sort out the bad ones. Also, because the spheres are poly-disperse with sizes from 0.5 to 5 micrometers, we performed a selection of spheres (within the limited resolution of the optical microscope at 1000x magnification) having a diameter from 2.0 to 2.5 micrometers approximately. This is very important because the size of the sphere determines which resonant modes posses a frequency within the transmission wavelength range of the silicon waveguide and can therefore be coupled to it.

Optical transmittance measurements were performed on the selected microspheres, one by one, in a wide wavelength range, namely from 1 o 4 micrometers. We used a Fourier Transform Infrared Spectrometer Bruker IF 66/S for that purpose. This allows identifying the resonant modes and determining precisely the sphere diameter by fitting the measured signal to Mie theory [3]. Therefore, only those microspheres having resonant modes within the transmission range of the waveguides were considered as candidates to build up the devices.

Finally, the placement of the candidate microspheres on top of the silicon waveguides was realized by micromanipulation techniques. Different needle-shaped tools were fabricated for the pick and place operation and for the fine positioning of the spheres on the waveguides.

III. RESULTS AND DISCUSSION

Figure 1 shows an optical microscopy image (top view) of a Si microsphere on top of a waveguide. The diameter of the sphere, determined by the procedure described above, is 2490 nanometers. The inset shows the direction and the polarization of light with respect the waveguide-microsphere device.

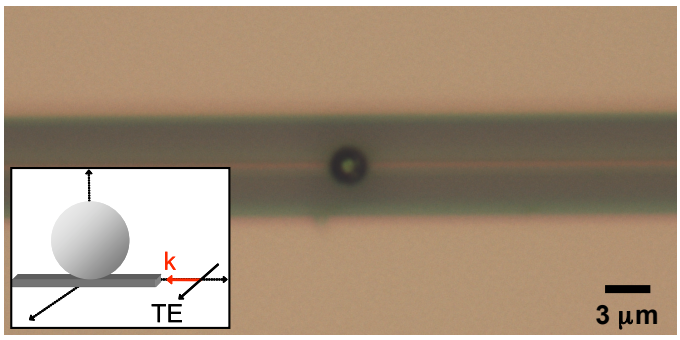


Figure 1. Optical microscopy image at 1000x magnification of a silicon microsphere placed on top of a silicon waveguide. Inset, schematic of the sphere and the waveguide showing the polarization of the transmitted light.

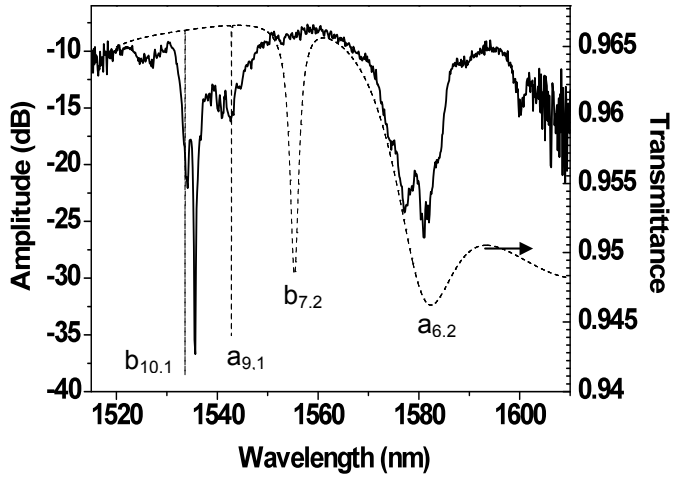


Figure 2. Measured light transmittance through a silicon waveguide with a silicon microsphere positioned on it (solid line, left axis). Simulation of the transmittance of the same silicon microsphere being isolated (dashed line, right axis).

Figure 2 shows the transmitted light through the waveguide with the microsphere placed on it (solid line, left axis), as well as the calculation by Mie theory of the transmission of light that would produce the same microsphere being isolated, i.e. without being placed on any substrate (dashed line, right axis). The deeps in transmission in the last case correspond to whispering gallery modes (WGM) that are indicated in the figure by letters 'a' and 'b' for TM an TE modes respectively, followed by two sub-indexes that account for the mode order [3]. We have associated the deeps in the transmitted signal through the waveguide to the coupling of light to the resonances of the microsphere. This way, the pronounced deep placed around 1535 nm would be originated from $b_{10.1}$ mode and the much wider deep placed around 1580 nm from $a_{6.2}$ mode. However, some discrepancies between theory and experiment are present. Some modes like $a_{9.1}$ and $b_{7.2}$ did not give rise to a coupling effect and the coupled modes ($b_{10,1}$ and $a_{6.2}$) split into two deeps respectively. Several reasons may account for these discrepancies. Firstly, while in the calculation the sphere is considered to be isolated, in the experiment it is placed on the silicon waveguide, therefore mode degeneracy would be broken due to the waveguide coupling. Secondly the control on the position of the microsphere is limited in the direction perpendicular to the waveguide, thus different coupling effects can be produced depending on this position. Thirdly, the microsphere may have some defects that could not be detected by optical microscopy and some type of absorption could be present. This would decrease the quality factor of the resonances. Nevertheless, it should be stressed the strong and peaked attenuation of the signal, of about 25 dB, achieved around 1535 nm.

IV. CONCLUSIONS

We have demonstrated the coupling between a silicon waveguide and a silicon microsphere. The light transmitted through the waveguide has been attenuated up to 25 dB for a wavelength corresponding to one of the microsphere resonating modes. A splitting effect of the modes has also been observed.

ACKNOWLEDGEMENT

The authors wish to acknowledge financial support from projects MAT2006-03097, Consolider Nº 18411 Nanolight.es, and TEC2008-06145 of the Spanish Education and Science Ministry, project PROMETEO/2008/092 of Generalitat Valenciana and project Apoyo a la investigación 2009 from Universidad Politecnica de Valencia, nº reg. 4325. J.D. Doménech acknowledges the FPI research grant BES-2009-018381. E. Xifré-Pérez acknowledges the financial support from the program Juan de la Cierva (Spanish Ministerio de Educación y Ciencia).

REFERENCES

[1] K.J. Vahala, "Optical microcavities," Nature, vol. 424, pp. 839–846, 2003.

[2] L. Pavesi, in Silicon Photonics, Eds : D.J. Lockwood, Springer, Berlin, Germany 2004.

[3] R. Fenollosa, F. Messeguer, and M. Tymczenko, "Silicon Colloids: from microcavities to photonic sponges," Adv. Mater., vol. 20, pp. 95–98, 2008.

[4] S. Noda, A. Chutinan, and M. Imada, "Trapping and emission of photons by a single defect in a photonic bandgap structure," Nature, vol. 407, pp. 608-610, 2000.

[5] V. R. Almeida, C. A. Barrios, R. R. Panepucci, and M. Lipson, "All-optical control of light on a silicon chip," Nature, vol 431, pp. 1081-1084, 2004.

[6] Y. O. Yilmaz, A. Demir, A. Kurt, and A. Serpengüzel, "Optical Channel Dropping With a Silicon Microsphere," IEEE Phot. Tech. Lett., vol 17, pp. 1662-1664, 2005.

[7] D. Taillaert, F. V. Laere, M. Ayre, W. Bogaerts, D. V. Thourhout, P. Bienstman, and R. Baets, "Grating couplers for coupling between optical fibers and nanophotonic waveguides," JJAP Part-1, vol. 45, pp. 6071-6077, 2006.

Bandwidth tunable filter based on silicon microring-MZI structure

Yunhong Ding[1,2], Xinliang Zhang[1], Dexiu Huang[1],
[1]Wuhan National Laboratory for Optoelectronics,
School of Optoelectronics Science and Engineering,
Huazhong University of Science and Technology,
Wuhan, 430074, Hubei, People's Republic of China
hustdyh@smail.hust.edu.cn

Minhao Pu[2], Liu Liu[2], Jing Xu[2], Christophe Peucheret[2],
Haiyan Ou[2]*
[2]Department of Photonics Engineering,
Technical University of Denmark,
2800 Kgs. Lyngby, Denmark
*haou@fotonik.dtu.dk

Abstract—**A novel bandwidth tunable bandpass filter based on a silicon microring-MZI structure is proposed and demonstrated. By thermally tuning the resonance offset between the two microring resonators, and adding the two drop transmissions together, the bandwidth of the microring-MZI filter can be easily linearly tuned with low in-band ripples.**

Key words—*bandwidth tunable; thermal tunable; optical filter; microring; optical signal processing.*

I. INTRODUCTION

Optical filters are one of the basic components in modern optical applications, especially in wavelength division multiplexing (WDM) optical networks. An optical filter is typically applied to filter out the required channel from a WDM signal. A bandwidth tunable filter is much more flexible since it can adapt to the bit rate of the selected channel, or select several channels simultaneously. To obtain such tunability, many approaches have been proposed and demonstrated so far. For example, a bandwidth tunable filter based on a single microring resonator has been demonstrated by micro-electronic-mechanical-system (MEMS)-tuning the coupling coefficient of the resonator [1, 2]. However, to realize MEMS tunability, a high actuation voltage of nearly 40 V should be applied. In another demonstration, the coupling of the microring resonator was tuned with a Mach-Zehnder interferometer (MZI), resulting in bandwidth tunability of the through transmission [3]. However, for the single microring resonator scheme, the tunability is limited, and as the bandwidth is tuned, the extinction ratio (ER) of the drop transmission is deteriorated. To improve the tunability and ER, high order microring resonators have also been used [4]. However, those are relatively complex and hard to control.

In this paper, we propose and demonstrate a simple and novel bandwidth tunable bandpass filter based on a silicon microring-MZI structure. The drop transmissions of the two identical microring resonators are combined together in the MZI structure. By thermally tuning the resonance offset between the two microring resonators, the bandwidth of our device can be easily linearly tuned over a large range with nearly constant ER and small in-band ripples.

II. FILTER PRINCIPLE

The proposed device is illustrated in Fig. 1. The drop

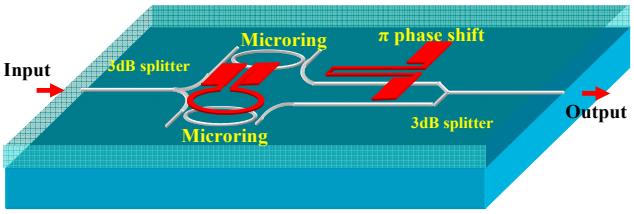


Figure 1. Structure of the microring-MZI bandwidth-tunable filter. It consists of two 3 dB splitters and two identical microring resonators. One heater is added on top of one microring resonator for resonance offset tuning. Another heater is added on top of one straight waveguide for phase tuning of the MZI.

transmission of a single microring resonator can be expressed as

$$t = -\frac{\kappa^2\sqrt{a\exp(-j\theta)}}{1-a(1-\kappa^2)\exp(-j\theta)} \quad (1)$$

where κ is the field coupling coefficient of the coupling region of the microring resonator, and θ and a are the roundtrip phase shift and transmission coefficient, respectively. As shown in Fig. 2(a), the wavelength-dependent phase shift induced by a single microring resonator over one free spectral range (FSR) is π. The two drop transmissions of the two microring resonators are partly overlapped by tuning the resonance of one ring. At the wavelength corresponding to the crossing point between the two drop transmissions (see Fig. 2(a)), a phase shift difference close to π is obtained between the two propagation paths in the MZI. Thanks to the additional π phase shift induced by the heater over the straight section of one MZI arm, the phase shifts in both arms can be made nearly equal, resulting in constructive interference and addition of the two drop transmissions, as shown in Fig. 2 (b). The bandwidth of the filter can then be tuned by adjusting the resonance offset between the two drop transmissions. At the same time, outside the combined passband of the two drop transmissions, the induced extra π phase shift will lead to a destructive interference and subtraction of the two drop transmissions, which further improves the ER of the proposed filter.

An optical filter is normally characterized by its 3 dB bandwidth, in-band ripple and ER, as defined in Fig. 2(b). For our application, a device with large tunability, high ER and small in-band ripples is preferred.

This work was supported by the National Natural Science Foundation of China (Grant No. 60577007), the National Basic Research Program of China (Grant No. 2006CB302805) and the Chinese Scholar Council (CSC).

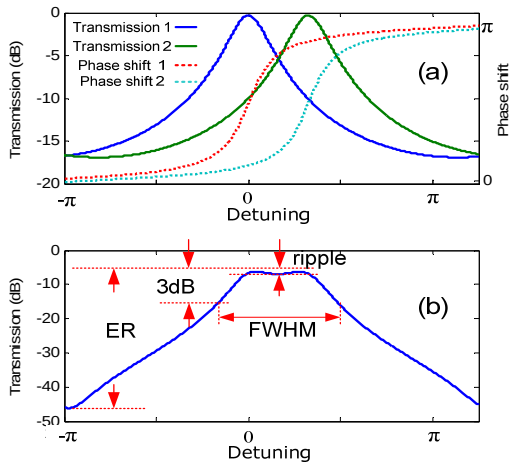


Figure 2. Principle of the bandwidth tunable filter. (a) Transmission and phase shift of the two microring resonators. (b) Characteristics of the bandwidth tunable filter. Here, we assume $\kappa = 0.5, a = 0.99$.

III. Filter Fabrication and Characterization

Fig. 3 shows the fabricated device. The device is fabricated on a SOI wafer with top silicon thickness of 250 nm and buried silicon dioxide of 3 µm. Diluted (1:1 in anisole) electron-beam resist ZEP520A is spin-coated on the wafer to form a ~110 nm-thick mask layer. The microring-MZI structure is then defined using electron-beam lithography (JEOL JBX-9300FS). After that, the sample is etched by inductively coupled plasma reactive ion etching (ICP-RIE) to transfer the patterns to the top silicon layer. Afterwards, a top cladding layer of 550 nm benzocyclobutene (BCB) is spin-coated for planarization, and a layer of 400 nm ZEP520A is spin-coated in sequence as the mask layer for the heaters. Electron-beam lithography is used again to define the patterns of the heaters and pads. Finally, 100 nm thick titanium heaters and pads are formed by evaporation and lift-off techniques. The radii of the microring resonators are 10 µm, with the waveguide width of 430 nm and coupling gap of 97 nm for both through and drop coupling regions, as shown in Fig. 3(a).

Due to fabrication uncertainties, the transmissions of the two microring resonators may not coincide initially. Since the thermal tuning will lead to a red-shift in the resonance of the microring resonator [5], one of the resonators is slightly blue-shifted by design. To ensure equal loss in the two arms of the MZI, and since heaters may cause excess loss, they are implemented on top of both straight sections. However, only one of them is used, with a heating electrical power of 88 mW,

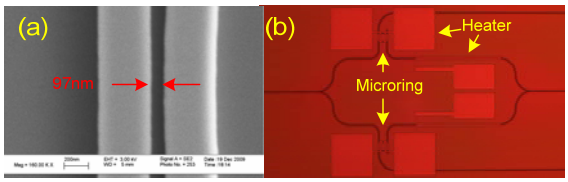


Figure 3. (a) Scanning electron microscope (SEM) top view image of the coupling region of the microring resonator. (b) Optical microscope picture of the fabricated device. Two identical add-drop microring resonators with micro-heaters are inserted in the two arms of the MZI structure. The straight sections of the two arms are also both implemented with heaters.

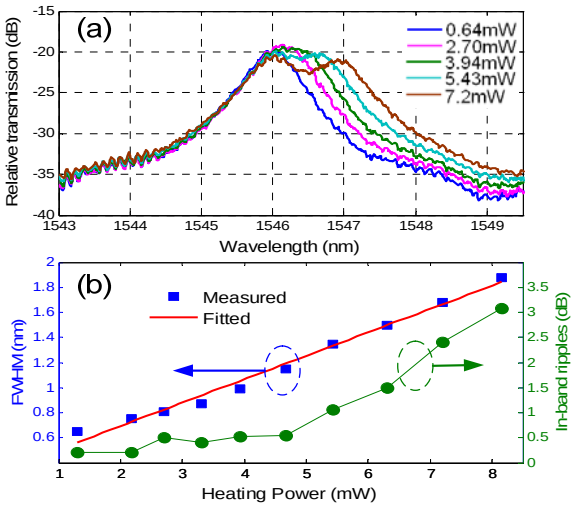


Figure 4. (a) Measured transmissions of the filter with different microring heating powers for the TE mode of the filter. (b) Measured bandwidth and in-band ripples versus microring heating power.

in order to introduce the desired π phase shift.

Fig. 4(a) shows the measured transmissions for the TE mode of the fabricated device, with the microring heating power from 0.64 mW to 7.2 mW. A clear bandwidth broadening can be observed. Fig. 4(b) illustrates the further measured tunability and the in-band ripples. The bandwidth linearly increases with the heating power. The in-band ripples remain below 1 dB when the heating power is under 5.43 mW. In this range, the 3 dB bandwidth can be linearly tuned from 0.65 nm to 1.35 nm. However, if the heating power further increases, the in-band ripple gradually increases. The ER of the filter is always larger than 15 dB, as shown in Fig. 4(a), which makes it practical in real applications.

IV. Conclusion

We have proposed and demonstrated a bandwidth tunable filter based on a silicon microring-MZI structure. An effective bandwidth tuning range from 0.65 nm to 1.35 nm, with nearly constant ER and small in-band ripples below 1dB, is obtained with a microring heating power between 1 mW and 5.43 mW. Based on the proposed structure, further improvement of the tunability can be realized by combining more microring resonators.

References

[1]. M.-C. M. Lee, and M. C. Wu, "Variable bandwidth of dynamic add–drop filters based on coupling-controlled microdisk resonators," Opt. Lett. **31**, 2444 (2006).

[2]. J. Yao, and M. C. Wu, "Bandwidth-tunable add-drop filters based on micro-electro-mechanical-system actuated silicon microtoroidal resonators," Opt. Lett. **34**, 2557 (2009).

[3]. L. Chen, N. Sherwood-Droz, and M. Lipson, "Compact bandwidth-tunable microring resonators," Opt. Lett. **32**, 3361 (2007).

[4]. B. Little, C. Sai, C. Wei, J. Hryniewicz, D. Gill, O. King, F. Johnson, R. Davidson, K. Donovan, C. Wenlu, and S. Grubb, "Tunable bandwidth microring resonator filters," in European Conference on Optical Communication, ECOC 2008. paper Th.2.C.2 (2008).

[5]. F. Gan, T. Barwicz, M. A. Popovic, M. S. Dahlem, C. W. Holzwarth, P. T. Rakich, H. I. Smith, E. P. Ippen, and F. X. Kartner, "Maximizing the thermo-optic tuning range of silicon photonic structures," in IEEE/LEOS Photonics in Switching 2007, paper TuB3.3 (2007).

Potential of Si-nc MOS devices as Transceivers for interchip optical links

A. Marconi, A. Anopchenko, L. Pavesi
Nanoscience Laboratory, Department of Physics
University of Trento
Via Sommarive 14, 38121 Povo (Trento) Italy
marconi@science.unitn.it

G. Pucker
Microtechnologies Laboratory
Bruno Kessler Foundation
Via Sommarive 18, 38121 Povo (Trento) Italy

Abstract—**New silicon nanocrystal (Si-nc) transceiver is present in this work. Both light emitter and receiver share the same circuit that is fabricated in a standard cMOS line and linked together in free-space with an optical fiber. A high efficiency is achieved which makes good promises for optical links in integrated silicon photonics and numerous applications.**

Si-nc devices; Transceiver; interchip optical link

I. INTRODUCTION

Integration of a transceiver in a single chip requires the integration of a light source and a photodetector. These transceivers when realized in silicon have enormous potential market for high speed optical interconnections, for optical signaling in harsh environments with high magnetic and electric field, for (bio)chemical sensing, etc. Many approaches have been tried in order to demonstrate the feasibility of a monolithically integrated transceiver, i.e. all in silicon. In [1] a silicon solar cell was bonded on top of another one; a good optical coupling and system efficiency was shown but the devices were very large, the wavelength mismatch between the light emitted and absorbed yields only 33% of coupling efficiency and the complexity of the cells makes integration difficult. In [2] on-chip integration is shown using a III-V substrate while only 10^{-4} % of power conversion (power from emitter revealed by the receiver) was achieved.

Our approach considers two cMOS capacitors, the simplest structure achievable, where the gate oxide is replaced by a Si-nc multilayer used as active material. Under forward bias Si-nc structure emits light efficiently in visible and under reverse bias the same Si-nc device work as photoreceiver. Each cMOS capacitor could play the role of the emitter as well as of the receiver. The optical link was done by a fiber optic in order to prove the feasibility of a monolithically integrated transceiver useful in telecommunication or sensing application. The silicon based technology needed to grow such system allows potentially low fabrication cost.

II. EXPERIMENTAL

A. Devices and Setup Description

The devices structure is a metal-oxide-semiconductor (MOS) capacitor. Alternating layers of stoichiometric SiO_2 and silicon rich silicon oxide (SRO) were grown on p-type Si wafer by PECVD. This active layer is composed of 5 layer of SRO and has a nominal thickness of about 25 nm.

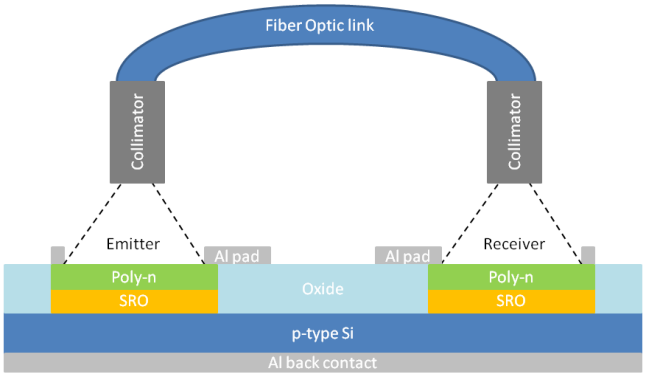


Figure 1. Scheme of the transceiver. Two identical devices are used as emitter and as receiver. The optical link if formed with an optical fiber.

During an high thermal annealing silicon nanocrystals are formed in the SRO layer. This is used as the gate oxide in our capacitors. The top contact is formed by 100 nm n-type polycrystalline-silicon, while 500 nm thick Al grid is used to connect the active area of 10^{-3} cm^2 with the bonding pad.

Recently Si-nc LED emitting in the visible range with the best efficiency reported so far was demonstrated by us [3]. The devices are also able to work efficiently as a detector at low light intensity [4]. More details on the devices and its characteristics are reported elsewhere [5]. Fig. 1 shows the scheme of the setup used to make the optical link. The devices have a diameter of 300 μm and are chosen at a distance of 5 cm in order to prevent interferences through the substrate. A visible multimode fiber optic is used to couple the two devices together. The coupling is optimized with a micromanipulator using each LED as emitter and maximizing the signal at a Si APD detector.

B. Electrical and Opto-Electrical Characterizations

In order to understand the electrical behavior of the devices under test Fig. 2 shows the Current-Voltage characteristics under dark and under illumination. Notice that two different scales are used to emphasize the electroluminescent region in forward bias (at the right) and the detection region in reverse bias (at the left). The dots reported on the I-V curve, in forward

bias, represent the current values where electroluminescence is observed.

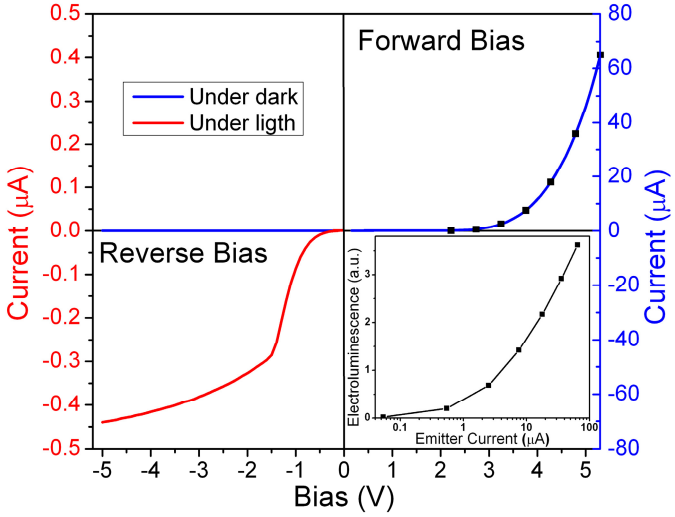


Figure 2. Current-Voltage characteristics under dark (blue) and under illumination (red). Black dots show current values at which EL signal (shown in the inset) was recorded. Left panel shows the photodetector region of the receiver.

In this region I-V characteristic is not affected by the illumination while in reverse bias the characteristics differ due to the contribution of the photogenerated current.

In order to measure the power conversion efficiency of the system the receiver was polarized at -4V and a voltage sweep on the source was done. Fig. 3 shows the photocurrent at the receiver versus the injected current at the source. Under dark a current of 0.5 pA flow through the detector whith a power consumption of 2 pW. Under the illumination the current grow up to 5 pA and the dissipated power is rather low. For the source, as shown in [3], the emission power efficiency reach its maximum at low injecting current because the electroluminescent intensity grow more slowly than the injecting current due to high losses at high biasing.

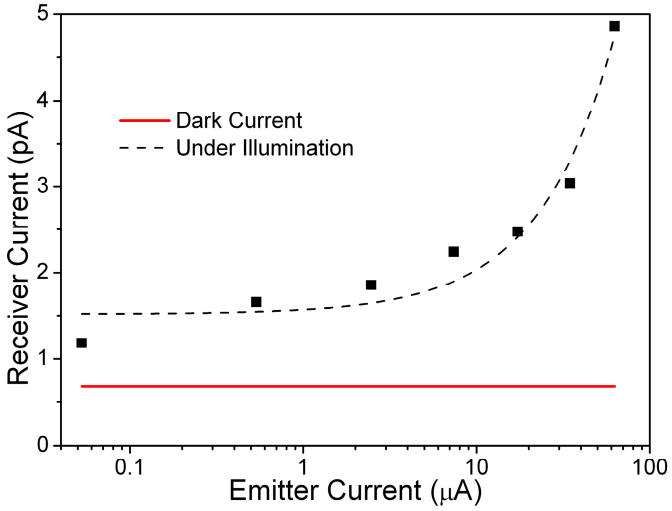


Figure 3. Photocurrent measured at the receiver versus the injected current at the source.

Fig. 4 show the power conversion efficiency of the system:

$$\eta\,\% = \frac{P_{Rl}-P_{Rd}}{P_{Rl}+P_E}\cdot 100.$$

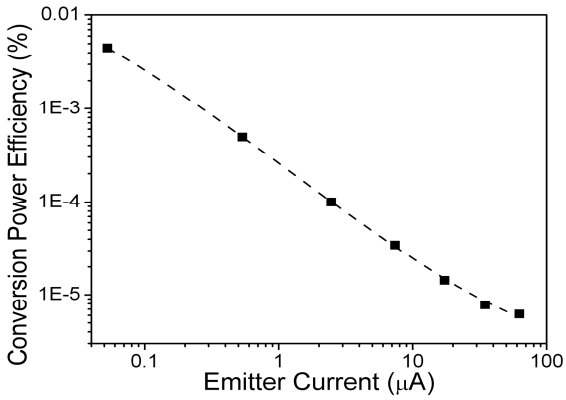


Figure 4. Power conversion efficiency versus source current

P_{Rl} is the power at the receiver under illumination, P_{Rd} the power at the receiver under dark and P_E the power injected at the source. From this figure it is clear that the system is more efficient at low injection current due to the higher efficiency of the emitter at this injection. Even with a not optimized optical coupling due to the crude coupling whit the optical fiber, it was possible to obtain efficiency up to 0.01%. This is attributable to the fact that the visible emission from the emitter can be absorbed by receiver with an efficiency larger than 80%.

III. Conclusion

In this paper we have demonstrated a proof-of-concept for an efficient silicon based transceiver for interchip communication made by standard cMOS technology. It is based on the use of the very same device both as emitter as well as a receiver. Despite the crude optical coupling the results here reported are very encouraging. More characterizations on the behavior of the system, also in pulsed regime, will be presented during the conference.

Acknowledgment

The authors acknowledge Dr. M. Wang for devices fabrication. This research has been supported by EC through the HELIOS FP7-ICT 224312 project and by a grant of INTEL.

References

[1] J. Zhao, M. A. Green, and A.Wang, "High-efficiency optical emission, detection, and coupling using silicon diodes," J. App. Physics, vol. 92, pp. 740–741, September 2002.

[2] P. Huertas, G. Mier, M. L. Dotor, J. V. Anguita, D. Golmayo, and F. Briones, "Monolithically integrated LED, waveguide and photodetector optical system for near-infrared biosensor," Sens. Actuators, vol. 37-38, pp. 512–515, 1993.

[3] A. Marconi, A. Anopchenko, M. Wang, G. Pucker, P. Bellutti, and L. Pavesi, "High power efficiency in Si-nc/SiO_2 multilayer light emitting devices by bipolar direct tunneling," App. Physics Letters, vol. 94, 221110, 2009.

[4] N. Daldosso, and L. Pavesi, "Nanosilicon Photonics", Laser & Photon. Rev., vol. 3, pp. 508-534, 2009.

[5] A. Anopchenko, A. Marconi, E. Moser, S. Prezioso, M. Wang, L. Pavesi, G. Pucker, P. Bellutti, "Low-voltage onset of electroluminescence in nanocrystalline-Si/SiO_2 multilayers", J. Appl. Physics, vol. 106, 033104, 2009.

High Efficiency Silicon-on-Insulator based Corner Turning Mirrors

D. G. Sun, S. Abdul-Majid, I. Hasan, J. Udoeyop, Z. Hu, T. J. Hall
School of Information Technology & Engineering
University of Ottawa
Ottawa, Canada
dsun@site.uottawa.com

G. Tarr
Department of Electronics
Carleton University
Ottawa, Canada

(An oral presentation is preferred)

***Abstract*:** Low propagation loss and low turning loss are very important for photonic integrated circuits. In this work, the silicon-on-insulator based corner mirrors having high optical transfer efficiency optimized in previous numerical calculation are further validated with FDTD simulation and then fabrication and test. An experimental optical access loss of 0.8dB is obtained.

Keywords: Silicon-on-insulator, corner turning mirror, optical transfer efficiency, optical access loss

I. INTRODUCTION

Photonic network systems, especially those using reconfigurable optical add-drop multiplexing (ROADM), have led to the need for larger-scale photonic integrated circuits (PIC) [1]. As a result, silicon-on-insulator (SOI) waveguide is a maturing technology and its inherent capabilities and advances are encouraging intensive research on the hybrid integration of active/passive components on one chip [1-3]. However, the minimum tolerable radius curvature of a conventional rib waveguide bend is still quite large, so the development of a low-loss compact SOI waveguide corner turning mirror is a paramount research topic [4]. In this work, we optimized the SOI waveguide corner mirrors with our numerical theory and commercial software tools, and then validated the predictions with experiments.

II. NUMERICAL MODELING AND PERFORMANCE SIMULATION

Figure 1(a) schematically shows the corner mirror structure of SOI rib waveguide and Fig. 1(b) is the cross-sectional view of SOI rib waveguide. This corner mirror structure is formed by an input waveguide channel, an output waveguide channel and a reflector. Certainly the angle between the input and the output waveguide channels θ meet the total internal reflection (TIR) at the interface of the waveguide and reflector materials. H is the silicon film thickness, h is the rib height and W is the rib width; n_1 and n_2 are the refractive indices of the core and the cladding of the effective channel waveguide, respectively, and n_m is the refractive index of the reflector material.

In this TIR process between the reflector material and waveguide material, the Goos-Hanchen effect results in shift of the effective reflecting interface from the real mirror interface, which impact the transfer efficiency. The Goos-Hanchen shift (GHS) is defined as [5]:

$$d_{TE} = \frac{1}{k_0[n_1^2 \sin^2(\frac{\theta}{2}+\varphi) - n_m^2]^{1/2}} \quad (1a)$$

$$d_{TM} = \frac{n_m^2}{n_1^2 \sin^2(\frac{\theta}{2}+\varphi) - n_m^2 \cos^2(\frac{\theta}{2}+\varphi)} \quad (1b)$$

where d_{TE} and d_{TM} are the GHS for TE and TM polarization states, respectively, and φ is the tilt-angle of mirror plane. Our numerical calculation shows the GHS in this structure has a bearing upon the transfer efficiency of a corner mirror [5]. Namely, if the mirror plane has a negative shift to compensate the GHS, this structure has the best transfer performance to the optical guided mode and is more robust to impaired surface roughness and mirror plane tilt angle errors.

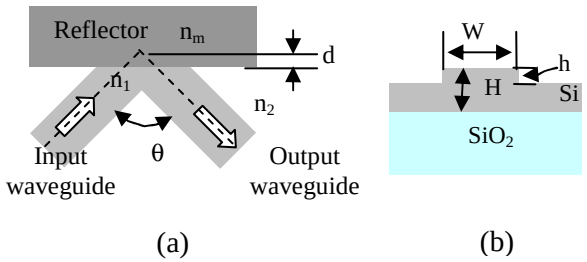


Figure 1: (a) Schematic geometry of SOI based corner mirror; (b) cross-sectional view of SOI rib waveguide

This work is sponsored by the Ontario Centre for Excellences (CR-60017-08) of Canada, D&T Photonics, and benefited from a Fabrication Grant IPDTTDTP provided by CMC Microsystems.

By selecting the device parameters of a 90° corner turning mirror: H=1.5μm, h=0.5μm, and W=3.0μm, the refractive indices of Si and SiO_2 as 3.45 and 1.45, respectively, at wavelength λ=1550nm and TE polarization, we obtained the FDTD simulation result of beam propagation process and guided mode output with this corner turning mirror as shown in Fig. 2(a) and (b), respectively

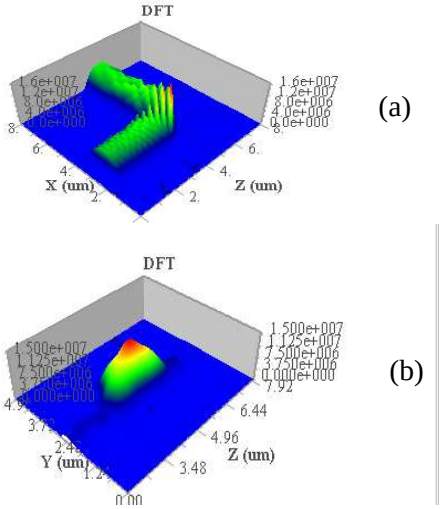
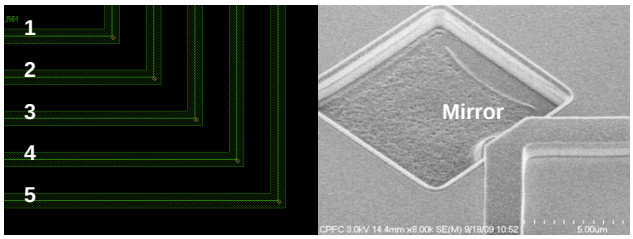


Figure 2: FDTD simulations with the selected corner mirror: (a) the propagation optical beam and (b) the output mode

III. FABRICATION AND EXPERIMENT

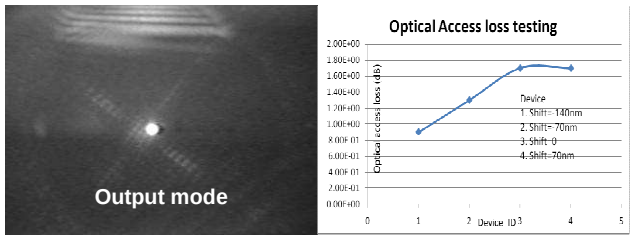
According to above optimization, we designed five corner mirror structures to correspond with the reflecting plane shift of -140, -70, 0, 70, and 140nm, then fabricated the corner turning mirror devices in Canadian Photonics Fabrication Centre (CPFC) with a fabrication grant of Canadian Microsystems Corporation (CMC). A SOI based device of corner turning mirror with incident/reflection waveguides was fabricated as shown in Fig. 3(b), where the mirror is the deep air trench. The measurement shows the sidewall verticality of the deep air trench has achieved 90±0.4°.



(a) **(b)**

Figure 3: (a) Five corner turning mirror devices having five different mirror plane shifts and (b) the SEM image of a mirror

With the fabricated device, at the wavelength of λ=1550nm, a guided mode output is observed as shown in Fig. 4(a), and the measured results of its optical access loss is shown in Fig. 4(b), the lowest value of 0.9dB is from the device with the shift of -140nm and this structure also gives a relatively lower polarization dependence of the optical access loss, which are completely consistent with the predictions of our previous work [5].



(a) **(b)**

Figure 4: (a) an experimental optical guided-mode output and (b) the measured values of optical access loss for four devices

IV. CONCLUSION

In accordance with our previous work on the modeling and numerical calculation, we further validated the optimization for the optical energy transfer efficiency of SOI waveguide corner mirrors with FDTD commercial software with a consideration of GHS. Then we fabricated a serial of corner turning mirror devices and finally obtained experimental results of guided mode output and optical access loss, which are agreeable with the values obtained in both numerical calculation and simulations.

ACKNOWLEDGMENT

Authors would like to thank Professor Pierre Berini of the School of Information Technology & Engineering and his group members: Ewa Lisicka, Asad Sadkhan and Fan Hui for their kind help to the experimental/testing work of this project. Authors also thank Professor Karin Hinzer and her group Ph.D student Simon Chow for their assistanc. Mr. Peng Liu of D&T Photonics is acknowledge for his support of this project.

REFERENCES

[1] W. J. Tomlinson, "Evolution of passive optical component technologies for fiber-optic communication systems," *J. Lightwave Technol.* Vol. 26, No 12, pp. 1046-1063, 2008.

[2] G. Roelkens, D. V. Thourhout, and R. Baets, "Silicon-on-insulator ultra-compact duplexer based on a diffractive grating structure," *Optics Express*, Vol.15, pp.10091-10096, 2007.

[3] B. Jalali and S. Fathpour, "Silicon photonics," *J. Lightwave Technol*, Vol. 24, no 12, pp. 4600-4615, Dec. 2006.

[4] Y. Qian, S. Kim, J. Song, and G. P. Nordin, "Compact and low loss silicon-on-insulator rib waveguide 90° bend," *Opt. Exp.*, Vol.14, pp.6020-6028, 2006.

[5] D. G. Sun, X. Li, D. Wong, Y. Hu, F. Luo, and T. J. H, "Modeling and numerical analysis for silicon-on-insulator rib waveguide corners," J. Lightwave Technol. Vol. 27, No 20, pp. 4610-4618, 2009.

SiON integrated optics elliptic couplers for Fizeau-based Optical Coherence Tomography

V. Duc Nguyen, T.G. van Leeuwen, and J. Kalkman
Biomedical Engineering & Physics,
Academic Medical Center, University of Amsterdam
Amsterdam, The Netherlands
D.V.Nguyen@amc.uva.nl

N. Ismail, F. Sun, B. I. Akca, A. Driessen, M. Pollnau, R. M. de Ridder, and K. Wörhoff
Integrated Optical Microsystems Group,
MESA+ Institute for Nanotechnology, University of Twente
Enschede, The Netherlands

Abstract—**The use of integrated optics for Optical Coherence Tomography (OCT) can offer significant cost reductions and new applications. We designed, fabricated, and characterized Silicon oxynitride (SiON) elliptic couplers that are used to focus light from a chip into the off-chip environment. Fizeau-based OCT measurements are performed and compared to calculations.**

Keywords- optical coherence tomography; integrated optics; elliptic coupler;

I. INTRODUCTION

Optical Coherence Tomography (OCT) [1] is a non-invasive optical technique for imaging biological tissue to a few millimeters depth with micrometer resolution. OCT is gaining widespread use in the clinic, in particular its use in ophthalmology for imaging the retina is becoming routine clinical practice. OCT uses interferometry to detect the time-of-flight of light reflected from a tissue. Nowadays, most OCT systems are Fourier-domain OCT systems, measuring the interference spectrum, formed by the reflection of a reference arm and biological tissue, by using a spectrometer or a swept source. Fourier-domain OCT systems are composed of many bulk optical components, such as: optical fibers, (focusing) lenses, beam splitters, and galvanometric scanners that all are necessary to relay the optical signal through the OCT system. The combination of all these components makes OCT systems bulky, expensive, and complex. Integrated optics can integrate these bulk components that make an OCT system onto a single optical chip. Therefore, integrated optics can make OCT systems smaller and more cost efficient. Thus far, only work has been presented about the integration of beamsplitters and waveguides in integrated optics for OCT [2], however many other OCT components also can be integrated. In addition, integrated optics can offer additional OCT functionality that would be too difficult or complex to achieve with bulk optics.

One key OCT component is a sample arm focusing lens. Here we present integrated optics elliptic couplers designed and fabricated in Silicon oxynitride (SiON) as an integrated-optics solution to focus light from the chip to the off-chip environment.

This work is supported by the Dutch Smartmix-Memphis project.. The authors gratefully acknowledge the technical support by G. Sengo.

II. ELLIPTIC COUPLERS

An integrated optics elliptic coupler consists of a straight index guiding waveguide followed by one half of an elliptic-shaped index guiding section [3], as shown in Fig.1. The elliptic coupler ends in an air region where sensing in the off-chip environment can take place. In a ray optics view, all rays emanating from one focal point of an ellipse are imaged onto the second focal point. Since the straight waveguide exits close to the first focal point, and it is thus to be expected that many rays will be imaged close to the second focal point. Some of the rays exiting the straight waveguide are not reflected on the boundary of the elliptic coupler and propagate without being focused into the air region.

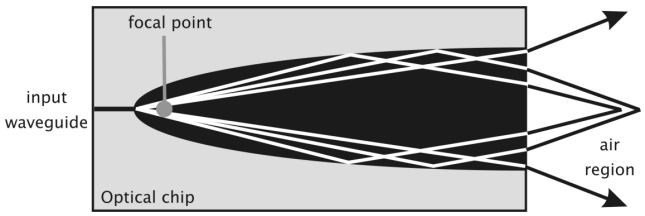


Fig. 1. Integrated optics elliptic coupler geometry. Rays from the input waveguide reflect off the elliptic coupler edge and are focused in the air region.

III. MATERIALS AND METHODS

We designed and fabricated straight waveguides/elliptic couplers in SiON technology [4]. The SiON layer has a thickness of 820 nm (n=1.5337) and is surrounded by SiO_2. For single mode operation we designed the straight waveguides with 2.5 μm width.

The electric field in the air region is determined in two ways. First, we perform beam propagation method (BPM) simulations of the electric field in the plane of the chip. Second, the beam profile intensity is measured in the plane of the chip using a knife-edge set-up and an infrared power meter. Finally, the field exiting from the elliptic coupler is modeled by Gaussian optics using the simulated and measured beam waists.

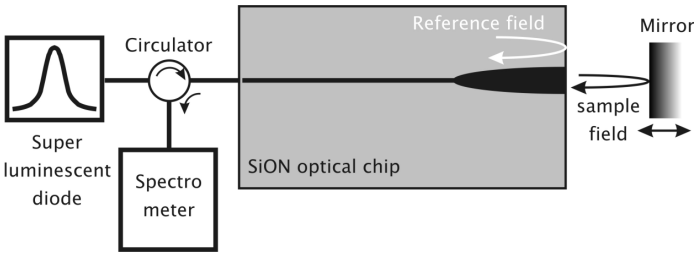


Fig. 2. Fizeau-based spectral-domain OCT set-up. Broadband light is coupled into the elliptic coupler and light reflected from the end-facet and the mirror is directed through the circulator into the spectrometer. The beam profiles are measured with a knife edge at the exit of the elliptic coupler.

Interferometric measurements are performed using a common path Fizeau-based OCT measurements, see Fig. 2. In short: light from a broadband lightsource operating at 1300 nm wavelength is coupled through a circulator into a tapered fiber. Via the tapered fiber light is coupled into waveguides with elliptic couplers at the other end of the optical chip. The field is reflected on the end facet of the elliptic coupler and on a mirror that is mounted on a moveable stage. The reflected light is guided through the circulator to a spectrometer where it is detected. Due to interference of the two fields, the spectrum is modulated and a depth profile is calculated by taking the Fourier transform of the spectrum. After a correction of the OCT signal for the intrinsic OCT system sensitivity with depth the OCT signal is only determined by the field evolution in the air region.

IV. OCT MEASUREMENTS

Figure 3 and 4 show the results for an elliptic coupler with a semimajor axis length of 1000 µm and a semiminor axis length of 35 µm. Figure 3 shows the beam waist for various distances from the end facet (intensity at $1/e^2$ level) measured in the plane of the chip with the knife-edge method. It can be clearly observed that the beam is focused at a distance of 500 µm and that the measured beam waists are in good agreement with the BPM simulations. In the out of plane direction the beam is strongly divergent.

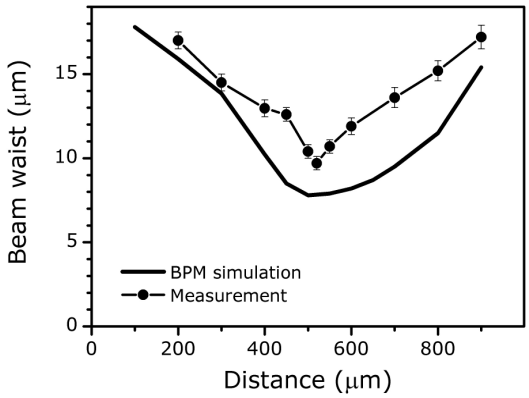


Fig. 3 Beam profile measurements in the plane of the chip as a function of distance for an elliptic coupler with semimajor axis length of 1000 µm and a semiminor axis length of 35 µm (dots). The experimental results are compared to BPM simulations (solid line)

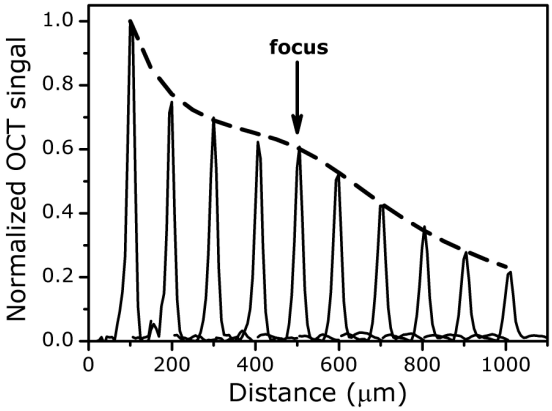


Fig. 4. Fizeau-based OCT depth profiles for a mirror at various distances from the end facet. The measurements for the various distances are superimposed on top of each other. The dashed line shows the decrease of the signal in depth calculated from the measured beam waist (see Fig. 3).

Figure 4 shows several OCT depth profile measurements overlaid on top of each other for various distances of the mirror relative to the end facet. The signal is normalized to the signal at 100 µm depth. As can be observed, the OCT signal strength decreases with depth, which is primarily caused by the divergent beam in the out of plane direction. In the in-plane direction the elliptic coupler focuses the beam at a distance indicated by the arrow. Gaussian optics calculations that are based on the measured beam waist are overlaid on the data (dashed line). Good agreement between the measurement and the calculations is observed.

V. DISCUSSION/CONCLUSIONS

We characterized several elliptic couplers. All show good focusing properties in the in-plane direction. Fizeau-based OCT measurements show good agreement with calculations for all elliptic couplers. Compared to a straight waveguide elliptic couplers show a clear increase of the signal with depth. The strong decrease of the OCT signal with depth is mainly due to the strong divergence in the out-of-plane direction where no focusing takes place. The strong out-of-plane divergence is caused by the small height of the waveguide resulting in a strongly divergent field. We propose tapering of SiON waveguides to decrease the out-of-plane divergence of these elliptic couplers.

REFERENCES

[1] D. Huang et al., "Optical coherence tomography" Science **254**, 1178 (1991)

[2] D. Culemann, A. Knuettel, and E. Voges, "Integrated optical sensor in glass for optical coherence tomography", IEEE J. Select. Topics Quantum Electron. **5**, 730 (2000)

[3] C. Wei, F. Groen, M. K. Smit, I. Moerman, P.Van Daele, and R. Baets, "Integrated opical elliptic couplers: modeling, design, and applications," J. Lightwave Techol. **l 15**, 906 (1997)

[4] K. Wörhoff, C. G. K. Roeloffzen, R. M. de Ridder, A. Driessen, and P.V. Lambeck, "Design and application of compact and highly tolerant polarization-independent waveguides," J. Lightwave Technol. **25**, 1276 (2007)

Reduction of N-H Absorption Peaks by B or P Doping of PECVD SiON Layers for Integrated Optics

F. Sun, A. Driessen, and K. Wörhoff
Integrated Optical MicroSystems Group, MESA+ Institute for Nanotechnology,
University of Twente, Enschede, The Netherlands
F.Sun@ewi.utwente.nl

***Abstract*—Boron or Phosphorous doped PECVD silicon oxynitride layers were fabricated and thermally treated. From the FTIR absorption spectra of the layers, N-H concentrations were obtained as functions of dopant concentration and annealing temperature. Significant reduction of N-H bonds has been observed after annealing at a temperature as low as 700˚C.**

Keywords- Silicon oxynitride, integrated optics, boron and phosphorus doping

I. INTRODUCTION

The excellent properties of silicon oxynitride (SiON), such as high transparency, adjustable refractive index and good stability, add to the attractiveness of this amorphous material for application in integrated optics [1-4]. High-quality SiON layers are reliably grown by chemical vapor deposition (CVD). However, the hydrogen-containing precursors applied in the deposition processes will inevitably lead to incorporation of hydrogen (H) bonds (Si-H, N-H, O-H) into the as-deposited SiON films. Those bonds, are well-known to cause absorption peaks at wavelength ranges around 1.5 μm [3, 4]. Annealing at high temperature (>1100˚C) can be applied to reduce the H-content and to achieve SiON-based optical waveguides with low loss [2, 3]. However, the high temperature required for sufficient hydrogen removal induces several undesired side effects such as inter-layer diffusion and micro-cracks [3].

The above problems can be addressed by introducing boron (B) and/or phosphorous (P) into the layers. Because of the weakening of chemical bonds induced by the dopants within the layers, the hydrogen bond formation will be suppressed, and annealing at lower temperatures is sufficient for further H reduction.

In our study, 5% B_2H_6/Ar and 5% PH_3/Ar were added into the gas precursors of plasma enhanced (PE) CVD processes, in order to fabricate B and P-doped SiON layers, respectively. The samples were annealed in nitrogen ambient at temperatures varying from 600-900°C. The H-bond concentrations were measured by Fourier transform infrared (FTIR) spectroscopy.

II. CHARACTERIZATION

In Fig. 1 the full FTIR spectrum of a SiON layer is shown including the positions of the absorption peaks corresponding to the three H bonds. In the FTIR spectra of all the samples, no Si-H peaks were observed within the detection limit, while the N-H peaks dominate the O-H peaks, as can be seen from the inset of Fig. 1. Therefore we only consider the change of N-H peaks for simplicity. The concentration of N–H bonds can be calculated by the method of Lanford and Rand [5].

Detailed analysis showed that the N-H absorption peak can be deconvoluted into two symmetric Gaussian peaks, notated as NH1 and NH2 (inset of Fig. 1). Peak NH1 is the contribution from the stretching of N-H…N, the bonding between the H atom in N-H bond and the lone pair electrons of another N atom nearby [6]. Compared to normal N-H stretching modes (NH2 peak), the NH1 peak is significantly broader and shifts to lower vibration frequencies.

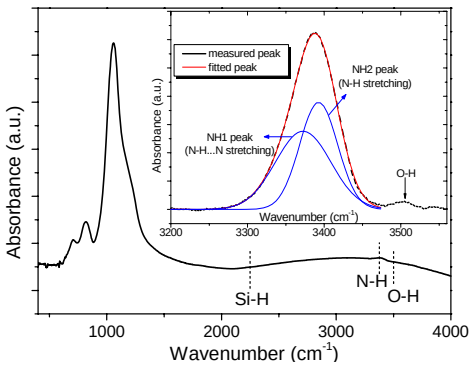


Figure 1. FTIR spectrum of SiON layer with indication of the absorption peak positions corresponding to Si-H stretching, N-H stretching and O-H stretching. (The inset shows details of N-H and O-H absorption peaks after baseline correction, where the N-H peak is deconvoluted into two Gaussian peaks)

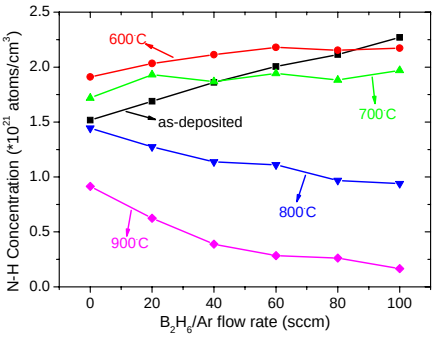


Figure 2. N-H concentration changes with annealing temperature and flow rates of gas precursors in B-doped SiON layers

This work is financially supported by the MEMPHIS Project of the Smart Mix programme of the Dutch Ministry of Econonic Affairs

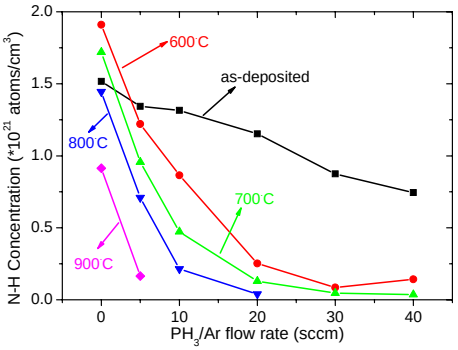


Figure 3. N-H concentration changes with annealing temperature and flow rates of gas precursors in P-doped SiON layers

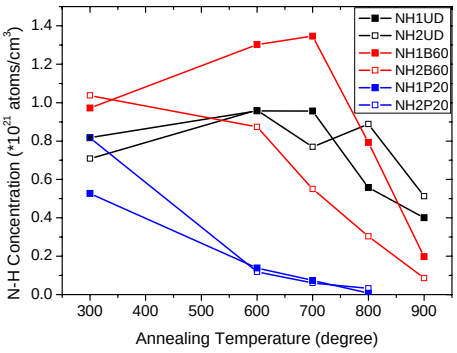


Figure 4. NH1 and NH2 concentration changes as a function of annealing temperature in undoped, B60 and P20 samples

III. Discussion

The influences of the annealing temperature and the dopant gas flow rates on the N-H-bond concentration are shown in Fig. 2 and Fig. 3. As can be seen in Fig. 2, in as-deposited B-doped SiON, the N-H concentration increases with the B_2H_6/Ar flow rate. There is no monotonous correlation between N-H concentrations and annealing temperatures. In undoped layers as well as in most of the B-doped layers, the N-H concentration first increases slightly with annealing temperature, followed by significant N-H reduction when the temperature increases further. The efficiency of N-H removal by annealing increases with the flow rate of B_2H_6/Ar. In sample B100 (B_2H_6/Ar=100sccm), for example, the highest N-H concentration among all the as-deposited B-doped layers was measured, while these N-H bonds are easiest to be eliminated by thermal treatment. After annealing at 800˚C, B100 presents the lowest N-H concentration. More significant N-H reduction was observed in P-doped SiON layers. As shown in Fig. 3, the N-H concentration decreases not only at higher PH_3/Ar flow rate, but also more rapidly with the increase of annealing temperature. The N-H reduction in P-doped samples is highly efficient; in layers grown at higher PH_3/Ar flow rates and/or annealed at higher temperatures, the N-H peak decreases below the detection limit and can not be observed in the FTIR spectra. In sample P40 (PH_3/Ar=40sccm), for example, the N-H concentration decreases to a level very close to the detection limit after annealing at 700˚C, and can not be detected any more after further increase of the temperature.

Based on the deconvolution of N-H absorption peaks in the FTIR spectra of all samples, further investigations on the concentration variations of N-H…N bonds and normal N-H bonds, corresponding to NH1 and NH2 peaks in the inset of Fig. 1, were carried out. Fig. 4 presents the concentration change of NH1 and NH2 with annealing temperature in three samples. In the undoped layer (UD), the concentrations of N-H…N bonds and normal N-H bonds have similar variation trends with temperature and remain approximately the same in both as-deposited and annealed films. In B-doped SiON layers, the initial increase of N-H…N concentration with annealing temperature is more prominent than that of normal N-H bonds, followed by a more rapid N-H…N bonds elimination with further increase of temperature. Thus the N-H…N bonds can dominate N-H bonds at moderate annealing temperatures. In P-doped SiON layers, however, normal N-H bonds are more preferable than N-H…N bonds in as-deposited films. After annealing, the concentration of these two types of bonds becomes almost identical.

IV. Conclusions

The concentrations and configurations of N-H bonds in B-doped and P-doped PECVD SiON layers were investigated and discussed. Our analysis showed that N-H bonds can be eliminated more efficiently in P-doped samples. After annealing at a temperature as low as 700˚C, the N-H absorption peak in the FTIR spectra of P-doped SiON films can be reduced to the detection limit. Further study shows that the contribution of N-H…N bonds to the whole N-H absorption peaks varies with annealing temperature and dopant type. More efficient N-H reduction can be expected by means of further improvements on the deposition and annealing processes. Therefore, B- and/or P- doping of SiON films is very promising for the realization of low-loss photonic devices exploiting CVD technology.

References

[1] O. P. Agnihotri, R. Tyagi, and I. Kato, “Silicon oxynitride waveguides for optoelectronic integrated circuits,” Jpn. J. Appl. Phys., vol. 36, pp. 6711-6713, November 1997.

[2] G. L. Bona, R. Germann, and B. J. Offrein, “SiON high-refractive-index waveguide and planar lightwave circuits,” IBM J. Res. & Dev., vol. 47, pp. 239-249, March/May 2003.

[3] K. Wörhoff, A. Driessen, P. V. Lambeck, L. T. H. Hilderink, P. W. C. Linders, and Th. J. A. Popma, “Plasma enhanced chemical vapor deposition silicon oxynitride optimized for application in integrated optics,” Sens. Act., vol. 74, pp. 9-12, January 1999.

[4] F. Ay, and A. Aydinli, “Comparative investigation of hydrogen bonding in silicon based PECVD grown dielectrics for optical waveguides,” Opt. Mat., vol. 26, pp. 33-46, January 2004.

[5] W. A. Lanford, and M. J. Rand, “The Hydrogen Content of Plasma-deposited Silicon Nitride,” J. Appl. Phys., vol. 49, pp. 2473-2477, April 1978.

[6] Z. Yin, and F. W. Smith, “Optical Dielectric Function and Infrared-Absorption of Hydrogenated Amorphous-Silicon Nitride Films: Experimental Results and Effective-Medium-Approximation Analysis,” Physical Review B, vol. 42, pp. 3666-3675, August 1990.

New Technique for Loss Measurement of a Direct UV Written Silica-on-Silicon Waveguide using Integrated Bragg Grating Structures

H. L. Rogers, J. C. Gates, S. Ambran, P. G. R. Smith
Optoelectronics Research Centre
University of Southampton
Southampton, UK
hlr1g09@orc.soton.ac.uk

Abstract—**We present an elegant new method for measuring the loss of a silica-on-silicon waveguide using integrated Bragg grating structures. This technique has been used to measure the losses of UV written FHD waveguides exhibiting losses of 0.23dB/cm.**

Keywords- direct UV written; Bragg grating; propagation loss; attenuation.

I. INTRODUCTION

Measuring the attenuation of a planar waveguide has many associated problems. These can be attributed to the short waveguide geometries which typically exhibit low total loss. A successful measurement technique must be able to differentiate between absorption loss and other losses associated with the waveguide, such as coupling losses and Fresnel reflections. There are many techniques which can be used to calculate losses within a waveguide; these include the cut-back method [1], prism-coupling technique [2] and the Fabry-Perot technique [3].

In this paper we present a new technique that is a variant on the cut-back approach. It removes uncertainty due to coupling losses, avoids the need for physical cut-back and by interrogating each grating with forward and backward propagating light provides a robust way of assessing loss.

Direct UV writing [4] produces waveguides within the photosensitive core layer of silica-on-silicon planar samples. Svalgaard and Kristensen [5] report propagation loss of <0.2dB/cm in silica-on-silicon waveguides produced by plasma

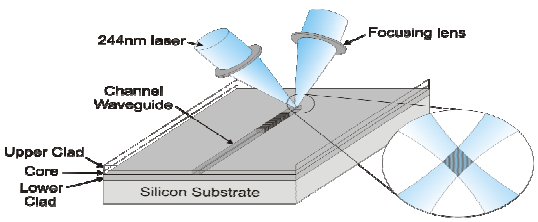


Figure 1. Direct UV written waveguide with integrated Bragg grating structure. Schematic shows focused crossed beam detail (inset).

We would like to thank the EPSRC for funding this research.

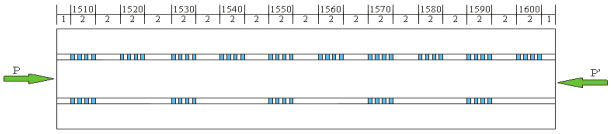


Figure 2. Direct UV written waveguide with integrated Bragg grating structure. Schematic shows focused crossed beam detail (inset).

enhanced chemical vapor deposition (PECVD). Samples produced by flame hydrolysis deposition (FHD) are expected to have similar loss characteristics.

Bragg grating structures are made using the direct grating writing (DGW) technique [4]. Precise modulation of the interference pattern produced by the crossed beams defines Bragg grating structures within the waveguide (Fig. 1). The wavelength of a Bragg grating is dependent on the local refractive index, so can be used to detect conditions at the device surface such as the presence of chemicals [6]. Additionally, measurement of the Bragg grating's response can be used to characterize the waveguide.

In this case, by simultaneous definition of Bragg gratings within the UV written waveguide, a variation on the cut-back method is used to calculate propagation losses within the waveguide. The method allows spatial mapping of the losses within integrated optical devices.

II. EXPERIMENTAL

The silica-on-silicon sample was fabricated via FHD to create three index matched doped silica layers on a silicon wafer. The core layer was doped with germanium to induce photosensitivity, which was further enhanced by hydrogen loading prior to waveguide fabrication. Exposure to UV radiation (λ=244nm) caused an increase in the refractive index of the local core region, forming the waveguide.

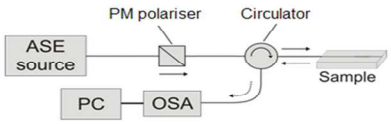


Figure 3. Characterization arrangement for analysis of Bragg grating spectra.

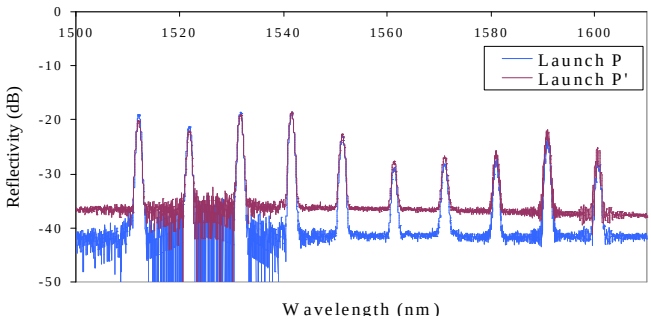


Figure 4. Reflected spectra from waveguide containing ten Bragg gratings, with light launched from directions P and P'.

The waveguides were produced in a 40mm sample, each containing a number of Bragg gratings with specific reflected wavelengths (Fig. 2). The arrangement shown in Fig. 3 was used to characterize the reflected spectra from the waveguide. Light was launched from each end of the sample in turn to obtain information on the spatial dependence of the reflectivity of the gratings. The normalized spectra obtained for the waveguide containing ten Bragg gratings can be seen in Fig. 4.

The loss of the waveguide can be calculated using the elegant relation

$$L = \frac{(P_1 - P_2) + (P_2' - P_1')}{4d}. \quad (1)$$

L is the attenuation in dB/cm, and d is the absolute distance between the centre points of the gratings in cm. P_1, P_2, P_1' and P_2' are the reflected power from gratings 1 and 2 in dB, when launching in directions P and P' respectively. The equation shows that the loss in a section of waveguide between a pair of Bragg gratings is independent both the insertion loss and launch power. In this experiment the magnitude of the peaks were obtained by applying a Gaussian fitting algorithm.

This analysis assumes that the gratings are weak and so have identical spectra from opposing directions. A second assumption is that the waveguide is of sufficient quality to support Bragg grating structures.

III. Results

Fig. 5 shows the reflected power ratio against the distance for the waveguide containing ten gratings. The gradient of this plot gives the average loss of the waveguide to be 0.235dB/cm.

To consider the loss of the gratings within the waveguide, a second waveguide was fabricated and characterized containing five gratings. Fig. 6 shows the plot of attenuation against absolute position of grating for this waveguide, and shows an average attenuation of 0.227dB/cm. This data suggests that the gratings provide no significant additional loss to the waveguides.

The simple relation (1) shows that this method provides more accurate loss measurements than the cut-back technique, as information about the reflectivity of the end facets of the waveguide is not required.

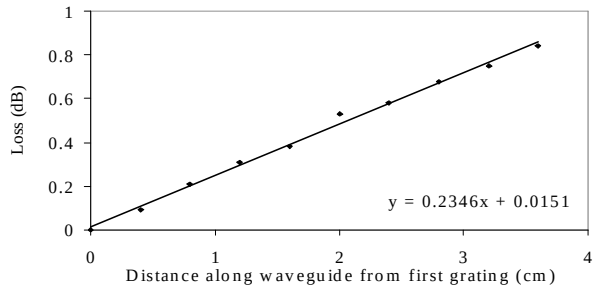


Figure 5. Shows the loss of each grating against the position of the grating within the waveguide. Waveguide contains ten gratings.

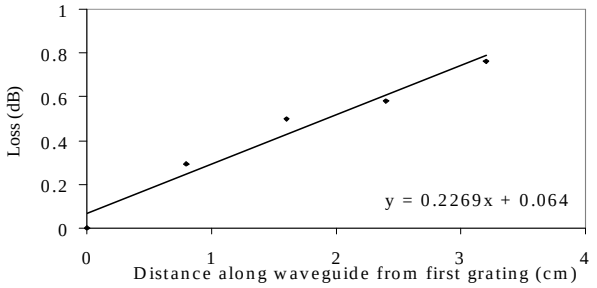


Figure 6. Shows the loss of each grating against the position of the grating within the waveguide containing five gratings.

IV. Conclusion

This work demonstrates a method of measuring loss in silica-on-silicon waveguides which could be applied to any photosensitive waveguide such as arrayed waveguide gratings (AWGs) or waveguides in chalcogenide glasses. We show that our UV written waveguides have a loss of 0.23dB/cm. We will present our latest studies on defects and losses of components such as micromachined grooves and couplers.

Acknowledgment

This research was funded by EPSRC, UK.

References

[1] A. Ghatak and K. Thyagarajan. Introduction to Fiber Optics, pages 413–416. Cambridge University Press, New York, 1998.

[2] Y.H. Won, P.C. Jassaud and G.H. Chartier. "Three-prism loss measurements of optical waveguides". Appl. Phys. Lett., 37(3): 269–271, 1980.

[3] T. Feuchter and C. Thirstrup. "High-Precision Planar Waveguide Propagation Loss Measurement Technique Using a Fabry-Perot Cavity". IEEE Photonics Technology Letters, 6(10):1244–1247, 1994.

[4] G.D. Emmerson, S.P. Watts, C.B.E. Gawith, V. Albanis, M. Ibsen, R.B. Williams, P.G.R. Smith. "Fabrication of directly UV-written channel waveguides with simultaneously defined integral Bragg gratings" *Elec. Lett.*, 38, 1531-1532, 2002.

[5] M. Svalgaard and M. Kristensen. "Directly UV written silica-on-silicon planar waveguides with low loss" *Elec. Lett.*33 (10), 861-863, 1997.

[6] R.M.Parker, J.C.Gates, M.C.Grossel, P.G.R.Smith. "In vacuo measurement of the sensitivity limit of planar Bragg grating sensors for monolayer detection." *Appl. Phys. Lett*. 2009 Vol.95 pp.173306.

Modelling Ge/Si Avalanche Photodiodes

F. Gity, J. M. Hayes, B. Corbett
Photonics Center, Tyndall National Institute
Lee Maltings, Prospect Row
Cork, Ireland
Farzan.Gity@Tyndall.ie

A. P. Morrison
Department of Electrical and Electronic Engineering
University College Cork
Cork, Ireland
a.morrison@ucc.ie

Abstract—**Ge/Si separate absorption, charge and multiplication avalanche photodiodes are investigated. The influence of the absorption thickness and doping, along with the charge and multiplication layer doping on the gain-profile, the breakdown voltage and the gain-bandwidth product are determined.**

Keywords-avalanche photodiode; gain-bandwidth product; germanium; optoelectronic devices; structural parameters

I. INTRODUCTION

Long wavelength Avalanche Photodiodes (APDs) are required for telecommunication optical integrated circuits due to their higher sensitivity and internal gain compared to PIN photodiodes. On the other hand, the avalanche multiplication process causes an internal noise related to the ratio of the electron and hole ionization coefficients [1] which limits the performance of the device. Si has a large asymmetry of electron and hole ionization coefficients, which makes it a useful candidate for APDs. However, Si is not able to absorb light at telecommunication wavelengths, unlike smaller band-gap materials such as Ge and InGaAs. InGaAs APDs have high multiplication noise that limits the gain-bandwidth product (GBP). APDs using Ge for absorption and Si for charge multiplication are more promising candidates having shown higher GBP [2]. Currently there are two approaches to fabricate Ge/Si APDs, Ge epitaxy on Si [2] and Ge/Si wafer bonding [3]. In this paper, a generalized structure is modelled to help decide the most appropriate fabrication approach and design of structural parameters depending on the APD requirements.

II. APD STRUCTURE

A schematic of the generalized Ge/Si separate absorption, charge and multiplication avalanche photodiode (SACM-APD) structure is shown in Fig. 1. The structure consists of a Ge absorption layer and a Si multiplication layer, separated by a p-doped Si charge layer, which is used to control the electric field distribution in the device. An additional Si layer is introduced between the charge layer and the physical interface in the Ge/Si SACM-APD structure. This layer separates the charge layer from the interface between the materials which may attract extra charge and therefore reduce control of the electric field in the multiplication region. The example device is cylindrical with a diameter of 30 µm and is simulated using the Silvaco TCAD simulation tool [4] under illumination of -30 dBm at 1.33 µm.

The static APD electric field for two different bias points is shown in Fig. 1. For bias voltages below breakdown voltage (red curve) the electric field in the multiplication region is below the critical value ($E_c \approx 4\times10^5$ V.cm^{-1} [4]) for Si for initialization of impact ionization. By increasing the bias voltage above breakdown (blue curve), the electric field distribution over the device is increased particularly in both the multiplication and the absorption regions. As a consequence, impact ionization and avalanching can take place. Higher electric field in the absorption layer will cause the minority carriers to travel toward the electrodes with higher velocity thereby increasing the bandwidth of the detector.

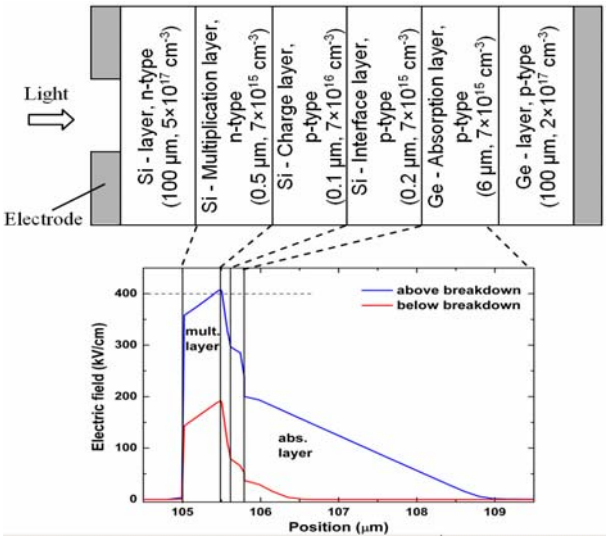


Fig. 1. Schematic of the Ge/Si SACM-APD base structure used in this work along with the static electric field distribution across the selected regions for two bias voltages.

III. SIMULATION RESULTS AND DISCUSSIONS

A. Gain Profile and Breakdown Voltage

Fig. 2 shows the dependence of the gain on voltage and on the thickness of the low doped Ge absorption layer. For absorption layer thicknesses less than 6 µm, the breakdown voltage varies significantly (inset Fig. 2), consequently the bias voltage referenced to the breakdown voltage (V_{bd}) of each structure is used (V_{bias} - V_{bd}) to allow fair comparison between devices. As shown in Fig. 2, by changing the absorption layer thickness, the peak gain and the full width at half maximum (FWHM) of the gain profile change. By increasing the thickness of the Ge absorption layer the voltage drop over this region is also increased, thereby increasing the absolute value of V_{bd} ($|V_{bd}|$). Hence, by designing the absorption layer thickness, the device will show a flat and a more stable gain-voltage profile.

This work is sponsored by Science Foundation Ireland (SFI) under grant 07/SRC/I1173.

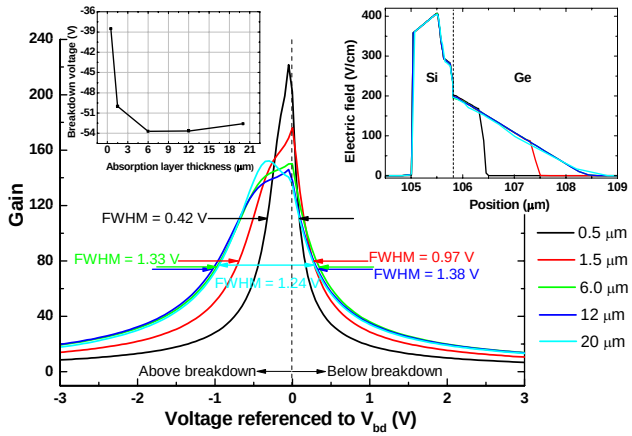


Fig. 2. Dependence of the Ge/Si APD gain on the absorption layer thickness. The insets show breakdown voltage and electric field dependence.

Fig. 3 shows the variation of the APD gain with the doping concentration in a 6 μm thick absorption layer. For any particular bias voltage a higher-doped absorption layer results in a smaller depletion penetration into this layer. As a result the greatest fraction of the electric field will be inside the multiplication layer. Therefore, the peak of the gain increases and the $|V_{bd}|$ decreases (inset of Fig. 3). Because the electric field is concentrated over the multiplication region, any small voltage drop due to high current flow near the breakdown voltage will cause the electric field inside this layer to drop below the critical value for impact ionization. The electric field reduction in the multiplication region results in a reduction in the gain which in turn will cause the gain-voltage profile to be very narrow. For the case of a lower-doped absorption layer, a portion of the electric field will be distributed across the absorption layer and hence the electric field drop near breakdown will be divided between the absorption and the multiplication layers, thus it will not decrease suddenly in the multiplication region. It is clear that reducing the doping level of the absorption layer, reduces the dependence of the gain on bias voltage.

B. Gain-Bandwidth Product (GBP)

Figs. 4 (a) and (b) show the voltage dependence of the GBP versus doping concentration in the multiplication and charge regions, respectively. By increasing the doping level in the multiplication layer the electric field distribution in some parts of this layer decreases dramatically (as indicated in the inset). As a result the gain reduces significantly which in turn reduces the avalanche build up time leading to an increase of the bandwidth [5]. However this increase in bandwidth is not enough to prevent the GBP from decreasing.

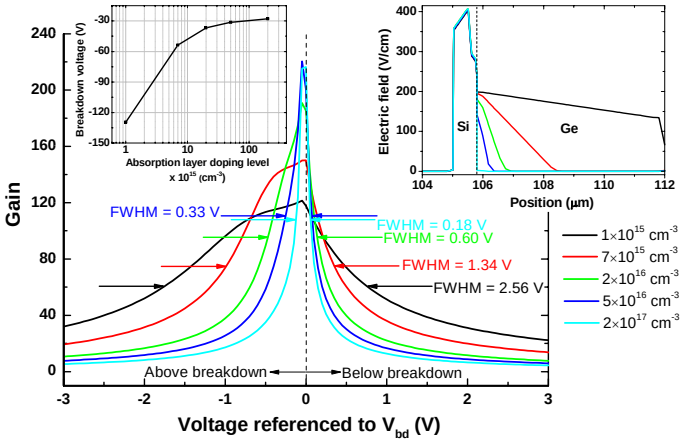


Fig. 3. Ge/Si APD gain-voltage profile for different absorption layer doping concentrations. The insets show breakdown voltage and electric field dependence.

As illustrated in Fig. 4 (b), by increasing the charge layer doping concentration the depletion region is kept inside the multiplication layer and the electric field increases (inset of Fig. 4 (b)). The GBP continues to increase after breakdown up to a point because the decreasing gain causes the bandwidth to increase and compensate the GBP.

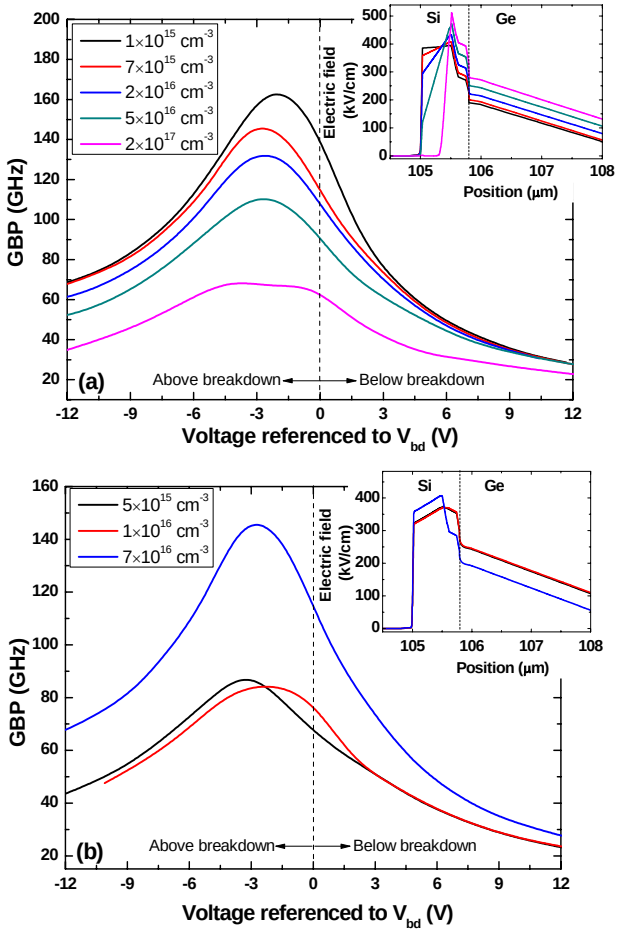


Fig. 4. GBP for different (a) multiplication layer and (b) charge layer doping concentrations. The insets show the electric field profiles for each structure.

REFERENCES

[1] R. J. McIntyre, "Multiplication noise in uniform avalnche diodes," IEEE Trans. Electron. Devices, vol. ED-13, no. 1, pp. 164-168, 1966.

[2] Y. Kang et al., "Monolithic germanium/silicon avalanche photodiodes with 340 GHz gain-bandwidth product," Nature Photonics, vol. 3, pp. 59-63, 2009.

[3] H. Kanbe, M. Miyaji, and T. Ito, "Ge/Si heterojunction photodiodes fabricated by low temperature wafer bonding," Appl. Phys. Express, vol. 1, article no: 072301, 2008.

[4] Atlas user's manual, Silvaco International, USA.

[5] T. Kaneda, and S. R. Forrest, Semiconductor and Semimetals, vol. 22, part D, Academic Press, 1985, pp. 258-382.

Tailored Chromatic Dispersion in Silicon-on-Insulator Slot Waveguides

Sara Mas, José Caraquitena*, José V. Galán, Pablo Sanchis, and Javier Martí
Nanophotonics Technology Center
Universidad Politécnica de Valencia
Valencia 46022, Spain
*E-mail: jcaraqui@ntc.upv.es

***Abstract*— We investigate the chromatic dispersion properties of silicon channel slot waveguides in a broad spectral region centered at ~1.5 μm. The variation of the dispersion profile as a function of the slot fill factor, i.e., the ratio between the slot and waveguide widths, is analyzed. Two different dispersion regimes are identified.**

Keywords- integrated optics; silicon photonics; dispersion.

I. INTRODUCTION

The recent progress in nanofabrication techniques has enabled the development of basic photonic building blocks on a silicon-on-insulator platform including light sources, modulators, and photodetectors [1]. In general, any silicon-based photonic component is affected by chromatic dispersion. Then, the design and optimization of silicon photonic devices requires a very precise knowledge of the dispersion properties. In this context, the chromatic dispersion of a simple silicon waveguide with a cross-sectional area of a few μm^2 is primarily determined by the intrinsic silicon dispersion [2]. In contrast, when the cross-sectional area is reduced, the optical confinement is stronger and, then, the effective dispersion is the result of the interplay between the material and the waveguide or geometrical dispersion [3,4]. In fact, a careful control of the waveguide shape and size allows for the tailoring of the group-delay dispersion (GVD) so that normal, anomalous, or even zero GVD can be achieved in the spectral region centered at ~1.5 μm [3,4].

On the other hand, the so-called silicon nanophotonic slot waveguides have been proposed and fabricated for different applications [5,6]. In these waveguide structures, the optical field is strongly confined in a very thin region of low refractive index material which is sandwiched between two silicon layers and, as a result, the nonlinear optical performance is highly enhanced [6]. An early analysis of the dispersion properties of symmetric slot waveguides was reported by Zheng et al. [7]. However, the analysis by Zheng et al. was limited to a small spectral range of only 0.15 μm centered at ~1.55 μm and the dispersion control capabilities were unexplored.

In this contribution, we perform a detailed analysis of chromatic dispersion in silicon channel slot waveguides. In particular, we analyze the influence of the slot on the GVD of the channel waveguide by considering different slot fill factors. Two different dispersion regimes are distinguished. In general, the slot fill factor determines the dispersion regime in which the guiding structure operates.

This work has been funded by the Spanish MEC (TEC2008-06333 and TEC2008-06380) and by the Generalitat Valenciana (GV/2009/44).

II. DISPERSION IN NANOPHOTONIC SLOT WAVEGUIDES

Let us first consider a conventional silicon channel waveguide consisting on a silicon channel embedded in a silica cladding, as shown in Fig. 1(a). Throughout this paper, three different cross-sectional areas are considered, 1 μm^2, 0.5 μm^2, and 0.1 μm^2, for both, conventional and slot waveguides. In addition, for simplicity, a fixed aspect ratio of 1-to-1.5 (height-to-width) will be assumed. Our numerical simulations are performed by using a full-vectorial mode solver based on the beam propagation method. In Fig. 1(a) a typical electric field profile of the fundamental quasi-TE mode is plotted.

By using the mode solver, we compute the effective index, $n_{eff}(\lambda)$, in a broad spectral range and by numerical differentiation the GVD parameter as a function of wavelength, $D_\lambda=-(\lambda/c_o)d^2n_{eff}/d\lambda^2$, is obtained. It is worth mentioning that our analysis includes the contribution of material dispersion to the GVD, by considering the Sellmeier equations for both silicon and silica. In Fig. 2, we show the resultant GVD profiles for the three cross-sectional areas under analysis. For comparison, the normal dispersion of pure crystalline silicon is also plotted. On the one hand, note that for larger cross-sectional areas, the GVD profile is similar to that corresponding to the silicon dispersion in such a way that the GVD gradually increases for longer wavelengths. We name this GVD behavior as material dispersion regime. A vertical up shifting in the dispersion profile is observed so that, eventually, a region with anomalous GVD is found. The more the cross-sectional area is reduced, the more the anomalous GVD region is increased. On the other hand, for smaller areas, the GVD profile is quite different having a maximum GVD along the spectral region and two zero GVD wavelengths when the maximum dispersion value is positive, as shown in the figure. These GVD characteristics describe the geometrical dispersion regime. Two different qualitative dispersion behaviors are then observed depending on the cross-sectional area of the channel waveguide.

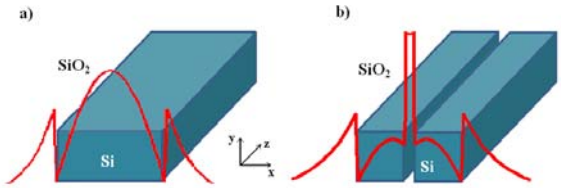


Figure 1. (a) Conventional and (b) slot silicon-on-insulator channel waveguides with same cross-sectional area. The electric field distribution of the quasi-TE mode in the *x* dimension and λ=1.5 μm is plotted.

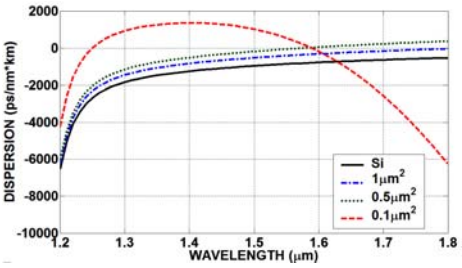


Figure 2. GVD for the fundamental quasi-TE mode of a silicon nanophotonic channel waveguide with a fixed aspect ratio of 1:1.5 and three different cross sectional areas. The intrinsic pure crystalline silicon dispersion is also plotted.

We now turn our attention to the case of silicon waveguides with a vertical slot. In Fig. 1(b), a typical geometry of a slot waveguide is shown. Note that the modal electric-field distribution has a strong discontinuity at the high-index-contrast interfaces and the optical field is significantly increased in the slot region. We have computed the dispersion properties of three different slot waveguides with the above introduced cross-sectional areas, i.e., 1 μm^2, 0.5 μm^2, and 0.1 μm^2, with the same aspect ratio. The resultant GVD curves are shown in Fig. 3(a-c), respectively. For each cross-sectional area, different slot fill factors have been considered, namely, 1:5, 1:10, 1:25, and 1:50. The fill factor is defined as the normalized ratio between the slot and the waveguide widths. Generally, in Fig. 3(a-c) the dispersion profiles can be grouped into the two dispersion regimes previously defined for a conventional waveguide. As expected, when the slot fill factor is decreased, the GVD profiles asymptotically converge to the dispersion of conventional channel waveguides.

The effect of the slot on the waveguide dispersion is different for each particular cross-sectional area. For a cross-sectional area equal to 1 μm^2, Fig. 3(a), a change in the slot fill factor translates into a relatively small variation in the GVD curve. In fact, all the dispersion profiles lie in the so-called material dispersion regime. Note that for larger fill factors, the dispersion profile exhibits a zero-GVD wavelength and, as a result, a spectral region with anomalous dispersion is found. For intermediate cross-sectional areas ~0.5 μm^2, Fig. 3(b), we find that the slot width strongly determines the dispersion regime in which the waveguide operates. More particularly, for the fill factors 1:5 and 1:10 we have GVD profiles in the geometrical dispersion regime while the fill factors 1:25 and 1:50 present GVD curves quite similar to the silicon material dispersion profile. For small cross-sectional areas, 0.1 μm^2, Fig. 3(c), we find that the slot waveguide mostly works in the geometrical dispersion regime. Note that the dispersion curve is significantly up shifted when the slot fill factor is decreased while the wavelength with maximum-GVD is nearly constant at 1.4 μm. Interestingly, for 1:5 slot fill factor, a dispersion curve with a flat profile is obtained in the ~1.4 μm – 1.6 μm spectral range.

We have also analyzed the dispersion behavior of asymmetric slotted structures, i.e., when the slot is placed in a region different than the geometrical center of the waveguide. Numerical simulations show that, in general, the asymmetry degree significantly modifies the GVD of the guiding structure.

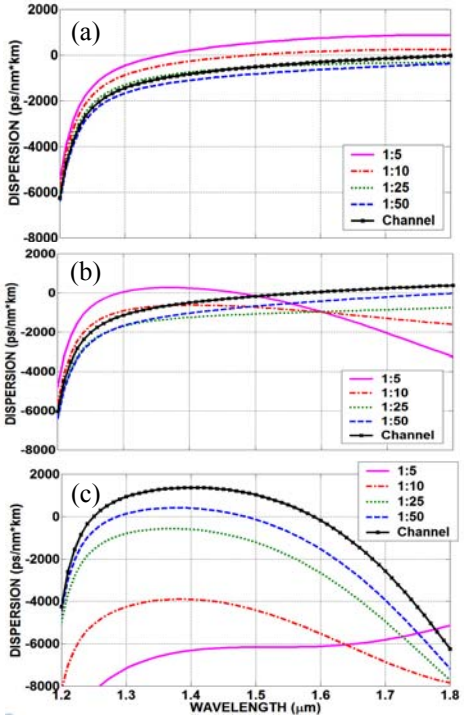


Figure 3. GVD of symmetric slot waveguides as a function of the slot fill factor. Three different cross-sectional areas have been considered: (a) 1 μm^2, (b) 0.5 μm^2, and (c) 0.1 μm^2, with a fixed aspect ratio equal to 1:1.5. The dispersion curve of a conventional channel waveguide is also plotted.

III. CONCLUSIONS

A detailed analysis of the dispersion properties of silicon-on-insulator vertical slot waveguides has been performed. Our study shows that, in general, the dispersion behavior of slot waveguides strongly depends on the slot dimension and location. Two different dispersion regimes have been qualitative distinguished. Our study shows that a careful control of the slot structural parameters enables the tuning of the GVD characteristics.

REFERENCES

[1] M. Lipson, "Guiding, modulating, and emitting light on silicon – Challenges and opportunities," J. Lightwave Technol., vol. 23, pp. 4222-4238, 2005.

[2] H. K. Tsang, C. S. Wong, T. K. Liang, I. E. Day, S. W. Roberts, A. Harpin, J. Drake, and M. Asghari, "Optical dispersion, two-photon absorption and self-phase modulation in silicon waveguides at 1.5 μm wavelength," Appl. Phys. Lett., vol. 80, pp. 416-418, 2002.

[3] E. Dulkeith, F. Xia, L. Schares, W. M. J. Green, and Y. A. Vlasov, "Group index and group velocity dispersion in silicon-on-insulator photonic wires", Opt. Express, vol. 14, pp. 3853-3863, 2006.

[4] A. C. Turner, C. Manolatou, B. S. Schmidt, M. Lipson, M. A. Foster, J. E. Sharping, and A. L. Gaeta, "Tailored anomalous group-velocity dispersion in silicon channel waveguides," Opt. Express, vol. 14, pp. 4357-4362, 2006.

[5] V. R. Almeida, Q. Xu, C. A. Barrios, and M. Lipson, "Guiding and confining light in void nanostructure," Opt. Lett., vol. 29, pp. 1209-1211, 2004.

[6] P. Sanchis, J. Blasco, A. Martínez, and J. Martí, "Design of silicon-based slot waveguide configurations for optimum nonlinear performance," J. Lightwave Technol., vol. 25, pp. 1298-1305, 2007.

[7] Z. Zheng, M. Iqbal, and J. Liu, "Dispersion characteristics of SOI-based slot optical waveguides," Opt. Commun., vol. 281, pp. 5151-5155, 2008.

320 fs Pulses from an Ultrafast Laser Inscribed Waveguide Laser Utilizing a Carbon Nanotube Saturable Absorber

S. J. Beecher, R. R. Thomson, N. D. Psaila and A. K. Kar
School of Engineering and Physical Sciences,
Heriot-Watt University,
Edinburgh, Scotland
sb215@hw.ac.uk

Z. Sun, T. Hasan, A. G. Rozhin and A. Ferrari
Engineering Department,
University of Cambridge,
Cambridge, United Kingdom

***Abstract*—We report the generation of sub-picosecond modelocked pulses from an ultrafast laser inscribed Er-doped waveguide laser. 320 fs pulses at a repetition rate of 40 MHz and energy of 31 pJ were facilitated via passive modelocking by a carbon nanotube saturable absorber.**

Keywords-component; waveguide devices; ultrafast optics

I. INTRODUCTION

The intensities attainable in the focal region of tightly focused ultrafast lasers can be used to locally modify the structure of transparent materials. These structural changes manifest themselves in a variety of ways, one example of which may be a refractive index modification. This refractive index modification can be used to inscribe optical waveguides by translating the material through the focus [1]. This technique is known as ultrafast laser inscription (ULI). ULI is attracting considerable research interest, one particularly exciting area of which is the development of active optical devices, including waveguide amplifiers [2,3] and waveguide lasers [4,5].

The emphasis of many research groups now is in the optimization of these devices, increasing the output powers and range of wavelengths over which they operate. There is also an interest in developing Q-switched and mode-locked waveguide lasers. To date there has been only one successful report of a ULI-fabricated mode-locked waveguide laser [4]. This laser produced 1.6 ps pulses, however the round trip net gain of the cavity was insufficient for femtosecond pulse generation. Here we report on a high gain ULI fabricated Er-doped bismuthate glass waveguide amplifier used in conjunction with a carbon nanotube (CNT) saturable absorber for the generation of 320 fs pulses.

II. WAVEGUIDE AMPLIFIER DEVELOPMENT

The glass substrate used in this study was an Er-doped bismuthate glass containing > 70 wt. % Bi_2O_3 and doped with 0.63 wt. %. Er. The glass was supplied by AGC in Japan. Waveguides were inscribed using a custom designed, variable repetition-rate master-oscillator power-amplifier (MOPA) ultrafast fiber laser system supplied by Fianium Ltd. The repetition-rate of the laser was set to 500 kHz and the pulse duration was measured to be ≈ 350 fs, full-width at half maximum (FWHM). The central wavelength of the laser radiation was 1064 nm and the polarization was adjusted to be circular. The pulse train was focused into the sample using a 0.4 NA aspheric lens and the sample was translated through the focus using computer controlled x-y-z air-bearing stages (Aerotech). The cross section of the waveguide was controlled using the multiscan fabrication technique [3] with each waveguide fabricated using 20 scans of the substrate through the laser focus, with each scan separated by 0.4 µm. The optimum waveguide was inscribed using 133 nJ pulses and a translation speed of 1.0 $mm.s^{-1}$. To reduce back reflections the sample was ground and polished at an angle of 3.0° to the waveguide axis, leaving the final waveguide 87.0 mm long.

Prior to constructing a laser cavity, the performance of the optimum waveguide was characterized. The passive performance was assessed by measuring the fiber-to-fiber insertion loss outside the Er^{3+} absorption band at a wavelength of 1618 nm. The waveguide exhibited a background insertion loss of 4.0 dB when coupled to OFS Clearlight 980-16 coupler fiber. When pumped with ≈ 1.0 W of 980 nm light, the waveguide amplifier exhibited a peak fiber-to-fiber net gain of ≈ 16.0 dB at 1533.0 nm, and greater than 10.0 dB of net gain from 1527 nm to 1563 nm.

III. MODE-LOCKED WAVEGUIDE LASER CONSTRUCTION AND OPERATION

A fiber ring cavity was constructed around the Er-doped bismuthate waveguide amplifier, as shown in Fig. 1. The pump light is delivered to the waveguide amplifier via two fused fiber wavelength division multiplexers (WDMs). Mode-locking is initiated by a well developed CNT-polymer composite saturable absorber [6-10], which is sandwiched between 2 FC/PC fiber connectors. The optical isolator ensures unidirectional operation, reducing instabilities caused by reflections. Output coupling is achieved using a broadband 80:20 fused fiber directional coupler.

This work was funded by the UK Engineering and Physical Sciences Research Council (EPSRC) (Grant Nos. EP/D047269/1, EP/G030227/1 and EP/GO30480/1), the Royal Society, European Research Council Grant NANOPOTs and King's College, Cambridge.

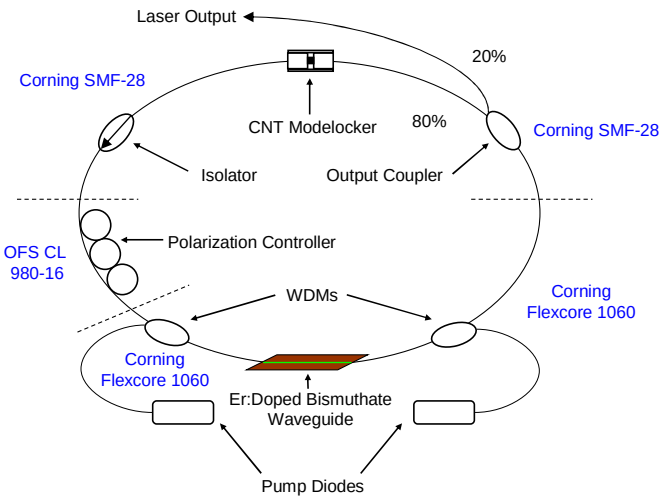


Figure 1. Schematic of the modelocked waveguide laser cavity

Under application of 130 mW of co-propagating and 220 mW of counter-propagating pump, the laser produced an average output power of 1.25 mW. A fast photodiode and RF spectrum analyzer confirmed a pulse repetition frequency of 40 MHz with no Q-switch instabilities observed. Greater pump power was available but previous studies had shown degradation of the polymer host of the saturable absorber for average powers greater than 5 mW. The laser output was coupled into a non-linear autocorrelator and the fiber polarization controller adjusted to minimize the duration of the pulse. Fig. 2 is a plot of the interferometric autocorrelation with the inferred intensity autocorrelation. From Fig.2, a pulse duration of 320 fs FWHM is derived assuming a $Sech^2$ temporal pulse profile consistent with soliton modelocking stabilized by a saturable absorber. Figure 3 plots the optical spectrum of the laser radiation, the central wavelength was 1560 nm with a spectral FWHM of 8.9 nm yielding a time bandwidth product of 0.351 close to the 0.315 expected for transform limited $sech^2$ pulses. The discrepancy can be accounted for by dispersion from the ~0.8 m piece of SMF-28 between the cavity and the autocorrelator.

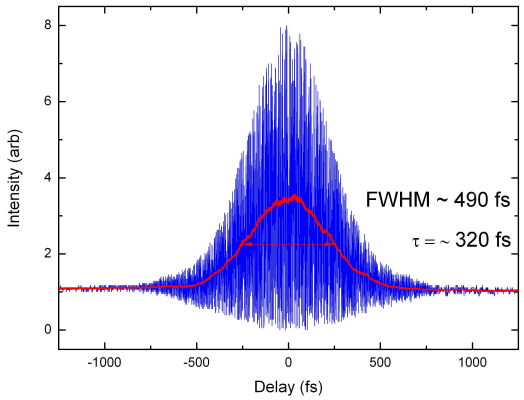


Figure 2. An interferometric autocorrelation of the output from the laser (Blue), with inferred intensity autocorrelation (Red).

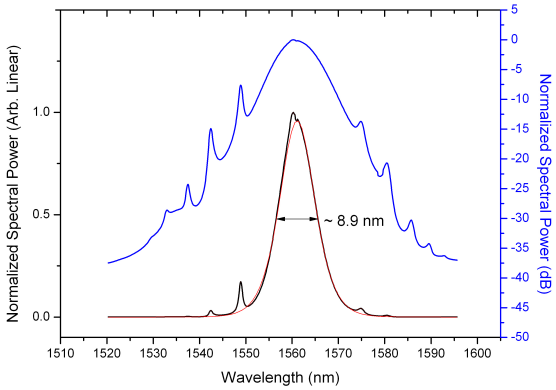


Figure 3. Optical spectrum of the modelocked waveguide laser, linear (Black) with $Sech^2$ fit (Red), and logarithmic (Blue).

IV. Conclusions

We have demonstrated a ULI fabricated, mode-locked waveguide laser producing 320 fs pulses with a FWHM spectral width of 8.9 nm. We believe this work will pave the way to compact, high-efficiency and high repetition-rate mode-locked lasers using the two novel technologies of ULI and CNT based saturable absorbers.

Acknowledgment

We sincerely thank Fianium Ltd. for their support and AGC-Japan for supplying the Er-doped bismuthate glass used in this study.

5. References

[1] K. M. Davis, K. Miura, N. Sugimoto, and K. Hirao, "Writing waveguides in glass with a femtosecond laser," Opt. Lett. **21**, 1729-1731 (1996)

[2] G. Della Valle et al., "C-band waveguide amplifier produced by femtosecond laser writing," Opt. Express **13**, 5976-5982 (2005)

[3] R. R. Thomson, S. Beecher, N. D. Psaila and A. K. Kar, " Ultrafast Laser Inscription of a High Gain Er-doped Bismuthate Glass Waveguide Amplifier," in *Advanced Solid-State Photonics*, OSA Technical Digest Series (CD) (Optical Society of America, 2010), paper AWB7.

[4] G. Della Valle et al., "Passive mode locking by carbon nanotubes in a femtosecond laser written waveguide laser," Appl. Phys. Lett. **89**, 231115 (2006)

[5] F.M. Bain et al., "Ultrafast laser inscribed Yb:KGd$(WO_4)_2$ and Yb:KY$(WO_4)_2$ channel waveguide lasers," Opt. Express **17**, 22417-22422 (2009)

[6] F. Wang et al., "Wideband-tuneable, nanotube mode-locked, fibre laser," Nat. Nanotechnol. **3**, 738-742 (2008).

[7] V. Scardaci et al., "Carbon Nanotube Polycarbonate Composites for Ultrafast Lasers." Adv. Mater. **20**, 4040-4043 (2008).

[8] E. J. R. Kelleher et al., "Nanosecond-pulse fiber lasers mode-locked with nanotubes," Appl. Phys. Lett. **95**, 111108 (2009).

[9] Z. Sun et al., "L-band ultrafast fiber laser mode locked by carbon nanotubes." Appl. Phys. Lett. **93**, 061114 (2008).

[10] T. Hasan et al., "Nanotube-Polymer Composites for Ultrafast Photonics," Adv. Mater. **21**, 3874-3899 (2009).

Ultra Low Loss Split Y- Junctions: Application to QPSK- Lithium Niobate Modulators

J. Hauden, *member, OSA*, N. Grossard, and H. Porte, *member, IEEE*
Photline Technologies
25000 Besançon, FRANCE
jerome.hauden@photline.com

The use of especially suited low-loss split-Y junctions greatly reduces the optical losses of complex optical structures such as QPSK- modulators. Optical losses as low as -4dB were measured, including optical connectors on an optical window covering the entire S & C- telecommunications bands and part of the L- one.

Quadrature phase shift keying, lithium niobate, Y-junction, optical losses.

I. INTRODUCTION

Over the last few years, driven by the increase of data- rates in optical telecommunication, integration complexity is increasing in particular since Quadrature Phase Shift Keying (QPSK) -like modulation formats require the use of several interferometers nested inside one another; thereby increasing the number of Y-junctions per device [1][2]. Moreover the proximity of several high speed modulators on the same chips force to enlarge separation between the interferometers in order to avoid microwave and optical cross-talk [3]. Excess losses in Y- junctions can thus become a limiting factor in terms of optical budget in a link. They have to be reduced as the complexity of chip integration increases.

Besides different ways to design low-loss Y- junctions [4][5][6], we use and report on a specially designed split structure based on mode shaping. This design is easy to apply in technological processing and highly reproducible at industrial level in particular for lithium niobate integrated structures [7][8]. We report here the application of such split Y- junctions in complex structure like QPSK- broadband modulators that includes six Y- junctions per device. The resulting overall optical insertion losses are less than 4dB including optical connectors for 2x 25Gbs 1550nm- QPSK modulators integrated by titanium indiffusion on X- Cut $LiNbO_3$ substrates.

II. DESCRIPTION AND PRINCIPLE OF SPLIT Y-JUNCTIONS

Regular single-mode Y- junctions are based on a simple structure: one input single mode waveguide connected to two other ones with a separation angle, see Fig 1. They can be seen as the succession of, a straight guide section of width Wi, a tapered section where the width expands progressively from Wi to 2Wo+D, and a branching section of half angle α and width Wo [9]. This kind of Y- junction suffers from modal instabilities due to the large taper that supports higher order propagation modes. Theoretically, the truncated tip of size D is considered to be null. In practice, resulting from technological process limitations it is typically of the order of one micron. It induces optical losses that can reach 0.5 dB for wavelengths around 1550 nm.

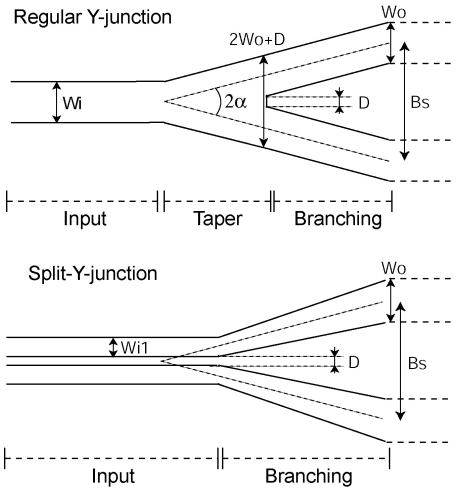


Fig. 1: Scheme of a conventional Y-junction (above) and of a split Y-junction (bottom).

A split Y- junction does not require the use of a tapered section. It consists in two symmetric waveguides structures placed side- by- side, see Fig 1. A first singlemode input section is made of two narrow straight waveguides of width Wi1, positioned in close proximity. The gap between them is D. The following part is a branching section of angle 2α where the waveguide width varies from Wi1 to Wo; Wo being the width of the output waveguides that have to be connected. For a suitable choice of Wi1 and D, the input section acts as an efficient mode filter- shaper. It insures a highly stable power splitting ratio; thus increases the resulting extinction ratios of the MZI using this kind of split junction [7]. As there is no longer truncation at the beginning of the branching section, no excess losses are generated at the transition.

Samples were made by titanium indiffusion in lithium niobate X-Cut wafers, including regular and split Y- junctions. Both kind of junctions had the same length and the same output separation. For conventional Y junctions, the optical losses were measured in the range 0.5-0.6 dB while they were

in between 0.25dB and 0.38dB for the split Y- ones. The mean gain on excess losses expressed in dB, is 45% per Y-junction.The impact can obviously be noticeable as the number of junctions increases like for a Dual Parallel Modulator (QPSK) where six Y-junctions are required with large branch separation.

III. Application to X-Cut $LiNbO_3$ QPSK- Modulator

A QPSK modulator is composed of two sub-Mach-Zehnder interferometers nested inside a larger one as described on Fig. 2.

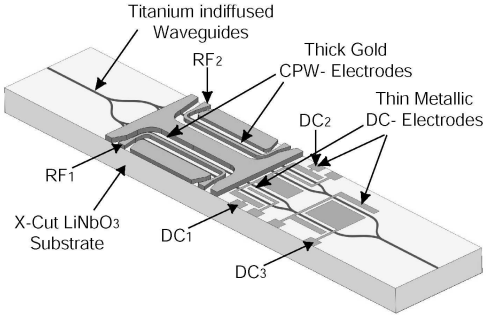


Fig.2: X-Cut LiNbO3
Broadband QPSK modulator chip design.

The waveguide structure is made by titanium indiffusion in X-Cut $LiNbO_3$ substrate. The optical waveguide pattern, as depicted in Fig 3, includes six split Y- junctions. Each split input section is made as described in previous section. The Y-output branching separations, center to center, are 25µm ("g" in Fig. 3). The two main input-output split- Y- junctions are followed by S-bent waveguides so as to reach a 140 µm- gap ("G"). The total length of the structure is 60 mm.

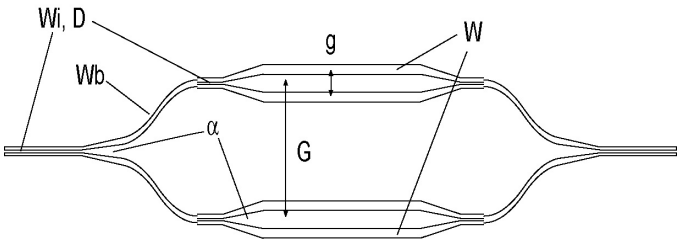


Fig. 3: scheme of the optical waguide structure of the fabricated QPSK modulator using split-Y junctions.

A set of RF and DC electrodes are fabricated on the top surface as for a broadband intensity modulator. The chips are optically polished and pigtailed with polarization maintaining, ended by APC- connectors. The optical losses and the static extinction ratio have been measured from 1460 nm to 1580 nm, covering the entire S- and C- telecommunication bands and part of the L- one. As seen in Fig. 4, the resulting insertion losses are about –4 dB over the whole wavelength range, including connectors, which is to our knowledge far below what has been reported to date on X-cut Ti:$LiNbO_3$ QPSK modulators. The resulting extinction ratios are better than 30dB, showing highly stable power propagation and splitting in all the Y- junctions.

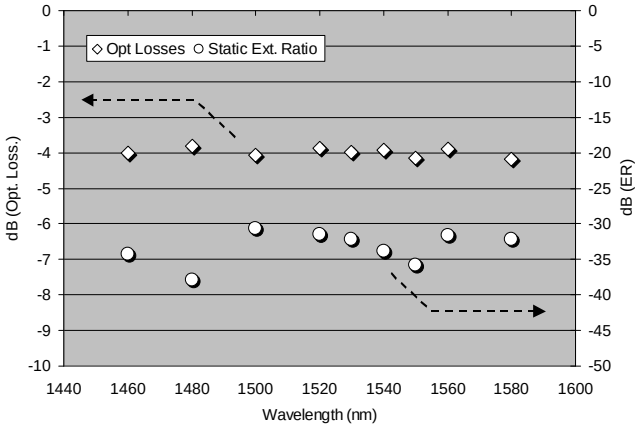


Fig. 4: Plots of optical losses and static extinction ratios vs. optical wavelength.

IV. Conclusions

We have fabricated a broadband QPSK modulator integrated in X-cut lithium niobate by titanium indifusion using very low-loss split Y- junctions. The resulting optical losses including optical connectors were as low as -4 dB from 1460 nm to 1580 nm. This represents a net gain of at least 2dB compared to the insertion losses of QPSK modulators based on standard Y- junctions. The measured extinction ratios were better than 30dB in the same optical bandwidth.

References

[1] G. Charlet, “Progress in Optical Modulation Formats for High-Bit Rate WDM Transmissions” IEEE Journal of Selected Topics in Quantum Electronics, VOL. 12, n°. 4, Jul.-Aug. 2006

[2] R. Griffin, “Integrated DQPSK Transmitters”, Optical Fiber Communication Conference, 6-11 March 2005. Technical Digest. Volume 3, paper OWE3.

[3] L. Terlevich, S. Balsamo, S. Pensa, M. Pirola, G. Ghione, "Design and characterization of a 10Gb/s dual-drive Z-cut Ti:LiNbO3 electrooptical modulator" IEEE Journal of Lightwave Technology, Volume 24, n° 6, pp. 2355- 2361, June 2006.

[4] Sakamaki, Y.; Saida, T.; Hashimoto, T.; Takahashi, H., "Low-Loss Y-Branch Waveguides Designed by Wavefront Matching Method", IEEE Journal of Lightwave Technology, n° 27, pp. 1128 – 1134, May 2009.

[5] Q. Wang, S. He, L. Wang, "A low-loss Y-branch with a multimode waveguide transition section", IEEE Photonics Technology Letters, Volume 14, n° 8, pp. 1124 – 1126, Aug. 2002.

[6] C. Yeh, Y. Liao, R. Lu, "low loss Y-branch with duty cycle varied figure type period segmented waveguides", in proceedings of OptoElectronics and Communications Conference, 2009, pp1-2, 13-17 July 2009, paper ThA2.

[7] N. Grossard, J. Hauden, H. Porte, “Low-loss and stable integrated optical Y-junction on lithium niobate modulators”, in proceedings of ECIO’2007, Copenhagen, Denmark, April 25-27, 2007. paper ThG08.

[8] World patent WO2006129035A2, "Optical integrated circuit Comprising a light guide forming at least one optical separation", 2006, May 25th.

[9] M. Izutsu, A Enokihara, T Sueta, "Optical-waveguide hybrid coupler", Optics Letters, no. 7, p. 136, 1982.

Optical Damage Resistant Near-stoichiometric Ti:Mg:Er:$LiNbO_3$ Strip Waveguides

E. Y. B. Pun, D.L. Zhang, and P.R. Hua
Department of Electronic Engineering,
City University of Hong Kong,
Kowloon, Hong Kong, P. R. China.
Email: eeeybpun@cityu.edu.hk

D.L. Zhang and P.R. Hua
Department of Optoelectronics & Information Engineering,
Tianjin University,
Tianjin 300072, P. R. China.
Email: dlzhang@tju.edu.cn; prhua@tju.edu.cn

***Abstract*—We report optical damage resistant near-stoichiometric Ti:Mg:Er:$LiNbO_3$ single-mode strip waveguides fabricated on congruent $LiNbO_3$ by Er diffusion, Mg/Ti co-diffusion, and vapor-transport-equilibration process. The waveguide optical properties, compositions, crystalline phases and Mg, Er and Ti profiles were characterized, and stable signal enhancement has been measured with >200mW pump power.**

Keywords- *Ti:Mg:Er:$LiNbO_3$ strip waveguide; Near-stoichiometry; Photorefractive effect; Optical amplifier.*

I. INTRODUCTION

Over the past years, a family of Ti-diffused Er:$LiNbO_3$ (Er:LN) waveguide devices have been demonstrated [1-4]. However, the photorefractive effect not only affects the performances of these devices, but also limits both the pumping and operating wavelengths, and hence hinders further development of new devices. To suppress this effect, two methods have been proposed. One is by propagating along the optical axis *Z* [2]. A disadvantage of this scheme is that it sacrifices the larger electro-optic coefficient r_{33}. Another method is by using ZnO-diffused waveguide on an Er:LN codoped with >5 mol% MgO [3]. In this approach, heavy MgO doping causes difficulty in growing high quality Er/Mg-codoped single-crystal, and extremely low Er diffusivity and solubility in the case of local Er-doping. A near-stoichiometric (NS) LN doped with lesser amount of MgO (> 0.8 mol%) can also effectively suppress the photorefractive effect [5]. The realization of a NS Ti:Mg:Er:LN waveguide would open up some new applications, such as 980nm pumped green upconversion and mid-infrared (2.7μm) lasers, and various quasi-phase-matching devices based on periodically poled lithium niobate (PPLN) waveguides.

Recently, we have demonstrated NS Ti:LN strip waveguides fabricated using vapor transport equilibration (VTE) process [6,7]. The realization of NS Ti:Mg:Er:LN waveguide is a challenge. In this work, we report the first demonstration of NS Ti:Mg:Er:LN strip waveguides using VTE process.

II. EXPERIMENT AND RESULTS

A 11-nm-thick Er metal film was coated onto the surface of a 0.8-mm-thick *Z*-cut pure congruent LN substrate followed by diffusion at 1100 °C for 100 h in air. Then, four groups of Ti strips, with thickness of 169nm and strip width from 4 to 7μm, were patterned onto the Er-diffused surface. Next, a 120nm thick MgO film was deposited over the Ti-strips. Simultaneous diffusion of Ti and Mg ions was then carried out at 1100°C for 2h in a wet O_2 environment. Finally, VTE process was carried out by annealing the sample at 1100°C for an additional 10 h in a Li-rich atmosphere, that is, Li-rich VTE.

The two facets were then polished, and end-fire coupling measurements show that waveguiding exists for all guides. All the waveguides are single-mode at 1.5μm wavelength, and just like proton-exchanged waveguides on a *Z*-cut LN, only TM mode was guided. Fig. 1(a) shows the TM mode patterns of the guides. In the width direction the mode field intensity follows a Gaussian function $A_x\exp[-2(x/W_x)^2]$. In the depth direction the mode field intensity follows a Hermite-Gaussian function $A_y y^2\exp[-2(y/W_y)^2]$. The initial Ti-strip width dependence of $W_{x,y}$ is shown in Fig. 1(b). The measured waveguide loss is ~ 1.4dB/cm for the 7μm wide waveguide.

Optical absorption study shows that the VTE process resulted in ~ 1 ± 0.3 nm blueshift of the optical absorption edge, confirming that the VTE process has brought the crystal surface (and hence the waveguide layer) closer to the stoichiometric composition. Furthermore, VTE process simulation shows that the Li_2O content in the waveguide layer is near-stoichiometric and has a homogeneous value of ~ 49.8 ± 0.1 mol%. The measured 1.5μm amplified simultaneous emission spectrum under 0.98μm wavelength laser diode excitation is a clear π-polarized spectrum, and is similar to that of a normal Er-doped LN, confirming that the Er ion presence in the waveguide layer is in the LN phase.

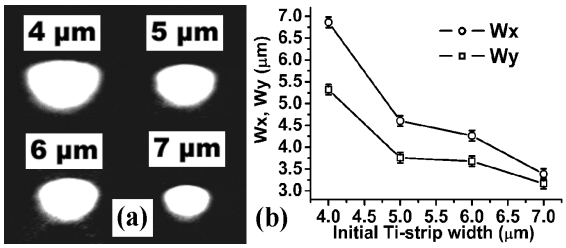


Fig. 1 (a) Near-field TM mode patterns of NS Ti:Mg:Er:LN strip waveguides at 1.5μm wavelength. (b) Mode size versus initial Ti-strip width.

The photorefractive effect of the NS waveguides was studied in comparison with that of the congruent waveguides. The congruent waveguides were fabricated by Ti indiffusion of 7μm wide, 106nm thick Ti strip into bulk Er (1 mol%)/MgO (1.5 mol%)-codoped *Z*-cut congruent substrate at 1060°C for 9h in wet O_2. The stability of the signal enhancement of small-signal (1μW) 1.531μm input light from a tunable laser under 0.98μm wavelength laser diode pump power was examined. The signal enhancement, defined as the ratio of the signal power at the output facet with pump light on to that with pump light off, was measured as a function of coupled pump power. The signal enhancement for the congruent waveguides drops significantly when the pump power exceeds 20mW. Under 220mW coupled pump power, a maximum signal enhancement of 1.5dB/cm was obtained for congruent Ti:Mg:Er:LN which lasts for ~1s, and then the value drops quickly. These features show that the optical damage is serious in the congruent waveguides. In contrast, for the NS Ti:Mg:Er:LN waveguides the maximum signal enhancement is 2.8dB/cm and is stable up to the maximum available coupled pump power of 216 mW. The stable enhancement implies that the photorefractive effect is suppressed in the NS waveguides.

Secondary ion mass spectrometry (SIMS) was used to analyze the surface profile of Ti ions [Fig. 2(a)] and the depth profiles [Fig. 2(b)] of all ions ^{7}Li, ^{93}Nb, ^{16}O, ^{48}Ti, ^{24}Mg and ^{166}Er in 6-μm-wide waveguides. The scattered curves in Fig. 2 represent the measured Ti or Er profiles and the overlapped solid lines denote the best fits. The fitted expressions are indicated for each Ti or Er profile. The Ti concentration follows a sum of two error functions along the lateral direction of the waveguide with a diffusion width 13 ± 0.5 μm, and a Gaussian function in the depth direction with a 1/e depth 5.1 ± 0.2 μm. The Er ion profile also follows a Gaussian function with a 1/e depth of 4.3 ± 0.2μm and a surface concentration of ~ 1×10^{20} atoms/cm^3, and these values are comparable to those of normal congruent Ti:Er:LN devices [1]. The excellent Gaussian fittings in the depth direction show that the Ti and Er diffusion reservoirs were exhausted under the diffusion conditions adopted.

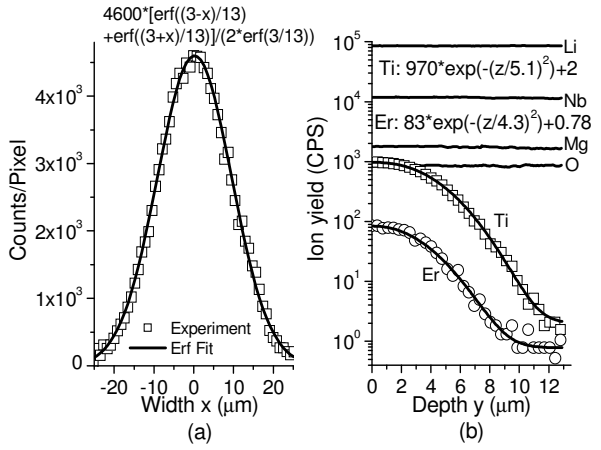


Fig. 2 (a) Surface ^{48}Ti profile and (b) depth profiles of ^{7}Li, ^{93}Nb, ^{16}O, ^{24}Mg, ^{48}Ti and ^{166}Er in 6-μm-wide NS Ti:Mg:Er:LN strip waveguide

As shown in Fig. 2(b), the distribution of Mg ions in the waveguide layer is homogeneous. For application purposes this is highly desirable. By analyzing a standard MgO (5 mol% in melt)-doped congruent LN crystal using SIMS and referencing the relative ratios of the yields of Mg and Nb ions, the Mg concentration is evaluated to be (3.9 ± 0.6) × 10^{20} atoms/cm^3 or 2.1 ± 0.6 mol%. This value is above the optical damage concentration threshold (~ 0.8 mol%) and is consistent with the absence of photorefractive effect measured results. Based upon the law of mass conservation and known Mg ion concentration, the 1/e Mg diffusion depth is evaluated to be 20 ± 3μm, indicating that the Mg diffusion is much faster than the Ti or Er diffusion in the depth direction, hence the Mg diffusion reservoir was also exhausted.

III. CONCLUSION

We have demonstrated NS Ti:Mg:Er:LN single-mode strip waveguides using in-diffusion and VTE process. The NS waveguides are optical-damage-resistant, support TM mode only, and retain the LN phase. To compensate the refractive index decrease arising from the Mg in-diffusion and the VTE process, thick Ti-film is required. The SIMS results show that all of the Er, Ti and Mg diffusion reservoirs were exhausted, and all of the diffused ion depth profiles are either the desired homogeneous or Gaussian types with adequate diffusion depths. No photorefractive effect was observed in the NS waveguides with up to 216mW 0.98μm pump light. With further optimization the combined in-diffusion and VTE method would open a way towards the fabrication of new NS devices.

ACKNOWLEDGMENT

This work was supported by the Research Grants Council of the Hong Kong Special Administrative Region, China, under CityU Project 119407, and by the National Natural Science Foundation of China under Projects 50872089 and 60577012.

REFERENCES

[1] Ch. Becker, T. Oesselke, J. Pandavenes, R. Ricken, K. Rochhausen, G. Schreiberg, W. Sohler, H. Suche, R. Wessel, S. Balsamo, I. Montrosset and D. Sciancalepore, "Advanced Ti:Er:$LiNbO_3$ waveguide lasers," IEEE J. Sel. Top. Quantum Electron., vol. 6, no. 1, pp. 101-113, January/February 2000.

[2] J. Amin, J. A. Aust, and N. A. Sanford, "Z-propagating waveguide lasers in rare-earth-doped Ti:$LiNbO_3$," Appl. Phys. Lett., vol. 69, no. 25, pp. 3785-3787, December 1996.

[3] C. H. Huang, and L. McCaughan, "Photorefractive-damage-resistant Er-indiffused MgO:$LiNbO_3$ ZnO-waveguide amplifiers and lasers," Electron Lett., vol. 33, no. 19, pp. 1639-1640, September 1997.

[4] G. Schreiber, D. Hofmann, W. Grundkotter, Y. L. Lee, H. Suche, V. Quiring, R. Ricken, W. Sohler, "Nonlinear integrated optical frequency conversion in periodically poled Ti:$LiNbO_3$ waveguides," Proc. SPIE, vol. 4277, pp. 144-160, 2001.

[5] Y. Furukawa, K. Kitamura, S. Takekawa, A. Miyamoto, M. Terao, and N. Suda, "Photorefraction in $LiNbO_3$ as a function of [Li]/[Nb] and MgO concentrations," Appl. Phys. Lett., vol. 77, no. 16, pp. 2494-2496, October 2000.

[6] D. L. Zhang, P. Zhang, H. J. Zhou and E. Y. B. Pun, "Characterization of near-stoichiometric Ti:$LiNbO_3$ strip waveguides with varied substrate refractive index in guiding layer," J. Opt. Soc. Am A, vol. 25, no. 10, pp. 2558-2569, October 2008.

[7] D. L. Zhang, P. R. Hua and E. Y. B. Pun, "Near-stoichiometric Ti:$LiNbO_3$ strip waveguides fabricated by standard Ti diffusion and post VTE," IEEE Photon. Technol. Lett., vol. 21, no. 22, pp. 1655-1657, November 2009.

Tm^{3+}/Yb^{3+} codoped aluminum germanate ion-exchanged glass waveguide amplifiers

D.L. Yang, E.Y.B. Pun
Department of Electronic Engineering
City University of Hong Kong,
Hong Kong, PR China
Email: eeeybpun@cityu.edu.hk

J. Zhang, H. Lin
Faculty of Chemical Engineering and Materials
Dalian Polytechnic University
Dalian, PR China
Email:lhai8686@yahoo.com

Abstract—**K^+–Na^+ ion-exchanged waveguide amplifiers have been fabricated in Tm^{3+}/Yb^{3+} aluminum germanate (NMAG) glasses. The quantum efficiency of the $^3H_4$ level is ~ 23.8%, and a relative gain of 3.47dB at 810nm wavelength has been obtained in a 2.20 cm long waveguide under 457mW 980 nm laser diode excitation.**

Keywords-component; Tm^{3+}/Yb^{3+} co-dopants; NMAG glasses; Waveguide amplifiers, Integrated optics

I. INTRODUCTION

In optical telecommunications, the first window wavelength (FWW) band (around 800-850 nm) which used multi-mode optical fibers has not been explored fully due to the high loss and large dispersion associated with the wavelength band. Recently, with the rapid expansion of the local area network (LAN) and intercity fiber-to-home net-work, FWW band has come into the focus for short-range communication. Thus, designing efficient optical amplifiers working at this wavelength region is highly desirable [1-3]. For signal amplification in FWW band, anti-Stokes upconversion emission plays an essential role. Up to now, rare-earth (RE) ions doped fibers have achieved effective signal gains in the first telecommunication window, and encourage researchers to re-examine the window again [4,5]. In addition, with the growing demand of compact and large capability communication systems, much of the research interest center on waveguide amplifiers owing to their potential applications in short-length, high-gain, and multi-channel signal amplification.

Recently, we have made high-quality and low phonon energy (~880cm^{-1}) aluminum germanate (NMAG) glasses, and have successfully demonstrated S-band and C-band ion-exchanged waveguide amplifiers [6,7]. In this work, we report the fabrication of high concentration Tm^{3+}/Yb^{3+} codoped NMAG glass waveguides, and obtain efficient integrated FWW band amplifiers. The results indicate that the Tm^{3+}/Yb^{3+} codoped NMAG waveguide amplifiers are suitable for short-range communications.

II. EXPERIMENTS

Tm^{3+}/Yb^{3+} codoped NMAG glasses, were prepared from high-purity Na_2CO_3, Al_2O_3, MgO, GeO_2, Tm_2O_3 and Yb_2O_3 powders, and followed the preparing procedures described in [6]. Considering the ion concentration dependence on upconversion efficiency, energy transfer rate and fluorescence quenching, 1wt% Tm_2O_3 and 2wt% Yb_2O_3 were used to dope the glasses. Yb^{3+} ions are used as an important sensitizer to produce efficient upconversion fluorescence under the 980nm laser excitation. Before preparing K^+–Na^+ ion-exchanged channel waveguide, Tm^{3+}/Yb^{3+} codoped NMAG glass substrates were optically polished and cleaned. A 200-nm-thick aluminum film was thermally deposited on the glass surfaces, and groups of 6-μm-wide channels were opened by standard micro-fabrication process and wet chemical etching method. The two end-faces of the waveguides were polished for further optical measurements.

The input end of an optical fiber was connected to the Tm^{3+}/Yb^{3+} co-doped NMAG glass channel waveguides, and under the excitation of a 980nm wavelength laser diode the ASE upconversion emission spectra were collected and recorded by a HORIBA Jobin Yvon FL3-21-iHR luminescence spectrometer. Gain measurements of the Tm^{3+}/Yb^{3+} codoped NMAG glass waveguide amplifiers were carried out as follows: Fiber-pigtailed 980nm and 810nm wavelength single-mode laser diodes were used as the pump and signal sources, respectively, and a wavelength division multiplexing (WDM) fiber coupler was used to combine both the pump and signal lights and lights were launched into the waveguide amplifer. The amplified light from the output facet of the waveguide amplifier was collected by a single-mode fiber connected to an HP86140B optical spectrum analyzer (OSA).

III. RESULTS AND DISCUSSION

Fig. 1 shows the ASE upconversion emission spectra of Tm^{3+}/Yb^{3+} co-doped NMAG glass channel waveguides under 980nm wavelength excitation.

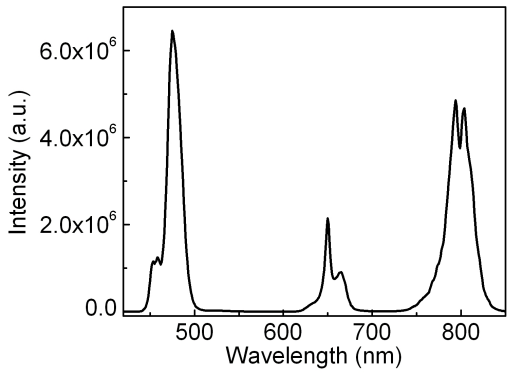


Fig. 1 The ASE upconversion emission spectra of Tm^{3+}/Yb^{3+} co-doped NMAG glass channel waveguides under 980nm wavelength laser diode excitation.

Three main ASE upconversion emission bands were observed at 475, 650, and 794 nm, corresponding to the radiative transitions of $^1G_4 \rightarrow {}^3H_6$, $^1G_4 \rightarrow {}^3F_4$, and $^3H_4 \rightarrow {}^3H_6$, respectively. The excitation mechanism is similar to that in other RE doped glass substrates, and in Tm^{3+}/Yb^{3+} codoped NMAG glasses the blue and red emissions are due to a three-photon excitation process, and the NIR emission is due to a two-photon excitation process. The absorption σ_{abs} and stimulated emission cross-section σ_{em} of Yb^{3+} were calculated using the reciprocity method [8], and the maximum values are 1.51×10^{-20} and 1.44×10^{-20} cm^2 at 976.5 and 977.0nm, respectively. Both values are higher than those in fluoride, fluorophosphate and bismuth borate glasses, and close to that of tellurite-based glasses. Large absorption and emission cross-sections of Yb^{3+} are beneficial in absorbing enough pumping energy and transferring considerable energy to Tm^{3+} ions in codoped NMAG glass system. Based on the experimental analysis, the quantum efficiency of the $^3H_4$ level is derived to be ~23.8% from the ratio of the measured lifetime to the calculated radiative lifetime.

The devices were multimode waveguides, and the propagation losses were measured to be ~0.42dB/cm using the cut back method.

Fig.2 shows the OSA spectra recorded under 457mW pump power and presents the small signal enhancement in the first telecommunications window. The relative gain G_R is defined as

$$G_R = 10\log_{10}[(P_{Sig(PumpOn)} - P_{ASE})/P_{Sig(PumpOff)}], \quad (1)$$

where $P_{Sig(PumpOn)}$ and $P_{Sig(PumpOff)}$ are the signal powers from the output end of the waveguide amplifier with and without pump power, respectively, and P_{ASE} is the amplified spontaneous emission power. From the measured OSA spectra, the relative gain for the 810nm wavelength signal in a 2.20-cm-long waveguide is 3.47dB, hence the gain coefficient is 1.58dB/cm. The gain coefficient obtained in NMAG planar glass waveguide amplifiers is 2 orders of magnitude higher than those in long length silicate and alumino-germao-silicate glass fibers, and an order of magnitude or several times higher than the values in ZBLAN glass fibers [1,4,5]. This is due to the higher dopant concentration and the efficient upconversion emission of Tm^{3+} in the glasses. With further optimization of the glass composition and the dopant concentration higher gain value can be expected.

The dependence of G_R on pump power was also investigated. As expected, G_R increases with increasing pump power at the initial stage, and becomes saturated when the pump power exceeds 248mW.

IV. CONCLUSION

In conclusion, Tm^{3+}/Yb^{3+} co-doped NMAG ion-exchanged glass waveguide amplifiers have been fabricated and characterized. Efficient upconversion emission for $^3H_4 \rightarrow {}^3H_6$ transition has been observed, and a relative gain of 3.47dB at 810 nm has been obtained in a 2.2cm long device. The value is higher that those reported for other glass hosts, and the broad near-IR emission band from 790 to 830nm indicate that Tm^{3+}/Yb^{3+} co-doped NMAG glass material is attractive for realizing compact efficient FWW band waveguide amplifiers.

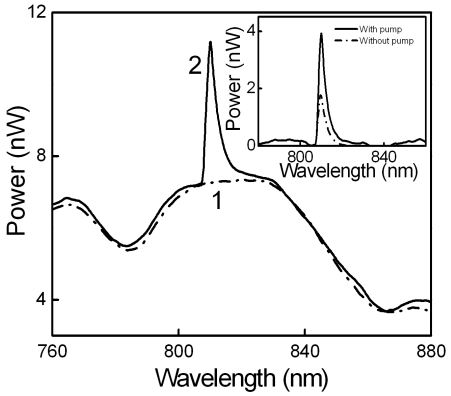


Fig.2 OSA spectra recorded from the output end-facet of 2.2 cm long Tm^{3+}/Yb^{3+} codoped NMAG glass waveguide amplifier. Curve 1: Amplified spontaneous emission (ASE). Curve 2: ASE together with amplified 810nm signal under 457mW 980nm wavelength laser diode excitation. Inset: 810nm signal without pumping and with 457mW 980nm laser pumping with removal of ASE.

ACKNOWLEDGMENT

The research work was supported by Research Grants Council of the Hong Kong Special Administrative Region, China (Grant No. CityU 1197/08) and Scientific Research Foundation for Universities form Education Bureau of Liaoning Province (Grant No. 2009A080).

REFERENCES

[1] R.D.T. Lauder, J.N. Carter, D.C. Hanna, A.C. Tropper, H.M. Pask, S.T. Davey, and D. Szebesta, "Efficient amplification in the first telecommunications window," J. Non-Cryst. Solids, vol. 161, pp.274–276, 1993.

[2] R. M. Percival, D. Szebesta, J. R. Williams, R. D. T. Lauder, A. C. Tropper, and D. C. Hanna, "Diode pumped operation of thulium doped fluoride fiber amplifier suitable for first window systems," Electron. Lett., Vol 30, pp. 1598–1599, 1994.

[3] D. A. Simpson, W. E. K Gibbs, S. F. Collins, W. Blanc, B. Dussardier, G. Monnom, P. Peterka, and G. W. Baxter, "Visible and near infra-red up-conversion in Tm^{3+}/Yb^{3+} co-doped silica fibers under 980 nm excitation," Opt. Express, vol. 16, pp. 13781–13799, 2008.

[4] P. R. Watekar, S. Ju, and W. T. Han, "800-nm Upconversion Emission in Yb-Sensitized Tm-Doped Optical Fiber," IEEE Photonics Technol. Lett., vol. 18, pp. 1609–1611, 2006.

[5] Y. Akasaka, H. Inoue, S. S. Yam, and Y. Kubota, "Thulium doped fiber amplifier for the first window from 790nm to 850nm with 690nw/140Onm dual pumping." in Proc. Optical Fiber Conf., vol. 3, Paper OWF3, 2005.

[6] D. L. Yang, E. Y. B. Pun, B. J. Chen, and H. Lin, "Radiative transitions and optical gains in Er^{3+}/Yb^{3+} codoped acid-resistant ion exchanged germanate glass channel waveguides," J. Opt. Soc. Am. B, vol. 26, pp. 357–363, 2009.

[7] D.L. Yang, E.Y.B. Pun, and H.Lin, "Tm^{3+}-doped ion-exchanged aluminum germanate glass waveguide for S-band amplification," Appl. Phys. Lett., vol.95, no.15, Art No 151106, 2009.

[8] K.S. Lim, P. Babu, C.K. Jayasankar, S.K. Lee, V.T. Pham, and H.J. Seo, "Optical spectroscopy of thulium-doped oxyfluoroborate glass", J. Alloys Comp., vol. 385, pp. 12–18, 2004.

Rapid Prototyping of Planar Infrared Waveguides

Christopher J. Rowlands, Dr. Lei Su and Prof. Stephen R. Elliott*
University Chemical Laboratory
Cambridge University
Cambridge, UK
*sre1@cam.ac.uk

***Abstract*—A method for creating planar As_2S_3 waveguides with a minimum of processing steps is proposed, and the resulting waveguides have been characterized. When the processing parameters are optimized, the losses are low enough for practical use. The authors demonstrate this by creating serpentine waveguides with multiple bends and lengths in excess of 23cm.**

Keywords-component; chalcogenide glass; optical waveguides; rapid prototyping; infrared.

I. INTRODUCTION

Planar optical waveguides offer a great deal of flexibility in terms of the incorporation of active elements[1], coupling of multiple waveguides[2], multiplexing / demultiplexing[3] and so on. Currently though, while planar waveguides based on SiO_2 and certain polymers are relatively common[4,5], waveguides operating in the infra-red are less well-developed. This lack of development is of particular importance for chemical sensing; many common analytes have absorbances in the infra-red, allowing them to be effectively characterized, but current technology makes analysis on a planar waveguide device difficult.

We present the development of a method for the rapid prototyping of optical waveguides based on amorphous arsenic trisulfide (As_2S_3), a chalcogenide glass. This material has several useful properties, such as transparency from 650 to 12000nm and photosensitive changes in refractive index, solubility and optical absorption. This method exploits the change in solubility to employ the As_2S_3 both as photoresist and as the waveguiding material itself, significantly reducing the time and number of processing steps required to create an infra-red waveguide over existing methods[6].

II. RESULTS AND DISCUSSION

Previous literature results suggest that annealing of As_2S_3 waveguides unavoidably leads to cracking, and hence poor performance of the waveguide[7]. We have determined that cracking can be eliminated in almost all cases if the waveguides are cooled sufficiently slowly after annealing, on the order of 20°C / hour. We have used this discovery, along with the fact that our waveguides are fully etched, as opposed to the more common shallow rib waveguides, to remelt the waveguides into a hemispherical cross-section with very smooth side-walls (see Figure 1).

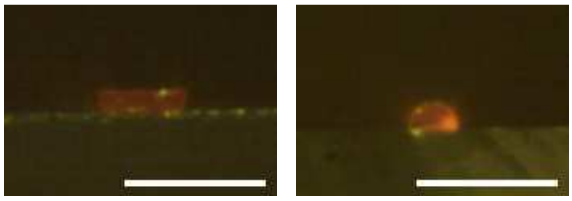


Figure 1. Unmelted and melted waveguides. The unmelted waveguide on the left (annealed at 230°C) retains its rectangular cross-section whereas the waveguide on the right, annealed at 290°C, has a hemispherical cross-section.

The waveguide dimensions were optimized by manufacturing large numbers of waveguides with different thicknesses and widths and measuring the transmission losses. It was found that the losses were not particularly sensitive to waveguide thickness, provided that they were not so thin that the waveguide partially evaporated during annealing (<4μm when annealed at 260°C) or that the aspect-ratio was too high (thicknesses >11μm combined with widths <10μm). The optimum thickness appeared to occur at approximately 8.5μm, although thicknesses between 4 and 10μm were acceptable.

The loss measurements were similarly insensitive to waveguide widths (under current processing parameters); provided the waveguides were between 9 and 33μm wide, there appeared to be little difference in the loss values.

The losses were found to be much more sensitive to annealing temperature; all annealing tests were performed for 2 hours under nitrogen atmosphere. The glass-transition temperature for As_2S_3 is approximately 180°C; waveguides annealed at 170°C had losses on the order of 2-3dB/cm, compared to approximately 5-10dB/cm for unannealed waveguides.

Increasing the annealing temperature unexpectedly increased the waveguide losses; when inspected under a microscope, these waveguides appeared to be darker in places. This was attributed to a roughening of the surface. The origin of this effect is not clear, but we hypothesize that it is due to microscopic inhomogeneities in the glass leading to either localized remelting on a nanoscopic length-scale, or partial microcrystallisation. With more time, this phenomenon would be investigated further. Once the annealing temperature passed 260°C though, the roughening was no longer observed. At temperatures on the order of 290°C and above, partial evaporation of the waveguides was observed, placing an upper

limit on the practical annealing temperature when performed at ambient pressure.

The optimum waveguides were found to be those with thicknesses of 8.5µm, widths of 9µm, and which were annealed at 260°C for two hours under nitrogen atmosphere before being cooled slowly; losses were found to be on the order of 1.2±1dB/cm.

Several different structures were created using the waveguides outlined above. Firstly, waveguides bends were demonstrated. Since the waveguides are fully-etched, the lateral confinement is very good. Waveguides with bend radii of >4mm were found to have almost negligible increase in loss over that of a straight waveguide, although smaller bend radii were still possible; radii < 1mm had appreciable additional losses, but these appeared to be limited to approximately 6dB/cm for a 287µm bend radius. Utilising these bends, a serpentine waveguide with a total length of 238mm was created; waveguiding was demonstrated over the whole length.

Y-splitters were also created, and light coupled into the input waveguide could be observed in both arms of the output waveguides. The design splitting ratio was 1 : 1, but the measured ratio was found to be between 1 : 1.6 and 1 : 8.8.

III. Experimental

As_2S_3 was synthesized from a mixture of arsenic (99.9999%, ABCR) and sulfur (99.9995%, Alfa Aesar) in the correct stoichiometric ratio. The elements were sealed in a quartz-glass ampoule, heated to 750°C for 12 hours in a rocking furnace to ensure a homogenous melt, and then cooled rapidly by removing the ampoule from the furnace and immersing it in water. The As_2S_3 glass was removed from the ampoule and broken into small lumps. These lumps were then placed in a molybdenum evaporation boat which was, in turn, placed in a vacuum chamber for thin-film deposition.

A series of glass microscope slides were cleaned by immersion in aqua regia for 12 hours, followed by immersion in a solution of Decon 90 (Decon Laboratories Ltd.) for 1 hour and rinsing in distilled water. The slides were then dried with a stream of compressed nitrogen. They were mounted in a rotating sample holder in the vacuum chamber, and a thin layer of As_2S_3 deposited by Joule heating of the molybdenum boat. Deposition rate and thickness were monitored by a film thickness monitor.

Once the slides had been removed from the vacuum chamber, they were placed in a custom-built direct-write laser system and a series of optical waveguide designs were written into the thin film by exposure to a tightly-focussed laser spot (532nm continuous-wave frequency-doubled Nd:YVO, lasing at 100mW with a spot size of approximately 10µm). The spot size could be controlled by defocusing the laser from a diffraction-limited spot to approximately 500µm diameter, and changing the laser power to maintain the same fluence.

Once laser-writing was complete, the slides were placed in an etching solution of 3.5×10^{3}M diisopentylamine in dimethyl sulfoxide[8] and etched until the surrounding unexposed regions had completely dissolved (20-30 minutes at room temperature and pressure). The slides were then washed in dichloromethane to remove any excess etchant and left to dry. Finally, the slides were heated in a nitrogen atmosphere for 2 hours to anneal the waveguides.

Transmission losses were characterized using the method of Okamura, Yoshinaka and Yamamoto[9]. Briefly, infra-red light is coupled into one end of the waveguide and the waveguide is imaged from above. Assuming the density of scattering centers in the waveguide is constant, the intensity of light scattered from the waveguide is proportional to the intensity of light in the waveguide itself, and hence by plotting the intensity of scattered light versus the distance along the waveguide and fitting to an exponential decay, the waveguide losses in dB/cm can be calculated independently of coupling losses.

IV. Conclusions

We have demonstrated a method for the creation of fully-etched As_2S_3 waveguides that requires a minimum of processing steps, yet yields waveguides with low losses and very strong confinement. We have used this method to create waveguides with lengths in excess of 23cm as well as with several bends and splitters, demonstrating the practical application of our method. Further details can be found in [10].

Acknowledgment

Christopher Rowlands would like to thank the Oppenheimer Fund for a studentship and Dr. Lei Su would like to thank the Home Office for financial support.

References

[1] J. J. Degnan, “The Waveguide Laser: A Review”, Appl. Phys., vol. 11(1), pp. 1-33, 1976.

[2] Z. Zhou, X. Liao, X. Ren and X Duan, “The Refractive Index Distribution of Tl^{+}-Na^{+} Ion-exchanged Glass Waveguide Optical Splitter in Branch District”, J. Non. Cryst. Sol., vol. 353(11-12), pp. 1164-1166, 2007.

[3] S. Janz et al., “Planar Waveguide Echelle Gratings in Silica-On-Silicon”, IEEE Photonic Tech. L., vol. 16(2), pp. 503-505, 2004.

[4] Y. P. Li and C. H. Henry, “Silica-based optical integrated circuits”, IEE Proc.-J, vol. 143(5), pp. 263-280, 1996.

[5] H. Ma, A. K.-Y. Jen and L. R. Dalton, “Polymer Based Optical Waveguides: Materials, Processing and Devices”, Adv. Mater, vol. 14(19), pp. 1339-1365, 2002.

[6] Ta’eed et al., “Broadband Wavelength Conversion at 40Gb/s Using Long Serpentine As_2S_3 Planar Waveguides”, Opt. Express, vol. 15(23), pp. 15047-15052, 2007

[7] A. Zakery, Y. Ruan, A. V. Rode, M. Samoc and B. Luther-Davies, “Low-loss Waveguides in Ultrafast Laser-Deposited As_2S_3 chalcogenide films”, J. Opt. Soc. Am. B, vol. 20(9), pp. 1844-1852, 2003

[8] S. Wong et al., “Direct Laser Writing of Three-Dimensional Photonic Crystals with a Complete Photonic Bandgap in Chalcogenide Glasses”, Adv. Mat., vol. 18(3), pp. 265-269, 2006.

[9] Y. Okamura, S Yoshinaka and S.Yamamoto, “Measuring Mode Propagation Losses of Integrated Optical Waveguides: a Simple Method”, Appl. Opt., vol. 22(23), pp. 3892-3894, 1983.

[10] C. J. Rowlands, L. Su and S. R. Elliott, “Rapid Prototyping of Low-Loss IR Chalcogenide-Glass Waveguides by Controlled Remelting”, unpublished.

Nd-doped aluminum oxide integrated amplifiers at 880 nm, 1060 nm, and 1330 nm

K. van Dalfsen, J. Yang, F. Ay, K. Wörhoff, and M. Pollnau
Integrated Optical MicroSystems Group, MESA+ Institute for Nanotechnology, University of Twente
Enschede, The Netherlands
k.vandalfsen@utwente.nl

Abstract—**Neodymium-doped Al_2O_3 layers were deposited on thermally oxidized Si substrates and channel waveguides were patterned using reactive-ion etching. Internal net gain on the Nd^{3+} transitions at 880, 1064, and 1330 nm was investigated, yielding a maximum gain of 6.3 dB/cm at 1064 nm. Values for the energy-transfer upconversion parameter for different Nd^{3+} concentrations were deduced.**

Keywords—Neodymium, aluminum oxide, channel waveguide, optical amplifiers, energy-transfer upconversion

I. INTRODUCTION

Integrated optical channel waveguides doped with rare-earth ions have been subject to investigations over the last two decades. Various host materials and different waveguide fabrication techniques have been employed to demonstrate gain in Nd-doped channel waveguides [1-4] and lasers [5,6]. Amorphous aluminum oxide is an excellent host for rare-earth ions, having low optical loss and high refractive index [7,8]. The latter allows for small bending radii and correspondingly small on-chip devices. In this work, optical gain in Al_2O_3:Nd^{3+} is investigated at 880, 1064, and 1330 nm. We report a maximum gain of 6.3 dB/cm for the transition at 1064 nm. In addition, internal net gain is reported for 880 and 1330 nm. Values of the energy-transfer upconversion (ETU) parameter were obtained from the measured gain by simulations.

II. CHANNEL WAVEGUIDE FABRICATION

Al_2O_3:Nd layers with a thickness of 600 nm were reactively co-sputtered onto thermally oxidized 10-cm Si wafers. Al and Nd targets of high purity were sputtered using Ar guns, while oxygen was supplied as a gas. By varying the Nd-target power, different Nd^{3+} concentrations from 0.65×10^{20} cm^{-3} to 2.95×10^{20} cm^{-3} have been obtained. The dopant concentrations were confirmed by Rutherford Backscattering Spectroscopy (RBS). Straight channel waveguides with a width of 2.0 µm were fabricated in the layers by means of reactive ion etching (RIE). The channels were shallow etched by 70 nm. These channels are single-mode at a wavelength of 1064 nm and multi-mode at the pump wavelength of 802 nm. The channel waveguides use air as the cladding.

III. EXPERIMENTAL RESULTS

The luminescence spectrum of Fig. 1 was obtained by pumping the Nd^{3+} ions at 802 nm from the $^4I_{9/2}$ ground level into the $^5F_{5/2}$ level and collecting light from the waveguide top into a spectrophotometer (Jobin Yvon iHR550). The obtained luminescence spectrum was corrected for the response of the used InGaAs detector. The measured $^4F_{3/2} \rightarrow {}^4I_{11/2}$ luminescence at 1064 nm is approximately five times stronger than the $^4F_{3/2} \rightarrow {}^4I_{9/2}$ and $^4F_{3/2} \rightarrow {}^4I_{13/2}$ luminescence at 880 nm and 1340 nm, respectively. The luminescence at 1330 nm has a value equaling 75% of the peak value at 1340 nm.

Small-signal internal net gain investigations were performed using a pump-probe method. A Ti:Sapphire laser (Spectra-Physics 3900s) was employed as the pump source at 802 nm, while diode lasers at 880 nm and 1330 nm and a Nd:Yag laser at 1064 nm were employed as signal sources. Attenuation of the signal to a power of 1-10 µW ensured operation in the small-signal regime. Signal light modulated by a mechanical chopper and pump light were combined via a dichroic mirror and coupled into and out of the waveguides using high-numerical-aperture (0.85 and 0.4 NA, resp.) microscope objectives. The unabsorbed pump light was filtered from the signal light using a high-pass filter at 850 nm placed behind the outcoupling objective, while the signal light was measured by a Germanium detector and amplified by a lock-in amplifier connected to the chopper. The optical gain was determined by measuring the ratio of the transmitted intensities in the pumped and unpumped case, I_p and I_u, respectively. The internal net gain per unit length was obtained by dividing by the sample length l and subtracting the combined measured propagation and absorption losses (α):

$$g_{meas}(l) = 10 \cdot \log_{10}(I_p(l)/I_u(l))/l - a(l) \qquad (1)$$

Figure 2a shows the measured internal net gain per unit length as a function of Nd^{3+} concentration at a launched power of 45 mW. At a concentration of 1.68×10^{20} cm^{-3}, a maximum optical gain of 6.3 dB/cm and 1.93 dB/cm was found at 1064 and 1330 nm, respectively. At a concentration of 1.40×10^{20} cm^{-3}, a maximum of 1.57 dB/cm was found at 880 nm.

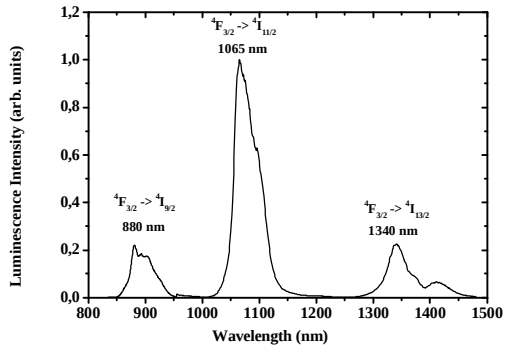


Figure 1. Broadband luminescence spectrum of a Al_2O_3:Nd channel waveguide

The internal net gain per unit length at these optimum concentrations as a function of launched power is displayed in Fig 2b. Both the decrease in gain per unit length as a function of Nd^{3+} concentration in Fig. 2a and the gain saturation visible in Fig. 2b are mainly attributed to energy-transfer upconversion (ETU) processes from the $^4F_{3/2}$ level into higher-lying energy levels [9,10].

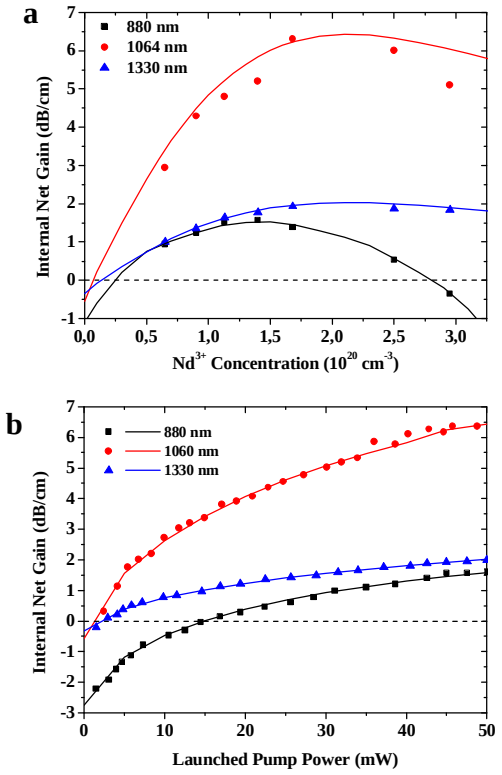


Figure 2. Measured (dots) and calculated (lines) internal net gain per unit length at 880, 1064 and 1330 nm versus (a) Nd^{3+} concentration for a launched power of 45 mW and (b) launched pump power for the samples with maximum gain per unit length in (a)

IV. Gain Simulations

The optical gain in Fig. 2 was simulated by numerically solving a rate-equation model using the ETU parameter as a fitting parameter to the experimentally obtained gain. The simplified rate-equation model describing the population mechanisms of the Nd^{3+} system can be described as follows:

$$dN_4 / dt = R_{05} - R_{4i} - R_{04} - t_4^{-1} N_4 - W_{ETU} N_4^2 \quad (2)$$

$$N_0 = N_d - N_4 \quad (3)$$

where N_4 and τ_4 are the population density and lifetime of the $^4F_{3/2}$ level, respectively, N_0 is the ground-state population and N_d is the dopant concentration. W_{ETU} is the combined upconversion coefficient of three ETU processes originating in the metastable $^4F_{3/2}$ level [9,10]. The pump absorption rate from the $^4I_{9/2}$ ground-state into $^4F_{5/2}$ is expressed by R_{05}, stimulated emission from $^4F_{3/2}$ into the lower-lying levels i = 0, 1, and 2 for 880 nm, 1064 nm, and 1330 nm, respectively, by R_{4i}, and reabsorption from the ground state into $^4F_{3/2}$ by R_{04} (taken into account only for the 3-level transition at 880 nm). The values for the ETU parameter at 1064 nm thus obtained are 0.51, 0.89, 1.32, and 2.32×10^{-16} $cm^3 s^{-1}$ for Nd^{3+} concentrations of 0.65, 1.13, 1.68, and 2.95×10^{20} cm^{-3}, respectively.

V. Conclusions

Al_2O_3:Nd^{3+} layers have been deposited onto thermally oxidized Si substrates and single-mode channel waveguides have been fabricated. A maximum small-signal gain of 1.57 dB/cm, 1.93 dB/cm, and 6.3 dB/cm at 880, 1330, and 1064 nm, respectively, was obtained. By fitting the simulated to the measured gain, values for the ETU parameter in Al_2O_3:Nd^{3+} at four different Nd^{3+} concentrations have been obtained.

References

[1] E. Lallier, J. P. Pocholle, M. Papuchon, M. De Micheli, M. J. Li, Q. He, D. B. Ostrowsky, C. Grezes-Besset, and E. Pelletier, "Nd:MgO:$LiNbO_3$ waveguide laser and amplifier," Opt. Lett., vol. 15, pp. 682-684, June 1990.

[2] Y. Sikorski, A. A. Said, P. Bado, R. Maynard, C. Florea, and K. A. Winick, "Optical waveguide amplifier in Nd-doped glass written with near-IR femtosecond laser pulses," Electron. Lett., vol. 36, pp. 226-227, February 2000.

[3] A. Peled, M. Nathan, A. Tsukernik, and S. Ruschin, "Neodymium doped sol-gel tapered waveguide amplifier," App. Phys. Lett., vol. 90, 161125, April 2007.

[4] J. Yang, M. B. J. Diemeer, D. Geskus, G. Sengo, M. Pollnau, and A. Driessen, "Neodymium- complex-doped photodefined polymer channel waveguide amplifiers," Opt. Lett., vol. 34, pp. 473-475. Feb. 2009.

[5] D. S. Gill, A. A. Anderson, R. W. Eason, T. J. Warburton, and D. P. Shepherd, "Laser operation of an Nd:$Gd_3Ga_5O_{12}$ thin-film optical waveguide fabricated by pulsed laser deposition," Appl. Phys. Lett., vol. 69, 10-12, July 1996.

[6] J. Yang, M. B. J. Diemeer, C. Grivas, G. Sengo, A. Driessen, and M. Pollnau, "Rare-earth-ion complex-doped fluorinated polymer for steady-state lasing," submitted (2010).

[7] K. Wörhoff, J. D. B. Bradley, F. Ay, D. Geskus, T. P. Blauwendraat, and M. Pollnau, "Reliable low-cost fabrication of low-loss Al_2O_3:Er^{3+} waveguides with 5.4-dB optical gain,"IEEE J. Quantum Electron., vol. 45, pp. 454-461, May 2009.

[8] J. D. B. Bradley, F. Ay, K. Wörhoff, and M. Pollnau, "Fabrication of low-loss channel waveguides in Al_2O_3 and Y_2O_3 layers by inductively coupled plasma reactive ion etching," Appl. Phys. B, vol. 89, pp. 311–318, Oct. 2007.

[9] M. Pollnau, P. J. Hardman, W. A. Clarkson, and D. C. Hanna, "Upconversion, lifetime quenching, and ground-state bleaching in Nd^{3+}:$LiYF_4$," Opt. Commun., vol. 147, pp. 203-211, Feb. 1998.

[10] M. Pollnau, P. J. Hardman, M. A. Kern, W. A. Clarkson, and D. C. Hanna, "Upconversion-induced heat generation and thermal lensing in Nd:YLF and Nd:YAG," Phys. Rev. B, vol. 58, 16076-16092, Dec. 1998.

Electron Beam Lithography of Bulk Zinc Oxide Wafers using a Polythiophene-based Charge Dissipation Layer

Rafal Dylewicz, Richard De La Rue and Faiz Rahman,
Department of Electronics and Electrical Engineering
University of Glasgow
Glasgow, United Kingdom
Email: r.dylewicz@elec.gla.ac.uk

Szymon Lis
Faculty of Microsystem Electronics and Photonics
Wroclaw University of Technology
Wroclaw, Poland

***Abstract*—The ability of thin conductive polythiophene layers to dissipate electrons in electron-beam lithography process on ZnO is presented for the first time. Quick and inexpensive processing method is shown for an EBL exposure of dense and high-resolution patterns in hydrogen silsesquioxane (HSQ) negative-tone resist deposited on bulk ZnO sample.**

Keywords-electron-beam lithography; zinc oxide; hydrogen silsesquioxane (HSQ); conductive polymer; PSS:PEDOT; photonic crystal

I. INTRODUCTION

Zinc oxide (ZnO) is a wide bandgap semiconductor that is attracting much attention these days due to its potential for fabricating blue light emitting devices. This II-VI oxide semiconductor has about the same bandgap (~ 3.4 eV) as gallium nitride (GaN) which is now the standard material for making short wavelength light emitting diodes and laser diodes. ZnO has a number of advantages over GaN when it comes to making similar devices. These include higher exciton binding energy and availability of bulk substrates. On the other hand, processing of ZnO is still developing and research groups are working on a number of areas that still require significant work [1, 2]. Electron-beam lithography pattering of ZnO is usually performed with a thin conducting metal layer (e.g., aluminium) deposited on top of the e-beam resist, due to electrostatic charging problem encountered with this material. Removal of Al layer after the exposure process is difficult because ZnO, being an amphoteric oxide, is easily attacked by both acids and bases used for this purpose. In this paper we describe the successful use of electrically conducting polymer – polythiophene – as a charge dissipation material for ZnO patterning through e-beam lithography.

II. EXPERIMENTAL DETAILS

We used commercially available 2.5% water-based dispersion of Poly(2,3-dihydrothieno-1,4-dioxin)-poly(styrenesulfonate), i.e. PEDOT:PSS from Sigma-Aldrich. Four point measurements of 6 μm thick films give surface resistivity values of 1200 Ω/square which falls to values below 500 Ω/square when films are made 20 μm thick. This later value corresponds to conductivity values in the range of 140-150 S/cm. The high electrical conductivity and good oxidation resistance of these polymer films make them suitable for electromagnetic shielding and noise suppression applications.

The bulk zinc oxide wafers, grown by a hydrothermal process, were cleaned by a wet chemical cleaning routine, followed by two hours of sample pre-bake on a hot plate. For trial exposures, 670 nm of undiluted hydrogen silsesquioxane (HSQ) negative e-beam resist was deposited on the samples by spin-coating at 2000 rpm for 60 seconds. Successful usage of HSQ as both the electron-beam resist and hard-mask for dry etching process was reported earlier for the fabrication of high-aspect ratio features in InP-based materials, with the use of chlorine-based inductively coupled plasma (ICP) dry etching [3, 4]. For comparison purposes three different samples were prepared: one sample with a single HSQ resist layer without any conductive film and two other samples with additional electron dissipation layers: one with an Al layer and one with a PEDOT:PSS layer. The conductive Al layer (40-nm-thick) was deposited with an electron-beam evaporator on the top of HSQ resist. For the last sample, PEDOT:PSS was deposited on HSQ surface by spin-coating at 5000 rpm for 60 seconds. This resulted in a conductive polymer layer with a thickness of 100 nm. Test features were defined directly in the HSQ mask layer using electron-beam lithography with a Vistec VB6 UHR machine operating at 100 kV. Software-based proximity correction was applied to the design prior to the exposure process in order to minimize electron backscattering effects on dense patterns. The fabricated patterns included a 50 μm × 10 μm area of pattern W1 (one row of holes removed) and W3 (three rows of holes removed) photonic crystal waveguide structures with a triangular lattice of holes (periodicity of 550 nm, designed hole diameter of 440 nm, radius to lattice period r/a ratio of 0.4). For each sample 25 different electron beam doses were investigated, with exposure doses varying in the range of 300 μC/cm^2 - 700 μC/cm^2. After exposure and prior to sample development, the polymer conductive layer was removed by using a warm bath of deionized water (55°C) for 2 hours. Samples were further investigated with a scanning

electron microscope, while image processing and analysis were performed with the use of ImageJ software [5].

III. Results and Discussion

The results of SEM micrograph analysis for each investigated case are presented in Fig. 1, while micrographs of PhC structures exposed with two different doses (333 and 474 μC/cm^2) are shown in Fig. 2. It is seen that the diameter of a single hole located within a photonic crystal lattice decreased with the increase of exposure dose, as expected for a negative-tone resist. For HSQ resist exposed without any electron dissipation layer (Fig. 1, square points), a steep dependence of hole dimensions against applied doses is noticed with a large scattering of experimental points. Additionally, severe overexposure of the dense pattern was observed for the majority of doses used in the experiment, starting from a dose of ~ 390 μC/cm^2. For a lower applied dose, i.e. 333 μC/cm^2, holes are slightly underexposed and not very sharply defined (Fig. 2a, SEM picture on the left). Usage of a higher dose (474 μC/cm^2) resulted in properly defined features on the edges of an array, while the middle part of the PhC lattice exhibited signs of strong proximity effect (Fig. 2a, micrograph on the right).

For a standard metal layer and conductive polymer layer, more gentle and gradual pattern variations were achieved. Sharply defined holes of similar size were obtained within highly uniform photonic crystal lattices, both for Al and PEDOT:PSS layers, as shown in Figs. 2b and 2c. For a wide range of doses, performance curves of these two conducting materials were highly comparable. Additionally, for lower exposure doses better definition of holes was noticed when 100-nm-thick PEDOT:PSS was used as the charge dissipation layer. The conductive polymer layer assured appropriate shape preservation within the whole range of investigated doses. While for Al, underexposed patterns with insufficient hole definition were observed for doses < 345 μC/cm^2 (Fig. 2b, on the left).

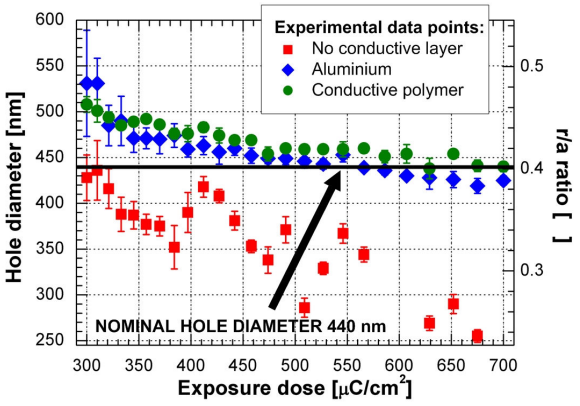


Figure 1. Experimental values of hole diameter and corresponding radius to lattice period (r/a) ratio against electron-beam lithography exposure dose, for three different exposure conditons: without any conductive layer (square points), with 40-nm-thick Al layer used (rhombus points) and 100-nm-thick PEDOT:PSS layer used (circle points).

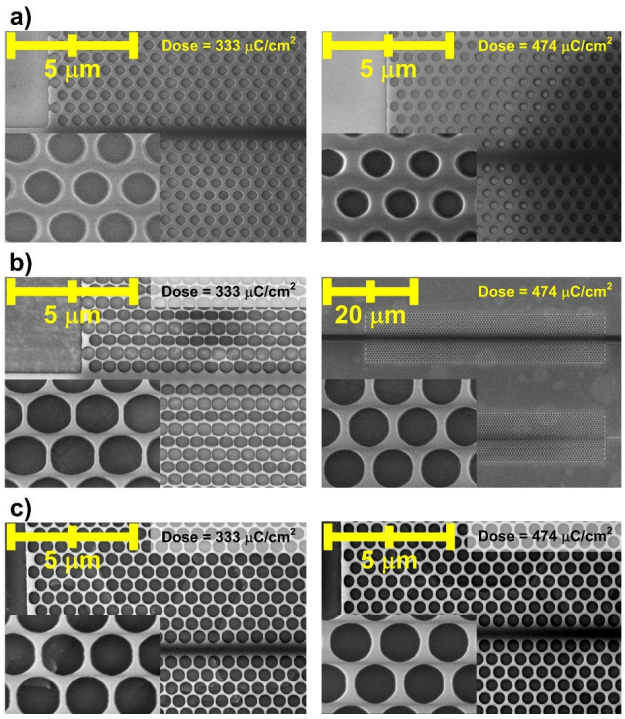


Figure 2. SEM micrographs of overall photonic crystal lattice and hole shape evolution in HSQ resist for doses of 333 and 474 μC/cm^2 and different exposure conditons: a) exposure without any conductive layer; b) 40-nm-thick Al layer used; c) 100-nm-thick PEDOT:PSS conductive polymer layer used.

IV. Conclusions

The excellent performance of PEDOT:PSS conductive polymer to dissipate charge in electron-beam lithography, in comparison with typically used metal layers, e.g. aluminium, was demonstrated experimentally. The new approach provides the ability to make ZnO sample processing much simpler, quicker and less expensive, but it may also be extended to EBL exposures of many other semiconductor/dielectric materials as well as to their observations in scanning electron microscopes.

References

[1] K. Ip, G. T. Thaler, H. Yang, S. Y. Han, Y. Li, D. P. Norton, S. J. Pearton, S. Jang and F. Ren, "Contacts to ZnO," J. Cryst. Growth, vol. 287, pp. 149–156, 2006.

[2] W. Lim, L. Voss, R. Khanna, B. P. Gila, D. P. Norton, S. J. Pearton and F. Ren, "Dry etching of bulk single-crystal ZnO in CH_4/H_2-based plasma chemistries," Appl. Surf. Sci., vol. 253, pp. 889-894, 2006.

[3] R. Dylewicz, "High aspect ratio ICP etching of InP/InGaAsP/AlGaInAs materials," Innovations - Surface Technology Systems Newsletter, issue 10, pp. 6-7, March 2009.

[4] R. Dylewicz, L. Hou, G. Mezősi, A. C. Bryce, "Development of single-step and high-resolution ICP dry etching for a wide range of InP-based materials," Compound Semiconductor Magazine, vol. 15, no. 6, pp. 34-36, September 2009.

[5] M. D. Abramoff, P. J. Magelhaes, S. J. Ram, "Image processing with ImageJ," Biophotonics International, vol. 11, issue 7, pp. 36–42, 2004.

Er - doped $KY_{1-x-y}Gd_xLu_y(WO_4)_2$ surface channel waveguides

Western Bolaños, Joan J. Carvajal, Xavier Mateos, Magdalena Aguiló and Francesc Díaz
Física i Cristal·lografia de Materials i Nanomaterials (FiCMA-FiCNA)
Universitat Rovira i Virgili, C/Marcel·lí Domingo s/n
43007, Tarragona, Spain
joanjosep.carvajal@urv.cat

Ganapathy Senthil Murugan, Hamish C. Hunt, Ananth Subramanian and James S. Wilkinson
Optoelectronics Research Centre (ORC)
University of Southampton
Highfield , Southampton, Hampshire, SO17 1BJ,
United Kingdom
jsw@orc.soton.ac.uk

Abstract— **Channel waveguides on $KY_{1-x-y}Gd_xLu_y(WO_4)_2$ epitaxial films doped with Er^{3+} were obtained by ion beam milling and guided modes at wavelengths near 1.5 µm confirmed single mode behaviour. Absorption and emission spectra of these waveguides agree with those of bulk crystals of the same family, showing potential for a planar waveguide laser.**

Keywords- tungsten compounds; epitaxial growth; dielectric films; optical strip waveguides; etching.

I. Introduction

Novel materials for integrated optics applications are under intense investigation. The interest in using the rare earth potassium double tungstates, $KRE(WO_4)_2$ (or KREW, for short, where RE = Y, Gd and Lu), is mainly because they: (i) exhibit large values of absorption and emission cross sections for the active lanthanide ions, allowing high gain to be obtained and hence laser generation; (ii) possess large ion to ion distance, which allows high doping levels of the active ions without the quenching of fluorescence; and (iii) have high refractive index values of about 2.0, which makes them suitable for the fabrication of compact integrated optical devices. Planar waveguide lasers using KREW have already been reported [1-2], however, Er-doped KREW planar waveguide lasers have not been yet reported and in this work we explore the possibility to obtain these planar waveguide lasers. Through a systematic study [3], we determined the optimum composition of a $KY_{1-x-y}Gd_xLu_y(WO_4)_2$ film which exhibits both low lattice mismatch and high refractive index contrast with the $KY(WO_4)_2$ substrate. This composition, corresponding to a $KY_{0.59}Gd_{0.19}Lu_{0.22}(WO_4)_2$ layer was successfully grown by liquid phase epitaxy on a **b** oriented $KY(WO_4)_2$ substrate without cracking and with a refractive index contrast with the substrate of the order of 2×10^{-3} at λ = 632.8 nm, allowing the demonstration of passive waveguiding; with scattering losses ~ 1 dB/cm. More recently we have doped our lattice matched layer with 1 at% Er^{3+} and 1 at% Tm^{3+}, maintaining the high structural quality and the refractive index contrast [4]. These layers had the following chemical compositions: $KY_{0.60}Gd_{0.18}Lu_{0.21}Er_{0.01}(WO_4)_2$ and $KY_{0.59}Gd_{0.18}Lu_{0.22}Tm_{0.01}(WO_4)_2$. We are interested in exploiting the 1.5 µm transition from Er^{3+} which matches the third telecommunications window very well. Surface and buried channel waveguides fabricated from monoclinic double tungstates have only been reported by Borca et al [5-6] using femtosecond laser writing and reactive ion etching (RIE), respectively. In this work we report on the fabrication and characterization of surface channel waveguides on $KY_{0.60}Gd_{0.18}Lu_{0.21}Er_{0.01}(WO_4)_2$ epitaxial layers grown on $KY(WO_4)_2$ substrates, structured by Ar ion beam milling using standard UV photolithography for the mask deposition.

II. Experiment and Results

$KY_{0.60}Gd_{0.18}Lu_{0.21}Er_{0.01}(WO_4)_2$ layers were grown on $KY(WO_4)_2$ substrates by Liquid Phase Epitaxy, (LPE). The refractive indices n_g and n_m were measured by ellipsometry in the range 300 nm – 1600 nm. From these measurements and using the approximation reported in [7], we determined the dimensions of the channels which would provide for single mode operation 1.5 µm. A channel design of 8 µm width and 7 µm height was chosen.

The epitaxial layers were polished to a thickness of 7 µm and cut with their edges perpendicular to the N_g and N_m optical directions and the four edges were also polished to laser quality [3]. Our early experiments using RIE with CHF_3 and SF_6 gases on $KY(WO_4)_2$ substrates were not satisfactory because we obtained an etch rate of 200 nm/h, too low for our purposes. We then explored the Ar ion beam milling technique. A 4 µm thick S1828 photoresist (PR) film was spun onto a $KY(WO_4)_2$ substrate. The system (PR + substrate) was exposed to the Ar ion beam for different etching times. In this way we determined an etch rate of 1.134 µm/h for the substrate and 1.014 µm/h for the photoresist. We therefore selected this method due to its improved etch rate and acceptable selectivity for structuring the KREW's.

After spinning photoresist of about 8 µm thickness in two stages on the $KY_{0.60}Gd_{0.18}Lu_{0.21}Er_{0.01}(WO_4)_2$ / $KY(WO_4)_2$ slab waveguide, straight channels were patterned using standard UV photolithography. The slab waveguide patterned with

This work was supported by the Spanish government under projects MAT 2008-06729-C02-02/NAN and PI09/90527 and the Catalan government under project 2009SGR235 and the fellowship (W. Bolaños) 2009FI_B 00626 and 2009 BE1000481.

photoresist was exposed to dry etching for 6 hours after which, we found that the etch rate of the epitaxial guiding layer (1.333

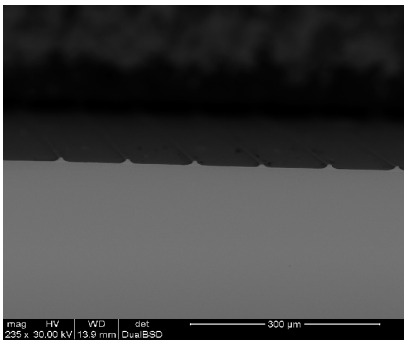


Figure 1. Cross-sectional image of the surface channels patterned on a $KY_{0.60}Gd_{0.18}Lu_{0.21}Er_{0.01}(WO_4)_2$/ $KY(WO_4)_2$ slab waveguide.

µm/h) was slightly higher than that of the substrate. Figure 1 shows a cross-sectional view of some of the channels obtained by Ar ion beam milling on the $KY_{0.60}Gd_{0.18}Lu_{0.21}Er_{0.01}(WO_4)_2$/ $KY(WO_4)_2$ slab waveguide.

Instead of a rectangular channel cross-section, a trapezoidal shape was obtained; nonetheless at wavelengths near 1.5 µm the light was well confined in the channels, as can be seen in figure 2, and monomode operation was obtained, confirming the prediction made using [7].

We determined the photoluminescence spectra of the $KY_{0.60}Gd_{0.18}Lu_{0.21}Er_{0.01}(WO_4)_2$/ $KY(WO_4)_2$ waveguides, at room temperature, in the wavelength region of the $^4I_{13/2} \rightarrow {}^4I_{15/2}$ transition upon excitation at 974 nm. Figure 3 shows the emission spectrum which is similar to those reported for this active ion in other crystals of the same family [8]. The maximum emission intensity was found at 1533 nm; no broadening of the peaks due to the presence of multiple ions (Y, Gd and Lu) occupying the same structural site was observed.

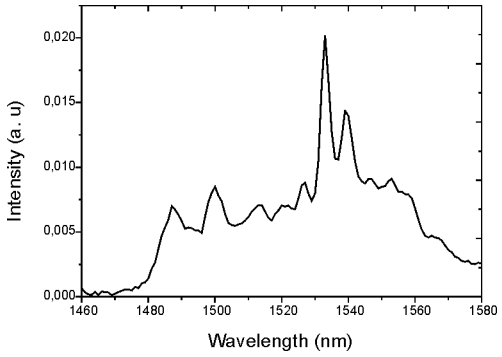


Figure 3. Emission spectra measured at room temperature corresponding to the $^4I_{13/2} \rightarrow {}^4I_{15/2}$ transition of Er^{3+} in $KY_{0.60}Gd_{0.18}Lu_{0.21}Er_{0.01}(WO_4)_2$/ $KY(WO_4)_2$ slab waveguide.

III. Conclusions

Surface channel waveguides were fabricated from $KY_{0.60}Gd_{0.18}Lu_{0.21}Er_{0.01}(WO_4)_2$/ $KY(WO_4)_2$ slab waveguides using the Ar ion beam milling. The slab waveguide was characterized in terms of refractive indices and allowed the measurement of the photoluminescence spectra whilst the

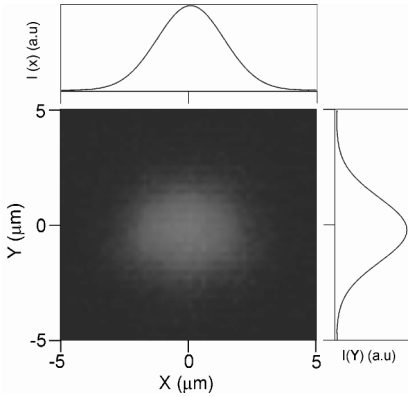


Figure 2. Near field intensity at 1.5 µm corresponding to a 8 µm width $KY_{0.60}Gd_{0.18}Lu_{0.21}Er_{0.01}(WO_4)_2$ channel.

channel waveguides were characterized in terms of guided modes. Experiments to realise a waveguide laser for wavelengths near 1530 nm are ongoing

Acknowledgment

The authors like to express their gratitude to David Sager and Neil Sessions for their support in the clean room.

References

[1] D. Geskus, S. Aravazhi, E. Bernardi, C. Grivas, S. Harkema, K. Hametner, D. Günter, K. Wörhoff and M. Pollnau, "Low-threshold, highly efficient Gd^{3+}, Lu^{3+} co-doped $KY(WO_4)_2$:Yb^{3+} planar waveguide laser,"Laser Phys. Lett. vol. 6, pp. 1-6, Aug. 2009.

[2] F. M. Baim, A. A. Lagatskiy, S. V. Kurilchick, V. E. Kisel, S. A. Guretsky, A. M. Luginets, N. A. Kalanda, I. M. Kolesova, N. V. Kuleshov, W. Sibbett and C. T. A. Brown, "Continous-wave and Q-switched operation of a compact, diode-pumped Yb^{3+}:$KY(WO_4)_2$ planar waveguide laser,"Opt. Express. vol. 17, pp. 1666-1670, Feb. 2009.

[3] W. Bolaños, J. J. Carvajal, M. C. Pujol, X. Mateos, G. Lifante, M. Aguiló and F. Díaz, "Epitaxial growth of lattice matched $KY_{1-x-y}Gd_xLu_y(WO_4)_2$ thin films on $KY(WO_4)_2$ substrates for waveguiding applications,"Cryst. Growth & Des. vol. 9, pp. 3525-3531, May. 2009.

[4] W. Bolaños, J. J. Carvajal, X. Mateos, M. C. Pujol, N. Thilmann, V. Pasiskevicius, G. Lifante, M. Aguiló and F. Díaz, "Epitaxial layers of $KY_{1-x-y}Gd_xLu_y(WO_4)_2$ doped with Er^{3+} and Tm^{3+} for planar waveguide lasers,"Opt. Mat. vol. 32, pp. 469-474, May. 2010.

[5] C. N . Borca, V. Apostolopoulus, F. Gardillou, H. g. Limberger, M. Pollnau and R. P. Salathé, "Buried channel waveguides on Yb-doped KY(WO4)2 crystals fabricated by femtosecond laser irradiation," Appl. Surf. Sci. . vol. 253, pp. 8300-8303, Feb. 2007.

[6] C. N. Borca, Y. E. Romanyuk, F. Gardillou, M. Pollnau, M. P. Bernal and P. Moretti,. "Optical channel waveguides in Yb-doped $KY(WO_4)_2$:Yb^{3+}," in Proc. Lasers Electro-Opt., Tech. Dig. 2005, pp.

[7] R. A. Soref, J. Smidtchen and K. Petermann, "Large single-mode rib waveguides in GeSi-Si and Si on SiO_2,"IEEE J. Quantum Electron. vol. 27, pp. 1971-1974, Aug. 1991.

[8] X. Mateos, R. Solé, Jna. Gavaldá, M. Aguiló, J. Massons, and F. Díaz, "Crystal growth, optical and spectroscopic characterisation of monoclinic $KY(WO_4)_2$ co-doped with Er^{3+} and Yb^{3+},"Opt. Mat. vol. 28, pp. 423-431, June. 2005.

UV laser-assisted fabrication of ridge waveguides in lithium niobate crystals

C. L. Sones, Y. J. Ying, R. W. Eason, S. Mailis
Optoelectronics Research Centre, University of Southampton, Southampton, SO171BJ, U.K
cls@orc.soton.ac.uk

P. Ganguly
Advanced Technology Development Centre, Indian Institute of Technology, Kharagpur, 721302, India.

E. Soergel
Institute of Physics, University of Bonn, Wegelerstrasse 8, 53115 Bonn, Germany.

Abstract—**We present a UV laser-assisted method for the fabrication of ridge waveguides in lithium niobate. The UV laser irradiation step provides the refractive index change required for the vertical light confinement in the waveguide and also defines the ferroelectric domain pattern which produces the ridge structures after chemical etching.**

I. INTRODUCTION

Lithium niobate (LN) is an optical ferroelectric crystal with a distinctive combination of inherent physical properties. This has resulted in its use for a diverse range of applications such as mobile and optical telecommunications, optical wavelength conversion, and for integrated optical devices such as high speed electro-optic modulators.

As the need for further improvement of the efficiency and compactness of integrated optical devices is increasing it is necessary to use superstructures such as ridge waveguides (instead of conventional diffused waveguides) that provides better lateral confinement of the optical mode due to the higher index contrast. Additionally, the stronger optical confinement and smaller modal dimensions enhance the efficiency of any nonlinear processes implemented using these waveguide.

Several different methods have been trialled to produce ridge waveguides in LN. In general almost all of these methods utilize an etching step that defines the ridge geometry and a separate waveguide fabrication step, such as ion-diffusion or proton-exchange which requires lithographic alignment with the ridge structure. Delineation of the ridge is achieved either via wet etching in an acid mixture containing HF acid or through dry etching processes such as ion beam milling [1] or plasma etching [2]. Since acid-based wet etching for structuring of LN is commonly based on the differential etching behaviour of the two complementary crystalline *z*-faces, domain inversion [3] has also been reported as an obvious and easy choice for defining ridges in LN. Interestingly, ridge waveguides have also been fabricated by mechanical dicing of planar MgO:LN bonded on to LN [4].

The mandatory step required to induce the vertical refractive index contrast either precedes or succeeds the wet or dry etching process. The compatibility of the two steps is essential and hence the recipe with the right sequential steps has to be adhered to for producing ridge waveguides in LN.

In this contribution we report on a method for producing ridge waveguides in *z*-cut LN whereby the definition of the ridge pattern and the vertical confinement are defined by a *single* step of direct continuous wave (c.w.) UV laser waveguide writing [5, 6]. This initial UV exposure of the +*z* face of LN crystals is known to inhibit domain inversion locally during subsequent electric field poling (EFP) [7]. As a result a ferroelectric domain structure which corresponds to the UV irradiated tracks is formed after EFP. In conjunction with wet etching this effect then provides an easy alternative method for fabricating useful domain and surface relief structures [7]. UV-induced refractive index change and poling-inhibition, pave the way to self-aligned ridge waveguides in LN.

II. EXPERIMENTS AND RESULTS

The first step in the sequence for the fabrication of the ridge waveguide structures involves the inscription of a refractive index change in LN using the UV direct writing procedure. This initial direct writing step not only helps to establish the vertical refractive index contrast for the ridge waveguides, but will also precisely outline the actual shape of the formed superstructures. A beam from a c.w. Ar-ion laser, which was focused to a spot radius of ~3 µm, was used for the writing on the +*z* face of a congruent un-doped LN crystal. Precise control over the positioning and exposure of the illuminating laser beam was achieved by a computer-controlled, three-axis stage system coupled with a mechanical shutter. The laser wavelength used in our experiments was 275 nm. Sets of parallel lines were drawn on the +*z* faces of the crystals along the crystallographic *y* direction by moving the stages at speeds ranging from 0.1 to 1 mm/s. The incident intensity was varied between 1 – 2 GW/m^2.

The samples with the sets of UV exposed parallel lines were then poled using the EFP set-up described in [7].The sample was first cycled through several forward and reverse poling cycles before the final forward poling step. In this final poling step, the voltage was ramped at 0.1 kV/s to a value of ~ 10 kV which corresponds to an electric field of ~20 kV/mm across the 0.5 mm thick sample. This lower value of the

This work was supported by the European research project 3D-DEMO STREP033297.

applied electric field (less than coercive field) ensures that domain inversion occurs slowly, which is desirable since the kinetics of the domain wall motion is seen to greatly influence the shape, quality and more essentially the continuity of the resultant ridge structures. As described in [7], the UV written lines inhibit subsequent domain inversion and retain their +z domain orientation whereas the rest of the un-illuminated crystal undergoes domain inversion to a –z orientation. Because of the differential etch characteristics of the complementary z faces, whereby the +z face does not etch, when the poled samples with the sets of UV written parallel lines, are etched in pure HF acid at room temperature, sets of parallel ridges are formed. Fig. 1 shows an optical microscope image of two sets of parallel ridges formed using this fabrication route. All of the ridges have been produced by scanning the c.w. UV laser beam at a speed of 0.1 mm/s, however, the set of four lines on the left of the image have been written with a slightly higher incident intensity of ~ 1.4 GW/m^2 whereas the ones on the right have been written using ~ 1.2 GW/m^2. A slight variation in the widths of these two set of ridges is a result of the difference in the incident power which influences the width of the poling-inhibited region. Fig. 2 shows a plot of the etched poling-inhibited width, which corresponds to the width of the ridge structure, as a function of the UV laser intensity. As shown in the plot a range of laser intensities exists where the width increases almost linearly with the laser intensity. The cross-section of a polished end face of one such a ridge is shown in the scanning electron microscopy (SEM) image presented in Fig. 3. The trapezoidal cross-section of the ridge is possibly a consequence of the inherent etching behaviour of different crystalline planes that are revealed during the etch process. The width of the ridge near the top is ~ 7 µm, and its height is ~ 3.1 µm. As the ridges have been formed by drawing lines parallel to the crystallographic *y* direction they consequently have a symmetric cross-sectional profile. The noticeable roughness along the sidewall of the ridge is a consequence of the wet etching process which was performed in pure HF. However, use of modified etchant mixture have been reported to produce smoothly-etched surfaces [8]. Further optimization of the etching conditions will be investigated in order to eliminate the deleterious sidewall roughness. The current choice of etching conditions was driven mainly by speed rather than quality. The UV laser intensity, during the UV writing step, has a significant impact on the quality of the ridge structures. Specifically, UV intensities higher than ~ 1.6 GW/m^2 lead to damage of the top-surface, whereas intensities lower than ~ 1.1 GW/m^2 result in poorly defined ridge side-walls. After edge polishing of the samples laser light (633 nm HeNe laser) was end-fire coupled into the ridge waveguides using a microscope objective lens in order to investigate the optical characteristics of the structures. Fig. 4 shows the near-field intensity profile collected using a second objective lens to image the output of the ridge on to a CCD camera. This mode profile corresponds to a ridge structure formed using a UV laser scanning speed of 0.1 mm/s and an incident intensity of ~ 1.2 GW/m^2. We did not observe any deterioration of the vertical confinement in the UV written waveguides after the EFP and wet etching processing steps. Contrary to that we did observe a significant refractive index change increase (more than 50 %) in the UV written optical waveguides following the poling-inhibition step (before etching to fabricate the ridges).

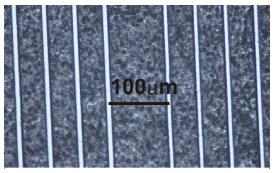


Figure 1. Optical microscope image of two sets of ridges.

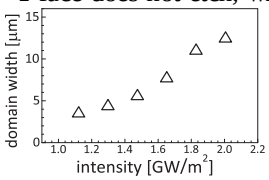


Figure 2. Plot showing variation of poling-imhibited domain width versus intensity.

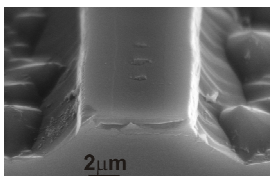
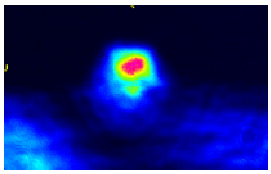


Figure 3. SEM of the polished end face of the ridge


Figure 4. Near-field intensity profile obtained at 633nm

III. CONCLUSIONS

In conclusion we have presented preliminary results on a UV laser-assisted method for the fabrication of ridge waveguides in LN crystals. The method utilizes UV laser direct writing to i) provide the vertical confinement of the light in the waveguide and ii) assist the domain engineering process (poling-inhibition) which, after chemical etching, defines the ridge structures.

REFERENCES

[1] A. Guarino, G. Poberaj, D. Rezzonico, R. Degl'Innocenti and P. Gunter, "Electro-optically tunable microring resonators in lithium niobate", Nature Photonics, 1, 407-410, 2007

[2] K. Noguchi, O. Mitomi, H. Miyazawa and S. Seki, "A Broad-Band Ti-$LiNbO_3$ Optical Modulator With A Ridge Structure", Journal of Lightwave Technology, 13, 1164-1168, 1995

[3] I. E. Barry, G. W. Ross, P. G. R. Smith and R. W. Eason, "Ridge waveguides in lithium niobate fabricated by differential etching following spatially selective domain inversion", Applied Physics Letters, 74, 1487-1488, 1999

[4] M. Iwai, T. Yoshino, S. Yamaguchi, M. Imaeda, N. Pavel, I. Shoji and T. Taira, "High-power blue generation from a periodically poled MgO : $LiNbO_3$ ridge-type waveguide by frequency doubling of a diode end-pumped Nd : Y3Al5O12 laser", Applied Physics Letters, 83, 3659-3661, 2003

[5] S. Mailis, C. Riziotis, I. T. Wellington, P. G. R. Smith, C. B. E. Gawith and R. W. Eason, "Direct ultraviolet writing of channel waveguides in congruent lithium niobate single crystals", Optics Letters, 28, 1433-1435, 2003

[6] P. Ganguly, C. L. Sones, Y. J. Ying, H. Steigerwald, K. Buse, E. Soergel, R. W. Eason and S. Mailis, "Determination of Refractive Indices From the Mode Profiles of UV-Written Channel Waveguides in $LiNbO_3$-Crystals for Optimization of Writing Conditions", Journal of Lightwave Technology, 27, 3490-3497, 2009

[7] C. L. Sones, A. C. Muir, Y. J. Ying, S. Mailis, R. W. Eason, T. Jungk, A. Hoffmann and E. Soergel, "Precision nanoscale domain engineering of lithium niobate via UV laser induced inhibition of poling", Applied Physics Letters, 92, 3, 2008

[8] H. Hu, R. Ricken, W. Sohler and R. B. Wehrspohn, "Lithium niobate ridge waveguides fabricated by wet etching", IEEE Photonics Technology Letters, 19, 417-419, 2007

Šolc-type wavelength filters based on TE↔TM mode conversion utilizing periodically poled Ti-diffused lithium-niobate channel waveguides

Hong-Sik Jung
Dept. of Electronic & Electrical Engineering
Hongik University
Seoul, Korea
hsjung@wow.hongik.ac.kr

Abstract—We have demonstrated the Šolc-type wavelength filters in a 52mm long periodically poled Ti diffused lithium niobate channel waveguide which has a domain period of 16.6μm. At room temperature, the center wavelength and the full-width at half maximum of the filter were about 1272.49nm and 0.23nm, respectively. The nearest side-lobe is about 7dB. New structure of optical add/drop multiplexer (OADM) utilizing Šolc-type TE↔TM mode converters was proposed for the first time

Keywords- Šolc-type wavelength filter, Ti:PPLN, polarization mode conversion, periodic poling, lithium-niobate ($LiNbO_3$), optical channel waveguide, optical add/drop multiplexer(OADM)

I. INTRODUCTION

The development of periodic poled Ti-diffused lithium niobate channel waveguides (Ti:PPLN) utilizing the electric-field poling techniques[1] allow good quality quasi phased matched (QPM) waveguide devices which can be used in various optical application fields. Among the various periodically poled ferroelectric materials, a periodically poled lithium niobate (PPLN) is particularly attractive for various QPM devices due to its large nonlinear-optic coefficient and easy integration. The main application fields of QPM devices based on periodical poled titanium-diffused optical channel waveguides (Ti:PPLN) are all-optical wavelength conversion[2], optical pulse compression[3], all-optical switching [4], and all-optical logic gate because of their ultrafast nonlinear optical response and high conversion efficiency. Actually, the electric-field poling of lithium niobate modulates not only the nonlinear optical coefficients but also the electro-optical coefficients due to periodically domain-inversion. These kinds of modulated structures can be used to compensate the phase mismatch between the ordinary and extraordinary wave in birefringent lithium niobate optical channel waveguides.

Recently, the electric-field poling technique allows a new type of narrowband Šolc filter based on PPLN, which has thousands of birefringent plates [5]. Although the Šolc filter was proposed more than 50 years ago, difficulties with the fabrication technology in making a large number of birefringent plate stacks have prevented the appearance of a practical narrowband Šolc-type wavelength filter [6]. Optical wavelength filtering and polarization mode conversion are key functions in an optical signal processing and communication systems. Optical wavelength filters have attracted much attention in applying to WDM systems due to their constant availability and reliability in the spectrum division and narrowing [7]. Among the diverse optical narrowband wavelength filters, birefringent Šolc-type wavelength filters can allow narrow and tunable spectral band.

Section II of this paper reviews the operation principles of a Šolc-type wavelength filters based on TE-TM mode conversion. Section III discusses the fabrication processes of Ti:PPLN and some experimental observations including propagation loss, near-field mode patterns and measurements of second harmonic generation. Section IV describes the performance of a Šolc-type wavelength filters and section V suggests an add/drop optical multiplexer consisting of Šolc-type TE↔TM mode converters and polarization beam splitters (PBS).

II. OPERATION PRINCIPLE OF ŠOLC FILTERS

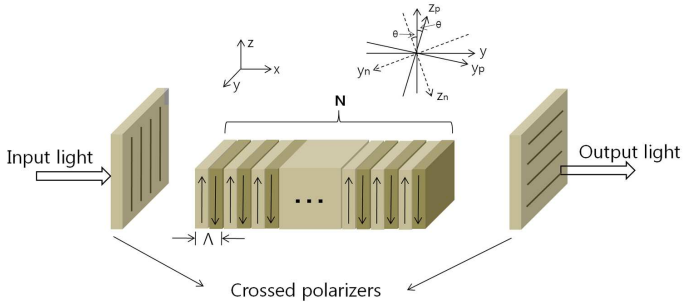


Fig. 1. Set-up for a PPLN Šolc-type wavelength filter

In a folded Šolc-type wavelength filter a series of half-wave plates are contained between crossed polarizers as shown in Fig. 1. The optical axes of the half-wave plates are alternately aligned at angles of +θ and –θ with respect to the plane of polarization of the input light. The angle θ is called the rocking angle because the angle can't be changed after poling process. The experimental observation of the Šolc-type

filter indicates that there is rocking angle θ between the optical axes of the positive and negative domains. Even though the origin of this rocking angle is not clear, the fabricating defect of the PPLN is suspected to cause the rocking angle. Namely, the crystal-axis (namely, Z-axis) is not exactly perpendicular with the crystal surface such that the crystal-axis of the negative domain after poling may have a very small deviation angle θ from the crystal-axis of the positive domain [5]. When a rocking angle θ exists between domains, the input light at the center wavelength which is polarized along the Y-axis rotates by an angle of 2θ after passing through the first set of positive and negative domains. The center wavelength λ_o is defined by [8]

$$\lambda o = \frac{2}{2m+1}(n_o - n_e)d, \qquad m = 0,1,2,- - - \qquad (1)$$

where n_o and n_e are refractive indices of the ordinary and extraordinary wave, respectively, and d is the domain thickness. Thus, after passing through N domains (N/2 sets), the rotation angle of the polarization is Nθ. In this case the transmission of power is described by $T=\sin^2(N\theta)$. Therefore, when $N\theta=90^o$ at the filter, light of wavelength does not experience loss in passing through the crossed polarizer as shown in Fig. 1. Light at other wavelengths does not satisfy the above condition and is therefore quickly attenuated at the crossed output polarizer. The transmissivity T of the Šolc-filter can be expressed by

$$T = \left[\frac{\sin\left(\frac{1}{2}\pi\sqrt{1+(N\cdot\frac{\Delta\Gamma}{\pi})^2}\right)}{\sqrt{1+(N\cdot\Delta\Gamma/\pi)^2}}\right]^2 \qquad (2)$$

where ΔΓ is the change of phase retardation defined by

$$\Delta\Gamma = -\pi(\lambda - \lambda_o)/\lambda_o \qquad (3)$$

where λ_o is the center wavelength of the filter. The FWHM of the filter is proportional to the inverse of the number of domains as given by

$$\lambda_{FWHM} \cong 1.6\{\lambda_m/[(2m+1)N]\} \qquad (4)$$

Therefore, we can control the bandwidth of filter by changing the length of device. Such a narrow bandwidth is caused by the numerous domains in the Ti:PPLN channel waveguide.

In a lithium niobate crystal, if an external electric field along the Y axis is applied refractive-index ellipsoid deforms and consequently the Y and Z axes of the Z-cut lithium niobate rotate by a small angle Φ about the X axis. X, Y, and Z represent the principal axes of the original index ellipsoid of the lithium niobate crystal. The rotation angle Φ is given by [9]

$$\Phi \approx \frac{\gamma_{51}E}{\left(\frac{1}{n_e^2}\right)-\left(\frac{1}{n_o^2}\right)} \qquad (5)$$

where E is the electric field intensity and r_{51} is the off-diagonal electrooptic coefficient. Note that the coefficient r_{51} changes its sign in the negative domains because of the 180° rotation of the crystal structure. Thus, even in the presence of a uniform electric field along the Y axis, the rotation angle of the Y and Z axes changes sign from positive to negative domains. For a PPLN with alternatively positive and negative domains whose length is given by eq. (1), a folded Šolc-type wavelength filter can be easily formed by application of a uniform electric field along the Y axis. Since the rotation angle Φ given by eq. (5) is proportional to the intensity of the applied voltage, the transmission intensity at a given wavelength can be electrically modulated by the applied electric field. Furthermore very narrow spectrum filters can be achieved by employment of a longer PPLN crystal since the line width of the transmission spectrum is governed by both the number and order of the half-wave plates.

In general, it is very difficult to predict and adjust the rocking angle θ by only poling to make $N\theta=90^o$ for a given device length. Therefore, the Nθ may be greater or smaller than 90° and eventually transmittance should be degraded. The amount of deficiency and surplus of Nθ can be adjusted to 90° by the rotation angle Φ, applying an external electric field along the Y axis. In this case, the transmission of power can be described by $T=\sin^2(N\theta \pm \Phi)$. A maximum spectral transmittance can be achieved at the condition $N\theta \pm \Phi=90^o$.

III. Fabrication Processes of Ti:PPLN and Characterizations

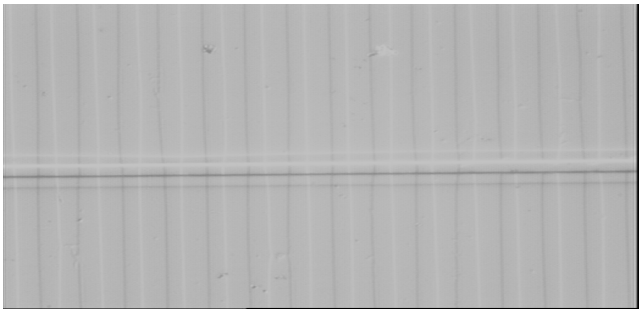


Fig. 2. HF-etched Ti:PPLN surface after domain-inversion

A channel waveguide with a width of 7μm was fabricated by diffusing ~100nm thick Ti stripes on –Z face of a 60mm long, 12mm wide, and 0.5mm thick Z-cut $LiNbO_3$ substrate along its X-axis. Afterwards, a micro-domain inversion structure with a periodicity of 16.6μm was generated by using an electrical field poling technique with liquid electrodes and annealed to remove the stress happened during electrical field poling. Fig. 2 shows periodic domain inversion structure on Ti-diffused channel waveguide in lithium niobate after selective chemical etching. We confirmed the qualities of QPM structure and waveguide in a Ti:PPLN device by the

measure of the second-harmonic wave, the propagation loss of waveguide and near field mode profiles, respectively. Fig. 3 shows the second harmonic curve at room temperature. The conversion efficiency was measured to be 473%/W at a wavelength of 1529.80nm. Such a narrow bandwidth and high conversion efficiency indicate that a good QPM structure was fabricated through the whole length of waveguide. The propagation losses of TM and TE polarization mode at 1529.80nm were measured to be 0.03 and 0.01dB/cm, respectively. At the same time, the near-field mode profiles of Ti:PPLN channel waveguide at the both polarization were measured to be 6.83μm x 4.69μm and be 4.77μm x 3.47μm for TM and TE polarization mode, respectively. From the waveguide characterization, we confirmed that the fabricated Ti:PPLN channel waveguides can guide TM and TE polarization beam simultaneously with a single mode profile. The shorter wavelength side ripples of a phase peak as shown in Fig. 3 seem to be influenced by slight variation of the refractive index difference between fundamental and second harmonic waves.

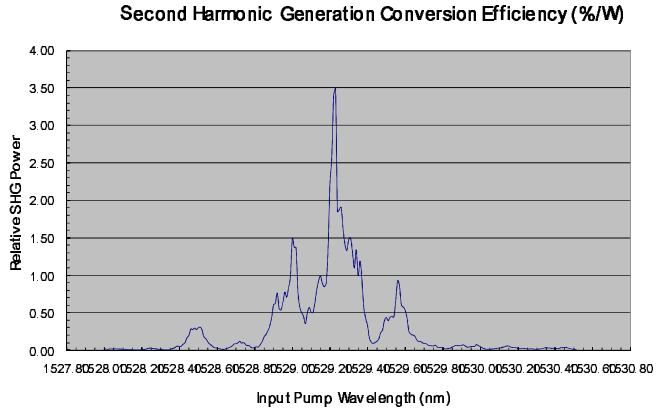


Fig. 3. Second-harmonic generation curve for Ti:PPLN

IV. ŠOLC FILTERS PERFORMANCES

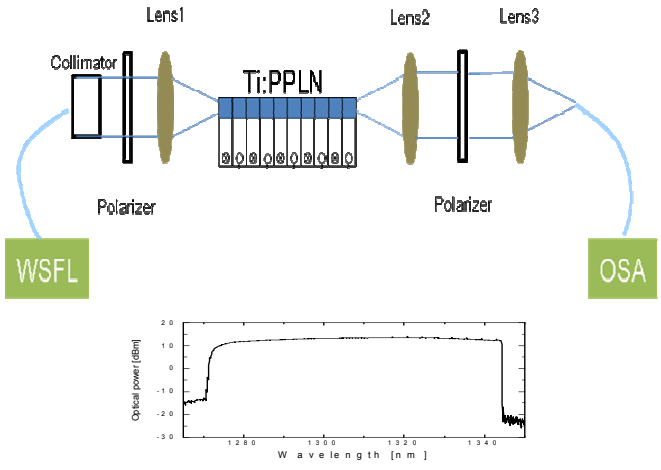


Fig. 4. Measurement set-up of Ti:PPLN Šolc-type filter

The experimental setup to perform the wavelength filtering based on the TE-TM mode conversion of Ti:PPLN channel waveguide is shown in Fig. 4. An incident optical wave from a wavelength swept fiber laser based on a semiconductor optical amplifier and a Fabry-Perot tunable filter was collimated and end-fire coupled into polarizer by x10 objective lens. The polarization direction of input mode was adjusted parallel to the Y-axis and output signal was observed by an optical spectrum analyzer. The optical spectrum of the wavelength swept fiber laser was shown in Fig. 4. The average power and sweeping frequency of the optical signal were 10mW and 15 KHz, respectively. The swept bandwidth of the laser was about 70nm (from 1260-1333nm).

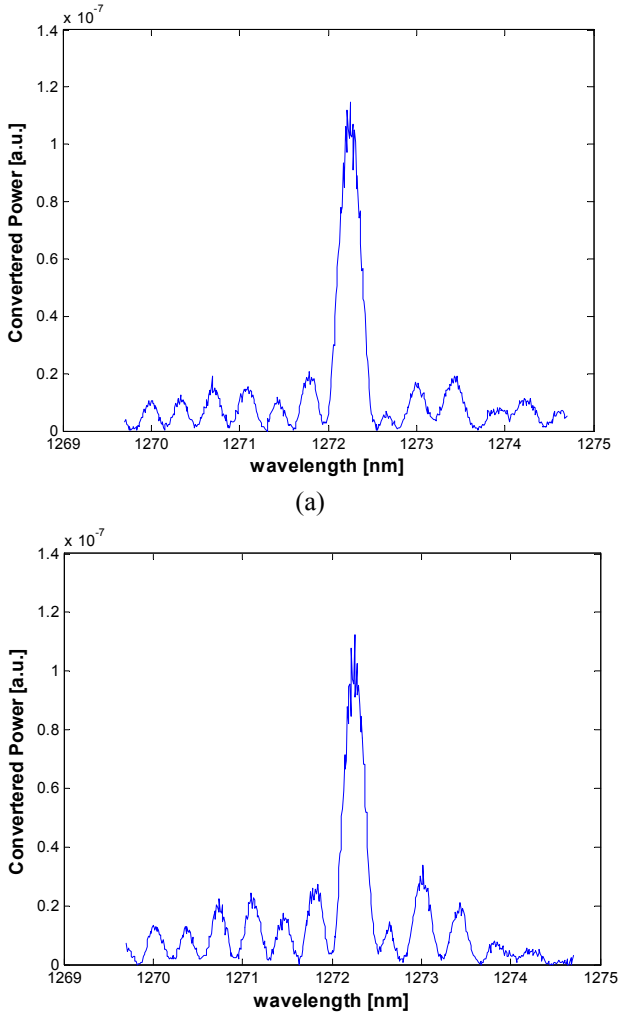


Fig. 5. Measured transmission optical power versus wavelength of Ti:PPLN Šolc-filter at center wavelength (a) 1272.49nm and (b) 1272.3nm, respectively

The measured transmission spectra of the waveguide-type Šolc-filter based on the Ti:PPLN waveguide are shown in Fig. 5 (a) and (b). The transmission spectra were measured at room temperature (25°C.). The measured center wavelength

and full-width at half-maximum (FWHM) of the filters in Fig. 5 (a) and (b) are 1272.49 nm and ~0.23nm, and 1272.3nm and ~0.24nm, respectively, which is almost the same as the predicted value in theoretical calculation. The largest sidelobe occurring on the transmission curve was measured about 7dB below the maximum transmission. A bandwidth of ~0.23nm is narrow enough for use in wavelength filtering in optical communications. The FWHM of the filter is proportional to the inverse of number of domains as given by eq. (4). Therefore, we can control the bandwidth of the filter by changing the length of Ti:PPLN devices. The normalized transmittance shows less than 10% because the rocking angle θ and entire device length were not enough to convert TE to TM entirely. However, the transmittance can be improved utilizing the rotation angle Φ by application of electric field along the Y-axis of the PPLN.

V. OPTICAL ADD/DROP MULTIPLEXERS UTILIZING TI:PPLN ŠOLC-FILTER

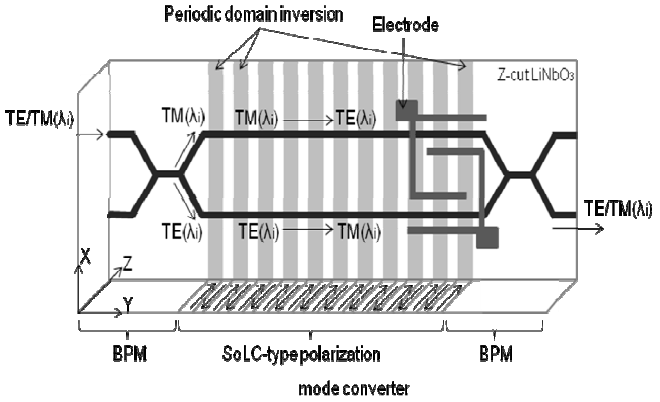


Fig. 6. Schematic diagram of optical add/drop multiplexer (OADM) consisting of Šolc-type polarization mode converters and polarization beam splitters

The schematic diagram of optical add/drop multiplexer (OADM) as shown in Fig. 6 was proposed for the first time to the best of our knowledge. It consists of three sections: two identical polarization beam splitters (PBS) near the input and output ends that are joined by a pair of parallel channel waveguides in which Šolc-type polarization mode conversion and wavelength tuning occur. The PBSs based on two-mode interference are basically a kind of passive directional couplers that leave an incident TM component in the straight-through arm, and route an input TE component to the cross-over arm. At the center polarization mode converter (PMC) section the separated polarized components undergo wavelength dependent Šolc-type polarization mode conversion in each of the parallel Ti:PPLN waveguide arms which has thousands of birefringent plates on Ti diffused channel waveguide.

VI. CONCLUSION

We have demonstrated the Ti:PPLN channel waveguide Šolc wavelength filter which has a domain period of 16.6μm. We observed that the FWHM, ~0.23nm of wavelength filter was narrow enough for use in an optical filter for all-optical wavelength switching. From a practical point of view, the optical waveguide-type PPLN Šolc wavelength filter is more useful than bulk-type Šolc filters. Among the various waveguide-type PPLNs, the Ti:PPLN waveguide is the most promising device for the Šolc filter because it can support both TE and TM polarization mode simultaneously with single-mode profile and low insertion loss. The new configuration of optical add/drop multiplexer (OADM) utilizing Šolc-type polarization mode converters was proposed for the first time to the best of our knowledge. We believe that the Šolc-type wavelength filter and polarization mode converter based on a Ti:PPLN channel waveguide will be a very useful optical device for a future tunable wavelength filter in optical communication.

ACKNOWLEDGMENT

This work was supported by the Korea Research Foundation Grant funded by the Korean Government (MOEHRD, Basic Research Promotion Fund) (KRF-2008-521-D00305).

REFERENCES

[1] Y.L. Lee, H. Suche, G. Schreiber, R. Ricken, V. Quiring and W. Sohler, "Periodical domain inversion in single mode Ti:MgO:$LiNbO_3$ channel waveguides", Electronics Letters, Vol. 38, No. 15, pp. 812-815, 2002.

[2] M. H. Chou, I. Brener, M. M. Fejer, E. E. Chaban, and S. B. Christman, "1.5-μm-Band Wavelength Conversion Based on Cascaded Second-Order Nonlinearity in $LiNbO_3$ Waveguides", IEEE Photonics Technol. Lett., Vol. 11, No. 6, pp. 653-655, 1999.

[3] M. A. Arbore, O. Marco, and M. M. Fejer, "Pulse compression during second-harmonic generation in a periodic quasi-phase-matching gratings", Opt. Lett., Vol. 22, pp. 865-867, 1977.

[4] T. Suhara and H. Ishizuki, "Integrated QPM sum-frequency generation interferometer device for ultrafast optical switching", IEEE Photonics Technol. Lett., Vol. 13, No. 11, pp. 1203-1205, 2001.

[5] J. Shi, X. Chen, Y. Chen, Y. Zhu, Y. Xia, and Y. Chen, "Observation of Šolc-like filter in periodically poled lithium niobate", Electron. Lett., Vol. 39, pp. 224-225, 2003

[6] I. Šolc, "Birefringent chain filters", J. Opt. Soc. Amer., Vol. 55, pp. 621-625, 1965.

[7] S. J. B. Yoo, "Wavelength conversion technologies for WDM network applications", J. Lightwave Technol., Vol. 14, pp. 955-966, 1996.

[8] C. Y. Huang, C. H. Lin, Y. H. Chen, and Y. C. Huang, "Electro-optic Ti:PPLN waveguide as efficient optical wavelength filter and polarization mode converter," Optics Express, Vol. 15, No. 5, pp. 2548-2554, March 2007.

[9] A. Yariv and P. Yeh, Optical Waves in Crystal: Propagation and Control of Laser Radiation, Wiley New York , 1984.

Rare Earth Doped Epitaxial Layers of $KY_{1-x-y}Gd_xLu_y(WO_4)_2$ as Active Waveguides

Western Bolaños, Joan J. Carvajal, Xavier Mateos, Maria Cinta Pujol, Magdalena Aguiló and Francesc Díaz
Física i Cristal·lografia de Materials i Nanomaterials (FiCMA-FiCNA), Universitat Rovira i Virgili (URV)
Tarragona, Spain

Ginés Lifante
Advanced Materials for Integrated Guided Optics (AMIGO), Departamento de Física de Materiales, Universidad Autónoma de Madrid
Madrid, Spain

e-mail: diaz@quimica.urv.es

***Abstract*—Active planar waveguides based on monoclinic double tungstates doped with Er^{3+} and Tm^{3+} are presented. The incorporation of these ions into the lattice matched $KY_{0.59}Gd_{0.19}Lu_{0.22}(WO_4)_2$ epitaxial layers grown on $KY(WO_4)_2$ substrates was successfully achieved without loss of optical quality, and keeping a high refractive index contrast between the epitaxial layer and the substrate. Both spectroscopic and waveguiding properties of the epitaxial layers have been characterized. Results indicate that high performance waveguide lasers operating at the IR can be realized in these dielectric media.**

Keywords- active waveguides, lasers, liquid phase epitaxy

I. INTRODUCTION

A wide range of dielectric materials, such as oxides, fluorides, glasses [1], and more recently monoclinic double tungstates, $KRE(WO_4)_2$ [2,3] and rare-earth doped sesquioxides [4], have been studied to develop waveguide lasers. The main advantages of lasers in waveguide configuration are the reduction of the cavity mode-volume, high optical gain, low threshold and easy on-chip integration with other photonics components. Since the family of monoclinic double tungstates, $KRE(WO_4)_2$, includes a rare earth ion in its structure, it is an excellent host materials for active lanthanide ions such as Yb^{3+}, Tm^{3+}, and Er^{3+}, for laser applications [5–8], including thin disk configuration [9]. In addition, $KRE(WO_4)_2$ crystals containing different rare earths present different refractive indices, and therefore by choosing a suitable combination of the constitutive rare earth ions in these materials, active waveguide with good refractive index contrast can be fabricated. We have chosen Er^{3+} and Tm^{3+} as active ions for doping the passive layer, due to their attractive characteristics for several integrated optical applications.

II. EXPERIMENTAL DETAILS

Er^{3+} and Tm^{3+} doped $KY_{1-x-y}Gd_xLu_y(WO_4)_2$ bulk single crystals were grown by the Top Seeded Solution Growth method (TSSG) in a vertical tubular furnace using **b**-oriented seeds of $KY(WO_4)_2$. $K_2W_2O_7$ was used as solvent in a ratio solute:solvent 12:88 mol%. The crystals were grown cooling by 15 K the temperature of the solution from the saturation temperature at a cooling rate of 0.03 K/h. The lattice parameters of Er^{3+} and Tm^{3+} doped $KY_{1-x-y}Gd_xLu_y(WO_4)_2$ single crystals were determined by X-ray powder diffraction using a Bruker-AXS D8-Discover diffractometer.

Liquid Phase Epitaxy was used to grow Er^{3+} and Tm^{3+}-doped $KY_{1-x-y}Gd_xLu_y(WO_4)_2$ epitaxial layers on **b**-oriented $KY(WO_4)_2$ substrates. The solution prepared for the epitaxial growth was composed of 7 mol% solute and 93 mol% solvent ($K_2W_2O_7$). Once the T_s was established, the $KY(WO_4)_2$ substrate was introduced into the furnace, and it was kept at 1 mm above the surface of the solution for 45 min to reach the same temperature that the solution used for growing the epitaxial layer. After that, the substrate was submerged into the solution at 1 K above T_s, during 5 min. Then, we decreased the temperature of the solution suddenly by 4 K below T_s, to reach the growth temperature, T_g. After 3 h, the substrate was taken out from the solution, and the furnace was cooled down to room temperature at 20 K/h to prevent cracking of the epitaxies by thermal shocks. Chemical composition of the samples was determined by Electron Probe Microanalysis (EPMA) with a CAMECA SX 50 equipment, performed at 20 mA of beam current, 20 kV of acceleration voltage.

Optical absorption spectra were taken with a VARIAN CARY-5E-UV–VIS–NIR 500 Scan Spectrophotometer, while photoluminescence spectra were performed by using a Ti:sapphire laser as excitation source and recorded in a 90º configuration by a double monochromator with a focal length of 0.46 m, by means of a cooled NIR photomultiplier.

Refractive indices of the Er^{3+} and Tm^{3+} doped $KY_{1-x-y}Gd_xLu_y(WO_4)_2$ epitaxial layers as well as those of the substrates were measured by the prism-film coupling technique using a Ti:sapphire laser and a He-Ne laser. The TE polarization allowed us to measure the refractive indices, n_g and n_m, associated to the N_g and N_m principal dielectric directions, respectively, while the TM polarization was used to determine the refractive index n_p, associated to the third principal dielectric direction, N_p.

III. RESULTS AND DISCUSSION

Crack-free and macroscopic defect free epitaxial layers of $KY_{0.60}Gd_{0.18}Lu_{0.21}Er_{0.01}(WO_4)_2$ and $KY_{0.59}Gd_{0.18}Lu_{0.22}Tm_{0.01}(WO_4)_2$ on **b**-oriented $KY(WO_4)_2$ substrates were obtained by the LPE technique. The chemical composition of these epitaxial layers was analyzed by EPMA. The scheme of the

atomic percent of Gd^{3+}, Lu^{3+}, Er^{3+} and Tm^{3+} measured by this technique across the substrate and the epitaxial layer shows no diffusion of these ions from the epitaxial layer to the substrate (see Fig. 1). The as-grown epitaxies had an epitaxial layer on every {010} face of the substrate. So, to fabricate waveguides, we removed one of the epitaxial layers, preferably that grown on the (0-10) face. Then, the epitaxial layer grown on the (010) face of the substrate was lapped and polished to a final thickness of 10 μm. The resulting sample was cut as a slab with dimensions of 5x5x2 mm^3 along the N_g, N_m and N_p directions, respectively. Finally, the four lateral edges of the sample were polished to high quality to facilitate the coupling of light into the epitaxial layer through the edge. The refractive indices of the substrate and the epitaxial layers were measured at different wavelengths with a Ti:sapphire laser coupled to a prism-film coupler system.

At 632.8 nm the refractive index contrast between the doped films and the substrate is, in both cases, of the order of 10^{-3}, which is high enough to guide light along the three principal optical directions of the epitaxial layer. For the Er^{3+} emission wavelength at 1533 nm, the n_g refractive index of the film, estimated by the Cauchy fitting, seems to be lower than that of the substrate. This means that light would be not guided when the electric field of the incident beam oscillates parallel to N_g direction. On the contrary, the n_m and n_p refractive indices of the film seem to be greater than those of the substrate. This would indicate the possibility to demonstrate an erbium-based waveguide laser for light oscillating parallel to N_m and N_p directions. In the case of the Tm^{3+} emission wavelength at 1769 nm, it seems that we would only expect to obtain a Tm-based waveguide laser for light polarized parallel to N_m direction since the estimated n_g and n_p refractive indices of the film seem to be lower than those of the substrate. According to the results, a $KY_{0.60}Gd_{0.18}Lu_{0.21}Er_{0.01}(WO_4)_2/KY(WO_4)_2$ waveguide will be monomode for guided light at λ = 1533 nm when the thickness of the film is around 6 μm, while at λ = 1769 nm the $KY_{0.59}Gd_{0.18}Lu_{0.22}Tm_{0.01}(WO_4)_2/KY(WO_4)_2$ waveguide will only guide one mode when the thickness of the film is ~5 μm.

Through the same prism-film coupler system we recorded the dark-mode spectra for the doped layers. At λ = 633 nm we observed five and four TE guided modes for 10 μm-thick epitaxial films when the electric field oscillates parallel to the N_g and N_m optical directions, respectively, and five TM guided modes when the magnetic field oscillates parallel to the N_p optical direction. The guided modes observed in the dark-mode spectra at λ = 632.8 nm were excited and visualized by the end-coupling technique using a 40x microscope objective to focus the laser beam at the input of the waveguide and a 60x microscope objective at the opposite edge to collect the near field intensity on a CCD camera.

We finally established an upper limit for propagation losses of the waveguides by measuring the intensity of the scattered light along the waveguide with a CCD camera. The upper limit in the two waveguides studied was about 1 dB/cm for the three principal optical directions.

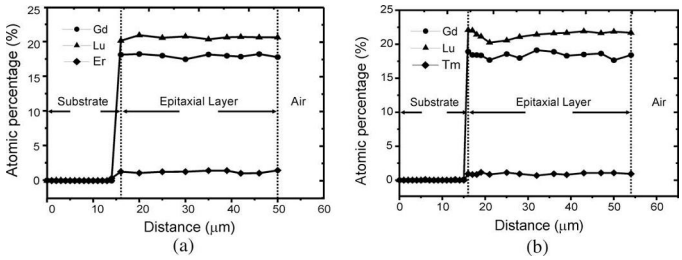


Fig. 1.- Extended profiles of the chemical composition across the interface substrate/epitaxial layer in (a) $KY_{0.60}Gd_{0.18}Lu_{0.21}Er_{0.01}(WO_4)_2$ and (b) $KY_{0.59}Gd_{0.18}Lu_{0.22}Tm_{0.01}(WO_4)_2$ samples.

IV. CONCLUSIONS

We have successfully introduced Tm^{3+} and Er^{3+} ions in $KY_{1-x-y}Gd_xLu_y(WO_4)_2$ epitaxial layers without loosing optical quality and keeping a low lattice mismatch and a high refractive index contrast with the $KY(WO_4)_2$ substrate. The Er^{3+} and Tm^{3+} ions concentrations in these epitaxial layers were $7.8x10^{-19}$ and $6.4x10^{-19}$ cm^{-3}, respectively, high enough to allow laser generation. Finally, the waveguiding properties of these epitaxial layers at λ = 632.8 nm were studied by dark-mode spectroscopy. It was found that these waveguides can support up to four TE and TM modes, allowing monomode propagation at the IR. Experiments to demonstrate planar waveguides lasers and routes for fabricating channel waveguide configuration in this material are ongoing at present.

ACKNOWLEDGMENTS

This work was supported by the Spanish Government under projects MAT 2008-06729-C02-02/NAN and the Catalan Authority under project 2009SGR235. The authors are grateful to the Serveis Cientifico-Tècnics of the University of Barcelona for EPMA measurements. W. Bolaños thanks the Catalan Government for the funds provided through the fellowship 2008FI_B00626. J.J. Carvajal is supported by the Education and Science Ministry of Spain and European Social Fund under the Ramon y Cajal program, RYC2006 – 858.

REFERENCES

[1] J.I. Mackenzie, IEEE J. Selected Topics Quant. Electron. **37** (2007) 626.

[2] Y.E. Romanyuk, C.N. Borca, M. Pollnau, S. Rivier, V. Petrov, U. Griebner, Opt. Lett. **31** (2006) 53.

[3] S. Rivier, X. Mateos, V. Petrov, U. Griebner, Y.E. Romanyuk, C.N. Borca, F. Gardillou, M. Pollnau, Opt. Exp. **15** (2007) 5885.

[4] A. Khan, S. Heinrich, H. Kühn, K. Petermann, J.D.B. Bradley, K. Wörhoff, M. Pollnau, G. Hüber, Opt. Exp. **17** (2009) 4412.

[5] X. Mateos, V. Petrov, M. Aguiló, R. Solé, Jna. Gavaldá, J. Massons, F. Díaz, U. Griebner, IEEE J. Quantum Electron. **40** (2004) 1056.

[6] O. Silvestre, M.C. Pujol, M. Rico, F. Güell, M. Aguiló, F. Díaz, Appl. Phys. B **87** (2007) 707.

[7] X. Mateos, R. Solé, Jna. Gavaldá, M. Aguiló, J. Massons, F. Díaz, Opt. Mater. **28** (2006) 423.

[8] C. Zaldo, M. Rico, C. Cascales, M.C. Pujol, J. Massons, M. Aguiló, F. Díaz, P. Procher, J. Phys.: Condens. Matter **12** (2000) 1.

[9] [12] S. Rivier, X. Mateos, O. Silvestre, V. Petrov, U. Griebner, M.C. Pujol, M. Aguiló, F. Díaz, S. Vernay, D. Rytz, Opt. Lett. **33** (2008) 735.

Acousto-optic tunable optical diode based on periodically poled LiNbO3

Qin Wang, Fei Xu, Zi-yan Yu, Xiao-shi Qian, Xi-kui Hu, Yan-qing Lu and Hui-Tian Wang
National Laboratory of Solid State Microstructures
Nanjing University,
Nanjing 210093, China

***Abstract*—**we propose a bidirectional acousto-optic tunable optical diode based on a periodically poled lithium niobate (PPLN) waveguide with defect. An acoustic wave propagates together with the light beam so that a collinear photon-phonon interaction happens, which affects the nonlinear optical processes in PPLN.

Keywords-QPM;optical diode;acousto-optic

I. INTRODUCTION

Recently, the nonreciprocal structures become hot topics. Periodically poled lithium niobate (PPLN) waveguides with geometrical asymmetries are promising nonreciprocal materials[1], which have been designed as optical diodes alternative to standard magneto-optic Faraday rotators. When the fundamental wave (FW) propagates in a PPLN waveguide with a defect, the second-harmonic wave (SH) and FW would go through different degrees of disturbance owing to the introduced phase discontinuity ($\delta\varphi$) at the defect area. Both the FW and SH thus are sensitive to the defect's parameters like its position and thickness. As long as the defect is not just at the middle of the PPLN waveguide, lights to opposite directions would see different structures then different FW and SH are obtained at the output ports. An extreme case is that one wave, e.g., the FW only may be detected at a single direction. The opposite FW is totally converted to SH. A unitary contrast $C = (T_\lambda^+ - T_\lambda^-)/(T_\lambda^+ + T_\lambda^-)$ was defined the degree of optical isolation, where T_λ^+ and T_λ^- are the FW transmission on forward and backward direction respectively. The contrast is greatly affected by phase discontinuity $\delta\varphi$, the position of $\delta\varphi$, and the fundamental input power. For a given PPLN diode, the $\delta\varphi$ and its location has been fixed. The contrast only can be tuned by the intensity of input power, which is not very convenient.

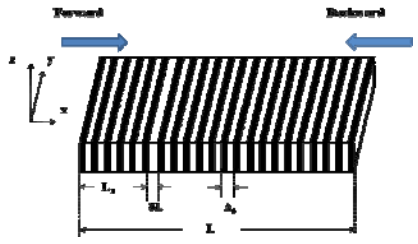


Fig. 1. Schematic diagram of a nonreciprocal PPLN waveguide (Dark and bright sections indicate positive and negative domains respectively). Λ_0 is the period of grating. A defect of length δL is introduced at x=L_1.

In this letter, the acoustic wave is introduced in asymmetric PPLN waveguides. The isolation of contrast could be tuned more flexible from -1 to 1, by just adjusting the intensity of acoustic wave. This makes the manufacturing and operation of the diode to be more convenient.

The nonreciprocal PPLN waveguide is sketched in Fig. 1. A defect is introduced in a PPLN of length L and period Λ_0. When an acoustic wave travels in it, a periodic index modulation is built up due to the elasto-optic effect, which could induce the acousto-optic (AO) polarization. The polarization rotation effect may be existed for either FWs or SHs depending on the phonon's frequency. Let's assume the FW's polarization is rotated, thus the original FW, the polarized FW and the SH are coupled together. To make use of the largest nonlinear coefficient d_{33}, the input FW is chosen to be Z-polarized. For simplicity, the propagation loss is ignored, and the wave vector mismatching for SHG and polarization rotation are compensated by the reciprocal vector (G1) of PPLN and the acoustic wave vector (H) respectively. The coupling equations could be deduced as follows with consideration of both nonlinear optic and AO interactions.

$$\begin{aligned} dA_{1z}/dx &= -iK_1 A_{1z}^* A_{2z} - iK_2 A_{1y} \\ dA_{2z}/dx &= -\tfrac{i}{2} K_1 A_{1z}^2 \\ dA_{1y}/dx &= -iK_2^* A_{1z} \end{aligned} \qquad (1)$$

Where $A_{j\xi} = \sqrt{n_{j\xi}/\omega_j}\,E_{j\xi}$, $K_1 = d_{33} g_1 / c\sqrt{\omega_1^2 \omega_2 / n_{1z}^2 n_{2z}}$, $K_2 = \omega_1 (n_{1y} n_{1z})^{1.5} p_{41} S / 4c$ $E_{j\xi}$, ω_j, $n_{j\xi}$, (the subscripts j = 1, 2 refer to the FW and SH, respectively, and $\xi = y, z$ represent the polarization) are the electric fields, the angular frequencies and the refractive indices, respectively. c is the velocity of light in vacuum. g_1 is the amplitude of the reciprocal vector G_1 whom is adopted to compensate the nonlinear phase match. p_{41} is the corresponding elasto-optic coefficient. S = HD is the amplitude of acoustic wave induced strain. H is the vector of acoustic wave to compensate the polarization rotation phase-matching and D is the amplitude of acoustic wave. A longitudinal acoustic wave along X-axis is considered.

This work was supported by 973 Program （ 2010CB327803 and 2006CB921805）, by the National Natural Science Foundation of China (60977039 and 10874080), The work of F. Xu and Y. Q. Lu was supported by Program for New Century Excellent Talents in University and Changjiang Scholars Program

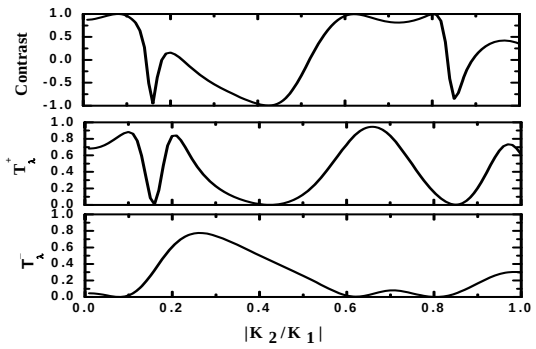


Fig. 2. The contrast is tuned by the intensity of acoustic wave. Here L_1 =4/10 L. The dephasing is 0.3 π. The red solid and green dashes represent the optical isolation with contrast C = 1 and -1 respectively.

Equations (1) are satisfied in the both uniform segments of PPLN waveguide in Fig. 1. In the domain of δL, a phase jump $\delta\varphi$ between FWs and SH is brought in. We suppose δL is short enough to ignore any influences on amplitude changes or phase-matching for both SHG and polarization rotation. While the waves travel forward, the z-polarized FW, y-polarized FW and z-polarized SH are coupled together along the PPLN in the segment L_1 (< 1/2 L). There are two competition processes: SHG and polarization rotation, which are governed by the coupling coefficients K_1 and K_2 and their ratio. When the light waves pass through the defect, their relative phase is changed and the SHG process is not standard any more. Then the seeded SHG and polarization rotation is engaged in the second segment L-L_1-δL. In the backward case, the same approach is adopted, except that the waves travel along the second segment L-L_1-δL firstly and thus the affection induced by dephasing $\delta\varphi$ is different. In both situations, K_2 could be easily controlled by tuning the intensity of acoustic wave (S) that makes the orientation of PPLN diode's unidirection optional.

At the room temperature, we set the pumping FW intensity 10 MW/cm^2 at 1550 nm, L = 1 cm, d_{33} = 25.2 pm/V, p_{41} = -0.05, Λ_0 =18.98 μm to satisfy the QPM condition. On the case of L_1 =4/10 L, $\delta\varphi$ = 0.3 π and π, the contrast and transmission in both directions for z-polarized FW is plotted in Fig. 2. It's obvious that the optical isolation with contrast (C) could be tuned nearly from -1 to 1 by adjusting the ratio of $|K_2/K_1|$, *i.e.*, the intensity of acoustic wave. When $\delta\varphi = 0.3\pi$, $C \approx 1$ (red solid, the forward transmission T_λ^+ = 83.73% and the backward transmission $T_\lambda^- \approx 0$) represents an optical diode which only allows the forward transmission. While $C \approx$ -1 (green dash, the forward transmission $T_\lambda^+ \approx 0$ and the backward transmission T_λ^- = 45.38%) represents the same diode but only allows the backward transmission. Thus, the bidirectional optical diode is achieved by tuning acoustic wave.

Simulations have also been done for unequal lengths of L_1, various dephasing $\delta\varphi$, and different input power. Figure 3 shows the tunable range of contrast versus dephasing $\delta\varphi$ with different lengths of L_1 at a lower input power than Fig. 2. Black dashes and red solids represent the achieved maximum

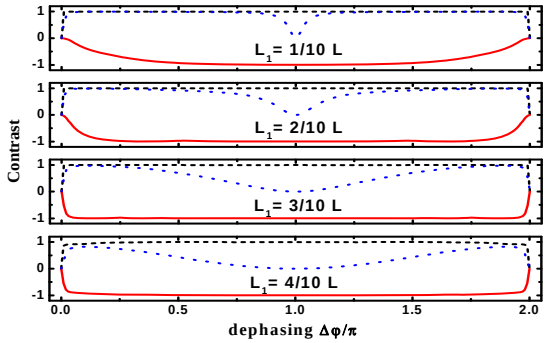


Fig.3. The tunable range of contrast C versus different dephasing $\delta\varphi$ with different lengths of L_1. Black dashes and red solids represent the maximum and minimum contrast by tuning the intensity of acoustic wave, respectively. The blue dots show the contrast without acoustic wave.

and minimum values of the isolation contrast by tuning the intensity of acoustic wave, respectively. The blue dots show the contrast without any acoustic. From Fig. 3:

(I) The contrast is symmetric with regard to π, because the influence induced by positive and negative phase jumps between FWs and SH is equal, i.e., $C(\delta\varphi) = C(-\delta\varphi)$. And the tuning range reaches the largest at $\delta\varphi = \pi$;(II) Although the isolation would be affected by varying $\delta\varphi$, the range of contrast still can be tuned from -1 to 1 at a very large domain of dephasing by tuning the intensity of acoustic wave;(III) Different lengths of L_1 also influence the value of contrast. While the length of L_1 becomes shorter enough, the tuning range shrink on the both sides of dephasing axis. And it makes sense that the shrinkage only exists in the backward isolation. In the backward case, the impact of defect couldn't restore the original FW power efficiently with short L_1. Anyway, the tuning range is from -1 to 1 at the vast majority of $\delta\varphi$s. While the length of L_1 becomes longer (always < 1/2 L), the tuning effect appears better. However, when L_1 is very close to the value of 1/2 L, the tuning range also shrinks, because the spatial nonreciprocity is not obvious any longer;(IV) In Fig. 3, we turn down the input power to one quarter of that in Fig. 2, and the tuning range of isolation contrast is still nearly from -1 to 1. A word, the influences brought by the value and location of $\delta\varphi$, power of incident FW and the intensity of acoustic wave were studied. We found that the affection induced by the first two could be completely covered by the last, which makes our device more tolerant and easy to implement. Moreover, by tuning the intensity of acoustic wave, even the orientation of the optical diode's unidirection could be changed. Finally, another PPLN can be integrated into the device to generate the acoustic wave; it is very compact and has great potential in photonic integrated circuits (PIC)

In summary, we proposed a bidirectional tunable optical diode in an asymmetric PPLN waveguide through cascading SHG and AO interaction. The optical isolation contrast could be tuned from -1 to 1 by adjusting the intensity of an induced acoustic wave. The influence of dephasing, location of defect, input power and the intensity of acoustic wave were discussed.

[1] K. Gallo, and G. Assanto, "Analysis of lithium niobate all-optical wavelength shifters for the third spectral window," J. Opt. Soc. Am. B **16**, 741-753, 1999.